CERN Yellow Reports: Monographs CERN-2020-002

SPS Beam Dump Facility

Comprehensive Design Study

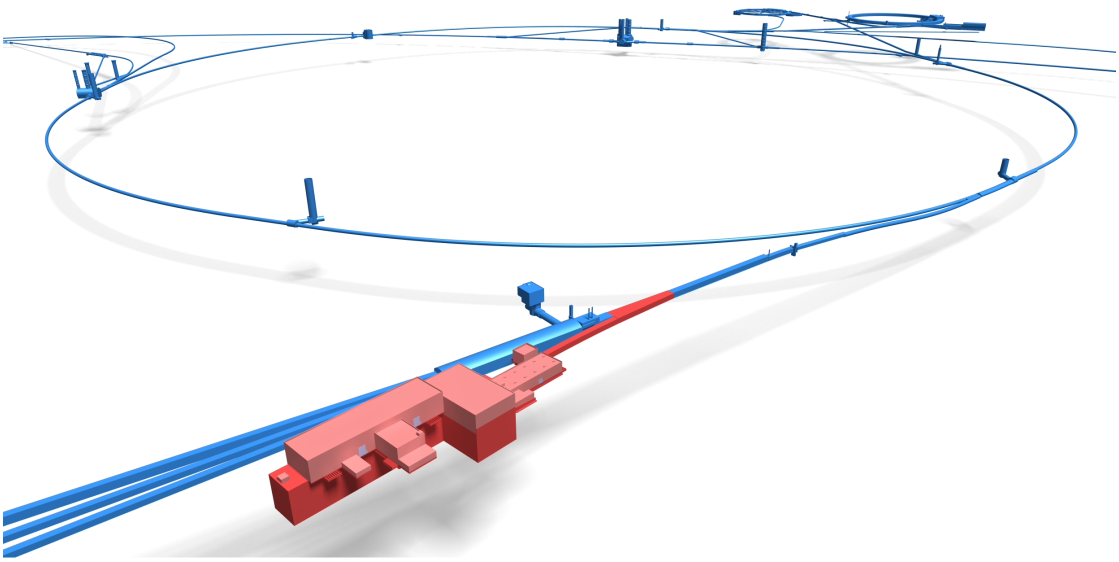

CERN Yellow Reports: Monographs
Published by CERN, CH-1211 Geneva 23, Switzerland

ISBN 978-92-9083-558-5 (paperback)
ISBN 978-92-9083-557-8 (PDF)
ISSN 2519-8068 (Print)
ISSN 2519-8076 (Online)
DOI https://doi.org/10.23731/CYRM-2020-002

Accepted for publication by the CERN Report Editorial Board (CREB) on 19 March 2020

This volume is indexed in: CERN Document Server (CDS) and INSPIRE.

This volume should be cited as:

SPS Beam Dump Facility : Comprehensive Design Study,
M. Calviani, B. Goddard, R. Jacobsson and M. Lamont (eds.),
CERN Yellow Reports: Monographs, CERN-2020-002 (CERN, Geneva, 2020)
https://doi.org/10.23731/CYRM-2020-002.

Abstract

The proposed Beam Dump Facility (BDF) is foreseen to be located in the North Area of the Super Proton Synchrotron (SPS). It is designed to be able to serve both beam-dump-like and fixed-target experiments. The SPS and the new facility would offer unique possibilities to enter a new era of exploration at the intensity frontier. Possible options include searches for very weakly interacting particles predicted by Hidden Sector models, and flavour physics measurements. Following the first evaluation of the BDF in 2014–2016, CERN management launched a Comprehensive Design Study over three years for the BDF. The BDF study team has executed an in-depth feasibility study of proton delivery to target, the target complex, and the underground experimental area, including prototyping of key subsystems and evaluations of radiological aspects and safety. A first iteration of detailed integration and civil engineering studies has been performed to produce a realistic schedule and cost. This document gives a detailed overview of the proposed facility together with the results of the in-depth studies, and draws up a road map and project plan for a three years Technical Design Report phase and a five–six years construction phase.

Authors

C.C. Ahdida[1], G. Arduini[1], A. Arnalich[1], P. Avigni[1], F. Bardou[1], M. Battistin[1], J. Bauche[1], L. Bianchi[1], M. Brugger[1], J. Busom Descarrega[1], M. Calviani[1*], J. Canhoto Espadanal[1], M. Casolino[1], N. Colonna[2], L. Dougherty[1], Y. Dutheil[1], E. Fornasiere[1], R. Franqueira Ximenes[1], M.A. Fraser[1], R. Garcia Alia[1], L. Gatignon[1], J. Gall[1], S. Gilardoni[1], B. Goddard[1*], J-L. Grenard[1], D. Grenier[1], M. Guinchard[1], C. Hessler[1], R. Jacobsson[1*], V. Kain[1], K. Kershaw[1], E. Koukovini Platia[1], M. Lamont[1*], E. Lopez Sola[1], S. Marsh[1], J.M. Martin Ruiz[1], R. Morton[1], Y. Muttoni[1], P. Ninin[1], J.A. Osborne[1], A. Perillo Marcone[1], J. Prieto Prieto[1], B. Riffaud[1], F. Sanchez Galan[1], P. Santos Diaz[1], S. Schadegg[1], S. Sgobba[1], L. Stoel[1], C. Torregrosa Martin[1], Heinz Vincke[1], Helmut Vincke[1], F.M. Velotti[1], V. Vlachoudis[1], P. Vojtyla[1], T. Wijnands[1], O. Williams[1].

[1] *European Organization for Nuclear Research, CERN CH-1211 Geneva 23, Switzerland*

[2] *INFN-Bari, Italy*

[*] *Editors—corresponding editor Mike.Lamont@cern.ch*

Contents

Chapter 1

Introduction

1.1 Context and motivation

The proposed Beam Dump Facility is foreseen to be located in the North Area of the Super Proton Synchrotron (SPS). It is designed to be able to serve both beam-dump-like and fixed-target experiments. 'Beam dump' in this context implies a target which is aimed at provoking hard interactions of all of the incident protons and the containment of most of the associated cascade. In the first instance, the exploitation of the facility, in beam dump mode, is envisaged to be for the Search for Hidden Particles (SHiP) experiment [1, 2, 3].

Several recently proposed experiments [4, 5] highlight that operating the SPS in beam dump mode or in fixed-target mode would be an excellent way to go beyond the current SPS programme and enter a new era of physics studies at the intensity frontier. These studies would complement the exploration of the high-energy frontier at the Large Hadron Collider (LHC) after 2026. Papers have been submitted [6, 7, 8] to demonstrate the unique potential of such a facility in searches for particles predicted by Hidden Sector models and in flavour physics measurements.

The multiuser design and full exploitation of the SPS accelerator with its present performance could allow the delivery of an annual yield of up to 4×10^{19} protons on target with a beam momentum of 400 GeV/c while respecting the beam requirements of the HL-LHC, and while maintaining the operation of the existing SPS beam facilities. Currently, CERN has no experimental facility which is compatible with this beam power. The consolidation and upgrades of the CERN injector complex and the continued operation of the SPS, with the unique combination of the high-intensity proton beam and slow beam extraction, motivate the construction of a new high-intensity experimental facility which is capable of fully exploiting its capacity in parallel with the operation of the HL-LHC. CERN's North Area has a large area next to the SPS beam transfer lines which is for the most part free of structures and underground galleries, and which could accommodate the proposed facility. In addition, the facility may be designed with future extensions in mind. On a longer time-scale, the possible future large-scale programmes at CERN could also pave the way for upgrading the facility to take advantage of new or upgraded injectors.

Following the first evaluation of the Beam Dump Facility (BDF) in 2014–2016, submitted together with the SHiP Technical Proposal and Physics Case, the CERN management launched a Comprehensive Design Study over 3 yr for SHiP and the BDF. The BDF study team has executed an in-depth feasibility study of proton delivery to target, the target complex, and the underground experimental area, including prototyping of key subsystems and evaluations of the radiological aspects and safety. A first iteration of detailed integration and civil engineering studies has been performed to produce a realistic schedule and cost. Complementing the SHiP physics and detector studies, the following document gives a detailed overview of the proposed facility together with the results of the in-depth studies, and draws up a road map and project plan for a 3 yr Technical Design Report phase and a 5–6 yr construction phase. The document shows that the feasibility has been proven, that the technologies and techniques, although challenging, appear to be within CERN's established competencies, and that the project, given the resources, is ready to move towards the detailed design and execution phase.

1.2 Objectives

The lack of firm hints as to the mass scale of new particles calls for a concerted effort by direct searches and precision measurements. At the same time, the absence of new particles is not necessarily due to their high scale of masses but could equally be due to their weak scale of couplings with the Standard

Model particles. This motivates investing in an ambitious complementary programme to investigate the possibility of a light Hidden Sector coupled to the Standard Model.

Beam dump experiments are potentially superior to collider experiments in sensitivity to GeV-scale hidden particles, given potential luminosities several orders of magnitude larger than those at colliders. The large forward boost for light states gives good acceptance despite the smaller angular coverage and allows efficient use of filters against background between the target and the detector, making the beam dump configuration ideal for searching for new particles with long lifetimes.

The detailed specification of the BDF is, in the first instance, mainly driven by the requirements of the SHiP experiment. SHiP has been optimized to search for light long-lived particles produced in decays of charm and beauty hadrons and radiative processes, and consists of two complementary apparatuses which are sensitive to both the decay of hidden particles and the scattering signatures of light dark matter. The combination of the intensity and the energy of the SPS proton beam allows the production of a very large yield of the processes potentially capable of giving rise to the different Hidden Sector particles. During 5 yr of operation with 4×10^{19} protons on a high-density target per year, it is expected to produce $\mathcal{O}(10^{18})$ charmed hadrons and more than 10^{21} photons above 100 MeV. In addition, it has been found that the 400 GeV/c proton beam at the SPS provides a good compromise between a large yield of heavy hadrons and photons, and a manageable background. Furthermore, the unique feature of slow extraction of a debunched beam on a time-scale of around a second allows tight control of combinatorial background.

The new Beam Dump Facility would also allow the performance of unprecedented measurements with tau neutrinos. Five years of operation on the BDF target at 400 GeV/c would yield $\mathcal{O}(10^{16})$ tau and antitau neutrinos. The first direct observation of the antitau neutrino and the measurement of tau neutrino and antitau neutrino cross-sections are among the goals of the SHiP experiment. As charm hadron decays are also a source of electron and muon neutrinos, it will also be possible to study neutrino-induced charm production from all flavours with a dataset which is more than one order of magnitude larger than those collected by previous experiments, performed solely with muon neutrino interactions.

The BDF beam line offers a potential opportunity to host and operate in parallel an experiment [7] to search for lepton flavour violation and rare decays with the very large production of tau leptons and D mesons. Intercepting about 2% of the intensity delivered to SHiP with a thin target, the experiment would have access to about 8×10^{13} tau leptons and 10^{16} D^0 and $\mathrm{D_s}$ meson decays.

In the medium term, extensions of the long-lived particle search programme at the BDF could be possible with a large-volume light dark matter and neutrino-scattering detector located downstream of the SHiP detector. Assuming the same angular acceptance and a liquid argon target, the mass equivalent to the current proposal with a 10 tonne scattering target of lead at 30 m from the target would be a $\sim$450 tonne detector at 120 m.

In the longer term, beyond, say, 2035, depending on future large-scale projects at CERN after the HL-LHC, upgraded or new injectors could open up a new search region. Continued operation of the SPS leaves several options open for the BDF depending on the development of the physics landscape. Findings at SHiP could motivate continued operation with protons to further establish or measure properties of new particles, but also potentially operation with electrons. An upgrade of the SPS to a superconducting machine at 0.9–1.3 TeV, in conjunction with an upgrade of the slow extraction and the transfer lines, could open a new mass window in the searches for weakly coupled particles. Alternatively, with a reconfigured target system, the facility could also host a kaon physics experiment in the future, such as the proposed experiment KLEVER [8], which aims at making a measurement of the branching ratio for the $\mathrm{K_L} \to \pi^0 \nu \overline{\nu}$ decay.

1.3 Interested community

The physics community's interest in Hidden Sector physics has grown rapidly in recent years, with an important increase in the activity of operational experiments, in the domain of both direct and indirect searches, as well as new proposals for experiments. SHiP formed an official collaboration with 45 institutes shortly after the submission of an Expression of Interest [1] in 2013 as part of the recommendation from the CERN management to prepare a Technical Proposal. Today the collaboration consists of 50 institutes and four associated institutes from 18 countries, CERN, and JINR. Several institutes in already associated and new countries are showing interest, and the collaboration is expected to grow significantly upon approval to proceed with technical design reports. Co-operation has already been established with the NA62 and LHCb collaborations, both on physics and on detector development, and in particular on the LHCb detector upgrade programmes. It is expected that this synergy will increase further. The proposed light dark matter/neutrino-scattering detector is also expected to stimulate further interest in the light dark matter search community and could lead to extensions of the current concepts.

Other potential users of the BDF include the TauFV and KLEVER proposals, both of which are in the domain of flavour physics. A dedicated TauFV study group has been active since the end of 2017, and the proposal, as developed so far, is presented in Appendix C of this document. The flavour physics community is large and worldwide. Violation of lepton universality has received particular interest from the community in Europe, the US, and Japan for several decades and has attracted even more interest in recent years. The TauFV proposal is complementary to LHCb and BELLE-II [9] in this respect. It is expected that the proposal will rapidly stimulate interest and attract collaborators. The project is technologically very challenging, requiring detectors with performances similar to those of the HL-LHC and FCC [10] detectors. A collaboration to draw up a plan for detector R&D is already under way. The KLEVER experiment draws on experience from NA62 and is expected to receive strong support from the kaon physics community. Its potential realization at ECN3 in the SPS North Area is also under consideration.

The development required for the target/dump design and construction and for the target complex technologies could have important implications for facilities worldwide. Collaboration is currently being explored and could be expanded upon project approval in order to optimize resources and costs, and to increase the impact of any technological breakthroughs.

The target/dump assembly is based on diffusion bonding via the hot isostatic pressing technique, employing refractory metals such as pure tungsten, molybdenum alloys, tantalum, and tantalum alloys. New developments such as the Second Target Station at the Oak Ridge National Laboratories Spallation Neutron Source [11] might benefit from such R&D and experience. Similarly, upgrade projects at the UK-based ISIS spallation neutron source might benefit from the technologies developed for the CERN Beam Dump Facility. Development of W-based technologies and radiation damage studies would create natural links with the European Spallation Source currently under construction.

The target complex, operating with a system that includes a purification technology for the helium vessel loop, currently under design, might be very beneficial for the upgrade of the T2K J-PARC neutrino beam line, both in the framework of the current operation and for the Tokai to Hyper-Kamiokande (T2HK) project [12] at present under consideration. Similar interest and collaborative opportunities exist in the framework of the LBNF/DUNE [13] neutrino project in the US. The radiation levels close to the production target would be extremely useful for irradiation purposes in the framework of the RaDIATE Collaboration [14] and would open up unprecedented equipment- and material-testing possibilities for CERN related to the Radiation to Electronics (R2E) project.

1.4 Overview of the Beam Dump Facility

The BDF relies on slow extraction of protons from the SPS, from an upgraded extraction channel in Long Straight Section 2 (LSS2). After about 600 m of the present TT20 transfer line, a new splitter/switch magnet system, which will maintain compatibility with the existing North Area (NA) operation, will deflect the beam into a dedicated new transfer line. The new line will be connected by a modified junction cavern to the existing tunnel. The beam is dumped on a high-power target housed in a purpose-built, heavily shielded target complex. Beyond the target complex, a muon shield is followed by an experimental hall. The scope of the facility studies includes these elements plus the associated civil engineering and service infrastructure. The proposed location and overall layout of the facility are shown in Fig. 1.1. A description of the key features of the new facility and a brief overview of the progress made by the study on the technical aspects follows.

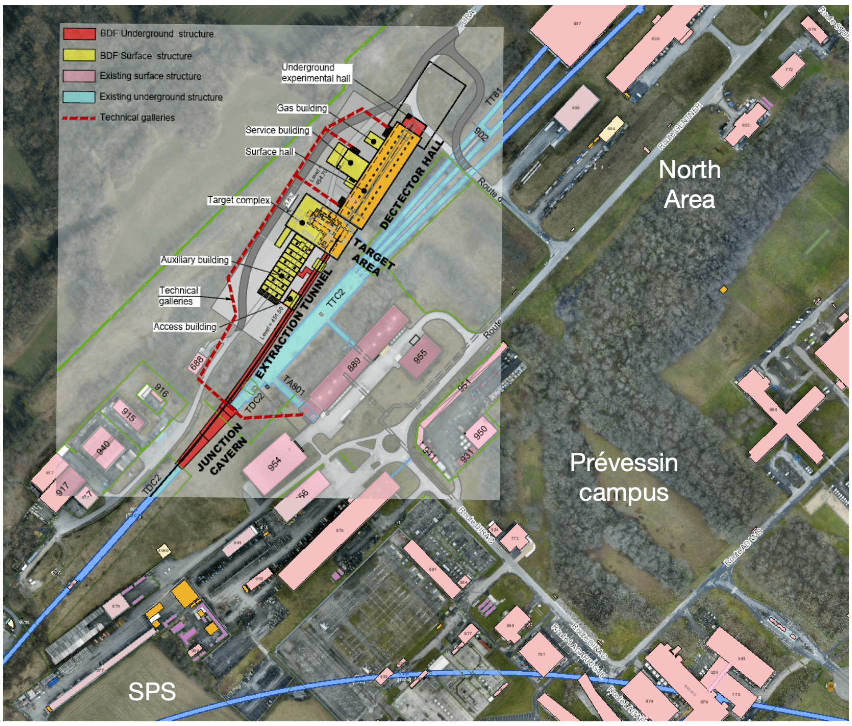

Fig. 1.1: Overview of the proposed implementation of the BDF in the SPS North Area at the CERN Prévessin campus.

1.4.1 Extraction from SPS

Third-integer slow extraction of 400 GeV/c protons from the SPS is well established. Beam losses of a few per cent on the septum wires are intrinsic to the process and result in machine activation, reduce component lifetime, and place severe limitations on personnel access and maintenance. Significant operational effort already goes into minimizing these losses and ensuring a high-quality, uniform spill. The proton intensity on target (PoT) requested by SHiP poses significant challenges [15], and improvements will need to come from a combination of lower beam loss per extracted proton, reduced activation per lost proton, and improved or remote interventions. The most effective solution is to reduce the beam loss per extracted proton, since this also reduces the radiation dose to cables and high-voltage feedthroughs. A factor of four reduction is needed.

Methods to reduce the losses concerning the extraction process, hardware, and controls were developed and tested in 2018, both with a SHiP cycle and with the longer NA cycle.

The Q-sweep method used for slow extraction in the SPS since its construction has been replaced by a new method, Constant-Optics Slow Extraction (COSE), where the optics are kept constant in normalized strength while the whole machine momentum is ramped. COSE has several advantages over the Q-sweep method, since it keeps the orbit and separatrix angle at the electrostatic septum (also referred to as the ZS) fixed through the spill. Since mid 2018, COSE has been systematically deployed in NA operation.

For loss reduction, both passive scatterers and bent silicon crystals have been developed and tested as diffusers to locally reduce the proton density at the ZS wires. For a passive diffuser [16], a 240 μm wide, 30 mm long array of Ta wires achieved a loss reduction of 15%, consistent with an effective ZS width of 500–600 μm. For a bent silicon crystal [17], a 780 μm wide and 2.5 mm long crystal with a large channelling angle of 150 μrad gave a loss reduction of slightly over 40%, again consistent with a ZS width of around 500 μm. Both diffuser types were tested for 12 h periods with the full beam intensity of 3×10^{13} protons per spill, and demonstrated that the ZS shadowing was stable and reproducible.

A separate technique of loss reduction by separatrix folding [18] was also tested successfully. The extraction sextupoles which govern the speed of diffusion across the ZS wires were increased in strength to reduce the particle density and losses, while octupole fields slowed the diffusion speed at higher amplitude to avoid increased losses on the ZS cathodes. In beam tests, this method also reduced the losses by slightly over 40%. Importantly, the method was successfully tested in combination with crystal ZS shadowing. The combination of the two methods gave a loss reduction of slightly more than a factor of three.

The alignment of the five ZS anodes is a crucial factor in the overall beam loss, since it determines both the absolute beam loss and the potential gain from the shadowing methods. The control of the alignment was improved to a resolution of below 50 μm, while numerical optimizers were simulated and deployed to align the five anodes with the extracted beam. The alignment time (with nine degrees of freedom) was reduced from 8 h to 40 min.

1.4.2 Transfer lines, switching, and dilution

The location of the BDF target complex allows the re-use of about 600 m of the present transfer line TT20, which is already operated with slowly extracted beam at 400 GeV/c. After the upgraded switch/splitter element, a new 380 m long section of beam line (TT90) is required to deliver the beam to the target.

The powering scheme for the TT20 transfer line will remain largely unchanged. The design of TT90 uses 23 standard bending magnets with a field of up to 1.9 T in a FODO structure to ensure adequate separation between the new and existing beam lines, and to minimize the longitudinal extent of the civil engineering works in the new junction region. Six standard focusing quadrupole magnets provide flexibility and tunability of the beam spot size and dispersion at the proton target. The line optics have been finalized with the completion of trajectory correction and aperture studies, and the feasibility of the parameters at the target has been demonstrated with the use of existing magnet designs.

The transfer line design replaces the three existing splitter magnets by laminated versions with dual functionality: either splitting the beam destined for the NA targets as today, or deflecting the entire beam into TT90 for transport to the BDF target. For the BDF beam sent to TT90, the entire beam will be steered through the switch/splitter aperture without losses. This solution maintains full compatibility with the present NA operation.

The present splitter magnet is an in-vacuum Lambertson septum with a yoke machined from solid iron, with the coil based on a water-cooled lead made of copper with insulation made of compacted MgO powder. For the new magnets, a laminated yoke is required to perform the polarity switch between SPS cycles in about 2 s.

A magnetic and mechanical design has been done and the magnet performance simulated, complicated by the details of the possible mechanical errors and their effect on the beam losses. Prototyping of the laminated yoke design is under way to evaluate the feasibility of the very tight mechanical tolerances required to maintain low beam losses. MgO coils will provide the required radiation resistance. Procurement of parts for the construction of a short magnet prototype will start in early 2019.

The beam dilution sweep will be implemented with two sets of two orthogonal kicker magnets with Lissajous powering functions to produce a circular sweep at 4 Hz. With a free drift length for the beam of about 120 m and a bending angle of 0.5 mrad per plane, the sweep radius will be 50 mm. Since the survival of the proton target relies critically on the beam dilution, the SPS beam will be interlocked with the beam dilution system and the instantaneous loss rate at the target. New concepts for interlocking of the slow extraction have been developed.

A straightforward reconfiguration of the existing beam elements in the BDF extraction channel would allow the accommodation of the drift space required to implement the in-line target and experimental zone for the tau lepton flavour experiment.

1.4.3 Production target/dump

The BDF/SHiP target can be considered as a beam dump, as it has to safely absorb the full 400 GeV/c SPS primary beam every 7.2 s. The target is required to maximize the production of charm and beauty hadrons and to maximize the re-absorption of pions and kaons, which implies a high-Z material with a short nuclear interaction length, in contrast to a neutrino-producing target. The high deposited power is the most challenging aspect, with up to 355 kW average power deposited in the target and 2.56 MW over the 1 s spill. To produce sufficient dilution of the energy density in the target, the slow extraction needs to be combined with a beam spot of at least 8 mm root mean square in both planes and a 300 mm long sweep of the beam over the target surface.

Detailed energy deposition and thermomechanical design studies have been performed. The required performance may be achieved with a longitudinally segmented hybrid target consisting of blocks of four nuclear interaction lengths (58 cm) of a titanium–zirconium-doped molybdenum alloy (TZM, density 10.22 g/cm^3) in the core of the proton shower followed by six nuclear interaction lengths (58 cm) of pure tungsten (density 19.3 g/cm^3).

A medium-density material is required in the first half of the target to reduce the energy density and resulting thermally induced stresses. The thickness of each block and the location of each cooling slot have been optimized to provide uniform energy deposition and sufficient energy extraction. The blocks are interleaved with 5 mm wide slots for water cooling. Tantalum alloy cladding of the TZM and tungsten blocks, by means of diffusion bonding via hot isostatic pressing, will prevent corrosion and erosion of the core material by the high water flow rate. The design limits the peak power density in the target to below 850 J/cm^3/spill and compressive stresses to below 130 MPa.

The target blocks will be assembled in a double-walled helium vessel. The inner vessel will enforce a high-flow 35 m^3/h water circulation between the proton target blocks at 20 bar to avoid boiling of the water. The outer vessel acts as a safety hull to contain hypothetical leaks, and is filled with He gas to prevent corrosion.

A prototype target built to the BDF/SHiP design was installed and tested with beam in the North Area target area (TCC2) in 2018. Lower-intensity 1 s spills of 4×10^{12} protons without dilution sweep were used to achieve stress levels comparable to those in the final target. The prototype was successfully operated with beam for over 14 h, accumulating 2.4×10^{16} PoT. Online measurements of strain and temperature on instrumented target blocks showed very good agreement with simulations. In 2019, the target blocks will be disassembled and analysed in a dedicated facility to quantify the behaviour of the target material under irradiation conditions.

1.4.4 Target complex

The target will be subject to severe radiological constraints, and will be located in a shielded bunker around 15 m below ground level. Remote handling for manipulation of the target and surrounding shielding will be mandatory owing to the high residual dose rates expected after operation. The target complex has been designed to house the target and its shielding in a helium vessel, along with cooling, ventilation, and helium purification services below ground level. The SPS beam will enter the surrounding helium vessel through a removable beam window, and then pass through a collimator which serves to protect the target and adjacent equipment from misalignment of the incident SPS beam and to protect the equipment in the extraction tunnel from particles (essentially neutrons generated by the target) travelling backwards relative to the incident beam.

The target will be surrounded by approximately 3700 t of cast iron and steel shielding (part of it water-cooled to dissipate the deposited power) with outer dimensions of around $6.8 \times 7.9 \times 11.2$ m^3 (the so-called bunker/hadron absorber) to reduce the prompt dose rate during operation and the residual dose rate around the target during shutdown. The target and its surrounding shielding will be housed in a vessel containing gaseous helium slightly above atmospheric pressure to reduce air activation and reduce the radiation-accelerated corrosion of the target and surrounding equipment. The design allows for removal and temporary storage of the target and shielding blocks in the cool-down area below ground level and includes dedicated shielded pits for storage of the highest-dose-rate equipment.

In 2018, the target complex design was developed in detail, with full definition of the handling and remote handling operations required throughout the life of the facility. This work demonstrated the feasibility of the construction, operation, and maintenance of the BDF target complex, along with decommissioning of the key elements. The remote handling of highly activated radioactive objects, such as the target, beam window, collimator, shielding blocks, and magnetic coil, along with their connection and disconnection within the target complex building, was studied in detail, including foreseen remote handling operations such as target exchange as well as unforeseen operations needed to recover from failures or damage to equipment.

The study included the conceptual design of lifting, handling, and remote handling equipment for the highly activated objects along with the necessary water, helium, and electrical connections compatible with the radiation environment and remote handling constraints. These have been integrated into the overall target complex design [19].

1.4.5 Muon shield

The total flux of muons emerging from the proton target with a momentum larger than 1 GeV/c amounts to $\mathcal{O}(10^{11})$ muons per spill of 4×10^{13} protons. To control the background from random combinations of muons producing fake decay vertices in the detector decay volume and from muon deep inelastic scattering producing long-lived neutral particles in the surrounding material, and to respect the occupancy limits of the subdetectors, the muon flux in the detector acceptance must be reduced by at least six orders of magnitude over the shortest possible distance. To this end, a muon shield based entirely on magnetic deflection has been developed [20]. The first section of the muon shield starts within the target complex shielding assembly, 1 m downstream of the target, with a magnetic coil which magnetizes the hadron stopper, made of US1010 steel, with a field of 1.6 T over 4.5 m. The rest of the muon shield consists of six free-standing magnets, each 5 m long, located in the upstream part of the experimental hall.

1.4.6 Experimental area

The BDF is designed to house a multipurpose, large-scale experimental programme using a single beam line and a single main target station. The initial design of the experimental area (Fig. 1.2) has been dictated to a large extent by the requirements of the SHiP experiment. All phases of the experiment, including assembly, construction, and installation, as well as operation, have been taken into consideration. The complex consists of a 120 m long underground experimental hall, centred on the beam axis. To reduce background from particle scattering in the walls, the underground hall is 20 m wide along its entire length. A 100×26 m^2 surface hall is located on top of the underground hall. The installation plan foresees pre-assembly in the surface hall in three principal work zones with the help of a 40 tonne and a 10 tonne crane, in parallel with final assembly in the underground hall using a dual 40 tonne hoist crane and a single 40 tonne hoist crane. Three 14.5×18 m^2 access openings between the surface hall and the underground hall provide direct access to the principal detector installation areas. For shielding purposes, each opening will be covered by 18 concrete beams during operation. A 20×34 m^2 three-storey service building, adjacent to the service hall, houses all services related to the infrastructure and the detector, control room, workshop, labs, and offices.

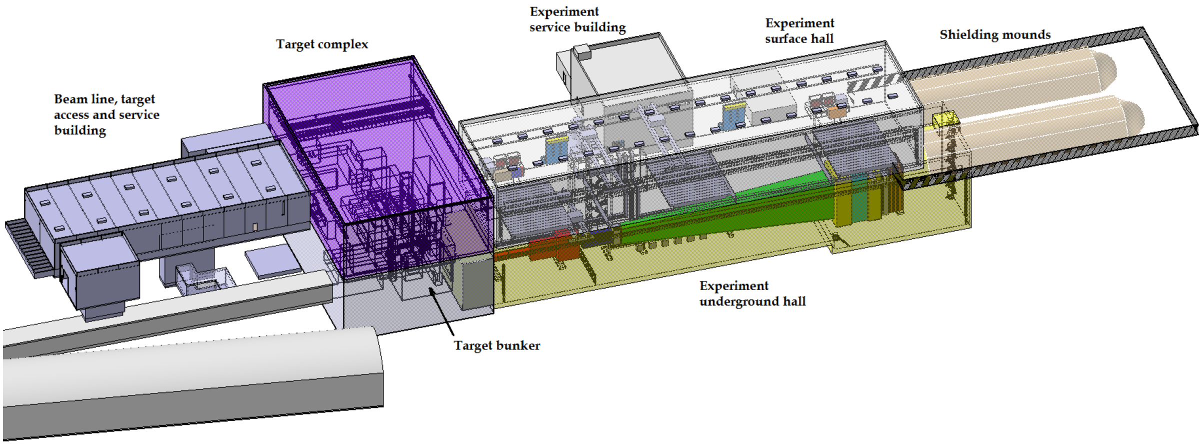

Fig. 1.2: Overview of the target complex and experimental area

1.4.7 Summary

The above outline presents a succinct overview of the proposed facility. Since the inception of the BDF feasibility study in 2016, the BDF team has attempted to address all pertinent technological challenges, along with a detailed look at the deployment of such a facility on the proposed site.

By end 2018, in-depth studies and prototyping had been performed or were already well under way for all critical components. Through a mixture of novel hardware development, beam physics, and technology, the study and prototype validations have shown that the SPS can deliver a beam with the required characteristics and with acceptable losses, to a robust target housed in a suitable target complex. The detailed results of these studies are presented in the following chapters.

With the delivery of this report, and the corresponding document from the SHiP Collaboration, it may be argued that the BDF and SHiP are mature proposals, and are ready, with appropriate approval, to move into the Technical Design Report phase.

References

[1] W. Bonivento et al. *Proposal to Search for Heavy Neutral Leptons at the SPS*. Oct. 2013. arXiv: 1310.1762 [hep-ex].

[2] SHiP Collaboration. *A Facility to Search for Hidden Particles (SHiP) at the CERN SPS*. Technical Proposal. Geneva: CERN, Apr. 2015. arXiv: 1504.04956. URL: https://cds.cern.ch/record/2007512.

[3] S. Alekhin et al. "A facility to search for hidden particles at the CERN SPS: the SHiP physics case". In: *Rep. Prog. Phys.* 79.12, 124201 (Dec. 2016). DOI: 10.1088/0034-4885/79/12/124201. arXiv: 1504.04855 [hep-ph].

[4] R. Alemany et al. *Summary Report of Physics beyond Colliders at CERN*. Feb. 2019. arXiv: 1902.00260 [hep-ex].

[5] J. Beacham et al. *Physics Beyond Colliders at CERN: Beyond the Standard Model Working Group Report*. Jan. 2019. arXiv: 1901.09966 [hep-ex].

[6] SHiP Collaboration. "The SHiP experiment at the SPS Beam Dump Facility". Submitted to European Particle Physics Strategy Update 2018–2020.

[7] I. Bezshyiko et al. "TauFV: a fixed-target experiment to search for flavour violation in tau decays". Submitted to European Particle Physics Strategy Update 2018–2020.

[8] M. Moulson. "KLEVER: an experiment to measure BR($K_L \to \pi^0\nu\bar{\nu}$) at the CERN SPS". In: *39th International Conference on High Energy Physics (ICHEP 2018) Seoul, Korea, July 4–11, 2018*. 2018. arXiv: 1812.01896 [physics.ins-det].

[9] T. Abe et al. *Belle II Technical Design Report*. Nov. 2010. arXiv: 1011.0352 [physics.ins-det].

[10] M. Benedikt et al. *Future Circular Collider*. Tech. rep. CERN-ACC-2018-0057. Submitted for publication to *Eur. Phys. J. Spec. Top.* Geneva: CERN, Dec. 2018.

[11] R. L. Kustom. "An overview of the Spallation Neutron Source project". In: *eConf* C000821 (2000), TU101. arXiv: physics/0008212 [physics.acc-ph].

[12] T. Ishida. "T2HK: J-PARC upgrade plan for future and beyond T2K". In: *15th International Workshop on Neutrino Factories, Super Beams and Beta Beams (NuFact2013) Beijing, China, August 19–24, 2013*. 2013. arXiv: 1311.5287 [hep-ex].

[13] R. Acciarri et al. *Long-Baseline Neutrino Facility (LBNF) and Deep Underground Neutrino Experiment (DUNE) Conceptual Design Report Volume 1: The LBNF and DUNE Projects*. Jan. 2016. arXiv: 1601.05471 [physics.ins-det].

[14] K. Ammigan and P. Hurh. "Status and update of the RaDIATE Collaboration R&D program". In: *13th International Topical Meeting on Nuclear Applications of Accelerators (AccApp '17), Quebec City, Quebec, Canada, July 31–August 4, 2017*. 2017. arXiv: 1803.08563 [physics.acc-ph]. URL: http://lss.fnal.gov/archive/2017/conf/fermilab-conf-17-563-ad.pdf.

[15] M. A. Fraser et al. "Slow extraction at the SPS: extraction efficiency and loss reduction studies". In: *Proceedings, Injector MD Days 2017: CERN, Geneva, Switzerland, March 23—24, 2017*. 2017, pp. 87–94. DOI: 10.23727/CERN-Proceedings-2017-002.87.

[16] B. Goddard et al. "The use of a passive scatterer for SPS slow extraction beam loss reduction". In: *Proceedings, 8th International Particle Accelerator Conference (IPAC 2017): Copenhagen, Denmark, May 14–19, 2017*. 2017, MOPIK044. DOI: 10.18429/JACoW-IPAC2017-MOPIK044.

[17] F. Velotti et al. "Reduction of resonant slow extraction losses with shadowing of septum wires by a bent crystal". In: *Proceedings, 8th International Particle Accelerator Conference (IPAC 2017): Copenhagen, Denmark, May 14–19, 2017*. 2017, MOPIK050. DOI: 10.18429/JACoW-IPAC2017-MOPIK050.

[18] L. Stoel et al. "Phase space folding studies for beam loss reduction during resonant slow extraction at the CERN SPS". In: *Proceedings, 8th International Particle Accelerator Conference (IPAC 2017): Copenhagen, Denmark, May 14–19, 2017*. 2017, MOPIK046. DOI: 10.18429/JACoW-IPAC2017-MOPIK046.

[19] K. Kershaw et al. "Design development for the Beam Dump Facility target complex at CERN". In: *J. Instrum.* 13.10, P10011 (2018). URL: https://doi.org/10.1088/1748-0221/13/10/P10011.

[20] SHiP Collaboration. "The active muon shield in the SHiP experiment". In: *J. Instrum.* 12.05, P05011 (2017). DOI: 10.1088/1748-0221/12/05/P05011. arXiv: 1703.03612 [physics.ins-det].

Chapter 2

Delivery of beam from the SPS

2.1 Introduction

The SPS serves several clients in sequence via a repetitive operational sequence (‘supercycle’) with a length of a few tens of seconds. Users may include the LHC, the Advanced Proton Driven Plasma Wakefield Acceleration Experiment (AWAKE), the High-Radiation to Materials (HiRadMat) facility, and the North Area. The NA receives a primary proton beam at 400 GeV/c, where the full SPS beam is slowly extracted over a flat top of typically several seconds. The recent maximum slowly extracted proton intensity was about 3.5×10^{13} protons over 4.8 s. This proton flux is transported and shared through two series of splitter magnets onto three primary targets, T2, T4, and T6, from which the NA secondary beam lines are served. The targets are housed in TCC2, the target hall of the SPS North Area. Important limitations on the intensities extracted to the NA are the losses inherent in slow extraction and in the splitting process. A schematic overview of the SPS and its associated facilities is shown in Fig. 2.1.

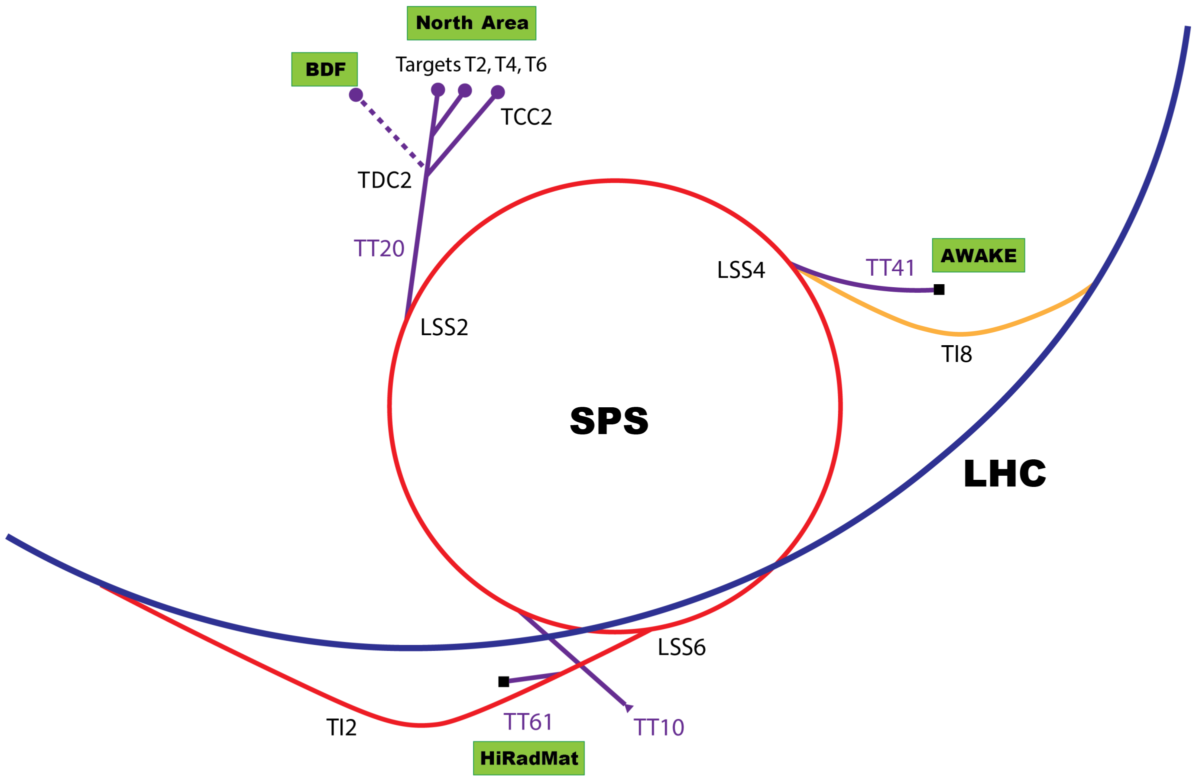

Fig. 2.1: Schematic layout of the SPS and its associated facilities. Abbreviations used extensively in this report are shown. These include LSS, Long Straight Section; TT20, the beam lines to the North Area targets; TCC2, the target hall of the SPS North Area; and TDC2, the tunnel/cavern before the target hall containing the splitters and downstream beam lines leading to TCC2.

The beam and SPS cycle parameters foreseen for SHiP [1] at BDF are shown in Table 2.1. Of note is the total beam intensity, the relatively short slow-extraction spill length, and the high beam power on target.

A detailed study of possible future proton sharing between potential SPS users was performed previously and was reported in Ref. [2]. This chapter summarizes a new study, taking into account

Table 2.1: Key SPS beam and cycle parameters foreseen for SHiP

Momentum	400 GeV/c
Beam intensity per cycle	4.2×10^{13}
Beam intensity on target	4.0×10^{13}
Cycle length	7.2 s
Spill duration	1.0 s
Average beam power on target	355 kW
Average beam power on target during spill	2560 kW
Protons on target (PoT)/yr	4.0×10^{19}
Total PoT in 5 yr data taking	2.0×10^{20}

operational experience from recent years in terms of machine time usage and SPS users, supercycle compositions, limitations arising from activation, and recent progress in loss reduction for the SPS slow extraction on the third-order resonance achieved in Machine Development (MD) studies. Furthermore, new considerations about the machine-interlocking strategy for the operation of the NA and the SHiP experiments are provided. Finally, future operational scenarios with varying spill lengths to the NA targets are discussed.

2.2 SPS intensity reach for slowly extracted beams

2.2.1 SPS intensity reach

The maximum beam intensities accelerated so far and extracted from the SPS (peak values) in the last 20 yr together with the peak operational parameters from the 2018 run are listed below (the durations quoted correspond to the cycle length):

- 4.8×10^{13} p/cycle (1997, slow and fast slow extraction, 9.6 s, 450 GeV/c);
- 4.5×10^{13} p/cycle (2008, CNGS, fast extraction, 6.0 s, 400 GeV/c);
- 4.0×10^{13} p/cycle (2009, slow extraction, 15.6 s, 400 GeV/c);
- 3.5×10^{13} p/cycle (2018, slow extraction, 10.8 s, 400 GeV/c).

The intensity reach for fixed-target beams from the SPS was studied in the past in preparation for the CERN accelerator complex serving the CERN Neutrinos to Gran Sasso (CNGS) facility [3]. The maximum intensity accelerated in the SPS during MD (but not extracted) was 5.3×10^{13} p/cycle (in 2004) [4]. The main intensity limitation for these beams was identified to come from losses in the Proton Synchrotron (PS) and the SPS. In particular, losses are encountered at PS-to-SPS transfer owing to the extraction process and in the SPS itself owing to losses at the vertical aperture and to Radio Frequency (RF) power limitations.

To mitigate the losses at PS extraction, the ‘Continuous Transfer’ (CT) [5] scheme, in which the beam was split by the extraction septum, was replaced by the ‘Multi-Turn Extraction’ (MTE) [6] scheme, in which the beam is split magnetically. This scheme has been used operationally since 2015 and has reduced activation levels in the PS significantly [7]. The maximum intensity used operationally with MTE has been about 3.5×10^{13} p/cycle in the SPS (during the 2018 run). A beam intensity of 4.0×10^{13} p/cycle could be accelerated in the SPS in a recent high-intensity test (in 2017) [8]. During this test, no particular issues were encountered related to the high beam intensity in combination with MTE.

The fact that the beam transmission in the SPS degrades with intensity is mostly related to an increase in the vertical emittance proportional to intensity (due to the beam production in the PSB) and to particles lost at the vertical aperture of the SPS. With the connection of Linac4 to the PSB during

Long Shutdown 2 (LS2) as part of the Large Hadron Collider (LHC) injector upgrade (LIU) project [9, 10], the vertical emittance of the fixed-target beam is expected to be reduced by up to a factor of two, which will improve transmission in the SPS. In addition, it should be mentioned that the SPS RF system will receive a major upgrade as part of the LIU project, and hence more RF power will become available after LS2. This could allow the intensity reach for fixed-target beams in the SPS to be further increased. A beam intensity of 4.2×10^{13} p/cycle can therefore be safely assumed as the future average intensity accelerated in the SPS with MTE deployed in the PS. A summary of the SPS intensity records is shown in Fig. 2.2.

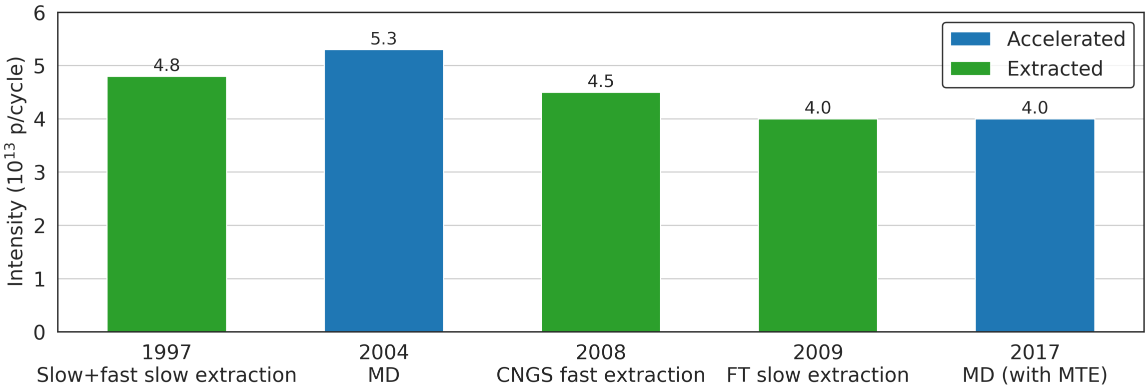

Fig. 2.2: Intensity per cycle achieved in the SPS

2.2.2 Limitations from slow extraction and splitting losses

An overview of the PoT delivered by the SPS in recent years to different experiments using resonant extraction schemes is shown in Fig. 2.3. For SHiP, the beam will be extracted on the third-integer resonance using the LSS2 extraction channel as for the NA beams.

Slow extraction using third-integer resonance and thin electrostatic septa (ES) is a process with inherent beam loss. For the 400 GeV protons required for the present NA operation, this beam loss already results in machine activation, reduced component lifetime, and severe limitations on personnel access and maintenance. With the request from SHiP for an additional 4.0×10^{19} PoT annually, the instantaneous and integrated loss levels become key limitations.

The activation and radiation doses in LSS2 and also at the splitters in TT20 are correlated with the total PoT and also with other less tangible aspects of the SPS operation and extraction channel set-up, such as the beam stability, the alignment of the extraction septa, any hardware faults, and the beam quality. There is therefore a significant scatter in the activation levels per proton, depending on the specific combination of conditions and also the level and quality of the follow-up both of the hardware and of the operation.

The residual dose after the end of proton operation has been measured over many years. Figure 2.4 shows the results for both LSS2 and LSS6. To keep the residual activation levels at around 5 mSv/h while extracting around 5.0×10^{19} PoT will require a reduction in the activation per proton by about a factor of four[12, 13, 14, 15] compared with the results obtained with around 1.0×10^{19} PoT annually.

The SHiP study has developed and tested methods to reduce the losses per proton at extraction by a factor of four. Since the beam for SHiP will pass through the gap of the splitter system in an essentially loss-free transport, this gain will mean that the present loss levels both in the extraction channel and in the splitter region can be maintained for the simultaneous delivery of 4.0×10^{19} to SHiP and 1.0×10^{19} to the NA (via lossy splitting). Studies will be launched in 2019 to investigate whether there are ways to reduce the losses per proton during the splitting process, but before these conclude, the present situation needs to be assumed.

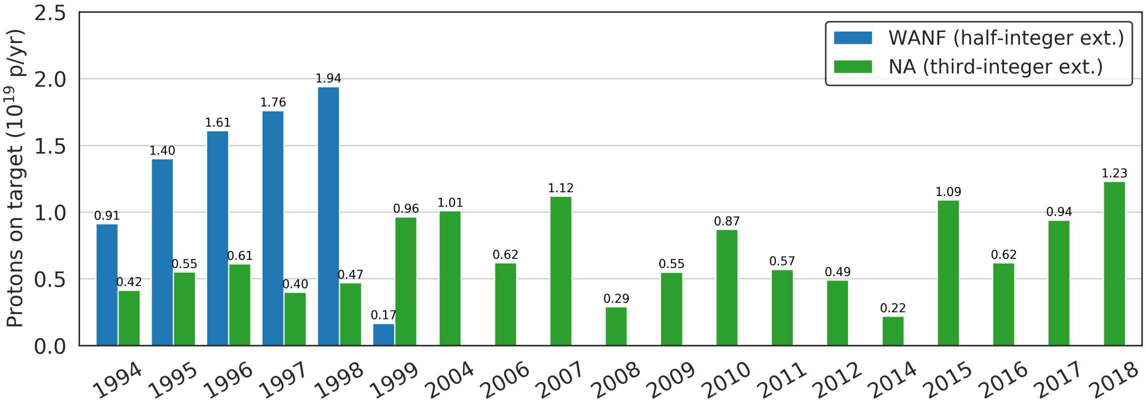

Fig. 2.3: Protons on target delivered by the SPS in recent years (there is no single infallible reference source for data, but the data have been cross-checked as best as possible with SPS operation logging data, SPS reports and minutes, radiation protection reports, etc.). Intensity data taken using secondary emission foils located in the NA transfer lines and in front of the targets might be affected by calibration uncertainties [11].

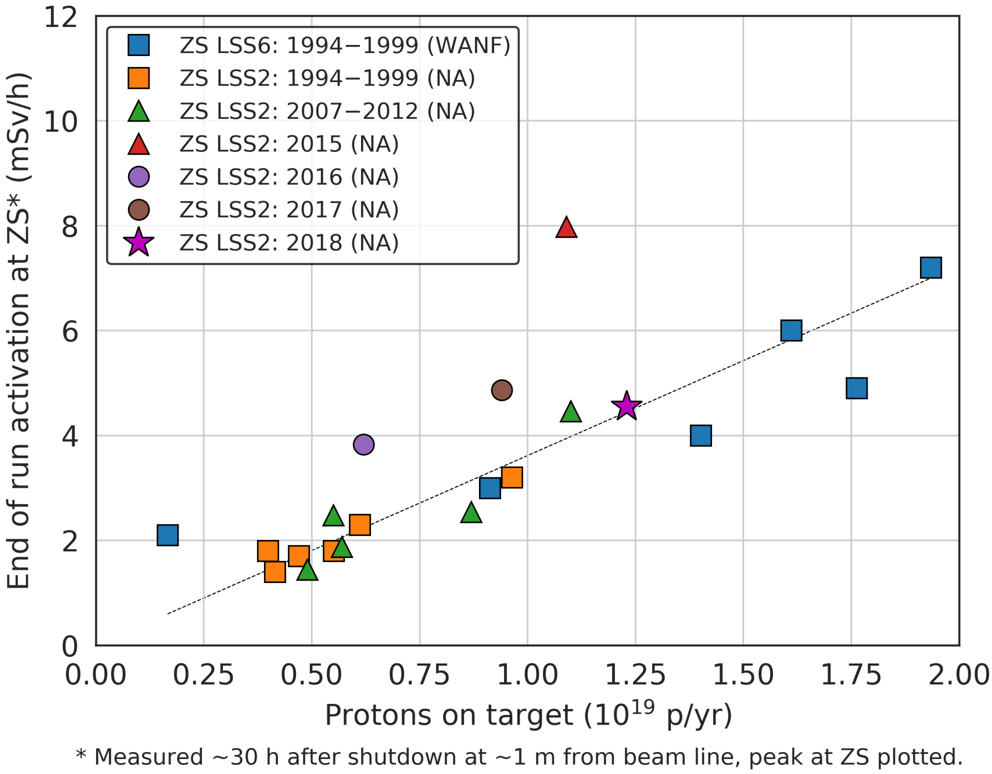

Fig. 2.4: Comparison of activation levels in the SPS extraction channels

The radiation dose to the cables and extraction equipment depends on the beam loss at extraction and the total number of protons extracted. If the factor of four loss reduction can be applied to both SHiP and NA extraction, then the limitation on the total number of protons extracted per year (to whatever target) will be 5.0×10^{19}. At these dose levels, a full recabling of the extraction channel region (control, high-voltage, and d.c. cables) will be required after about 8 yr of operation, or every other long shutdown.

The slowly extracted beam is distributed via a network of transfer lines in the NA and delivered simultaneously to multiple experimental targets by splitting the beam directly on steel Lambertson septa magnets [16]. This process, when combined with the extraction and transfer efficiency, introduces a transmission from ring to targets that is typically measured at approximately 70%. The splitting efficiency also depends on the splitting ratio and intensities demanded by each target. Because of systematic errors in the absolute calibration of the intensity monitors in the NA, this number is intrinsically uncertain and should be taken with caution. The limitations discussed above are plotted graphically in Fig. 2.5. It should be emphasized that, in this plot, the beam loss per proton in the LSS2 extraction channel of the SPS is assumed to be reduced by a factor of four compared with present operational values.

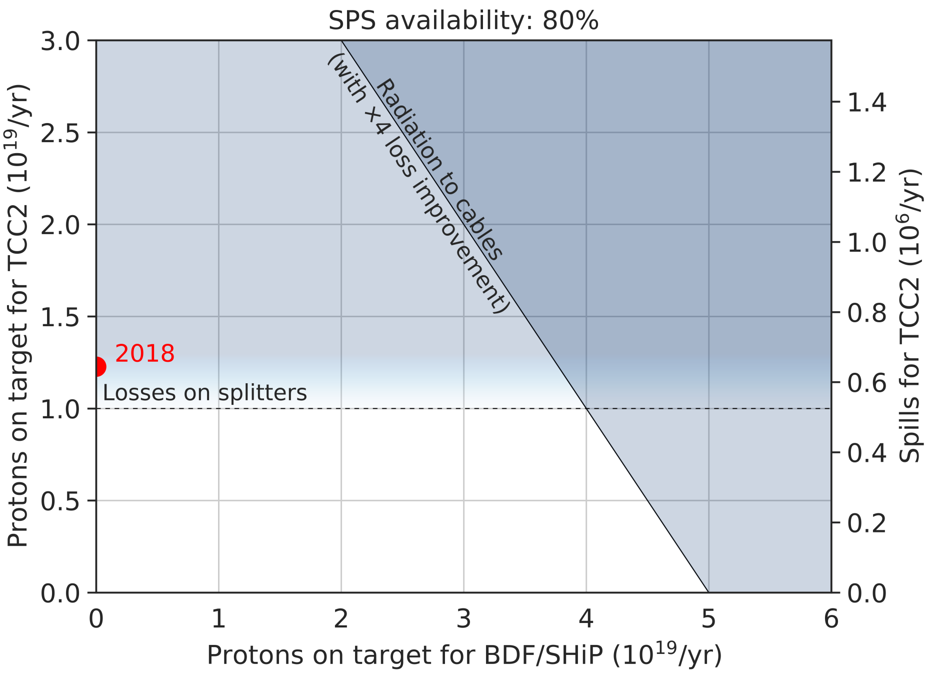

Fig. 2.5: Intensity limitations (shaded areas) from SPS slow extraction and operationally achieved protons on target in 2018. The secondary axis shows the number of spills.

2.2.3 Beam parameters considered for SHiP

Slow extraction on the third integer to TT20 on a time-scale of 1 s is retained as a baseline for the SHiP beam parameters, taking into account the following considerations:

- maximum acceptable instantaneous particle flux at the detector;
- calculations of the power and power density deposition on the target.

SHiP assumes a proton beam of 400 GeV/c. This beam momentum corresponds to the momentum of the proton beam extracted to the NA targets T2, T4, and T6 during proton fixed-target operation. In the past, it was assumed that one would define different extraction momenta for the beams circulating in the SPS according to their destination to allow proper interlocking. In the case of SHiP, the present machine-interlocking approach will not rely on different beam momenta. Instead, both the beam to the NA targets and the beam for the SHiP experiment will be extracted at 400 GeV/c. The programmed timing destination will be used to distinguish between beam to SHiP and beam to the NA targets in the extraction interlock system.

The minimum cycle length that is compatible with the above parameters is 7.2 s, provided that it can be proven that an extraction of 4.2×10^{13} p/cycle over 1 s can be performed without damaging the electrostatic septa or significantly increasing the spark rate. In the West Area Neutrino Facility (WANF) era in LSS6, intensities of 1.5×10^{13} p were extracted in a spill length of under 10 ms, twice per cycle. Although there were relatively frequent stops due to damage to the electrostatic septum, many improvements were made and these instantaneous rates are considered acceptable. During machine development studies in 2017 and 2018, up to 1.0×10^{13} p/cycle slowly extracted over 1 s was demonstrated on a SHiP cycle. Extracting higher intensities on such a cycle has not been attempted yet.

2.3 Proton sharing

2.3.1 SPS cycles and sharing of machine time in 2018

In its present configuration, the SPS delivers beam to the LHC, the NA, AWAKE, and HiRadMat. In addition, a rich programme of MD studies is being carried out to improve the machine performance and prepare for future beam requests. Table 2.2 shows a representative selection of cycles used during SPS operation in 2018.

Table 2.2: SPS cycles from 2018

	Length (s)	Power (MB+MQ) (MW)
AWAKE	7.2	31.23
BDF/SHiP	7.2	32.50
HiRadMat	22.8	16.83
LHC filling	22.8	16.83
LHC pilot	12.0	31.67
MD dedicated	22.8	16.83
MD parallel	7.2	2.98
Scrubbing	22.8	16.83
TCC2	10.8	52.79
Zero	1.2	0.10
Degauss	3.6	4.77

Note that in the 'zero' and 'degauss' cycles it is not possible to inject any beam. The latter cycle is typically placed in front of the fixed-target cycle (here called the 'TCC2' cycle) to achieve reproducible magnetic behaviour of the machine for optimizing transmission and slow-extraction conditions. The parallel MD cycle has a short, flat bottom for measurements (about 3 s) and a short ramp to 200 GeV/c to establish the magnetic reference of the main magnets for the cycle after (typically the TCC2 cycle).

The maximum acceptable average resistive power dissipated in the main dipole magnets for the SPS is 37.9 MW, while the total average power for the main dipoles and main quadrupoles is 44 MW. This constraint limits the possible supercycle combinations. A list of the supercycles used during 2018 operation is shown in Table 2.3. In both this table and the preceding one, the quoted power corresponds to the sum of the power in the main dipoles and main quadrupoles.

To calculate the number of cycles and the number of protons to the NA targets, the time sharing between the different supercycle configurations during the operational run has to be taken into account. The 2018 proton run was scheduled over 31 weeks with two planned technical stops of 30 h. This corresponds to a total of 5148 h machine time allocated for operation. The time sharing between the different SPS users as obtained from the 2018 injector schedule is summarized in Table 2.4.

The left column of Table 2.4 shows the bare hours for which the corresponding supercycle (see Table 2.3) was scheduled. The right column shows the effective hours expected taking into account the LHC filling and LHC set-up periods. Based on these numbers, the total number of cycles per user over the entire run can be obtained. Figure 2.6 shows the sharing of the SPS machine time per user, comparing

Table 2.3: SPS supercycles used in 2018

	AWAKE	BDF/SHiP	HiRadMat	LHC filling	LHC pilot	MD dedicated	MD parallel	Scrubbing	TCC2	Zero	Degauss	Length (s)	Power (MW) (MB+MQ)
AWAKE	2	–	–	–	–	–	–	–	2	–	2	43.2	37.60
AWAKE with parallel MD	2	–	–	–	–	–	2	–	2	–	–	50.4	32.40
Dedicated MD	–	–	–	–	–	1	–	–	–	–	–	22.8	16.83
HiRadMat	–	–	1	–	–	–	–	–	1	–	1	37.2	26.10
LHC filling	–	–	–	1	–	–	–	–	1	–	1	37.2	26.10
LHC set-up	–	–	–	–	1	–	–	–	1	6	2	37.2	26.48
Physics	–	–	–	–	–	–	–	–	2	–	2	28.8	40.79
Physics with parallel MD	–	–	–	–	–	–	2	–	2	–	–	36.0	32.87
Scrubbing	–	–	–	–	–	–	–	1	1	–	–	33.6	28.39
Thursday MD	–	–	–	–	–	1	–	–	1	–	–	33.6	28.39

Table 2.4: SPS supercycle sharing from schedule of 2018 proton run

	Scheduled (hours)	Effective (hours)
Physics	1852.00	1389.00
Physics with parallel MD	1356.00	1017.00
HiRadMat	240.00	180.00
AWAKE with parallel MD	265.51	199.13
AWAKE	742.49	556.87
Dedicated MD	370.00	277.50
Thursday MD	250.00	187.50
Scrubbing	72.00	54.00
LHC set-up (10% of time)	–	514.80
LHC filling (15% of time)	–	772.20
Total	5148.00	5148.00

the actual numbers from 2018 (left) with the expected values obtained from the analysis described above (right).

The agreement is very good, thus validating the approach. Small differences can be explained by the fact that the ion setting-up was not included explicitly in the schedule and the TCC2 cycle was played slightly more frequently compared with the schedule as it was present in the supercycle during some dedicated MD (without taking beam). This kind of modelling will be used for the projection of future proton sharing presented in what follows.

2.3.2 Future proton-sharing scenarios

The proton-sharing scenarios in the SHiP era were generated in the following way: the maximum number of protons to the TCC2 experiments is obtained assuming an operational year without SHiP, similarly to the analysis performed for the 2018 run. On the other hand, the maximum number of protons for SHiP is

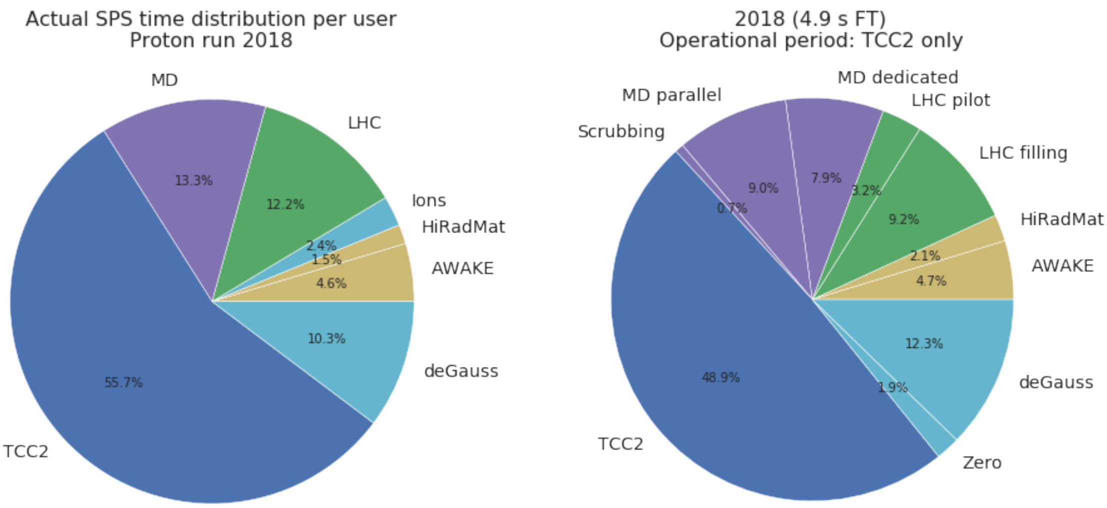

Fig. 2.6: Distribution of the actual machine-time sharing in 2018. Data (left), provided by J. Dalla-Costa, are compared with the expectation from schedule (right).

obtained assuming that the SPS serves both SHiP and the TCC2 targets throughout the entire run using supercycle configurations with a high duty cycle for SHiP. Any intermediate scenario can be obtained by splitting the operational run into periods with only TCC2 experiments and periods with both TCC2 and SHiP experiments with corresponding duration.

2.3.2.1 Scenarios with 4.9 s flat top for TCC2 experiments

The SHiP baseline scenario considers operational runs with protons only, i.e. there is no operational period with ions. Instead, the duration of the proton run is extended to a total of 245 days, including two times of 30 h for technical stops. The supercycle time sharing considered is summarized in Table 2.5. The corresponding supercycle compositions for the two possible running periods are summarized in Table 2.6 (serving only the TCC2 experiments) and in Table 2.7 (serving both TCC2 and SHiP experiments). In both cases, it is assumed that the SPS serves in addition the LHC, AWAKE, HiRadMat, and MD users similarly to the operational run in 2018.

Table 2.5: Supercycle sharing considered for a run with protons only

	Scheduled (hours)	Effective (hours)
Physics	2332.0	1749.0
Physics with parallel MD	1548.0	1161.0
HiRadMat	240.0	180.0
AWAKE with parallel MD	268.1	201.1
AWAKE	739.9	554.9
Dedicated MD	370.0	277.5
Thursday MD	250.0	187.5
Scrubbing	72.0	54.0
LHC set-up (10% of time)	–	582.0
LHC filling (15% of time)	–	873.0
Total	5820.0	5820.0

The resulting machine time sharing for the two running periods is shown in Fig. 2.7. As expected,

Table 2.6: Future SPS supercycles (running period without BDF/SHiP)

	AWAKE	BDF/SHiP	HiRadMat	LHC filling	LHC pilot	MD dedicated	MD parallel	Scrubbing	TCC2	Zero	Degauss	Length (s)	Power (MW) (MB+MQ)
AWAKE	2	–	–	–	–	–	–	–	2	–	2	43.2	37.60
AWAKE with parallel MD	2	–	–	–	–	–	2	–	2	–	–	50.4	32.40
Dedicated MD	–	–	–	–	–	1	–	–	–	–	–	22.8	16.83
HiRadMat	–	–	1	–	–	–	–	–	1	–	1	37.2	26.10
LHC filling	–	–	–	1	–	–	–	–	1	–	1	37.2	26.10
LHC set-up	–	–	–	–	1	–	–	–	1	–	1	26.4	36.64
Physics	–	–	–	–	–	–	–	–	2	–	2	28.8	40.79
Physics with parallel MD	–	–	–	–	–	–	2	–	2	–	–	36.0	32.87
Scrubbing	–	–	–	–	–	–	–	1	1	–	–	33.6	28.39
Thursday MD	–	–	–	–	–	1	–	–	1	–	–	33.6	28.39

Table 2.7: Future SPS supercycles (running period with BDF/SHiP)

	AWAKE	BDF/SHiP	HiRadMat	LHC filling	LHC pilot	MD dedicated	MD parallel	Scrubbing	TCC2	Zero	Degauss	Length (s)	Power (MW) (MB+MQ)
AWAKE	2	3	–	–	–	–	–	–	1	–	1	50.4	34.50
AWAKE with parallel MD	2	3	–	–	–	–	1	–	1	–	1	57.6	30.56
Dedicated MD	–	–	–	–	–	1	–	–	–	–	–	22.8	16.83
HiRadMat	–	4	1	–	–	–	–	–	–	–	–	51.6	25.58
LHC filling	–	1	–	1	–	–	–	–	–	–	–	30.0	20.59
LHC set-up	–	4	–	–	1	–	–	–	–	–	–	40.8	32.26
Physics	–	4	–	–	–	–	–	–	1	–	1	43.2	35.26
Physics with parallel MD	–	4	–	–	–	–	1	–	1	–	–	46.8	32.64
Scrubbing	–	–	–	–	–	–	–	1	1	–	–	33.6	28.39
Thursday MD	–	2	–	–	–	1	–	–	1	–	1	51.6	27.89

without SHiP the main user of SPS machine time remains the NA, with slightly more than 50% overall. On the other hand, during operational periods with both NA and SHiP more than 50% of the machine time would be used for the SHiP cycles, while the TCC2 cycles would use only about 15% of machine time. Note that the number of 'degauss' cycles is also reduced, as they are mostly needed to reduce the r.m.s. power of the SPS main magnets when playing the NA cycle. Furthermore, the amount of parallel MD time in this running period would also be reduced owing to the lower duty cycle in the supercycle configurations considered for SHiP. Figure 2.8 shows a similar comparison of the machine time sharing during the proton run for an operational year with both proton and ion-physics-like operation in 2018.

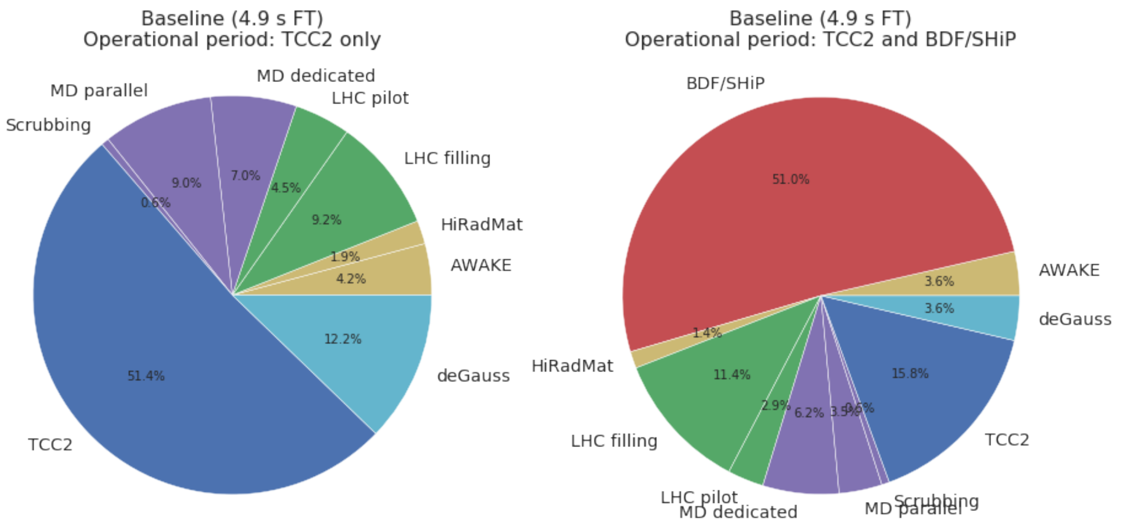

Fig. 2.7: Projected future distribution of machine time usage for a running period without BDF/SHiP (left) compared with a running period with BDF/SHiP (right).

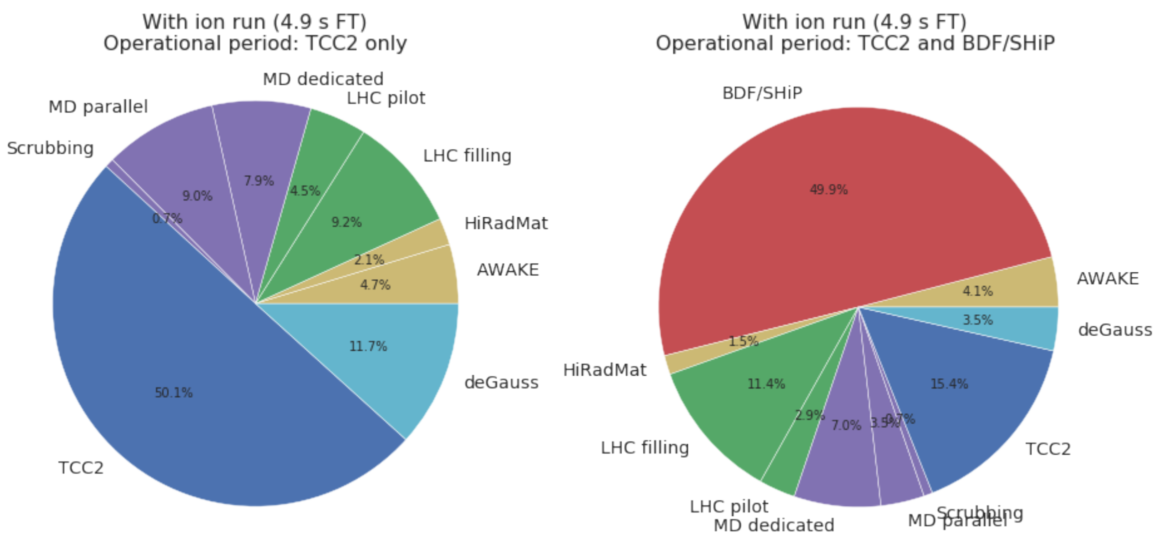

Fig. 2.8: Projected future distribution of machine time usage for a running period without BDF/SHiP (left) compared with a running period with BDF/SHiP (right) with ion run as in 2018.

With the transmission values considered and the intensity per cycle as summarized in Table 2.8, the resulting proton sharing is shown in Fig. 2.9. Furthermore, a machine availability of 80% was considered, which is a realistic but conservative number (in 2018 the SPS availability was 80%, slightly lower than in previous years). The curve labelled “With ion run” corresponds to a schedule as in 2018, i.e. with the supercycle sharing given in Table 2.4. The 4.9 s flat top for the TCC2 experiments maximizes the total proton flux to the NA and the BDF/SHiP experiment. This would be optimum if there are experiments in the NA that require a large proton flux (e.g. KLEVER).

2.3.2.2 Scenarios with 9.7 s flat top for TCC2 experiments

If the main interest of the NA experiments were in test beams with limitations on the instantaneous proton flux, a longer flat-top cycle would be more advantageous (similar to what was done during the operation of the CNGS experiment). Proton-sharing scenarios with a 9.7 s flat top for the TCC2 experiments have

Table 2.8: Transmission and intensity per cycle considered

	TCC2	BDF/SHiP
Extraction transmission	0.99	0.99
TT20 transmission	0.96	0.96
Splitting transmission	0.80	1.00
Total transmission	0.76	0.95
Protons per spill (10^{13})	4.00	4.20
Protons on target per spill (10^{13})	3.04	3.99

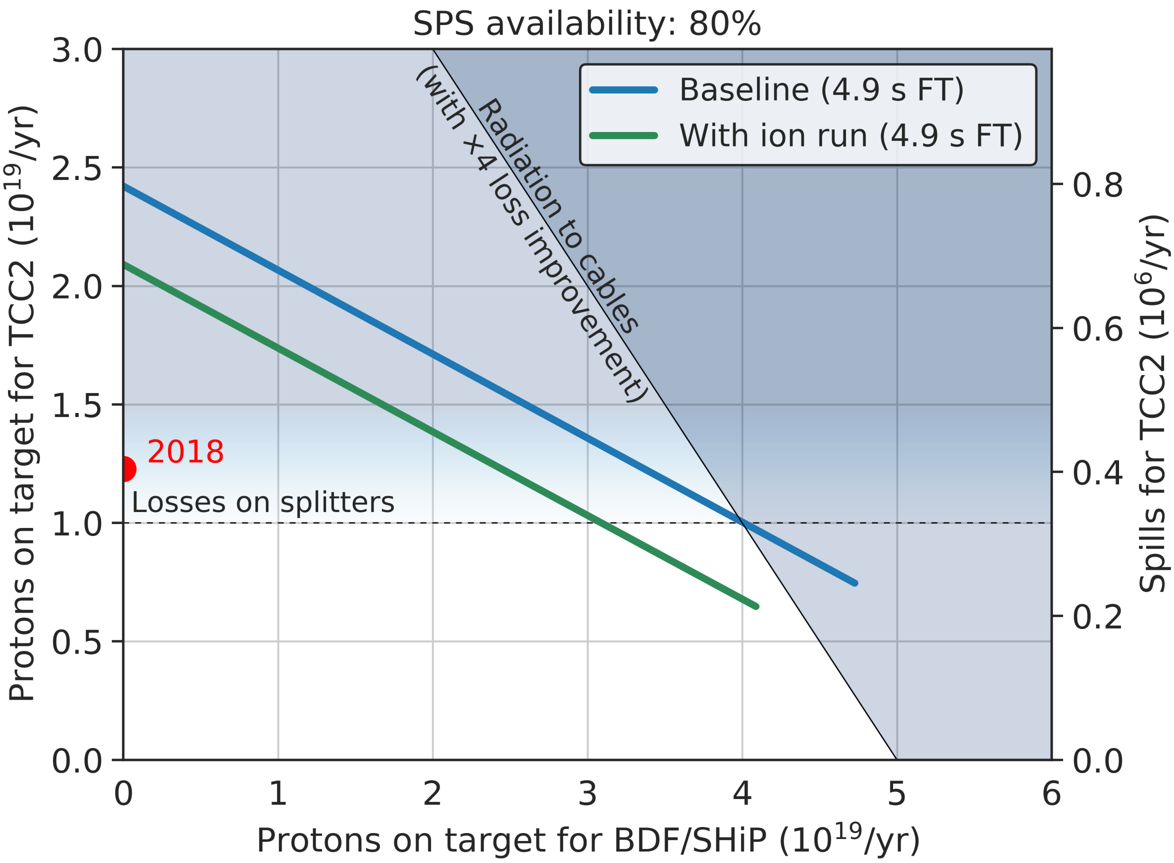

Fig. 2.9: Future proton-sharing scenarios with (green) and without (blue) ion operation. A 4.9 s flat-top (FT) length is considered for the TCC2 experiments.

been calculated as presented below. The total length of the TCC2 cycle with a 9.7 s flat top is 15.6 s, with an average power (main bends and quadrupoles) of 63.6 MW. Assuming again the supercycle sharing of Table 2.5 for operational runs with only protons and Table 2.4 for operational runs with protons and ions, the resulting time sharing between the different users is given in Figs. 2.10 and 2.11. The supercycle compositions considered are summarized in Tables 2.9 and 2.10.

The scenarios for proton sharing between the TCC2 experiments and the BDF/SHiP experiment obtained are shown in Fig. 2.12. The secondary vertical axis on the right side of the plot shows the number of spills for the TCC2 experiments in units of "4.9 s equivalent" spills, which is obtained by

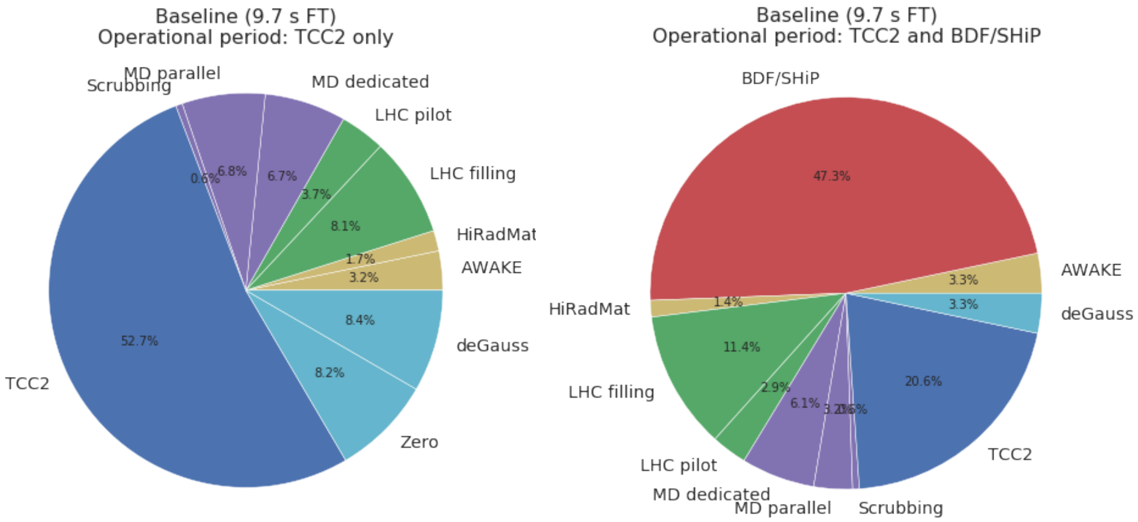

Fig. 2.10: Projected future distribution of machine time usage for a running period without BDF/SHiP (left) compared with a running period with BDF/SHiP (right) with a 9.7 s flat-top duration.

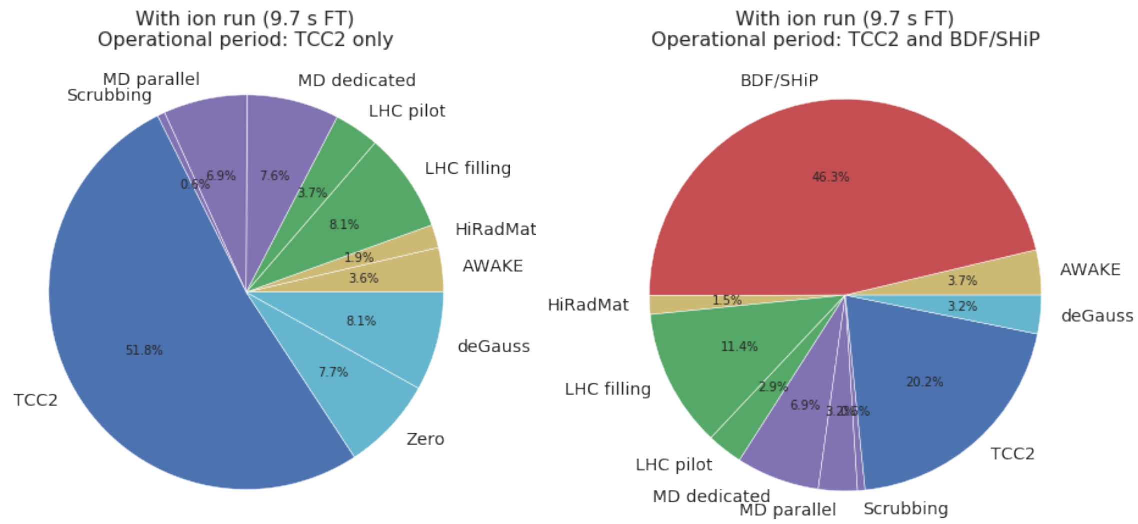

Fig. 2.11: Projected future distribution of machine time usage for a running period without BDF/SHiP (left) compared with a running period with BDF/SHiP (right), with an ion run and with a 9.7 s flat-top duration.

multiplying the number of actual spills by the ratio of the flat-top lengths (9.7/4.9). This represents the situation where the TCC2 experiments are limited in the instantaneous proton flux available and therefore would profit from longer spills. In other words, a flat top of 9.7 s gives double the data-taking time compared with a 4.9 s flat top, at a constant spill rate.

2.4 Summary and conclusions

The SPS serves a large variety of physics users. A detailed analysis has been performed to analyse the compatibility and possible proton-sharing scenarios between the TCC2 experiments and proposed future experiments such as BDF/SHiP, taking into account the parallel operation of the LHC, AWAKE, HiRadMat, and MD. The analysis is based on the actual operational conditions and constraints of the 2018 proton run, in order to be as realistic as possible. The methodology presented in this chapter has been benchmarked against the operational period of 2018: the operationally obtained number of protons for the TCC2 targets of the 2018 run was correctly reproduced for the corresponding parameters. For

Table 2.9: Future SPS supercycles (running period without BDF/SHiP)

	AWAKE	BDF/SHiP	HiRadMat	LHC filling	LHC pilot	MD dedicated	MD parallel	Scrubbing	TCC2	Zero	Degauss	Length (s)	Power (MW)
AWAKE	1	–	–	–	–	–	–	–	1	2	1	28.8	42.86
AWAKE with parallel MD	1	–	–	–	–	–	1	–	1	–	–	30.0	41.28
Dedicated MD	–	–	–	–	–	1	–	–	–	–	–	22.8	16.83
HiRadMat	–	–	1	–	–	–	–	–	1	–	1	42.0	33.17
LHC filling	–	–	–	1	–	–	–	–	1	–	1	42.0	33.17
LHC set-up	–	–	–	–	1	–	–	–	1	1	1	32.4	42.89
Physics	–	–	–	–	–	–	–	–	1	4	1	24.0	42.08
Physics with parallel MD	–	–	–	–	–	–	2	–	2	1	–	46.8	43.32
Scrubbing	–	–	–	–	–	–	–	1	1	–	–	38.4	35.83
Thursday MD	–	–	–	–	–	1	–	–	1	–	–	38.4	35.83

Table 2.10: Future SPS supercycles (running period with BDF/SHiP)

	AWAKE	BDF/SHiP	HiRadMat	LHC filling	LHC pilot	MD dedicated	MD parallel	Scrubbing	TCC2	Zero	Degauss	Length (s)	Power (MW)
AWAKE	2	3	–	–	–	–	–	–	1	–	1	55.2	39.15
AWAKE with parallel MD	2	3	–	–	–	–	1	–	1	–	1	62.4	34.98
Dedicated MD	–	–	–	–	–	1	–	–	–	–	–	22.8	16.83
HiRadMat	–	4	1	–	–	–	–	–	–	–	–	51.6	25.58
LHC filling	–	1	–	1	–	–	–	–	–	–	–	30.0	20.59
LHC set-up	–	4	–	–	1	–	–	–	–	–	–	40.8	32.26
Physics	–	4	–	–	–	–	–	–	1	–	1	48.0	40.53
Physics with parallel MD	–	4	–	–	–	–	1	–	1	–	–	51.6	37.78
Scrubbing	–	–	–	–	–	–	–	1	1	–	–	38.4	35.83
Thursday MD	–	2	–	–	–	1	–	–	1	–	1	56.4	33.00

future proton-sharing scenarios, operational periods with and without dedicated ion physics have been considered. Two different flat-top lengths for the slow extraction to the TCC2 experiments have been analysed, taking into account realistic supercycle compositions and respecting the SPS limits on power dissipation in the magnets. The intensities considered for the TCC2 cycle and the BDF/SHiP cycle are based on operationally achieved values during the CNGS era of the SPS. The limitations arising from losses at the splitters to the TCC2 targets and the intensity limitation arising from activation of the slow-extraction equipment have also been taken into account. With all these assumptions, the target of 4.0×10^{19} PoT for the BDF/SHiP experiment can be achieved in different scenarios. The PoT for the TCC2 experiments then depends on the chosen flat-top length and the total number of days of physics (i.e. whether there is an ion run or not). However, it should be stressed that the PoT numbers would be

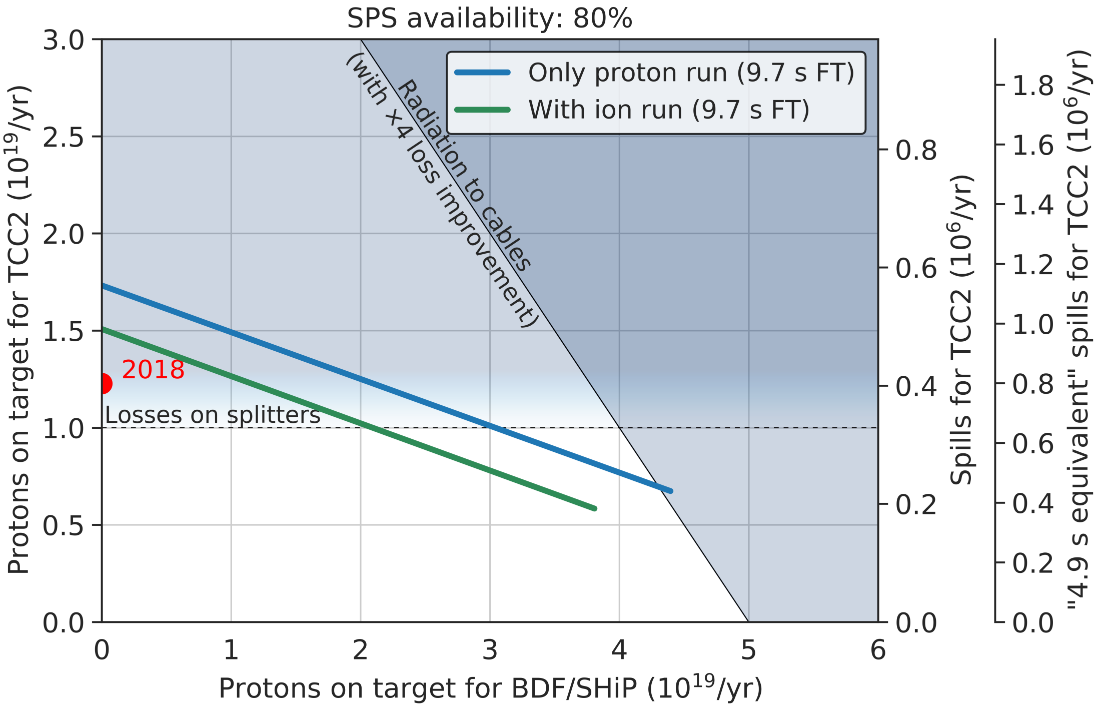

Fig. 2.12: Future proton-sharing scenarios with (green) and without (blue) ion operation. A 9.7 s flat-top length is considered for the TCC2 experiments.

reduced in the case of more frequent LHC fillings than in today's operation (which might be required if one of the back-up operational scenarios with reduced LHC fill lengths is needed operationally during the HL-LHC era).

References

[1] G. De Lellis. "Search for Hidden Particles (SHiP): a new experiment proposal". In: *Nucl. Part. Phys. Proc.* 263–264 (2015), p. 71. DOI: 10.1016/j.nuclphysbps.2015.04.013.

[2] G. Arduini et al. *The SPS Beam Parameters, the Operational Cycle, and Proton Sharing with the SHiP Facility*. Technical Report CERN-SHiP-NOTE-2015-004. CERN, 2015.

[3] M. Meddahi and E. Shaposhnikova. *Analysis of the Maximum Potential Proton Flux to CNGS*. Technical Report CERN-AB-2007-013-PAF. CERN, 2007. URL: https://cds.cern.ch/record/1027754.

[4] E. Shaposhnikova et al. "Recent intensity increase in the CERN accelerator chain". In: *Proc. of 2005 Particle Accelerator Conference (PAC'05)* (Knoxville, Tennessee). May 2005. DOI: 10.1109/PAC.2005.1590452. URL: http://accelconf.web.cern.ch/AccelConf/p05/PAPERS/ROPC004.PDF.

[5] C. Bovet et al. "The fast shaving ejection for beam transfer from the CPS to the CERN 300 GeV machine". In: *IEEE Trans. Nucl. Sci.* 20 (1973), p. 438. DOI: 10.1109/TNS.1973.4327144.

[6] R. Cappi and M. Giovannozzi. "Novel method for multiturn extraction: trapping charged particles in islands of phase space". In: *Phys. Rev. Lett.* 88, 104801 (2002). DOI: https://doi.org/10.1103/PhysRevLett.88.104801.

[7] S. Abernethy et al. "Operational performance of the CERN injector complex with transversely split beams". In: *Phys. Rev. Accel. Beams* 20, 014001 (2017). DOI: 10.1103/PhysRevAccelBeams.20.014001.

[8] A. Huschauer et al. "Approaching the high-intensity frontier using the multi-turn extraction at the CERN Proton Synchrotron". In: *Proc. HB2018*. 2018. DOI: 10.18429/JACoW-HB2018-WEA1WA02.

[9] J. Coupard et al. *LIU Technical Design Report, Volume I: Protons*. CERN-ACC-2014-0337. 2014. URL: https://cds.cern.ch/record/1976692.

[10] J. Coupard et al. "LIU Technical Design Report, Volume II: Ions". In: CERN-ACC-2016-0041. 2016. URL: https://cds.cern.ch/record/2153863.

[11] M. A. Fraser et al. "Slow extraction efficiency measurements at CERN SPS". In: *Proc. of International Particle Accelerator Conference (IPAC'18)* (Vancouver, BC, Canada). Apr. 2018. DOI: https://doi.org/10.18429/JACoW-IPAC2018-TUPAF054. URL: http://accelconf.web.cern.ch/AccelConf/ipac2018/papers/tupaf054.pdf.

[12] M. A. Fraser et al. "SPS slow extraction losses and activation: challenges and possibilities for improvement". In: *Proc. of International Particle Accelerator Conference (IPAC'17)* (Copenhagen, Denmark). May 2017. DOI: https://doi.org/10.18429/JACoW-IPAC2017-MOPIK045.

[13] F. M. Velotti et al. "Reduction of resonant slow extraction losses with shadowing of septum wires by a bent crystal". In: *Proc. of International Particle Accelerator Conference (IPAC'17)* (Copenhagen, Denmark). May 2017. DOI: http://dx.doi.org/10.18429/JACoW-IPAC2017-MOPIK050.

[14] K. Brunner. "Improving the slow extraction efficiency of the CERN Super Proton Synchrotron". MA thesis. Eötvös Loránd University, 2018. URL: https://cds.cern.ch/record/2650734.

[15] B. Goddard et al. "The use of a passive scatterer for SPS slow extraction beam loss reduction". In: *Proc. of International Particle Accelerator Conference (IPAC'17)* (Copenhagen, Denmark). May 2017. URL: http://accelconf.web.cern.ch/AccelConf/ipac2017/papers/mopik044.pdf.

[16] L. R. Evans et al. "The steel septum magnets for beam splitting at the CERN SPS". In: *Proc. 6th International Conf. on Magnet Technology (MT-6), Bratislava, Slovakia, CERN-SPS-ABT-77-13*. 1977.

Chapter 3

Slow extraction from the SPS

3.1 Introduction

3.1.1 Slow extraction in the SPS

Third-integer slow extraction from the SPS uses a set of suitably located extraction sextupoles to create a stable area in horizontal phase space. In the standard scheme (Q-sweep), the beam is debunched with the chromaticity set to a large negative value, and the machine tune moved towards the third integer. The extraction is done in combined momentum and betatron space, with the lowest-momentum particles coming into resonance and being extracted first across the electrostatic septum (note that 'ZS' is used synonymously with 'electrostatic septum' when discussing the installed hardware). There is a momentum ramp of the extracted beam during the spill as it sweeps through the intrinsic momentum spread of the circulating beam, which couples into changes in the separatrix position and angle with time at the ES. For the newly developed constant-optics slow extraction, the normalized machine optics are set constant and the momentum of the entire beam is trimmed to move into the resonance, which has the advantage of keeping the separatrix presentation to the ES constant.

The SPS currently provides beam to the North Area fixed-target physics programme with spill lengths of several seconds; in recent years spills were extracted with a flat-top length of 4.8 s. The extraction system is located in Long Straight Section 2 and is composed of an ES (or ZS) upstream of magnetic septa (referred to as Magnet Septum Thin (MST) and Magnet Septum Extractor (MSE)), as shown in Fig. 3.1. Dedicated protection devices, e.g. the extraction collimator (TCE) and the fixed septa protection absorber (TPST), are strategically positioned to intercept and absorb a large part of the beam energy that would otherwise be deposited in the septa and quadrupoles. The largest-amplitude particles jumping into the ES are deflected off into the extraction channel, leaving the SPS via the coil window of the wide-aperture quadrupole QDA.219.

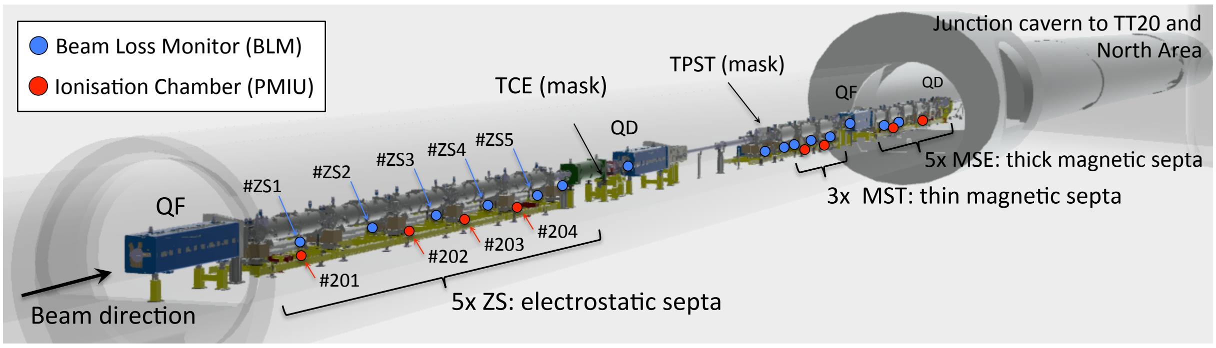

Fig. 3.1: LSS2 slow-extraction region towards the TT20 transfer line and the NA [1]

The ES is divided into five separate tanks, 3.15 m long, each containing an array of 2080 tungsten–rhenium (WRe) wires that create the boundary delimiting the low- and high-electric-field regions. The wires are made as thin as possible (ZS1–2, ⌀ 60 µm; ZS3–5, ⌀ 100 µm) to reduce beam losses, but a small fraction of beam is unavoidably scattered on the wires, inducing radioactivity in LSS2. Five such units are needed to extract the beam at 400 GeV, individually aligned with the beam to minimize overall losses. Primary proton scattering on these wires is the dominant source of beam loss. To minimize the effective thickness of the septum seen by the beam, the anode supporting the wires is made as straight as possible with a very accurate positioning system, but nevertheless several per cent of the beam is lost in the extraction process.

3.1.2 Implications of protons-on-target request

The radiation dose and induced radio-activation in LSS2, and also at the splitters in TT20, are correlated with the total PoT as well as with other less tangible aspects of the SPS operation and extraction channel set-up, such as the beam stability, the alignment of the extraction septa, any hardware faults, and the beam quality. There is therefore a significant scatter in the activation levels per proton, depending on the specific combination of conditions and also the level and quality of the follow-up both of the hardware and of the operation. The residual dose after the end of proton operation has been measured over many years, and is summarized in Fig. 3.2, showing the results for both LSS2 and LSS6. To keep the residual activation levels at around 5 mSv/h after 30 h of cool-down while extracting around 5×10^{19} PoT per year will require a reduction in the activation per proton of approximately a factor of four.

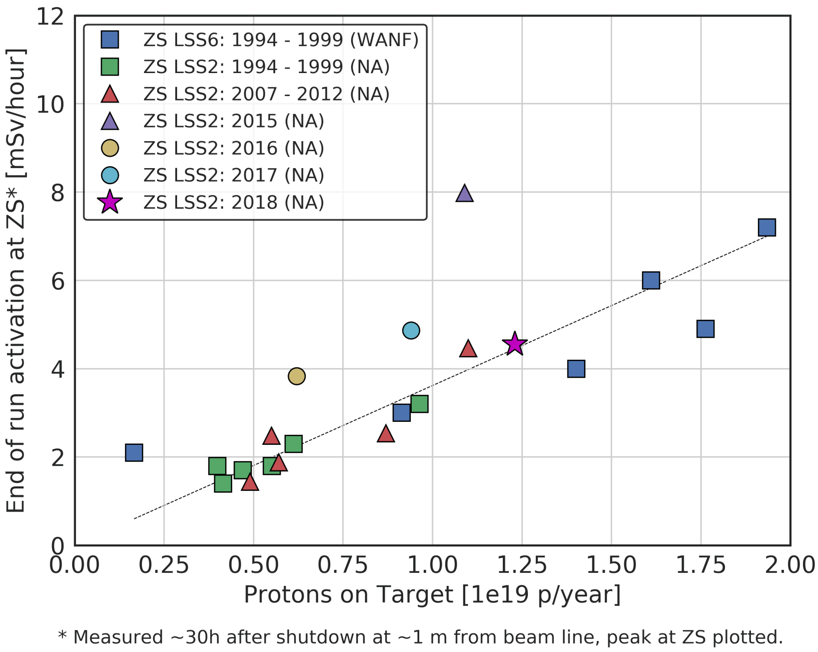

Fig. 3.2: Induced activation as a function of PoT per year for the ES in the slow-extraction channels LSS2 and LSS6.

The high losses and activation observed in 2015 were problematic for the hands-on maintenance of the systems, and also were likely contributors to the severe failures seen in 2018, where both a High-Voltage (HV) feedthrough broke on one ZS and the main HV cable powering all the ZS failed. Accumulated dose is known to be a major factor in the lifetime of both of these critical elements, and since changes to the ZS tank or anode materials will not help with the dose to equipment, the reduction in the induced radioactivity per extracted proton is critical for equipment performance.

The transfer line TT20 to the NA shows several zones of rather high activation but the highest occurs at the radiation-resistant Lambertson splitter septa, which are protected by an upstream collimator. The fraction of beam lost on the splitters is about 3%, as estimated by intensity monitors in the NA. For the future BDF, one major advantage of the concept is that the splitters will be used in a 'switch' mode, where the beam is not split or shared, but steered towards the new beam line and target. Since the beam for the BDF will pass through the gap of the splitter system in an essentially loss-free transport, this gain will mean that the present loss levels both in the extraction channel and in the splitter region can be maintained for the simultaneous delivery of 4×10^{19} to the BDF and $\sim 1 \times 10^{19}$ to the NA.

Further, the radiation dose to the cables and extraction equipment depends on the beam loss at extraction and the total number of protons extracted. If the factor of four loss reduction can be applied to both SHiP and NA extraction, then again the limitation on the total number of protons extracted per year (to whatever target) will be 5.0×10^{19}. At these dose levels, a full recabling of the extraction channel region, e.g. the control, HV, and d.c. cables, is required after about 8 yr of operation or every other long shutdown, based on experience.

3.1.3 Overview of challenges, possibilities for improvement, and associated R&D efforts

In 2018, the highest integrated number of protons in the history of the NA was slowly extracted from the SPS for the fixed target (FT) physics programme. At well over 1.2×10^{19} PoT, this represented the highest annual figure for almost two decades, since the West Area Neutrino Facility was operational. The high-intensity PoT requests look set to continue in the foreseeable future, especially in view of the proposed SPS BDF and experiments, e.g. SHiP [2]. Without significant improvements, the attainable annual PoT will be limited to well below the total the SPS machine could deliver, owing to activation of accelerator equipment and associated personnel dose limitations. The instantaneous and integrated loss levels are therefore strong limitations on the annual attainable PoT.

Over the past 3 yr, significant effort has been made on several fronts to conceive, design, deploy, and test where possible methods to reduce the extraction beam losses or to mitigate their effects through different material choices or handling. In this chapter, the requirements on, constraints on, and potential improvements to the slow-extraction system in the SPS are described. The present and future challenges are numerous, including machine stability and reproducibility, monitoring and surveillance of the extraction, carrying out interventions and remote handling of equipment in the activated extraction region, and improving the extraction inefficiency. Several possibilities to reduce dose to personnel during hands-on maintenance, which is considered as one of the most important figures of merit alongside machine availability, are being investigated, spanning improved spill quality, manipulation and control of the extracted separatrix, alternative or upgraded extraction hardware concepts, including diffuser devices (passive and active) upstream of the ZS, low-activation materials, and the extended use of remote handling techniques.

It is clear that there will not be one single solution but rather a combination of improvements, which together may achieve the factor of four reduction in extraction beam loss desired. Interestingly, some of the methods for reduction of loss, activation, and personnel dose can be combined directly, with a multiplicative gain. The techniques evaluated are compared in terms of what has been learnt from simulations and recent measurements with beam, and what can be expected operationally from a realistic extrapolation of the results.

3.1.4 Dose rate and cool-down predictions in BDF era

To understand how the extracted proton flux affects the build-up and subsequent cool-down of the induced radio-activation of the extraction straight section and make predictions for the BDF scenario, a model based on a simple empirical relationship has been developed [3] and shown to predict the measured radioactive decay in ionization chambers in LSS2. The empirical model was first developed in the mid 1990s, with dedicated measurements of the induced radioactivity (IR) in the LSS6 extraction region, to understand the build-up of activation during the high-intensity operation of the West Area Neutrino Facility [4, 5, 6]. To put the relative intensities in perspective, consider that the BDF is requesting 20×10^{19} PoT over 5 yr, compared with the 7×10^{19} PoT delivered to the WANF over a similar period. During this period the model was developed to fit the measured data as a function of the extracted proton flux, allowing predictions of cool-down times to be made during operation. More recently, and with much improved software and analysis tools, the model was revived and exploited as a predictive tool for estimating cool-down times as a function of extracted proton flux.

The instrumentation relevant to this study is shown in Fig. 3.1. Beam Loss Monitors (BLMs) placed along the extraction region are used to measure the prompt beam loss induced by the small fraction of the beam that impacts the wires of the ZS septum during extraction. In addition to the BLMs, a series of ionization chambers (Radiation **P**rotection **M**onitor for dose rates due to **I**nduced Radioactivity (PMIU)) are used to measure the IR. Unlike the BLMs, the PMIU detectors have a fixed gain and saturate during extraction owing to the high prompt loss signal but give a reliable signal during periods of cool-down.

The objective of this work was to estimate the cool-down times required for the PoT requested annually by the NA experiments and to estimate the improvement in the extraction efficiency required to keep cool-down times reasonable for the future BDF.

3.1.4.1 *Empirical models of IR(t)*

One of the most challenging aspects of predicting the evolution of the IR is the non-linear time dependence of its effective half-life arising from the mixture of different radionuclides produced both during the initial irradiation and in the resulting chains of radioactive decay. After irradiation, the exponential decay of the IR can be expressed as

$$\mathrm{IR}(t) \propto \exp\left(-\frac{t}{\tau(t)}\right), \tag{3.1}$$

where different functional forms have been proposed for the time evolution [4]. The most suitable model for the SPS was shown empirically to take the above exponential form with

$$\tau(t) = \frac{t}{k_1 \ln(t)^{k_2}}, \tag{3.2}$$

where k_1 and k_2 are decay constants. By differentiating Eq. (3.1) with respect to time and rewriting the result as a first-order linear ordinary differential equation, one can write the effective half-life of the empirical model by inspection as

$$t_{1/2}(t) = \frac{t}{k_1 k_2 \ln(t)^{k_2-1}} \ln(2). \tag{3.3}$$

A similar derivation, based on another empirical model developed by Sullivan and Overton, can be found in Ref. [7]. As one would expect for a physical effective half-life describing a mixture of different radioisotopes, each with different populations and half-lives, the expression continually increases at an exponentially slower rate towards stability, i.e. $\lim_{t\to\infty} t_{1/2}(t) = \infty$ and $\lim_{t\to\infty}(\partial t_{1/2}(t)/\partial t) = 0$, for $k_1, k_2 \in \mathbb{R}_{>0}$ and $k_2 > 1$, which is not the case for many of the empirical models that have been proposed to date [8, 9]. The model fits the empirical data well, as well as simulated data generated by activating different materials with a 400 GeV proton beam for 200 days using the ActiWiz code [10]. The fit constants showed good agreement with the simulated activation of stainless steel, which is the dominant material component of the ZS, and also with the fit constants obtained empirically.

A predictive model of the build-up and decay of the IR as a function of time was developed by introducing the measured extracted proton flux $P_{\mathrm{ex}}(t)$ and the prompt normalized loss per proton $N_{\mathrm{L}}(t)$. The introduction of N_{L}, as measured on the BLMs next to the ZS, was an attempt to introduce changes in the extraction efficiency over time into the model. The model was discretized in time, using bins of duration Δt, and an exponential decay function was generated at every bin with a starting value proportional to both P_{ex} and N_{L}. At the nth bin, the IR can be expressed as a sum of exponentials arising from all previous bins according to

$$\mathrm{IR}_n = G \sum_{i=1}^{n} N_{\mathrm{L},n+1-i} P_{\mathrm{ex},n+1-i} \exp\Big(-k_1 \ln(\Delta t(i-1))^{k_2}\Big), \tag{3.4}$$

where G is a constant conversion factor that depends on the primary beam energy, material composition, and geometry of the machine, including the relative positions of the detectors and their calibrations. This relatively simple analytic function depends on only three constants, determined empirically by applying a non-linear least-squares fitting routine on logged measurement data taken during past operational years. An example is shown in Fig. 3.3, using data logged during 2016. In this example,

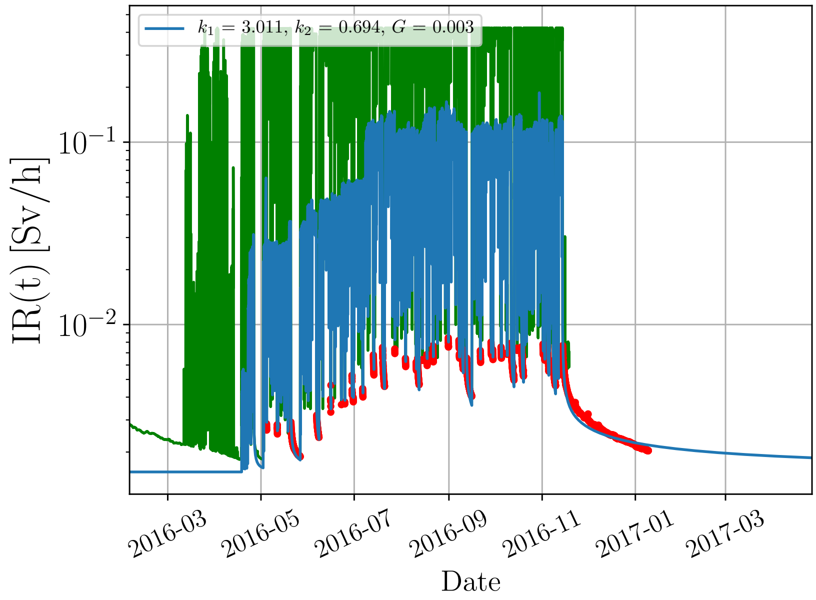

Fig. 3.3: IR model (blue) fitted to measured filtered data (red): first 5 h of data after beam stops and saturated PMIU data are filtered from the raw data (green); $\Delta t = 0.5\,\mathrm{h}$.

PMIU.202 was paired with its closest BLM on ZS2 to account for variations in the extraction efficiency. The agreement between the measurement and the fit is better than 10% from a few days to 2 months of cool-down. The IR measured on the PMIU detectors has to be filtered to remove saturated values acquired in the presence of beam, as well as data taken immediately after a stop in operation. The quality of the fitting over longer time periods is limited by the fast initial variation of the half-life caused by the rapid decay of short-lived radioisotopes and the length of the stops during the operational year over which the fitting is done. The convergence of the fit is improved significantly if the first few hours of data are removed; the amount of data removed is a free parameter chosen to improve the fitting in the time range of interest.

The fit constants determined from the logged 2016 data are shown in Table 3.1, where each PMIU is paired with its nearest BLM. The variation in G can be attributed to the relative positions and differences in calibration of the PMIUs and BLMs. The variations in the decay constants k_1 and k_2 indicate localized differences in the decay rate. A spatial dependence of the cool-down rate is indeed observed along LSS2 and is likely caused by local differences in the material composition of the equipment in the proximity of the detectors. The effect is most prevalent in the first days of cool-down. The fitting was also carried out on the average of all detectors next to the ZS to give a more global description of the IR, from which similar fit constants were also obtained.

3.1.4.2 Predictive power of the IR(t) model

The predictive power of the model was tested on data logged in 2011 and 2015 by applying the 2016 fit constants. The discrepancy with the model was tested using PMIU.202 and BLM.ZS2, and the model was accurate to within 10%. The model has been used in recent years to predict the end-of-year activation for different operational scenarios. An example during the 2017 physics run is shown in Fig. 3.4, where

Table 3.1: Empirical constants determined from 2016 data

BLM.ZS no.	PMIU no.	k_1	k_2	G (Sv h^{-1} Gy^{-1})
1	201	3.14	0.69	0.0062
2	202	3.01	0.69	0.0027
3	203	2.73	0.66	0.0007
4	204	2.44	0.76	0.0008
Average		3.31	0.67	0.0016

it was required to assess the impact on the cool-down time during the Year-End Technical Stop (YETS) in view of a possible exchange of the second ZS tank. Using the planned intensity and the injector accelerator schedule as input, the model was able to accurately predict the measured induced radioactivity during the YETS.

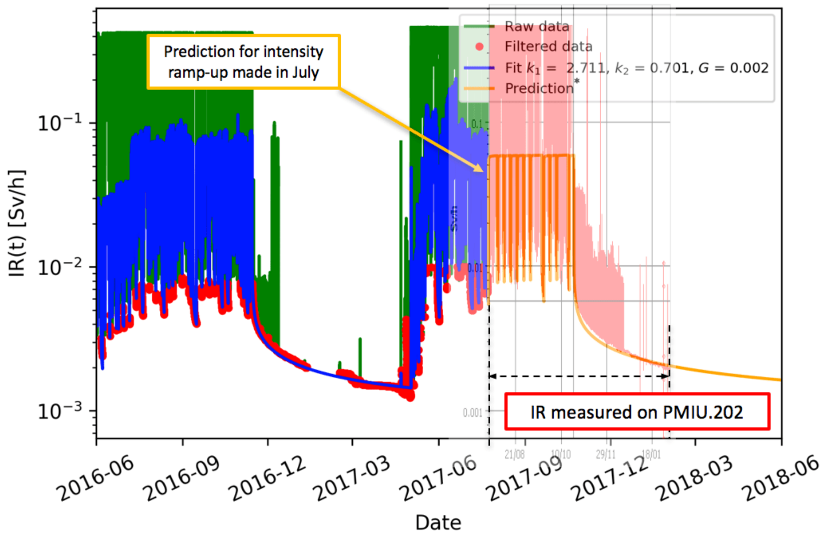

Fig. 3.4: IR model (blue) fitted to measured filtered data (red dots) and extrapolated (orange) in view of the requested increase in PoT: the prediction is compared with the measured IR (red shaded line) on PMIU.202. PPP, protons per pulse.

With increasing amounts of good-quality, precisely logged data, the model is reaching its full potential and several years can be strung together to consider the build-up of longer-term induced radio-activation. Figure 3.5 demonstrates this, with both of the years 2016 and 2017 included in the fitting algorithm and extrapolated to give predictions of the end-of-run activation and cool-down into Long Shutdown 2 based on the 2018 request for proton flux by the NA experiments. In 2018, the model was also used to predict the cool-down time and expected dose to personnel in the event that the tank in which the HV feedthrough broke would need replacing.

3.1.4.3 Impact of future BDF operational scenario on IR

During the shutdown period early in 2016, several ZS tanks had to be exchanged for preventive maintenance owing to problems observed in 2015. Using the actual dose received by the personnel involved in these interventions and the measured IR at PMIU.202 as a reference, the dose for given cool-down times was estimated for future operational scenarios. In the following estimates, the cool-down times are

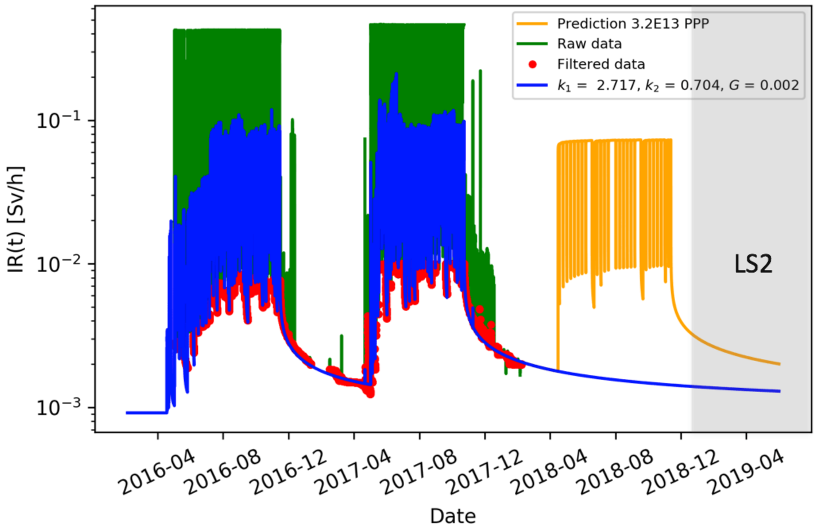

Fig. 3.5: IR model (blue) fitted to measured filtered data (red dots) and extrapolated (orange) in view of the 2018 PoT request and cool-down into LS2.

quoted at the end of an operational year for a 5 mSv collective dose using the exchange of ZS tank 2 on 19 February 2016 as the reference; the collective dose received was 1.7 mSv after 100 days of cool-down.

An intensity profile $P_{\text{ex}}(t)$ based on the draft 2017 CERN injector schedule was assumed and parametrized by the number of Spills Per Day (SPD), Protons Per Pulse (PPP), and N_{L}, where the extraction efficiency is inversely proportional to N_{L}. The cool-down times parametrized in terms of SPD and N_{L} are shown in Fig. 3.6 for an intensity of 4×10^{13} PPP, as requested by both the NA in 2017 and the future SPS BDF. In this case a model pairing PMIU.202 with BLM.ZS2 was used. The cool-down times scale almost quadratically with N_{L} and intensity. In 2017, an average of 3300 SPD was predicted, whereas for the BDF over 6000 SPD would be needed to meet the requested PoT. Assuming the same average extraction efficiency as measured on BLM.ZS2 in 2015 ($N_{\text{L}} = 1.8 \times 10^{-14}$ Gy/p), one can expect cool-down times of approximately 17 days. For the SPS BDF, the cool-down times would extend to over 7 weeks with today's extraction efficiency. An improvement of at least a factor of three is required to keep future waiting times below a week during operation of the BDF.

The estimates assume that the shape of the activation profile along LSS2 does not change significantly and that no local hot spots arise. As observed in recent operation, localized hot spots could significantly affect the dose received during interventions, and the conclusions drawn with the above assumptions should be taken with care. The model provides a powerful tool to understand changes in the activation levels as a function of the extracted proton flux and extraction efficiency, which could permit the identification of hot spots before the end-of-year radio-protection survey.

Further work is needed to understand the build-up of the induced radioactivity arising from longer-lived radioisotopes over extended periods of operation and to tune the model to the these time-scales. To this end, the LSS2 geometry has been implemented in FLUKA code to generate loss and activation maps.

3.2 Understanding today's extraction efficiency

Since careful attention was given to the operational alignment of the ZS after Long Shutdown 1 (LS1) owing to the increasing proton flux to the North Area and induced radio-activation of LSS2, it has become evident that the measured extraction efficiency is lower than what one would expect from simulations of the extraction process with scattering, including even relatively conservative mechanical and alignment tolerances. The measured extraction inefficiency indicates values a little over 3% [11], improving over

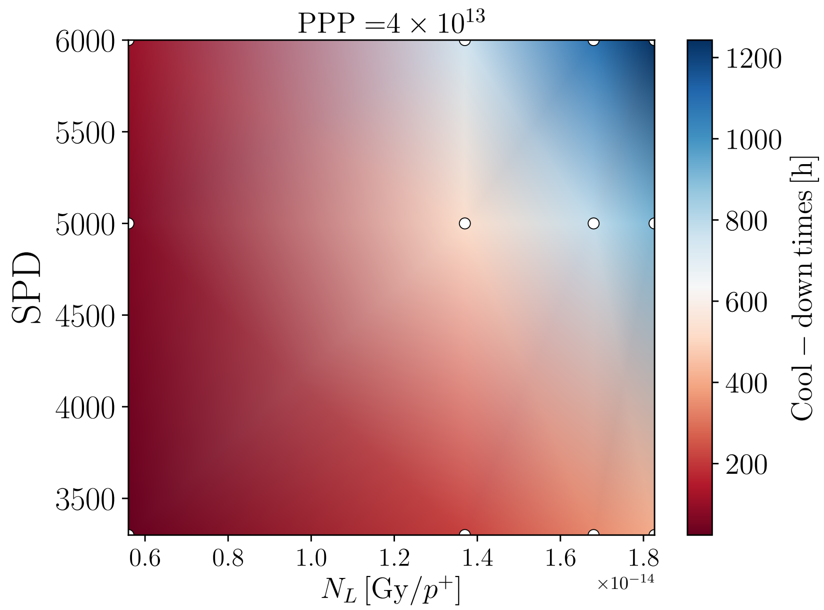

Fig. 3.6: Parametric study of waiting times for the reference intervention: ZS2 tank exchange with 5 mSv collective dose.

recent years, but simulations of the nominal extraction system suggest that the values should be closer to 1%. Recent FLUKA simulations do indeed confirm that the measured prompt beam loss is higher than expected, consistent with a thicker septum. The increased effective thickness is expected to arise from a combination of electromechanical and thermomechanical deformation as well as the relative alignment of the separate ZS tanks. The studies summarized in this section focus on recent work to mitigate and reduce the extraction losses as well as to understand the present limitations and identify where future effort is needed to improve the extraction efficiency. In particular, the tests of the prototype diffusers with beam provided important information about the effective ZS width and the angular spread of the beam at the ZS, among other things.

3.2.1 Slow-extraction efficiency measurements at the SPS

The high efficiency of most slow-extraction systems makes quantifying the exact amount of beam lost in the process extremely challenging. This is compounded by the lack of time structure in the extracted beam, as is typically requested by high-energy physics experiments, and the difficulty of accurately calibrating d.c. intensity monitors in the extraction line at count rates of $\approx 1 \times 10^{13}$ Hz. As a result, it is common for the extraction inefficiency to be measured by calibrating the beam loss signal induced by the slow extraction process itself. The ability to accurately measure the extraction efficiency is becoming more relevant at a time when global research efforts [12] to find loss mitigation methods to meet the demanding requests for higher-intensity slowly extracted beams are intensifying. Accurate efficiency measurements are also important in order to compare (i) the expected performance of different extraction techniques with simulations and (ii) the state-of-the-art performance achieved at different laboratories.

The efficiency (ϵ) of the extraction process is a very important figure of merit because the IR is directly proportional to the number of protons lost in the extraction process:

$$\text{IR} \propto 1 - \epsilon \,. \tag{3.5}$$

As $\epsilon \to 1$, it becomes more accurate to measure the extraction inefficiency ($\bar{\epsilon}$) and to infer ϵ from the relation

$$\epsilon + \bar{\epsilon} = 1 \,. \tag{3.6}$$

Even relatively large systematic errors in $\bar{\epsilon}$ result in small absolute errors in ϵ. To illustrate this point, assume $\epsilon = 0.99$; a systematic error of 10% in a measurement of $\bar{\epsilon}$ yields a systematic error of only 0.1% in an indirect measurement of ϵ. The measured beam loss during extraction, which is proportional to the number of protons lost, can be calibrated and used to measure the inefficiency. The challenge is to carefully calibrate the beam loss measured on a BLM system with respect to the number of protons lost. Most laboratories use beam loss measurements to quantify their slow-extraction efficiency [13, 14, 15, 16, 17, 18, 19].

At the CERN SPS, a technique developed at FNAL's Main Ring in the 1970s was applied to calibrate the response of the BLM system as a function of the extraction efficiency by gently skewing the ZS [20, 21]. The measurement concept is described schematically in Fig. 3.7. Equation (3.6) can be expressed in terms of the intensity measured in the external transfer line I_{ext}, the extracted intensity inferred from measurements of the circulating beam intensity in the machine I_{circ}, and the total beam loss signal summed over the BLM system:

$$\underbrace{k\frac{\sum \text{BLM}}{I_{\text{circ}}}}_{\bar{\epsilon}} = 1 - \underbrace{\frac{1}{C}\frac{I_{\text{ext}}}{I_{\text{circ}}}}_{\epsilon}, \tag{3.7}$$

where k and C are calibration constants. Once the calibration constants are determined empirically, the extraction efficiency can be measured online using the relationship

$$\epsilon \approx 1 - kC\frac{\sum \text{BLM}}{I_{\text{ext}}}. \tag{3.8}$$

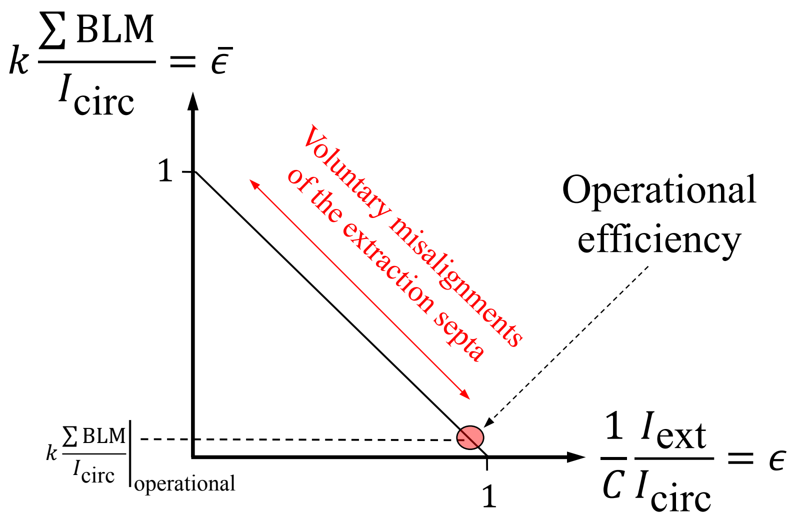

Fig. 3.7: FNAL efficiency measurement concept [20]

The alignment of the ES was deliberately skewed during dedicated measurement sessions with low-intensity extractions of approximately 2×10^{12} protons. The downstream end of the girder on which all five of the ES tanks sit was moved in steps to a maximum excursion of $\approx \pm 1.5$ mm, therefore rotating the septum by up to $\approx \pm 100$ µrad. The beam intensity in the extraction beam line was measured on a secondary emission monitor (BSI) composed of titanium foils and placed in the beam approximately 200 m downstream of the ES. The results of the measurement campaigns are summarized in Table 3.2. More recent measurements were also made in 2018, with similar results to the 2017 data; however, the results were less conclusive owing to several problems such as missing BLM signals during start-up due to a hardware electronics failure, incorrect gain settings of the BSI foils, and the limited machine development time available, with other higher-priority topics such as tests of the diffusers and extraction with octupoles taking precedence. These results and the difficulties encountered are documented in Ref. [22].

Table 3.2: SPS slow-extraction efficiency measurement results using BSI.210279

Year	BSI plate	Girder scan direction	k (10^{13} p$^+$ mGy^{-1})	C ($I_{\text{ext}}/I_{\text{circ}}$)	$\epsilon = 1 - \bar{\epsilon}$ ($\% \pm \delta_\epsilon$)
2016	A	All data	24.0 ± 1.2	0.66 ± 0.005	95.7 ± 0.8
	A	Towards outside ring	21.7	0.78	97.0 ± 0.6
2017	A	Towards inside ring	26.3	0.79	96.4 ± 0.7
	A	All data	23.8 ± 0.9	0.78 ± 0.005	96.6 ± 0.7
	B	Towards outside ring	21.3	0.94	97.1 ± 0.6
2017	B	Towards inside ring	27.0	0.93	96.4 ± 0.7
	B	All data	25.9 ± 1.0	0.93 ± 0.005	96.6 ± 0.7

An example dataset from 2017 is shown in Fig. 3.8, where an Ordinary Least Squares (OLS) regression analysis was performed alongside a Deming Regression (DR) (to account for errors in both scattered variables), plotted with the corresponding 1σ Confidence Level (CL) and Prediction Level (PL).

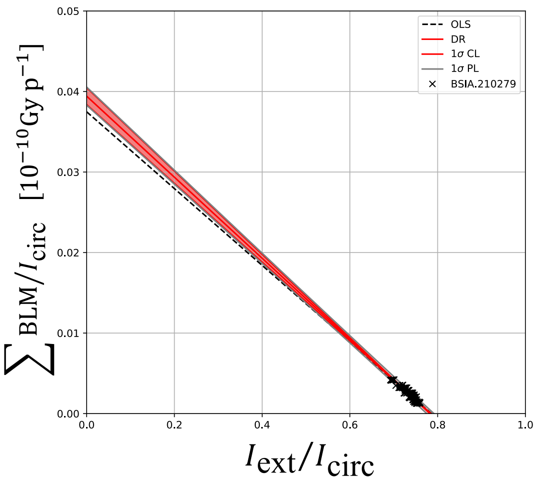

(a)

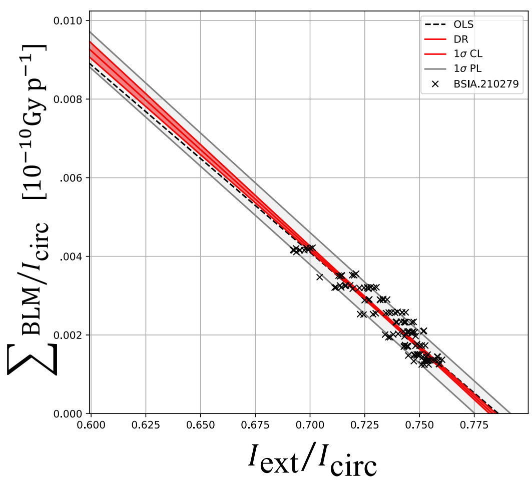

(b)

Fig. 3.8: Measurement data: BSIA.210279 taken in 2017. (a) Large extrapolation to determine $k = (23.8 \pm 0.9) \times 10^{13}$ p$^+$ mGy^{-1}. (b) Extrapolation to determine $C = 0.78 \pm 0.005$.

The inefficiency in 2016 was measured as $4.3 \pm 0.8\%$ and improved by 20% in 2017 and 2018. The measured inefficiency should be compared with the theoretical value of approximately 1.2% computed using MADX, *pycollimate* [23, 24], and FLUKA [25, 26, 27, 28] simulations with an ES set to an effective thickness of 200 µm. The empirical determination of k showed a strong dependence on the direction of the movement of the ZS girder, which is an indicator that the changing loss profile as measured on the BLM system is a source of non-linearity and systematic error. The error in ϵ quoted is an estimation based on the systematic variations observed in the girder scan direction, including a propagation of the errors from the regression analysis.

Unlike at FNAL, where a dedicated longitudinal (coaxial) BLM was installed on the ceiling of the accelerator tunnel, relatively far from and vertically above the beam line, no dedicated longitudinal BLM is currently available in LSS2. The BLMs are well distributed but located relatively close to the beam line, in the plane of extraction (horizontal) and biased by their position on the inside of the ring. FLUKA simulations have been launched to understand the dependence of the systematic errors in the measurements on the location of the BLMs in LSS2 [29]. There is a BLM on main quadrupole 218 in LSS2 that failed in 2017. Although it was replaced for the 2018 run, the BLM is saturated during high-intensity operation, affecting the measurement of the efficiency. These issues may systematically affect the efficiency measurements. An online measurement of the extraction efficiency will be implemented as part of the SPS quality control application.

3.2.2 Calibration of beam intensity monitors in the extraction and transfer lines

As a result of the measurements of the slow-extraction efficiency, large calibration errors in the transfer line intensity monitors were identified, which were far from guaranteeing an accuracy of a few per cent. The first results in 2016 identified a large discrepancy between the calibration of the monitor BSI.210279 located at the upstream end of the TT20 extraction line and the Beam Current Transformer (BCT) in the ring, i.e. $C = 0.66 \pm 0.005$. To complicate issues, the BSI assembly is composed of a stack of two measurement plates (A upstream of B) with a bias plate in between [30].

To further understand the discrepancy and the behaviour of the BSI, plate A was removed at the end of the 2016 physics run and installed in the TT10 transfer line between the PS and the SPS, where a fast BCT is available for cross-calibration purposes. The difference in the Secondary Emission Yield (SEY) due to the lower beam energy, which is a factor of $\sim$30 below the SPS extraction energy, is expected to be negligible. The BSI plates in TT20 were replaced by two new titanium plates, with a third, new plate installed at position B in TT10. The measurements in TT10 indicated that exposing the old plate to air during its displacement from TT20 to TT10 affected its SEY, which increased by about 10%. The calibration constant determined using the extraction efficiency measurements in LSS2 was confirmed by the TT10 measurements in 2017, although drifting of the SEY throughout the year was observed, as shown in Fig. 3.9. The measurements also confirmed a systematically higher signal by $\sim$15% measured on plate B compared with A, consistent with the LSS2 measurements, with the likely explanation being that secondary electrons generated on plate A reach plate B.

Work is actively ongoing to provide accurately calibrated intensity measurements in the extraction transfer lines, and a summary of the analysis can be found in Ref. [31]. For now, one must take the numbers recorded by the BSIs with caution and assume systematic errors on the order of 10–20%.

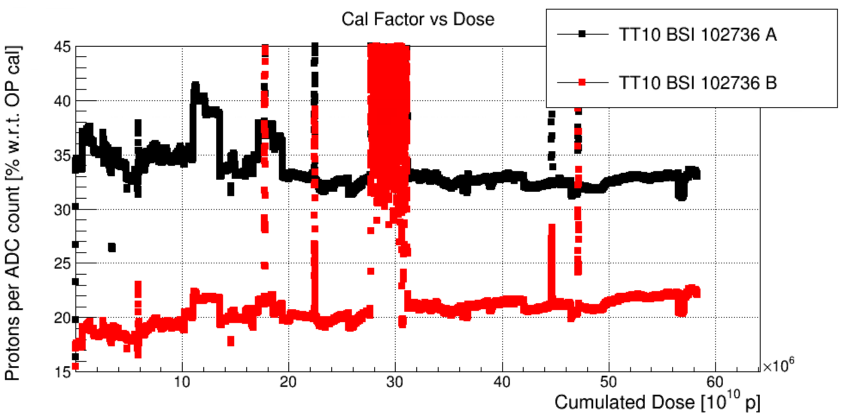

Fig. 3.9: Measured BSI calibration factors in 2017 [31]

3.2.3 ZS alignment

The alignment of the ZS has improved iteratively over the last few years as operational knowledge of the system has improved along with the required tools, both operational and simulation. An important improvement was to check the size of the extracted beam and its impact on beam loss on the cathodes of the ZS. For most of the last 2 yr of operation, the first two cathodes were retracted slightly to help reduce losses arising from this source, which helped in alignment and especially in reducing the loss contribution from particles scattered back into the machine and returning at large amplitude after three more turns of the synchrotron. The improvement is best illustrated in Fig. 3.2, where, since the 2015 physics run, the end-of-year Radiation Protection (RP) survey based on measurements close to the ZS 30 h after operation has improved year on year, and is now lying back on the historical trend as a function of total extracted flux.

3.2.3.1 Simulation of alignment procedures

The active length of the ZS is over 16 m and composed of five separate units, containing separate wire arrays that can be moved independently. The tanks are all mounted on a single support structure that can move the ensemble coherently. As a result, the large number of positional degrees of freedom complicates the alignment procedure in operation. Obtaining and maintaining accurate alignment with the beam is therefore crucial for minimizing beam loss. The particles impinging on the ZS are shown in phase space in Fig. 3.10(a), along with a sample of trajectories with misaligned anode wires and scattering in Fig. 3.10(b).

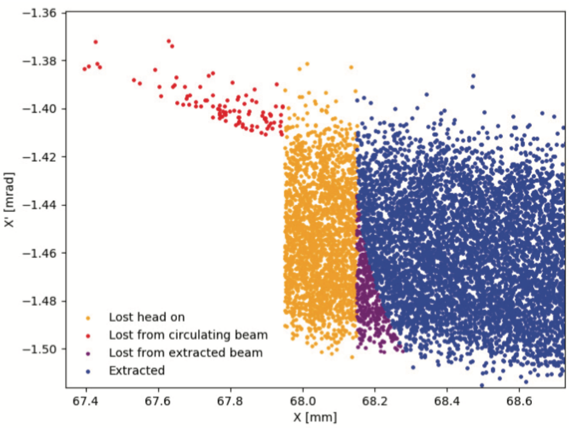

(a)

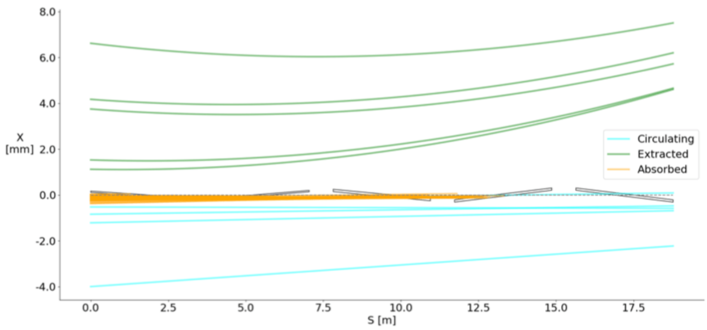

(b)

Fig. 3.10: (a) Phase space upstream of ZS and losses (black-body absorber model). Particles lost or extracted are shown for the nominal alignment with simplified ZS geometry (effective thickness 200 µm, no gaps between tanks) in the black-absorber approximation. Most particles are lost owing to non-zero wire thickness at the ES upstream (orange). The remaining losses stem from the angular spread of the beam, which occur downstream, from both the inside (purple) and the outside (red) of the ZS. (b) Particle trajectory (*pycollimate* scattering model) along the ZS. Particle trajectories along the ZS in the presence of scattering.

To understand and investigate the efficacy of different alignment procedures, particle-tracking simulations were carried out and the beam loss along the extraction straight section was computed as a function of the relative positions of each of the five separate ZS units. An important aspect of the study was to understand the alignment tolerance and motor precision required to achieve optimum extraction efficiency for a given configuration of wire-array thicknesses. The anode wires were taken as nominally designed, without imperfections, between 60 µm (tanks 1 and 2) and 100 µm (tanks 3–5) thick. The upstream and downstream ends of the anodes and the girder can be moved independently, yielding a total of 12 degrees of freedom. By fixing the upstream end of the girder and the first tank, together with the extraction bump amplitude, the spiral step (transverse extracted beam size) was kept constant, reducing the dimensionality of the problem to 10 degrees of freedom. Random misalignments between the tanks mean that the effective thickness of the anode wires is increased and the probability of particles being scattered and lost increases.

Simulations, such as FLUKA simulations or even multiturn tracking simulations with MADX coupled to *pycollimate*, demand a level of detail that is computationally very expensive. Given the relatively high dimensionality of our problem, simplified models are necessary to cut down the simulation time to reasonable values when running large batches of error seeds. To reduce the simulation time, a fixed particle distribution at the upstream end of the ZS was pre-computed by MADX and then sampled for every alignment error seed tested. Sampled particles were then tracked along the ZS, taking into account wire misalignments. Only the last three turns before extraction were simulated, giving a large speed-up in the simulation time. If a particle hit the wires, it was handed over to *pycollimate* to simulate the scattering process. Particles that were scattered back to the circulating side were then tracked around the ring until they were either extracted, absorbed by the ZS in an inelastic nuclear interaction, or lost somewhere on an aperture restriction. The tracking around the ring was done with a simplified lattice containing only linear elements and non-linear thin-lens extraction sextupoles. This scheme allows us to reduce the number of turns for which the particles are tracked by a factor of $\sim 10^4$, since the bulk of the work has to be done only once in MADX. The simulation code can be found on GitLab [32] and has been made in such a way that different custom or off-the-shelf optimizers can be easily plugged into the library.

Currently, the ZS tanks are aligned manually in a few 8 h shifts over the course of the commissioning period at the beginning of the operational year. In 2017 and 2018, once the alignment was adjusted and the losses were acceptable for high-intensity operation, the ZS could be kept in the same position throughout the rest of the year's operation.

The procedure is as follows. Once the slow extraction has been correctly set up with the orbit flattened in LSS2, and the extraction bump and sextupoles have been correctly scaled, the angle of the girder is scanned, while holding the upstream position constant. The position that yields the lowest losses, as measured by the LSS2 BLMs, is chosen. The alignment set-up of the ZS is carried out at low intensity to minimize the risk of damaging the septum and to minimize the induced radio-activation. Next, similar scans are repeated for all the anode motors, starting from the downstream end of ZS1, before moving onto the upstream end of ZS2 and moving downstream sequentially. The anode scans are then repeated until no improvement in beam loss is observed. The sum of the extraction losses in LSS2 during the alignment procedure over 6 h for a single iteration during the 2018 recommissioning is shown in Fig. 3.11 and compared with large-scale error study simulations with two different tolerances for the starting misalignment of the anodes.

Since the procedure is labour-intensive, requiring several dedicated sessions of about 8 h each, and the loss profiles for each scan are reproducible, the automation of the procedure was investigated. In addition, these studies were motivated by the pressure for physics time that severely limits the number of iterations that can be carried out. For example, it was evident that an algorithm exploiting the global structure of the problem instead of locally optimizing each degree of freedom would be of interest. Different optimization and alignment algorithms capable of yielding similar performance with faster

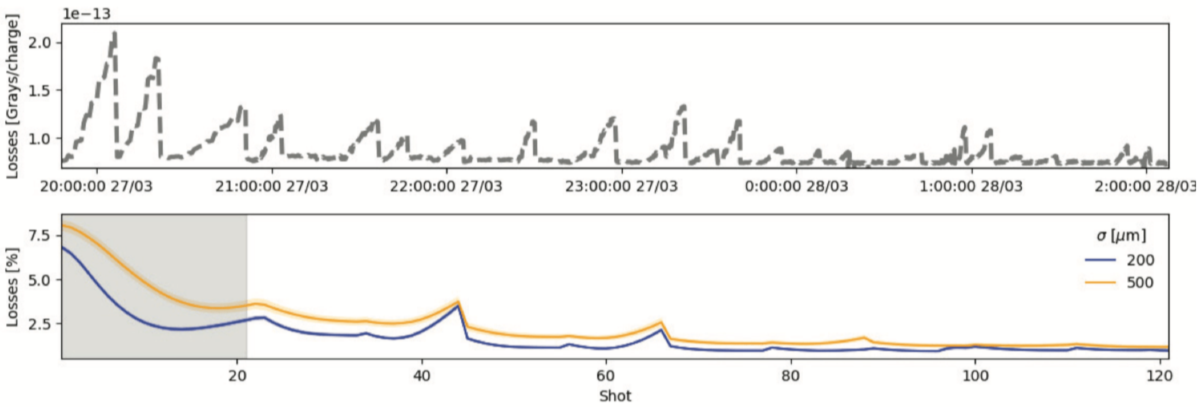

Fig. 3.11: Top: normalized BLM losses measured during the last alignment procedure over 6 h for a single iteration of alignment during 2018 recommissioning. The overall improvement was 31%. Bottom: 500 anode scan simulations with normally distributed initial misalignments. The average and 95% confidence interval of the losses is shown. The shaded area indicates the girder scan, with subsequent scans following ZS tank anodes 1–5.

convergence were investigated. A full summary of the study can be found in Ref. [33].

The current operational algorithm was simulated and compared with a gradient descent algorithm that computed the gradient of the loss function with respect to nine degrees of freedom by moving each ZS anode motor left and right by a given step size, with the upstream end fixed, as described in detail in Ref. [34]. At each iteration, all anodes were moved in the direction of greatest descent of the total loss function before repeating the gradient computation, with an exponentially shrinking step size. Each error seed drew its initial misalignments from a random normal distribution with $\sigma = 500\,\mu\mathrm{m}$. When studying motor errors, a random shift drawn from a normal distribution was added on top of the requested anode position. The results, summarized in Fig. 3.12, show the stark difference in the efficiency of the current operational procedure compared with the gradient descent algorithm, both in the number of shots needed for convergence and in the end scatter of the data. The results are highlighted by the improved clustering of the final positions of the anodes, summarized in Fig. 3.13.

3.2.3.2 Simulation with motor accuracy error

The simulations presented in Fig. 3.14 indicate that the required motor precision depends heavily on the type and efficacy of the alignment algorithm employed. The simulations indicate that for today's scenario a motor precision of 50 µm is sufficient, whereas the accuracy could be relaxed in the future should improved alignment algorithms be successfully deployed.

3.2.3.3 Simulation of higher-voltage ZS

It goes without saying that the fewer independent septum tanks that one needs to align, the simpler and more efficient the alignment procedure. In addition, if higher voltages could be applied, less material would be presented to the beam and the extraction efficiency would be significantly higher. This was demonstrated in simulations by increasing the voltage and extracting with just two ZS tanks, as is the case at J-PARC [33]. Although the improvement is dramatic, it is unfeasible when one considers that one would need electric fields surpassing 11 MV/m with voltages of over 500 kV. The electric field is limited by today's technology used for the large electrodes, and the gap sizes.

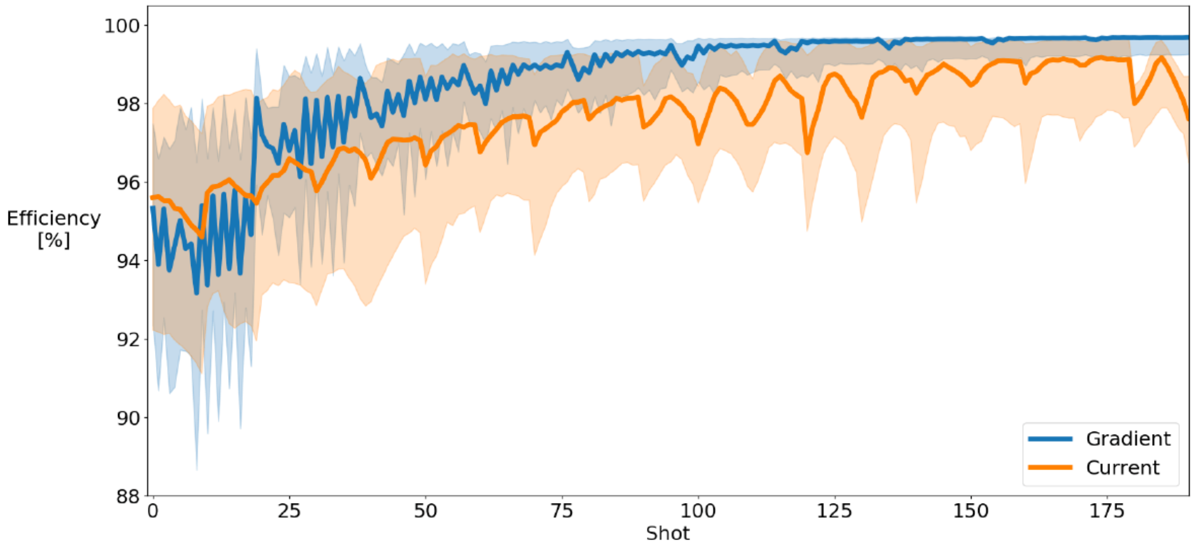

Fig. 3.12: Simulated evolution of the current operational alignment procedure compared with a gradient descent optimizer algorithm starting from random initial anode alignments with $\sigma = 500\,\mu\mathrm{m}$. The median and 90% confidence interval of the error seeds are plotted.

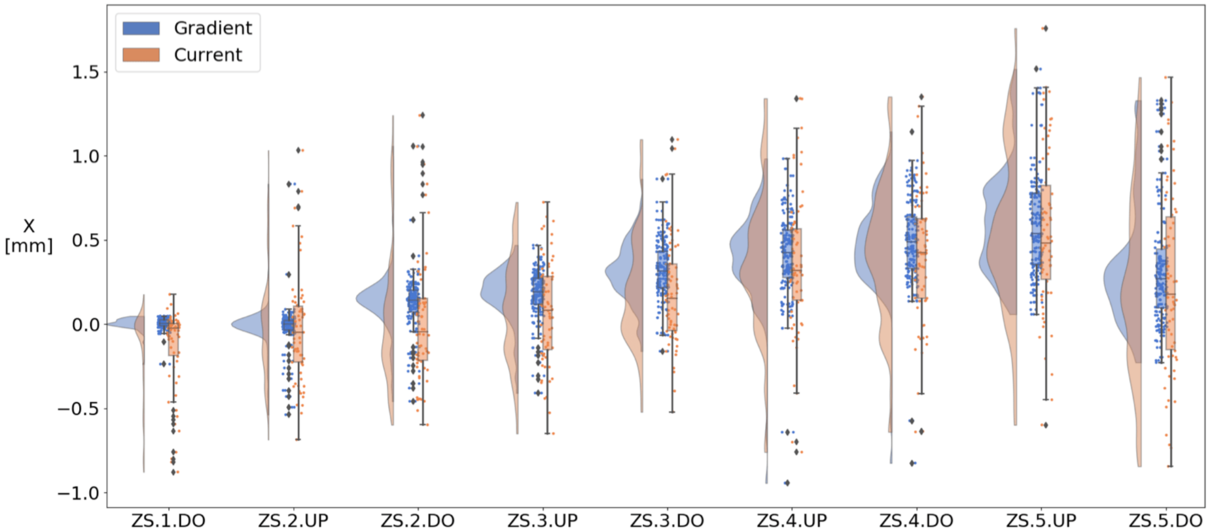

Fig. 3.13: Simulated ZS anode positions at the end of one iteration of the current operational alignment procedure compared with a gradient descent optimizer algorithm starting from random initial anode alignments with $\sigma = 500\,\mu\mathrm{m}$.

3.2.3.4 Operational implementation of an automatic ZS alignment procedure

In a recent beam test, an operational optimizer based on a Powell optimization algorithm was applied to the ZS alignment problem. The septum was successfully aligned in about 40 min of beam time and about 130 shots, reducing the time needed by over an order of magnitude. The optimizer acted on the nine degrees of freedom while observing and minimizing the normalized losses of all BLMs in LSS2. Future studies will concentrate on algorithms which memorize (speeding up full alignment to a few cycles) and possibly generalize the automation via reinforcement learning. These first promising results, reported in Ref. [35], give us confidence that the septum can be aligned far quicker in the future and potentially with a better extraction efficiency. Further beam tests are needed to understand the improvement of the

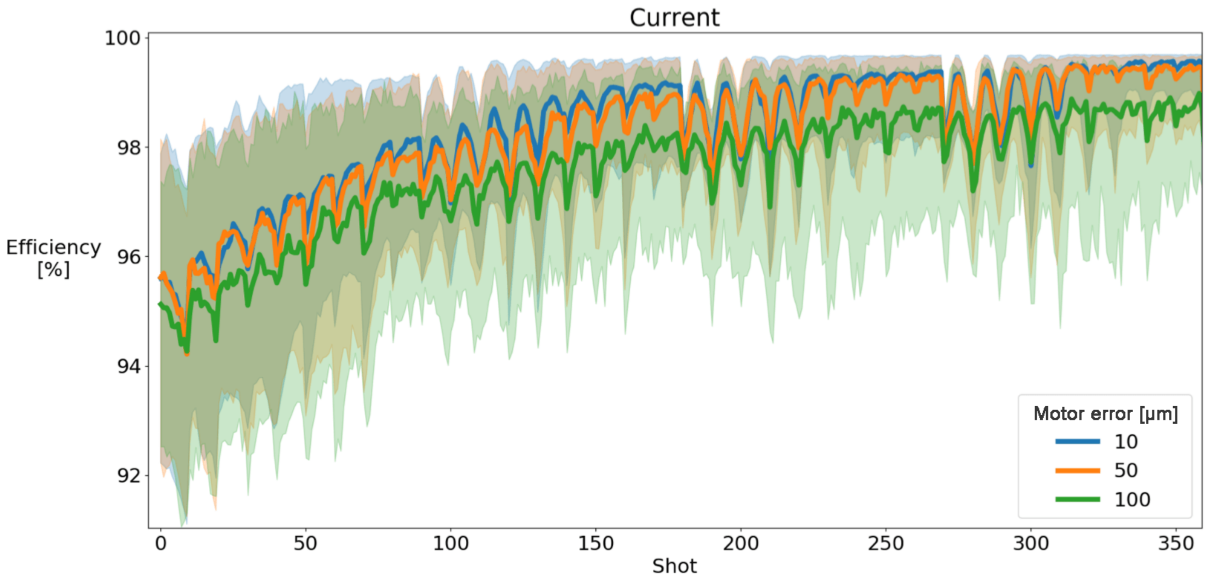

(a)

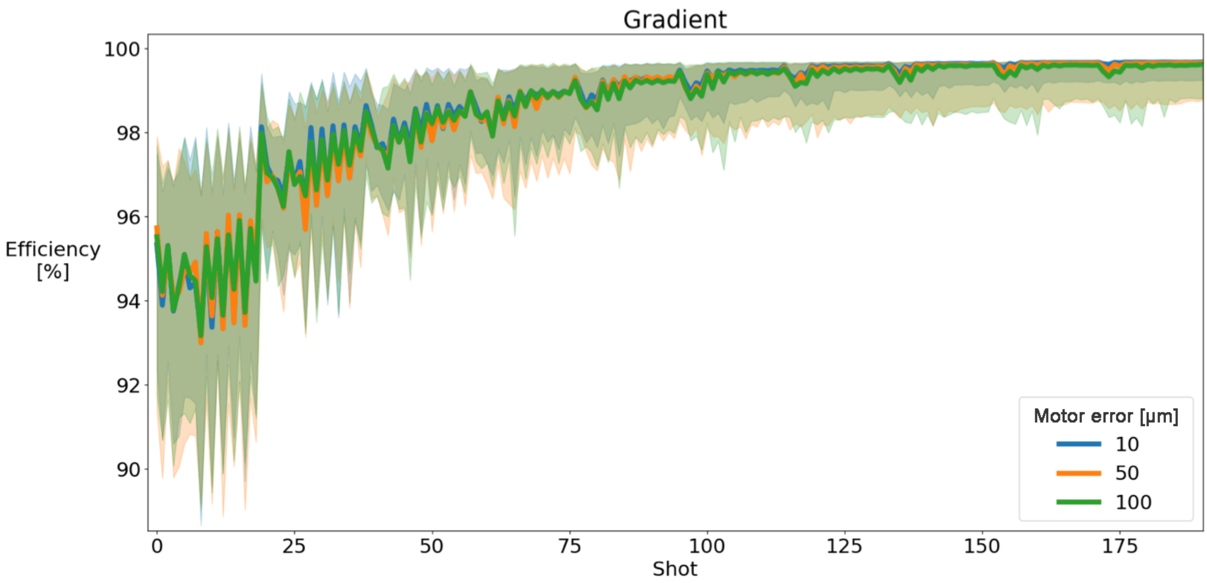

(b)

Fig. 3.14: Simulations of the alignment procedure in the presence of different random motor errors. (a) Simulated evolution of the current operational alignment procedure including random motor position errors of different magnitude. (b) Simulated gradient descent optimizer including random motor position errors of different magnitude.

extraction efficiency that can be obtained with a dedicated optimization algorithm, as well as to assess the role of noise in the optimization.

3.2.4 Impact of bunched beam extraction on extraction efficiency

To provide slowly extracted beams with a time structure on the order 5–100 MHz, the RF system of the SPS must remain on to keep the beam bunched during the extraction. Because of the non-zero chromaticity used in the present extraction scheme, the resulting synchrotron motion induces a tune modulation in a similar way to a strong ripple on the current of the main power converters [36]. The difference in this case is that the tune modulation is not coherent; the modulation frequency and phase of each particle depend on its initial location in the bunch (longitudinal action and angle). In recent simulations of the extraction efficiency, the extracted beam emittance and spill quality for a 5 ns bunch structure with an RF voltage of 7 MV was investigated and is summarized in Fig. 3.15. The spill quality degrades, with a duty factor of $F = 0.55$, with the spill length effectively halving. This is because particles undergoing synchrotron motion visit the lower half of the bucket every $\sim$40 turns. As the tune sweep progresses in momentum from the lower tip to the centre of the RF bucket, virtually every particle will have the chance to become resonant and be extracted. Thus, when the sweep reaches halfway and matches on-momentum particles, the extracted intensity drops as all particles have been pushed through resonance by their synchrotron motion. The tune sweep can be easily adjusted for the bunched case.

A threefold increase in the extraction inefficiency was observed. This can be attributed to the higher angular spread of the extracted beam at the ES. As in the case of ripple, particles coming in and out of resonance do not follow clean trajectories along the separatrix.

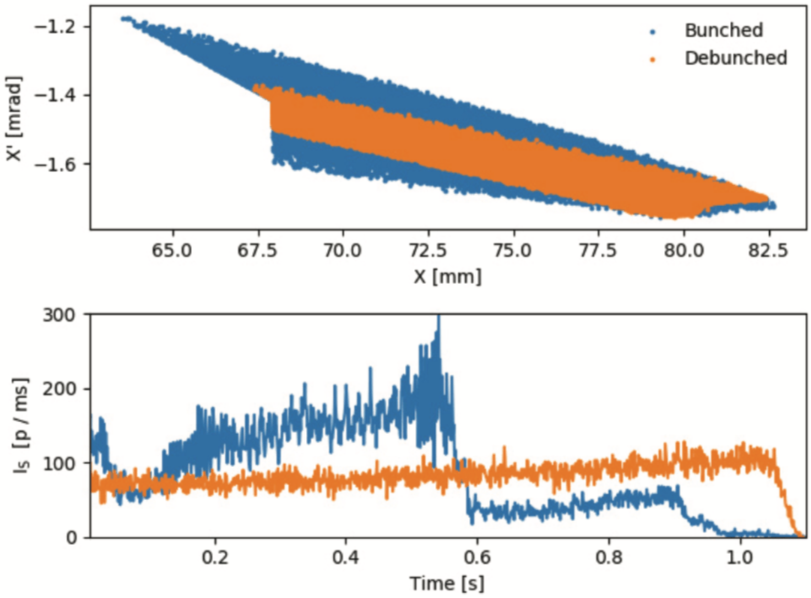

Fig. 3.15: Comparison of debunched and bunched (V_{RF} = 7 MV) chromatic extraction. Top: horizontal phase space at the extraction point, showing particles lost on the ZS or extracted. Bottom: spill rate.

Slowly extracted beams have been provided to the NA in the past for irradiation tests of LHC components with a 25 ns bunch structure. However, the extraction inefficiency was reported to be as much as 10 times worse, limiting the intensity that could be delivered. For experimental requests with a larger bunch spacing than 5 ns, e.g. 25–100 ns, the extra cycle time required in the PS to carry out the required RF manipulations will have a severe impact on the duty cycle in the SPS.

These results highlight the need to fundamentally rethink the extraction scheme in the face of experimental requests for beam with a megahertz time structure. Other extraction schemes are a matter of ongoing study, but they have their own shortcomings. For instance, a similar scheme with near-zero chromaticity has been shown to reduce the angular spread of the extracted beam; however, this comes at the cost of having to make a slower tune sweep, thus increasing the sensitivity to ripple. Possible ways of smoothing the spill with zero chromaticity by applying transverse RF noise were successful in beam tests in 2018 and will be investigated further.

3.2.5 FLUKA modelling of LSS2 beam loss profile

An extensive FLUKA model of the SPS LSS2 was developed to study the energy deposition in the beam line elements and evaluate the response of the BLMs as a consequence of the protons lost during the slow extraction process. The model, shown in Fig. 3.16, consists of:

- all beam elements from QFA.216 to QDA.219, including the electrostatic septa (ZS), the magnetic septa (MST and MSE), the bumper magnets, and the beam-intercepting devices (TCE and TPST);
- the SPS BLMs;
- a detailed description of the aperture of the beam line elements;
- the time-constant magnetic fields of the quadrupoles, MST, and MSE;
- the electric field of the ZS, emulated by an equivalent magnetic field.

The ZS wires are modelled as a 200 μm thick WRe ribbon with a scaled density (to maintain the same mass as the real wires) and are perfectly aligned along the five ZS tanks. It was checked that the modelling of the wire array as a scaled-density ribbon did not change significantly the loss pattern with respect to a case where each single wire was modelled.

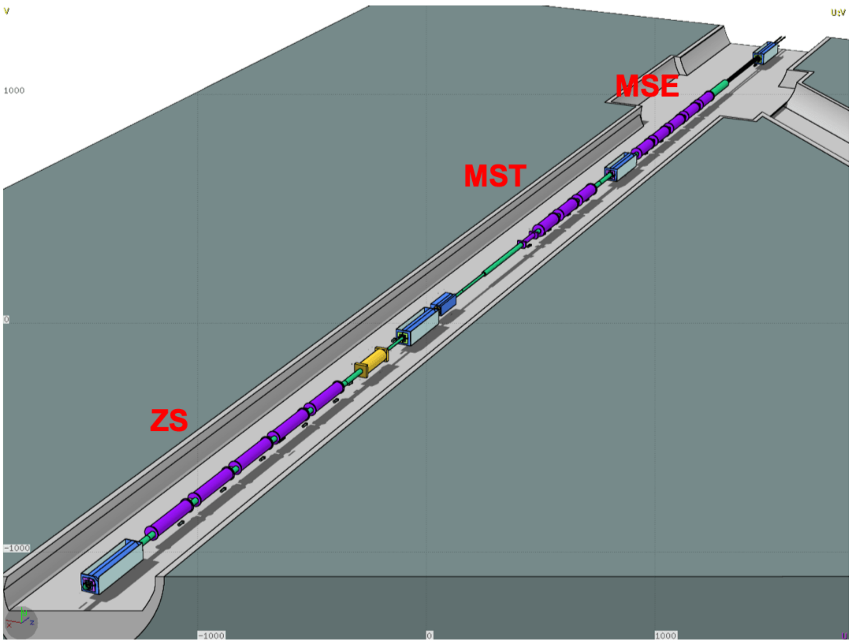

Fig. 3.16: FLUKA model of the SPS-LSS2. The geometry extends from QFA.216 to QDA.219

The proton distribution used as the source term for the FLUKA calculations is computed by MADX tracking, and the last four turns for each particle are given at a position upstream of the ZS. Two distributions were used:

- the first, referred to as the *black* distribution, where the ZS wires are treated as black absorbers, i.e. any proton hitting the ZS wire is not transported any more;
- the second, referred to as the *full* distribution, where the MADX tracking is linked to *pycollimate* [24]. In this case, a proton scattered by the ZS wires is tracked for additional turns until it is extracted, hits the vacuum chamber aperture, or undergoes a nuclear interaction in the ZS.

Figure 3.17 compares the measured pattern of the BLMs installed in the SPS LSS2 with that simulated by FLUKA. The simulated losses along the ZS are mainly due to the single-pass effect and are a factor of three below the measured values. The losses at TPST and QFA.218 are, instead, due to protons scattered by the ZS that make additional turns in the SPS.

The inefficiency of the slow extraction process, defined as the number of protons lost divided by the number of protons extracted towards TT20, is 0.7% and 1.2% for the *black* and *full* distributions, respectively.

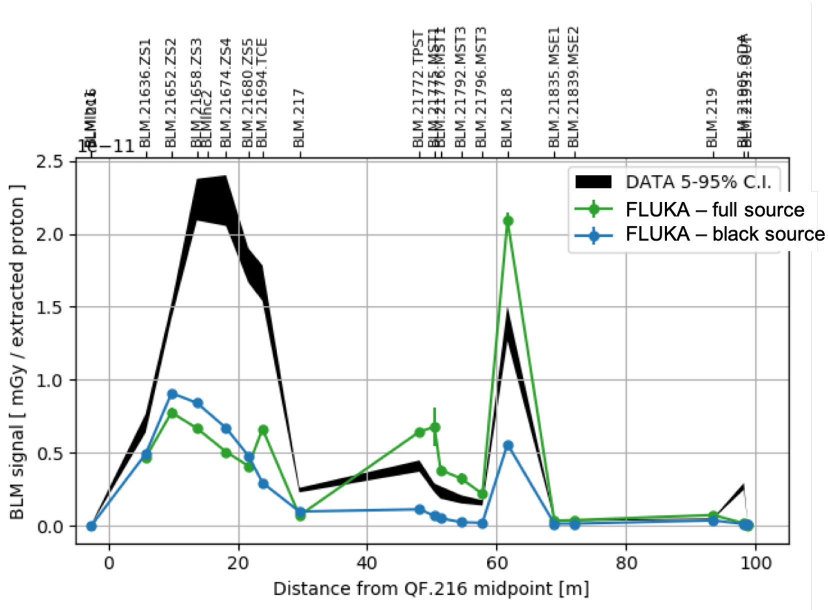

Fig. 3.17: Normalized loss pattern of the SPS LSS2 BLMs. Black: measured data from 15 to 18 April 2018. BLM responses computed by FLUKA using the *black* distribution (blue) and the *full* distribution (green) are also shown. BLM.21694.TCE was misplaced in the geometry model used with the *black* distribution. For this reason, its signal is increased by a factor of two.

The relative energy deposition in the ZS wires is shown in Fig. 3.18, which reports also the corresponding temperature increase. The latter was computed to a first approximation by assuming a constant specific heat capacity and considering no mechanism of heat transfer. For a perfectly aligned geometry, the peak is located at the beginning of the upstream end of the wire array, while the downstream wires are in their shadow.

As an illustration of the effect of wire misalignment, loss patterns with different effective thicknesses of the wire ribbon (the uniform ribbon density is scaled accordingly) are compared in Fig. 3.19. The measured loss pattern along the ZS matches the simulation when the wire ribbon is ∼800–1000 µm thick. At the same time, the losses at TPST and QFA.218, due to the protons scattered off by the ZS, are clearly overestimated. It should be pointed out that ribbon is assumed to be straight and therefore aligned. Recent studies have shown that coherent deformation of the anode support holding the wires worsens the inefficiency compared with the ribbon approximation. The computed inefficiency of the slow extraction process is 3.1% and 3.9% for an 800 and a 1000 µm thick wire ribbon, respectively, consistent with recent measurements giving $3.4 \pm 0.7\%$ [22]. Further investigations are ongoing to assess potential coherent misalignments of the wires and the interplay between the scattering of protons off the ZS and multiturn effects.

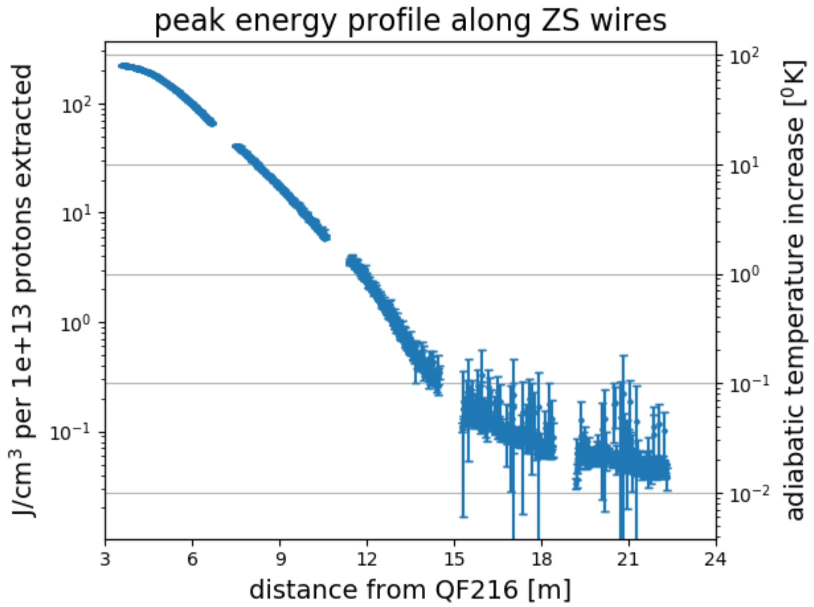

Fig. 3.18: Energy density profile along the ZS wire array normalized to 10^{13} protons extracted. The right vertical axis indicates the corresponding adiabatic temperature increase.

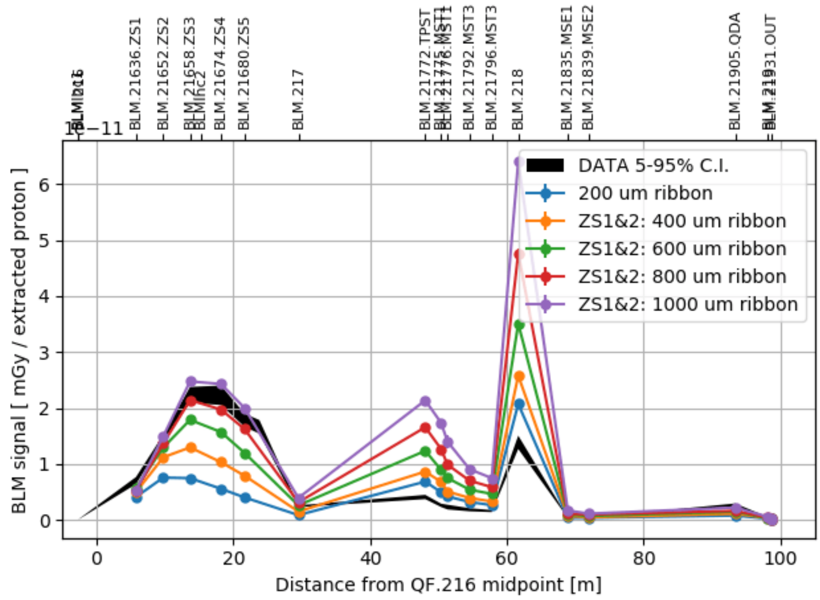

Fig. 3.19: Energy density profile along the ZS wire array for different ribbon thicknesses

3.3 Extraction loss reduction techniques

3.3.1 Constant-optics slow extraction

As described above, the SPS slow extraction is a quadrupole-driven chromatic extraction. The machine tune is changed in time during the spill to extract particles with increasing momentum as a function of time. In the SPS, this has been done by ramping the main quadrupoles to change the horizontal tune, and this is referred to as the Q-sweep method in this document. As the rest of the machine's elements are stationary during the spill, the optics seen by the particles with the resonant tune are different from the nominal optics, changing the presentation of the separatrix as a function of momentum, i.e. time. The imperfect overlap in time of the extraction separatrix actually results in an increase in the angular spread of the beam at the ZS entrance, which also results in a higher number of particles that intercept the ZS, i.e. losses. The change of optics with time also means that the phase advance between the ZS and the resonance-driving term are different (see Fig. 3.20), as well as the beta-beating and the variation of the natural chromaticity. The concept and results briefly discussed in this section can be found published in more detail in Ref. [37].

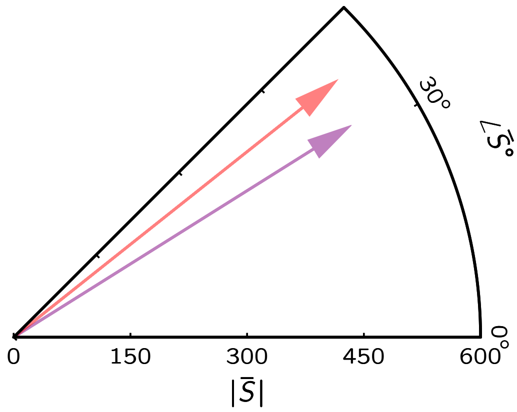

Fig. 3.20: Schematic view of the evolution of the resonance-driving term in time (violet is for $t = 0$ and red is for $t = 4.8\,\mathrm{s}$).

3.3.1.1 *Dynamic bump*

In order to keep the extracted separatrix at the same phase space location at the ZS, the first idea was to directly act on the position and angle of the beam. This could be done using orthogonal independent steering bumps, for angle and position, with time-varying amplitudes to follow the beam variations, as implemented already at the J-PARC Main Ring [38]. Theoretical studies and experimental tests were carried out, showing the ability to act on the beam presentation at the entrance to the ZS wires over time. Although a possible reduction in the order of 10% was predicted in simulations, it was never experimentally confirmed [39]. The machine tests only highlighted the operational complexity of the dynamic bump concept at the SPS. The beam presentation change at the electrostatic septum was identified as coming from the variation of the machine optics during the spill. Eventually, it was realized that the SPS control system offers the possibility to eliminate the optics change without applying dynamic bumps.

3.3.1.2 *Implementation at SPS*

The SPS is operated by controlling high-level parameters thanks to its control infrastructure, the so-called LHC Software Architecture (LSA) [40]. The LSA offers the ability to work in physics parameters, e.g. the tune (Q), the machine momentum (p), the charge (q), etc. The framework takes care of translating these into hardware settings such as voltage or current. The spill structure of the slow extraction in Q-sweep mode is optimized by acting directly on the horizontal tune parameter. All magnetic parameters in the SPS are defined normalized to p/q in the control room tools, where $q = 1$ for protons. The p-parameter links the defined normalized magnetic strength with the required magnetic field and current (by applying the calibration function).

To drive chromatic slow extraction, either the machine tune is varied to select the resonant particles according to their tune (Q-sweep) or the machine tune is adjusted to the resonant value for the particle with the lowest momentum, and then the p-function is increased accordingly to extract all other momenta across the beam's momentum distribution. For the latter, the machine tune and the entire machine optics stay constant for the particles on resonance. This is the concept of COSE. Figure 3.21 shows the resonant driving term with COSE. It does not change any more with time, as the optics are frozen during the extraction process. Locking the optics during the spill results in an overall reduction of the angular spread of the separatrix at the ZS wires of about 20% in simulation, from 12 to 9.5 µrad as shown in Fig. 3.22. This should also result in a loss reduction at the ZS.

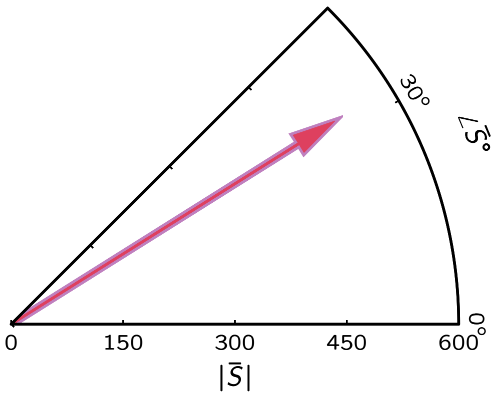

Fig. 3.21: Schematic view of the evolution of the resonance-driving term in time (violet is for $t = 0$ and red is for $t = 4.8\,\mathrm{s}$) for COSE. The two arrows overlap.

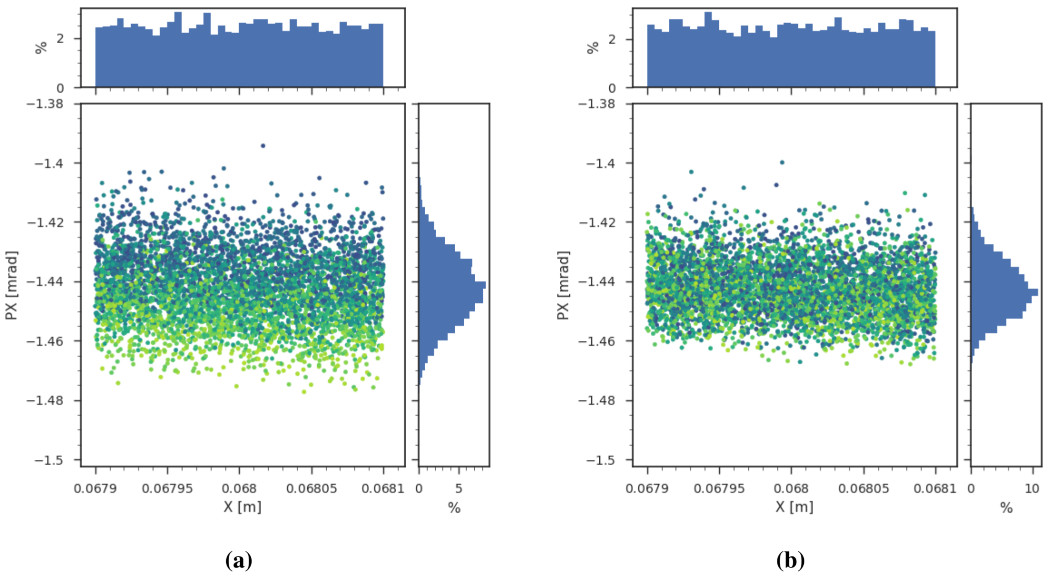

Fig. 3.22: Simulated angular spread of the beam presented to the ZS wires across a 200 µm thickness. (a) Q-sweep ($\sigma_{x'} = 12\,\mu\mathrm{rad}$). (b) COSE $\sigma_{x'} = 9.5\,\mu\mathrm{rad}$.

Several low-intensity MD studies were dedicated to detailed studies of COSE and the preparation of an operational procedure for its deployment during the 2018 run. During these studies, no clear loss reduction was observed compared with the Q-sweep method, but, owing to its operational simplicity and elegance and as a prerequisite for other loss reduction schemes, it was deployed on the operational cycle for beam to the North Area targets in September 2018. A comparison between 10 days of operation with Q-sweep and COSE in terms of extraction losses was carried out. A slight reduction of losses of approximately 5% was observed when comparing periods with similar PoT delivered and duty cycle.

Also, no increase in overall losses around the machine was measured. More systematic studies will be required to conclude whether or not the apparent loss reduction was a direct consequence of the implementation of COSE. For example, changes in the relative alignment between the ZSs could account for loss differences before and after the implementation of COSE after the technical stop; the ZS girder was not aligned before the switch, and girder alignment was performed right after the deployment of COSE.

3.3.2 Passive diffuser (wire array)

A passive diffuser, or pre-scatterer, in a suitable configuration has been predicted to reduce beam loss on the ES significantly, with the actual gain factor depending on the parameters and details of the extraction process and hardware. In this section, the optimization of diffuser configurations is investigated for the SPS, and the sensitivity to the available parameters explored via simulation results. The design, construction, and installation of a prototype diffuser are described, together with the experimental results obtained from its use in the SPS. The expected performance gain for an optimized design is discussed and quantified by simulation, in view of the experimental results obtained.

3.3.2.1 Concept and theoretical potential

A diffuser, as initially postulated by Durand [41], is a promising approach to reducing the performance-limiting beam loss at the ES in the SPS [42]. The scatterer generates an angular spread in the particle distribution, which reduces the transverse density at the septum wires and can result in an overall beam loss reduction. This technique has been used at CERN in the PS and is under study for SHiP [42, 43], and also for the Mu2e beam from the Fermilab debuncher [44, 45].

The distance of the diffuser from the septum entrance determines the extent to which the angular scattering is translated into a positional spread at the ES. Small distances, corresponding to only a few degrees in betatron phase, have been tested, in a local configuration with the diffuser in the extraction bump. Much larger phase advances may be advantageous in a non-local configuration, with the added complexity of needing a second bump system at the diffuser's location elsewhere in the SPS.

The diffuser works because the main loss source is particles traversing the ES with a small impact angle. A small scattering angle upstream of the ES produces a spread in the particle positions at the ES, illustrated in Fig. 3.23. If this spread is large enough, an overall reduction in beam loss is produced, provided that the additional losses induced by the diffuser itself remain small.

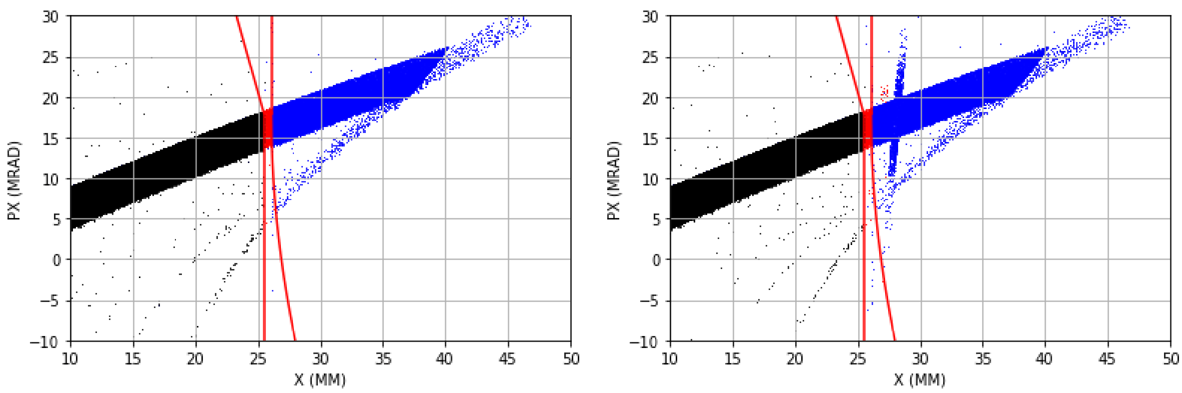

Fig. 3.23: Separatrix (in normalized phase space) with lost (red) and extracted (blue) particles at ZS without (left) and with (right) a diffuser placed at a phase advance 4° upstream. The diffuser here is not at the optimum alignment to shadow the ZS. The coordinates of particles lost at the diffuser are also plotted.

The required r.m.s. Multiple Coulomb (MC) scattering angle θ_{MC} can be estimated by assuming that the diffuser has negligible length and that the ES losses are proportional to the ES hits. The position spread at the septum is

$$X_{\mathrm{ES}} \approx \beta_x \sqrt{(\mu_x^2 \theta_{\mathrm{MC}}^2 + w_s^2/12)}\,, \tag{3.9}$$

for a phase advance μ_x, a diffuser width w_s, and a beta function at the ES and diffuser β_x.

With the 4° of phase advance available for a realistic diffuser location in the SPS, a factor of two loss reduction is possible for a scattering angle of $\approx 30\,\mu\mathrm{rad}$. Clearly, compared with a crystal, the incoherent diffuser suffers because the peak density of the scattered particle distribution is always at zero scattering angle and aligned with the ES, so that a large scattering angle is needed to produce a significant loss reduction factor. The material length of the diffuser needed to produce the given scattering angle is crucial for the overall loss reduction factor, which depends on the number of nuclear interaction lengths of material.

For the diffuser, the ratio of the radiation length X_0 to the nuclear interaction length λ_{I} should be small, since a large λ_{I} minimizes loss through nuclear scattering, while a short X_0 maximizes the MC scattering angle.

A comparison of the materials considered and the lengths needed to achieve a 30 µm r.m.s. scattering angle with a momentum of 400 GeV/c is shown in Table 3.3. The total loss includes all protons scattered inelastically, and those scattered elastically by more than 0.5 mrad.

Somewhat counter-intuitively, denser materials are actually significantly better for the SPS. The use of a dense diffuser such as $W_{75}Re_{25}$ (widely used for ES wires) can provide over a factor of 10 gain in the loss per impacting proton at the diffuser itself (for the length needed to generate a specific MC scattering angle), compared with materials with a lower atomic number such as carbon.

Table 3.3: Diffuser length and loss fraction for $\theta_{\mathrm{MC}} = 30\,\mu\mathrm{m}$

Parameter	$^{9}_{4}$Be	$^{12}_{6}$C	$^{28}_{14}$Si	$^{96}_{42}$Mo	$^{181}_{73}$Ta	$^{184}_{74.3}$($W_{75}Re_{25}$) alloy
ρ (g/cm^3)	1.8	2.0	2.3	10.2	16.7	19.7
λ_{n} total (cm)	29.9	29.6	30.2	9.1	6.6	5.6
λ_{I} inelastic (cm)	42.1	42.9	46.5	15.3	11.5	9.8
X_0 (cm)	35.3	21.4	9.4	0.96	0.41	0.35
Length (cm)	26	16	7.0	0.70	0.32	0.26
θ_{e} (µrad)	237	215	162	108	87	87
Inelastic loss (%)	46	31	14	4.5	2.5	2.6
Total loss (%)	56	40	19	6.4	3.6	3.7

3.3.2.2 Mechanical design of prototype diffuser

For the demonstration tests of the SPS prototype diffuser, the local shadowing option with the diffuser installed close to the ES was selected as being the most straightforward to integrate and to test with beam. A suitable location in the SPS lattice was identified (Fig. 3.24) and the diffuser specification was developed with the help of particle-tracking simulations.

A prototype diffuser was built in collaboration with the Wigner Institute, Hungary. A single degree of freedom was used, for translation of the wires in and out of the beam, using a precision screw driven by a stepping motor permitting a step size of 10 µm. Tantalum wire of diameter 0.2 mm was chosen for the diffuser material; the ⌀ 0.2 mm wire is much more malleable than similar-thickness WRe and could be mounted with good straightness. Its performance, as specified in Table 3.3, is almost identical to that of WRe in terms of the loss produced for a given scattering angle. The mounted wire array had a 0.26 mm effective thickness, which was obtained by offsetting half of the wires. The mechanical design of the device is shown in Fig. 3.25.

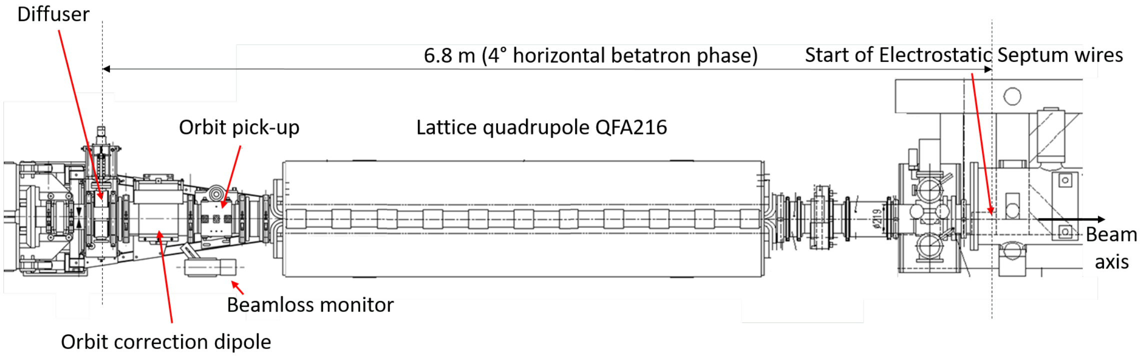

Fig. 3.24: Integration of prototype diffuser in SPS, upstream of the electrostatic septum and focusing lattice quadrupole (QFA.21610).

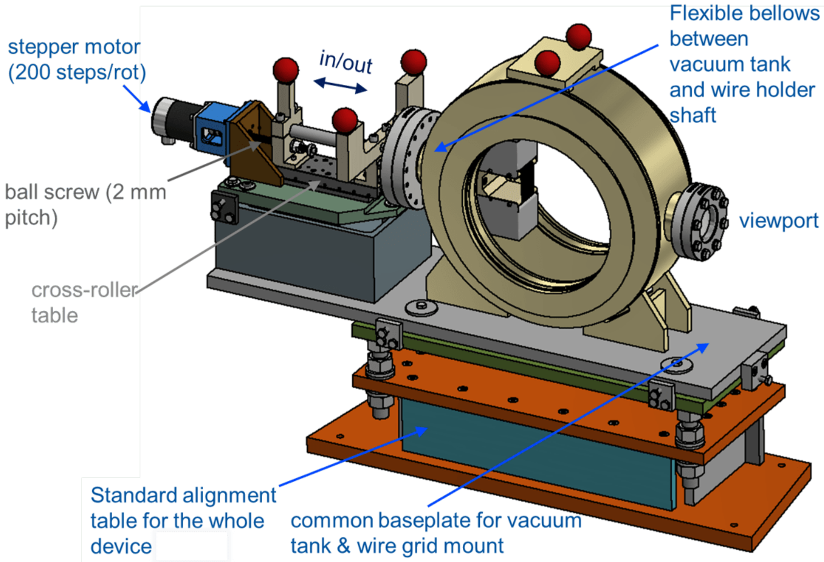

Fig. 3.25: Prototype diffuser installed in SPS. The device has 20 Ta wires of diameter 200 µm, aligned in two halves with a 60 µm offset, and spaced by 1.5 mm over a total length of 30 mm.

3.3.2.3 Summary of main results of machine development and operational tests

A series of tests were done in 2018 with simple scans of the diffuser position in front of the ZS wires, initially with a low-intensity beam of 2×10^{12} protons per spill. The results were highly reproducible, with a reduction in the overall beam loss on the ZS (summed over all extraction BLMs) of 15% compared with extraction with no diffuser. A typical loss response profile is shown in Fig. 3.26, compared with simulation results. There is very good agreement with the simulation in terms of the simulated loss reduction and the side features of the profile for a ZS width of 0.6 mm, which is significantly larger than expected (the wires of the first ZS are only 0.06 mm in diameter). The specified positioning accuracy of the diffuser's wire array of $\pm 50\,\mu$m was confirmed to be necessary, and attainable.

The diffuser was also deployed for a 23 h period on the operational beam to the NA, with an intensity of 3×10^{13} protons per spill. After the beam was inhibited, it took 3 min to move the diffuser to the operational position and a further 22 min to optimize the position with respect to the beam. No issues were seen during this longer test period, although the extraction loss reduction factor was slightly lower, at 10%. A total of 1.2×10^{17} protons were extracted with the diffuser in beam. A period of 2 h each side of the insertion where the SPS was in stable operation with no supercycle changes or LHC filling

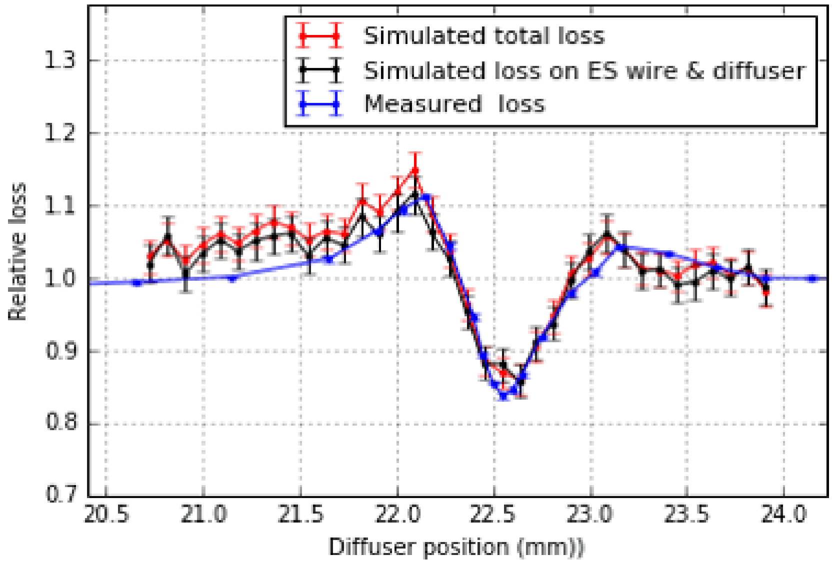

Fig. 3.26: Measured diffuser response (total loss in extraction region) compared with simulation using 0.6 mm ZS thickness.

was analysed; see Fig. 3.27. There was a short initial period of outgassing where the vacuum pressure increased from 1×10^{-8} to 2×10^{-7} mbar, but it recovered within about 15 min. No re-alignment of the ZS girder was possible, and further optimization to the 15% gain may have been possible.

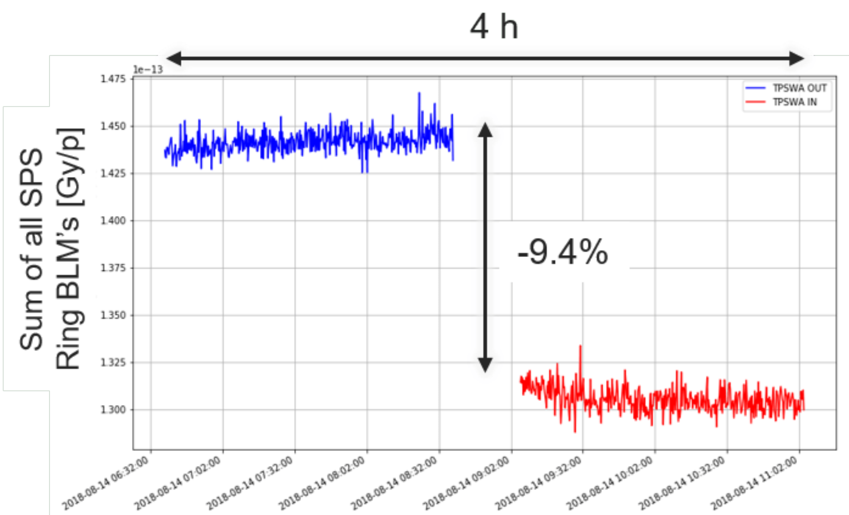

Fig. 3.27: Total SPS beam loss (integral over BLMs around the full ring) for a 4 h period spanning the insertion of the prototype diffuser into the operational beam.

3.3.2.4 *FLUKA simulations of the diffuser*

The response of the BLMs to the linear scan of the diffuser was measured during MD time and compared with the FLUKA model, discussed in more detail below. Despite the difference in the absolute comparison, as was indicated in Fig. 3.17, the functional pattern is fairly well reproduced and, in particular, the height and width of the loss dip are in reasonable agreement with the experimental observations. Figure 3.28 compares the measured loss response with the FLUKA simulation and the sum of the six BLMs along the ZS and TCE, where the data are normalized to the same minimum value found empirically.

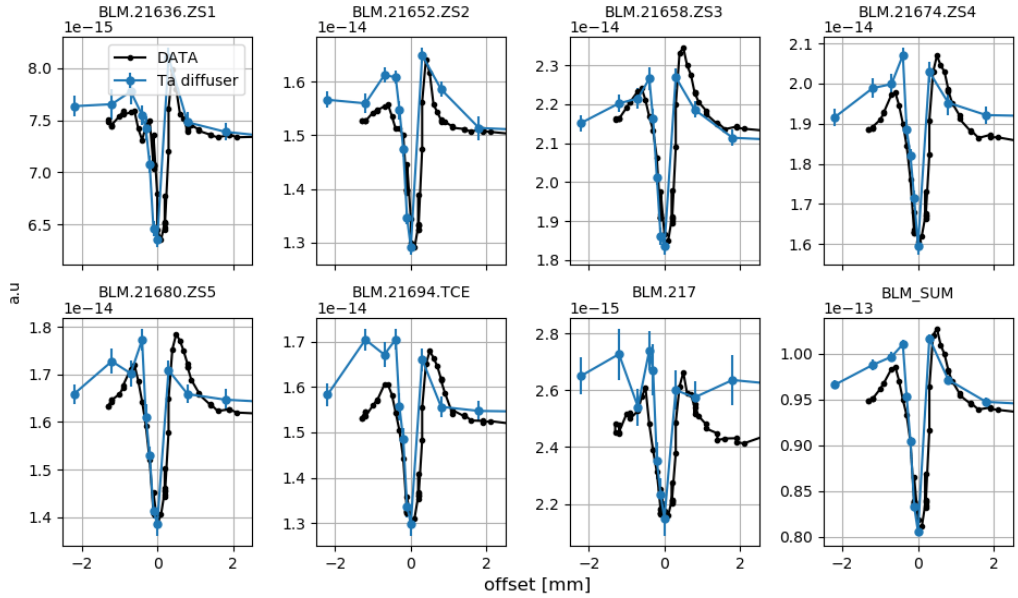

Fig. 3.28: Relative comparison of the signal of the BLMs along the ZS, TCE, and QF.217 measured as a function of the diffuser position with the result of the FLUKA simulation. The bottom right plot displays the sum of the signals of the five BLMs along the ZS and the TCE. The simulation points are normalized to the minimum value of the experimental data.

The response of BLM.216, which is located near the diffuser, is sensitive to the linear density of the extracted beam. For this BLM, the FLUKA estimation of the signal per extracted proton is $\sim$15% systematically higher than the measured signal. Figure 3.29 shows the experimental data and the results of the simulation. This figure also shows a curve obtained with a high-statistics run (with about 100 times the number of events) but with the model geometry including only the diffuser and BLM.216 in order to speed up the computing time and investigate the statistical convergence of the observable. The systematic difference in the signal of BLM.216 may stem from an incorrect calibration factor. In the simulation, the conversion from the energy deposited in the active gas volume of the BLM to dose is computed using the mass of the gas, and the same factor is applied to all BLMs. Therefore, the factor of three in the underestimation of the losses at the ZS by the FLUKA simulations is not compatible with a systematic error, but is likely to originate from effects that increase the effective thickness of the septum that have not yet been taken into account in the simulation model.

3.3.2.5 Issues and challenges observed

The increased beam loss at the location of the diffuser is a concern, since this zone is a ‘low-dose’ area used for access during interventions on the much more radioactive ZS. The dose at this location with the diffuser in beam measured on the BLM on quadrupole 216 was indeed observed to increase by a factor of 7.5. Although the expected remnant dose at the diffuser is expected to be more than an order of magnitude less than at the ZS, this increase in this previously low-radiation area needs to be taken into consideration in the overall optimization.

3.3.2.6 Outlook for design of operational device

The key parameter for an operational device is the effective ZS width, as seen from Fig. 3.24, and is estimated as approximately 0.6 mm, while from the results with the crystal a width of 0.5 mm was derived. The diffuser width needs to be matched precisely to this value to obtain the optimum loss

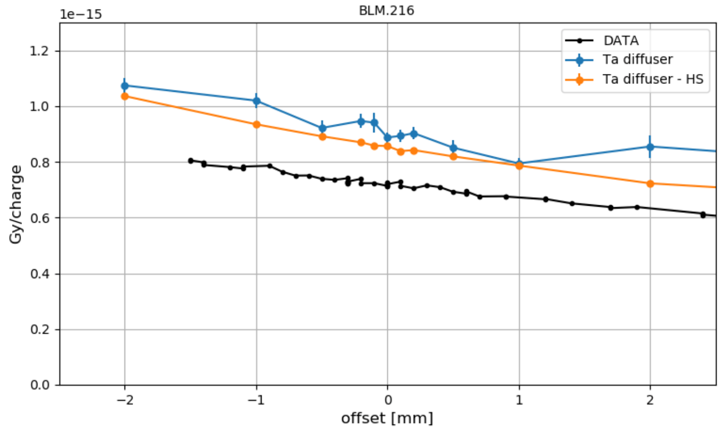

Fig. 3.29: Absolute comparison of the signal of BLM.216 measured as a function of the diffuser position with the FLUKA simulation. Black: measured data. Blue: Monte Carlo points from the same simulation as in Fig. 3.19. Orange: Monte Carlo points from a high-statistics run with a geometry model including only the diffuser and BLM.216. All curves are normalized to the extracted current.

reduction; too narrow and unscattered particles will directly impact the ZS, too wide and the losses from nuclear scattering in the diffuser are unnecessarily large. A Ta diffuser with a width of 0.6 mm would allow approximately 30% loss reduction in regular operation, depending on the separatrix angular width that can be achieved. This reduction could be improved for a thinner ZS, to 50%; so, for the SPS, the diffuser is significantly less effective than the crystal, albeit with simpler operation expected.

3.3.2.7 Conclusions

The Wigner prototype passive diffuser (referred to as TPSWA) in LSS2 was tested successfully in dedicated MD and for almost 24 h with operational beam. A total of 1.2×10^{17} PoT were extracted to the NA during the test, with just 3 min of downtime caused by the deployment. A 9.4% reduction of slow-extraction beam loss was recorded on the SPS BLM system, with no impact on TT20 losses or on experiments. For a well-aligned ZS, the loss reduction of 15% is consistent with a ZS width of 0.6 mm. A redesigned diffuser for this ZS effective width could reduce the extraction losses by approximately 30%.

3.3.3 Active diffuser (thin bent crystal)

3.3.3.1 A novel extraction scheme

The application of bent silicon crystals has been pursued at CERN for various applications involving the deflection of high-energy particles in the SPS and LHC [46, 47, 48]. The beam loss on a thin electrostatic extraction septum can be reduced by aligning a thin, bent crystal with both the beam and the septum to deplete the beam density impinging on the blade of the septum in a scheme we term ‘shadowing’. The particles that would have otherwise hit the septum blade are deflected into the extraction channel by the crystal. The concept and results briefly discussed in this section can be found published in more detail in Ref. [49].

3.3.3.2 Concept and theoretical potential

Because of the highly non-linear regime of the beam dynamics during the third-integer slow extraction process, particle-tracking simulations were carried out to assess the performance reach of this novel extraction concept. To simulate the effect of the crystal on the beam, the thin-tracking module of MADX was used and coupled with *pycollimate* [24] to simulate the interaction with the crystal and the ES. The different processes that generate deflections of charged particles interacting with the crystal lattice can be divided into different regimes. The probability of a charged particle undergoing each process occurs as a function of the incidence angle of the particle with respect to the crystal. To design and specify the extraction scheme, measurements performed in 2014 on a UA9 bent silicon crystal (SFT45) [50] were used to map the relation between the input and output angles of particles impinging on the crystal. A 2D probability density function (Fig. 3.30) was implemented in *pycollimate* to simulate the effect of the crystal throughout the slow extraction process. The results refer to single-pass effects of the crystal measured on an experimental transfer line (H8) in the NA. In MADX, particles that interact with the crystal are given a thin kick assigned randomly from the probability density function. For an incoming angular range of $\pm 10\,\mu\mathrm{rad}$, the single-pass channelling efficiency in the simulation is approximately 55%.

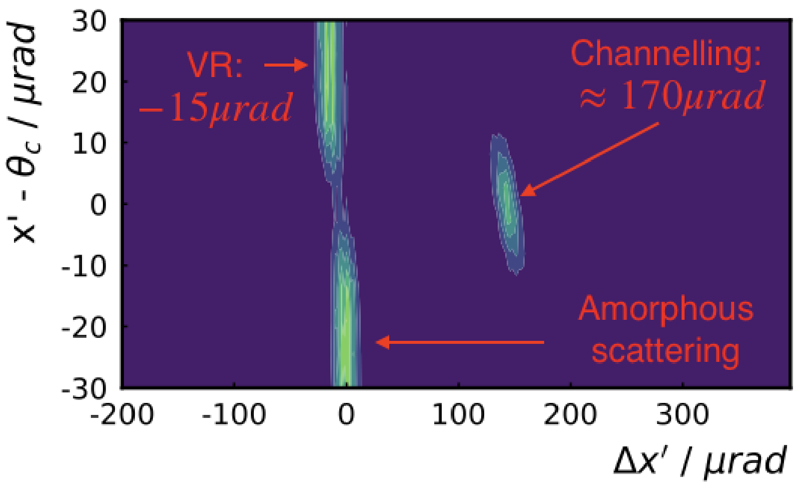

Fig. 3.30: Probability density function describing particle interaction with a bent crystal as implemented in *pycollimate* from data obtained by the UA9 Collaboration, taken in H8.

To avoid restricting the aperture of the synchrotron at injection, a fast-actuating crystal or a series of high-energy magnetic bumpers is needed to move the beam close to the crystal. The latter option is preferable for mechanical reasons. There are two ways to shadow the ES wires: (i) locally, by installing a crystal immediately upstream of the ZS inside the extraction bump, or (ii) non-locally, by installing it at a favourable optical location in the ring that is equipped with another set of bumpers. Both options have been studied in detail for the SPS and reported in Ref. [51]. The first option was chosen for the prototyping of the concept because of its apparent advantages for ease of operation and optimization, although the performance reach of a non-local system is expected to be better than that of a local system owing to the flexibility in choosing the phase advance.

The results of the –*pycollimate* tracking simulations are shown in Fig. 3.31, where the beam presentation to the upstream crystal and the downstream electrostatic septum is shown in phase space. The crystal thickness was specified as 0.6 mm, with a deflection angle of 170 µrad [52]. A clear region of intensity depletion can be observed at the location of the ZS wires, with a consequent increase in the number of extracted particles. The simulated loss reduction at the ES is a factor of two for the local case, as shown by the transverse beam density in Fig. 3.32.

In a similar way to a passive diffuser, the relative thickness of the crystal and the ES plays an important role in the overall loss reduction potential of the concept. To maximize the efficiency of the scheme and improve the loss reduction, the angular spread of the beam at the crystal must be minimized such that it fits well inside the channelling acceptance. In the original concept, it was thought that this

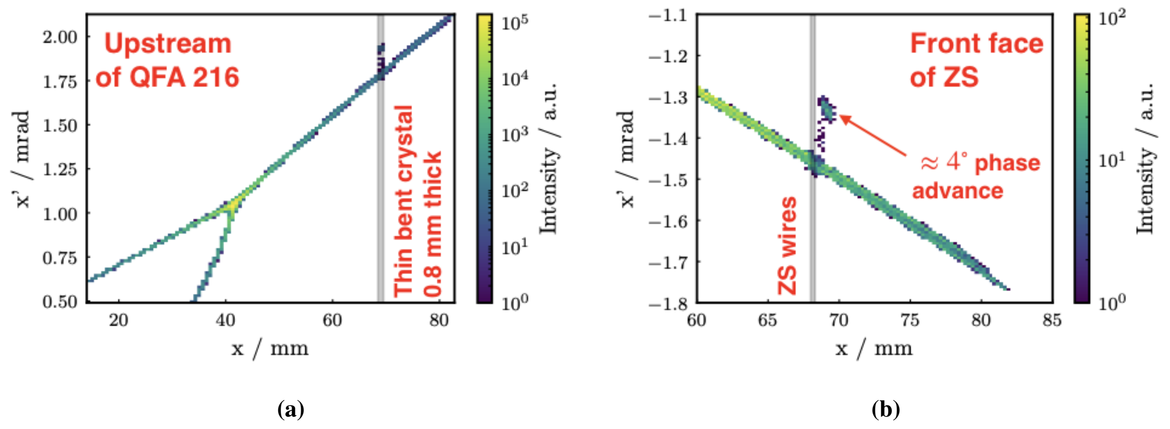

Fig. 3.31: Phase space presentation of the resonantly extracted beam at the crystal and close to the wires of the ZS. (a) Phase space presentation at the crystal. (b) Phase space presentation at the ZS.

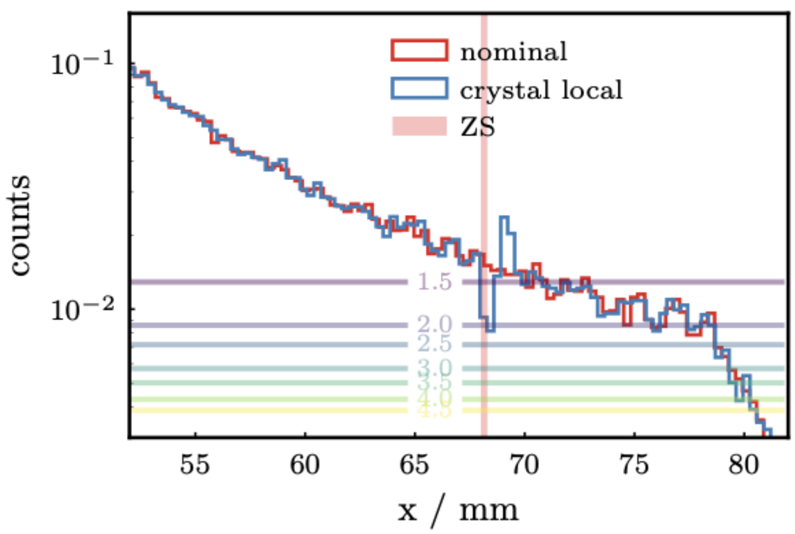

Fig. 3.32: Histogram of the horizontal particle distribution at the ZS. The case for a nominal SPS FT extraction is shown in red, and the density for ZS local shadowing in blue.

could be achieved with a dynamic extraction bump, which is varied together with the horizontal tune to compensate for the beam movement throughout the spill. As discussed previously, the implementation and set-up of the dynamic bump are operationally complex, and the problem was instead solved by employing the COSE extraction technique.

The prototype crystal was installed in LSS2 of the SPS, just upstream of the ZS (0.6 m upstream of the QFA.21610). In this case, a crystal with a large channelling angle is required because the phase advance between the crystal and the ZS is only a few degrees. Also, the crystal should be installed such that the channelled particles are deflected towards the outside of the ring. The expected loss reduction using this extraction configuration is about a factor of two. When the crystal is aligned for volume reflection, a density-depleted region is also formed, with particles being kicked back into the machine to circulate for another three turns, before being extracted as part of the tail at large amplitude on the extracted beam. The expected loss reduction factor is 3.4 for the non-local case with a crystal located in LSS4 of the SPS.

3.3.3.3 Prototype mechanical design

The UA9 prototype crystal diffuser tank (TECS.21602) is installed in the same location as the passive diffuser (see Fig. 3.24), which was swapped out during the second Injectors Technical Stop in September 2018. The crystal is 2.5 mm long and 0.8 mm wide with a 175 μrad bending angle. It is mounted on a holder with a large vertical clearance and a 35.8 mm horizontal clearance to allow the resonantly extracted beam to jump past the crystal. The holder is mounted inside a tank equipped with a goniometer, which is needed to allow the correct angular alignment of the crystal with respect to the incoming beam. Figure 3.33 shows the prototype of the crystal installed in the SPS.

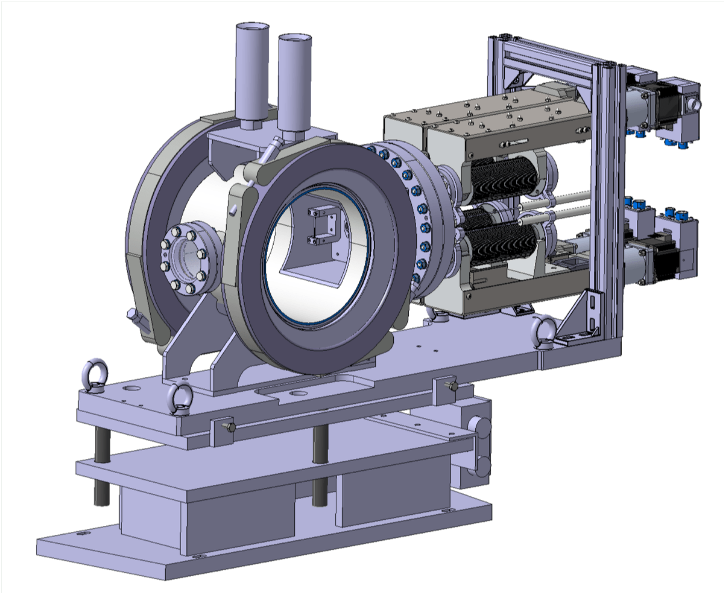

Fig. 3.33: Prototype of the compact vacuum tank TECS.21602 installed in the SPS, which contains the goniometer and the crystal.

The alignment of the crystal is accomplished by two linear stage motors: the first one moves the crystal transversely, and the second changes the orientation of the crystal with respect to the beam. The lever arm between the two motors is 10 cm. The measurement of the position of each stage motor is performed by means of a Linear Variable Differential Transformer (LVDT) sensor. The motor gears experience backlash when the direction of movement is reversed. The backlash of the two motors was measured in vacuum in the SPS and was 62 μm and 37 μm, respectively. In terms of the crystal angle, the backlash affects the absolute value of the crystal orientation by up to a few hundreds of microradians.

For the prototype goniometer, this can be only partially corrected using the LVDT measurements, as they were affected by a variation in the pulsed currents in the nearby main magnets. The design of a future operational crystal device would implement appropriate measures to minimize these effects in view of the lessons learnt.

3.3.3.4 Issues and challenges observed

The particles channelled by the aligned crystal and entering the transfer line as a coherent beamlet caused losses measured at a specific location at the beginning of TT20. With the new BDF optics developed for TT20, it was possible to transport the channelled beamlet to the targets with no additional losses recorded along the line by applying local trajectory bumps to avoid the aperture restrictions. This is also expected to be the case for the transport along the new transfer line to the BDF target. It should be noted that the trajectory excursions predicted for the channelled beamlet in the TT20 operational optics for the NA are more severe and require further investigation to understand whether the beamlet can also pass through the splitters and be transferred to the targets or whether it will need collimating in the transfer line.

3.3.3.5 Summary of main results of machine development and operational tests

The majority of the machine tests took place in parallel with the test of the dedicated prototype BDF target, where a 1 s spill was used to slowly extract 400 GeV/c protons towards the T6 target in the NA. The advantage of such a parasitic test was the high duty cycle achieved and the large number of position and angular scans that could be made with the crystal being actuated to its required position and angle between cycles, before staying fixed and not moving during each extraction. A significant amount of data was also taken using the crystal with ions in parallel with operation in 2018 at different beam energies, which is not discussed here.

The creation of a channelled beamlet was directly observed on screens at different locations in the transfer line, and, most impressively, the expected manipulation of the horizontal beam density was clearly observed on the wire-grid profile monitor located directly upstream of the ZS, as shown in Fig. 3.34.

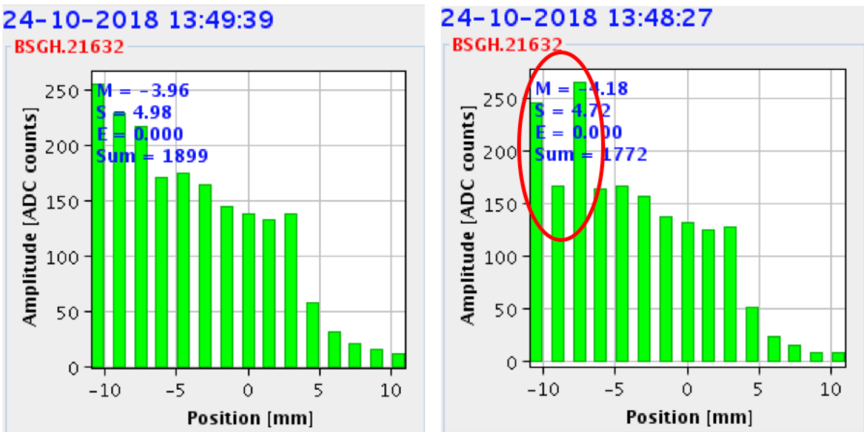

(a) **(b)**

Fig. 3.34: Horizontal beam density measured on a wire-grid profile monitor directly upstream of the ZS, with the observed depletion of intensity at the ZS wires circled in red. (a) Crystal as amorphous scatterer. (b) Crystal aligned and channelling.

To find the optimum settings for the shadowing, i.e. to maximize the loss reduction, many angular scans were performed at different transverse positions of the crystal in front of the ZS. The results from the first measurement campaign are shown in Fig. 3.35. For the best position and angle, a loss reduction of about 40% was observed. This was obtained when the crystal was correctly aligned with the beam angle, permitting the protons impinging on the crystal to be channelled. Another interesting regime for loss reduction was observed to be volume reflection [53]. Under these conditions, the particles on the separatrix are instead coherently deflected towards the inside of the machine by a small angle ($\approx$−15 µrad) and extracted three turns later. This leads to a loss reduction of $\sim$20% when the crystal is oriented for volume reflection. The tests are well summarized in Fig. 3.36, where the loss reduction factor is shown by linear scans of the crystal position aligned either for channelling or for volume reflection.

One of the main initial concerns was regarding the beam stability, because the channelling angular acceptance of the crystal is limited to about $\pm$10 µrad for 400 GeV protons. The tests demonstrated that the loss reduction could be achieved with remarkable stability. The stability was tested in channelling and volume reflection, resulting in an r.m.s. stability of 1.1% and 0.4%, respectively, as shown in Fig. 3.37. The stability was even acceptable at an angle between channelling and amorphous scattering, where the slope of the loss with respect to angle was steepest.

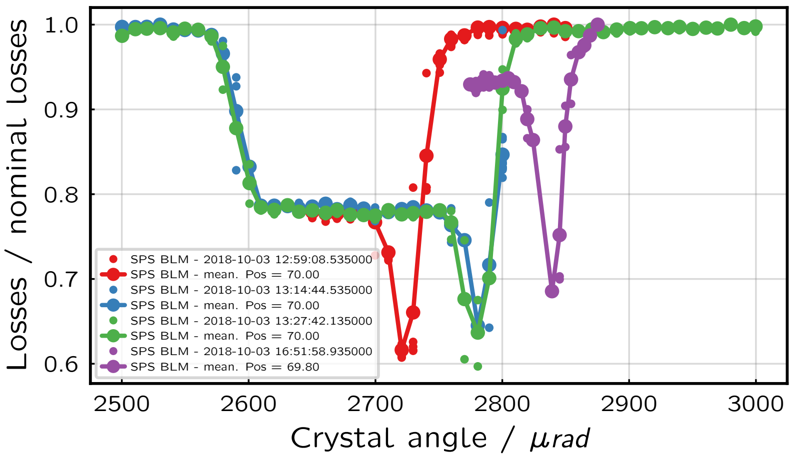

Fig. 3.35: Measured relative evolution of the total loss in the LSS2 extraction channel as a function of the crystal angle.

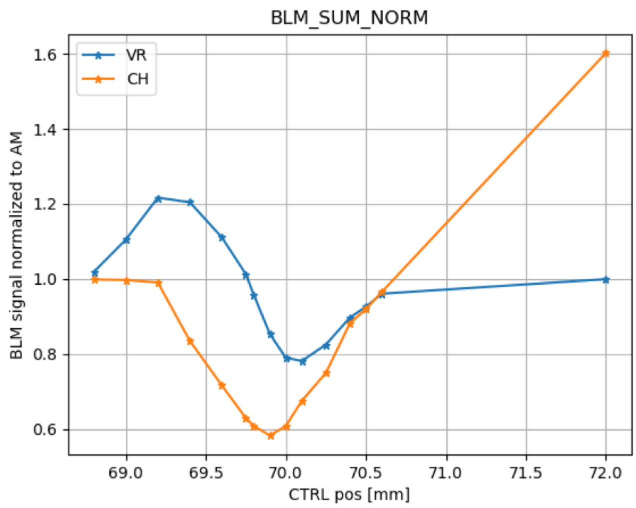

Fig. 3.36: Measured loss reduction factor when the crystal is aligned either for channelling (CH) or for volume reflection (VR) as a function of the crystal position. The losses are normalized to the amorphous (AM) crystal orientation.

Angular scans performed at different transverse positions were used to map the phase space presentation of the extracted beam separatrix to the crystal. Analysis of the data to include corrections using the LVDT measurements of the motor position is ongoing. The data, when compared with the simulation, also provide information about the effective thickness of the ES, as shown in Fig. 3.38, where values of close to 500 μm are found, consistent with the passive-diffuser results.

The crystal was aligned for volume reflection and tested for 13 h on the operational beam to the NA, with an intensity of 2.8×10^{13} protons per spill. A total of $\sim 6 \times 10^{16}$ protons were extracted. The test was carried out in volume reflection to avoid causing downtime to operation from losing the channelled beamlet on an aperture restriction in TT20. The operational transfer line optics are different from those used during the MD tests and could not be tested in advance. The crystal was aligned with only 10 min of downtime, and the performance is shown in Fig. 3.39 for a period of 2 h each side of the removal of the crystal at the end of the 13 h. The expected loss reduction of 20% was demonstrated,

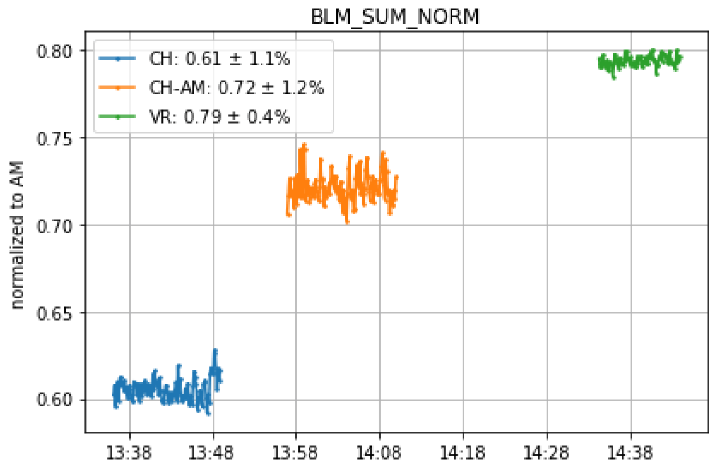

Fig. 3.37: Loss level normalized to amorphous during stability checks. The crystal was fixed in the channelling, channelling–amorphous, and volume reflection regimes. The loss reduction factors and the r.m.s. values are indicated in the legend.

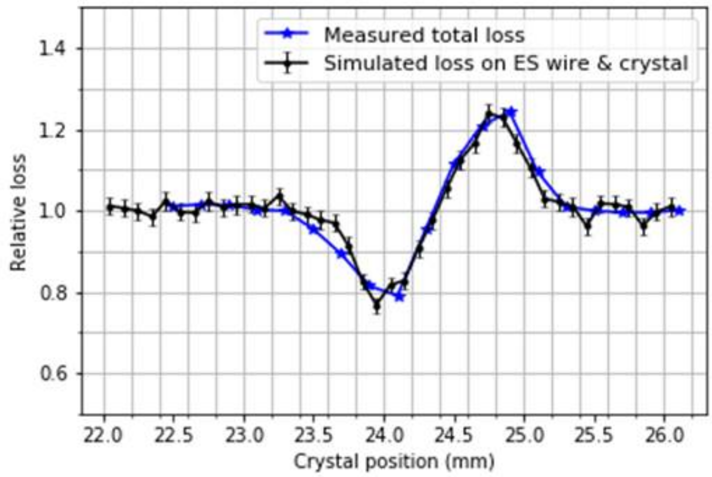

Fig. 3.38: Linear-scan data in volume reflection fitted to simulation with an effective ZS thickness of 0.5 mm.

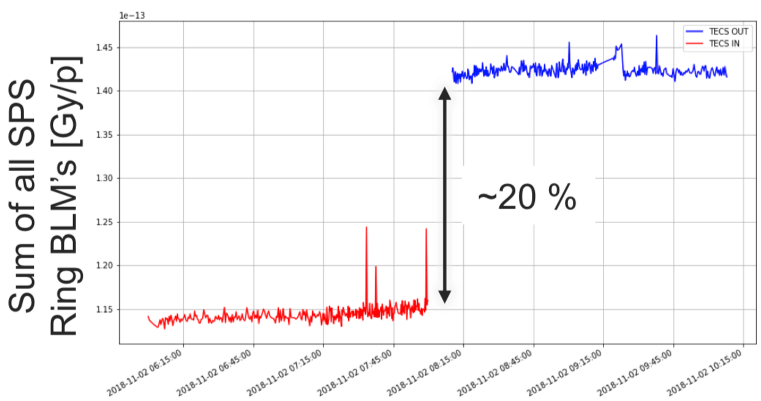

Fig. 3.39: Total SPS beam loss (integral around the full ring) for the 4 h period spanning the retraction of the prototype crystal after 13 h in the operational beam.

with evidence that the extracted beam intensity was increased with the crystal inserted. A negligible amount of outgassing was observed when the crystal was inserted, an order of magnitude lower than that observed for the passive diffuser. The absolute prompt dose level observed upstream of QDA.216 with the crystal inserted was a factor of two lower than for the passive diffuser, with only 1% of the total dose saved around the SPS ring being increased locally at this location.

3.3.3.6 Conclusions

The prototype thin bent crystal provided by the UA9 Collaboration for ZS shadowing tests showed huge promise for the significant extraction loss reduction factors being sought, with up to 40% loss reduction being demonstrated. The tests made on the operational beam showed ease of alignment and excellent stability, even in operation at high intensity and duty cycle, with a stable loss reduction of approximately 20%. Further improvements and optimization of the shadowing concept could yield even more significant gains and are being studied for future implementation. Important lessons were also learnt regarding the crystal hardware itself.

3.3.4 Phase space folding with octupoles

Higher-order multipoles can be added to the sextupole-driven extraction to manipulate the phase space trajectories in such a way that a 'folded' separatrix can be extracted. This can lower the particle density at the ZS wires and increase the density in the extraction aperture, leading to reduced beam loss per proton extracted. Theoretical and experimental studies at SPS have shown that the normalized loss can be reduced by over 40% [39, 54, 55].

3.3.4.1 Kobayashi Hamiltonian

The Kobayashi Hamiltonian, upon which the theory of slow extraction is based, is conventionally shown for only a sextupole field. When we add octupoles as well, the Hamiltonian in non-dimensionalized coordinates $(\hat{X}, \hat{P}) = K_2 \cdot (X, P)$ reads

$$\hat{H} = \frac{\epsilon}{2}\left(\hat{X}^2 + \hat{P}^2\right) + \frac{1}{4}\left(\hat{X}^3 - 3\hat{X}\hat{P}^2\right) + \frac{9}{32}\kappa_3\left(\hat{X}^2 + \hat{P}^2\right)^2 ,$$

where $\epsilon = 6\pi\,(Q - Q_{\text{res}})$ is a measure of the distance of the tune from resonance, $\kappa_3 = K_3/K_2^2$, and

$$K_n = \frac{1}{n!}\frac{L}{B\rho}\left[\frac{\partial^n B_y}{\partial x^n}\right]_{x=y=0}\beta_x^{(n+1)/2}$$

are the normalized multipole strengths. Its equivalent in polar coordinates reads

$$\hat{H} = \frac{\epsilon}{2}\hat{A}^2 + \frac{1}{4}\hat{A}^3\cos(3\hat{\theta}) + \frac{9}{32}\kappa_3\hat{A}^4 ,$$

showing the threefold symmetry more clearly. For zero octupole strength, the Kobayashi Hamiltonian shows a stable triangle with a size dependent on the distance to resonance, and separatrix arms extending towards infinity. With the addition of octupoles, we still see a stable triangle on one side of the resonance, but with the separatrix arms coming out of the stable triangle and bending around three new stable points, returning towards the stable triangle. At resonance, the stable triangle shrinks to a point, and on the other side of the resonance the stable triangle exists only in a narrow range of tunes, as the corners of the stable triangle merge with the other stable points to leave a fully stable phase space.

It is also theoretically possible to reduce the normalized extraction losses by adding decapoles to the extraction instead of octupoles. However, simulations have shown that in the case of the SPS the required decapole strengths would be unfeasible [56].

3.3.4.2 Driving-term rotation

The strong curvature of the separatrix with added octupoles means that the angle of particles on the separatrix at the position of the ZS wires changes significantly. Therefore, a 'knob' was designed that can change the angle of the effective sextupole driving term without changing the effective sextupole strength [39]. This knob makes use of the extraction sextupoles that are already present in the SPS but are not normally used in operation. Since this knob uses sextupoles but does not affect the effective sextupole strength, it is referred to as the 'orthogonal sextupole knob'.

The knob was tested in MD. The first observations showed minor changes in the extracted beam profile at the upstream end of the ZS, but a movement of several millimetres at the grid 90° downstream, as expected for a rotation of the separatrix arm. Furthermore, the normalized losses on the ZS BLMs were recorded and compared with those for a scan of the girder on which the ZS sits. Since in one case we were changing the angle of the ZS with respect to the beam, and in the other we were changing the beam angle with respect to a stationary ZS, the scan results were expected to be similar. Figure 3.40 shows that this is indeed the case, confirming that the knob works. The shift in the baseline losses is explained by the fact that the girder scan had been performed several months earlier, and the relative alignment of the ZS tanks had changed in the meantime.

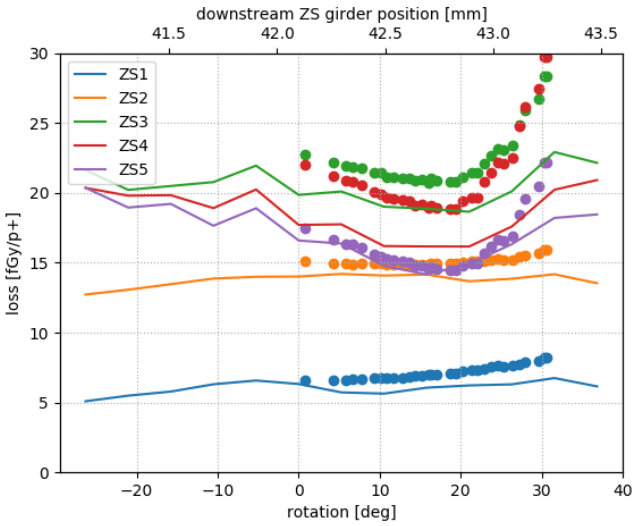

Fig. 3.40: Measured normalized losses on the ZS BLMs during a scan of the rotational knob (solid lines, lower horizontal scale) compared with those during an earlier scan of the downstream ZS girder position (dots, upper horizontal scale). The two horizontal scales have been aligned so that the minima correspond, and stretched in accordance with simulation results for the scale equivalence.

3.3.4.3 Simulated extraction

The LOF (lattice octupoles focusing) octupoles in the SPS are nominally unused during the slow extraction and are installed at high β_x, making them good candidates to use for separatrix folding. These octupoles were used in simulations to curve the separatrix and extract a 'folded' separatrix, in combination using with the orthogonal sextupole knob to correct the angle of the beam at the ZS wires back to the nominal value. To eliminate changes in the optics with momentum, all simulations used the COSE extraction method.

The simulated extracted beams are shown in Fig. 3.41. In the simulation, a reduction of up to 43% in the number of particles impinging on the ZS wires was observed, shown in Fig. 3.41(c). The shape of the extracted beam varies greatly with the multipole settings. Therefore, the optics in TT20 would need to be rematched in order to transport the beam to the target. In these simulations, the orthogonal sextupole knob was used to rotate the separatrix arm in such a way that the beam angle at the ZS wires was at the nominal value. The advantage is that the ZS girder alignment would not have to be changed, but the drawback is that the beam centre moves, both at the upstream ZS and at the handover point, which would require a steering correction in the extraction channel in LSS2 and the upstream part of TT20.

3.3.4.4 Machine protection

A procedure for the MD tests was discussed and approved by the SPS and LHC Machine Protection Panel [57]. Even though a combination of octupoles and sextupoles can be used to reduce normalized losses, a wrong configuration could also increase normalized losses and potentially damage the ZS wires. When the octupoles are too strong compared with the sextupoles, the horizontal extent of the beam in the extraction aperture becomes very small. In extreme cases, the separatrix can even be bent so strongly that particles become trapped at large amplitudes without being extracted. When the beam is trapped at large amplitudes, near the ZS wires, there is a risk of collimating the circulating beam directly onto the ZS wires, which is to be avoided at all costs.

This trapping effect was confirmed in machine studies (under safe conditions), and safe octupole limits for several sextupole strengths were identified. Since the safe sextupole and octupole limits are interdependent, interlocking for the general case is not possible with the current SPS Interlock System (SIS). If extraction with octupoles were to be used operationally, one would need either to define safe settings around the new operational parameters, or to require an updated SIS with a functionality for interdependent interlock settings.

3.3.4.5 Summary of main results of machine development

Several combinations of octupole and sextupole strengths, listed in Table 3.4, were tested in the machine, and a scan of the angular-rotation knob was carried out for each. In the best case, the summed losses were reduced by 42%. In this best-case scenario, unlike for the other configurations, the loss signal at BLM 219 increased. The most likely cause of the increased losses at BLM 219 is beam losses at the downstream end of the MSE. These losses can probably be avoided either by moving the downstream end of the MSE or by correcting the trajectory of the beam through LSS2.

Table 3.4: Optimized ZS losses for several combinations of octupole and sextupole strengths. For these settings, the rotation could not be used to fully optimize the ZS losses, since the losses at BLM 219 increased as the ZS losses decreased.

$k_2L/(k_2L)_{\mathrm{ref}}$	k_3L per LOF (m^{-3})	Rotation (deg.)	Loss ZS1–5 (fGy/p$^+$)	Loss BLM 219 (fGy/p$^+$)
0.95	0.0	15.8	69.4	2.7
0.95	1.7	−35.8	67.8	3.6
1.4	−2.25	50.0	47.0	10.0
2.1	−2.25	14.2	43.7	9.9
2.1	−2.45	28.5	40.2	18.5

3.3.5 Phase space folding with a massless septum

An alternative approach to folding the separatrix in phase space, using the fringe field region of a massless septum to deliver a kick to part of the separatrix arm, has also been studied [58, 59]. Like the octupole method, this allows the use of higher sextupole strengths. Initial studies showed a loss reduction of 50%. The simulated optimum used the sextupoles at 2.3 times their nominal strength and with a massless septum placed between the final sextupole and the ZS. Although the preliminary studies are promising, the aperture requirements in the ring have not yet been taken into account in the simplified simulation

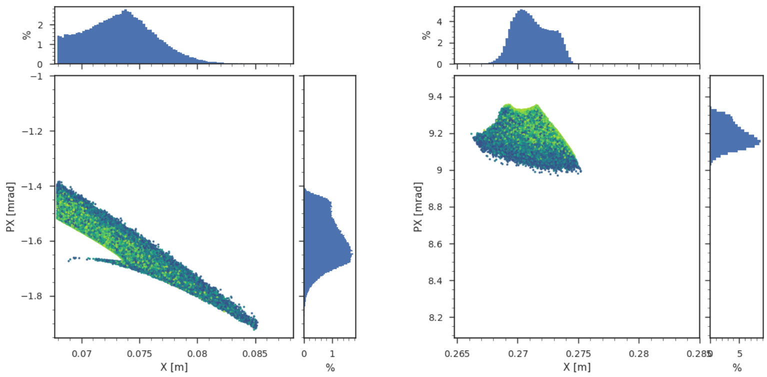

(a)

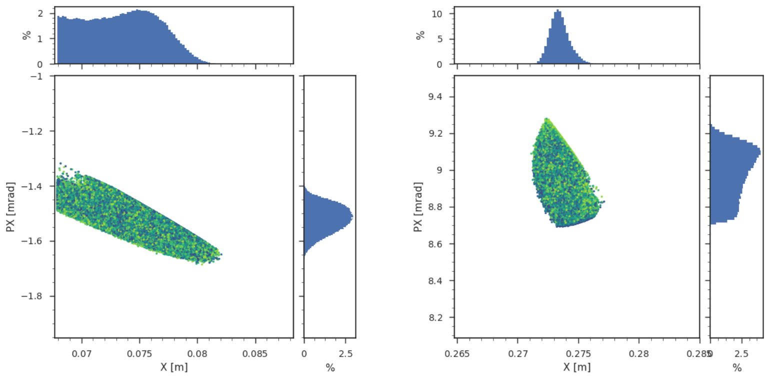

(b)

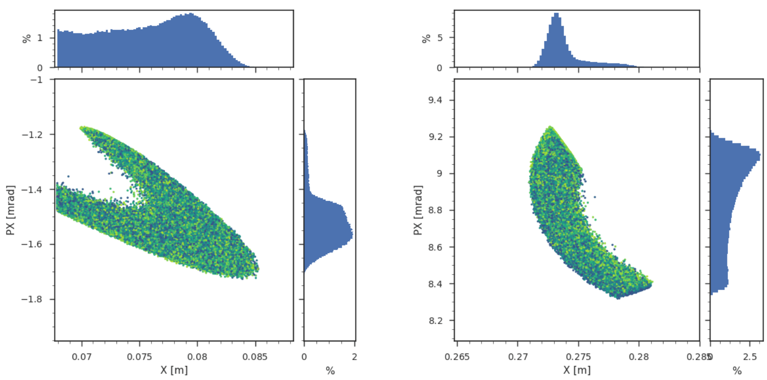

(c)

Fig. 3.41: Extracted beam in phase space at the upstream end of the ZS (left) and at the LSS2–TT20 handover point (right) for several multipole settings. Simulated particles are coloured according to momentum from blue (low) to yellow (high). Nominally, 2.66% of the beam impacts the ZS wires. (a) Extraction with nominal sextupole strength, $k_3L = 4.5\,\mathrm{m}^{-3}$ per octupole, and −85° driving-term rotation, resulting in 1.74% of the beam impacting the ZS wires. (b) Extraction with 1.4 $\times$ nominal sextupole strength, $k_3L = -2.5\,\mathrm{m}^{-3}$ per octupole, and 50° driving-term rotation, resulting in 2.35% of the beam impacting the ZS wires. (c) Extraction with 2.0 $\times$ nominal sextupole strength, $k_3L = -2.2\,\mathrm{m}^{-3}$ per octupole, and 30° driving-term rotation, resulting in 1.52% of the beam impacting the ZS wires.

code used, which is likely to be a limitation. It has not yet been determined whether or not folding with octupoles and folding with massless septa can be combined to achieve an even greater loss reduction.

3.3.6 Combining loss reduction techniques: phase space folding applied together with crystal shadowing

In a final test with protons, the crystal was aligned with the octupoles powered and COSE implemented. During the crystal alignment scans, a loss reduction factor at the ZS BLMs of over 3 was achieved when the crystal was channelling; see Fig. 3.42. More dedicated tests will be needed in the future to assess the stability of the combined extraction technique, as time was limited to that required to collect the data shown in Fig. 3.42. The angular spread of the beam at the crystal in the presence of octupoles is an important consideration for the specification of a future extraction system combining the two techniques. The same can be said about transporting or collimating the channelled beamlet in the transfer line in the presence of a larger horizontal emittance created by the octupoles.

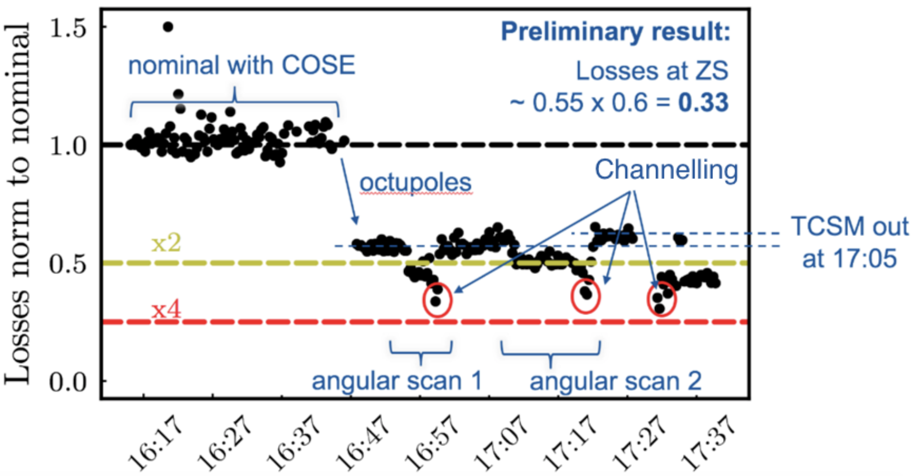

Fig. 3.42: Relative loss reduction when COSE, phase space folding with octupoles, and shadowing with the crystal were combined on 1 November 2018. In this case, the octupoles were powered as mentioned in the text, i.e. $k_2L/(k_2L)_{\rm ref} = 2.1$ and $k_3L = -2.45\ \mathrm{m}^{-3}$ per LOF. A fortuitously-located LHC-type collimator (TCSM) in LSS5 was used to safely define and restrict the aperture to protect the cathode on the outside of the extraction aperture.

3.4 Machine stability, reproducibility, and operation

The SPS provides different beams to serve multiple users on different magnetic cycles played in a sequence, the so-called supercycle (SC). The composition of the SC is changed several tens of times every day. Proton and ion beams are accelerated for fixed-target physics in the North Area hall, the SPS assembles and accelerates the LHC injection trains, and beams are also provided to the HiRadMat irradiation facility [60], the AWAKE plasma wakefield facility [61], and machine development users, who often fill any remaining space in the SC to push the performance and prepare for future running scenarios. In addition, a dynamic economy system has been introduced to save energy by ramping the main power supplies only if beam is received on the injection plateau. The frequent changes to the magnetic cycling of the machine impact the reproducibility, the effects of which are most noticeable on the resonant fixed-target cycle, with degradation of the uniformity of the slowly extracted spill. There is evidence to suggest that hysteresis, which amounts to just a few gauss at flat top, is responsible for these variations on time-scales of hours.

In addition to the hysteresis effects, the longer-term stability of the closed orbit in the bending plane of the synchrotron has been shown to drift by over a millimetre on time-scales of several weeks in the LHC extraction regions of the SPS [8]. This makes it very difficult to maintain the relative alignment between the ZS and the beam, demanding regular realignment of the septa. The source of the drift has not yet been identified.

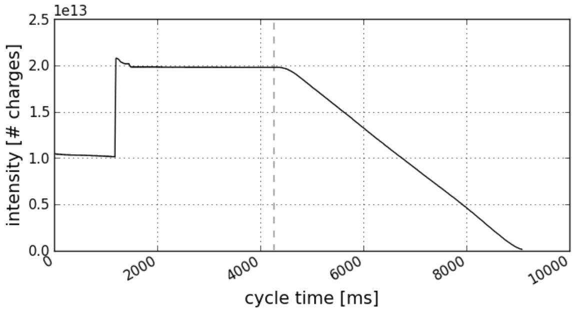

Fig. 3.43: Evolution of the intensity through the fixed-target cycle in the SPS in 2016. The dashed line indicates the moment at which the slow extraction starts.

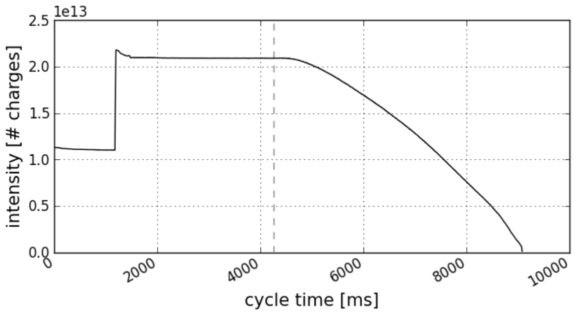

Fig. 3.44: Evolution of the intensity through the fixed-target cycle in the SPS in 2016 after a supercycle change. The dashed line indicates the moment at which the slow extraction starts. The beam is not extracted at a constant rate.

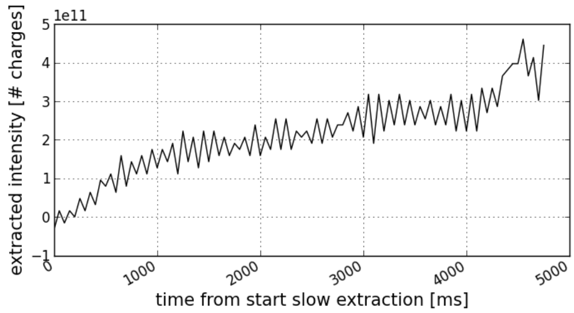

Fig. 3.45: Extracted intensity as a function of time on the extraction plateau of the fixed-target cycle calculated from the intensity evolution shown in Fig. 3.44.

3.4.1 Spill quality and effect of spill length

For the NA experiments and the BDF, the quality of the slowly extracted spill is important for several reasons. The experiments are sensitive to combinatorial background, and large spikes in the extracted proton rate have an impact on the sensitivity. In addition, the target is designed for a certain maximum transverse proton density, which could be exceeded if the spill shape departs too far from the ideal trapezoid. A measure of the uniformity of the spill is the 'effective spill length' [62], which is defined as

$$t_{\text{efs}} = \frac{[\int_{t_1}^{t_2} f(t)\, dt]^2}{\int_{t_1}^{t_2} [f(t)]^2\, dt}, \tag{3.10}$$

where $f(t)$ is the extracted intensity as a function of time. Figures 3.43 shows the evolution of the circulating intensity and extracted intensity calculated from the decay of the intensity during the extraction flat top. The ramp-up of the extracted intensity at the beginning of the spill was introduced on purpose, as the RF structure takes roughly 500 ms to diminish to an acceptable level for the North Area experiments. Any events during this time are not taken into account. The situation in Fig. 3.43 corresponds to a well-adjusted spill, and the effective spill length calculated according to Eq. (3.10) is $t_{\text{efs}} \approx 4500$ ms. If LHC 450 GeV/c cycles are added to the SC or the dynamic economy mode is enabled, where the cycles are not fully played in cases where no beam is injected, the beam parameters will change. The effect on the extracted intensity before running the feedforward algorithm is shown in Figs. 3.44 and 3.45. The effective spill length is reduced to 3800 ms in this case.

For the SPS, the quoted effective spill length is derived from the BCT measurement, sampled at 200 Hz during the extraction flat top, as indicated in the figures above. The effective spill length derived in this manner is a measure of the macrostructure of the spill. Often also the spill duty factor is quoted, which corresponds to $t_{\text{efs}}/(t_2 - t_1)$, where $t_2 - t_1$ is the flat-top length in the SPS. A typical value for the SPS spill duty factor is 95%. Figure 3.46 shows the distribution of the effective spill length over 4 weeks in July 2018. The mean effective spill length was 4450 ms.

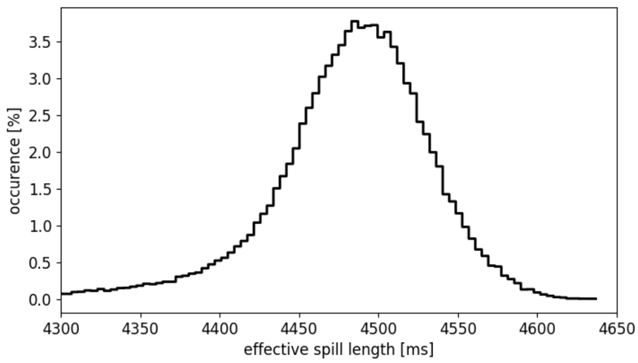

Fig. 3.46: Distribution of effective spill length during 4 weeks in July 2018. The spread is roughly from 4250 to 4600 ms.

3.4.2 Possible origin of changes in spill macrostructure

The various SPS cycles differ not only in the maximum energy reached but also in the optics used (see e.g. [63]). This implies that, following an SC change, not only will the magnetic history of the main bends be different, but also that of the main quadrupoles. It was observed that variations in the SC reduced the spill duty factor (red curve in Fig. 3.47) by a few per cent. Interestingly, the losses in the slow-extraction channel were not affected (black curve in Fig. 3.47). This can be explained by the fact that the beam position at the electromagnetic septum (ZS) is not significantly perturbed by SC changes.

In Fig. 3.48, the difference between the measured mean horizontal positions of the beam during the slow extraction cycle, before and after an SC change, is shown. It can be seen that, except for the

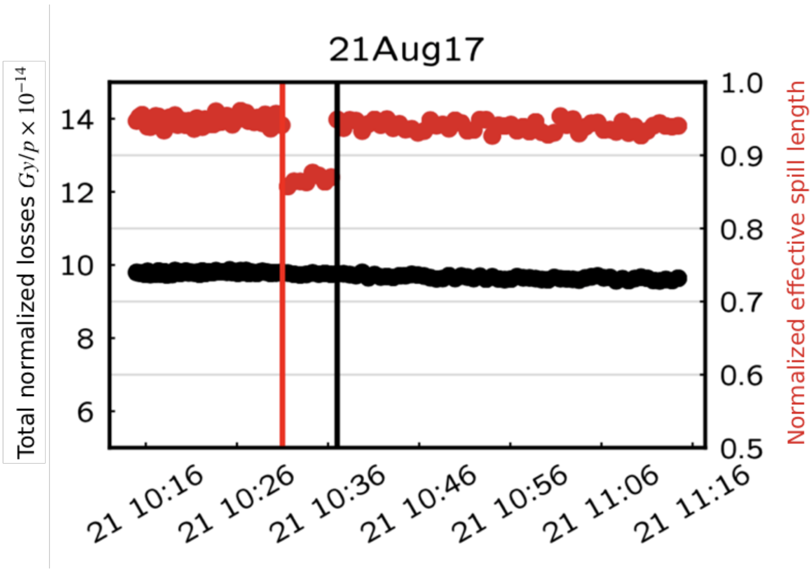

Fig. 3.47: Time evolution of normalized effective spill length and total extraction losses in the slow extraction channel. The vertical red line represents a change in the SC, and the black vertical line the correction applied to the tune to readjust the spill quality.

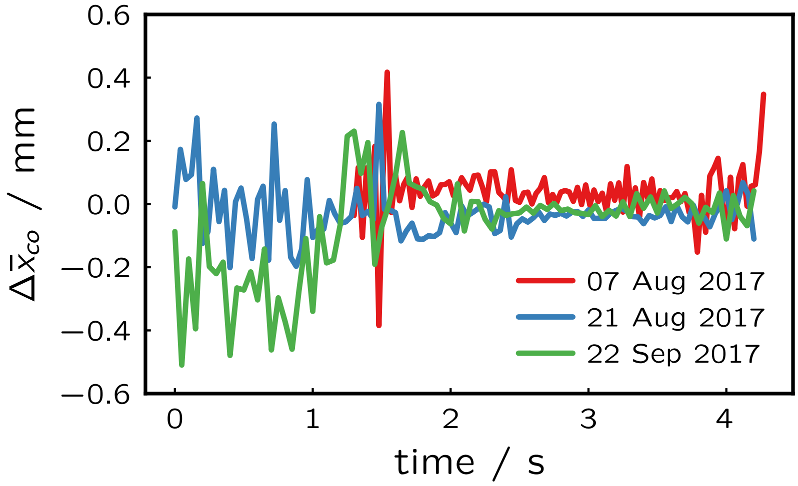

Fig. 3.48: Difference in mean horizontal closed orbits of the beam during FT cycle before and after an SC change on three different dates.

difference at flat bottom, which can be explained by the fact that the radial loop is activated at the start of the ramp, the mean of the horizontal orbit does not change.

During the same measurement period as in Fig. 3.47, the transverse tunes were also measured (Fig. 3.49). At injection, the SC change shifts both the horizontal and the vertical tune by 0.04%. Then, thanks to the radial loop, the difference in tune from one cycle to another is kept zero for more than half of the acceleration ramp. When the flat top is approached (starting from around 310 GeV/c), the difference diverges from zero, reaching about 0.02% at flat top. Such a difference, mainly in the horizontal tune, provokes the above-mentioned spill quality degradation. Earlier investigations of the errors in the response of the main dipoles and quadrupoles, and their compensation, are detailed in Ref. [64]. It was observed that, starting from 300 GeV/c and until the flat top was reached, an error between the demanded and measured field was present on all SPS cycles. This effect is more critical for the FT cycle owing to its faster ramp. The difference in the tune functions could originate from the differences in behaviour between the main bends and the quadrupoles when the saturation levels are approached. Also, the radial loop is still active at that moment, which could have an additional effect.

The good reproducibility of the tune variation following an SC change shown here could be used to eliminate the observed spill quality degradation by feedforward compensation. Further analysis and measurements are still needed to fully draw conclusions about the origin of the observed effect and to possibly cure it at source.

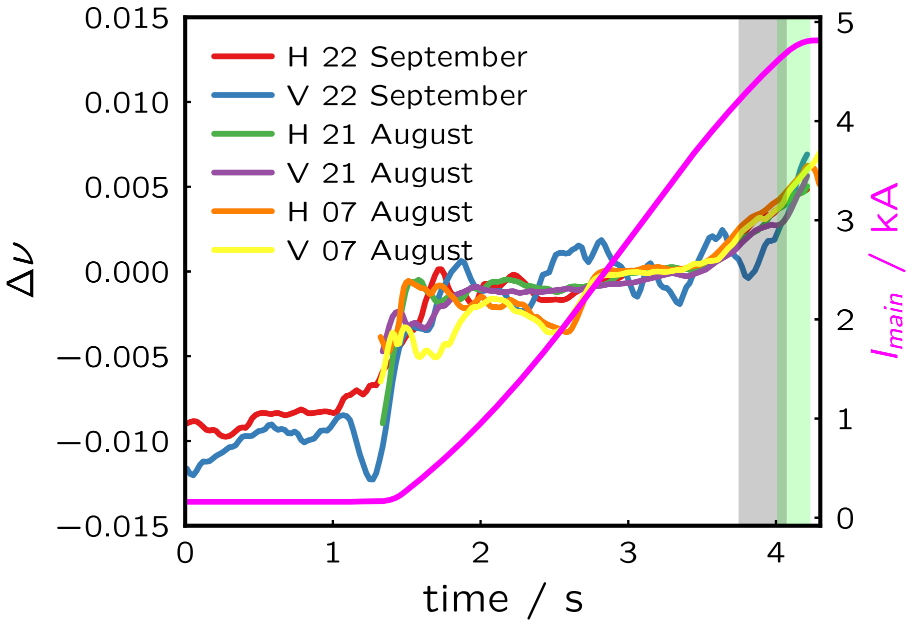

Fig. 3.49: Difference in horizontal and vertical tunes during FT cycle before and after an SC change. The magenta line represents the current time evolution of the main SPS power supplies.

Insufficient tracking of the demanded current function by the main quadrupole power converter leads to another possible spill quality degradation factor. At the round-off to the extraction flat top of the current function, the power supplies tend to overshoot. These current variations lead to spikes in the extracted intensity before slow extraction is supposed to start.

3.4.3 Effect of power supply noise on spill quality and correction of spill ripple

Spill quality is also significantly influenced by noise in the machine power supplies. The harmonic content of the spills can be measured using the 2.5 kHz-bandwidth intensity monitor installed in the extraction transfer line to the NA. Without correction, the intensity is almost 100 % modulated during the flat top. The main source of the noise has been identified to originate from the main power supplies, especially those of the focusing quadrupoles (denoted QF). As already shown in the literature [65, 66], the figure of merit for the sensitivity of the spill to power supply noise is the transfer function between each individual converter and the extracted intensity. In 2017, a campaign of measurements to characterize the transfer function for all SPS main power supplies was carried out. The results for the main focusing and defocusing quadrupoles (the latter denoted by QD) are shown in Fig. 3.50. The observed behaviour is that measured and explained in Ref. [65, 66], i.e. the dynamics of the slow extraction and of the machine with its vacuum chambers act as a low-pass filter for noise [36]. At about 300 Hz, a reduction of about one order of magnitude in the amplitudes passing can be observed. The same measurements were carried out in two different ways. The blue curve in Fig. 3.50 shows the normalized ratio between the Fourier spectra of the measured currents in the QF and QD circuits and the extracted intensity over time. The yellow markers, in contrast, show results obtained by injecting external noise into the magnet circuits at each individual frequency and measuring the effect on the extracted spill. Both measurements are in good agreement with the theoretical prediction presented in Ref. [65].

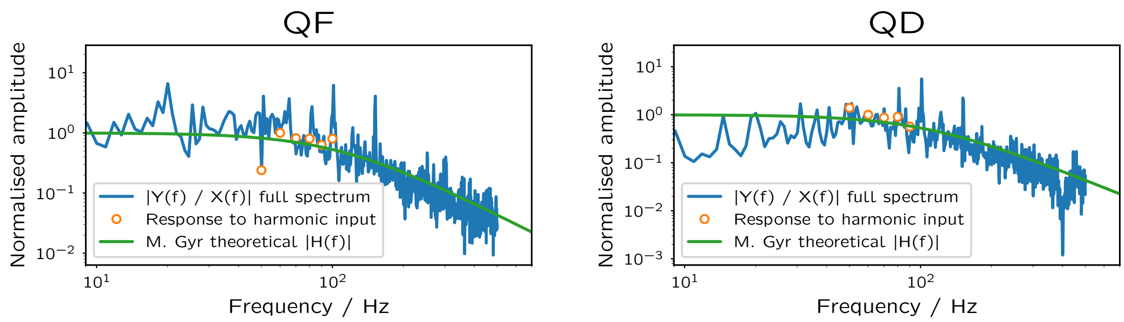

Fig. 3.50: Transfer function between QF current and extracted intensity (left), and between QD current and extracted intensity (right).

3.4.3.1 Simulations of spill with power supply noise

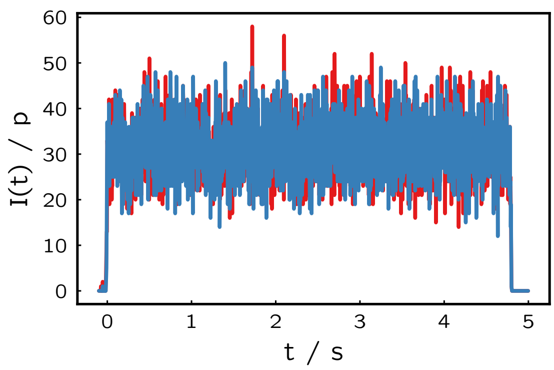

Fig. 3.51: Example of simulations of spill structure using the semi-analytic model described in the text. Red, the expected spill structure when 50, 100, and 150 Hz noise on the horizontal tune is injected. Blue, the expected spill structure when the same noise is used but the extraction speed is increased by 50 %, together with the extraction sextupole strength.

To predict the expected spill quality from a measured current waveform, a semi-analytic model was built. The driving idea was to simplify the slow-extraction simulations and make them less time-consuming. The simplified code was benchmarked with more sophisticated simulation tools such as [36, 67]. This tool will be used to optimize slow-extraction parameters and, in the best case, propose ways to reduce the impact of noise, e.g. by increasing the absolute value of the chromaticity and hence increasing the speed of the tune sweep during extraction.

The first version of this model was built by parametrizing the probability that a particle can be extracted judging by its transverse amplitude, its momentum, and the distance from resonance. Such a probability was parametrized as Gaussian in momentum space and exponential in amplitude space. Then, it was shaped using the classic stop-bandwidth definition [68] according to the instantaneous machine tune, and hence the distance from resonance, accounting for chromaticity and individual momentum.

The input current was fed into the model by decomposing it into its main harmonics and adding it to the main-quadrupole current function driving the slow extraction. This was used as input to evaluate at each step in time the exact machine tune and the size of the stable area for each particle.

The main SPS machine and beam parameters that play a role in the slow extraction process were taken into account, i.e. chromaticity, sextupole strength, emittance, and momentum distribution. An example of two simulated spills (using two different machine configurations) is shown in Fig. 3.51. The gain in the spill noise level achievable from increasing the machine chromaticity (and hence the slow-extraction speed) by 50 % was simulated to be about 30 % for the main harmonics (50, 100, and 150 Hz). Measurements are still needed to benchmark these predictions. As a first benchmark, the results from this model were compared with an analytical description [69] of the effect of a faster tune sweep on the non-extracted intensity; see Fig. 3.52.

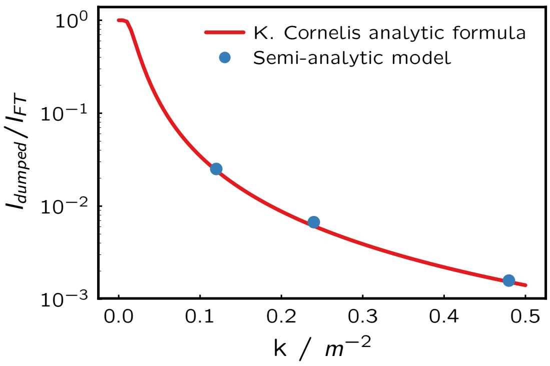

Fig. 3.52: Evolution of non-extracted particles, normalized by the total intensity, as a function of the sextupole strength. The analytic formula presented in Ref. [69] is shown in red. The blue markers represent the results obtained with the semi-analytic model.

Until the 2018 proton run, the spill harmonic content was corrected with a dedicated servo-quadrupole system consisting of four short QMS quadrupoles installed in cell 116. This is equipped with a power converter capable of providing modulation of the current at 50, 100, 150, and 300 Hz with an adjustable phase and amplitude on top of its reference function, which is zero nowadays. A measurement of the network 50 Hz signal was made available in the control room to deterministically find the correct phase with respect to the 50 Hz modulation of the spill. Figure 3.53 shows a typical spill of the 2018 proton run corresponding to a total extracted intensity of 2.7×10^{13} protons with the servo-quadrupole harmonic correction on. Unfortunately, the correction settings do not remain valid for long, because of amplitude and phase drift. The time-scale of the drift of the 50 Hz amplitude is illustrated in Fig. 3.54. The SPS quality check (SPS QC) software monitors the effective spill length and harmonic content and issues a warning if the spill quality has deteriorated below a given threshold. Increased awareness of the operations crew, better tools, and automatic algorithms for spill correction have much improved the spill quality and the stability of correction over the years. Figure 3.55 shows the improved control of the 50 Hz amplitude in the slowly extracted spill between 2017 and 2018. For about 85% of the time, the 50 Hz content was well corrected in 2018, compared with only 60% of the time in 2017.

The electronics of the servo-quadrupole $n \times 50$ Hz injection system are obsolete and a new way of correcting the spill ripple has been proposed. It will be based on directly injecting a current modulation at $n \times 50$ Hz into the QF main power supply circuit, which powers 108 quadrupoles. the amplitude and phase can be adjusted. The first tests in 2018 looked promising, and the SPS will start up with correction of the harmonic content of the spill via the QF circuit in 2021. Additional improvements will come from the spill measurement system. Currently, the acquisition system of the spill-monitoring system (BSI) is in the surface building BA1 close to the servo-quadrupole system. The long cables from the surface building BA2 to BA1 add noise. After LS2, the acquisition system will be directly placed in BA2 to

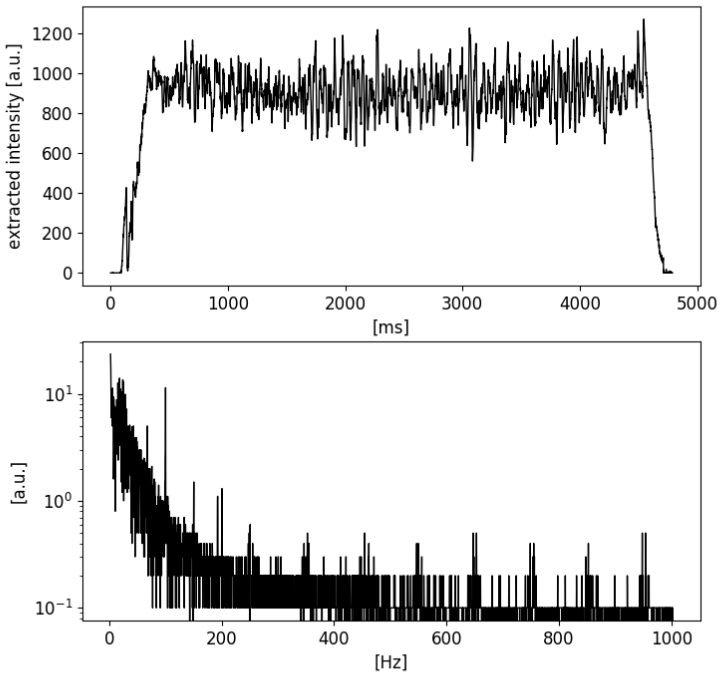

Fig. 3.53: Typical spill measured by the BSI foil in the transfer line TT20 for ~2.7×10^{13} protons extracted at 400 GeV/c on 4 November 2018 at 12:29 (upper plot), and fast Fourier transform of spill (lower plot). The 100 Hz component is not well corrected. The 50 Hz amplitude is within tolerance, with an amplitude 50 a.u.

improve the signal-to-noise ratio, such that even low-intensity ion spills will be measurable.

3.4.4 Spill quality at higher frequency

3.4.4.1 Medium frequencies (synchrotron revolution period): 46 kHz

The fixed-target beam spectrum of the SPS has a pronounced structure at the revolution frequency of 43 kHz and its second harmonic at 86 kHz due to the filling of the SPS from the PS, where the 2.1 µs PS single turn is injected into the SPS in five turns, leading to a pattern of two trains of 10.5 µs of beam with two gaps of 1 µs. The time needed for the beam to completely debunch to wash out this structure is much longer than the $\sim$1 s time available for the extraction.

3.4.4.2 Higher frequencies (RF time structure): 200 MHz

The main SPS accelerating RF system imposes a 200 MHz structure on the proton beam. When the RF is switched off just prior to extraction, the protons start to debunch, helped by the large (increased by RF gymnastics) momentum spread. The particles with negative momentum offset move forward in phase while those with positive offset move backwards. As measured by a pick-up in the SPS ring, after some 10 ms the debunching is complete, as the particles with negative offset in one bunch overlap fully with the positive-offset particles from adjacent bunches. However, as the slow extraction effectively selects a narrow band of momentum (via the large chromaticity), the 200 MHz structure is still present in the extracted beam for several hundreds of milliseconds, until the debunching and phase space mixing are complete. It is important to understand this structure and how it varies throughout the spill for experiments at the BDF.

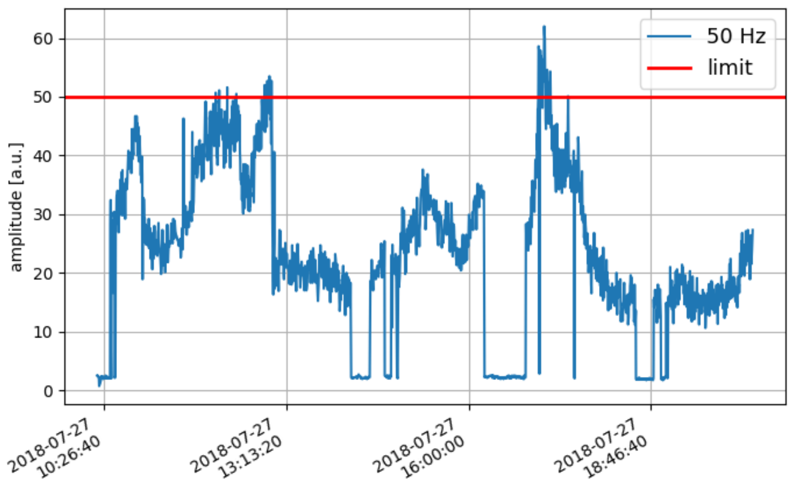

Fig. 3.54: Typical evolution of the 50 Hz amplitude of the spill over a duration of 10 h. Data were obtained on 27 July 2018.

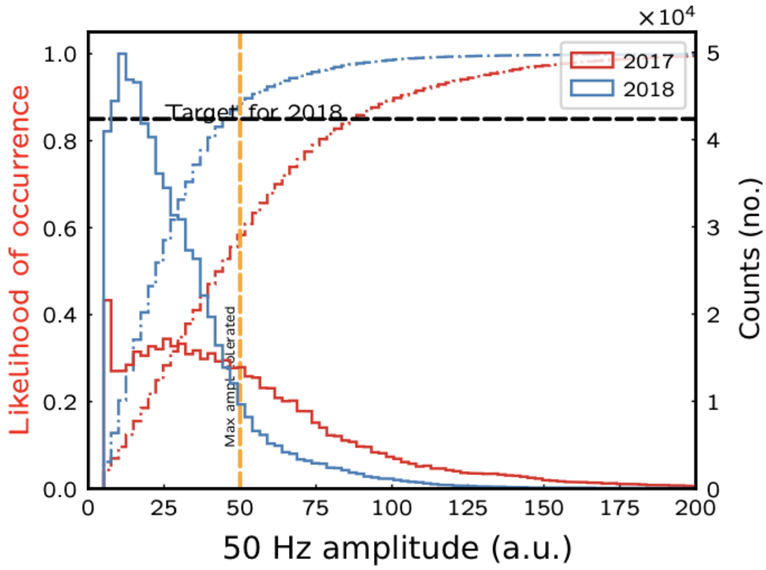

Fig. 3.55: Distribution of 50 Hz amplitude of spill for both 2017 (red) and 2018 (blue). The dashed curves represent the cumulative distribution functions for the two sets of data.

In this context, research has been launched to provide higher-bandwidth spill measurement using a detector based on Cherenkov radiation, allowing the decay of the 200 MHz main RF component of the SPS and other components induced by the machine's impedance to be measured during extraction [70, 71, 72]. Options for suppressing higher-frequency spill components are being investigated, including lowering the chromaticity (extracting using amplitude detuning instead of chromaticity via momentum) and applying longitudinal noise (stochastic extraction; see e.g. [73]).

3.5 Extraction hardware, activation, and interventions

3.5.1 Low-Z septa

To extract the beam from the accelerator, electrostatic septa (ZS) and magnetic septa (MS) are used. The magnetic septa are protected from accidental beam impact by a diluter (TPST) installed in front of the first magnetic septum (MST1). A fraction of the slowly extracted beam impacts the wire arrays of the electrostatic septa, provoking secondary particle showers to develop, which then activate equipment further downstream. Hence, there is a strong interest in septa fabricated from materials with a low atomic number (Z), which will provoke only a minimal amount of loss via scattering, and cause less activation per proton lost. Low-Z septa therefore serve two purposes:

- to reduce the interaction of the septum wires with the beam, thus reducing the production of secondaries;
- to limit activation by minimizing interactions of the equipment with stray particles and secondaries.

3.5.1.1 Low-Z septum wires

Low-Z electrostatic-septum wires yield an immediate gain in prompt extraction losses by reducing the production of secondary particle showers [74]. The quantity of secondaries produced by scattering of the beam from the septum wires is obviously also dependent on the wire thickness and the straightness of the anode (see Section 3.5.2), in particular in the upstream part of the septum, where the beam has not yet been deflected significantly.

Historically, the septum wires have been made of tungsten–rhenium alloy owing to its high melting temperature and ductility. Encouraged by the initial experience with Carbon NanoTube (CNT) wires at KEK [75], a comparison of the surface finishes of polished WRe wires and CNT wires was done using a microscope; see Fig. 3.56. It can be concluded that the surfaces of these two wires are comparable. The yield stress of the CNT wire was tested at CERN [76], and was higher than the yield stress of WRe wire of the same cross-section. WRe wire is difficult to fix mechanically, and in the ZS the wires are clamped with rods onto the ZS anode. CNT wire is delivered on reels, and it is anticipated that a similar fixation system can be used with it. CERN has ordered ⌀ 100 µm CNT wires from Hitachi-Zosen, Japan, with the aim of testing the behaviour of these wires as an anode under high electric fields, since the behaviour of the CNT material under HV is a key issue for the feasibility of its deployment as a septum (anode) material.

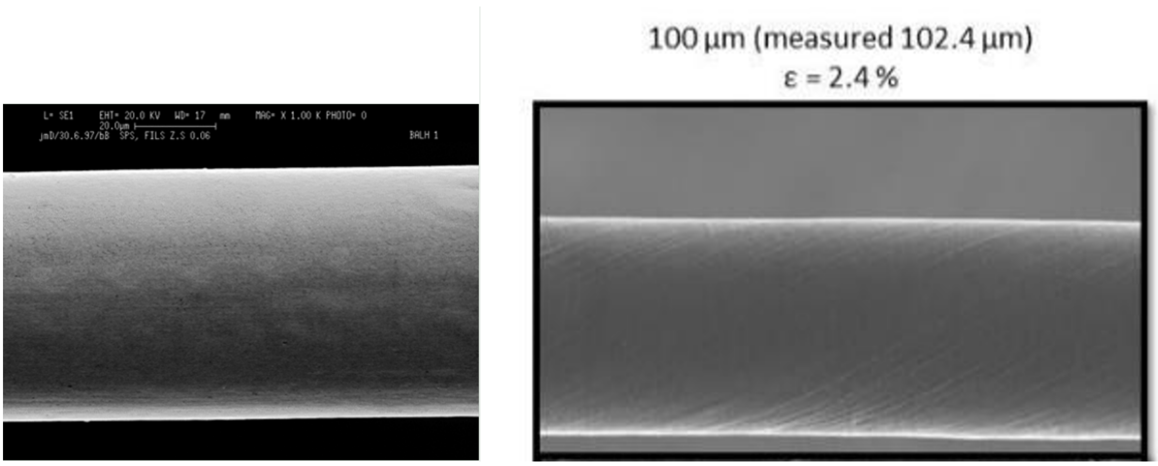

Fig. 3.56: Surface finish of 60 µm polished WRe wire (left) and 100 µm CNT wire (right), as observed under an electron microscope.

3.5.1.2 Low-Z components

The activation of the equipment due to direct beam loss and secondary beam showers can be reduced by carefully selecting low-Z materials or low-density geometries for equipment components.

In the ZS, the WRe wires and their anode supports also heat up when the beam is extracted. To avoid deformation of the anode support, it is made of Invar (FeNi36, an alloy with a very low thermal expansion coefficient) for the first three (out of a total of five) ZSs. Changing the wires to low-Z materials will result in less heating of the wires and their support. In this case, it would be of interest to study the possibility of using low-Z materials for the anode support, such as aluminium. Aluminium anode supports are used in the CERN PS electrostatic septa. Most notably, aluminium was used in the beam-slicing septum PE.SEH31 for the continuous transfer extraction scheme up to 2017.

One can also think of different manufacturing methods to achieve low-Z septa. The electrodes, i.e. the anode support and the cathode, are at present made of solid materials. An alternative approach that could be explored is the manufacture of hollow electrodes. This could be achieved by the conventional sheet metal approach, as shown in Fig. 3.57, where a test electrode was made of thin titanium sheet instead of solid material. An alternative approach to be explored is the manufacture of components such as anode supports by additive layer manufacturing. This may allow designs that use material only where needed for mechanical strength and stability, reducing the weight and hence the chance of particles of interacting with the anode support. Also, the solid HV deflectors installed on the insulating support rods and HV feedthroughs could be made lighter using one of these techniques.

Fig. 3.57: Stainless steel electrode machined from solid material, weighing 432 g (left), and hollow titanium electrode, weighing 66 g (right), made using sheet-metal working techniques.

3.5.2 Anode straightness and positioning control

The ZS wires are attached to precision-machined anode supports. The straightness of these anode supports prior to wire installation was measured to be better than 20 µm at ambient temperature [77]. In the five successive ZSs, the first three anode supports are made of Invar and the last two of stainless steel. This was done to preserve the straightness as much as possible during extraction, when beam is lost on the wires and the anode supports are heated. To limit the beam loss on the first ZSs, the first two ZSs employ ⌀ 60 μm wires, while the last three are equipped with ⌀ 100 μm wires.

The wires are tensioned using springs. These springs ensure a tensile force of approximately 1 N for the ⌀ 60 μm wires and 5 N for the ⌀ 100 μm wires. This equates to roughly 20% of their breaking strength. The wires are subjected to a force due to the electric field and are deflected towards the cathode. This deflection is proportional to the tension applied to the wire, to the wire diameter, and to the electric field. Consequently, the ⌀ 60 μm wire will be deflected by more than the ⌀ 100 μm wire. A simple analytic calculation, neglecting frictional forces, predicts deflections of 75 and 27 μm for the ⌀ 60 μm and ⌀ 100 μm wires, respectively, for an electric field of 11 MV/m [78].

A measurement of the wire deflection due to the electric field was carried out using the following set-up. A ZS equipped with a DN150 viewport on the upstream flange was put under vacuum. An optical system was installed to allow observation of the radial displacement of a wire due to the electric field. The cross-hairs of a theodolite were aligned with a wire. Once this wire was subjected to the full electric field, the displacement of the wire could not be measured directly, owing to the angle between the wire array and the line of sight. Therefore, using the radial displacement system of the anode, the anode position was adjusted to line up the wire with the previously set cross-hairs of the theodolite. This radial displacement then yielded the displacement of the wire.

These measurements yielded a radial displacement of 105 μm for the 60 μm wire and 45 μm for the 100 μm wire, both for a main field of 11 MV/m. Additional measurements on wires at the extremities of the anode support (not subject to the field) confirmed that those wires did not move, i.e. their displacement was 0 μm, and so validated the measurement method.

As can be seen in Fig. 3.58, the wire array is longer than the cathode. The field on the central portion of the anode supports is uniform, but the wires installed close to the extremities of the anode support are subject to a gradually decreasing field (see Fig. 3.59). These regions are about 80 mm upstream and downstream of each ZS. The subsequent wire displacement is shown in Fig. 3.60. Here it can be observed that the effective septum thickness is increased by the wire deflection due to the electric field.

Since the shape of the end field is well known at the nominal position, a deliberate offset of the anode wires (by machining the anode support) could be considered in order to compensate this effect. Note that perfect wire alignment can be obtained only for a predetermined (nominal) cathode voltage and gap width. In addition, the leakage, or stray, field penetrating the anode wires is being investigated as another source of the large measured effective thickness.

The present motorization system of the anodes is based on d.c. motors with position feedback using potentiometers. This allows a positioning accuracy and reproducibility of about 25 μm. Since the power is switched off after displacement, the anode position remains unchanged even if a drift is observed on the potentiometer.

To obtain a more accurate positioning system, one could consider replacing the present system with a new system using radiation-hard stepping motors and encoders. It is expected that this could improve the positioning accuracy to 5 μm. To allow the verification of the anode positions when the ZSs are installed in the tunnel and are under vacuum, external alignment references have been added directly on the anode shafts. By installing targets on these supports, an accurate measurement referring directly to the upstream and downstream mechanical wire positions can be performed. The advantage of this method is that it allows a local measurement of the wire position independent of the tilt error of the installed magnet and the tank deformation due to vacuum forces. Unfortunately, this approach will not allow an online readout, but will instead require the help of surveyors.

3.5.3 Interventions

3.5.3.1 Present case study

Since the lessons learnt from the high dose levels in LSS2 during 2015, it has become policy that no major in situ repairs are carried out on the ZS. It is now preferable to replace the ZS tanks with an operational spare to limit dose and to preserve HV performance. During the Extended YETS of 2016, three ZS tank exchanges were carried out, with dose to personnel improving each time from the experience gained, which was used to improve training and procedures. Ultimately, the goal is to respect CERN's As Low As Reasonably Allowable (ALARA) guidelines, with hard limits currently set for Level 2 at a collective dose of 5 mSv for all participants per intervention, and with far stricter limits on individuals. As explained earlier, the exchange of the second ZS tank on 19 February 2016 was used as a case study to estimate the doses and cool-down times required in future operational scenarios, using the dose measured in the ionization chamber PMIU.202 and the 1.7 mSv collective dose to personnel that was recorded for the intervention. Dose measurements at PMIU.202 are used to scale the predicted dose to an intervening team using this reference.

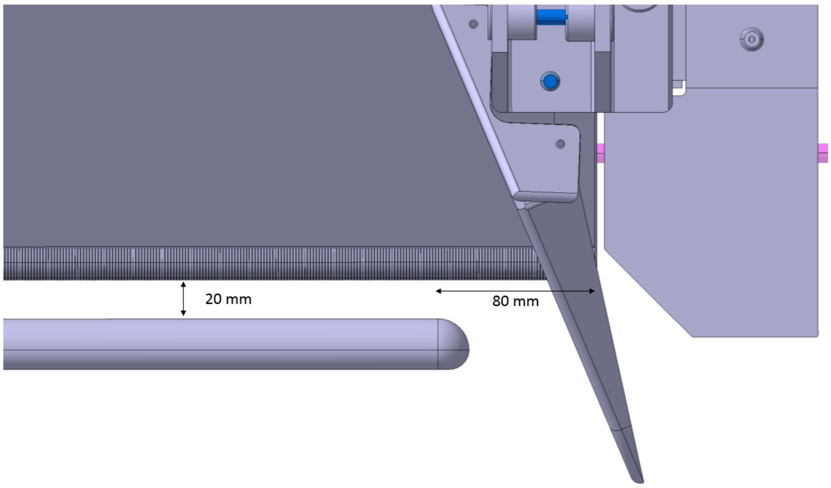

Fig. 3.58: Top view of the ZS electrode extremities, showing the cathode (bottom), the edge of the anode support (top), and a field deflector (placed diagonally, on the right).

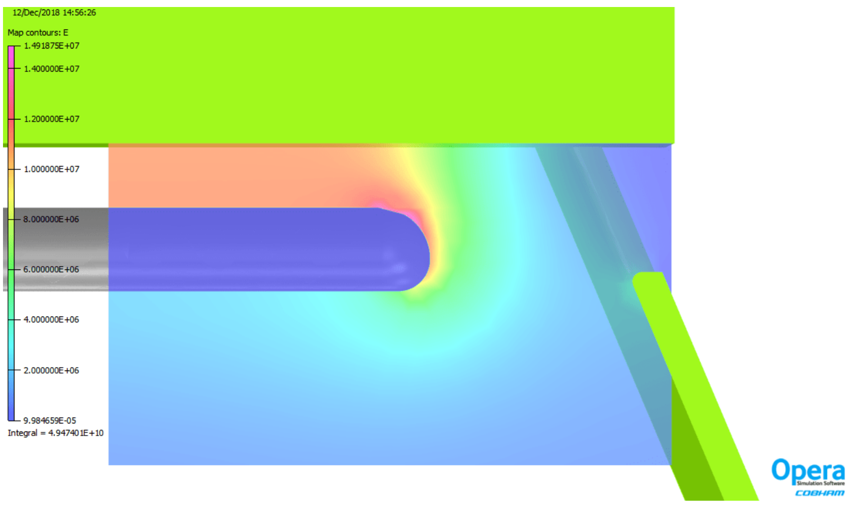

Fig. 3.59: Radial electric field in the midplane near the extremity of the ZS anode

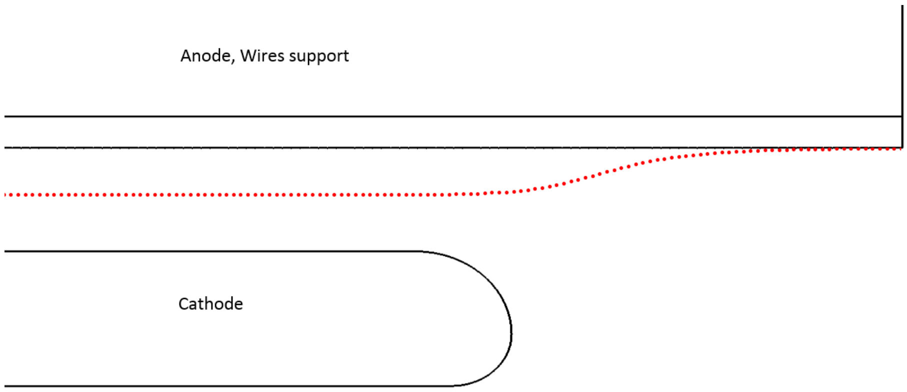

Fig. 3.60: Wire displacement near the extremities of the anode support (not to scale)

3.5.3.2 *Remote handling*

Remote handling during the exchange of a ZS tank offers a significant reduction in dose to personnel and potentially less machine downtime. The first steps have already been taken in this direction, with the recent ZS tank exchanges being partially carried out with remote handling techniques. It will be important to include the required modifications in the design of new devices to fully benefit from remote handling techniques in the future.

3.5.4 Radiation effects on equipment

The Replacement of Irradiated and Ageing Cables (RIAC) working group was established in 2009 to develop a cable replacement strategy based on quantifiable ageing of cables. Cable samples were placed in the CERN accelerators and a plan was defined for their collection and testing during the following years, up to Long Shutdown 5. The working group was discontinued in 2014, but cable samples installed in LSS2 were analysed in 2017 [79] and the results indicated clearly that the cables in LSS2 were severely degraded by ageing and radiation. In particular, the cross-linked polyethylene (XLPE) cables used to supply the ZS tanks with HV from the surface are prone to radiation damage. These cables are split into two main parts.

- Two cables (of which one is spare) in the shaft from BA2 (the surface building where the HV generator is installed) to a junction box where the cable enters the tunnel. These two cables were installed during the construction of the SPS in the 1970s.
- Two (of which one is spare) cables in the tunnel, from the junction box (downstream of the MSEs in LSS2) and alongside the extraction equipment in a cable tray, towards a distribution box upstream of the ZS.

After 10 yr of operation, in 2008, the operational cable in the tunnel broke down and operation resumed after switching to the spare cable. In the subsequent technical stop, both the operational cable in the tunnel and the spare were replaced by new cables from the same production batch as the previous ones (manufactured around 1987). In 2018 the operational cable in the tunnel broke down again, and switching to the spare cable permitted finishing the run with only 21 h of downtime for this fault. Since this cable was from the same manufacturing batch as the cables installed previously, this indicates clearly that the cable lifetime is reduced to approximately 10 yr owing to the radiation in LSS2. This is even more evident when one takes into account the cable that has been installed in the shaft for around 50 yr and has not been subject to radiation from the accelerator except for its final few metres.

Historically, the extraction regions were recabled every 10 yr. The cable sample campaigns launched by the RIAC working group have not been able to demonstrate that this frequency is unsuitable. More concretely, the fact that the XLPE HV cable failed in 2008 and 2018 shows clearly that little margin exists for recabling the extraction region. However, owing to a lack of resources, during LS2 only the ZS region will be recabled, since new, upgraded ZS tanks (in the context of LIU-SPS) need to be installed. The cables in the remainder of the extraction region (for example around the MS tanks) will only be recabled at a later date (likely LS3). The consequence of this situation is that no equipment will be changed in these other regions, nor will other major work be done, to limit the risk of damaging the degraded cables.

Concerning radiation damage to feedthroughs, one can observe that the number of feedthrough failures has dropped significantly since the early 2000s. This coincides with the disappearance of leptons in the SPS, and hence the reduced amount of synchrotron radiation to which the feedthroughs were subjected.

3.5.5 Induced radioactivity and dose to personnel

The slow extraction process in LSS2 provokes losses and induces radio-activation most prominently at locations where the septa cause an aperture restriction for the beam. Figure 3.61 shows the residual-dose-rate profile measured 30 h after the beam stop 1 m from the beam axis at the end of the 2017 run. The measured dose rate profile highlights the fact that the most critical elements for the residual activation hazard of the extraction equipment are the ZS tanks, TPST, and the MST tanks.

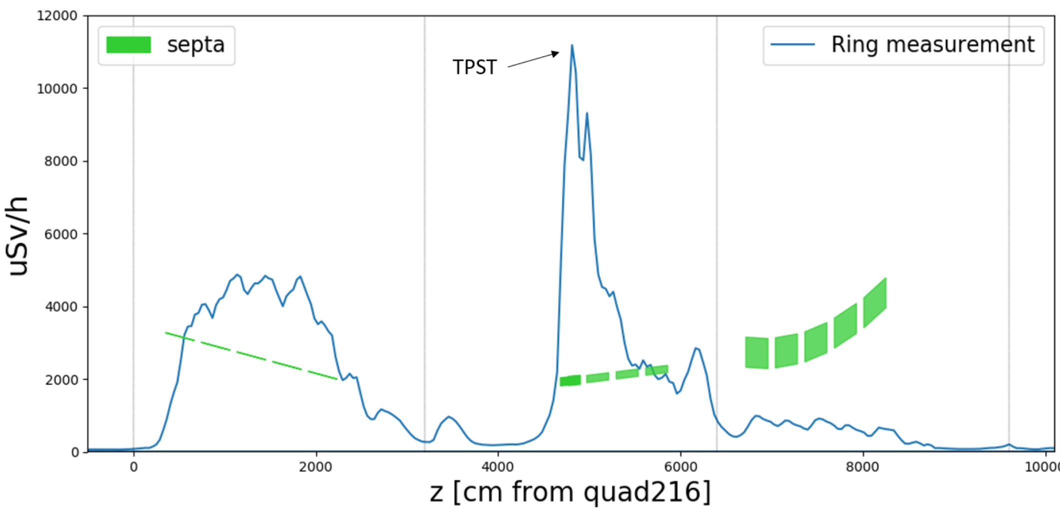

Fig. 3.61: Dose rate profile of LSS2 measured 30 h after beam stop on 24 October 2017. The radiation hazard is most prominent at the ZSs, TPST, and the MST tanks.

3.5.5.1 *Electrostatic-septum materials*

Currently at CERN, the electrostatic septa (ZS, for example; see Fig. 3.62) use mostly stainless steel (for vacuum vessels and mechanical supports), some aluminium (for the cathodes and HV deflectors), and Invar (as anode supports in the first ZSs). These materials become considerably activated, and the remnant radio-activation imposes severe constraints on interventions as described above. Instead, low-Z materials could be selected for the vacuum vessel or even the anode support to improve this. Experience with alternative materials exists, such as in the following examples:

- J-PARC has built and installed a septum with a titanium vacuum vessel, anode support, and end plates to reduce residual radioactivity [75];
- LEP used aluminium vacuum chambers;

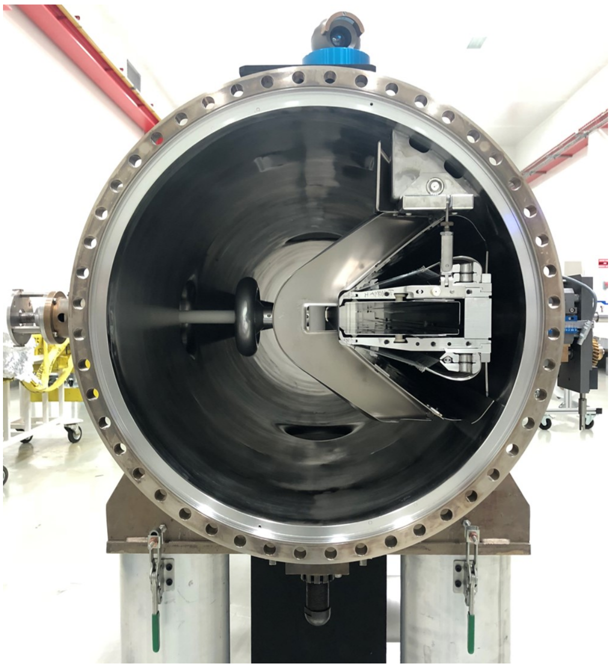

Fig. 3.62: ZS septum, showing circular stainless steel vacuum vessel and the Invar C-shaped anode support on the right inside the vacuum vessel.

– the electrostatic septa in the PS (PESEH23/31) use aluminium anode supports.

To evaluate the potential of changing some of the ZS materials, the software package ActiWiz [10] was used to assess the impact on the radiological hazards. This software package, developed at CERN, allows a fast and simple analysis, and as such is very suitable for a first look into alternative materials for the different ZS components. ActiWiz provides hazard values (risk factors) that allow a linear comparison of activation-triggered consequences for different materials and different irradiation cases. The higher the risk factor, the higher the activation. For the global radiation risk, an average value is provided for the material after activation for 1 day, 1 week, 200 days, and 20 yr. The operational values presented consider a sum of weighted dose rate contributions for 10 cooling times between 1 h and 20 yr, while for the waste only a cooling time of 20 yr is taken into account.

To this end, a very simplistic model of the ZS was used. This model for the currently installed ZS is made up of:

– *the tank:* a 3.2 m $\times$ $\varnothing$ 0.6 m tank made of 6 mm thick 304L stainless steel, with 30 mm thick covers;
– *the anode support:* a 3.1 m $\times$ 200 mm $\times$ 94 mm C-shaped support made of Invar or stainless steel.

Looking into alternative materials, the following assumptions were made for the tank:

– stainless steel: the baseline, with dimensions as stated above;
– aluminium, but using 67% thicker material (i.e. 10 mm tank body, 50 mm covers) to take into account the reduced yield stress of aluminium compared with stainless steel;
– titanium, but assuming 33% thinner material (i.e. 4 mm tank body, 25 mm covers); this choice probably gives an optimistic indication, since it does not take into account that Ti has a much lower Young's modulus, and may need additional reinforcement to maintain the required rigidity.

For the anode support, the dimensions were kept constant for all material alternatives, since these are driven by the space requirements, not the mechanical stress. The material properties assumed in the calculations are shown in Table 3.5. In this table, the global radiation risk in the vicinity of a 400 GeV/c beam (at 10 cm lateral distance to the target) is also listed for the operational case, as well as for the case of disposal of the device as waste.

Table 3.5: Material properties and radiation risk factors for the different materials considered

	Inox 304L	Al (6061)	Ti-A6-V	Invar
Young's modulus (GPa)	200	69	120	148
Yield strength (MPa)	200	120	760	483
Density (Mg/m^3)	7.85	2.7	4.43	8.05
Thermal expansion (10^{-6}/K)	17	23	9	1.5
Global radiation risk at 400 GeV/c (operation)	1.6	0.27	0.94	2.13
Global radiation risk at 400 GeV/c (waste)	0.83	0.35	1.16	0.81

To establish the radiological hazard factors for each tank/anode support material combination, the following approach was used.

- To calculate the operational hazard factor, the volume of each topology (tank volume) was multiplied by the compound risk factor for each material.
- To determine the waste hazard factor, a normalized hazard factor was calculated based on the weight of the anode and the tank ratio.

The hazard factors for the different tank/anode support material combinations are shown in Figs. 3.63 and 3.64. This preliminary analysis showed that changing materials could be beneficial for the activation of the ZSs, and further, more detailed studies were undertaken.

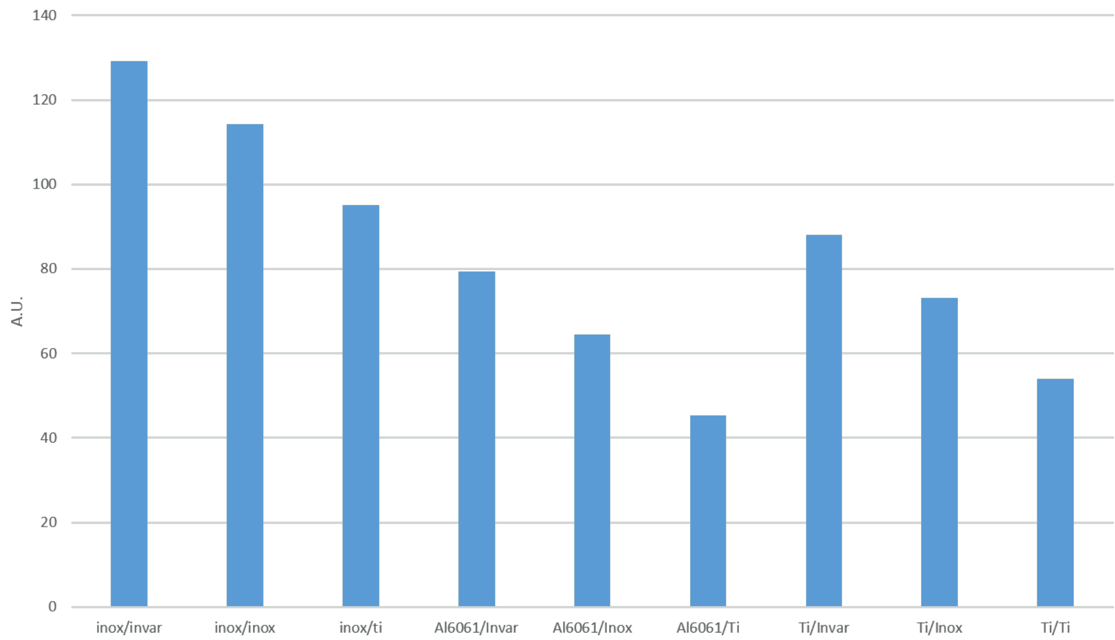

Fig. 3.63: Global radiation hazard factor for a ZS tank in operation for different tank/anode support material combinations. Currently, ZS1-3, Inox/Invar; ZS4-5, Inox/Inox.

3.5.5.2 *Material alternatives to reduce the radiation hazard in the extraction region*

Encouraged by the potential radiation hazard reduction offered by alternative materials, we have used the newly developed LSS2 FLUKA model [1, 25, 26, 27, 80] to evaluate alternative materials while taking

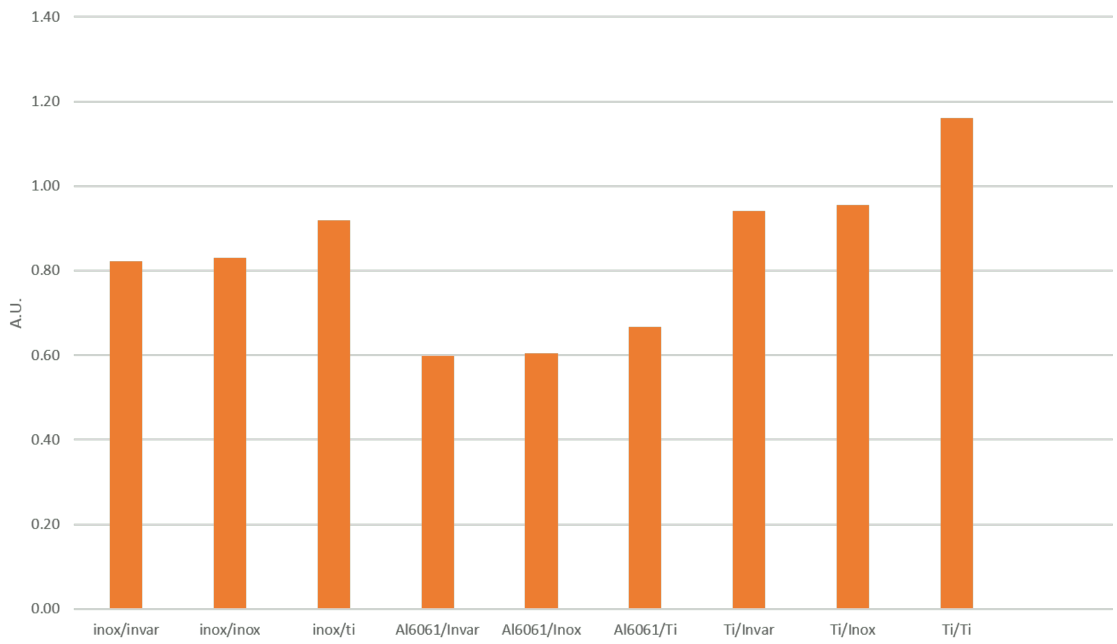

Fig. 3.64: Normalized global radiation hazard factor for a ZS tank as waste for different tank/anode support material combinations. Currently, ZS1-3, Inox/Invar; ZS4-5, Inox/Inox.

into account both the spatial complexity of the extraction beam line and the specific radiation fields produced during and after the extraction process. This section presents the material exchanges that were found to reduce the residual-dose-related hazards of the radioactive elements of the extraction beam line. The suggestions in Table 3.6 for lower-Z materials were found to be advantageous either directly through the FLUKA model, or indirectly from the particle fluence spectra obtained with the model, to be used as input for ActiWiz [10]. The differences in the magnitudes of the hazards estimated with ActiWiz do not take account of geometrical considerations, such as component shadowing or the internal distribution of the radioisotopes within the components themselves.

Figures 3.65 and 3.66 show ActiWiz estimates of the impact that different material choices have on residual dose rates 1 m from the ZS anode wire and the ZS anode support. The estimations of the septum materials were evaluated from particle fluences in separate FLUKA simulations, all of which assumed the same volume of wires averaged over the full ribbon volume as explained in Section 3.2.5.

Constructing the ZS anode wire septa from lower-Z material will both change their radiological contribution by a factor of 0.001–0.1 (Fig. 3.65) and change the overall residual dose rate in the ZS region by at least a factor of 0.6 in the case of carbon-based wires (in this case simulated as graphite), as shown in Fig. 3.67. The overall radiation hazard in the region will be decreased because fewer secondary particles are produced as a result of the reduced probability of hadronic interactions between the beam and the nuclei of the wire septa. The nuclear fragments produced by nuclear interactions of the beam with lower-Z materials will have decreased variety and be less likely to further activate the machine, as a result of the release of fewer neutrons from the process of nuclear evaporation. The fact that the residual activation is reduced outside the wire septa themselves is shown in Fig. 3.67, which compares FLUKA simulations of the current set-up with a set-up where the wire septa of ZS1 and ZS2 are replaced with graphite of the same volume. The comparison shows that all ZS elements and the downstream TCE element are activated less after the septum materials of the first two ZS elements are exchanged for lower-Z materials.

The aluminium alloy Al6061 was found to be favourable compared with stainless steel for the vacuum tank containers of the extraction elements and for the beam pipe in the region; see Figs. 3.68 and

Table 3.6: Radiologically beneficial component material exchanges for extraction equipment

Element	Component	Current material	Beneficial material	Dose rate reduction factor
ZS	Anode wires	Rhenium/ tungsten	Titanium or graphite	0.2–0.6 integrated reduction after 30 h. 0.1–0.001 anode contribution at 1 m distance (Figs. 3.65 and 3.67)
ZS	Anode support	Stainless steel or Invar	Titanium	0.25–0.33 after 1 week, 1 m distance (Fig. 3.66)
ZS	Vacuum tank	Stainless steel	AL6061	0.6 after 1 week, 1 m distance (Fig. 3.68)
TPST	Vacuum tank	Stainless steel	AL6061	0.8 after 1 week, 1 m distance (Fig. 3.68)
MST	Vacuum tank	Stainless steel	AL6061	0.5 after 1 week, 1 m distance (Fig. 3.68)
MSE	Vacuum tank	Stainless steel	AL6061	0.7 after 1 week, 1 m distance (Fig. 3.68)
	Beam pipe	Stainless steel	AL6061	Up to 0.1 in contact after 1 week (Fig. 3.69)

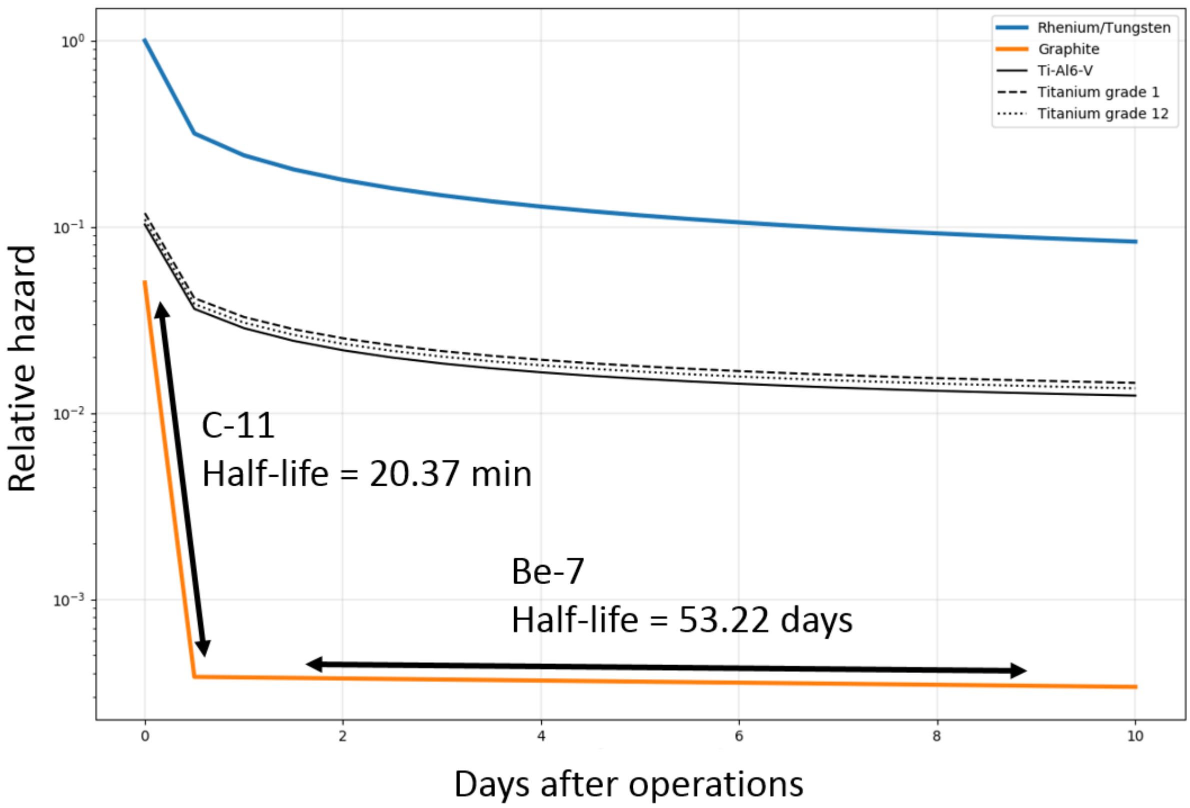

Fig. 3.65: ActiWiz comparison of residual-dose-rate contributions for different ZS septum materials at 1 m distance assuming an identical wire volume for each material choice.

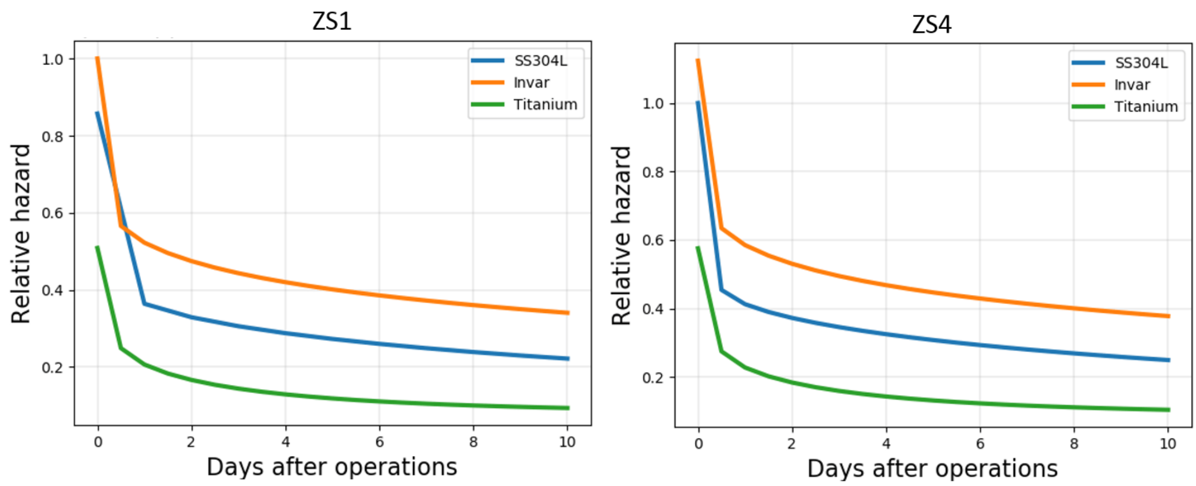

Fig. 3.66: ActiWiz comparison of residual-dose-rate contributions for different ZS anode support materials at 1 m distance.

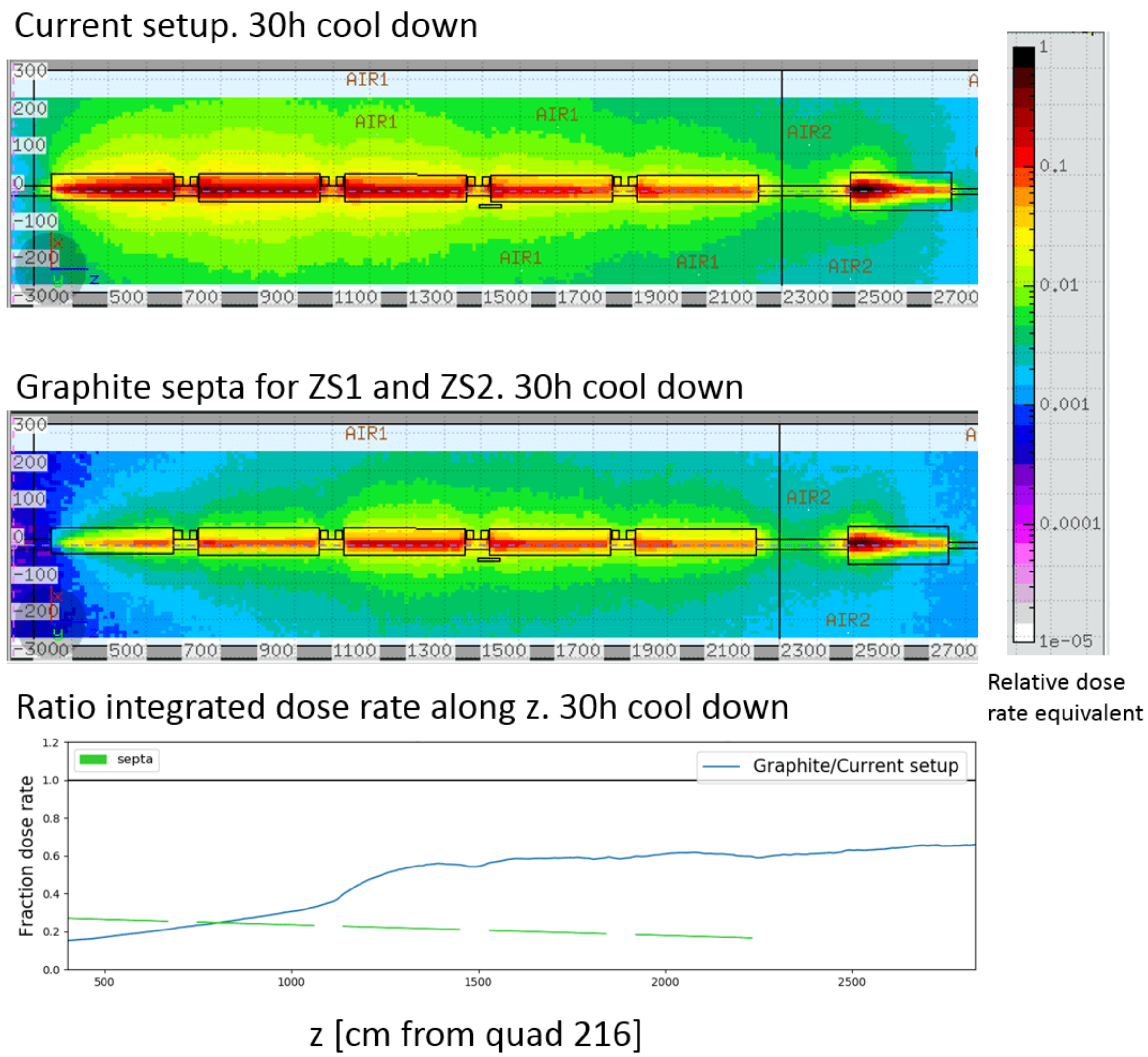

Fig. 3.67: FLUKA residual-dose-rate comparison for changing the wire septum material to graphite for ZS1 and ZS2 only. The reduced activation extends outside the exchanged wire septa.

3.69. The activation reduction with the Al6061 vacuum tanks is particularly useful since it can be used to reduce the residual activation hazard of the most critical elements of the extraction region without interfering with their functionality. Changing the beam pipe material to Al6061 will be most radiologically beneficial in close proximity to the beam pipe in locations where frequent work is performed in their vicinity.

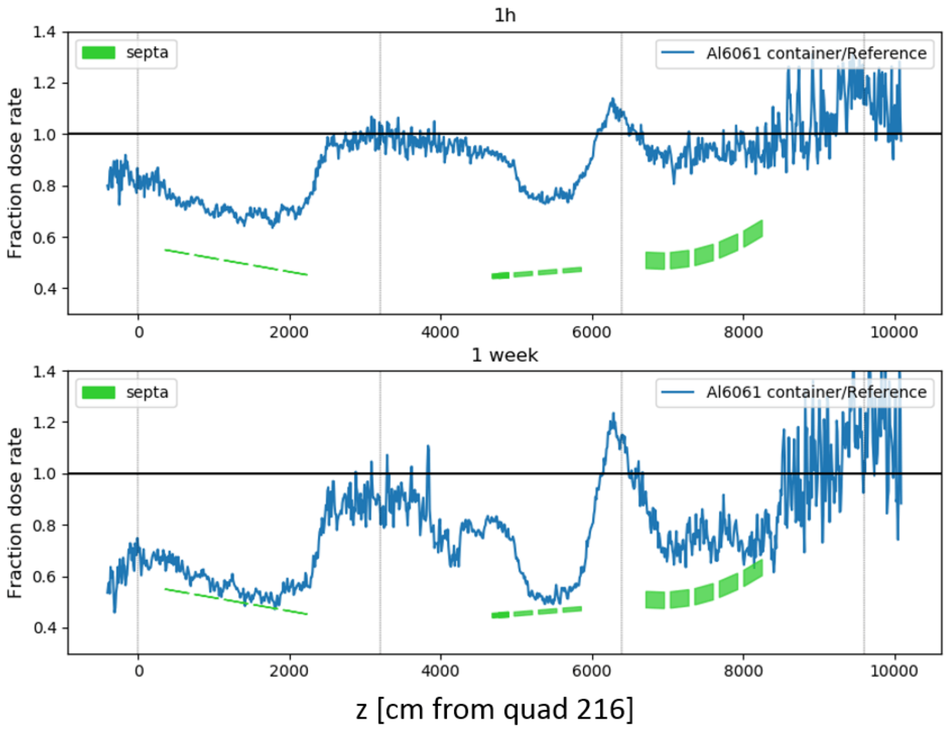

Fig. 3.68: FLUKA estimate of dose rate reduction for Al6061 vacuum tank exchange for the ZSs, TPST, the MSTs, and the MSEs.

3.5.5.3 Shielding design and impact on radiation hazard

The extraction protection element TPST is currently protecting the downstream magnetic septa from stray particle showers provoked by scattering from or interactions with the upstream ZS anode wires. The number of hadronic interactions with the TPST blade is sufficient to make this protection element the hottest part of the extraction beam line; however, recent operational improvements in the set-up of the extraction are seeing this device cool year on year. Figure 3.70 shows that shielding TPST within a marble encasement can reduce the residual dose rate 1 m from the beam axis by a factor of 10 after 1 week of cool-down. Shielding the highly activated TPST addresses the most radioactive part of the extraction region.

3.5.5.4 Conclusion

The typical residual-dose-rate profile of the extraction region shows peaks for the first few ZSs, and around TPST and the first MST. Studies have shown that changing the materials used for the septa can be beneficial for reducing this dose rate. As such, changing all vacuum tanks and beam pipes from stainless steel to aluminium would be favourable, and could potentially reduce the activation of the septa by around 25%, with a consequent reduction in dose to personnel intervening in this equipment for maintenance and or repairs. Before aluminium vacuum vessels can be designed, however, the following aspects need to be considered.

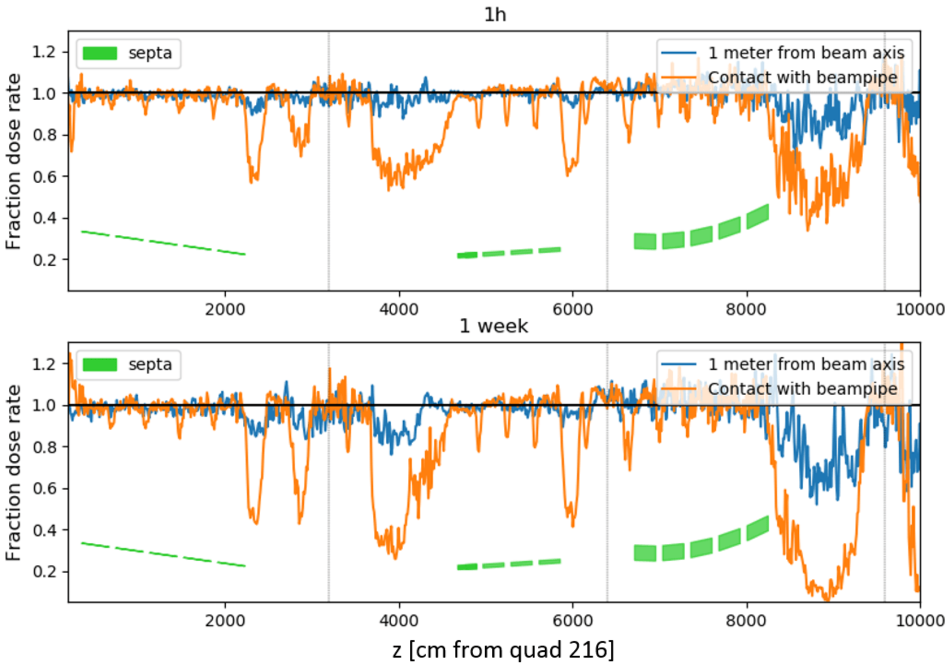

Fig. 3.69: FLUKA estimate of dose rate reduction for Al6061 beam pipe in contact and at 1 m distance from beam axis.

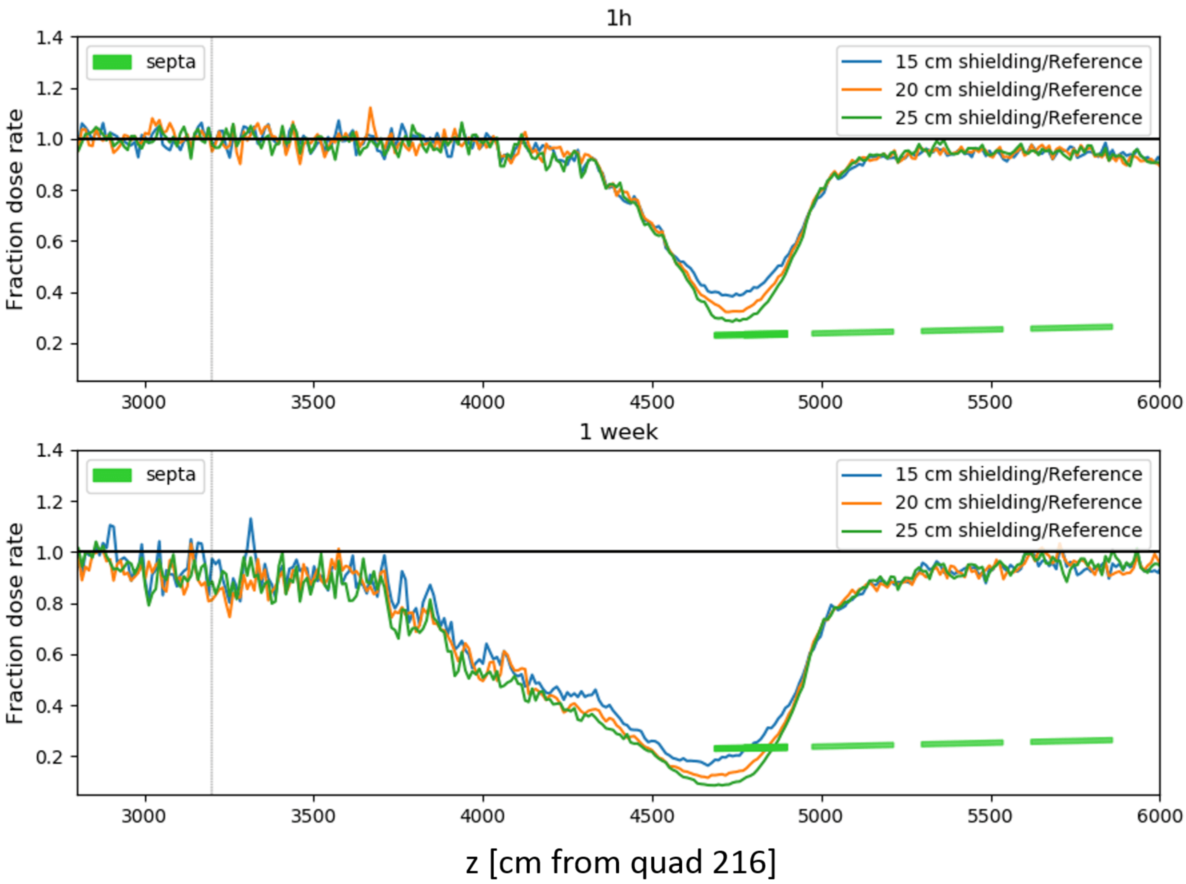

Fig. 3.70: FLUKA estimate of residual-dose-rate reduction from marble shielding of TPST at 1 m from beam axis for different cooling times.

– Aluminium Conflat flanges are being developed at CERN but are not yet commercially available.
– Bimetal Conflat flanges (stainless steel/aluminium) are commercially available.
– Larger-diameter flanges or aluminium flanges to replace 'Suchet' or 'Wheeler' flanges will have to be developed.

Replacing the tungsten–rhenium wires of the first two ZS septa with carbon wires appears very promising, and will reduce the activation of all ZSs owing to the reduced production of nuclear fragments during interaction of the beam with the wires. Before this can be considered, the compatibility of carbon wires as an anode material for the ZS septa needs to be demonstrated. To this end, carbon nanotube wires have been ordered, and will be tested in the foreseeable future.

Using titanium instead of Invar or stainless steel as an anode support could be a good alternative, if combined with carbon wires and after further studies have demonstrated that the energy deposition in the titanium anode supports is sufficiently reduced compared with the present Invar/tungsten anodes to avoid the anode support deforming in operation.

To reduce the residual dose rate for personnel near the extraction protection element TPST, the best option is to shield the device using 15–25 cm of marble, depending on the limitations of the girder support on which TPST is installed together with the MSTs.

3.6 Conclusion

The study of slow extraction in the SPS for the BDF has actively developed and tested methods to reduce the prompt beam loss per proton during extraction. A variety of approaches have been applied to the extraction process, including hardware and controls, and deployed on the SPS in tests and put into operation, both with the shorter SPS BDF (SHiP) cycle and with the longer NA cycle.

The Q-sweep method used for slow extraction in the SPS since its construction has the disadvantage that the machine optics changes through the spill as the machine tune is varied. A new type of slow extraction was developed and deployed operationally, where the optics is kept constant in normalized strength while the whole machine momentum is ramped. This COSE method has several advantages over Q-sweep and is now systematically used for regular NA operation. It is also a prerequisite for exploiting the full potential of diffusers by minimizing the angular spread of the beam presented to the septum. In addition, the recent improvements in the quality of the spill have been important, allowing the experiments to better exploit the extracted flux. Looking to future high-intensity operation, further improvements in the spill quality will be important to ensure that every extracted proton is exploited to its full potential.

The alignment of the ZS anodes is also a crucial factor in the overall beam loss, since the effective width determines both the absolute beam loss and the potential gain factor obtained from the shadowing method. The control of the alignment was improved to a resolution below 50 µm, and numerical optimizers have been simulated and tested with beam to align the five anodes with the extracted beam, bringing the alignment time down from over 8 h to 40 min. Measurements coupled with simulations of the extraction efficiency and tests with diffusers have provided strong evidence that the effective thickness of the ZS is far larger than expected. Investigations are under way to understand the source of this discrepancy.

Both passive scatterers and thin, bent silicon crystals have been been developed and prototypes tested to reduce the proton density at the ZS wires during extraction. In the case of a passive diffuser, a 260 µm wide, 30 mm long array of Ta wires achieved a loss reduction of 15%, consistent with an effective ZS width of 500–600 µm. For a bent silicon crystal 780 µm wide and 2.5 mm long, the large channelling angle of 175 µrad allowed a loss reduction of slightly over 40%, again consistent with a ZS width of around 500 µm and with the angular spread in the beam expected with the COSE extraction. Both diffuser types were tested with the full operational beam intensity of approximately 3×10^{13} protons per spill, demonstrating that the concept of ZS shadowing is stable and reproducible.

In addition, a separatrix-folding technique to reduce the beam loss at the ZS was tested successfully. In this method, the extraction sextupoles that govern the speed of diffusion across the ZS wires are increased in strength to reduce the particle density and losses, while octupole magnets are used to slow the diffusion speed at higher amplitude, folding the extracted beam back to avoid beam losses on the ZS cathodes caused by the limited ZS gap size. This method demonstrated a beam loss reduction of slightly over 40%. Most importantly, it was also tested in combination with the crystal aligned for channelling and shadowing the ZS. The combination of methods gave a loss reduction factor at the ZS BLMs of up to $\sim$3.1 and demonstrated that some of the methods for reduction of loss, activation, and personnel dose can be combined directly, with a multiplicative gain.

It is expected that after further optimization of the different concepts presented in this study, a factor of four reduction of the prompt extraction losses in LSS2 is within reach for operational scenarios. Since the beam for the BDF will pass through the gap of the splitter system in an essentially loss-free transport, this gain will mean that the present loss levels both in the extraction channel and in the splitter region can be maintained during the simultaneous delivery of 4.0×10^{19} protons to SHiP and 1.0×10^{19} protons to the NA (via the lossy splitting). Nevertheless, studies will be launched in 2019 to investigate whether there are ways to reduce the losses per proton during the splitting process to the NA.

The radiation dose to cables, extraction equipment, and personnel carrying out interventions depends on both the beam loss at extraction and the total number of protons extracted, and remains a limitation. In addition to developing loss reduction concepts, significant effort is ongoing to investigate new low-Z hardware to reduce losses and minimize the radiation hazard in the extraction region, as well as to ensure interventions can be carried out with minimum dose to personnel.

The reduced radiation hazard that can be obtained from material exchanges and shielding designs looks promising for the future. Implementing these improvements will allow the SPS to increase the beam intensities delivered to the North Area without losing availability from increased activation of the machine.

References

[1] D. Björkman. “Progress on the LSS2 FLUKA model”. Presented at the SPS Losses and Activation Working Group meeting, CERN, Geneva, Switzerland. 5 Apr. 2017. URL: https://indico.cern.ch/event/621754/.

[2] A. Golutvin et al. *A Facility to Search for Hidden Particles (SHiP) at the CERN SPS*. Tech. rep. CERN-SPSC-2015-016 (SPSC-P-350). CERN, Geneva, Switzerland, 2015.

[3] M.A. Fraser et al. “Modelling the radioactivity induced by slow extraction losses in the CERN SPS”. In: *Proc. of the 8th International Particle Accelerator Conference* (Copenhagen, Denmark, May 14, 2017–May 19, 2017), pp. 1897–1899. ISBN: 978-3-95450-182-3. DOI: 10.18429/JACoW-IPAC2017-TUPIK086.

[4] F. Ferioli and R.L. Keizer. *Analysis of the Induced Radioactivity in the SPS Extraction Channels during 1994*. Tech. rep. SL-Note-95-06-BT. CERN, Geneva, Switzerland, 1994.

[5] R. L. Keizer. *High Intensity Running and Radiation Problems*. Tech. rep. SL-Note-95-14-BT. CERN, Geneva, Switzerland, 1995.

[6] R. L. Keizer. *1995 SPS Operation*. Tech. rep. SL Memorandum. CERN, Geneva, Switzerland, 1996.

[7] G. R. Stevenson. *Activation in Accelerators*. Tech. rep. CERN-TIS-RP-90-10-CF. CERN, Geneva, Switzerland, 1990.

[8] A. H. Sullivan and T. R. Overton. “Time variation of the dose-rate from radioactivity induced in high-energy particle accelerators”. In: *Health Phys.* 11 (1964), pp. 1101–1105.

[9] G. R. Stevenson. *Induced radioactivity dose-rates from steel and lead*. Tech. rep. CERN-HP-72-106. CERN, Geneva, Switzerland, 1972.

[10] H. Vincke and C. Theis. "ActiWiz—optimizing your nuclide inventory at proton accelerators with a computer code". In: *Health Phys.* 4 (2014), pp. 228–232. DOI: `10.15669/pnst.4.228`.

[11] M. A. Fraser et al. "Slow extraction efficiency measurements at CERN SPS". In: *Proc. of the 9th International Particle Accelerator Conference* (Vancouver, Canada, Apr. 29, 2018–May 4, 2018), pp. 834–837. ISBN: 978-3-95450-184-7. DOI: `10.18429/JACoW-IPAC2018-TUPAF054`.

[12] "Slow Extraction Workshop 2017". CERN, Geneva, 9–11 November 2017. URL: `https://indico.cern.ch/event/639766`.

[13] F. Scheck Y. Baconnier O. Barbalat. "Status of studies of the CPS slow extraction". In: *Proc. of the 7th International Conference on High-Energy Accelerators* (Yerevan, USSR, Aug. 27, 1969–Sept. 2, 1969), pp. 565–575.

[14] V. Gvozdev. "Measurement of the synchrophasotron slow-extraction efficiency". In: *Part. Accel.* 6 (1974), pp. 53–55.

[15] M. Tanaka et al. *SEB Extraction Study I: Calibrations of the Ring Loss Monitor (RLM) and the Secondary Emission Chamber (SEC) by Changing the Electrostatic Septum Position and Skew*. Tech. rep. AGS Studies Report 219. BNL, USA, 1987.

[16] M. Tanaka et al. *SEB Extraction Study II: Investigations of the Apparent Beam Intensity Dependence of Extraction Efficiency*. Tech. rep. AGS Studies Report 222. BNL, USA, 1987.

[17] M. Tanaka et al. *SEB Extraction Study III: Measurement of Extraction Efficiency during the Spill*. Tech. rep. AGS Studies Report 229. BNL, USA, 1987.

[18] R. A. Andrews et al. "Extraction for the Main Ring at NAL". In: *Proc. of the 9th International Conference on High-energy Accelerators* (SLAC, Stanford, CA, USA, May 2, 1974–May 7, 1974), pp. 456–461.

[19] M. Tomizawa et al. "Performance of resonant slow extraction from J-PARC Main Ring". In: *Proc. of the 3rd International Particle Accelerator Conference* (New Orleans, LA, USA, May 20, 2013–May 25, 2013), pp. 481–483. ISBN: 978-3-95450-115-1.

[20] F. Hornstra. "The system for precise measurement of accelerator extraction efficiency". In: *Nucl. Instrum. Meth.* 128 (1975), pp. 435–440. DOI: `10.2172/1155350`.

[21] F. Hornstra and E. Bleser. *A Method and a Simple Device to Precisely Measure Accelerator Extraction Efficiency and Beam Line Transport Efficiency*. Tech. rep. FN-252. FNAL, USA, 1973.

[22] M. A. Fraser. "Extraction efficiency". Presented at the SPS Losses and Activation Working Group meeting, CERN, Geneva, Switzerland. 23 May 2018. URL: `https://indico.cern.ch/event/730812`.

[23] D. Björkman. "Status of slow extraction simulation studies (alignment, diffuser)". Presented at the SPS Losses and Activation Working Group meeting, CERN, Geneva, Switzerland. 23 Aug. 2017. URL: `https://indico.cern.ch/event/659556`.

[24] F. M. Velotti. "Higher brightness beams from the SPS for the HL-LHC era". Ph.D. Thesis. Ecole Polytechnique de Lausanne, Mar. 2017. URL: `https://cds.cern.ch/record/2265703`.

[25] G. Battistoni et al. *The FLUKA code: description and benchmarking*. Ed. by M. Albrow and R. Raja. 2007.

[26] A. Fasso et al. *FLUKA: A Multi-particle Transport Code*. Tech. rep. CERN-2005-10 and SLAC-R-773. 2005.

[27] T. T. Bahlen et al. "The FLUKA code: developments and challenges for high energy and medical applications". In: *Nucl. Data Sheets* 120 (2014), pp. 211–214. DOI: 10.1016/j.nds.2014.07.049. URL: https://cds.cern.ch/record/2109973.

[28] L. Esposito and D. Björkman. "Establishing a FLUKA model for slow extraction in LSS2". Presented at the SPS Losses and Activation Working Group meeting, CERN, Geneva, Switzerland. 24 Jan. 2018. URL: https://indico.cern.ch/event/687186.

[29] L. Esposito. "First FLUKA results of LSS2 loss maps". Presented at the SPS Losses and Activation Working Group meeting, CERN, Geneva, Switzerland. 7 Feb. 2018. URL: https://indico.cern.ch/event/701592.

[30] K. Bernier et al. *Calibration of Secondary Emission Monitors of Absolute Proton Beam Intensity in the CERN SPS North Area*. Tech. rep. CERN-97-07. Geneva, CERN, Switzerland, 1997.

[31] F. Roncarolo. "Investigation of BSI calibrations". Presented at the SPS Losses and Activation Working Group meeting, CERN, Geneva, Switzerland. 21 Feb. 2018. URL: https://indico.cern.ch/event/701595.

[32] J. P. Prieto. "pyTrack library on CERN's Gitlab". Project ID: 35657. URL: https://gitlab.cern.ch/jprietop/pyTrack.

[33] J. P. Prieto. "ZS alignment and loss reduction studies". Presented at the SPS Losses and Activation Working Group meeting, CERN, Geneva, Switzerland. 10 Oct. 2018. URL: https://indico.cern.ch/event/761066.

[34] M. Szakaly. "Case study 2: comparison of alignment algorithms". Presented at the Automatic ZS Alignment meeting No. 4, CERN, Geneva, Switzerland. 31 Aug. 2018. URL: https://indico.cern.ch/event/751972.

[35] S. Hirlander. "Automated ZS alignment MD". Presented at the SPS Losses and Activation Working Group meeting, CERN, Geneva, Switzerland. 21 Nov. 2018. URL: https://indico.cern.ch/event/774574.

[36] J. P. Prieto et al. "Beam dynamics simulations of the effect of power converter ripple on slow extraction at the CERN SPS". In: *Proc. of the 9th International Particle Accelerator Conference* (Vancouver, Canada, Apr. 29, 2018–May 4, 2018), pp. 818–820. ISBN: 978-3-95450-184-7. DOI: 10.18429/JACoW-IPAC2018-TUPAF050.

[37] V. Kain et al. "Resonant slow extraction with constant optics for improved separatrix control at the extraction septum". Submitted to *Phys. Rev. Accel. Beams*.

[38] M. Tomizawa et al. "Slow extraction from the J-PARC main ring using a dynamic bump". In: *Nucl. Instrum. Meth.* 902 (2018), pp. 51–61. DOI: 10.1016/j.nima.2018.06.004.

[39] L. S. Stoel. Ph.D. Thesis. To be published.

[40] M. Albert et al. *LHC Software Architecture: TI8 Commissioning*. Tech. rep. LHC-Project-Note-368, CERN-LHC-Project-Note-368. Geneva, CERN, Switzerland, 2005.

[41] A. Durand. "On the scattering of protons at 400 GeV in a wire array placed at the front of an electrostatic septum". In: *Nucl. Instrum. Meth.* 127 (1975), pp. 349–354. DOI: 10.1016/S0029-554X(75)80004-8.

[42] B. Goddard et al. "The use of a passive scatterer for SPS slow extraction beam loss reduction". In: *Proc. of the 8th International Particle Accelerator Conference* (Copenhagen, Denmark, May 14, 2017–May 19, 2017), pp. 607–610. ISBN: 978-3-95450-182-3. DOI: 10.18429/JACoW-IPAC2017-MOPIK044.

[43] A. Durand. "Efficacitie d'un réseau de fils placé devant la plaque du septum du transfer continu a 12 GeV/c". Personal communication with C. Germain. 22 Apr. 1974.

[44] V. Nagaslaev and I. Rakhno. "MARS tracking simulations for the mu2e slow extracted proton beam". In: *Proc. of the 6th International Particle Accelerator Conference* (Richmond, VA, USA, May 3, 2015–May 8, 2015), pp. 4010–4012. ISBN: 978-3-95450-168-7. DOI: 10.18429/JACoW-IPAC2015-THPF125.

[45] B. Goddard et al. "Optimization of diffuser (pre-scatterer) configurations for slow extraction loss reduction at electrostatic septa". In: *Proc. of the 9th International Particle Accelerator Conference* (Vancouver, Canada, Apr. 29, 2018–May 4, 2018), pp. 830–833. ISBN: 978-3-95450-184-7. DOI: 10.18429/JACoW-IPAC2018-TUPAF053.

[46] W. Scandale et al. "First results on the SPS beam collimation with bent crystals". In: *Phys. Lett. B* 692 (2010), pp. 78–82. DOI: 10.1016/j.physletb.2010.07.023.

[47] W. Scandale et al. "Comparative results on collimation of the SPS beam of protons and Pb ions with bent crystals". In: *Phys. Lett. B* 703 (2011), pp. 547–551.

[48] W. Scandale et al. "Strong reduction of the off-momentum halo in crystal assisted collimation of the SPS beam". In: *Phys. Lett. B* 714 (2012), pp. 231–23. DOI: 10.1016/j.physletb.2012.07.006.

[49] F. M. Velotti et al. "Septum shadowing by means of a bent crystal to reduce resonant slow extraction beam loss". Submitted to *Phys. Rev. Accel. Beams*.

[50] R. Rossi et al. "Measurements of coherent interactions of 400 GeV protons in silicon bent crystals". In: *Nucl. Instrum. Meth. B* (2015), pp. 369–373. DOI: 10.1016/j.nimb.2015.03.001.

[51] F. M. Velotti et al. "Reduction of resonant slow extraction losses with shadowing of septum wires by a bent crystal". In: *Proc. of International Particle Accelerator Conference (IPAC'17)* (Copenhagen, Denmark). May 2017. DOI: http://dx.doi.org/10.18429/JACoW-IPAC2017-MOPIK050.

[52] B. Goddard M. A. Fraser and F. M. Velotti. *Functional Specification for a Thin Bent Crystal Located in LSS2 for the Shadowing Tests of the ZS Wires in 2018*. Tech. rep. Geneva, CERN, Switzerland, 2017. URL: edms.cern.ch/document/1783433/2.0.

[53] M. Ivanov et al. "Volume reflection of a proton beam in a bent crystal". In: *Phys. Rev. Lett.* (2006), p. 144801. DOI: 10.1103/PhysRevLett.97.144801.

[54] L. S. Stoel et al. "Investigating beam loss reduction with octupoles during slow extraction in the CERN SPS". In: *Proc. of the 9th International Particle Accelerator Conference* (Vancouver, Canada, Apr. 29, 2018–May 4, 2018), pp. 822–825. ISBN: 978-3-95450-184-7. DOI: doi:10.18429/JACoW-IPAC2018-TUPAF051.

[55] M.A. Fraser et al. "Demonstration of slow extraction loss reduction with the application of octupoles at the CERN Super Proton Synchrotron". In: *Phys. Rev. Accel. Beams* 22 (2019), p. 123501.

[56] L. S. Stoel et al. "Phase space folding studies for beam loss reduction during resonant slow extraction in the CERN SPS". In: *Proc. of the 8th International Particle Accelerator Conference* (Copenhagen, Denmark, May 14, 2017–May 19, 2017), pp. 615–618. ISBN: 978-3-95450-182-3. DOI: 10.18429/JACoW-IPAC2017-MOPIK046.

[57] M. A. Fraser L. S. Stoel and F. M. Velotti. *Separatrix Folding with Octupoles during Resonant Slow Extraction*. Tech. rep. Geneva, CERN, Switzerland, 2018. URL: edms.cern.ch/document/2014948.

[58] K. Brunner et al. "Use of a massless septum to increase slow extraction efficiency". In: *Proc. of the 9th International Particle Accelerator Conference* (Vancouver, Canada, Apr. 29, 2018–May 4, 2018), pp. 862–865. ISBN: 978-3-95450-184-7. DOI: doi:10.18429/JACoW-IPAC2018-TUPAF061.

[59] K. Brunner. "Improving the slow extraction efficiency of the CERN Super Proton Synchrotron". MA thesis. Eötvös Loránd University, 2018. URL: https://cds.cern.ch/record/2650734.

[60] I. Efthymiopoulos et al. "HiRadMat: a new irradiation facility for material testing at CERN". In: *Proc. of the 2nd International Particle Accelerator Conference* (San Sebastian, Spain, May 4, 2011–May 9, 2011), pp. 1665–1667. ISBN: 978-92-9083-366-6.

[61] P. Muggli et al. "Physics of the AWAKE project". In: *Proc. of the 4th International Particle Accelerator Conference* (Shanghai, China, May 12, 2013–May 17, 2013), pp. 1179–1181. ISBN: 978-3-95450-122-9.

[62] V. Kain et al. *SPS Slow Extracted Spill Quality during the 2016 Run*. Tech. rep. CERN-ACC-2017-121. Geneva, CERN, Switzerland, 2017. DOI: 10.18429/JACoW-IPAC2017-MOPIK049.

[63] H. Bartosik et al. "Optics considerations for lowering transition energy in the SPS". In: *Proc. of the 2nd International Particle Accelerator Conference* (San Sebastian, Spain, May 4, 2011–May 9, 2011), pp. 619–621. ISBN: 978-92-9083-366-6.

[64] J. Wenninger et al. *Dipole Field, Tune and Chromaticity Correction at the SPS: from Converter Tracking to Eddy Currents*. Tech. rep. AB-Note-2007-009 OP. Geneva, CERN, Switzerland, 2007.

[65] M. Gyr. *SPS Spill Quality*. Tech. rep. SL 95–103 (BT). Geneva, CERN, Switzerland, 1995.

[66] J. Wenninger et al. *SPS Spill Quality*. Tech. rep. AB-Note-2004-0YY OP. Geneva, CERN, Switzerland, 2003.

[67] F. M. Velotti et al. "Characterisation of the SPS slow-extraction parameters". In: *Proc. of the 7th International Particle Accelerator Conference* (Busan, Korea, May 8, 2016–May 13, 2016), pp. 3918–3921. ISBN: 978-3-95450-147-2. DOI: 10.18429/JACoW-IPAC2016-THPOR055.

[68] M. Benedikt. "Optical design of a synchrotron with optimisation of the slow extraction for hadron therapy". Ph.D. Thesis. Vienna, Tech. U., Oct. 1997.

[69] K. Cornelis. *Momentum Cleaning in the LHC with Resonant Extraction*. LHC Project Note 176. Geneva, CERN, Switzerland, 1998.

[70] B. Goddard M. A. Fraser. *Functional Specification for a Cherenkov Beam Diagnostic System for Slow Extraction at SPS*. Tech. rep. Geneva, CERN, Switzerland, 2015. URL: edms.cern.ch/document/1500135/1.0.

[71] F. Addesa. "An in-vacuum Cherenkov detector to study the slow extraction spill at SPS". Presented at the 15th SHiP Collaboration Meeting, CERN, Geneva, Switzerland. 7 Nov. 2018. URL: https://indico.cern.ch/event/765293.

[72] F. M. Addesa. "Cherenkov light in vacuum beam monitor for crystal-assisted beam manipulations". Ph.D. Thesis. Sapienza Università di Roma and INFN, Sept. 2018.

[73] M. Gyr. *Slow extraction at 400 GeV-c with stochastic RF noise*. Tech. rep. CERN-SPS-AOP-MG-jf, CERN-SPS-Impr-Rep-80-179. Geneva, CERN, Switzerland, 7 Dec. 1978.

[74] D. Veres. "Case study 1: effect of carbon wires and passive diffuser". Presented at the Automatic ZS Alignment meeting #4, CERN, Geneva, Switzerland. 31 Aug. 2018. URL: https://indico.cern.ch/event/751972.

[75] M. Tomizawa. "Slow extraction at J-Parc". Presented at Slow Extraction Workshop, Darmstadt, Germany. 1–3 June 2016. URL: https://indico.gsi.de/event/4496.

[76] A. Mariet. "Report on CNT test results". Geneva, CERN, Switzerland, to be published.

[77] R. L. Keizer and R. Oberli. *The Construction of Electrostatic Septa with Invar Anodes and Ultrathin Wires*. Tech. rep. CERN-SPS-Tech-Note-86-005-ABT. Geneva, CERN, Switzerland, 1986. URL: http://cds.cern.ch/record/88375.

[78] B. Balhan. *ZS Wires Displacement under Electrostatic Field*. Tech. rep. Geneva, CERN, Switzerland, 20 Dec. 2018. URL: edms.cern.ch/document/2065257.

[79] I. Petrova and D. Ternova. *Findings Considering Cable Samples in SPS Zone 2*. Tech. rep. Geneva, CERN, Switzerland, 15 May 2018. URL: edms.cern.ch/document/1964320.

[80] D. Björkman. "Optics and loss profile of the LSS2 FLUKA model". Presented at the SPS Losses and Activation Working Group meeting, CERN, Geneva, Switzerland. 24 Jan. 2018. URL: https://indico.cern.ch/event/687186/.

Chapter 4

Transfer to target

4.1 Introduction

The Beam Dump Facility is foreseen to be located on the side of the present SPS North Area towards the Jura mountains (Fig. 1.1). This position allows the re-use of the existing slow-extraction channel from the SPS and the TT20 transfer line to the North Area up to the first splitter (MSSB2117), which is in total about 600 m of existing beam line. The present layout of the TT20 line is shown in Fig. 4.1.

The existing splitter, consisting of three individual magnets, has to be replaced by a new laminated, bipolar design, which will permit the deflection of the entire beam to the left into a new beam line leading to the BDF target complex while maintaining the possibility to operate the North Area in the present mode by splitting the beam into two parts sent towards the T2 and T6 targets. The new splitter will be able to switch between the destinations of the BDF and the North Area on a cycle-by-cycle basis. The new beam line is approximately 360 m long and will transport, enlarge, and dilute the slowly extracted beam on its way to the target.

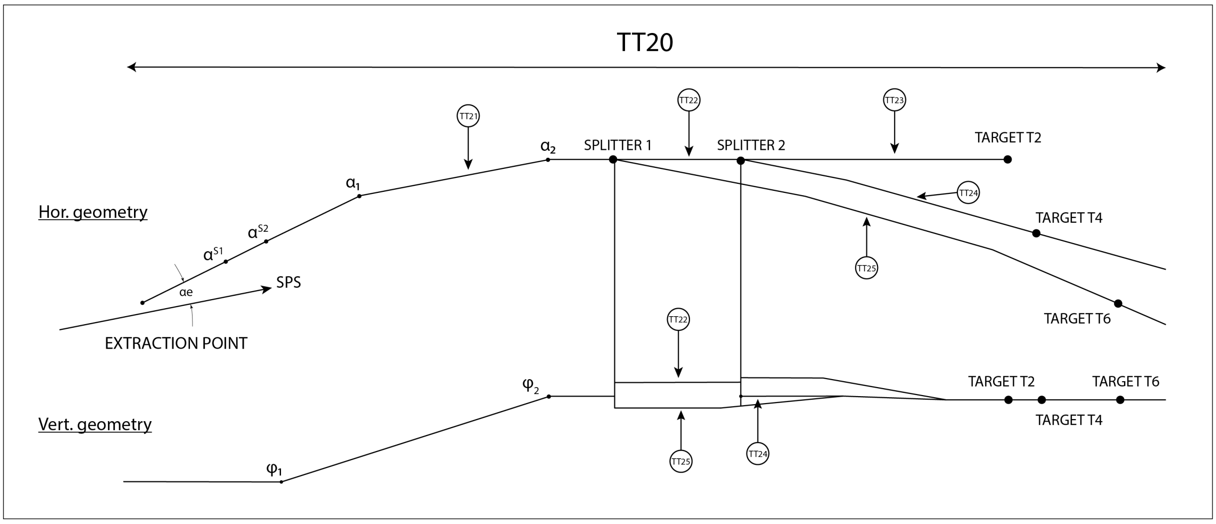

Fig. 4.1: Present TT20 layout showing the position of splitters and North Area targets. The proposed new beam line would branch off towards the BDF at splitter 1.

4.2 Extraction line optics

4.2.1 Beam parameters

Extraction methods were discussed in Chapter 3, and Fig. 4.2 shows the resulting horizontal distributions at the start of the extraction line. The vertical plane is not shown, as it remains unchanged by the extraction process and is considered Gaussian.

Figure 4.2 shows all extracted particles in blue. A relative cut around the central momentum of $\pm 1.5 \times 10^{-4}$ leads to the particles in red and better represents the phase space transported in the line, since the dipoles ramp during extraction to follow the extracted momentum. The constant-optics extraction method provides a constant phase space during extraction, and Fig. 4.2b shows only the total extracted phase space. The red and blue ellipses are defined using the covariance matrix of the associated distributions and are such that their projections cover the space between $\pm 1\sigma$.

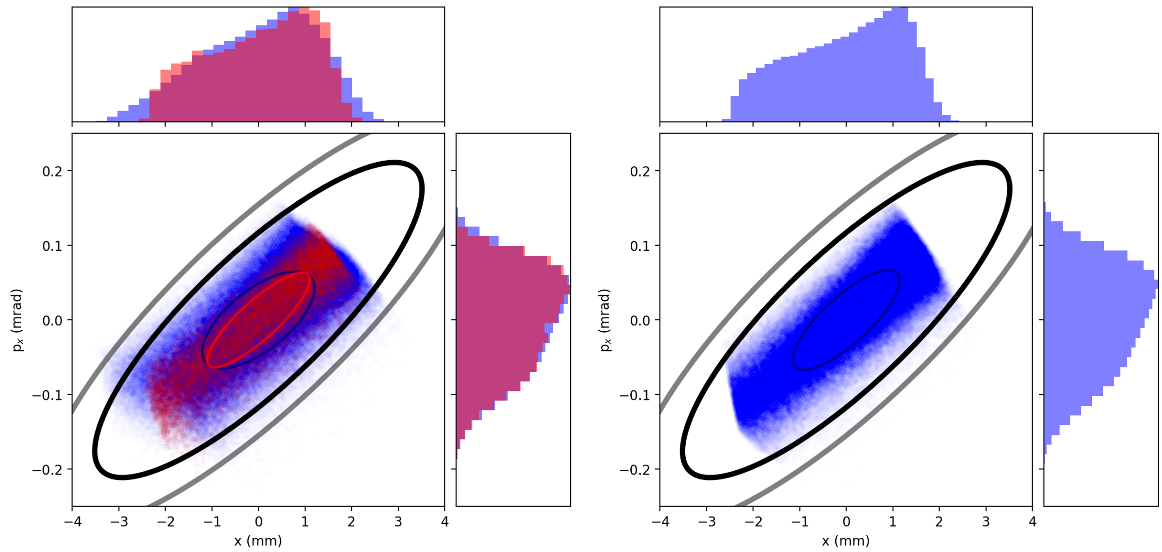

(a) **(b)**

Fig. 4.2: Horizontal phase space and projections of the extracted beam at the start of the extraction line for the current extraction method (a) and for the constant-optics method (b).

Table 4.1 lists the simulated beam parameters associated with the above ellipses. In the horizontal plane, the horizontal phase space distribution depends strongly on the extraction method. We therefore have decided to use some approximate beam parameters as a reference in this document. A visual representation of these reference beam parameters in the horizontal plane is shown in Fig. 4.2 as the black and grey ellipses, the projections of which cover $\pm 3\sigma$ and $\pm 4\sigma$, respectively, of the matched Gaussian distribution. Measurements conducted during the SPS BDF extraction cycle in 2017 are also listed in Table 4.1. The reference beam parameters considered are based on simulations, measurements, and the fact that more precise instrumentation (see Section 4.4) will allow a more accurate setting of the extraction line to minimize the emittance and effective momentum spread transported during operation.

Table 4.1: Beam parameters at the start of the extraction line

Condition	α_x	β_x (m)	ϵ_x^N (mm·mrad)	α_y	β_y (m)	ϵ_y^N (mm·mrad)
						From simulations
Current method	−0.87	24.7	26.0	−3.79	140.4	5.0
Current method, with cut	−1.62	33.1	16.2	−3.79	140.4	5.0
COSE method	−1.30	28.2	20.6	−3.79	140.4	5.0
						From 2017 measurement [1]
1 s spill	−0.85(8)	25.8(9)	37.0(1)	−4.2(4)	162(18)	4.5(4)
						Selected reference
Reference	−1.50	30.0	20.0	−3.79	140.4	5.0

In the vertical plane, the beam is essentially unperturbed by the extraction process and has the circulated beam parameters. Table 4.1 shows measurements taken in 2017, which are in good agreement with the simulated quantities. The simulated beam parameters were therefore chosen as a reference and used thereafter.

The final characteristic of the beam to be considered is the correlation between the relative momentum of the particles and their position or angle in both the horizontal and the vertical plane. We refer to these correlations as the dispersion (D) and dispersion prime (D') in the given plane. Depending on the extraction method, the horizontal dispersion may be zero or small. In the vertical plane, the dispersion is the same as for the circulating beam and zero or very small, since the SPS is planar and horizontal. Furthermore, the evolution of the dispersion in the extraction line is dominated by long sections of bending magnets that bring the beam from the extraction point to the North Area. Therefore D and D' in both planes are set to zero at the extraction point.

Because of the ramp of the dipole in the line during the extraction process, the effective momentum spread of the beam is much lower than the momentum spread extracted from the ring (see Section 3.1.1). We use a value primarily based on experience of a transported relative momentum spread of $\sigma_{dp/p} = 1 \times 10^{-4}$.

4.2.2 Trajectory and optics

The extracted beam needs to be transported from the SPS to the BDF target. Unlike for North Area operation, the beam will not undergo transverse splitting during its transport. At the target, the beam is required to be circular with a transverse size of $\sigma = 8\,\mathrm{mm}$. Additionally, we impose the condition that the dispersion in both planes should be zero at the target.

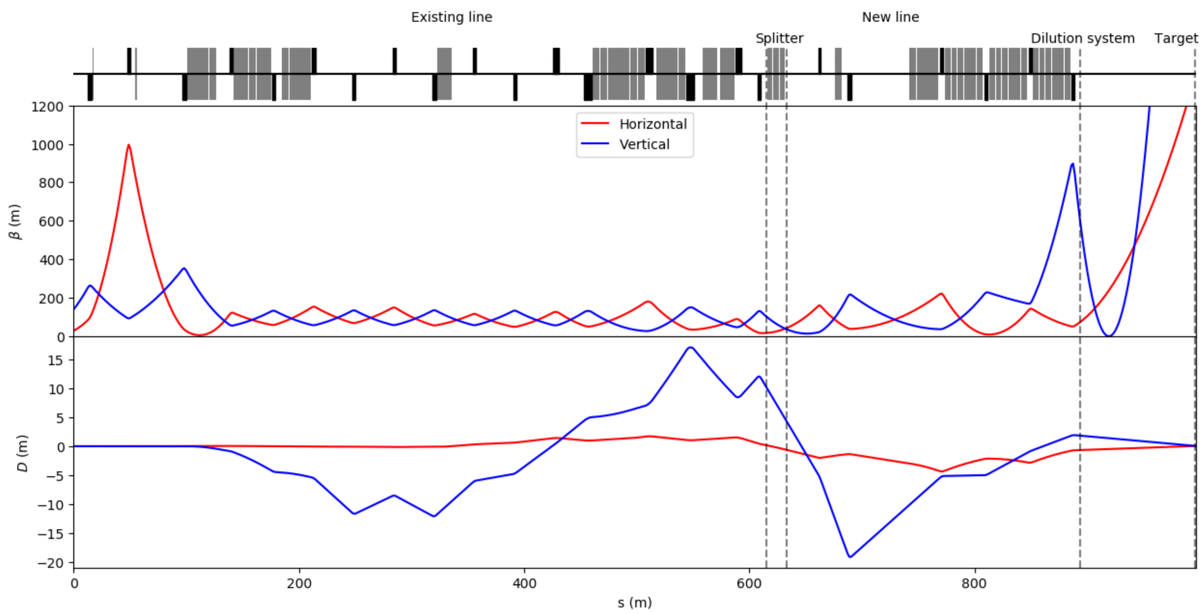

Fig. 4.3: Synoptic view and optical functions along the transfer line from the SPS to the BDF target. Dipoles are represented as grey bars, and quadrupoles are represented as black squares above the centre line for focusing and below it for defocusing.

The beam optics for the BDF transfer line have been studied in detail using the simulation code. Figure 4.3 shows the resulting optics, taking into account input from the integration work detailed in Chapter 8. The optics in the existing part of the line are essentially the same as for current North Area operation. However, in contrast to the existing optics, the optical functions are kept small at the splitter, as no splitting is performed for the BDF beam. The positions and powering of all quadrupoles were optimized to use the available magnets and to allow integration in the available space near the TT22 line.

Complete cancellation of the dispersion at the target is achieved using carefully tuned phase advances and quadrupole settings in both the existing and the new line. Optical functions of 1364 m and

5456 m in the horizontal and vertical planes, respectively, allow a round-beam size on the target of $\sigma = 8\,\mathrm{mm}$ to be reached using the reference emittances defined in Section 4.2.1. The optical functions in Fig. 4.3 have been clipped above 1200 m for easier visualization but follow a typical quadratic evolution. The magnet choices and the powering scheme will be discussed in Section 4.3.

4.2.3 Aperture and correction scheme

It is critical to consider the fact that magnetic characteristics and device positioning cannot be perfect. Both lead to offsets between the ideal and the effective beam trajectory. In this section, we study the effects of such errors with the help of realistic modelling of the beam that includes apertures and the beam size.

Static errors, which comprise the alignment of the magnets and monitor and systematic field errors, were studied here. Using Ref. [2], we decided to consider the following realistic errors:

- in the dipole field of the `RBEND` elements, a relative error of $\mathcal{N}\left(0, (2.5\times10^{-4})^2\right)$[1] truncated at $\pm2\sigma$;
- in the quadrupole field of the `QUADRUPOLE` elements, a relative error of $\mathcal{N}\left(0, (2.5\times10^{-4})^2\right)$ truncated at $\pm2\sigma$;
- in the tilt around the longitudinal axis of the `RBEND` elements, an angle of $\mathcal{N}\left(0, (1.6\times10^{-6})^2\right)$ rad truncated at $\pm4\sigma$;
- in the transverse position of the `QUADRUPOLE` elements, a vertical and horizontal misalignment of $\mathcal{N}\left(0, (0.2\times10^{-3})^2\right)$ m truncated at $\pm3\sigma$;
- in the transverse position of the `MONITOR` elements, a vertical and horizontal misalignment of $\mathcal{U}\left(-0.5\times10^{-3}, 0.5\times10^{-3}\right)$ m;[2]
- in the transverse position at the start of the line, a vertical and horizontal misalignment of $\mathcal{N}\left(0, (0.5\times10^{-3})^2\right)$ m truncated at $\pm2\sigma$;
- in the transverse angles at the start of the line, a vertical and horizontal angle of $\mathcal{N}\left(0, (0.05\times10^{-3})^2\right)$ rad truncated at $\pm2\sigma$.

These errors were introduced in the model of the line, and 500 different sets of errors were generated. For each set of errors, correction was simulated using the beam centroid position at each monitor and finding the set of corrector strengths that minimized the offset at those monitors. Here, a total of 13 horizontal monitors, 16 vertical monitors, 5 horizontal correctors, and 11 vertical correctors were used. The new correctors are discussed in detail in Section 4.3.2, and the new monitors in Section 4.4.

Figure 4.4 shows the maximum expected envelopes of the beam obtained from the correction scheme modelling. Each of the 500 corrected trajectories is plotted along the line and is visible in the centre around the centre line for each plane. An envelope's maximum Z is defined as

$$\pm Z = N \times \sqrt{\epsilon\beta_z + \left(\sigma_{dp/p} \times D_z\right)^2} + z_{\max}\,, \tag{4.1}$$

where z stands for either x in the horizontal plane or y in the vertical plane. The absolute maximum excursion of the trajectory after correction is $z_{\max}$. The Twiss parameters are β and D, and the beam parameters ϵ and $\sigma_{dp/p}$ were discussed in Section 4.2.1. The envelopes shown in Fig. 4.4 by dashed lines use $N = 4$ and refer to the transport, with error and after application of the correction scheme, of the grey ellipse shown in Fig. 4.2.

It is clear that the correction scheme allows transport of the beam along the line, within the aperture of both the existing and the new elements. In the vertical plane, the envelope remains well within the

[1] $\mathcal{N}\left(\mu, (\sigma)^2\right)$ describes a normal distribution with median μ and standard deviation σ.

[2] $\mathcal{U}\left(a, b\right)$ describes a uniform distribution bounded by a and b.

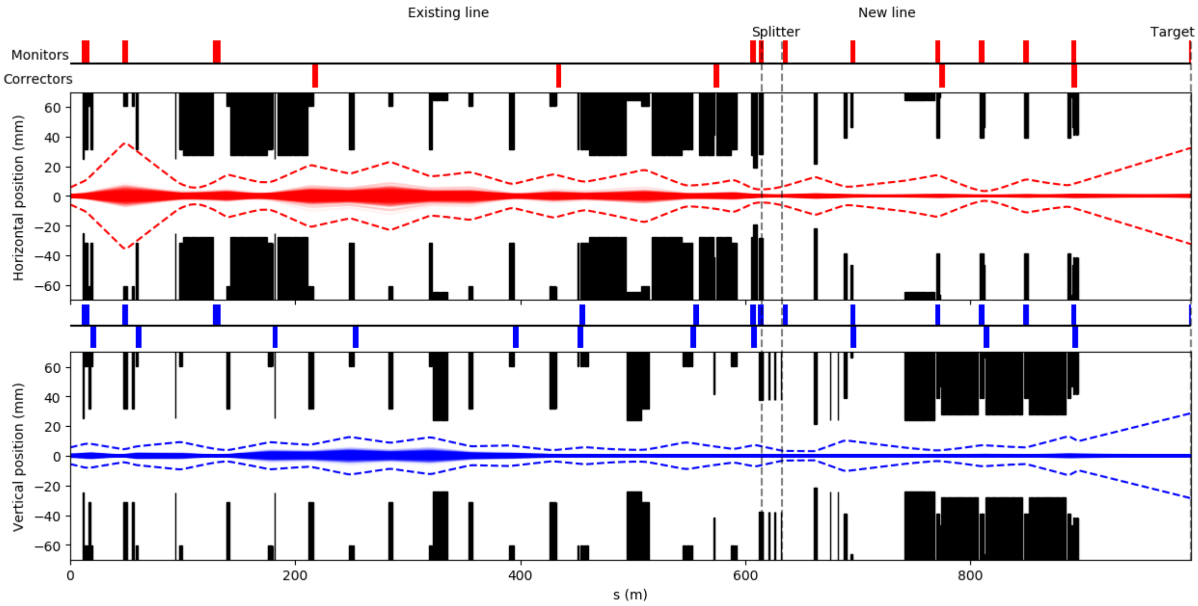

Fig. 4.4: Beam size along the line after correction of the trajectory in the horizontal and vertical planes, with element apertures shown in black. A synoptic view of the line shows the position, for each plane, of each monitor and each corrector magnet above and below the centre line, respectively.

aperture of all elements along the line. In the horizontal plane, Fig. 4.4 omits some specific apertures in the first few tens of metres of the new line, but these are discussed below.

At the splitter, the BDF beam travels in the lower-field region of the three magnets. The splitter magnets are aligned and symmetric, as discussed in more detail in Section 4.3.4. Therefore, as the BDF beam is bent towards the target, the left side of the aperture closes with the reference trajectory. Figure 4.5 shows a zoom of the envelope in the horizontal plane, with the splitter aperture closing with the beam envelope. This representation is relative to the ideal reference trajectory but quickly allows one to confirm that the size and aperture of the new splitter are compatible with the transported beam.

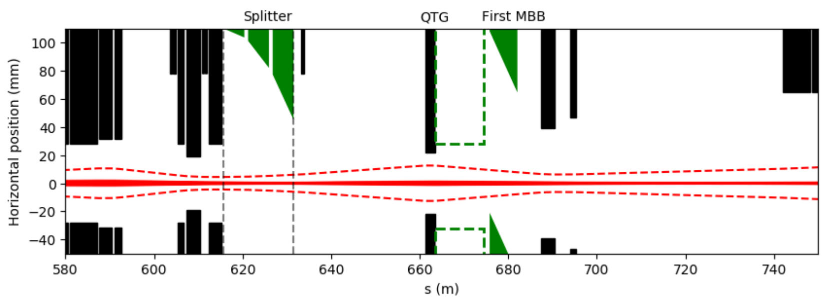

Fig. 4.5: Horizontal beam size after correction in the early part of the new line, with specific aperture limitations shown in green.

Because of the limited space immediately downstream of the splitter (see Section 8.2.4.3), the first quadrupole of the new line, of QTG type [3], features a smaller aperture than the other quadrupoles used in the extraction line. The smaller aperture of the quadrupole also allows tighter transverse external sizes and a stronger maximum gradient, both useful here. The aperture presented in Fig. 4.5 refers to the largest inscribed radius fitting within the magnet poles after accounting for the thickness of the vacuum pipe. This is a very conservative choice, as the beam is not round in this location and the real beam pipe has a lozenge section. Nevertheless, the envelope shown in Fig. 4.5 fits well within the aperture of the quadrupole.

Again because of size constraints, the upstream side of the first dipole is shifted away from the TT22 line by 40 mm, as discussed in Section 8.2.4.1. Owing to the curvature of the beam within the magnet and the angle between the two lines, the downstream side of the magnet is aligned with the reference trajectory of the BDF beam. Figure 4.5 shows the resulting aperture relative to the reference trajectory, and the aperture reduction caused by the shift of the upstream side of the magnet. The modelled beam envelope remains away from that limiting aperture and confirms the validity of the solution.

Lastly, the vacuum chamber used between the QTG quadrupole and the first dipole had to be reduced from the usual circular chamber of internal diameter 156 mm to a rectangular vacuum chamber of internal dimensions under vacuum of 154 mm in the vertical and 60.4 mm in the horizontal direction. In the vertical direction, the size is large enough to be ignored and well beyond the scale of Fig. 4.4. Figure 4.5 shows in dashed green lines the position of this aperture limitation in the horizontal plane. The aperture is rather close to the beam but still far enough away to pose no risk of clipping the BDF beam.

4.2.4 Modification to the TT22 line

As discussed in Sections 8.2.4.1 and 8.2.4.3, the existing TT22 line has to be slightly modified to accommodate the new BDF line.

The first modification consists of the relocation of the first horizontal dipole corrector in the TT22 line, MDAH.220118. Figure 4.6(b) shows the dipole corrector moved from upstream to downstream of the two focusing quadrupoles QTAF.2202 and QTAF.2203, to around $s = 670\,\mathrm{m}$. This change is required to integrate the new BDF line, as discussed in Section 8.2.4.1. The full correction scheme for the line has not been studied here, but Fig. 4.6(a) shows that the effect of the shift on the trajectory offset created by this dipole is minimal. Furthermore, the operating current of the corrector is always around −20 A, well below the rating of 330 A of the magnet. Therefore, the relocation of that dipole corrector would only marginally modify the behaviour of the TT22 line.

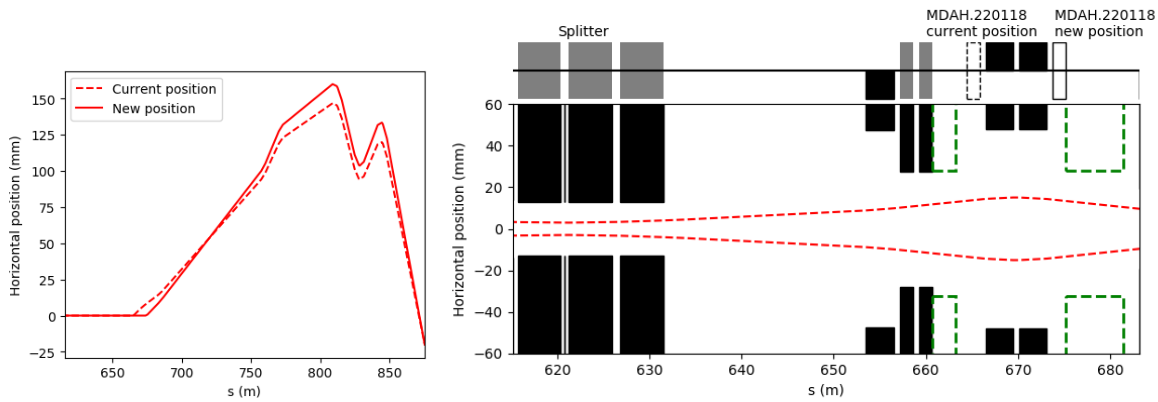

(a) (b)

Fig. 4.6: Trajectory offset in TT22 created by a kick of 1 mrad at MDAH.220118 at its current location (dashed line) and at its new location (solid line) (a). Apertures and beam size downstream of the splitter in the TT22 line, with synoptic representation of the lattice (b).

The second modification required on the TT22 line is a reduction of the dimensions of the vacuum chamber (see Section 8.2.4.3). Figure 4.6(b) shows the evolution of the $N = 4$ envelope with dashed red lines, according to Eq. (4.1) and following the horizontal beam parameters discussed in Section 4.2.1, but it does not include trajectory correction. The new vacuum chamber is rectangular, of internal dimensions under vacuum of 154 mm in the vertical and 60.4 mm in the horizontal direction. The chamber aperture, shown by dashed green lines, remains well away from the beam envelope. Even though the correction scheme and trajectory offsets were not considered here, the large distance that remains between the new aperture and the beam envelope validates this change.

Other changes not impacting on beam dynamics also have to be made. In particular, the secondary emission monitor grid BSGV.220075 has to be redesigned to accommodate the new BDF line. This modification is discussed in Sections 8.2.4.2 and 4.4.1.1.

4.3 Magnets

4.3.1 Main dipoles and quadrupoles

The new part of the line was designed with the intention of using magnets already available at CERN. Table 4.2 shows the magnets used in the current design of the BDF line. In particular, the apertures shown here were those used in Section 4.2.3 (Fig. 4.4) and refer to the total internal size, accounting for chamber compression effects from vacuum and from fitting the magnets. In the case of the quadrupoles, the aperture used corresponds to the diameter of the largest inscribed circle fitting within the poles, reduced by the thickness of the vacuum chamber. This definition of the aperture underestimates the available space when the beam size is not circular, but has proved to be sufficient for our study.

Table 4.2: Main magnet types used for the new BDF line, and their specifications

Function	Type	Number	Magnetic length	Aperture		Max. current	Max. field or gradient
				x	y		
			(m)	(mm)		(A)	(T or T/m)
Dipole	MBB [4]	5	6.26	129	48.5	5750	2.02
Dipole	MBN [5]	18	5.0	152	55.5	1340	1.8
Quadrupole	QTG [3]	1	2.2	43	43	530	34
Quadrupole	QTL [6]	5	2.99	78	78	416	24

4.3.1.1 Powering scheme

A detailed powering scheme was investigated, and this provided a comprehensive input for the costing of the project. It was developed to provide a 7.2 s repetition cycle with a 1.2 s magnetic flat top, coherent with the most demanding scenarios discussed in Chapter 2. Present standards for new beam lines at CERN require that all magnetic elements be pulsed and that the power supply be able to recover the inductive energy to minimize power consumption. All the power converters identified for powering the magnets of the new BDF line are part of the new SIRIUS family [7].

Table 4.3 shows the result of the power supply study and presents some important parameters. The nominal currents are associated with the optics discussed in Section 4.2.2 and will be achievable in the most stringent cycle considered. The strongest constraint on this powering scheme is that every circuit needs enough internal energy storage capacity to limit its electrical consumption to the compensation of the ohmic losses in each circuit.

The powering scheme is sized to provide currents of up to 5% and 20% beyond the nominal values for the dipoles and quadrupoles, respectively. The values for the maximum power supply current and associated field in Table 4.3 are indicative only, and may not be reachable by the system with the nominal repetition rate or associated ramp rate. Furthermore, the quadrupole power supplies must be designed for four-quadrant operation and thus be capable of changing polarity.

Table 4.3: Powering schemes, with nominal currents and indicative maximum fields achievable. Negative values refer to quadrupoles used for defocusing.

Type	Number of power circuits	Nominal		Power supply maximum	
		Current (A)	Field (T or T/m)	Current (A)	Field (T or T/m)
MBB	1	5493	1.92	5750	2.02
MBN	6	1070	1.46	1800	>1.8
QTG.01	1	297	23.5	450	28.9
QTL.02	1	−287	−16.6	900	>24.0
QTL.03	1	251	14.5	450	>24.0
QTL.04	1	−160	−9.2	450	>24.0
QTL.05	1	248	17.3	450	>24.0
QTL.06	1	−396	−21.3	900	>24.0

4.3.2 Dipole corrector magnets

The new BDF line requires dipole correctors with an integrated field $Bl \approx 0.5\,\mathrm{T\,m}$ and a laminated core to handle the pulsing of the BDF cycle. Unlike the main dipoles and quadrupoles, no existing dipole corrector magnets in storage at CERN could be used for the design of the new line. An existing short dipole corrector based on a solid core exists, however: the MDX corrector magnet [8]. A laminated version of the MDX magnet is already being developed in the context of another project [9]. Table 4.4 summarizes the preliminary specifications for the dipole correctors used in our study.

Table 4.4: Preliminary specifications for the laminated MDX magnet design

Aperture in bending plane	140 mm
Aperture in non-bending plane	100 mm
Total length	630 mm
Maximum integrated field	0.509 T·m
Maximum current	240 A
Resistance	320 mΩ
Inductance	221 mH

A total of five of these correctors are used along the new line to correct the trajectory. An additional single dipole corrector, the VREF, is provisioned to impart a small vertical angle to the BDF line if required because of incoherence in the current 3D integrated model related to a change in the definition of verticality between the Meyrin and Prévessin sites. A further four of those correctors will be required for the dilution system, which will be discussed in Section 4.3.3.1. In total, 11 of the new laminated MDX-type dipole correctors will be used in the new BDF line.

The six correctors and the single VREF will each be powered by a single four-quadrant power supply capable of recovering and storing the inductive energy between cycles. The voltage specifications will also allow small changes during the spill to compensate for any systematic motion of the beam during the 1 s spill.

4.3.3 Dilution system

As discussed in Section 5.5.4.2, the target cannot handle the extracted beam for a full 1 s spill, despite the relatively large round beam of $\sigma = 8\,\mathrm{mm}$. A dilution system aim at moving the beam spot across the target during the spill is necessary. The simulations presented in Section 5.5.4.2 show that a circular pattern of radius 50 mm repeated four times during the spill will be sufficient. This dilution scenario is considered the nominal case.

4.3.3.1 Dilution system design

The last 100 m of the BDF line is empty of magnetic elements. It is natural that the dilution system would make use of this drift space by imparting a small angle to the beam that translates into the required offset at the target.

The angle required to be imparted to the beam 100 m upstream of the target to reach an offset $R = 50\,\mathrm{mm}$ is $\theta_{\mathrm{max}} = 500\,\mu\mathrm{rad}$. Using the magnetic rigidity of a 400 GeV/c proton beam, we find that the maximum integrated field required is $Bl_{\mathrm{max}} \sim 0.667\,\mathrm{T{\cdot}m}$. This integrated gradient can be achieved using two laminated MDX magnets (see Table 4.4) powered at $I_{\mathrm{max}} \sim 160\,\mathrm{A}$.

The required pattern can be obtained by driving each quadrupole with a sinusoidal current at a frequency of $f_{\mathrm{dil}} = 4\,\mathrm{Hz}$. We need to consider both the voltage $U(t)$ and the current $I(t)$ as a function of time t for this application:

$$I(t) = I_{\mathrm{max}} \times \sin\left(2\pi f_{\mathrm{dil}} t\right) , \tag{4.2}$$

$$U(t) = I_{\mathrm{max}} \times \left(2\pi f_{\mathrm{dil}} t \times L \times \cos\left(2\pi f_{\mathrm{dil}} t\right) + R \times \sin\left(2\pi f_{\mathrm{dil}}\right)\right) , \tag{4.3}$$

where R and L are the magnet resistance and inductance, respectively, listed in Table 4.4. Figure 4.7 shows the evolution of the current and voltage during a full spill. The large required maximum voltage per magnet of $U_{\mathrm{max}} \sim 890\,\mathrm{V}$ prevents the use of more than one magnet per power supply. Therefore each of the two magnets needed to achieve the offset R is to be powered by a dedicated power supply through a dedicated pair of cables.

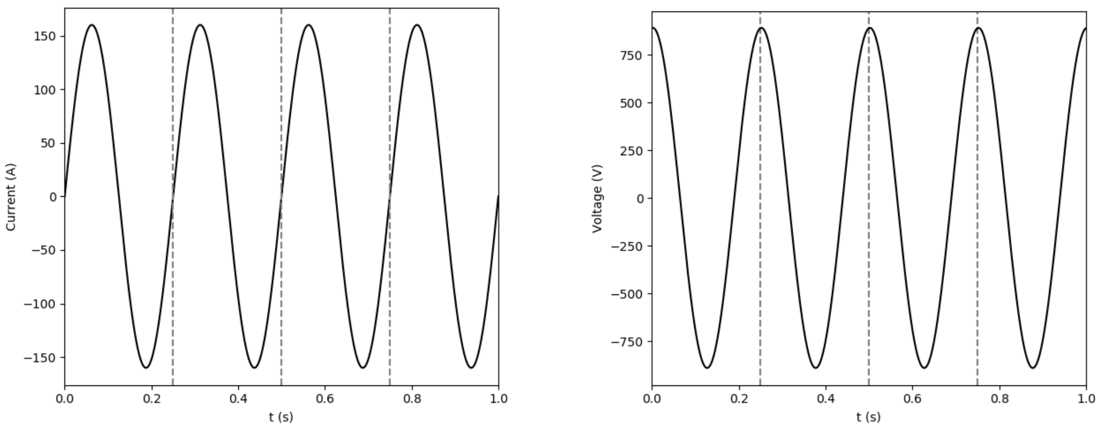

(a) **(b)**

Fig. 4.7: Required current (a) and voltage (b) for the MDX magnet for the dilution system as a function of time.

The power supply selected for this application may reach up to 900 V and 450 A. Here, the frequency translates directly into high voltages owing to the inductance of the magnet. The margin between the required maximum voltage U_{max} and the power supply rating is particularly small. A more complex voltage function, however, such as a clipped sinusoidal function, may be applied to increase the maximum current reached with only a small effect on the shape of the current function.

Since we need two independent circuits to reach the integrated field Bl_{max}, we need four independent circuits to obtain a circular pattern of the beam on the target. This can be achieved by splitting the four circuits into two groups, referred to as 0 and $\pi/2$, in which the magnets are oriented horizontally and vertically, respectively. Each group is driven by the current functions

$$\begin{aligned} I_0(t) &= I_{\max} \times \sin(\omega t) \ , \\ I_{\pi/2}(t) &= I_{\max} \times \sin(\omega t + \pi/2) \ , \end{aligned} \tag{4.4}$$

where $\omega = 2\pi f_{\mathrm{dil}}$. We refer to this scheme as the $\pi/2$ dilution scheme. This scheme provides the required circular pattern, with a radius of 50 mm on the target.

Given that there are four independently powered circuits, we can investigate a more complex scheme. By rotating each magnet by $\pi/4$ and powering them with the correct dephasing, we can achieve the same circular dilution pattern. Each of the four magnets is then oriented along a direction θ and powered by a current function I_θ as follows:

$$\begin{aligned} I_0(t) &= I_{\max} \times \sin(\omega t) \ , \\ I_{\pi/4}(t) &= I_{\max} \times \sin(\omega t + \pi/4) \ , \\ I_{\pi/2}(t) &= I_{\max} \times \sin(\omega t + \pi/2) \ , \\ I_{3\pi/4}(t) &= I_{\max} \times \sin(\omega t + 3\pi/4) \ . \end{aligned} \tag{4.5}$$

(4.6)

This arrangement is called the $\pi/4$ scheme.

The two schemes detailed here provide the same dilution pattern on the target. Therefore the simpler $\pi/2$ scheme would be favoured. We will go into more detail, however, about the advantages of the $\pi/4$ scheme when we study failure cases in Section 4.5.1.

4.3.4 Splitter

To allow switching of the BDF beam in the direction opposite to the existing North Area beams, three MSSB splitters of a new design are planned to be installed in place of the existing first splitter triplet (MSSB.2117). In the present configuration, the beam can be sent straight towards T2 or bent to the right towards T6. The new MSSB design will add the capability to switch the beam towards the BDF target complex while maintaining full compatibility with the operation of existing experiments in the North Area.

To allow the switching of the beam, the magnets must have the possibility of reversing their polarity in a relatively short time between cycles of the machine. The main way to achieve this is to replace the present solid iron yoke with laminations, so as to mitigate the eddy currents induced by the field variation associated with the switch in polarity.

The high radiation levels and the fact that the iron yoke is enclosed in a vacuum tank imply that the insulating coating on the laminations has to be inorganic and vacuum-compatible. Another radiation-hardness measure is the use of mineral-insulated copper conductors (MICC) to build the coils of the magnets. These conductors use compacted magnesium oxide (MgO) powder as an insulator instead of an epoxy resin–glass fibre composite. A water-cooled MICC has been successfully employed in the existing MSSB design and is still in operation. To reduce the inductance of the magnet and improve compatibility with the powering circuit, the number of turns in the coil will be reduced from 48 to 35 and the current correspondingly increased, with a simultaneous increase in the conductor cross-section. To allow quick exchange of a magnet in the case of a fault, all connections, both hydraulic and electrical, will be of a plug-in type. This will also allow automatic alignment of the magnet without the necessity to enter the high-radiation area.

The construction of a short prototype of the laminated top yoke is currently under study. The aim of the prototype is to validate the proposed manufacturing technology and prove that the mechanical tolerances required are achievable over a 5 m long laminated yoke. The main area of interest is the septum blade region, in which even small imperfections can drastically increase beam losses.

4.4 Instrumentation

4.4.1 Beam position and profile monitors

The beam position and beam size will have to be measured at several locations along the line. The measurement system will also be used to measure the evolution of the beam position and beam size during the extraction process, with a temporal resolution of 100 ms. The system should also be able to function over a wide range of intensity, i.e. for beams of 1×10^{11} to 4×10^{13} protons per second.

4.4.1.1 Upgrade of existing transfer line

The existing TT21 line up to the first splitter is shared by all beams. The instrumentation of these lines is being reviewed, as some systems no longer fulfil present and foreseen operational requirements. The expected time line for renovation is during Long Shutdown 3 (LS3), but funding has yet to be found. However, in the scope of the current BDF work, a few specific monitors and their specifications have been identified.

Table 4.5: Required modifications for the TT21 beam line instrumentation. “BSP” refers to split foils used to measure position.

s	Current name	Horizontal		Vertical	
		Resolution	Coverage	Resolution	Coverage
(m)		(mm)		(mm)	
181	BSP.210508	1.5	22.5	1.5	22.5
318	BSP.210858	2.5	37.5	2.5	37.5
397	None	None		2.5	37.5
515	BSPH.211411	5.0	75.0	None	

Table 4.5 summarizes the specifications of the monitors for which replacement is being requested. The proposed solution is to provide 16 wires per grid per plane, consistent with the above requirements, while keeping cabling and electronics costs reasonable.

The new beam line layout impacts an existing secondary emission monitor grid tank (BSGV.220075), which must be modified mechanically as the present tank is too wide. A new tank where the external diameter does not exceed 225 mm is under study, with the grid movement operated from below. All other parameters, including the number and position of the wires, of this secondary emission monitor grid are expected to remain unchanged.

4.4.1.2 New BDF line

In the new beam line which branches off downstream of the first splitter (MSSB.2117), a total of five beam position (centroid) and beam size measurement devices should be provided. The specifications in terms of coverage and resolution are summarized in Table 4.6.

The proposed solution is here also to provide secondary emission monitor grids with 16 wires per grid per plane, consistent with the above requirements, while keeping cabling and electronics costs reasonable.

4.4.1.3 Target beam monitoring

A new target screen monitor (BTV) is requested at a location approximately 50 m upstream of the target, where the beam r.m.s. size is expected to be around 5 mm in both planes. It should provide a 2D image of the beam, allowing the beam position and size to be extracted. The total area to be covered is 70×70 mm, with images taken every 100 ms for offline analysis.

Table 4.6: Specifications for the beam instrumentation of the new BDF line

s	Provisional name	Horizontal		Vertical	
		Resolution	Coverage	Resolution	Coverage
(m)		(mm)		(mm)	
692	BDF.02	1.5	22.5	1.5	22.5
769	BDF.03	2.5	37.5	0.8	12
808	BDF.04	0.8	12	1.5	22.5
847	BDF.05	1.5	22.5	1.5	22.5
889	BDF.06	1.5	22.5	2.5	37.5

4.4.2 Other instruments

4.4.2.1 Intensity measurement

It is requested to measure the beam intensity at one specific location, close to the monitor BDF.06 in the new beam line. The intensity should be provided throughout the slow extraction with a time resolution of 100 ms. The intensity range to be covered ranges from 1×10^{11} to 4×10^{13} charges, with a resolution of 5×10^{10} charges and an accuracy on the level of 1%.

4.4.2.2 High-frequency spill structure monitor

The high-frequency time structure of the beam is relevant for the facility up to 10 GHz. R&D efforts are to start after LS2 to provide a spill monitor covering frequencies up to and including 200 MHz.

4.4.2.3 Beam loss monitors

A total of nine new ionization monitors are requested along the new beam line at locations yet to be defined. If losses exceed operational thresholds during the slow extraction, a hardware interlock should trigger a beam dump with a reaction time not exceeding 10 ms.

4.5 Failure scenarios and machine protection

As shown in Table 2.1, both the instantaneous and the average beam power are very high. This calls for a specific approach to studying failure scenarios to prevent catastrophic machine damage. The results of preliminary investigations are presented below. A rigorous study should be conducted in the preparatory stage of the Technical Design Report.

4.5.1 Dilution system failure

The dilution system is required in order for the target to handle the full spill from the SPS. Uninterrupted extraction without the nominal dilution pattern is potentially a very serious incident for the target. For instance, a single full spill without dilution would lead to a complete failure of the BDF target (see Section 5.5.4.2).

4.5.1.1 Dilution failure patterns

Because of the four fully independent dilution kickers, a wide range of patterns are possible, depending on the scheme used and the power supply failure that occurs. Figure 4.8 shows the different dilution patterns possible on the target and represents the extent of a round beam of $\sigma = 8\,\mathrm{mm}$ in transparent shading.

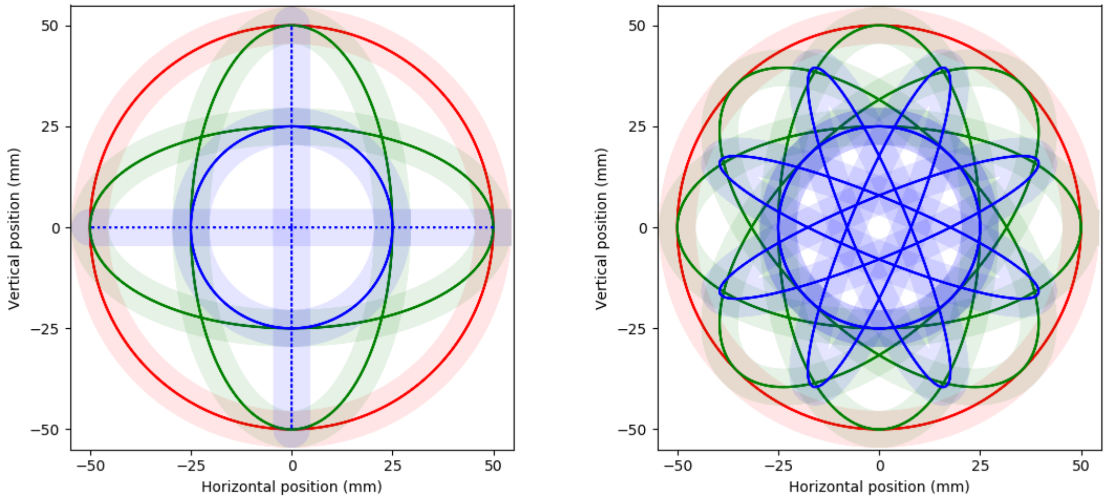

Fig. 4.8: Possible dilution patterns on the target with all four circuits (red), three circuits (green), and only two circuits (blue). Part (a) shows patterns for the $\pi/2$ scheme, while the possible patterns for the $\pi/4$ scheme are shown in (b).

The loss of one single circuit causes the dilution pattern to take a oblong shape, shown in green in Fig. 4.8. This scenario is referred to as case 1 in Section 5.5.4.2 and would not require replacement of the target.

In the eventuality of the loss of two dilution circuits, multiple different patterns may be considered. We can see here the effect of the $\pi/4$ magnet scheme introduced in Section 4.3.3.1. In the case of the simplest, $\pi/2$ scheme, the simultaneous loss of two circuits may lead to a flat dilution pattern in 33% of cases, and this is represented by dotted lines in Fig. 4.8b. In the case of the $\pi/4$ scheme, no two circuits share the same axis. This prevents the loss of two power supplies leading to a flat dilution pattern. In this $\pi/4$ scheme, the loss of two circuits leads to a flattened elliptical pattern in 66% of cases.

The loss of two circuits with the $\pi/2$ scheme and the flat pattern, and with the $\pi/4$ scheme and the elliptical pattern are referred to as case 3 and case 4, respectively, in Section 5.5.4.2. It was established that both scenarios would require replacement of the target. Case 2, which refers to a smaller circular pattern of radius 25 mm, would likely not necessitate replacement of the target. Therefore the $\pi/2$ scheme is favoured, since the loss of two circuits would require replacement of the target in 33% of occurrences, while the corresponding probability would be 66% for the $\pi/4$ scheme. It is the $\pi/2$ scheme, with two horizontal and two vertical dilution circuits, that is implemented in the drawings of the line presented in Section 5.5.4.2.

Finally, the simultaneous loss of three circuits would lead to a 50 mm long flat dilution pattern. This scenario would also require replacement of the target.

4.5.1.2 *Mitigation systems and interlocks*

The currents in the power supplies (in the dilution system or elsewhere in the transfer line) can be monitored continuously during the execution of the programmed function. The front-end power converter control system (Function Generator/Controller (FGC)) provides the possibility to interlock on a regulation error (i.e. a power converter not following the programmed function within a predefined tolerance) [10] at a frequency of 1 kHz. The output of the FGC needs to be connected to a dedicated slow-extraction Beam Interlock System (BIS), the details of which will be discussed below. The trigger to the BIS can occur within 200 µs. The time it takes to stop slow extraction will have to be evaluated taking cable lengths all the way to the SPS beam dump system into account. The total BIS reaction time will, however, be significantly below 100 ms, as was studied in case 6 in Section 5.5.4.2. As additional protection to ensure that the correct functions are loaded to the power converters, a rough absolute-current-value interlocking should be provided by the SPS software interlock system (SIS) for all converters except the ones used in the dilution system. The flat-top current function loaded should be compared with a reference current value at the start of acceleration in the SPS. The tolerances have to be sufficiently large to allow for COSE. This consistency check will ensure that not only are the power converters following the programmed functions, but also they are all consistent with each other for a given mode of operation, either BDF or NA. For the dilution system, another software application/makerule will have to be prepared that allows one to load only functions fulfilling certain criteria. The current settings for the dilution system should be managed by the use of the Management of Critical Settings (MCS) system.

The monitoring system discussed in Section 4.4.1.3 will also be used to validate the performance of the dilution system. After every extraction cycle, data from the system will be automatically analysed and compared with the nominal dilution pattern. The system can use other information sources, such as power supply currents or radiation levels in the tunnel. Only once the normality of the previous cycle has been confirmed will a new extraction cycle be permitted. Such an automatic post-operation checking system is already used for the LHC dump [11], but would need to be completed here within no more than $\sim$4 s.

The methods for interlocking the dilution system presented in this section so far have in common that they are software-based solutions. Taking into account the criticality of the beam dilution on the target, an additional hardware-based system is advisable for interlocking the dilution system. Such a hardware interlock could be realized by obtaining a signal proportional to the sweep velocity by analogue signal processing of the current measurement signals of the horizontal and vertical dilution magnets, which are proportional to the horizontal and vertical beam positions on the target. This sweep velocity should be constant during the flat top in regular operation. By comparing the sweep velocity signal with a reference, a deviation can be detected and the beam interlock triggered.

4.5.1.3 Failure probability listing

We have established that it is not possible to absolutely prevent failure of the dilution system. Therefore, a statistical approach to the failure cases can give us an objective expectation of the performance of the system and direct studies towards more complex protection systems if needed.

The SIRIUS power converters expected for the dilution system have not yet been operated at CERN. Hence no measured failure probabilities are available. Furthermore, the complexity of the power converters prevents an accurate estimation of the mean time between failures). Only the design goal lifetime of 50 000 h is known. As the SIRIUS system will be operated to power the TT10 line magnets, experimental numbers will become available after LS2.

4.5.2 Interlocking slow extraction at the CERN SPS

Beam interlock controllers (BICs) are used to gather the interlock signals (True or False) from different systems such as beam loss monitors and power supplies. The inputs are combined by a logical AND, and the result is input to a so-called master BIC.

The TT21 BIC will combine signals from the extraction equipment (ZS voltage and magnetic septa) and from power converters, the SIS software, and BLM interlocks before the first splitter. The NA BIC will have inputs from the current of the first splitter, from beam loss monitors, and from the TT22/TT25 power converter interlocks. Finally, the BDF BIC will cover the power converters in the new BDF line, the muon shield, the dilution kickers, etc.

Faults due to BDF systems should not stop operation of the NA or any other beams in the SPS, and vice versa. For this purpose, a concept of arbitration between slow-extraction interlocking for the

NA and the BDF has to be provided. Timing destinations are a useful concept for this purpose. The master BIC would have as additional inputs the destination BDF or NA (provided by the timing system) and take only the relevant BICs into account in its output. For example, if the destination is BDF, only the TT21 and BDF BICs have to give a green light. At the same time, if neither of the destinations BDF or NA is provided by the timing system, none of the TT21, BDF, or NA BICs are taken into account. The output of the master BIC is connected to an unmaskable input to the SPS ring permit BA2 BIC. If any input of a ring permit BIC goes false, an SPS beam dump is triggered. The simplified master BIC equation is

$$\begin{aligned}&[\neg \mathrm{destination}_{\mathrm{BDF}} \wedge \neg \mathrm{destination}_{\mathrm{NA}}] \vee \\ &\qquad [\mathrm{BIC}_{\mathrm{TT21}} \wedge [(\mathrm{destination}_{\mathrm{BDF}} \wedge \mathrm{interlocks}_{\mathrm{BDF}}) \vee (\mathrm{destination}_{\mathrm{NA}} \wedge \mathrm{interlocks}_{\mathrm{NA}})]] \,. \end{aligned} \tag{4.7}$$

As timing destinations are not rigorously enforced, and BDF interlocks are taken into account only if the correct timing destination is set, a mechanism has to be provided so that no slow extraction is possible without the correct timing destination. A way to achieve this is to modify the power converter controls of the SPS extraction bumper and the SPS extraction sextupole circuits, such that they pulse only if a timing destination of either NA or BDF is set for the given cycle.

References

[1] C. Hessler et al. “Beam optics studies for BDF and for tests of a prototype target”. In: *Proc. of 9th International Particle Accelerator Conference (IPAC 2018), Vancouver, BC, Canada*. 2018, TUPAF033. DOI: 10.18429/JACoW-IPAC2018-TUPAF033.

[2] W. Herr and M. Meddahi. “Trajectory correction studies for the CNGS proton beam line”. In: *9th European Particle Accelerator Conference (EPAC 2004) Lucerne, Switzerland, July 5–9, 2004*. 2004.

[3] *Norma Database, QTG design*. norma-db.web.cern.ch/magdesign/idcard/583/.

[4] *Norma Database, MBB design*. norma-db.web.cern.ch/magdesign/idcard/497/.

[5] *Norma Database, MBN design*. norma-db.web.cern.ch/magdesign/idcard/501/.

[6] *Norma Database, QTL design*. norma-db.web.cern.ch/magdesign/idcard/647/.

[7] G. Le Godec. *SIRIUS Power Converter: Technical Specification*. Tech. rep. CERN, Geneva, Switzerland, 2016. URL: edms.cern.ch/document/1586436/2.

[8] *Norma Database, MBN design*. norma-db.web.cern.ch/magdesign/idcard/231/.

[9] O. Crettiez. *Design report for the MDX L corrector magnet*. Tech. rep. CERN, Geneva, 2019. URL: https://edms.cern.ch/document/1892265.

[10] D. Nisbet. Personal communication. Sept. 20, 2018.

[11] E. Gallet et al. “Automatic post-operational checks for the LHC beam dump system”. In: *Proc. of 11th European Particle Accelerator Conference, EPAC 2008, Genoa, Italy, June 23–27, 2008*. Vol. C0806233. 2008, WEPP059.

Chapter 5

Production target design and R&D

5.1 Introduction and target requirements

The Beam Dump Facility target assembly is the core of the proposed Beam Dump Facility. The BDF target sits at the core of the installation, with a double function. On the one hand, it must absorb safely and reliably the full SPS primary beam. On the other hand, its design has been optimized from a physics point of view (in terms of geometry, material, gaps, etc.) to maximize the production of charmed mesons. It can be considered as a beam dump/absorber, since it will contain most of the cascade generated by the interaction with the primary beam. The high power deposited is one of the main challenges of the BDF target design, with 320 kW of average power deposited and 2.56 MW over the 1 s slowly extracted spill.

Such a high beam power expected on the target requires beam dilution, as well as a large beam spot diameter, to avoid target failure. The dilution pattern generated by the upstream magnets and the beam size have been optimized taking into account the aperture restrictions of the extraction line magnets and the mechanical performance of the target. As a result, the SPS primary beam will be diluted into four turns of a 50 mm radius circle for each 1 s pulse, with a beam spot size of 8 mm 1σ.

The materials sought for the BDF target are high-Z materials with a short nuclear interaction length, to increase the re-absorption of pions and kaons produced in the intranuclear cascade process. Details of the design will be discussed in Section 5.2 and later paragraphs, which will include energy deposition and radiation damage considerations (Section 5.3), thermomechanical and Computational Fluid Dynamics (CFD) simulations (Sections 5.5 and 5.6), and the preliminary mechanical design of the assembly (Section 5.7). A description of the design of the BDF target is also reported in detail in a separate publication [1]. A discussion of the selection of the target materials will be presented in Section 5.8, and a detailed presentation of the BDF target prototype, which was irradiated during 2018, will be given in Section 5.9.

5.2 Introduction to the target design

5.2.1 Selection of production target materials

The proposed Beam Dump Facility production target is a hybrid mechanical assembly, consisting of several collinear cylinders of TZM (0.08% titanium–0.05% zirconium–molybdenum alloy) and pure tungsten (W), clad with a W-containing Ta alloy, Ta2.5W (2.5% tungsten–tantalum alloy), as depicted in Fig. 5.1. The function of the target is to produce particles for the downstream experiment, but at the same time also to fully absorb the primary energy beam from the SPS. For this reason, the assembly is often referred to as the target/dump device of the BDF infrastructure.

To match the physics requirements for the BDF, the target/dump assembly should be characterized by the highest possible density and shortest possible nuclear interaction length. Thermomechanical and technical constraints, however, limit the possibilities for potential materials.

- For the first part of the target core, which will absorb a large fraction of the total beam power deposited in the target, TZM has been considered as the absorbing material. The material has a sufficiently high density to fulfil the requirements of the experiment, but it leads to energy deposition and stresses lower than those which would be encountered if materials with a higher density, such as pure tungsten, were chosen. This Mo-based alloy was selected because of its higher strength, better creep resistance, and higher recrystallization temperature compared with pure molybdenum [2].

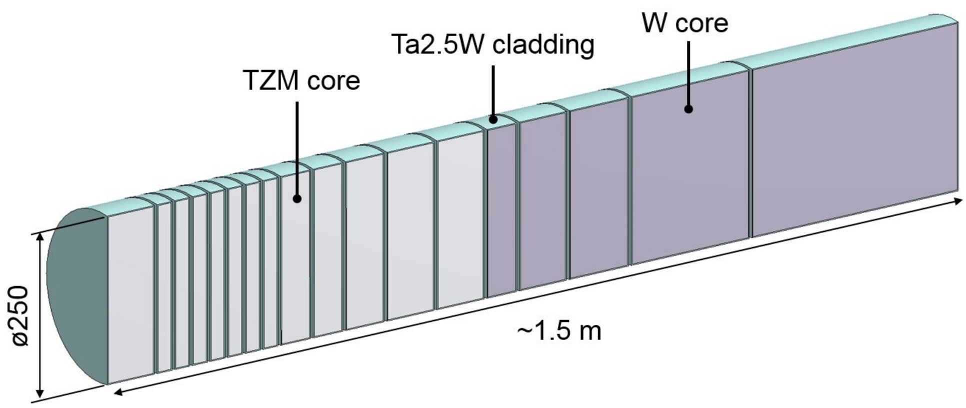

Fig. 5.1: Layout of the Beam Dump Facility target core, showing the first part, made of TZM, and the second part, made of pure W, both clad with Ta2.5W.

- For the second part of the target, which will receive much less power deposition from the primary beam, pure W has been chosen, since it fulfils the physics requirements and has proven good performance under irradiation [3].

The target needs to be actively cooled by water, given the high energy deposited and the high temperatures reached during operation. The cooling-system design is based on high-velocity water flowing through the 5 mm gaps foreseen between the target blocks. The high-speed water flow over the surface of the blocks allows an effective Heat Transfer Coefficient (HTC) between the cooling medium and the target that will dissipate the power deposited by the SPS primary beam. More details of the cooling-system design are given in Section 5.6.

The high-velocity water flow in contact with the pure W and TZM blocks could induce undesired corrosion–erosion effects. Therefore, all the target core blocks will be clad via diffusion bonding achieved by means of the Hot Isostatic Pressing (HIP) method with Ta2.5W [4, 5], a compound of Ta alloyed with W. This material was selected as the cladding material owing to its high corrosion resistance and its convenience as a high-Z material with a short interaction length. Ta2.5W has enough ductility to become plastic and allow diffusion bonding with the target core materials, and is soluble in molybdenum and tungsten, reducing the risk of forming intermetallic layers during the HIP diffusion bonding.

In the preliminary target design phase, pure tantalum was considered as a cladding material for the target core blocks, given the vast experience with tantalum-clad targets in other operating facilities such as the ISIS spallation neutron source at the Rutherford Appleton Laboratory [6] in the UK. However, structural calculations performed on the BDF target blocks (which are detailed in Section 5.5.2) have shown that the maximum stresses reached in the tantalum layer may be critical for the operation of the target, limiting its lifetime significantly. For that reason, Ta2.5W was considered an as alternative cladding material, with the advantage of a considerably higher strength at high temperatures and similar corrosion–erosion resistance [7, 2].

An exhaustive R&D study has been carried out in the framework of the BDF project to test the quality of bonding of Ta2.5W with TZM and with pure tungsten after the HIP process. The mechanical tests on the interface performed have proven that the intermetallic bonding strength of TZM or W with Ta2.5W is comparable to that with pure tantalum, validating the selection of Ta2.5W as the target cladding material. The procedures, results, and conclusions of the R&D studies carried out have been published in Ref. [8]. The selection of the target materials and their properties will be detailed further in Section 5.8.

As a further validation of the use of Ta2.5W in the cladding of the BDF target blocks, a prototype of the BDF target has been tested under beam in the North Area of CERN [9]. The BDF target prototype consists of a scale replica of the BDF target, with identical length and reduced diameter. Pure tantalum and Ta2.5W were used as cladding materials for the BDF target prototype, to compare the performance of both materials under beam irradiation. A Post-Irradiation Examination (PIE) campaign is planned during the course of 2019–2020 on several blocks of the target prototype, to characterize the mechanical bonding of the cladding and core materials after irradiation. A description and the results of the BDF target prototype beam tests in 2018 have been published in a separate paper [10].

5.2.2 Beam parameters and target design optimization

The 400 GeV/c proton beam pulse, with 4×10^{13} protons/pulse, will be extracted from the SPS to impact the target for 1 s, delivering an average power of 2.56 MW, followed by cooling for 6.2 s. Out of the 355 kW average beam power impacting the target, roughly 305 kW will be deposited inside the target assembly, while the rest will be lost in the surrounding (water-cooled) shielding of the BDF target complex. A detailed list of the BDF operational beam parameters is presented in Table 5.1.

Table 5.1: Baseline beam parameters of the BDF target operation

Proton momentum (GeV/c)	400
Beam intensity (p^+/cycle)	4×10^{13}
Cycle length (s)	7.2
Spill duration (s)	1.0
Beam dilution pattern	Circular
Beam sweep frequency (turns/s)	4
Dilution circle radius (mm)	50
Beam sigma (H, V) (mm)	(8, 8)
Average beam power (kW)	356
Average beam power deposited in target (kW)	305
Average beam power during spill (MW)	2.3

The BDF target core is made up of 18 collinear cylinders with a diameter of 250 mm and variable thicknesses, from 25 to 80 mm for the TZM blocks and from 50 to 350 mm for the pure tungsten blocks, giving a total effective target length of around 1300 mm. The length of the target cylinders was iteratively adjusted to reduce the level of the temperatures and stresses reached in the materials. Table 5.2 summarizes the target core materials and the longitudinal thicknesses of the blocks.

Figure 5.2 shows the maximum energy deposition in the longitudinal direction after the impact of one proton on the target, obtained via FLUKA Monte Carlo simulations [11]. Because Ta2.5W has a higher density than TZM, the peak energy deposition is reached in the cladding of the target blocks. The maximum values of energy for the TZM core part (first half of the target) are concentrated in blocks 2–8, which were segmented to have the shortest length (25 mm). The reduced thickness of these blocks allows more effective heat dissipation by the water flowing through the 5 mm gaps between the target cylinders, with the aim of reduction of the temperatures reached in the core and on the surface. The thicknesses of the following blocks increase gradually as the total energy deposition decreases. A similar approach is used for the second, higher-density, part of the target, made of pure tungsten: the first block is the most loaded one in terms of heat deposition, similarly to blocks 9 and 10 (with a TZM core), and hence the thickness of this block was set to 50 mm. The length of the following tungsten-core blocks then increases progressively as the energy deposited decreases.

The optimization of the target block thicknesses is essentially based on the distribution of the maximum energy deposition per block (shown in Fig. 5.2). As will be discussed in Section 5.5, the most critical stresses and cladding temperatures will be reached in the upstream thin blocks (i.e. blocks 3–6), where the interaction with the primary beam leads to the highest values of peak energy deposition and

Table 5.2: Summary of the longitudinal thickness and material configuration of the cylinders of the final BDF target, including the core and the cladding.

Block number	Core material	Cladding material	Length (mm)
1	TZM	Ta2.5W	80
2	TZM	Ta2.5W	25
3	TZM	Ta2.5W	25
4	TZM	Ta2.5W	25
5	TZM	Ta2.5W	25
6	TZM	Ta2.5W	25
7	TZM	Ta2.5W	25
8	TZM	Ta2.5W	25
9	TZM	Ta2.5W	50
10	TZM	Ta2.5W	50
11	TZM	Ta2.5W	65
12	TZM	Ta2.5W	80
13	TZM	Ta2.5W	80
14	W	Ta2.5W	50
15	W	Ta2.5W	80
16	W	Ta2.5W	100
17	W	Ta2.5W	200
18	W	Ta2.5W	350

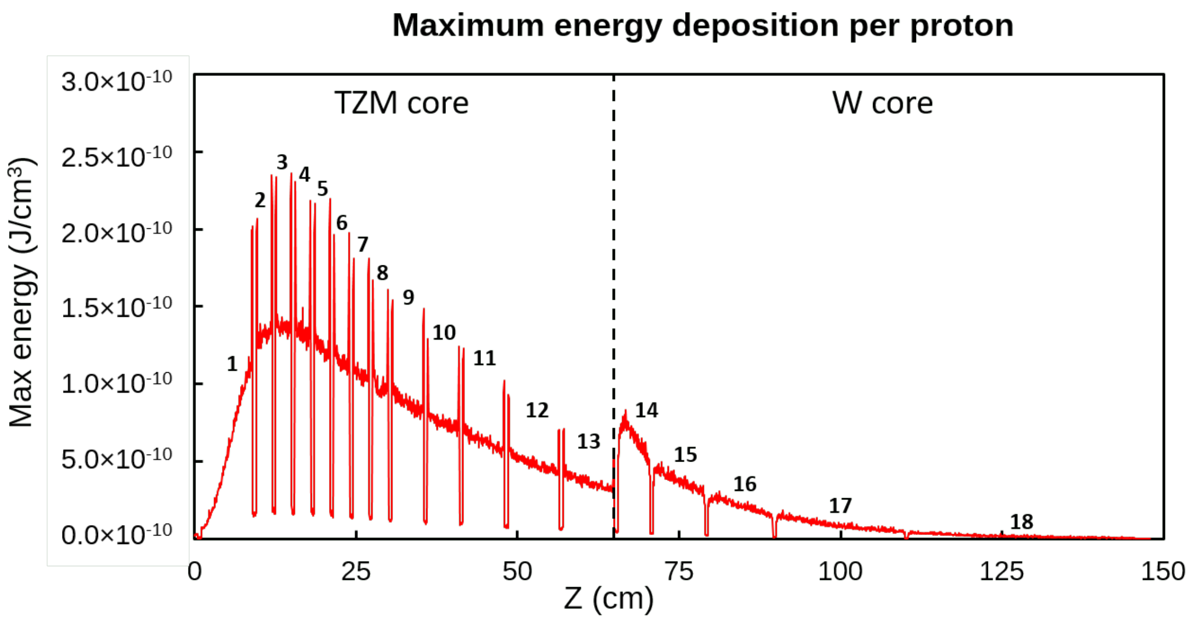

Fig. 5.2: Maximum energy deposition (per unit volume and per proton) in the BDF target blocks along the longitudinal axis, obtained via FLUKA Monte Carlo simulations.

power density.

A further improvement of the target design aimed at increasing its operational lifetime could be possible through additional segmentation of the low-thickness target blocks. However, the insertion of supplementary water gaps into the target design is not desirable from a physics perspective, since the presence of water in the longitudinal direction reduces the production of charmed mesons for the experiment, leading to higher background.

The advanced optimization of the target block thicknesses would require an evaluation of the temperatures and stresses in parallel with the variation of the lengths of the different cylinders. These calculations would be very costly in terms of time and computational power, given the high complexity of the thermal and structural Finite Element Model (FEM) simulations carried out for the evaluation of the performance of the target (see Section 5.5). The optimization of the target block thicknesses could be the subject of future studies if the operational conditions require it.

The total energy deposited in each target block is reported in Fig. 5.3; it can be observed that the total energy distribution for blocks 1–8 is rather uniform, with an energy deposition per block of around 100 kJ/pulse, lower than that for the more downstream cylinders. This is explained by the fact that the volumes of the first target blocks are much smaller than those of the rest of the blocks, the thickness of blocks 2–8 being the smallest (25 mm). Blocks 9–18 also show a quite uniform distribution of total energy, around 150 kJ/pulse, except for the last three tungsten blocks, where the energy deposition is considerably lower, owing to the dump/absorber nature of the target (roughly a total of 12 nuclear interaction lengths).

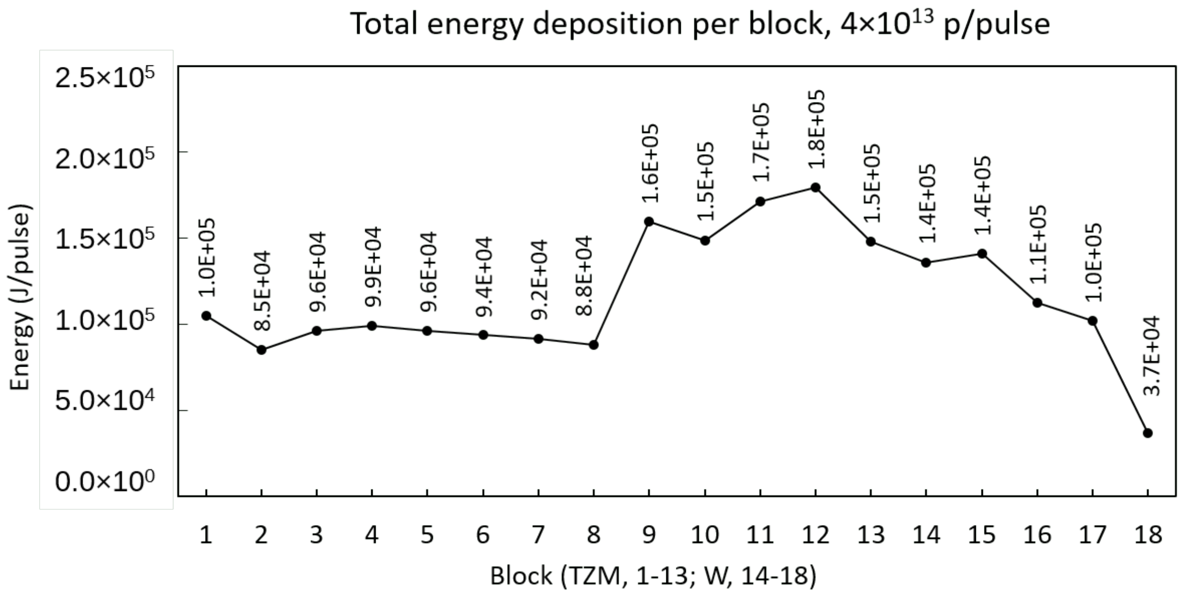

Fig. 5.3: Total energy in every block of the BDF target, assuming a nominal pulse intensity of 4×10^{13} protons.

5.2.3 Dilution system for target

The high energy deposited in the target requires beam dilution by the upstream magnets in the TDC2, as detailed in Chapter 4, since the impact of a non-diluted beam would lead to premature target failure by fracture of the core or cladding or both (melting is not likely to occur, given the high melting point of the target materials). The pattern used for the beam dilution has been optimized taking into account the mechanical performance of the target and the restrictions imposed by the upstream magnets. As a result, the SPS primary beam is foreseen to be diluted following a circular pattern, with four turns over a 50 mm radius circle for each 1 s pulse (Fig. 5.4).

The dilution system design has been improved with respect to the initial design, which consisted in an idealized Archimedean spiral with a radius from 5 to 35 mm, and five turns in 1 s. To evaluate the performance of the target with different dilution systems, thermomechanical calculations were carried out for one of the most loaded target blocks, to compare the maximum temperatures reached after several

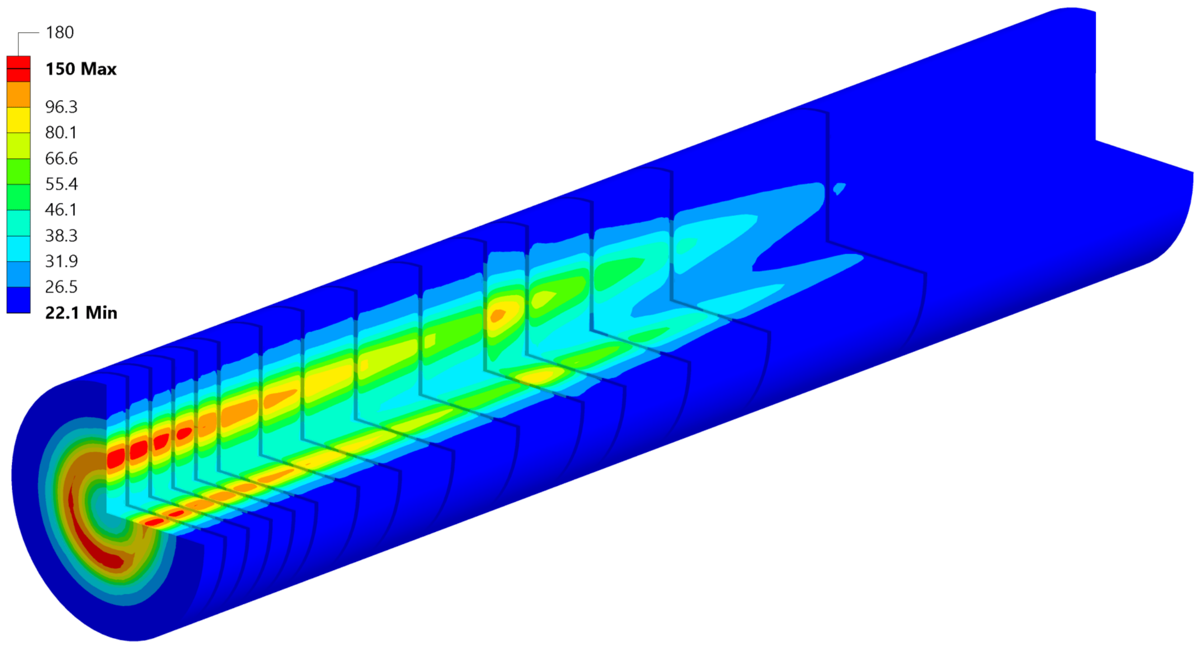

Fig. 5.4: Temperature distribution (in degrees Celsius) in the BDF target/dump when beam dilution is used. The BDF beam dilution scheme currently consists in four turns of the beam sweep over a 50 mm radius circular pattern during 1 s (i.e. 250 ms per circle).

pulses for each dilution scenario.

Figure 5.5(a) presents the evolution of the maximum temperature in the Ta2.5W cladding during a 1 s beam pulse (after several beam pulses) for different dilution scenarios. A similar trend is observed for both the TZM and the W cores. An increase in the sweep radius has a considerable impact in terms of reduction of the maximum temperature; it can be seen that the temperatures reached for a beam sweep over a 4–52 mm radius spiral are 200°C lower than for the first dilution design, with a 5–35 mm radius spiral. The dilution amplitude was therefore increased to the limits accepted by the upstream magnets (around 50 mm).

Furthermore, it can be observed that for an almost equivalent dilution amplitude of 50 mm, a circular sweep of the upstream magnets leads to a level of temperature in the cladding that is comparable to that for the spiral dilution pattern. The complexity of the dilution system is substantially reduced by using a circular dilution pattern instead of a spiral pattern: the spiral pattern requires a controlled variation of frequency and amplitude from the dilution magnets, while the circular sweep of the beam requires constant amplitude and frequency. Therefore, a circular dilution of radius 50 mm was chosen as the baseline sweep pattern for the magnet dilution system.

Finally, Fig. 5.5(b) presents a comparison of the maximum temperature build-up for circular dilution over a 50 mm radius circle using several numbers of turns for a 1 s pulse. It can be seen that an increase in the number of turns reduces the maximum temperature reached in the cladding to approximately 160°C. Four circular turns were selected as an optimal compromise between reducing the temperature and stress levels and keeping the dilution frequency within reasonable limits for the dilution magnets. More details of the beam dilution system can be found in Chapter 4.

As a further improvement to the dilution system design, the transverse beam size at the target/dump position has been maximized taking into account the limitations imposed by the aperture of the upstream magnets. It was shown that a larger beam spot size leads to lower temperatures and stresses in the target, since the energy deposition is more distributed in the volume of the material. The need for a compromise between maximizing the spot size of the round beam and the aperture restrictions of the transfer line

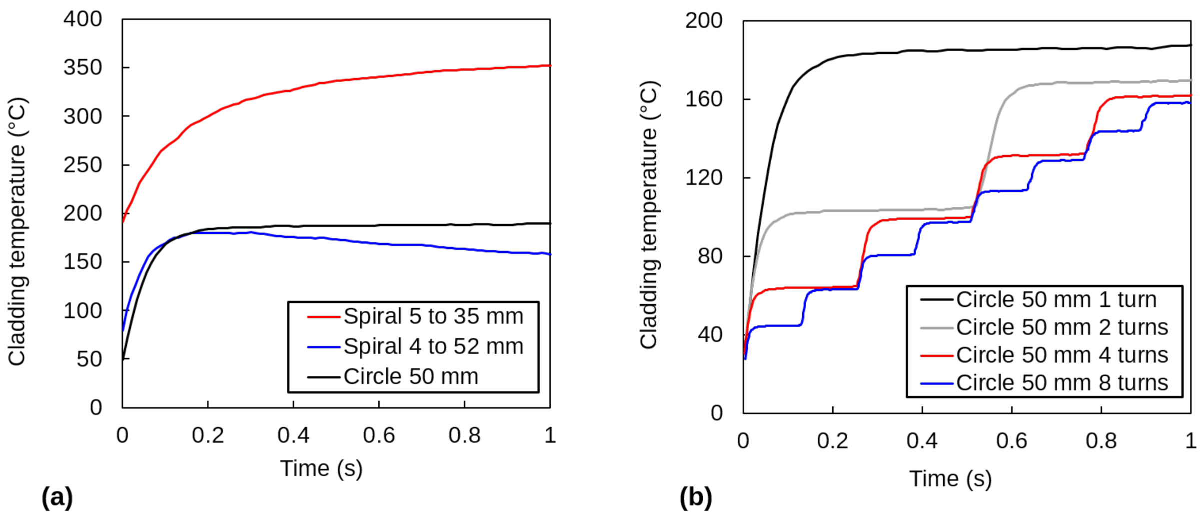

Fig. 5.5: Comparison of the maximum cladding temperature for (a) spiral and circular dilution patterns and (b) several circular turns.

magnets (see Chapter 4) led to the selection of a beam size on target of 8 mm 1σ.

5.3 Energy deposition in the target and radiation damage studies

5.3.1 Introduction

FLUKA Monte Carlo simulations [11, 12] have been performed to evaluate the energy deposited in the target blocks and to study radiation damage around the target.

The target core is composed of 18 cylinder blocks of 125 mm radius and different thicknesses. The thickness were iteratively adjusted as discussed in the previous sections. The first 13 blocks are made of TZM, while the remaining blocks are pure tungsten (W). Every block is clad with tantalum alloy 1.5 mm thick. The FLUKA model of the BDF target assembly can be seen in the left part of Fig. 5.6, visualized using the FLAIR [13] interface. The blocks and the target vessels are displayed, including the energy deposition in the blocks normalized to one pulse with 4×10^{13} protons. On the right, the figure shows the radial energy deposition (in J/cm^3) in the BDF target for one pulse of 4×10^{13} protons.

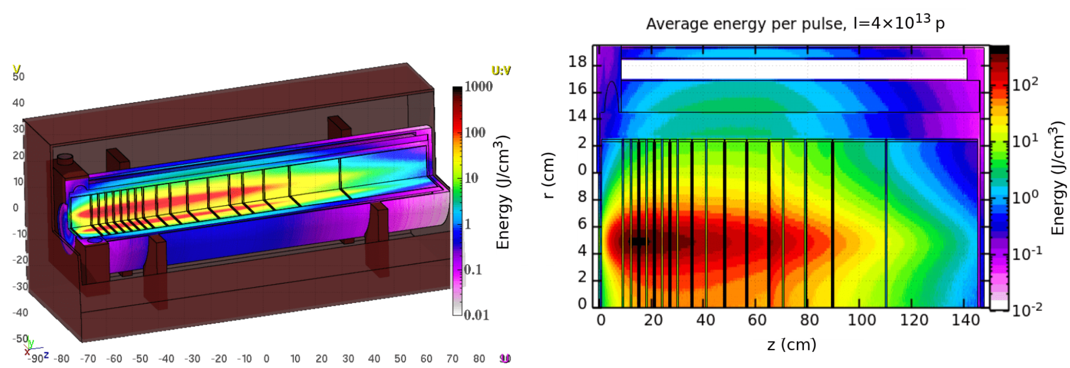

Fig. 5.6: Left, FLUKA model of the BDF target, including the target, the container, and the energy deposition. Right, radial energy deposition (in J/cm^3) in the BDF target in one pulse of 4×10^{13} protons.

The FLUKA simulations were performed using version 2011.2x.6, with a 400 GeV/c proton beam of Gaussian shape with 8 mm sigma on target, in a circular sweep of 5 cm radius, to reproduce the shape referred to in Section 5.2.2. The sweeping of the beam helps to dissipate the destructive effect of the beam on the material, such as a high peak in the energy deposition or damage to the material structure itself. The energy deposition was normalized to one pulse with 4×10^{13} protons, and the numbers of displacements per atom (dpa) and the R2E parameters were normalized to 1 yr of irradiation assuming 4×10^{19} protons.

5.3.2 Energy deposition

Figure 5.7 shows the average energy deposited per normalized pulse along the beam axis (z axis) for several radii. The energy density in the target can reach values between 0.1 J/cm^3 and a maximum of 500 J/cm^3. From the distribution, the transition between the TZM and tungsten blocks can be clearly seen. Similarly, the right part of the figure shows the total energy deposited in each of the blocks. From block 8 to block 9, the total energy increases because the thickness changes from 25 mm to 50 mm. The energy deposited in the 18 blocks is approximately 2.2 MJ per pulse, which means that they absorb about 78% of the total proton beam energy.

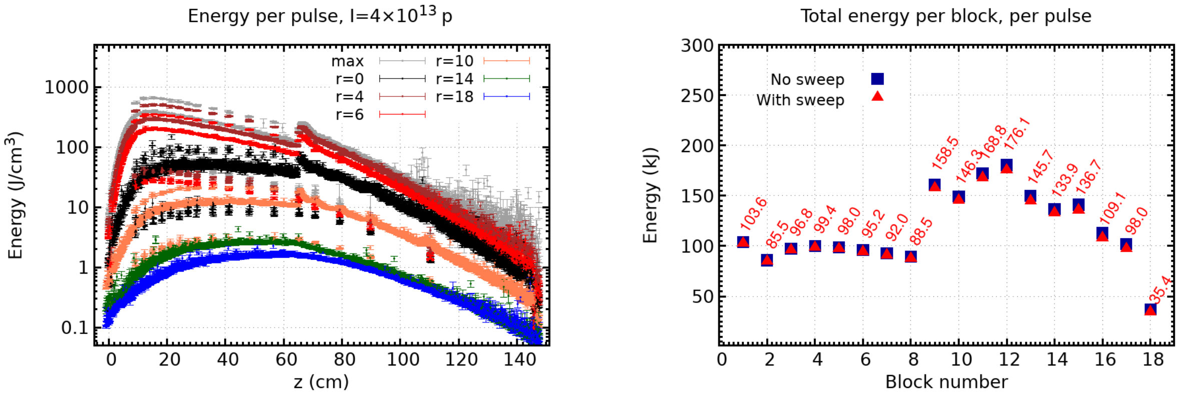

Fig. 5.7: Left: average deposited energy density along the beam axis (z) for several radii for one pulse of 4×10^{13} p. Right: total energy deposited per block and per pulse. For the latter, a comparison between the case with and without a sweep is shown.

Using a beam with same shape but in a swept path or concentrated in the centre gives approximately the same energy deposition per block, as can be seen in the right part of Fig. 5.7. However, if the beam is not dissipated in a circular path, the maximum energy density deposited in the target per pulse is about 10 times higher (as shown in Fig. 5.8). This would significantly increase the temperature and pressure gradients in the material, and would increase the risk of failure, even though the total energy per block remain similar.

5.3.3 Dose around the target

The BDF target is subjected to a considerable number of protons per year, expected to be in the order of 4×10^{19} protons/yr. Owing to the high average beam power and the high density of the production target, extremely high radiation levels are expected for the components around the target assembly. Information about the cumulative dose is important for determining the radiation hardness of the target and the proximity shielding, and of the water-cooling plug-in system, for example, and other equipment placed nearby. To this end, the same FLUKA Monte Carlo code model was employed.

In Fig. 5.9, the FLUKA model is shown cut away to display the centre of the target. Similarly, the left part of Fig. 5.10 shows the yearly average dose averaged around the target centre, while the right part shows the dose value at different distances from the central axis of the target. At 25 cm from the target centre, the dose can reach values of around 300 MGy per year, and at about 40 cm from the target centre, it reaches $\sim$100 MGy per year.

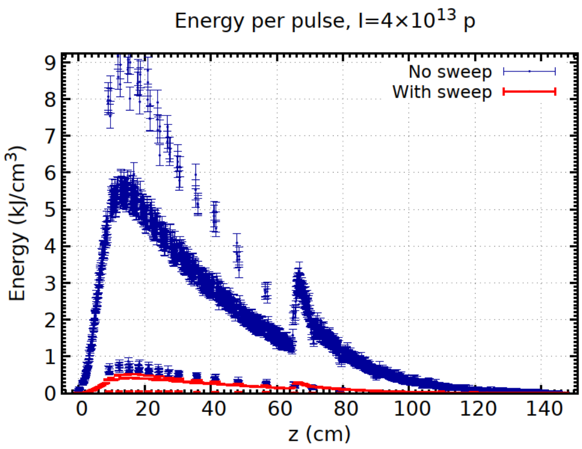

Fig. 5.8: Maximum deposited energy density along the beam axis (z) for the same beam, concentrated in the centre (blue) or swept in a circular path (red). The swept version is the one considered for the target.

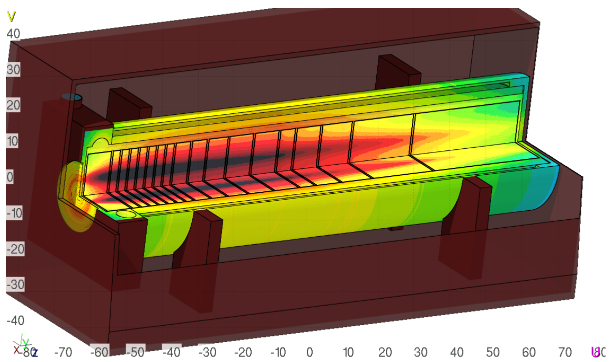

Fig. 5.9: Isometric view of the FLUKA model, including the dose in the target per year assuming 4×10^{19} p.

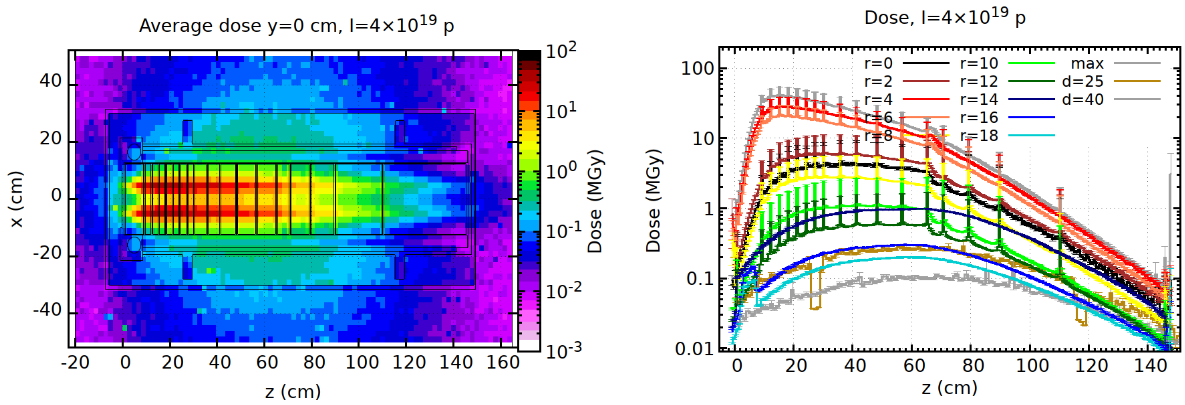

Fig. 5.10: Left: yearly average dose in $y = [-1, 1]$ cm around the target centre. Right: dose along the beam axis (z) for several radii, and outside the target at 25 and 40 cm from the target axis. Outside the target, the cylindrical geometry is lost, so the positions $d = 25$ and $d = 40$ cm correspond to the average in $y = [-1, 1]$ cm and $x = 25$ or 40 cm, respectively. Results normalized for 1 yr, with 4×10^{19} p.

5.3.4 Neutron and proton fluence

The fluence of particles in the materials is also important for understanding the potential damage to the materials. In Fig. 5.11, the yearly proton fluence (p/cm^2) is shown on the left, while the yearly maximum fluences of protons, neutrons, and high-energy hadron equivalent are shown on the right.

The neutron thresholds were considered at thermal energies, while the proton thresholds were set to 100 keV. The target will see a maximum fluence of $\sim 3 \times 10^{18}$ protons/cm^2 per year around blocks 8 and 9 (TZM, $\sim$30 cm). The yearly maximum fluence of neutrons is around block 15 (W, $\sim$75 cm), with 2.5×10^{20} n/cm^2. More discussion of the material properties and their variation with irradiation is presented in Section 5.8.6.

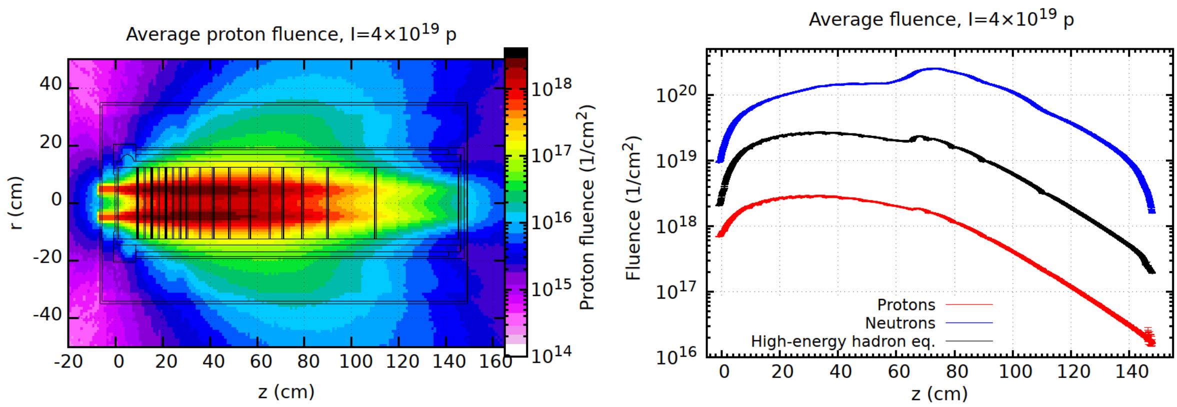

Fig. 5.11: Left: average proton fluence in $y = [-1, 1]$ cm around the target centre for 1 yr of irradiation. The effect of the beam dilution is evident by the presence of an apparent double-impact beam around the target centre. Right: maximum proton and neutron density and high-energy hadron equivalent along the beam axis (z). Results normalized for 1 yr, assuming 4×10^{19} p.

5.3.5 Radiation damage (displacements per atom and gas production)

The materials of the target are expected to suffer significant variations in their mechanical properties owing to the high cumulative number of protons colliding with them. More precisely, the number of dpa and the amount of H and He gas production in the core provide an indication of the extent of such effects on the thermophysical and mechanical properties. The same FLUKA model was used to simulate these values for a year of operation (4×10^{19} p). The energy required to permanently displace an atom (damage energy threshold) for TZM was assumed equal to that for pure molybdenum (i.e. 60 eV), while 90 eV was assumed for pure tungsten. The value for pure Ta was assumed to be 53 eV, and that for stainless steel (316L) 40 eV.

Figure 5.12 shows the radial distribution of the dpa, as well as the maximum dpa at different radii. The maximum dpa occurs at 5 cm from the centre, where the beam is focused, and is larger between the TZM blocks 9 and 12, where it could reach values of about 0.1 per year. If the beam was focused on the centre instead of a circular sweep being used, considerably higher values would be expected. In Fig. 5.13, a comparison between the dpa reached in the case of no beam sweep and the baseline configuration case can be seen. The material, assuming an unswept beam, would suffer about five times more dpa than for the sweeped beam.

The production of the gases hydrogen and helium is very important for the properties of metallic materials in operation, since gas bubbles can have severe life-limiting consequences for materials, even at low concentrations. This is especially important in the case of helium owing to its low solubility in the crystal lattice. The gas production can accumulate, producing bubbles and defects in the metal, which can lead to swelling or grain-boundary embrittlement, or both, of the materials.

In one year of operation, a maximum of about 40 ppm hydrogen and about 15 ppm helium can be produced in the target core, as shown in Fig. 5.14.

Another important factor to be considered is the ratio of the gas content to the dpa. Figure 5.15 shows this ratio for hydrogen (left) and for helium (right). It can be seen that the ratio is about 600 and 200 for hydrogen and helium, respectively.

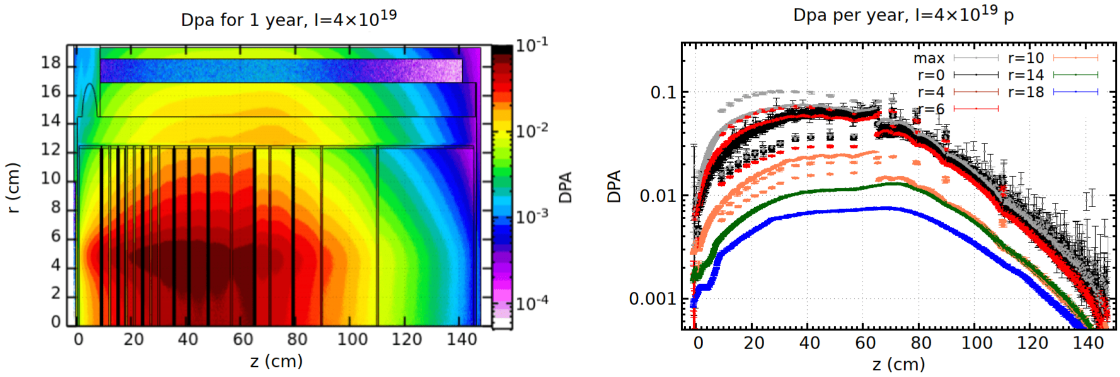

Fig. 5.12: Displacements per atom for the BDF target in 1 yr of operation (4×10^{19} p). Left: radial average versus z (beam direction). Right: maximum dpa along the beam axis (z) for several radii.

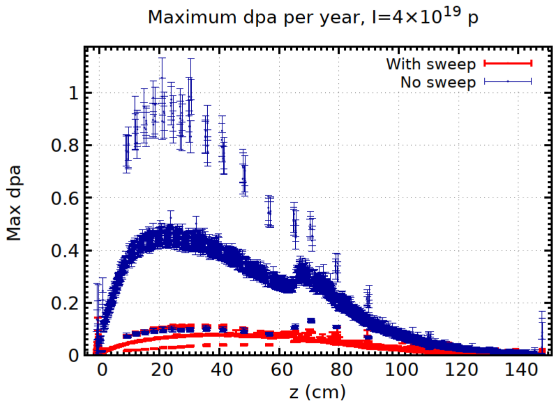

Fig. 5.13: Maximum dpa per year along the beam axis (z) for the same beam concentrated in the centre (red) or swept in a circular path (blue).

For a summary of the results, the average maxima along z are reported in Table 5.3. To avoid statistical fluctuations, the values correspond to the maximum of the average of three points. The Ta cladding receives slightly more dose, dpa, and H/He production since it is at boundaries between blocks and has a high density.

Table 5.3: Summary of the maximum values for TZM, W, and Ta2.5W cladding, considering each parameter reported in this section. HeHad corresponds to the high-energy hadron equivalent. For the Ta cladding, there are three bins in z per slice of cladding. The maximum here corresponds to the maximum of the average of the three bins per slice (to reduce fluctuations).

Material/ position	Dose (GGy)	p fluence (1/cm^2)	n fluence (1/cm^2)	HeHad (1/cm^2)	dpa	H (appm)	He (appm)	H/dpa	He/dpa
TZM/	~40	2.9×10^{18}	1.7×10^{20}	2.7×10^{19}	0.074	37.9	15	~650	~275
block no.	4	9	13	9	10	8	8	1	1
W/	~14	1.8×10^{18}	2.5×10^{20}	2.3×10^{19}	0.053	30	13	~560	~300
block no.	14	14	15	14	14	14	14	14	18
Ta2.5W/	~54	2.9×10^{18}	2.5×10^{20}	2.7×10^{19}	0.053	51	30	~900	~280
block no.	3–4	8 and 9	15	9	9	9–10	9–10	1	1 and 2

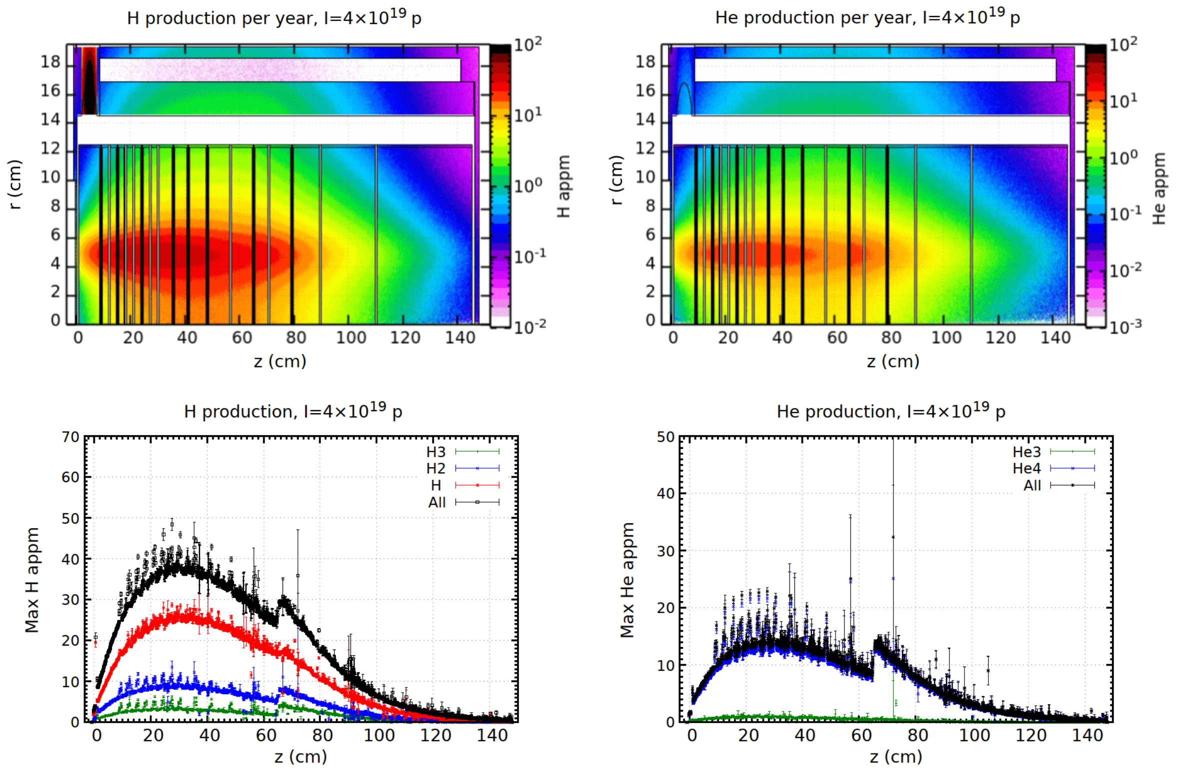

Fig. 5.14: Gas production in the BDF target per year of operation: hydrogen production (left) and helium production (right). Top, average dpa around the target core; bottom, maximum along the beam axis (z).

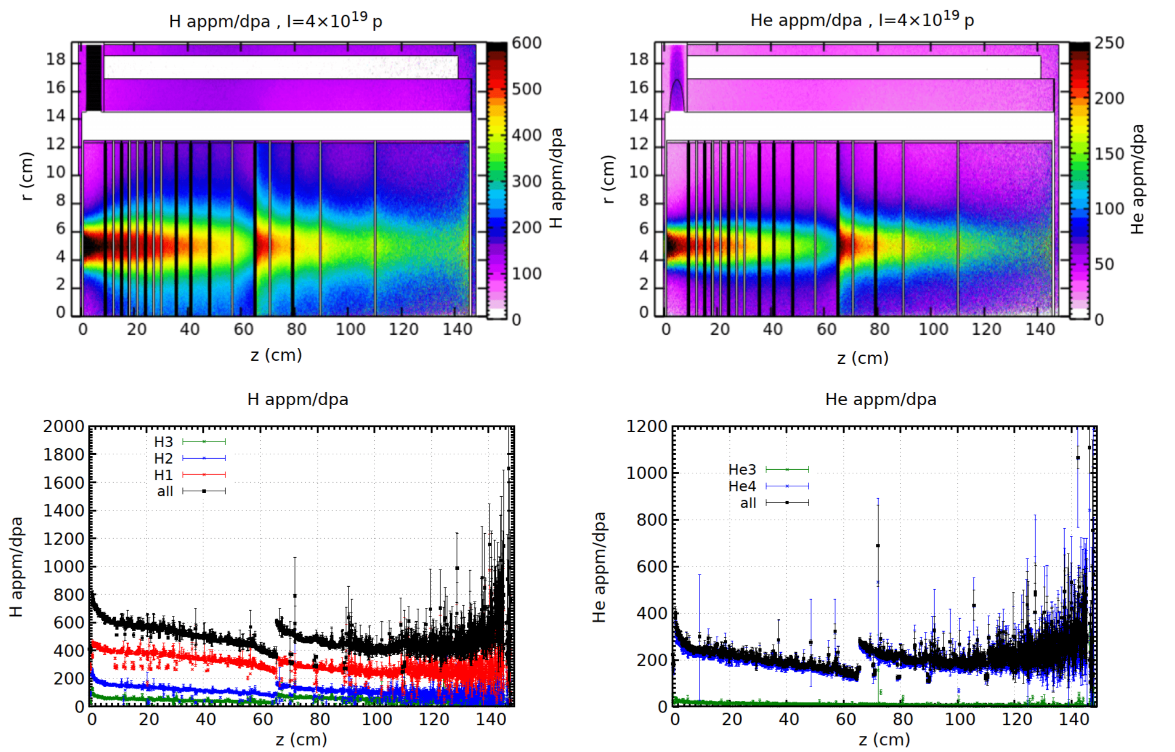

Fig. 5.15: Ratio of gas (H or He) production to dpa: hydrogen production (left) and helium production (right). Top, average ratio in 2D; bottom, maximum along the beam axis (z).

5.4 Summary of radiation protection considerations for BDF target

This section summarizes the radiological assessment for the final BDF target. The high-intensity beam power deposited in the target poses challenges with respect to radiation protection for all maintenance interventions. The studies include expected residual dose rates, and storage and transport considerations. Finally, studies on target disposal were conducted. The studies are based on extensive simulations with the FLUKA Monte Carlo particle transport code [11, 12] and with ActiWiz 3 [14]. Figure 5.9 shows the target as implemented in FLUKA. All studies assume 4×10^{13} protons on target per spill (with a duration of 7.2 s) and an integrated total of 2×10^{20} protons on target over 5 yr of operation, each year with 83 days of operation followed by 272 days of shutdown.

Figure 5.16 shows the expected residual dose rates for the target for different cooling times. The highest dose rates are in the order of 10^8 µSv/h after 4 h of cooling. For this reason, target exchange is a delicate procedure, which is carefully addressed in Chapter 6.

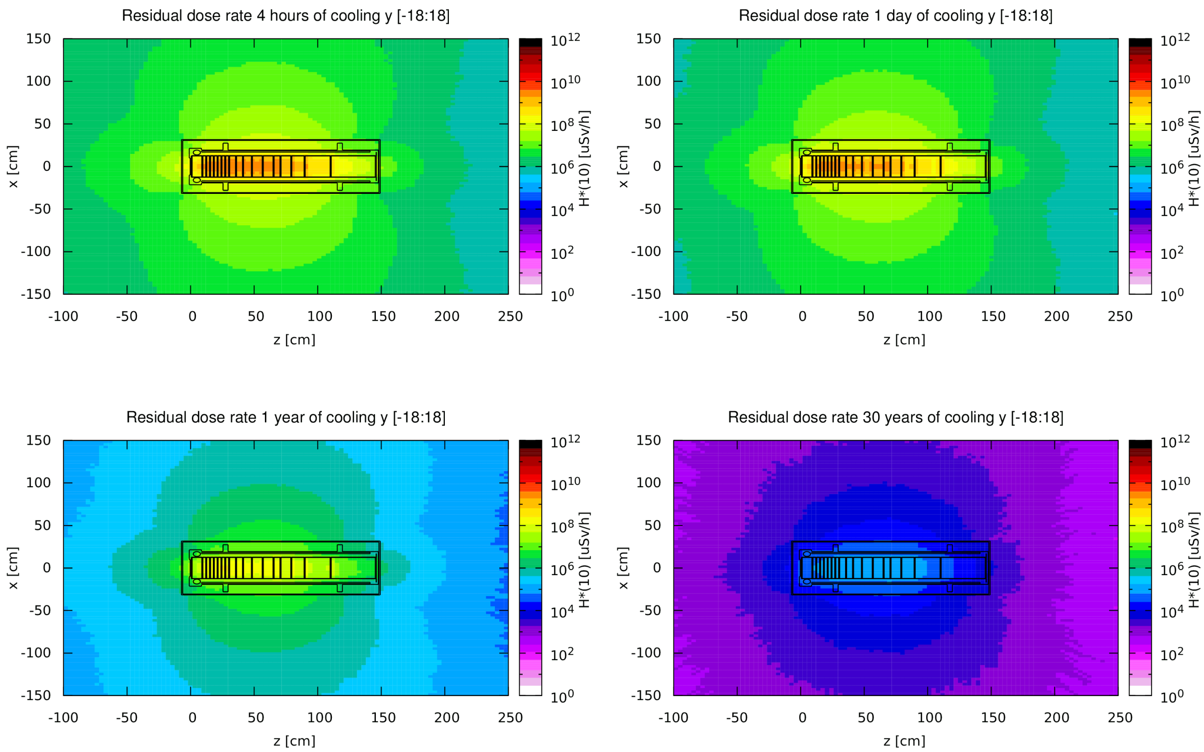

Fig. 5.16: Residual dose rates in microsieverts per hour after (a) 4 h, (b) 1 day, (c) 1 yr, and (d) 30 yr of cooling.

Even after 30 yr of cooling, the dose rates at 40 cm will still be in the order of a few millisieverts per hour, and thus dedicated storage place was designed in the facility to safely store the target. For transportation of radioactive materials, as indicated in Ref. [15], the maximum dose rate level at any point on the external surface of a package should not exceed 2 mSv/h. Therefore, the container will be made out of iron with a thickness of 30 cm on all sides. This transportation cask will be used as well during the exchange procedure in order not to expose the target.

Some preliminary studies were performed for the disposal of the BDF target after irradiation. The results of ActiWiz 3 calculations are reported in terms of the Swiss Liberation Limits (LLs) (see Ref. [16]). In the calculations, the same irradiation profile was assumed, but with only 1 yr cooling time. The total dose rate level in units of the LL is 5.6×10^8 and 6.3×10^7 for the TZM and W block respectively, with Y-88 ($\approx$ 87%LL) and Ta-182 ($\approx$ 42% LL) as top contributors for TZM and W, respectively. The time evolution of the dose rate level is shown in Figure 5.17; even after a 30 yr cool-down period the level is still above the liberation limit. The target will need to be treated as radioactive waste in event of disposal. A proper assessment of the disposal will be performed in the future.

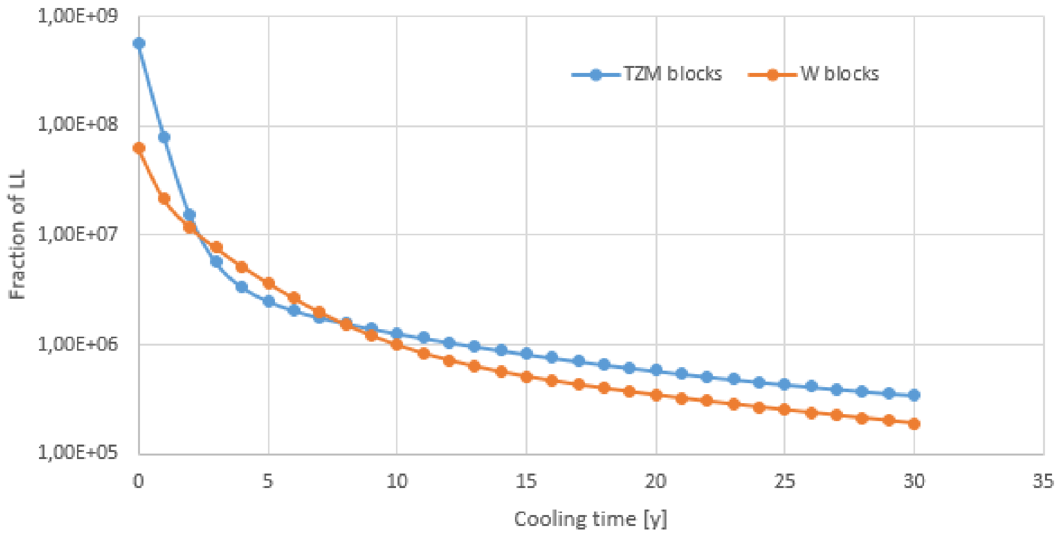

Fig. 5.17: Time evolution of the dose rate level for TZM and W blocks

5.5 Thermomechanical simulations of target

5.5.1 Thermal calculations

As discussed above (Section 5.3), the energy deposited by the primary proton beam in the target was obtained via FLUKA Monte Carlo simulations [11, 12]. The energy induced by beam–matter interactions was imported into ANSYS© Mechanical to perform FEM thermomechanical calculations, to evaluate the performance of the target during operation.

Forced convection was applied on the surfaces of the target blocks as a boundary condition for the FEM thermal simulations, with an estimated value of the film coefficient of 20 000 $W/m^2{\cdot}K$ and a water temperature of 30°C. The value of the film coefficient is consistent with the average heat transfer coefficient calculated via CFD simulations, as will be shown in Section 5.6.

One of the most challenging aspects of the thermal calculations performed was the implementation of the proton beam dilution in the FEM software. An ANSYS APDL code has been developed to simulate the beam sweep trajectory, where the FLUKA data corresponding to one single proton impact are imported into a thermal analysis done with ANSYS Mechanical and moved in the target following a circular pattern identical to that of the dilution system design. As a result, the temperature distribution in the target blocks is obtained as a function of time. Table 5.4 summarizes the maximum temperatures reached in the different target materials for the most critical blocks in terms of the thermal load on each material.

Table 5.4: Maximum temperatures reached in the BDF target materials for the most critical blocks.

Material	Block number	Maximum temperature (°C)
Ta2.5W	4	160
TZM	9	180
W	14	150

Figure 5.18(a) shows the evolution of the maximum temperature during three pulses for TZM, W, and Ta2.5W, while Fig. 5.18(b) shows the temperature distribution in the Ta2.5W cladding of block number 4 after a beam impact. The beneficial effect of beam dilution in terms of reducing the maximum temperature can be observed in both figures.

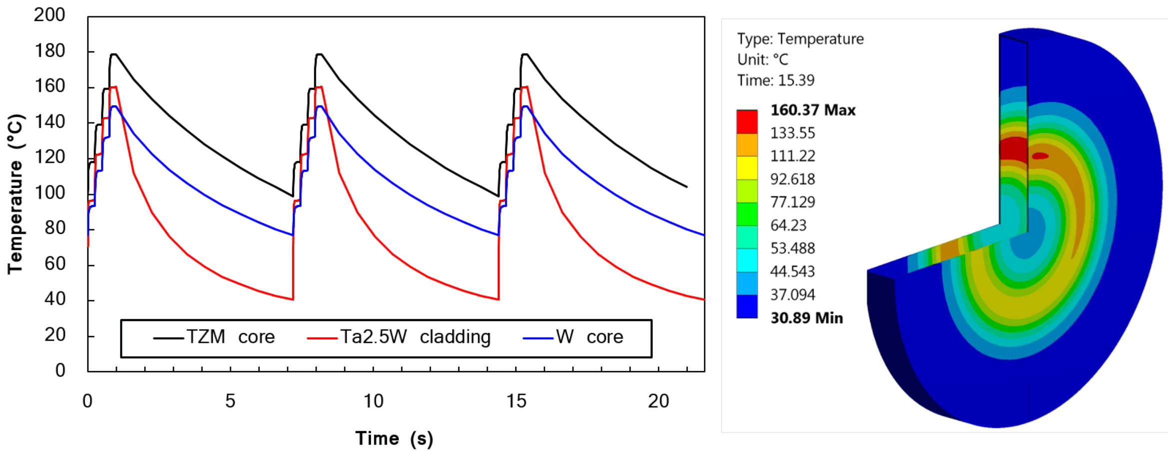

Fig. 5.18: (a) Evolution of maximum temperature in the BDF target materials during three beam pulses after long-term operation: results for the most loaded target blocks. (b) Temperature distribution in the Ta2.5W cladding of block number 4 at the time of maximum temperature.

The temperature reached in the target core and cladding materials is around $0.1T_\mathrm{m}$ (where T_m is the melting temperature), and these materials do not undergo any allotropic transformation in this range of temperature. As a consequence, the physical and mechanical properties are expected to evolve gradually with temperature, without abrupt changes. There are several limitations, however, associated with the high temperatures expected during operation. First, the degradation of the material properties at high temperatures, especially for Ta2.5W, leads to a reduction in the strength of the materials (see Section 5.5.2). This is the main reason for the selection of a tantalum alloy as the cladding material instead of pure tantalum, the latter having a reported yield strength reduction from 185 MPa at room temperature to 70 MPa at 200°C [17].

Furthermore, it is undesirable to reach temperatures above the boiling point of water at the target surface, as this could lead to localized boiling of the cooling water, inducing severe degradation of the heat dissipation from the blocks. This issue will be reported in more detail in Section 5.6. Finally, the thermal loads applied to the target will induce high levels of stress, in particular in the cladding material, where the temperature increase after each proton beam impact can reach 120°C, as shown in Fig. 5.18.

5.5.2 Structural calculations

5.5.2.1 Transient structural simulations

5.5.2.1.1 Review of properties of target materials

As mentioned in the previous section, considering the level of thermally induced stresses reached in the target materials, it is important to consider the degradation of the material properties with temperature, since the target materials are expected to reach temperatures of around 150°C during operation. The evolution of the yield and tensile strength of Ta2.5W, TZM, and pure tungsten as presented in the literature is shown in Fig. 5.19, as an indication of the reduction in strength with temperature. The yield strength of tungsten is not plotted, given the brittle nature of this material below 250°C, as will be clarified later in this section.

As a general trend, the yield strength and tensile strength decrease with temperature for the three

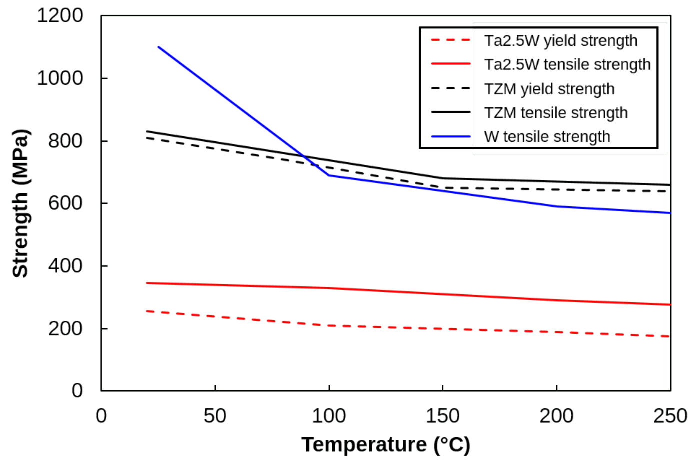

Fig. 5.19: Yield strength and tensile strength as a function of temperature for TZM [18], tungsten [19], and Ta2.5W [20].

materials. Ta2.5W shows much lower strength values than TZM and W over the entire range of temperature. Note, however, that the differences in mechanical properties between products made from the same material can be significant, and they depend greatly on the geometry and the manufacturing process used.

The strength of the target materials is a crucial parameter for estimating the target lifetime, and thus for performing target design. A material characterization campaign is currently ongoing within the framework of the BDF Project, and will help to elucidate the properties of Ta2.5W, TZM, and W for the purpose of a more robust target design. In the following list, the most relevant values of yield and tensile strengths that have been measured or can be found in the literature are presented.

- The yield and tensile strengths of Ta2.5W were measured at room temperature on specimens obtained from Ta2.5W discs treated with a HIP cycle identical to that used to produce the BDF target blocks. The measured yield strength was 270 MPa, and the tensile strength 360 MPa [21]. These results are compatible with the ones plotted in Fig. 5.19 at room temperature, even though the material suppliers were different in the two cases. For comparison purposes, pure tantalum specimens with identical geometry were also tested after the HIP process, and showed a much lower yield strength (170 MPa) and tensile strength (220 MPa). The low strength shown by pure tantalum would probably compromise the target lifetime, as mentioned in Section 5.2.1.
- Regarding the TZM core material, samples obtained from a 200 mm diameter, 100 mm length rod were tested at 20 and 700°C [22]. At room temperature, the measured yield strength and mean tensile strength were 480 and 525 MPa, respectively, which are significantly lower than the values shown in Fig. 5.19. This is probably due to the larger grain size obtained in the production of rods of such a large diameter and length, which is also the case for the TZM rods produced for the BDF target. Considering this reduction in material strength, the estimated yield strength at 200°C is around 370 MPa.
- Pure tungsten shows brittle behaviour at room temperature, and for common commercial tungsten products the ductile-to-brittle transition temperature (DBTT) is around 300°C in most cases [23, 24]. Furthermore, the DBTT of tungsten can be strongly affected by the manufacturing process and by radiation damage to the material; studies have shown an increase in the DBTT of tungsten at low levels of radiation damage (around 0.1 dpa) to values above 400°C [25]. It is therefore predicted that the tungsten in the BDF target will behave in a brittle manner during operation, when the maximum temperatures reached in the tungsten are expected to be around 150°C. The tensile strength of tungsten specimens produced via sintering and HIPing has been reported in

Ref. [26], showing much lower strength (567 MPa) than the values in Fig. 5.19. This value is more relevant to study of the BDF target material properties, given that the large diameter and length of the tungsten blocks in the BDF will most probably constrain the production of the tungsten cylinders to the sintering and HIPing method instead of forging or rolling (see Section 5.7). Taking into account the reduction in tensile strength with temperature shown in Fig. 5.19, the estimated Ultimate Tensile Strength (UTS) at 150°C is around 330 MPa.

Table 5.5 summarizes the strength data found in the literature and via mechanical testing that are relevant for the BDF operational conditions. Data for different materials at room temperature and high temperature are presented to show meaningful data for the operational temperatures of the target.

Table 5.5: Yield and tensile strengths of BDF target materials at Room Temperature (RT) as obtained from the literature and from mechanical testing [21, 22, 26]. The material strength at high temperatures was estimated according to the trend shown in Fig. 5.19.

Material	Yield strength at RT (MPa)	UTS at RT (MPa)	Yield strength at 200°C (MPa)
Ta2.5W	270	360	190
TZM	480	525	370

Material	UTS at RT (MPa)	UTS at 150°C (MPa)
W	567	330

5.5.2.1.2 Simulation results

The stresses induced by the high temperatures reached in the target materials were estimated by means of FEM calculations. The preliminary simulations performed showed that the level of the stresses was substantially reduced if the target blocks showed free-body expansion after the temperature rise generated by a beam impact. Therefore, in the analysis the target cylinders were assumed to be resting on the support surface (and not fixed or clamped to the support). A detailed description of the target assembly will be given in Section 5.7.

The temperature distribution in each of the blocks was imported as a thermal load for the structural analysis. A transient structural analysis was performed to evaluate the evolution of the stress over time given the temperature distribution at each time step. The pulse duration of 1 s was considered sufficiently long for beam-induced dynamic effects to be negligible, however, and for that reason the structural analysis can be regarded as quasi-static.

Ta2.5W and TZM show ductile behaviour at the operational temperatures, and are expected to deform elastically under the thermal loading induced by the beam; if the yield point of the materials is reached, the blocks will start deforming in the plastic regime. Cyclic plastic deformation of the core or cladding over a long period could lead to premature fracture of the material or to detachment of the cladding from the base refractory metal, however, reducing or blocking the heat dissipation through the cladding material. Therefore, the von Mises yield criterion was used to evaluate the safety margin of the stresses reached in the Ta2.5W cladding and TZM core with respect to the yield strength of these materials.

For pure tungsten, which was considered as a brittle material at the operational temperatures of the target, the Christensen criterion [27] was considered the most suitable failure criterion. Owing to the low availability of compressive-strength data for tungsten under the operational conditions of the target, however, the maximum-normal-stress criterion was used to assess whether the maximum stresses reached in the tungsten core were within the safety limits of the material.

Table 5.6 summarizes the maximum stresses found in each material, as well as the safety margin with respect to the yield strength or ultimate tensile strength of the material at the operational temperatures.

Table 5.6: Maximum stresses reached in the BDF target materials, and safety factors with respect to the material limits presented in Table 5.5.

Material	Maximum von Mises equivalent stress (MPa)	Yield strength at 200°C (MPa)	Safety factor
TZM	128	370	3
Ta2.5W	95	190	2

Material	Maximum normal stress (MPa)	UTS at 150°C (MPa)	Safety factor
W	80	330	4

The impact of the beam on the target blocks leads to high stresses that follow the geometrical distribution of the beam dilution, as can be seen in Fig. 5.20. The highest von Mises equivalent stress in the cladding is reached in block number 4, in the beam impact region at the end of the pulse, the maximum stress being located in the interface with the core of the block. For the TZM, the highest von Mises equivalent stress is found in the centre of the core of block 4, where high compressive stresses develop, as well as in the interface with the tantalum cladding. The maximum principal stress in the pure tungsten blocks is reached at the upstream face of block 14, following the beam dilution pattern.

As discussed in Section 5.2.2, the largest values of stress are found in the most upstream blocks (3–6). The stress distribution inside one of the most critical target blocks is displayed in Fig. 5.20(d), showing an abrupt stress variation in the interface between the target cladding and the core.

The stress increase in the target blocks during a beam impact is highly influenced by the beam dilution pattern. Figure 5.21 presents the evolution of the stresses in the locations of maximum stress during the 1 s SPS beam pulse. The maximum-stress locations studied can be seen in Fig. 5.20. The sweep of the beam, following four circular turns, leading to a stress increase when the beam approaches the specific location plotted and to a stress decrease as the beam moves away, can be clearly observed.

For TZM, the maximum von Mises equivalent stress is well below the yield strength of the material, and so the TZM core is not expected to show any plastic deformation during operation. In the case of pure W, the maximum principal stress is considerably lower than the tensile strength of the material at 150°C, leading to a high safety margin even considering the brittle behaviour of tungsten at the operational temperatures of the target. The Ta2.5W cladding of the target is the most critical part of the target operation, with a safety factor that is acceptable with respect to the limits in the design criteria, but lower than for the TZM and tungsten cores.

5.5.2.2 Fatigue analysis

5.5.2.2.1 Review of fatigue literature

The SPS primary beam is foreseen to impact the BDF target for 1 s every 7.2 s, and the total number of cycles expected during the target lifetime is of the order of 10^7. The target will operate under cyclic structural loads, and so it is necessary to evaluate the fatigue life of the target materials under high-cycle

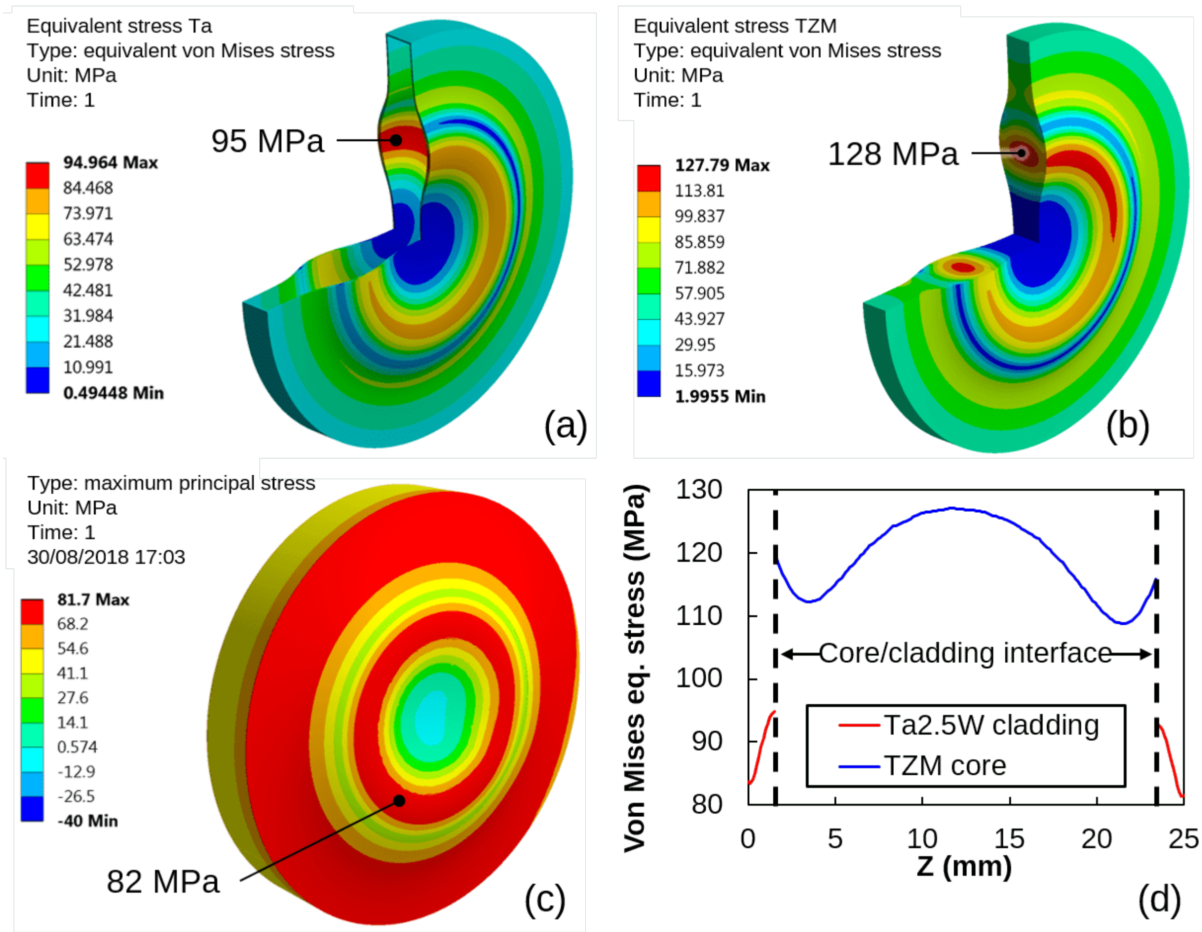

Fig. 5.20: Distribution of von Mises equivalent stress after one beam pulse in the most loaded blocks for each target material: block 4 for Ta2.5W (a) and TZM (b), and block 14 for W (c). Stress distribution on the longitudinal axis at the beam dilution position ($Y = 50$ mm) in block 4 (d).

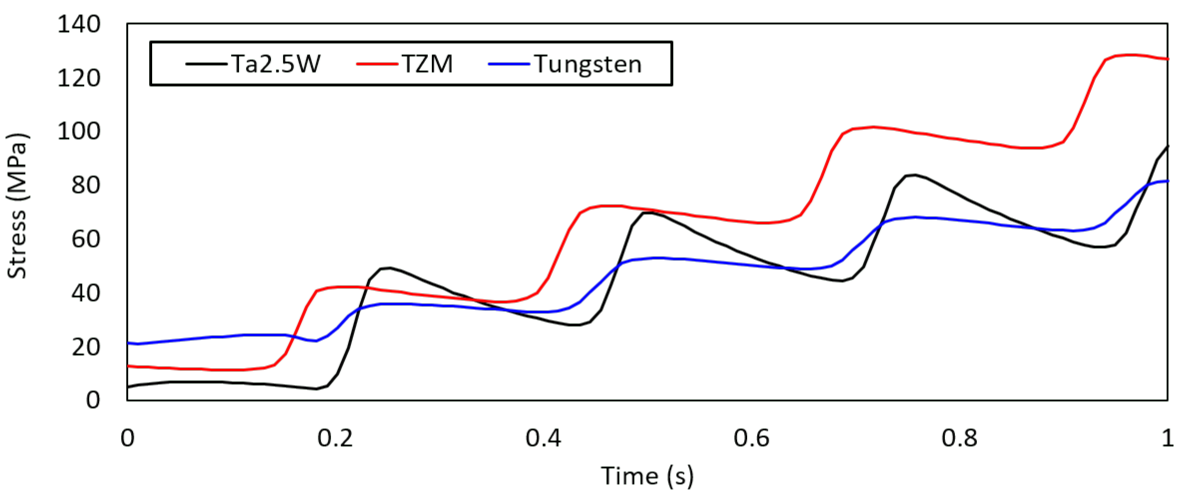

Fig. 5.21: Effect of beam dilution on the evolution of the stresses in the target materials. Results plotted for the locations of maximum stress shown in Fig. 5.20. The stress values correspond to the von Mises equivalent stress for TZM and Ta2.5W, and to the maximum principal stress for tungsten.

loading.

A literature study was carried out to obtain fatigue data for the target materials under loading conditions similar to those of the BDF target. The literature on fatigue life is very limited, especially for fatigue behaviour at high temperatures and under irradiation. This makes the estimation of fatigue properties for the BDF target materials especially difficult, as the different material and test conditions (geometry, heat treatment, purity, test mode, test stress ratio, test temperature, test frequency, ...) can significantly change the resulting fatigue strength values. A material characterization campaign is foreseen in the framework of the BDF Project in order to acquire experimental data on the fatigue life of the target materials at room and high temperature and to allow a robust engineering design of the BDF target.

Fatigue data for TZM are available in Ref. [28], with the special point of interest that the fatigue limit at 10^7 cycles was analysed at room and high temperature. The most relevant source for fatigue of pure tungsten can be found in recent studies from the European Spallation Source (ESS), where the fatigue limits of several tungsten specimens produced by different manufacturing routes was evaluated for 2×10^6 cycles [26]. For Ta2.5W, the fatigue data are even more limited. Such data can be found in the material database of a tantalum supplier [2], which includes data for fully reversed bending fatigue at 10^7 cycles for 1 mm plates.

Table 5.7 summarizes the fatigue data reported in the papers studied, which are considered to represent the conditions closest to the operation of the BDF target. Nevertheless, it is worth mentioning that some of the testing conditions were not identical to those of the BDF target materials (e.g. fatigue data given at room temperature, and different material production routes).

Table 5.7: Summary of the reviewed high-cycle fatigue data relevant to the operational conditions of the BDF target. Sources: TZM [28], tungsten [26], Ta2.5W [2]. P/M, powder metallurgy; Aw, as worked; HIP, hot isostatic pressing; Rxx, recrystallized; RT, room temperature.

Material	Production process	Dimensions	Test mode	Number of cycles	Stress ratio, temperature, frequency (Hz)	Fatigue limit (MPa)
TZM	P/M, Aw	⌀ 50 mm bar	Push–pull	10^7	−1, RT, 25 −1, 850°C, 25	440 250
W	Sintered + HIP	⌀ 5 mm bar	Push–pull	2×10^6	0, RT, 25	180
	Rolled + annealed	⌀ 5 mm bar	Push–pull	2×10^6	0, RT, 25	350
Ta2.5W	P/M, Rxx	Plate 1 mm	Bending fatigue	10^7, 50% fracture	−1, RT, 25	310

It can be seen that TZM shows the highest fatigue strength at $N = 10^7$, with a value of 440 MPa at room temperature, and the fatigue limit decreases at high temperatures as expected. Pure tungsten shows the lowest fatigue strength, of 180 MPa, for the sintering and HIPing manufacturing route, which is considered closer to the BDF target case. The measured fatigue strength of 180 MPa can be considered as conservative because it does not correspond to fully reversed loading, since all the tests presented in Ref. [26] were carried out in the tensile regime. Ta2.5W shows a fatigue strength of 310 MPa at room temperature, which is relatively close to the tensile strength of the material.

5.5.2.2.2 Simulation results

As a result of the high temperatures reached during operation for every impact of the beam on the target, the target materials are subjected to significant mean stresses and stress amplitudes, which may be critical for the operation of the target. The fatigue data found in the literature were usually obtained from uniaxial fully reversed tests (with a mean stress equal to zero). However, the state of stress in the target blocks is multiaxial and has a non-zero mean stress. To correlate the stresses calculated for the BDF target with the available fatigue strength, a two-step approach is necessary.

– First, an equivalent mean stress and an equivalent stress amplitude must be calculated, which are expected to give the same fatigue life under uniaxial loading as the multiaxial stress state found in the target.
– Then, it is necessary to compute an equivalent fully reversed stress from the values of the equivalent mean stress and equivalent stress amplitude. This equivalent fully reversed stress must take into account the contribution of the mean stress to the fatigue life of the target materials, to allow us to compare it with the fatigue strength under fully reversed loading found in the literature.

For TZM and Ta2.5W, which are considered as ductile materials, the Sines method [29] is considered the most suitable for this analysis. However, given the low availability of fatigue strength data under loading with non-zero mean stresses for the target materials, a similar approach requiring only data for fully reversed fatigue was adopted.

The octahedral-shear-stress (von Mises) theory applied to a multiaxial state of stress was used to calculate the equivalent stress amplitude $\sigma_{\mathrm{q,a}}$ and the equivalent mean stress $\sigma_{\mathrm{q,m}}$ from the evolution of the principal stresses in the target materials [29], following

$$\sigma_{\mathrm{q,a}} = \sqrt{\frac{(\sigma_{1,\mathrm{a}} - \sigma_{2,\mathrm{a}})^2 + (\sigma_{2,\mathrm{a}} - \sigma_{3,\mathrm{a}})^2 + (\sigma_{3,\mathrm{a}} - \sigma_{1,\mathrm{a}})^2}{2}} \tag{5.1}$$

and

$$\sigma_{\mathrm{q,m}} = \sqrt{\frac{(\sigma_{1,\mathrm{m}} - \sigma_{2,\mathrm{m}})^2 + (\sigma_{2,\mathrm{m}} - \sigma_{3,\mathrm{m}})^2 + (\sigma_{3,\mathrm{m}} - \sigma_{1,\mathrm{m}})^2}{2}}\,, \tag{5.2}$$

where $\sigma_{i,\mathrm{a}}$ and $\sigma_{i,\mathrm{m}}$ are the stress amplitude and the mean stress for the maximum, middle, and minimum principal stresses.

This equivalent-stress method is limited to proportional loading conditions, where the principal directions remain unchanged during the loading cycle, which is the case for the BDF target blocks. The von Mises equivalent-stress approach is also limited to the case in which the principal stresses are in phase. In some areas of the target materials, the maximum and minimum principal stresses are in opposite phases (i.e 180° out of phase). The methodology applied takes this situation into account by adding a negative sign to the out-of-phase component, as described in Ref. [30].

Note that the value of $\sigma_{\mathrm{q,m}}$ obtained from the von Mises equation is always positive, and does not take into account the possible beneficial effects of compressive mean stresses. Given that the mean principal stresses of the target materials are compressive in most of the cases, the method applied can be regarded as conservative.

For pure tungsten, which is assumed to be a brittle material, the maximum-stress criterion is considered [29]. It is expected that the fatigue endurance of the tungsten core under the multiaxial state of stress during operation will be principally influenced by the tensile contribution of the stress tensor. Therefore, the equivalent mean stress and the equivalent stress amplitude for pure tungsten were taken from the maximum cyclic variation of the principal stress:

$$\sigma_{\mathrm{q,a}} = \sigma_{1,\mathrm{a}} \quad \text{and} \quad \sigma_{\mathrm{q,m}} = \sigma_{1,\mathrm{m}}\ . \tag{5.3}$$

Figure 5.22 shows the equivalent mean stress and stress amplitude calculated at the locations of maximum stress for the three target materials and illustrates the evolution of the equivalent stress during three SPS beam pulses. The evolution presented corresponds to uniaxial loading and is expected to be equivalent in terms of fatigue life to the actual evolution of the multiaxial stress in the target materials.

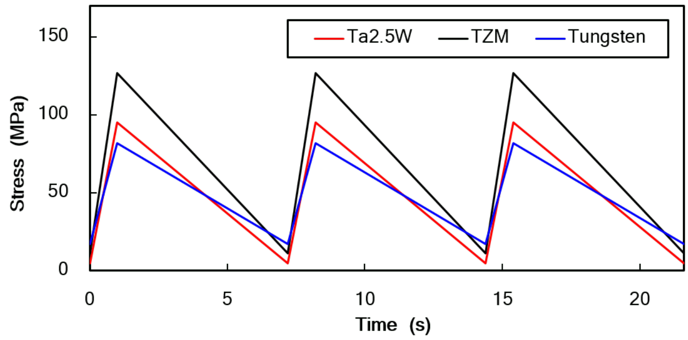

Fig. 5.22: Evolution of the equivalent stresses during three beam pulses in the most loaded areas of the BDF target materials.

TZM displays the highest equivalent stress amplitude and mean stress, followed by Ta2.5W. The results displayed do not take into account the stress variations during the circular sweep of the beam presented in Fig. 5.21. The effect of the beam dilution on the fatigue life of the target materials will be studied further in the future, but the preliminary calculations performed have shown that it is not expected to significantly affect the target lifetime.

The influence of the mean stress on the fatigue life has been studied in depth [31], with the general conclusion being that non-zero mean stresses have a detrimental effect on the fatigue behaviour of materials. The following modified Goodman equation was used:

$$\sigma_{\mathrm{q,f}} = \frac{\sigma_{\mathrm{q,a}}}{(1 - \sigma_{\mathrm{q,m}}/\sigma_{\mathrm{UTS}})} \leqslant \sigma_{\mathrm{fat}} \quad , \tag{5.4}$$

where σ_{UTS} is the ultimate tensile strength of the material, which was taken for the present calculations from the measured values at room temperature cited in Section 5.5.2, and σ_{fat} is the fatigue limit of the material. This equation was used as a design criterion to compare the stresses calculated for the BDF target materials, which have a non-zero mean stress, with the fully reversed stress amplitude found in the literature. The equation relates the mean stress $\sigma_{\mathrm{q,m}}$ and equivalent stress amplitude $\sigma_{\mathrm{q,a}}$ obtained from Eqs. (5.2), (5.1), and (5.3) to an equivalent fully reversed stress amplitude $\sigma_{\mathrm{q,f}}$ which is assumed to give the same fatigue life.

Table 5.8 presents the equivalent mean stress, stress amplitude, and Goodman equivalent stresses calculated for the target materials, as well as the fatigue endurance for each material and the safety margin achieved. The stresses found in the BDF target are well within the endurance limits found in the literature. The thermomechanical calculations performed have proven that it is unlikely that the target blocks will fail owing to high-cycle fatigue. In this case the Ta2.5W cladding is not a critical aspect for target operation, because the fatigue limit of the material is relatively close to its tensile strength (85% of the UTS at room temperature).

Further studies are required to evaluate the effects of radiation damage on the target materials, which could eventually reduce the fatigue life of the target, even though the safety margin appears to be sufficient. Additional fatigue data under more representative loading conditions are necessary for an accurate estimation of the fatigue life of the target materials in operation.

Table 5.8: Summary of stresses in the BDF target under high-cycle fatigue loading. Comparison with the fatigue strength of the target materials for 10^7 cycles, obtained from Refs. [26, 28, 2]. The values of the UTS used for the calculation of the Goodman equivalent stress can be found in Refs. [21, 22, 26].

Material	$\sigma_{q,m}$ (MPa)	$\sigma_{q,a}$ (MPa)	σ_{UTS} (MPa)	$\sigma_{q,f}$ (MPa)	Fatigue limit (MPa)	Safety margin
TZM	68	58	525	66	440	6.7
W	49.5	32.5	567	36	180	5
Ta2.5W	50	45	360	53	310	5.8

5.5.3 Residual stresses

The HIP process carried out for the production of the BDF target blocks is crucial to ensuring mechanical and chemical bonding between the cladding and core materials. The TZM and tungsten cylindrical parts are inserted into a Ta2.5W tube with a small gap (around 0.1 mm in radius), and then closed by two Ta2.5W discs. The top and bottom Ta2.5W discs are welded under vacuum to the tube by means of electron beam welding, to make the assembly leak-tight. Finally, the target block assembly undergoes a HIP cycle, reaching a temperature of 1200°C and a pressure of 150 MPa for 2 h. Figure 5.23 describes the HIP cycle proposed to be applied in the production of the BDF target blocks. Note that other HIP cycles have been investigated, as presented in Section 5.8.2.2.

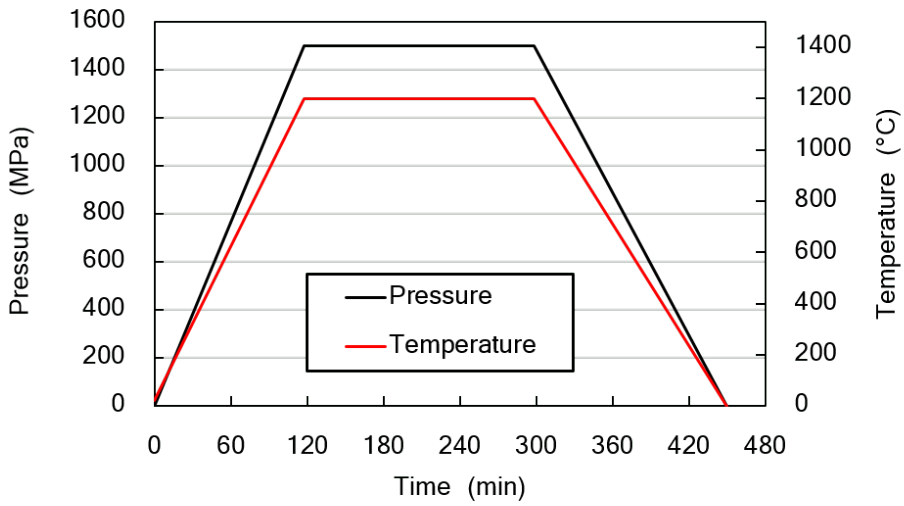

Fig. 5.23: Hot isostatic pressing cycle applied in target block production

During the cool-down phase of the HIP process, residual stresses appear in the target blocks owing to the different Coefficients of Thermal Expansion (CTEs) of the target materials. At high temperatures, these stresses are expected to be relieved, but as the temperature decreases below a certain temperature, residual stresses appear in the blocks owing to differential thermal contraction.

This so-called 'lock-in' temperature, as thoroughly described in Ref. [32], has a strong influence on the level of residual stresses reached. The literature regarding the lock-in temperature is very limited and shows a large scatter. An experimental set-up has been tested at the Rutherford Appleton Laboratory (RAL), UK, measuring a lock-in temperature for tantalum-clad tungsten blocks in the range of 350–500°C [33]. Concerning the case of the BDF target blocks, the effect of the residual stresses on the expected target lifetime has been studied through FEM calculations, by calculating the residual stresses appearing in the target for an assumed lock-in temperature of 500°C.

The maximum stresses reached after several beam pulses have also been computed considering the residual stresses in the blocks, as well as the Goodman equivalent stress, calculated using Eqs. (5.2)–(5.4), to evaluate the fatigue life of the target materials.

5.5.3.1 Ta2.5W-clad TZM blocks

For the Ta2.5W-clad TZM blocks, the residual stresses are higher in the Ta2.5W cladding, reaching around 105 MPa for the most beam-loaded block. This residual stress is purely tensile in the Ta2.5W layer. After a beam impact, the maximum von Mises equivalent stress obtained is higher than in the previously studied case, reaching around 150 MPa. The reason for this is that the beam-induced stresses in the external part of the cladding are highly tensile in the radial direction, and add to the tensile residual stresses. This value is still below the yield strength of the material at 200°C, however. Figure 5.24 illustrates the distribution of the von Mises equivalent stress in the Ta2.5W cladding of block 4 after the HIP process and after one beam impact on the target (after steady state is reached).

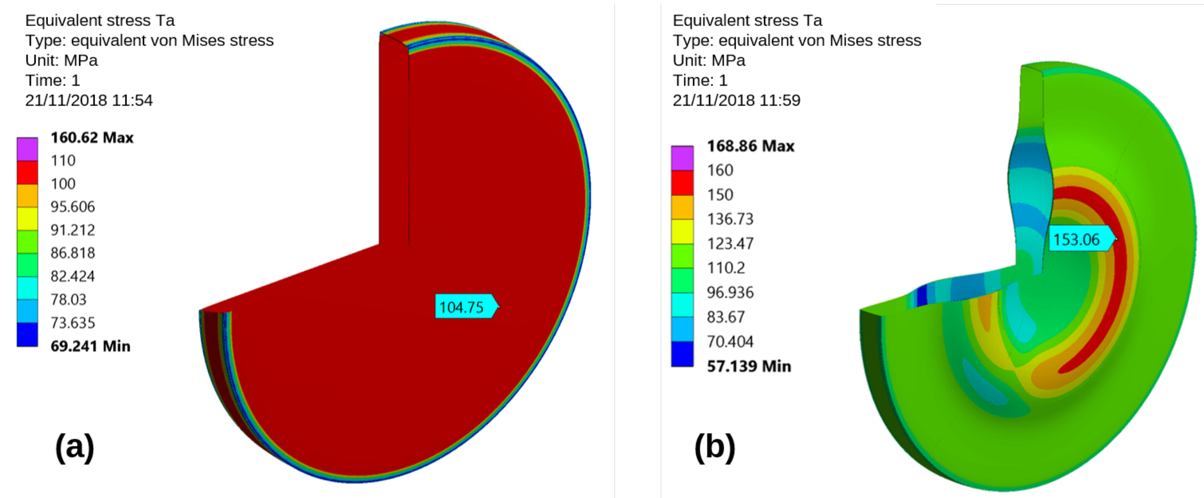

Fig. 5.24: Distribution of von Mises equivalent stress in the Ta2.5W cladding of block 4: (a) after HIP (residual stress); (b) after beam impact.

In terms of fatigue life, the equivalent stress amplitude is reduced with respect to the values without residual stresses, and the mean stress is considerably increased by the residual stresses. The reduction in stress amplitude turns out to be apparently beneficial for the estimation of the fatigue life of the target, as the calculated Goodman equivalent stress is slightly lower than in the previous scenario.

For the TZM part, the residual stresses are quite low, around 15 MPa, and purely compressive. The equivalent stress amplitude after the beam irradiation is similar to the case without residual stresses, but the equivalent mean stress is higher (15 MPa more). This is explained by the fact that the stresses induced by interaction with the beam in the TZM core are mainly compressive in the circumferential direction, and are added to the compressive residual stress already present in the material. As a result, the maximum von Mises equivalent stress is higher, but well within the material limits, reaching 140 MPa (Fig. 5.25).

Regarding fatigue life, the Goodman equivalent stress is slightly higher than that obtained without considering residual stresses, mainly owing to the increase in the mean stress. Because of the small difference between the two scenarios, it is considered that the target lifetime will not be reduced.

Table 5.9 summarizes the most relevant calculation results for the Ta2.5W-clad TZM blocks. The values obtained from the calculations without residual stresses shown in Section 5.5.2 are displayed in parentheses for comparison purposes. Figure 5.26 presents the fatigue behaviour for the cladding and core materials of block number 4 as described previously.

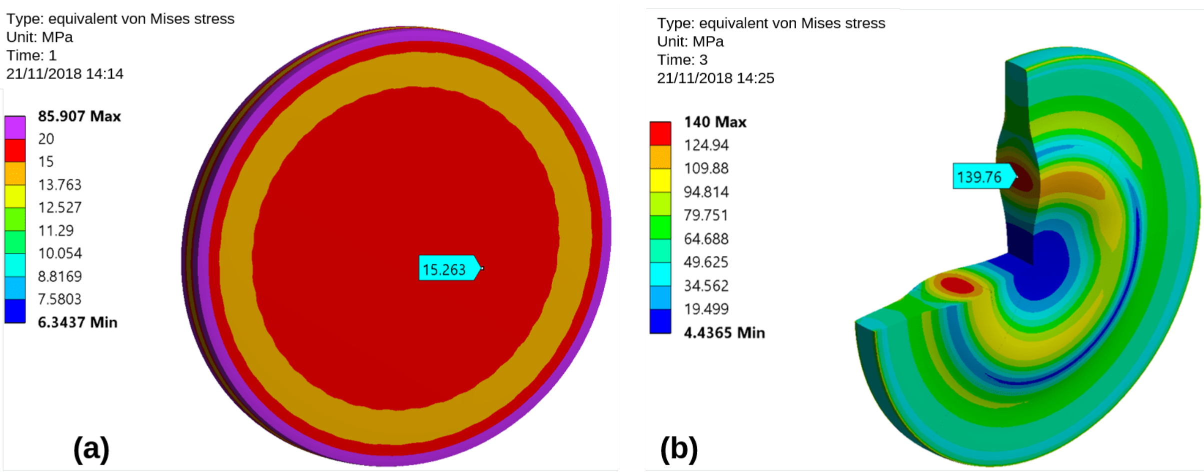

Fig. 5.25: Distribution of von Mises equivalent stress in the TZM core of block 4, after HIP (residual stress) (a) and after beam impact (b).

Table 5.9: Summary of FEM calculations performed to evaluate the influence of residual stresses on the behaviour of the target materials for the most loaded TZM block (number 4). The values obtained in Section 5.5.2 without residual stresses are presented in parentheses and italic font for comparison. Yield strength values were obtained from Refs. [21, 22] and fatigue limits from Refs. [28, 2].

Material	Maximum residual stress (MPa)	Maximum stress after beam impact (MPa)	Yield strength (MPa)	Goodman equivalent stress (MPa)	Fatigue limit (MPa)
Ta2.5W	105	153 *(95)*	190	50 *(53)*	310
TZM	15	140 *(128)*	370	68 *(66)*	440

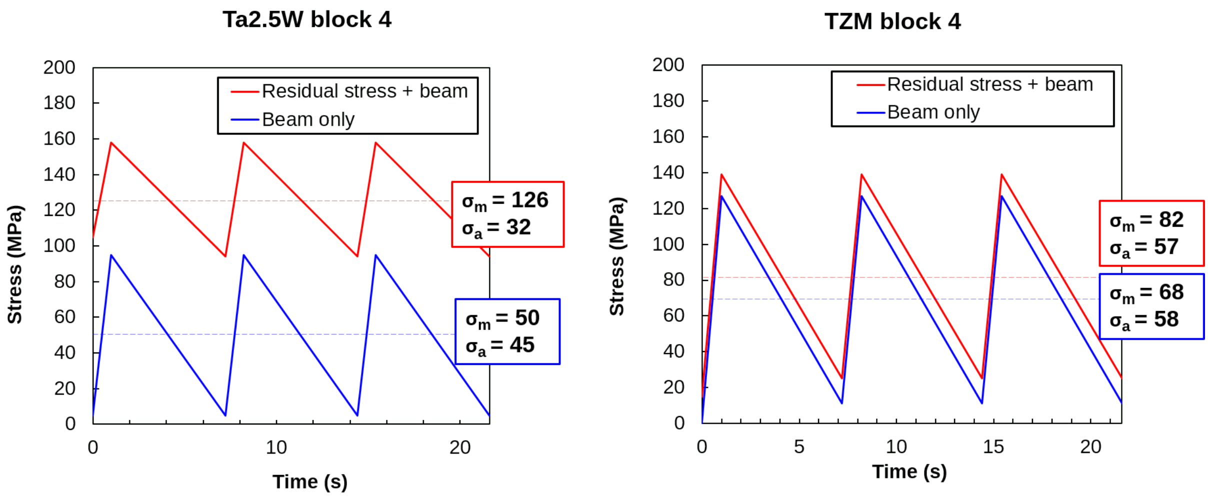

Fig. 5.26: Equivalent mean stress and stress amplitude for the Ta2.5W cladding and TZM core of block 4. Comparison between the simulation results for a beam impact on the block with or without residual stresses due to HIP.

5.5.3.2 Ta2.5W-clad tungsten blocks

Concerning the Ta2.5W-clad tungsten blocks, the residual stresses that appear in the Ta2.5W cladding are very high, owing to the high difference in CTE between Ta2.5W and pure tungsten. A deeper investigation is needed in this case to evaluate the amount of residual stress in the cladding. A temperature-dependent plasticity model was used to predict the behaviour of the cladding, taking into account the evolution of the yield strength presented in Fig. 5.19. The calculations performed showed that the cladding was not expected to suffer any plastic deformation during the HIP cool-down phase, but the residual stresses appearing in the Ta2.5W layer were very close to the yield strength of the material. The remaining residual stress in the Ta2.5W after the HIP cycle is around 250 MPa over all the cladding, leading to a low safety margin with respect to the yield strength of the material, which is assumed to be 270 MPa at room temperature, as shown in Section 5.5.2. Figure 5.27 displays the distribution of the von Mises equivalent stress in the Ta2.5W cladding after the HIP process and after a beam impact.

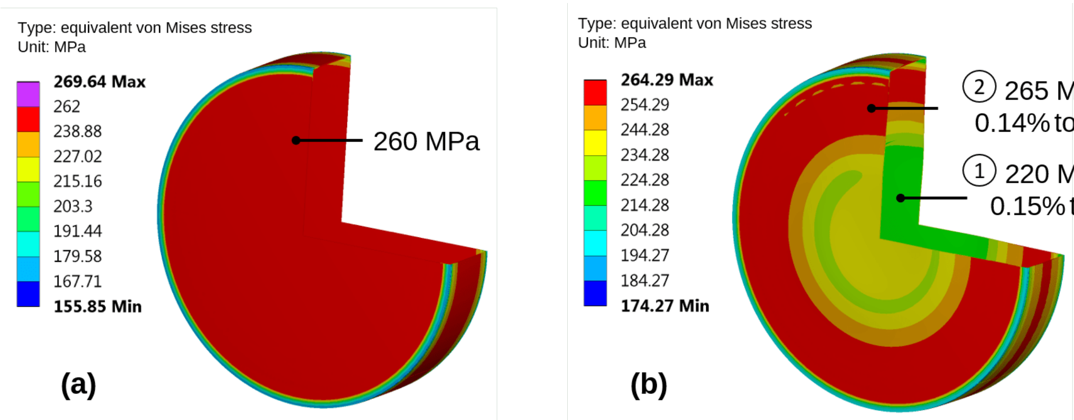

Fig. 5.27: Von Mises equivalent stress corresponding to the residual stress after HIP (a), and after beam impact (b) in the cladding of block 14 (Ta2.5W cladding, tungsten core).

During and immediately after the proton beam impact, the target block temperature rises significantly, with a subsequent reduction in the yield strength of the Ta2.5W. Given that the residual stresses in the Ta2.5W layer are already close to the yield strength at room temperature, the cladding is expected to deform plastically after the beam pulse. Two different regions have been studied in detail to evaluate the effect of the residual stresses in the cladding.

- In the beam impact region and the internal part of the cladding (point 1 in Fig. 5.27), the highest temperature rise is found, reaching 125°C. The stresses induced by the beam interaction are highly compressive in the circumferential direction in this region, and they relieve the existing tensile residual stresses. The maximum von Mises equivalent stress found in the beam dilution area is 220 MPa. This stress is slightly above the yield strength of the material at 125°C, producing plastic deformation of the cladding. The deformation in the plastic regime is quite low, though, thanks to the fact that the residual stresses have been relieved, and the total strain obtained is 0.15% after the beam pulse. The cladding is not expected to fail, since the total strain is well below the elongation to failure of Ta2.5W, which is around 10% at 150°C [20].
- In the external part of the cladding (point 2 in Fig. 5.27), far from the path of the diluted beam, some of the stresses generated by the beam impact are tensile in the circumferential direction, and they add to the tensile residual stress. The beam-induced tensile stresses are very small in that area, however, and the temperatures reached are of the order of 50°C, much lower than in the beam impact region. The von Mises equivalent stress obtained is 265 MPa, slightly above the yield strength of Ta2.5W at 50°C, which leads to plastic deformation in the cladding. The calculated total strain is 0.14% after the beam pulse, greatly below the elongation limit. It can be

concluded that, as expected, the whole cladding will show plastic behaviour, but the amount of plastic deformation will be quite low and well within the material limits.

It can be concluded that in several areas of the cladding of some of the target blocks, plastic deformation is expected as a consequence of the first beam pulse after the HIP process. The cyclic plastic deformation of the cladding might eventually lead to detachment of the latter, which is undesirable for operation as it would reduce heat dissipation. However, the calculations performed have shown that the cladding will always operate in the elastic regime during the steady-state beam pulses (i.e. it will show elastic shakedown), after the first plastic deformation produced by the first beam impact post-HIP.

This behaviour can be observed in Fig. 5.28, where the evolution of the von Mises equivalent stress and the total and plastic strain at point 1 of the cladding is plotted. The residual stress builds up during the HIP process, always in the elastic regime, and increases slightly until steady-state operation is reached. With the first beam impact after steady state is reached, the residual stresses are relieved, and the cladding deforms plastically owing to the rise in temperature (and subsequent decrease in yield strength). The maximum plastic strain reached is around 0.03%. During the subsequent pulses, no further plastic deformation occurs; the deformation after the beam impacts takes place in the elastic regime (there is elastic shakedown). For this reason, it is considered that there is no risk of further plastic deformation or ratcheting, which could be potentially harmful for the target lifetime.

Regarding the fatigue life of the Ta2.5W cladding on the tungsten-core blocks, the maximum Goodman equivalent stress calculated is 50 MPa, and is found in the path of the diluted beam. This value is higher than that obtained without considering residual stresses at the same location in block 14, mainly owing to a substantial increase in the mean stresses. In any case, however, this value is similar to the Goodman equivalent stress obtained for block 4 (TZM core, Ta2.5W cladding) without residual stresses, and is very far from the fatigue limit; this means that the residual stresses are not expected to have a detrimental effect on the target lifetime from this point of view.

In the pure tungsten core, similarly to the TZM blocks, the residual stress is compressive, reaching around 18 MPa. After a beam impact, the values of the maximum principal stress reached are lower than they are without residual stresses, since the beam-induced tensile stresses are applied to a stress field which is purely compressive. Therefore, the safety margin with respect to the UTS of the material is higher than for a non-stressed block. For the same reason, the maximum compressive stresses are higher than in the previous scenario, but since the compressive strength of tungsten is much superior to its tensile strength, the maximum-principal-stress criteria was used, as presented in Section 5.5.2. Figure 5.29 shows the distribution of the residual stress after HIP and the distribution of the maximum principal stress at the peak of the pulse in the pure tungsten core of block number 14.

The calculated Goodman equivalent stress is similar to the previous case without residual stresses (around 35 MPa); therefore it is considered that the residual stress will not have a detrimental influence on the target lifetime from this point of view.

Table 5.10 summarizes the main results obtained from the FEM simulations for the Ta2.5W-clad tungsten blocks. It can be concluded that in general the residual stresses post-HIP are not likely to reduce the target lifetime considerably, given that the values of the maximum stress and Goodman equivalent stress are close to the calculated values without residual stresses. The residual stresses may even be beneficial in some cases, as in the case of pure tungsten, where the compressive residual stress leads to an increase in the safety margin between the maximum tensile stress and the UTS of the material. However, the fact that the cladding is expected to show plastic deformation in some of the target tungsten blocks requires further investigation of this subject. In order to evaluate the residual stresses in the HIPed blocks, experimental measurements with different techniques (hole drilling, ring core technique, neutron diffraction, ...) are foreseen. The experimental set-up and the results of these measurements will be presented in a separate paper.

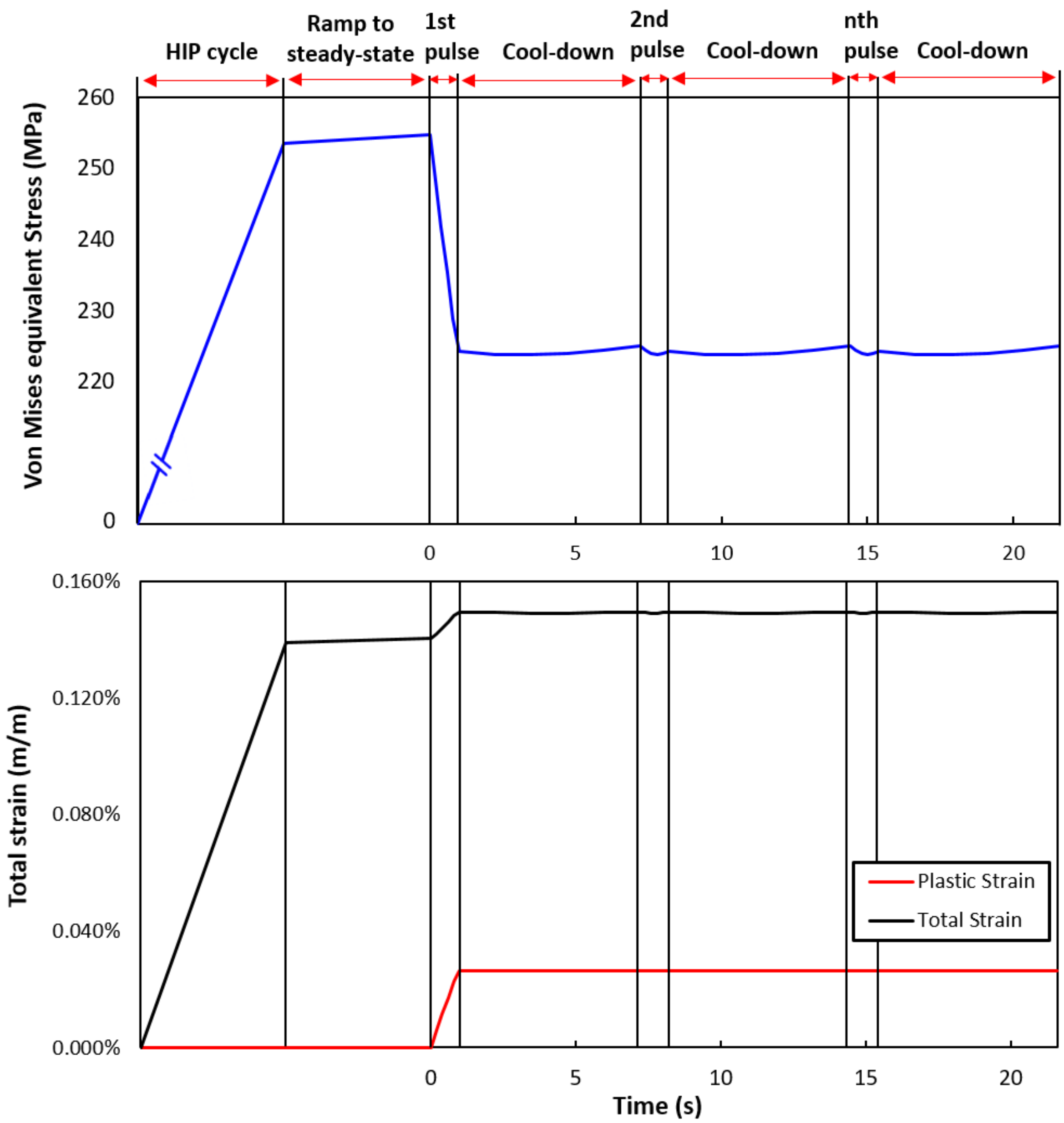

Fig. 5.28: Evolution of the von Mises equivalent stress and total and plastic strain in the external part of the cladding (point 1) in Fig. 5.27.

5.5.4 Accident scenarios and target survivability

5.5.4.1 Cooling-system failure

The cooling circuit of the target is critical for the successful operation of the BDF target. A disconnection or rupture of the cooling pipes or a failure of the cooling-system equipment could lead to a sudden stop of the water circulation or a loss of cooling water in the circuit. Even if the circuit pressure and flow rate are continuously monitored and interlocked to stop irradiation of the target in the case of a cooling-system failure, there are several operational (and other) risks associated with the loss of active cooling in the target.

In the event of a cooling accident with the beam stopped, the heat produced by the decay of the long-term-irradiated target materials will dissipate at a very slow rate, owing to the absence of forced

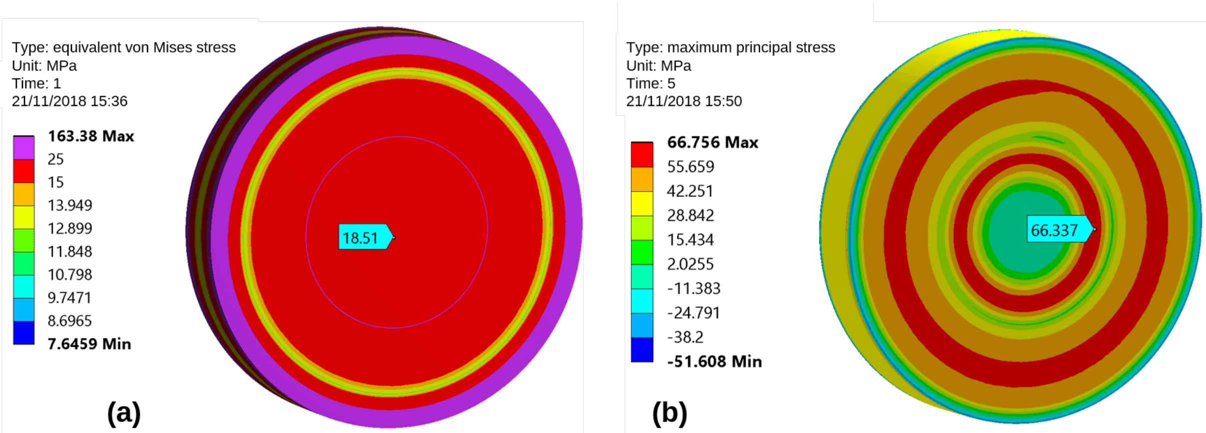

Fig. 5.29: Distribution of von Mises equivalent stress in the Ta2.5W cladding of block 14 after HIP (residual stress) (a) and maximum principal stress after beam impact (b).

Table 5.10: Summary of FEM calculations performed to evaluate the influence of residual stresses on the behaviour of the target materials. Results are shown for the most loaded W core block (number 14). The values obtained in Section 5.5.2 without residual stresses are presented in parentheses and italic font for comparison. The strength limit values were obtained from Refs. [21, 26] and the fatigue strength from Refs. [26, 2].

Material	Maximum residual stress (MPa)	Maximum stress after beam impact (MPa)	Strength limit (MPa)	Goodman equivalent stress (MPa)	Fatigue limit (MPa)
Ta2.5W	260	265 (plastic) *(63)* Total strain 0.15%	Elongation to failure 10%	50 *(25)*	310
W	18	67 *(80)*	370 (UTS)	34 *(36)*	180

cooling, increasing the temperature of the target materials for hours and days following the accident. Two different scenarios have been considered.

- In the case of a sudden water circulation failure, where the water remains inside the inner tank of the target, the heat will be mainly dissipated through the stagnant water via natural convection, with a low convection coefficient. The main risks associated with this scenario are melting or cracking of the target due to the high temperatures reached, and possible overpressure in the tank in the case of vaporization of water.
- In the event of a loss-of-coolant accident, where all the cooling water is lost from the circuit, the decay heat can be dissipated only by natural convection in air or helium, with a much lower convection coefficient than that of water. In this case, the main risk is the possible melting of the target materials given the high concentration of heat in the target, and the production of tungsten trioxide (WO_3) species, which are highly volatile.

The decay heat produced in the target materials has been estimated for different periods via FLUKA simulations. Figure 5.30 displays the heat distribution in all the target blocks one week after the event, obtained from FLUKA. It can be seen that the decay heat is dominated by the decay of tantalum isotopes.

Figure 5.31 presents the maximum decay heat in the target blocks along the Z axis for different time steps, from 60 s to 2 yr; the power generated is of the order of 600 W one minute after the failure.

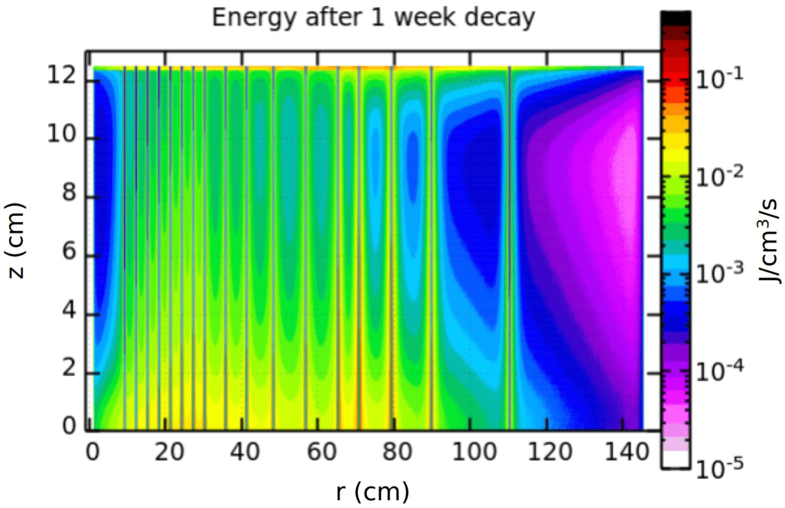

Fig. 5.30: Decay heat in the BDF target blocks after 1 week. FLUKA calculation results considering 5 yr of operation with a total of 2×10^{20} PoT.

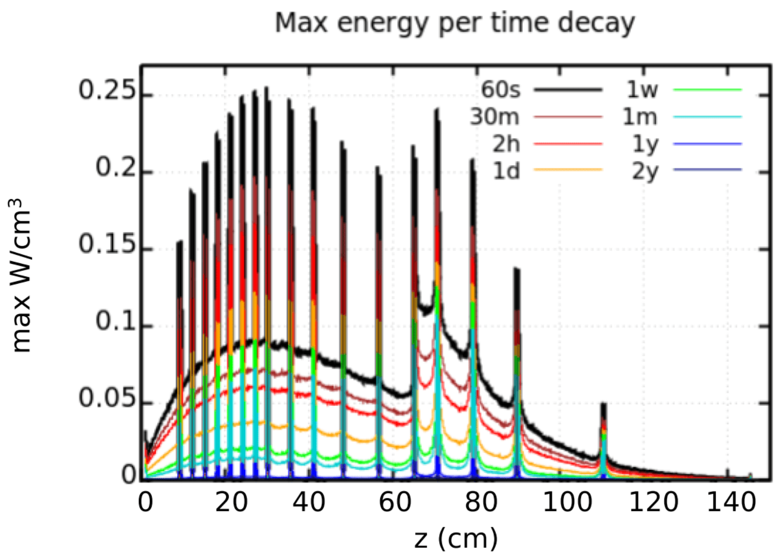

Fig. 5.31: Plot in the longitudinal direction of the maximum decay heat in the BDF target blocks for different time steps. FLUKA calculation results conservatively considering 5 yr of operation with a total of 2×10^{20} PoT before failure of the cooling system.

Thermal calculations were carried out to evaluate the effects on the target of a cooling-system failure. In a preliminary study, a low convection coefficient of 1 W/m^2·K was selected as the boundary condition for the calculations. Such a film convection coefficient could be considered as conservative for natural convection in air, helium, or water. Under these conditions, the evolution of the temperature in the target blocks was estimated. Figure 5.32 presents the evolution of the maximum temperature in the target blocks after a cooling-system failure over 2 yr. The maximum temperature in the target blocks is around 350°C and is reached 1 week after the accident; it is sufficiently low to avoid oxidation even if the tungsten is breached. Further studies are required to understand the possibility of producing oxidation at these temperatures in TZM.

Figure 5.33 presents the temperature distribution in the target blocks one week after the failure. It can be observed that the temperatures found are different from one block to another, and that the peak

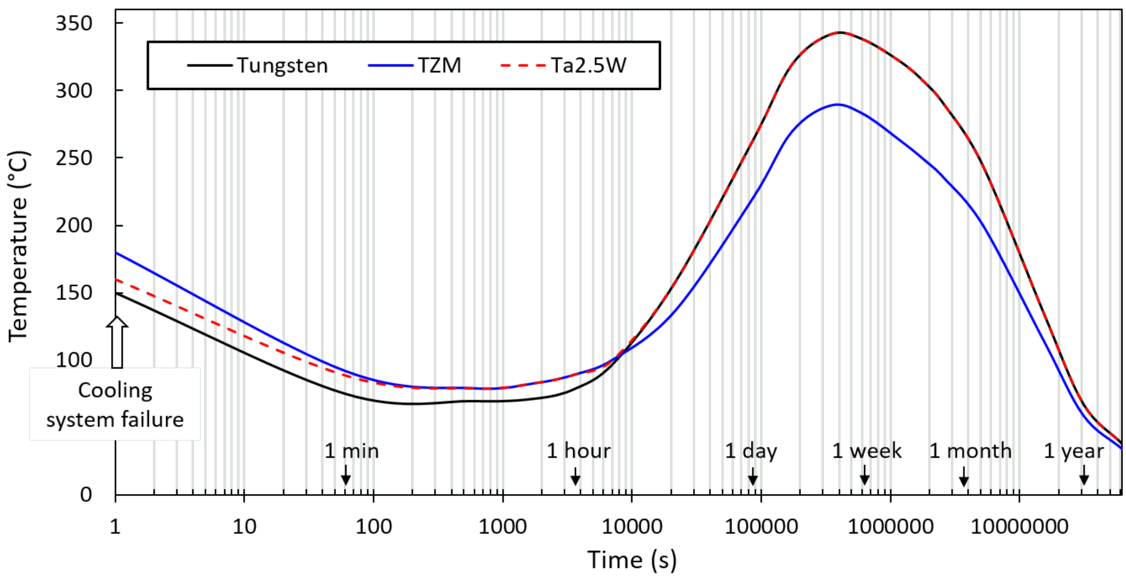

Fig. 5.32: Evolution of the maximum temperature in the target materials after a cooling-system failure due to the decay heat generated in the target.

temperature is reached in block number 15 (tungsten core), coincident with the position of maximum energy in the core materials shown in Fig. 5.31.

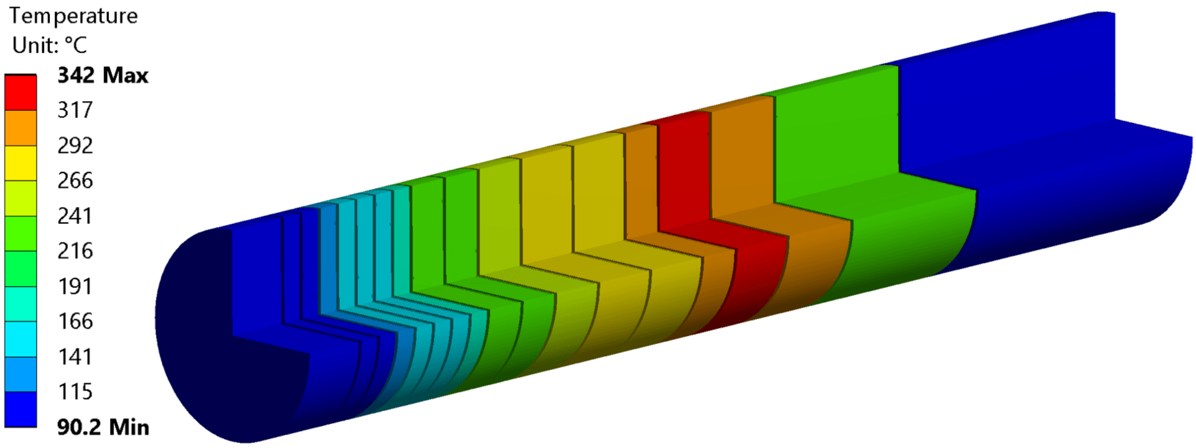

Fig. 5.33: Temperature distribution in the target blocks 1 week after a cooling-system failure. The maximum temperature is approximately 350°C, located in block 15.

The temperatures expected in the target for this accident scenario are well below the melting point of the materials. The stresses induced by the thermal loads were also calculated. The equivalent von Mises stress and maximum principal stress in the core materials (TZM and tungsten) are below 20 MPa for all the blocks during the whole period considered (2 yr), according to the structural calculations carried out. Hence, the target core materials are not expected to compromise the survival of the target after the cooling-system failure.

In the Ta2.5W cladding, higher stresses are expected, given the high amount of heat generated by the decay of tantalum isotopes. Figure 5.34 presents the distribution of the von Mises equivalent stress in the Ta2.5W cladding of the target blocks at the moment of maximum temperature, i.e. one week after the cooling-system failure.

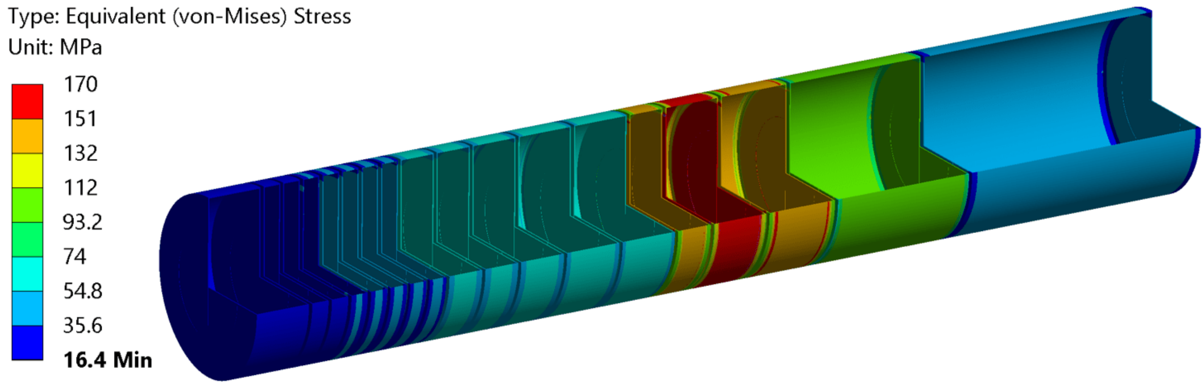

Fig. 5.34: Distribution of von Mises equivalent stress in the cladding of the target blocks 1 week after a cooling-system failure. The maximum stress is approximately 170 MPa, located in block 15.

The maximum stress is around 170 MPa, found in the cladding of block 15. This value is above the yield strength of the material at 350°C, which is estimated to be around 140 MPa. Therefore, a certain amount of plastic deformation is expected in the Ta2.5W cladding if the cooling system is not restarted after several days. Fracture of the cladding is not expected, since the maximum stress is below the tensile strength of the material and the total strain is very low compared with the elongation to failure of Ta2.5W.

Further study should be done to evaluate whether or not the plastic deformation produced has a detrimental effect on the target behaviour if operation is resumed after more than one week. Given that the plastic strain is quite low (0.02%) and localized, it is expected that the plastic deformation provoked by the decay heat will not impact on the lifetime of the target.

The FEM calculations performed have shown that a cooling-system failure could lead to high temperatures in the target materials, which would not be critical in terms of melting or fracture of the target, but could induce plastic deformation in the cladding of some of the blocks. However, the preliminary calculations performed have several limitations with respect to fully understanding the consequences of a cooling-circuit failure in the target.

– First, they do not take into account the increase in water temperature as the heat is dissipated into the stagnant water, in the case of a sudden stop of the cooling circuit. Therefore, it is not possible to estimate the risk of vaporization of water and overpressure in the tank.
– Then, further studies are required to evaluate the possibility of volatile isotopes being released at high temperature. This is a possibility for pure tungsten, which has been reported to form oxide layers above 400°C [34] and release tungsten trioxide (WO_3) species at 800°C [35]. Additional studies are required to investigate potential volatile isotope production by TZM and Ta2.5W.
– Finally, the convection coefficient used has a considerable influence on the temperatures reached in the target. Figure 5.35 shows a comparison between the maximum temperatures expected in the target for four different heat transfer coefficients used as boundary conditions in the FEM calculations: 0.5 W/m^2·K, 1 W/m^2·K (used for the thermal simulations presented above), 10 W/m^2·K, and 100 W/m^2·K. It can be seen that the variation of the film coefficient leads to very different scenarios for the target materials. Further dedicated studies are required to be able to provide a firmer assessment of the situation.

To achieve accurate modelling of the behaviour of air, helium, or water after a cooling-system failure accident, CFD studies are currently ongoing. These will allow precise calculation of the natural convection coefficient and the temperatures reached in the target, thereby allowing us to assess the survivability of the target in the scenarios considered.

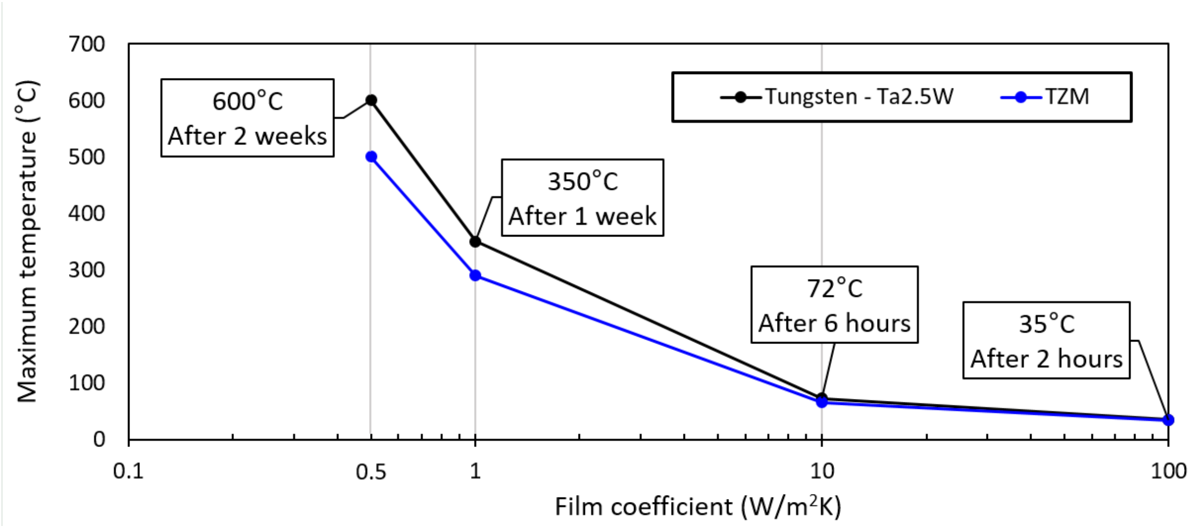

Fig. 5.35: Maximum temperature in the target materials obtained via FEM calculations for four different heat transfer coefficients used as boundary conditions to model natural convection. The value used for the detailed thermal simulations was 1 W/m^2·K, which is considered to be realistic and conservative.

5.5.4.2 Dilution system failure

The beam dilution system is critical for the ability of target to absorb safely the full SPS primary beam without damage. The transfer line design considers four independent dilution magnets powered by four different power supplies. Several dilution failure patterns are possible, depending on the number of power supplies failing and the dilution scheme used. Two different dilution schemes were considered, one with two pairs of magnets rotated by $\pi/2$ and another with four magnets rotated by $\pi/4$. More details of the transfer line dilution systems and the possible failure scenarios are given in Chapter 4.

Figure 5.36 displays the possible dilution failure patterns that could occur during operation. A beam size of σ = 8 mm is also represented, in transparent shading.

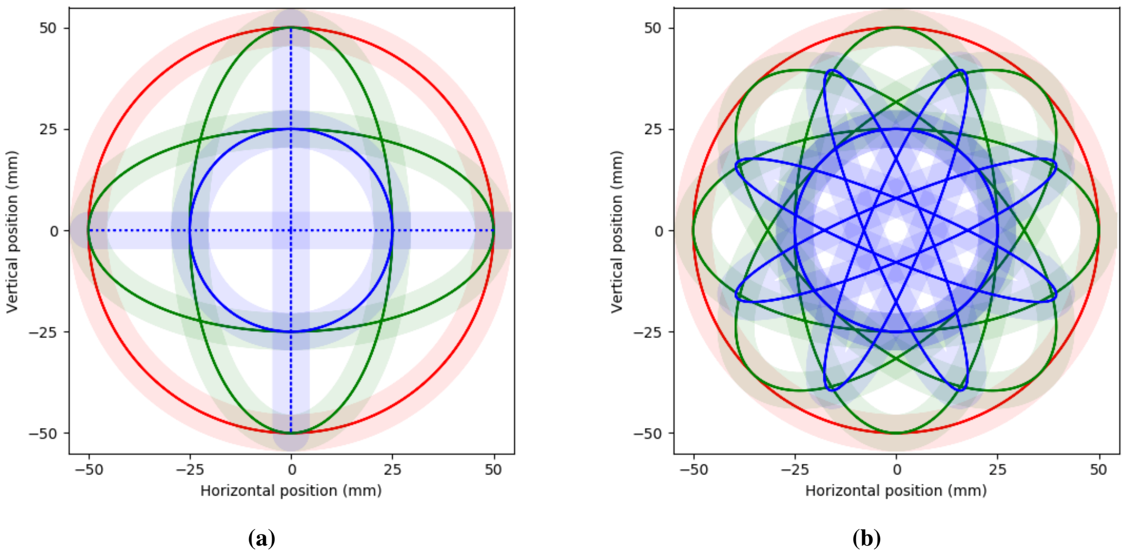

Fig. 5.36: Possible dilution patterns on the target with all four circuits (red), with three circuits (green), and with only two circuits (blue). (a) Patterns for the $\pi/2$ scheme, (b) possible patterns for the $\pi/4$ scheme. See Chapter 4 for more details of the beam dilution system.

It is necessary to evaluate the thermally induced effects on the target for the different dilution failure scenarios foreseen, to estimate the probability of target failure and to decide whether or not a continuous monitoring system is required for the dilution system. The results presented in this section summarize the thermomechanical calculations performed for that purpose.

The survivability of the target in the different failure cases was evaluated by studying two parameters that are considered to be among the most critical for target operation: (1) the maximum von Mises equivalent stress in the Ta2.5W cladding, which should be lower than the yield strength of Ta2.5W at the operational temperature (as discussed in Section 5.5), and (2) the surface temperature of the blocks, which has to be maintained below the boiling point of water (as will be shown in Section 5.6).

5.5.4.2.1 *Case 1: loss of a single dilution power supply*

The loss of one single power supply leads to an oval dilution pattern (for both the $\pi/2$ and the $\pi/4$ scheme), as shown in green in Fig. 5.36. This scenario induces a maximum temperature of 310°C in the blocks and a maximum surface temperature of 280°C, which can lead to very localized boiling of water for a short period of time. The maximum von Mises equivalent stress in the Ta2.5W cladding was found to be 140 MPa, below the yield strength at 300°C, which is estimated to be around 160 MPa.

Given that the amount of boiling in this case will be negligible, and that the probability of plastic deformation of the cladding is low, it is considered that in the event of failure of one power supply, the target would survive and no replacement would be needed.

5.5.4.2.2 *Case 2: loss of two dilution power supplies (circular dilution pattern)*

The loss of two dilution circuits may lead to different dilution patterns. The first one considered is a small circular pattern of radius 25 mm, shown in blue in Fig. 5.36.

This failure scenario leads to a maximum temperature of 340°C in the blocks and a maximum surface temperature of 300°C, which again could induce very localized boiling of water for a short period of time. The maximum von Mises equivalent stress in the Ta2.5W cladding was found to be 170 MPa, above the yield strength at 350°C, which is estimated to be around 140 MPa. This means that local plastic deformation is expected, and further analysis was performed as described below.

The behaviour of the target after the dilution failure was simulated to understand the effects on the target of such a failure scenario. A plastic model with temperature-dependent hardening was used to simulate the behaviour of the material above the yield point and after plastic deformation. The maximum von Mises equivalent stress reached after a beam impact subsequent to the dilution failure is 95 MPa, exactly as in the baseline case (see Section 5.5.2), and no further plastic deformation takes place. The situation described is illustrated in Fig. 5.37.

It can be concluded that a residual stress is created by the plastic deformation induced after the beam dilution failure, but this residual stress is negligible and is not expected to affect the target behaviour in normal operation. Taking into account these considerations, it is considered that—according to current knowledge—in this failure scenario the target would survive and no replacement would be needed.

5.5.4.2.3 *Case 3: loss of two dilution power supplies (flat dilution pattern)*

Another possible dilution pattern produced by the failure of two power supplies is a flat line 50 mm wide, represented by blue dotted lines in Fig. 5.36(a), obtained only for the $\pi/2$ scheme. In this case, the maximum temperature reached is 450°C in the blocks and a maximum surface temperature of 400°C is found, with temperatures of over 250°C in large areas of the surfaces of the blocks. Boiling of water is not considered to be negligible under these operational conditions, and could pose a risk for target operation.

The maximum von Mises equivalent stress in the Ta2.5W cladding is found to be 215 MPa, well

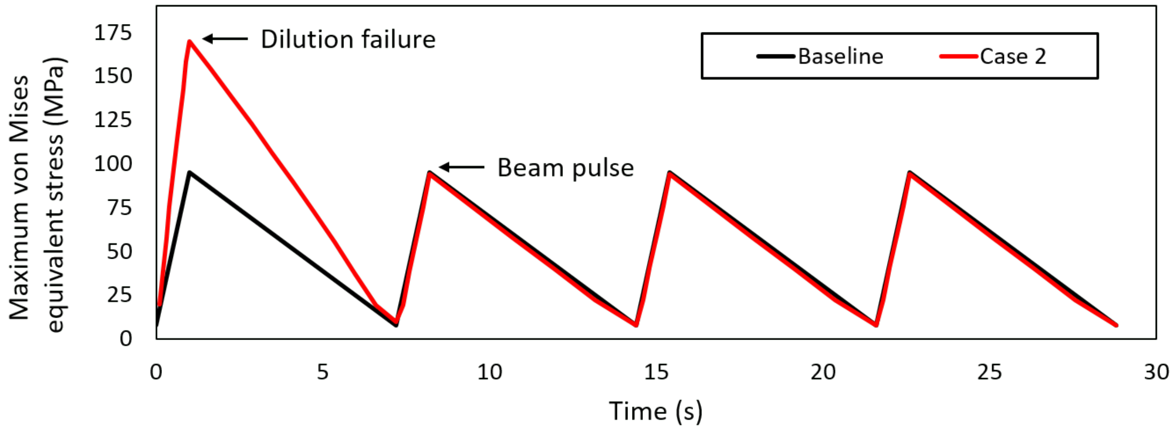

Fig. 5.37: Evolution of stresses during three pulses after the beam dilution failure presented in case 2. Comparison between the results of the baseline case and case 2 for the maximum von Mises equivalent stress found in the Ta2.5W cladding.

above the yield strength at 400°C, which is estimated to be around 125 MPa. This means that local plastic deformation is expected. The maximum von Mises equivalent stress is lower than the UTS of the material at 400°C, and the calculated total strain is well below the elongation limit of Ta2.5W; hence the risk of fracture ofthe cladding is considered to be very low.

The plastic deformation created by a beam impact with dilution failure could lead to residual stresses that affect the lifetime of the target. Similarly to case 2, the maximum von Mises stress reached in the Ta2.5W cladding after the first beam impact subsequent to the beam dilution failure was estimated to have a value of 145 MPa. This stress is below the yield strength of Ta2.5W at the operational temperatures, and no further plastic deformation is expected to occur during subsequent pulses.

The stress level is around 1.5 times higher than that in the baseline case, however, and it is considered that the dilution failure will affect the target behaviour by creating residual stresses, modifying the stress state in the target, and increasing the maximum stress during operation. It is concluded that the target should be replaced in this failure scenario.

5.5.4.2.4 Case 4: loss of two dilution power supplies (elliptical dilution pattern)

This scenario has effects on the target very similar to those in case 3. In this configuration, the failure of two power supplies leads to a flattened elliptical pattern, represented by a blue ellipse in Fig. 5.36(b). The maximum temperature reached is 470°C in the blocks and a maximum surface temperature of 415°C is found, with temperatures over 250°C in large areas of the surfaces of the blocks. Boiling of water is not considered to be negligible under these conditions, and could be a risk for target operation.

The maximum von Mises equivalent stress in the Ta2.5W cladding is found to be 215 MPa, well above the yield strength at 400°C, which is estimated to be around 140 MPa. As in case 3, local plastic deformation is expected. The risk of cladding fracture is again considered to be very low, given that the maximum von Mises equivalent stress is lower than the UTS of the material at 400°C, and the calculated total strain is well below the elongation limit of Ta2.5W.

The maximum von Mises stress reached in the Ta2.5W cladding after the first beam impact subsequent to the beam dilution failure is around 120 MPa, 1.25 times higher than the maximum stress in the baseline case. Figure 5.38 illustrates the aforementioned situation, comparing the results for the baseline case and cases 3 and 4. As in case 3, it is considered that the dilution failure will affect the target lifetime, and that replacement of the the target should be performed in this case too.

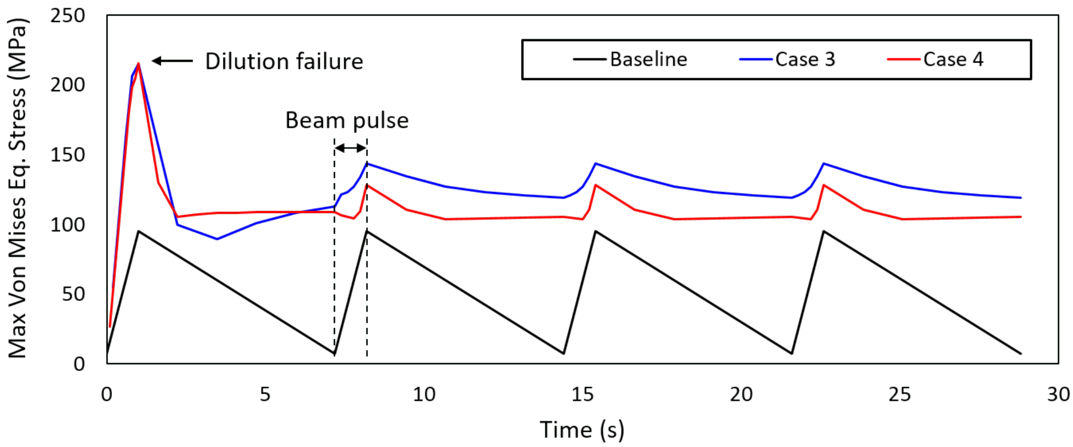

Fig. 5.38: Evolution of stresses during three pulses after the beam dilution failure presented in cases 3 and 4. Comparison between the results for the baseline case, case 3, and case 4 for the maximum von Mises equivalent stress found in the Ta2.5W cladding.

5.5.4.2.5 Case 5: loss of three dilution power supplies

The simultaneous failure of three dilution circuits would lead to a flat line pattern of length 25 mm. The calculations performed showed that the temperatures reached in the target would be around 550°C, with large areas of the target surface exposed to boiling water. The maximum von Mises equivalent stress obtained is 225 MPa, above the UTS of Ta2.5W at 500°C (estimated to be around 200 MPa), leading to a high risk of fracture of the cladding. Therefore, it is concluded that this scenario would require replacement of the target.

5.5.4.2.6 Conclusions

Table 5.11 summarizes the effects on the BDF target of the different dilution failure scenarios considered up to now in the study. Further studies will be required in the Technical Design Report phase to validate the technical solution to be implemented in the final project.

Table 5.11: Summary of effects on target foreseen for the five different cases of dilution system failure considered in the present study, evaluated via FEM calculations.

Dilution failure	Number of failing power supplies	Effects on target	Additional risks	Target replacement
Case 1	1	Low risk of plastic deformation in the cladding	Localized water boiling	No
Case 2	2	Localized plastic deformation in the cladding No influence on target lifetime	Localized water boiling	No
Case 3	2	Plastic deformation in the cladding Increased stress after pulse ($\times$1.5) Influence on target lifetime	Water boiling	Yes
Case 4	2	Plastic deformation in the cladding Increased stress after pulse ($\times$1.25) Influence on target lifetime	Water boiling	Yes
Case 5	3	Possible fracture of the Ta2.5W cladding	Water boiling	Yes

5.6 Target cooling system and CFD simulations

5.6.1 Cooling-system design

The cooling system of the target is one of the most critical parts of the BDF target design, given the high energy and average power deposited in the target during operation. Pressurized water has been chosen as the cooling medium, as other coolants such air or helium would require a much higher flow rate to dissipate such a high amount of power. A rotating target, as employed in other similar spallation targets, has been excluded for the moment owing to the additional technical complexity. Several requirements were considered in the design of the cooling system. First, a high water velocity is necessary to obtain a sufficiently high HTC between the cooling medium and the target blocks. Then, the pressure of the circuit should be high, and the pressure drop minimized, to ensure that the water in contact with the solid blocks is always below the boiling point. Furthermore, the design should be optimized to limit the increase in temperature in the circulating water while minimizing the necessary flow rate.

Figures 5.39 and 5.40 describe the circulation path of the cooling system around the target blocks. The target cylinders are separated by 5 mm channels that allow the passage of water between the blocks. The water circulation is designed to cool effectively the flat faces of the target cylinders, which are impacted by the diluted beam and will reach the highest temperatures during operation. The proposed cooling-system design consists in a serpentine configuration (series flow) with two parallel streams. A serpentine circulation can provide high water speeds in the channels with quite a low flow rate, while maintaining a reasonable pressure drop across the entire assembly.

The cooling circuit of the target was designed to allow the circulation of two streams in parallel. This configuration was aimed at reducing the total pressure drop in the circuit and the increase in temperature of the water from inlet to outlet. Another reason for this arrangement is to avoid a complete failure of the cooling-water circuit if one of the channels is blocked because of swelling of the blocks due to thermal expansion or because of debris in the circuit. If one of the channels is blocked, the water flow

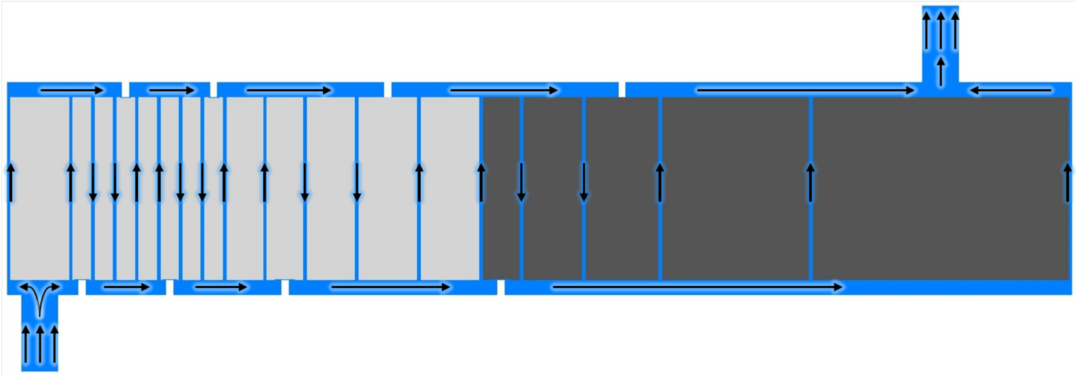

Fig. 5.39: Longitudinal cross-section of BDF target. Top view of the cooling circulation path. The beam comes from the left side; the blocks shown in light grey are made of TZM, while those in dark grey are made of pure W.

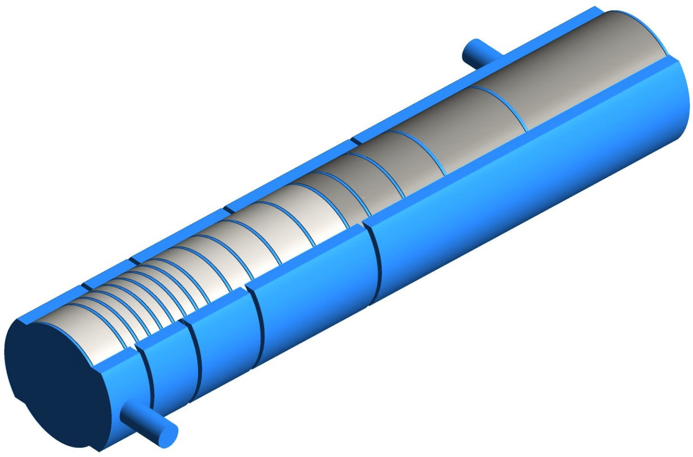

Fig. 5.40: 3D model of the BDF target cooling system, showing in blue the water volumes around the target core.

can continue through the other parallel channel, improving the reliability of the circuit. The last three channels are in parallel, since the number of channels is odd and the last tungsten blocks are the ones that receive the lowest amount of energy and have the lowest rise in temperature during operation.

The channels are connected by 'manifolds' that receive the water from two channels and distribute it to the following two. The size of the manifolds has been reduced to minimize the total water volume of the cooling system, and is also constrained by the design of the target support, which will be described in Section 5.7. At the same time, the cross-section of the manifolds has been designed to be large enough to avoid increasing the pressure drop in the circuit. The water velocity in the manifolds is not a critical parameter for the cooling-system design, given that the cylindrical side faces of the target core blocks will not receive a direct beam impact.

The serpentine circulation is horizontal, to avoid the formation of air pockets during the filling process, as well as to prevent stagnant water being left after draining. If a vertical configuration was chosen, the manifolds would be placed on top of and below the channels, and it would be very likely that air bubbles would remain in the top manifolds during the filling process, and stagnant water could remain in the bottom manifolds during draining of the circuit. The design, construction, and operation of the BDF target prototype (see Section 5.9), which will be detailed in a separate publication, has improved the understanding of the requirements on and limitations of the design of the cooling system for the final BDF target.

The operational pressure of the water-cooling circuit chosen was 22 bar. The thermal–fluid-dynamics simulations carried out in the study and detailed in the next sections have shown that the maximum surface temperature in the target blocks will be around 110°C at the peak of the pulse, well below the boiling point of water at 22 bar, which is 212°C. The main risk of having localized boiling is the loss of heat transfer between the solid blocks and the water, which would prevent the dissipation of heat by convection. The safety margin between the expected water temperature and the damaging effects of boiling is considered sufficiently large because the first phase of boiling that occurs beyond the boiling point is so-called nucleate boiling. During nucleate boiling, the heat flux is increased with respect to that achieved by convection in liquid water, and therefore the effects on heat dissipation are not detrimental but rather beneficial. This phase takes place after the boiling point is reached, and continues until this temperature is exceeded by around 30°C, at which point the critical heat flux is reached and the heat flux decreases drastically, leading to a significant reduction in the heat dissipation that could be harmful for the behaviour of the target. At 22 bar, the critical heat flux is reached at around 240°C, much higher than the expected maximum water temperature in the circuit. Figure 5.41 illustrates this effect.

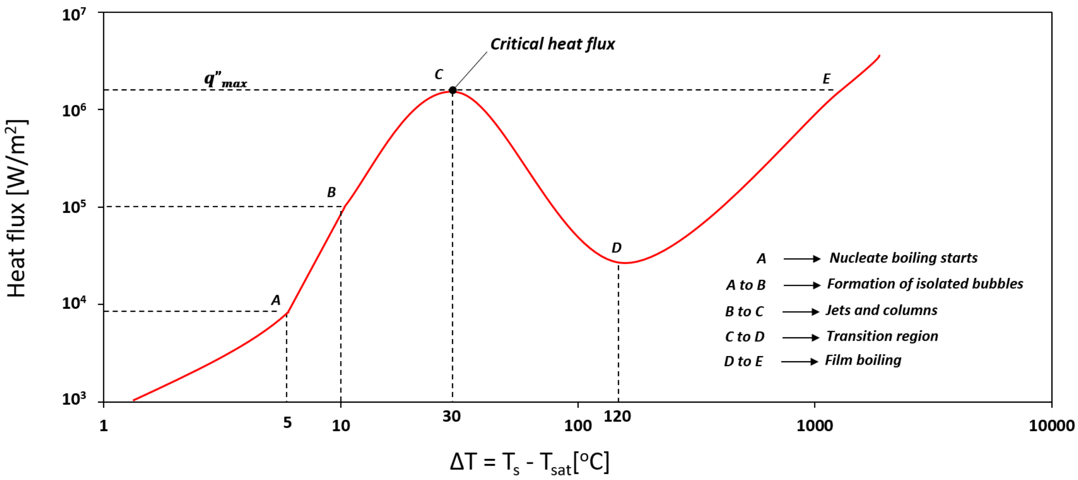

Fig. 5.41: Typical boiling curve for water at 1 atm. Surface heat flux as a function of difference of temperature from the saturation temperature [36].

The design water flow rate is 9 kg/s, leading to a rather uniform water velocity in the channels of around 5 m/s, as will be shown in the following section. The water velocity in the channels was limited by design to 5 m/s, to avoid potential undesired erosion effects on the tantalum–tungsten surface. Other spallation sources, such as ISIS at RAL, currently use high water velocities of up to 10 m/s in operational tantalum-clad targets (such as TS1) [33]. At the present conceptual design stage of the BDF target, it has been considered sufficient to apply a safety factor of 2 with respect to this value to ensure the safe operation of the target. As will be shown in the following sections, the average HTC obtained with a velocity of 5 m/s in the channels is sufficiently high to ensure temperatures and stresses well within the operational limits of the target.

5.6.2 Analytical calculations

Based on a fundamental knowledge of flow dynamics and heat transfer, analytical calculations were performed to provide a preliminary idea of the behaviour of the water flow in the cooling channels and the manifold. The average fluid–solid interface temperature and the average heat transfer coefficient on the walls of the cooling channels were also calculated. The properties of water at 20 bar and 30°C were conservatively used.

As discussed earlier, a channel velocity of 5 m/s was considered as an initial design parameter. A comparative study with channel velocities of 1, 2.5, 7.5, and 10 m/s will be reported later in this section. From Fig. 5.39 it can be observed that after the water enters the cooling domain from the inlet, it becomes bifurcated into two streams of parallel channels passing adjacent to the first target blocks. A zoomed view of Fig. 5.39 including two cooling channels and the inlet is shown in Fig. 5.42.

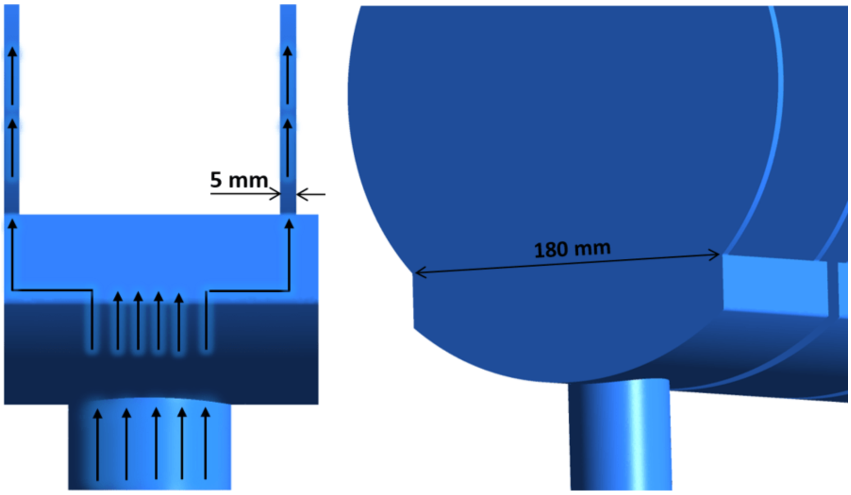

Fig. 5.42: Channel dimensions for the BDF target cooling circuit and flow bifurcation

Owing to the serpentine nature of the flow, the same pattern as shown in Fig. 5.42 is found in the following sections of the domain, which means that the sums of the mass flow rates in each pair of parallel cooling channels are identical and are also equivalent to the inlet mass flow rate. In the last part of the cooling domain, however, there are three channels in parallel and therefore the average velocities in these channels are less than 5 m/s.

Using the principle of mass conservation, the inlet mass flow rate can be calculated as follows:

$$\dot{m} = 2\rho A_c v_{\text{channel}}\,, \tag{5.5}$$

where ρ is the density of water, v_{channel} is the velocity of water in the channel, and A_c is the cross-sectional area of the cooling channels, which can be simplified to a rectangular cross-section with a channel thickness of 5 mm and a width of 180 mm. Using this information, the mass flow rate can be calculated, and the result is $\dot{m} \approx 9$ kg/s.

Using the energy balance equation (Eq. (5.6)), the temperature rise of the water from the inlet to the outlet of the flow configuration can be evaluated:

$$Q = \dot{m} C_p \Delta T\,, \tag{5.6}$$

$$\Delta T = \frac{Q}{\dot{m} C_p} \approx 8.1°\text{C}\,, \tag{5.7}$$

where Q is the average beam power deposited in the target core (305 kW) and C_p is the specific heat capacity of water.

The primary focus is on resolving the flow and heat transfer in the channels (and not in the manifolds) for two reasons.

– The beam impacts along the longitudinal direction of the target blocks, and hence the maximum energy deposition will be located mainly along the path of the diluted beam, and not at the cylindrical surfaces of the blocks, for all blocks.

– The conjugate heat transfer is primarily dependent on the flow speed and the contact area (between solid and fluid), and, since the average velocity of the water in the channels is approximately five times more than in the manifold, it can be safely assumed that the main heat dissipation will take place in the channels.

Using the velocity of water in the channels, the average Reynolds number inside the channels can be calculated as follows:

$$Re_{\mathrm{c}} = \frac{\rho \times v_{\mathrm{channel}} \times D_{\mathrm{H}}}{\mu}\,, \tag{5.8}$$

where μ is the dynamic viscosity of water and D_{H} is the hydraulic diameter of the channels, which can be calculated from

$$D_{\mathrm{H}} = \frac{4 \times A_{\mathrm{c}}}{P_{\mathrm{c}}} = 0.00973\ \mathrm{m}\,, \tag{5.9}$$

where P_{c} is the wetted perimeter of the channel cross-section. Using this value in Eq. (5.8), the average Reynolds number Re_D inside the channels is around 60 000, showing that the flow is highly turbulent in the cooling-circuit channels.

The HTC at the fluid–solid interface can be analytically calculated using the following expression:

$$h = \frac{Nu \times k}{D_{\mathrm{H}}}\,, \tag{5.10}$$

where k is the thermal conductivity of the water and Nu is the Nusselt number. Several convection correlations can be used to calculate the value of Nu for turbulent flow in a channel. Assuming that the water is flowing over a smooth surface, either the Dittus–Boelter or the Gnielinski equation can be used [36] (the Gnielinski equation, however, gives a higher level of accuracy, and will be employed in the following sections). The Dittus–Boelter equation can be written as

$$Nu_D = 0.023\, Re_D^{4/5} Pr^n\,, \tag{5.11}$$

which is valid for $0.6 \leq Pr \leq 160$, $Re_D \geq 10\,000$, and $L/D \geq 10$. n in Eq. (5.11) is 0.4 if the solid temperature is higher than the liquid temperature and 0.3 if the liquid temperature is higher than the solid temperature. The Gnielinski equation [37] can be written as

$$Nu_D = \frac{(f/8)(Re_D - 1000)Pr}{1 + 12.7(f/8)^{1/2}(Pr^{2/3} - 1)}\,, \tag{5.12}$$

which is valid for $0.5 \leq Pr \leq 2000$ and $3000 \leq Re_D \leq 10^6$. f is the friction factor, which can be calculated by use of the Petukhov relationship [38] as given in the following equation:

$$f = \left(0.79 \ln(Re_D) - 1.64\right)^{-2}, \quad \text{valid for} \quad 3000 \leq Re_D \leq 5 \times 10^6\,. \tag{5.13}$$

Using the above relationship and the value of Re_D, the friction factor in the channel was found to be $f = 0.02$. The Prandtl number for water at 30°C was taken as 5.4 [36], and was assumed to be constant for the flow. Using the values of f, Re_D, and Pr, Nu_D can be calculated from Eqs. (5.11) and (5.12):

$$Nu_D = 300 \quad (\text{using Dittus–Boelter equation})\,, \tag{5.14}$$
$$Nu_D = 350 \quad (\text{using Gnielinski equation})\,. \tag{5.15}$$

It is recommended to use the value of Nu_D obtained from the Gnielinski equation if a higher level of accuracy is desired [36]. Using the value of Nu_D from Eq. (5.15) in Eq. (5.10), the HTC can be estimated as

$$h = \frac{350 \times 0.61}{0.00973} \quad \Rightarrow \quad h \approx 22\,000\ \mathrm{W/(m^2 \cdot K)}\,. \tag{5.16}$$

The high HTC value calculated using the above equation is attributed to the large velocities reached in the channels. A comparative analytical study was been performed taking 1, 2.5, 7.5, and 10 m/s as the average channel velocity. Table 5.12 reports a comparison between the results for different channel velocities.

Table 5.12: Comparison of various analytical results for different channel velocities

Case no.	v_c	$\dot{m}$	ΔT	f	Nu (using Eq. (5.12))	HTC (using Eq. (5.12))
1	1	1.8	41	0.03	86	5 400
2	2.5	4.5	16	0.024	190	12 000
3	5	9	8.1	0.02	350	22 000
4	7.5	13.4	5.4	0.018	490	31 000
5	10	18	4.1	0.017	630	40 000

As can be seen, the temperature rise from inlet to outlet in the cooling domain is around 41°C and 16°C in cases 1 and 2, respectively. However, it was assumed in the design of the cooling stations for the target that the temperature rise should be limited to 10°C. Furthermore, it can be seen that the HTC values for cases 1 and 2 are much lower (four and two times less, respectively) than the values obtained for a velocity of 5 m/s.

In cases 4 and 5, even though the temperature rise is within the design limits and the HTC values are above those obtained for 5 m/s, the high speeds of the water (7.5 and 10 m/s) in the channels may induce long-term erosion effects in the cladding, which is undesirable for reliable target operation. In addition, higher water velocities lead to a correspondingly higher pressure drop in the circuit, as will be shown in the following section.

These analytic calculations give us a broad idea about the characteristics of the flow and heat transfer in the cooling circuit and, specifically, in the cooling channels. In spite of that, however, an extensive CFD study of the full-scale cooling system is needed because of the complexity of the flow in the turbulent regime, and because of the need to resolve the flow and heat transfer in the boundary layer of the channels.

5.6.3 CFD calculations

5.6.3.1 Simulation set-up

A commercial CFD code, ANSYS Fluent, was used to perform the extensive 3D turbulence modelling of the flow configuration. In conjugate heat transfer problems (such as the present one), the heat transmitted from the solid body to the liquid is highly dependent on the thermal boundary layer. Therefore, sophisticated turbulence models (such as the k–ω SST model or a realistic k–ϵ model with enhanced wall treatment) must be used to resolve the boundary layers.

A schematic model of the full-scale 3D flow domain along with the target blocks is shown in Fig. 5.40. A velocity of 5 m/s in the cooling channels was selected as a design parameter, and hence a velocity of 4.58 m/s was specified as the inlet boundary condition, the inlet diameter being 50 mm. A homogeneous Neumann boundary condition for the pressure was specified at the outlet (constant outlet pressure). A no-slip boundary condition was specified at the walls of the cooling circuit and at the target blocks. A non-uniform energy deposition was specified on all the target blocks; the energy deposition map was imported from the FLUKA Monte Carlo [11, 12] simulation results to the ANSYS Fluent model with the help of a user-defined function. The turbulence model used for all the simulations presented in this section was the k–ω SST model, unless otherwise mentioned explicitly.

Figure 5.43 illustrates the mesh used for the present model, which consists of both structured and unstructured elements. In all the target blocks and the cooling channels, hexahedral elements are used, which is imperative for improving the mesh quality (skewness, orthogonality, etc.) and achieving faster convergence of the simulation. Wedge elements are used in all of the boundary layer region, which is made up of several inflation layers, as shown in Fig. 5.44. The inflation layers are necessary in turbulent-flow simulations near the wall region to resolve the flow in the boundary layer region.

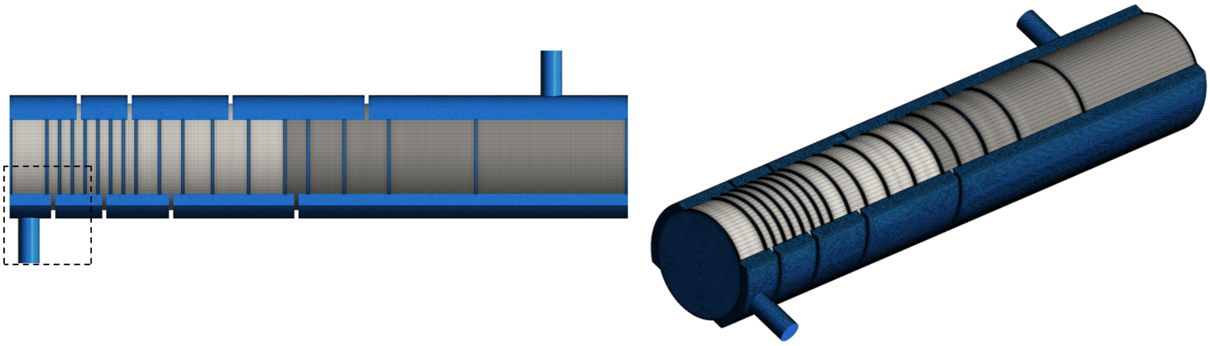

Fig. 5.43: Computational hybrid grid used for the 3D CFD calculations (top view)

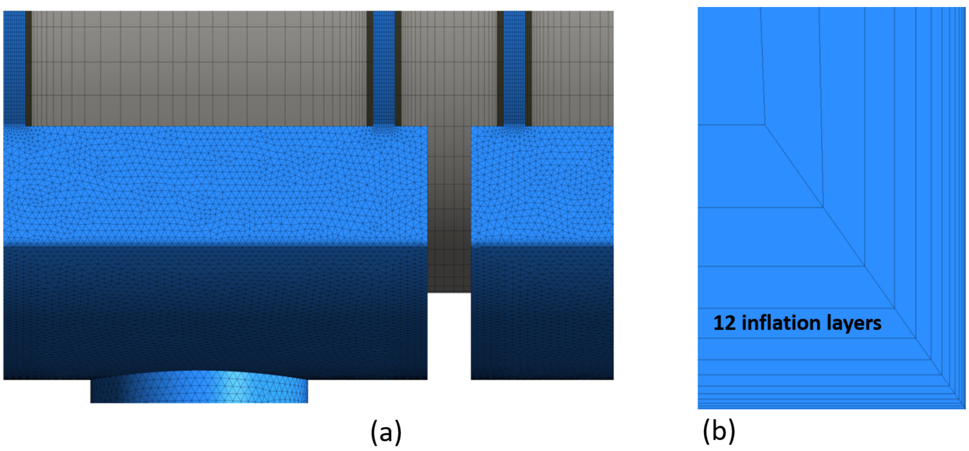

Fig. 5.44: Parts of the computational grid zoomed: (a) part of Fig. 5.43 (rectangular dashed box); (b) near the solid–liquid interface in the cooling channels.

5.6.3.2 Steady-state results

Steady-state simulations were carried out to investigate the flow and heat transfer behaviour in the cooling domain and the target.

Figure 5.45 shows contours of the static pressure distribution in the cooling system. As is illustrated in the figure, the pressure drop in the domain from inlet to outlet is around 3.2 bar, which means that the absolute pressure at the outlet would be $(22 - 3.2) = 18.8$ bar. This pressure is acceptable, since the boiling point at this pressure is over 200°C.

Figure 5.46 illustrates velocity contours in the cooling domain in the longitudinal plane of the BDF

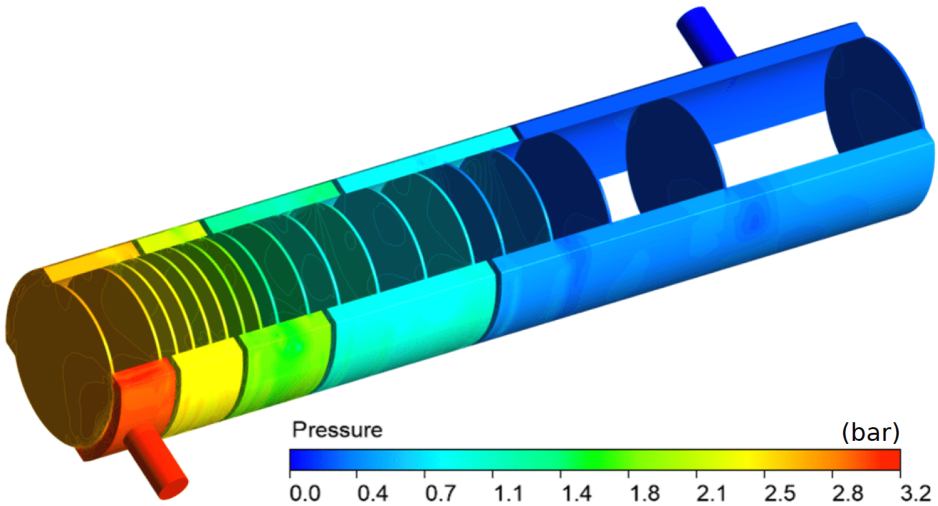

Fig. 5.45: Map of relative pressure variation in the target cooling system, assuming an outlet pressure set to 0 bar.

)

target. It can be seen that the average velocities in the cooling channels vary between approximately 4 and 6 m/s, except for the last three channels, where the average velocity is around 3–4 m/s. In the manifolds and in the outlet pipe, the blue regions denote recirculation zones due to flow separation. A recirculation zone was also observed in the cooling channels because of their circular shape. Figure 5.47 illustrates the 3D velocity distribution in the cooling system.

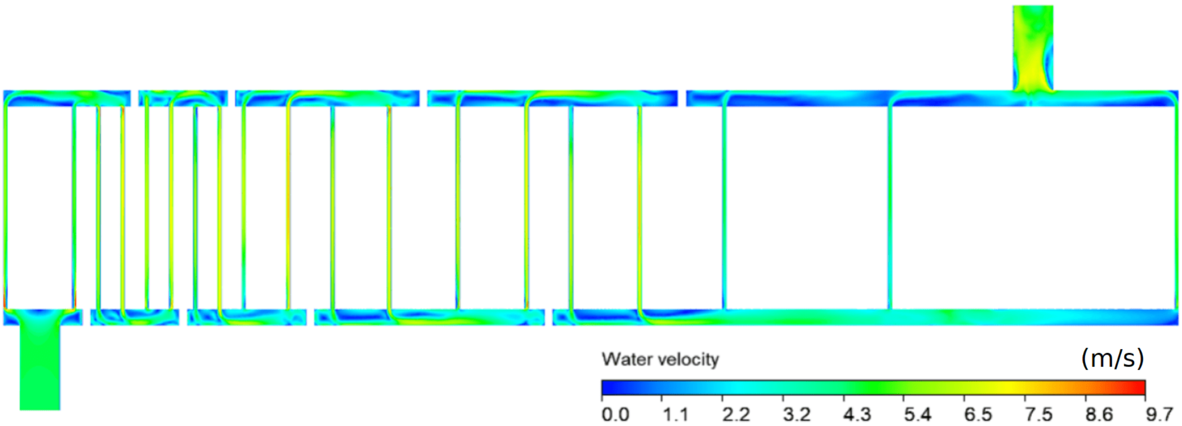

Fig. 5.46: Velocity contours in the cooling system in the central longitudinal plane of the BDF target

Figure 5.48 displays the average velocity of the water in all 19 channels. As can be seen from the figure, the average velocity in the channels is around 5 m/s for the first 16 channels and around 3 m/s for the last three channels. As the water stream enters the cooling system from the inlet, the flow is bifurcated into two streams, which enter the channels with similar mass flow rates. Hence, the average velocities in the first two cooling channels are almost identical. However, owing to the presence of blockers (which make the serpentine design possible), the mass flow rate in the even channels is higher than that in the odd channels. This effect is highlighted in Fig. 5.48 by the 'zigzag' pattern from channel 3 to channel 16.

Figure 5.49 shows a plot of the distribution of y^+ near the walls of the channels. It can seen that the value of y^+ in all the walls of the channels is near 1, and hence it can be concluded that the boundary layer is sufficiently resolved in the cooling channels using the k–ω SST turbulence model. The top and

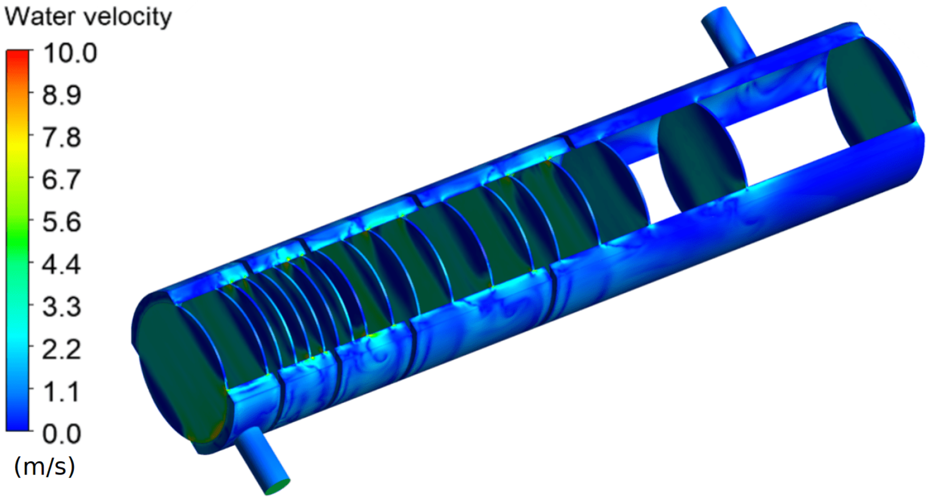

Fig. 5.47: 3D velocity distribution in the BDF target cooling system. The recirculation zones in the channels and manifolds can be seen in dark blue.

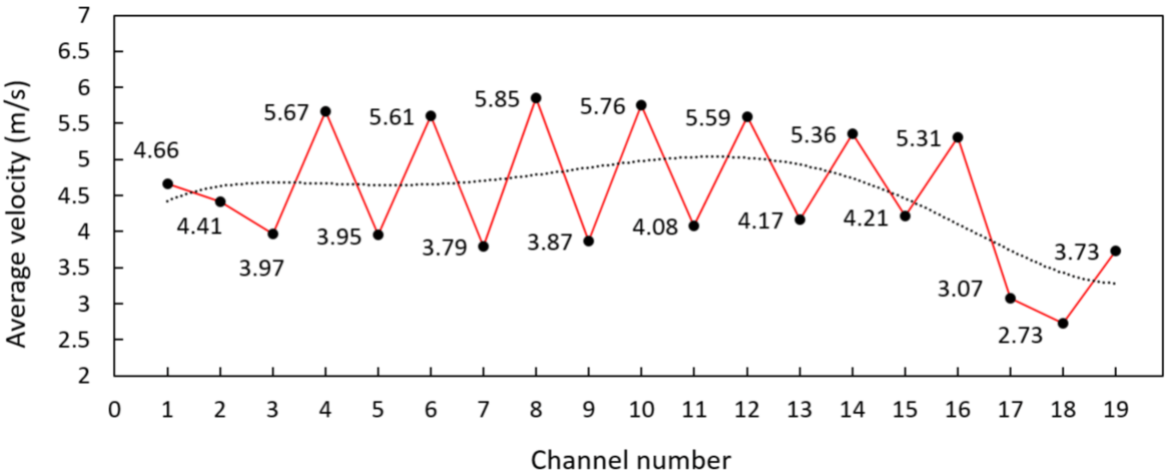

Fig. 5.48: Variation of average velocities in the water channels of the target. The trend line of the values plotted is represented by a dotted line.

bottom parts correspond to the manifolds and show higher y^+ values (above 30).

The total temperature rise at the outlet obtained from the steady-state CFD simulations performed is around 8°C. This behaviour is illustrated in Fig. 5.50, which shows the temperature contours in the cooling circuit in the YZ plane. The temperature rise found is in good agreement with the temperature rise calculated from the energy balance (Eq. (5.6)). In the transient case, however, the temperature at the outlet will fluctuate under the influence of the impact of the beam on the target, as will be shown in the following section.

Figure 5.51 displays the average heat transfer coefficient for all 19 channels of the cooling domain. Analytical values obtained as in Eq. 5.16 using the average channel velocities shown in Fig. 5.48 are also plotted for comparison purposes. As shown by the trend line of the simulated average HTC values, the HTC in the target cooling channels oscillates between 15 000 and 25 000 W/(m^2·K) in the first 16 cooling channels, where the velocity is around 5 m/s, as predicted by the analytical calculations. From this plot it can also be concluded that the HTC values obtained using the k–ω SST turbulence model are in good agreement with the analytical solution.

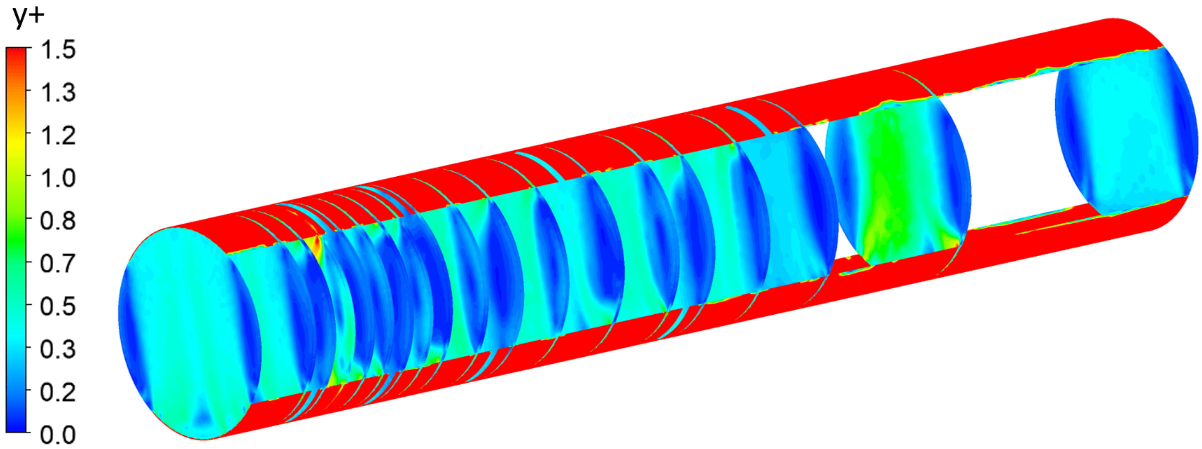

Fig. 5.49: Contours of y^+ on the surface of the cooling channels for the BDF target

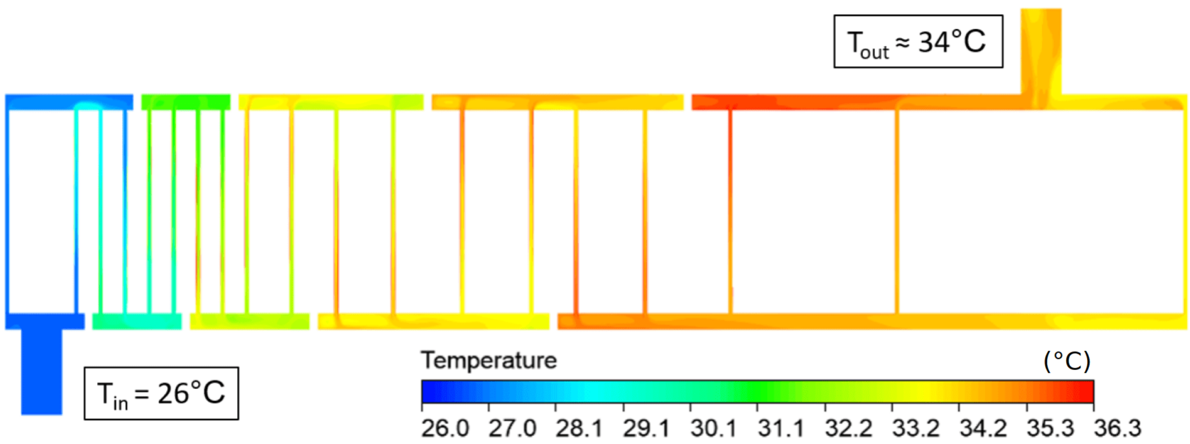

Fig. 5.50: Temperature contours in the cooling circuit in the YZ plane. Results from steady-state thermal CFD simulations.

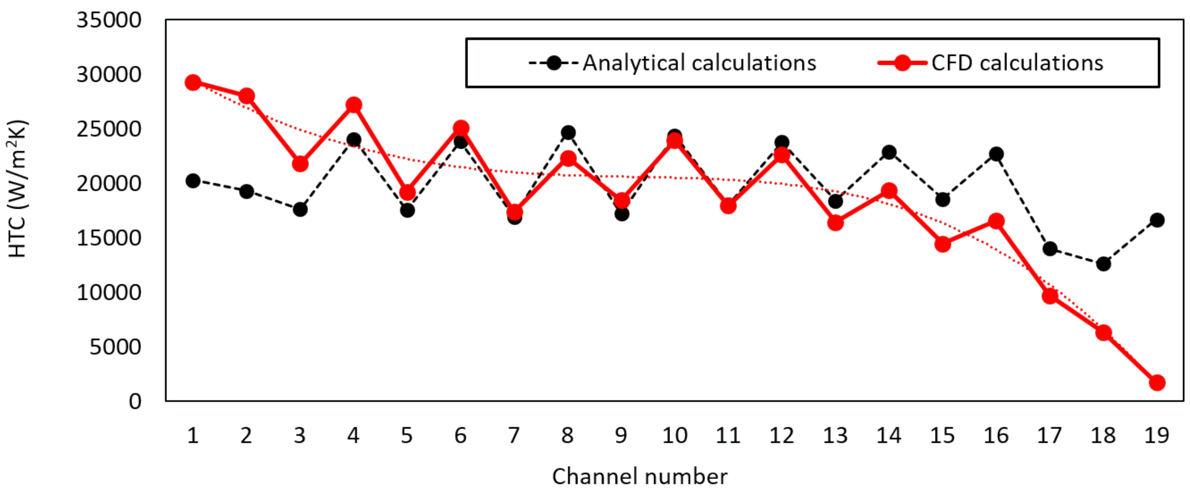

Fig. 5.51: Average HTC in the cooling channels. Comparison between values obtained from analytical calculations and from numerical simulations (k–ω SST turbulence model). The trend line of the average HTC values obtained from CFD simulations is shown as a dotted line.

Figure 5.52 illustrates the HTC distribution at the solid–liquid interface for the 9th, 10th, and 12th blocks, where it can be seen that, locally, higher values of the HTC (above 30 000 W/(m^2·K)) are reached on the surface of the blocks. It can be observed that for each block one of the two interfaces shows higher values of the HTC, which is attributed to the higher velocities reached in that particular channel (as shown in Fig. 5.48).

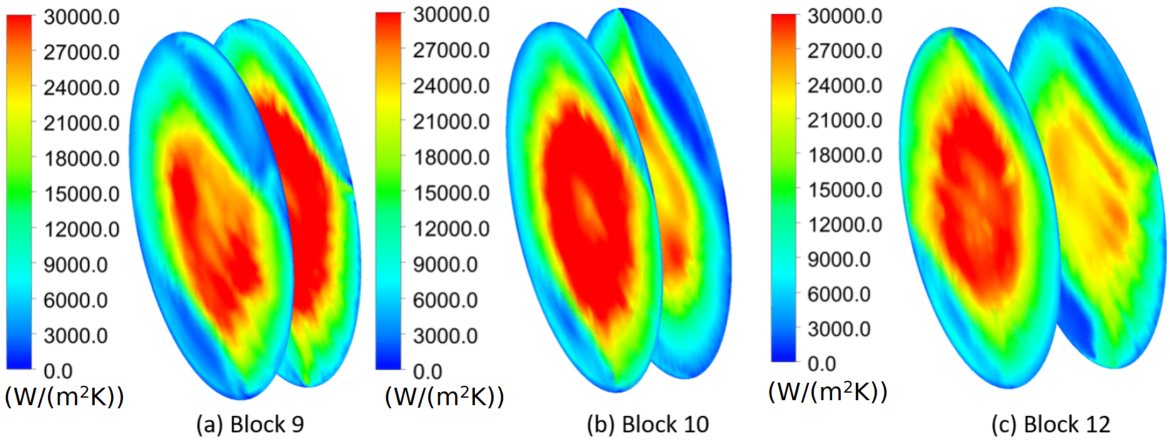

Fig. 5.52: Distribution of convective heat transfer coefficient at the water–target interface for different blocks in the channel.

The HTC, as explained earlier, is highly dependent on the flow velocity and contact area at the interface. A comparative study to investigate the effect of different channel velocities (1, 2.5, 5, 7.5, and 10 m/s) on the average HTC value in the cooling channels was performed. The results are shown in Fig. 5.53. Good agreement was found between the average values of the HTC obtained numerically and analytically (see Table 5.12). From the figure, it can be concluded that the heat transfer coefficient at the solid–liquid interface increases as the velocity of the water is increased. On the other hand, high velocities in the channel can lead to erosion of the solid surface, as well as a higher pressure drop in the circuit. A compromise between the two effects is found at the selected value of 5 m/s, leading to a high HTC (20 000 W/(m^2·K)) while reducing the risk of erosion of the tantalum and tungsten.

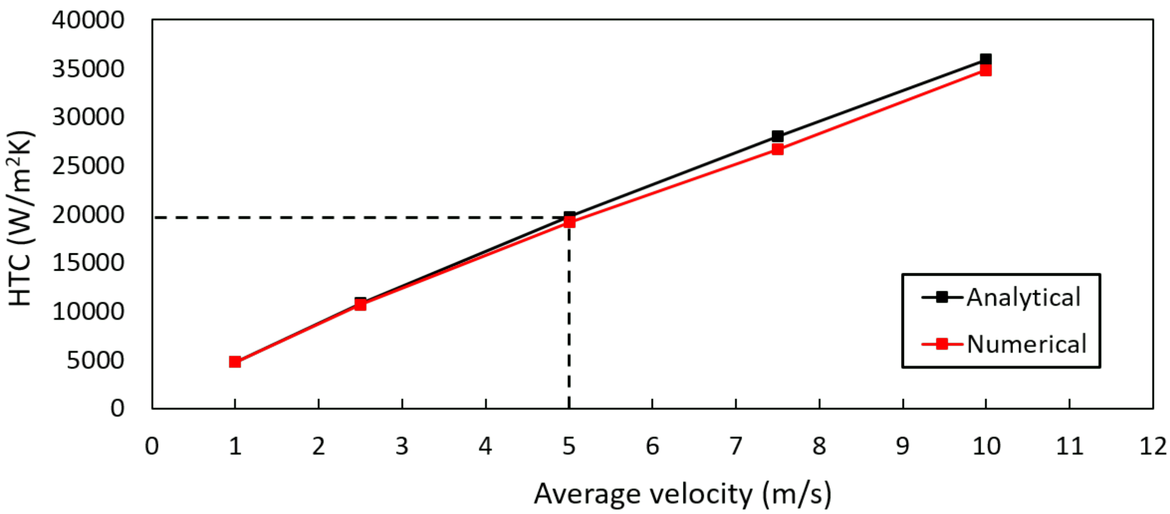

Fig. 5.53: Variation of convective heat transfer coefficient with channel velocity. Comparison between results of analytical and CFD calculations, showing good agreement between the two.

5.6.3.3 Transient results

Transient simulations were performed for the model described in the previous section, with an identical beam size, computational grid, and boundary conditions. In this case, the user-defined function responsible for importing the map of energy deposition on the target blocks was modified such that the energy deposited by the primary beam was applied to all the target blocks for 1 s and then removed for 6.2 s, thereby simulating the 7.2 s BDF/SHiP cycle. The results of the steady-state simulations were provided as the initial condition.

Figure 5.54 illustrates contours of the temperature distribution in a longitudinal section at the midplane of all the target blocks at the peak of the pulse (1 s). The corresponding temperature profile in the blocks following a line parallel to the Z axis at a distance of 50 mm from the axis (coincident with the beam impact location) is plotted in Fig. 5.55. From this figure, it can be noticed that the maximum temperatures are found in blocks 9 and 12, with similar temperatures (around 160°C) in the cores of the blocks owing to heat diffusion during the 1 s-long pulse.

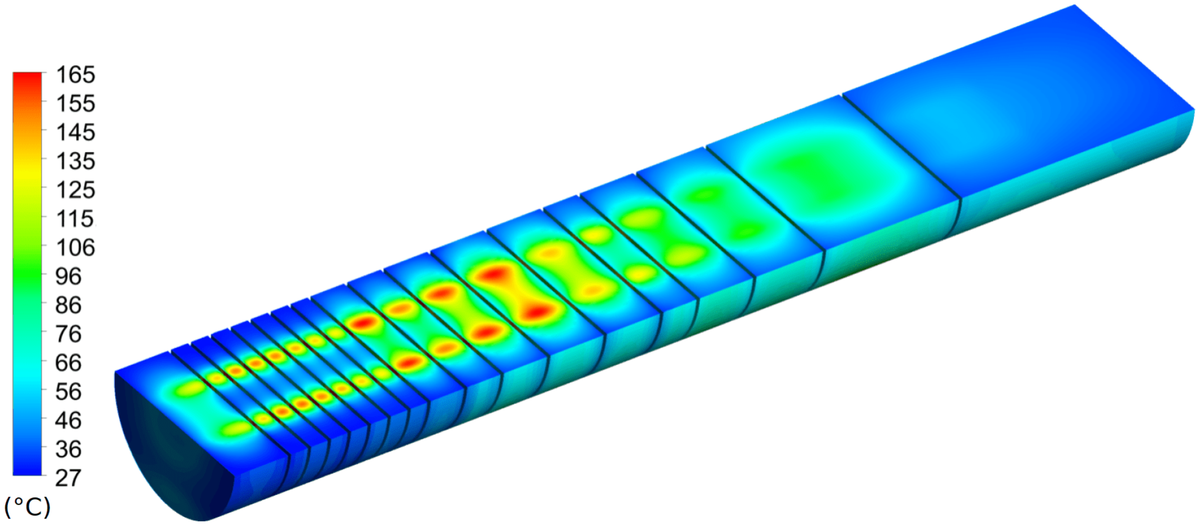

Fig. 5.54: Temperature contours in the target blocks at the end of the 1 s proton pulse

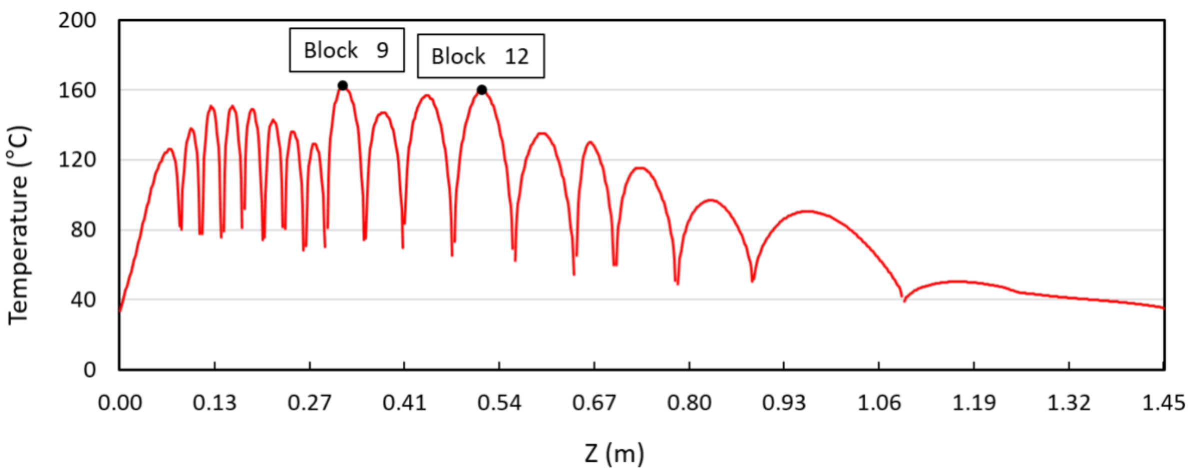

Fig. 5.55: Temperature variation in all the target blocks at the end of the 1 s pulse along the longitudinal axis at Y = 50 mm.

Figure 5.56 shows the temperature distribution in block number 12 at the end of the proton pulse, the maximum temperature in the TZM core of the block being 165°C. It can be observed that the circular surfaces of the block which are not in direct contact with water (the top and bottom surfaces) are nearly 30°C warmer than the side surfaces, which are cooled by water passing through the manifold.

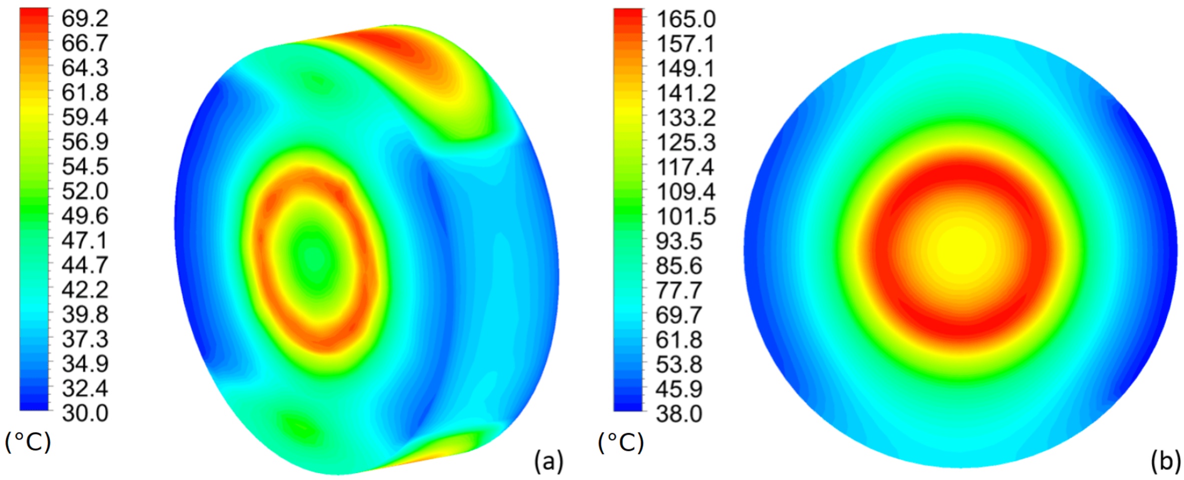

Fig. 5.56: Temperature contours in the 12th block at the peak of the pulse (1 s). (a) Side view, (b) mid section.

As presented in Section 5.5, the Ta2.5W cladding is one of the most critical aspects of the BDF target design, owing to the high intensity of the SPS pulse. Hence, it is important to investigate the maximum temperature reached in the Ta2.5W layer to ensure that mechanical failure does not occur because of excessive thermal stresses. Figure 5.57 shows the maximum temperature in the left and right layers of the Ta2.5W cladding of each block at the peak of the pulse. The maximum temperature is obtained in the left side layer of blocks 3 and 5, with a value of around 120°C.

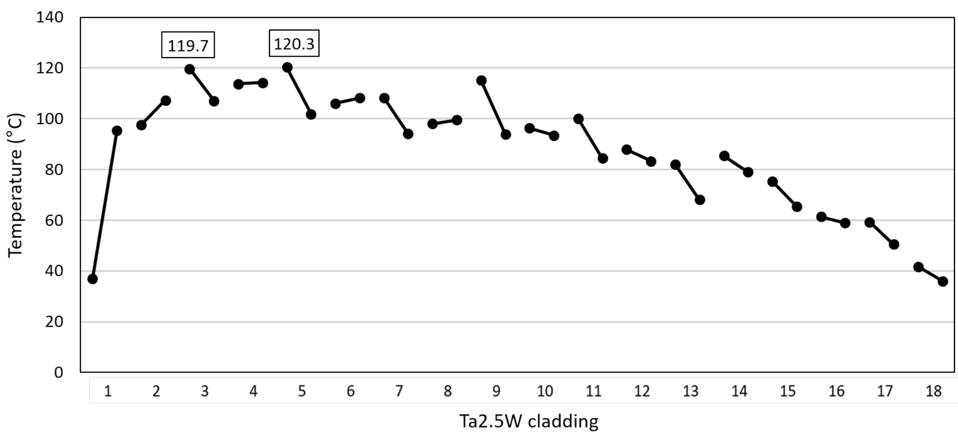

Fig. 5.57: Maximum temperature in the left and right Ta2.5W layers of the target blocks.

It is worth mentioning that the maximum temperatures obtained in the core and cladding materials via CFD calculations differ from the results of the FEM simulations shown in Section 5.5. The maximum temperature in the Ta2.5W cladding is not obtained in block number 4 as in the FEM calculations, but in blocks 3 and 5 (see Fig. 5.57).

Figure 5.58 displays a comparison of the longitudinal profiles of the temperature in the target blocks at 50 mm from the target axis for the two cases. It can be seen that the maximum temperature obtained in the core of the target blocks is around 20°C lower in the CFD simulations, and the surface temperature of the blocks is also substantially reduced. This difference can be explained by the fact that the HTC used as the boundary condition in the FEM simulations was constant, with a value of 20 000 W/(m^2·K), while in the CFD calculations the HTC was iteratively calculated and could reach values of over 30 000 W/(m^2·K), as shown in Fig. 5.52.

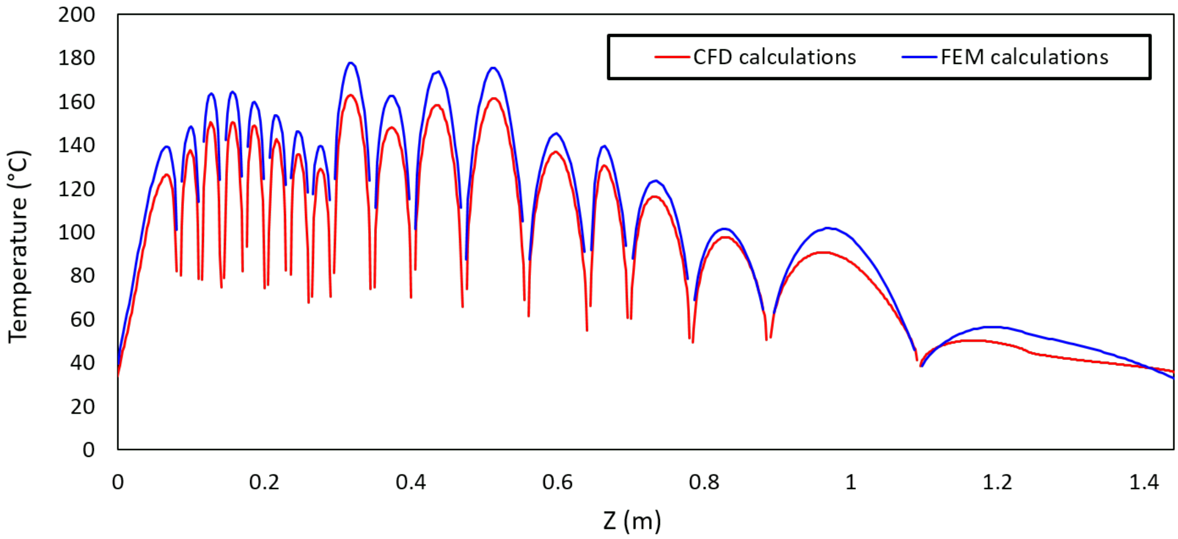

Fig. 5.58: Comparison between FEM and CFD calculation results for the temperature profile along the longitudinal axis 50 mm from the target centre. Results obtained for $t = 1$ s (end of pulse).

Therefore, the stresses calculated in Section 5.5.2 by importing the temperatures obtained via FEM calculations are conservative, and the safety margin with respect to the material limits is expected to be higher. For accurate modelling of the state of stress in the BDF target during operation, a temperature map obtained from CFD calculations should be imported into the FEM structural code. This activity remains as part of a future study, even though the results of the present calculations are conservative and appear to be well within the limits of the target materials.

Figure 5.59 presents the maximum temperature found at the surface of the target blocks, displaying the maximum value for the left and right fluid–solid interfaces of every block. It can be observed that the maximum surface temperature is around 90°C, reached in the left interface of target blocks 3 and 5. This temperature is less than half the boiling point of water at 22 bar, which is 212°C. It can be concluded from the results of the CFD calculations that boiling of water is not likely to occur during normal operation of the BDF target.

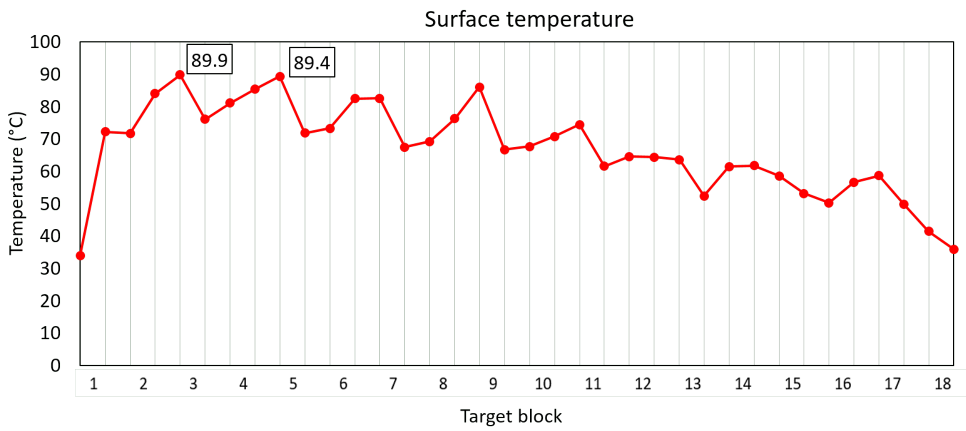

Fig. 5.59: Maximum temperature at the left and right surfaces of the target blocks. The maximum surface temperature is approximately 90°C.

5.7 Mechanical design of the BDF target and target assembly

5.7.1 Target assembly design

The BDF target assembly consists essentially of four main parts: the target core blocks, an inner tank that supports the target blocks, a leak-tight outer tank that encloses the inner tank, and a helium container that contains the whole assembly. A section of the inner and outer tanks supporting the target blocks can be seen in Fig. 5.60. The helium container enclosing the full target assembly, which is also the interface for the handling system in the target complex design, is shown in Fig. 5.61.

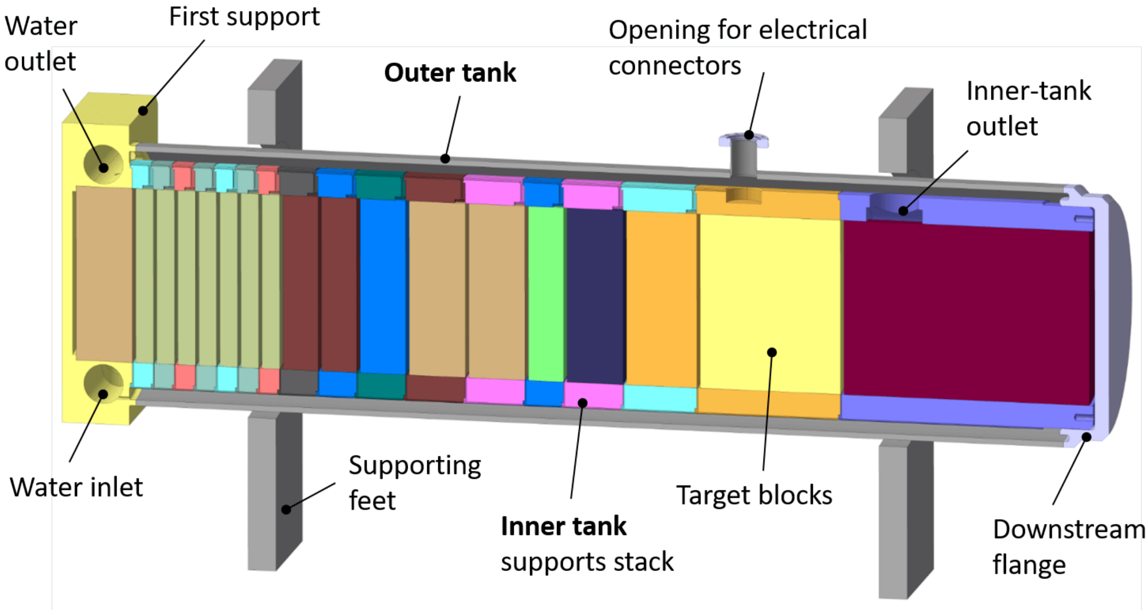

Fig. 5.60: Longitudinal section of the inner- and outer-tank structure of the BDF target. The target core blocks supported by the inner tank can be seen, as well as many functional elements of the cooling circuit and the supporting structure of the target itself.

5.7.1.1 Target block production

To assess the feasibility of the target assembly, a preliminary study of the mechanical design of the target and its assembly procedure has been executed. The BDF target core blocks consist of two different parts.

- A TZM or W cylinder with a length depending on the position of the block in the target core. Preliminary investigations showed that all the TZM cylinders can be manufactured via multiaxial forging, but not all the pure tungsten cylinders can be manufactured by this method [39]. The length of some of the tungsten cylinders, which reach up to 350 mm long, is a limiting factor in applying both longitudinal and radial forging. For that reason, it is foreseen that the W cylinders will be produced via sintering and subsequent HIPing, this process leading to an isotropic material structure and an acceptable density of around 97%.
- The Ta2.5W cladding, which encloses the TZM or W cylinder and consists of a tube of variable length and two discs. The Ta2.5W tubes can be rolled, and must be seamless as this is a requirement for the HIP process described later on. The Ta2.5W discs can be obtained via forging.

For the production of the target blocks, the TZM or W cylinder is inserted into the Ta2.5W tube and closed above and below by the two Ta2.5W discs. The discs and the cylinder have to be precisely machined to ensure a gap of around 0.1 mm between the disc and cylinder diameters and the inner diameter of the Ta2.5W tube. This gap should be sufficient for insertion of the discs and cylinder into

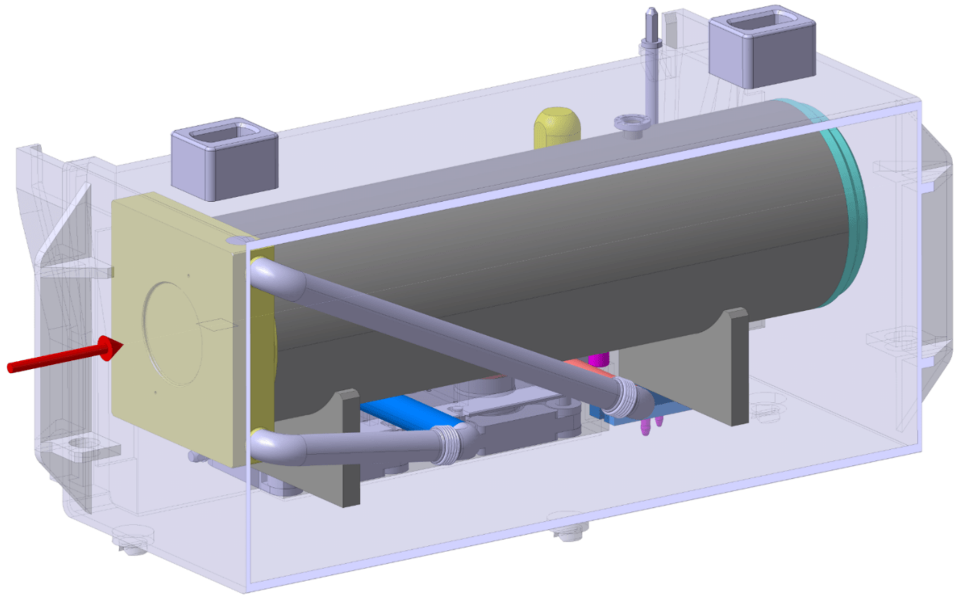

Fig. 5.61: Full assembly of BDF target: view of the helium container, outer tank, upstream and downstream flanges, and inlet and outlet pipes.

the Ta2.5W tube, but tight enough to achieve diffusion bonding between the materials during the HIP process. As an example, Fig. 5.62 shows the different parts necessary for the production of the target blocks, in this case for the production of a reduced-scale target block (25 mm thick, 80 mm in diameter) for the BDF target prototype tested in the North Area of CERN 5.9.

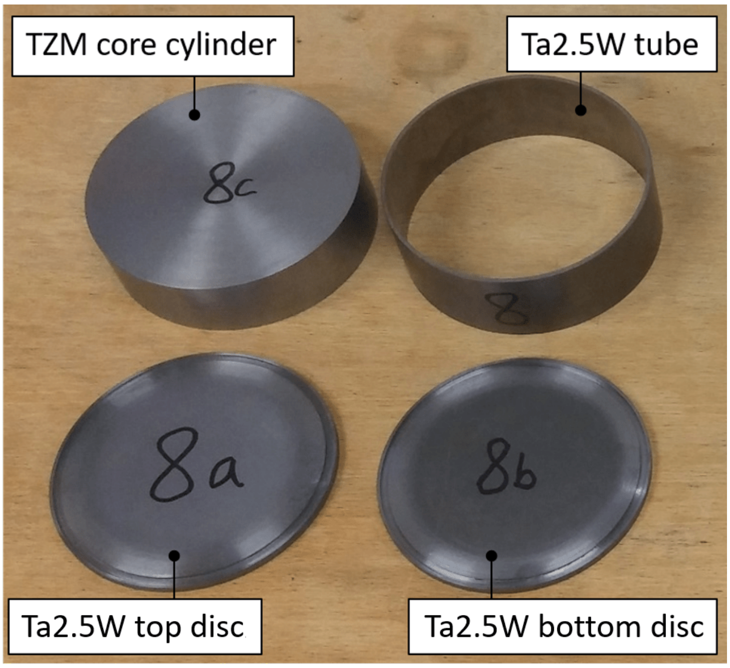

Fig. 5.62: Refractory metal parts required for the production of an 80 mm diameter, 25 mm thick Ta2.5W-clad TZM target block for the BDF target prototype test in the North Area of CERN (see Section 5.9).

Before the HIP run, the top and bottom Ta2.5W discs are electron-beam welded to the Ta2.5W tube, and the whole assembly is tested under vacuum to guarantee the leak-tightness of the capsules. After that, the capsules are covered with zirconium foil to prevent oxidation. Then, every assembled target block undergoes a HIP cycle, reaching a temperature of 1200°C and a pressure of 150 MPa for 2 h. Figure 5.23 illustrates the HIP cycle applied in the production of the BDF target blocks.

Once the HIP cycle has been completed, the target blocks have to be machined to ensure that the design dimensions are respected. The HIP process carried out in the production of the BDF target blocks is crucial to ensuring mechanical and chemical bonding between the cladding and core materials. A separate publication will detail the studies carried out to investigate different HIP cycles and evaluate the bonding quality achieved. Further studies are currently ongoing to explore other cladding cycles that could be similarly adopted to improve the cladding process.

5.7.1.2 Inner stainless steel tank of target vessel

The inner tank is composed of several ‘supports’ that are assembled together, made out of SS316LN (see Table 5.13 for more information). Each target block has its own support, which also acts as a handling tool. The target blocks may be very heavy, up to 300 kg for the heaviest tungsten cylinder, making a handling mechanism necessary for their assembly. Each support holds the corresponding target block in a vertical position during assembly, and all the supports are stacked on top of each other starting from the first support. Figure 5.63 shows a description of the supports that make up the inner tank, and Figs. 5.64 and 5.65 depict the handling and assembly process of the inner tank. This is a preliminary assessment of the constructability of the assembly, which will be further developed during the Technical Design Report phase.

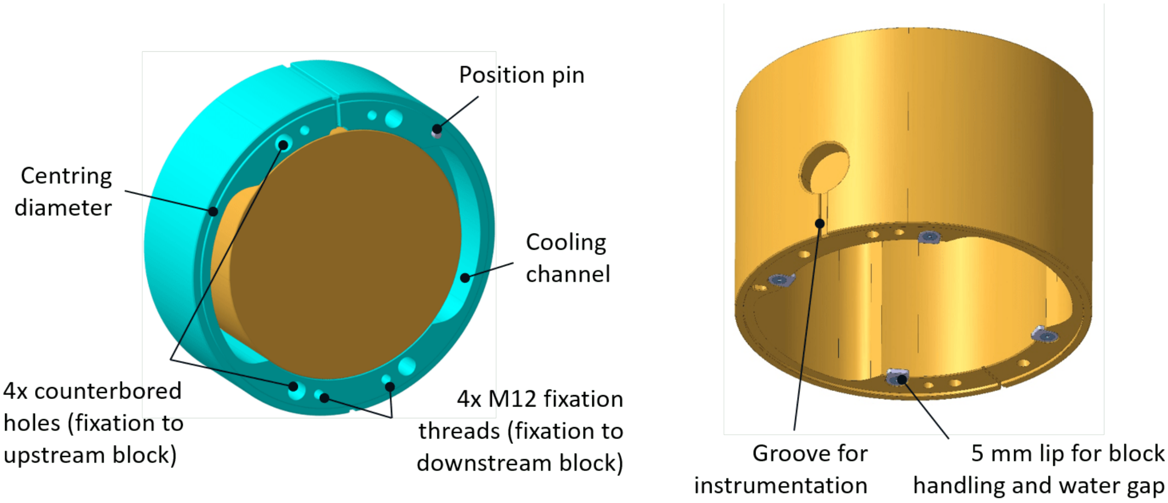

Fig. 5.63: Description of the supports of the target inner tank. Each support integrates different elements that permit assembly with the previous and following supports, as well as water circulation around the target blocks.

The supports are progressively bolted together, making one whole supporting structure. Once the assembly is completed, the supporting structure for the target blocks (hereafter referred to as the inner tank) is placed in a horizontal position for subsequent operations. The inner-tank structure is held by the first support on one side and by the outer-tank downstream flange on the other side. The structure has been designed to safely withstand the weight of all the target blocks, with an acceptable vertical deformation in the centre of around 0.1 mm, as will be shown in Section 5.7.2. Figure 5.60 presents a longitudinal cross-section of the inner-tank structure in the horizontal position; the target core blocks can be seen enclosed by the various supports, as well as the outer tank containing the whole assembly.

Another function of the inner tank is to enclose the target cooling system. The supports include dedicated grooves to provide the circulation path foreseen for the cooling water, compatible with the cooling-system design presented in Section 5.6. The 5 mm gaps between the blocks necessary for the water channels are ensured by a 5 mm ‘lip’ added to the supports, which also allows the blocks to be

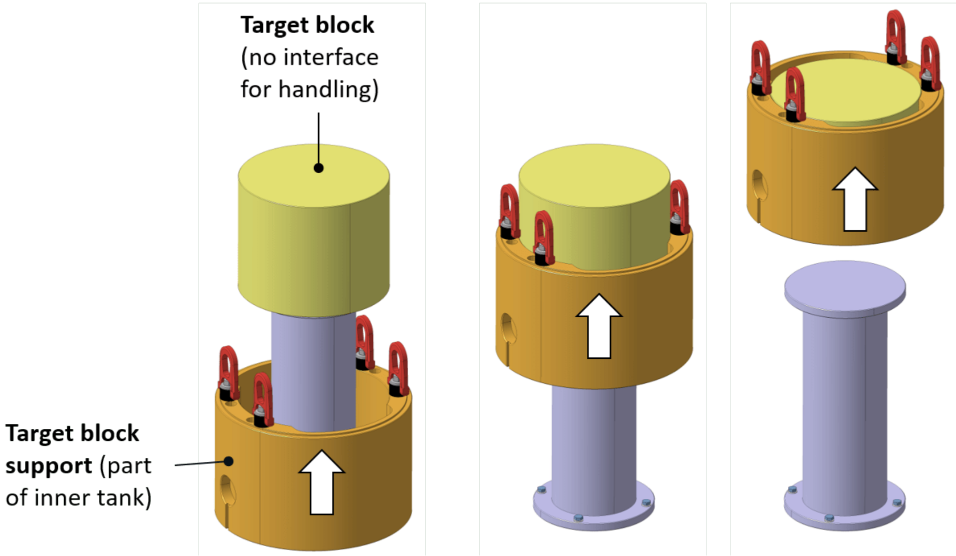

Fig. 5.64: Handling process for the target blocks: each target block is lifted by a corresponding support, which includes a dedicated interface for the target-block-handling operation.

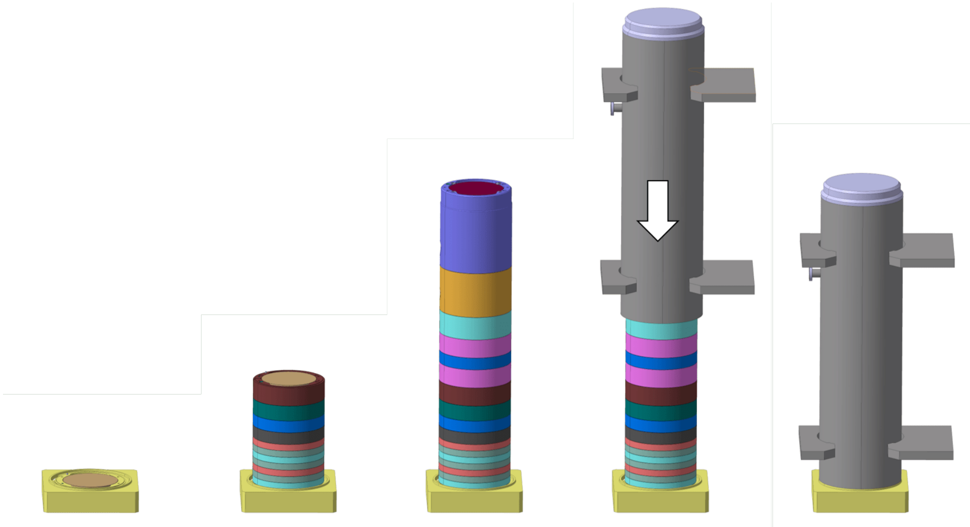

Fig. 5.65: Assembly process for target inner tank and fitting the outer tank: (i) each support is mounted on top of the previous one in a vertical position; (ii) once all the supports have been assembled, the outer tank is installed and welded to the first support, enclosing the whole inner tank; (iii) the whole assembly is placed in a horizontal position (Fig. 5.60).

held in a vertical position during the handling process (Fig. 5.64). The inlet of the target cooling system is located in the first support, and the outlet in the last one. The inlet is placed at the bottom of the first support, making it the lowest point of the whole cooling circuit. This arrangement provides more effective draining of the water if it is necessary to empty the circuit, avoiding water stagnation points. Finally, the inner tank also includes grooves for instrumentation cabling, since it is foreseen that the temperature and strain in several blocks will be monitored during operation.

5.7.1.3 Outer stainless steel tank of target vessel

The outer tank—also made out of SS316LN (see Table 5.13 for more information)—is responsible for providing leak-tightness of the target assembly and structural stability of the equipment. The cooling circuit is enclosed by the inner tank, but the inner-tank structure is, by design, not sealed against water leaks. Given the high number of connections between the supports that constitute the inner tank, and the complexity of the water circulation path, an external tank was chosen as the most reliable barrier to prevent leaks from the cooling system. The outer tank is welded to the first support on one side and to the downstream flange on the other side (see Fig. 5.60). Regarding the assembly procedure, once all the inner-tank supports have been stacked and bolted on top of one another, the outer tank is inserted and welded to the first inner-tank support. The fact of having only two welds adds simplicity and robustness to the target manufacture and assembly process, while ensuring good reliability of the system.

To avoid any stagnation of water between the inner and outer tanks, a gap is foreseen that is sufficiently large to force water circulation in the volume between the two tanks, creating an 'external' cooling loop. The outer-tank diameter was optimized taking into account the pressure drop, which should be minimized, and the water velocity, which should be high enough to provide continuous water circulation. CFD calculations were carried out, concluding that the optimal inner diameter of the external tank should be of the order of 360 mm, leading to a pressure drop of 1.5 bar in the volume enclosed between the two tanks and an average water velocity of 1 m/s (see Fig. 5.66). The outer tank lies on two rectangular feet and is 8 mm thick; it has been designed to withstand an internal pressure of 31 bar (22 bar with a safety factor of 1.43) and an external pressure of 1 bar, and to support the whole weight of the inner tank and the blocks.

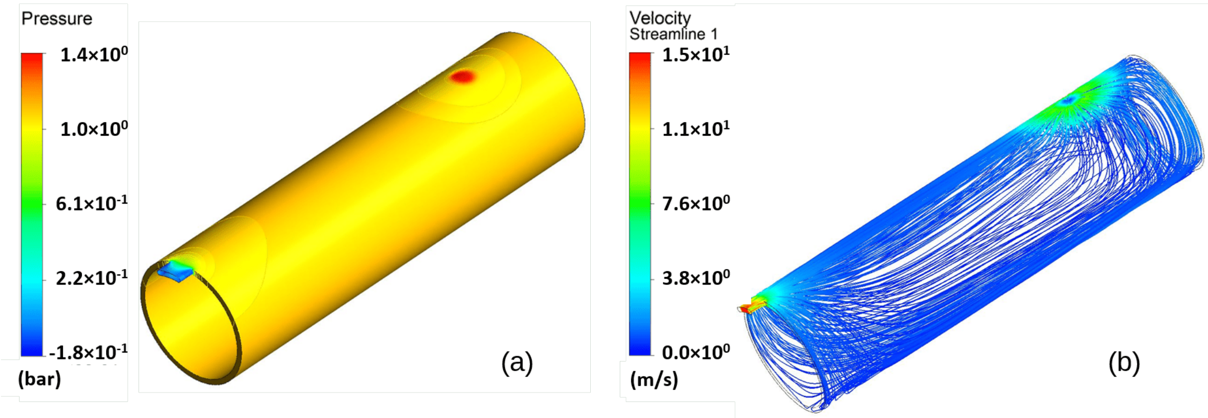

Fig. 5.66: Pressure (a) and velocity (b) distribution in the external cooling circuit obtained via CFD calculations. Maximum pressure drop $\approx$ 1.5 bar, average velocity $\approx$ 1 m/s.

Figure 5.67 details the layout of the first support of the inner tank, which is one of the key elements of the target assembly. This support acts as the upstream flange of the outer tank, and includes both the inlet of the internal cooling circuit and the outlet of the external cooling circuit. The water outlet is at the highest point of the circuit, preventing the formation of air pockets during the filling process; the presence of air bubbles could be harmful to the operation of the cooling system. The cooling pipes providing the water circulation are welded to the sides of the first support, and are routed below the outer tank, facilitating the drainage of water for target replacement, as shown in Fig. 5.60.

The first support assembly includes also the proton beam window. The thickness of the central part of the first support, where the impact of the diluted beam will take place, was reduced to 15 mm. This dimension was optimized to obtain a beam window thick enough for good mechanical reliability, taking into account the internal pressure of 22 bar, and thin enough to avoid critical levels of energy deposition by the beam.

The outer tank also provides an interface with the electrical connections of the target. As mentioned in the previous section, a groove is provided in the inner-tank supports for instrumentation cabling. When the outer tank is inserted, the cabling can be collected into a larger groove machined into one of the target supports (see Fig. 5.60), and the electrical connectors can be extracted from an opening in

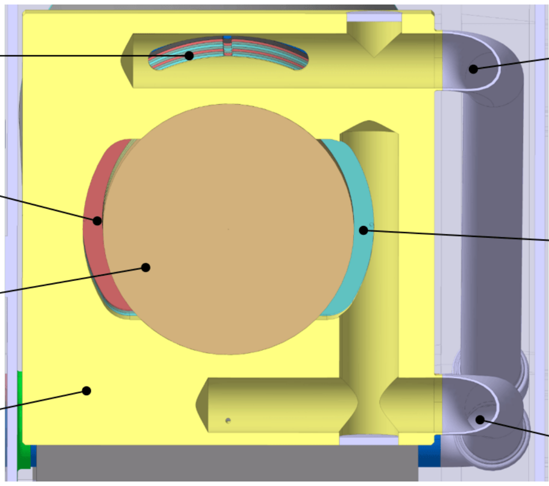

Fig. 5.67: Layout of the first support of the target inner tank, and also the upstream flange of the outer tank.

the outer tank. The connectors will then be connected to a feedthrough to ensure leak-tightness of the outer tank. The number of target blocks to be instrumented, as well as the physical parameters to be monitored and the type of instrumentation to be used, is yet to be defined. The aforementioned test of the target prototype under beam, where some of the target blocks have been instrumented employing several different technologies (Pt100 sensors, strain gauges, optical fibres), coupled with operating experience of spallation neutron sources such as ISIS (UK), SNS (US), and MLF (JP), will be of particular interest for clarifying this subject.

5.7.1.4 Target helium tank

The whole target assembly is contained inside a square-section tank filled with an inert gas (He at the current stage), as shown in Fig. 5.61. The presence of helium gas ensures a dry and controlled environment for target operation, reducing the risk of corrosion of the target assembly components. Additionally, the closed circulation of helium allows the monitoring of possible water leaks from the target vessel.

The mounting process of the outer tank in the helium container is summarized in Fig. 5.68. To ensure the leak-tightness of the helium tank and the feasibility of the welds inside the container, it is necessary to define several steps in the assembly procedure. First, the water inlet and outlet attached to the remote handling connections are inserted into the helium tank through two dedicated holes in the side. Then, leak-tightness is achieved by inserting two joints around the inlet and outlet pipes that avoid any possible passage of helium or water to the target complex environment. The next step is to install the outer tank of the target inside the helium tank, and attach the supports of the tank to the container to ensure proper alignment of the target assembly. Then, the connection between the pipes coming from the water supply of the target complex and the inlet and outlet of the BDF target cooling circuit is performed. Two water pipes are welded to the first support of the target and to the external pipes for that purpose. Finally, the side cover of the helium container is welded to the tank, ensuring leak-tightness and reliability of the whole assembly.

In the case of target failure, it is foreseen that the whole helium tank will be replaced together with the internal components. A comprehensive study of the handling in and integration of the target complex has been performed, and is reported in detail in a separate publication [40] and in Chapter 6. The target assembly design is fully compatible with the integration of the target complex, in which remote disconnection and exchange of the target helium container are foreseen. All the electrical, water, and helium interfaces of the helium tank that can be seen in Fig. 5.61 have been designed to be disconnected via remote handling, and are detailed in Ref. [40] and in Chapter 6.

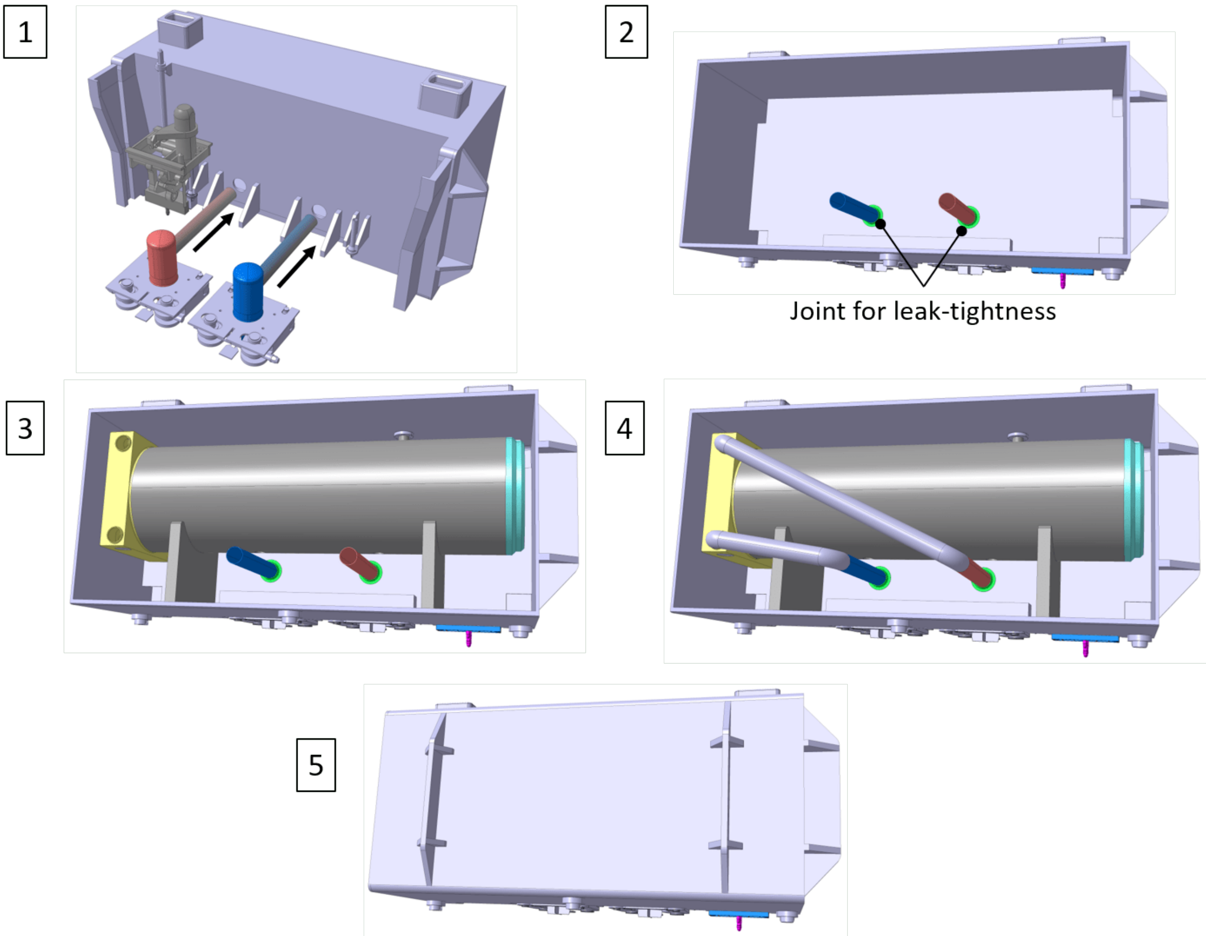

Fig. 5.68: Simplified assembly process of the BDF target outer tank in the helium-containing tank

5.7.2 Structural calculations for the target vessel

5.7.2.1 Scope of analysis

The model investigated was the BDF target assembly, 373 mm in diameter, approximately 1500 mm long, and 1.5 t in weight, which will be subject to cooling with pressurized water at 22 bar under operational conditions, but the water pressure will be ramped up to 31 bar during the test phase. The goal of the analysis was to check the structural resistance of the inner-tank support stack and determine the size and number of bolts required. An additional part of the scope of the analysis was to assess the vertical deflection of the structure, with an assigned threshold of 1 mm. The relative displacement between the end of the stack and the supporting housing structure, as a consequence of the self-weight-induced bending deformation of the assembly, was also checked to ensure that no locking occurred. Detailed results are described in Ref. [41].

5.7.2.2 Material selection

The mechanical properties of the different materials used in the target structure are reported in Table 5.13.

5.7.2.3 Failure criteria

5.7.2.3.1 Deformations and stresses

It was required that the vertical displacement did not exceed 1 mm. Also, the relative motion between the end of the stack and the supporting structure was checked to ensure that no locking occurred. The stresses

Table 5.13: Material properties. ρ, density; E, Young's modulus; ν, Poisson's ratio.

Property	Stainless steel 1.4404	Stainless steel 1.4435	TZM	Tungsten	Stainless steel A4-100
ρ (kg/m^3)	8000	8000	10220	19300	8000
E (GPa)	200	200	288	405	200
ν	0.3	0.3	0.28	0.28	0.3
$R_{\mathrm{p}0.2}$ (MPa)	190	200	764	1350	940
$R_{\mathrm{p}1.0}$ (MPa)	225	235	–	–	–
R_{m} (MPa)	490	520	965	1670	1000
A	35%	45%	10%	2%	9%

in the model were assessed against the standard for pressure vessels EN 13445-3 [42]. This standard defines the maximum allowable values of the nominal design stress for pressure vessel components, under operating conditions and during testing, according to the specification of the steel and its minimum rupture elongation. As a conservative approach, the properties of stainless steel 1.4404, an austenitic steel with a minimum elongation after fracture larger than 35%, were assumed in the calculation of the maximum allowable stresses. The maximum allowable value of the nominal design stress for the present vessel under operating conditions is

$$f_{\mathrm{d}} = \max\left[\left(\frac{R_{\mathrm{p}1.0/\mathrm{T}}}{1.5}\right); \min\left(\frac{R_{\mathrm{p}1.0/\mathrm{T}}}{1.2}; \frac{R_{\mathrm{m/T}}}{3}\right)\right] = 163.3\,\mathrm{MPa}\,. \tag{5.17}$$

The maximum allowable stress during testing is

$$f_{\mathrm{test}} = \max\left[\left(\frac{R_{\mathrm{p}1.0/\mathrm{T\,test}}}{1.05}\right); \left(\frac{R_{\mathrm{m/T\,test}}}{2}\right)\right] = 245\,\mathrm{MPa}\,. \tag{5.18}$$

5.7.2.3.2 *Bolt assessment methodology*

The bolts were assessed against VDI 2230-1 [43]. In so doing, the pre-load to be applied to the bolts was estimated taking into account the effects of external forces, so as to guarantee that the loads acting on the planes orthogonal to the main axes of the bolts were equilibrated by frictional forces arising between the surfaces joined together (the number of bolts acting on the same joint was also considered): a conservative friction coefficient of 0.1 was assumed. The necessary tightening torque to be applied to each bolt was assessed, verifying that it did not exceed the prescribed limit value. Finally, the die used in the manufacture of the bolts was also verified, and the minimum required engagement length was estimated.

5.7.2.4 Boundaries and load conditions

In all analyses, the whole model was fixed to the ground at the bottom faces of the two vertical supports, and standard earth gravity was applied. As shown in Fig. 5.69, a pressure of 0.1 MPa mimicking atmospheric pressure was applied on all the external faces, while a pressure of 3.1 MPa was applied on the surfaces inside the structure to simulate the maximum pressure that the target will suffer during the test phase.

5.7.2.5 Results

Numerical simulations were used to perform a static structural analysis of the target support, to evaluate its deformations and stress levels and the reaction forces in the bolts.

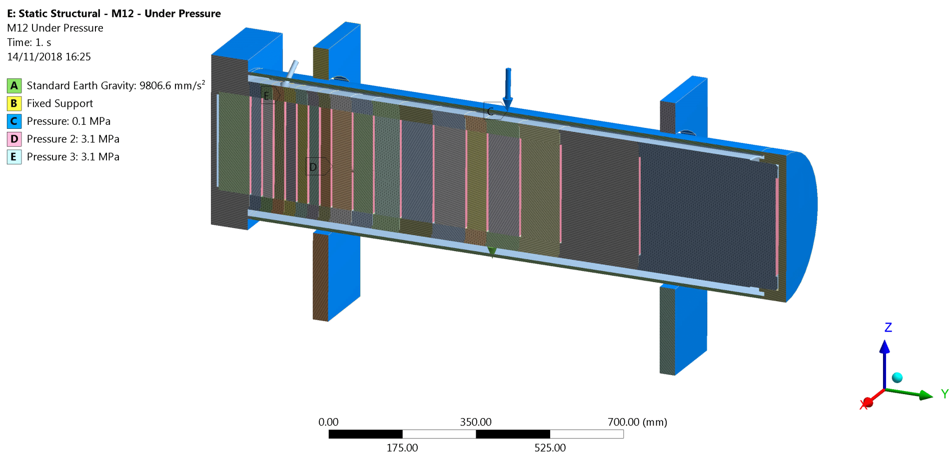

Fig. 5.69: Initial conditions of the numerical model required to assess the structural robustness of the BDF target assembly.

5.7.2.5.1 *Displacements*

The vertical deformation of the model was calculated. Figure 5.70 shows the vertical deformation of the assembly. It can be seen that the maximum displacement is 0.11 mm. Hence, the criterion of a maximum displacement of 1 mm is fulfilled.

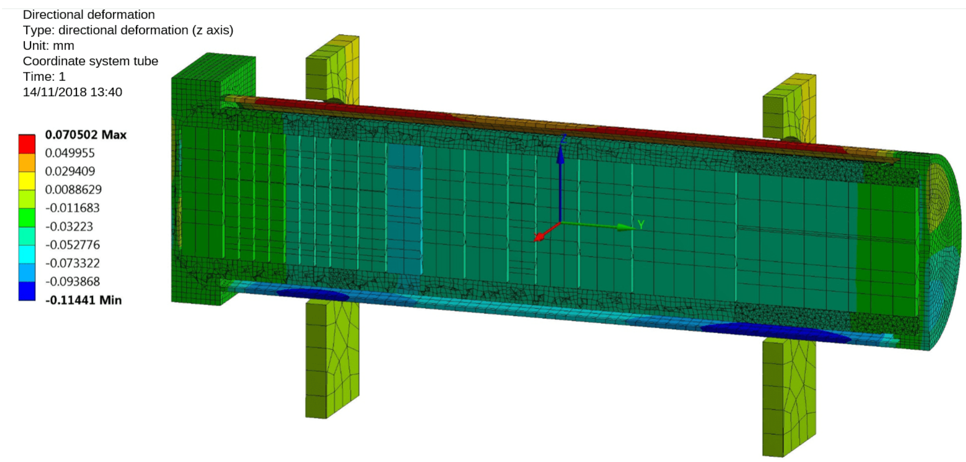

Fig. 5.70: Vertical displacement of the BDF target assembly

5.7.2.5.2 *Relative displacement between end of stack and supporting housing structure*

The annular support at the end of the stack is embedded in the closing flange. The relative displacement between these two parts needed to be evaluated to ensure that no locking occurred. The reference system was fixed to the closing flange, and the displacements of the annular support were assessed in this reference system. The most critical case is when the assembly is subjected only to its own weight. As shown in Fig. 5.71, the maximum displacement at the end of the stack relative to the supporting housing structure is 0.066 mm. Consequently, a minimum radial gap of 0.1 mm between the two parts should prevent locking.

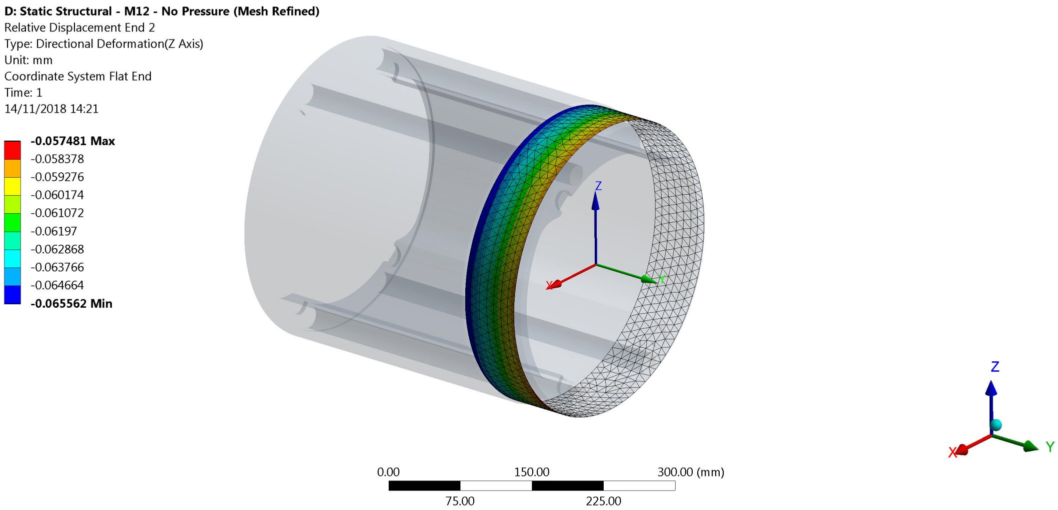

Fig. 5.71: Relative displacement at the end of the BDF target stack

5.7.2.5.3 *Equivalent stress*

The stresses in the model were evaluated according to EN 13445-3. According to this standard, the maximum design limit in the simulation should not exceed f_{test} = 245 MPa. The stresses arising at the contacts simulating the cross-sections of the bolts were been excluded from this evaluation, as the analysis of the reaction forces associated with the contacts simulating the bolts was carried out according to VDI 2230-1. Figure 5.72 shows the equivalent stress. The stress levels in the model are globally below 200 MPa. Only a few points are close to the maximum allowable stress during testing. As they are very localized and in regions that are non-critical, they could be tolerated.

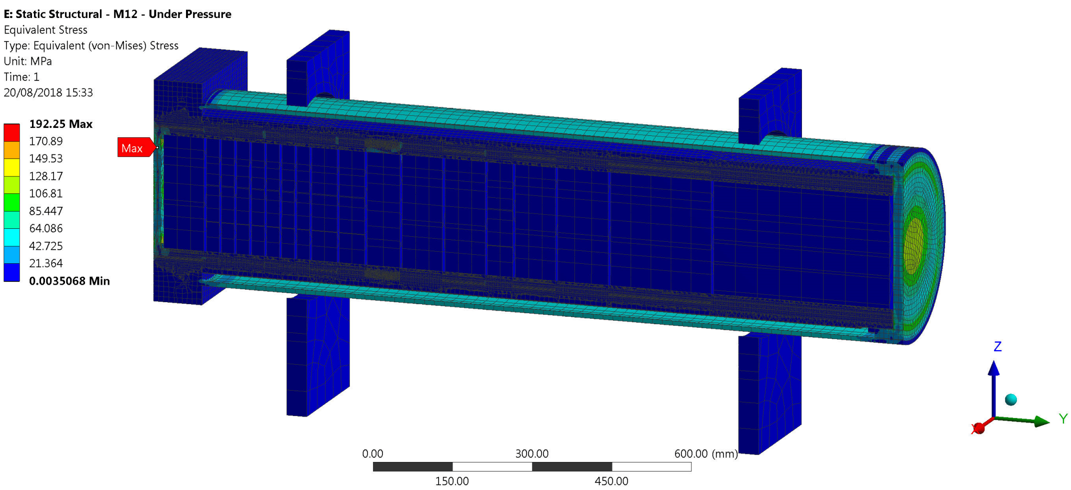

Fig. 5.72: Equivalent (structural (von Mises) stresses in the BDF target assembly

A stress linearization in the through-thickness direction was performed according to EN 13445-3: in particular, given the static nature of the loads acting on the structure, the condition $\sigma^{\text{eq}}_{\text{P+Q}} < 1.5 \times f_{\text{test}}$ was conservatively considered as a design limit. The maximum equivalent principal membrane stress had a value $\sigma^{\text{eq}}_{\text{Pm}} = 68.5$ MPa and was found in the middle of the outer tube, while the maximum equivalent local membrane stress had a value $\sigma^{\text{eq}}_{\text{Pl}} = 45.5$ MPa and was found in the first block support, at an extremity of the window. The equivalent total stress $\sigma^{\text{eq}}_{\text{P+Q}} = 140$ MPa was found in the middle of the first block support, as shown in Fig. 5.73. The target stress distribution appears to be compliant with

EN 13445-3:

$$\sigma_{\mathrm{Pm}}^{\mathrm{eq}} < f_{\mathrm{test}} \,, \tag{5.19}$$

$$\sigma_{\mathrm{Pl}}^{\mathrm{eq}} < f_{\mathrm{test}} \,, \tag{5.20}$$

$$\sigma_{\mathrm{P+Q}}^{\mathrm{eq}} \leqslant 1.5 \times f_{\mathrm{test}} \,. \tag{5.21}$$

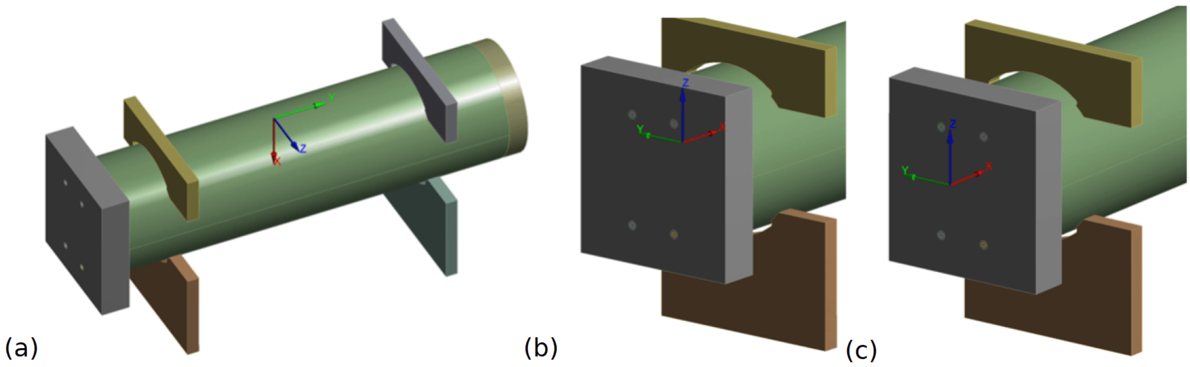

Fig. 5.73: Locations of (a) maximum equivalent principal membrane stress $\sigma_{\mathrm{Pm}}^{\mathrm{eq}}$, (b) maximum equivalent local membrane stress $\sigma_{\mathrm{Pl}}^{\mathrm{eq}}$, and (c) maximum equivalent total stress $\sigma_{\mathrm{P+Q}}^{\mathrm{eq}}$.

5.7.2.5.4 Bolt assessment

For each bolt, the reaction force was calculated numerically and was used to estimate analytically the necessary pre-load. In parallel, the admissible pre-load corresponding to the bolt type was estimated, as well as the tightening torque, according to VDI 2230-1. Table 5.14 summarizes the values for the design and the reference values, calculated according to VDI 2230-1.

Table 5.14: Results for the calculated parameters of the bolts required for the BDF target inner-tank assembly.

Parameter	Value
Maximum necessary pre-load	33.5 kN
Admissible pre-load	42.5 kN
Maximum necessary tightening torque	100 N·m
Admissible tightening torque	107.7 N·m
Actual length of engagement	17.2 mm
Required length of engagement	11.1 mm

The admissible pre-load for an M12 bolt made from A4-100 stainless steel is 42.5 kN, and the necessary pre-loads calculated for the bolts in the design are all below this value (the maximum required pre-load is 33.5 kN). An estimation of the tightening torque shows that 100 N·m is enough to guarantee the necessary pre-load. The length of engagement of the bolts was also calculated according to VDI 2230-1, and it can be seen that the actual length of engagement is larger than the minimum recommended. Therefore, the design parameters for the bolts are compliant with the VDI 2230-1 standard.

5.7.2.6 Conclusion on structural calculations for BDF inner tank

The structural strength of the inner and outer tanks of the BDF target has been reviewed assuming that atmospheric pressure and an internal pressure of 31 bar are applied. The vertical displacement does not exceed the limit of 1 mm. An analysis of the relative displacement between the end of the inner-tank stack and the supporting housing structure revealed that a minimum gap of 0.1 mm between the two parts will ensure that no locking occurs. The simulations showed that the stress levels were below the acceptability limits, in accordance with EN 13445-3. Analytical calculations, based on numerical results and following the VDI 2230-1 standard, demonstrated the compliance of the fixings of the supports in terms of bolt area, length of engagement, and necessary pre-load for each bolt.

5.8 Considerations on material selection for BDF target

5.8.1 Target material selection

Based on simulations involving a spallation target split into a Mo-based and a W-based portion, the suitability of these metals and their alloys has been considered. Starting from the available physical and mechanical properties, it was checked whether these materials can guarantee sufficient strength. The most severe stresses are in the tensile regime, up to $\sim$140 MPa for Mo (see Fig. 5.9) and $\sim$70 MPa for W (see Fig. 5.10), in a temperature range between 100 and 180°C for Mo and between 80 and 150°C for W (see Fig. 5.18 for both materials). The above figures arise from the results of the simulations summarized in Section 5.5.

The spallation materials will experience 10^6 cycles of thermomechanical fatigue under irradiation conditions each year, and hence fatigue strength and irradiation resistance have to be considered.

5.8.1.1 Mo and Mo alloys

The mechanical properties of pure Mo are highly dependent on its state of temper. Stress-relieved Mo shows sufficient yield strength and tensile strength at room temperature. However, data on the tensile properties of recrystallized Mo are quite limited [19]. Independently of the temper state, the values of the yield and tensile strengths are diminished by 10–15% at 200°C with respect to room temperature [2]. In all cases, a stress-relieved temper should be preferred for Mo and its alloys.

Mo features an elevated fatigue strength at room temperature in the high-cycle fatigue regime (up to 10^8 cycles), which is also highly dependent on the state of temper. As an example, fatigue strength values of 500 MPa (68% of the UTS) and 300 MPa (44% of the UTS) have been reported for as-worked and recrystallized 25 mm rods, respectively, as can be observed in Fig. 5.74 [2].

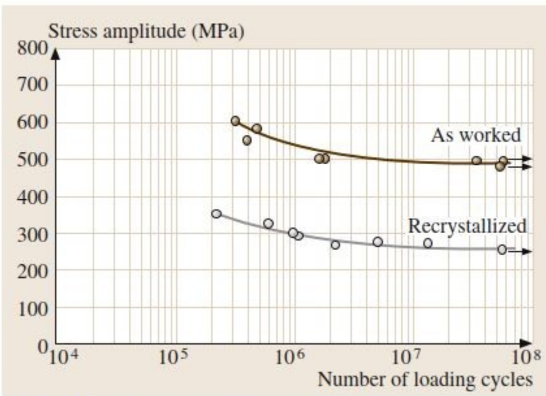

Fig. 5.74: Rotatory-bending fatigue test results for as-received and recrystallized Mo rods 25 mm in diameter, tested at room temperature [2].

Irradiation of Mo leads to a general loss of tensile ductility compared with the unirradiated state in the case of irradiation temperatures below 700°C. These phenomena have been observed uniformly for two types of irradiation at representative fluences, namely protons (2.0×10^{20} p/cm^2) and neutrons (1.5×10^{22} n/cm^2) [44, 45].

Among the Mo alloys, one of the most widely available commercially and most extensively tested is TZM (0.5% titanium–0.08% zirconium–0.03% carbon–molybdenum alloy). In the unirradiated state, TZM features a higher strength and ductility than pure Mo for both stress-relieved and recrystallized tempers over a wide temperature range (up to 1600°C; see Fig. 5.75) [2].

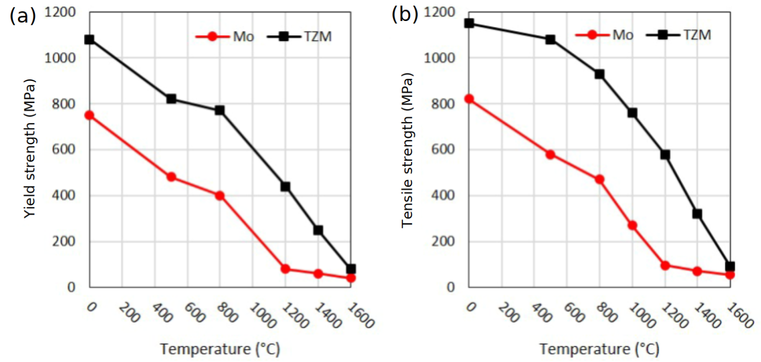

Fig. 5.75: (a) Yield strength and (b) ultimate tensile strength versus temperature for Mo and TZM 1 mm thick stress-relieved sheets [2].

TZM is equally sensitive to the temper state to pure Mo. The tensile strength for stress-relieved 1 mm sheets at room temperature is 820 MPa, while for the recrystallized temper the tensile strength is 550 MPa. For the same material grade, the fatigue strength at representative cycles (10^7) has been measured as 620 and 390 MPa for stress-relieved and recrystallized tempers, respectively, the values representing 70% of the tensile strength [46].

The alloying elements in TZM form carbides that precipitate during the manufacturing process and act as recrystallization inhibitors. In consequence, the recrystallization temperature rises by roughly 400 K with respect to pure Mo. The full recrystallization temperatures for 1 h annealing of 1 mm sheets with a similar deformation degree were found to be 1000°C for Mo and 1450°C for TZM [2]. The recrystallization temperature becomes of importance when one considers the thermal cycling that the target materials will be subjected to during the bonding to the cladding material, as described in Section 5.8.2.2. As stated above, the mechanical properties are significantly enhanced for stress-relieved tempers, and thus recrystallization should ideally be avoided during material processing.

Irradiation data for TZM are currently mainly available for neutron irradiation. With representative neutron fluences (0.9×10^{22} n/cm^2), a significant strength increase was found when the material was irradiated below 650°C at representative strain rates (10^{-3} s^{-1} to 10^{-1} s^{-1}), as can be observed in Fig. 5.76(a). Moreover, the DBTT increased from -85°C to 150°C [3], resulting in a potential loss of ductility under the operational conditions of the target. Figure 5.76(b) shows the fatigue behaviour of TZM for similar neutron fluences, resulting in a fatigue life increased by a factor of two in the irradiated state [47].

5.8.1.2 W and W alloys

Pure W is available in different product forms, including rolled plates (thickness up to 20 mm), billets, rods (diameter up to 80 mm), and forgings, that are relevant to application in the BDF target. Rolled plates can feature a fully dense microstructure, but one which becomes layered and hence strongly anisotropic. Flat grains parallel to the rolled surface affect the mechanical properties and result in a potential risk of delamination. Double-forged (radially and axially) W blanks feature a more isotropic

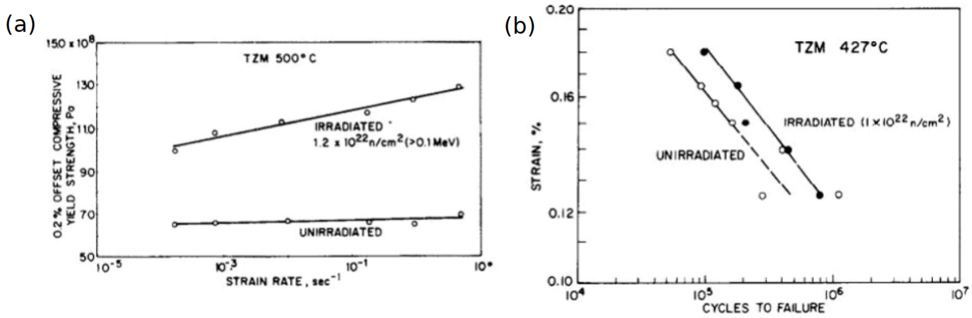

Fig. 5.76: (a) Effect of strain rate on the compressive yield strength of irradiated and unirradiated TZM at 500°C. (b) Effect of total strain per half cycle on the fatigue life of notched specimens of irradiated and unirradiated TZM at 427°C in vacuum [47].

microstructure than unidirectionally forged shapes. It is considered by the fusion community that double-forged (multidirectional) W should act as a reference grade for establishing a reliable materials database for finite element calculations [48].

The DBTT of pure W is highly influenced by the degree of deformation applied below the recrystallization temperature, as shown in Fig. 5.77. With a sufficient degree of deformation, the DBTT can be lowered to 200–400°C. With annealing, the DBTT rises until it reaches that of the recrystallized metal. Thus, multidirectionally forged products in the stress-relieved state are the preferred W products for offering the maximum strength and potential ductility [19].

Sufficient tensile strength is exhibited by the latter W products at the operational temperatures of the target, with values above 1100 MPa at room temperature and 600 MPa at 200°C for rolled sheets. These strength values are halved for the same product in the recrystallized state [19].

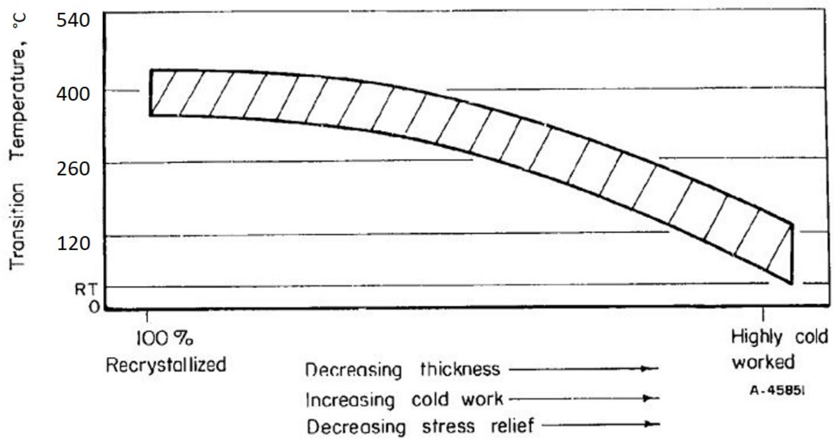

Fig. 5.77: Influence of processing parameters on the DBTT of flat-rolled powder-metallurgy W products [19].

Nevertheless, owing to the brittle nature of W, the use of any grade of W in structural components at low temperatures (<500°C) is subject to a suitable design to limit thermal stresses [49]. Even in the case of a low DBTT achieved with severe deformation, at irradiation fluences of 0.3–0.5 dpa (representative of the target material) any ductility achieved will have already vanished [49]. Therefore, a W grade with the best available mechanical properties should be employed to maintain a high safety factor with respect to the operational stress field.

Relevant data on the mechanical properties of neutron-irradiated W are available in the literature. The effect of irradiation at low temperatures (300°C and below) is considered minor for fluences around 5×10^{19} n/cm^2 (with $E > 0.1$ MeV). Nevertheless, at neutron fluences of 0.9×10^{22} n/cm^2, such irradiation results in a yield strength increase and a diminution of ductility (see Fig. 5.78) [50, 3]. Analogous behaviour is also observed in representative proton irradiations (0.5–1 dpa) at target operational temperatures (50–150°C), with an increase in the compressive yield strength and a decrease in ductility [51].

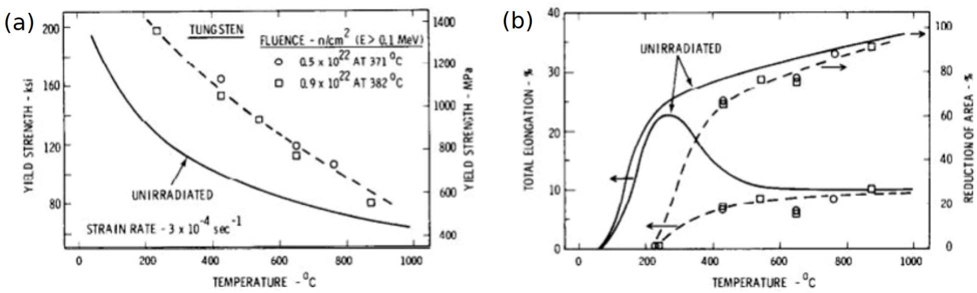

Fig. 5.78: Temperature dependence of the strength (a) and ductility (b) of unirradiated and irradiated W [3].

Fatigue data for unirradiated W have recently been reported for two grades: rolled plates and sintered + hot-isostatic-pressed plates. Data were reported in the tensile regime for high-cycle fatigue (2×10^6 cycles). The material grade was shown to be a key factor in the fatigue performance, with fatigue strengths of 350 and 180 MPa for rolled W and sintered + HIP W, respectively. Both values represent a percentage of 30–35% with respect to the static tensile strength [26].

Concerning W alloys, WRe alloys have the advantage of featuring a higher recrystallization temperature and a lower DBTT compared with pure W, and of preserving ductility after recrystallization [52]. The effect of Re addition is significant above 3%, and towards the lower end of the range (3% to 5%) it has a favourable effect on the ductility in the non-irradiated state. However, under neutron irradiation it results in more rapid and severe embrittlement than is observed for pure W [48]. High activation of Re is also expected under neutron (and proton) irradiation [53], owing to its high thermal-neutron cross-section.

Similarly, less mechanical strength and an increased loss of ductility compared with pure W were found for particle-strengthened W alloys such as W–1% La_2O_3 "when tested up to 700°C" [48].

An exception among all the W alloys explored is mechanically alloyed W-TiC, which offers better machinability and improved ductility compared with pure W (for the latter, both characteristics are a major concern). The addition of TiC allows an isotropic, fine grain structure to be formed that is maintained even in the recrystallized condition. Moreover, the finer dispersoids of TiC particles improve the low-temperature impact toughness [48].

Ultrafine-grained W-TiC (with additions in the range of 0.25–0.8% TiC) has been developed for use in irradiation environments. It has been observed that, in contrast to pure W, this alloy shows no hardening when irradiated with neutrons at a fluence of 2×10^{24} n/cm^2 at 600°C. However, W-TiC is not yet available on an industrial scale [54, 55]. Such materials were tested with a high-intensity proton beam at the HiRadMat facility in the HRMT48-PROTAD experiment during 2018.

Among the different W alloys available, unalloyed W has been the choice of target material in several neutron spallation facilities (ISIS [56], LANSCE [57], KENS [5]) for decades. The operational conditions of those targets are relevant to the BDF target in terms of the target configuration, the magnitude of cyclic thermal loads, and the irradiation conditions. Extensive operational experience of the use of W as a target material has been built up with no major issues reported, and therefore pure W remains the reference grade as a spallation target material for future facilities (such as ESS [58]).

5.8.1.3 Conclusions on target material selection

In conclusion, for the Mo-based components, a Mo alloy should be preferred to pure Mo. TZM, with a stress-relieved temper, is a promising candidate because of better mechanical properties and a lower recrystallization temperature. Preliminary investigations have indicated that this material can fulfil the target material requirements in terms of physical and mechanical properties, considering the irradiation environment. Accordingly, TZM was selected as the baseline material for the first half of the BDF target.

Concerning the W-based components, the available literature on plasma-facing applications recommends avoiding the use of W under heavy cyclic thermal loads at temperatures below 500°C. However, the BDF target conditions are much less critical in terms of temperature gradients, strain rates, heat flux factors, etc. Conditions in neutron spallation targets are more representative of the conditions in the BDF target, and many facilities have successfully operated W-based targets. The literature on material properties combined with operational feedback from facilities indicates that pure W can fulfil the requirements on physical and mechanical properties, considering the irradiation environment. Thus, pure W with forged and stress-relieved tempers was chosen as the baseline material for the second half of the BDF target. Nevertheless, the brittle nature of pure W should be taken into account in the target design, to avoid issues related to machinability and residual stresses, which can be accentuated under irradiation conditions. W alloys such W-TiC could be considered as an alternative, although they are not yet industrially available.

Radiation damage effects on the target material and the corresponding variations of thermophysical and mechanical properties under representative proton irradiation still remain to be addressed by specific tests so that a robust target design can be produced.

5.8.1.4 Target protection: protective cladding

W and TZM have limited corrosion resistance in high-temperature flowing water (up to 320°C), even when stringent control of the oxygen content of the water (<1 ppm) is maintained [59]. Under these conditions, phenomena such as exfoliation have been observed for W. Furthermore, the corrosion rates of these materials are expected to be enhanced in irradiation environments owing to the build-up of radiolysis products, an effect already reported for pure W [60, 61]. As a consequence, high corrosion rates can lead to significant amounts of activated material in the cooling circuit and generate operational issues, as has been reported at facilities such as LANSCE [57].

Alternative materials such as Zircaloy, stainless steels, titanium alloys, and tantalum alloys exhibit excellent corrosion and erosion–corrosion resistance in aqueous environments [62]. The physics performance of the target, however, may be severely impaired because of longer interaction lengths and lower Z, therefore limiting their application as target materials. Covering the target material with a layer of one of these materials, while keeping the maximum amount of the target volume made of W and TZM, has been suggested as an elegant solution to protecting the target materials without limiting the ability to meet the physics requirements [56, 5, 57].

5.8.1.5 Selection of cladding materials

From among several options, tantalum was selected as the protective material because of its good bondability to W and Mo alloys. Ta has complete solubility in W and Mo, avoiding the possibility of development of brittle crystalline phases at interfaces when it is bonded to the target. Tantalum also has a similar thermal expansion to W and Mo, which is required to minimize the stresses at the interface during thermal cycling [63, 64, 65].

The BDF target will face approximately 10^6 beam pulses per year of operation, and therefore the same number of thermal cycles. Mechanical stresses are expected in the interface between the target and the protective layer owing to the unavoidable thermal-expansion mismatch. Hence, strong and reliable bonding between the Ta and the target material is mandatory to avoid detachment during the lifetime of the target. Any loss of contact could cause a loss of heat transfer to the cooling water, blocking of the cooling channels, or accelerated cladding/target failure.

Thanks to extensive R&D studies (see Section 5.8.4), the applicability of a protective Ta layer has been fully validated. The optimal configuration was determined as a Ta layer 1–2 mm thick, diffusion bonded to the target material by means of HIP (see Section 5.8.2.2).

Thermal and structural simulations revealed that, in some of the most loaded blocks, the stress and temperature field can reach up to 100 MPa and 150°C at some points of the cladding (see Section 5.5). Considering that the yield stress of unalloyed Ta is approximately 80 MPa at this temperature, the accumulation of cyclic plastic strain could lead to premature failure of the cladding. Alternative cladding materials which could offer higher strength but also offer good erosion–corrosion resistance and HIP-assisted diffusion-bonding compatibility with the target materials were sought. The material explored was a commercial Ta alloy, solution strengthened with 2.5% of W. This material presented the advantage of a chemistry close to unalloyed Ta but with enhanced mechanical properties. The theoretical yield strength of this material at the operational temperatures of the BDF is over 200 MPa, offering a sufficient operational safety margin. The alloy can withstand the conditions of a HIP cycle, and both Ta and W have complete solubility in the target materials, resulting in interfaces without undesirable formation of brittle intermetallic phases. The alloy shows improved corrosion resistance with respect to Ta, proven under severe conditions such as in hot H_2SO_4 and HCl, both environments where employing Ta is required. Furthermore, the hydrogen embrittlement resistance is enhanced [66].

Unalloyed Ta sheet shows sufficient yield and tensile strengths of 185 and 200 MPa, respectively, at room temperature. However, these strengths are reduced to 70 and 180 MPa, respectively, at 200°C. A recrystallized temper was assumed in the materials selection process, since the HIP thermal cycle will certainly induce full recrystallization of the Ta microstructure. Ta2.5%W sheet shows greater yield and tensile strengths at the operational temperatures of the target, with values of 255 and 345 MPa at room temperature and 190 and 290 MPa at 200°C [20, 17]. Solution strengthening of Ta with W also results in a decrease in the sensitivity of the material to the strain rate, as can be observed from Fig. 5.79, which shows results from several compression tests [67].

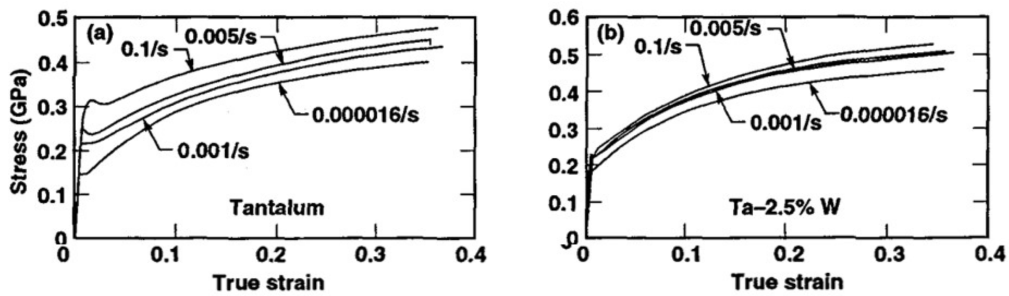

Fig. 5.79: Stress–strain compression curves at different strain rates for (a) unalloyed Ta and (b) Ta2.5W [67].

Fatigue data for both materials are available but limited to certain conditions, i.e. fully reversed loading and at room temperature. Recrystallized Ta and Ta2.5W sheets show fatigue strengths of 200 and 270 MPa, respectively, in high-cycle fatigue regimes ($\sim 10^7$ cycles) [2, 68].

Extensive irradiation data are available for unalloyed Ta under representative conditions. Irradiation with 800 MeV protons at temperatures of 25–250°C resulted in progressive hardening up to 11 dpa. For the same specimens, the strain to necking was rapidly reduced from 30% to 10% at 0.6 dpa but remained constant at 10% up to 11 dpa [69]. The effects of alloying on the evolution of the mechanical properties after irradiation do not show clear trends: in a Ta-10%W alloy, increased irradiation hardening compared with Ta was observed when the material was irradiated with protons; in contrast, hardening similar to that for Ta was observed for the alloy T111 (Ta-8%W-2%Hf) under comparable neutron irradiation conditions [70, 71].

Only a small amount of specific irradiation data exists for the alloy Ta2.5W. Reference [72] reported that alloying Ta with W delayed the radiation-induced lattice damage, as observed by irradiating several Ta alloys (Ta, Ta2.5%W, and Ta-10%W) with a proton beam at 3 MeV. Further studies are re-

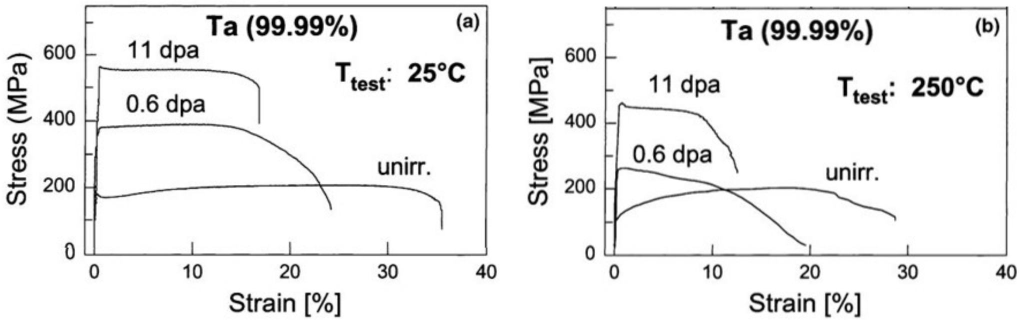

Fig. 5.80: Stress–strain curves of Ta specimens tensile tested at a strain rate of 10^{-3} s^{-1} at (a) RT and (b) 250°C [69].

quired to explore radiation damage under beam conditions representative of the BDF, and activities are ongoing in the framework of the RaDIATE Collaboration [73, 74]. More details of the present activities are given in Section 5.8.6.2.

To our knowledge, there is no reported experience in the literature corresponding to diffusion bonding of Ta2.5W by means of HIP, and thus Ta2.5W was included in the R&D studies as an alternative cladding material to unalloyed Ta. Successful results in the R&D studies led to Ta2.5W being chosen as the baseline cladding material for the BDF target rather than unalloyed Ta (see Section 5.8.4).

5.8.2 Target block manufacture

5.8.2.1 Manufacture of target materials

The baseline material grade for the production of the target materials is multidirectionally forged products. The use of this material grade is basic to ensuring an isotropic microstructure, which is required because the stresses in the target are equally severe along all three axes, as presented in Section 5.5. Forging can also ensure the maximum material density and the best mechanical properties.

Since the W and TZM blocks are conceived as having cylindrical shapes, the most obvious products available commercially from which to build the target blocks are 2D (radially) forged rods, which are then cut to the required lengths. The maximum available rod diameters from known providers are 80 mm for W and 120 mm for TZM, much smaller than the final target block diameter (250 mm). One potential solution proposed by a vendor to obtain the target blocks would be to cut rods of the maximum available diameter to a certain length and then upset forge the rods to increase the diameter to 250 mm. This procedure would additionally improve the mechanical properties in the axial direction, and the target blocks would had been forged in three directions (2D radially + 1D axially from the upset forging). Nevertheless, the upset forging operation is limited by the height/diameter (H/D) ratio, which needs to be smaller than a certain value to avoid buckling and excessive accumulated strain in the material. The maximum aspect ratio for forging is normally considered to be between 2 and 3. This limitation might be an issue for the longest blocks of the BDF target. In the case of TZM, the longest blocks are blocks 1 and 13, with a length of 80 mm. To obtain this geometry from 120 mm diameter rods, upset forging would need to start with a 350 mm long rod. The H/D ratio in this case is 2.9, and therefore upset forging is possible for all the TZM blocks (see Fig. 5.81). For the W blocks, the longest block is block 18, with a length of 350 mm. Starting from an 80 mm diameter rod, the length required for upset forging would be 3500 mm. The H/D ratio in this case is 27.5, much greater than the recommended limit.

As a consequence, the production of the longest W target blocks by the upset forging route was discarded. Several alternative manufacturing routes were explored.

– The use of sintered W pre-shapes with an aspect ratio similar to that of the target blocks, which are then densified by means of hot isostatic pressing (see Fig. 5.82(a)). The main advantage of

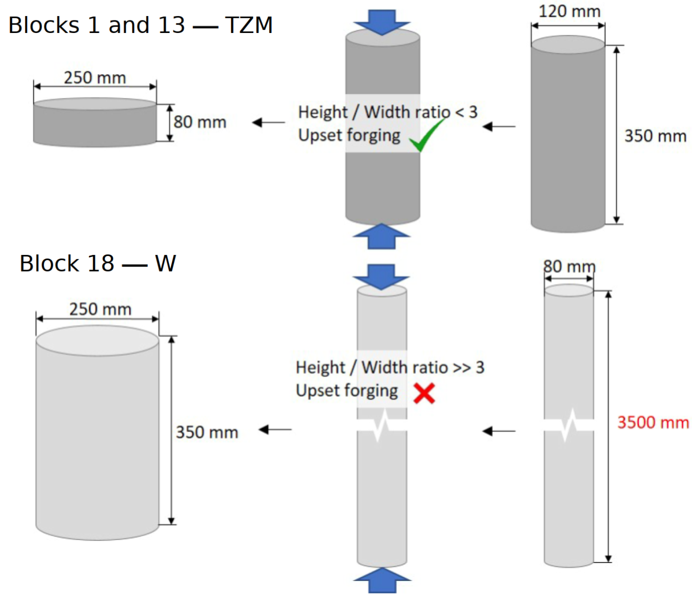

Fig. 5.81: Schematic illustration of the upset forging process for the longest target blocks, applicable to BDF target blocks made of TZM and W.

this production route is the flexibility in terms of shape and dimensions that can be achieved. As discussed before, the mechanical properties of W are highly dependent on the density and deformation grade of the material below the recrystallization temperature [19]. The density and deformation achieved by this production route are significantly lower than for forging, and hence the mechanical properties are inferior to those of forged W grades (see Section 5.8.3.2) [26].

– Employing two different W grades in the same target block. A multidirectionally forged rod with the maximum available diameter would form the central part of the target block. This ‘core’ would then be covered with a ‘shell’ of sintered + HIP W grade to reach the required 250 mm diameter. Intimate union between the two parts would be achieved afterwards by means of HIP-assisted diffusion bonding (see Fig. 5.82(b)).
– Employing target blocks composed of two or several 3D forged W cylinders bonded coaxially. Since the length of the target blocks is the main limitation of upset forging, cylinders of reduced length would be individually upset forged, piled up coaxially to reach the desired target block length, and finally diffusion bonded by means of HIP (see Fig. 5.82(c)).

The FEM simulations (see Section 5.5) predict moderate mechanical requirements on the W target blocks, which will face maximum cyclic stresses below 100 MPa. Commercial forged W shows a tensile strength in the order of 1000 MPa, while sintered + HIP W shows a tensile strength in the order of 500–600 MPa [26]. Despite the significant strength reduction, the strength of sintered + HIP W appears to fulfil the target requirements. The combination of satisfactory mechanical properties and the flexibility of the production method prompted the choice of sintered + HIP W grade as the baseline over other options.

On one hand, the option of using two different W grades in the same target block would allow forged W grade to be employed in the target core, resulting in improved mechanical properties. Additionally, ductility might be enhanced, but it would soon vanish under irradiation as described in Section 5.8.1. On the other hand, ensuring reliable thermal conductivity and therefore mechanically strong bonding between the core and the external part would be a mandatory condition for the applicability of this option. Preliminary studies such those presented later (see Section 5.8.4) revealed difficulties in diffusion bonding W to W even in simplified geometries (bonding flat to flat surfaces). Diffusion bonding

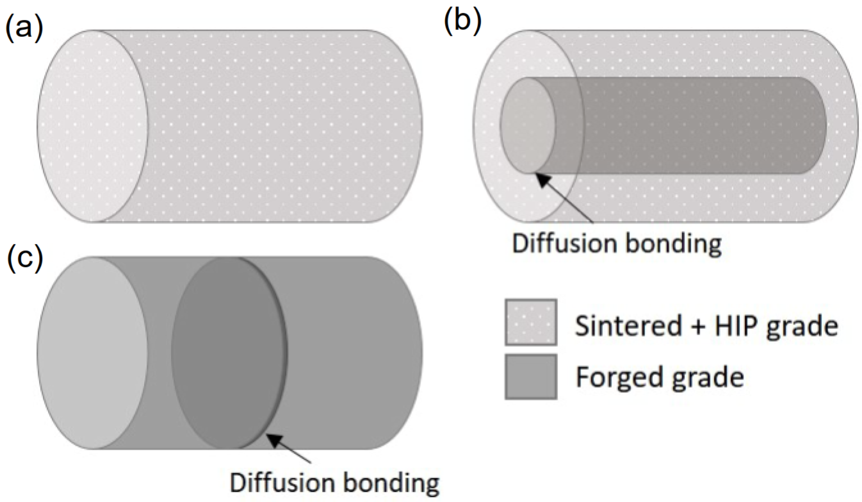

Fig. 5.82: Schematic illustration of different fabrication possibilities for the target W blocks

of two concentric cylindrical surfaces would also represent a challenge in terms of tolerances owing to difficulties in machining the W. This option was abandoned in view of the added complexity and the substantial amount of prototyping and additional development which would be required.

A third option was considered, and results from prototyping are currently being awaited. As already said, diffusion bonding of two flat surfaces was found to present difficulties during preliminary R&D activities (see Section 5.8.4). Nevertheless, promising results were obtained when interfacial aids to diffusion such as interfoils were placed between two target blocks (see Section 5.8.4). The solution appears to be validated by this work, but the reliability of the interface under cyclic thermal fatigue remains unclear.

5.8.2.2 *Process of bonding cladding to target*

As mentioned in Section 5.8.1.5, the target blocks will be protected with an external Ta-based layer 1–2 mm thick. The Ta layer will be diffusion bonded to the target blocks by means of HIP. The principles of the bonding process are highlighted in this part.

5.8.2.2.1 *Principles of diffusion bonding*

In diffusion bonding, the nature of the joining process is essentially the coalescence of two atomically clean solid surfaces. The process can be divided into three stages, listed below and illustrated schematically in Fig. 5.83 [75].

- Firstly, because of inherent surface roughness, the contact between the surfaces is limited to a small fraction of the area. With the application of pressure, time, and temperature, the contact area increases through plastic deformation of asperities and creep.
- Atoms diffuse to the remaining voids to reduce the surface free energy. In parallel, interfacial grain boundaries migrate out of the plane of the joint to achieve a lower-energy equilibrium.
- The remaining intragranular voids are eliminated through diffusion of atoms though the volume of the grains.

5.8.2.2.2 *HIP-assisted diffusion bonding*

When one wishes to diffusion bond complicated geometries, such as a continuous Ta layer over a cylindrical geometry, conventional diffusion-bonding techniques (uniaxial, rolling) are not applicable. This is

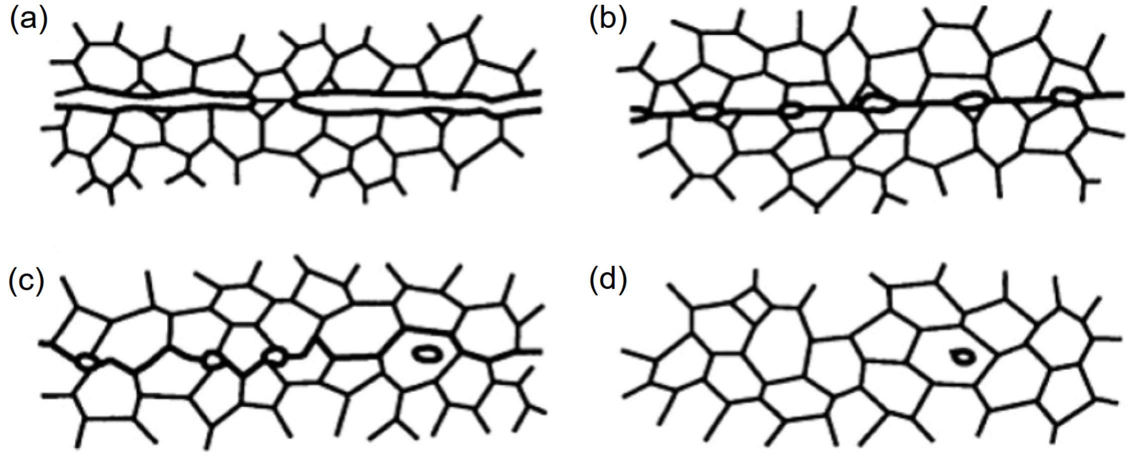

Fig. 5.83: Stages of diffusion bonding. (a) Initial contact, limited to a few asperities. (b) First stage: deformation of surface asperities by plastic flow and creep. (c) Second stage: diffusion of atoms to voids, and grain boundary migration. (d) Third stage: volume diffusion of atoms to voids [75].

due to the difficulty of applying uniform pressures to the base materials. HIP allows applying isostatic pressure even with complicated geometries thanks to a pressurized gas.

To bring the cladding into intimate contact with the target and allow subsequent diffusion bonding, isostatic pressure only on the external side of the cladding material is required. To achieve this, a continuous, hermetic cladding-material capsule is fabricated around the target by welding several parts of cladding together (e.g. two plates and a tube surrounding the target cylinder in our case). Before welding, the air between the cladding capsule and target material must be removed. Any infiltration of gas between the cladding material and the target cylinder would equalize the pressure on both sides of the cladding material and cancel the applied pressure on the target.

HIP is carried out in a chamber which allows continuous, controlled application of high gas pressures (up to 2000 bar) and high temperatures (up to 1500–2000°C). During the HIP cycle, the gas pressure and temperature are simultaneously ramped up and held for a certain time. The internal surface of the cladding and the target are brought into contact and diffusion-bonding phenomena (as described above) take place between them. Further details of the preparation procedure and HIP parameters are given in Section 5.8.4). The different steps of the HIP-assisted diffusion bonding process are illustrated schematically in Fig. 5.84.

5.8.3 Target material properties

After validation of the material selection (see Sections 5.8.1 and 5.8.2), it was necessary to gather together the available material properties from the literature and internal studies. Careful analysis of the available data was performed to determine their applicability to the BDF target. Finally, the necessary materials testing was carried out to complete the available data and provide a reliable input for the FEM simulations and the target design. All of these steps are presented in this section.

5.8.3.1 Relevant material properties

The energy deposition from the pulsed proton beam will be translated into a cyclic temperature increase in the target materials. A knowledge of physical properties of the materials, such as the heat capacity (C_p) and thermal conductivity, is required to determine the evolution of the temperature field in the target. At the same time, the evolution of the temperature in the blocks will induce thermal expansion. Physical properties such as the coefficient of thermal expansion and Young's modulus are required to determine the resulting stress field. The yield strength, tensile strength, elongation at failure, and fatigue

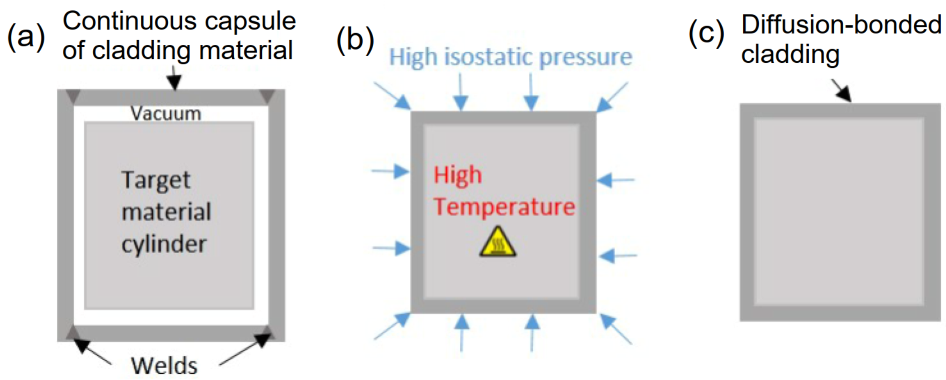

Fig. 5.84: Schematic illustration of the different stages of HIP-assisted diffusion bonding: (a) welding a continuous, hermetic claddding-material capsule over the target material, (b) application of isostatic pressure and temperature to bring the two surfaces together and start diffusion bonding, and (c) resulting geometry after the HIP cycle, with diffusion-bonded cladding.

strength are crucial properties for determining whether the target will retain its integrity when subjected to the cyclic stress field, either in normal operation or in failure scenarios. Many of these properties are dependent on temperature, and thus it is relevant to know how they evolve within the operational temperature range of the target.

In parallel with the ability to withstand the mechanical loads, the resistance of the cladding material to corrosion in demineralized water is of extreme importance to assessing the reliability of the target. Furthermore, all of the target materials will be subject to irradiation conditions, which can affect material properties. These two factors are discussed in separate sections (see Section 5.8.5 for corrosion considerations and Section 5.8.6 for irradiation considerations).

5.8.3.2 Review of literature on BDF target material properties

5.8.3.2.1 Physical properties

Some physical properties of the four target materials and their evolution with temperature are reported in Fig. 5.85. The physical properties of these materials are not sensitive to the type of material product, the microstructure, the purity, or the thermal history. Generic values are available for W, TZM, and Ta for the entire range of operational temperatures, while data for Ta2.5W are mostly limited to room temperature.

5.8.3.2.2 Static mechanical properties

The static mechanical properties are highly dependent on the type of product, the microstructure, the purity, and the thermal history. The literature values are therefore presented together with a discussion of their applicability to material selection for the BDF target. The stress fields in the target materials have similar intensities in both tensile and compressive behaviour. Tensile values are presented (if available) because they offer a more conservative approach.

For the BDF target, two W grades from two production routes were considered, forged material and sintered + HIP material. For the forged W grade, the most representative (and conservative) data are for recrystallized forged rods [19]. The HIP diffusion-bonding cycle will bring the W close to the recrystallization temperature for 3 h and therefore recrystallization can occur. Specimens were tested at a representative strain rate (10^{-3} s^{-1}) but the diameter and grain size of the rods were not reported. The values obtained and their evolution with temperature are plotted in Fig. 5.86. The values of the tensile strength are 600 MPa at 20°C and 350 MPa at 200°C. The brittle nature of the material over the entire temperature operational range can be noticed. Data for sintered + HIP W grade are available only at room temperature [26]. The value of the tensile strength is similar to that of the forged grades, at 560 MPa at

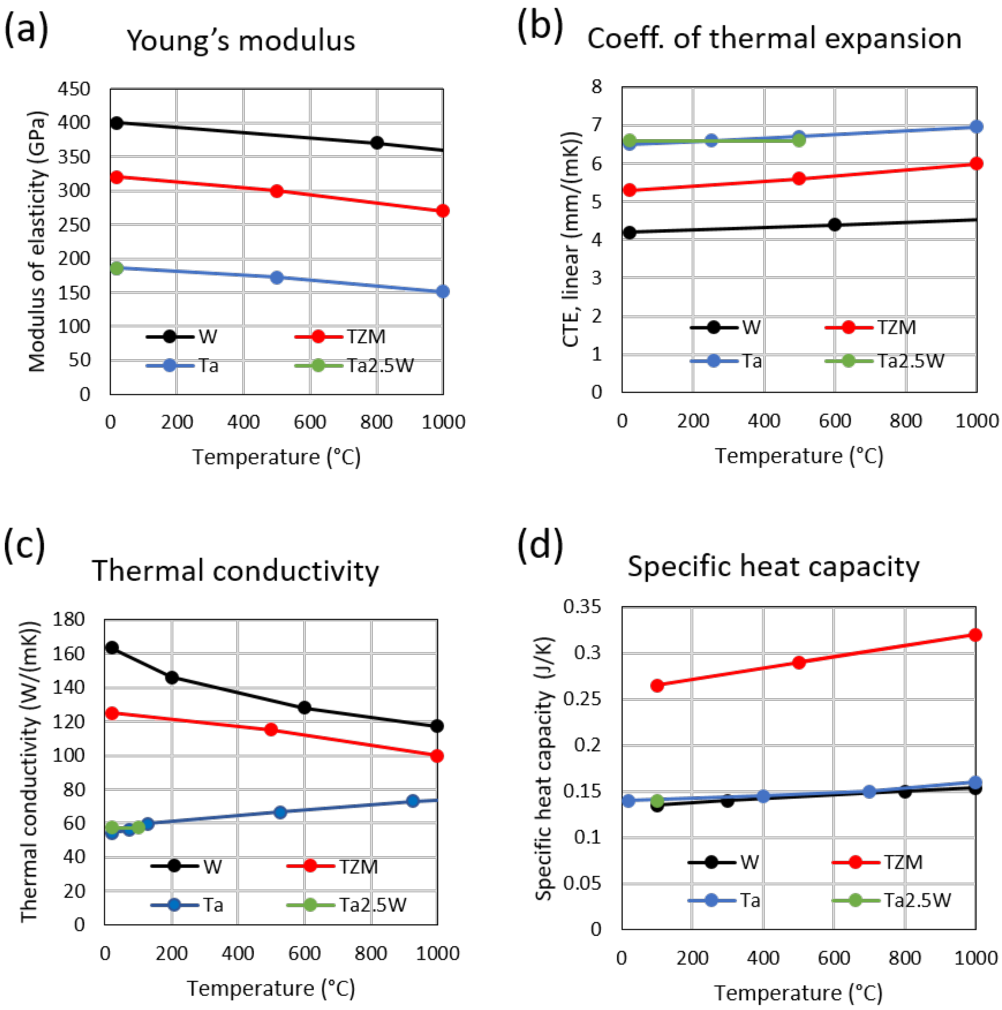

Fig. 5.85: Physical properties of the target materials: (a) Young's modulus, (b) coefficient of thermal expansion, (c) thermal conductivity, and (d) specific heat capacity [2, 20, 76].

RT, and no plastic deformation was observed either. Samples were tested at representative strain rates (10^{-2} s^{-1}), but no references to the material product were given.

Extensive data on static mechanical properties are available for TZM. Most of the data were obtained from rolled sheet products up to 20 mm thick, not representative of the cylindrical TZM forgings to be used in the target. Nevertheless, the data obtained from TZM sheet are useful for understanding the evolution of the properties with temperature. Data for stress-relieved sheet from Plansee, with a grain size of 190 µm (longitudinal) × 35 µm (transverse) tested at a strain rate of 10^{-3} s^{-1}, are given in Fig. 5.87 [18]. This material is characterized by a high tensile strength and elongation at failure, which at room temperature reach values of 830 MPa and 21%, respectively. Representative data are available for cylindrical TZM forgings of diameter 200 mm and length 100 mm, with a production route and dimensions similar to those of the BDF target but tested at only two temperatures (20 and 700°C). In this case the tensile strength (in the axial directions) is much lower, with values of 525 MPa at 20°C and 320 MPa at 700°C. The low ductility offered by this product at room temperature is also noticeable. The significant difference in the mechanical properties between the two material products is due to the degree of deformation applied. The high strength of TZM limits the deformation degree that can be achieved with conventional forging equipment, which becomes relevant for large cross-sections (e.g. forgings). For small sections (e.g. sheets or plates), a lower load is required and a greater deformation degree can

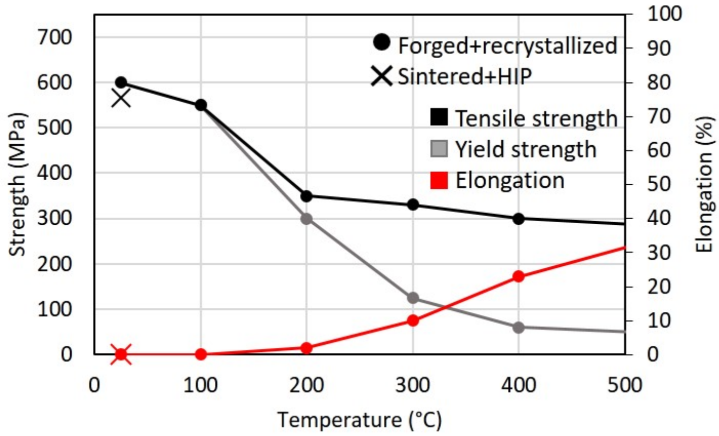

Fig. 5.86: Tensile properties of two W grades, forged + recrystallized [19] and sintered + HIP [26]

be achieved, resulting in superior mechanical properties.

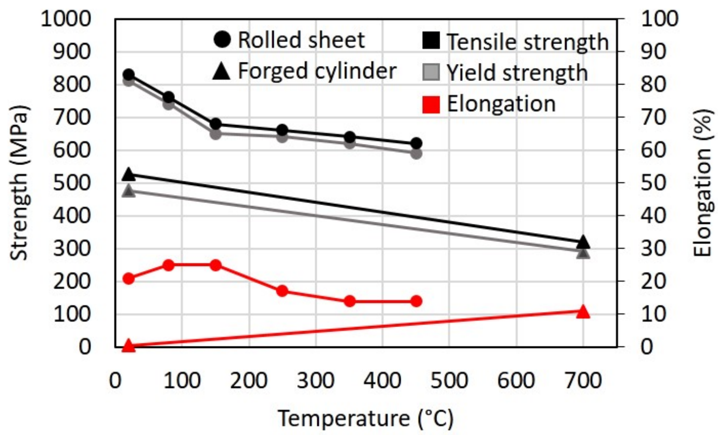

Fig. 5.87: Tensile properties of two TZM grades, stress-relieved rolled sheet [18] and forged cylinders (internal data).

The evolution of the tensile properties with temperature for Ta is available in the literature for a quite representative material: cold-rolled and recrystallized 1 mm thick sheet, tested at a strain rate of 1.5×10^{-3} s^{-1} (Fig. 5.88 [17]). Some measurements on Ta sheet specimens extracted from Ta-clad W/TZM prototypes were carried out internally and resulted in similar values at room temperature, with a yield strength of 170 MPa and a tensile strength of 220 MPa (see Fig. 5.88).

In the case of Ta2.5W, the evolution of the tensile properties with temperature is available only from the minimum guaranteed properties of H.C. Starck's Ta2.5W products [20]. Even though no information about the product tested is given, the values are similar to those of in-house Ta2.5W sheet specimens extracted from Ta2.5W-clad W/TZM prototypes, tested at room temperature (Fig. 5.89). For the latter, values of 270 and 360 MPa were measured.

A summary of the data reviewed is given in Table 5.15, which compiles the data on static mechanical strength relevant to the BDF operational conditions available from the literature and obtained via mechanical testing; these data were used as an input to the FEM simulations.

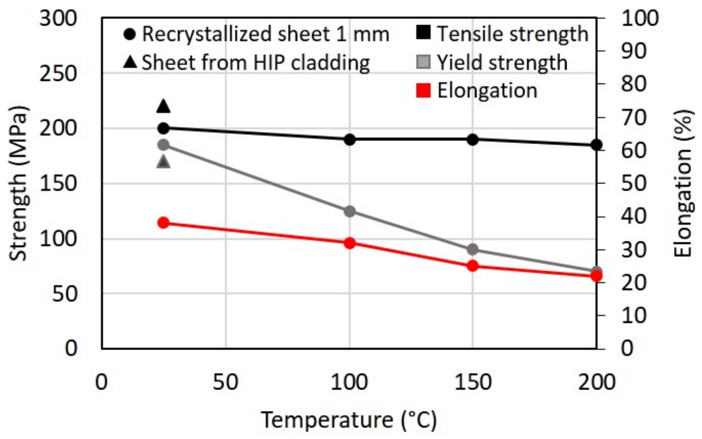

Fig. 5.88: Tensile properties of Ta, recrystallized rolled sheet (1 mm thickness) [17], and sheet from HIP cladding (internal data).

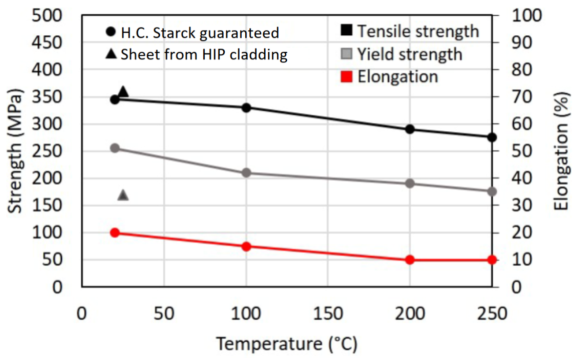

Fig. 5.89: Tensile properties of Ta2.5W: guaranteed values from H.C. Starck [20] and for sheet from HIP cladding (internal data).

Table 5.15: Yield and tensile strength of BDF target materials at room temperature as obtained from available literature and mechanical testing. The material strength at high temperatures was estimated according to the trend shown in Figs. 5.86 and 5.89.

Material	Yield strength (MPa)		Tensile strength (MPa)		Total elongation (%)	
	RT	200°C	RT	200°C	RT	200°C
W	–	300	560	350	0	2
TZM	480	425	525	475	0.5	3
Ta	180	70	200	180	35	22
Ta2.5W	270	190	360	290	20	10

5.8.3.2.3 *Dynamic mechanical properties*

The dynamic mechanical properties are highly dependent on two factors, the material grade (product, microstructure, purity, thermal history, ...) and the testing set-up (specimen dimensions, specimen surface preparation, testing mode, testing frequency, ...). Literature values are presented together with a discussion of their representativeness for the BDF target materials. Representative data are considered to be values obtained for products equivalent to the target (forged rods for TZM and W, recrystallized sheet for Ta and Ta2.5W) and tested under conditions similar to those during operation (push–pull mode, 10^7 cycles, operational temperatures, stress ratio ~ 0, frequency <100 Hz).

Fatigue data for sintered + HIP W are limited to the work presented in Ref. [26], although they are highly representative for the BDF target application. Specimens were tested in a push–pull configuration for 2×10^6 cycles, with a stress ratio $\sim$0, a testing frequency of 25 Hz, and at RT. The fatigue strength under these conditions is 175 MPa, 31% of the UTS. The same authors studied the fatigue behaviour of forged plates 90 mm thick, representative of an alternative W grade. The fatigue strength under the same conditions is similar to that of the sintered + HIP grade, with values of 170–200 MPa (34–38% of the UTS). In that work, high-temperature tests were also carried out, resulting in fatigue strengths of 250 MPa at 280°C and 190 MPa at 480°C, employing the same testing conditions [77].

For TZM, fatigue properties have been extensively reported in the literature, but the data for the most representative conditions for the BDF target are given in Ref. [28]. Samples were extracted from 50 mm bar, as-worked, and were tested in push–pull fatigue for up to 10^8 cycles. The testing conditions were stress ratio -1, testing frequency 25 Hz, and temperatures RT and 850°C. The fatigue strength at 10^7 cycles was measured as 440 and 250 MPa, respectively. The Wöhler curves obtained are shown in Fig. 5.90.

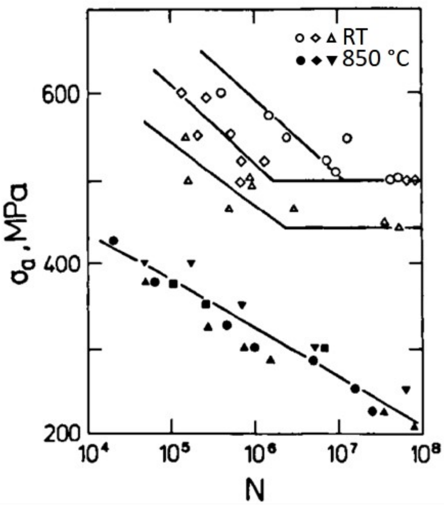

Fig. 5.90: Fatigue strength for different numbers of cycles (N) for TZM at two temperatures, RT and 850°C [28].

For Ta and Ta2.5W, representative fatigue data exist but are limited to room temperature. For Ta, fatigue strengths of 180 and 210 MPa were found for 2 mm thick recrystallized plate at 10^7 cycles, tested in push–pull mode, at a stress ratio of -1 and frequencies of 0.05 and 10 Hz, respectively [68]. The Wöhler curves are shown in Fig. 5.91. For Ta2.5W, fatigue strengths between 270 and 310 MPa were found in the bending fatigue mode, at 10^7 cycles, stress ratio -1, and 25 Hz. These values represent between 60% and 70% of the UTS of the material [2].

Table 5.16 summarizes the available fatigue data that are most relevant to the BDF operational conditions, which were used as an input in the FEM simulations.

5.8.3.3 Materials characterization campaign

A literature review was convenient for validating the material selection for the target and defining a preliminary materials database for the FEM simulations. However, specific materials properties obtained from representative materials are required to validate the target design. Thus, a dedicated campaign of characterization was launched for the target materials within the framework of the BDF project.

The justifications for a specific characterization campaign and the objectives of that campaign were the following.

– The W and TZM material products, which are large forged cylinders, are not conventional prod-

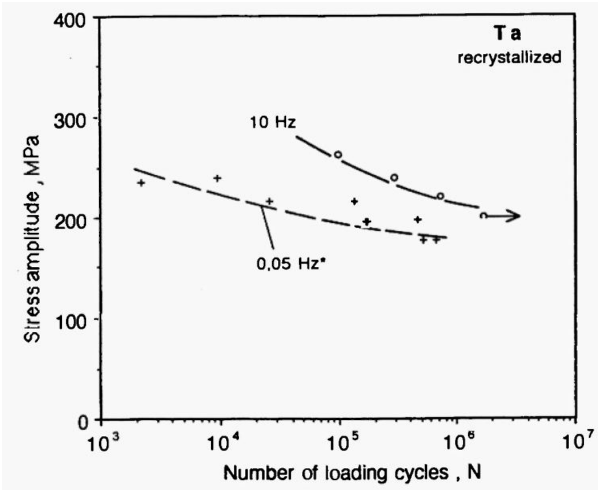

Fig. 5.91: Fatigue strength for different numbers of cycles (N) for Ta at room temperature and two different frequencies, 0.05 Hz and 10 Hz [68]

Table 5.16: Summary of the reviewed high-cycle fatigue data relevant to the operational conditions of the BDF target. Sources: TZM [28], W [26, 77], Ta [68], Ta2.5W [2]. P/M, powder metallurgy; Aw, as worked; Rxx, recrystallized

Material	Production process	Dimensions	Test mode	Number of cycles	Stress ratio, temperature, frequency (Hz)	Fatigue limit (MPa)
TZM	P/M, Aw	50 mm bar	Push–pull	10^7	−1, RT, 25 −1, 850°C, 25	440 250
W	Sintered + HIP	5 mm bar	Push–pull	2×10^6	~0, RT, 25	180
	Forged	90 mm thick plate	Push–pull	2×10^6	~0, RT, 25 ~0, 280°C, 25 ~0, 480°C, 25	170–200 250 190
Ta	Rxx	2 mm thick plate	Push–pull	1×10^7	-1, RT, 0.05 −1, RT, 10	180 210
Ta2.5W	Rxx	1 mm thick plate	Bending fatigue	1×10^7 50% fracture	−1, RT, 25	270–310

ucts. The mechanical properties of refractory metals depend greatly on the deformation applied below the recrystallization temperature. The application of deformation is limited (in quantity and homogeneity) owing to the large dimensions of the forgings. Hence, the microstructure and mechanical properties differ greatly between large forged cylinders and conventional rolled sheet, the latter being the main source of literature data. One clear example of these differences is in the static mechanical properties of TZM presented in Section 5.8.3.2.

- The target materials will be subjected to the HIP cycle necessary to bond the cladding material to the target material. This represents a thermal treatment for roughly 3 h at temperatures which might exceed the recrystallization temperature of the target material (most certainly for Ta and Ta2.5W). The material properties might be affected by several factors, such as grain growth, recrystallization, segregation, and gas absorption. The literature on material properties after these thermal treatments is scarce and not representative.
- There are material properties, sampling procedures, or testing parameters that are not reported in

the literature or that differ from the target application conditions. The effect of these differences on the properties is unknown, but it could eventually become significant. One example occurs in dynamic mechanical testing, which is extremely sensitive to specimen geometry, surface preparation, and testing parameters. Reference [77] reported an endurance limit of 150 MPa for sintered + HIP W, which increased to 240 MPa with only specimen polishing (electropolishing) before testing. Another example is the sensitivity of body-centred cubic metals to strain rate; in Ref. [78], several refractory materials were tested in fatigue at a high number of cycles, and endurance values of 250 and 350 MPa were reported for Ta at low (100 Hz) and high (20 kHz) frequencies, respectively. The frequency change on its own affected the endurance value significantly, and it even changed the fracture mode of the samples from ductile to brittle when the testing frequency was increased.

5.8.3.3.1 Testing matrix

The material characterization was carried out on the same materials as those used for the BDF target prototype (see Section 5.9), with the same characteristics and production route; these materials are expected to be highly representative of the final target. The characteristics of each material are given in Table 5.17.

Table 5.17: List of materials employed for characterization, with production route, product form, densification method, and product dimensions. These correspond to the blocks acquired for the execution of the tests on the BDF target prototype reported in Section 5.9. P/M, powder metallurgy; EB, electron beam melting.

Material	Production route	Product	Dimensions	Densification route
TZM	P/M	Rod	80 mm diameter	Radial forging (2D)
W	P/M	Rod	80 mm diameter	HIP
Ta	EB	Sheet	1.5 mm thickness	Rolling
Ta2.5W	EB	Sheet	1.5 mm thickness	Rolling

All of the materials afterwards followed a HIP cycle analogous to that followed by the target blocks to bond the target and cladding materials, to obtain fully representative microstructures. The pressure and temperature were ramped up to 1500 bar and 1200°C, respectively, and held for 3 h. The evolution of the pressure and temperature during the HIP cycle is shown in Fig. 5.92. Images of the materials, wrapped in getter foils, before and after the HIP cycle are shown in Fig. 5.93.

The characterization was focused on measuring the relevant properties of the four target materials over the entire operational temperature range. Three groups of properties were measured, the thermophysical (specific heat capacity, linear thermal expansion, and thermal diffusivity or thermal conductivity), static mechanical (tensile testing), and dynamic mechanical properties (high-cycle fatigue testing). The testing conditions for the characterization are given in Tables 5.18, 5.19, and 5.16, respectively. The characterization results were not yet available at the time of writing this document, but will be part of a dedicated publication.

Table 5.18: Characterized thermophysical properties of the BDF target materials, with corresponding testing conditions.

Properties	Test conditions
Specific heat capacity (C_p)	
Thermal diffusivity or thermal conductivity	RT–500°C
Linear thermal expansion (CTE)	

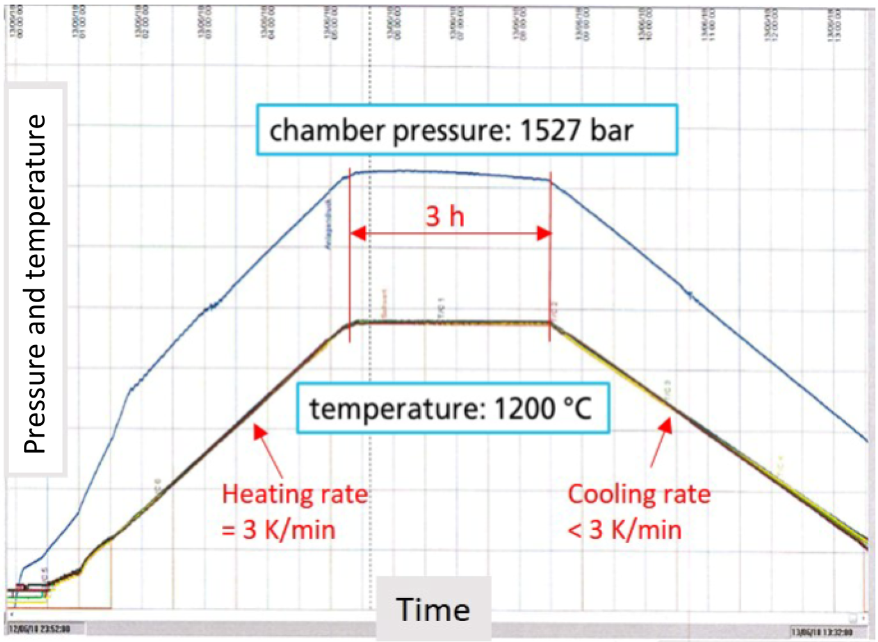

Fig. 5.92: Evolution of pressure and temperature during the HIP cycle

5.8.4 Studies and development of target cladding via HIPing process

5.8.4.1 Selection of cladding technique

During the preceding years (2015–2018), strong efforts had already been made to obtain reliable bonding between W and Mo in cylindrical geometries and external protective Ta layers surrounding them.

The first investigations explored the application of a Ta layer via coating. A chemical vapour deposition technique was employed to grow Ta layers with thicknesses ranging from 0.25 to 0.5 mm directly on W rods of diameter 20 mm. Several sample rods were coated, as shown in Fig. 5.94(a). Metallographic inspections at the interface level revealed point detachments and cracks, which eventually propagated into the bulk W (Fig. 5.94(b)–(d)) [79].

The second attempt was undertaken using an opposite approach. W rods of diameter 20 mm were fitted inside 1 mm thick Ta tubes and contact between the two materials was maintained by the elasticity of Ta. Various samples were produced, as shown in Fig. 5.95(a). Metallographic inspections at the interface level showed recurrent detachments up to a few micrometres wide (Fig. 5.95(b)–(d)) [80].

Following these trials, solid-state diffusion bonding was considered as a potential route, since it had already been applied to refractory metals in the 1960s, as explained in Refs. [81] and [63]. Simultaneous application of elevated pressure and temperature maintained over a certain time would eventually lead to surface diffusion processes between the Ta and the W or TZM.

The candidate technique was hot isostatic pressing. The utilization of this technique to clad Ta to W was first reported in Ref. [56], where it was used to protect a water-cooled W target at ISIS (Didcot, United Kingdom). The construction of successive spallation neutron targets at KENS (KEK, Japan) in 2000 and at LANSCE (LANL, United States) in 2010 based on this concept significantly increased knowledge about this application. In contrast, no publications have reported HIP diffusion bonding of Ta and Ta alloys to Mo alloys.

Several actors in the refractory metals industry were asked to provide W, Mo, and TZM cylinders of different diameters clad with a Ta layer 2 mm thick, diffusion bonded by means of HIP. ATM (Beijing, China) provided two Ta-clad W prototypes (Fig. 5.96(a)) in which the diffusion bonding was successful, with homogeneous and defect-free interfaces. The cladding thickness was found to be variable among

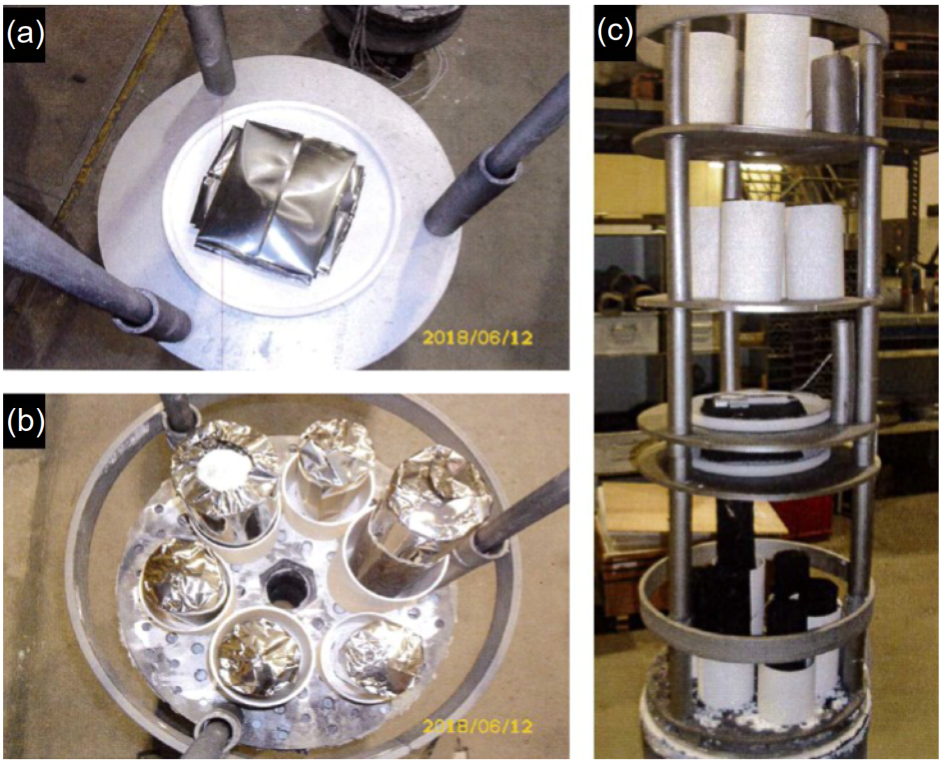

Fig. 5.93: Images of the set-up for HIP. (a) Ta and Ta2.5W sheet wrapped with getter foils before HIP, (b) W and TZM cylinders wrapped with getter foils before HIP, (c) full set of samples after HIP.

the prototypes, however, and the W material showed heterogeneous grain growth and some cracking (Fig. 5.96(b) and (c)) [82].

Plansee (Reutte, Austria) supplied eight prototypes made of W, Mo, and TZM [83], some of them visible in Fig. 5.97(a) after cutting. The diffusion bonding with Ta was successful and, additionally, all of the prototypes showed homogeneous interfaces and homogeneous cladding thicknesses. The Ta layer was first applied by using a welded Ta tube covering the cylindrical surface and two Ta plates covering the flat ends of the cylinder. The two plates were welded to the tube by Tungsten–Inert Gas (TIG) welding before HIP to obtain a hermetic seal. Interfacial defects were observed in the vicinity of the welds (Fig. 5.97(b) and (c)). Furthermore, since the Ta tube was welded, significant Ta grain growth was observed in the surroundings of the welds (Fig. 5.97(d)) [84].

Moreover, some actions were taken to resolve the issues observed in the prototypes: subsequent prototypes employed seamless Ta cladding tubes, the welds before the HIP operation were carried out at the cylinder edges and with an external lip so as not to interfere with the diffusion-bonded interface, and the welds were carried out employing electron beam welding to minimize the energy deposition and consequent Ta grain growth.

In view of the promising results, HIP was chosen as the baseline technique for bonding a 1–2 mm Ta layer to the target materials. Numerous reduced-scale target prototypes have been produced and characterized since then, with continuous improvement, in the framework of a collaboration with Fraunhofer IFAM (Dresden, Germany) (see Fig. 5.98). Successful diffusion bonding with homogeneous interfaces free of defects was achieved.

In parallel, owing to the potential fabrication issues with the largest W blocks required for the BDF target (see Section 5.8.2), development of the diffusion bonding of two forged blocks coaxially was explored with Fraunhofer IFAM. Preliminary exploration of this option was carried out employing

Table 5.19: Characterized static mechanical properties of the BDF target materials, with corresponding testing conditions.

Properties	Test conditions				
	Standard	Temperature (°C)	Strain rate (s^{-1})	Sampling direction	Atmosphere
Young's modulus Yield strength Tensile strength Elongation at failure	ASTM E8 (RT) ASTM E21 (HT)	TZM: RT–125–200–450–800 W: RT–125–200–350–450–800 Ta and Ta2.5W: RT–125–200–300–450	1×10^{-3}	TZM: Axial W: Axial Ta: Long. Ta2.5W: Long.	Inert gas for Ta and Ta2.5W at T >250°C Inert gas for TZM and W at T >400 °C
		TZM: 200 W: 200 Ta: 200 Ta2.5W: 200	1×10^{-1}	TZM: Axial W: Axial Ta: Long. Ta2.5W: Long.	
		TZM: 200 W: 200 Ta: 200 Ta2.5W: 200	1×10^{-3}	TZM: Radial W: Radial Ta: Trans. Ta2.5W: Trans.	

Table 5.20: Characterized dynamic mechanical properties of the BDF target materials, with corresponding testing conditions.

Properties	Test conditions						
	Temperature (°C)	Stress ratio	Frequency (Hz)	Number of cycles	Sampling direction	Atmosphere	Test method
Fatigue strength	TZM: RT–200 W: RT–200 Ta: RT–200 Ta2.5W: RT–200	0	<100	10^7	TZM: Axial W: Axial Ta: Long. Ta2.5W: Long.	Inert gas for $T = 200$°C	Staircase method

spark plasma sintering to diffusion bond small cylinders coaxially (Fig. 5.99(a)). The bonding operation between W–W and TZM–TZM pairs of cylinders was carried out at 1200°C with an axial pressure of 45 MPa for 1 h. Diffusion phenomena were limited to a few regions, and it was concluded that the pressure applied was too low (Fig. 5.99(b)). Hence, it was decided to explore HIP-assisted diffusion bonding because of the higher pressure that could be applied (up to 200 MPa).

Successful bonding of TZM to TZM and Mo to Mo was reported in Refs. [63] and [85], but always employing interfacial aids such as metal and refractory metal foils (Ta, Re, V, Ni, Ti, . . .) a few tens of micrometres thick. The effectiveness of and need for interfacial aids in the diffusion bonding of W to W and TZM to TZM required specific development.

5.8.4.2 Studies on development of HIP-assisted diffusion bonding

Several points related to the bonding of the materials still remained open. Therefore an ambitious specific R&D study was launched in collaboration with Fraunhofer IFAM. The results presented below have been

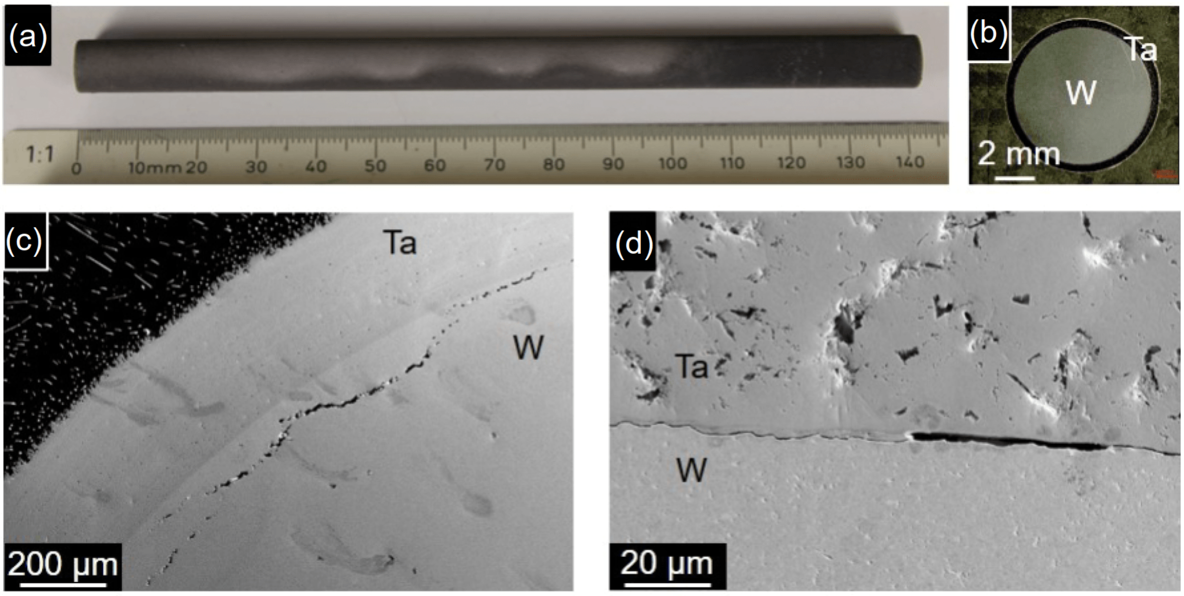

Fig. 5.94: (a) Image of a Ta-coated W rod sample; (b) optical microscope image of a cross-section of a rod; (c), (d) Scanning Electron Microscope (SEM) images of a cross-section of a rod at the Ta–W interface.

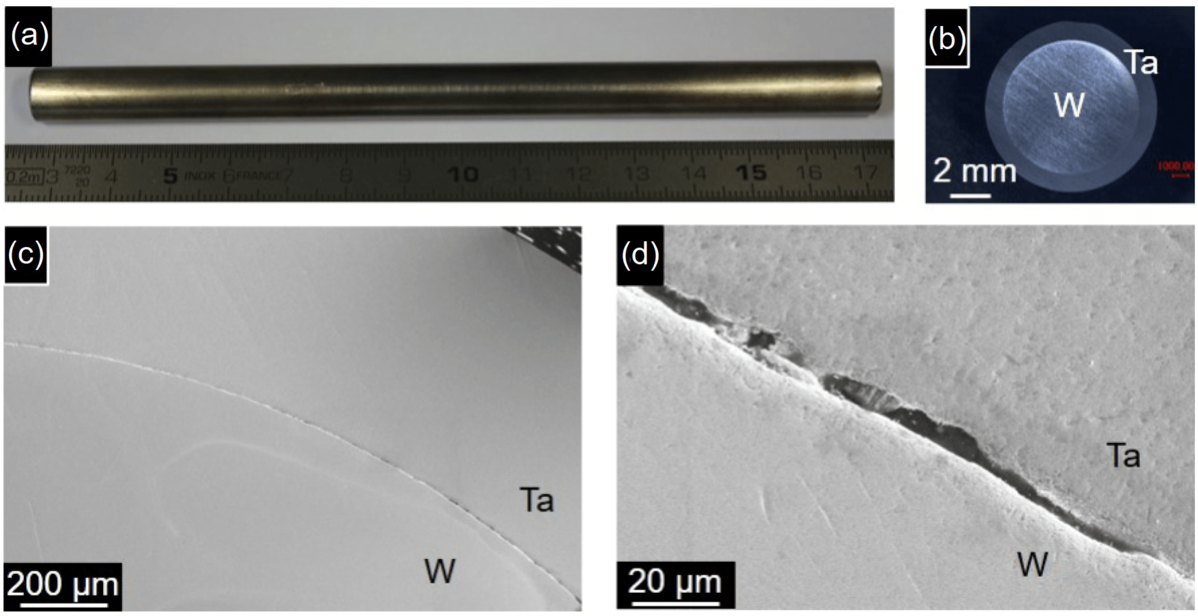

Fig. 5.95: (a) Image of a W rod sample fitted inside a Ta tube; (b) optical microscope image of a cross-section of a rod; (c), (d) SEM images of a cross-section of a rod at the Ta–W interface.

published in Ref. [8].

The objectives of the study were multiple. First, to validate the use of diffusion bonding by HIP for all of the cladding and target candidate materials for the BDF, especially for the alternative cladding material Ta2.5W. Second, to study the potential for bonding between several target cylinders by HIP-assisted diffusion bonding. Third, to study the potential use of interfacial aids (such as Ta foil) in the two previous cases. In parallel, there was also interest in exploring different HIP parameters to optimize the bonding properties and to study how the HIP cycle affects the bulk materials. To this end, several downscaled target block prototypes were built to extract bonding specimens for subsequent

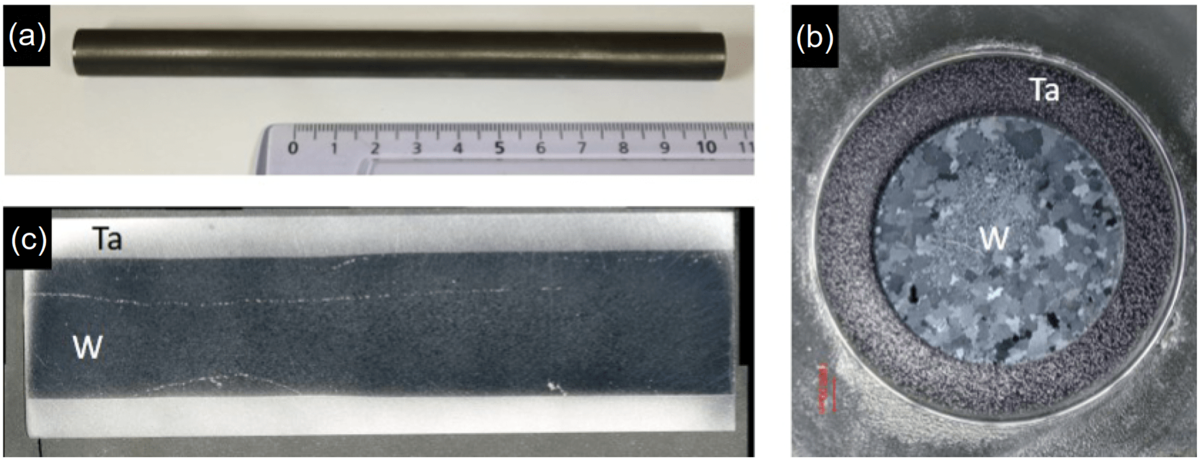

Fig. 5.96: (a) Image of an HIP-assisted diffusion-bonded Ta-on-W rod; (b) optical microscope image of a cross-section of a rod, showing the significant W grain growth observed after the HIP cycle; (c) optical microscope image of a longitudinal cross-section of a rod.

characterization at three levels: microstructural, mechanical, and thermal.

Several similar studies, especially those in Refs. [5] and [57], have included efforts to improve prototype preparation routines, improve the cladding–target interface, and solve surface-state-related problems. The prototype preparation routine was optimized in previous internal studies (as described above), and no surface-related problems were observed in that work, thanks to the application of vast prior experience from Refs. [5, 57] as well as private communications with RAL/ISIS. Hence, the study was specifically addressed to the cladding–target interface.

5.8.4.2.1 Materials for prototyping

Four materials were employed in the fabrication of the prototypes, unalloyed W and a molybdenum alloy (TZM) as target materials and unalloyed tantalum and a tantalum alloy (Ta2.5W) as cladding materials. W was supplied by Plansee in the form of forged and annealed 25–50 mm-diameter rods, with a minimum density of 99.97% and a hardness of HV 420–480. TZM was also supplied by Plansee in the form of forged and annealed 25–50 mm-diameter rods, with a hardness of HV 250–310. Ta and a Ta alloy with 2.5% W (Ta2.5W) were supplied by Plansee and WHS Sondermetalle, respectively, both in the form of plates, seamless tubes, and foils and all in the annealed state. The surfaces of all the materials employed in the study did not show any specific surface preparation other than conventional machining. Henceforth, these materials will be referred to simply as W, TZM, Ta, and Ta2.5W, respectively.

5.8.4.2.2 Prototype configuration

For this study, prototypes with geometries equivalent to the final target configuration were considered to have already anticipated any geometrical issues in the conception of the target.

The prototypes were built using one or two cylinders of the target material (W or TZM) with diameters between 25 mm and 50 mm and total lengths between 50 mm and 100 mm. The cylinders were fitted inside a tube made of the cladding material (Ta or Ta2.5W) and closed at the two ends by two covers, also made from the cladding material. The thickness of the cladding material was 1.5 mm in the cylindrical part but was increased to 10 mm in the two covers to allow the extraction of larger bonding specimens, required for mechanical testing. The bonding of the cladding material to the target material was created by HIP, a technique already introduced in Section 5.8.2.2.

Two types of prototype were built, with either one or two target cylinders. The single-cylinder prototypes were used to study the target-to-cladding-material bonding, while the double-cylinder prototypes

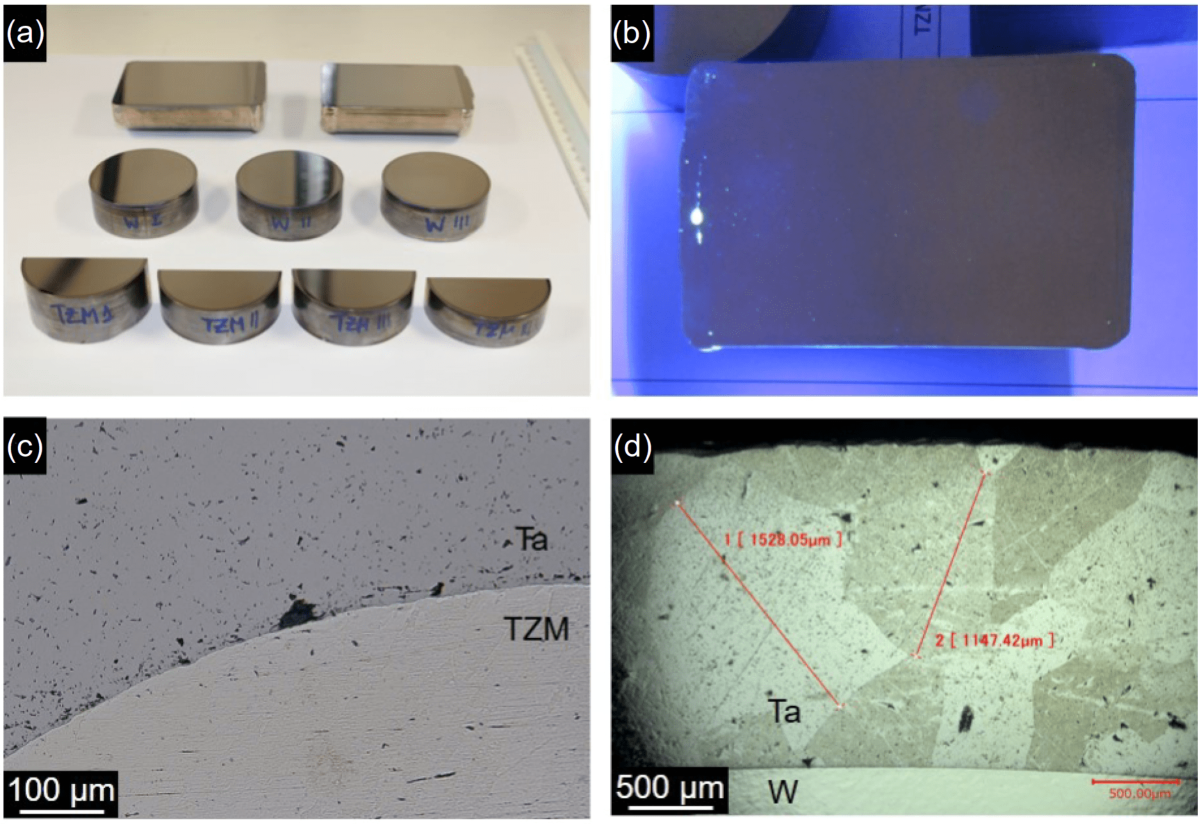

Fig. 5.97: (a) Image of HIP-assisted diffusion-bonded Ta-on-W cylinders after cutting; (b) image of a longitudinal cross-section of a prototype after fluorescent dye penetrant testing, which revealed indications of defects at the interface level; (c) SEM image at the Ta–TZM interface level; (d) optical microscope image of the Ta layer microstructure.

were intended to study the target-to-target-material bonding. The two types of prototype are illustrated schematically in Fig. 5.100 together with their components. Ta interfoils 50 µm thick were introduced between the two materials (cladding and target or target and target) as interfacial bonding aids in some cases.

5.8.4.2.3 Prototype fabrication

Before assembly of each prototype, the target material cylinder and the two cladding-material covers were machined to a diameter 100 µm smaller than the tube. This tolerance requirement was aimed at ensuring sufficient spacing for the introduction of the target material cylinder inside the cladding-material tube but was narrow enough to avoid corrugation of the cladding during the HIP cycle.

A continuous, hermetic (gas-tight) cladding-material capsule covering the target material cylinder was required to ensure application of isostatic pressure between the cladding and target materials during the HIP cycle. To this end, electron beam welding was employed to weld together the tube and covers of each prototype. The covers had a machined lip to facilitate the welding operation and to keep the heat-affected zone far from the cladding–target-material interface. Electron beam welding was performed at STD Strahltechnologie (Dresden, Germany). The prototypes were evacuated overnight before welding at 10^{-2} mbar to remove the entrapped air between the cladding and target materials. After the welding, each prototype was leak-tested with helium to ensure the leak-tightness of the cladding-material capsules around the target material cylinders. Images of the production of the capsules are presented in Fig. 5.101.

A HIP cycle was carried out on the prototypes to diffusion bond the cladding material to the target

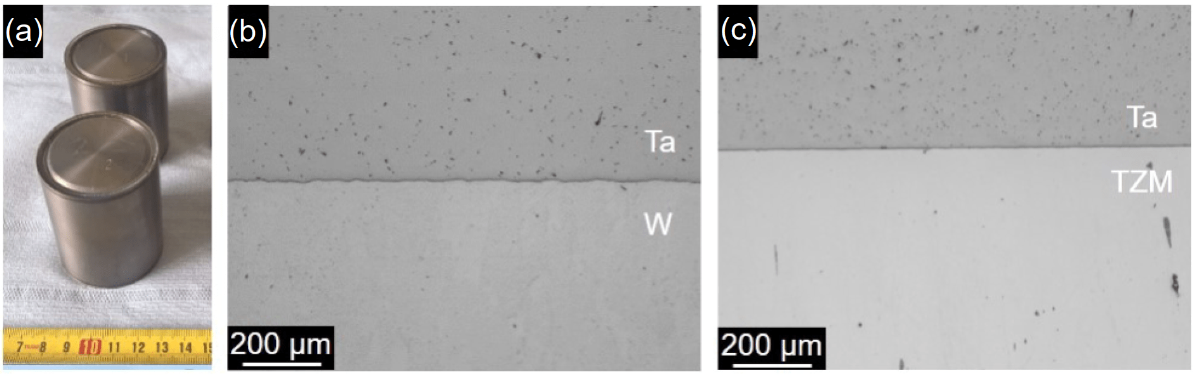

Fig. 5.98: (a) Image of HIP-assisted diffusion-bonded Ta-on-W and Ta-on-TZM cylinders, (b) SEM image at the Ta–W interface level, (c) SEM image at the Ta–TZM interface level.

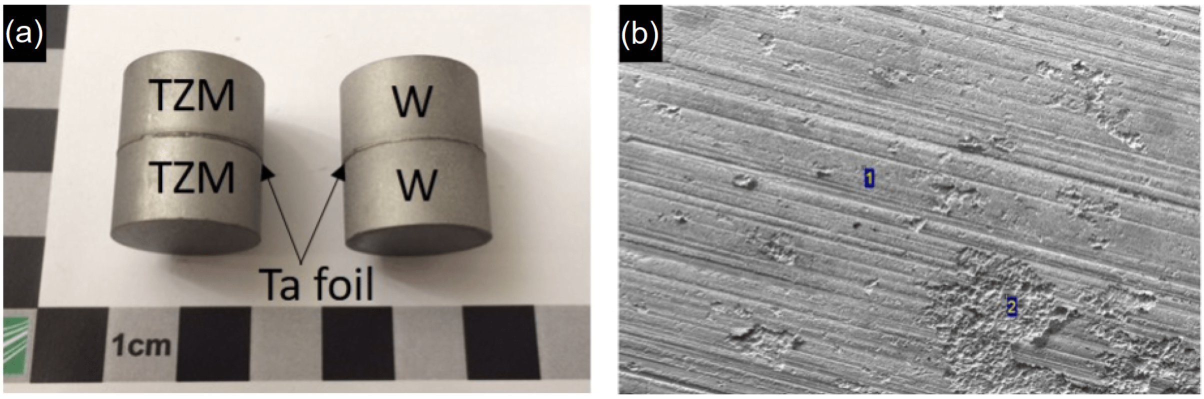

Fig. 5.99: (a) Image of two samples where the bonding between target materials TZM and TZM and between W and W was explored. (b) SEM image of a W cylinder surface after bonding operation. Bonding was limited to the areas with 'machining-like' lines.

material and, if possible, also to bond the target materials together. The HIP cycle was carried out by HIP PM Volker (Dorfen, Germany). Special attention was paid to the HIP furnace atmosphere to minimize the amount of impurities in the Ar atmosphere, which could potentially be absorbed by the cladding surface. Reference [5] reported a study of the effect of different purities of the atmosphere in the HIP furnace during the application of a HIP cycle to bond Ta cladding to W. The growth of fragile TaC and Ta_2O_5 layers was observed on the Ta surface, which was attributed to impurities from the atmosphere and from the furnace. From this valuable experience, the HIP atmosphere for the study was chosen as 5.0 purity grade argon, in a furnace with a Mo heater. Additionally, all the prototypes were wrapped with one Ta and one Zr foil to getter the remaining impurities in the furnace atmosphere.

The heating rate during the HIP cycle was fixed at 10 K/min, and the dwell time at the nominal temperature and pressure was 3 h. The temperature and time of the HIP cycle are determining parameters for the plastic deformation, interdiffusion kinetics, and microstructure of the materials. In this work, two sets of HIP cycle parameters were employed: 1200°C and 150 MPa, from now on referred to as 'L', where the temperature remained below the recrystallization temperatures of W and TZM [2], with the objective of achieving diffusion bonding and at the same time preserving the refined microstructure in the target materials; and 1400°C and 200 MPa, from now on referred to as 'H', where the temperature was raised above the recrystallization temperatures of the W and TZM target materials, with the objective of obtaining the best diffusion bonding even though the properties of the materials would be partially sacrificed owing to recrystallization or grain growth.

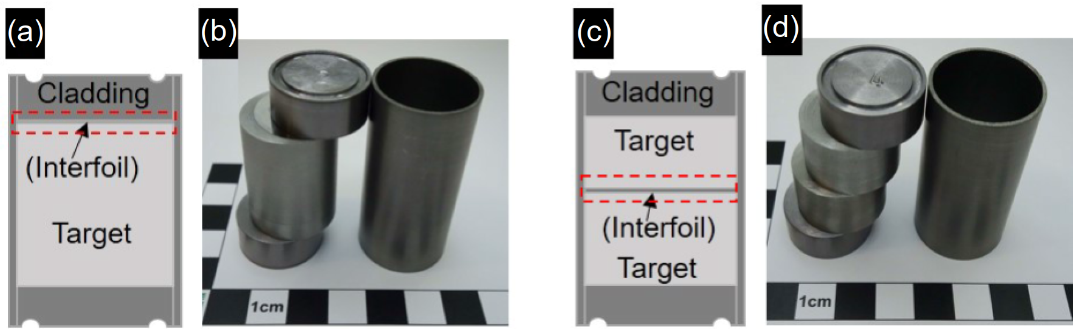

Fig. 5.100: (a) Schematic cross-section of the prototypes used to study the target-to-cladding-material bonding; (b) image of the target-to-cladding-material prototype components before assembly; (c) schematic cross-section of the prototypes used to study the target-to-target-material bonding; (d) image of the target-to-target-material prototype components before assembly [8].

After the HIP cycle, EDM was employed to extract specimens from the prototypes. The specimens were extracted from the areas marked in red in Fig. 5.100. The target-to-cladding-material interface specimens were extracted from the prototypes shown in Fig. 5.100(a), and the target-to-target-material interface specimens from the prototypes shown in Fig. 5.100(c).

Inspections of the interface microstructure were carried out with an SEM. Samples were prepared by conventional mechanical grinding and polishing. The interface strength was measured by tensile testing, carried out on miniaturized tensile specimens with a 5 mm gauge length and a square section of 4 mm^2. When the strength of the bonded interfaces was measured, the interface was coincident with the minimum specimen section. Because of the small gauge length, the elongation could not be precisely measured, and therefore only values of the tensile strength are reported here. Testing was carried out at a strain rate of 2×10^{-4} s^{-1}. Hardness measurements were carried out on bulk materials employing a Falcon 500 system from INNOVATEST with a Vickers indenter and a load of 5 N (HV5). The thermal conductivity was measured indirectly by employing the following relation:

$$\lambda = \alpha * C_p * \rho \, , \tag{5.22}$$

where α is the measured thermal diffusivity, C_p is the heat capacity, and ρ is the density.

5.8.4.2.4 Testing matrix

The number of prototypes made for the study was determined by the requirement to obtain all combinations of target material and cladding material, all target materials bonded to the same target material, the use or non-use of a Ta interfoil, and the two possible HIP cycles. A list of the specimens studied resulting from all of these combinations is given in Table 5.21.

5.8.4.3 Results of interface study

5.8.4.3.1 Bonding between target and cladding materials

The bonding interfaces between the target and cladding materials are observable in the SEM images shown in Fig. 5.102. Apart from the specimens for bonding between W and Ta2.5W, which did not show any apparent bonding after HIP cycle L (Fig. 5.102(d)), all of the specimens showed interfaces in which the two materials were in perfect contact, indicating potential diffusion bonding. Difficulties were encountered in imaging the diffusion layer owing to specimen preparation artefacts and the small layer thickness, which was measured to be approximately 1 µm when measurement was achievable. This value is in concordance with Ref. [5], in which a diffusion layer thickness between 0.5 and 2 µm was estimated for the HIP parameters employed in the study. In the interfaces between the target and

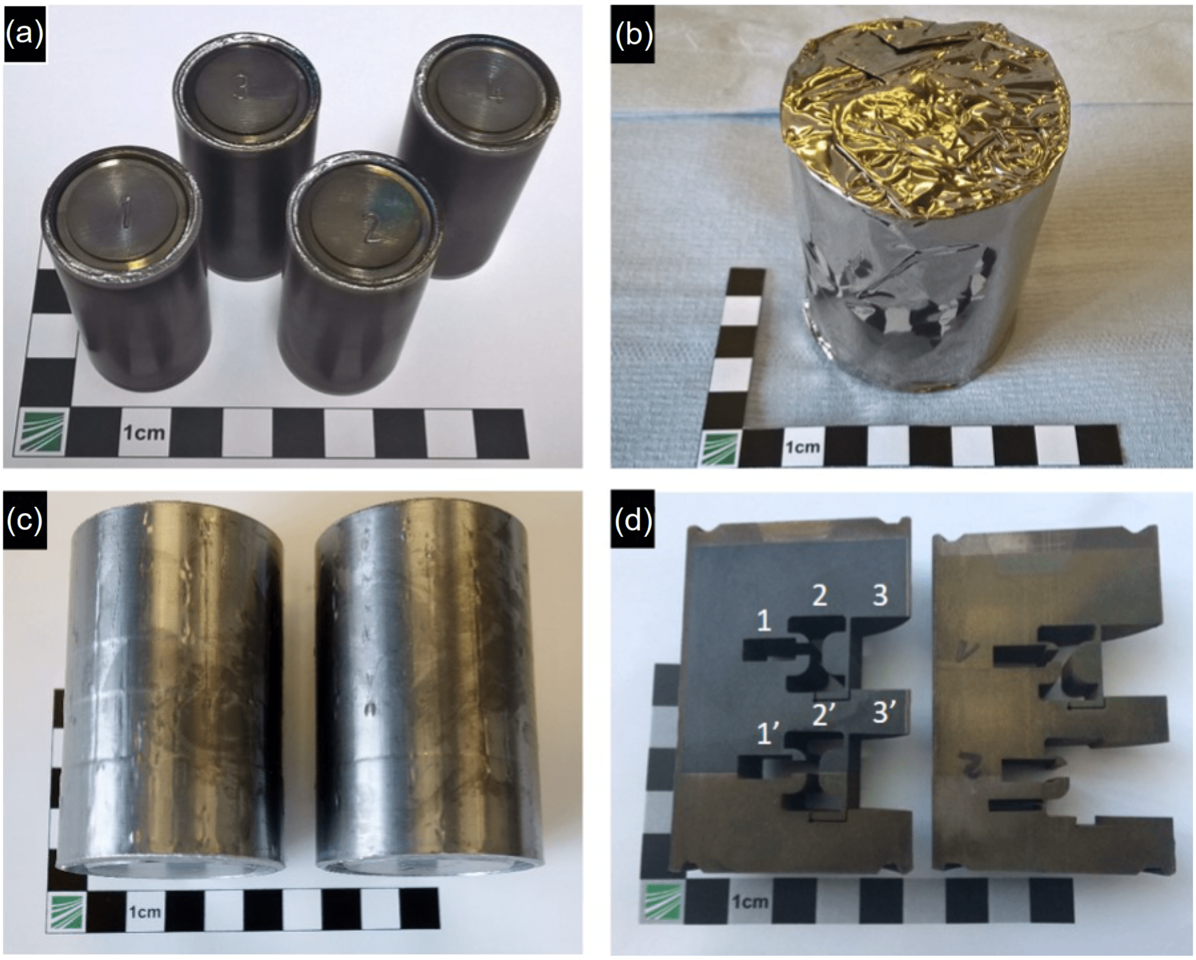

Fig. 5.101: (a) Photograph of four prototypes after welding of the Ta/Ta2.5W capsule. (b) Photograph of one prototype wrapped with getter foils before the HIP cycle. (c) Photograph of two prototypes after the HIP cycle and removal of the getter foils. Deformation and corrugation of the cladding can be observed. (d) Photograph of two half prototypes after cross-sectional cutting with Electro-Discharge Machining (EDM). Areas where specimens were extracted can be observed: 1, 2, and 3 for target-to-target material bonding and 1′, 2, 3′ for cladding-to-target material bonding. Specimens '1' were for thermal-conductivity measurements, '2' for tensile testing, and '3' for interface microscopy [8].

cladding materials, no features such as heterogeneities or retained porosity were observed. However, in the interfaces between the Ta interfoil and Ta2.5W, barely visible microporosity aligned with the interface level was observed in the specimens processed with HIP cycle L. Such features were not observed in the specimens processed with HIP cycle H.

For the tensile testing, three tensile specimens were tested for each bonding combination, and the average values of the results are given in Fig. 5.103. Both of the cladding materials show lower strength than the target materials, and, thus, all of the bonding tensile strengths were theoretically limited by the cladding materials. The tensile strengths of the cladding materials were measured as 360 MPa for Ta2.5W and 220 MPa for Ta, employing the same set-up as for the interface specimens used in the study. Most of the bonding specimens failed at the interface level, and therefore the interface strength was measured. Some of them failed (tests marked with an asterisk) in the base materials, however, and therefore the interface strength might be greater.

In general terms, strong bonding was achieved for the combinations TZM–Ta2.5W (330 MPa), TZM–Ta (215 MPa), and W–Ta (185 MPa); all of these values are close to the tensile strength of the

Table 5.21: List of specimens related to the BDF target studied in this work, together with the corresponding materials, the use or non-use of an interfoil, and the HIP cycle used [8].

Bonding-specimen number	Target to cladding			
	Target material	Cladding material	Interfoil	HIP cycle
1	TZM	Ta2.5W	•	L
2			–	
3		Ta	–	
4	W	Ta2.5W	•	
5			–	
6		Ta	–	
7	TZM	Ta2.5W	•	H
8			–	
9		Ta	–	
10	W	Ta2.5W	•	
11			–	
12		Ta	–	
	Target to target			
	Target material I	Target material II	Interfoil	HIP cycle
13	TZM	TZM	–	L
14			•	
15	W	W	–	
16			•	
17	TZM	TZM	•	H
18	W	W	•	

respective cladding material. Nevertheless, for the pair W–Ta2.5W (230 MPa), the highest mechanical strength was 60–70% of the tensile strength of Ta2.5W.

For TZM as the target material, the strongest bonding was reached with Ta2.5W as the cladding material and HIP cycle H, independently of the use of Ta foil. For W as the target material, the highest bonding strength was achieved with Ta2.5W as the cladding material but required the use of a Ta interfoil. Stronger bonding was always achieved for HIP cycle L.

Higher bonding strengths were achieved for Ta2.5W, most probably owing to the higher strength of this cladding material compared with Ta. However, in certain cases (the W–Ta specimen, HIP cycle L), Ta2.5W required the use of a Ta interfoil to create bonding with W.

Interfoils increased the bonding strength only in the case of bonding of Ta2.5W to W for cycle L. For all other combinations, the Ta interfoil affected the bonding strengths negatively. Nevertheless, the use of a Ta interfoil was the only option for obtaining successful bonding of W to Ta2.5W with HIP cycle L.

On one hand, the HIP cycle with the higher temperature was useful for increasing the bonding strength of the Ta2.5W claddings. At the same time, the higher-temperature cycle reduced the bonding strength of the Ta claddings.

The thermal conductivity of the specimens was mainly limited by the bulk-material conductivity of Ta and Ta2.5W (55 W/m·K), which is much lower than those of TZM and W (120 and 179 W/m·K, respectively). The thermal conductivity was measured across the cladding–target-material interface, and the values obtained are given in Fig. 5.103. The values are compared with the theoretical thermal conductivities, calculated with the thermal-resistance law and assuming perfect bonding without losses at the interface. The theoretical thermal conductivity for the pairs W–Ta and W–Ta2.5W was calculated

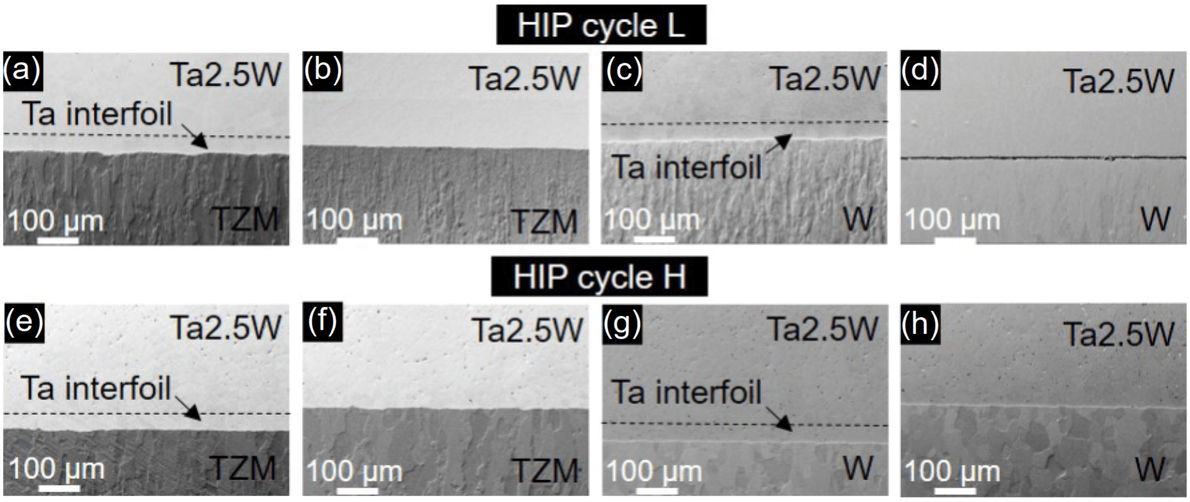

Fig. 5.102: Secondary electron micrographs at the interface level for the specimens under study at 150× magnification, for the two HIP cycles described in the text [8].

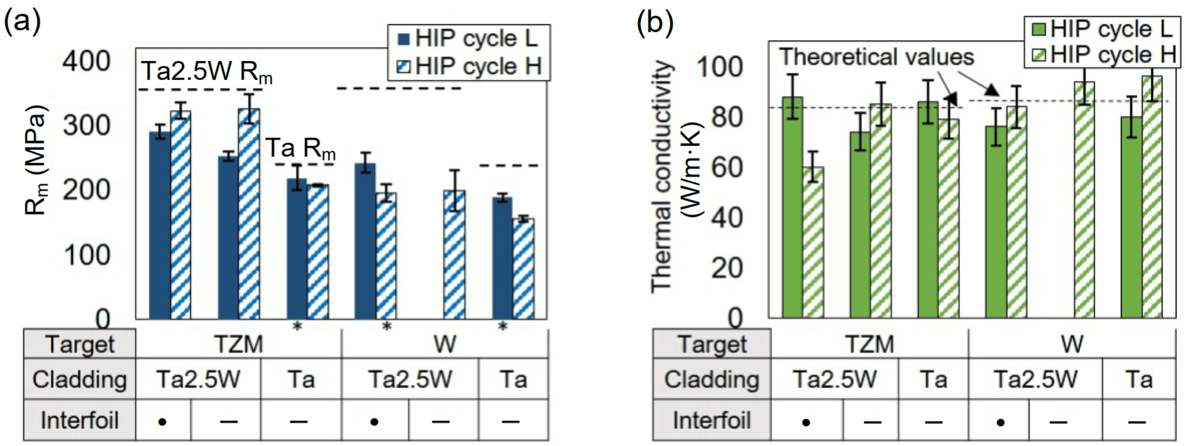

Fig. 5.103: (a) Measured average tensile strength for each type of bonding between cladding and target materials. The tensile strengths of Ta2.5W and Ta are included as references. Specimens marked with and asterisk failed outside the gauge length. (b) Measured thermal conductivity for each type of bonding between cladding and target materials. The theoretical thermal conductivities for bonding without losses at the interface are included as references [8].

to be 85 W/m·K, and for the pairs TZM–Ta and TZM–Ta2.5W 82 W/m·K. The thermal conductivity of the combination W–Ta2.5W without a foil and with the low-temperature cycle was considered to be zero owing to the absence of mechanical bonding. Only one specimen, the TZM–Ta2.5W specimen with a foil and HIP cycle H, showed a significantly reduced thermal conductivity, with a value of 60 W/m·K, 73% of the theoretical value. For all the other specimens, thermal-conductivity values close or equal to the theoretical conductivity were observed independently of the type of bonding, ranging from 74 W/m·K (89% of the theoretical value) for the TZM–Ta2.5W specimen with HIP cycle L to 96 W/m·K (113% of the theoretical value) for the W–Ta specimen with HIP cycle H. No clear tendency was observed in the thermal conductivity with respect to the target and cladding materials, the use of an interfoil, or the HIP cycle.

5.8.4.3.2 Bonding between target materials

The bonding interfaces between the target materials are observable in the SEM images shown in Fig. 5.104. The interfaces between the target materials showed incomplete diffusion bonding when no interfoil was used: the interface between TZM and TZM showed some bonding, but it was limited to some areas and there were recurrent gaps; the interface between W and W did not show any bonding. The interfaces between target materials, when they contained an interfoil, showed potential complete diffusion bonding. The interfaces were homogeneous with no features such as pores, voids, segregations, or any other heterogeneity. A diffusion layer was not discernible, as for the target-to-cladding material bonding.

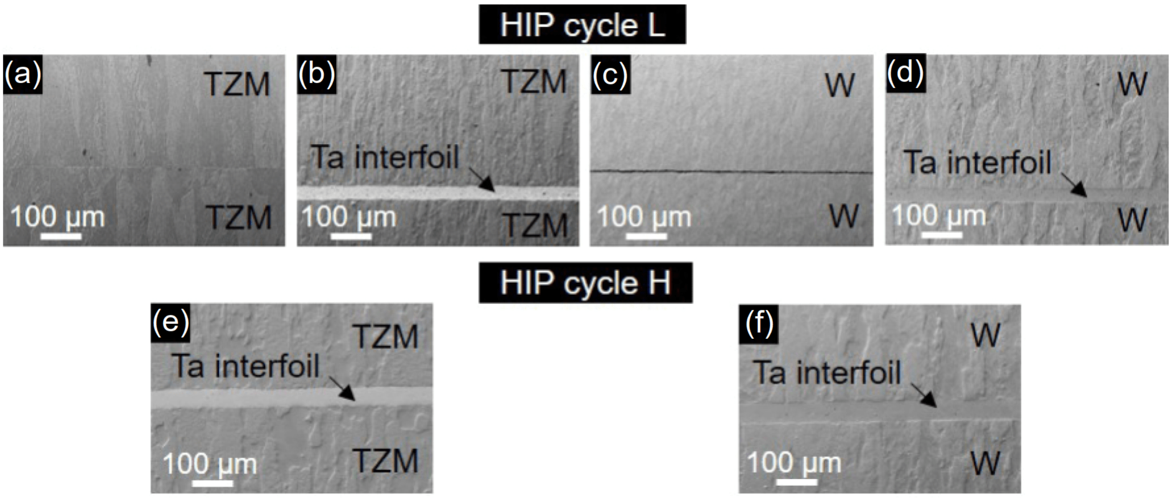

Fig. 5.104: Secondary electron micrographs at the interface level for the specimens studied at 150 × magnification, for the two HIP cycles [8].

For the tensile testing of the target-to-target-material interfaces, three tensile specimens were tested for each interface combination, and the average values obtained are given in Fig. 5.105(a). The tensile strength of Ta is given in the figure for ease of interpretation. All of the specimens tested failed at the bonded interfaces. The bonding strength of the interfaces without an interfoil showed extremely low values for the pair TZM–TZM (5 MPa), and no mechanical bonding for the pair W–W. Strong bonding was observed when an interfoil was used, however. The W–W interface showed tensile strengths of 200 MPa when an interfoil was used, independently of the HIP cycle, a strength which is close to the tensile strength of Ta. The TZM–TZM interface shows much higher tensile strengths of 550 MPa (cycle L) and 475 MPa (cycle H) when a Ta interfoil was used, much stronger than the tensile strength of Ta.

The thermal conductivity was measured across the target-to-target-material interfaces, and the values obtained are presented in Fig. 5.105(b). In the case of TZM–TZM bonding, the thermal conductivity showed values ranging between 120 and 126 W/m·K, values equal to the thermal conductivity of bulk TZM, indicating perfect conductivity across the interface independently of the bonding parameters. The W–W bonding showed thermal-conductivity values slightly lower than those of bulk W, from 126 W/m·K for bonding without an interfoil to 158 W/m·K when an interfoil and HIP cycle H were employed. In general terms, a slight increase in the thermal conductivity was observed when an interfoil was used and with HIP cycle H.

5.8.4.3.3 Bulk material properties

The temperatures of the HIP cycles could be equal to or higher than the recrystallization temperatures of the materials under study. Subsequently, the materials could show recrystallization, grain growth, softening, and degradation of thermal properties. To evaluate these effects, hardness and thermal-conductivity measurements were additionally carried out on bulk material specimens taken from the prototypes.

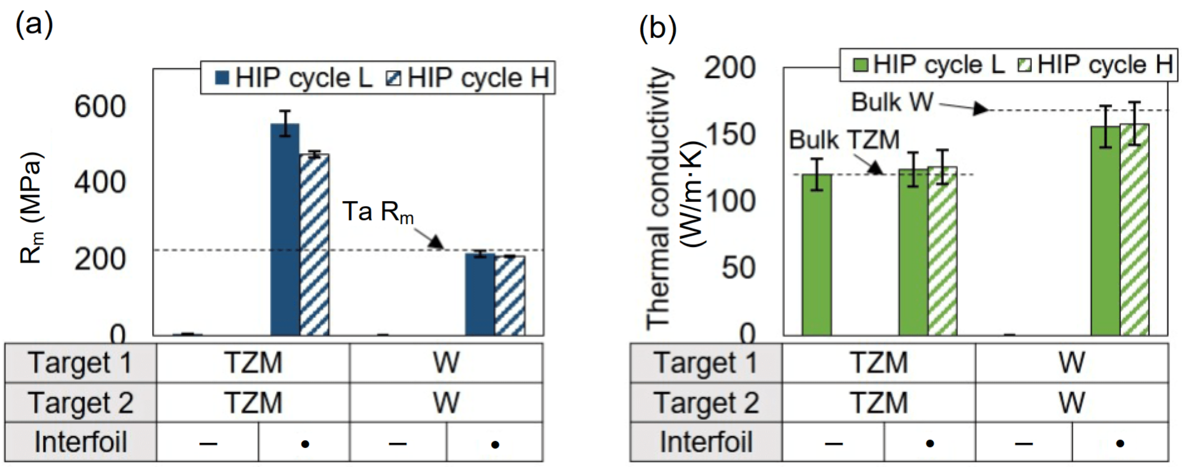

Fig. 5.105: (a) Measured average tensile strength for each type of bonding between target materials. The tensile strength of Ta is included as a reference. (b) Measured thermal conductivity for each type of bonding between target materials. The thermal conductivities of the bulk materials are included as references [8].

The microstructure of the TZM and W was observable in the micrographs in Figs. 5.102 and 5.104. TZM and W showed deformed and elongated grains after HIP cycle L, indicating a microstructure as worked, without any indications of recrystallization. A similar microstructure but with slightly larger grains was observed after HIP cycle H, most probably as a result of slight grain growth. This growth was more pronounced for W and an even equiaxial microstructure was observed in Fig. 5.102(h), indicating potential recrystallization. The microstructure of Ta and Ta2.5W was not observable in the micrographs but no significant differences were expected, since the temperatures of the two HIP cycles were significantly above the recrystallization temperatures of the materials.

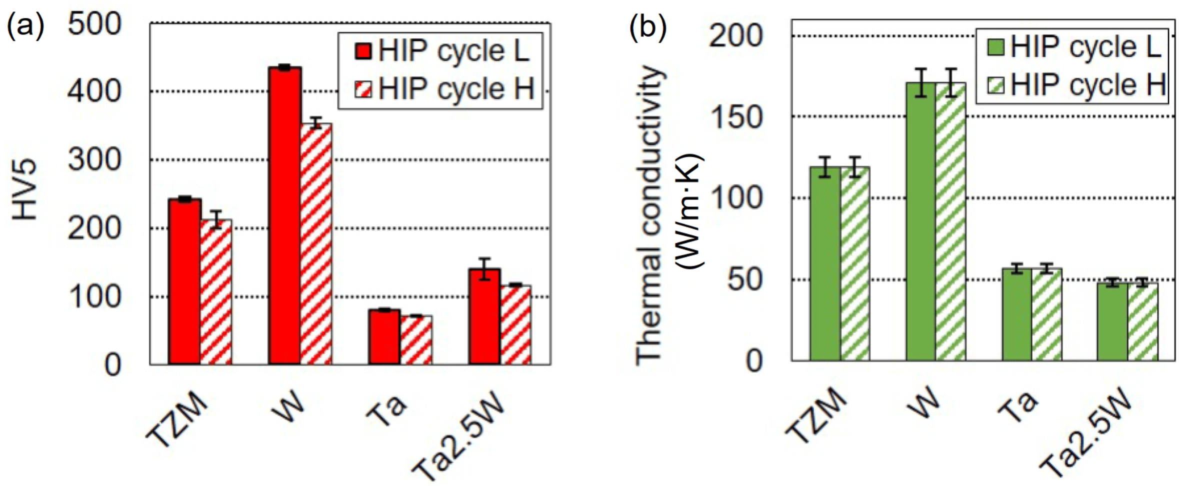

Fig. 5.106: (a) HV5 microhardness and (b) thermal-conductivity values for the four materials after HIP cycles [8].

Vickers hardness values were measured for the four materials after each HIP cycle. The measured values are plotted in Fig. 5.106(a). The four materials showed lower hardness values for HIP cycle H than for HIP cycle L. The reduction was at similar levels for the four materials: 13% for TZM, 19% for W, 10% for Ta, and 17% for Ta2.5W.

The thermal conductivity of the four materials was measured after each HIP cycle. The measured values are given in Fig. 5.106. No significant changes in the thermal conductivity due to the different

HIP cycles were observed in the materials.

5.8.4.4 Discussion

Successful diffusion bonding was achieved for all of the combinations of target materials (TZM and W) and cladding materials (Ta and Ta2.5W), and only some difficulties were encountered when bonding W and Ta2.5W with HIP cycle L. Microscopic inspection of the interfaces did not provide exploitable information about the extent of diffusion bonding, since the diffusion layers were extremely thin (around 1 μm). However, microscopy proved useful for observing the morphology of the interfaces, which, apart from the above-mentioned exception, were homogeneous and did not show any defects such as voids, pores, or segregations. Only in the case of Ta-to-Ta2.5W interfaces and for cycle L was slight retained porosity observed at the interface level.

The evaluation of diffusion bonding at the interfaces was done mainly by means of parameters that are critical for the application and performance of such joints, such as the mechanical strength and thermal conductivity of the interface.

Ta provided satisfactory results as a cladding material with either TZM or W as the target material. With TZM, a tensile strength of 100% of the yield strength of Ta and a thermal conductivity of 100% of the theoretical interfacial thermal conductivity were achieved. For W, slightly lower performance was achieved, with a tensile strength in the range of 70–90% of the yield strength of Ta, but 100% of the theoretical interfacial thermal conductivity was maintained.

Ta2.5W alloy was chosen in view of the increased cladding strength that it offered at the operational temperatures of the BDF target (up to 200°C). Moreover, it could additionally offer improved corrosion resistance in demineralized water and resistance to proton irradiation. Ta2.5W was successfully validated as an alternative cladding material to the widely used Ta. Diffusion bonding to TZM was successful in all cases, and a tensile strength of 330 MPa (92% of the tensile strength of Ta2.5W) and a thermal conductivity of 88 W/m·K (107% of the theoretical interface thermal conductivity) were obtained. Diffusion bonding to W required either higher temperature and pressure parameters in the HIP (cycle H) or the use of a Ta interfoil. Under these conditions, an interface tensile strength of 240 MPa (67% of the tensile strength of Ta2.5W) and a thermal conductivity of 95 W/m·K (110% of the theoretical interface thermal conductivity) were achieved. The difficulties in bonding W directly to Ta2.5W could be due to the higher strength of Ta2.5W compared with Ta. This enhanced strength could limit the plastic deformation of the cladding, required to adapt to the W, and therefore reduce the contact area where diffusion could take place. This phenomenon was not observed with TZM as the target material, most probably because the increase in strength of the cladding was compensated by the higher ductility of TZM.

The parameters of the HIP cycle such as the temperature and pressure were found to have a high influence on the bonding properties. For Ta2.5W as the cladding material, the use of a higher temperature and pressure (cycle H) was beneficial for generating bonding and for increasing the mechanical strength. For Ta as the cladding material, good mechanical bonding was already achieved with a lower temperature and pressure (cycle L). A lower strength was found when a higher temperature and pressure (cycle H) were used, most probably because of softening of the materials owing to recrystallization or grain growth.

The effect of using an interfacial aid such an interfoil showed strong synergies with other factors. As example, when Ta2.5W was bonded to TZM, using an interfoil increased the thermal conductivity from 74 to 88 W/m·K when only HIP cycle L was used. In contrast, if HIP cycle H was used, the interfoil reduced the thermal conductivity from 85 to 60 W/m·K. Thus, the influence of an interfoil requires assessment case by case.

Successful diffusion bonding was also accomplished in the case of the two target-to-target material combinations (between TZM and TZM and between W and W) but only when interfacial aids (Ta interfoils) were used. In these cases, interface microscopy could not image the diffusion layers, but it revealed homogeneous, defect-free interfaces. The extent of diffusion bonding in the interfaces was evaluated in the same manner as for the target-to-cladding-material bonding, by measuring the interfacial mechanical strength and thermal conductivity. In the case of bonding between W target materials, high-quality bonding was achieved, with a mechanical strength of 215 MPa (90% of the Rm of Ta) and a thermal conductivity of 158 W/m·K (93% of the value for bulk W). In the case of bonding between TZM target materials, the results were outstanding, with a mechanical strength of 550 MPa (250% the Rm of Ta) and a thermal conductivity of 126 W/m·K (105% of the value for bulk TZM). In contrast to the target-to-cladding bonding, the HIP parameters did not play an important role, with only a small reduction in bonding strength being observed for HIP cycle H, most probably as a result of softening of the bulk material. Nevertheless, the use of interfacial aids was of extreme importance in the mechanical strength of the bonding: the bonding strength for TZM–TZM bonding increased from 5 to 550 MPa, and for W–W bonding it increased from 0 to 215 MPa. Even though the thermal conductivity might attain high values, however, the mechanical strength of the bonding without an interfoil was found to be only residual.

For both types of bonding (of cladding to target materials and of target to target materials), it was found that incipient diffusion bonding was enough to obtain high values of the thermal conductivity. In contrast, the tensile strength of the bonding was a stronger indication of the extent of diffusion bonding.

A decrease of 10–20% in the hardness values was found for the four materials studied after HIP cycle H compared with HIP cycle L. For the target materials, a higher decrease was found for W, most probably because of the lower recrystallization temperature of this material compared with TZM, confirmed by the micrograph in Fig. 5.104(h). A significant decrease in hardness was also found for both Ta and Ta2.5W. This softening phenomenon could be the cause of the decrease in interfacial strength for the specimens with Ta as a cladding material, since the decrease in tensile strength for the specimens processed with cycle H is also 10–20%. The diffusion bonding of Ta cladding could already be completed with HIP cycle L, and so the increase in temperature and pressure for cycle H could act only in a detrimental way on the bulk properties of the Ta. In contrast, the bonding of Ta2.5W was not complete for HIP cycle L, and therefore the strength was increased by the higher temperature and pressure of HIP cycle H. The same reasoning can be used for the bonding of target to target materials: diffusion bonding with an interfoil is already complete with HIP cycle L, and increasing the temperature and pressure leads to a bond with less strength owing to softening of the bulk material.

5.8.4.5 Conclusions

Several reduced-scale prototypes for the BDF target were successfully built and clad with Ta-based materials by HIP. The microstructure, mechanical properties, and thermal properties of the bonding in the resulting prototypes were studied. HIP has been proven as a valid technique for bonding the candidate target materials (W and TZM) to Ta-based erosion–corrosion-resistant claddings in geometries representative of the final target. Several previous studies with different techniques had led to unreliable bonding. In the present study, bonds with homogeneous interfaces, stronger than the cladding material and with thermal conductivities equal to the theoretical values, were achieved for the combinations Ta–TZM, Ta–W, and Ta2.5W–TZM. The same was valid for the combination Ta2.5W–W but with a slightly lower strength (70% of that of the cladding material). To achieve the desired target geometry and at the same time employ multidirectionally forged material, the division of a target block into smaller multidirectionally forged blocks, coaxially bonded inside the Ta-based cladding, was explored. Diffusion bonding assisted by HIP was successfully used to bond W to W and TZM to TZM in cylindrical geometries. Homogeneous and defect-free interfaces, bonding strengths of 550 and 215 MPa (for TZM-TZM and W-W, respectively), and thermal conductivities equal to the theoretical values were achieved. The use of interfacial aids was mandatory in both cases, however. The mastering of key parameters such as the interfacial aids and HIP parameters was shown to be of special importance for optimizing the interface and bulk material properties of the final target.

5.8.5 Target corrosion considerations

In this section, we present an assessment of the potential corrosion phenomena in Ta and Ta2.5W, the target materials which will be exposed to the target coolant environment.

5.8.5.1 Target conditions

The target blocks will be actively cooled by demineralized water, at a temperature between RT and 110°C and at a high pressure (20 bar) and velocity (5 m/s). The detailed design of the target cooling has already been presented in Section 5.6. Under these conditions, several corrosion phenomena are potentially applicable:

- general/localized corrosion of the Ta and Ta2.5W due to direct contact between target and coolant;
- galvanic corrosion of the Ta and Ta2.5W due to direct contact and through-coolant contact between the target and vessel materials;
- hydrogen embrittlement of the Ta and Ta2.5W, inherent to both materials;
- erosion–corrosion of the Ta and Ta2.5W due to the high velocity of the coolant and possible particles suspended in the coolant;
- irradiation-enhanced corrosion.

The applicability of each corrosion phenomenon is discussed below.

5.8.5.2 Literature review

5.8.5.2.1 General/localized corrosion

According to the *ASM Metals Handbook*, Ta shows no corrosion in de-ionized water at 40°C [86]. Moreover, failures due to exposure to steam condensate have not been recorded, with many cases operating at temperatures up to 250°C. Only a general recommendation on maintaining the pH below 8 is given.

The corrosion behaviour of Ta in high-temperature water was studied in Ref. [59]. The corrosion rate of Ta was measured in flowing water at 180°C (the maximum water temperature in the target), 260°C, and 320°C, with stringent control of dissolved oxygen (<1 ppm). Extremely low corrosion rates in the order of 0.001–0.004 mm/yr were reported. In addition, no occurrence of exfoliation or spallation was observed [59].

No specific data are available for general or localized corrosion in water environments for Ta2.5W. Nevertheless, as mentioned above, Ta2.5W has been proven to have equal or improved corrosion resistance compared with Ta, in critical environments such as hot nitric and sulfuric acid, environments where Ta and its alloys are generally employed [66, 87].

5.8.5.2.2 Galvanic corrosion

The target blocks will be supported in a stainless steel vessel (AISI 316L), and the cooling water will circulate between the inner and the outer tank (see Section 5.2). Hence, it is of interest to assess the potential galvanic corrosion between the two materials. Data on the galvanic coupling between Ta and 316L are available from internal studies under representative conditions, in demineralized water at 20°C and 80°C, with two oxygen levels, 0.1 and 10 ppm. In all cases, the measured galvanic currents were negligible, below 2 $\mu A/cm^2$ [88]. No specific data are available for Ta2.5W but, because the chemistry is close to that of Ta, no large differences in the corrosion potential are expected for this alloy. Further tests will, however, be required in the follow-up to the BDF project.

5.8.5.2.3 Hydrogen embrittlement

In the presence of stray currents or when coupled to a less noble material (e.g. low-carbon steel) in an acidic medium, tantalum can become the cathode in the galvanic cell created and absorb hydrogen, with subsequent embrittlement. Although the stray currents and coupling may be transient, hydrogen absorption is cumulative in its effect. Even if no stray currents are expected and the Ta is coupled to a more noble metal (such as AISI 316L), the Ta might eventually become cathodic given sufficient time. Therefore it is desirable to prevent galvanic-cell formation by providing adequate electrical insulation from other metals [86].

Substitutional alloying of Ta can reduce the hydrogen absorption. References [66, 87] reported reduced hydrogen absorption in a hot sulfuric acid environment particularly for Ta2.5W.

5.8.5.2.4 Erosion–corrosion aspects

Erosion–corrosion deals with simultaneous interactions between erosion and corrosion, with synergies which can increase significantly the metal loss beyond the addition of the two phenomena independently.

Erosion–corrosion studies were reported in Ref. [62] for several metals (AISI 304L, AISI 316L, Ti, Ta, Ta2.5W, and Zr). In areas of the specimens protected from the impinging alumina particles, no alteration of the Ta or Ta2.5W surface was observed, even in an aggressive medium (10% HCl). Nevertheless, owing to the lower hardness of Ta compared with stainless steels, this metal was found to be susceptible to failure caused by impinging particles. Even with additions of alloying elements such as W, the presence of abrasive particles in the coolant induced severe erosion–corrosion.

An erosion–corrosion test was carried out on a Ta cladding at RAL [89]. A water jet impinged on the Ta surface at 34 m/s at an angle of 25°. In this test, the water was filtered before impinging on the surface and therefore erosion–corrosion was limited to liquid erosion. After more than 3000 h of testing, the Ta did not show any signs of pitting or erosion.

5.8.5.2.5 Irradiation-enhanced corrosion

Corrosion behaviour in water in irradiation environments presents specific conditions. The interaction of high-energy protons with water produces decomposition of water molecules into various species (radiolysis), which can attack the metal surface. The data in the published literature on the corrosion behaviour of Ta in irradiation environments are limited to Ref. [60]. Ta specimens were introduced into a corrosion loop containing de-ionized water at 30°C. The Ta specimens were continuously irradiated with 800 MeV protons inside the corrosion loop. Thanks to careful pre-cleaning of the circuit and the employment of hydrogen water chemistry, the formation of radiolysis products was mitigated, and the corrosion rate of the target was extremely low, less than 0.12 µm/yr.

5.8.5.2.6 Remarks

From the above literature review on the corrosion behaviour of Ta and Ta2.5W, it can be concluded that no significant potential issues related to corrosion are expected for Ta and Ta2.5W if several points, listed below, are properly addressed in the design of the water circuits. Nevertheless, dedicated R&D will be pursued further to quantitatively clarify this point.

- The water chemistry should be carefully monitored and controlled (oxygen and hydrogen concentrations, pH, conductivity, . . .).
- The water should be continuously filtered to avoid recirculation of spallation products, either from the target or from other parts of the cooling circuit.
- Circuit cleaning should be performed before initiation of target operation.
- If feasible, the target blocks should be isolated electrically from other metals.

Dedicated corrosion studies are planned for the future.

5.8.6 Radiation damage considerations and R&D studies

In this section, a literature review of the effects of irradiation on the target materials is presented, with a discussion of its representativeness. Ongoing and planned specific irradiation studies are then presented.

5.8.6.1 Literature review

Irradiation of the target materials will affect the properties of those materials. Irradiation causes lattice damage through atom displacements (measured by the dpa) and generation of gas atoms (mainly hydrogen and helium) in the material. The dpa and gas generation introduce microscopic defects into the lattices of the materials, which translate into macroscopic changes in the material properties. The extent of this damage is directly related to the type and fluence of the irradiation. The irradiation temperature plays also an important role, since high temperatures promote defect annihilation by thermal recovery.

The irradiation conditions that the target will be subject to during 1 yr of operation are summarized in Table 5.22 for the four target materials (taken from Sections 5.3 and 5.5).

Table 5.22: Irradiation conditions for each BDF target material with approximate maximum annual fluences, dpa, and gas production, as presented in Section 5.3.

Material	Irradiation type	Irradiation temperature (°C)	Fluence	dpa	Gas production
TZM	Proton + neutron	35–180	3×10^{18} p/cm^2, 2×10^{20} n/cm^2	0.1	38 appm H, 15 appm He
W	Proton + neutron	35–150	2×10^{18} p/cm^2, 3×10^{20} n/cm^2	0.1	30 appm H, 16 appm He
Ta/Ta.25W	Proton + neutron	35–160	3×10^{18} p/cm^2, 3×10^{20} n/cm^2	0.06	51 appm H, 30 appm He

It should be highlighted that most of the irradiation damage will be concentrated in areas in the centre of the target because of the location of the beam impact, and the damage will decrease gradually towards the outside. The microscopic effects of irradiation are not discussed in this part, but only the macroscopic effects, which impact directly on the thermophysical and mechanical properties of the BDF target assembly.

Swelling due to irradiation is a concern for the target materials. Since most of the target volume is occupied either by W or by TZM, even a small swelling of 1–2% in these materials could drastically reduce the spacing between the target blocks and reduce the cooling-water flow. The literature on both materials at representative neutron fluences reports swelling, which starts at irradiation temperatures above 300°C and becomes critical at 600°C, with values of swelling of up to 1.5% for W and 2.5% for TZM. Therefore, swelling of materials under neutron irradiation appears not to represent a significant concern within the range of operational temperatures of the target [90, 91]. Further studies will be required to assess the situation under representative proton irradiation, however, as gas production, which contributes to swelling, is significantly larger for proton irradiation than for (thermal) neutron irradiation.

A review of the available literature on the mechanical properties of the materials of the target after irradiation is summarized in Table 5.23. The minimum temperature for initiation of thermal recovery in the target materials is estimated as 600°C. Therefore, data for irradiation temperatures between RT and 600°C are considered representative and are presented in this review.

Table 5.23: Literature review of effects of irradiation on the mechanical properties of the four materials. UTS, ultimate tensile strength; YS, yield strength; FS, fracture strength; FT, fracture toughness; E, elongation at failure; MH, microhardness; NH, nanohardness; SR, strain rate.

Product form	Irradiation type	Irradiation temp. (°C)	Fluence	dpa	Gas	Strength	Ductility	Ref.
TZM								
Bar 6 mm	Proton	35–400	–	0.4–0.7	50–70 appm He	UTS +20%	E: 8% to 0%	[92]
Plate 6.35 mm	Neutron	300–560	0.7–2.5 × 10^{22} n/cm^2	3.9–12.3	–	YS: +5–100%		[93]
Sheet 1.52–6.35 mm	Neutron	500–600	1–5.5 × 10^{22} n/cm^2	–	– 10 appm He	YS: +50%, SR: + sensitive FS: +	DBTT: 430–500°C	[47]
Bar 105 mm diam.	Neutron	380	0.5–0.9 × 10^{22} n/cm^2	–	–	YS: 60–70% at 200°C	E: 25–0% at 200°C	[3]
Sheet 0.3 mm thick	Neutron	50–100	1.5 × 10^{20} n/cm^2	–	–	UTS: +50–120%	E: 3–11% to 0%	[94]
Rods 3.1 mm diam.	Neutron	40–475	2.9–3.5 × 10^{20} n/cm^2	0.29–0.35	–	YS: +50%, FT: −	E: 30–50% to 0% at RT–200°C	[95]
W								
Rod 3 mm diam.	Proton	50–270	–	0.6–23.3	200–11 000 appm H, 40–2020 appm He	YS: 30% increase at 1 dpa	E:+	[96] [51]
Rod 3–6 mm diam.	Proton	<300	3.1 × 10^{14} p/cm^2	–	–	MH: +18%	E: 0%	[97]
Plate	Self-ion	500	–	0.5–5	–	NH: +18% at 0.2 dpa, +40% at 5 dpa		[98]
Wire 1 mm diam.	Neutron	100	5 × 10^{19} n/cm^2	–	–	No significant differences		[50]
–	Neutron	330–450	1–1.5 × 10^{21} n/cm^2	–	–	YS: − (ann), + (def)	E: 0%	[45]
Bar 105 mm diam.	Neutron	380	0.5–0.9 × 10^{22} n/cm^2	–	–	YS: +55% at 200°C	DBTT: 60–240°C	[3]
Ta								
Plate	Proton	<200	0–1.7 × 10^{21} p/cm^2	0–11.3	0–580 appm He	MH: +80% at 1 dpa, +150% at 11 dpa	E: 15% at 11 dpa	[69]
–	Proton	150–260	–	6.5–16.3	–	UTS: +170% at 7.3 dpa	E: 2%–10% at 15 dpa	[99]
Sheet 0.5 mm thick	Proton	385–400	4.8 × 10^{19}–5.3 × 10^{20} p/cm^2	0.26–2.9	–	UTS: up to +85%	E: 22–2%	[100]
–	Neutron	60–100	1.1 × 10^{17}–4.2 × 10^{20} n/cm^2	0.00004–0.14	–	UTS: +200% at 0.14 dpa	E: 2–12% at 0.14 dpa	[101]
Ta2.5W								
Ta–1.2W	Neutron	60–100	1.1 × 10^{17}–4.2 × 10^{20} n/cm^2	0.00004–0.14	–	UTS: +100% at 0.14 dpa	E: 10% at 0.14 dpa	[101]
Ta–1.2W	Proton+ neutron	50–160	8.3 × 10^{20}–3.6 × 10^{21} p/cm^2 and 2.9 × 10^{20}–1.1 × 10^{21} n/cm^2	0.7–7.5	–	UTS: +120% at 7.5 dpa	E: 10% at 7.5 dpa	[101]

For TZM, quite representative data were reported in Ref. [92], with the irradiation temperature, type, dpa, and He generation representative of 3–5 yr of target operation. Under these conditions, TZM exhibits a higher UTS (+20% with respect to the unirradiated case) even though it fractures before yielding, as can be observed in Fig. 5.107. This underlines the embrittlement of the base materials, which show negligible ductility. Data for neutron irradiation are less representative of the target conditions, but the effects on the mechanical properties provide a general indication. Moreover, studies with neutron irradiation have reported additional irradiation effects: a slight increase in the strain rate sensitivity, fatigue life, and fracture strength was reported in Ref. [47] and a slight decrease in fracture toughness was reported in Ref. [95].

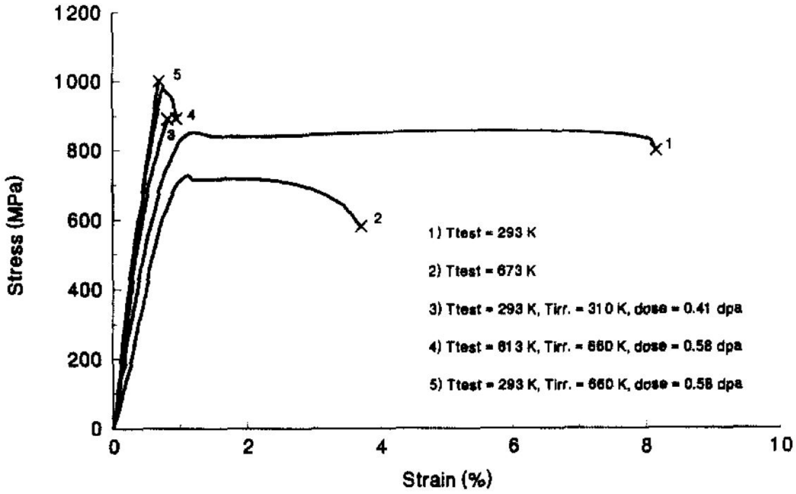

Fig. 5.107: Tensile deformation curves for TZM, irradiated at different temperatures and doses, as presented in Ref. [92].

Data for equivalent irradiation conditions with a wide range of dpa and He content are available for pure W from Ref. [96, 51]. An increase in the compressive yield strength of 30% was measured at 0.6 dpa (40 appm He), equivalent to 5–6 yr of target operation. This value stayed constant up to 4 dpa (290 appm He). Cracking on the sides of the irradiated specimens indicated a decrease in ductility, which was confirmed in Ref. [97] in bending tests on proton-irradiated W. Less attention is commonly given to the physical properties. Reference [26] recently reported a significant decrease in the thermal diffusivity of proton-irradiated W, as depicted in Fig. 5.108.

Several studies on pure Ta irradiated with protons are available and are applicable to the target conditions. The literature agrees in reporting a fast increase in the strength of Ta at low dpa values (0.1–0.3); the rate of increase is then reduced but remains constant up to several tens of dpa (see Fig. 5.109). Less agreement is shown on the embrittlement rate of Ta with increasing dpa values. While Ref. [100] reported a severe elongation reduction even at 0.3 dpa, Ref. [69] reported a 15% elongation up to 8.4 dpa, as can be observed in Fig. 5.109. This different behaviour was attributed to the purity level of the Ta. In accordance with this, Ref. [101] also reported severe embrittlement of Ta, which was attributed to oxygen pick-up during annealing.

No specific data are available for the effects of irradiation on the mechanical properties of Ta2.5W. Reference [101], however, presented a study of the effects of combined irradiation (neutron + proton) of two different Ta alloys with W in solid solution, namely Ta–1%W and Ta–10%W. It was found that Ta–1%W exhibited a significant plastic region up to 10 dpa, much greater than that for Ta or Ta–10%W at high dpa, as can be seen in Fig. 5.110.

For all of the target materials, data for proton irradiation are limited and most of the data are available for neutron irradiation. Neutron data are difficult to correlate with proton data, since the effects on the material are different: He gas production can reach higher values of appm per dpa for high-

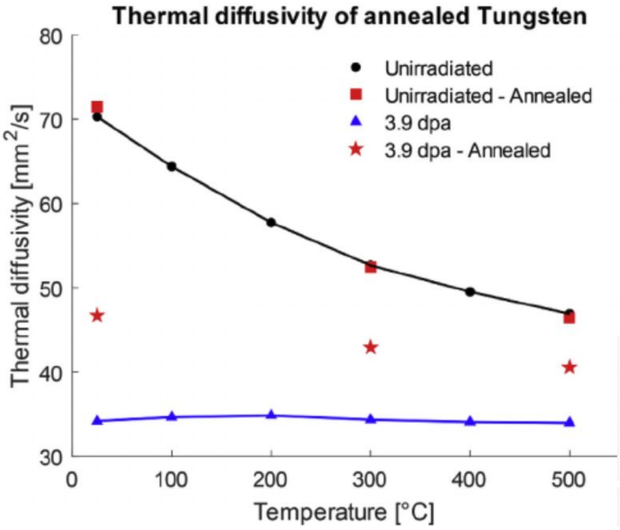

Fig. 5.108: Thermal diffusivity of irradiated W at 25–500°C, as presented in Ref. [26].

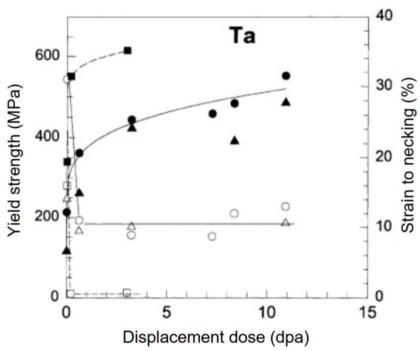

Fig. 5.109: Yield strength (filled symbols) and strain to necking (open symbols) as a function of the displacement dose for Ta. The circles and triangles indicate the results for high-purity Ta tested at RT and 250°C, respectively (from Ref. [69]); the squares indicate data for less pure Ta from Ref. [100].

energy proton irradiation compared with fission reactor neutron irradiation [102]. Moreover, there are many difficulties in correlating the existing data, since many parameters can affect the consequences of irradiation apart from the irradiation conditions, such as impurities in the material, heat treatment, grain size, and cold work. These parameters are not always reported or considered during the experiments.

In general terms, many of the irradiation studies agree on the consequences of irradiation for the materials, by showing an increase in tensile strength combined with reduced ductility (i.e. a significant increase in DBTT). It is widely accepted that embrittlement at low irradiation temperatures is the major concern at working temperatures below $0.3T_\mathrm{m}$ for these materials [103].

By putting together the estimated radiation damage in the target materials, it can be expected that the W and TZM will become slightly harder but brittle after only few years of operation. Nevertheless, it is expected that the Ta and Ta2.5W will become slightly stronger but retain significant ductility if high-purity material is employed.

There are several material properties relevant to the target design for which irradiation effects have not been studied or correlation is difficult. Data on fatigue behaviour, fracture toughness, and thermal properties after irradiation are scarce for refractory metals. This is a critical aspect that requires to be addressed in order to produce a robust target design with sufficient safety margins in terms of radiation damage. A plan in the framework of the RaDIATE Collaboration [73, 74] is being defined. Further

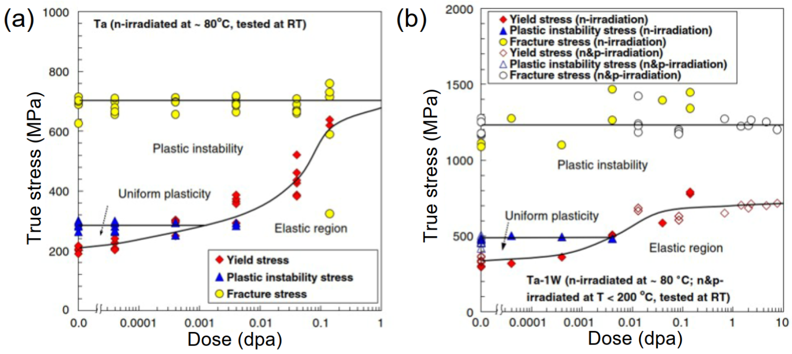

Fig. 5.110: Macroscopic deformation maps for (a) pure Ta and (b) Ta–1%W alloy, from Ref. [101]

discussions are reported in Section 5.8.6.2.

5.8.6.2 BLIP studies

5.8.6.2.1 Introduction to RaDIATE Collaboration

With the increase in power of proton accelerator particle sources such as target facilities, there is a pressing need to better understand and predict long-term radiation damage effects in structural window and target materials. In this framework, CERN joined the Radiation Damage In Accelerator Target Environments (RaDIATE) Collaboration in 2017 [104]. Many research institutes in the accelerator domain, such as Fermilab, Argonne, FRIB, Brookhaven National Laboratory (BNL), and Pacific Northwest National Laboratory (PNNL), were already members of the RaDIATE Collaboration. Its final goal is to be able to predict as best as possible the operating lifetimes of materials used in target facilities in terms of integrated proton fluence and the high-energy proton accelerator parameter space (e.g. temperature, dose rate, duty factor, and dynamic stress).

To achieve its final goal [104],

> the RaDIATE Collaboration draws on existing expertise in related fields in fission and fusion research [. . .] to formulate and implement a research program that will apply the unique combination of facilities and expertise at participating institutions to a broad range of high power accelerator projects of interest to the collaboration. The broad aims are threefold:
>
> – to generate new and useful materials data for application within the accelerator and fission/fusion communities;
> – to recruit and develop new scientific and engineering experts who can cross the boundaries between these communities;
> – to initiate and coordinate a continuing synergy between research in these currently disparate communities, benefiting both proton accelerator applications in science and industry and carbon-free energy technologies.

5.8.6.2.2 Introduction to BLIP facility and experiment

The Brookhaven Linac Isotope Producer (BLIP) facility at BNL has the mission of producing medical isotopes using a 116 MeV primary proton beam [105, 106]. It delivers a rastered beam with a peak current of 165 µA and a fluence of 7×10^{13} p/cm$^2 \cdot$ s (with a 3 cm diameter footprint) to isotope targets. The BNL linac is capable of delivering protons up to 200 MeV, however. Therefore, it is possible to operate BLIP at higher energies in tandem with material targets upstream of the isotope targets. In this operating mode, the optimal beam energy and proton flux still need to be delivered to the downstream isotope targets to preserve isotope yield. This can be achieved by *selecting* target materials with defined parameters (such as the thickness and the Z number of the materials through which the proton beam passes) to control the degradation of the initial beam energy. Taking also into account the type of tests to be performed after irradiation, significant fine tuning and multiple sensitivity studies were performed to optimize and configure the sample sizes, the sample configuration inside the capsule, and the final target array composition.

One big advantage of the BLIP experiment is that it offers a unique opportunity to irradiate materials with protons with energies above 100 MeV. Reactor studies of materials with neutron fluxes with energies between 1 and 14 MeV are limited in relevance to the target systems. The effects of low-energy neutron irradiations are not equal to the effects of high-energy proton irradiations. The typical irradiation parameters obtained for proton irradiation ($E_{\mathrm{p}^+} \geq 100$ MeV) and neutron irradiation ($1 \leq E_{\mathrm{n}} \leq 14$ MeV) are summarized in Table 5.24. For proton irradiation, the dpa rate and gas production obtained are higher by a factor of two at least [107].

Table 5.24: Typical parameters for proton irradiation ($E_{\mathrm{p}^+} \geq 100$ MeV) and neutron irradiation ($1 \leq E_{\mathrm{n}} \leq 14$ MeV) obtained in irradiated materials.

Irradiation source	dpa rate (dpa/s)	He gas production (appm/dpa)	Irradiation temperature (°C)
Mixed-spectrum fission reactor	3×10^{-7}	1×10^{-1}	200–600
Fusion reactor	1×10^{-6}	1×10^{1}	400–1000
High-energy proton beam	6×10^{-3}	1×10^{3}	100–800

5.8.6.2.3 Framework and objectives

In the context explained above, CERN had the possibility to irradiate materials in the proton line of the BLIP facility at BNL [105]. The BLIP experiment will complement the studies of long-term radiation damage effects in materials (such as iridium, TZM, and Ta2.5W) used in target and dump applications such as the BDF, for example. Results obtained from the BLIP irradiation campaign will provide important knowledge about the mechanical and thermal behaviour of the materials of interest.

The main objectives for CERN were to design a new irradiation capsule to accommodate the samples and in which to send the capsules to BNL for irradiation. Additionally, post-irradiation examination work had to be defined prior to irradiation. A complete PIE procedure had to be written, taking into account several aspects: reception of capsules and handling of activated capsules, disassembly, mechanical and thermal tests, and metallographic observations.

All of the information presented here is well documented and summarized in documents stored in the CERN Engineering Data Management Service (EDMS) [108, 109, 110]. The reader can refer to these documents for more details.

5.8.6.2.4 RaDIATE irradiation run

Various materials relevant to the participating institutions were irradiated for up to 8 weeks in the framework of the RaDIATE Collaboration. The target box arrangement in the BLIP beam line, containing various materials just upstream of the isotope target box, is depicted in Fig. 5.111 [105]. The target box was configured to degrade the 181 MeV incoming linac beam to the exact energy required for optimal isotope production. Each material type was enclosed in its individual stainless steel capsule, separated in series by a 2.5 mm wide gap of flowing cooling water.

Three capsules were built, shared between two runs. Several samples were irradiated, such as iridium, TZM, copper alloy, Ta2.5W, and Si samples, to provide insight into the behaviour under proton

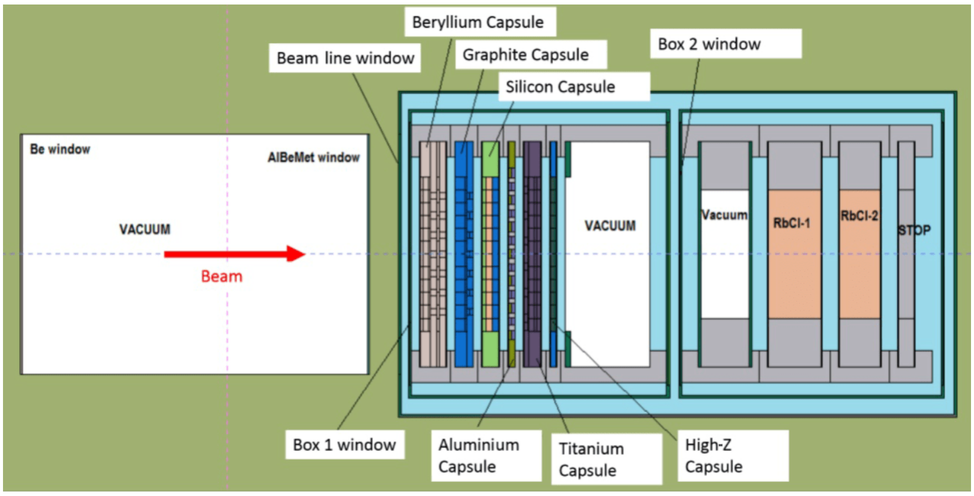

Fig. 5.111: Target arrangement in BLIP beam line [105]

irradiation of materials used for future beam-intercepting devices at CERN. The irradiation of the first two capsules took place successfully in July 2017 at BNL. Finally, the success of the first BLIP test campaign led to the carrying out of a second irradiation test campaign, completed in March 2018. The different runs, capsule configurations, times of irradiation, and protons on target are summarized in Table 5.25 [111]. BLIP run 1 comprises two irradiation phases, where capsules could be swapped.

Table 5.25: Capsule configurations, different runs, times of irradiation, and protons on target for the BLIP irradiation campaign.

Capsule name	CERN High-Z capsule	CERN Silicon Capsule	CERN High-Z capsule II
Irradiated materials and associated experiments	Iridium (AD) TZM (BDF) CuCrZr (SPS internal dump) PGS graphite	Silicon (SPS internal dump) SiC-coated graphite (KEK muon production target) Sigraflex® graphite	Ta2.5W (BDF) Mo-coated CFC and Mo-coated MoGr. (materials for collimators) Monocrystalline Si (Crystal collimation) PGS graphite
Run	BLIP run 1		BLIP run 2
Capsule position in the array	6	3	3
Irradiation phases	2	1, 2	3
Weeks of irradiation	1.8	3.15	4.7
PoT	1.03×10^{21}	1.76×10^{21}	2.81×10^{21}
Completion of irradiation	July 2017		March 2018

5.8.6.2.5 Capsule configuration

High-Z capsule. The High-Z capsule, enclosed in vacuum, contained 40 samples of TZM (a candidate material for the BDF target) as well as iridium and CuCrZr specimens. Figure 5.112 shows a sketch of the bending-specimen layers for the different materials and a picture of the capsule during its assembly. Because of the high density of the materials, this capsule was irradiated for only two weeks to minimize the residual dose rate and stay below the limits for handling and transportation. In addition, the proton budget allowed for our materials (<10 MeV/capsule) was a limiting factor on the thickness of the samples to be irradiated. The dimensions of the samples were minimized to $20 \times 2 \times 0.5$ mm for micromechanical testing. All samples were manufactured to be tested in four-point bending. The sample dimensions together with the peak temperatures reached during irradiation are summarized in Table 5.26. More information about the temperatures obtained can be found in Section 5.8.6.2.6.

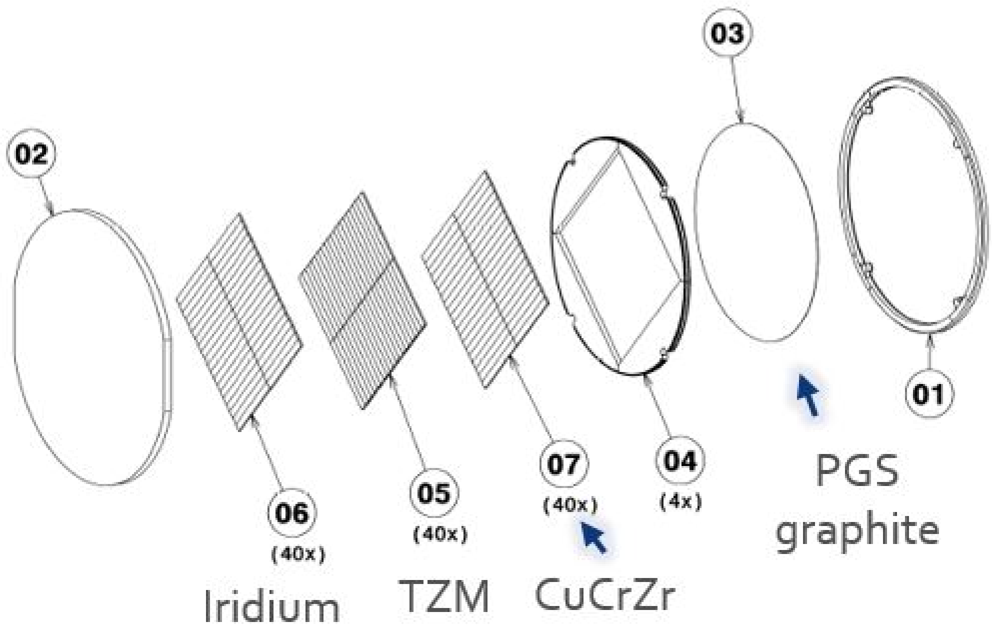

Fig. 5.112: Sketch of the arrangement of bending-specimen layers for the different materials in the High-Z capsule.

High-Z II capsule. The High-Z II capsule was also vacuum-sealed and was irradiated during run 2, and received the highest number of PoT (2.81×10^{21} total POT; see Table 5.25). The estimated peak irradiation temperatures were calculated to be reasonably low (around 330°C; see Table 5.26) thanks to the systematic use of PGS in between the arrays of materials. Among other materials, the capsule contained 40 samples of Ta2.5W (used as a cladding material for the TZM and W blocks of the BDF target) for four-point bend tests.

5.8.6.2.6 *Irradiation results*

To calculate the temperatures and stressed reached in each of the capsules and their sample materials, thermomechanical calculations using the commercial Finite-Element (FE) software package ANSYS Mechanical [112] were performed. For these calculations, a FLUKA Monte Carlo code [12] was first used to generate an input file for the thermal heat load arising from the irradiation. The generated file was then mapped to the ANSYS mesh and applied as an internal heat generation source. The transfer from one code to the other was performed using an APDL script [113]. The values obtained could fluctuate depending on the models used, and therefore we present the most reasonable estimates obtained here. Unfortunately, the values estimated by simulations could not be confirmed by measurements during irradiation owing to the obvious difficulty of the operation.

Calculations of the dpa and gas production were performed by means of FLUKA Monte Carlo simulations [108]. The peak dpa obtained during irradiation and the gas production are depicted in Figs. 5.114 and 5.115, respectively. Materials are presented following the order of Table 5.26. For the High-Z capsule with a PoT of 1.03×10^{21}, TZM reached 0.19 dpa. Ta2.5W reached the highest dpa obtained, 0.88, for a PoT of 2.81×10^{21} in the High-Z II capsule.

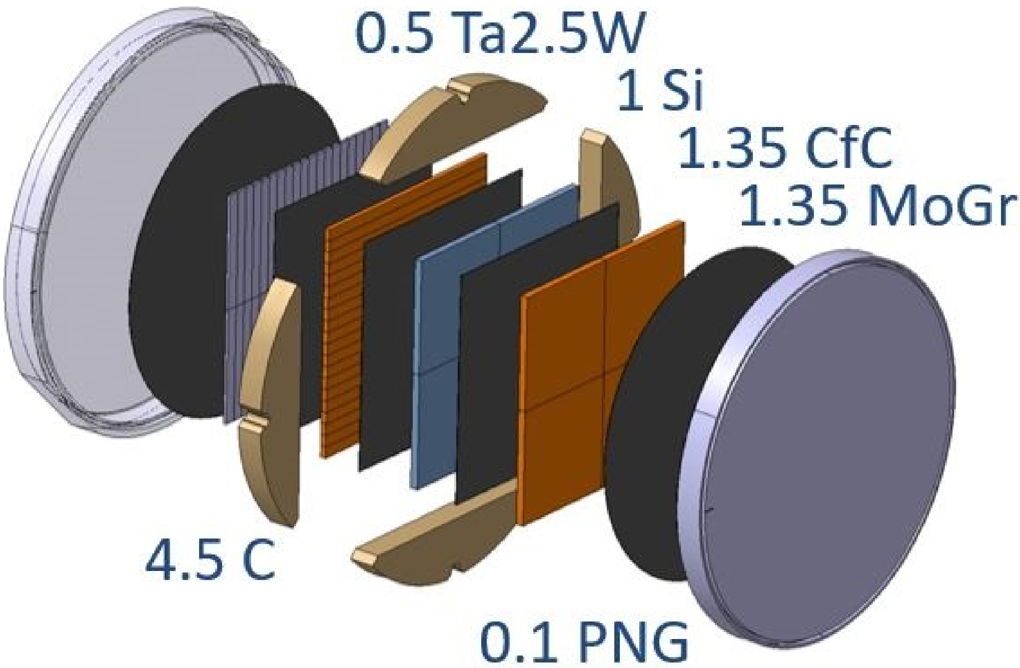

Fig. 5.113: 3D view of the arrangement of bending-specimen layers for the different materials in the High-Z II capsule.

Table 5.26: Sample configuration, sample size and thickness, dpa reached, and temperature during the BLIP irradiation campaigns.

Capsule	Material	Sample size $l \times w$ (mm × mm)	Sample thickness (mm)	Peak temperature (°C)
High-Z	Iridium	20 × 2	0.5	860
High-Z	TZM	20 × 2	0.5	820
High-Z	CuCrZr	20 × 2	0.5	230
High-Z	PGS graphite	⌀ 55.5	0.1	165
Silicon	Silicon	40 × 2	1	220
Silicon	SiC	⌀ 9.8	0.2	220
Silicon	Graphite	⌀ 9.8	0.8	220
Silicon	Sigraflex® graphite	⌀ 55.5	2	190
High-Z II	Ta2.5W	40 × 2	1	270
High-Z II	Mo-CFC	20 × 20	1.35	330
High-Z II	Mo-MoGr	20 × 20	1.35	250
High-Z II	Single crystal Si	20 × 2	0.5	320
High-Z II	PGS graphite	⌀ 55.5	0.1	290

5.8.6.2.7 BLIP post-irradiation examination

During the irradiation, the interaction of the proton beam with the targets and dump materials creates radioactive isotopes in the materials through nuclear fragmentation processes, resulting in their activation. After irradiation, a sufficient cooling time is necessary before one can proceed with the treatment, handling, and processing of the samples. The capsules were shipped to the various institutions of the RaDIATE Collaboration for the PIE work. Thus, a cooling time of the capsules sufficient to meet the

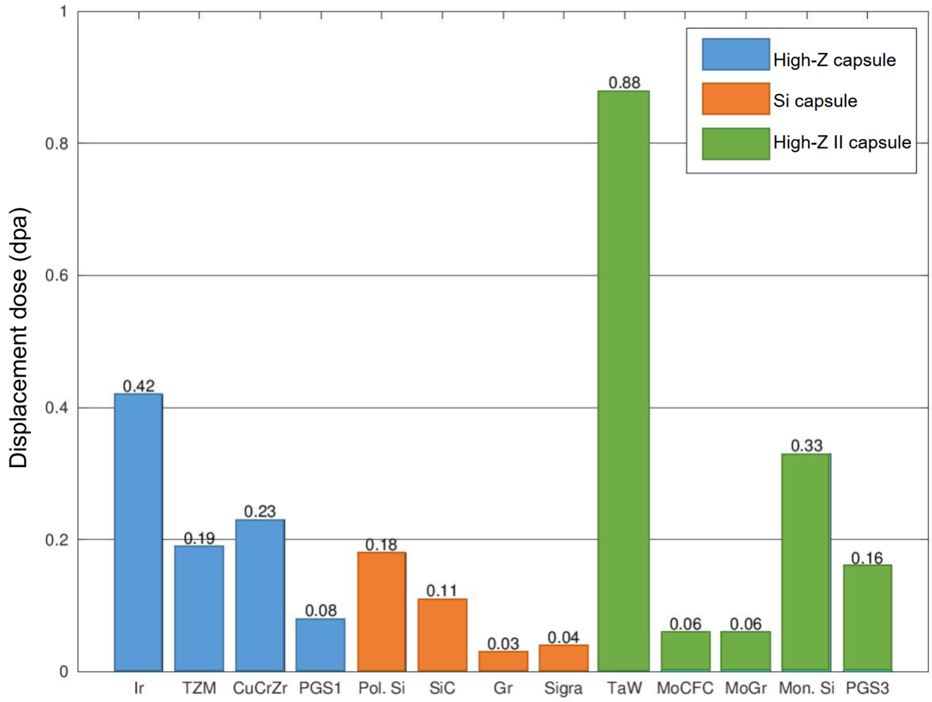

Fig. 5.114: Values of dpa reached in CERN materials irradiated at BLIP

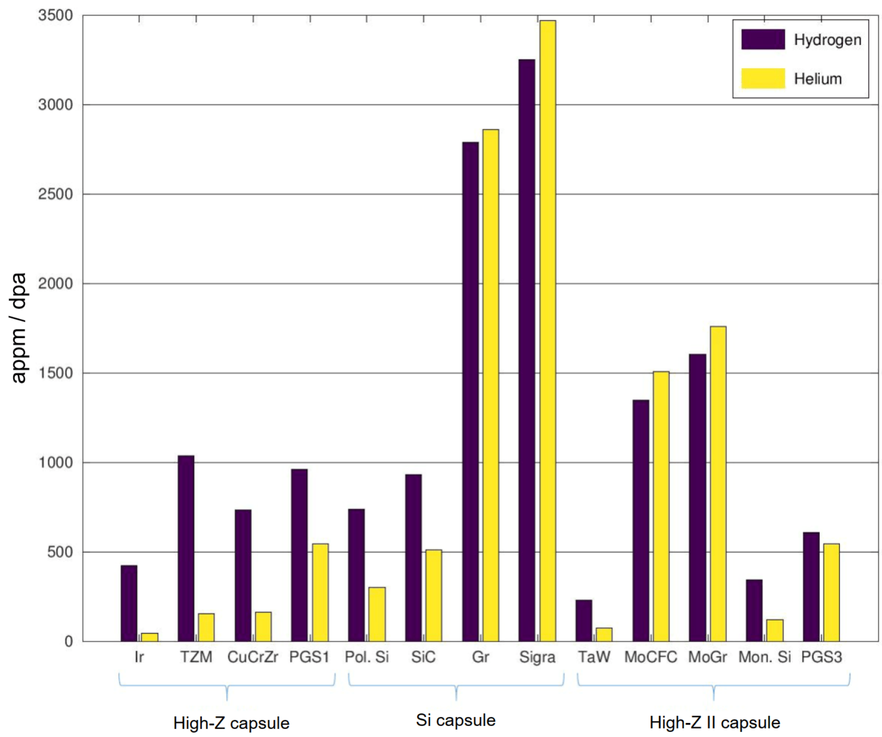

Fig. 5.115: Peak gas production rate in CERN materials irradiated at BLIP

requirements for Type A radioactive shipments was required. The PIE will characterize changes in the strength and thermal and microstructural properties of the material due to radiation damage effects.

Together with the fact of coping with brittle materials and the small amount of available space inside the capsule, micromechanical methods were chosen for material testing. For four-point bending tests, in accordance with the available proton budget (see Section 5.8.6.2.5), the design and dimensions of the samples were chosen to accommodate the ASTM E-1820 and ASTM E-399 standards as guidelines for the test campaign.

The mechanical tests that are required to be performed on the irradiated samples, the sample preparation for metallographic observations, the metallographic investigation techniques to be used (such as optical microscopy and scanning electron microscopy), the thermal tests on the flexible graphite, and the analysis of results required have all been documented in detail in a technical specification procedure for the PIE [114]. For CERN, all PIE work on the specimens will be performed at PNNL. For the High-Z capsule, PIE work will start in the current year, 2019, while for the High-Z II capsule, PIE work is foreseen during 2020.

5.9 Development of a BDF target prototype for beam tests

5.9.1 Introduction to and motivation for the construction of the BDF target

Given the unprecedented regime of temperature and stresses in the BDF target, a beam test of a target prototype during 2018 was proposed back in 2017 to provide timely feedback for the European Strategy for Particle Physics process. To reach similar operational scenarios, representative beam scenarios had to be reproduced.

Since the BDF conditions require a slow extraction process, the HiRadMat facility could not be used. Considering that high-intensity slow extraction is available in the North Area target zone (TCC2), the experiment was proposed to take place upstream of the T6 primary target (thanks also to the absence of a vacuum beam pipe until roughly 15 m upstream of the T6 target assembly). This is allowed by the lack of wobbling magnets upstream of T6, unlike the case for T2 and T4. In addition, intensities of up to 10^{13} protons per pulse are regularly sent onto the T6 beryllium targets for the COMPASS experiment.

The experiment has been designed to produce levels of temperature and stress in the core and the cladding similar to what will be expected in the final BDF application, despite the different beam configuration.

The main objectives of the tests of the target prototype are summarized below.

- Reproduce experimentally the temperatures and the magnitude of the thermally induced stresses in the final target, despite the lack of dilution.
- Evaluate the response under thermal shock of the refractory-clad materials, which will be subjected to temperature increases of the order of 50–100°C per pulse.
- Cross-check the finite element model simulations performed. For that purpose, several blocks were instrumented to execute online measurements.
- Further explore the survivability of the instrumentation in challenging environments, including high levels of accumulated dose, high water speed, and pressure.
- Validate the performance of the target assembly cooling system and, specifically, the high velocity of water in contact with the blocks.
- Execute tritium out-diffusion experiments to quantitatively assess the diffusion coefficient that will be employed in the environmental impact study for the final installation.
- Perform detailed post-irradiation experiments after irradiation.

More details of these objectives will be given in the following sections.

5.9.2 Design of the target prototype

5.9.2.1 Mechanical design of target prototype

The target replica that was tested in the North Area consists in a reduced-scale prototype of the final BDF target. The target prototype cylinders have a diameter of 80 mm (instead of 250 mm), and the same length distribution as in the final target. The core materials used in the target replica are equivalent to those of the final target: the first 13 blocks are made out of forged TZM and the last five out of sintered + HIP pure tungsten. The cladding materials used are pure tantalum and Ta2.5W, to compare the performance of the two materials under beam irradiation conditions.

The pure tungsten blocks are all clad with pure tantalum and not with Ta2.5W. This is because at the design stage of the target prototype, good mechanical and chemical bonding between tungsten and Ta2.5W could not be achieved via HIPing. Successful bonding was accomplished later on by changing the HIP parameters (see Section 5.8), justifying the use of Ta2.5W as a cladding material for all of the target blocks [8].

A summary of the materials and dimensions of the target prototype cylinders is given in Table 5.27.

Table 5.27: Description of BDF target prototype blocks, with core and cladding material as well as total length and weight of each block.

Block number	Core material	Cladding material	Length (mm)	Weight (kg)
1	TZM	Ta	80	4.1
2	TZM	Ta2.5W	25	1.3
3	TZM	Ta2.5W	25	1.3
4	TZM	Ta2.5W	25	1.3
5	TZM	Ta2.5W	25	1.3
6	TZM	Ta2.5W	25	1.3
7	TZM	Ta2.5W	25	1.3
8	TZM	Ta	25	1.3
9	TZM	Ta2.5W	50	2.6
10	TZM	Ta	50	2.6
11	TZM	Ta	65	3.3
12	TZM	Ta	80	4.1
13	TZM	Ta	80	4.1
14	W	Ta	50	4.7
15	W	Ta	80	7.5
16	W	Ta	100	9.4
17	W	Ta	200	18.8
18	W	Ta	350	32.9

Similarly to the final BDF target, the prototype assembly includes two concentric stainless steel tanks. The outer tank ensures the leak-tightness of the assembly, compatible with an operational pressure of 22 bar; it provides an interface for the electrical and water connections; and it encloses an inner stainless steel tank. The inner tank supports the target blocks and encloses the prototype cooling circuit.

The prototype inner tank differs significantly from the final design of the target inner tank. In this case, the target prototype blocks are much lighter, and do not require a specific handling tool for assembly. The inner tank consists of two half-shells, clamped together with bolts. The target blocks sit on the lower shell of the inner tank, constrained only in the Z direction by two pins that allow free-body expansion of the blocks within a range of 50 µm, but ensure a gap of 5 mm between the blocks, necessary for the water cooling to act on the surface of the blocks.

The inner-tank shells were designed taking into account the water circulation foreseen for the cooling system of the target prototype. A more detailed description of the cooling circuit is given in the following sections. The inner-tank upper shell includes several grips to allow the removal of the half-shell via remote handling, which is necessary for the remote extraction of the target blocks for PIE (see Section 5.9.8). A schematic illustration of the inner tank can be seen in Figs. 5.117 and 5.116, where the target prototype blocks and the different materials used are also shown.

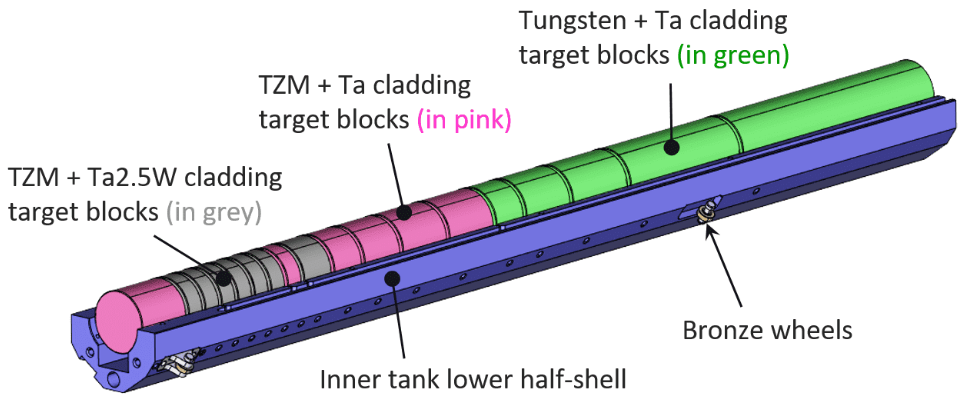

Fig. 5.116: Description of lower shell of inner tank and target blocks of BDF target prototype

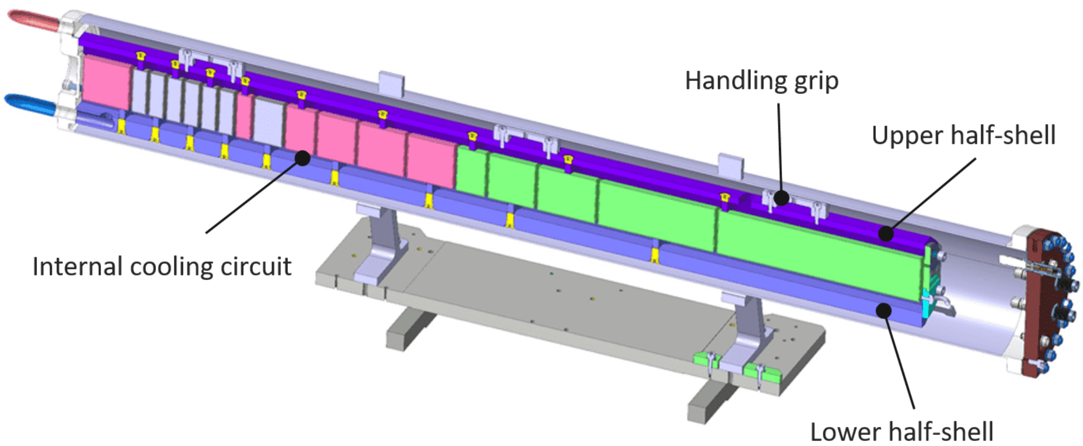

Fig. 5.117: Longitudinal cross-section of the target prototype inner tank inserted into the outer tank. The upstream and downstream flanges are also represented.

The target inner tank is mounted on four bronze wheels, which allow insertion of the tank into the outer tank. Once inserted, the inner tank is bolted to the upstream flange of the outer tank. The outer tank has two guides in its inner surface that serve as alignment guides for the inner tank, ensuring correct positioning of the target with respect to the beam axis.

The downstream part of the tank is closed by an end flange that includes all the feedthroughs for the target instrumentation (see Section 5.9.4). The water connections are located in the upstream flange of the outer tank, and the pressure drop in the whole target assembly can be measured via two pressure sensors installed in the water connection pipes. The outer tank is considered as a pressure vessel capable of safely withstanding the 22 bar operational pressure of the cooling system (tested to 31 bar, with a safety factor of 1.43 [42]). Figure 5.118 shows the outer-tank assembly with the inlet and outlet of the cooling system.

The whole target assembly is placed on a motorized table with a horizontal movement that permits

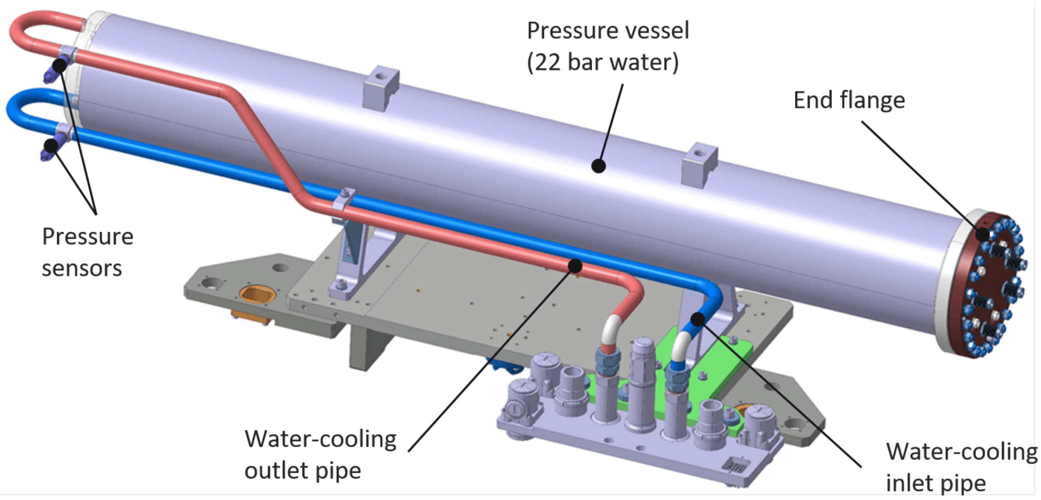

Fig. 5.118: Description of BDF target prototype outer tank. The modified LHC collimator plug-in, the water-cooling pipes, and the intermediate connection plate are visible.

one to align the target with the beam axis for beam tests, and remove it from the beam after operation. A modified LHC collimator plug-in table is used as an intermediate support between the outer tank of the target and the motorized table. The standard collimator support is made out of two plates designed in such a way that the upper plate can be installed on top of the lower plate by means of remote handling. This set-up allows the remote installation, replacement, and removal of the whole target assembly (inner tank, outer tank, and collimator top plate) by using only the remotely manipulated crane in the TCC2 target complex zone. This is a critical implementation owing to the limited access to TCC2 during installation, and the high dose rate expected at the end of the beam irradiation period.

Additionally, a specific interface was needed to perform the remote connection and disconnection of the water and electrical connectors. Because of the specific requirements of high water flow, high pressure, and high radiation levels, the LHC collimator plug-in connection had to be significantly modified. Dedicated R&D was carried out to develop a plug-in system for the water and signal connections suitable for the target prototype application, leading to a fully metallic system. Figure 5.119 describes the different subassemblies of the whole target prototype and support assembly (a), as well as the remote installation and dismantling procedure (b).

5.9.2.2 Beam parameters and thermomechanical calculations

5.9.2.2.1

Target prototype beam parameters

The target prototype was tested in TCC2 using a non-diluted primary proton beam (no diluter is available in the TDC2/TCC2 area) and the same cycle as for the final BDF target (i.e. a spill length of 1 s and a repetition rate of 7.2 s). Consequently, the beam intensity required to reach representative temperatures and stresses with respect to the final target was lower and was expected to be in the range of 3–4$\times 10^{12}$p^{+}/cycle. Table 5.28 shows a comparison between the beam parameters for the final BDF target and for the target prototype.

5.9.2.2.2 Thermal calculations

The energy deposited in the target by the SPS 400 GeV/c beam was calculated via FLUKA simulations, and imported into ANSYS Mechanical for thermostructural analysis. Detailed CFD calculations were also performed, defining the water-cooling parameters of the target prototype to obtain a homogeneous

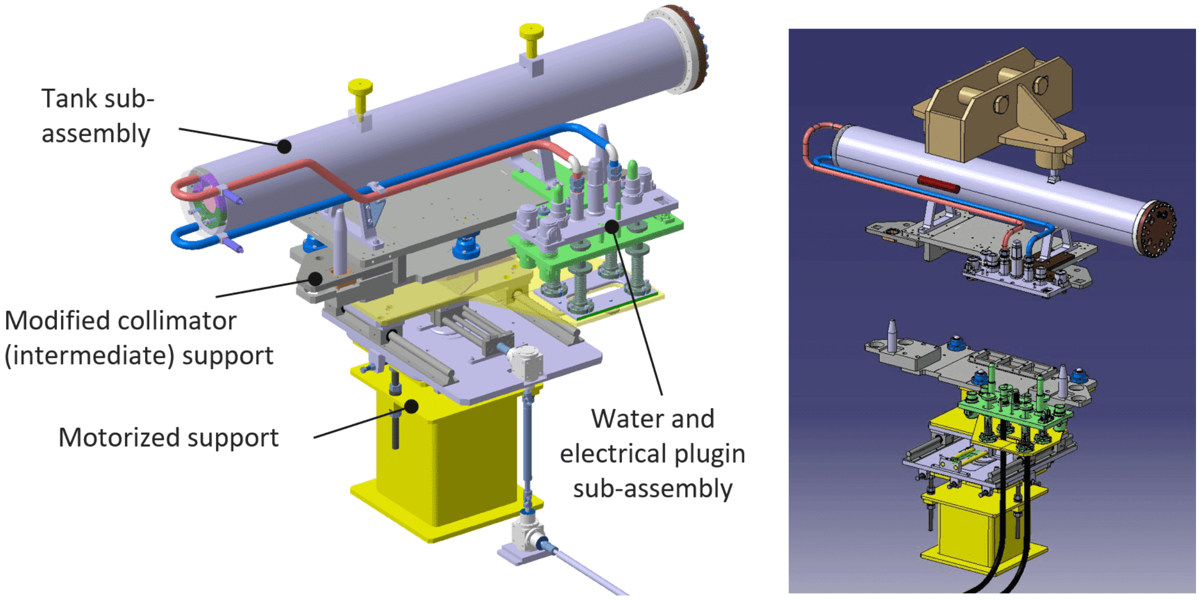

Fig. 5.119: (a) Motorized support, plug-in system, and intermediate support for BDF target prototype. (b) Representation of the remote installation/removal of the target assembly.

Table 5.28: Summary of beam parameters for final target and target prototype

Baseline characteristics	Final BDF target	BDF target prototype
Proton momentum (GeV/c)	400	400
Beam intensity (p^+/cycle)	4×10^{13}	$3–4 \times 10^{12}$
Beam dilution	4 circular sweeps/s	No
Expected beam spot size (H/V) (mm)	8/8	3/3
Cycle length (s)	7.2	7.2
Spill duration (s)	1.0	1.0
Average beam power (kW)	350	35
Average beam power on target (kW)	305	30
Average beam power during spill (MW)	2.56	0.26

water velocity distribution in the channels between the blocks (see next section). The estimated average value of the heat transfer coefficient on the surface of the blocks is around 16 000 W/($m^2 \cdot K$), which was used as a boundary condition for the thermal analysis.

A comparison between the maximum temperatures estimated in the materials of the final target and the prototype at two different beam intensities is shown in Fig. 5.120. The temperatures reached with 3×10^{12} and 4×10^{12} p^+/pulse in the TZM core and the cladding materials are higher than those expected in the final target. For the pure W core, the temperature reached with 3×10^{12} p^+/pulse is 20% lower than in the final application, which justifies the use of a higher-intensity beam for the prototype test. With 4×10^{12} p^+/pulse, the temperatures reached in the pure W core are comparable to those in the final target.

Figure 5.121 presents the temperature distribution in the target prototype at the end of a beam impact. It can be seen that the temperature distribution differs from that obtained in the final BDF target (see Fig. 5.4), which can be explained mainly by the fact that the beam is diluted into a circular trajectory in operation of the final BDF target, in contrast to the prototype test, where the beam impacts directly on the centre of the target.

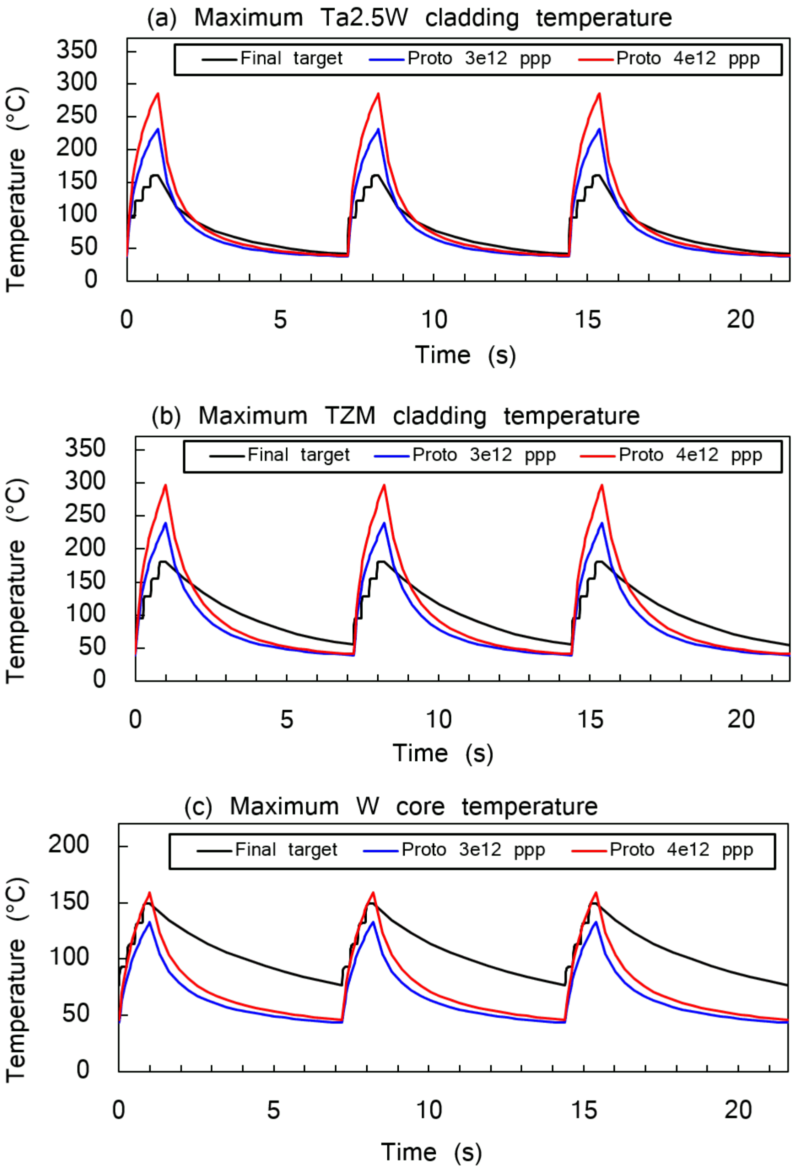

Fig. 5.120: Evolution of maximum temperature during three beam pulses after steady state for the different target materials: (a) Ta2.5W cladding of block 4 of the final and prototype targets, (b) TZM core of block 9 of the final target and TZM core of block 4 of the target prototype, (c) W core of block 14 of the final and prototype targets. Comparison of results for the operation of the final target and the prototype under 3×10^{12} or 4×10^{12} protons per pulse.

Despite the impacted area being different, the thermally induced stresses are expected to have the same effect on the interface between the refractory metal core and the cladding material, which is one of the main objectives of the beam test.

5.9.2.2.3 Structural calculations

The evolution of the temperature distribution with time was imported as an input for the structural analysis. The stresses induced by the temperature increase were considered as quasi-static (similarly to the case of the final BDF target), since the pulse duration of 1 s can be considered as long enough for the dynamic effects in the materials to be negligible.

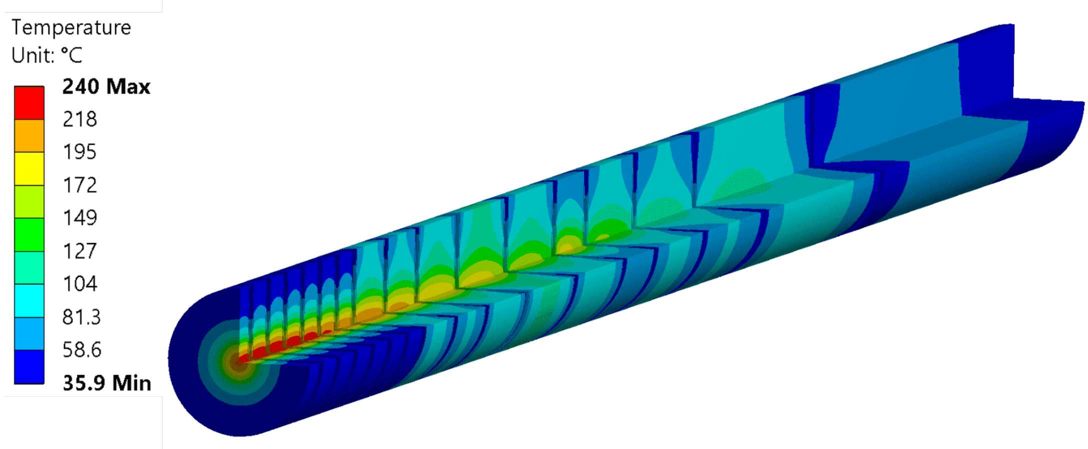

Fig. 5.121: Temperature distribution in the BDF target prototype after a beam impact. The maximum temperature reached is around 240°C, found in the TZM core of block 4.

Table 5.29: Maximum stresses expected in the target materials for the final target and the target prototype at two different intensities. For TZM and Ta2.5W, the maximum von Mises equivalent stress is shown; for pure tungsten the maximum principal stress is shown.

Material	Maximum stress (MPa)		
	Final target	Target prototype 3×10^{12} p^+/pulse	Target prototype 4×10^{12} p^+/pulse
TZM	128	116	160
W	80	70	85
Ta2.5W	95	90	120

A comparison between the maximum stresses in the different target materials obtained for the final BDF target and for the prototype in tests at two different intensities is shown in Table 5.29. It can be observed that for an intensity of 3×10^{12} p^+/pulse on the BDF target prototype, a similar level of stresses to that in the final BDF target is reached. Higher intensities such as 4×10^{12} were considered for the target prototype, which will be subjected to slightly more challenging conditions than the final BDF target. It can be seen that the level of stresses in this case is higher than for the final target, especially for the TZM core and the Ta2.5W cladding (20% higher stress), but still within the material limits. Higher intensities were also considered to compensate for beams expected to be slightly larger than those requested (3 mm 1σ).

The aim of the experiment was to reach around 10^4 pulses on target. This number of cycles is substantially lower than that one expected on the final BDF target ($N = 10^7$ over the lifetime of the assembly), but it will help in understanding the response of the materials to high-cycle fatigue and the robustness of the core/cladding interfaces. Figure 5.122 shows a comparison between the evolution of the maximum equivalent stresses in TZM, W, and Ta2.5W for the final BDF target and the target prototype at the two different intensities. The results plotted correspond to the position where the maximum stresses are reached in the most loaded target blocks (block 4 for TZM and Ta2.5W, and block 14 for tungsten).

The calculations performed showed that the mean stress and stress amplitude are expected to be well reproduced in the target prototype tests for the two different intensities. However, there are some limitations on recreating the stress state of the final target blocks. As shown in Fig. 5.123(a), the maximum von Mises equivalent stress in the cladding materials is reached in the external surface of the cladding, about 10 mm from the beam axis. For the core materials, the maximum stresses are reached in

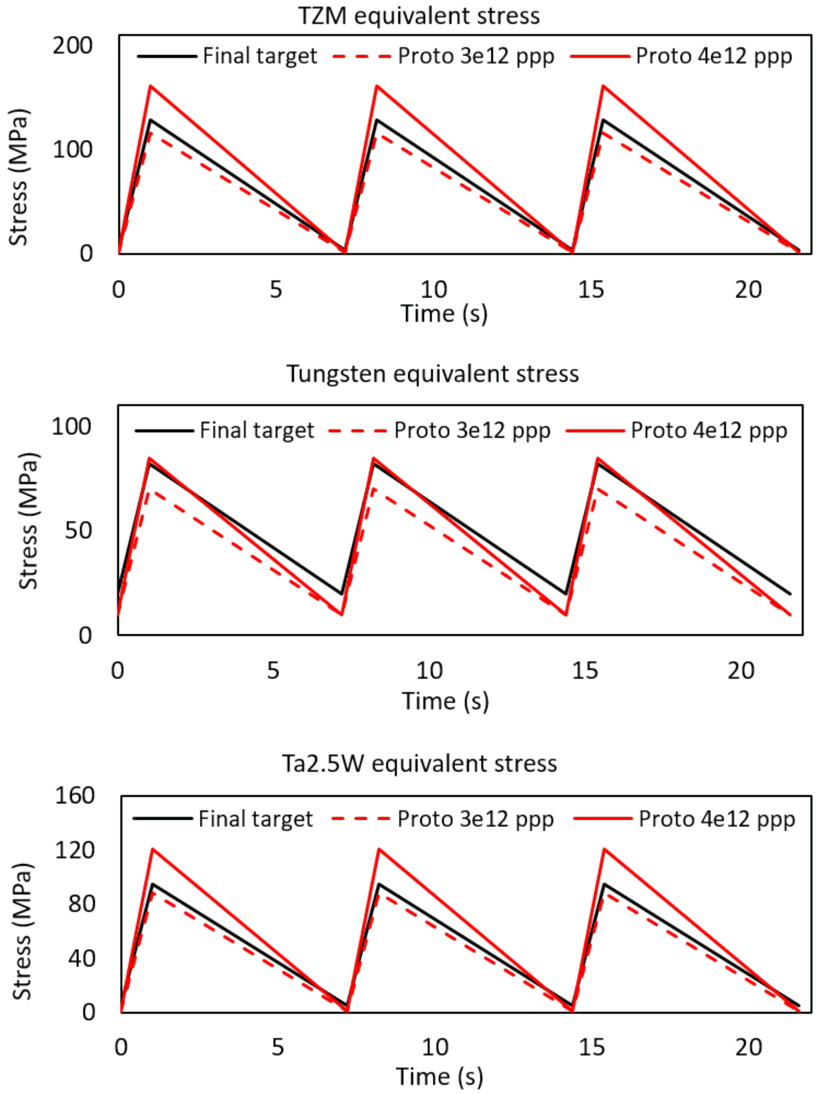

Fig. 5.122: Evolution of the equivalent stress in the target materials during three beam pulses (once steady-state conditions have been reached). The plots show a comparison between the final BDF target and the BDF target prototype at two different intensities.

the centre of the core and at the bonding interface with the cladding layer, 5–10 mm from the beam axis as well (Fig. 5.123(b)).

This stress distribution differs from that in the final BDF target, where the maximum stresses are expected to follow the beam impact trajectory (Fig. 5.20). The difference between the two stress distributions can be explained by the fact that the beam is diluted in one case and not in the other, leading to a different temperature distribution and therefore to a different stress field.

The evolution of the stresses at a given point in the target is also different depending on whether or not beam dilution is used. As shown in Fig. 5.21, the von Mises equivalent stress at a given point in the final BDF target increases, with a clear influence of the beam dilution. In the BDF target prototype the situation is different, since the beam impact always occurs in the centre of the target. A comparison between the evolution of the von Mises equivalent stress at the points of maximum stress in the Ta2.5W cladding of block 4 of the final target and of the target prototype at 3×10^{12} and 4×10^{12} p^{+}/pulse is presented in Fig. 5.124.

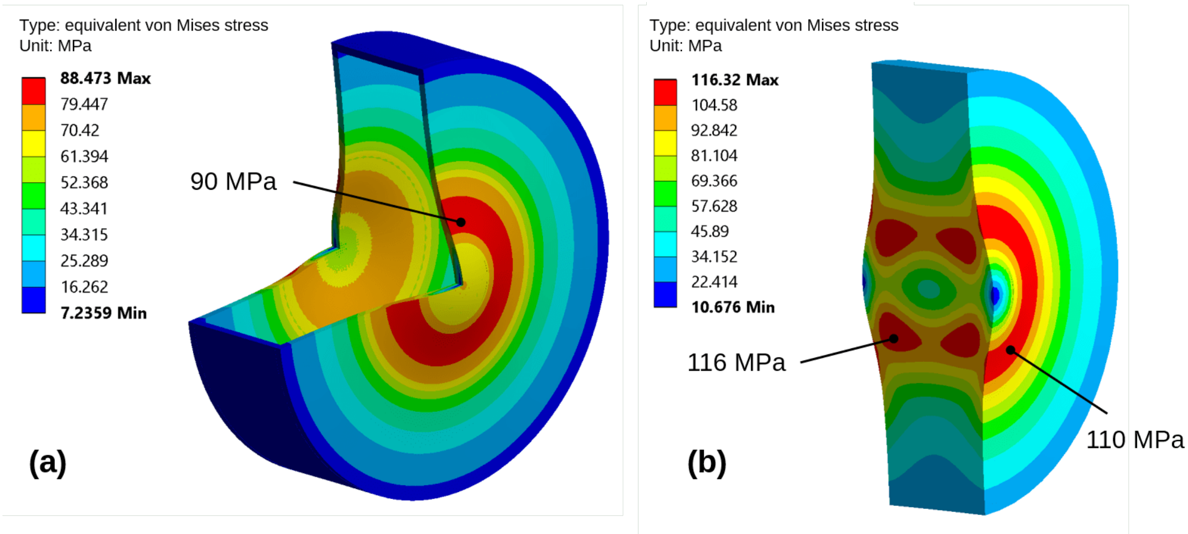

Fig. 5.123: Distribution of von Mises equivalent stress in the Ta2.5W target cladding (a) and in the TZM core (b) of block 4 of the target prototype. Results for 3×10^{12} p^+/pulse.

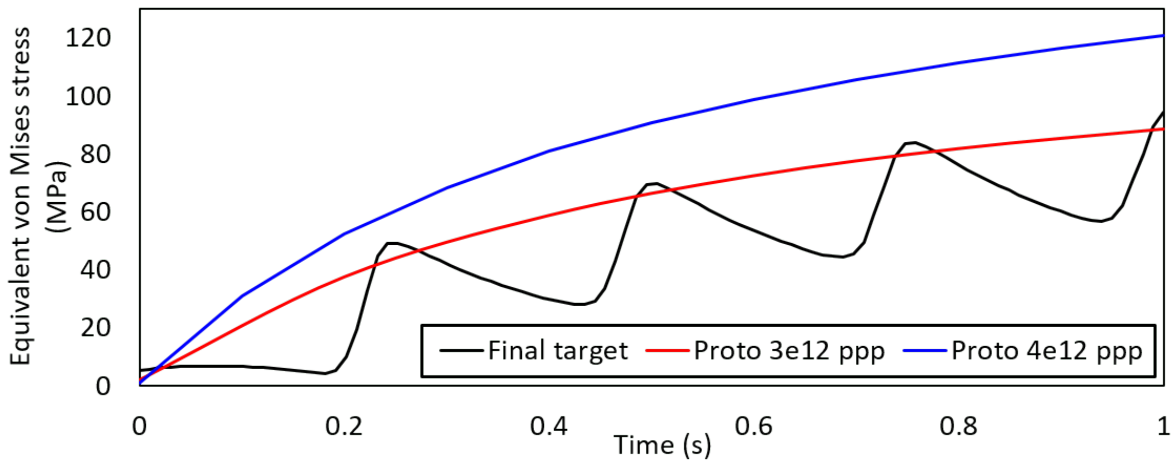

Fig. 5.124: Evolution of von Mises equivalent stress at the point of maximum stress of the Ta2.5W cladding (block 4) during a beam impact of 1 s. Comparison between the final target and the target prototype at two different intensities.

The absence of beam dilution in the target prototype tests leads to some limitations in reproducing the stress state in the prototype blocks. However, it has been shown that the maximum level of stress predicted in the final target is expected to be recreated and even surpassed in the operation of the target prototype, which will provide—when the data collected is fully exploited—fundamental information on the robustness of the design of the final BDF target.

5.9.2.3 Prototype cooling system and CFD analysis

The design of the target prototype cooling system was intended to provide an initial validation of the final design of the cooling system for the BDF target. The cooling design for the BDF target prototype replicates the major features of the final target cooling system:

– water cooling at a high pressure of around 22 bar;
– 5 mm channels (allowing the placement of sensors on the surface of the blocks);

- significant water speed between plates (up to 4 m/s);
- serpentine configuration of the water flow.

The prototype cooling design also includes some differences with respect to the final target, owing to the specific design of the experiments and the available SPS beams:

- reduced-size channels, owing to the diameter of the blocks being only 80 mm instead of 250 mm;
- a channel flow velocity lower than that expected in the final BDF target, i.e. 4 m/s rather than 5 m/s;
- one stream circulating in series instead of two parallel streams following the serpentine path.

Several flow configurations were investigated to minimize the required mass flow rate and at the same time obtain a uniform fluid velocity and high HTC in the channels. Each configuration had a specific combination of number of parallel channels and number of turns along the target body. For the specific set of parameters of the BDF target prototype, the single-channel (serpentine) configuration presented in Fig. 5.125 was found to be the optimal one in terms of flow velocity uniformity and overall mass flow rate.

Figure 5.126 shows the 3D flow distribution in the water volume of the inner vessel; the high velocity in the gap between the plates is very clear. Figure 5.127 illustrates the static pressure distribution at the surface of the fluid volume, and provides an estimate of about 2.5 bar for the pressure drop along the target.

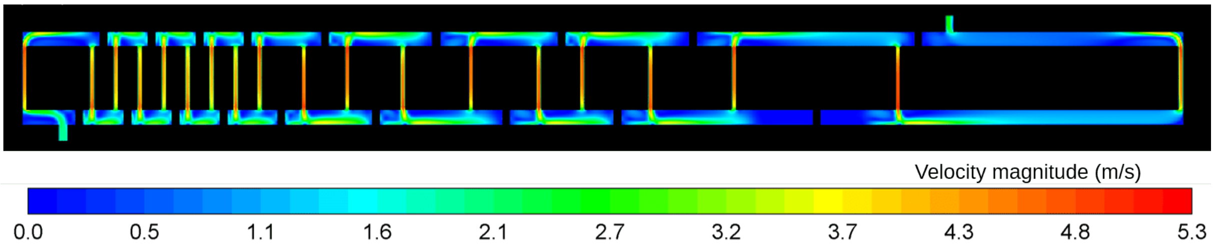

Fig. 5.125: 2D contours of velocity magnitude (m/s) in the target prototype cooling system, with a serpentine configuration.

The results of the thermal simulations described in the previous section show that, owing to a combination of low thermal conductivity, high power deposition, and potential localized boiling, the cladding temperature is a critical parameter. To limit the cladding temperature, a surface heat transfer coefficient of about 16 000 W/m^2·K was assumed in the FEM calculations by selecting the average flow velocity in the vertical gaps to be 4 m/s. In reality, the actual value of the HTC predicted by the simulations is slightly higher and non-uniform, as shown in Fig. 5.128, providing conservative values.

Transient simulations for this configuration showed that the predicted peak surface temperature at 3×10^{12} p$^+$/pulse in the cladding of block 4 (the most critical block from a thermal standpoint) is about 180°C, well below the boiling point of water at 22 bar ($\sim$ 212°C). The temperature distribution along the longitudinal axis in block 4 is shown in Fig. 5.129. The peak temperature after a beam impact is about 225°C, found in the centre of the TZM core.

It should be noted that the results of the CFD (Fig. 5.129) and FEM (Fig. 5.121) simulations show a discrepancy in the temperature field with a maximum value of 15°C. The peak temperature in the TZM core of block 4 obtained from the calculations in ANSYS Mechanical is around 240°C. This difference is due to the fact that the FEM simulation assumes a constant HTC value on all wetted surfaces (calculated from a correlation for fully developed flow), while the CFD simulation accounts for the actual HTC distribution. This discrepancy is negligible in the context of the corresponding analyses.

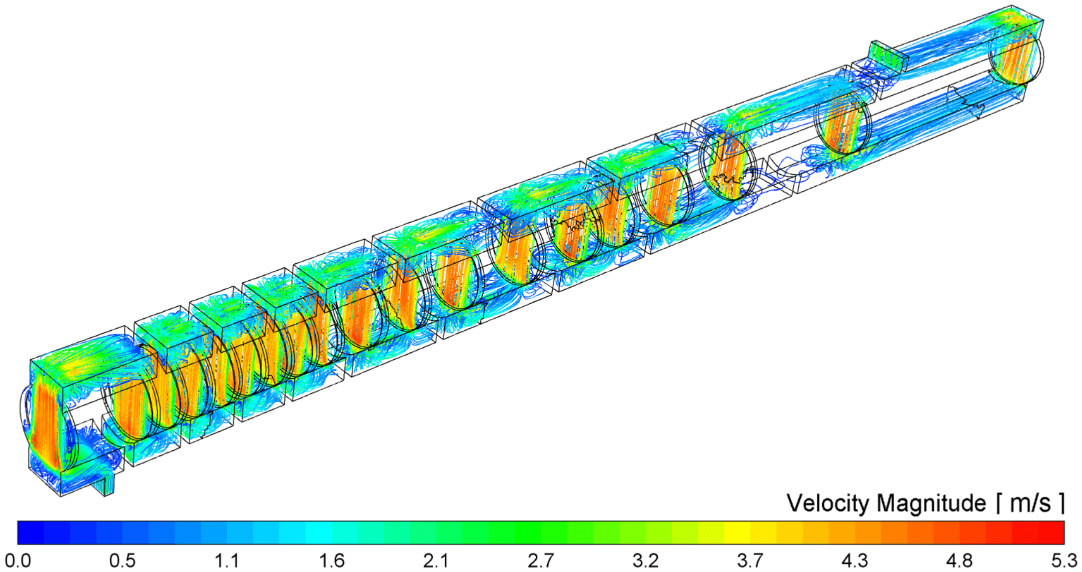

Fig. 5.126: Path lines coloured by velocity magnitude (m/s) from a 3D CFD simulation of the BDF target cooling system.

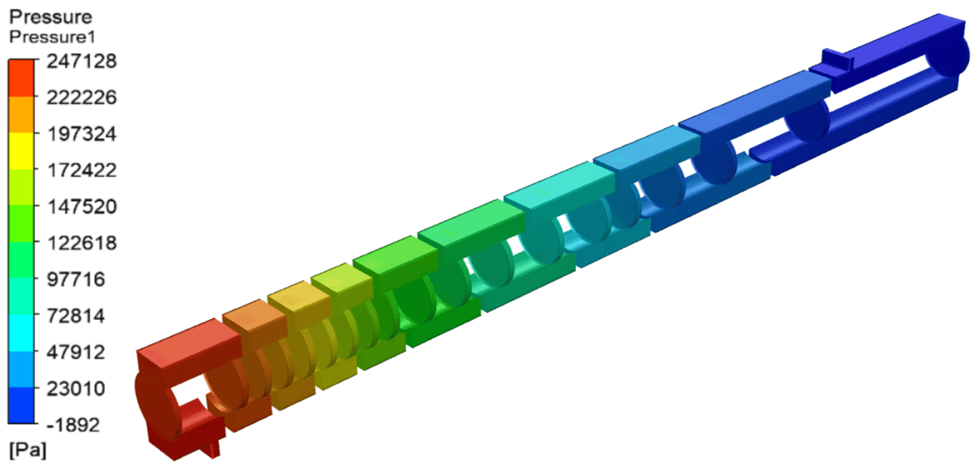

Fig. 5.127: Static pressure distribution (Pa) along the cooling circuit of the target. The total pressure drop is approximately 2.5 bar.

With respect to the water temperature distribution, the thermal inertia of the blocks smooths out the rapid variations of the power with time, and the resulting outlet water temperature oscillates only slightly around its average, as shown in Fig. 5.130.

5.9.3 Target prototype construction and assembly

5.9.3.1 Prototype construction

The manufacture of the target inner tank was carried out by an external contractor. In parallel, the outer tank was manufactured at CERN. Figures 5.131 and 5.132 present several views of the inner and outer tanks.

The production of the target core blocks was one of the most challenging aspects of the construction of the prototype. The prototype blocks were made out of different parts, following a similar process to the one foreseen for the production of the final target blocks (described in Section 5.7). For the manufacture of the prototype blocks via the HIP process, several parts made of different materials

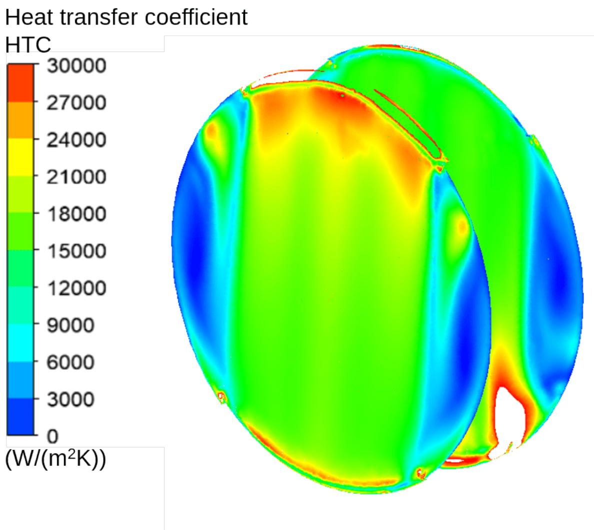

Fig. 5.128: Distribution of heat transfer coefficient in the front surface of block 4

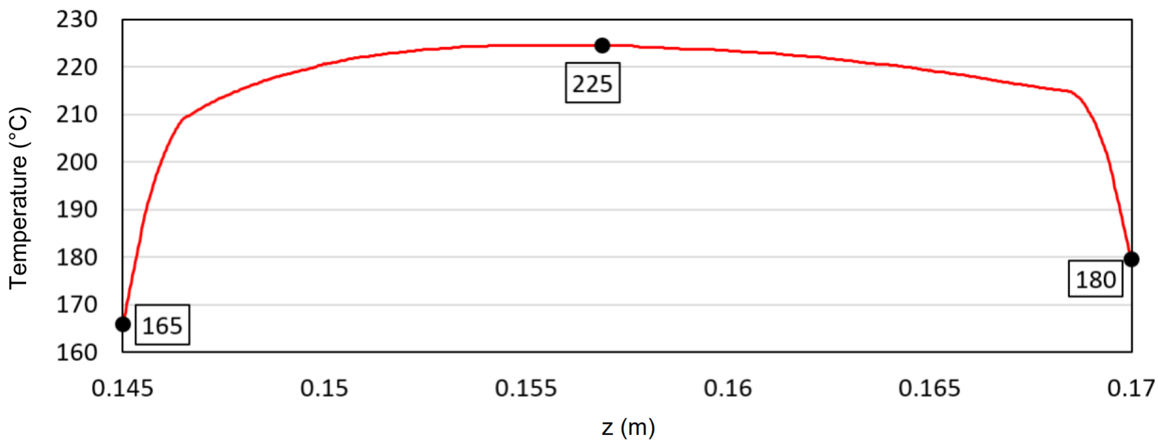

Fig. 5.129: Temperature distribution along z axis in block 4 at the end of the beam pulse (peak profile). Maximum temperature in the cladding surface $\approx 180°$C, peak temperature in the block $\approx 225°$C.

were needed. Each target block was made out of four different parts:

– one TZM or W cylinder with diameter 77 mm and a length according to the position of the block in the target;
– one Ta2.5W or Ta tube with inner diameter 77 mm, outer diameter 80 mm, and variable length;
– two Ta2.5W or Ta discs with diameter 77 mm and thickness 3 mm.

In the first stage, the parts were produced on the premises of an external supplier and received at CERN. All the parts were tested with ultrasound, and mechanical and chemical testing at the contractor's premises. Furthermore, vacuum leak testing was performed at CERN once the parts were received. The TZM and W cylinders and the Ta2.5W and Ta discs were requested to have larger diameters than the values mentioned above. Then, precise machining was performed at CERN to ensure the required 0.1 mm gap between the cylinders or discs and the Ta or Ta2.5W tubes. The machined parts prior to the HIP process can be seen in Fig. 5.62.

Once the machining was performed, the target parts were sent to an external contractor for the production of prototype blocks via HIPing. The manufacturing process of the prototype blocks was

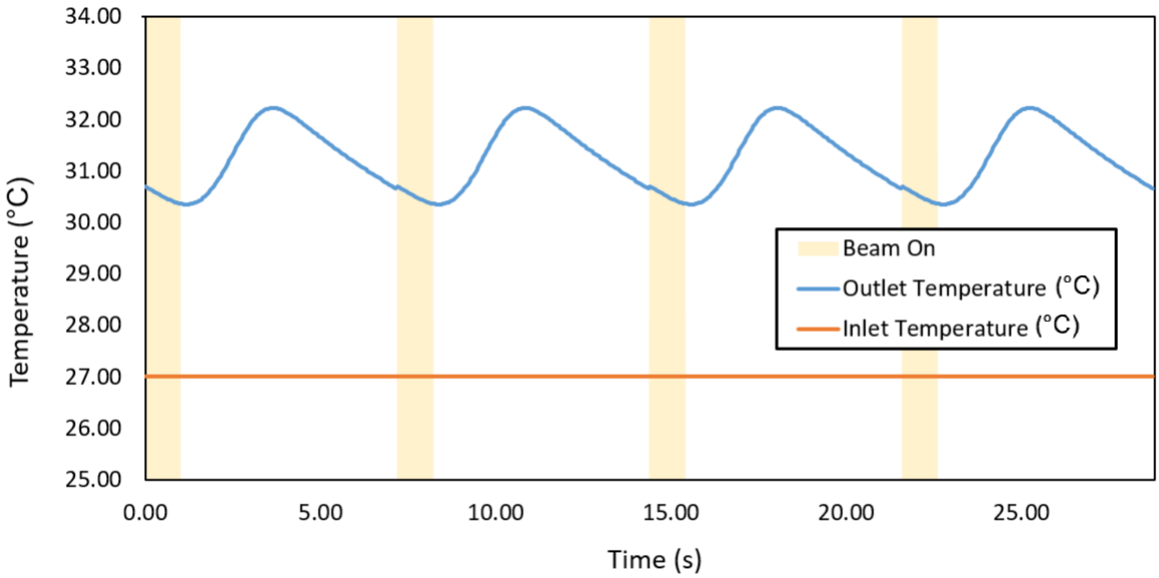

Fig. 5.130: Target inlet and outlet water temperatures as a function of time. Evolution during four beam pulses after long-term operation.

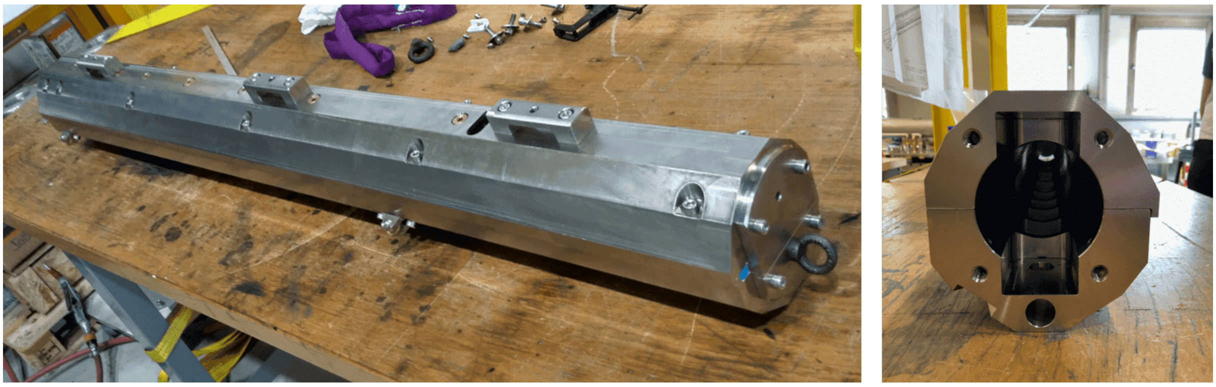

Fig. 5.131: Side and front views of BDF target prototype inner tank. Lower and upper half-shells mounted without target blocks. The right image shows clearly the housing of the target blocks.

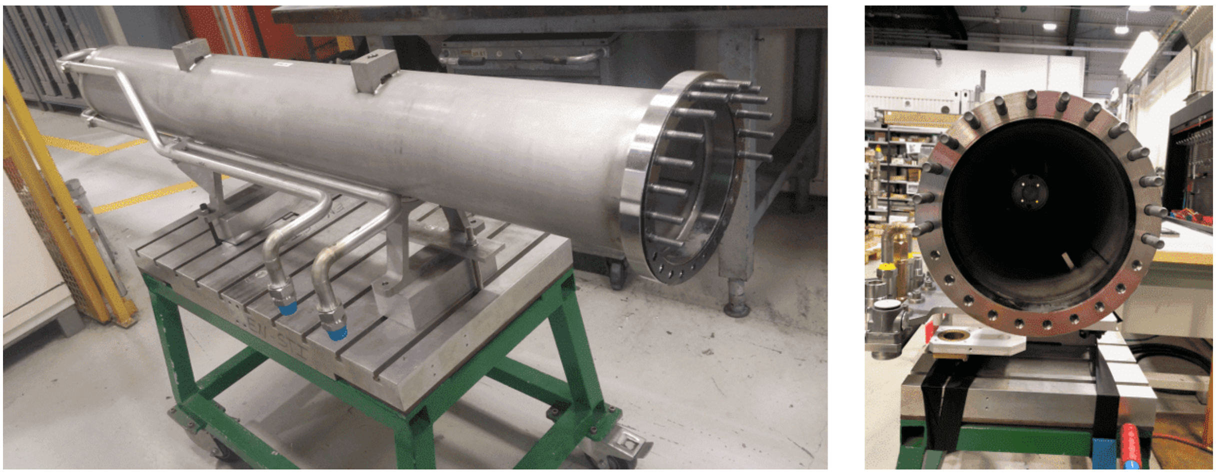

Fig. 5.132: Side and front views of BDF target prototype outer tank

identical to that of the final target blocks described in Section 5.7. Figure 5.133 shows the parts of one target block mounted before HIPing, and a finished target block after HIPing and final machining.

Fig. 5.133: Target block parts mounted before the HIP process (left), and after the HIP run and subsequent machining performed with the objective of matching the required sizes to house the blocks in the target inner tank (right).

5.9.3.2 Prototype testing and assessment

Prior to the full assembly of the target prototype, several tests on the target prototype housing were carried out.

- The target outer tank was tested at a pressure of 31 bar to assess the leak-tightness and pressure compliance of the tank with a safety factor of 1.43 with respect to the operation pressure of 22 bar [42].
- The fully metallic plug-in for the water and electrical connections was connected to the outer tank and tested at 31 bar static pressure and 22 bar with circulating water flow. Figure 5.134 shows the plug-in connection of the female and male plates before installation and the plug-in installed in the outer tank with the connection performed for testing.
- Several 'dummy' copper blocks were mounted on the inner-tank lower shell to perform and consolidate the assembly of the inner and outer tanks, as can be seen in Fig. 5.135. Some of the copper blocks were equipped with instrumentation cabling to simulate the instrumentation of the prototype blocks.
- Cooling tests were executed with the whole target assembly (with dummy copper blocks) to confirm the good functioning of the target cooling system. The measured value of the pressure drop was approximately 3 bar, very close to the value of 2.5 bar calculated via CFD simulations. Figure 5.136 shows the experimental set-up used for the preliminary tests of the cooling system.
- Several different tests were carried out with the remote-manipulation and heavy-handling teams to simulate several operations of the process of remote installation and dismantling (lifting, unscrewing, extracting the inner tank). Figure 5.137 illustrates some of the robotics and handling tests performed.

5.9.3.3 Target prototype assembly

The final assembly of the target prototype was carried out once the production of the final blocks was achieved. Four of the target blocks were instrumented and installed in the lower half-shell of the inner tank. More details of the instrumentation of the target blocks will be given in Section 5.9.4. Figure 5.138 shows the instrumented target blocks lying on the lower half-shell.

Finally, the remaining target blocks were installed in the inner-tank lower shell. Some of the target cylinders required dedicated handling tools owing to their heavy weight (see Table 5.27). Figure 5.139 illustrates the installation procedure, as well as the full target core installed in the inner tank.

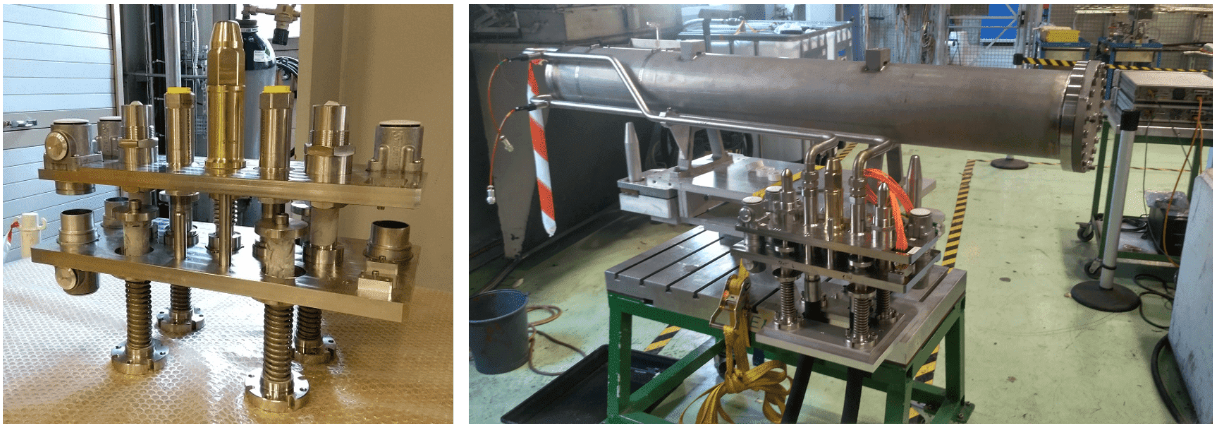

Fig. 5.134: Fully metallic connection for the water and electrical interfaces. Coupled male and female connection before installation (left); installed plug-in with coupled connection for testing (right).

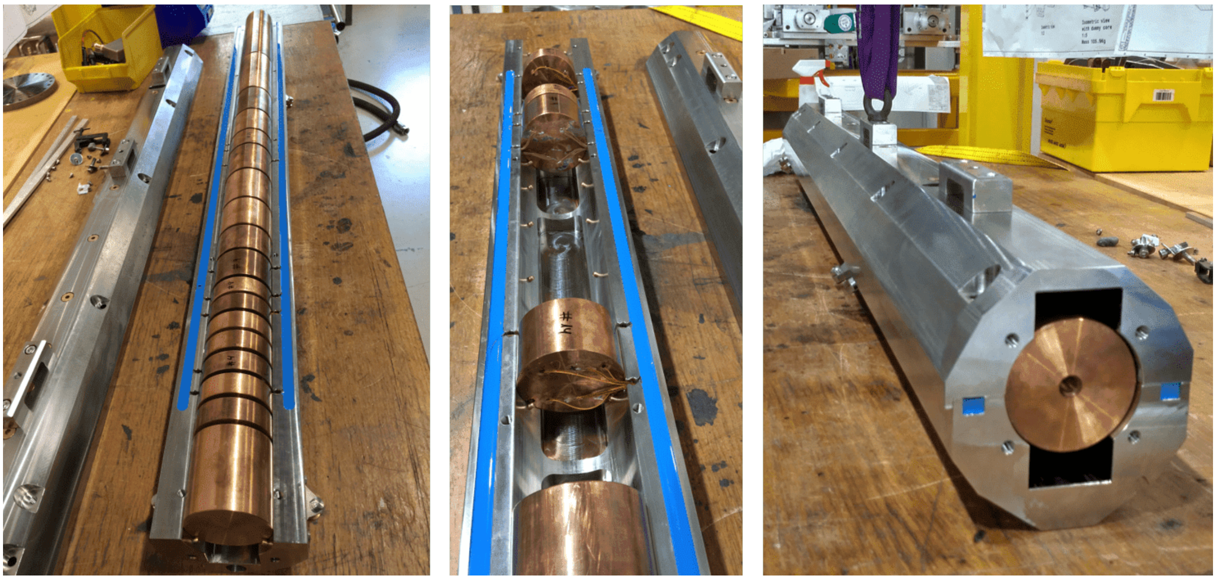

Fig. 5.135: Copper dummy blocks installed in the target prototype inner tank to validate the prototype assembly.

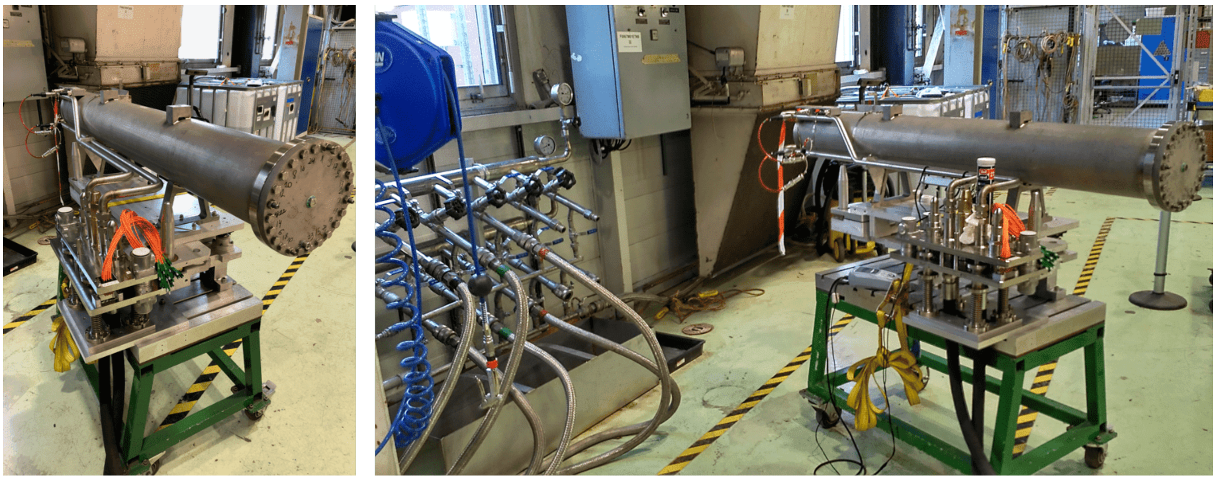

Fig. 5.136: Experimental set-up for preliminary cooling tests of the target prototype. The target prototype was tested under static pressure and under water circulation with and without 'fake' instrumentation in the copper blocks.

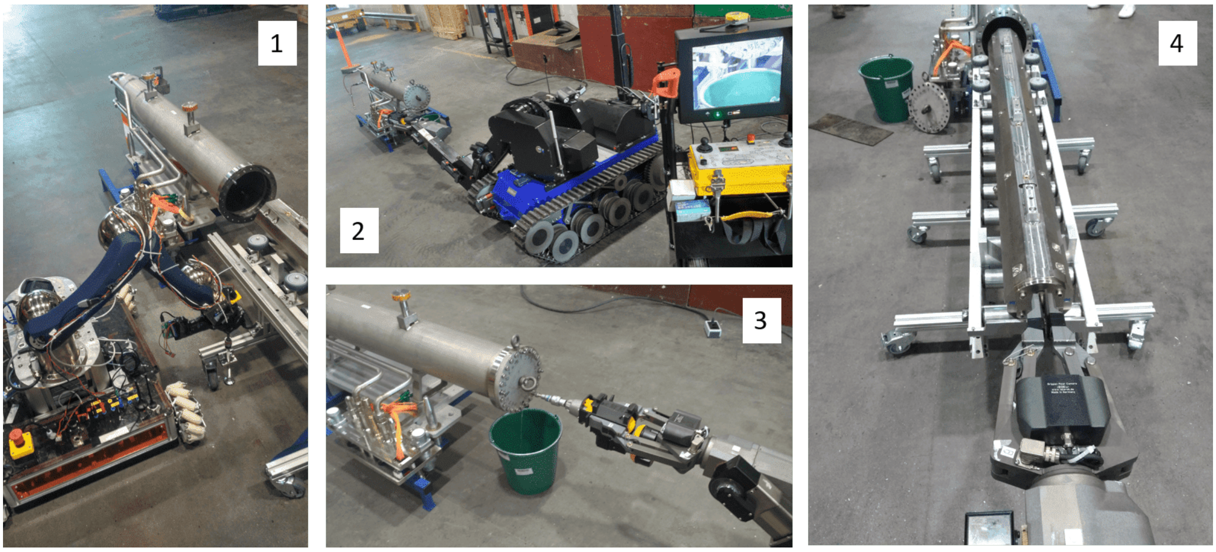

Fig. 5.137: Robot tests executed on the target prototype assembly with CERNBot (1) and Teodor (2). Simulation of dismantling operations: draining the target outer tank (3), where a bolt is unscrewed by the robot to remove all of the water remaining in the outer tank, and extraction of the inner tank (4), where the robot pulls the inner tank out of the outer tank with the help of an additional conveyor support.

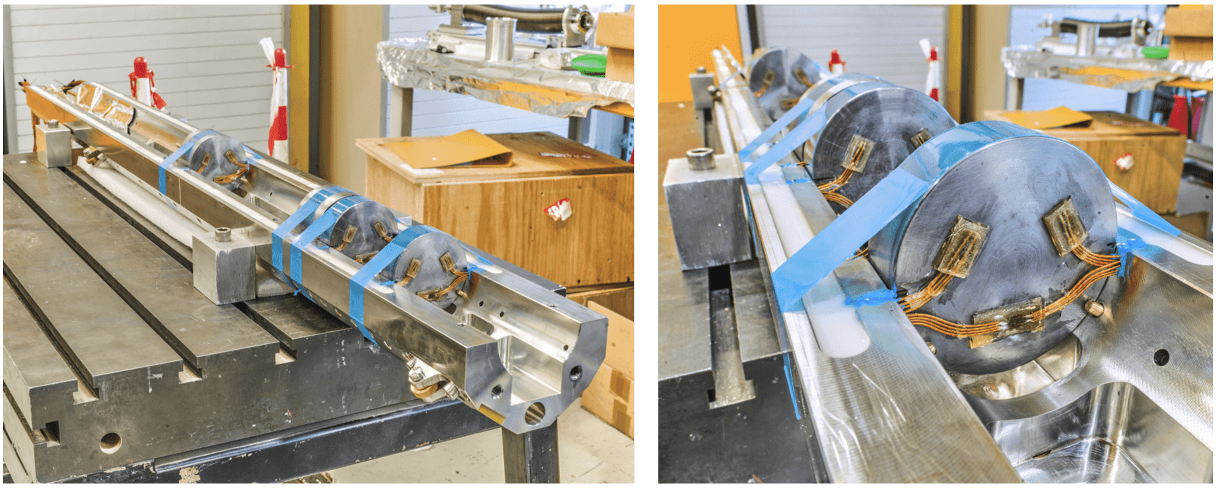

Fig. 5.138: Instrumented prototype blocks installed in the lower half-shell of the inner tank. (Photograph: J.M. Ordan [115].)

Once the inner-tank assembly was completed, it was inserted into the outer tank. Once again, dedicated tooling was necessary to safely insert the inner tank into the outer tank: a dedicated support with a conveyor mechanism aligned with the outer tank was manufactured to facilitate the insertion of the inner tank. The electrical connections from the inner tank to the feedthroughs in the downstream flange of the outer tank were performed, and the outer tank was finally closed so as to be ready for installation. Figure 5.140 illustrates the process. Before installation of the target in TCC2, cooling-water tests with the final target prototype assembly were carried out to assess the leak-tightness of the whole assembly.

Detailed pictures of the target assembly and installation can be found on the CERN Document Server [115, 116].

Fig. 5.139: Left: installation of the last tungsten block with dedicated handling equipment. (Photograph: J.M. Ordan [115]). Right: full target core assembly lying on the inner-tank lower shell.

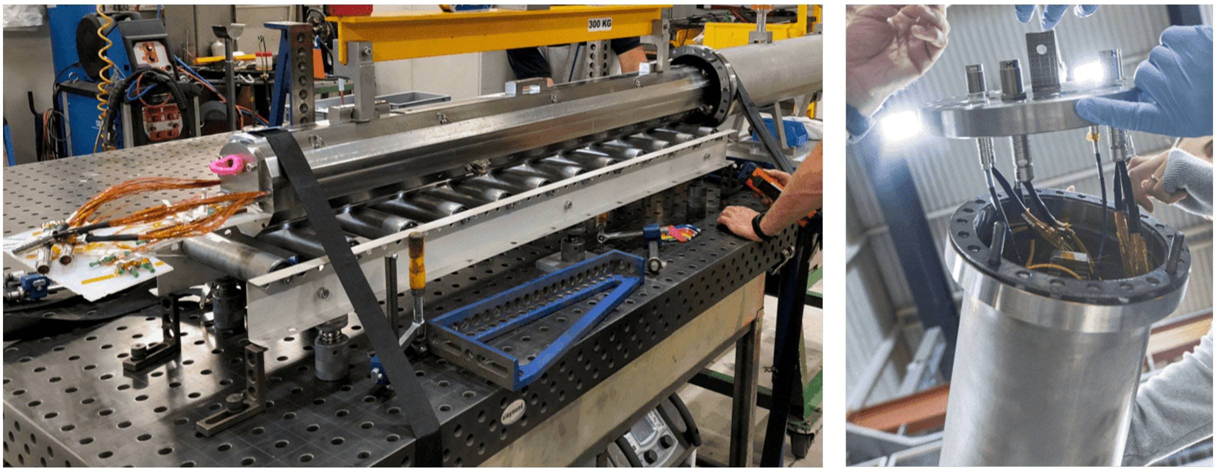

Fig. 5.140: Left: insertion of the inner tank into the outer tank with dedicated tooling. Right: connection of the instrumentation electrical wiring to the feedthroughs installed in the downstream flange of the outer tank before the tank was closed. (Photograph: J.M. Ordan.)

5.9.4 Design and development of the BDF target prototype instrumentation

5.9.4.1 Introduction

This section summarizes the design and selection of the instrumentation and electronics for the measurements of strain and temperature in four disc-shaped blocks of the BDF target prototype installed upstream of the T6 target in the TCC2 area. These sensors and services will be subjected to an underwater and pressurized environment, a high-speed water stream, high temperatures, and radiation.

The design of the instrumentation and services was done according to the results of preliminary simulations: some of the guidelines, such as expected temperature rise, strain response, and radiation dose, are shown in Fig. 5.141. The aim of the instrumentation was to validate the mechanical response and thermal models assumed for the materials and to compare the measured behaviour with the FEA simulations carried out. The locations and materials of the instrumented blocks, as well as the position of the groove for the extraction of the cabling, are indicated in Fig. 5.142.

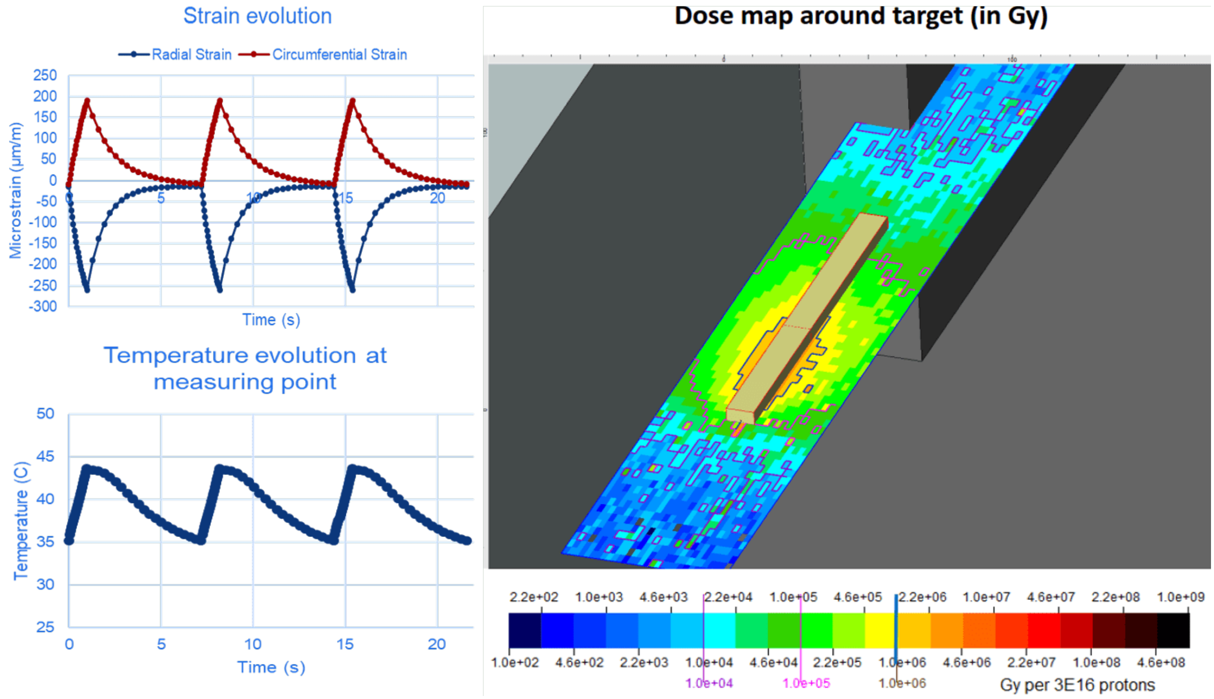

Fig. 5.141: Left: simulation of the temperature and radial and circumferential strain vs time at the measurement point. Right: total dose (in Gy) around the target at the end of the irradiation.

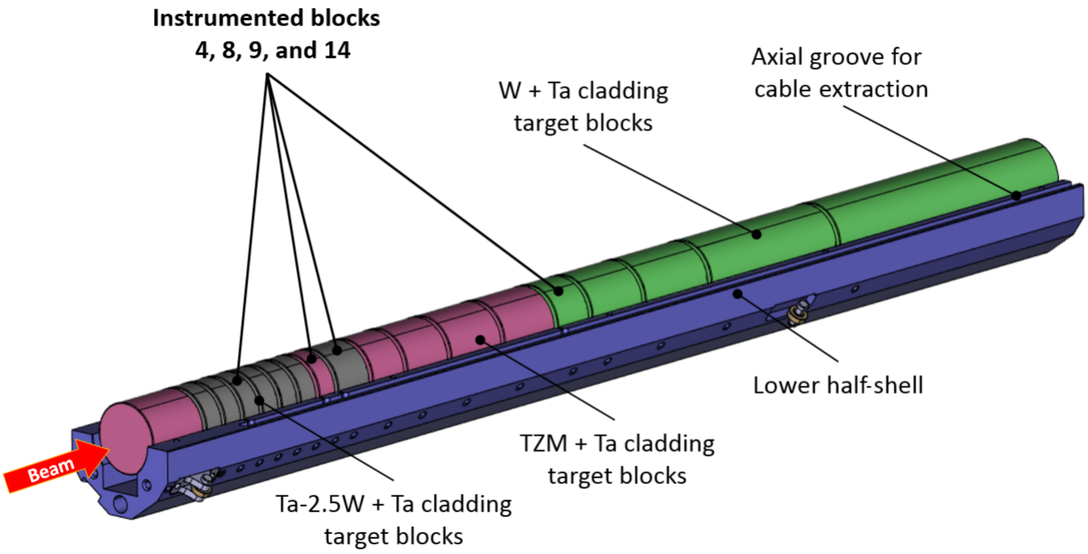

Fig. 5.142: Schematic view of the instrumented blocks for the BDF target prototype

5.9.4.1.1 Instrumentation requirements

It is required to measure the temperature and the radial and circumferential strain at several points on the flat surfaces (on the upstream and downstream sides) of the blocks. The first step in making the choice of instrumentation was to consider the harsh working environment of the experiment, which imposes some minimum requirements on the sensors for them to function, as shown in Table 5.30.

These requirements imposed the choice of waterproof/watertight, radiation-hard, and pressure-resistant equipment. The second step was to consider the capability to accurately measure the physical

Table 5.30: Requirements imposed on the instrumentation of the BDF target prototype by the environmental conditions of the experiment.

Environmental feature	Requirement/maximum value
Underwater	Waterproofness
Pressure (bar)	22
Water flow (m/s)	4.2
Maximum temperature (°C)	200
Total dose (MGy)	100

quantities of interest, meaning acquiring the related signal amplitudes and frequencies, as listed in Table 5.31.

Table 5.31: Requirements of measurements

Physical quantity	Requirement/maximum value
Strain (µm/m)	500
Time response of strain (ms)	100
Temperature (°C)	200
Time response of temperature (s)	1

Other restrictions were imposed by the design of the BDF target prototype and needed to be considered in order to implement correctly the application of the sensors and their cabling (such as restrictions on the maximum number of cables and their length). These are summarized in Table 5.32.

Table 5.32: Design requirements of BDF target prototype and their impact on instrumentation

Geometrical parameter	Value
Gap between neighbouring blocks (mm)	5
Max. distance from sensor to feedthrough flange (mm)	1560
Cross-section for cable passage through block (mm^2)	10×2
Cross-section for passage of axial cables (mm^2)	10×12

5.9.4.2 Proposed instrumentation and services

Taking into account the requirements and constraints of the beam experiment, it was proposed and agreed to instrument the following measurement points on the blocks (see Fig. 5.143).

- *Blocks 4, 8, and 14*: three measurement points at 120°on the upstream faces for radial and circumferential strain, one of the points coinciding with the vertical (with resistive biaxial strain gauges). Two measurement points at 180°on the downstream faces for radial and circumferential strain, coinciding with the horizontal (with optical fibre sensors based on Fibre Bragg Gratings (FBGs)). Two measurement points at 180°on the vertical of the downstream faces for temperature sensing (with Pt100 sensors).
- *Block 9*: same design as for the other blocks, but with the instrumentation of the upstream face placed on the downstream face and vice versa.

For information about the radiation hardness of the materials employed, see Ref. [117]. The following paragraphs explain the working principle of the sensors selected.

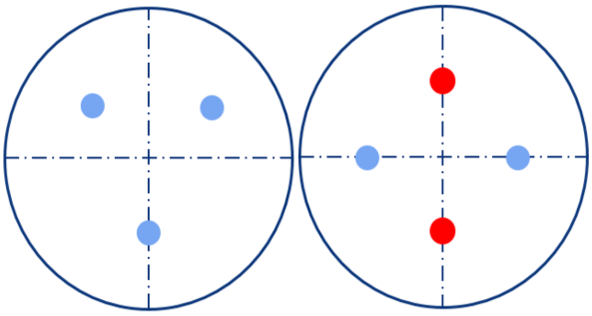

Fig. 5.143: Measurement points for strain (blue) and temperature (red). Design for upstream (left) and downstream (right) faces of blocks 4, 9, and 14.

5.9.4.2.1 Strain measurements

Electrical strain gauges. The working principle of electrical strain gauges relies on the relationship between the change in electrical resistance and the deformation: it is well known that all electrical conductors change their electrical resistance with mechanical strain. The change in resistance in a strain measurement is rather small, and therefore an electronic amplifier is necessary to perform the measurement. The sensitivity of strain gauges is determined by a gauge factor k (approximately 2) defined in the following equation; the value is stated by the manufacturer after testing a sample from each production lot, according to a standard procedure:

$$k = \frac{\Delta R/R_0}{\Delta l/l} = \frac{\Delta R/R_0}{\epsilon} \quad ((\Omega/\Omega)/(\mathrm{m/m}))\,. \tag{5.23}$$

The strain gauges for the BDF target prototype were of type 1-Y91-1.5/120 from HBM®, where two measurement grids are placed in a rosette to measure strain in perpendicular directions; their characteristics are listed in Table 5.33. The gauges feature a polyimide carrier and cover, while the measurement grids are embedded in a constantan foil.

Table 5.33: Characteristics of 1-Y91-1.5/120 resistive strain gauge

Property	Value
Nominal resistance (Ω)	120 ± 0.5
a, length of measuring grid (circumferential strain) (mm)	1.5
b, width of the measuring grid (radial strain) (mm)	1.2
k factor, a	$1.94 \pm 1.5\%$
k factor, b	$1.97 \pm 1.5\%$

Bonding and protection of the strain gauges. Good bonding is required between the specimen surface and a strain gauge, to minimize dissipation of the strain; curing adhesives, ceramic putties, flame-deposited ceramics, and spot welded joints are some possible methods. The strain gauges selected are not waterproof, but they can be employed in combination with a protective cover agent. The glue and protective agent used are listed in Table 5.34.

Wheatstone bridge circuit. A Wheatstone bridge circuit can be used to determine the absolute value of an electrical resistance or a relative change in resistance (in the range 10^{-4}–10^{-2} Ω/Ω).

In Fig. 5.144, the resistances R_1–R_4 represent the four arms of the bridge. V_S is the excitation voltage of the bridge, and is connected to points 2 and 3. V_o is the output voltage of the bridge (the measurement signal), and is measured between points 1 and 4. A direct or alternating voltage is usually

Table 5.34: Selected bonding and cover agents

Product	Name	Characteristics
Bonding material	Vishay® M-Bond 610	2-component epoxy phenolic adhesive, hot curing (−269°C; +260°C)
Cover agent	HBM® X280	Epoxy resin, cold-curing (−200°C; +200°C)

applied as the excitation voltage. In a voltage-fed bridge configuration, the deviations from linearity of strain gauges are automatically corrected.

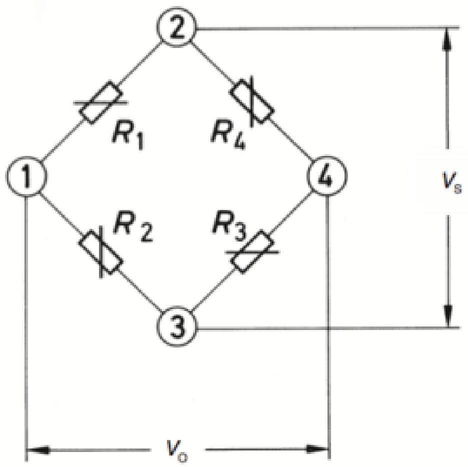

Fig. 5.144: Wheatstone bridge circuit

The Wheatstone bridge is a voltage divider. The voltage V_S is applied to points 2 and 3 and is divided in the two arms of the bridge R_1, R_2 and R_4, R_3. If the bridge is unbalanced, different voltages are measured in the two arms. The difference in voltage is calculated by use of the following equation:

$$V_\mathrm{o}/V_\mathrm{S} = (1/4)((\Delta R_1)/R_1 - (\Delta R_2)/R_2 + (\Delta R_3)/R_3 - (\Delta R_4)/R_4)\,, \tag{5.24}$$

or, in terms of strain,

$$V_\mathrm{o}/V_\mathrm{S} = (k/4)(\epsilon_1 - \epsilon_2 + \epsilon_3 - \epsilon_4)\,. \tag{5.25}$$

Equation (5.25) is true if all arms of the bridge are active. If only one gauge is active in the measurement, the circuit is called a quarter bridge circuit. The strain gauge and the connecting leads form one arm of the bridge and R_2, R_3, and R_4 are fixed resistances that complete the bridge circuit (Fig. 5.145). R_SG is the measuring strain gauge, $R_\mathrm{L1.1}$ and $R_\mathrm{L1.2}$ are the resistances of the connecting leads between the strain gauge and the rest of the bridge, and R_2–R_4 are the completion resistors. It is assumed that the strain measured is due to the bridge imbalance caused by the strain gauge:

$$V_\mathrm{o}/V_\mathrm{S} = (1/4)(\Delta R/R)_\mathrm{SG} \Rightarrow V_0/V_S = (k/4)\epsilon\,. \tag{5.26}$$

All of the resistive strain gauges in the experiment were installed in a quarter bridge, eight of them in a four-wire configuration and the others in a two-wire configuration.

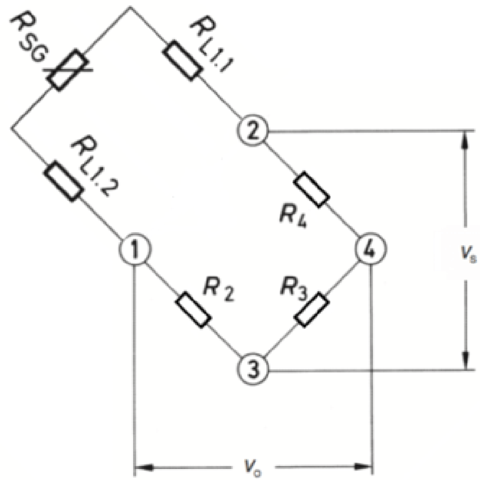

Fig. 5.145: Wheatstone bridge circuit with strain gauge

Optical fibre sensors for strain measurements. Optical fibres can be used to measure strain by means of the FBG technology, which exploits the photosensitivity of the fibre core material. The main features of this kind of sensor are robustness, extremely small dimensions, waterproofness, radiation hardness, immunity to electromagnetic fields, and the absence of a need for a power supply. Typically, FBGs are obtained from standard single-mode telecom fibres with an external diameter of 200 µm and a core diameter of 9 µm. The working principle is based on periodic modulation of the refractive index of the core of the grating, obtained by use of UV laser imprinting and a phase mask grating. Such gratings are able to reflect light with a wavelength λ given by the following equation (see Fig. 5.146):

$$\lambda = 2nD\,, \tag{5.27}$$

where n is the refractive index of the core and D is the distance between the modulations in the grating. The FBG is glued onto the surface of a piece subjected to deformation; when deformation occurs, the fibre stretches or shrinks and D changes. By monitoring the corresponding change in the wavelength of the reflected light, it is possible to determine the deformation from the linear relationship

$$\epsilon = \Delta\lambda/(k\lambda_{\mathrm{B}})\,, \tag{5.28}$$

where the k factor of the sensor is $0.78 \pm 2\%$.

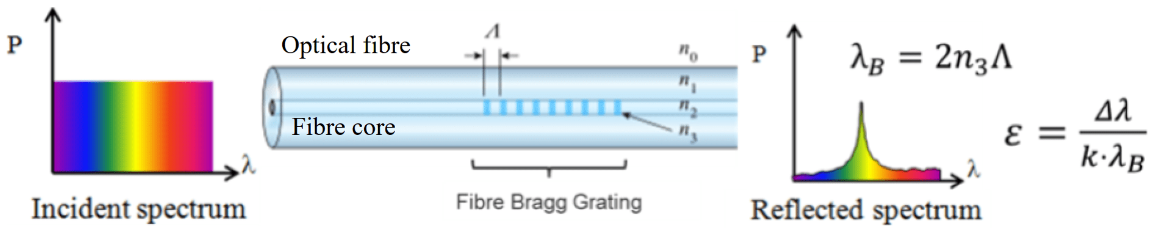

Fig. 5.146: Working principle of FBG

The sensors chosen were provided by HBM® FiberSensing, and their accuracy was determined in the Mechanical Measurement Laboratory in the Engineering Department at CERN [118]. The selected sensors have an FBG inscribed on the fly with a new technique based on femtosecond laser pulses. Their design is shown in Fig. 5.147, and some of their characteristics are listed in Table 5.35.

Bonding of the optical fibre sensors. The fibres were bonded to the surfaces following a procedure similar to that employed for the resistive strain gauges, which was designed especially to ensure a reduction in the quantity of glue ued. The adhesive used was Araldite® Standard (Ultra Strong), which is

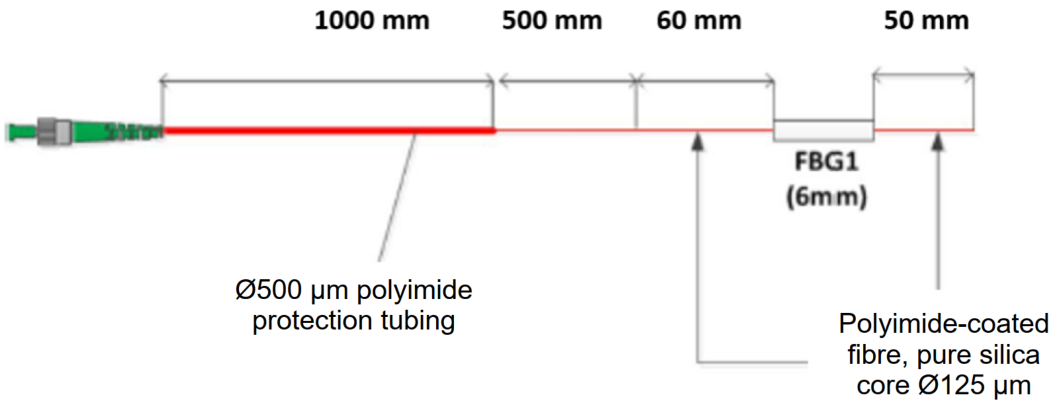

Fig. 5.147: Design of optical array for FBG sensor

Table 5.35: Characteristics of FBG sensors used

Property	Value
Core (pure silica) diameter (µm)	9
Coating (polyimide) diameter (µm)	125
Wavelength range (nm)	1515–1560
Strain measurement accuracy	<5%
Maximum strain (µm/m)	5000
Grating length (mm)	6
Temperature influence (pm/°C)	10
Maximum temperature (°C)	350

a cold-curing two-component epoxy glue. Since the fibres are waterproof, no protective agent was used with these sensors.

5.9.4.2.2 Temperature measurements

The electrical resistance of a metal changes with temperature. The relationship between the two is non-linear and can be described by a high-order polynomial,

$$R(t) = R_0(1 + A \cdot t + B \cdot t^2 + C \cdot t^3 + \dots)\,, \tag{5.29}$$

where R_0 is the nominal resistance at 0°C. The number of high-order terms is chosen depending on the required accuracy of the measurement. Platinum is the most commonly used material, thanks to its chemical stability, its simplicity of processing, the availability of wire in a highly pure state, and the excellent reproducibility of its electrical characteristics. The temperature measurement range varies from -200 to 961.78°C. For measurements between 0 and 100°C, the increase in resistance is linear, with a coefficient α defined by the following equation:

$$\alpha = (R_{100} - R_0)/(R_0 \cdot 100°\mathrm{C})\,. \tag{5.30}$$

For platinum, α is equal to 3.8505510°C^{-1}. The temperature can be determined from the following equation (where R_T is the resistance of a Pt100 sensor at temperature T, and $R_0 = 100\ \Omega$):

$$T = (R_T/R_0 - 1)/\alpha\,. \tag{5.31}$$

The Pt100 sensors selected for the experiment were provided by Radiospares (6117801); they are suitable for submerged environments, and the temperature range is from -50 to +500°C. The accuracy class is B.

Bonding of Pt100 sensors. A key factor to consider when selecting the glue for a temperature probe is that it must have a good thermal conductivity to minimize the error in the measurement. The glue selected was a cold-curing two-component epoxy adhesive called Stycast® 2850 FT. To protect the electrical connections from the water stream, the probes were embedded in the same protective agent as used for the resistive strain gauges (see Table 5.34).

5.9.4.3 Data acquisition system and software

A description of the data acquisition system and the software used with it was provided in paragraphs 4 and 5 of an EDMS document [119], to which we refer. Here, we aim to add information about the acquisition device for the optical strain sensors (the optical interrogator) and the combination of modules used.

5.9.4.3.1 Optical interrogator

Initially, a dynamic optical interrogator was intended to be used, sampling at 1000 Hz. For reasons explained below, it was eventually decided to employ two static interrogators from HBM®, type FS22SI, which have a lower sampling frequency (1 Hz).

5.9.4.3.2 Final acquisition system

The acquisition system, installed in building BA80, is composed of the following equipment:

- two HBM® Quantum X MX1615B, each with 16 channels, to read signals from the resistive strain gauges and Pt100 sensors;
- one HBM® Quantum X M640 dedicated to the pressure sensors installed on the inlet and outlet water pipes of the tank;
- one HBM® CX27 for synchronization between these three modules;
- two HBM® FS22SI optical interrogators;
- an Ethernet hub for connection of all of the devices to a PC.

The software allows synchronization between all of the signals, sampled at different frequencies and with different devices, thanks to the Network Time Protocol (NTP), and it allows one to monitor online the measured quantities of interest through a tailored front panel, shown in Fig. 5.148. The resistive strain gauges and pressure sensors are sampled at 1000 Hz, while the temperature probes are sampled at 100 Hz.

5.9.4.4 Integration

5.9.4.4.1 Connectors and feedthroughs

On the connection flange of the tank, there are five electrical four optical feedthroughs. These components, together with the plugs, must be watertight and resistant to pressure and radiation damage. These components allow the extraction of the signal from the electrical strain gauges, optical fibres, and temperature probes from the inside of the tank and also allow connection to a Staubli table. In this interface, there are three electrical connectors, with 48 pins, and one connector (Combitac) that allows 16 optical connections. Both the electrical and the optical feedthroughs were provided by Fischer Connectors and were tested in the same test set-up as that employed for the sensors (see Section 5.9.4.5). The electrical feedthroughs and plugs have 27 pins and belong to the Fischer stainless steel core series. The regular Viton O-rings were substituted with EPDM ones, owing to their better radiation hardness. These components are watertight and guaranteed for pressures up to around 30 bar. To increase their effectiveness against pressure, the feedthroughs are mounted with the female side towards the inner of the tank. The optical feedthroughs contain a gas-tight receptacle, and each of them can receive four optical fibres with

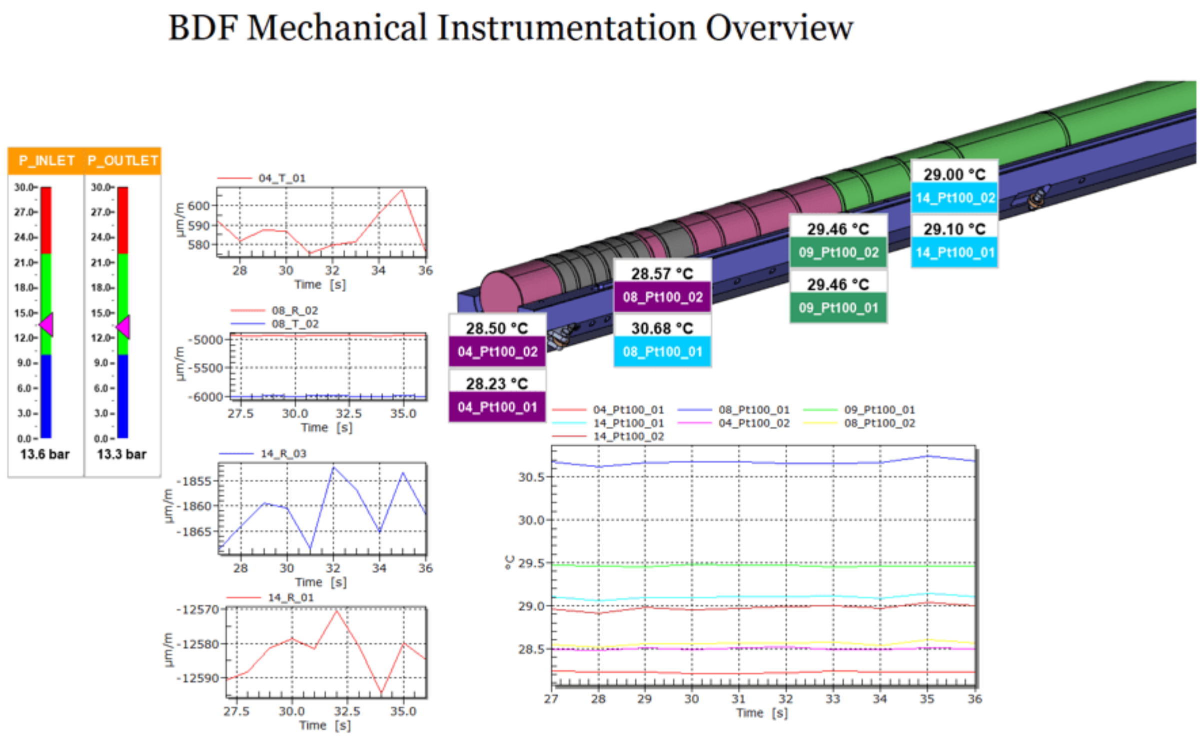

Fig. 5.148: Catman® front panel, showing an overview of online measurements

8° FC/APC connections. The manufacturer does not specify the maximum pressure that the connectors can withstand.

5.9.4.4.2 Cabling and installation

The following equipment has been installed to extract the signals from the sensors on the blocks to the upper Staubli plate:

- SCEM 04.01.63.C polyimide cables 0.25 mm^2;
- radiation-hard optical fibres;
- Fischer optical feedthroughs, FO4 P01P8 S9-001.4-00.3 CFCN8 AAA;
- Fischer electrical feedthroughs, ST-WDE 105 AZ102-130E;
- Staubli connection system.

The following equipment is used from the fixed table to the measurement devices:

- Staubli connection system;
- 3 × NE48 cables for electrical instrumentation;
- 16 optical fibres, DRAKKA radiation hard:
  - 10 × XPSS031 PCORD SIMPLEX SM-7A2 E2000/APC C1|FC/APC C1 1 m;
  - 6 × XPSS032 PCORD SIMPLEX SM-7A2 E2000/APC C1|FC/APC C1 2 m;
  - 15 × XPSS080 PCORD SIMPLEX SM-7A2 E2000/APC C1|SC/APC C1 5 m;
  - 1 × XPSS081 PCORD SIMPLEX SM-7A2 E2000/APC C1|SC/APC C1 7.5 m.

The data acquisition systems were installed in TCC2. The “Demande d’Installation de Cables” (DIC) are in attachments to the EDMS document [119].

5.9.4.5 Validation tests

A validation campaign was necessary to establish the behaviour and suitability of the equipment, owing to the lack of technical information available for the operational conditions of the BDF target prototype. None of the manufacturers could provide specifications of the effects of flow rate, and sometimes could not provide specifications of the watertightness and maximum admissible pressure. Therefore, a test rig was designed and manufactured to test the strain gauges, optical fibre sensors, plugs, and feedthroughs against pressurized water and high flow rates.

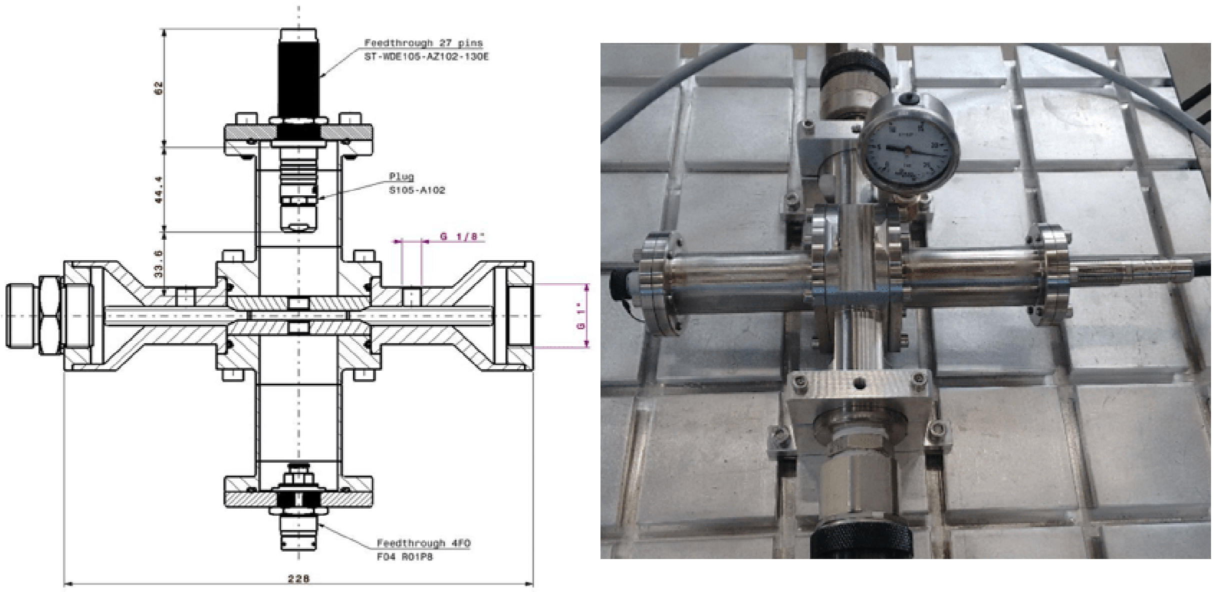

Fig. 5.149: Technical drawing of a dedicated test rig aimed at testing the instrumentation for the BDF target prototype, and installation in building 181.

As shown in Fig. 5.149, the set-up hosted two inserts, which were instrumented with the strain sensors (Fig. 5.150). The measurements from the candidates were compared with a reference electrical strain gauge (LE11-3/350), which was encapsulated and waterproof but not radiation hard, also glued to the same insert. Because of changes in the requirements on the instrumentation (different measurement points and directions), the tests were run with electrical strain gauges different from the Y series ones. The second insert was instrumented with an FBG. The system was run for several days with a circulating water flow of 4.2 m/s at 22 bar.

The main results of the tests were as follows.

- The electrical and optical feedthroughs could withstand the operational pressure without leakage.
- There was agreement between the strain measurements carried out with the two types of resistive strain gauge. In particular, it was possible to observe thermal expansion and contraction of the inserts due to changes in temperature between day and night (see Ref. [9] for examples of these measurements).
- The cover agent successfully protected the Y series strain gauges, which are not guaranteed against an underwater environment, and it did not influence the measurements.
- It was observed that the cover agent became stiff and easy to detach if it was exposed alternately to air and water (see Fig. 5.151). Therefore, once it is submerged it should stay wet until the end of the experiment.
- Tests done with and without protection of the optical fibres with a cover agent showed that protection of them was not necessary.

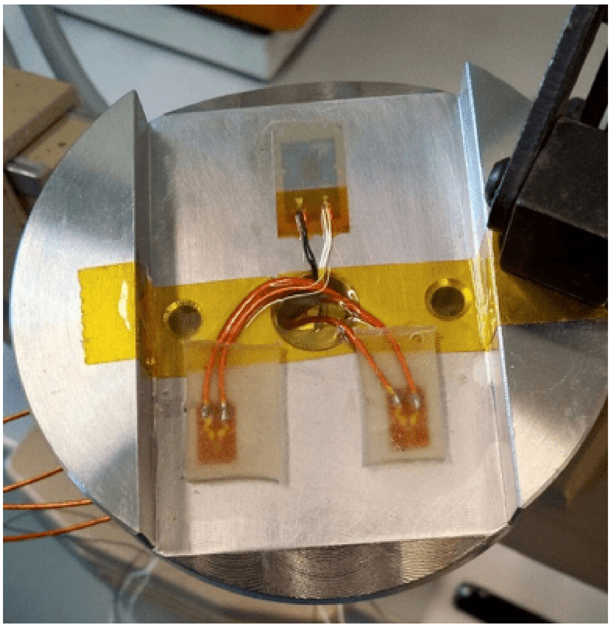

Fig. 5.150: Test-rig insert instrumented with electrical strain gauges. The LE11 strain gauge is on the top; it is encapsulated and waterproof. Two LY61 strain gauges are at the bottom, covered with protective agent.

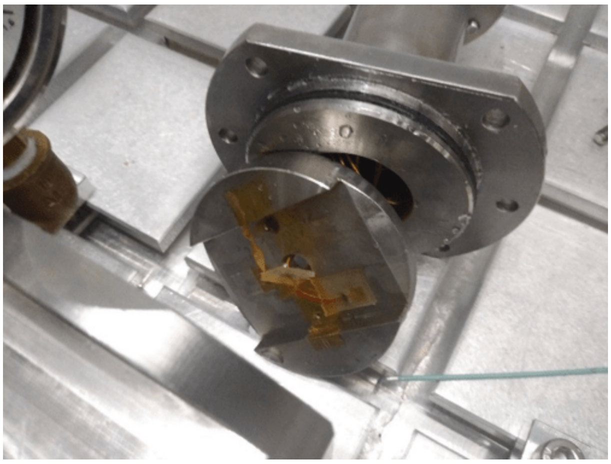

Fig. 5.151: One of the two LY61 strain gauges was found to be detached after the tests. This insert was tested underwater and then exposed to air during the CERN annual closure (2 weeks).

5.9.4.6 Instrumentation steps

5.9.4.6.1 Instrumentation of the blocks

The first step was to instrument the faces of the blocks with the electrical strain gauges (i.e. marking the positions, gluing the gauges, and application and curing of the cover agents) (Fig. 5.152). Only at the end of this process were the other faces instrumented with the Pt100 sensors, and the last sensors to be placed on the blocks were the optical fibre sensors (to avoid possible damaging manipulations in their surroundings).

5.9.4.6.2 Installation of the blocks

After application of the sensors, the blocks were positioned in the lower half-shell of the tank and the cabling extracted towards the connection flange through radial grooves machined next to every instrumented block, and two larger axial grooves machined all along the shell thickness. Once in place, all of

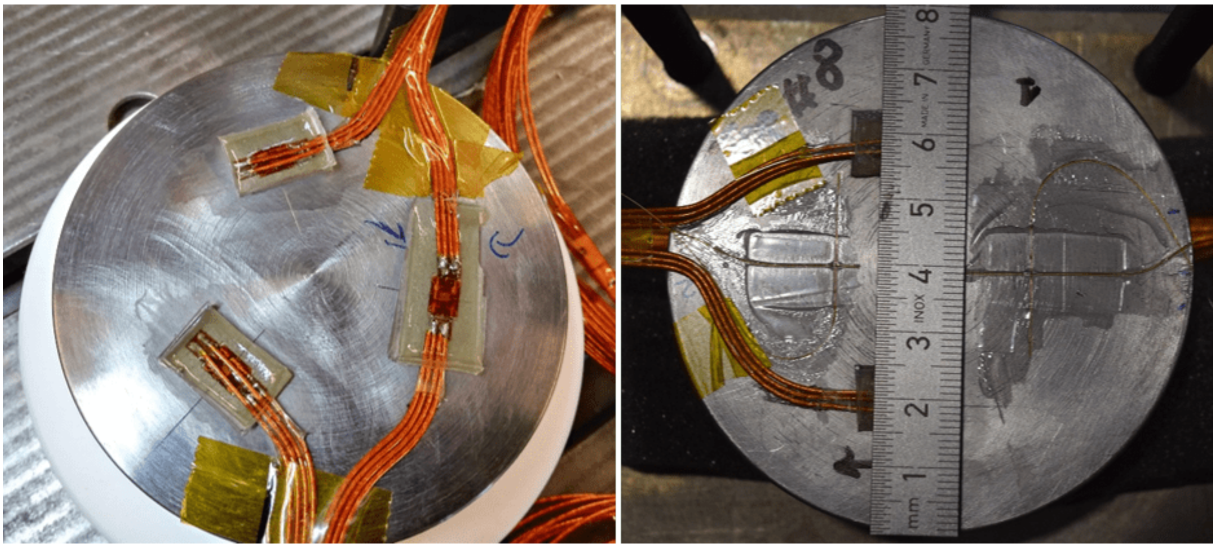

Fig. 5.152: Left: target block surface instrumented with biaxial resistive strain gauges, positioned at 120°and covered with protective agent to guarantee waterproofness. Right: surface instrumented with two Pt100 sensors and four FBGs.

the radial and axial grooves hosting the wires and optical fibres were covered with resin to avoid water leaks, and hot cured (Fig. 5.153).

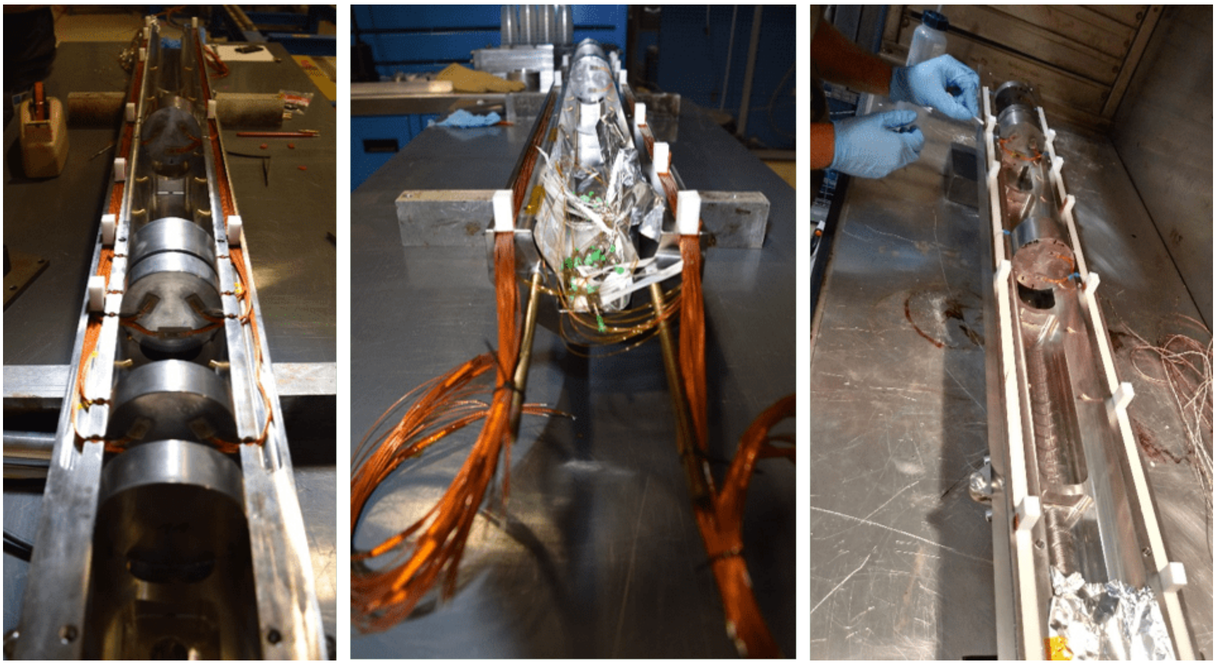

Fig. 5.153: Installation of blocks and wires (left and centre); application of the resin in the axial grooves (right).

After these operations, the placement of the other target blocks, and the installation of the optical and electrical feedthroughs, it was possible to place the upper half-shell and place the closing flange (Fig. 5.154).

Fig. 5.154: Adjustment of the wires inside the BDF target prototype tank and closing with the connector flange.

5.9.4.7 Test of the acquisition chain and signals

During the aforementioned operations, the electrical continuity of the resistive strain gauges and Pt100 sensors was checked frequently, always giving positive outcomes, and the optical fibres were checked after the curing of the resin in the grooves, also giving 100% positive results (one fibre of the 16 was broken during installation). During the pressure tests, four more fibres were lost. Figure 5.155 depicts the measured Bragg wavelengths of the 11 working sensors during the last pressure tests.

The optical connection line from the electronic rack in building BA80 to the mobile Staubli plate connector was checked in March 2018 by means of a test specimen instrumented with four FBGs. The line included the facility cables from the rack to the Combitac connector of the fixed Staubli plate, the Staubli Combitac connection, and the sensing elements connected to the Combitac connector of the mobile Staubli plate with FC/ACP-FC/APC adapters.

The connections were found to be good, as the signal back from the test specimen was strong, allowing good tracking of the peaks, with an example shown in Fig. 5.156.

Despite the positive outcomes of the tests performed on the different sections of the connection chain (the experimental tank and the BA80 installations), when the BDF target prototype was lowered underground and connected to the fixed Staubli plate, several problems arose in detecting the Bragg peaks. The signal-to-noise ratio was extremely low, making it impossible to distinguish the position of the Bragg peak in the full spectrum, and therefore to measure the strain. On the other hand, 100% of the signals from the resistive strain gauges, Pt100 sensors, and pressure sensors were detectable.

5.9.4.8 Operation

During 3 days of the experiment, the sensors were monitored online by remotely accessing the PC installed in BA80 from the CERN Control Centre. The online measurements allowed observation in real time of the movement of the target, the steering of the beam, and the beam impacts, as shown in Fig. 5.157. Only a small number of sensors have been lost since the beginning of the experiment. After more than 1 month since installation in the T6 area, in a continuous water flow, a pressurized environment, and a total PoT of 2.4×10^{16} accumulated during the experiments, 23 out of 24 resistive strain gauges and 6 out of 8 Pt100 sensors were still working at the moment of the disconnection of the acqui-

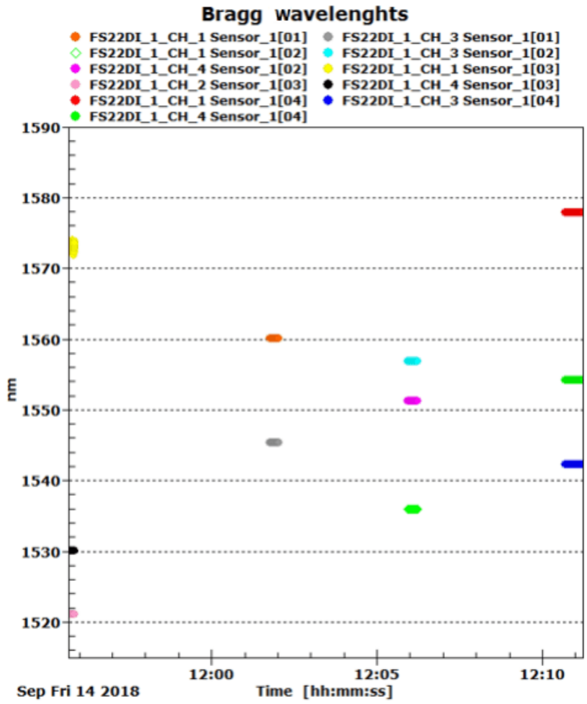

Fig. 5.155: Measurements of the Bragg wavelength of the optical sensors installed on the blocks during a water pressure test.

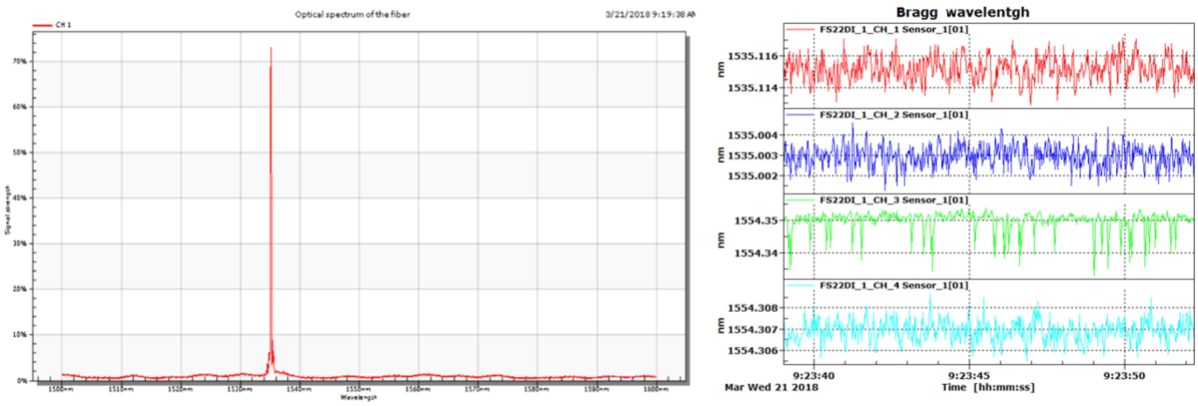

Fig. 5.156: Spectrum of one FBG on the test specimen (left), and measured wavelength for all of the sensors (right).

sition system.

5.9.5 Preparation of beam test area and execution

5.9.5.1 Overall layout of the area

The experimental set-up for the BDF target prototype was located in the North Area target zone (TCC2), upstream of the T6 target assembly (see Fig. 5.158). A new concrete bunker was constructed directly downstream of the T6 target to house the experiment.

As the test was expected to receive a significant number of protons, the target was placed in dedicated shielding to keep the dose to personnel low in the case of interventions in the area. The main target shielding was made out of standard concrete blocks, 2400 × 1600 × 800 mm. The first level was a base of 100 mm spacers to allow the passage of cables and pipes on the floor below the shielding.

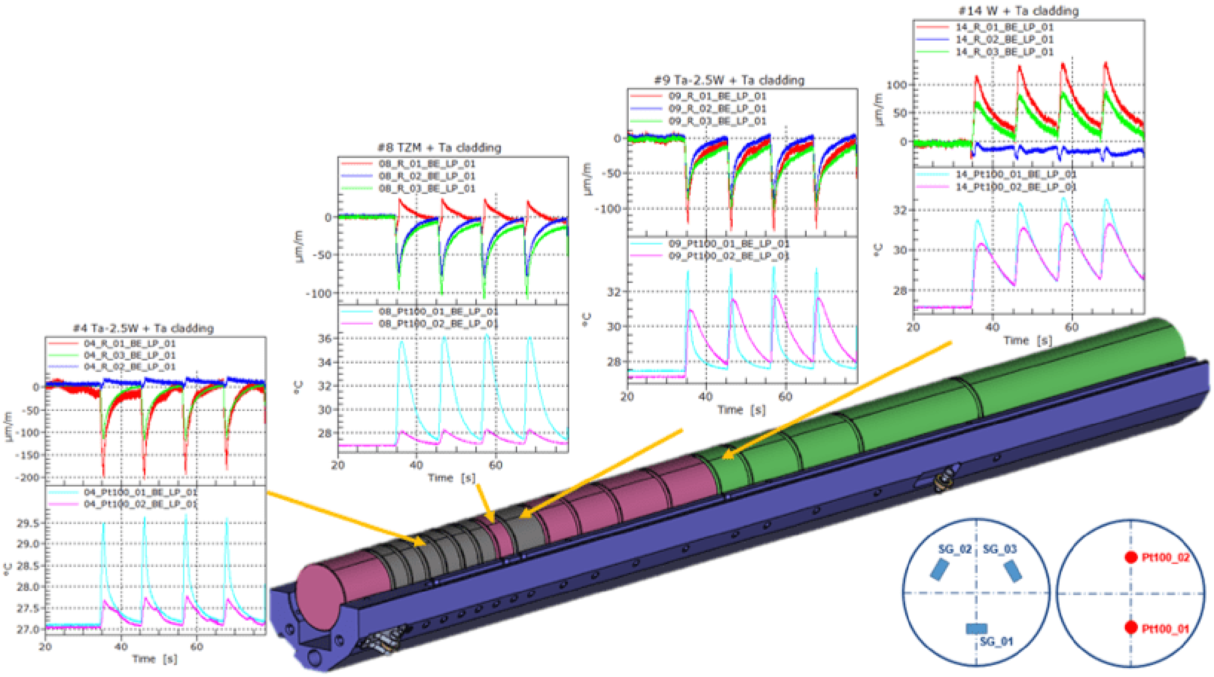

Fig. 5.157: Examples of strain and temperature measurements visible online during tests

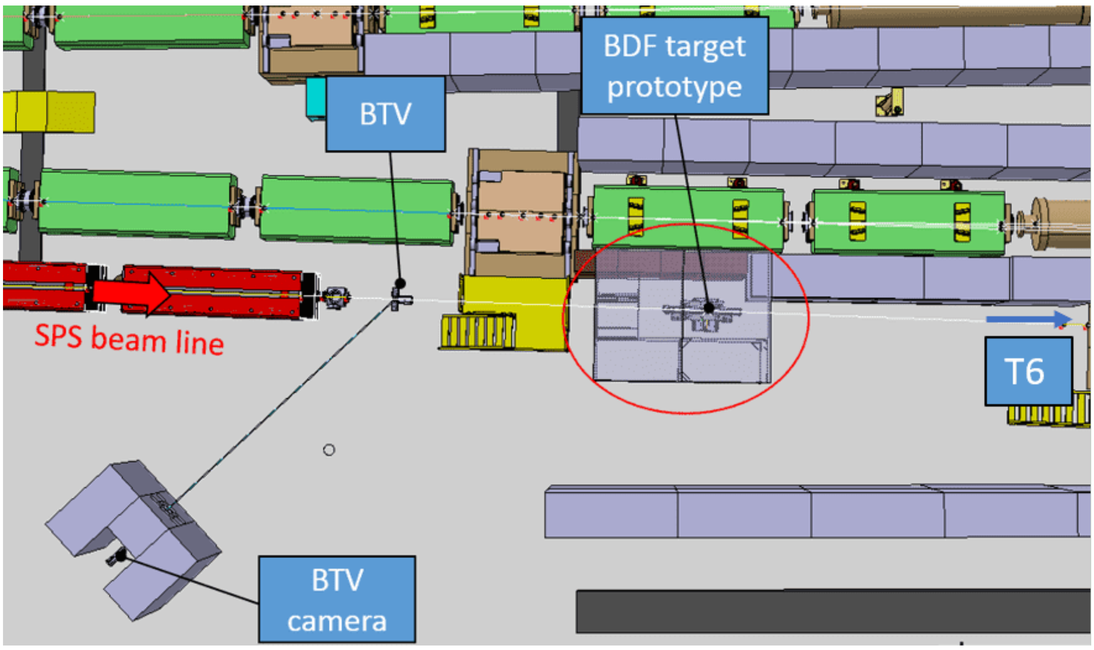

Fig. 5.158: Layout of TCC2 area, with a view of the target prototype bunker, the target beam screens (BTV), and the upstream BTV camera and camera shielding.

The construction was planned to be executed by stapling the different blocks together using the overhead crane.

On the upstream side of the shielding, a 100×200 mm opening for the beam passage was provided. On the downstream side, a passage to enter the bunker was created. If personnel access to T6 was required, an additional concrete block would be placed downstream of the target to reduce the residual dose rate from the BDF target. If required, the small hole upstream of the shielding could be closed as well to protect people intervening on the T4 target shielding assembly. The BDF target, once available, was inserted and removed by the crane from the top. During beam operation, the bunker was also closed at the top by two concrete blocks.

Two dedicated BTVs (beam screens) were installed, one upstream and one downstream of the experimental set-up, to measure the profile of the beam impinging on the target and to help in aligning the beam on the target. The digital camera aimed at the upstream BTV had to be protected from radiation damage: for that purpose, it was located inside a U-shaped shielding wall, made out of standard cast iron blocks (Fig. 5.159).

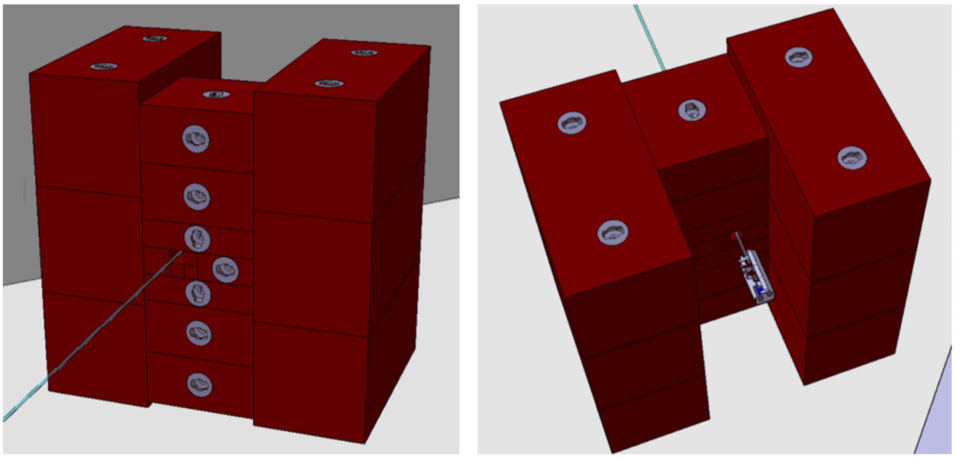

Fig. 5.159: Cast iron shielding for the BTV camera bunker

A dedicated cooling-system skid was provided, to avoid any possible contamination of the North Area primary cooling circuit in the case of target cladding failure. The cooling-system skid was installed in the access tunnel of TCC2 and TA801 (see Fig. 5.160).

Fig. 5.160: Layout of TCC2 and TA801 access tunnel, where the position of the target prototype and the dedicated cooling-system skid can be seen.

5.9.5.2 Preparation of the area during YETS 2017–2018

The prototype test area was prepared during the Year-End Technical Stop in 2017–2018, to profit from the lower radiation levels in TCC2. The target support and its motorization system were installed, as well as the surrounding shielding blocks. A mock-up of the target was installed on the target support for testing the alignment, remote handling, and cooling (Fig. 5.161).

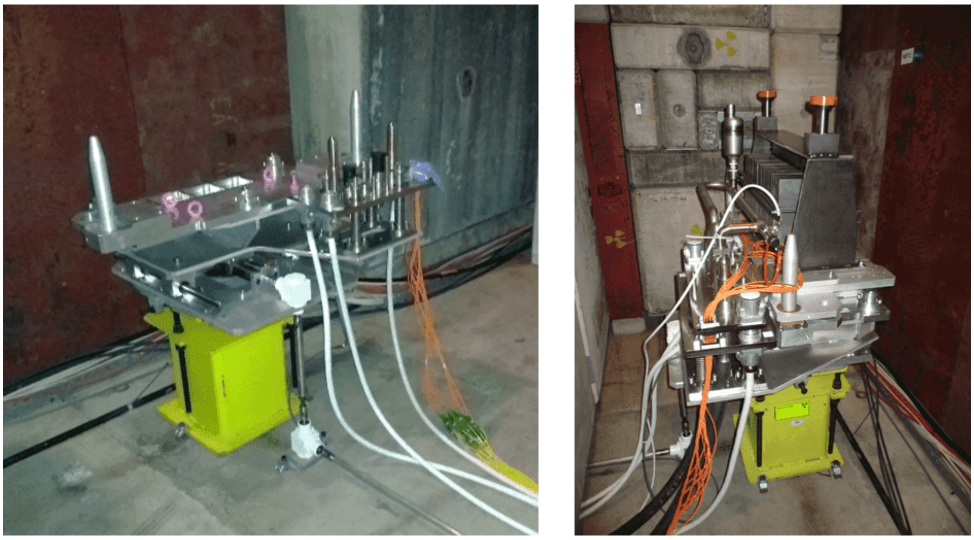

Fig. 5.161: Left: target prototype support installed in the TCC2 area. Right: mock-up of target prototype for robot, cooling, and alignment tests.

The upstream and downstream BTVs, as well as the shielding for the upstream BTV camera, were also installed (Fig. 5.162). Most of the cabling necessary for the target block instrumentation and the motor operation was put in place. The cooling-system skid was installed in the access tunnel, and most of the pipe connections required were performed, awaiting the installation of the target prototype at a later stage (Fig. 5.163).

Fig. 5.162: Upstream (left) and downstream (right) dedicated BTVs installed in the TCC2 area to provide beam alignment capabilities for the BDF target.

Fig. 5.163: Cooling-system skid for target prototype installed in the access tunnel to TCC2 (TA801).

5.9.5.3 Target prototype installation

The installation of the target prototype took place in September 2018. The installation required the combined effort of several teams, to cope with the radiation protection, remote handling, transport, cooling, and mechanical aspects of such an operation during a technical stop in the North Area.

The installation was performed fully remotely with the main crane of TCC2 and telemanipulation tools; the target was transported and placed on its support with the TCC2 area overhead crane, with the additional help of robot cameras. The water and electrical connections were performed by a robot, and a brief one-minute personnel access was granted for visual inspection for possible leaks (Fig. 5.164).

Fig. 5.164: Handling of BDF target prototype, with overhead crane towards the support location. (Photograph: J.M. Ordan [116].)

Additionally, concrete shielding was installed around the cooling-system skid to mitigate potential

R2E events in the electronics of the cooling system.

5.9.6 Radiation protection considerations for target prototype

This section summarizes the radiological assessment of the beam test of the BDF target prototype executed in September–October 2018. The target was irradiated in accordance with representative BDF/SHiP beam scenarios to provide insight into the material response. The evaluation of radiation protection risks was crucial to performing this experiment. The test beam required a slow extraction process at high intensity, currently available in the North Area target zone (TCC2). The experiment took place upstream of the T6 primary target (see Fig. 5.165). Quantifying the impact of this experiment on the activation of water and air was mandatory to ensuring that radiation protection requirements were fulfilled in the area. The studies done for that purpose were based on extensive simulations with the FLUKA Monte Carlo particle transport code [12, 11] and ActiWiz 3 [14]. The studies prior to the test assumed an integrated total of 3×10^{16} PoT, while in the two beam periods of the test integrated totals of 0.9×10^{16} and 1.6×10^{16} PoT were collected.

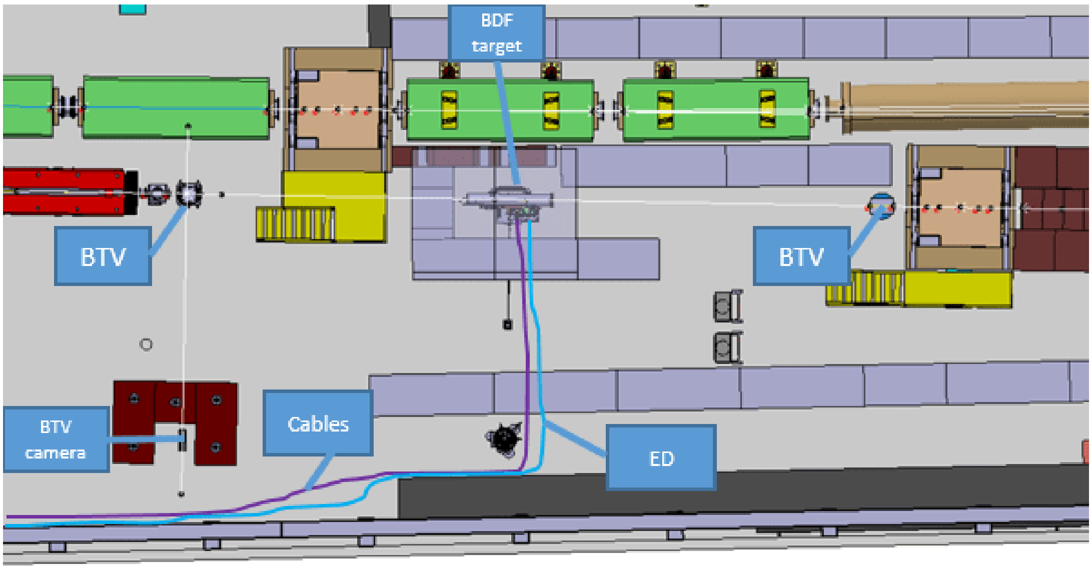

Fig. 5.165: Layout of TCC2, including the T6 bunker. The “BTVs” are beam screens and “ED” (Eau Demineralisée) is the connection to the cooling circuit.

As a significant number of protons were received during the test, the target was placed in dedicated shielding as shown in Fig. 5.166. This allowed the dose to personnel to be reduced in the case of interventions in the area. A new concrete bunker was placed between the T4 target passerelle and the T6 target. The main target shielding was constructed with standard concrete blocks of size $2400 \times 1600 \times 800$ mm^3.

On the downstream side, the shielding blocks were put in the ‘open’ position (see Fig. 5.167) to allow enough space for remote handling by a robot. If personnel access to T6 was required, the concrete blocks closest to T6 were moved to the ‘closed’ position (see Fig. 5.168) to reduce the residual dose rate from the target prototype. The residual dose rates in the ‘closed’ configuration, evaluated at different cooling times (4 h, 1 day, 1 week, and 6 months), are shown in Fig. 5.169. The residual dose rates around the bunker for short cooling times ($\leq$1week), which are interesting in the case of interventions, range between hundreds of microsieverts per hour to a few millisieverts per hour. For at least 6 months after irradiation, the target assembly must remain in the bunker in the ‘closed’ configuration before its removal during LS2. The removal of the target can be performed only by using remote handling owing to the high residual dose rates (O(20 mSv/h) at 40 cm) even after 6 months of cooling.

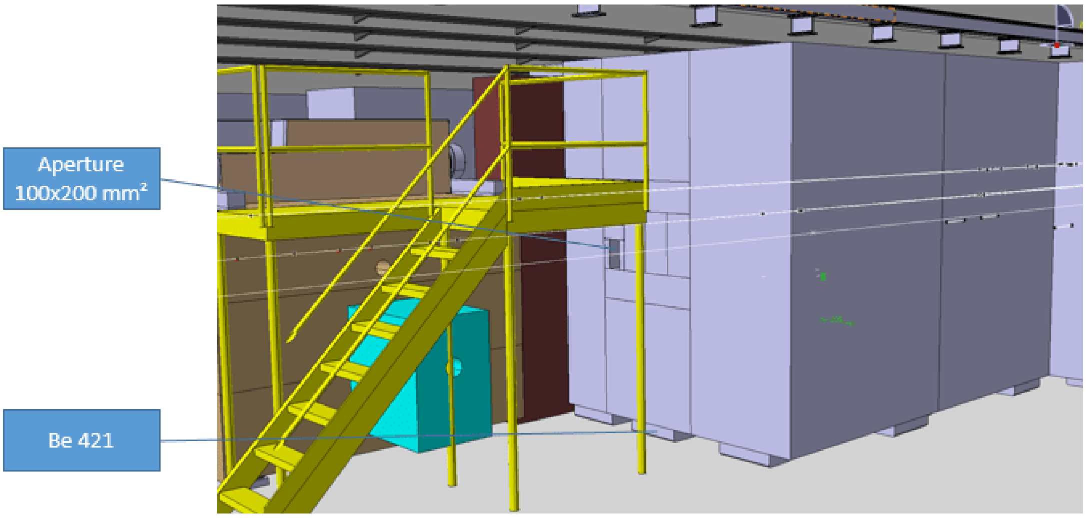

Fig. 5.166: View of the BDF target test bunker in T6

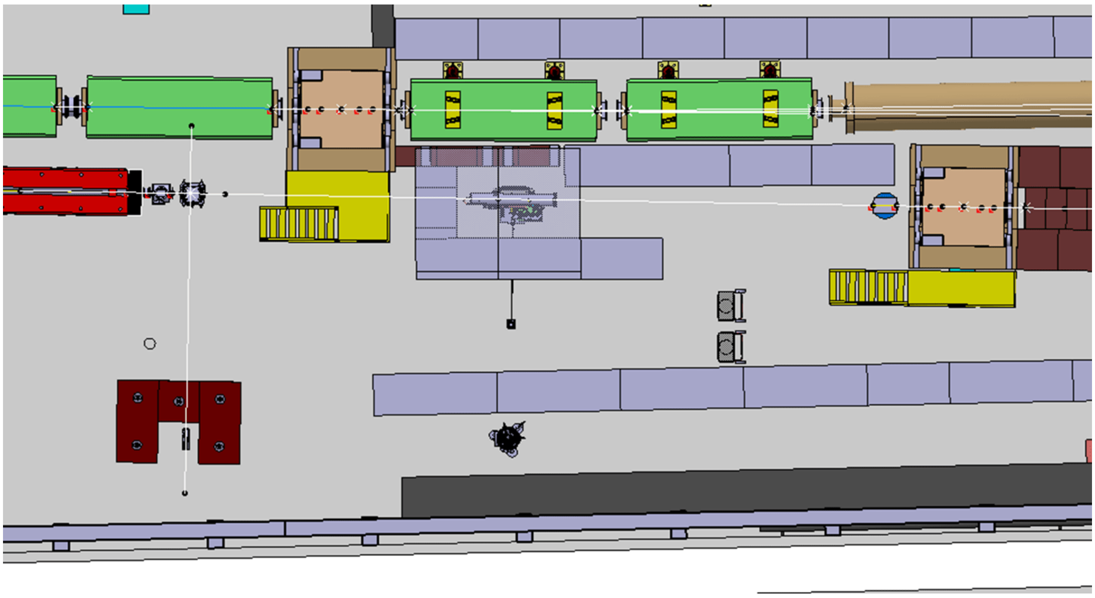

Fig. 5.167: Shielding configuration in the 'open' position

After the first beam period, the dose rates at a distance of 40 cm from the target were measured remotely after 1 week of cooling, reaching a maximum of 43 mSv/h. The simulations resulted in 30 mSv/h for the same number of PoT and therefore show relatively good agreement with the measurements, considering the uncertainty in the positioning of the detector held by the robot which performed the measurements.

The impact of the test on the activation of the air in TCC2 was negligible. As a matter of fact, the test required only 3×10^{16} PoT, which is equivalent to $\approx 1\%$ of the total PoT received by the T2, T4, and T6 targets during the year. Furthermore, those targets, in contrast to the BDF target prototype, are air cooled, leading to higher activation owing to the proximity of air to the targets. The BDF target, however, provides significant shielding power, reducing the radiation field prior to reaching regions of air. During beam operation in TCC2, the ventilation system is set into recirculation mode and the air is flushed only in the case of an intervention. Flushing the air requires 2 h of cool-down and 2 h of flushing, and thus 4 h is the minimum amount of time needed before an intervention can take place.

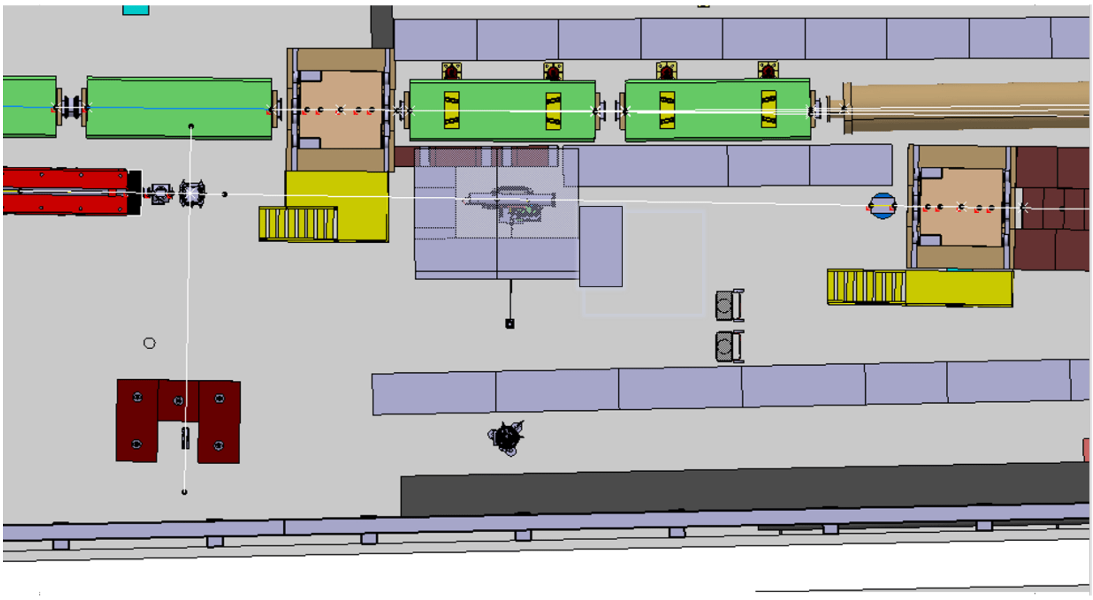

Fig. 5.168: Shielding configuration in the 'closed' position

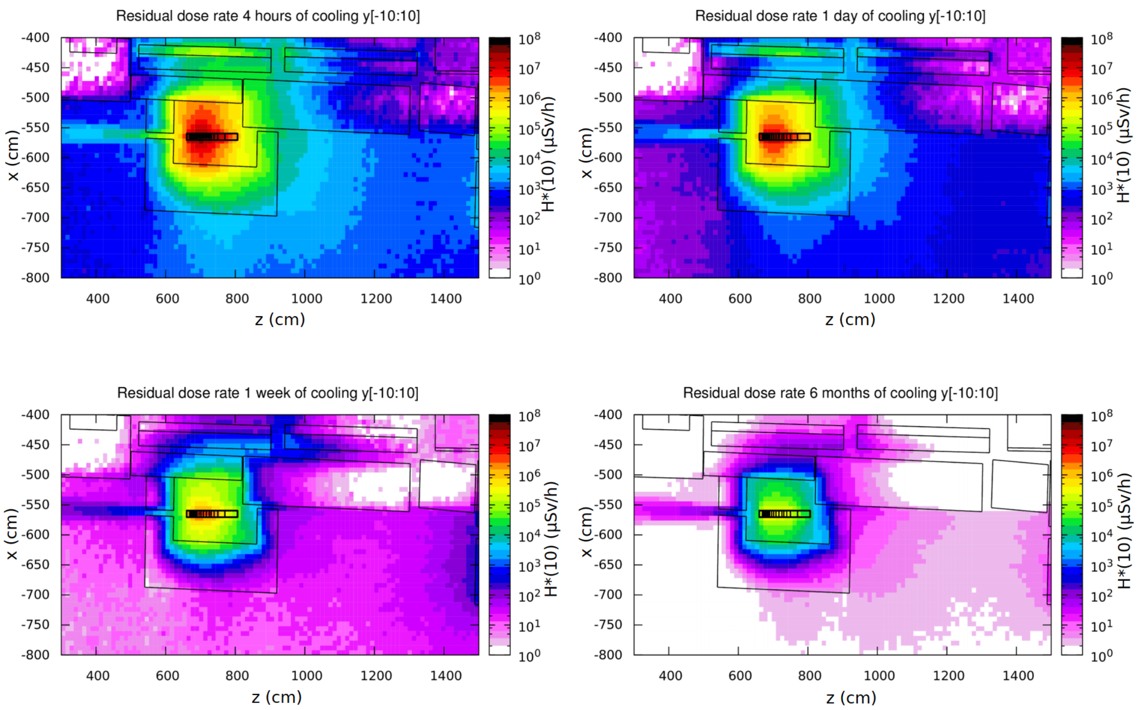

Fig. 5.169: Residual dose rates in microsieverts per hour after (a) 4 h, (b) 1 day, (c) 1 week, and (d) 6 months cooling.

A high water speed (5 m/s) was required in the channels between the target prototype blocks to remove the power deposited in the target. The circuit was supplied with demineralized water and equipped with mechanical filters and an ion exchanger to catch impurities and activated ions. The water activation was estimated using the ActiWiz 3 code. It was expected that some components of the cooling circuit would become contaminated with activated ions. For example, assuming that all of the isotopes were caught in the cartridge of the ion exchanger, the residual dose rate after 1 h of cooling at 40 cm from the cartridge was expected to be around 14.5 mSv/h. For the first beam period of the test, the residual dose rate after 1 h of cooling at 40 cm from the cartridge was expected to be around 10.3 mSv/h. These values showed good agreement with measurements made by a PMI, which was placed 40 cm away from the cartridge and gave a dose rate of 15.2 mSv/h after 1 h of cooling. In the case of an intervention, a longer cooling time should be considered (>4 h). In that case, the residual dose rate at 40 cm from the cartridge due to water activation would be around 75 µSv/h, with Be-7 as the main contributor. The main purpose of this test was to study the material response, and therefore the possibility of contamination of the water circuit with 1 g of material from the most radioactive part of the target was considered as an accident case (a conservative assumption, but a reasonable estimate in the case of an accident is O(1 µg)). This debris, assuming it is are collected in the filters or in the ion exchanger, results in a dose rate of ≈300 µSv/h after 1 h cooling at 40 cm. The irradiation of the high-Z material of the target also produces alpha emitters, which are considered as radiologically problematic. The main contributor among the ions produced is Gd-148, and in the aforementioned accident case ≈100 Bq of Gd-148 would be released into the cooling circuit. To avoid contamination of the existing cooling circuit, a dedicated cooling circuit for this experiment was put in place, as detailed in Section 5.9.2. The analysis of the gamma radiation emitted from water taken through a sampling valve showed the presence of spallation products in the water. Ongoing studies will characterize the dust found in the water.

To investigate the response of the materials, a PIE analysis is planned. Therefore, six blocks of the prototype BDF target will be sent out of CERN to a specialized company for analysis. The residual dose rates for these blocks after 6 months of cool-down are shown in Fig. 5.170; preliminary calculations with ActiWiz 3 interfaced with e-SHIP in Nucleonica [120] suggest that a Type A package will be needed for the shipment. After the cool-down period of at least 6 months, the BDF target prototype will be transferred out of the bunker into a transport container for storage before disposal. For transportation of radioactive materials, as indicated in Ref. [15], the maximum dose rate level at any point on the external surface of a package should not exceed 2 mSv/h. Therefore, the container will be made out of iron with a thickness of roughly 18 cm on the lateral sides and 15 cm on the upstream and downstream sides.

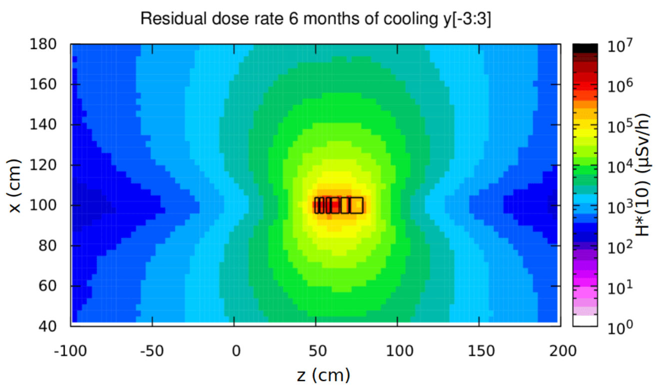

Fig. 5.170: Expected residual dose rate in microsieverts per hour after 6 months cooling for the blocks which will be shipped.

Some preliminary studies were performed for the disposal of the BDF target prototype after irradiation and the PIE tests. The results of the ActiWiz 3 calculations are reported in terms of the Swiss liberation limits (see Ref. [16]) for the two most radioactive blocks (one made of TZM and one of W). In the calculations, the same irradiation profile was assumed, but with a 1 yr cooling time. The total dose rate level in units of the LL is 1.53×10^6 and 1.17×10^6 for the TZM and W blocks, respectively, with Y-88 ($\approx$ 50% LL) and W-185 ($\approx$ 40% LL) as the top contributors for TZM and W, respectively. The time evolution of the dose rate level is shown in Fig. 5.171; even after a 20 yr cool-down period, the level is significantly above the exemption limit. The target will need to be treated as radioactive waste in the event of disposal. A proper assessment of the disposal will be performed in the future.

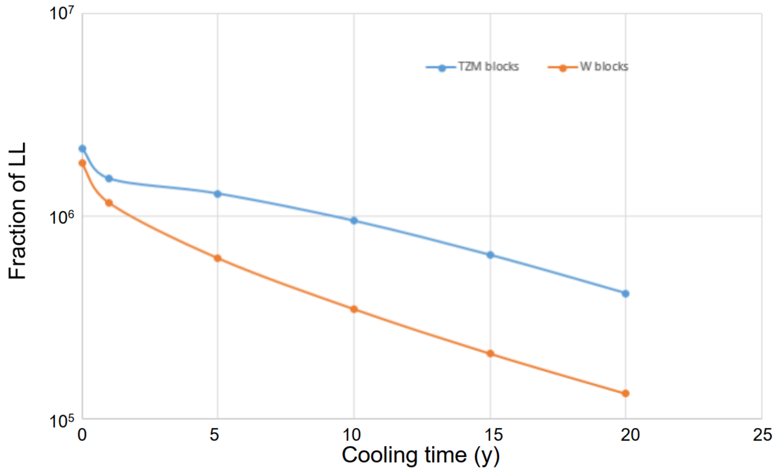

Fig. 5.171: Time evolution of the dose rate level for the TZM and W blocks

5.9.7 Target prototype beam tests

5.9.7.1 Beam tests, day 1

On 3 October 2018, the BDF target prototype received the first shots on the target. The beam steering and tuning to reach the target centre with the required beam spot dimensions were performed, profiting from the beam instrumentation installed (one BTV upstream of the target and another downstream; see Section 5.9.5).

The target prototype operated under the SHiP supercycle (i.e. 1 s spill, 7.2 s pulse) for several hours, and a total of 6 h of beam on target were achieved. Figure 5.172 presents a capture of the SPS Page 1 screen showing the dedicated SHiP supercycle. The accumulated number of protons on target during the first day of beam tests was around 1×10^{16}. One of the goals of the beam tests was to achieve 3×10^{16} protons on target, to obtain a representative number of cycles and a meaningful target irradiation, even if it was far from the expected PoT of the final BDF target.

The target instrumentation operated successfully for the duration of the whole test, despite the challenging experimental conditions. An example of the online monitoring recorded by the instrumentation sensors can be seen in Fig. 5.157. The response of the temperature and strain sensors to the impacts of the beam on the target can be observed; in this case four beam pulses and the subsequent cooling times are recorded.

5.9.7.2 Beam tests, day 2

The second day scheduled for the prototype tests was 24 October 2018. Before the first shots on the target, the upstream camera failed, most probably because of long-term radiation exposure. As a consequence, the beam tuning (alignment on the target) was performed using the downstream BTV, which was much less precise in terms of beam positioning and beam size. A total of 5.5 h of dedicated beam was accomplished during the day, and the total PoT after the test was 2.4×10^{16}.

During the execution of the test, the pump in the dedicated cooling-system skid for the target prototype failed. This event had already been registered after the installation of the cooling skid, and is thought to be related to R2E stochastic events in the control system of the skid. To avoid target failure in the case of such an event, a beam interlock was implemented to trip the beam after failure of the pump. The beam trip occurred after four pulses on target without cooling, which was clearly visible in the online measurements of the strain and temperature sensors. Figure 5.173 displays a view of the temperature measurements recorded following the failure of the cooling-skid pump. The accident was not thought to have damaged the target; hence, the system was successfully restarted and the beam tests

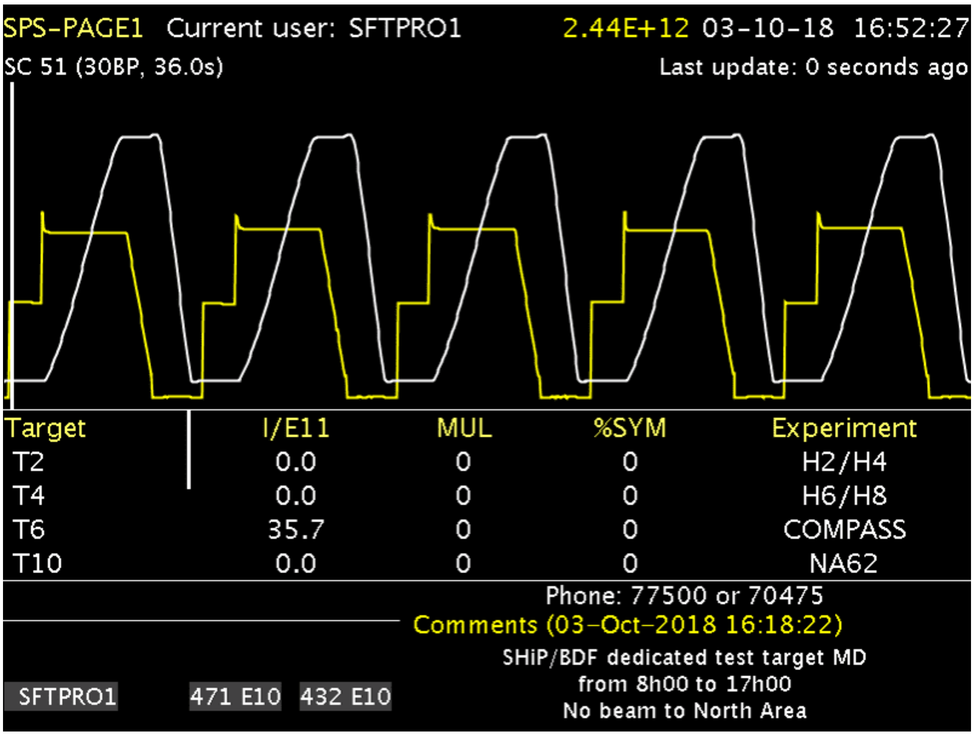

Fig. 5.172: SPS Page 1 screen during the execution of the beam tests of the BDF target prototype, with dedicated SHiP supercycle: 1 s spill, 7.2 s cycle, corresponding to a beam power of 35 kW.

were resumed.

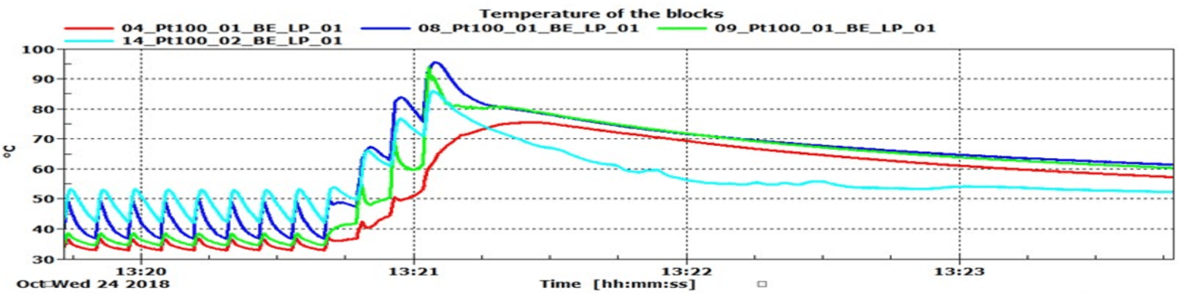

Fig. 5.173: Temperature sensor recording during the second day of beam tests on the BDF target prototype. The pump failure occurred around 13:20:45, and the temperature increased drastically during the next four pulses until the beam trip.

5.9.7.3 Beam tests, day 3

On 7 November 2018, the target prototype received two hours of non-dedicated beam, i.e. shared with other accelerators and experiments. Exchange of the upstream BTV camera was performed one week before, to ensure good accuracy in the beam position and dimensions.

The main aim of the test during this period was to cross-check the instrumentation measurements carried out in the previous tests. Several iterations were performed with several beam axis positions on the target to record the response of the instrumentation to the different beam impact coordinates.

In summary, at the end of the three beam test days, more than 14 h of beam was allocated to the target prototype, and a total of around 2.4×10^{16} PoT was reached. Figure 5.174 presents the evolution of the PoT during the two first days of beam tests (the contribution of the third day to the total PoT is negligible).

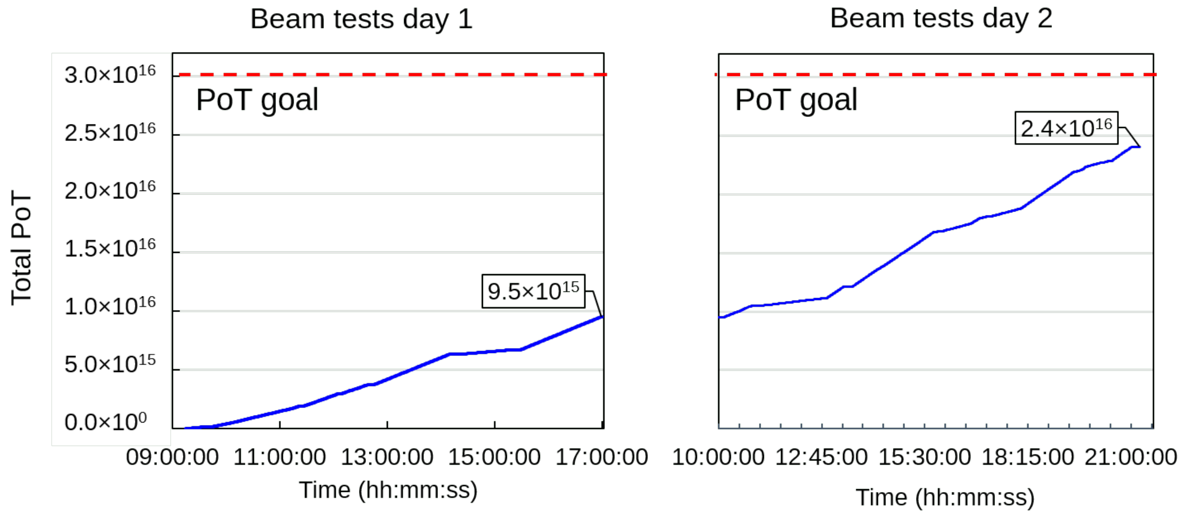

Fig. 5.174: Accumulation of protons on target during the first two days of beam tests. The total PoT achieved is around 2.4×10^{16}, close to the goal of 3×10^{16}.

It can be concluded that the beam tests were very successful, given that the beam instrumentation, the target block instrumentation, and all the related equipment worked proficiently during the tests. Additionally, much useful information could be extracted from the tests, and a large amount of data was gathered from the instrumentation measurements.

5.9.8 Plans for post-irradiation experiments

5.9.8.1 Objectives of post-irradiation examination

A post-irradiation examination of the BDF target prototype after the beam test is envisaged in order to achieve several objectives, aiming at understanding the effect of the proton beam on the target materials.

- Study the surface state and integrity of the cladding to validate the resistance of the cladding material to the cooling conditions.
- Validate Ta2.5W as a new cladding material and compare its performance with unalloyed Ta.
- Study the state of the cladding–target interface to assess its reliability under thermal cycling due to beam impacts. Identify any degradation of the interface properties (strength, thermal conductivity) or appearance of defects (detachments, segregations) for each different cladding–target pair (TZM–Ta2.5W, TZM–Ta, and W–Ta).
- Study the state of the target and cladding materials (W, TZM, Ta, and Ta2.5W) after thermal cycling due to beam impacts. Identify any degradation of the material properties (strength, thermal conductivity) or appearance of defects (cracks, voids, microstructure changes, segregation).
- Foresee any other potential issues related to target operation (target block movement or deformation, blocking of cooling channels, . . .) and provide feedback to the design of the actual target.

To this end, several target blocks will be extracted at CERN and shipped to an external contractor with the required PIE capabilities.

5.9.8.2 Description of samples

The PIE is planned to be carried out on several target blocks, representative of the dimensions of the different blocks, all the combinations of target and cladding materials, and several levels of cyclic stress.

The four blocks foreseen for PIE are highlighted in Fig. 5.175. The characteristics of these blocks are listed in Table 5.36 and summarized in Fig. 5.176. The target blocks will present residual dose rates in the order of several hundreds of millisieverts per hour, and therefore special considerations will be necessary for handling the blocks and shipping them to the PIE contractor, as described in Section 5.9.6.

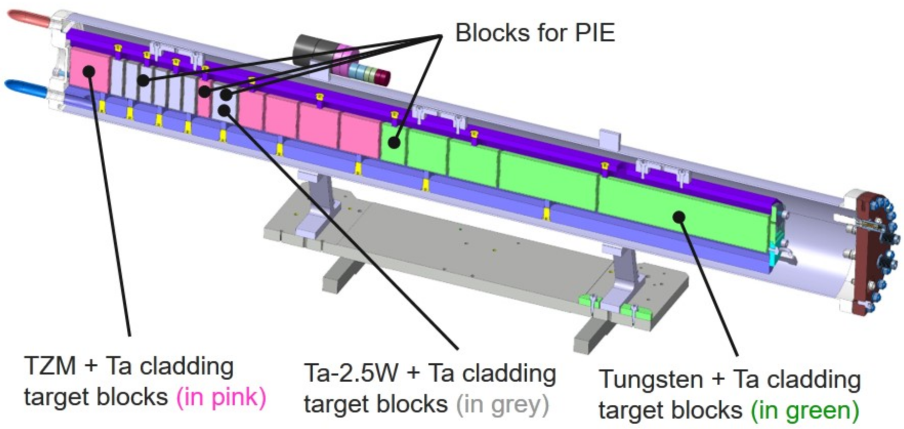

Fig. 5.175: Longitudinal cross-section of BDF target prototype, with the three different type of target blocks highlighted in different colours.

Table 5.36: Target prototype blocks foreseen for PIE, with dimensions and materials

Sample number	Shape	Dimensions			Materials		Comments
		Diameter (mm)	Length (mm)	Cladding thickness (mm)	Core	Cladding	
4	Cylindrical	80	25	1.5	TZM	Ta2.5W	
8			25		TZM	Ta	
9			50		TZM	Ta2.5W	50 μm thick Ta foil downstream
14			50		W	Ta	

5.9.8.3 *Description of tests envisgaed*

In the following section, a first proposal for the tests envisaged is presented. The final PIE will be subject to discussion with external contractors to match the desired testing, the contractor capabilities available, and the financial resources allocated. Each of the PIE steps described in the following will be performed for each of the blocks studied.

5.9.8.3.1 Surface inspection

Surface inspection is planned to be carried out on the samples before any destructive tests.

- *Visual inspection:* first, visual inspection should be carried out over the entire surface of the blocks. Any change in the surface colour and texture and the presence of any type of heterogeneity such as cracks, holes, or marks should be reported and properly localized.
- *Optical microscopy:* any features reported following visual inspection should be imaged with optical microscopy and micrographs should be recorded at different representative magnifications (e.g. 20×, 100×, and 500×,). Moreover, optical micrographs should be acquired on each flat surface (at centre, mid radius, and outer radius) and on the curved surfaces (next to the cylinder edges and in the middle of the length) according to Fig. 5.177, also at several representative magnifications.

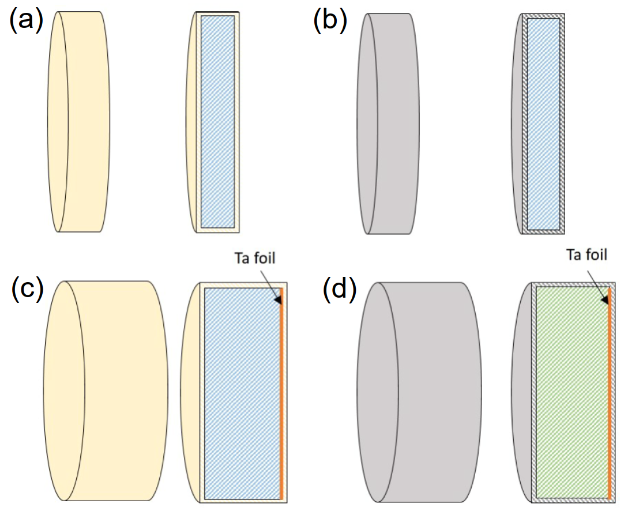

Fig. 5.176: Sketch of samples (a) 4, (b) 8, (c) 9, and (d) 14. A 3D view (left) and an axial cross-sectional view (right) are given for each sample. The colours indicate Ta2.5W (yellow), TZM (blue), and W (green). Blocks 9 and 14 contain a 50 µm Ta foil on the downstream side, between the target and the cladding material.

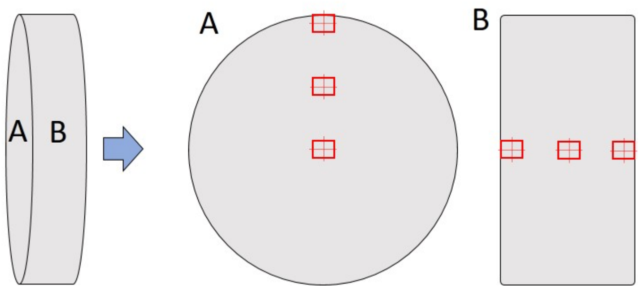

Fig. 5.177: 3D view of target block and 2D view of flat surface (A) and curved surface (B). Areas for optical microscopy outlined in red.

5.9.8.3.2 *Metrology requirements*

– For dimensional measurements, cylinder diameters should be measured along several diameters, according to Fig. 5.178(a). Cylinder lengths should be measured at different distances from the centre (or continuously) along two different perpendicular diameters, according to Fig. 5.178(b), to detect any cladding or target swelling.
– Surface roughness should be measured in several areas (the same areas as for optical microscopy in Fig. 5.177), to detect any surface morphology change due to cooling water.

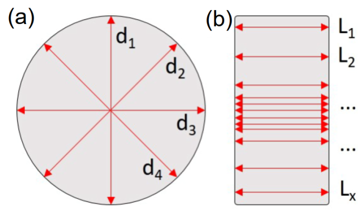

Fig. 5.178: Schematic illustration of a target block with (a) diameter measurements and (b) length measurements

5.9.8.3.3 Non-destructive testing

- *Penetrant testing:* the entire external surface of each block should be inspected with dye penetrant testing to reveal any weld imperfections, surface cracking, or other surface defects in the cladding which might not be perceptible by visual inspection.
- *Ultrasonic testing of interfaces:* the whole of the cladding–target interface should be examined by ultrasonic testing to detect any loss of contact between cladding and target. The sensitivity should be adjusted with artificial defects formed on unirradiated samples already available (see Fig. 5.179 for an example of an interfacial defect formed on the curved surface of a cylinder).
- *Ultrasonic testing of bulk material:* the entire volume of each block should be examined by ultrasonic testing to detect any defects in the bulk material. The sensitivity should also be adjusted with artificial defects formed in unirradiated samples.

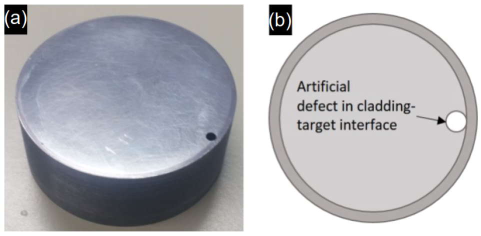

Fig. 5.179: (a) Image of an artificial interface defect prepared for previous internal studies, and (b) schematic illustration of the position of the defect with the side of the hole tangent to the cladding–target interface.

5.9.8.3.4 Specimen extraction

Once all the surface inspections, metrology, and non-destructive testing have been performed, specimen extraction should be carried out to allow further inspection. Careful cutting techniques such as EDM or low-speed sawing should be employed for specimen extraction to minimize introduction of artefacts due to cutting.

5.9.8.3.5 Metallographic inspection

Metallographic inspection should be performed on a slice of length equal to the block length $\times$ 20–30 mm $\times$ 10 mm located at the centre of each target block, as outlined in Fig. 5.180. The slice should be extracted in such a way that the surface to be prepared is slightly offset from the centre (by 0.5–2 mm). After the removal of material as a consequence of metallographic preparation (grinding and polishing), the surface to be examined will be coincident with the cylinder axis.

The specimen should be mounted in electrically conductive resin and the surface prepared with conventional metallographic preparation. Optical micrographs at representative magnifications should be acquired at the level of the cladding surface and of the cladding–target interface, on the upstream and downstream sides in both cases. Additionally, optical micrographs should be acquired from the bulk of the target material. Any detected feature or heterogeneity should additionally be imaged and reported.

Scanning electron micrographs should be acquired at the same places as the optical micrographs with secondary electron imaging to observe the surface morphology with additional resolution (e.g. 50$\times$, 1000$\times$, and 5000$\times$). In parallel, backscattered electron imaging should be employed to image any surface layer on the cladding (Ta oxides, contamination) and the diffusion layer in the cladding–target interface at representative magnifications. If any heterogeneity in chemical composition is detected with backscattered electron contrast (in the external cladding layer, diffusion layer, bulk material, . . .), micro-analysis techniques should be employed to identify the chemical nature of the feature.

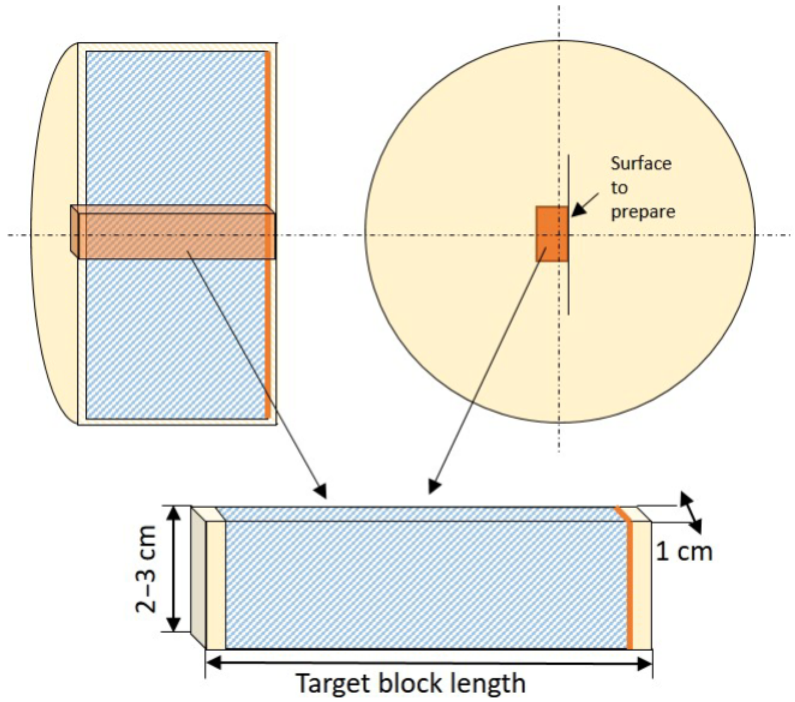

Fig. 5.180: Schematic illustration of target block with placement of the specimen for metallographic preparation.

5.9.8.3.6 Hardness testing

Microhardness testing should be carried out along several profiles on the same specimens as used for metallographic inspection, following an indentation pattern as shown in Fig. 5.181. Any phenomena affecting the mechanical properties of the material, such as plasticity, recrystallization, grain growth, or the appearance of voids or precipitates, would be measurable.

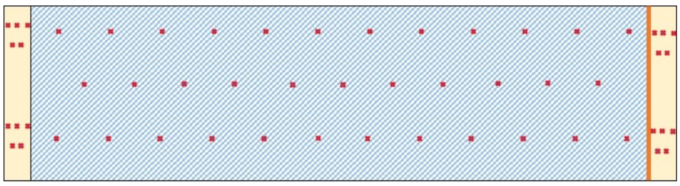

Fig. 5.181: Schematic illustration of a specimen used for metallographic inspection, with the microhardness indentations indicated in red.

5.9.8.3.7 Thermophysical properties

The thermal conductivity across the cladding–target interface should be measured to detect any change in the contact thermal resistance. Specimens should be extracted from both sides of the target blocks (upstream and downstream), as close as possible to the cylinder axis and with dimensions imposed by the measuring system.

5.9.8.3.8 Mechanical properties of cladding–target interface

The small thickness of the cladding materials on the target blocks does not allow the extraction of tensile specimens such as those used during the R&D activities on the cladding (see Section 5.8.4). Therefore, the strength of the cladding–target interface materials can only be measured by shear testing. Sample specimens and the set-up necessary for these measurements are depicted in Fig. 5.182. Tests will need to be carried out with miniaturized specimens owing to the small amount of material available. Specimens should be extracted in such a way that the cladding lip is obtained from a position as close as possible to the cylinder axis.

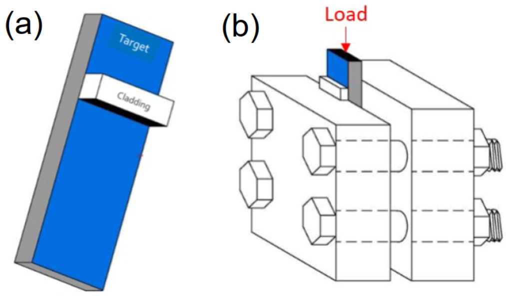

Fig. 5.182: (a) Schematic illustration of shear specimen and (b) schematic illustration of the set-up for shear testing.

References

[1] E. Lopez Sola et al. "Design of a high power production target for the beam dump facility at CERN". In: *Phys. Rev. Accel. Beams* 22 (11 Nov. 2019), p. 113001. DOI: 10.1103/PhysRevAccelBeams.22.113001. URL: https://link.aps.org/doi/10.1103/PhysRevAccelBeams.22.113001.

[2] W. Martienssen, H. Warlimont. "Refractory metals and alloys". In: *Springer Handbook of Condensed Matter and Materials Data*. Springer, 2005. Chap. 3.1.9, p. 318.

[3] J. M. Steichen. "Tensile properties of neutron irradiated TZM and tungsten". In: *J. Nucl. Mater.* 60 (1976), pp. 13–19. DOI: 10.1016/0022-3115(76)90112-4.

[4] A. T. Nelson et al. "Fabrication of a tantalum-clad tungsten target for LANSCE". In: *J. Nucl. Mater.* 431 (Dec. 2012), pp. 172–184. DOI: 10.1016/j.jnucmat.2011.11.041.

[5] M. Kawai et al. "Fabrication of a tantalum-clad tungsten target for KENS". In: *J. Nucl. Mater.* 296 (2001), pp. 312–320. DOI: 10.1016/S0022-3115(01)00533-5.

[6] L. G. Jones, D. Wilcox. "ISIS TS1 project target—design for manufacture". In: *J. Phys. Conf. Ser.* 1021 (2018). DOI: 10.1088/1742-6596/1021/1/012056.

[7] F. Cardarelli. "Tantalum and tantalum alloys". In: *Materials Handbook: A Concise Desktop Reference*. Springer International, 2018. Chap. 4.3.7, pp. 490–513. DOI: 10.1007/978-3-319-38925-7.

[8] J. Busom Descarrega, A. T. Pérez Fontenla, A. Perillo Marcone, E. Lopez Sola, M. Calviani, S. Sgobba, T. Weißgärber, T. Hutsch. "Application of hot isostatic pressing (HIP) technology to diffusion bond refractory metals for proton beam targets and absorbers at CERN". In: *Mater. Des. Process. Commun.* (2019). DOI: 10.1002/mdp2.101.

[9] E. Lopez Sola et al. "Beam Dump Facility Target: Design Status and Beam Tests in 2018". In: *Proc. 9th International Particle Accelerator Conference (IPAC'18), April 29–May 4, 2018* (Vancouver, BC, Canada). International Particle Accelerator Conference 9. Geneva, Switzerland: JACoW, June 2018, pp. 2604–2607. ISBN: 978-3-95450-184-7. DOI: doi:10.18429/JACoW-IPAC2018-WEPMG002. URL: http://jacow.org/ipac2018/papers/wepmg002.pdf.

[10] E. Lopez Sola et al. "Beam impact tests of a prototype target for the beam dump facility at CERN: Experimental setup and preliminary analysis of the online results". In: *Phys. Rev. Accel. Beams* 22 (12 Dec. 2019), p. 123001. DOI: 10.1103/PhysRevAccelBeams.22.123001. URL: https://link.aps.org/doi/10.1103/PhysRevAccelBeams.22.123001.

[11] T. T. Bohlen et al. "The FLUKA code: developments and challenges for high energy and medical applications". In: *Nucl. Data Sheets* 120 (2014), pp. 211–214. ISSN: 0090-3752. DOI: https://doi.org/10.1016/j.nds.2014.07.049. URL: http://www.sciencedirect.com/science/article/pii/S0090375214005018.

[12] A. Ferrari et al. *FLUKA: A Multi-particle Transport Code (Program Version 2005)*. CERN Yellow Reports: Monographs. Geneva: CERN, 2005. URL: https://cds.cern.ch/record/898301.

[13] V. Vlachoudis. "FLAIR: a powerful but user friendly graphical interface for FLUKA". In: *Int. Conf. on Mathematics, Computational Methods Reactor Physics (MC 2009)* (Saratoga Springs, New York). Apr. 2009.

[14] H. Vincke and C. Theis. "ActiWiz 3 – an overview of the latest developments and their application". In: *J. Phys. Conf. Ser.* 1046 (June 2018), p. 012007. DOI: 10.1088/1742-6596/1046/1/012007. URL: https://doi.org/10.1088/1742-6596/1046/1/012007.

[15] *Regulations for the Safe Transport of Radioactive Material: Specific Safety Requirements*. IAEA Safety Standards SSR-6 (Rev.1). Vienna: International Atomic Energy Agency, 2018. ISBN: 978-92-0-107917-6. URL: https://www.iaea.org/publications/12288/regulations-for-the-safe-transport-of-radioactive-material.

[16] Office federal de la santé publique (OFSP). *Ordonnance du 26 avril 2017 sur la radioprotection (ORaP)*. 2017. URL: https://www.admin.ch/opc/fr/classified-compilation/20163016/index.html.

[17] F. F. Schmidt, H. R. Ogden. *The Engineering Properties of Tantalum and Tantalum Alloys*. Defense Metals Information Center, Sept. 1963.

[18] G. Filacchioni et al. "Tensile and impact properties of TZM and Mo-5% Re". In: *J. Nucl. Mater.* 212–215, Part B (1994), pp. 1288–1291. DOI: https://doi.org/10.1016/0022-3115(94)91037-5. URL: https://www.sciencedirect.com/science/article/pii/0022311594910375.

[19] F. F. Schmidt, H. R. Ogden. *The Engineering Properties of Tungsten and Tungsten Alloys*. Defense Metals Information Center, Sept. 1963.

[20] H. C. Starck. *ULTRA 76 Tantalum for Corrosive Resistant Applications*. Online brochure. 2017. URL: https://www.hcstarck.com/ultra76_tantalum_alloy.

[21] Fraunhofer IFAM. *TaW-clad Refractory Metals*. Internal communication. 2017.

[22] Plansee GmbH. *TZM Measurements*. Internal communication. 2018.

[23] Y. Zhang et al. "Observations on the ductile-to-brittle transition in ultrafine-grained tungsten of commercial purity". In: *Mater. Sci. Eng. A* 503 (2009), pp. 37–40. DOI: https://doi.org/10.1016/j.msea.2008.07.074. URL: https://www.sciencedirect.com/science/article/pii/S0921509308013002.

[24] V. Krsjak et al. "Mechanical properties of tungsten in the transition temperature range". In: *J. Nucl. Mater.* 450 (2014), pp. 81–87. DOI: https://doi.org/10.1016/j.jnucmat.2013.11.019. URL: https://www.sciencedirect.com/science/article/pii/S0022311513012567.

[25] H. Ullmaier, F. Carsughi. "Radiation damage problems in high power spallation neutron sources". In: *Nucl. Instrum. Methods Phys. Res. B* 101 (1995), pp. 406–421. DOI: https://doi.org/10.1016/0168-583X(95)00590-0. URL: https://www.sciencedirect.com/science/article/pii/0168583X95005900.

[26] J. Habainy et al. "Fatigue properties of tungsten from two different processing routes". In: *J. Nucl. Mater.* 506 (2018), pp. 83–91. DOI: https://doi.org/10.1016/j.jnucmat.2017.10.061. URL: https://www.sciencedirect.com/science/article/pii/S0022311516312028.

[27] R. M. Christensen. "A comprehensive theory of yielding and failure for isotropic materials". In: *J. Eng. Mater. Technol.* 129 (2007), pp. 173–181. DOI: 10.1115/1.2712847.

[28] H. A. Calderon et al. "Microstructure and plasticity of two molybdenum-base alloys (TZM)". In: *Mater. Sci. Eng. A* 160 (1993), pp. 189–199. DOI: https://doi.org/10.1016/0921-5093(93)90447-M. URL: https://www.sciencedirect.com/science/article/pii/092150939390447M.

[29] R. I. Stephens, A. Fatemi, et al. "Stress-based criteria". In: *Metal Fatigue in Engineering*. 2nd ed. Wiley-Interscience, 2000. Chap. 10.3, p. 325. ISBN: 978-0-471-51059-8.

[30] D. F. Socie, G. B. Marquis. "Stress-based models". In: *Multiaxial Fatigue*. Society of Automotive Engineers, 2000. Chap. 5, p. 155. ISBN: 0-7680-0453-5.

[31] J. A. Collins. *Failure of Materials in Mechanical Design: Analysis, Prediction, Prevention*. Wiley-Interscience, 1993. Chap. 7: High-cycle fatigue.

[32] D. Wilcox et al. "Stress levels and failure modes of tantalum-clad tungsten targets at ISIS". In: *J. Nucl. Mater.* 506 (Nov. 2017), pp. 76–82. DOI: 10.1016/j.jnucmat.2017.10.075.

[33] D. Wilcox, RAL (UK). *Lock-in Temperature*. Internal communication. 2018.

[34] J. Habainy et al. "Formation of oxide layers on tungsten at low oxygen partial pressures". In: *J. Nucl. Mater.* 506 (2018), pp. 26–34. URL: https://doi.org/10.1016/j.jnucmat.2017.12.018.

[35] T. Millner and J. Neugebauer. "Volatility of the oxides of tungsten and molybdenum in the presence of water vapour". In: *Nature* 163 (1949), pp. 601–602. DOI: 10.1038/163601b0.

[36] F. P. Incropera et al. "Internal flow". In: *Fundamentals of Heat and Mass Transfer*. Wiley, 2011.

[37] V. Gnielinski. "New equations for heat and mass transfer in turbulent pipe and channel flow". In: *Int. Chem. Eng.* 16 (1976), pp. 359–368.

[38] B. S. Petukhov. "Heat transfer and friction in turbulent pipe flow with variable physical properties". In: *Adv. Heat Transf.* 6 (1970), pp. 503–564. DOI: 10.1016/S0065-2717(08)70153-9.

[39] Plansee GmbH. *Manufacturing of Refractory Metals*. Internal communication. 2017.

[40] K. Kershaw et al. "Design development for the Beam Dump Facility target complex at CERN". In: *J. Instrum.* 13 (2018), P10011. DOI: 10.1088/1748-0221/13/10/P10011. URL: https://cds.cern.ch/record/2631508.

[41] L. Giordanino. "Engineering evaluation of the BDF target". In: *EDMS* (2018). URL: https://edms.cern.ch/document/2059775/1.

[42] European Committee for Standardization. *EN 13445-3 Unfired Pressure Vessels—Part 3: Design*. 2014.

[43] Verein Deutscher Ingenieure. *VDI 2230, Part 1, Systematic Calculation of Highly Stressed Bolted Joints*. 2014.

[44] N. Simos et al. "Proton irradiation effects on the physio-mechanical properties and microstructure of cold-worked molybdenum". In: *J. Nucl. Energy Sci. Power Generat. Technol.* 4 (2017), p. 2.

[45] I. V. Gorynin et al. "Effects of neutron irradiation on properties of refractory metals". In: *J. Nucl. Mater.* 191-194 (1992). Fusion Reactor Materials Part A, pp. 421–425. ISSN: 0022-3115. DOI: https://doi.org/10.1016/S0022-3115(09)80079-2. URL: http://www.sciencedirect.com/science/article/pii/S0022311509800792.

[46] K. Furuya and T. Kainuma. "Effects of alloying and heat treatment on the endurance limit of molybdenum in high cycle fatigue tests". In: *J. Nucl. Mater.* 122.1-3 (1984), pp. 754–758.

[47] H. H. Smith and D. J. Michel. "The effect of irradiation on the fatigue and flow behavior of TZM alloy". In: *J. Nucl. Mater.* 66.1 (1977), pp. 125–142. ISSN: 0022-3115. DOI: https://doi.org/10.1016/0022-3115(77)90141-6. URL: http://www.sciencedirect.com/science/article/pii/0022311577901416.

[48] G. Pintsuk. "Tungsten as a plasma-facing material". In: *Comprehensive Nuclear Materials*. Ed. by R. J. M. Konings. Oxford: Elsevier, 2012, pp. 551–581. ISBN: 978-0-08-056033-5. DOI: https://doi.org/10.1016/B978-0-08-056033-5.00118-X. URL: http://www.sciencedirect.com/science/article/pii/B978008056033500118X.

[49] V. Barabash et al. "Armour materials for the ITER plasma facing components". In: *Phys. Scr.* 1999.T81 (1999), p. 74.

[50] M. J. Makin and E. Gillies. "The effect of neutron irradiation on the mechanical properties of molybdenum and tungsten". In: *J. Inst. Metals* 86 (1957).

[51] S. A. Maloy et al. "The effect of 800 MeV proton irradiation on the mechanical properties of tungsten at room temperature and at 475°C". In: *J. Nucl. Mater.* 343.1-3 (2005), pp. 219–226.

[52] W. D. Klopp, W. R. Witzke, and P. L. Raffo. *Mechanical Properties of Dilute Tungsten-Rehnium Alloys*. Tech. rep. National Aeronautics and Space Administration, Cleveland, OH, USA, 1966.

[53] V. Barabash et al. "Selection, development and characterisation of plasma facing materials for ITER". In: *J. Nucl. Mater.* 233-237 (1996), pp. 718–723. ISSN: 0022-3115. DOI: https://doi.org/10.1016/S0022-3115(96)00323-6. URL: http://www.sciencedirect.com/science/article/pii/S0022311596003236.

[54] H. Kurishita et al. "Current status of ultra-fine grained W–TiC development for use in irradiation environments". In: *Phys. Scr.* 2007.T128 (2007), p. 76.

[55] H. Kurishita et al. "Development of nanostructured tungsten based materials resistant to recrystallization and/or radiation induced embrittlement". In: *Mater. Trans.* 54.4 (2013), pp. 456–465.

[56] T. Broome. "ISIS target and moderator materials". In: *Proceedings of the Second International Workshop on Spallation Materials Technology, No. JUL-3450, in FZJ Report*. 1997, pp. 55–59.

[57] A. T. Nelson et al. "Fabrication of a tantalum-clad tungsten target for LANSCE". In: *J. Nucl. Mater.* 431 (Dec. 2012), pp. 172–184. DOI: 10.1016/j.jnucmat.2011.11.041.

[58] S. Peggs et al. *ESS Technical Design Report, Released 2.63*. 2013.

[59] Y. Ishijima et al. "Corrosion resistance of refractory metals in high-temperature water". In: *J. Nucl. Mater.* 307-311 (2002), pp. 1369–1374. ISSN: 0022-3115. DOI: https://doi.org/10.1016/S0022-3115(02)01066-8. URL: http://www.sciencedirect.com/science/article/pii/S0022311502010668.

[60] R. S. Lillard, D. L. Pile, and D. P. Butt. "The corrosion of materials in water irradiated by 800 MeV protons". In: *J. Nucl. Mater.* 278.2 (2000), pp. 277–289. ISSN: 0022-3115. DOI: https://doi.org/10.1016/S0022-3115(99)00248-2. URL: http://www.sciencedirect.com/science/article/pii/S0022311599002482.

[61] S. A. Maloy et al. "Water corrosion measurements on tungsten irradiated with high energy protons and spallation neutrons". In: *J. Nucl. Mater.* 431.1 (2012). Special Issue of the Tenth International Workshop on Spallation Materials Technology (IWSMT-10), pp. 140–146. ISSN: 0022-3115. DOI: https://doi.org/10.1016/j.jnucmat.2011.11.052. URL: http://www.sciencedirect.com/science/article/pii/S0022311511010075.

[62] M.-D. Bermúdez et al. "Erosion-corrosion of stainless steels, titanium, tantalum and zirconium". In: *Wear* 258.1 (2005). Second International Conference on Erosive and Abrasive Wear, pp. 693–700. ISSN: 0043-1648. DOI: https://doi.org/10.1016/j.wear.2004.09.023. URL: http://www.sciencedirect.com/science/article/pii/S004316480400256X.

[63] A. G. Metcalfe and T. B. Lindemer. *Diffusion Bonding of Refractory Metals*. Tech. rep. Solar Turbines International, San Diego, CA, USA, 1963.

[64] D. E. Dombrowski and S. A. Maloy. *Preliminary Results for HIP Bonding Ta to W Targets for the Materials Test Station*. Tech. rep. Los Alamos National Laboratory (LANL), Los Alamos, NM, USA, 2009.

[65] J.-F. Li et al. "Strength proof evaluation of diffusion-jointed W/Ta interfaces by small punch test". In: *J. Nucl. Mater.* 321.2 (2003), pp. 129–134. ISSN: 0022-3115. DOI: https://doi.org/10.1016/S0022-3115(03)00237-X. URL: http://www.sciencedirect.com/science/article/pii/S002231150300237X.

[66] L. A. Gypen, M. Brabers, and A. Deruyttere. "Corrosion resistance of tantalum base alloys. Elimination of hydrogen embrittlement in tantalum by substitutional alloying". In: *Mater. Corros.* 35.2 (1984), pp. 37–46.

[67] W. H. Gourdin et al. "The influence of tungsten alloying on the mechanical properties of tantalum". In: *J. Phys. IV* 4.C8 (1994), pp. C8–207.

[68] S. Kong et al. "Cyclic stress strain behaviour of high-melting point metals". In: *High Temp. Mater. Process.* 13.1 (1994), pp. 61–74.

[69] J. Chen et al. "Mechanical properties of pure tantalum after 800 MeV proton irradiation". In: *J. Nucl. Mater.* 298.3 (2001), pp. 248–254.

[70] T. T. Claudson and H. J. Pessl. "Irradiation effects on high temperature reactor structural materials". In: *BNWL* 23.Feb. (1965).

[71] F. W. Wiffen. *Tensile Properties of Fast-reactor Neutron-irradiated BCC Metals and Alloys*. Tech. rep. Oak Ridge National Laboratory, TN, USA, 1973.

[72] I. Ipatova et al. "Radiation-induced void formation and ordering in Ta-W alloys". In: *J. Nucl. Mater.* 495 (2017), pp. 343–350.

[73] Ammigan, K. and Hurh, P. "Status and update of the RaDIATE Collaboration R&D program". In: *Proc. of 13th International Topical Meeting on the Applications of Accelerators, Quebec, Canada, July 31–August 4*. 2018.

[74] Ishida, T. et al. "Recent progress on radiation damage studies at RaDIATE". In: *Proc. of 20th International Workshop on Neutrinos from Accelerators, Blacksburg, Virginia, August 12–18*. 2018.

[75] ASM International Handbook Committee and D. L. Olson. *Welding, Brazing, and Soldering*. ASM Handbook. ASM International, 1993. ISBN: 9780871703828. URL: https://books.google.ro/books?id=y0VLAQAAIAAJ.

[76] H.-J. Shi, C. Korn, and G. Pluvinage. "High temperature isothermal and thermomechanical fatigue on a molybdenum-based alloy". In: *Mater. Sci. Eng. A* 247.1–2 (1998), pp. 180–186.

[77] J. Habainy et al. "Fatigue behavior of rolled and forged tungsten at 25°, 280° and 480°C". In: *J. Nucl. Mater.* 465 (2015), pp. 438–447.

[78] M. Papakyriacou et al. "Influence of loading frequency on high cycle fatigue properties of bcc and hcp metals". In: *Mater. Sci. Eng. A* 308.1-2 (2001), pp. 143–152.

[79] A. T. Perez Fontenla. *Microscope Observation of Tantalum Coating on Tungsten Rod*. Tech. rep. CERN, 2015. URL: https://edms.cern.ch/document/1513398/1.

[80] A. T. Perez Fontenla. *Scanning Electron Microscope (SEM) Observation of Tantalum (Ta) Sleeved Tungsten (W) Rod*. Tech. rep. CERN, 2015. URL: https://edms.cern.ch/document/1538148/1.

[81] C. O. Tarr. *Jointing of Refractory Metals by Solidstate Diffusion Bonding*. US Patent 3,170,234. Feb. 1965.

[82] A. T. Perez Fontenla. *Quality Study of Tungsten (W) Rods and Tantalum (Ta)-cladded W Material*. Tech. rep. CERN, 2016. URL: https://edms.cern.ch/document/1566868/1.

[83] C. Torregrossa et al. "19th Plansee Seminar 2017". In: *Refractory Metals for Particle Producing Targets at CERN*. 2016.

[84] L. Gomez Pereira. *Quality Inspection of Potential Material Target for n-TOF*. Tech. rep. CERN, 2017. URL: https://edms.cern.ch/document/1749441/1.

[85] J. Hammond. *Method for Diffusion Bonding Refractory Metals and Alloys*. US Patent 3,714,702. Feb. 1973.

[86] S. D. Cramer. *Corrosion: Materials*. ASM Handbook 13b. ASM International, 2005.

[87] P. Aimone, E. Hinshaw, et al. "Tantalum materials in the CPI for the next millennium". In: *57th Annual NACE Conference, Houston, TX, USA*. 2001.

[88] F. Liautaud. *Electrochemical Study by CETIM-CERMAT on Corrosion Behaviour of Different Materials in Demineralized Water*. Tech. rep. CERN, 2016. URL: https://edms.cern.ch/document/1698449/1.

[89] O. Caretta, T. Davenne, and C. J. Densham. "Water erosion tests on a tantalum sample: a short communication". In: *J. Nucl. Mater.* 492 (2017), pp. 52–55.

[90] B. V. Cockeram et al. "The swelling, microstructure, and hardening of wrought LCAC, TZM, and ODS molybdenum following neutron irradiation". In: *J. Nucl. Mater.* 418.1-3 (2011), pp. 121–136.

[91] J. Matolich, H. Nahm, and J. Moteff. "Swelling in neutron irradiated tungsten and tungsten-25 percent rhenium". In: *Scr. Metall.* 8.7 (1974), pp. 837–841.

[92] G. V. Müller et al. "Postirradiation tensile properties of Mo and Mo alloys irradiated with 600 MeV protons". In: *J. Nucl. Mater.* 212 (1994), pp. 1283–1287.

[93] T. S. Byun et al. "Deformation and fracture properties in neutron irradiated pure Mo and Mo alloys". In: *J. Nucl. Mater.* 376.2 (2008), pp. 240–246.

[94] B. N. Singh et al. "Microstructure and mechanical behaviour of TZM and Mo-5% Re alloys irradiated with fission neutrons". In: *J. Nucl. Mater.* 223.2 (1995), pp. 95–102.

[95] M. Scibetta, R. Chaouadi, and J. L. Puzzolante. "Analysis of tensile and fracture toughness results on irradiated molybdenum alloys, TZM and Mo–5% Re". In: *J. Nucl. Mater.* 283 (2000), pp. 455–460.

[96] S. A. Maloy et al. "The effect of 800 MeV proton irradiation on the mechanical properties of tungsten". In: *Mater. Trans.* 43.4 (2002), pp. 633–637.

[97] W. F. Sommer et al. *Tungsten Materials Analysis Letter Report*. Tech. rep. LA-UR-95-220. Los Alamos National Laboratory, Los Alamos, NM, USA1, 1995, p. 51.

[98] T. Hwang et al. “Effect of self-ion irradiation on hardening and microstructure of tungsten”. In: *Nucl. Mater. Energy* 9 (2016), pp. 430–435.

[99] S. Saito and D. Hamaguchi. “Mechanical properties of W alloys and pure Ta irradiated at SINQ target 4”. In: *IWSMT-11*. 2012.

[100] R. D. Brown, M. S. Wechsler, and C. Tschaldr. “Tensile properties of several 800 MeV proton-irradiated bcc metals and alloys”. In: *Influence of Radiation on Material Properties: 13th International Symposium (Part II), Seattle, WA, USA, 23–25 June 1986*. Vol. 956. ASTM International. 1987, p. 131.

[101] T. S. Byun and S. A. Maloy. “Dose dependence of mechanical properties in tantalum and tantalum alloys after low temperature irradiation”. In: *J. Nucl. Mater.* 377.1 (2008), pp. 72–79.

[102] P. Jung. “Radiation effects in structural materials of spallation targets”. In: *J. Nucl. Mater.* 301.1 (2002), pp. 15–22.

[103] K. J. Leonard. “Radiation Effects in Refractory Metals and Alloys”. In: *Comprehensive Nuclear Materials*. Ed. by R. J. M. Konings. Oxford: Elsevier, 2012, pp. 181–213. ISBN: 978-0-08-056033-5. DOI: https://doi.org/10.1016/B978-0-08-056033-5.00088-4. URL: http://www.sciencedirect.com/science/article/pii/B9780080560335000884.

[104] Kavin Ammigan. *RaDIATE Collaboration*. Mar. 2019. URL: https://radiate.fnal.gov/index.html (visited on 03/21/2019).

[105] Brookhaven National Laboratory. *Brookhaven Linac Isotope Producer*. Mar. 2019. URL: https://www.bnl.gov/BLIP/ (visited on 03/21/2019).

[106] Kavin Ammigan et al. “The RaDIATE high-energy proton materials irradiation experiment at the Brookhaven linac isotope producer facility”. In: *Proc. of 8th International Particle Accelerator Conference (IPAC 2017), Copenhagen, Denmark, May 14–19, 2017*. 2017, WEPVA138. DOI: 10.18429/JACoW-IPAC2017-WEPVA138. URL: http://lss.fnal.gov/archive/2017/conf/fermilab-conf-17-582-ad.pdf.

[107] Patrick Hurh. *Overview of RaDIATE Organized Activities and Recent Results*. Presented at the 5th RaDIATE Collaboration Meeting (RaDIATE 2018), CERN, Geneva, Switzerland. 2018. URL: https://indico.cern.ch/event/718767/contributions/3194769/.

[108] J. P. Canhoto Espadanal. *FLUKA Damage Studies to the BLIP Irradiations*. EDMS Document 2114686 v.1. Geneva: CERN, 2019. URL: https://edms.cern.ch/ui/#!master/navigator/document?P:1003062245:100327351:subDocs.

[109] E. Fornasiere. *BLIP 2017 Activities*. EDMS Document 1760908 v.1. Geneva: CERN, 2017. URL: https://edms.cern.ch/ui/#!master/navigator/document?P:1003062245:1092806060:subDocs.

[110] E. Fornasiere. *BLIP Run 2*. EDMS Document 2114690 v.1. Geneva: CERN, 2019. URL: https://edms.cern.ch/ui/#!master/navigator/document?P:1003062245:100327359:subDocs.

[111] Kavin Ammigan et al. *Overview of RaDIATE-organized BLIP Irradiations*. Presented at the 5th RaDIATE Collaboration Meeting (RaDIATE 2018), CERN, Geneva, Switzerland. 2018. URL: https://indico.cern.ch/event/718767/contributions/3194778/.

[112] ANSYS Inc. *ANSYS Mechanical User’s Guide*. 2013.

[113] ANSYS Inc. *ANSYS APDL Command Reference*. 2013.

[114] E. Fornasiere. *Price Enquiry Post-Irradiation Experiment (PIE) of Samples Irradiated at the BLIP Facility*. EDMS Document 1836705 v.1. Geneva: CERN, 2017. URL: https://edms.cern.ch/ui/#!master/navigator/document?P:1003062245:1655424143:subDocs.

[115] CERN. *BDF Target Prototype Assembly*. 2018. URL: http://cds.cern.ch/record/2635418.

[116] CERN. *BDF Target Prototype Installation*. 2018. URL: http://cds.cern.ch/record/2638991.

[117] P. Beynel and P. Maier and H. Schonbacher. *Compilation of Radiation Damage Test Data. Part III: Materials Used around High-energy Accelerators*. Tech. rep. CERN-HS-RP-093. CERN, 1982. URL: https://cds.cern.ch/record/141784/files/CERN-HS-RP-093.pdf.

[118] M. Guinchard et al. "Validation of strain optical sensors". In: *EDMS* (2015). URL: https://edms.cern.ch/document/1555701/1.

[119] L. Bianchi et al. "BDF T6 prototype target instrumentation technical description". In: *EDMS* (2018). URL: https://edms.cern.ch/ui/file/1870655/0.1.

[120] Nucleonica GmbH. *Nucleonica Nuclear Science Portal*. URL: www.nucleonica.com.

Chapter 6

Target complex design and development

6.1 Introduction to the target complex

The target will be at the heart of the new facility. High levels of radiation (both prompt and residual) will be produced by the SPS beam hitting the target; a total accumulated dose near the target of around 500 MGy/yr is expected. The target will be located in an underground area (to contain radiation as much as possible) about 15 m below ground level. The depth of the infrastructure is determined by the location of the extraction line (TT20) from where the SPS beam will be deflected.

The target will be surrounded by approximately 5500 t of cast iron and steel shielding with outer dimensions of around 6.8 m $\times$ 9.5 m $\times$ 8 m high (the so-called hadron absorber) to reduce the prompt dose rate during operation and the residual dose rate around the target during shutdown. The target and its surrounding shielding will be housed in a vessel containing gaseous helium slightly above atmospheric pressure to reduce air activation and reduce the radiation-accelerated corrosion of the target and surrounding equipment.

The SPS beam will enter the helium vessel through a beam window and then pass through a collimator, which serves to protect the target and adjacent equipment from misalignment of the incident SPS beam and to protect the equipment in the extraction tunnel from particles (essentially neutrons generated by the target) travelling backwards relative to the incident beam. Downstream of the target, a magnetic coil and US1010 steel yoke will be used to produce a magnetic field of 1.5–1.6 T to sweep away high-energy muons produced in the target to reduce experimental backgrounds. The secondary beam will pass through the downstream helium vessel wall and leave the target complex via a 5 cm thick steel plate ‘window’ at the upstream end of the detector hall.

Schematic views are presented in Figs. 6.1–6.3.

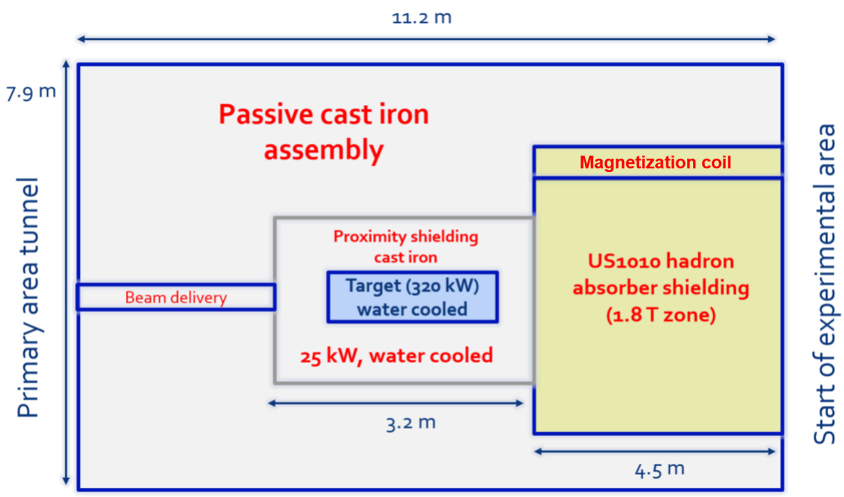

Fig. 6.1: Schematic view of the BDF target complex

The target and the shielding immediately around it will be water cooled. All of the shielding in the helium vessel will be built up from blocks, the layout and geometries of which are designed to avoid direct radiation shine paths and to minimize the number of block movements needed to allow exchange of failed equipment. A helium purification system will be provided to allow flushing of the air to ensure a 99.9% pure helium atmosphere in the vessel after initial installation and after maintenance

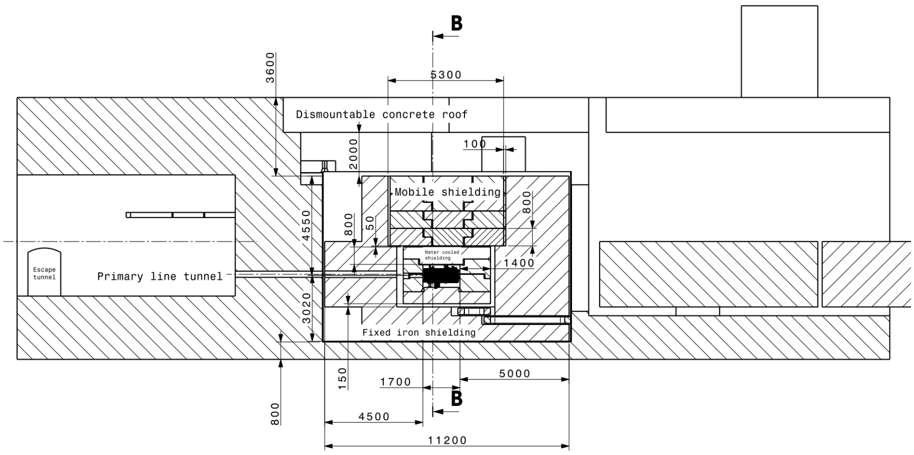

Fig. 6.2: Cross-sectional view of the BDF target complex

interventions. Ventilation of the target complex will use a cascade of pressure between different zones to provide containment of any radioactive contamination that could potentially be released according to ISO Standard 17873.

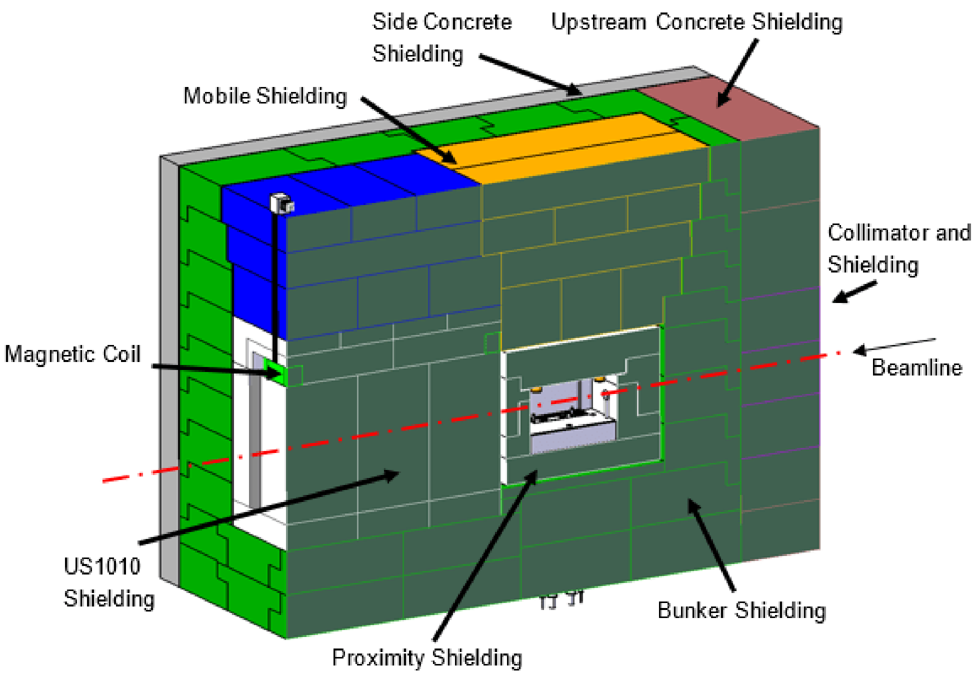

Fig. 6.3: Isometric view of the BDF target complex

Remote handling and manipulation of the target and surrounding shielding will be mandatory owing to the high residual dose rates. The target complex has been designed to house the target and its shielding in the helium vessel along with the cooling, ventilation, and helium purification services below ground level. The target complex design allows for removal and temporary storage of the target and shielding blocks in a cool-down area below ground level and includes dedicated shielded pits for storage of the highest-dose-rate equipment.

A 40 t capacity overhead travelling crane in the target complex building will be used for initial installation and will carry out the handling and remote handling of the shielding blocks and other equipment as needed for assembly and maintenance of the facility. All of the shielding blocks and other heavy equipment are designed to be compatible with the crane's lifting capacity. The target and beam elements are to be aligned within ± 10 mm with respect to the impinging proton beam.

6.2 Design study of handling and integration of the BDF target complex

6.2.1 Introduction to the handling and integration study

6.2.1.1 Aim of study

After the initial work to determine the main requirements and basic layout of the target complex as explained in the introduction, the target complex design was further developed by going into more detail about the handling and remote handling operations required throughout the life of the facility. This work aimed to demonstrate the feasibility of the construction, operation, and maintenance of the BDF target complex along with decommissioning of the key elements, and to provide an integrated design of the target complex. The output from the study was fed into the design work on the target, the magnetized muon shield system, the helium vessel, and the cooling and ventilation systems.

6.2.1.2 Deliverables of study

The deliverables of the study were in the form of reports, 2D drawings, 3D models of the target complex, and animations of the handling sequences. They are stored in CERN's EDMS in the document EDMS 1977049 v1, "BDF Target Complex Design: Final Results: May 2018" [1]. The study results were published in Ref. [2].

6.2.1.3 Scope of study

The remote handling of highly activated radioactive objects, such as the target, collimator, beam window, shielding blocks, and magnetic coil, along with their connection and disconnection within the target complex building, was studied by CERN in collaboration with Oxford Technologies Ltd to arrive at the integrated designs presented here. In addition to 'foreseen' remote handling operations, such as target exchange, the study considered 'unforeseen' remote handling operations needed to recover from failures or damage to equipment. The study included the conceptual design of lifting, handling, and remote handling equipment for highly activated objects along with the necessary water, helium, and electrical connections compatible with the radiation environment and remote handling constraints. These designs were then integrated into the target complex as a whole. The handling and integration studies concentrated on the target hall and its underground area—the integration of an adjacent service building housing the ventilation plant, access systems, controls, etc. was dealt with separately (Chapter 8).

6.2.1.4 Key design considerations

6.2.1.4.1 Shielding design

A large amount of the design is driven by radiation protection and safety considerations. For the shielding blocks in the helium vessel, this leads to requirements such as:

- minimizing and staggering gaps to avoid direct radiation shine paths;
- providing gaps to allow purging by the helium purification system;
- equipping the blocks with lifting features to allow remote handling;
- proportioning the blocks so that they are stable during transport and installation;
- achieving compatibility with the capacity of the crane in the building and with road transport.

6.2.1.4.2 Water and electrical connections

Experience at CERN has shown that connections in radiation environments are a source of problems such as water leaks—for this reason, particular attention was paid to connection and disconnection methods compatible with the radiation environment, along with repair in the event of failure and damage.

6.2.1.4.3 Whole life cycle

The study took into account the whole life cycle of the facility, in particular:

- initial installation and alignment;
- potential failures and damage during operation and maintenance, along with how to recover from them (using remote techniques where needed);
- reconfiguration of the facility for a different experiment in the future;
- decommissioning.

6.2.1.5 The two handling concepts studied (crane and trolley concepts)

Target complex designs based on two different handling concepts have been developed: the 'crane concept' and the 'trolley concept'.

6.2.1.5.1 Crane concept: using a remotely controlled overhead travelling crane

The crane concept relies on an overhead travelling crane in the target complex building for remotely controlled handling and transfer of the target, shielding, magnetic coil, etc. during the life of the facility.

The hook of the crane has motorized rotation to allow remote handling of radioactive equipment. Power and signal connection services are supplied to the pulley block of the hook to operate the spreader attachment features used to remotely pick up loads, and for the cameras on the spreaders (Fig. 6.4). More details of this building crane are given in Section 6.2.1.5.1.

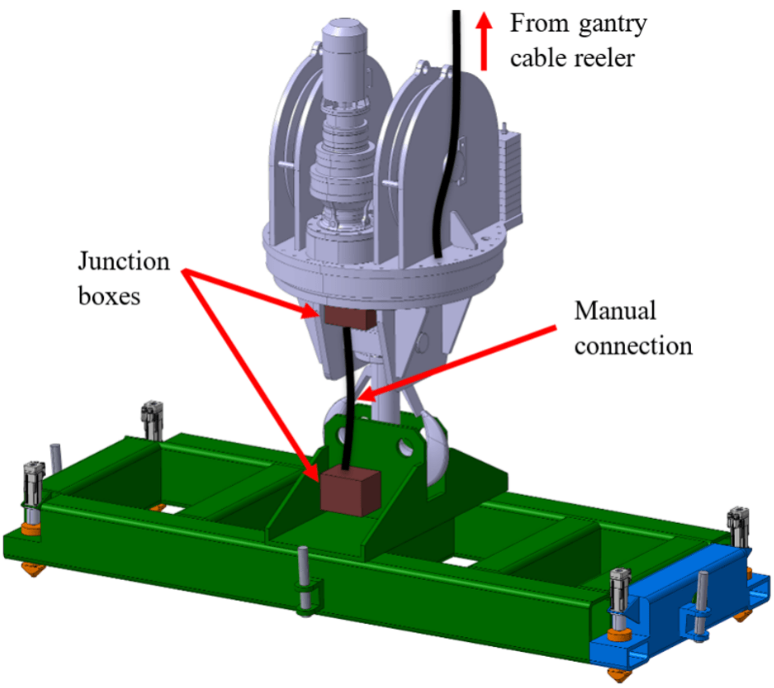

Fig. 6.4: Pulley block and hook (grey) of overhead travelling crane with remotely operated spreader beam for handling of shielding. The spreader shown has remotely operated ISO load attachments at each corner and is equipped with cameras.

Remotely operated spreader beams are needed to enable the crane to pick up and handle the different radioactive elements of the facility. More details of the spreader beam designs are given in the sections dealing with the handling of the key components of the facility.

6.2.1.5.2 Trolley concept

The trolley concept has the target and its main services installed on a mobile trolley running on rails. When the trolley retracts the target and shielding from the helium vessel, the target enters a remote handling 'hot cell' equipped with master–slave manipulators which allow the target to be disconnected from its services remotely and then exchanged without disturbing other equipment in the helium vessel. This concept is already used with ISIS at the Rutherford Appleton Laboratory in the UK (Fig. 6.5). For the handling operations on other equipment, the building crane is used in the same way as in the crane concept.

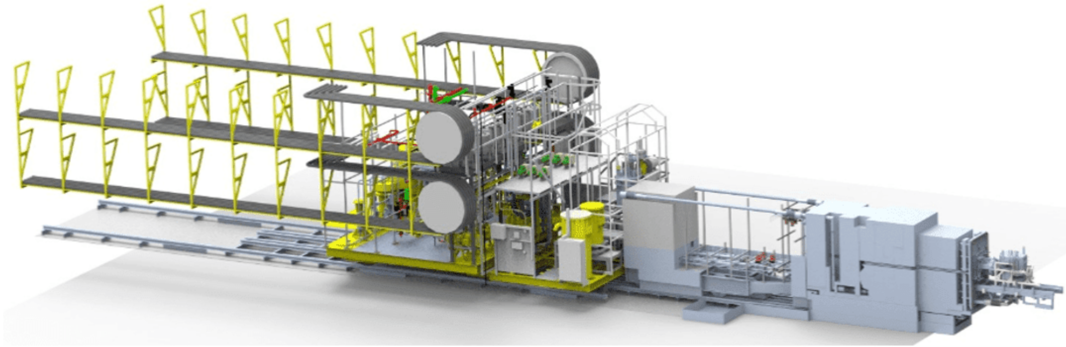

Fig. 6.5: ISIS target trolley. (Courtesy of RAL.)

6.2.1.5.3 Common features of and main differences between the crane and trolley concepts

For both concepts, the main elements (target core, beam window, helium vessel, collimator, magnetic coil, and US1010 shielding) are essentially the same and are common to the target complex designs produced for the two concepts. The designs for both concepts include cool-down areas, remote handling areas, cooling and ventilation areas, and sump rooms.

The main differences between the crane and trolley concepts are in the way the target and water-cooled proximity shielding are supported, installed, and removed from the helium vessel and how their services are connected and disconnected. These differences can potentially have a large impact on the reliability and operation of the facility.

6.2.1.6 Crane concept: overview of target complex

The target complex design for the crane concept is illustrated in Figs. 6.6–6.10. The target and its surrounding shielding are housed in a helium vessel in the target pit. An underground cool-down area, including a remote handling area, is used for storage and dismantling of activated components. A surface building equipped with an overhead travelling crane covers the underground areas. Transfers of radioactive equipment removed from the helium vessel in the target pit are carried out using the building crane while keeping the load below ground level to ensure compliance with radiation dose rate limits outside the building.

Cooling plant (for cooling of the equipment in the helium vessel and for helium purification) is also installed underground. Separate sump rooms are used to collect any water leaking from the equipment in the helium vessel. A surface building equipped with an overhead travelling crane covers all the underground areas. The complex is equipped with a ventilation system to ensure confinement for radiological safety. A vehicle airlock is attached to the surface building to allow vehicle movements without disrupting the ventilation system. More details of the cooling and ventilation systems are given in Section 6.5.

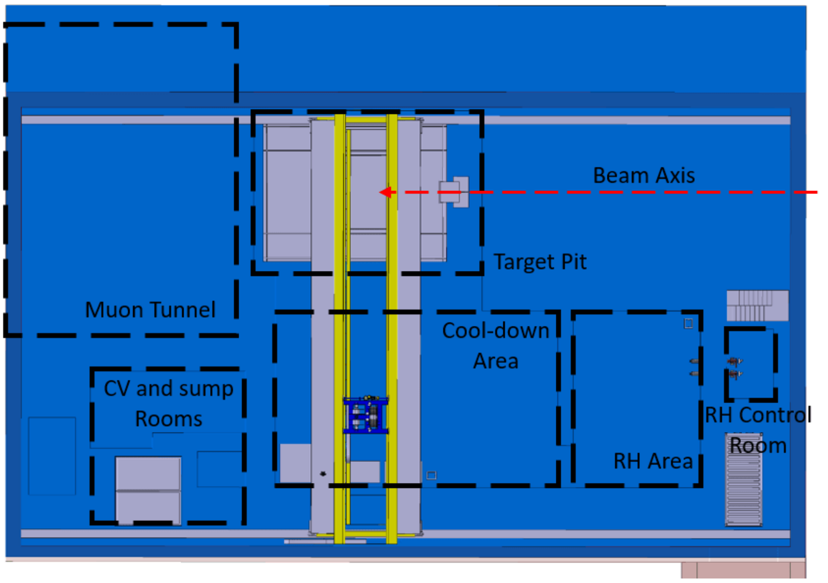

Fig. 6.6: Plan view showing the main areas of the crane concept target complex. The proton beam from the SPS enters from the right in the figure.

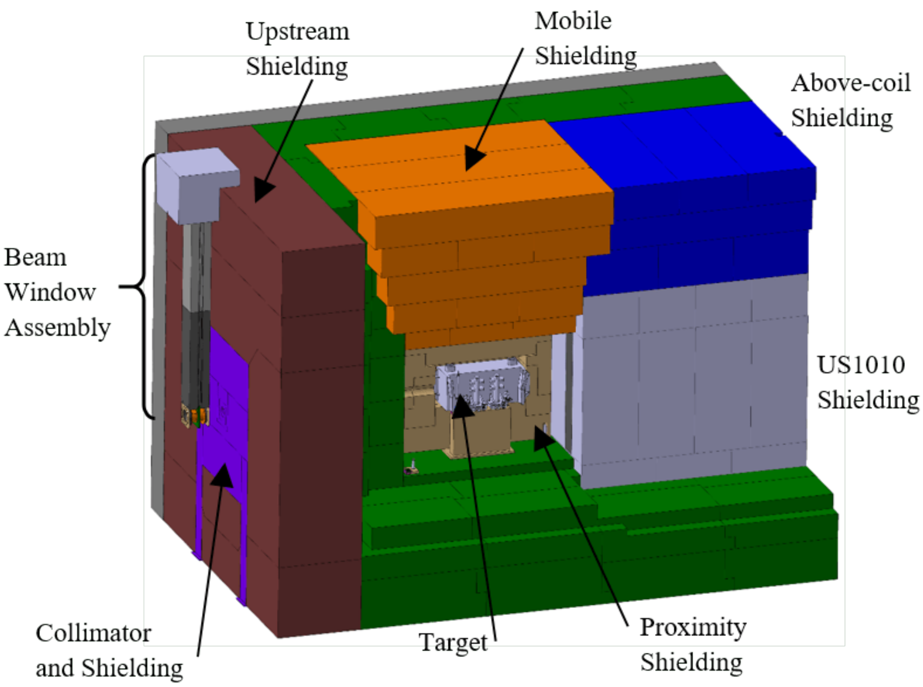

Fig. 6.7: Isometric cutaway view of crane concept equipment in the helium vessel

6.2.1.7 Trolley concept: overview of target complex

The target complex design for the trolley concept is illustrated in Figs. 6.11–6.18. As with the crane concept, the target and its surrounding shielding are housed in a helium vessel in the target pit. The main difference is that the target is supported on a trolley running on rails and enters the helium vessel from the side.

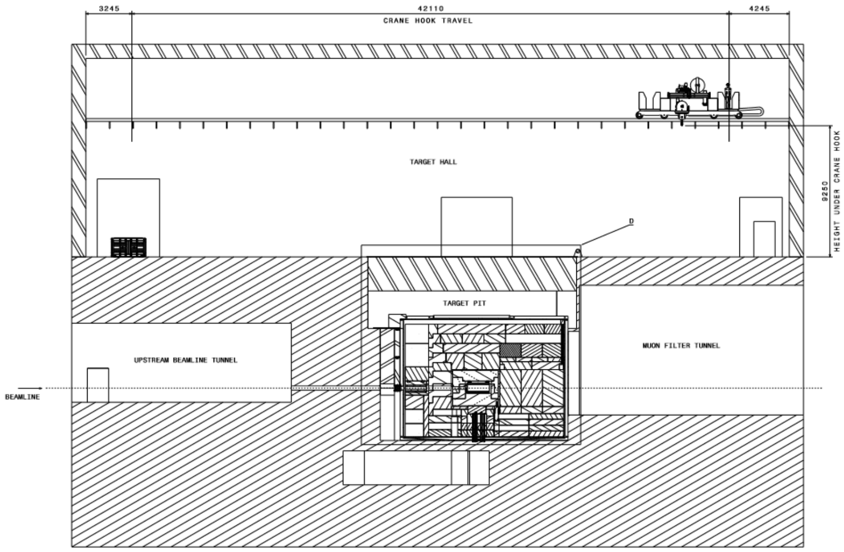

Fig. 6.8: Sectional view of crane concept target complex showing underground area and surface building—showing proton beam entering from left side of figure.

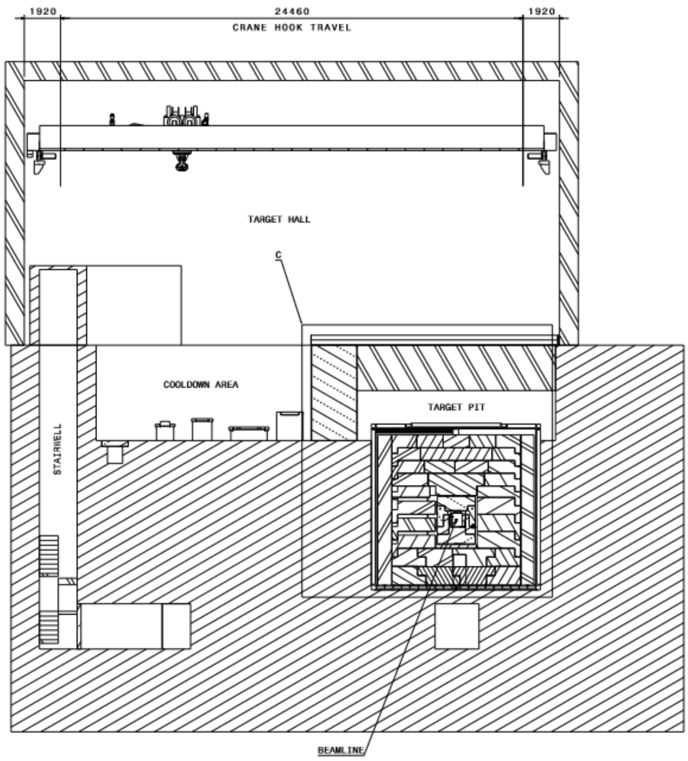

Fig. 6.9: Sectional view of crane concept target complex showing underground area and surface building—view along beam axis.

The target can be withdrawn from the helium vessel, without the need to remove the lid of the helium vessel or remove the shielding above the target, by rolling back the trolley. When the target is withdrawn from the helium vessel, it enters a hot cell equipped with a 3 t overhead travelling crane and two pairs of master–slave manipulators, which are primarily used to operate the clamp securing the target and to make and break water and electrical connections to the trolley in the event of target

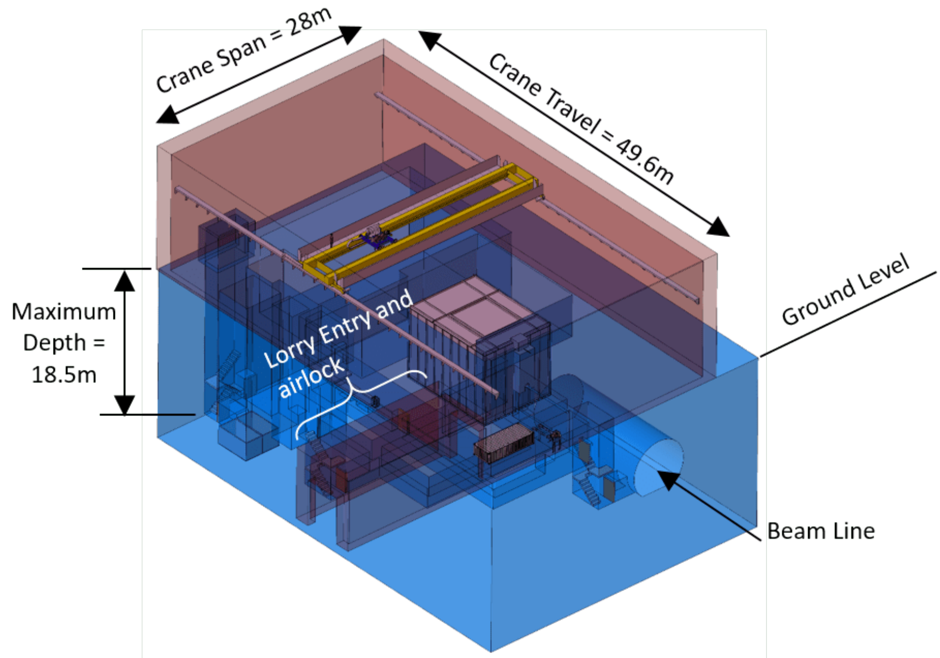

Fig. 6.10: Isometric view of crane concept target complex building

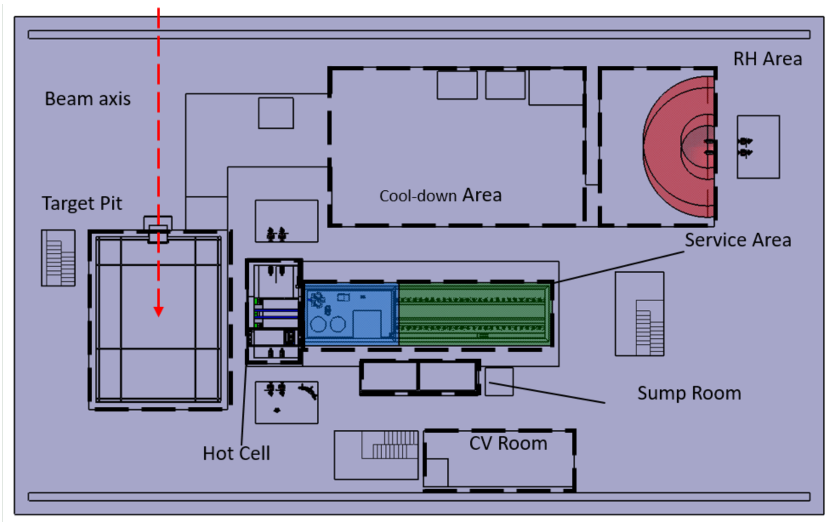

Fig. 6.11: Plan view showing main areas of trolley concept target complex

exchange. More details of the hot cell crane are given in Section 6.2.6.2.

The trolley supports the target on cantilever beams, which also support a 'plug' of cast iron shielding that moves into the helium vessel along with the target. All the services to the target, and the trolley-mounted water-cooled proximity shielding, are incorporated into the trolley.

A door equipped with inflatable EPDM seals is fitted to the trolley to close the helium vessel when the target is in its operating position (Figs. 6.19–6.21). The EPDM seal can be replaced using the manipulators in the hot cell.

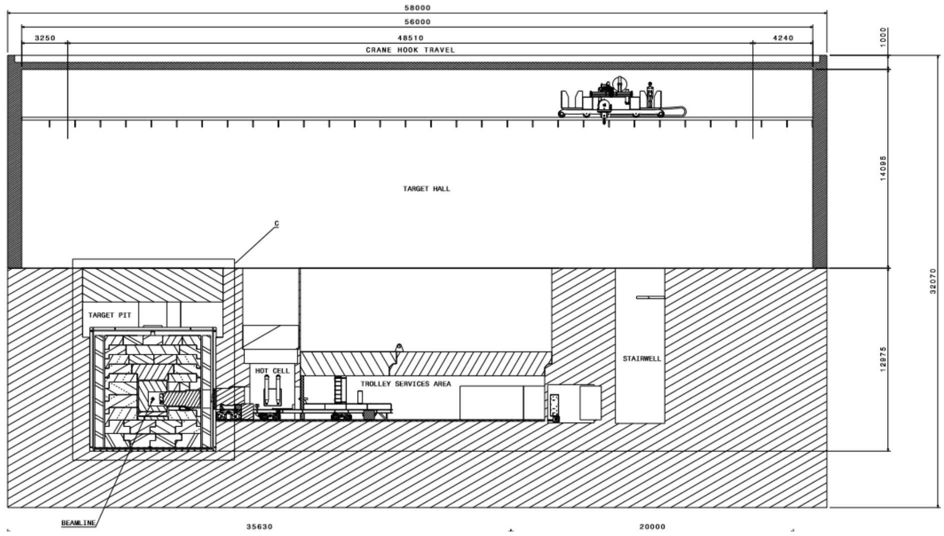

Fig. 6.12: Sectional view of trolley concept target complex showing underground area and surface building—view along beam axis.

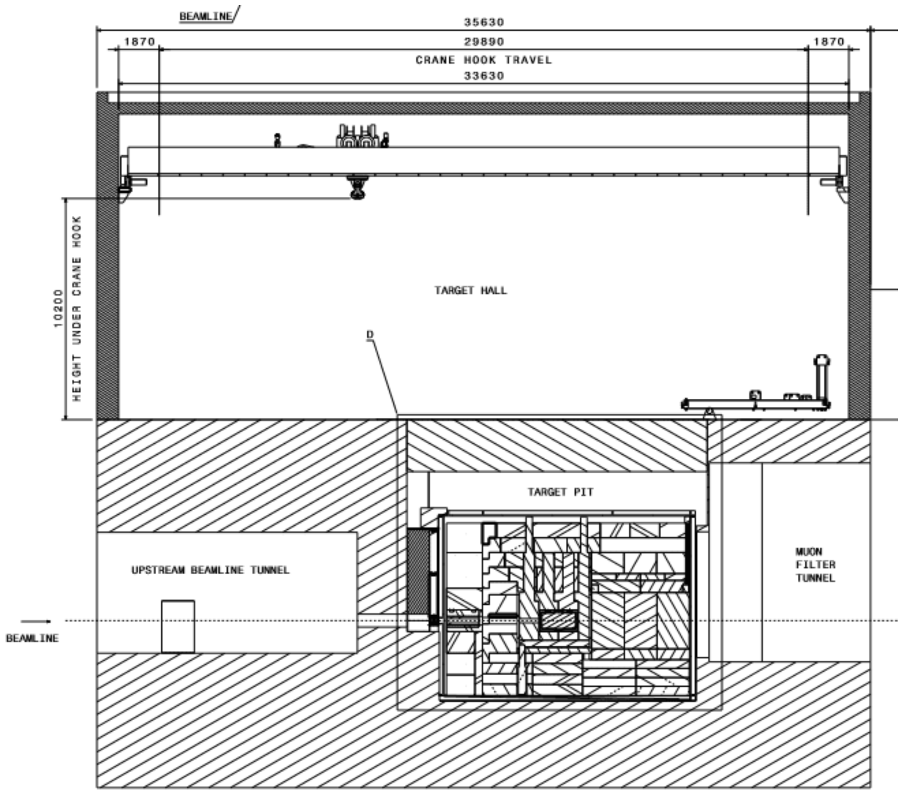

Fig. 6.13: Sectional view of trolley concept target complex showing underground area and surface building—proton beam entering from left side of figure.

6.2.2 Target support and handling

6.2.2.1 Target housing, supports, services, and connections: crane concept

The crane concept target is housed in a rectangular stainless steel container which incorporates support and alignment features, lifting points, handling guides, and water and electrical connectors (Fig. 6.22). Internal pipework connects the cooling channels of the target to the remotely operated connector clamps

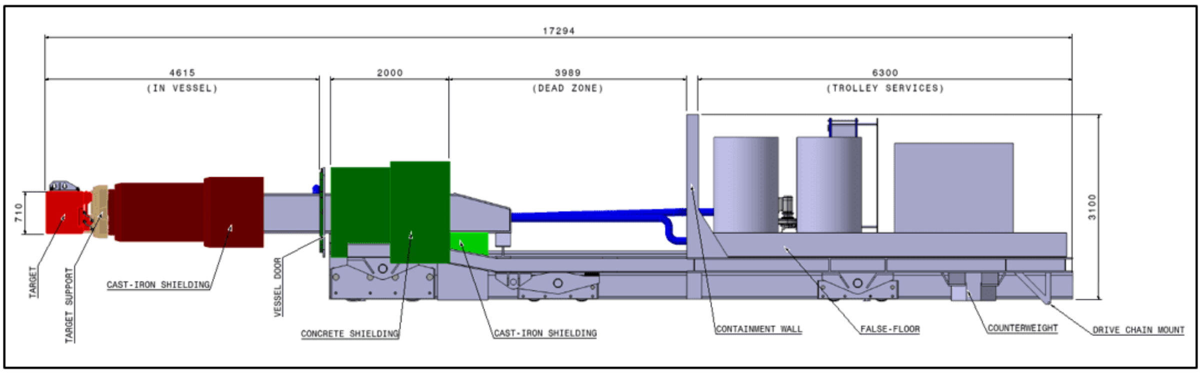

Fig. 6.14: Trolley layout with main elements and dimensions

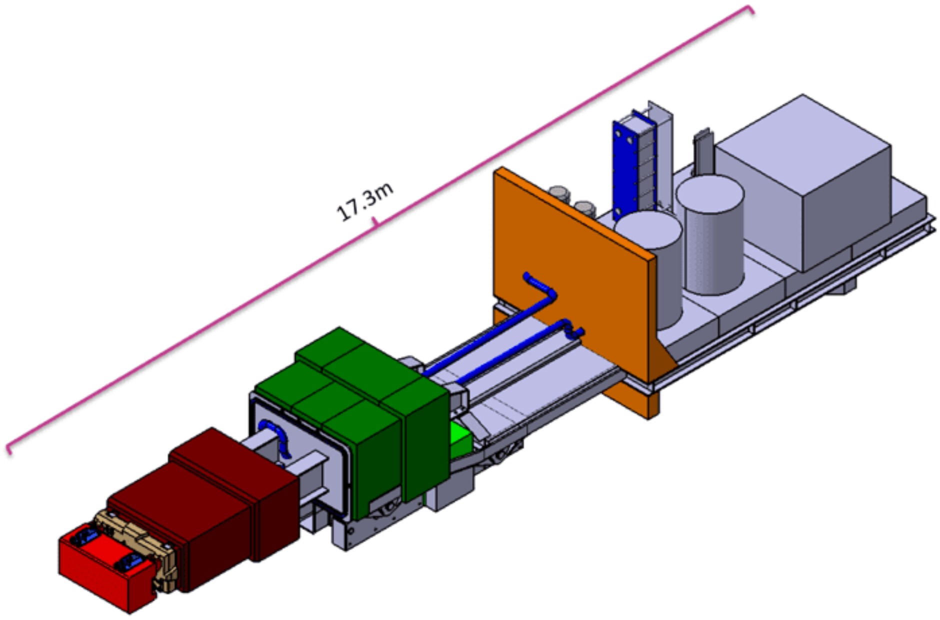

Fig. 6.15: Isometric view of BDF trolley with main components and size

near the base of the target container. The details of the internal pipework are covered by a separate study (Chapter 5).

The target is supported on three V and ball supports on the bottom layer of the proximity shielding, which in turn sits on top of three pre-aligned pillars. Cooling-water pipework and temperature sensor cables for the proximity shielding pass through the pillars. A separate service pillar supplies the target with its water, helium, and electrical connections (Figs. 6.23 and 6.24). Service galleries are therefore needed underneath the helium vessel to allow passage of the services and provide personnel access for installation and repair of the services.

Water connections to the proximity shielding and water and helium connections to the target are made using remotely operated clamp connections based on Grayloc® connectors (Fig. 6.25). Electrical connections are made remotely by radiation-tolerant, custom-designed connectors once the proximity shielding and target have been lowered onto their supports. Clamping and unclamping of the water and helium connections to the target are done with an ‘(un)locking tool’ lowered into position by the crane (Figs. 6.26–6.28).

A two-stage guidance arrangement is used to guide the target into position as it is lowered by the crane onto its supports. In the first stage, buffers on the target container (Fig. 6.29) provide an initial

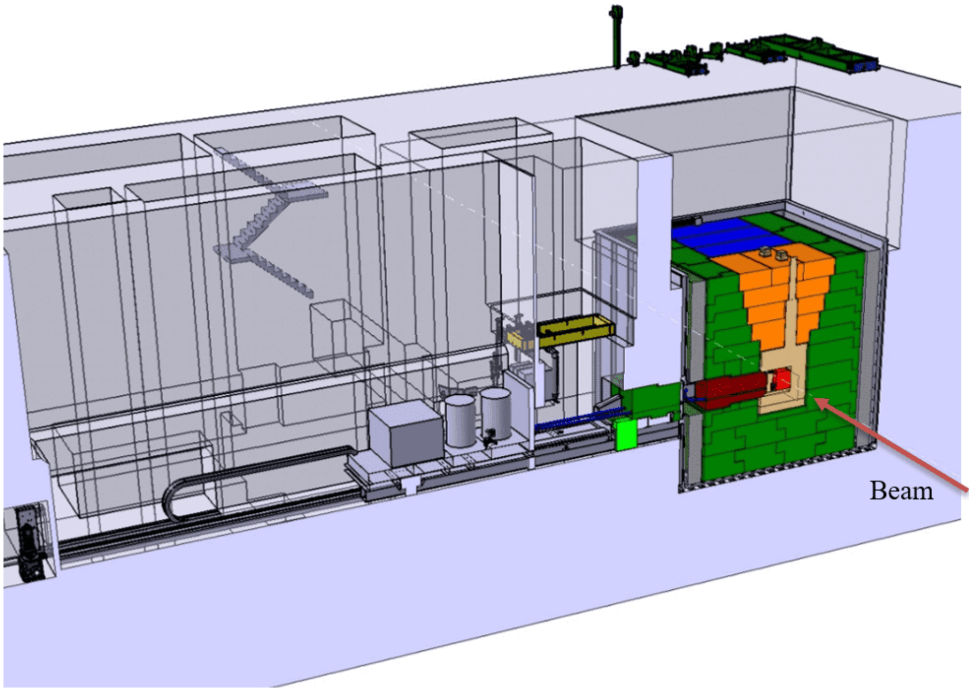

Fig. 6.16: Cutaway view of underground area of trolley concept target complex: target in operating position inside the helium vessel. Hot cell crane shown in yellow.

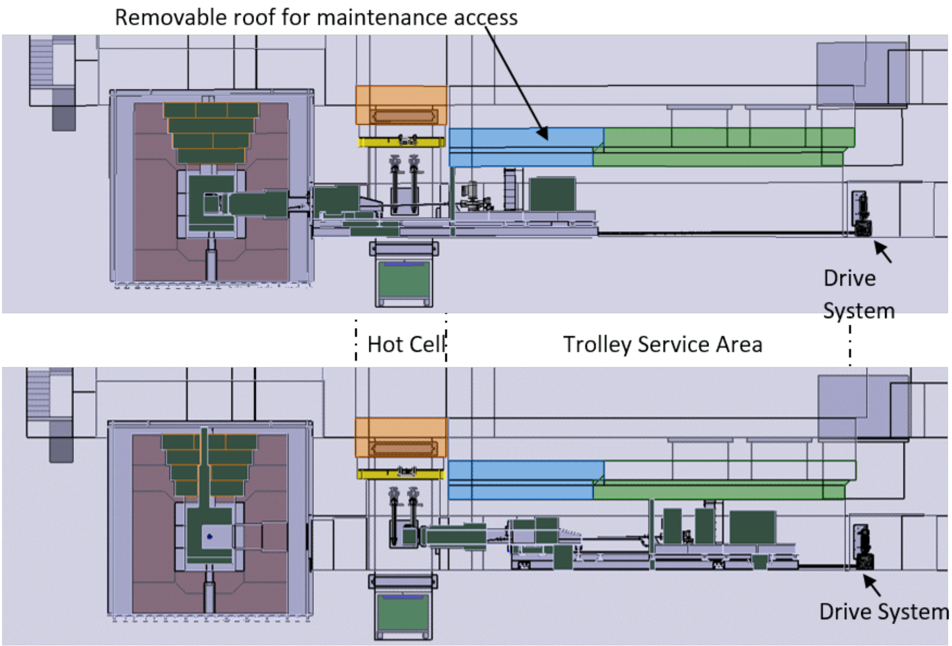

Fig. 6.17: Sectional views showing trolley with target in its operating position in the helium vessel (upper image) and withdrawn into the maintenance hot cell (lower image).

rough alignment to allow the target to engage with the conical upper sections of the second-stage guide pins. The guide pins ensure that the target is lowered accurately to allow helium and water connections to be made. The water and helium pipe connections include bellows and internal guides to ensure correct alignment and compliance during the installation and clamping operations (Fig. 6.30).

The electrical connections are not made as the target is lowered; once the target is in position, the

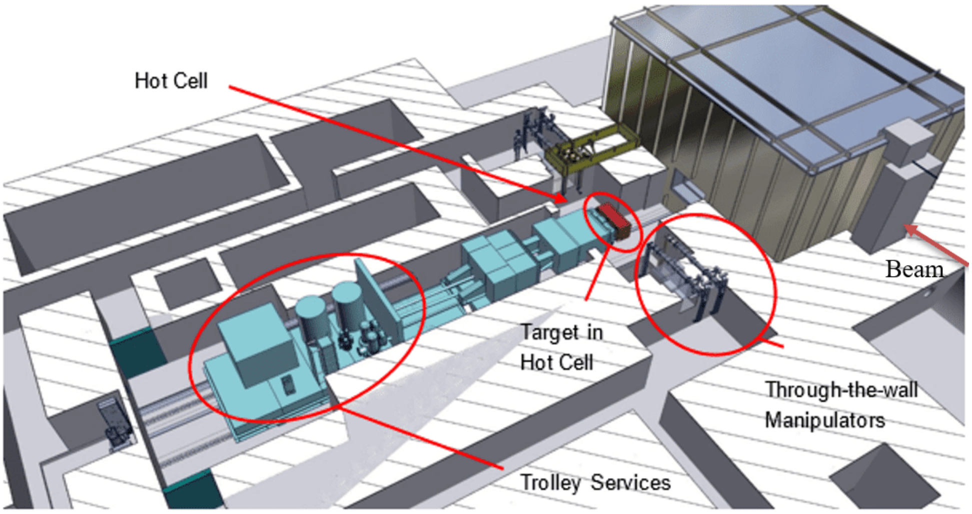

Fig. 6.18: Cutaway view showing trolley withdrawn from helium vessel with target in hot cell.

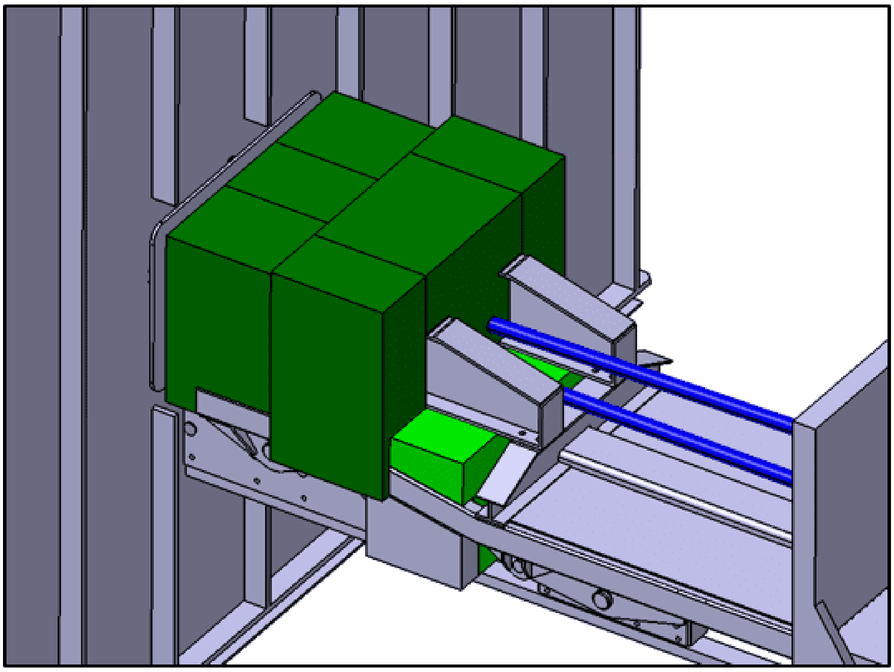

Fig. 6.19: Trolley moved to fully forward position: the helium vessel door is closed and the concrete shielding plug (green) fills the opening in the concrete shielding wall between the helium vessel and the hot cell (shielding wall not shown for clarity).

electrical connections are driven into contact using leadscrew drives mounted on the target container and remotely operated by the (un)locking tool (Fig. 6.31). The electrical connections are disconnected by reversing the leadscrew drive; however, the target can still be extracted if the leadscrew drive fails.

The crane concept target is held down onto its supports by springs (made up of Belleville washers) attached to the underside of the upper layer of proximity shielding (Fig. 6.32).

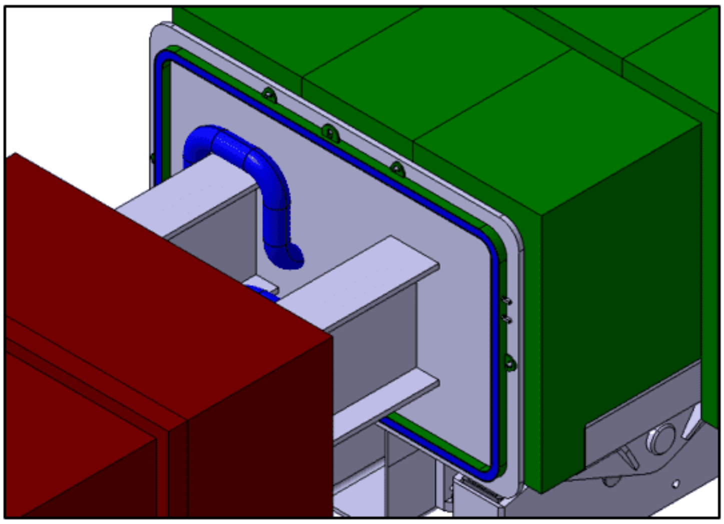

Fig. 6.20: Helium vessel door on trolley: the door is equipped with an inflatable EPDM seal which seals against the helium vessel wall when the trolley is in its fully forward position.

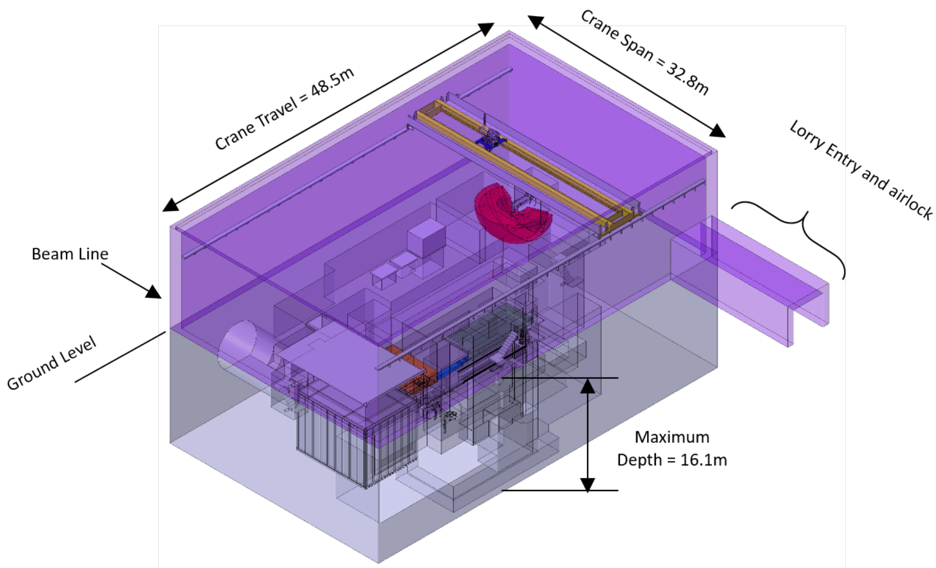

Fig. 6.21: Isometric view of trolley concept target complex building

6.2.2.2 *Target exchange sequence: crane concept*

In the crane concept, all installation and removal operations are carried out vertically using the building's overhead travelling crane. To exchange the target, it is necessary to first remove the small lid of the helium vessel, the 'mobile shielding', and the top layer of proximity shielding (Figs. 6.33–6.35).

A series of remotely operated spreader beams are used to lift the mobile and proximity shielding above the target and then the target itself. Disconnection of services from the proximity shielding and the target must be carried out before they can be lifted out. For the target, disconnection is carried out remotely using the target (un)locking tool described in Section 6.2.2.1. For the disconnection of the proximity shielding, (un)locking tools are incorporated into the remotely operated lifting spreaders; details of this are given in Section 6.2.3.2. The steps involved in target removal are given in Table 6.1. The installation of a new target follows the same procedure in reverse.

A shielded spreader is used for lifting and transfer of the target; it is equipped with a hoist system

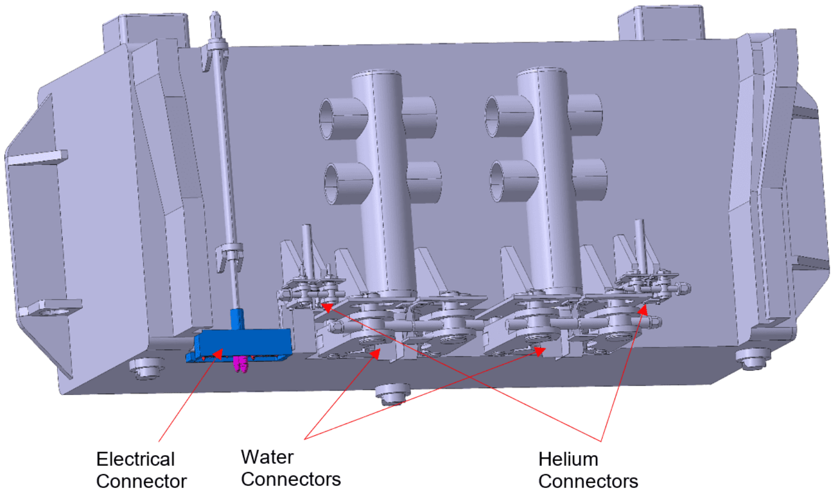

Fig. 6.22: Target container showing service connections (crane concept)

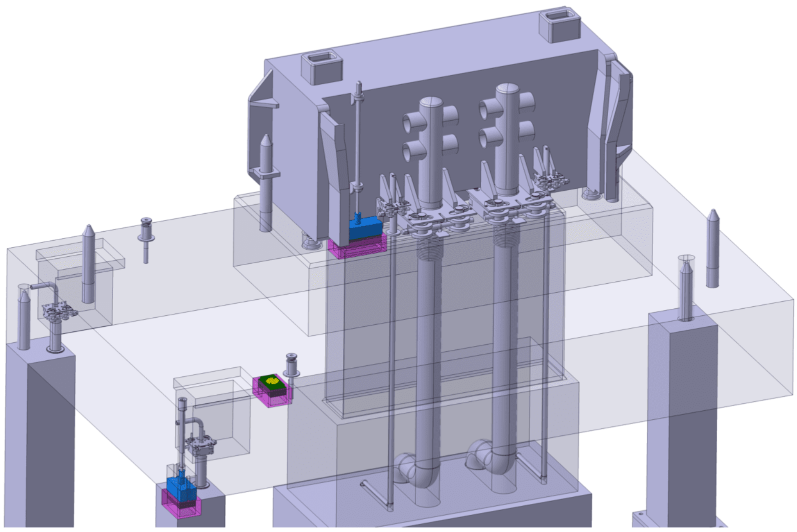

Fig. 6.23: Target sitting on bottom layer of proximity shielding (crane concept). Helium, water-cooling, and electrical connections for the target pass though the central support pillar. Services for the proximity shielding pass through the proximity shielding support pillars. Pipework connections are made by remotely operated screw-clamp connections.

(with remotely operated twist lock attachments) to lift the target inside the shielding before the target is transferred to the cool-down area. This transfer is carried out with the spreader kept as close as possible to the floor to minimize external radiation shine from the bottom of the target. Additional concrete shielding blocks may be installed along the transfer path to further reduce radiation levels in the target hall during transfers. The crane concept target transfer spreader is shown in Fig. 6.36.

6.2.2.3 Target housing, supports, services, and connections: trolley concept

The trolley concept target is housed in a rectangular stainless steel container which incorporates the support interfaces used to attach it to the front of the trolley, the lifting attachment points, and the water, helium, and electrical connectors (Fig. 6.37). Internal pipework connects the cooling channels of the target to the remotely operated connector clamps on the side of the target container. The design of the internal pipework was outside the scope of the handling study but was covered in the target design work

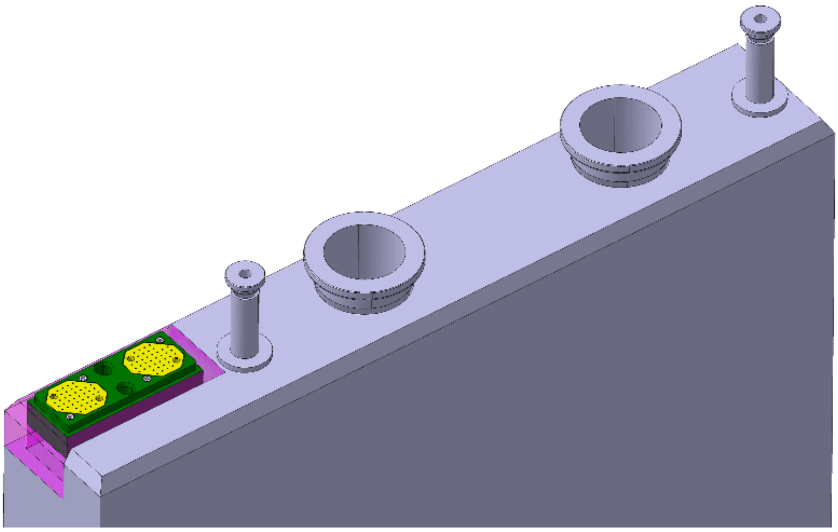

Fig. 6.24: Upper part of crane concept target service pillar showing helium, water, and electrical connections.

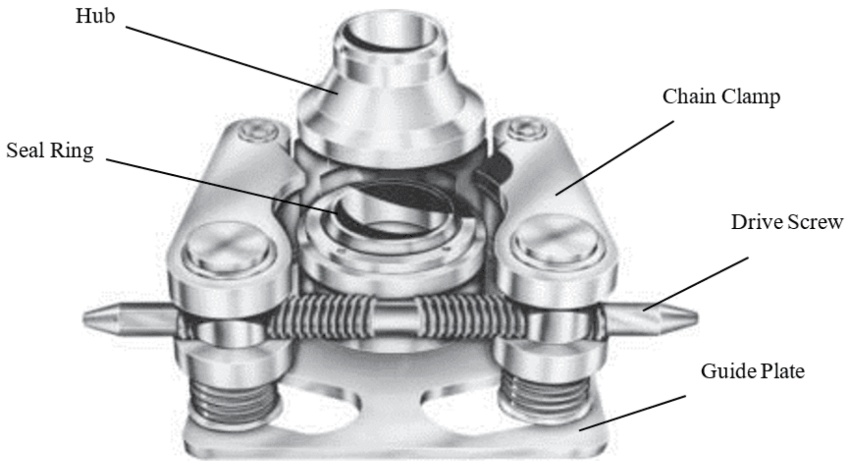

Fig. 6.25: Elements of Grayloc® connector clamping system: rotation of the drive screw clamps the hub welded onto one pipe to the other pipe hub, compressing the captive seal between the hubs.

Table 6.1: Steps for removal of target from the helium vessel and transfer to the cool-down area (crane concept).

Step	Task	Tooling
a	Open lid of helium vessel	Hands-on operation
b	Remove mobile shielding above target and transfer to cool-down area	Crane and remotely operated spreaders
c	Disconnect water connections to top layer of proximity shielding	Crane and spreader with (un)locking tool
d	Remove top layer of proximity shielding and transfer to cool-down area	Crane and spreader with (un)locking tool
e	Disconnect water connections to target	Crane and (un)locking tool
f	Lift out target with shielded spreader and transfer to cool-down area	Crane and shielded spreader for target transfer

(Chapter 5).

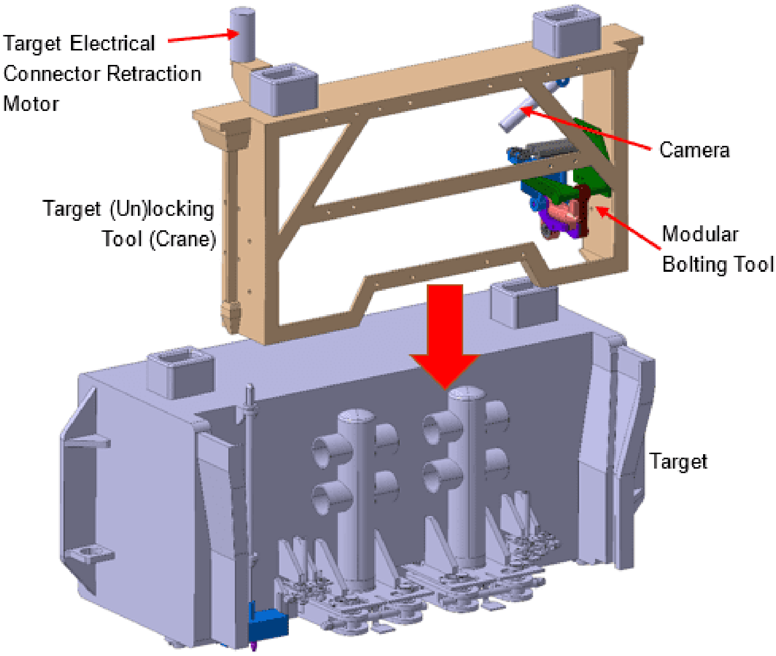

Fig. 6.26: (Un)locking tool for the remotely operated screw-clamp water and helium pipework connections of the target (crane concept). Electrical connections are also connected using a motor drive on the (un)locking tool. The tool is lowered into position by the crane; guidance rails on the target ensure the correct position of the tool.

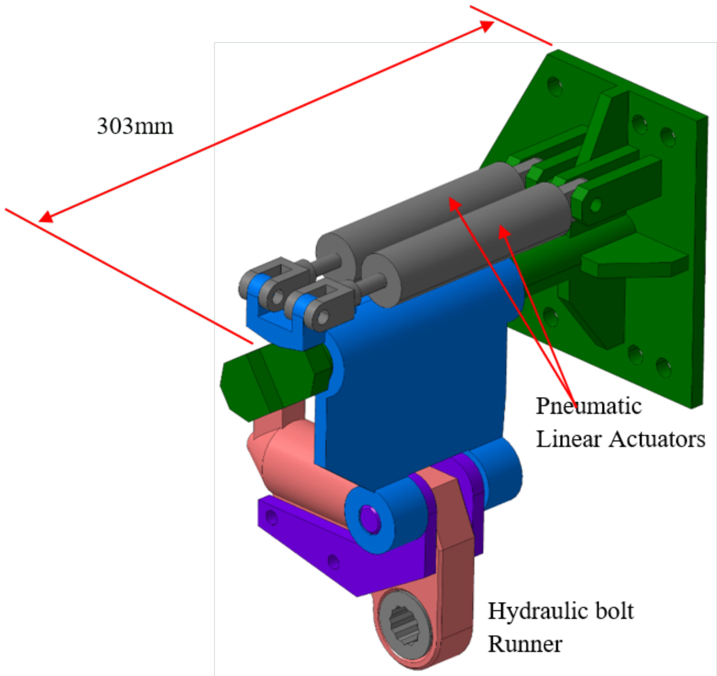

Fig. 6.27: Bolting module fitted to (un)locking tool—this is used to remotely tighten and loosen screw-driven pipe clamps on the crane concept target.

The target is supported on hooks at the 'nose' end of the trolley. It is lowered onto the hooks by the hot cell crane and guided into position by master–slave manipulators (Fig. 6.38). It is secured by a screw-driven clamp operated by a power tool that is positioned using the hot cell master–slave manipulators. All the service connections to the target arrive at the nose of the trolley. Once the target is fully lowered

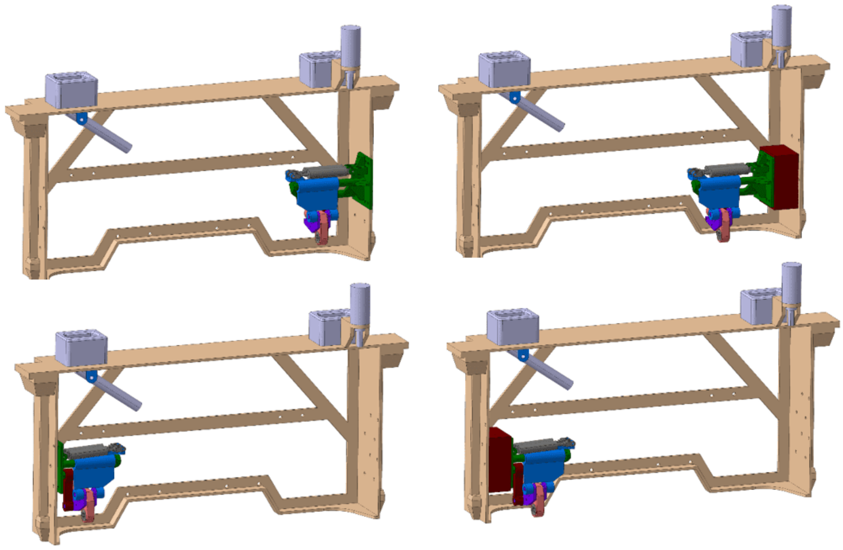

Fig. 6.28: (Un)locking tool with bolting module fitted in different positions to loosen or tighten the different pipe clamps.

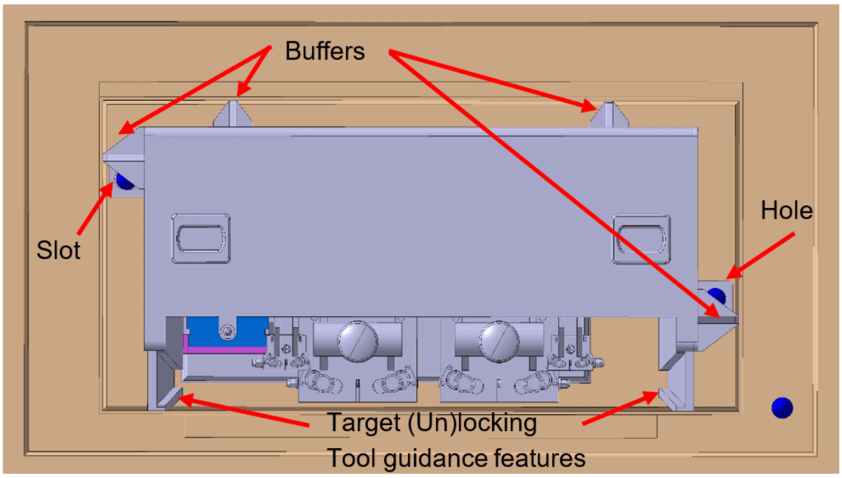

Fig. 6.29: Crane concept target container showing buffers for first-stage (rough) guidance during installation, the hole and slot that engage with the guide pins for more precise guidance during installation, and the guidance features of the (un)locking tool.

and the water connection pipes are engaged, the screw-clamp water connections are tightened using the hot cell manipulators. Electrical and helium connections are also made using the hot cell manipulators (Figs. 6.39 and 6.40).

6.2.2.4 *Target exchange: trolley concept*

Target exchange is carried out by driving the trolley backwards to withdraw it from the helium vessel and into the hot cell. After disconnection of services in the hot cell and release of the securing clamp using the master–slave manipulators, the target is lifted off the nose of the trolley and placed in a shielded target export trolley using the hot cell crane. The target is then transferred to the cool-down area in the target export trolley, which runs along the export tunnel under the hot cell (Fig. 6.41). Installation of a new target is the reverse of the removal procedure. The steps involved are summarized in Table 6.2 and illustrated in Figs. 6.42–6.49.

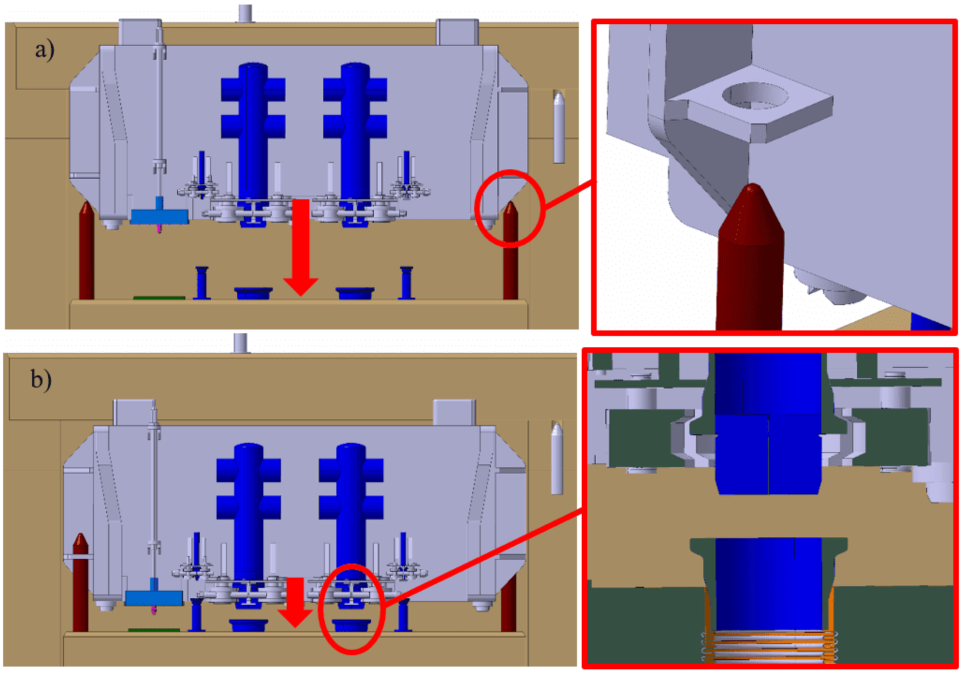

Fig. 6.30: Illustration of guidance stages during installation of target (crane concept). Upper images: as the target is lowered into position, guide pins guide the target to align it with the water and electrical connections. Lower images: guide fins in the target water connections align the fixed water connections (which are mounted on flexible bellows) as the target is lowered.

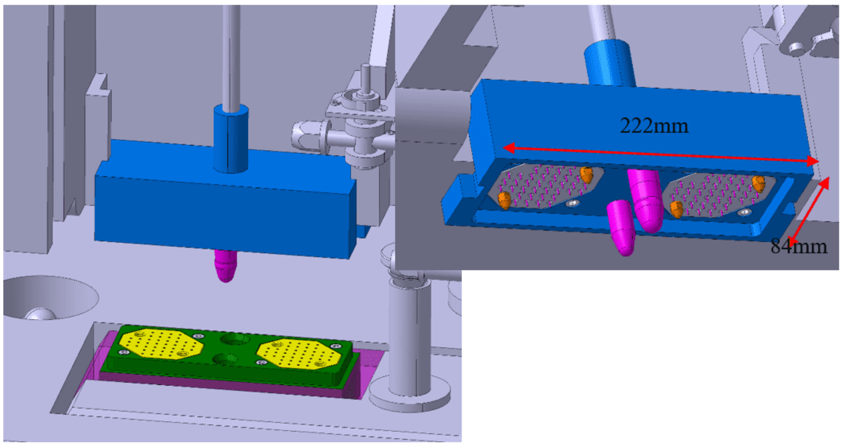

Fig. 6.31: Electrical connectors on the target and service pillar (crane concept). They are driven into their connected position using a leadscrew, which is turned by a motor on the (un)locking tool.

6.2.3 Design of target proximity shielding

6.2.3.1 Thermomechanical performance

The results for thermomechanical performance presented here are based on the design for the trolley concept proximity shielding. The trolley concept proximity shielding is in two main parts: the fixed proximity shielding, made up of blocks that are permanently installed in the helium vessel, and the trolley-mounted proximity shielding block.

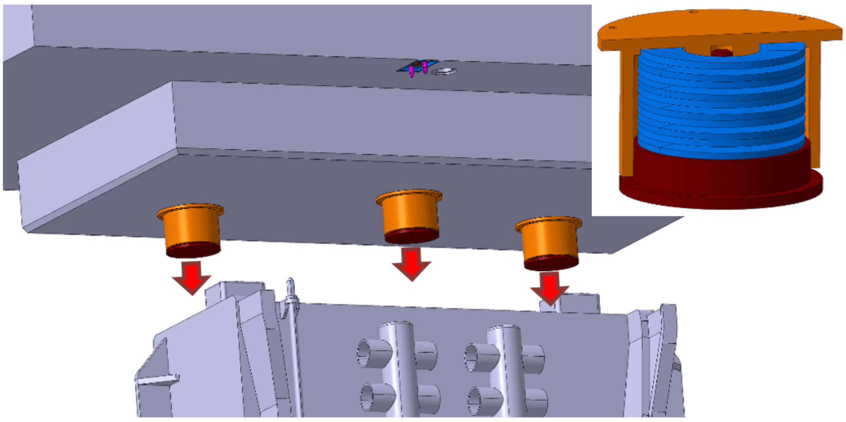

Fig. 6.32: Springs made up of Belleville washers attached to the underside of the upper layer of the crane concept proximity shielding hold the target down on its supports.

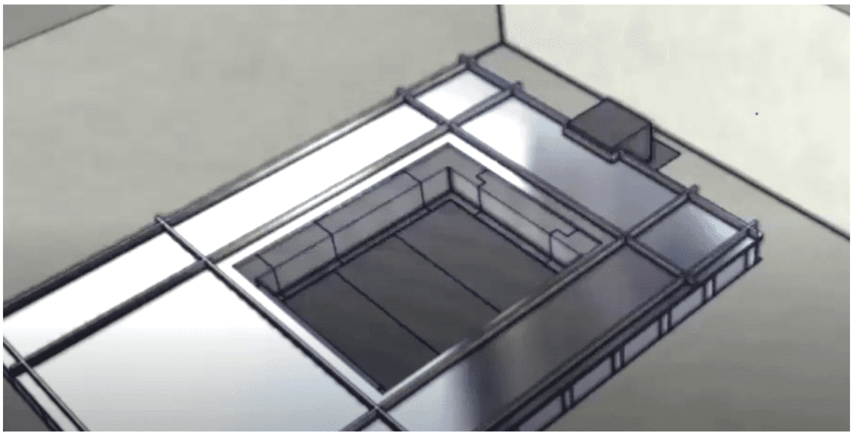

Fig. 6.33: Target exchange (crane concept): helium vessel with small lid and first layer of mobile shielding removed.

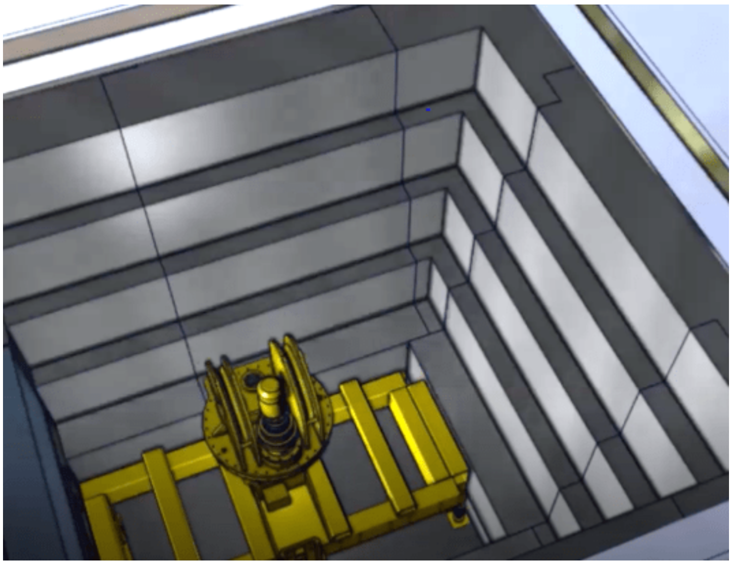

Fig. 6.34: Target exchange (crane concept): remotely operated spreader removing proximity shielding. Spreader equipped with (un)locking tools to disconnect electrical and water connections.

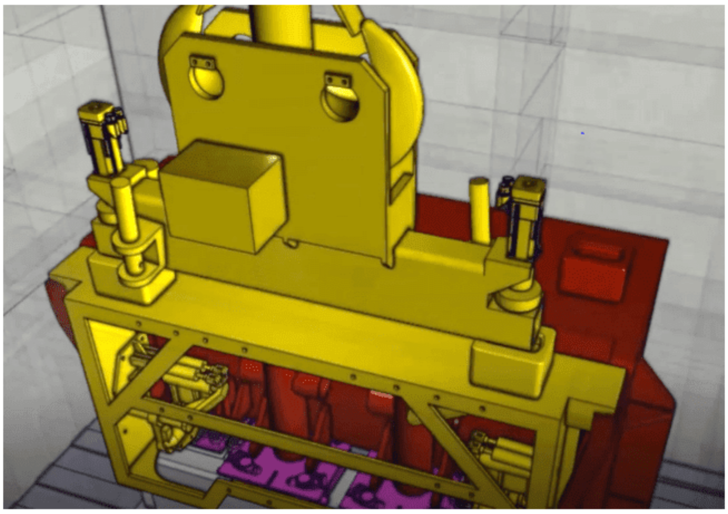

Fig. 6.35: Target exchange (crane concept): (un)locking tool lowered into place by crane to open target connections.

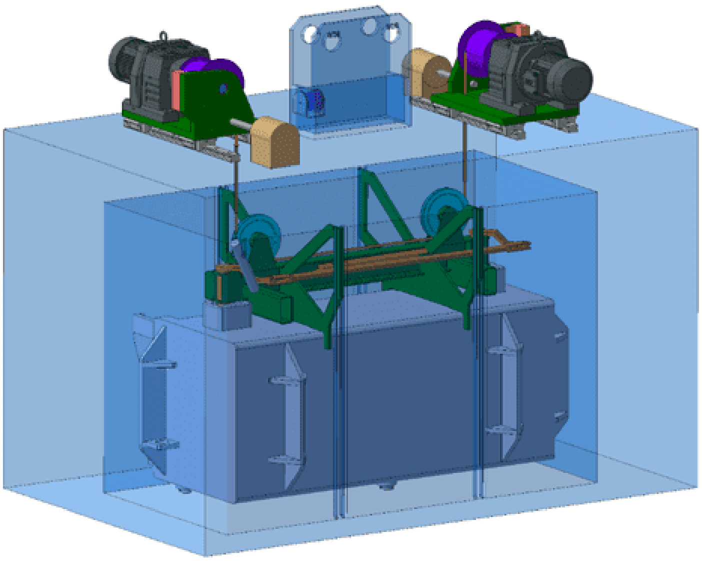

Fig. 6.36: Target exchange (crane concept): transfer spreader for shielded transfer of target from helium vessel to cool-down area. Two hoists are used for redundancy so that operations can continue if one hoist fails. Target shown inside shielding.

6.2.3.1.1 Fixed proximity shielding

The interaction of the primary beam with the BDF target produces a shower of secondary particles that interact with the proximity shielding. The energy deposited in the proximity shielding is not negligible, and will be dissipated via active cooling. Figure 6.50 shows a map of the energy deposition in the proximity shielding for the trolley concept obtained via FLUKA simulations. The total power deposited in the shielding blocks is around 12 kW.

The dissipation of heat in the proximity shielding is performed by the forced circulation of cooling water. The water flows through stainless steel pipes embedded in the cast iron blocks. In the trolley concept design, the water is brought to the shielding blocks through service chimneys. The cooling-system design is based on the cooling principle for the SPS Internal Dump (TIDVG) shielding, where 10 mm thick stainless steel pipes are embedded in the cast iron shielding of the dump [3]. The preliminary

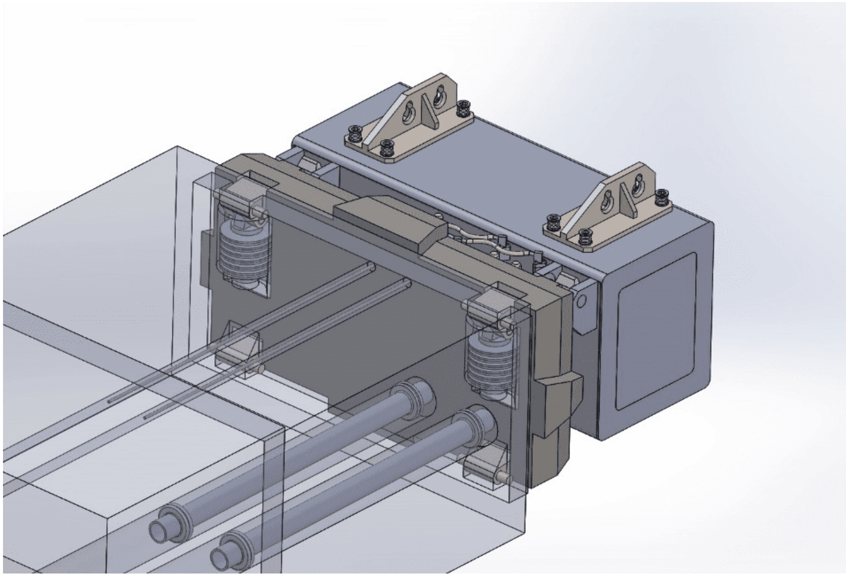

Fig. 6.37: Target supported on nose of trolley. Coolant and helium pipes pass through the shielding to the connectors on the side of the target housing.

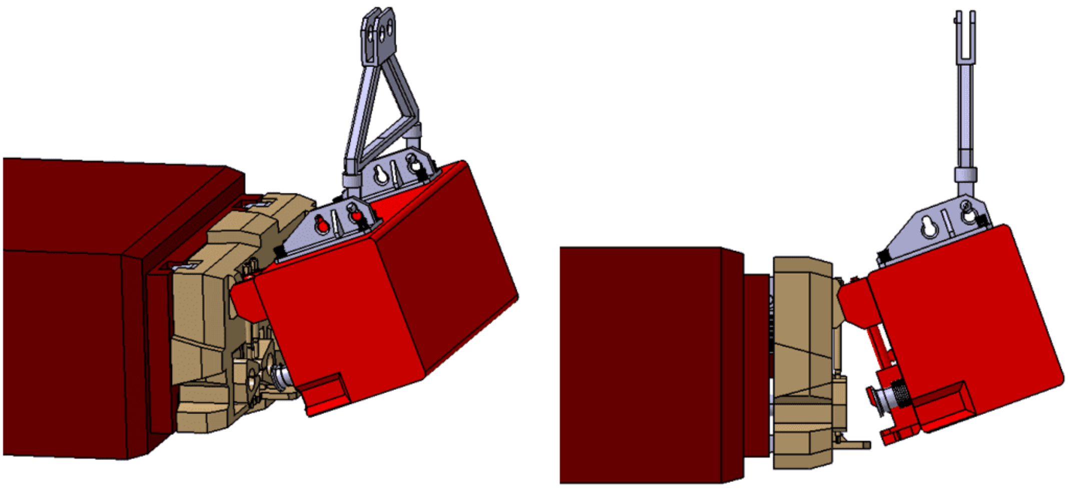

Fig. 6.38: Target being lowered onto support hooks at the end of the trolley. Once the target is engaged with the hooks, further lowering rotates the target so that the water connections on the side of the target engage with the screw-operated connection clamps on the nose of the trolley. The screw clamps are operated by the hot cell master–slave manipulator using appropriate tooling.

water circuit design consists of long pipes, with an internal diameter of 16 mm and outside diameter of 36 mm, that enter and exit the shielding blocks at the top. The internal and external diameters are equivalent to those of the SPS TIDVG shielding cooling, given the proven compatibility of the 10 mm thick pipe walls with the casting process.

The mass flow rate foreseen for each block water circuit is 0.25 kg/s, leading to a total mass flow rate of 1 kg/s at the water supply level. The water inlet temperature assumed is 28°C, and the maximum temperature increase expected is 5°C. The calculated water velocity in the cooling pipes is around 1.2 m/s—well below the design limit of 2 m/s, chosen to avoid damage to the pipes or fittings.

Thermal calculations were performed to evaluate the maximum temperatures reached in the proximity shielding. The heat loads are given by the beam energy deposition in the shielding, and the heat is

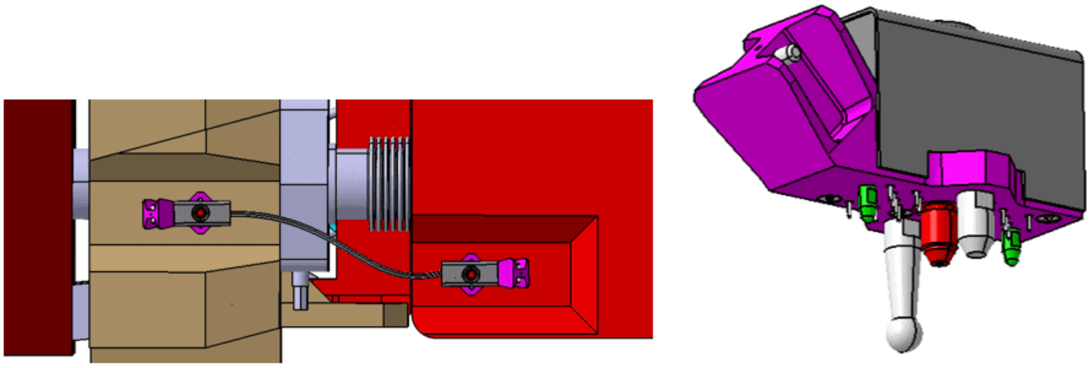

Fig. 6.39: Electrical connections to trolley concept target. Left: leads with connectors at each end are used for the connections. Right: electrical connectors are designed to be compatible with remote handling by the master–slave manipulators in the hot cell.

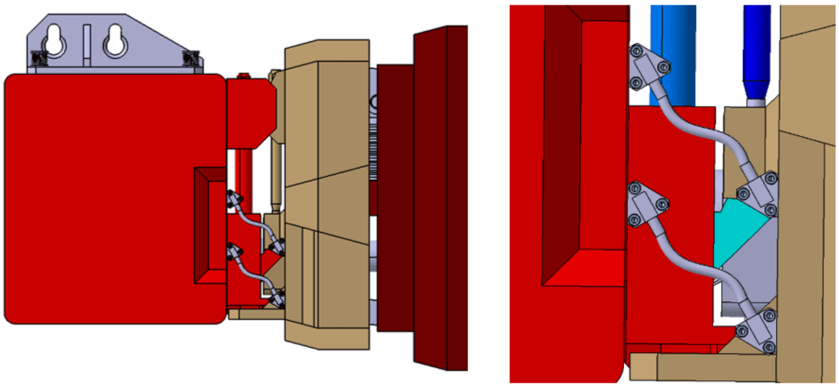

Fig. 6.40: Helium connections to the trolley concept target; the connections are screwed into position using the hot cell master–slave manipulators.

Table 6.2: Main steps for removal of target from the helium vessel and transfer to the cool-down area (trolley concept).

Step	Task	Tooling
a	Withdraw target on end of trolley from helium vessel into hot cell	Trolley
b	Disconnect helium, water, and electrical connections, and release target-securing clamp	Hot cell manipulators and hot cell crane
c	Attach lifting attachments to target, and remove target from trolley nose	Hot cell manipulators and hot cell crane
d	Lower target into export trolley and close lid	Hot cell manipulators, in-cell winch, hot cell crane
e	Transfer target to cool-down area and put into storage pit	Export trolley and cask, building crane

dissipated mainly by the water-cooling system. The heat removal by the cooling system was evaluated in two steps. First, the heat transfer coefficient from the water to the stainless steel pipes was obtained.

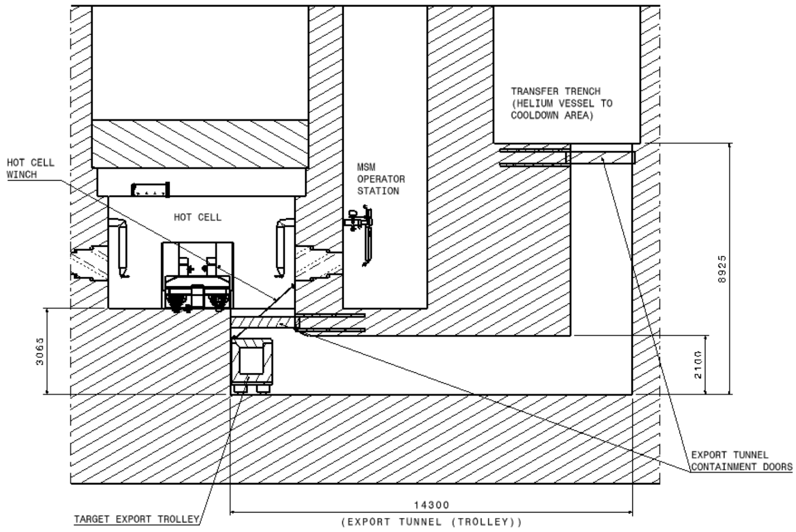

Fig. 6.41: Section through the trolley concept underground area showing the hot cell and target export trolley and the export tunnel linking the hot cell to the cool-down area.

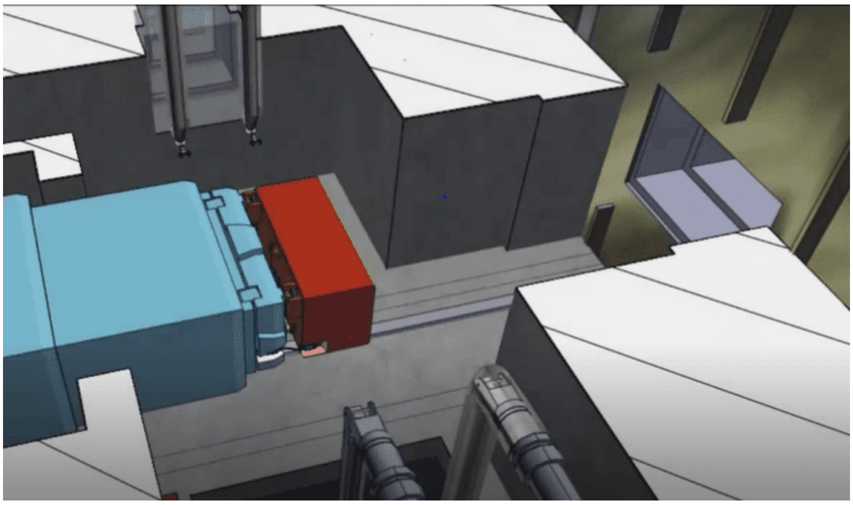

Fig. 6.42: Target exchange (trolley concept): withdrawal of target on end of trolley from helium vessel into hot cell.

Then, it was necessary to calculate the conduction through the stainless steel pipes in contact with the cast iron blocks. It was assumed that 50% of the outer surface of the stainless steel pipes was in perfect contact with the surrounding cast iron, as measured in a similar experimental set-up via ultrasound testing [4]. The 3D model used for the thermal calculations is presented in Fig. 6.51.

Figure 6.52 shows the steady-state temperature distribution obtained in the proximity shielding blocks. As a conservative approach, it was assumed that no heat conduction takes place from one block to another. The maximum temperature reached is around 90°C, well below the maximum service temperature of cast iron, which is between 230 and 300°C.

Additionally, transient thermal calculations were carried out, to evaluate the temperature increase during the impact of a beam pulse on the target. Figure 6.53 shows the evolution of the maximum temperature in the most thermally loaded shielding block. It can be observed that the maximum temperature increase for each pulse is below 0.1°C, and is therefore negligible.

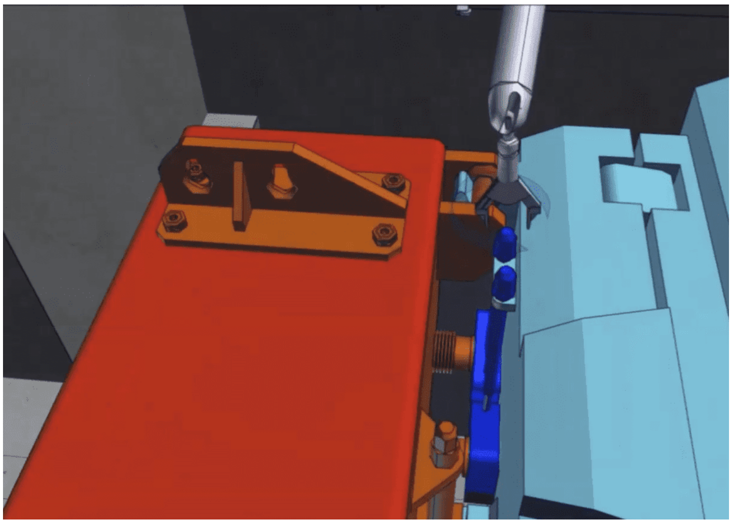

Fig. 6.43: Target exchange (trolley concept): disconnection of screw-driven pipe clamp using master–slave manipulator, with drive shafts used to provide an accessible rotation drive point. The master–slave manipulator would be used to handle a power tool (not shown) to undo the pipe clamps.

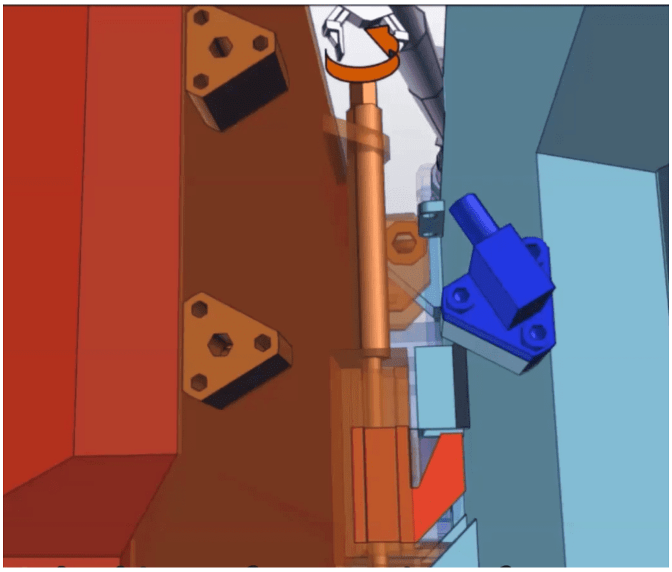

Fig. 6.44: Target exchange (trolley concept): release of screw-driven target-securing clamp (with downward movement to release) using master–slave manipulator.

6.2.3.1.2 Trolley-mounted proximity shielding block

The shielding block mounted on the target trolley also requires active water cooling, given the level of energy deposition in the block. The total heat deposited reaches 6 kW during beam operation. Figure 6.54 displays a map of the energy deposition in the trolley shielding block.

The cooling-system design is based on the same principle as for the rest of the proximity shielding blocks, with the exception that the water pipes are routed to the side, in the direction of the services that lie on the trolley.

The mass flow rate foreseen for the trolley block water circuit is 0.3 kg/s. The water inlet temperature assumed is 28°C, with an expected temperature increase of 5°C from inlet to outlet. The calculated water velocity in the cooling pipes is around 1.4 m/s, also below the design limit of 2 m/s. The 3D model used for the FEM simulations, along with the pipeline design, is shown in Fig. 6.55.

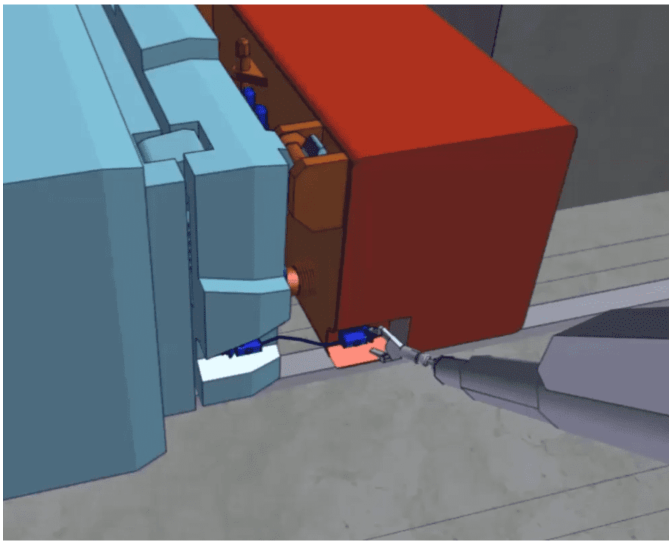

Fig. 6.45: Target exchange (trolley concept): disconnection of target electrical connections using hot cell master–slave manipulators.

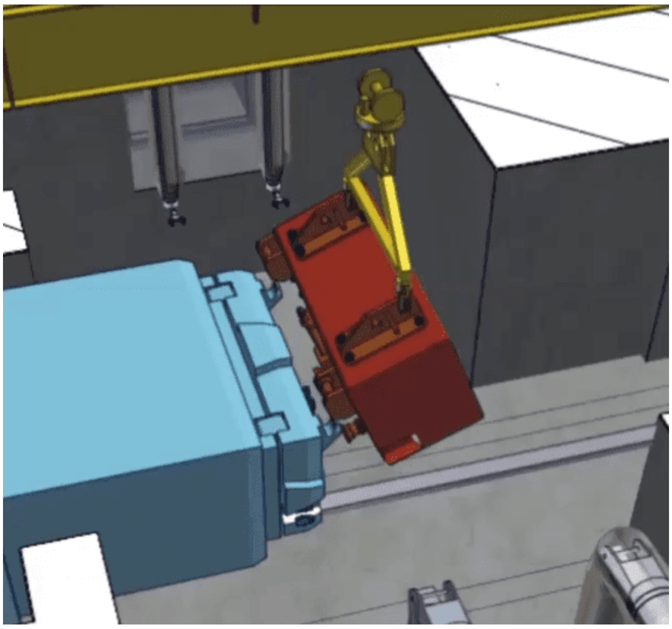

Fig. 6.46: Target exchange (trolley concept): lifting target off trolley support hooks using hot cell crane and spreader beam.

The boundary conditions considered in the thermal analysis were equivalent to those for the rest of the shielding blocks. Figure 6.56 shows the steady-state temperature distribution in the trolley shielding block. The maximum temperature reached is 73°C, well within the safety limits of the material. The transient thermal simulations performed showed that the maximum increase in temperature during each beam pulse was negligible.

6.2.3.2 Handling of proximity shielding: crane concept

The crane concept proximity shielding is built up of layers of cast iron with internal cast-in stainless steel thick-walled pipes to provide passages for cooling water (Fig. 6.57). The layers of proximity shielding are installed on top of support pillars (Fig. 6.58), which provide cooling and electrical services to the

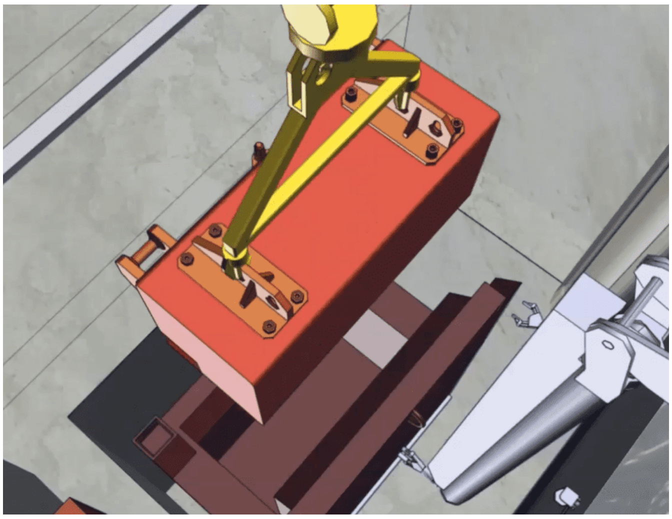

Fig. 6.47: Target exchange (trolley concept): lowering target into export trolley cask using hot cell crane and manipulators.

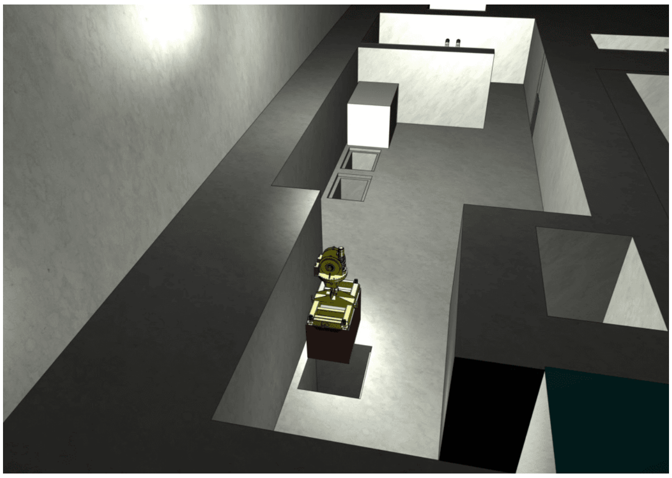

Fig. 6.48: Target exchange (trolley concept): moving target inside export trolley cask inside cool-down area using the building crane and remotely operated spreader.

proximity shielding. The coolant pipes are connected using remotely operated screw clamps as used for the target; the connections are made once each layer has been installed on top of the previous layer. Two (un)locking tools, similar to the ones used for the target, are mounted on the lifting spreader and used to operate the clamps (Figs. 6.59 and 6.60).

6.2.3.3 Handling of proximity shielding: trolley concept

The cast iron proximity shielding for the trolley concept is designed to allow the target to be installed and removed from the side. It is made up of four elements, which include service ‘chimneys’ which are used to provide the water-cooling and temperature sensor services and radiation protection shielding. The water and electrical connections to the proximity shielding are all made at the top of the helium vessel shielding, where residual radiation levels are sufficiently low to allow hands-on work. For alignment reasons, the proximity shielding is supported on a flat plate mounted on support pillars (Fig. 6.61). The mobile shielding above the trolley concept proximity shielding is handled using spreader beams equipped with legs to make it possible to work around the proximity shielding service chimneys (Fig. 6.62). The service chimneys include a lifting feature at the top which interfaces with a lifting attachment fitted to

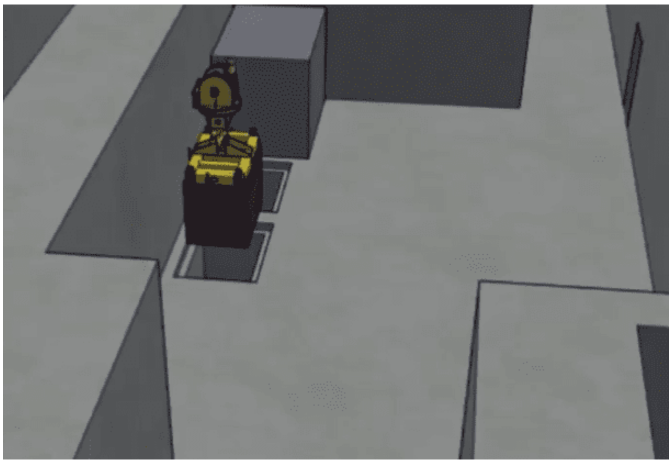

Fig. 6.49: Target exchange (trolley concept): moving target inside export trolley cask inside cool-down area using the building crane and remotely operated spreader (close-up view).

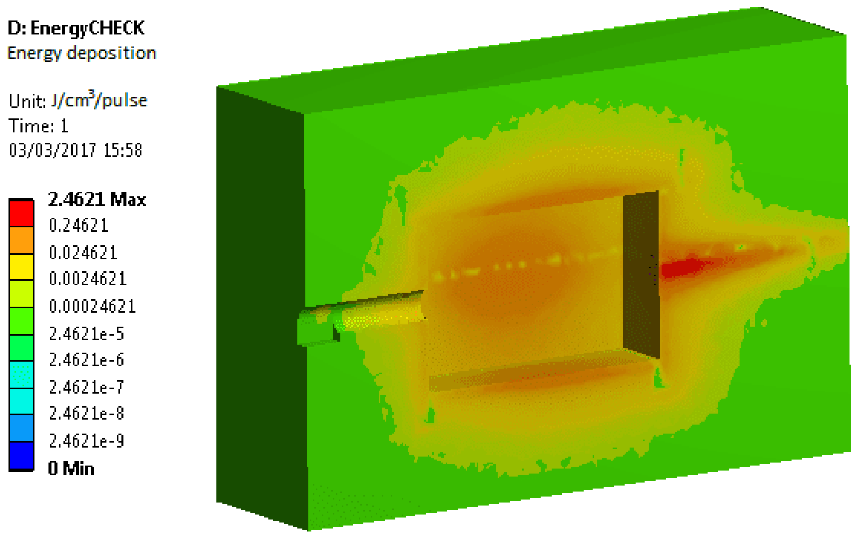

Fig. 6.50: Energy deposition distribution in a transverse section of the BDF proximity shielding blocks (logarithmic scale).

the crane hook (Figs. 6.63 and 6.64). The fixed proximity shielding elements and the mobile shielding, stacked in the cool-down area, are shown in Fig. 6.65.

6.2.4 Handling of other beam line equipment in the target complex

The handling of beam line equipment (other than the target and proximity shielding) is essentially the same for both the crane and the trolley concept.

6.2.4.1 Proton beam window design and handling

A beam window is required to isolate the helium vessel (which is at atmospheric pressure or above) from the vacuum in the beam pipe delivering protons from the SPS. It is necessary to design the beam window and its supports to allow replacement during the life of the facility. Because of the high levels of induced radioactivity, it is necessary to design for replacement using remote handling techniques. The beam window design produced as part of the handling study and the remote handling operations needed

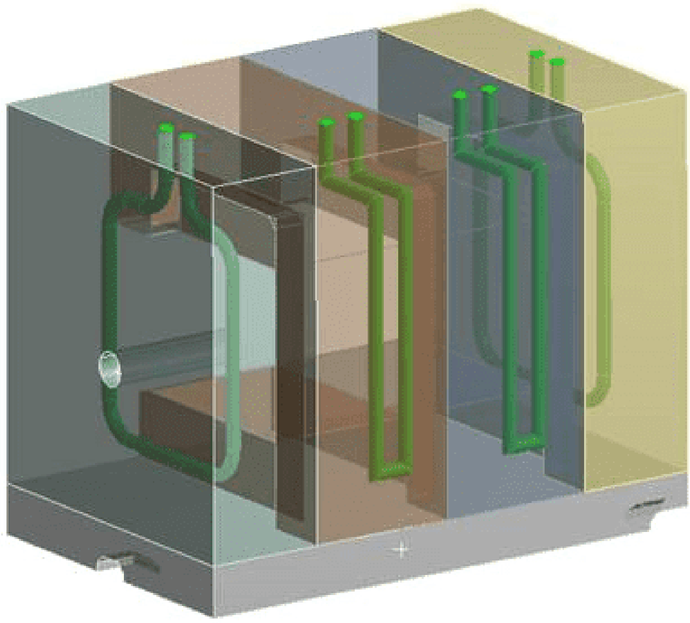

Fig. 6.51: 3D model of the proximity shielding blocks with embedded stainless steel pipes used for FEM calculations.

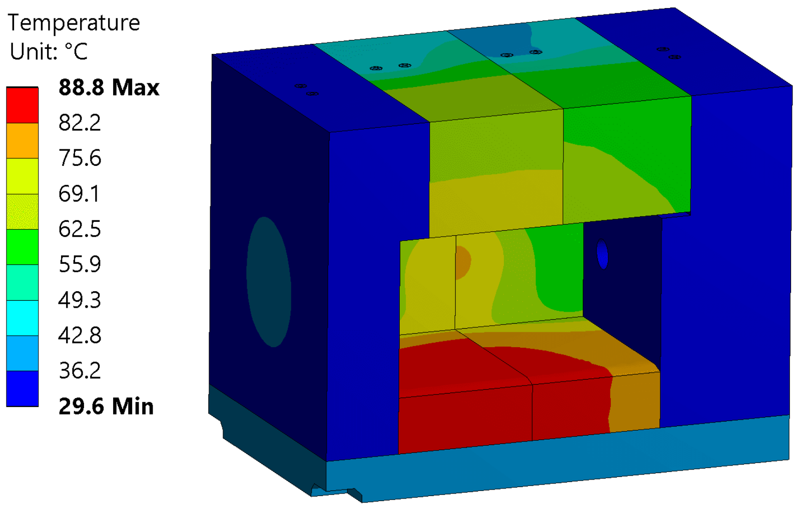

Fig. 6.52: Steady-state temperature distribution in the proximity shielding blocks. The maximum temperature reached is around 90°C.

to exchange it are described below. The beam window itself is similar in concept to the one used at T2K, shown in Fig. 6.66.

The beam window is mounted on the outside of the helium vessel (Fig. 6.67). It uses two inflatable pillow seals to seal it to the upstream beam pipe on one side and to the helium vessel on the other. The beam window assembly is designed to allow remote replacement using the overhead travelling crane in the target hall. The main elements of the beam window and its shield blocks, shielded cask, and extended remote lifting attachment are shown in Fig. 6.68. To remove the beam window, first the crane lifts out the upper shielding block and then the lower shielding block with the beam window attached to it. The shielding blocks are transferred to the remote handling section of the cool-down area, where the

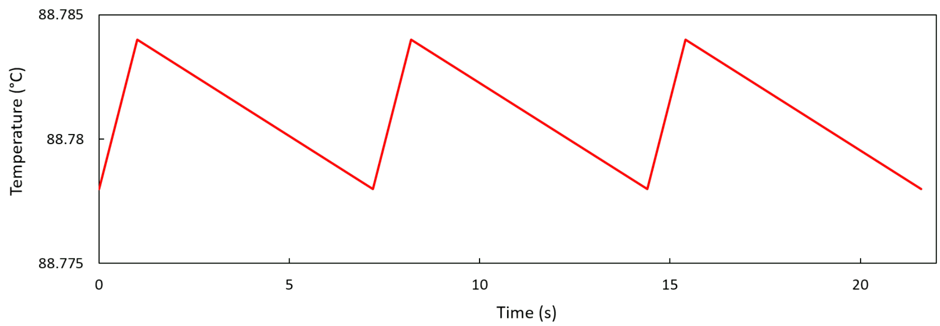

Fig. 6.53: Transient evolution of the temperature in the location of maximum temperature during three pulses after a long period of operation. The temperature increase is below 0.1°C.

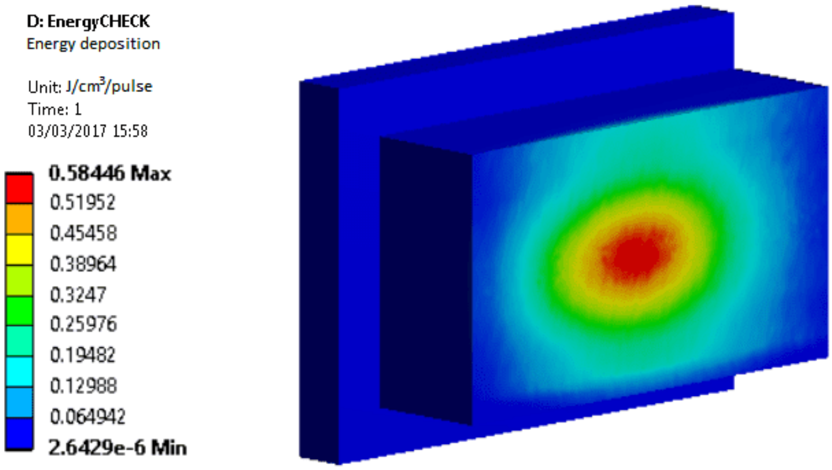

Fig. 6.54: Energy deposition distribution in the trolley shielding block

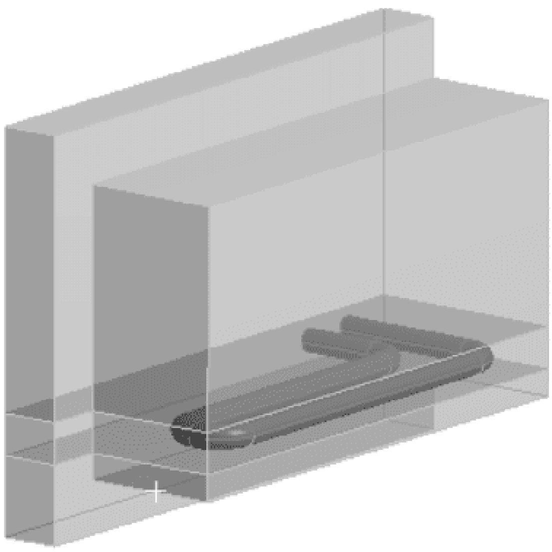

Fig. 6.55: 3D Model of the trolley shielding block with embedded stainless steel pipe used for FEM calculations.

beam window is then disconnected from the lower block using a pair of through-the-wall master–slave manipulators. The main steps in the removal of the beam window are listed in Table 6.3 and illustrated

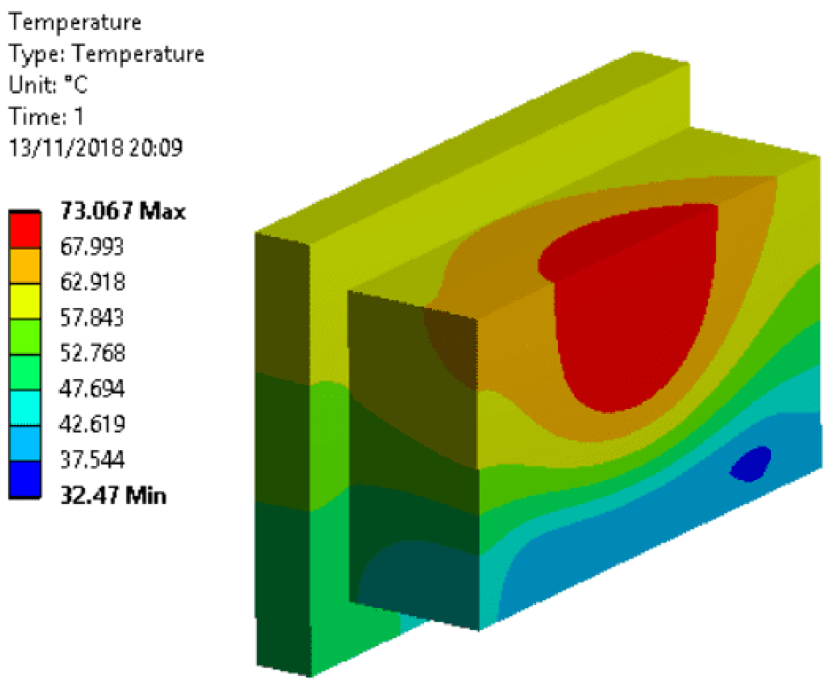

Fig. 6.56: Steady-state temperature distribution in the trolley shielding block. The maximum temperature reached is around 70°C.

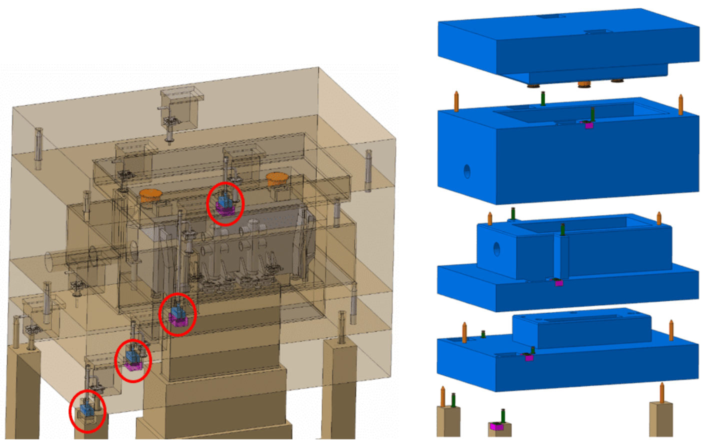

Fig. 6.57: Crane concept proximity shielding. Left: the layers of proximity shielding (crane concept) when assembled with the target in the middle. Electrical connectors are circled in red. Right: the proximity shielding layers are separated, showing alignment pins and cooling pipework stubs.

in Figs. 6.69 and 6.70.

Replacement is essentially the reverse of the removal procedure and can be carried out using a new beam window and new lower shield block or by fitting a new beam window onto the lower shielding block that has already been used. In front of the beam window, a second set of shielding blocks are used to fill in an access shaft—these blocks can be removed to provide access to the beam window extension on the vacuum vessel (Fig. 6.67). This access will be used for initial installation and connection of the vacuum pipe and for (remote) repair of the sealing faces on the helium vessel or vacuum pipe.

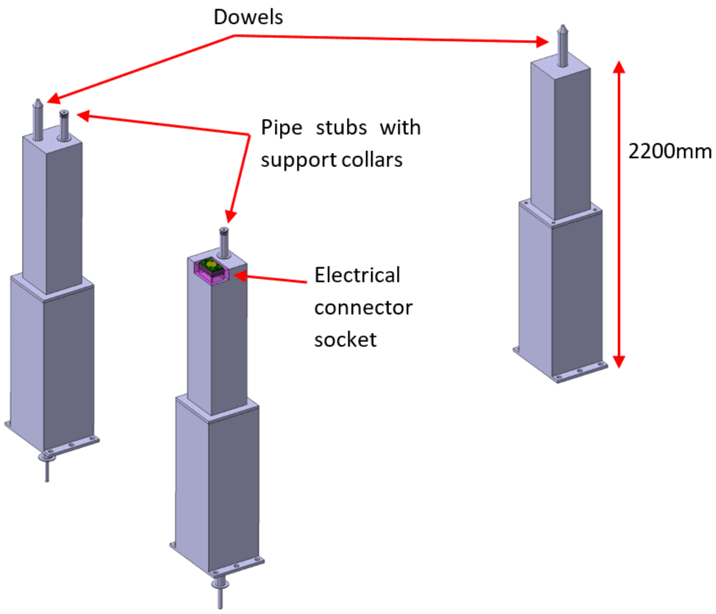

Fig. 6.58: Support pillars for crane concept proximity shielding, with water-cooling and electrical connections.

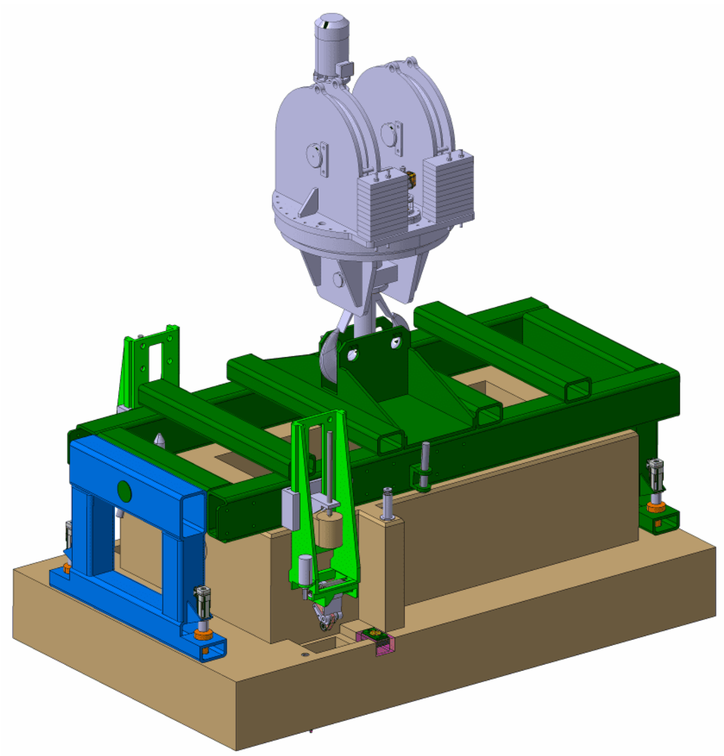

Fig. 6.59: Spreader beam for crane concept proximity shielding, equipped with two (un)locking tools, shown lifting proximity shielding block 3. The (un)locking tools can be repositioned on the spreader to suit the connection positions on the different layers of the proximity shielding.

6.2.4.2 Collimator handling

The collimator is formed as part of a removable block within the upstream shielding inside the helium vessel. It consists of a 150 cm long, 20 cm diameter graphite mask, employed to protect the downstream target and shielding assembly against beam misalignment. The graphite mask is incorporated into a

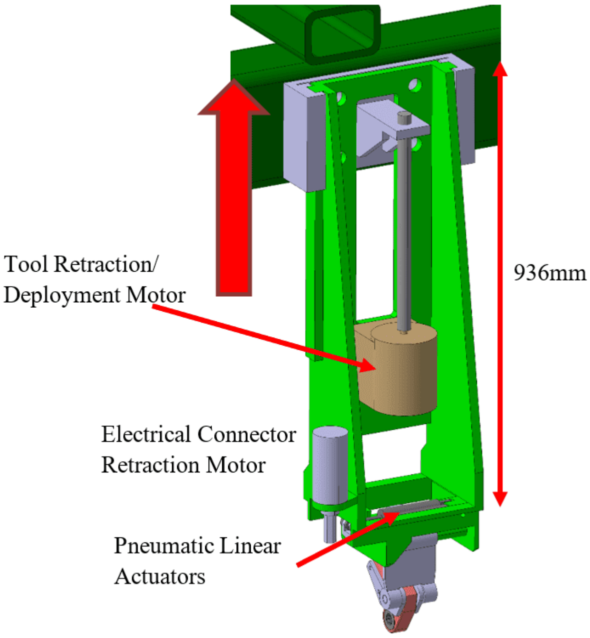

Fig. 6.60: Bolting tool for crane concept proximity shielding, used to remotely loosen or tighten water-cooling pipe clamps.

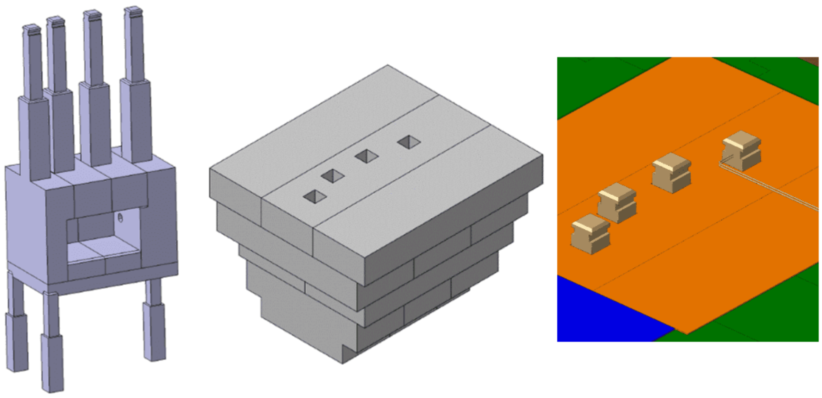

Fig. 6.61: Trolley concept proximity shielding. Left: the four blocks with their service 'chimneys' installed on a flat plate supported by three pillars. The service chimneys incorporate steps to avoid direct radiation shine paths. Middle: mobile shielding above the proximity shielding with passages for the service chimneys. Right: tops of the proximity shielding service chimneys protruding above the mobile shielding, with service connections shown on the right-hand chimney.

shielding block with lifting points so that it can be remotely installed and removed by the building crane. The shielding immediately around the collimator is supported on pillars to allow precise alignment of the collimator during initial installation (Fig. 6.71). The shielding above the collimator is designed to minimize the handling operations needed to exchange the collimator. The main steps and tooling required for collimator removal are listed in Table 6.4 and illustrated in Fig. 6.72.

6.2.4.3 Magnetic coil and US1010 shielding: handling aspects

The magnetic coil and US1010 shielding are designed to work together to provide a magnetic field of 1.5–1.6 T downstream of the target to sweep the muons produced in the target away from the detector acceptance, to reduce experimental backgrounds. More details are given in Section 6.3. The shielding

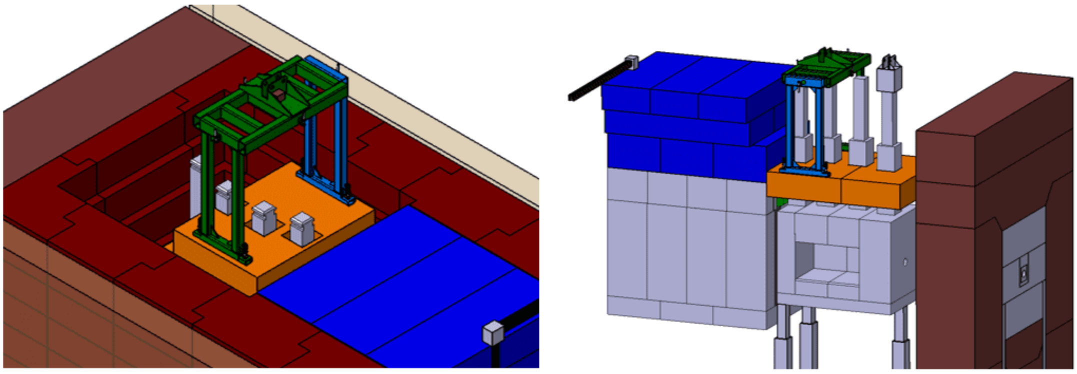

Fig. 6.62: Removing mobile shielding from above the trolley concept proximity shielding: the remotely operated spreader has 'legs' in order to be able to reach down to the lower levels of mobile shielding, while the main structure of the spreader is above the top of the service chimneys.

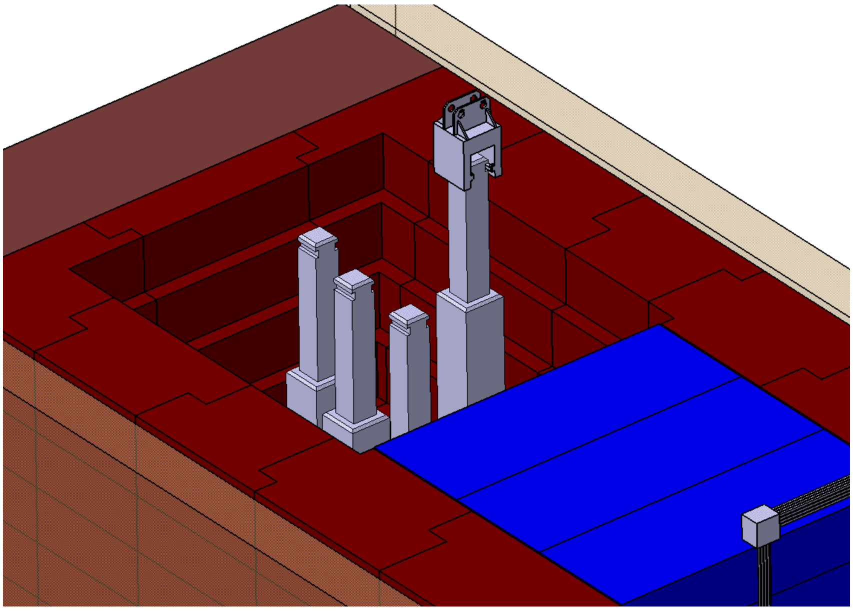

Fig. 6.63: Lifting the trolley concept proximity shielding: a lifting attachment fitted to the crane hook engages with lifting features at the top of the service chimneys. Lifting attachment shown engaged on right-hand service chimney.

includes two sections of non-magnetic stainless steel blocks (shown in black in Fig. 6.73) to ensure that the magnetic field is correctly guided through the US1010 steel yoke. The coil is lifted in and out of the helium vessel along with its surrounding US1010 shielding and its service connections, which protrude above the top layer of the shielding in the helium vessel (Fig. 6.74). The location of these service connections allows hands-on connection and disconnection above the bunker shielding. The design and layout of the US1010 blocks were optimized to give the minimum number of gaps seen by the magnetic field generated by the coil while remaining compatible with the achievable manufacturing and handling precision. To ensure that the individual components of the shielding can be safely left in a standing position during storage and initial installation, the US1010 and stainless steel parts are bolted together (Fig. 6.73). The coil is assembled into a module with a surrounding support structure made of US1010 steel, and is handled by the crane during installation in and removal from the helium vessel using lifting points in the support structure (Fig. 6.73). The main handling steps for removal of the coil in the event of failure are listed in Table 6.5 and illustrated in Figs. 6.75 and 6.76.

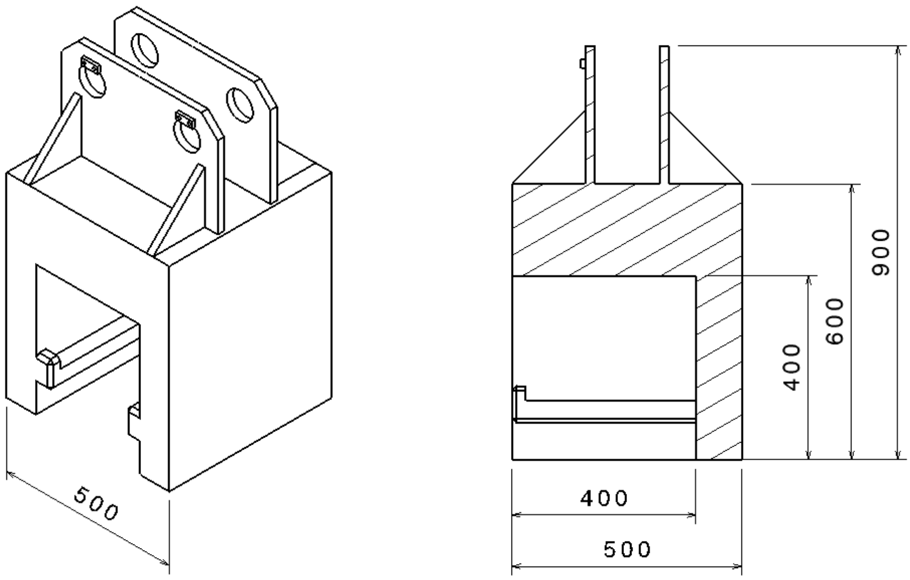

Fig. 6.64: Lifting attachment for trolley concept proximity shielding. The attachment is fitted manually to the crane hook and permits remote lifting of the proximity shielding.

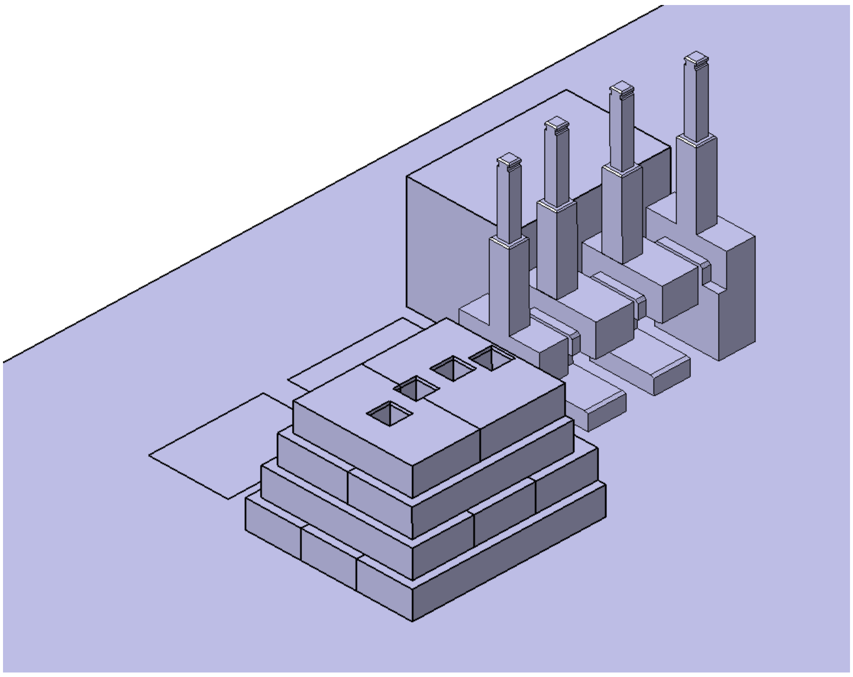

Fig. 6.65: Fixed proximity shielding elements for trolley concept, and mobile shielding stacked in the cool-down area.

6.2.5 Design of fixed bunker shielding: handling aspects

The fixed bunker shielding for the target is the shielding that fills in the space in the helium vessel around the sections of shielding that may need to be moved for maintenance reasons during the life of the facility. Figure 6.77 shows the different sections of iron and steel shielding in the helium vessel; the fixed bunker shielding is shown as semi-transparent in the figure. The design of the bunker shielding was carried out once all the other shielding had been designed. The requirements (for avoiding shine paths etc.) are, in general, the same as for the rest of the shielding, as set out in Section 6.2.1.4.

Fig. 6.66: T2K beam window with inflatable stainless steel pillow seals on both sides. (Image courtesy of T2K (Japan) and STFC (UK).)

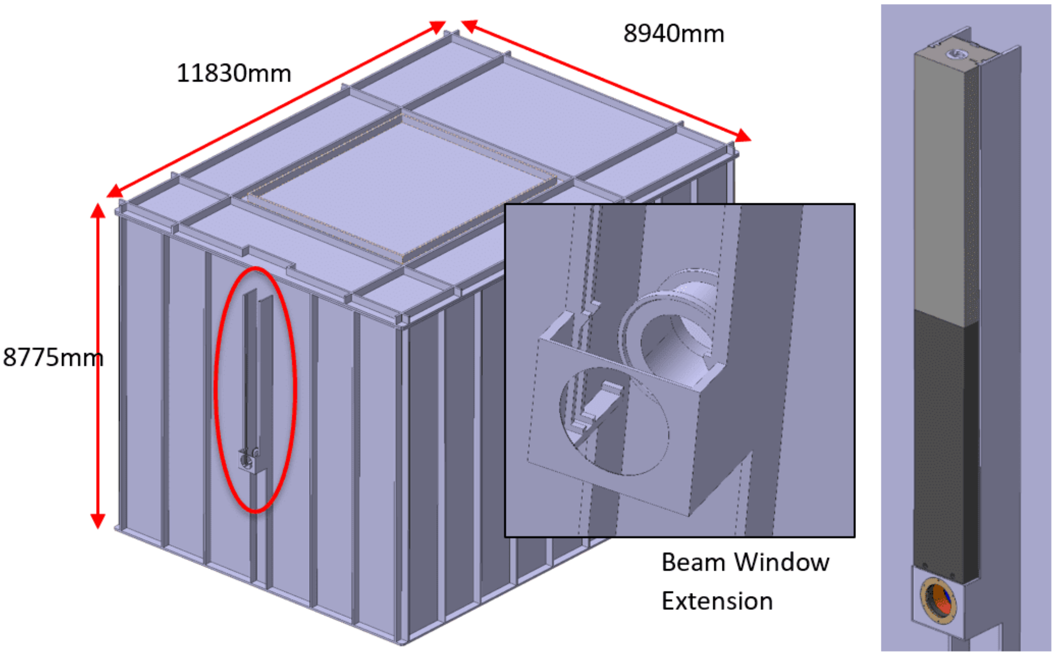

Fig. 6.67: Proton beam window. Left: BDF helium vessel with support features for the beam window and its shielding (ringed). Inset: beam window extension with sealing face for sealing the beam window to the helium vessel, and support for the end of the upstream beam pipe. Right: beam window and its shielding installed in the support on the helium vessel.

6.2.6 Global handling, integration, and operational aspects

6.2.6.1 Overhead travelling crane in target complex surface building (crane and trolley concepts)

Both the trolley and the crane concept have a remotely operated overhead travelling crane in the surface building to carry out the necessary handling operations for the installation and operation of the target complex. The crane runs on rails that run the length of the building, supported on the walls of the building. The capacity of the building crane was set at 40 t, giving a useful working load of around 36 t if 10% is reserved for spreader beams; this capacity is in line with road transport limitations, which is an

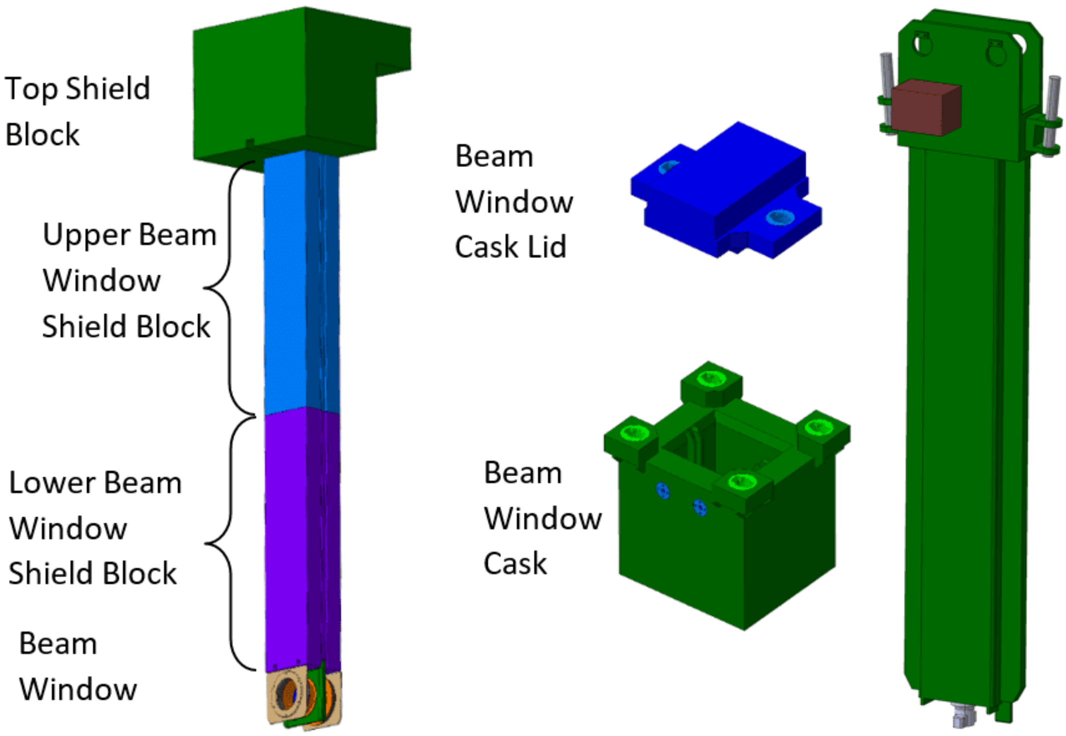

Fig. 6.68: Proton beam window. Left: main elements of the beam window and its shielding. Middle: shielded storage cask and lid for the beam window. Right: extended remote lifting attachment for lifting the lower shield block/beam window module.

Table 6.3: Main steps and tooling for removal of proton beam window from the helium vessel and transfer to the cool-down area for storage.

Step	Task	Tooling
a	Remove top shield block	Building crane (hands-on operation)
b	Disconnect services	By hand
c	Lift out upper shield block, transfer to storage support in cool-down area	Building crane and remote lifting attachment
d	Lift out lower shield block and beam window assembly, then transfer to beam window shielded cask in remote handling area	Building crane and extended remote lifting attachment
e	Disconnect beam window from lower shielding block (screw attachment designed for remote disconnection). Put lower shielding block in storage support.	Manipulators in remote handling area and building crane with remote lifting attachment
f	Cut off service connections to beam window	Manipulators + shear
g	Put lid on beam window cask	Building crane + manipulators

important consideration given the quantities of shielding blocks to be delivered and installed.

The crane hook rotation is motorized so that radioactive loads can be oriented without the need for the crane operator to be next to the load to rotate it manually—as is the case for normal crane operations. The crane hook is a size 20 ramshorn hook (according to DIN 15402). Electrical power and signal

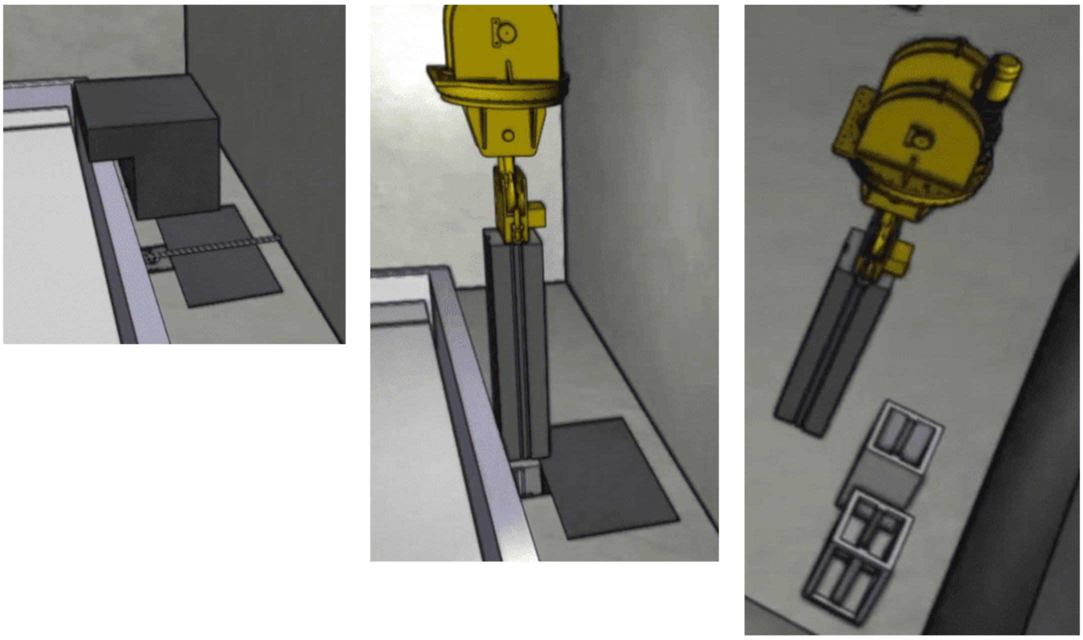

Fig. 6.69: Proton beam window removal (1). Left: removal of top shielding block. Centre: withdrawal of upper shielding block using building crane. Right: transfer of upper shielding block to storage support in cool-down area. The dark rectangle next to the beam window shaft represents shielding blocks which can be removed to access the beam window extension.

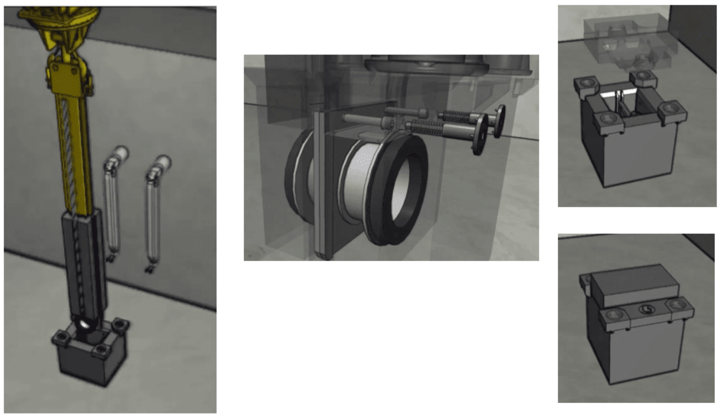

Fig. 6.70: Proton beam window removal (2). Left: withdrawal of lower shielding block and beam window assembly using extended lifting attachment and transfer to shielded cask in remote handling area. Centre: disconnection of beam window from lower shielding block using manipulators (via captive drivers in cask wall). Right: placing of lid on cask (after shearing beam window service pipes).

services are supplied down to the crane hook to operate spreader beams and their cameras. The crane is equipped with cameras and lighting on the crane bridge, trolley, and hook pulley block to illuminate the area around the loads being handled.

Spreader beams with remotely operated load attachment mechanisms are used in conjunction with the building crane. The spreaders are attached manually to the crane hook in an area away from radioactive equipment; electrical power and signal services are connected to the spreader beams at the same time to operate the remote load attachments and the spreader cameras.

Remote operation of the building crane is carried out from the control room in the experimental area service building. In addition to the controls for the crane, the control room has TV monitors for the

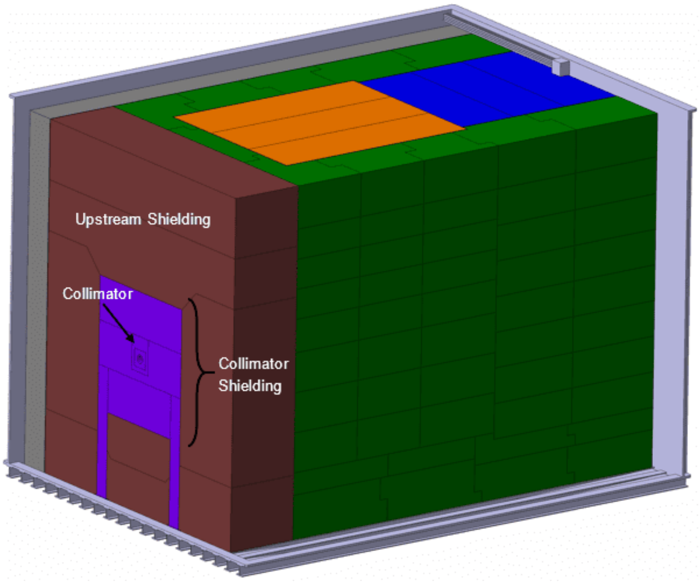

Fig. 6.71: Collimator and surrounding shielding, shown in cutaway helium vessel

Table 6.4: Main steps for removal of collimator from the helium vessel and transfer to the cool-down area.

Step	Task	Tooling
a	Remove helium vessel lid	Building crane (hands-on operation)
b	Disconnect electrical connections	By hand
c	Lift out two upstream shielding blocks above collimator and transfer to cool-down area	Building crane and remotely operated spreaders
d	Lift out collimator, then transfer to shielded cask in remote handling area	Building crane and remotely operated spreader
e	Cut off service connections	Manipulators + shear
f	Put lid on cask	Building crane + manipulators

Table 6.5: Main steps and tooling for removal of coil from the helium vessel and transfer to the remote handling area.

Step	Task	Tooling
a	Remove helium vessel lid	Building crane (hands-on operation)
b	Disconnect electrical connections	By hand
c	Lift out above-coil shielding and mobile shielding blocks and transfer to cool-down area	Building crane and remotely operated spreaders
d	Lift out coil, then transfer to remote handling area	Building crane and remotely operated spreader
e	Cut off service connections and separate coil from its support shielding	Manipulators + shear, building crane, and remotely operated spreader
f	Place in cask and put lid on cask	Building crane and remotely operated spreader

different camera views and controls for the pan–tilt–zoom drives of the cameras mounted on the crane, on the spreader beams, and around the building.

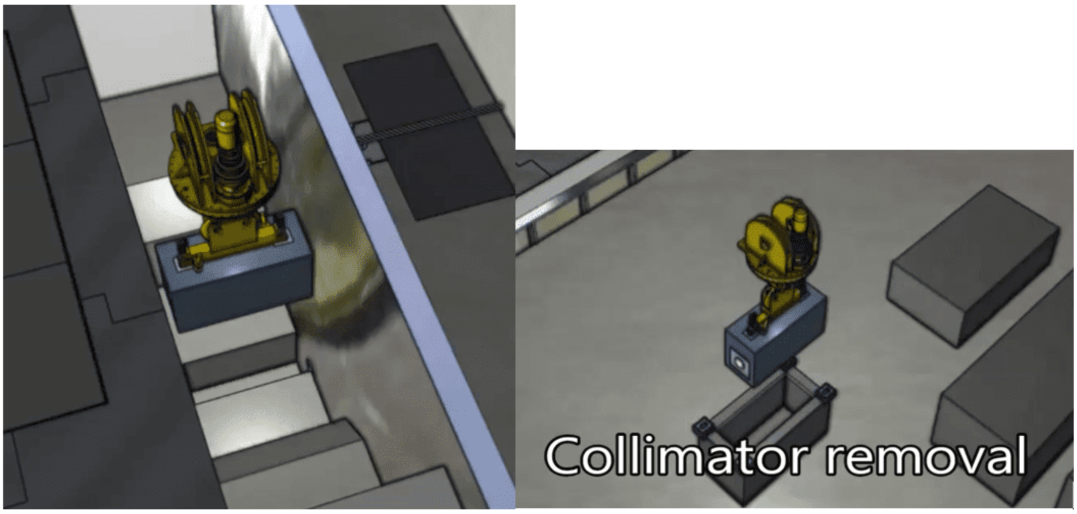

Fig. 6.72: Collimator removal. Left: crane lifting collimator out of helium vessel after removal of upstream shielding. Right: placing collimator in shielded cask.

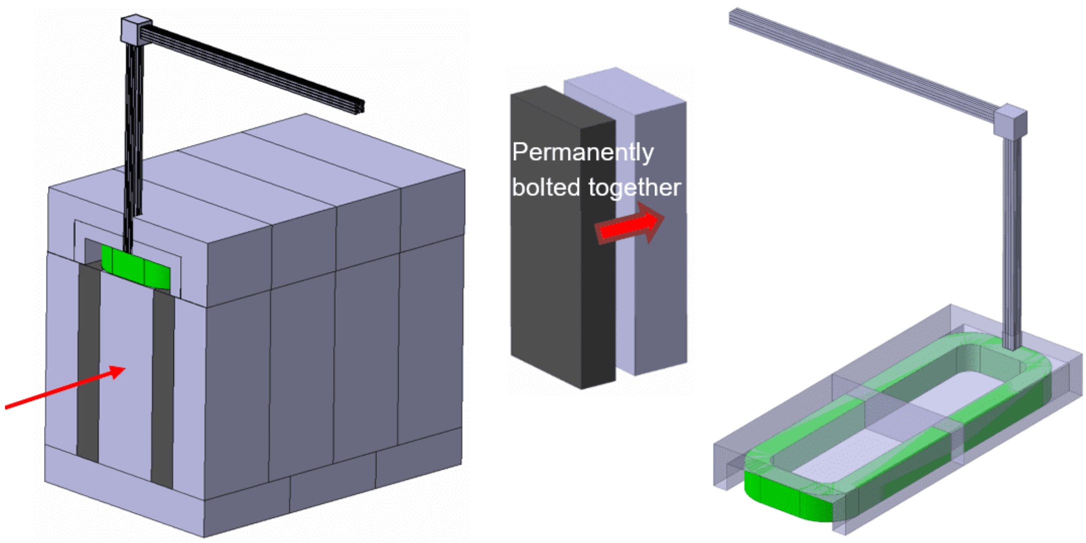

Fig. 6.73: Magnetic coil and US1010 shielding. Left: US1010 shielding downstream of the target and the magnetic coil. Right: magnetic coil with its surrounding US1010 support structure, which restrains the coil during operation and provides lifting points for the crane. The junction box between the horizontal and vertical portions of the service connections represents the connections which are made and disconnected by hands-on interventions.

The crane has no on-board electronics: electrical control cubicles are not installed on the crane, to avoid damage to the electronic components due to radiation and also to allow repair of the control electronics without the need to access the crane in the event of a failure. Position feedback from mechanisms on the crane is done by means of resolvers rather than encoders to avoid the presence of electronics on the crane. A cable festoon running the length of the building is used to transfer power and control signals between the control cubicles and the crane.

In the event of a crane breakdown during handling of a radioactive load, it is necessary to be able to move the load to a safe, shielded area. Recovery in the event of breakdown of the crane is ensured by siting the control electronics off the crane and designing in features such as redundancy of the hoisting, long-travel, cross-travel, and hook rotation drives along with their cabling. Repair of the crane can be carried out once the load is safely stored and the crane moved to an area at the end of the building where

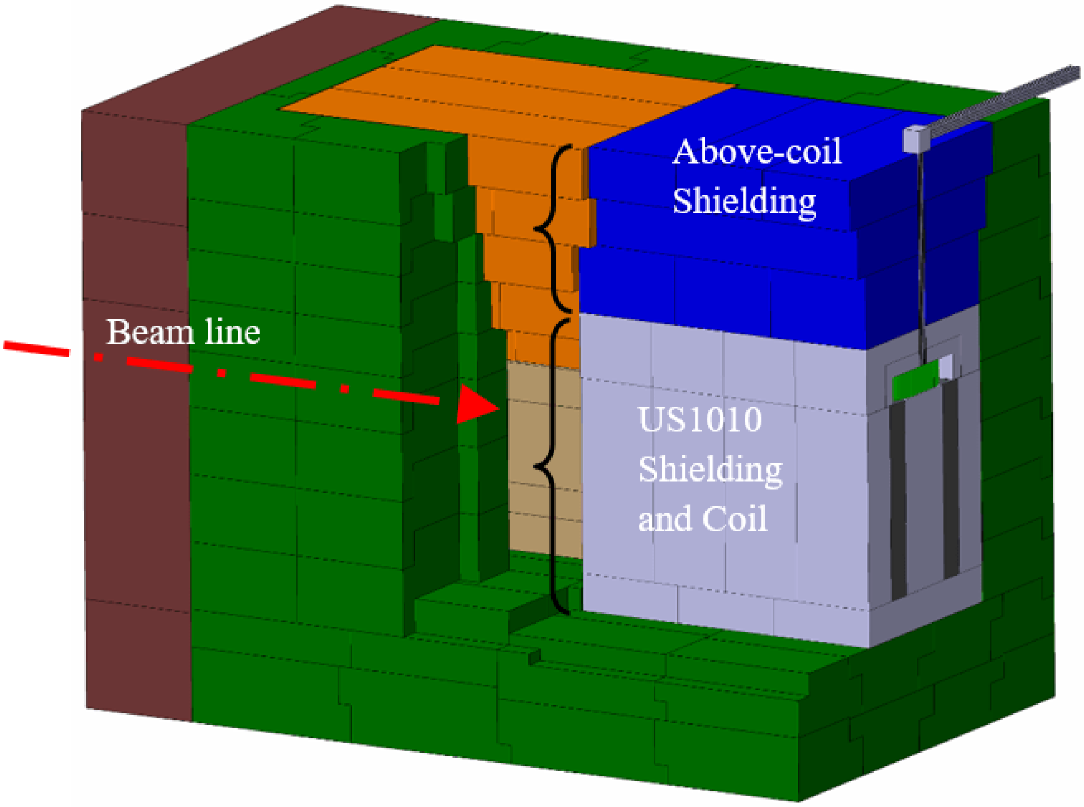

Fig. 6.74: Cutaway view of shielding in helium vessel showing the US1010 shielding and coil along with the above-coil shielding. Note staggering of joints between blocks to avoid direct radiation shine paths.

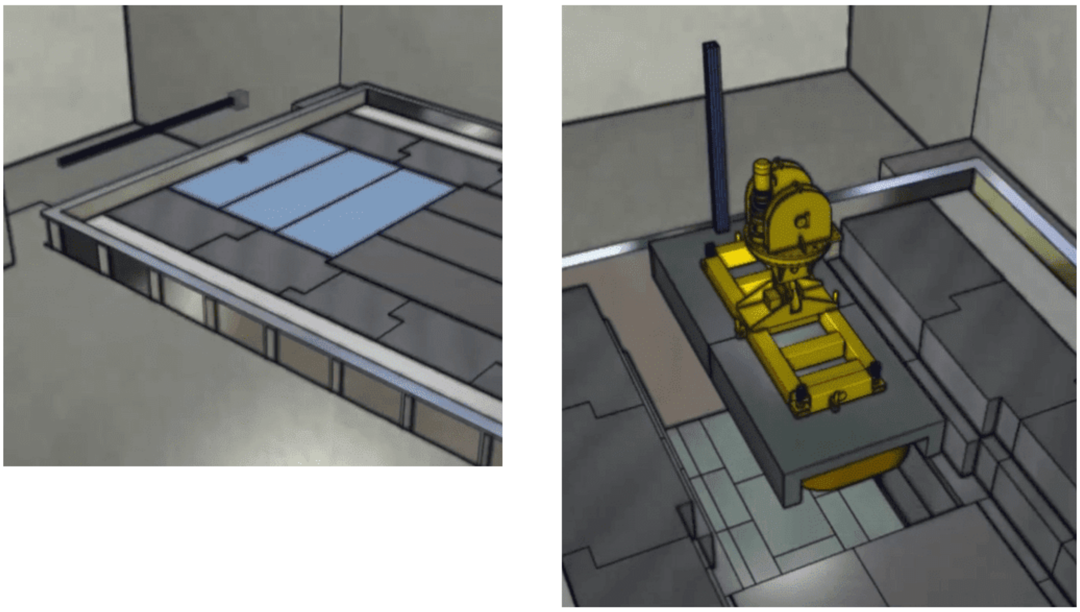

Fig. 6.75: Removal of magnetic coil. Left: disconnection of services above the shielding in the helium vessel. Right: lifting of the coil and its supporting shielding out of the helium vessel using the building crane and a remotely operated spreader.

radiation levels permit access for repairs.

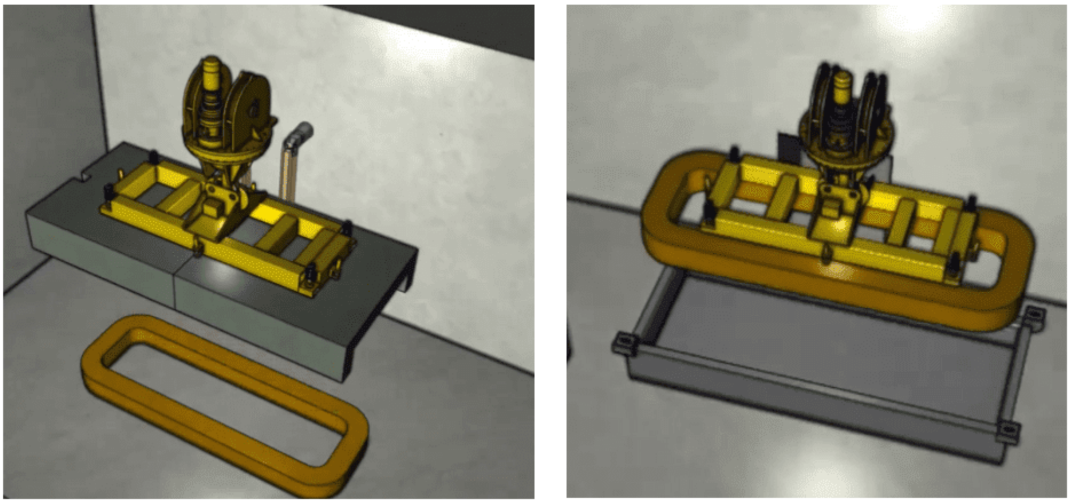

Fig. 6.76: Separation of magnetic coil and placing in storage cask. Left: separation of coil from shielding in the remote handling area. Right: placing the coil in the storage cask.

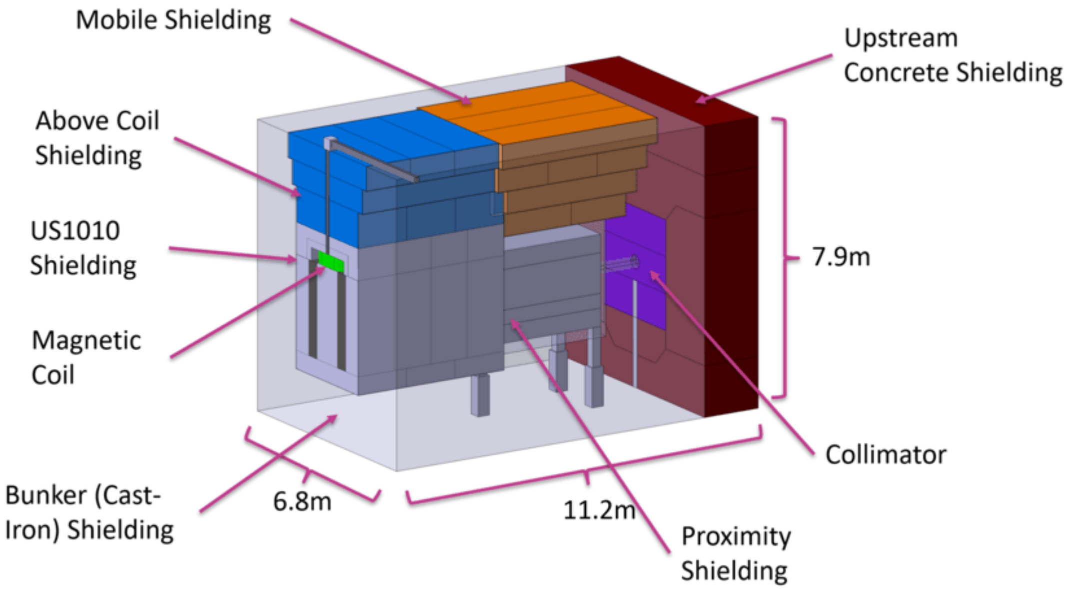

Fig. 6.77: Sections of shielding in the helium vessel. The fixed cast iron bunker shielding is shown as semi-transparent.

6.2.6.2 Hot cell crane for trolley concept

The trolley concept hot cell is equipped with a 3 t remotely operated overhead travelling crane to carry out target-handling operations inside the hot cell when the trolley is in its withdrawn position. The crane is fitted with a ramshorn hook with motorized rotation.

The crane is controlled from the area outside the hot cell next to the master–slave manipulator master arms; viewing of operations is done via the shielded windows of the hot cell and radiation-tolerant pan–tilt–zoom cameras installed in the hot cell.

The spreader beam used to lift the target is attached to the crane hook with the aid of the master–slave manipulators, and the manipulators can also guide the spreader beam to engage it with the target.

The crane has no on-board electronics: resolvers are used for position feedback of the crane motions. Recovery in the event of breakdown of the crane is ensured by siting the control electronics off the crane and designing in features such as redundancy of the hoisting, long-travel, cross-travel, and hook rotation drives along with their cabling. Repairs to the crane can be carried out by accessing the hot cell once the target is removed, either by moving it on the trolley into the helium vessel or by lowering it into the transfer cask and moving it into the storage area.

6.2.6.3 *Cameras and viewing*

6.2.6.3.1 *Cameras and viewing for remote handling operations with the target hall crane*

Cameras are needed for remote handling operations carried out by the crane. Pan–tilt–zoom cameras are mounted on the crane itself and around the target hall building (Fig. 6.78). Fixed cameras are mounted on the lifting spreaders (see Figs. 6.80 and 6.81).

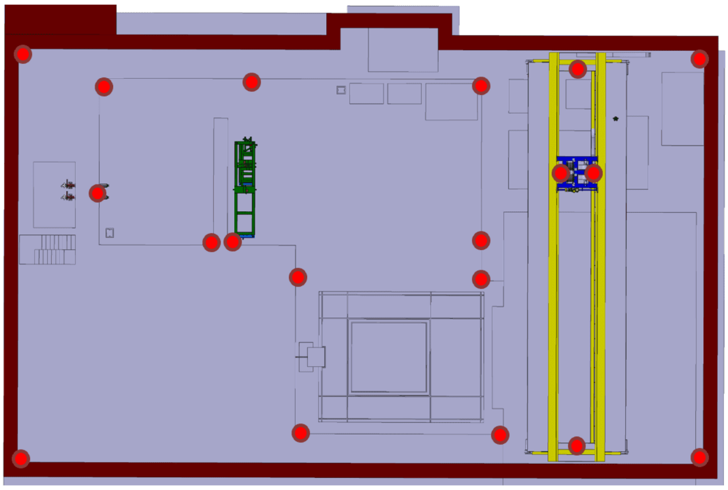

Fig. 6.78: Crane concept camera positions on the crane and in the target hall building (around the cool-down and remote handling areas and around the target pit).

6.2.6.3.2 *Cameras and viewing for the remote handling area and trolley cell*

The trolley concept hot cell and the remote handling areas for both concepts are fitted with lead glass shielded viewing windows and also pan–tilt–zoom cameras. In addition, cameras may be fitted to the manipulator arms to get a close-up view of the grippers (Fig. 6.79).

6.2.6.4 *Spreader beams and lifting interfaces*

The study included the conceptual design of spreader beams and lifting attachments used to lift the equipment that will become radioactive. The designs of some of the spreader beams and lifting attachments are explained and illustrated in the various sections of this report describing handling methods and sequences for the exchange of key components. Most of the spreader beams have motorized lifting interfaces to allow fully remote connection and disconnection of the loads.

Two different lifting interfaces are used in these spreader beams.

- ISO ‘twist lock’ lifting interfaces (as used on standardized transport containers): these have conical ends to allow easier remote operation and are rotated through 90° to lock on to the load. They have a load capacity of approximately 15 t each (see Fig. 6.80).
- CERN lifting attachments: these also are rotated through 90° to lock onto the load but do not have conical ends to facilitate remote use. They have a load capacity of 7.5 t (see Fig. 6.81).

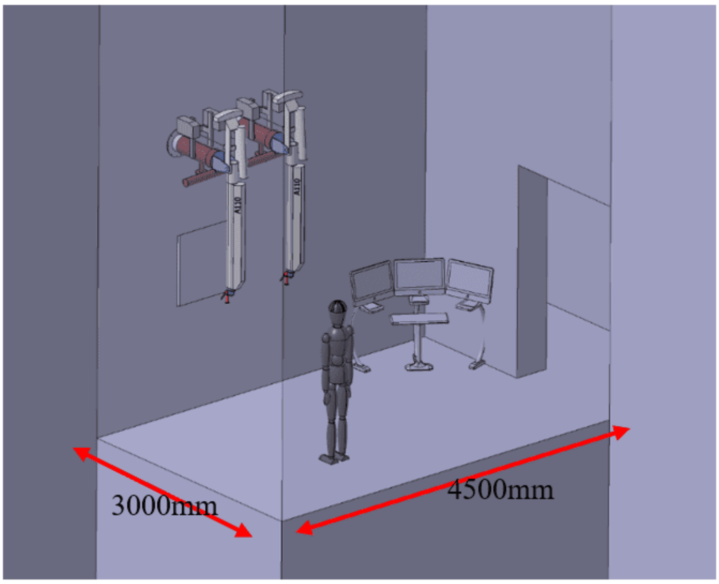

Fig. 6.79: Operating area for the trolley concept hot cell with manipulator master arms, shielded viewing window in the hot cell wall, and camera monitors.

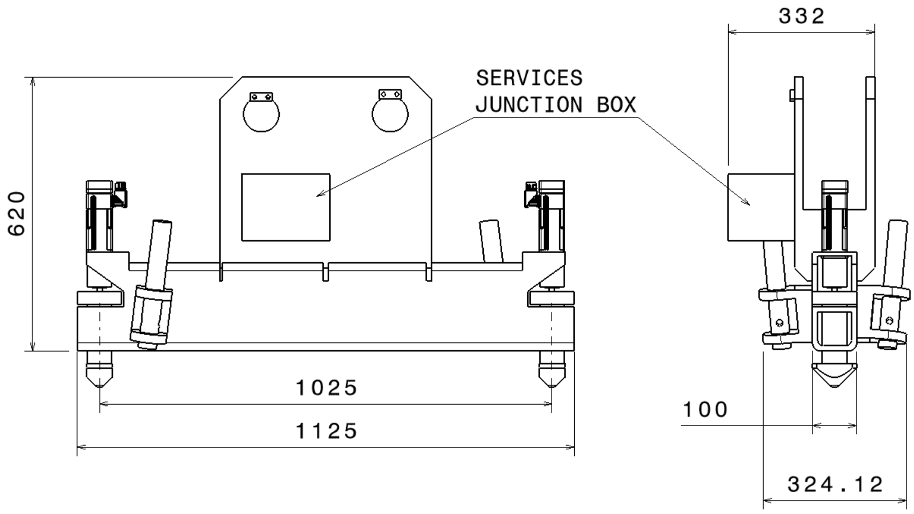

Fig. 6.80: Lifting spreader for collimator, equipped with four motorized ISO twist locks. Inclined cameras are installed on the spreader to allow the crane operator to view the engagement of the twist locks during remote operations.

6.2.6.5 Helium vessel and services: handling and integration

The helium vessel (Fig. 6.82) has to support the loads due to the shielding inside it, ensure good helium leak-tightness, allow the passage of services, permit the flushing of air with helium, and also allow draining of any water leaks.

To allow for flushing of helium and draining of water leaks, the floor of the vessel slopes down to a drain point. This drain point is connected to a sump room so that any water leaking into the vessel drains out even in the event of a pump failure. Service galleries are included in the civil engineering structure to allow connections between the Cooling and Ventilation (CV) and sump rooms.

The helium vessel designs for the two handling concepts have some differences in the position of

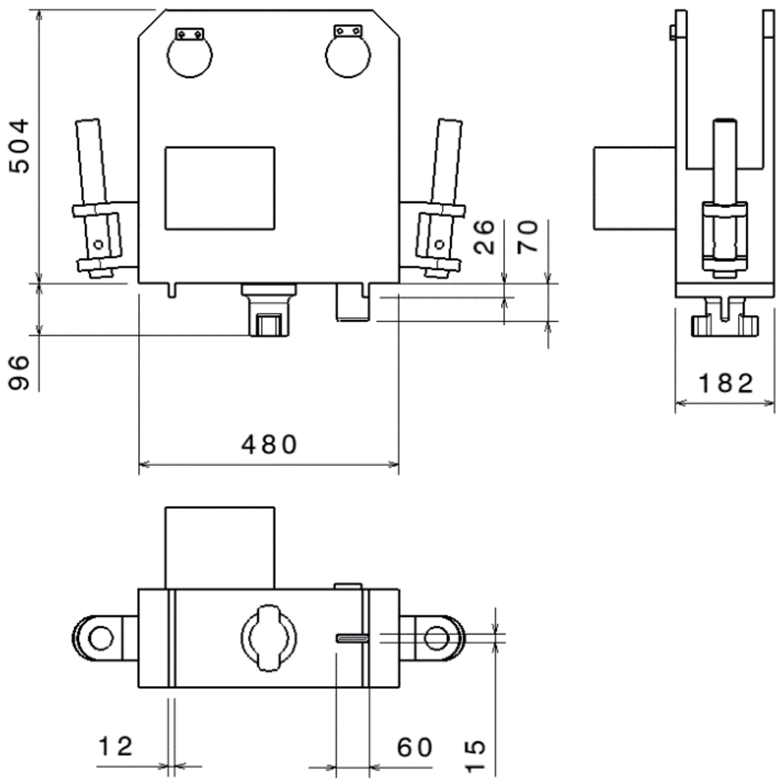

Fig. 6.81: Spreader for upper beam window shield block, equipped with a CERN twist lock interface

the service passages and access openings for target and shielding movement. In the crane concept design, the services (water, helium, electrical) for the target and proximity shielding enter the helium vessel from below, while the services for the magnetic coil enter from the vessel side close to the top (Fig. 6.82). In the trolley concept design, no services enter the helium vessel from below: the target services pass via the trolley, while the proximity shielding and coil services enter the helium vessel from the side above the upper surface of the shielding inside the vessel.

The structural design of the helium vessel is covered separately in Section 6.4.

6.2.6.6 Cool-down and remote handling areas

A cool-down area below ground level is provided for temporary storage of the target, shielding, magnetic coil, beam window, etc. The area has been designed to allow temporary storage and transfer as required, for all maintenance operations foreseen during the life of the facility. As part of the study, the space requirements in the cool-down area for each maintenance operation were determined in order to define the required dimensions of the cool-down area. Figures 6.83 and 6.84 illustrate typical storage space checks carried out as part of the design process.

In addition, a remote handling area, equipped with a pair of through-the-wall master–slave manipulators, has been included as part of the cool-down area to carry out operations such as disconnection of the beam window from its shielding block, removal of the magnetic coil from its surrounding shielding, and unforeseen repair work if needed (see Figs. 6.6 and 6.11).

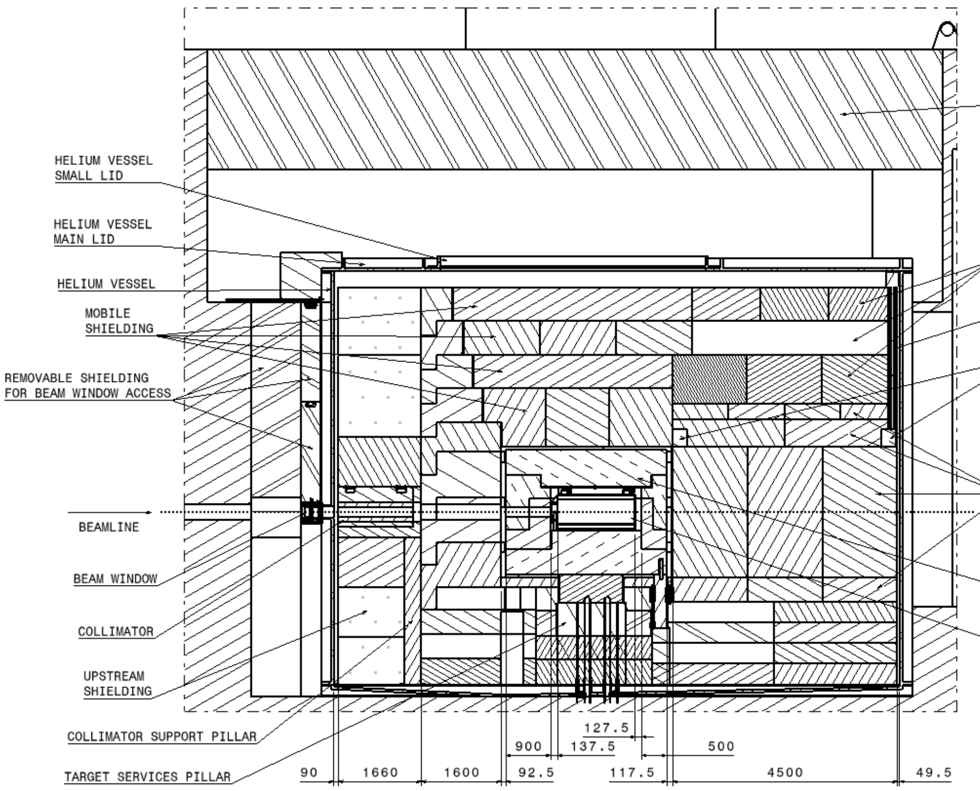

Fig. 6.82: Sectional view of helium vessel in the target pit showing the main elements and the different shielding areas (crane concept shown, which includes a small lid as part of the main lid; only the small lid needs to be removed for target exchange).

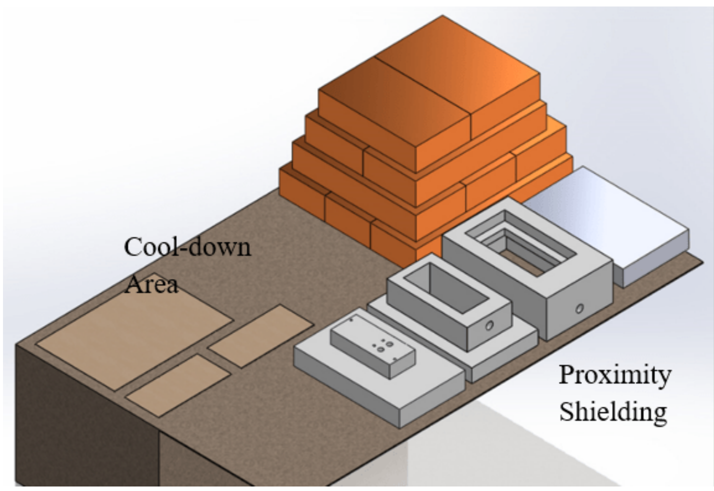

Fig. 6.83: Example of storage space checks used to determine the required dimensions of the cool-down area (in this case, the crane concept proximity shielding and mobile shielding are shown).

6.2.6.7 Cooling and ventilation services and equipment: handling and integration

The cooling and ventilation systems for the target complex consist of water-cooling systems for the target, proximity shielding, and magnetic coil; a helium purge and purification system for the helium vessel and the target; and a pressure cascade ventilation system for the target complex to ensure containment of any radioactive contamination. ANSYS simulations were used extensively to validate the cooling of the target and of the proximity shielding; the results of this work were fed into the design of the CV systems.

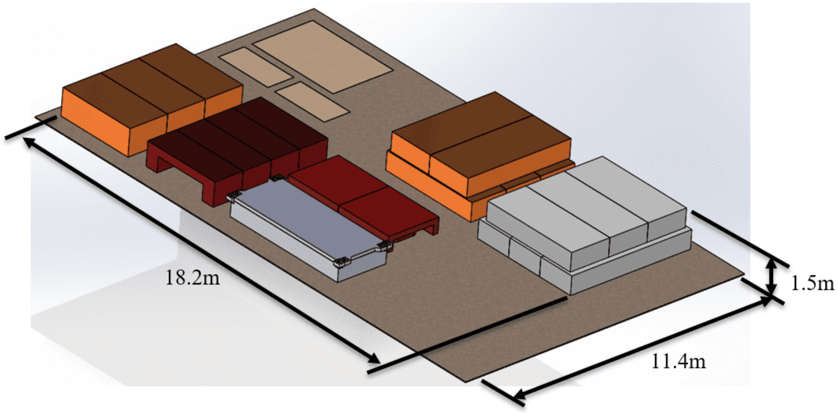

Fig. 6.84: Dimensions of cool-down area required for coil removal

More details of the CV systems are given in Section 6.5.

The equipment for water cooling and helium purification is housed underground in the target complex along with the sump room to collect any water leaks in the helium vessel. The pressure cascade ventilation ducts are integrated into the target complex building, while the rest of the ventilation system equipment and cooling towers are housed in an auxiliary building to be constructed next to the target complex building.

For the crane concept design, all of the cooling and helium system equipment for the target and proximity shielding is housed in the underground area (see Fig. 6.6); for the trolley concept, the cooling and helium systems for the target are installed separately on the rear of the trolley (see Figs. 6.14 and 6.18). The integration of the CV equipment into the target complex is explained in Section 6.5.

6.2.6.8 Recovery from beam line equipment failures: remote handling capabilities needed

Designing for recovery from failures was an important aspect of the handling and integration study, as the very high residual radiation dose rates for the target and the proximity shielding necessitate the use of remote handling techniques. In the event of failure of the beam window, collimator, or magnetic coil, the failed item would be replaced using the techniques and procedures described in Section 6.2.4, which are common to the crane and trolley concepts. However, for the connections to the target and proximity shielding, the two concepts use different remote handling approaches.

6.2.6.8.1 Trolley concept connector repairs

For the trolley concept, failures of connections to the target would be dealt with using the remote handling manipulators and custom-designed tools (adapted for remote use) within the hot cell. The trolley concept proximity shielding connections are outside the shielding and so can be repaired hands-on.

6.2.6.8.2 Crane concept connector repairs

For the crane concept, there is a need for special tooling to deal with connector failures; a solution based on the use of cutting tools incorporated into the frame of the (un)locking tool is used to deal with failure of the connector clamp (Fig. 6.85). However, if the fixed connections on the service pillars in the crane concept helium vessel are damaged, a mobile remotely operated manipulator system capable of reaching into the helium vessel and working at the level of the service pillar connections will be needed for repair. One potential solution is the use of a twin-arm force-reflecting servo manipulator mounted on a support platform which can be lifted into position by the building crane to carry out repairs using adapted tools. The master arms would be in the facility control room, with the power and control signals to the slave arm carried via a mixture of Ethernet and electrical cables (Fig. 6.86).

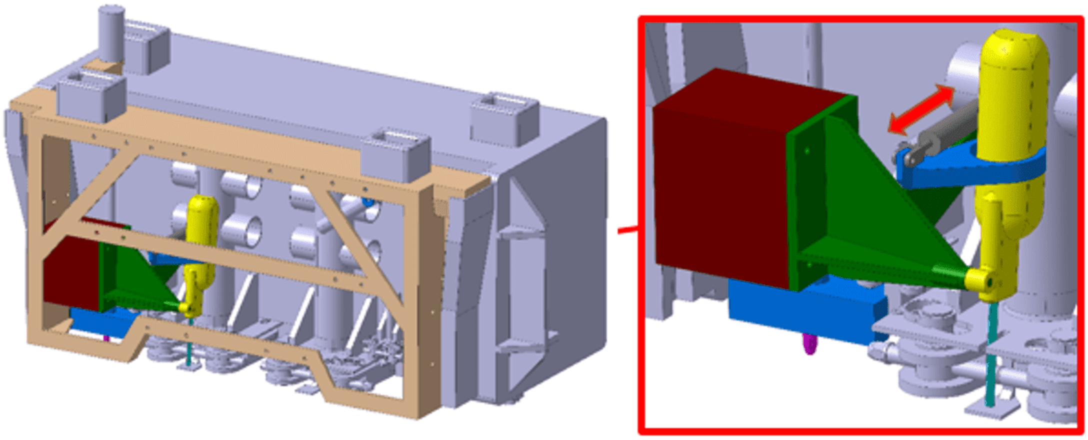

Fig. 6.85: Cutting a seized clamping screw on the target water connection using a saw module installed in the frame of the (un)locking tool. Saw module shown in zoom view on right. A second device then prises open the failed connector so that the target can be lifted.

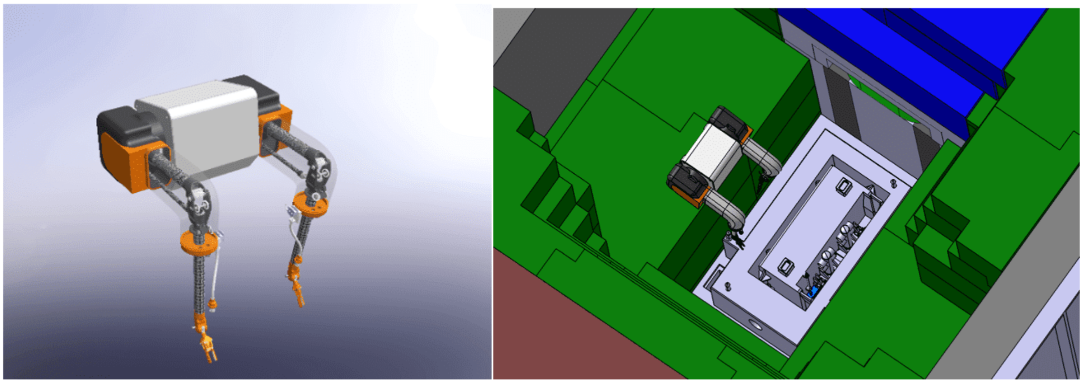

Fig. 6.86: Additional remote handling system for repair of damage to service pillar connections in crane concept. Left: twin-slave-arm master–slave servo manipulator 'Dexter', produced by Oxford Technologies. Right: illustration showing the slave arms in the helium vessel.

6.2.6.9 Reconfiguration and decommissioning

Reconfiguration of the facility could be required in the future to install a different experiment. For the purposes of the handling and integration study, reconfiguration was taken to mean replacement of all of the equipment in the helium vessel. Reconfiguration will therefore necessitate removal of the equipment in the helium vessel using the remote handling equipment and procedures already described. In addition, the service pillars for the crane concept could need to be removed or the nose of the trolley could need to be replaced.

Decommissioning of the facility would involve removal of all of the equipment in the helium vessel and of all other radioactive or contaminated equipment in the building. It is similar in scope to the equipment removal needed for reconfiguration but with extra work to dismantle and dispose of the helium vessel and, in the case of the trolley concept, the activated/contaminated parts of the trolley itself and of the hot cell.

6.2.7 Comparison of crane and trolley concepts: conclusions

Analysing the handling and remote handling operations needed during the lifetime of the facility (including those needed to recover from failures and damage) as part of the integration design work has led to a clearer understanding of the design requirements for the target complex; the design work forms a sound basis for further work as the BDF design study advances.

The remote handling methods are essentially the same for many elements of both concepts, and so they will not influence any decision on the choice of concept: for example, the beam window, collimator, magnetic coil, and US1010 shielding. To compare the two concepts, the following elements related to operation and construction of the target complex were considered:

- target exchange;
- water and electrical connections;
- shielding;
- helium vessel;
- design and development risks of the handling equipment;
- civil engineering;
- reconfiguration;
- decommissioning.

6.2.7.1 Target exchange

The trolley concept design offers a simpler and faster target exchange than the crane concept, as the target is withdrawn from the helium vessel without the need to remove the lid, remove the mobile shielding, and then disconnect and remove the proximity shielding. The pipework design in both concepts allows draining of the target before disconnection.

6.2.7.2 Water and electrical connections

Both concepts have remotely operated clamped water connections and remotely operated electrical connections to the target and proximity shielding that are exposed to high levels of radiation—this is a potential source of major problems because conventional industrial sealing solutions and materials cannot be used.

The water and electrical connections for the trolley concept offer some major advantages over the crane concept connections.

- The connections to the trolley concept fixed proximity shielding are above the helium vessel shielding—this allows hands-on access to connect and disconnect connections and to diagnose and repair faults once the helium vessel lid has been removed.
- There are no fixed (permanently installed) connectors in the trolley concept helium vessel. The crane concept has fixed connections in the service pillars, which will require an additional (relatively complex) mobile remote handling system along with custom-designed remotely operated tooling to repair them if they are damaged.
- The trolley concept design offers good access for remote handling (and viewing via the hot cell shielding windows) of the target connections on the trolley. This will allow the remote repair of failed or damaged connectors on the trolley by means of custom-designed tooling put in place by the hot cell master–slave manipulators.
- The connections to the crane concept fixed proximity shielding are built up in layers—this is a major disadvantage in the event of a leak. First of all, it will be hard to leak-test the circuits until all the layers are installed. Secondly, it will be difficult to diagnose the source of a leak—especially once the facility is in operation and it is not possible to have personnel access the area of the proximity shielding. Thirdly, repairing a leak will require removal and replacement of several layers of shielding and the use of relatively complicated custom-made remotely operated (un)locking and recovery tooling put in place by the building crane.

6.2.7.3 Helium vessel

The trolley concept helium vessel has the added complexity of the side opening for the trolley and the resulting risk of leaks in the event of damage to the door seal or to the sealing face. The seal would need to be replaced remotely using the hot cell master–slave manipulators and specially developed tooling. Damage to the sealing face would be very difficult to repair with remote techniques.

The crane concept helium vessel has added complexity due to the provision of services to the target and the proximity shielding through the vessel floor.

6.2.7.4 Shielding

The key differences between the shielding in the crane and trolley concepts arise from the differences in the layout of the proximity shielding. The proximity shielding blocks for both the crane and the trolley concept are of similar levels of complexity—and CERN already has experience of design and manufacture of large iron castings with embedded water-cooling pipes. The trolley concept service chimneys and surrounding mobile shielding will need to be particularly carefully designed, built, and installed to avoid shine paths above the target.

6.2.7.5 Design and development risks

A disadvantage of the trolley concept is the additional design and development work needed for the trolley itself, and the additional space required in the underground area of the building for it to operate.

The crane concept offers the advantage of a simpler facility/building design than the trolley concept. However, the tooling required to operate and recover from failure of the water connections in the helium vessel will be relatively complex and require extensive development and testing. For the crane concept, repair of damaged water or electrical connections in the helium vessel will also require an additional mobile remote handling manipulator system.

6.2.7.6 Civil engineering

The crane concept has the advantage of a smaller underground area than the trolley concept; the need to provide service galleries directly underneath the heavily loaded helium vessel of the crane concept, however, will add complexity and risk of settlement movement over the life of the facility.

6.2.7.7 Reconfiguration

The thicknesses of the shielding in the helium vessel have been determined in order to have minimal activation of the helium vessel. To allow maximum flexibility for reconfiguration of the target complex, the design should ideally allow the all of the equipment in the helium vessel to be easily removed so that a new kind of target (possibly of completely different dimensions) and shielding, etc. can then be installed.

Both the crane and the trolley concept place some restrictions on reconfiguration of the target complex. The service pillars in the crane concept (which will be radioactive) would need to be cut out to provide complete flexibility for a new design. The trolley concept is more restrictive because, to keep the cantilevered weight of shielding on the trolley as low as possible, the size of the opening in the shielding in the helium vessel has been kept to the minimum compatible with the existing target design. A larger target would therefore not be possible without major modification of the trolley and the helium vessel. Further restrictions on the size of a new target could be imposed by the size of the opening in the concrete wall between the helium vessel and the hot cell and the dimensions of the transfer passage between the hot cell and the cool-down area.

6.2.7.8 Decommissioning

Decommissioning of the trolley concept facility would produce a slightly higher volume of waste owing to the trolley itself if that became contaminated. Decommissioning of the crane concept facility would be complicated by the need to cut the service pillars out of the helium vessel and remove potentially contaminated pipework from the service galleries below the helium vessel.

6.2.7.9 Choice between crane concept and trolley concept

At the end of the study, after analysis and comparison of the two designs—mainly in view of the concerns explained above relating to the water and electrical connections inside the helium vessel—it was decided to consider the trolley concept as the baseline for the ongoing work being carried out on the integration of the whole facility, the studies of the cooling and ventilation, the studies of the helium vessel, etc.

6.2.8 The 'crane++' concept: a third concept combining the benefits of the crane and trolley concepts

6.2.8.1 Explanation of crane++ concept

After analysing and comparing the designs produced during the handling and integration study based on the crane and trolley concepts, it was realized that a third concept could combine the best features and advantages of both concepts. This third concept uses the crane for all handling but has service chimneys (as used with the trolley concept proximity shielding) for both the target and the proximity shielding. This third concept has been named the 'crane++' concept.

The proximity shielding in the crane++ concept is similar to that in the trolley concept, but the fixed portion has a U shape rather than a C shape to allow the target to be installed and removed vertically by the building crane (Fig. 6.87). The target is suspended from an upper plug of water-cooled shielding that is supported by the fixed, U-shaped portion of proximity shielding castings. This method of suspension will allow adjustment of the target alignment if necessary. The water cooling of the proximity shielding uses cast-in thick-walled stainless steel pipes as in the trolley concept. The pipework for water cooling of the target and electrical services passes through the two service chimneys attached to the upper plug of the proximity shielding.

The crane++ concept includes service passages in the helium vessel lid to provide fully accessible water and electrical service connections. Connections in the pipework below the helium vessel lid are welded to avoid the risk of leaks from mechanically clamped seal connectors. The water and electrical connections at the top of the service chimneys can be made, disconnected, and repaired hands-on rather than remotely; this reduces the complexity of the connectors and the risk of damage during connection work, and greatly simplifies fault diagnosis and repair.

The main features of the crane++ concept are illustrated in Figs. 6.87–6.93; it is proposed to further develop the concept in the next phase of the project.

6.2.8.2 Crane++ concept target exchange steps

In the crane++ concept (as in the crane concept), all installation and removal operations are carried out vertically using the building's overhead travelling crane. As in the crane concept, it is proposed to have a small lid as part of the helium vessel lid so that it is not necessary to remove the complete lid to exchange the target.

Before starting lifting operations, all of the connections to the target and proximity shielding service chimneys are manually disconnected from outside the lid of the helium vessel. To exchange the target, it is necessary to remove the small lid of the helium vessel and the 'mobile shielding' (Figs. 6.96 and 6.97).

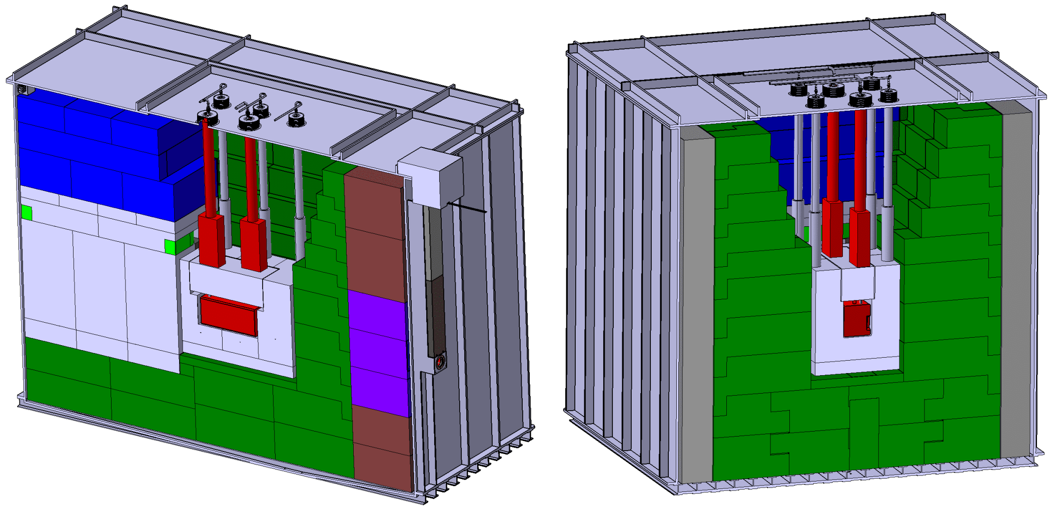

Fig. 6.87: Crane++ concept. Left: vertical section through the helium vessel parallel to the beam line showing the target (in red) in the centre surrounded by the proximity shielding (in grey). The target is suspended from an upper plug in the proximity shielding. The mobile shielding above the proximity shielding has been removed to show the service chimneys for the target (in red) and for the proximity shielding (in grey). Right: section through the helium vessel perpendicular to the beam line showing U-shaped proximity shielding.

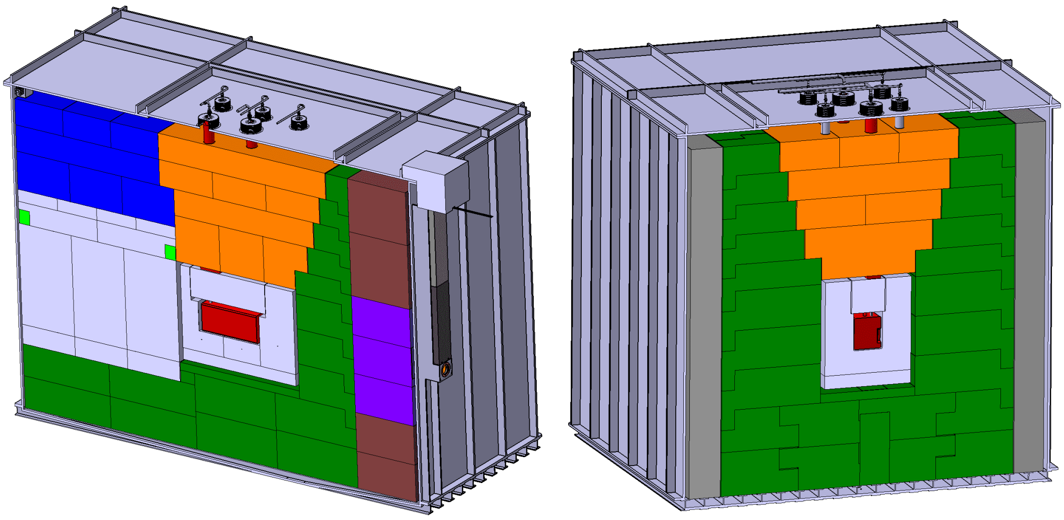

Fig. 6.88: Crane++ concept: vertical sections through the helium vessel with the mobile shielding (orange) installed above the proximity shielding.

Once the mobile shielding is removed, a shielded cask is lowered into position above the target. The target and the upper plug of the proximity shielding are then lifted, via a lifting attachment that interfaces with the top of the target service chimney in a similar way to the one used in the trolley concept (Figs. 6.59 and 6.60). As the target and the proximity shielding are lifted, the target enters the shielded transfer cask (Fig. 6.98). Further lifting of the target also lifts the shielded cask so that the target is shielded during transfer to the storage area and lowering of the target into a storage pit in the cool-down area (Figs. 6.99 and 6.100).

A series of remotely operated spreader beams (as used in the trolley concept—see Fig. 6.62) are used to lift the mobile shielding above the target and then the target itself. The steps involved in target removal are given in Table 6.6. The installation of a new target follows the same procedure in reverse.

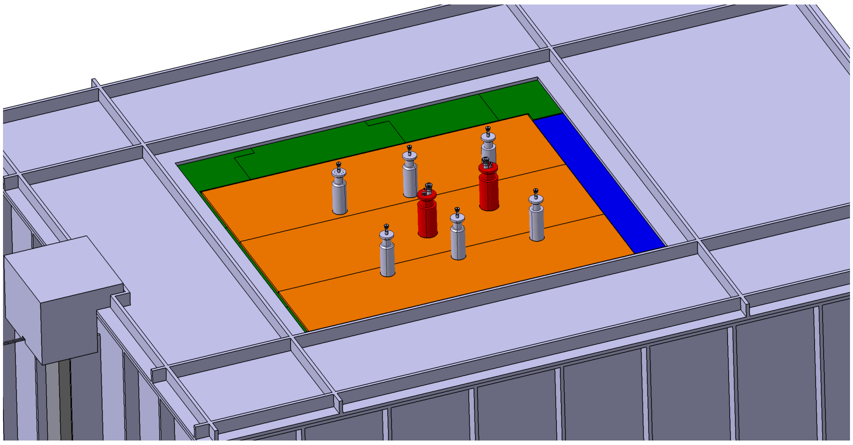

Fig. 6.89: Crane++ concept: view of the upper surface of the shielding in the helium vessel with the small lid removed, showing the tops of the service chimneys for the proximity shielding (in grey) and for the target (in red). The services for the proximity shielding plug above the target also pass through the target service chimneys.

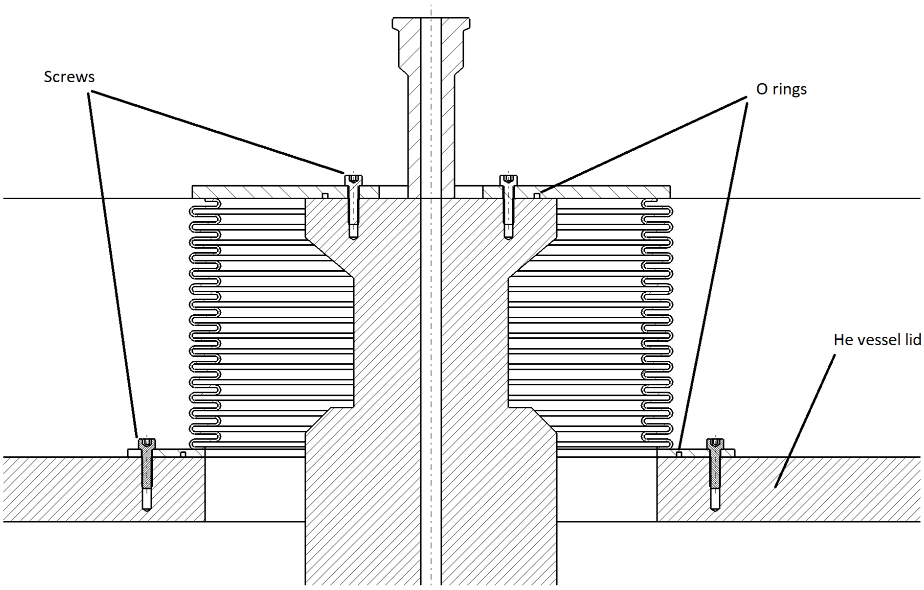

Fig. 6.90: Crane++ concept: service passages in the helium vessel lid. Sectional view illustrating outline concept for target water-cooling connections at the top of the service chimneys. A bellows unit is used to provide flexibility to adapt to misalignments (in XYZ+ tilt) of the service chimneys with respect to the He vessel lid and also to any movements of the lid due to pressure changes, etc.

The main steps involved in target removal for the crane++ concept are illustrated in Figs. 6.94–6.100.

6.2.9 Comparison of crane++ concept with crane and trolley concepts

Many elements of all three concepts are essentially the same, and so they do not influence any decision on the choice of concept, for example with respect to the beam window, collimator, magnetic coil, and US1010 shielding. It should be noted, however, that the approach in the crane++ concept of a service chimney design with connections accessible from outside the helium vessel could also be applied to the magnetic coil and collimator; this could improve availability owing to shorter fault diagnosis and repair times.

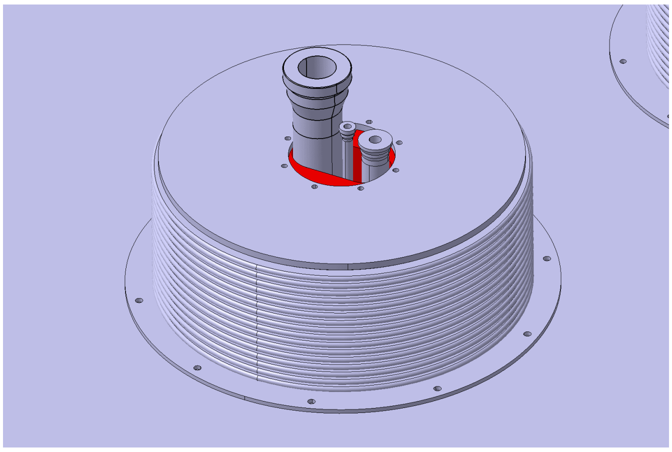

Fig. 6.91: Crane++ concept: service passages in the helium vessel lid. Close-up view of pipes coming out of target service chimney viewed from above the service vessel lid. Pipe clamps not shown. The large-diameter pipe is for target cooling; the smaller-diameter pipes are for cooling of the proximity shielding top plug and the helium supply to the target.

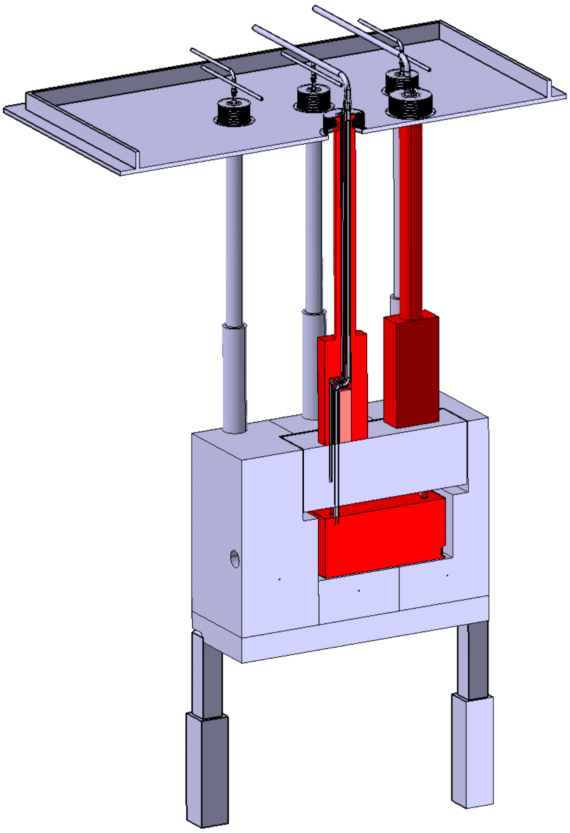

Fig. 6.92: Crane++ concept: service passages in the small helium vessel lid. Cutaway view of proximity shielding and target with service chimneys and small helium vessel lid.

To compare the crane++ concept with the other two concepts, the following elements related to operation and construction of the target complex were considered:

– target exchange;
– water and electrical connections;

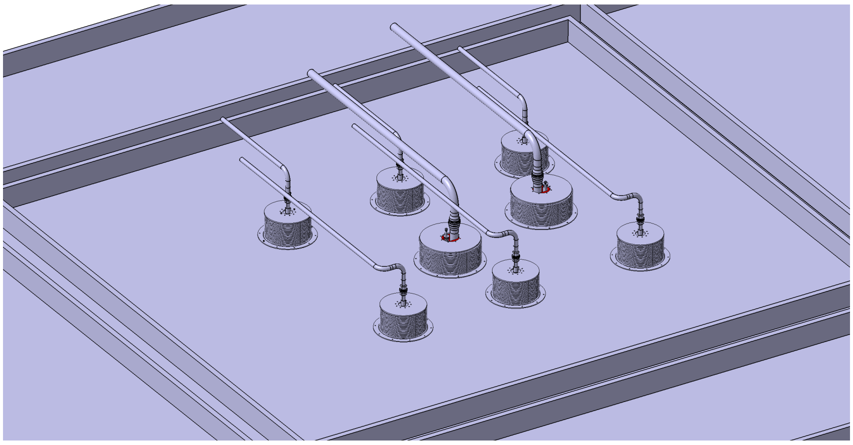

Fig. 6.93: Crane++ concept: service passages in the helium vessel lid. Isometric view of the main cooling pipes coming out of the target and proximity shielding service chimneys above the small helium vessel lid. Smaller cooling pipes for the proximity shielding top plug and helium pipes for the target are not shown.

Table 6.6: Steps for removal of target from the helium vessel and transfer to the cool-down area (crane++ concept).

Step	Task	Tooling
a	Disconnect water and electrical connections to target and proximity shielding upper plug	Hands-on operation, working on top of helium vessel
b	Open lid of helium vessel	Hands-on operation
c	Remove mobile shielding above target and transfer to cool-down area	Crane and remotely operated spreaders
d	Lower shielded transfer cask into position above target	Crane and remotely operated spreader
e	Lift out target with shielded transfer cask and transfer to cool-down area, placing target (and proximity shielding upper plug) in underground storage pit	Crane, remote lifting attachment, and shielded transfer cask

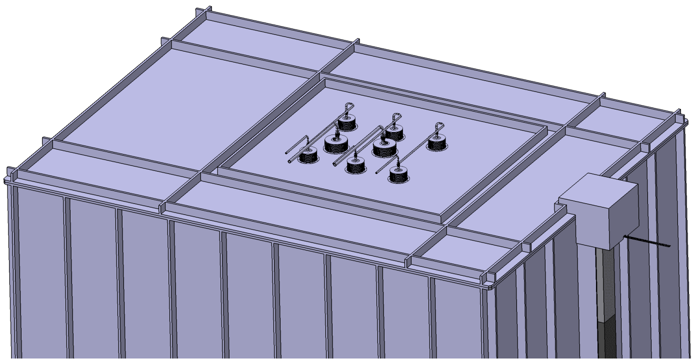

Fig. 6.94: Crane++ concept target exchange: isometric view of top of the helium vessel at the start of operations.

- helium vessel;
- shielding;
- design and development risks of the handling equipment;
- civil engineering;

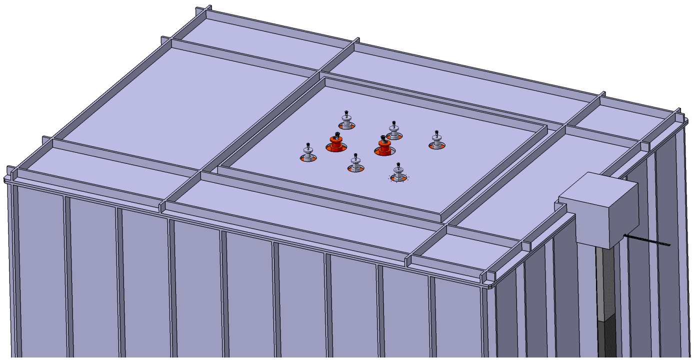

Fig. 6.95: Crane++ concept target exchange: pipework disconnected and removed. Note that this work is carried out 'hands-on' without the need for remote handling.

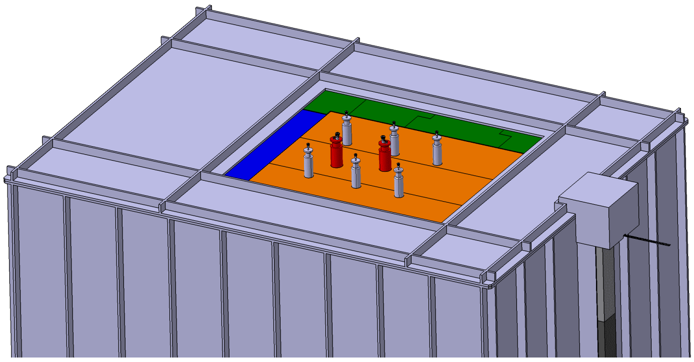

Fig. 6.96: Crane++ concept target exchange: small lid removed from helium vessel

– reconfiguration;
– decommissioning.

6.2.9.1 Target exchange

Target exchange in the crane++ concept is similar to that in the crane concept but has some key advantages:

– the water and electrical connections to the target and the upper plug of the proximity shielding are disconnected by hand;
– the shielded transfer cask does not need its own high-integrity hoist system.

6.2.9.2 Water and electrical connections

The major advantage of the crane++ concept is that the water and electrical connections are accessible for hands-on connection, disconnection, fault diagnosis, and repair. This can be expected to lead to higher reliability and availability of the facility along with lower construction and operation costs.

6.2.9.3 Helium vessel

As the water and electrical connections for the crane++ concept are accessible from outside the helium vessel, the risk of leaks and electrical problems requiring removal of the lid to repair them is minimized; there will therefore be less need to remove the whole helium vessel lid. This will reduce the number of times the helium has to be purified and reduce the risk of problems with the seals of the main and small lids.

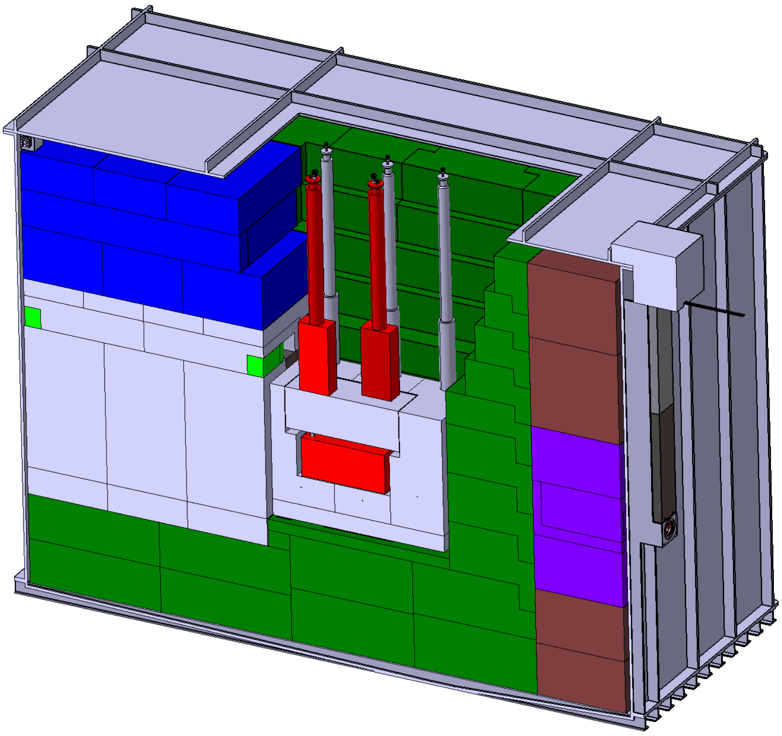

Fig. 6.97: Crane++ concept target exchange: mobile shielding above target removed. Note that this is carried out remotely.

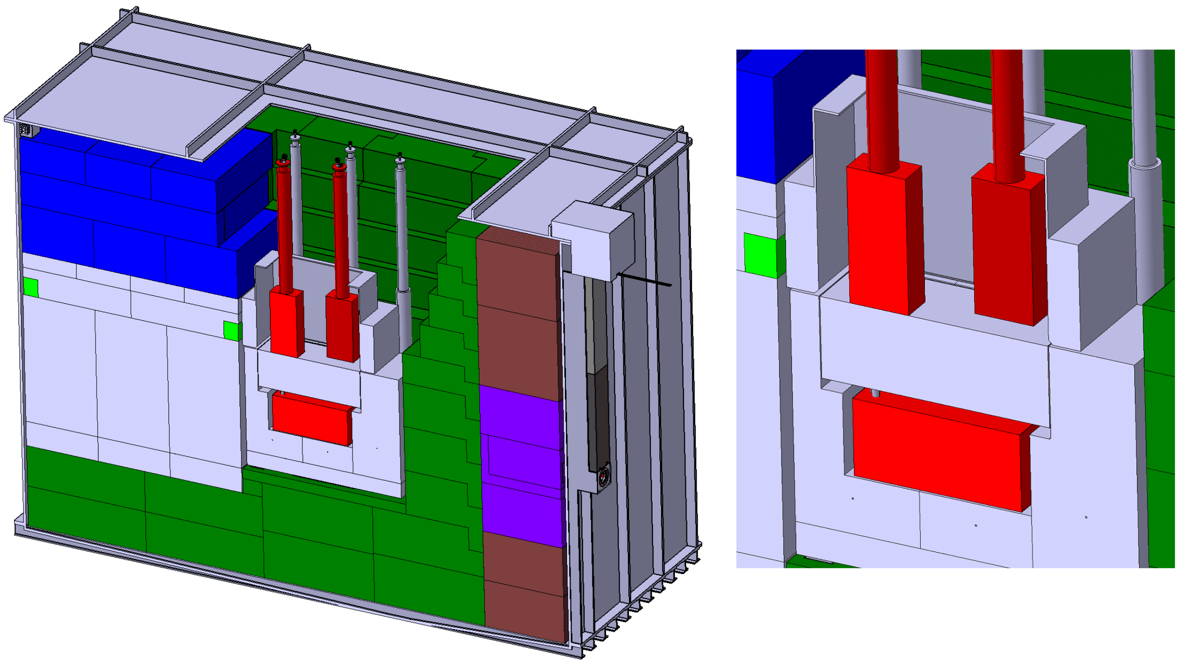

Fig. 6.98: Crane++ concept target exchange: shielded transfer cask lowered into position above target. Left: overview. Right: close-up of shielded transfer cask after being lowered into position over target, before the target is raised.

Not having the side door opening in the helium vessel wall that is needed for the trolley concept avoids the risk of leaks in or damage to the inflatable seal or sealing faces, which would need to be

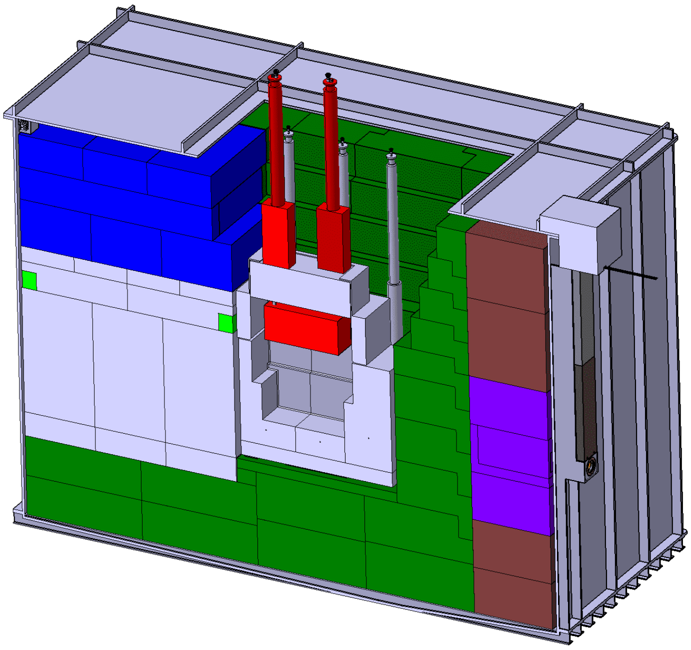

Fig. 6.99: Crane++ concept target exchange: target and proximity shielding plug lifted by the building crane in the target complex into shielded transfer cask.

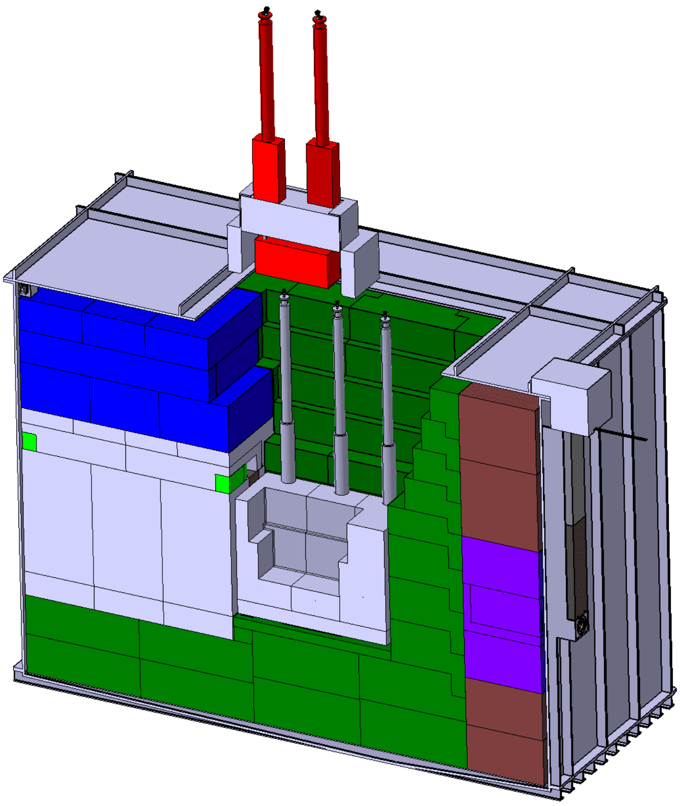

Fig. 6.100: Crane++ concept target exchange: further lifting of the target and shielding plug lifts the shielded transfer cask. The target is lifted out of the helium vessel inside the shielded transfer cask before transfer to the storage pit in the cool-down area (keeping close to the floor during transfer).

repaired via the trolley hot cell using remote handling techniques.

6.2.9.4 Shielding

The proximity shielding is very similar to that in the trolley concept, with the same sort of service chimneys. The mobile shielding above the proximity shielding is also similar to that in the trolley concept, with stepped openings for the service chimneys.

6.2.9.5 Handling-equipment design and development risks

The handling equipment is much simpler than for the crane concept, as there are no remotely operated (un)locking tools, remotely operated recovery tools, or mobile remote telemanipulator system to design and develop. The handling system is much simpler than for the trolley concept, as there are no trolley and trolley hot cell to design and develop. The remote handling area at the end of the cool-down area will be the same as for the crane and trolley concepts and will be used to disconnect beam window and coil services, as well as to disconnect the service chimneys from the target and proximity shielding for the crane++ concept before disposal.

6.2.9.6 Civil engineering

The civil engineering will be simpler than for the trolley concept, as there will be no need for the operating area and hot cell for the trolley. The civil engineering will be simpler than for the crane concept, as there will be no need for service galleries under the helium vessel.

6.2.9.7 Reconfiguration

The crane++ concept is more flexible than the trolley concept, as it does not have the restrictions on target size, weight, and cooling that are inherent in the trolley concept. Reconfiguration for the crane++ concept would be more flexible than for the crane concept, which has fixed service pillar positions and extensive remote tooling for connection operations, which are specific to the target vessel and proximity shielding designs for the crane concept.

6.2.9.8 Decommissioning

The crane++ concept offers the easiest decommissioning of all the concepts, as all radioactive parts inside the helium vessel can be easily lifted out (there is no need to cut out radioactive service pillars from the helium vessel and no need to dismantle radioactive parts at the front of the trolley). The dismantling of the service chimneys would be carried out in the cool-down remote handling area.

6.2.10 Further work: choice between crane, trolley, and crane++ concepts

At the current stage of development, the crane++ concept appears to offer a simpler, cheaper, and potentially more reliable (and hence offering higher availability) target complex design. It is therefore proposed to develop the design to a similar level of detail as that in the work already done for the other two concepts. If this does not show up any major weak points, then the crane++ concept will be used as the basis for the further work listed below.

6.2.11 Further work: integration of results of other studies

As increasingly detailed results from design studies on aspects of the target complex become available, the integration of the target complex will need to be updated (Fig. 6.101). Examples of the aspects concerned are:

– radiation protection;

– target and target container;
– helium vessel;
– magnetic coil and shielding;
– cooling and ventilation (including helium purification);
– access systems;
– general safety;
– electrical services;
– overhead travelling cranes.

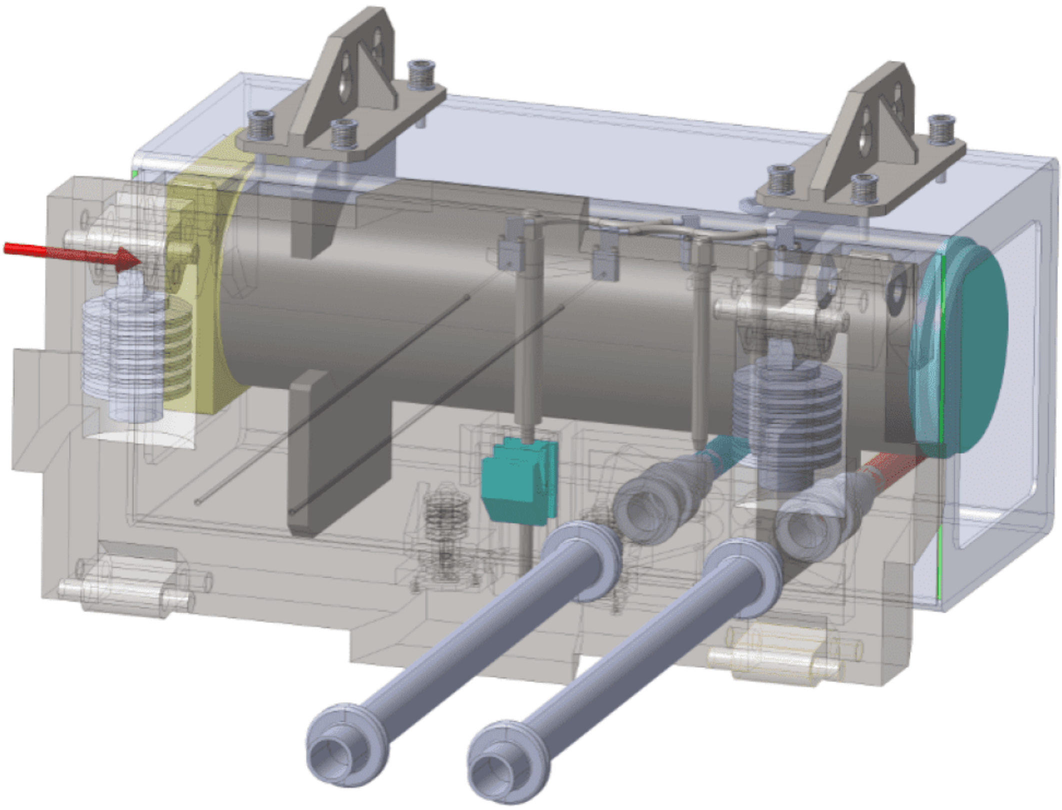

Fig. 6.101: Example of design work integrating the results of different studies: integration of BDF target core into target container (trolley concept container shown).

As explained above, it is expected that this next phase of integration work for the target complex will be based on the crane++ concept.

6.3 Hadron absorber and muon shield

One of the primary requirements of the SHiP experiment is to operate in an environment of extremely low background from ordinary physics processes. To meet this objective, the target system is immediately followed downstream by an important mass of shielding with several functionalities. Firstly, the shielding should absorb the electromagnetic radiation and hadrons emerging from the proton target. Secondly, SHiP employs a magnetic system, referred to as the *muon shield* [5], to deflect the large flux of muons emerging from the target away from the fiducial volume of the detector. The muon shield is designed to reduce the flux of muons by six orders of magnitude in the detector acceptance.

The shield includes a first set of magnets that deflect the positively and negatively charged muons to either side of the beam axis, irrespective of their initial direction. This allows creating a region around the beam line beyond this first set of magnets in which there are no charged particles. A second set of magnets which have their return field in this unoccupied region then provides further deflection. This configuration prevents muons deflected in the first section from being deflected back towards the detector by the return field in the second section.

Despite the aim of searching for particles with relatively long lifetimes, the sensitive volume of the SHiP experiment should be situated as close as possible to the proton target owing to the relatively large production angles. The length and the aperture of the magnetic system are minimized by applying the highest possible magnetic field as close as possible to where the muons are produced. It is very difficult technically to introduce a field across the target system and the proximity shielding, which makes up the first 0.8 m of the hadron absorber, and the field would interfere with the instrumentation of the target system. The rest of the absorber may, however, be magnetized with the help of a magnetic coil integrated into the shielding. The subsequent magnetic system downstream of the hadron absorber is composed of a set of free-standing magnets located inside the underground experimental hall. Their field configuration has been optimized using machine learning techniques. The separation between the magnetized volumes in the hadron absorber and in the first free-standing magnet is minimized by having a roughly 30 mm thick stainless steel window in the wall separating the target bunker from the experimental hall.

The overall physical dimensions of the hadron absorber are primarily driven by radiological considerations, as described in Section 6.7. Studies show that it is possible to almost entirely prevent radioactivation of the experimental area and its components with 5 m of iron shielding in total. The coil and the integration of the coil in the target shielding, however, are subject to several severe constraints related to radiation exposure (see Fig. 6.102), powering, heat extraction, and handling. As shown in Fig. 6.103, the preliminary design is based on a single set of coils which magnetizes the last 4 m of the hadron absorber after the proximity shielding. To reduce the radiation to the coil, it is located 1.30 m above the beam axis, which then also drives the requirement on the height of the volume that is magnetized. Two vertical non-magnetic stainless steel plates (shown in black in Fig. 6.103) ensure that the dipole field is correctly guided through the US1010 steel blocks making up the yoke. The design and layout of the US1010 blocks were optimized to ensure the minimum number of gaps seen by the magnetic field, while at the same time remaining compatible with the achievable precision in manufacturing and handling. Magnetic-field modelling of the whole assembly in Opera Vector Fields showed that a field of greater than 1.6 T can be achieved in the critical volume, as shown in Fig. 6.104. To deflect a sufficient fraction of the angular spread of the muon flux that would otherwise reach the detector acceptance, the width of the magnetized region must be around 1.60 m.

Initial calculations indicate that the thermal and electrical engineering of a coil of this size are manageable. An aluminium tape conductor is preferred for mass, radiation, and thermal reasons. The preliminary design considerations for the coil assembly are pursuing ideas for two different configurations, both of which are based on multiple coils powered and cooled independently to ensure redundancy (Fig. 6.105). The baseline consists of a single coil assembly, comprising several layers of coils stacked vertically and stretching the entire length of the volume to be magnetized. The second option comprises several coils located in a chain horizontally. The latter option has the advantage of reducing the mass of the individual coils and reducing the manufacturing complexity, but at the penalty of slightly reducing the integrated field. The impact on the routing of the services through the shielding and the helium vessel surrounding the entire shielding assembly is also under investigation.

The remote handling of the magnetic yoke blocks and the coil assembly, along with their connection and disconnection within the target complex, has been considered in the design study of the target complex handling and integration (Section 6.2.4.3).

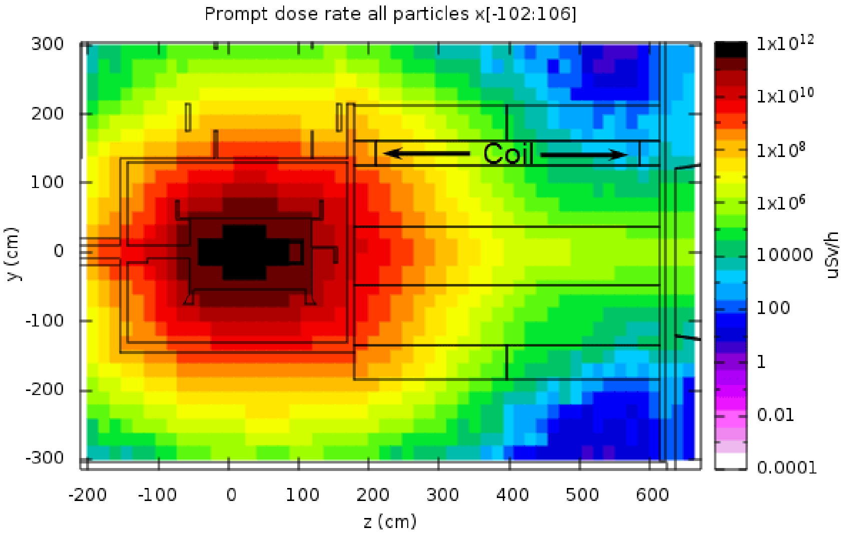

Fig. 6.102: Average annual radiation dose at coil height. The coil body will see an annual radiation dose of around 10^5 Gy at its closest point to the target, i.e. 0.1 MGy per year. At the location where the services arrive, the radiation dose is approximately 10^{-3} Gy/yr.

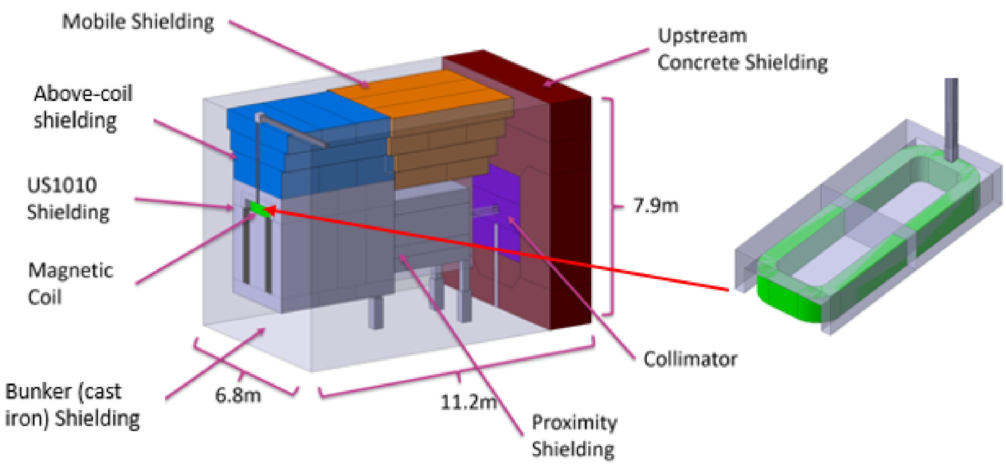

Fig. 6.103: View of the magnetized section of the target shielding with the yoke configuration and the coil. The coil is embedded in specially designed shielding blocks which restrain the coil during operation and which provide crane lifting points should an intervention be necessary. (Credits: V. Bayliss, J. Boehm, RAL (UK).)

6.4 Helium vessel containment

6.4.1 Introduction and requirements

The He vessel is an essential part of the BDF target complex, as it contains all beam-intercepting devices and shielding elements. Its role is to guarantee an inert atmosphere in the high-radiation area surrounding the spallation target, with the aim of reducing formation of short-lived air activation products and of NO_x, which could attack materials and produce radiation-accelerated corrosion.

The He vessel is designed to be slightly overpressurized with respect to the neighbouring areas to avoid entry of air into the vessel during operation. The following sections detail the design of the He vessel and the purification and circulation system.

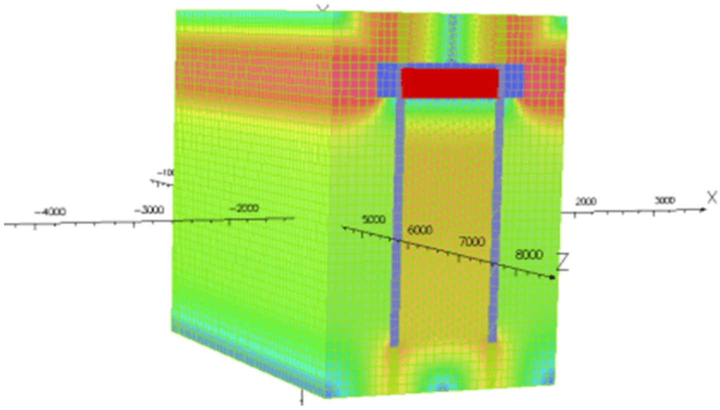

Fig. 6.104: Magnetic field in the magnetized volume of the hadron stopper. The coil is shown in red near the top of the shielding. (Credits: V. Bayliss, J. Boehm, RAL (UK).)

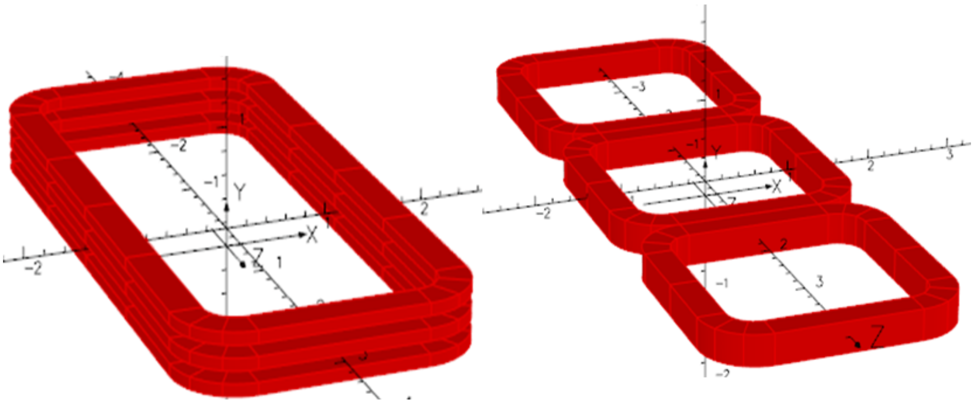

Fig. 6.105: The modular coil assemblies considered, with coils either stacked vertically (left) or aligned horizontally (right).

6.4.2 Design and preliminary structural assessment of He vessel

6.4.2.1 Design requirements

6.4.2.1.1 Dimensions and surrounding space

The minimum internal dimensions of the He vessel (the minimum available space for the target and its surrounding radio-protection shielding) will be 11330 mm × 8440 mm × 8275 mm high (approximately 790 m^3). The minimum space reserved for the mechanical structure will comply with the load resistance criteria described in Section 6.4.2.1.4. Adequate space will be reserved inside and outside the structure to allow assembly, testing, maintenance, and dismantling operations. A personnel access route (four persons maximum at the same time) will be reserved on the top surface of the structure to allow time-limited manual interventions outside the vessel during the operational phase when the beam is off.

6.4.2.1.2 Interface with civil engineering works

The He vessel will be installed in a rectangular pit of size approximately 12 000 mm × 9000 mm × 9000 mm deep. The mechanical structure will lie on the concrete floor without any other connections to civil engineering works. The interface between the mechanical structure and the concrete floor will be designed in compliance with civil engineering tolerances and the permissible floor load.

6.4.2.1.3 *Material constraints*

The choice of materials for the design of the He vessel will consider the following criteria: compliance with European construction codes (Eurocodes), resistance to corrosion, water and helium leak-tightness, respect of radiation protection rules, and cost.

6.4.2.1.4 *Load case*

The structure of the He vessel will be designed to withstand its own weight and an internal helium gas pressure of 0.1 barg (with a test pressure of up to 0.5 barg). The floor of the He vessel will be designed to withstand the weight of the target assembly and of its surrounding shielding (total weight approximately 5500 t, contact pressure approximately 60 t/m^2). The weight of four people working at the same time on the top surface of the structure will also be considered. The structure and what it contains will be designed to withstand a seismic action having a peak ground acceleration of 1.1 m/s^2. The He vessel will not be designed for internal vacuum.

6.4.2.1.5 *Lids and side window*

- *Top lid (large):* the entire top surface of the He vessel (11830 mm $\times$ 8940 mm) will be removable in one piece to allow installation, maintenance, and dismantling of internal components (the lid is expected to be opened once a year at most during the 5–10 yr lifetime of the experiment). The interface with the rest of the structure (the full perimeter of the lid) will be sealed according to the helium leak-lightness requirements described in Section 6.4.2.1.9. The seal will be put in place and removed manually, since the top of the He vessel will be personnel-accessible when the beam is off. Materials such as EPDM can be used as a sealing solution, as long as they are replaced at regular periods to avoid their becoming unsuitable owing to long-term exposure to radiation and loading.
- *Small lid (crane version only):* in the crane version, a smaller lid will be fitted in the top lid, to allow maintenance of the target assembly and its proximity shielding only. It is expected to be opened approximately three times a year during the 5–10 yr lifetime of the experiment. A similar solution to the one used for the top lid should ensure helium leak-tightness.
- *Side window (trolley version only):* in the trolley version, the maintenance of the target assembly will be done using an opening made in the side wall of the He vessel. Maintenance operations should occur a few times a year during the 5–10 yr lifetime of the experiment.

6.4.2.1.6 *Beam window*

The beam window will be mounted on the outside of the He vessel. The interface with the mechanical structure will be compatible with the remote handling installation and maintenance process, as well as provide leak-tight connection of the window.

6.4.2.1.7 *Service feedthroughs (water, gas, and electrical)*

Since the top part of the He vessel will be personnel-accessible once the shielding is in place, the service connections should preferably be routed to ports located in the upper part of the He vessel side walls, where feedthroughs can be permanently installed and where maintenance can be done without any consequence for the opening and closing of the lids and without removing the shielding blocks. The routing of the service connections for the target and its proximity shielding depends on the option which is chosen for handling (trolley or crane).

- *He vessel services:* Feedthroughs will be provided in the side wall of the tank for the connection to the helium purification system. They will be installed between the top level of the internal shielding and the main lid of the He vessel, to allow manual intervention.

– *Target services (crane version only):* water-cooling, helium gas, and electrical connections for the target will be supplied through pillars towards the floor, so the shielding can be removed without disconnecting the circuits.
– *Proximity shielding services:* for the trolley version, water-cooling feedthroughs will be provided in the side wall of the tank. They will also be installed between the top level of the internal shielding and the main lid of the He vessel. For the crane version, water cooling will be supplied through pillars towards the floor.
– *Coil services:* feedthroughs will be provided in the side wall of the tank for the supply and water cooling of the coil. They will also be installed above the top level of shielding and below the main lid of the He vessel.
– *Collimator services:* electrical feedthroughs will be provided in the side wall of the tank for connection of temperature sensors (Pt100).

6.4.2.1.8 Draining of water and helium

If a leak occurs in any of the cooling circuits contained in the He vessel, the coolant will be contained by the vessel itself and be drained by gravity through a dedicated circuit without any embedded components having to be removed. If leakage occurs outside the He vessel, the coolant will be collected by the drainage system designed by the civil engineering team.

6.4.2.1.9 Helium leak-tightness

All joints and components of the He vessel related to helium leak-tightness will be designed to comply with a maximum room temperature leak rate (both localized and global) of 0.1 mbar·l/s.

6.4.2.1.10 Temperature level

Every part of the He vessel will be designed to withstand a maximum temperature of 40 °C without any permanent damage or impact on the functional behaviour of the assembly.

6.4.2.1.11 Installation, maintenance, and dismantling

The design will allow the mounting of the He vessel inside the area within the constraints of space and access defined by the integration work. The design will be compatible with the transport of components of the He vessel within the handling capabilities (maximum weight and range) available. The design will be compliant with CERN safety regulations and radiation protection rules (ALARA) during installation, operation, maintenance, and dismantling.

6.4.2.2 Applicable norms and standards

6.4.2.2.1 Design according to Eurocode

The BDF He vessel, having a relatively low pressure of 0.1 barg, is not considered a pressure vessel within the scope of the Pressure Equipment Directive 2014/68/EU [6]. It will therefore be assessed as a steel structure to which Eurocode 3 applies. The structure has been classified as Level 2 in the following classes.

– Class of consequences (EN 1990 [7]), which is used for the purpose of reliability differentiation by considering the consequences of failure or malfunction of the structure. Class of consequences CC2 is applied when there are medium consequences for loss of human life and for economic, social, and environmental effects.
– Reliability class (EN 1990), which is associated with the class of consequences and has a direct impact on the reliability index β, on the multiplication factor $K_{\mathrm{FI}} = 1.0$ applied to the partial factors on actions, and on design supervision and inspections during execution.

– Execution class (EN 1090 [8]), which is related to quality of production in general, and to welding, bolting, riveting, and assembling of the structural members.

Eurocode 3 will be applied in the design of the structure together with the following relevant documents:

– EN 1993-1-1, for general rules and rules for buildings [9];
– EN 1993-1-5, for plated structural elements [10];
– EN 1993-1-6, for strength and stability of shell structures [11]; and
– EN 1993-1-8, for design of joints [12].

While there are good practices for choosing columns, beams and, joints, it is generally assumed that unconventional designs will be accepted by the Eurocode as long as it is proved that the design complies with the Ultimate Limit State (ULS) and Serviceability Limit State (SLS); see Section 6.4.2.2.2. All materials used will be considered in accordance with EN 1993 and EN 10025 [13]. At the time of writing this document, the material of choice is S235 steel for all columns and beams; its properties are in agreement with those listed in Table 6.7.

Table 6.7: Material properties considered for S235 in accordance with EN 10025

	f_y (N/mm^2)	f_u (N/mm^2)
S235	235	360

6.4.2.2.2 Assessment according to the Eurocode

The structure will be assessed against the ULS, which will guarantee structural integrity of the He vessel against all permanent, variable, and accidental actions. On the other hand, an assessment against the SLS will guarantee that the structure is fit for purpose. This last condition will limit the maximum displacements and the natural frequencies. Considering the STR limit state, which concerns the strength of the structure, the combination of actions may be expressed by using Eq. (6.10) of EN 1990, in which "+" means combination:

$$\sum_{j\geq 1} \gamma_{G,J} G_{k,j} \text{ " + " } \gamma_{Q,1} Q_{k,1} \text{ " + " } \sum_{i\geq 1} \gamma_{Q,i} \psi_{0,i} Q_{k,i} \,, \tag{6.1}$$

where

– $\gamma_{G,j}$ is taken from the EN 1990 French national annexe for design of structural members not involving geotechnical actions (STR) and corresponds to 1.35 for unfavourable actions and 1.0 for favourable actions;
– $G_{k,j}$ are the permanent actions of the self-weight (including the weight of the iron blocks inside the structure) and the internal pressure due to the helium;
– $\gamma_{Q,1}$ is also taken from the same national annexe and corresponds to 1.5 for an unfavourable action or 0 for a favourable one;
– $Q_{k,1}$ is the main variable action;
– $\gamma_{Q,i}$ is a factor for the remaining variable actions and is 1.5 or 0 in an unfavourable or favourable case, respectively;
– $\psi_{0,i}$ is a factor for buildings (Table A1.1 of EN 1990);
– $Q_{k,i}$ are the remaining variable actions.

Other variations of this equation suggested in the Eurocode will also be taken into account to find the least favourable combination. In the BDF He vessel, the permanent actions are the self-weight of the structural and non-structural members and the internal pressure, while the variable actions are the weight of four persons on the top of the roof. The only accidental action is an overpressure (1.5×), which will be applied as indicated in EN 1991-1-7:

$$\sum_{j\geq 1} G_{k,j} \text{ " + " } A_d \text{ " + " } \Psi_{1,1} Q_{k,i} \text{ " + " } \sum_{i\geq 1} \Psi_{2,i} Q_{k,i} \,. \tag{6.2}$$

The seismic assessment will be performed in accordance with EN 1998. As part of the ULS assessment, a non-linear buckling analysis will be performed by applying the nominal boundary conditions of the structure together with a deformation equivalent to the fabrication tolerances. This deformation will take the form of a scaled shape of the first mode obtained from a linear buckling analysis. The Eurocode does not consider such an analysis, and therefore the procedure followed will be according to the direct-route guidelines defined in the European code for pressure vessels EN 13445-3 [14].

6.4.2.2.3 Load cases

The actions imposed on the structure will be defined in accordance with Eurocode 1, specifically EN 1991-1-1 [15] (*Densities, Self-weight, Imposed Loads for Buildings*). Table 6.8 presents the different load cases and the actions that will be considered.

Table 6.8: Multipliers on actions to be considered for each load case

	Permanent actions		Variable actions	Accidental actions	Analysis		
Load cases/ actions	Self-weight	Pressure P	Weight of 4 people	Overpressure	Static	Modal	Buckling
			Serviceability limit state				
Nominal conditions	1	1	1	–	Yes	Yes	–
			Ultimate limit state				
Self-weight with roof	1.35	1.35	1.5	–	Yes	No	Yes
Self-weight without roof	1.35	–	–	–	Yes	No	Yes
Leak test	1.35	$1.35 \times P_{\text{test}}$	1	–	Yes	No	Yes
Assembly	1.35	–	–	–	Yes	No	Yes
Accidental	1	–	1.5	$1.5 \times P$	Yes	No	Yes
Seismic	1	1	–	–	Response spectrum analysis		

In the assembly load case, the joints between columns and beams will be assessed as cantilever load cases. These cases are expected to appear during assembly and are likely to be the most demanding load scenario for the joints. A fatigue assessment does not need to be performed, as the expected number of cycles is low. The roof lid will be open three times per year, so a maximum of four pressure cycles per year can be expected for a time frame of 15 yr, which amounts to a total of 60 cycles. While fire will not be assessed as an action, a risk analysis can be performed and prevention measures will be put in place as part of the installation of the equipment. Creep does not therefore need to be taken into account, as the temperature considered is only $40°$C.

6.4.2.3 Design principles

6.4.2.3.1 State of the art

The design work will be carried out in compliance with the acknowledged state of the art in the field of mechanical design. The rules issued by CERN for this type of activity as well as the applicable norms and standards (described in Section 6.4.2.2) will be respected.

6.4.2.3.2 Self-supporting structure

Since the He vessel cannot be in contact with civil engineering works except for the ground around the pit, the principle of a self-supporting structure will be applied in this case. This structure will be designed and built in compliance with the applicable norms and standards as described in Section 6.4.2.2.

6.4.2.3.3 Dismountable structure

Since the design will have to comply with CERN radiation protection rules, especially during the decommissioning phase, the principle of a dismountable structure will be applied in this case. For components to be assembled on-site, bolted connections will be preferred to welded joints. Welding operations done on-site (and therefore cutting on-site during dismantling operations) will be minimized, and the welded joints will be designed to be easily removed.

6.4.2.3.4 Transportable parts

To comply with transport and handling capabilities as well as space constraints in the Beam Dump Facility, every prefabricated component of the He vessel will have a maximum size of 6000 mm $\times$ 2000 mm $\times$ 500 mm and a maximum mass of 35 000 kg (the lifting capacity of the BDF crane). Some components will be assembled inside the facility near the pit (in a dedicated area) and therefore the size of the assembled elements may be greater than the value specified above, but the total mass of the assembly will not exceed 35 000 kg.

6.4.2.3.5 Separated functions

The two main functions of this mechanical structure are to guarantee structural resistance to the load case described in Section 6.4.2.1.4 and to ensure helium leak-tightness as described in Section 6.4.2.1.9. The design principle used in this case will be to separate these two functions, so that no structural element will be used to fulfil the leak-tightness requirement, and vice versa. This will, for example, minimize the mechanical stresses on components dedicated to leak-tightness.

6.4.2.3.6 Narrow or confined spaces

Since most of the structure will be assembled inside a pit, the design will be done in such a way that manual assembly, maintenance, and dismantling operations in narrow or confined spaces are minimized and can be performed in accordance with CERN safety standards.

6.4.2.3.7 Verification and testing

The design will be done in such a way that all quality, performance, and reliability checks (inspections or tests) can be carried out in accordance with CERN safety standards.

6.4.2.3.8 Cleaning

The design will be compatible with the application of an appropriate cleaning procedure to rid the tank (and, in particular, its internal components) of metallic and non-metallic particles that could be activated during beam operation.

6.4.2.4 Conceptual design

6.4.2.4.1 Concept

The basic concept will be to build a helium-tight envelope (the skin) surrounded by a support structure (the skeleton).

6.4.2.4.2 Self-supporting structure

– *Geometry and structural distribution:* the mechanical structure of the He vessel, as shown in Fig. 6.106, will consist of a floor whose main function will be to support the 5500 t of shielding for the target. On this floor will be fixed walls that will have the main mechanical functions of supporting their own weight, the weight of the top cover, the weight of equipment and of people who could be placed on it, and an internal pressure of 0.1 barg. The upper part of the He vessel will consist of a removable structure (lid) whose main mechanical functions will be to support its own weight, the weight of the equipment and of people who could be placed on it, and an internal pressure of 0.1 barg.
– *Material:* the support structure will be built mostly of structural steel (type S235) in standard profiles such as IPE400 and HEA240, as shown in Fig. 6.107. Welded structural parts will be made using Electrode, metal active gas (MAG), or TIG processes using filler metal E7018, S35, or ER7056, respectively. The material used for the bolts and nuts will be at least Steel 8.8. An adequate long-life surface treatment will be applied to profiles, welds, and bolts to minimize erosion–corrosion effects.
– *Total weight:* the total weight of the mechanical structure of the He vessel will be approximately 130 t, which is less than 3% of the total mass of the target assembly (target, internal shielding, and He vessel).

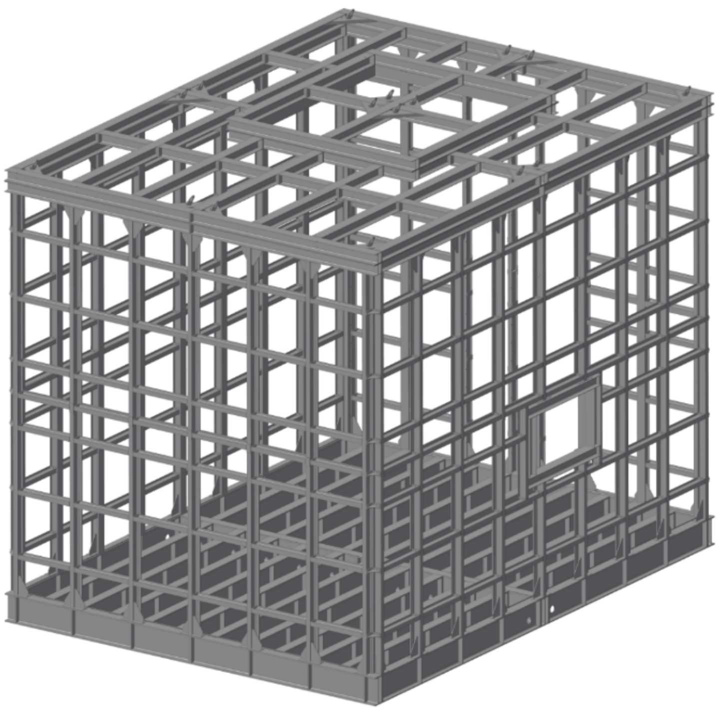

Fig. 6.106: He vessel support structure (skeleton)

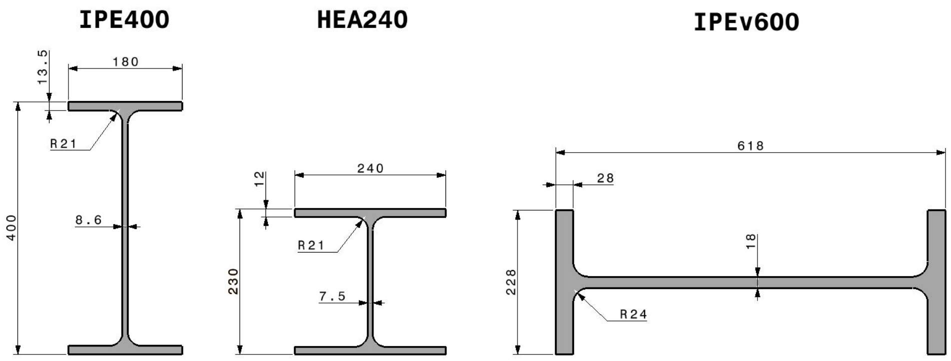

Fig. 6.107: Standard steel profiles used in the self-supporting structure

6.4.2.4.3 Floor

- *Geometry and structural distribution:* the floor structure will be made of reinforced IPEv600 profiles bolted together, as shown in Fig. 6.108. These components will be pre-assembled on-site (in a dedicated area) and then transported to the pit. The differences in flatness with respect to the concrete floor will be compensated by shims. Since the shims used will have a thickness of 1 mm and the flatness-monitoring system is expected to have a resolution of 1 mm, the flatness of the He vessel floor over its entire surface will be less than 10 mm, with local flatness differences of the order of a few millimetres. The use of IPEv600 profiles will provide the necessary space for the installation of supply services (such as the water drainage system) under the floor.
- *Water/air draining:* as shown in Fig. 6.109, the water drainage system will consist of stainless steel helium-tight retention containers (sloped), attached to the mechanical structure of the floor. Tightness between the containers will be ensured by stainless steel welded profiles that will cover the joints. The floor surface will then be covered with perforated stainless steel plates. The containers will be connected to the water drainage circuit, which can also be used for pushing air out by injection of helium from the top of the vessel.

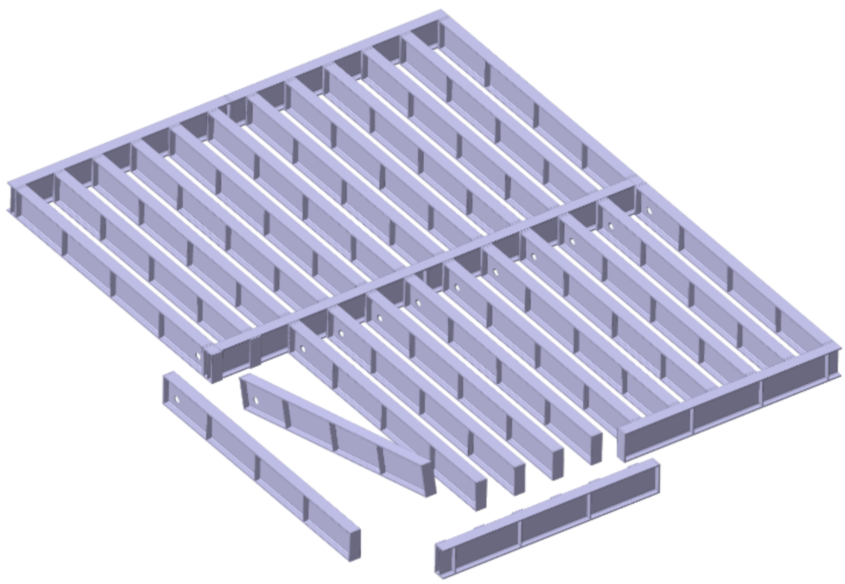

Fig. 6.108: Floor structure of He vessel

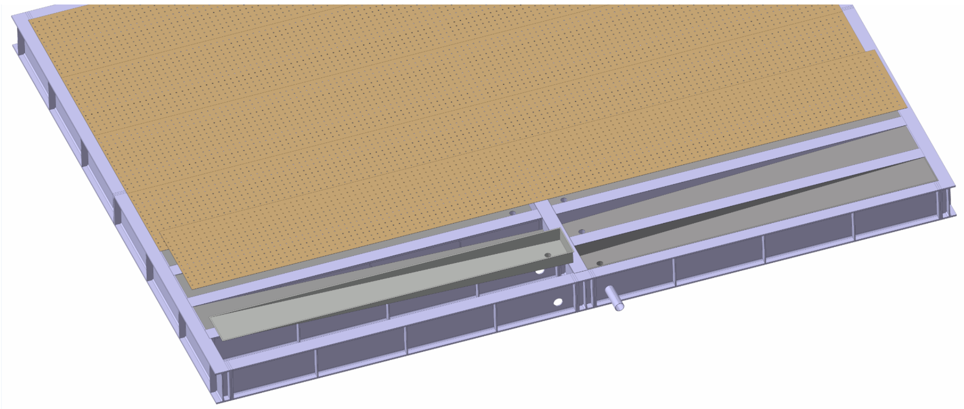

Fig. 6.109: Water and air drainage system of He vessel

6.4.2.4.4 *Helium leak-tightness*

- *Insulation:* Figs. 6.110 and 6.111 show how the helium-tight wall will be built using thin stainless steel panels bolted to the inside of the support structure. These panels will cover the inner surface of the He vessel. The joints and fasteners will be covered by stainless steel profiles that will be welded to the panels, to ensure the required leak-tightness. These profiles can be easily cut out to provide access to bolts during the dismantling phase.
- *Material:* the leak-tight envelope will be made out of thin plates of stainless steel (type EN 1.4306, thickness 2–4 mm). The material used for the bolts and nuts will be at least Steel 8.8. The filler used for the TIG welds of the insulation will be stainless steel 317LN (with no filler in the case of plasma welding).
- *Weld leak detection during construction phase:* each weld procedure will be qualified on samples. A strict follow-up on the production welds (operator, equipment, procedure, independent visual inspection, X-ray where possible) will be implemented. Samples will be produced again during the installation phase to verify that there is no deviation with respect to agreed quality. Multipass welds will be specified where possible to reduce the probability of leakage. Depending on geometry, intermediate leak tests will be specified.

6.4.2.4.5 *Lids and side window*

To comply with CERN radiation protection rules, the lids allowing access to the internal components of the helium tank will be held in position by bolted connections (welded connections will be excluded); see Fig. 6.112. The leak-tightness of the joints will be ensured by replaceable EPDM flat seals.

In the trolley version only, an opening (side window) will be built in the side wall of the He vessel (Fig. 6.113). This opening will be tightly closed using a movable door, which will be fixed to the trolley and closed by movement of the trolley. This opening/closing system will be compatible with the misalignment tolerance of the target ($\pm$10 mm in all directions) and with the maximum deformation in this area of the structure. EPDM-type seals will be used owing to the relatively low level of radiation in this location. Figure 6.114 illustrates the sealing solution for the trolley version.

6.4.2.4.6 *Prefabricated components*

The structure will be constructed from prefabricated elements (welded or bolted) composed of beams and panels that can be manufactured off-site and easily transported, with the objective of minimizing on-site assembly operations; see Fig. 6.115.

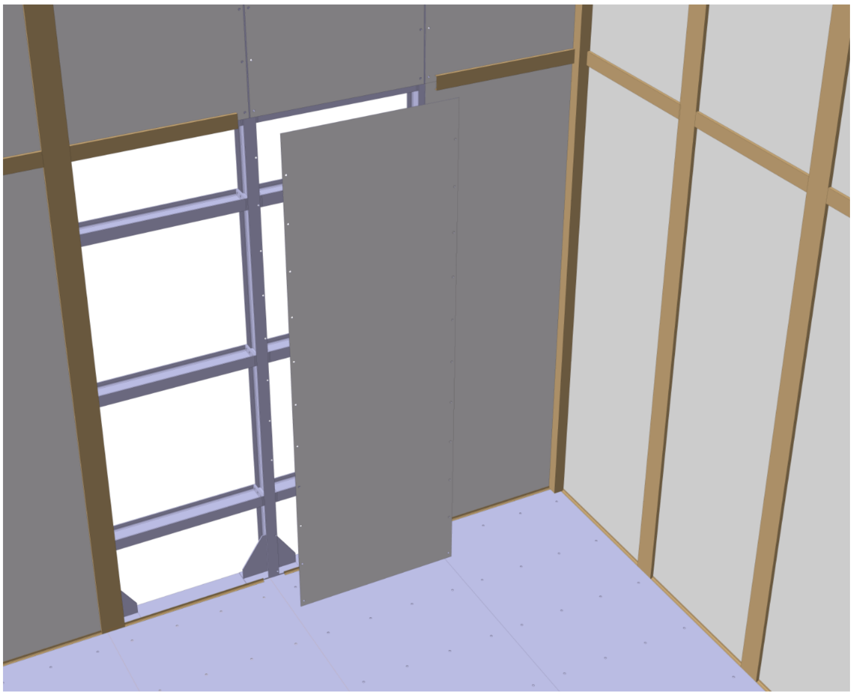

Fig. 6.110: Helium-tight walls (skin)

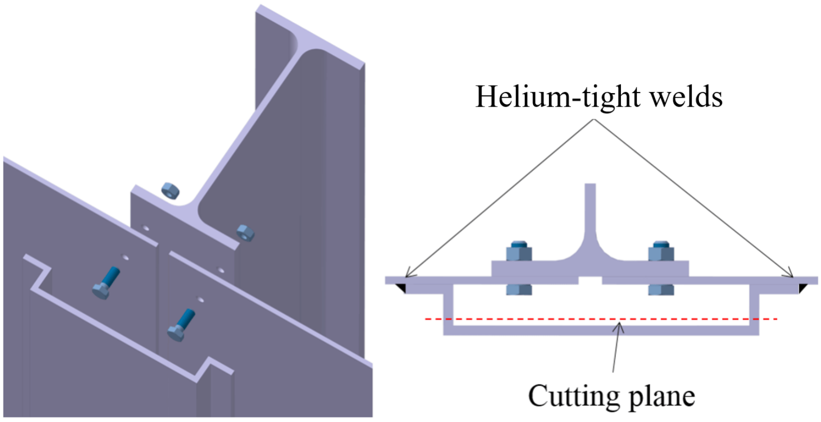

Fig. 6.111: Helium leak-tightness at joints

6.4.2.4.7 Beam window

A sliding system is located at the front of the structure, as shown in Fig. 6.116. It allows precise positioning of the beam window and its fixation on the structure (by remote handling). The slide is also used as a guide for the precise positioning of the shielding elements.

6.4.2.4.8 Interfaces

Standard interface modules will be bolted to the He vessel support structure (Fig. 6.117). These modules will contain fluid and electrical distribution systems (connectors, pumps, valves, etc.). Openings will be made in the helium-tight panels to allow services to be supplied inside the vessel. The use of flexible feedthroughs will minimize the transmission of mechanical stresses in the walls.

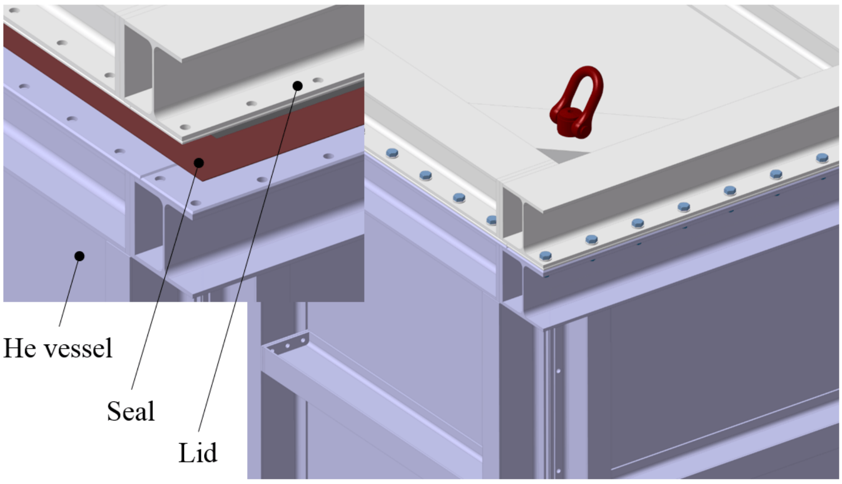

Fig. 6.112: Lid in open and closed positions, using bolted connections and EPDM seal

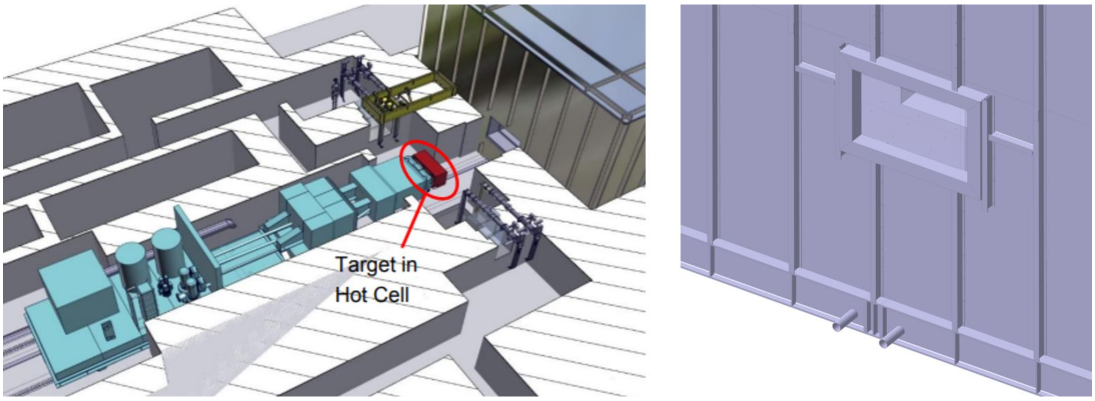

Fig. 6.113: Principle of opening and closing of side window for trolley concept

6.4.2.5 Structural assessment

The structural assessment of the He vessel will be performed using finite element methods. To model the structure, shell elements will be used for the beam webs and horizontal flanges and for the helium-tight plates. The joints will be assessed for their worst-case scenario (many of the joints will be similar, and there will be no need to assess all cases) using a submodel that is discretized with solid elements and details the welds and the bolt interfaces. The displacement fields (u, v, w, r_x, r_y, r_z) will be introduced at the boundaries of the submodels. While this approach is reliable for assessing the structural integrity of the He vessel, it is also computationally intensive and therefore will only be deployed once the geometry of the skeleton has been fully iterated. For the preliminary iterations, much simpler models will be used which discretize the geometries into shells and beam elements. Such modelling, even though simplified, allows fast comparison between two models and may be useful again in the future to quickly check the resistance and deformation of the structure in different load cases. In the following subsections, preliminary results for the He vessel and, in particular, the roof and the floor are presented for the SLS (nominal working conditions).

6.4.2.5.1 Self-weight analysis of roof

As the roof is joined by one perimeter edge of bolted connections, it can be considered as a pinned connection in a conservative fashion. The roof of the vessel is to be removed once per year and contains a lid which is to be removed three times per year, which justifies the bolted connections at both interfaces.

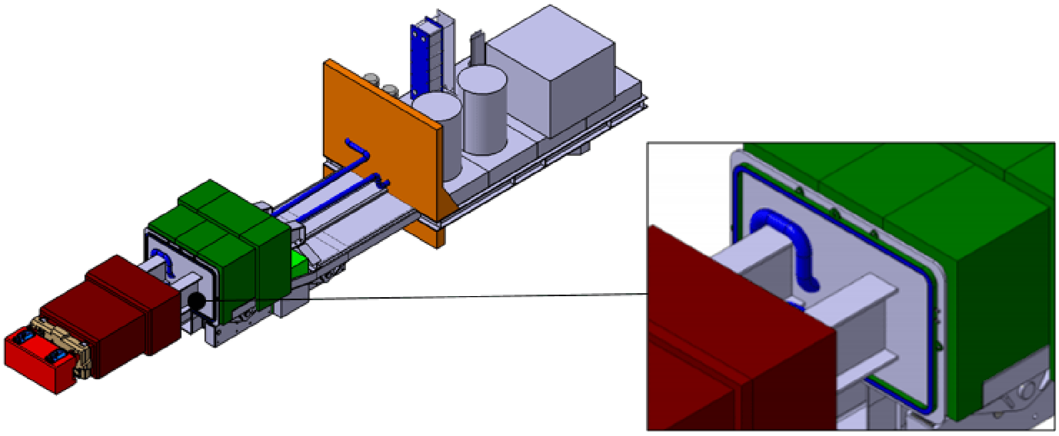

Fig. 6.114: Movable door and sealing solution for the trolley version of the BDF target

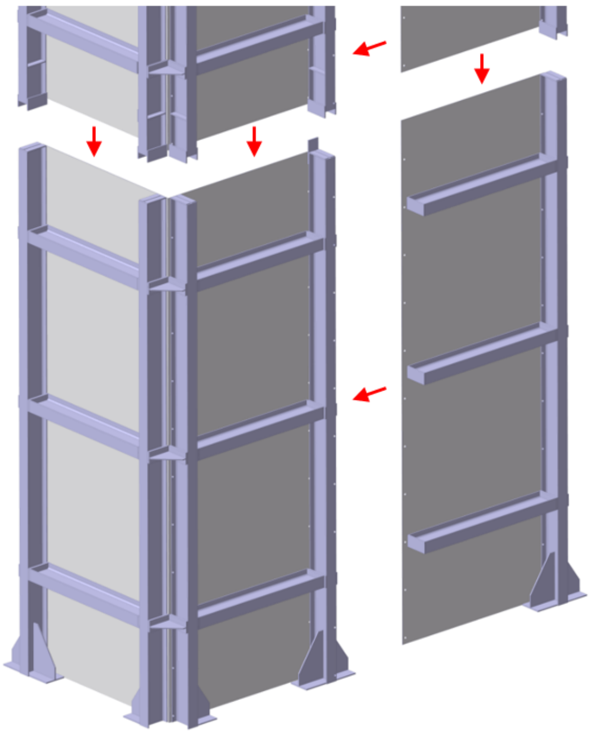

Fig. 6.115: Sketch of assembly of prefabricated components of He vessel

Using a simplified model made of beam elements and shell elements, as shown in Fig. 6.118, containing only 14 000 nodes, the distribution of roof beams was quickly optimized. Figure 6.119 shows the evolution of the configuration.

6.4.2.5.2 He vessel under internal pressure

The He vessel was modelled against internal pressure and self-weight. Using a simplified discretization, with only shell and beam elements, the model includes a total of 25 000 nodes, as shown in Fig. 6.120. With this model, it was possible to quickly evaluate the reaction forces in the joints, the impact of self-weight on the beams (compression/buckling), and the impact of internal pressure on the deflection of the beams and columns. Figure 6.121 shows an estimation of the deflection due to these loads on the beams.

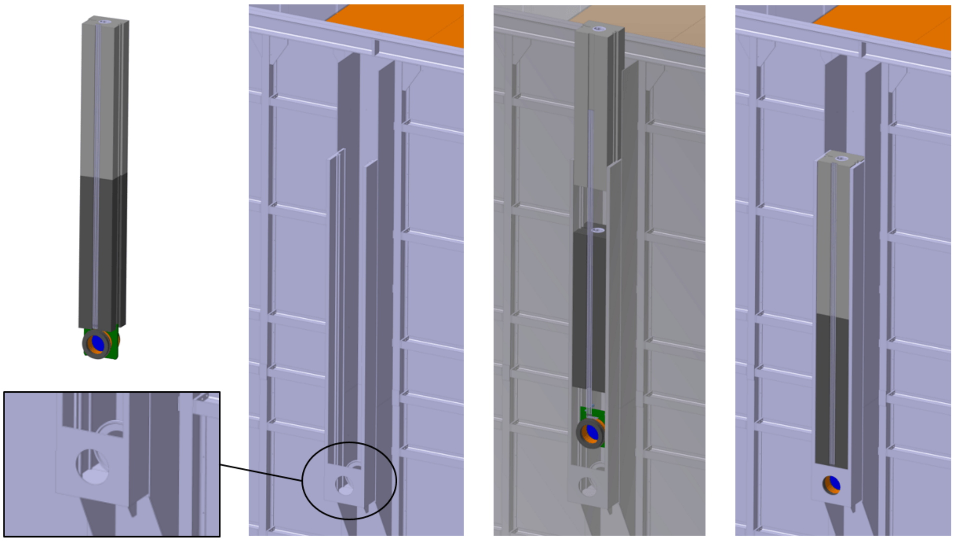

Fig. 6.116: Assembly of beam window of He vessel

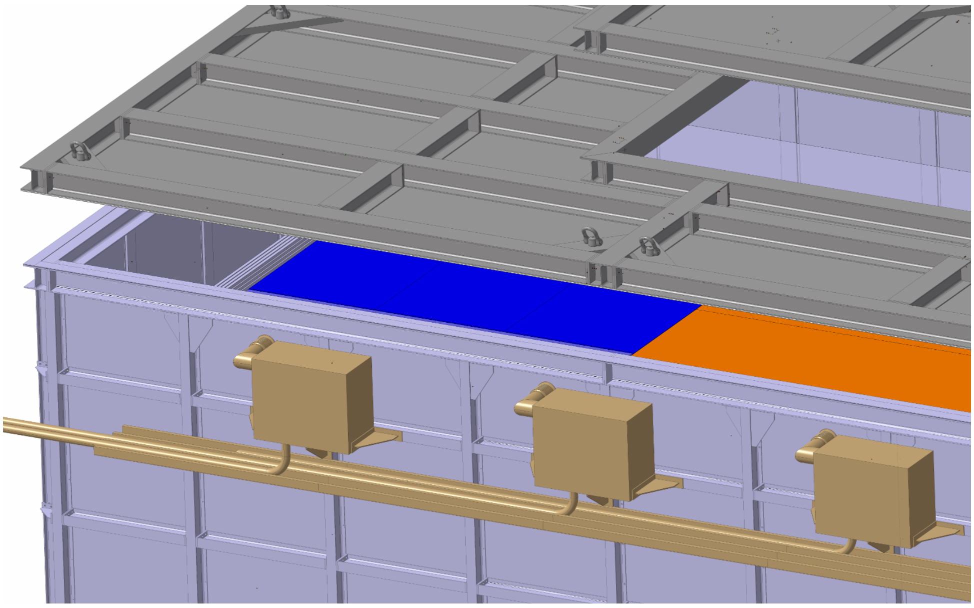

Fig. 6.117: Standard interface modules and feedthroughs

6.4.2.5.3 Weight acting on the lower beams

The equivalent weight of the iron blocks inside the vessel amounts to 5500 t, acting on the lower beams. Using shell elements to model the flanges and webs of the beams, an estimation of the stress involved in supporting this weight was obtained. A maximum stress of 42 MPa is expected, which is quite low compared with the yield strength of S235 steel (Fig. 6.122).

6.4.3 CFD analysis of He vessel system

6.4.3.1 Purpose

CFD simulations for the helium vessel have been run in support of the helium vessel design effort. The purpose of these simulations was to confirm that the helium will circulate properly in the helium vessel, and that the following general constraints are met.

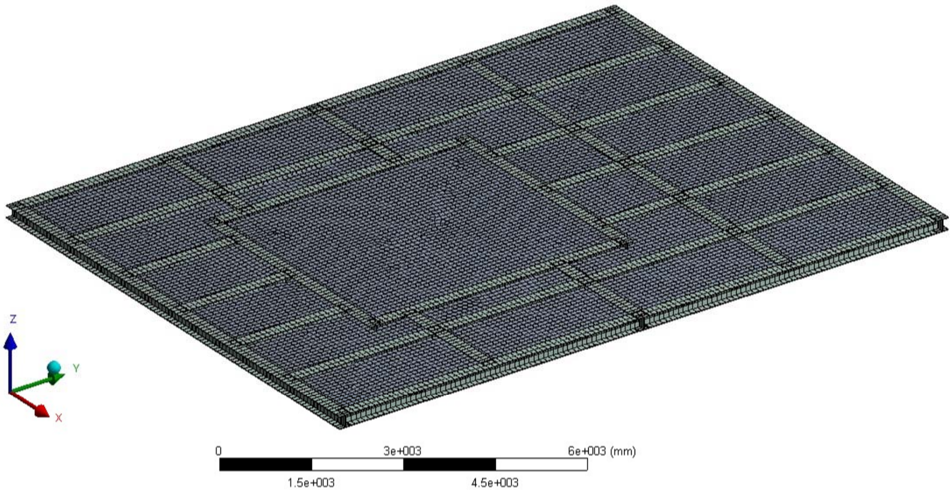

Fig. 6.118: Mesh representation of He vessel roof. The model has 14 000 nodes.

- During start-up of the helium passivation system, the formation of air pockets should be prevented so that the air-to-helium replacement procedure happens smoothly. This constraint will help to minimize the amount of pure helium lost to the atmosphere during flushing of the air–helium mixture; it will also minimize the overhead on the helium purification system during the purification phase of the start-up procedure.
- During operation of the helium passivation system, stagnation areas in the helium flow should be minimized. This constraint will help to minimize the amount of impurities remaining in the helium vessel (not treated by the helium purification system), thus reducing the potential activation of the gas mixture.

Because of the size of the problem to be solved and the characteristics of the mesh, the transient version of the problem turns out to be more challenging than the steady-state version. For this reason, the steady-state circulation of the helium was treated first, and is presented in this report before the time-dependent version, in opposition to what will be the chronological order of the operations (flushing first, then circulation).

6.4.3.2 Scope

The simulation of the helium circulation in the helium vessel is one aspect of the design of the helium passivation system [16, 17, 18] that will be operated in the BDF target complex. This helium passivation system will supply purified helium to the helium vessel that contains the BDF target and its shielding, and its primary purpose is to remove impurities from the gas mixture in the helium vessel. Helium provides a low level of activation by radiation from the primary beam; combined with the purification capability of the passivation system, this results in minimal activation of the gas mixture contained in the helium vessel. Moreover, a pure helium atmosphere will help protect the materials from oxidation, thereby increasing the lifetime of the components contained in the helium vessel. The helium is supplied at the top of the helium vessel and is collected from a location at the bottom; further details of the layout and components are provided in Ref. 6.4.3.3. In the start-up mode, pure helium from cylinders is injected and helium–air mixture is extracted from the system and vented to the atmosphere, until the

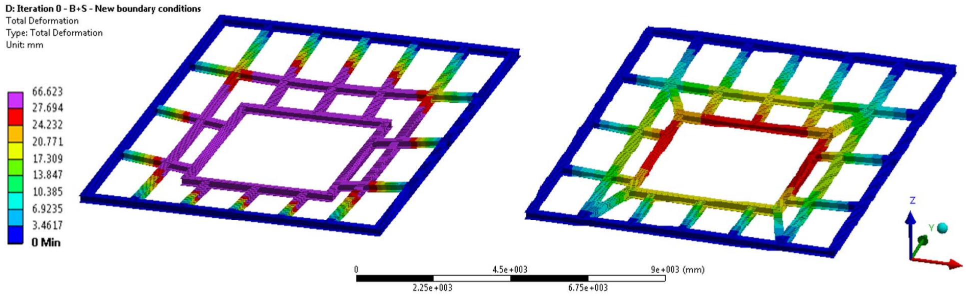

Fig. 6.119: Expected deflection of roof when placed on the He vessel with no internal pressure. Shells have been hidden from the image for better visualization. The left image represents the first model, and the right one the second iteration of it. There is a clear evolution between the two models.

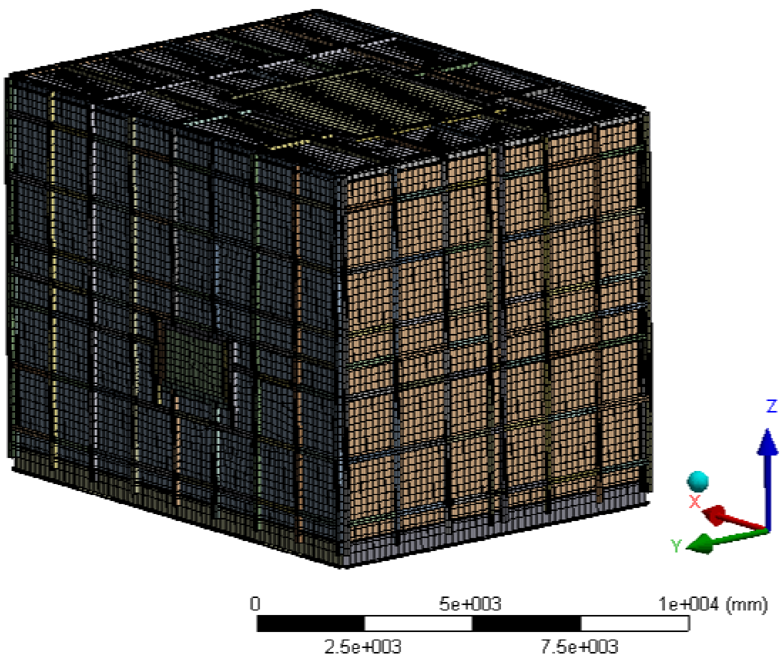

Fig. 6.120: Model of He vessel using shell and beam elements. The model contains 25 000 nodes.

helium purity reaches about 85%vol. At this point, the flushing is interrupted and the helium passivation system begins to purify the mixture by recirculating it through the vessel. During operation, whenever the purity decreases below a given threshold, the purification system will be turned on and purify the mixture to the desired level. In this context, an optimal flow distribution as described in 6.4.3.1 is desired.

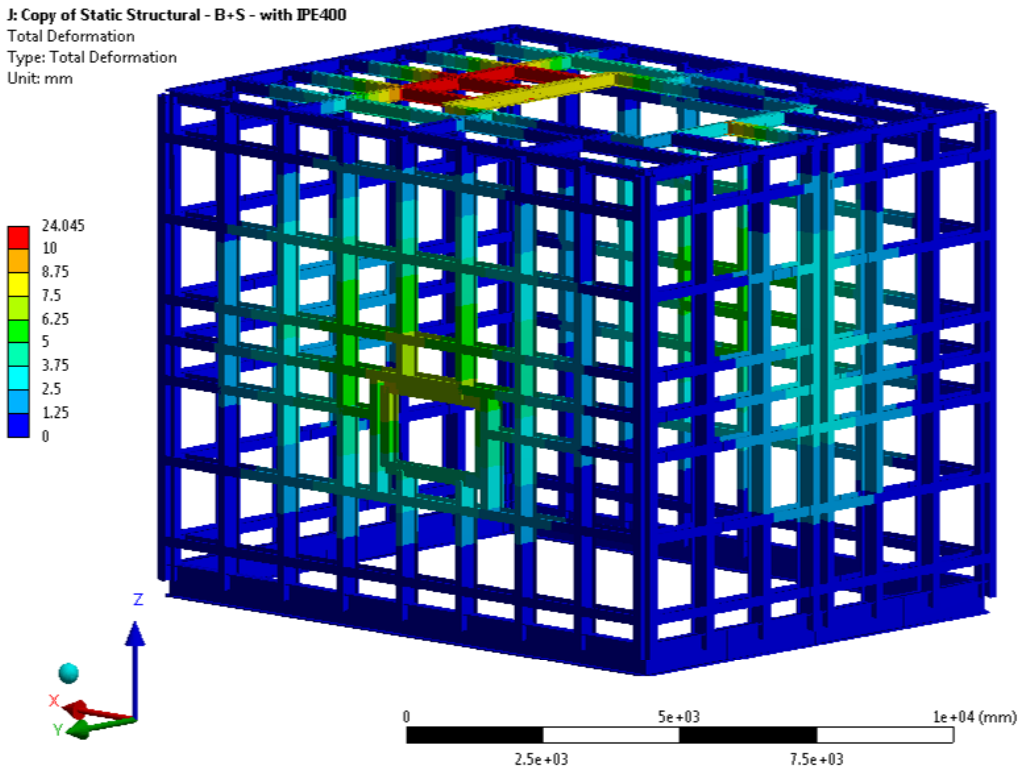

Fig. 6.121: Deflections of He vessel due to internal pressure. Shell elements representing the leak-tight envelope have been hidden for better visualization.

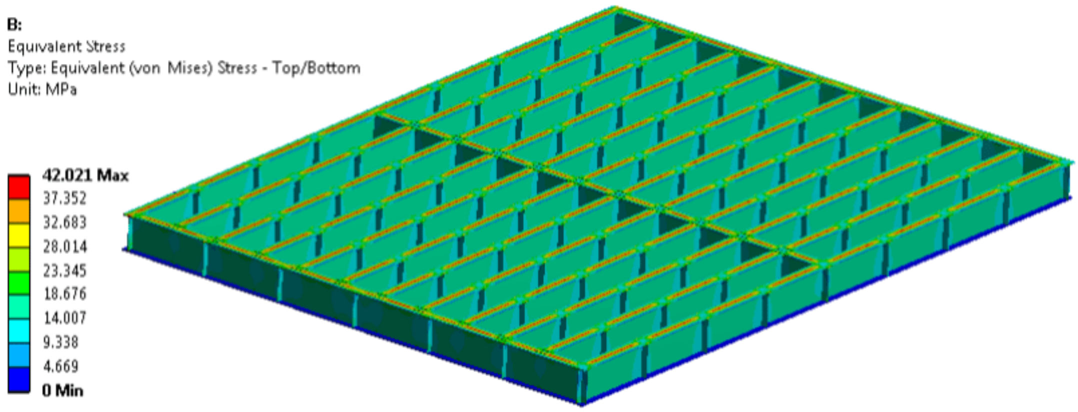

Fig. 6.122: Stress distribution in the lower beams

Section 6.4.3.3 presents the 3D model used for the simulation and a summary of the simulation set-up, while Sections 6.4.3.5 and 6.4.3.6 describe the steady-state and transient simulations, respectively.

6.4.3.3 3D model

The 3D model used for the CFD simulations was generated in SpaceClaim [19], starting from a model developed in Catia V5 by Oxford Technologies Ltd for CERN [1]. The initial model was partially cleaned up to remove components that were not relevant for the CFD simulations; also, some of the remaining components were simplified to ease the solution process. Figure 6.123 shows a view of the helium vessel after clean-up of the model. A series of ribs supports the steel containment on each face. For the purpose of this simulation, the lid was provided with six cylindrical penetrations (70 mm each) that represented the helium supply and distribution system. Similarly, the outlet was represented by three cylindrical penetrations, shown at the bottom left corner in Fig. 6.123. Figure 6.123 also shows the penetration and the door for the trolley that supports the target and allows its insertion and extraction from the helium vessel [1].

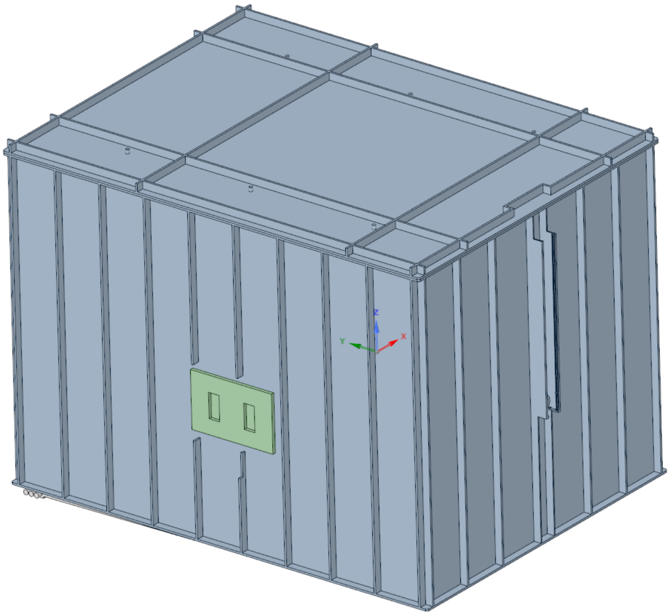

Fig. 6.123: 3D model of the helium vessel employed in the CFD studies

The final design of the helium vessel will likely have one single inlet penetration for the helium flow, positioned on one of the side walls of the structure, to minimize penetrations through the helium vessel. This is expected not to affect the conclusions of the CFD analysis, since the flow is mainly determined by the layout of the shielding blocks and the gaps between them.

Figure 6.124 shows a slice of the helium vessel in a vertical plane passing through the beam axis; the target is visible in red at the centre of the figure. Figure 6.124 also shows the following components:

– the collimator assembly components (pink);
– the concrete shielding of the collimator (grey);
– the proximity shielding (blue);
– the coil assembly blocks (blue);
– the bunker blocks (blue);
– the magnetic coil (red).

Figure 6.124 also gives an idea of the free volume available in the helium vessel. To facilitate the modelling, all gaps between blocks (except for those thicker than 10 mm) have been eliminated here; they will be generated again during the inflation phase of the meshing process. The resulting remaining free volume was extracted and is shown in Fig. 6.125.

6.4.3.4 Meshing

The size of the model and the presence of a high number of thin volumes make the meshing process relatively challenging. The mesh was developed using Fluent Meshing, using the following approach.

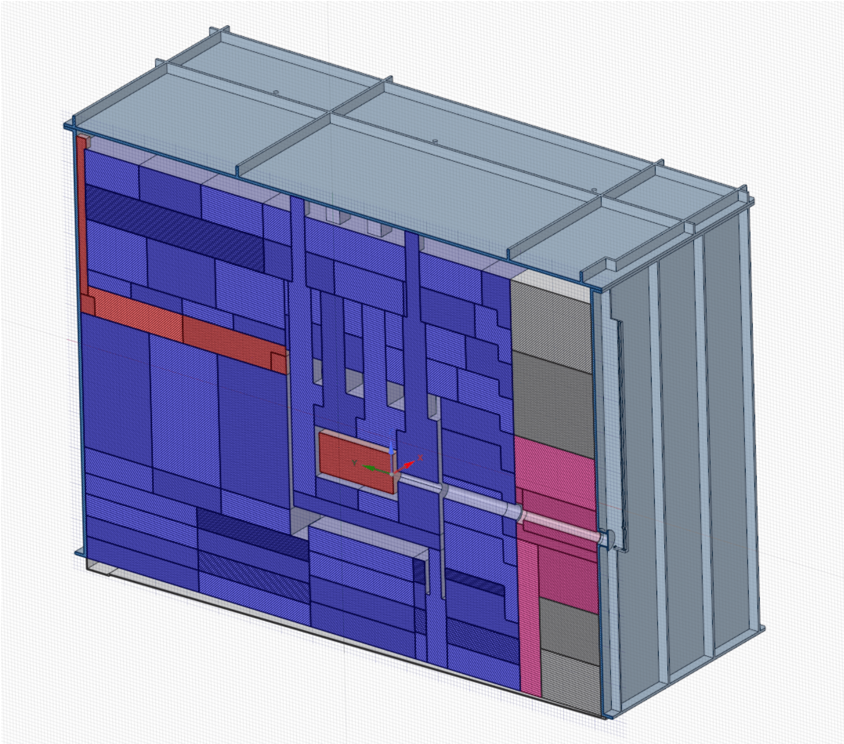

Fig. 6.124: Vertical slice of helium vessel model in a plane normal to the trolley insertion/extraction line.

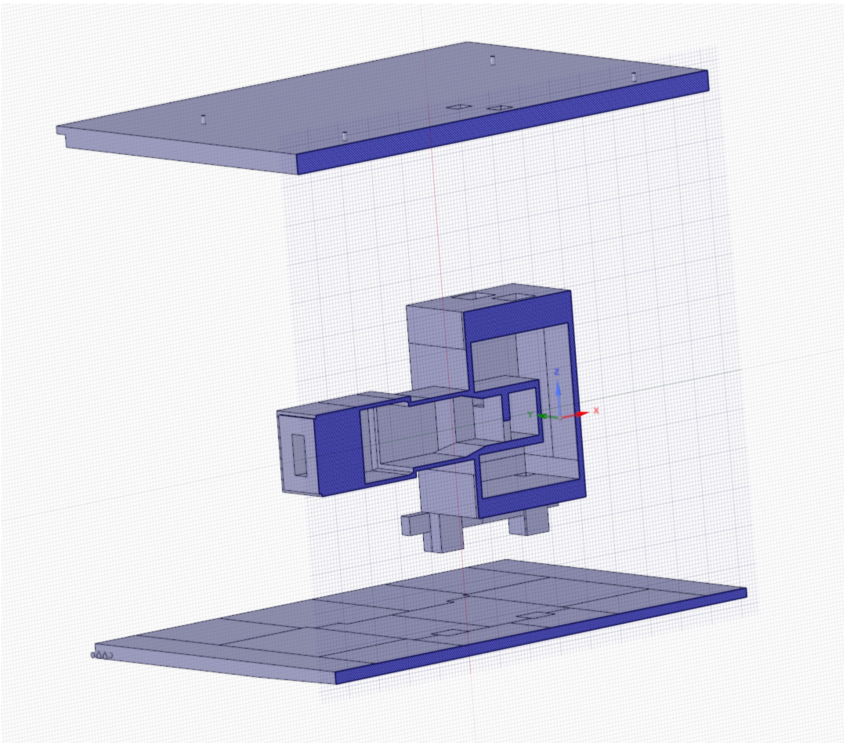

Fig. 6.125: Slice of the free volume in a plane normal to the beam axis crossing the centre of the BDF target.

– *Step 1.* The SpaceClaim model (6.4.3.3) is imported into Fluent Meshing using the CFD surface mesh option and the parameters listed in Table 6.9. This option produces a fully connected and conformal mesh based on an automatic size function.

– *Step 2.* Volumetric regions are computed, and a first scoped prism layer is defined according to the parameters in Table 6.10. With this prism growth configuration, each face grows two layers on both sides, for a total of four layers and a 10 mm gap thickness. Note that this mesh is based on the assumption that the gap between blocks is 10 mm for all gaps in the model.
– *Step 3.* A preliminary volume mesh with prisms is computed using the auto-fill-volume option. This step is performed with the aid of a journal file that, for each volume, grows the prism layer according to the definition of step 2 and fills it with tetrahedra. This process requires several hours to fill all 197 volumes in the model. At the end of the process, unutilized tetrahedral cell zones (corresponding to solid blocks) are deleted and the remaining volumes are merged to create a single fluid cell zone. Note that this is the step in which the gaps between blocks are created.
– *Step 4.* Two prism layers are grown on each face by morphing the existing mesh, thus resulting in a total of eight transverse cells per gap. The thicknesses of the two layers are 1 mm for the first and 1.5 mm for the second. The purpose of these two additional layers is to improve the velocity profile near the walls and enhance convergence. The mesh is now ready for final clean-up, transfer to solution mode, and conversion to polyhedra.

Table 6.9: CFD surface mesh parameters for He vessel

Parameter	Value	Units
Minimum size	25	mm
Maximum size	80	mm
Growth rate	1.2	–

Table 6.10: CFD prism definition parameters for He vessel

Parameter	Value	Units
Type	Uniform	–
First-layer thickness	2.5	mm
Number of layers	2	–
Maximum thickness	5	mm
Growth rate	1	–

Figure 6.126 shows the polyhedral mesh resulting from the meshing process. Table 6.11 presents the main parameters, statistics, and size of the mesh. Figure 6.127 shows a slice of the mesh in the area between the collimator and the target.

Table 6.11: Statistics of CFD mesh for He vessel

Parameter	Value	Units
Size	6 782 628	Cells
Allocated memory	10 982	Mbyte
Total volume	74.5	m^3
Minimum orthogonal quality	3.34	%
Maximum aspect ratio	328	–
Mesh check	Passed	–

The main contribution to the mesh size is made by the thin cells in the gaps between blocks. Figure 6.127 shows the distribution of gaps in a vertical slice passing through the beam axis and gives an idea of the number of gaps present in the model. Figure 6.128 shows a detail of the mesh in some

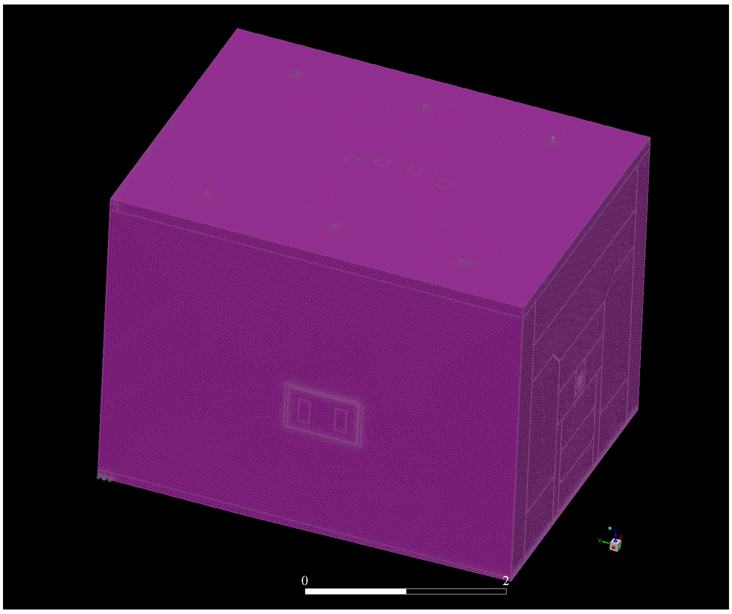

Fig. 6.126: Overview of polyhedral mesh

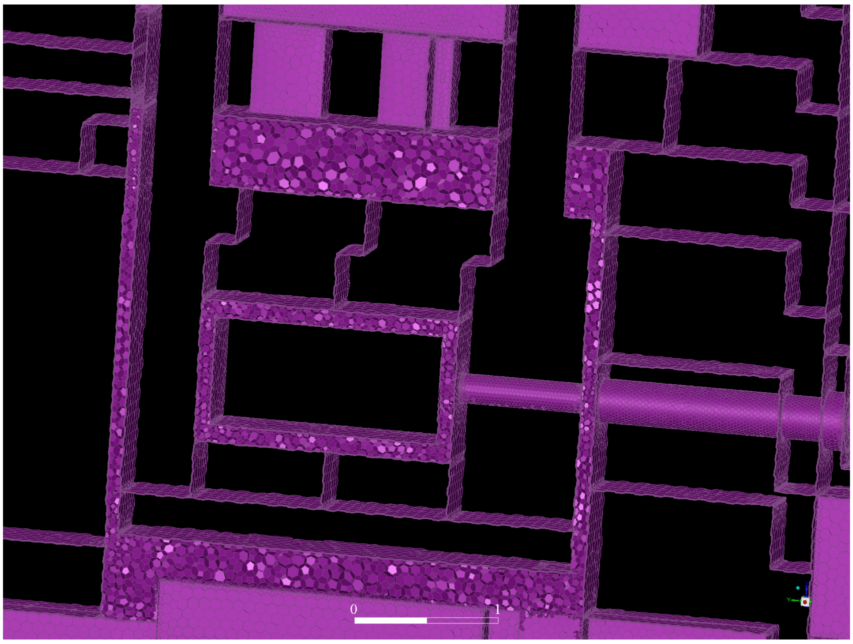

Fig. 6.127: Mesh slice in the collimator–target region of the He vessel

of these gaps. The cells in the gaps have a high aspect ratio, which becomes particularly critical in the proximity of intersections of different gaps, where the flow direction changes sharply. At these locations, convergence of the solution is more challenging; a reasonably converging solution has been obtained, however. On the other hand, a finer mesh could not be used, owing to limitations on computational power.

6.4.3.5 Steady-state simulation: helium circulation

A steady-state simulation of the helium circulation was run to analyse the pressure and velocity distributions and to identify locations where the helium velocity is particularly small.

Fig. 6.128: Detail of mesh in gaps between blocks

6.4.3.5.1 Simulation set-up

The set-up of the simulation was done according to the following points:

- solver type: pressure-based, for incompressible flow (the maximum velocity of helium is less than 30% of the speed of sound);
- turbulence modelling: realistic k with enhanced wall treatment;
- materials: the fluid was assumed to be pure helium gas with the properties listed in Table 6.12;
- boundary conditions:
  - six velocity inlets; inlet velocity equal to 10 m/s, normal to boundary; total flow for six inlets equal to 764.45 m^3/h;
  - three pressure outlets;
  - remaining surfaces modelled as walls.

Table 6.12: Thermophysical properties of helium as implemented in the CFD simulation

Parameter	Value	Units
Density	0.1625	kg/m^3
Molecular weight	kg/kmol	4.0026
Specific heat capacity	5193	J/kg·K
Thermal conductivity	0.152	W/m·K
Dynamic viscosity	1.99×10^{-5}	kg/m·s

The flow rate selected for the simulation, 764.45 m^3/h, represents the flow provided by the cooling compressor of the helium passivation system; note that the design flow of the purification part of the helium passivation system is much smaller, 75 m^3/h [17].

6.4.3.5.2 Solution set-up

The set-up of the solution was done according to the following points:

– solution method: SIMPLE scheme with second-order discretization for all equations and default under-relaxation factors;
– default hybrid initialization;
– the calculation was run for several hundred iterations; the steady-state solution was reached after about 525 iterations.

6.4.3.5.3 Steady-state results

Because of the large number of gaps and the relatively low number of cells across these gaps (which reduce the effectiveness of plots of path lines), it is difficult to provide an overall 3D representation of the resulting velocity distribution.

Figures 6.129 and 6.130 show the path lines coloured by velocity magnitude in the upper and lower plenums, respectively, in the He vessel. The plots are constrained to a maximum velocity of 0.5 m/s.

In the upper plenum, the flow distribution is dominated by recirculation zones in the proximity of the six inlet locations. Everywhere else, the velocity is smaller and the path lines are less well defined and less dense. Figure 6.129 also gives an idea of the complicated path of the flow through the upper blocks of the shielding.

The helium flow through the shielding is also visible in Fig. 6.130. Sudden acceleration and deceleration of the flow in the gap intersection areas make the flow distribution relatively irregular. The flow distribution, however, becomes more regular when the helium approaches the outlets.

Fig. 6.129: Path lines coloured by velocity magnitude in the upper plenum of the He vessel

Looking at the pressure distribution, Fig. 6.131 shows contours of the static pressure on the outer boundary faces of the model, those in contact with the helium vessel structure. Figure 6.132 shows the same contours in a vertical plane containing the beam axis. Both figures show that the pressure distribution grows uniformly from the upper plenum to the lower plenum, in such a way that the pressure drop across the helium vessel is on the order of 25 Pa.

Figure 6.132 shows that the presence of gaps does not significantly alter the pressure distribution in the internal channels of the helium vessel, in particular the fact that the pressure increases uniformly from top to bottom; this indicates that the flow distribution is acceptable.

The primary intent of the steady simulation was the identification of areas where the flow velocity was close to 0 m/s. Figure 6.133 shows a vector plot coloured by velocity magnitude and limited to 0.2 m/s; note that all vectors are scaled to the same length and, owing to the size of the model, the

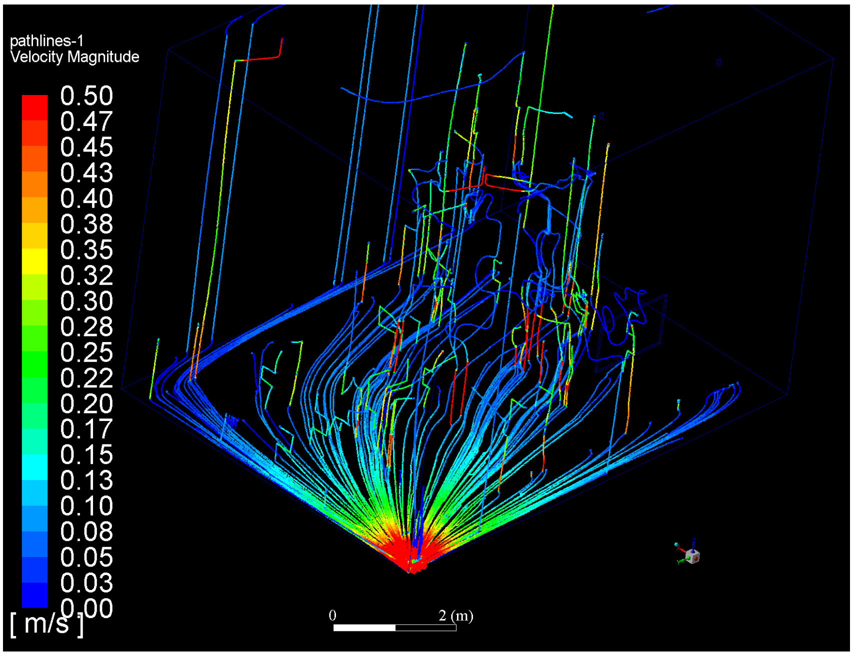

Fig. 6.130: Path lines coloured by velocity magnitude in the lower plenum of the He vessel

vectors resemble points. Excluding the inlet and outlet locations (where the velocity is well beyond 20 cm/s), the velocity distribution generally looks uniform and not higher than 10 cm/s. The plot does not, however, allow any critical locations to be identified.

To show areas of low velocity, the scale was reduced to a maximum velocity of 0.1 mm/s, corresponding to 6 mm/min. Figure 6.134 shows a vector plot coloured by velocity magnitude and clipped at 0.1 mm/s. The figure shows that the main critical areas are the trolley, the target, the proximity shielding, and the collimator assembly. Note that the areas identified in the upper and lower plenum are not as critical, because they are located in open volumes, in which recirculation and gravity will help to provide some mixing effect.

Figure 6.135 represents the same plot as in Fig. 6.134 (a vector plot coloured by velocity magnitude clipped at 0.1 mm/s) zoomed in on the target area. The following low-velocity areas can be identified:

– the collimator and beam pipe;
– the gaps between the proximity shielding blocks;
– the gaps below the proximity shielding;
– the trolley structure.

The collimator and trolley areas are less critical, because the gaps are not excessively thin; the transient simulation (6.4.3.6) provides deeper insight into the impurities left in these areas. On the other hand, the gaps between and below the proximity shielding blocks are more critical: since these blocks are open on one side, the helium prefers to flow around them rather than through them.

6.4.3.6 Transient simulation: helium-filling process

A transient simulation of the helium-filling process was run to identify air pockets that would remain in the helium vessel during flushing.

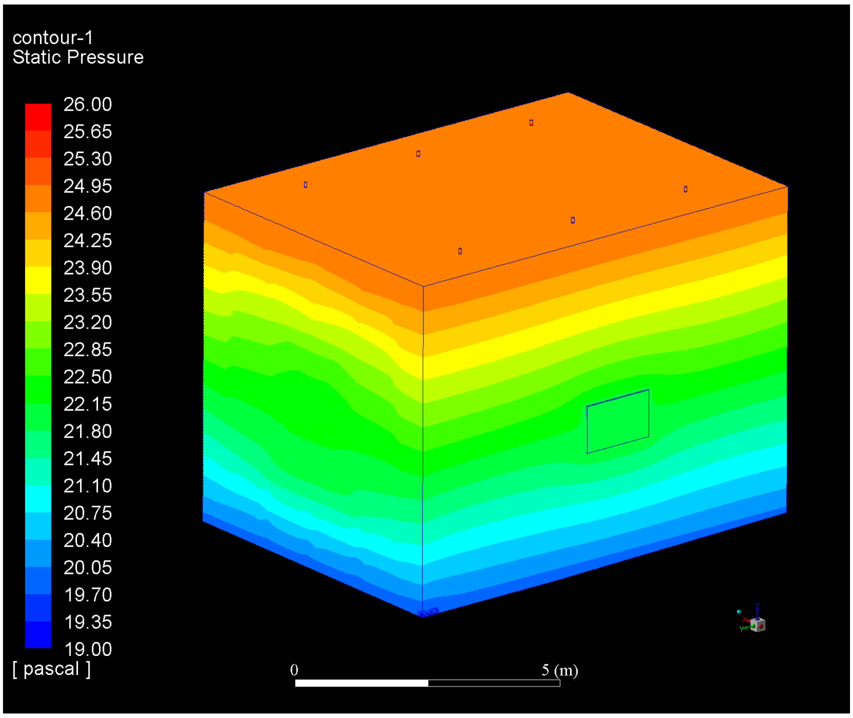

Fig. 6.131: Contours of static pressure on the boundaries of the model

6.4.3.6.1 Simulation set-up

The set-up of the simulation was analogous to that in Section 6.4.3.5 (steady-state simulation), except for the following points.

- Energy equation: on.
- Species model: species transport.
- Materials: a mixture of two fluids, helium and air. The properties of helium used are listed in Table 6.12; those of air in Table 6.13; and those of the mixture in Table 6.14.
- Boundary conditions: identical to those for the steady-state simulation; helium concentration at inlets 100%.

Table 6.13: Thermophysical properties of air as implemented in the CFD simulation

Parameter	Value	Units
Molecular weight	28.966	kg/kmol
Specific heat capacity	1006.43	J/kg·K
Thermal conductivity	0.0242	W/m·K
Dynamic viscosity	1.7894×10^{-5}	kg/m·s

6.4.3.6.2 Solution set-up

The set-up of the solution was analogous to that in Section 6.4.3.5 (steady-state simulation), except for the following points.

- Solution method: PISO scheme with four skewness correction iterations and 0 neighbour correction iterations.
- Spatial discretization: see Table 6.15.

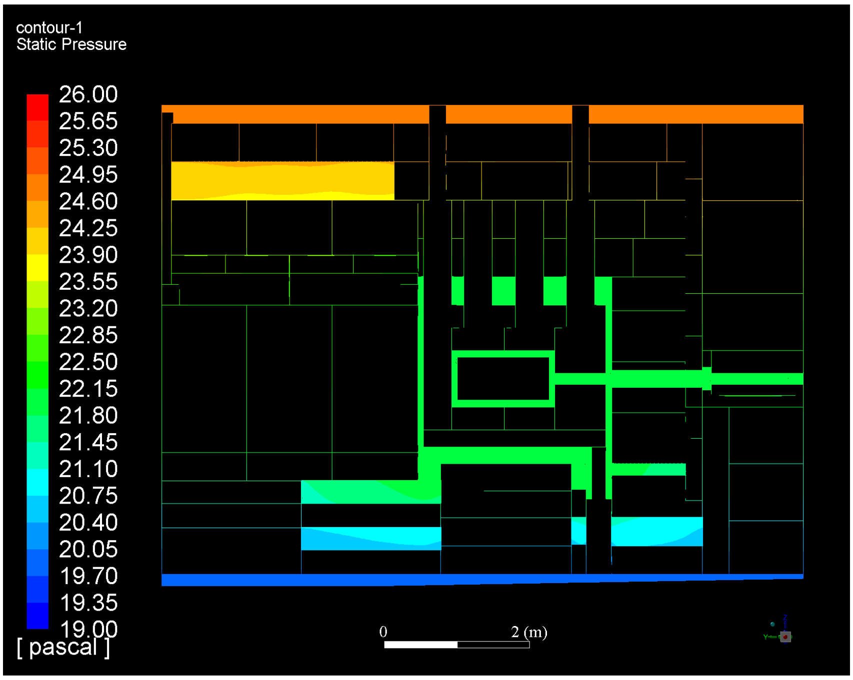

Fig. 6.132: Contours of static pressure in a vertical plane containing the beam axis

Table 6.14: Models selected for calculation of thermophysical properties of He–air mixture

Parameter	Model
Density	Ideal gas
Specific heat capacity	Mixing law
Thermal conductivity	Mass-weighted mixing law
Dynamic viscosity	Mass-weighted mixing law
Mass diffusivity	Constant dilute approximation

– Transient formulation: bounded second-order implicit.
– Under-relaxation factors: see Table 6.16.
– Hybrid initialization: air concentration equal to 100% at start of simulation in all cells.
– Transient calculation parameters: fixed time step (10 iterations maximum per time step), 0.1 s up to 10 s, then 1 s up to 784 s (final time). The total simulation time is equivalent to 166.5 m^3 of pure helium injected at 764.45 m^3/h. Since the free volume of the helium vessel is 74.5 m^3, this amount of pure helium is equivalent to 2.23 gas changes.

Note that one autosave file was about 2.29 GB in size, and so autosaving every 2 s resulted in an output file folder of about 898 GB on the hard drive.

6.4.3.6.3 Transient results

A transient simulation was performed to characterize the helium distribution inside the helium vessel during the flushing process.

Figure 6.136 shows a volume rendering of the distribution of the helium mole fraction (i.e. helium purity) in the helium vessel at six instants of time during the transient simulation. As a reference, the last snapshot of the series (8 min 34 s) corresponds to about 1.46 volumes of pure helium injected into the system. The volume rendering is a series of semi-transparent contour plots in about 20 vertical parallel planes normal to the translational direction of the trolley. Figure 6.137 shows the same purity contours

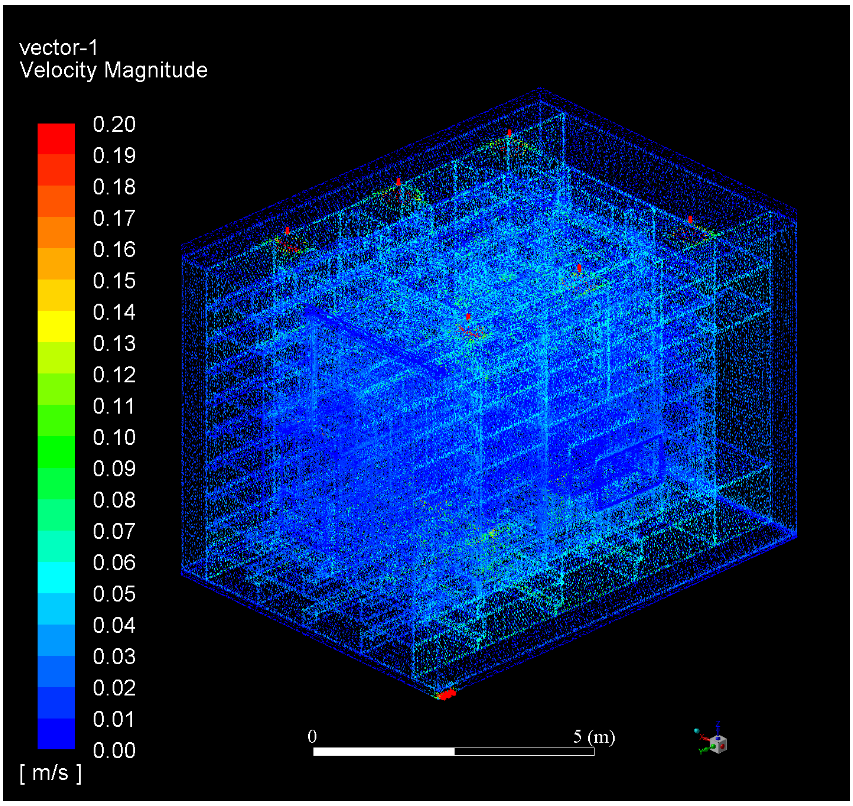

Fig. 6.133: Vector plot coloured by velocity magnitude and limited to 0.2 m/s

Table 6.15: Models selected for spatial discretization of Navier–Stokes equations. Higher-order models were used to reduce numerical diffusion.

Parameter	Model
Gradient	Least-squares cell based
Pressure	PRESTO!
Momentum	Third-order MUSCL
Turbulent kinetic energy	Third-order MUSCL
Turbulent dissipation rate	Third-order MUSCL
Air	Second-order upwind
Energy	Second-order upwind

in one of these planes, specifically, the one that intersects the three inlets on the side of the trolley door.

The series of plots shows that the helium flow gradually and uniformly fills the helium vessel, including its gaps, from top to bottom. This suggests that the helium purity level that is reachable via flushing is high; the plots do not, however, allow the identification of critical areas where the purity is lower than the average in the vessel.

The inlet flow rate, as mentioned in Section 6.4.3.5, is equal to 764.45 m^3/h, resulting in a 10 m/s inlet flow velocity. One volume change (74.5 m^3) is achieved in 5 min and 51 s. Note that the specified flow rate is:

– equal to the flow rate required for cooling of the internals of the helium vessel [17];
– higher than the purification flow rate, which is 75 m^3/h [17].

The pure helium for the flushing process would be provided by 200 bar compressed-helium cylin-

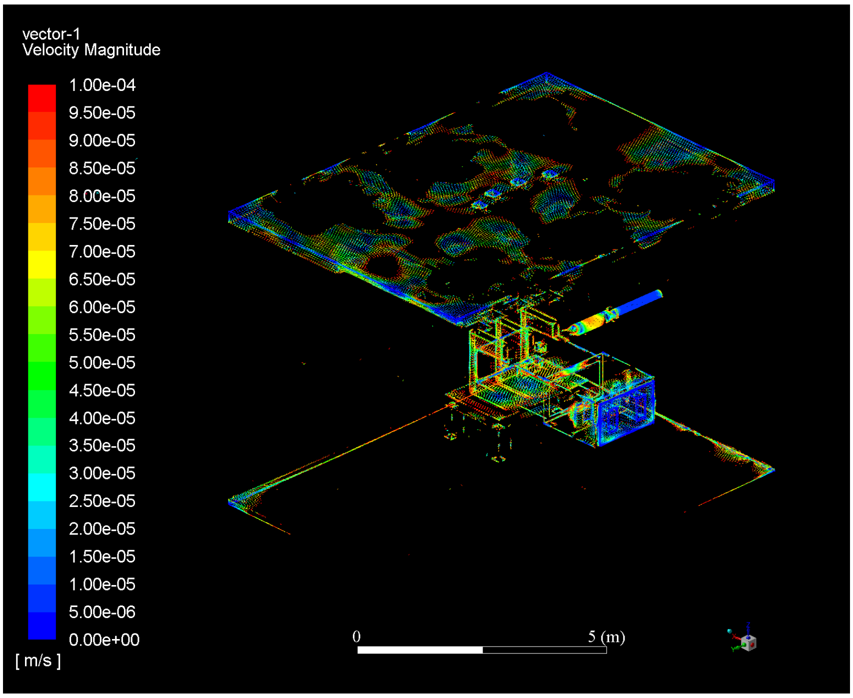

Fig. 6.134: Vector plot coloured by velocity magnitude and clipped at 0.1 mm/s

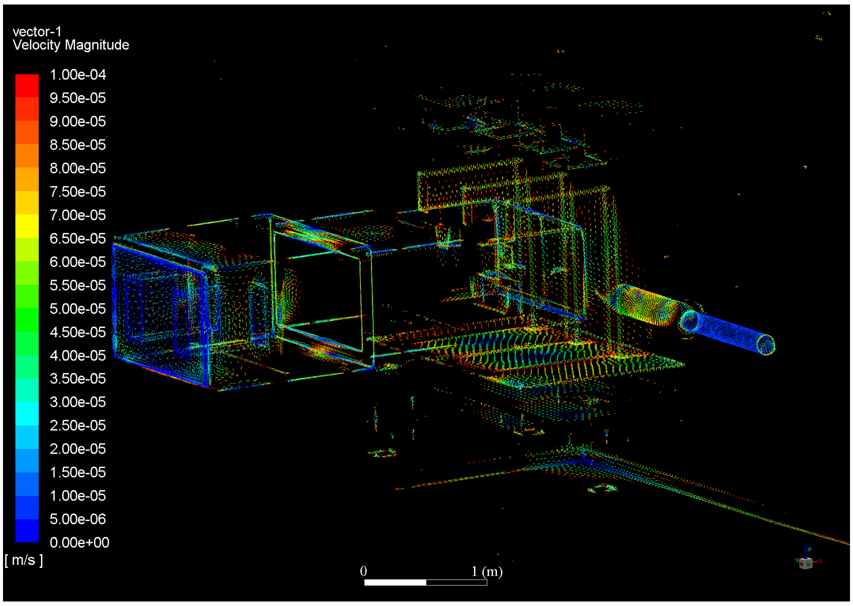

Fig. 6.135: Vector plot coloured by velocity magnitude and clipped at 0.1 mm/s

ders. The 764.45 m^3/h flow rate was selected because it was expected to be more critical than a lower flow rate (such as the purification flow rate) in terms of helium–air mixing: high velocity and high turbulence would be expected to enhance mixing between the two gases, thus increasing the time needed for flushing and the amount of pure helium lost. The results of the simulation, however, seem to contradict this expectation; factors that may influence this behaviour are the complicated geometry, which enhances the separation between helium and air, and mixing by diffusion, which has a smaller impact on small time-scales. Deeper investigation could be done of this aspect; however, the optimization of the helium flow rate was not the main purpose of these simulations, as long as it could be shown that the amount of pure helium required for reaching 85% average purity was less than two vessel volumes.

Table 6.16: Under-relaxation factors. Values lower than default were implemented to increase the numerical stability of the solution.

Parameter	Under-relaxation factor
Pressure	0.7
Density	0.9
Body forces	0.9
Momentum	0.3
Turbulent kinetic energy	0.7
Turbulent dissipation rate	0.7
Turbulent viscosity	0.7
Air	1.0
Energy	1.0

Figure 6.138 shows the evolution of the helium purity with time. The three datasets represent the following quantities.

– The injected volume fraction: the volume of pure helium injected into the vessel, normalized by the free volume of the vessel (74.5 m^3). This parameter is useful for identifying the number of gas changes: it reaches 1.0 when one volume change has been achieved. Since 1.0 is achieved after about 350 s, two volume changes (the threshold for loss of pure helium) are achieved at about 700 s.
– The outlet average fraction: the surface average of the helium purity (weighted by mass) at the outlets of the helium vessel. This is the purity that would be measured by a purity meter at the inlet of the purification system. Note that the peak at about 615 s is not physical (it is generated by local convergence issues during the simulation) and should be disregarded.
– The volume average fraction: the average helium purity in the helium vessel as a function of time.

The parameter of interest is the volume average fraction, or purity. The flushing process allows a high purity to be reached without losing a large amount of helium before it is possible to start the purification process: the volume average fraction reaches 85% (the threshold for the purification system [1]) at about 350 s, equivalent to about one volume change (i.e. an injected volume fraction equal to 1).

The behaviour of the volume average fraction is asymptotically increasing to 1; the average purity is 85% at one volume change and greater than 98% at two volume changes (at about 700 s).

The outlet average fraction is delayed (owing to the inertia of the system) and more oscillating; it consistently exceeds 90% only towards the end of the second volume change.

6.4.3.6.4 Identification of low-purity areas

Figures 6.139–6.144 represent the helium purity at different locations in the helium vessel at the end of the simulated transient, corresponding to 13 min 4 s, or 2.23 volume changes; the scale is clipped at a maximum purity of 98.5% to show areas of low purity. Figure 6.139 shows an overview of the low-purity areas. The minimum purity is about 82% and is likely to be located in the collimator area. Not many low-purity areas are identified, proving that the current design provides good circulation patterns for the helium. Note that the large impurity volume located in the lower plenum should be neglected, since it would naturally disappear with a longer simulation time. Figure 6.140 shows the same results from a different point of view, looking at the frontal collimator blocks.

The first low-purity area can be identified immediately below the C-shaped blocks of the proximity shielding (Fig. 6.141), in the horizontal gap between these blocks and the flat horizontal block. This area had already been identified in the steady simulation. The reason for the presence of this stagnation area

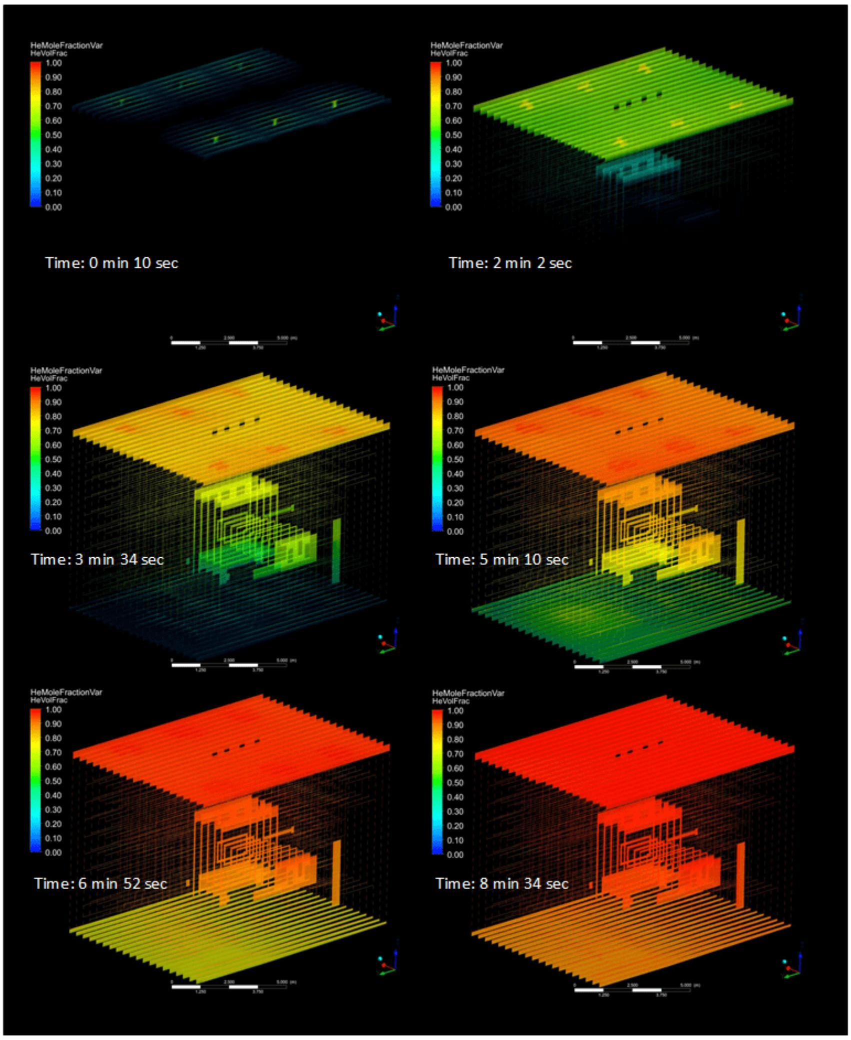

Fig. 6.136: Volume rendering of helium mole fraction during filling

is the fact that the helium prefers to flow around the proximity shielding blocks rather than through the gaps. Note also that vertical gaps still allow gravity to drive a flow induced by different molecular masses of the gases, so that impurities are removed, but horizontal gaps have no means to let these impurities flow out.

A second important stagnation area is located between the collimator and the block surrounding it (Fig. 6.142). This is the location where the purity is lowest. The stagnation is generated by the presence of multiple corners in series combined with a horizontal gap along the flow path, so that the pressure differential is not able to generate a flow through the gaps.

A series of stagnation areas can also be identified in the bunker shielding blocks. Figure 6.143 shows the front bunker blocks; stagnation areas can be found again where the already slow flow in the horizontal gaps is forced to stop at corners. These corners are required, however, to prevent stray radiation from reaching the outside rooms and buildings without shielding.

Analogous considerations hold for the back bunker blocks, represented in Fig. 6.144.

6.4.3.6.5 Recommendations for He vessel design in view of the CFD studies

The following conclusions can be drawn and recommendations made based on the simulation analysis.

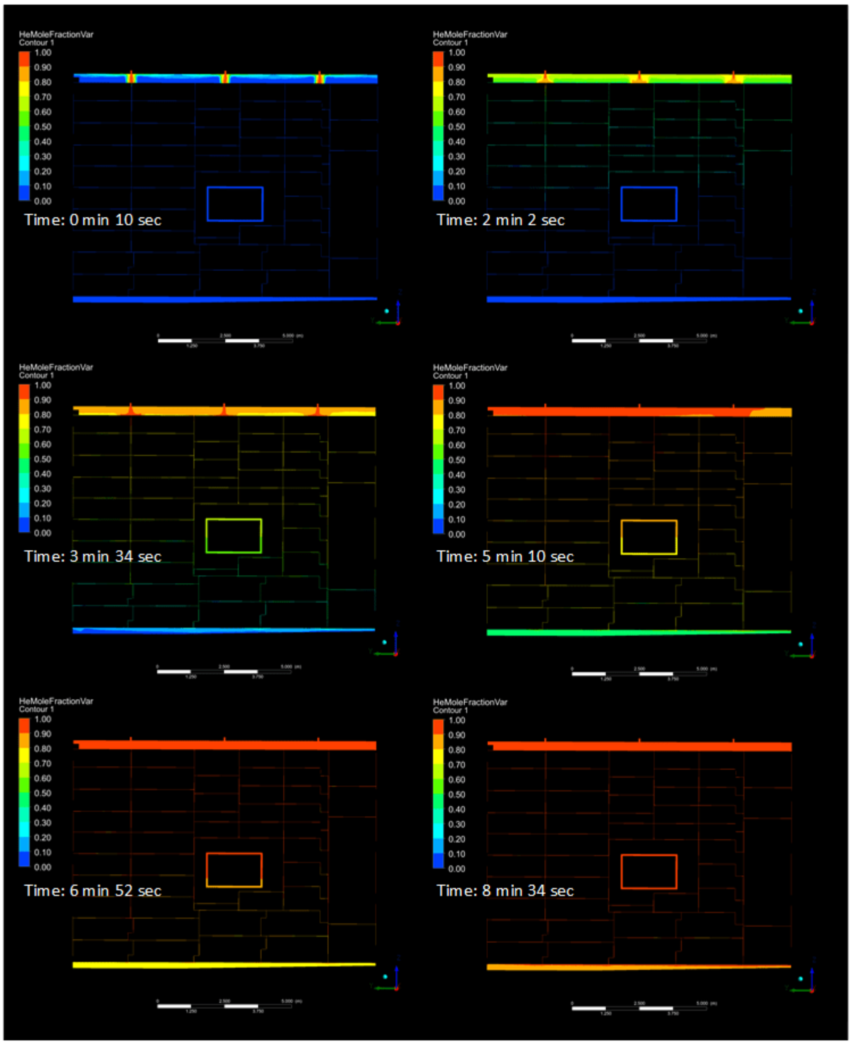

Fig. 6.137: Contours of helium mole fraction in a vertical plane crossing three inlets

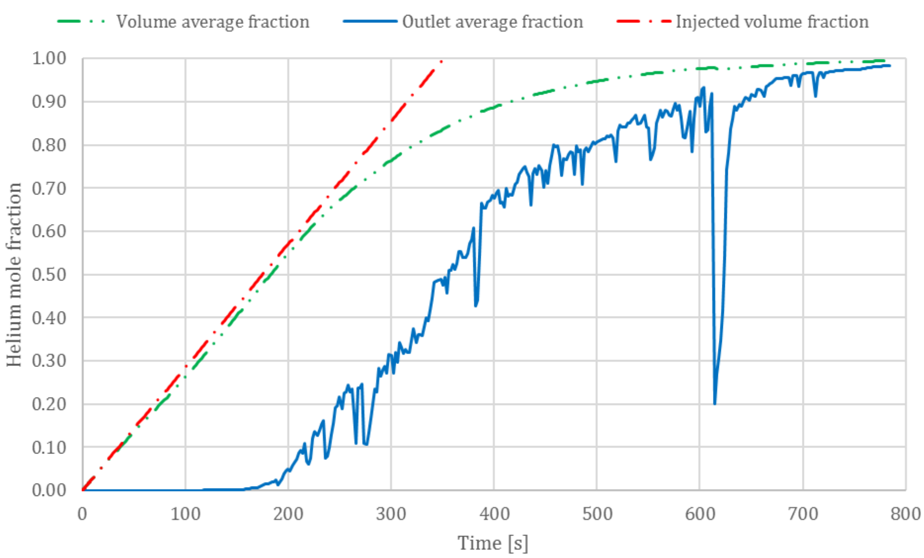

Fig. 6.138: Helium mole fraction as a function of time

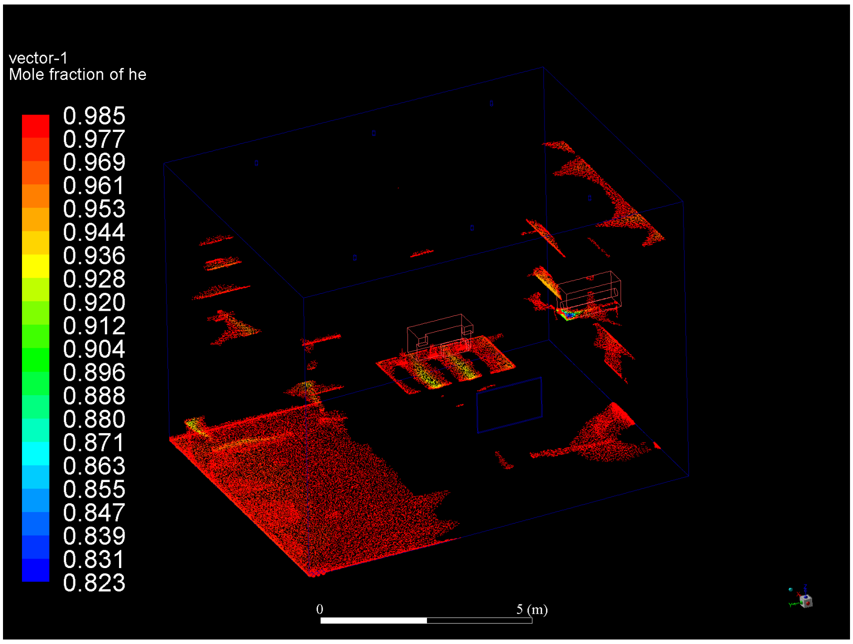

Fig. 6.139: Vector plot of helium mole fraction clipped at 98.5% (2.23 volume changes)

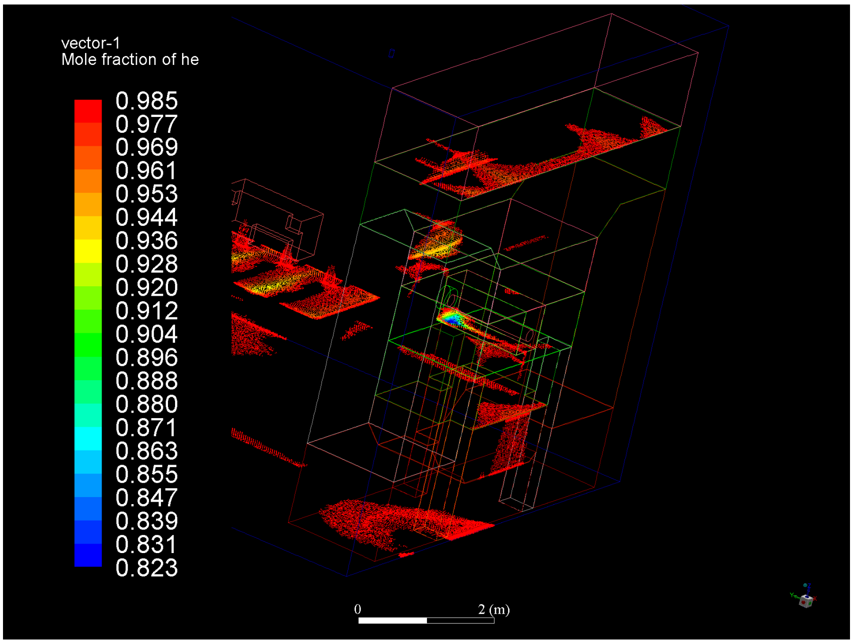

Fig. 6.140: Vector plot of helium mole fraction clipped at 98.5% (2.23 volume changes): front view, collimator area.

- The presence of a 10 mm gap between the blocks and the vessel internals provides an acceptable level of helium purity after flushing, even at a high inlet flow rate.
- The current design allows 85% average purity (the minimum required to start the purification system) to be achieved in the helium vessel well before 2.0 pure-helium volume changes are reached.
- 2.0 volume changes are still recommended before starting the helium purification system, so that not only the volumetric average purity but also the outlet surface average purity is beyond 85% before starting the purification.
- Control over the accuracy of the gap thicknesses is important to preventing the formation of un-

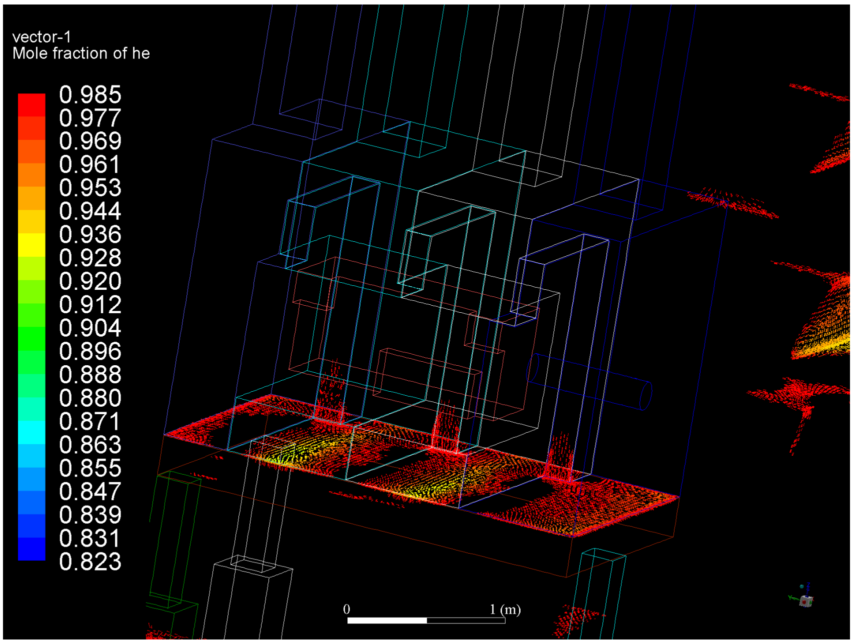

Fig. 6.141: Vector plot of helium mole fraction clipped at 98.5% (2.23 volume changes): proximity shielding.

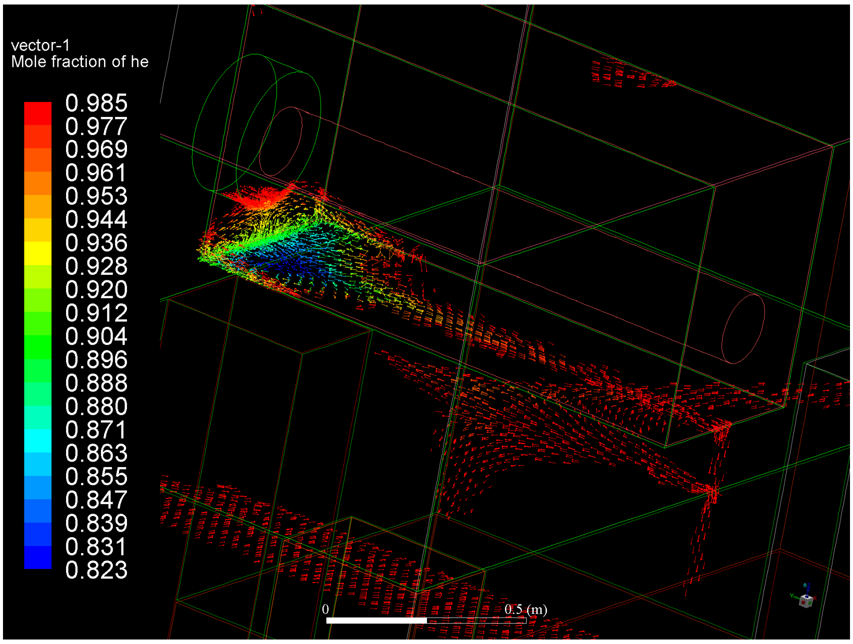

Fig. 6.142: Vector plot of helium mole fraction clipped at 98.5% (2.23 volume changes): collimator

expected stagnation areas or flow imbalances. This is particularly true for the lateral concrete shielding blocks, and for any location where a bypass flow could be generated by an unplanned variation of gap sizes, leaving some areas unventilated.

- The presence of corners combined with horizontal gaps generally makes stagnation areas more likely to appear.
- Horizontal gaps with a large surface area should be avoided as much as possible; if this is not possible, the dimensions and geometry of the gap should be defined, and a CFD analysis should prove that stagnation is limited as much as possible.

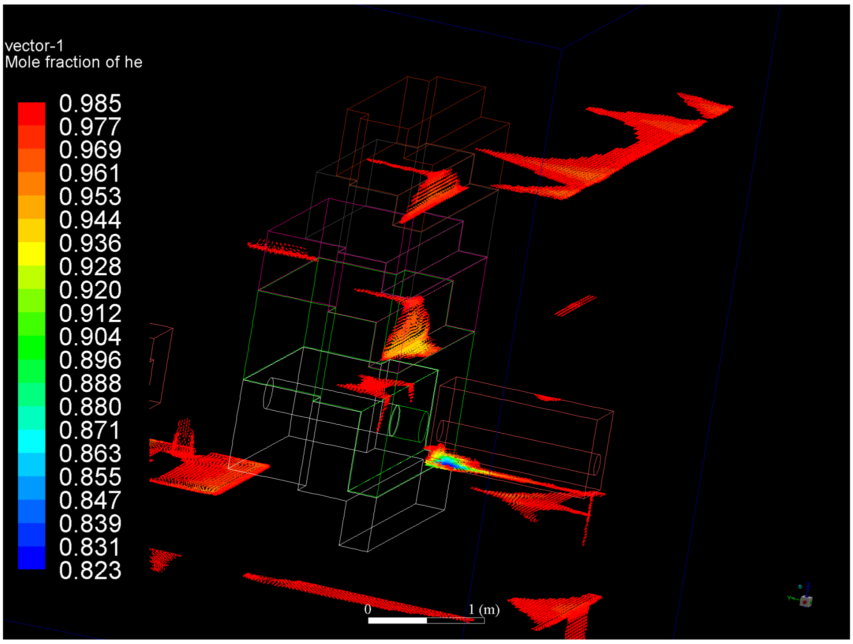

Fig. 6.143: Vector plot of helium mole fraction clipped at 98.5% (2.23 volume changes): front bunker blocks.

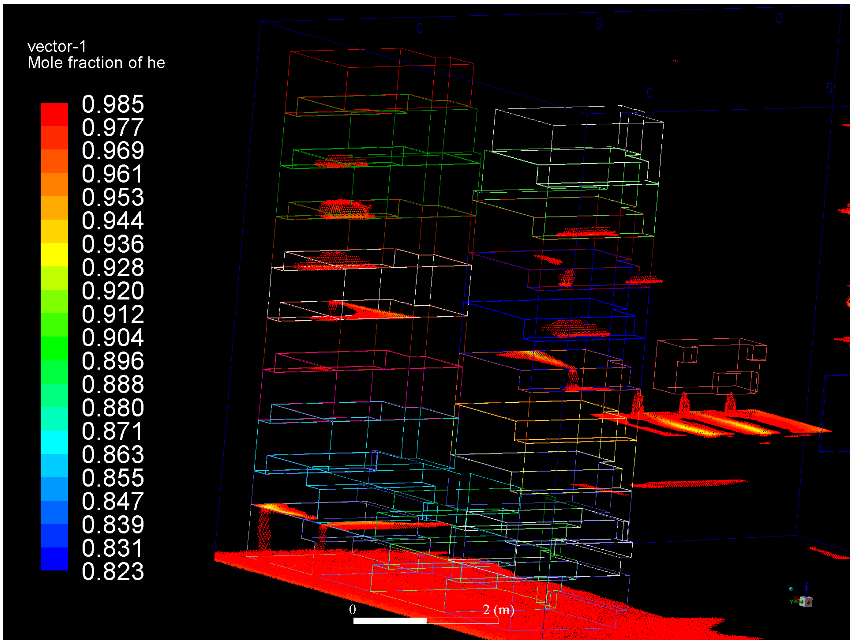

Fig. 6.144: Vector plot of helium mole fraction clipped at 98.5% (2.23 volume changes): back bunker blocks.

6.4.4 Preliminary technical considerations on the He purification and circulation system

6.4.4.1 General description

The helium passivation system supplies purified helium to the helium vessel that contains the BDF target and its shielding; its primary purpose is to remove impurities from the gas mixture so that it is not activated and remains inert from a chemical standpoint.

Helium provides a low level of activation by radiation from the primary beam; combined with the purification capability of the passivation system, this results in minimal activation of the gas mixture contained in the helium vessel. Moreover, a pure helium atmosphere will help to protect the materials from oxidation, thereby increasing the lifetime of the components contained in the helium vessel.

A simplified representation of the overall system is presented in Fig. 6.145; in particular, the passivation system consists of the green part of Fig. 6.145. The system is divided into two parallel units:

- a cooling unit equipped with a compressor, C2 (the "C2 unit");
- a purification unit equipped with a compressor, C1 (the "C1 line"), which includes a cold-box unit (light blue box).

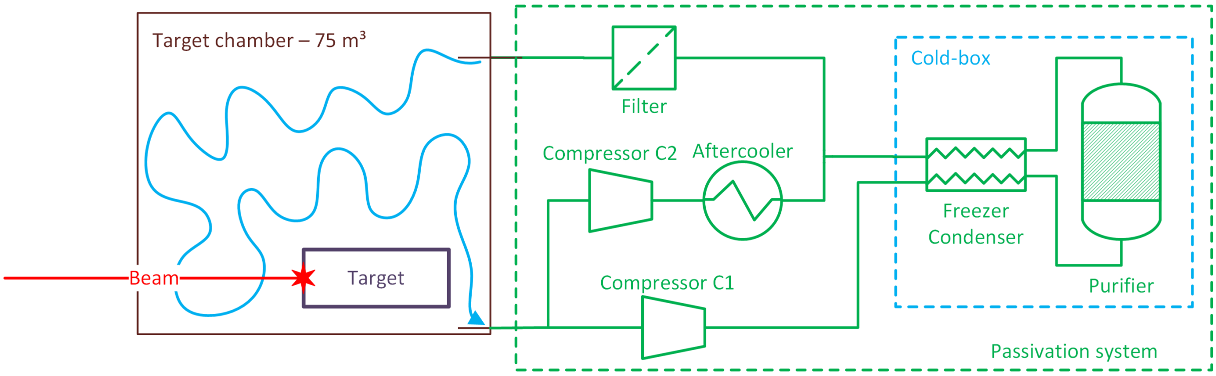

Fig. 6.145: Schematic representation of helium purification system, with the various components of the system.

The two main units (cooling and purification) are designed to comply with the following main requirements.

1. Purify the helium so that the purity at the outlet of the system is at least 99.99% (design purity);
2. Remove 3 kW from the helium in the chamber, with a maximum temperature increase of the helium in the chamber of 20 K. This value for the cooling power will need to be revised at a more advanced design stage to take into account the actual heat dissipation in the helium.

The helium is supplied from a distribution system at the top of the helium vessel, and is collected from a location at the bottom. In the start-up mode, pure helium from cylinders is injected and the helium–air mixture is extracted from the system and vented to the atmosphere, until the helium purity reaches about 85%vol. At this point, the flushing is interrupted and the helium passivation system begins to purify the mixture by recirculating it in the vessel. During operation, whenever the purity decreases below a given threshold, the purification system will be turned on and purify the mixture to the desired level.

The system has three operational modes:

1. Preparation mode: this mode is operated during the initial start-up phase, and prepares the cold-box unit, the target chamber, and the other components of the system for nominal mode operation.
2. Nominal mode: this mode is operated during the main experimental phase, when the beam is hitting the target; the purpose of this mode is to treat the helium so that its condition is compliant with the two main requirements listed above.
3. Purge mode: this mode is operated at the end of the experimental phase; it purges the helium from the target chamber and shuts down the system in a safe condition.

With respect to helium purity, the following two definitions are assumed.

- Design purity: 99.99%. This purity is the purity at which the helium should be provided at the outlet of the system after the purification process. The system should be capable of producing helium with a purity at least equal to the specified design purity.

– Nominal purity: 99.9%. This purity is the desired minimum purity in the target chamber during the operation of the system. During construction, compliance with this requirement will not be the responsibility of the contractor, because it is affected by the leak-tightness and internal configuration of the target chamber.

6.4.4.2 *Piping and instrumentation diagram and process description*

The low-temperature adsorption method is used in the helium purification unit. The implementation of this purification technology allows the design purity to be achieved. The basic principle of purification by this method is to remove impurities (moisture, air, nitrogen, etc.) by condensation and adsorption on an adsorbent bed that is maintained at a cryogenic temperature (about 77 K). To reach the design purity, the process must work at a pressure level of at least 15 bar.

The adsorbent bed allows impurities in the gas to be captured from the main helium stream. To achieve simultaneous adsorption of several gas components, a mixed bed of sorbents is used, typically a multisorbent based on coconut activated carbon (washed) and CMS-T3A.

A preliminary simplified process flow diagram of the helium purification unit is shown in Fig. 6.146 for the redundant-cold-box version. The process of helium purification is performed in the following steps.

1. Impure helium from the target chamber, at a pressure slightly above atmospheric and a temperature below 46°C, is supplied to the suction of compressor C1 (see Fig. 6.146).
2. In compressor C1 (the compressor for purification), the helium is compressed to a pressure of at least 15 bar.
3. The helium enters the shell space of the condenser–freezer E1 (see Fig. 6.146). In the condenser–freezer, helium is cooled to a temperature of about 88 K by the flow in the return line and the nitrogen vapour from the adsorber dewar. All impurities such as moisture, CO_2, and residual oil vapours from the compressor freeze out in the condenser–freezer.
4. After the condenser–freezer, the helium enters the purification block. The flow of helium is cooled further in the helium purification unit to a temperature of 77 K, and then enters the adsorbent bed. The adsorber is located in a tank, which is filled with liquid nitrogen.
5. The pure helium after the adsorber is directed back to the condenser–freezer E1 for pre-cooling of the main flow of impure helium.
6. After the condenser–freezer, the pure helium is filtered (to clean it of adsorbent particles, at PF3) and returns to the target chamber at the design purity.

The system is fully automated, because the target complex area is not accessible during the experimental phase and all operations need to be performed remotely.

6.4.4.3 *Layout and components*

The system is divided into two pieces: the cooling unit (C2 line: compressor C2 and aftercooler) and the purification unit (compressor C1 + cold-box) (Figs. 6.147 and 6.148). The units comply with the following requirements:

– the purification unit is supplied on a skid, whose maximum dimensions are 2.5 m (length) × 1.2 m (width) × 2 m (height); the skid is assembled and transported on-site, for connection and testing;
– the cooling unit, whose maximum dimensions are 2.5 m (length) × 1.5 m (width) × 2 m (height), is transportable and provided with lifting points on top of the structure;
– both units are equipped with their own electrical and control cubicles;
– both units are provided with connection flanges for the required services (water connections, helium cylinder connections, liquid nitrogen connections, connections to second cold-box).

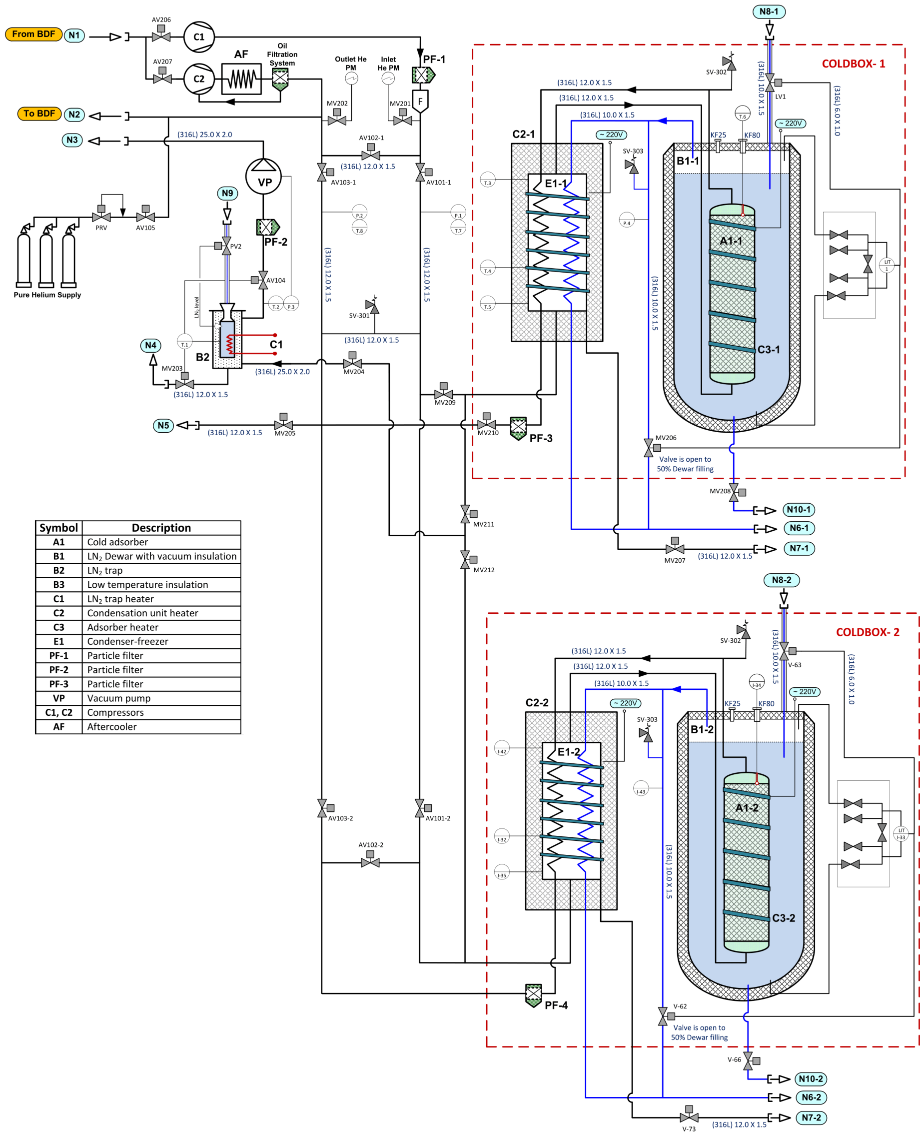

Fig. 6.146: Preliminary process flow diagram for the helium passivation system, showing two redundant cold-box units for continuous operation and a cooling and circulation unit.

The preliminary design of the system features two compressors, one for purification (C1) and another for circulation and cooling (C2). Compressor C1 has an adjustable flow rate and is provided with with an automatic control unit. The flow rate is determined so that the preparation process can be completed in less than 24 h. Compressor C1 has the following characteristics.

- To limit as much as possible and potentially eliminate oil vapour/aerosol content in the outlet helium flow, compressor C1 is oil-free.
- Compressor C1 will be operated in a radiation-controlled area. The selection of the compressor will ensure that preventive maintenance is needed no more than once per year.
- The compressor compresses helium to at least 15 bar.
- The compressor features an aftercooler.

Similar considerations hold for the compressor for circulation (C2) and its aftercooler. The compressor C2 and aftercooler have the following characteristics.

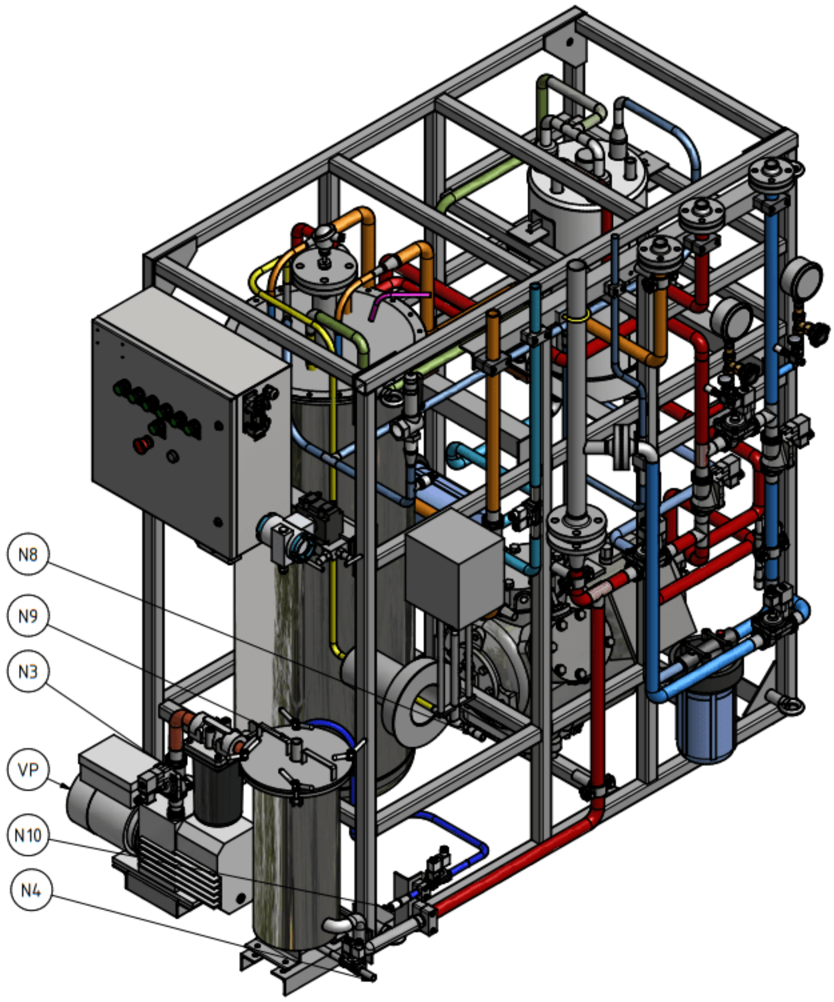

Fig. 6.147: Preliminary 3D model of the purification unit, including the cold-box, the regeneration system, and the electrical cubicle.

- The combination of compressor and aftercooler is capable of cooling helium from 46 to 26°C with a maximum of 3 kW thermal power (corresponding to roughly 700 m^3/h).
- The pressure head is at least 1000 Pa.

The purification system consists of two main blocks: the condenser–freezer and the adsorber.

The adsorber is a vessel made of stainless steel and filled with sorption material. To increase the sorption capacity, the absorber is submerged in a liquid nitrogen dewar. The main technical characteristics of the adsorber are listed in Table 6.17.

The adsorber is connected in series with the condenser–freezer, and they work simultaneously. The restoration of the sorption capacity (regeneration) of the adsorbent is done by heating and pumping out the cold-box cavities. A cold trap (B2 in Fig. 6.146) is installed to collect the impurities during the regeneration procedure.

The helium purification unit is designed in such a way that a single pass through the condenser–freezer and the adsorber is needed to achieve the design purity. The adsorber is dimensioned to provide a purification capacity of 6 h at a constant inlet gas purity of 85% and the nominal flow rate (as mentioned in Table 6.17). In this context, the purification capacity is defined as the operational time (at the specified constant flow rate and inlet purity) after which the adsorber saturates and requires regeneration. For the

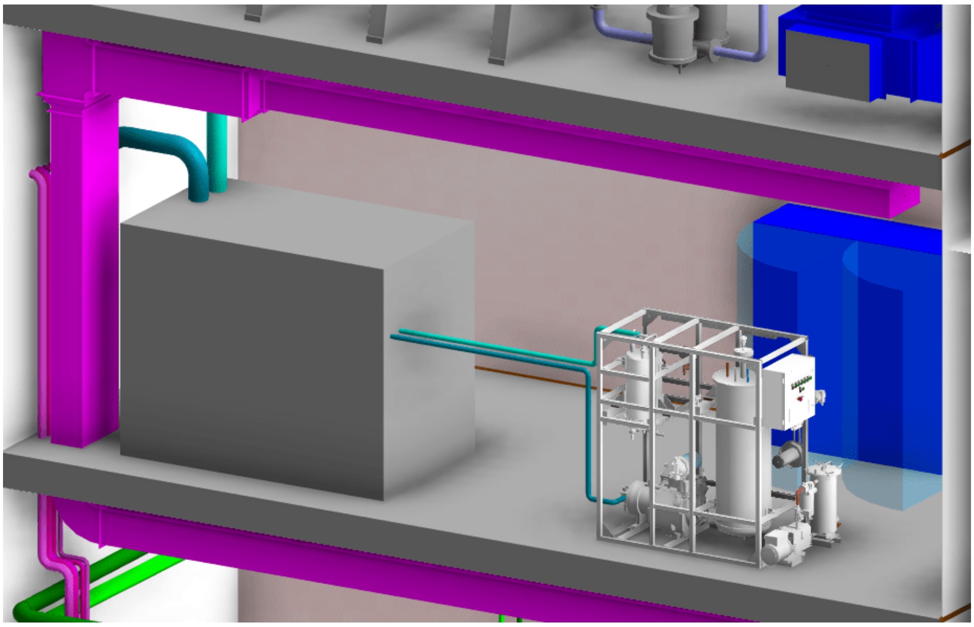

Fig. 6.148: Preliminary integration of the helium passivation system in the CV room of the BDF target complex. Both the purification and the circulation unit are illustrated.

Table 6.17: Technical requirements for the purification unit and the adsorber

Parameter	Units	Value
Design purity	%	99.99
Minimum operating pressure	bar	15.0
Minimum allowable pressure	bar	0.0
Maximum allowable pressure	bar	30.0
Inlet temperature	K	93.0–95.0
Operating temperature	K	77.0
Purification capacity (minimum working time before saturation) at 85% constant inlet gas purity	h	6

nominal operating conditions of the BDF, assuming an average impurity level in the helium vessel of 0.05%vol (consistent with 1 m^3/day of impurity ingress), the unit can work continuously for more than a month before regeneration is needed. Regeneration might, however, be needed much more frequently if a high level of moisture is present inside the vessel during operation, causing blockage of the condenser–freezer unit due to excessive icing.

The condenser–freezer is designed to freeze moisture, vapours, and CO_2, thus significantly reducing the load on the absorber and increasing its lifetime. The purpose of the condenser–freezer is twofold:

- to pre-cool the impure helium via heat exchange with reverse streams of pure helium and cold nitrogen vapours;
- to freeze and trap high-boiling components, such as moisture, carbon dioxide, and hydrocarbons.

The condenser–freezer is designed as a shell-and-tube heat exchanger. The tubes are double-walled, so that one fluid can flow in the annular gaps and another can flow in the internal, cylindrical pipes. The fluid distribution and flow direction in the condenser–freezer volumes are organized as follows:

- shell volume: direct flow of impure helium (coming from compressor C1);

- annular gaps: reverse flow of nitrogen gas (coming from dewar B1; see Fig. 6.146);
- cylindrical pipes: reverse flow of pure helium (coming from the adsorber in dewar B1).

As illustrated in Fig. 6.146, the purification unit is connected in bypass mode to the cooling unit. The entire system is finally connected to the helium vessel via piping going from the CV room to the helium vessel area.

6.4.4.4 Purification system upgrades

The following optional upgrades are foreseen for increasing the functionality of the purification system:

- an additional hydrogen removal system; two options are possible:
  - an additional catalytic recombination unit before entering the cold-box;
  - an additional specific cryogenic unit for hydrogen adsorption;
- an additional gas chromatography unit, including a gas chromatograph, a helium ionization detector, a thermal-conductivity detector, and control software;
- an upgrade of the compressor for circulation and its aftercooler unit to remove 10 kW of thermal power from the helium flow.

6.4.4.5 Pure helium supply

Pure helium is supplied from pressurized cylinders located in a designated area on the surface, next to the target complex (Fig. 6.149). One cylinder holds 50 l of pure helium at 200 bar, corresponding to roughly 10 Nm^3. The cylinders are supplied in groups of 12 on dedicated racks: each rack has a capacity of 120 Nm^3 of pure helium. Accounting for two start-ups per year, plus the equivalent for 1 yr of leaks, the amount of pure helium needed for the operation of the helium purification system for 1 yr is roughly 600 Nm^3. To provide this storage capacity, five racks (60 cylinders) are placed in the helium storage area (Fig. 6.149). Each rack is provided with a pressure indicator to allow timely replacement of exhausted cylinders; the helium storage reserve needs to be periodically checked (at least every six months and in any case after every helium-flushing operation) to make sure that the system does not run out of helium during operation. The helium storage area is provided with supply modules that include pressure regulators/reducers, relief valves, drain valves, and shut-off valves. If necessary, the supply pressure can be monitored on the module via a pressure transmitter, which is linked to alarms/warnings on the supervision system that are activated whenever the pressures in the racks are below a specified threshold.

6.4.4.6 Liquid nitrogen supply

Liquid nitrogen is needed to maintain the adsorber at cryogenic temperatures; the amount of liquid nitrogen needed for the operation of the passivation system is roughly 120 l for every start-up and a maximum of 10 l/h under nominal conditions. Assuming four start-ups per year, the overall need is roughly 90 000 l/yr, or 7500 l/month. A reasonable tank-refilling interval at CERN is on the order of 1 month.

Liquid nitrogen suppliers provide tanks of standard sizes; the sizes of interest for the BDF are 6000 l, 11 000 l, and 19 000 l, corresponding to an autonomy of 0.7, 1.3, and 2.1 months, respectively (accounting for losses). To avoid issues if one monthly refill is missed, the 19 000 l tank was selected; this tank has a diameter of 2.4 m and height of 8 m (Fig. 6.149). Its pressure-building coil needs to be sized for a liquid nitrogen supply of 10 l/h. The tank can be either rented or purchased. The pay-off time for such tanks is on the order of 6–7 yr. The operation of the BDF target is planned to be for 5 yr; in this context, the rental option is likely to be preferable. Instead, if the operation of the helium purification system is to be extended beyond 5 yr, the purchase option is recommended.

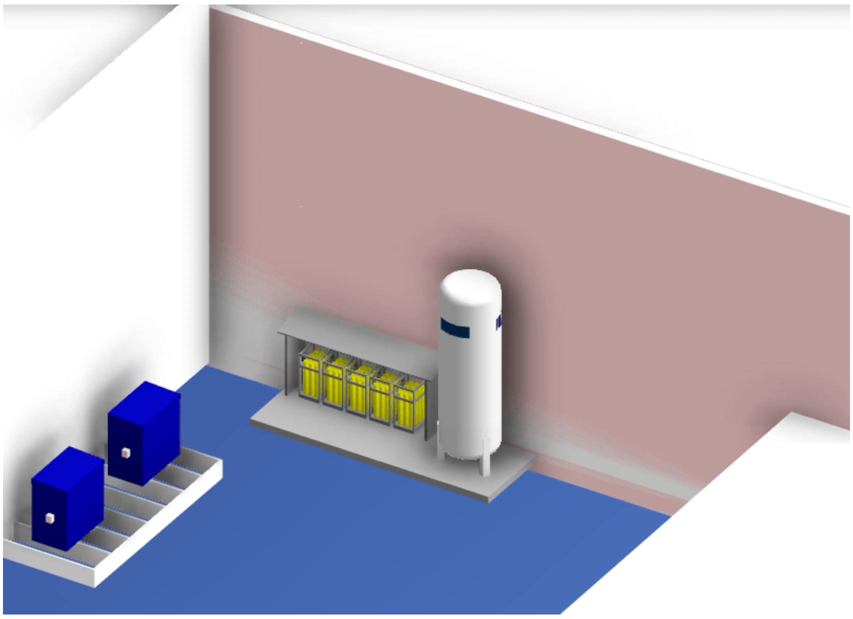

Fig. 6.149: Layout of pure helium and liquid nitrogen supply next to the target complex wall

6.4.4.7 Chilled-water cooling

The helium purification system is designed to remove a maximum of 10 kW of thermal load from the helium vessel. To provide this cooling, chilled water is supplied to the target complex CV room. Table 6.18 lists the main parameters of the aforementioned chilled-water cooling system.

Table 6.18: Chilled-water cooling parameters for the helium purification system

Parameter	Units	Value
Location	–	CV room
Temperature in	°C	6
Temperature out	°C	8.5
Temperature	°C	2.5
Flow rate	m^3/h	3.6
Piping size	–	DN25
Thermal load	kW	10
Type	–	Chilled water
Activation	–	No

6.5 Consideration of cooling and ventilation aspects

6.5.1 Introduction

This section presents the preliminary design of the cooling and ventilation systems for the target and target complex of the Beam Dump Facility; a detailed description of this design is provided in Ref. [20].

The BDF target complex (Fig. 6.150) houses the production target and its shielding, as well as services, handling facilities, cooling and ventilation systems, cool-down areas, and general equipment for supporting the reliable and long-term operation of the facility. The area surrounding the target is passivated by means of a helium cooling, circulation, and purification system, which preserves the integrity of the materials and enhances safety from a radiation protection standpoint. Parts of the cooling and ventilation systems are also located in the BDF auxiliary building, located upstream of the target complex building.

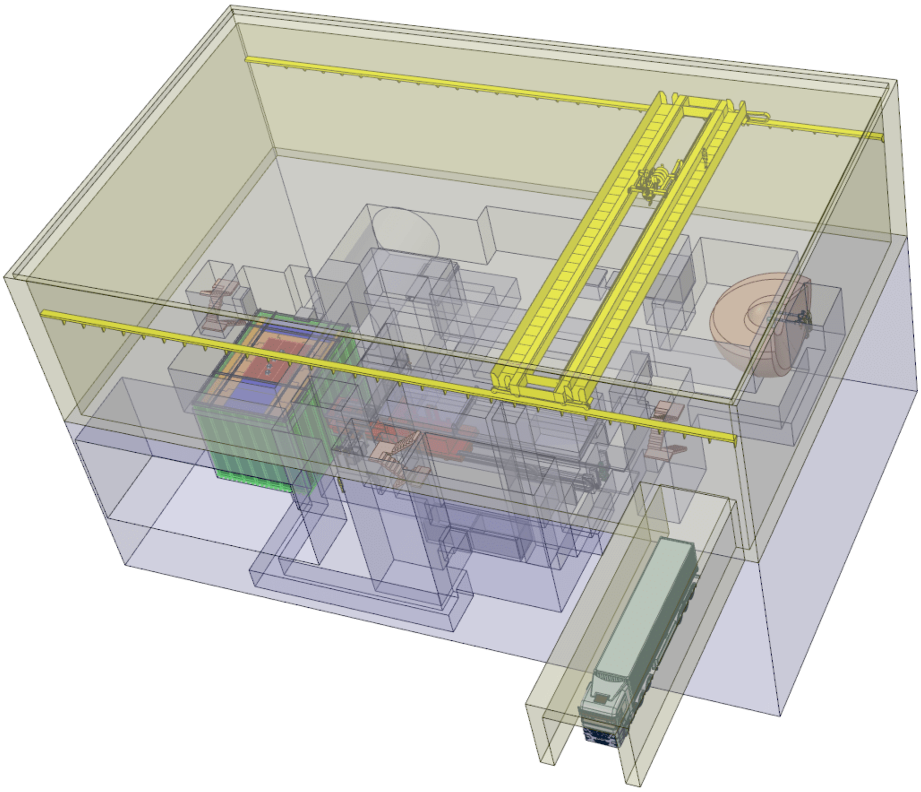

Fig. 6.150: View of preliminary 3D model of BDF target complex (Section 6.2)

6.5.1.1 *Building layout*

Figure 6.150 shows the preliminary 3D model of the BDF target complex, and Fig. 6.151 shows a top view of the rooms inside the target complex. The building is composed of the rooms listed in Table 6.19.

Table 6.19: Size of rooms in the BDF target complex

Room	Volume (m^3)
Surface hall	28 786
Stairs (He vessel)	47
Stairs (CV room)	340
Stairs (trolley)	231
Manipulator rooms	292
CV room	562
Sump shaft	340
He vessel top	333
Hot cell	173
Trolley area	240

The main purposes of the rooms listed in Table 6.19 are as follows:

- surface hall: to allow access to and manipulation of components during maintenance;
- stairs: to allow access to the underground areas;

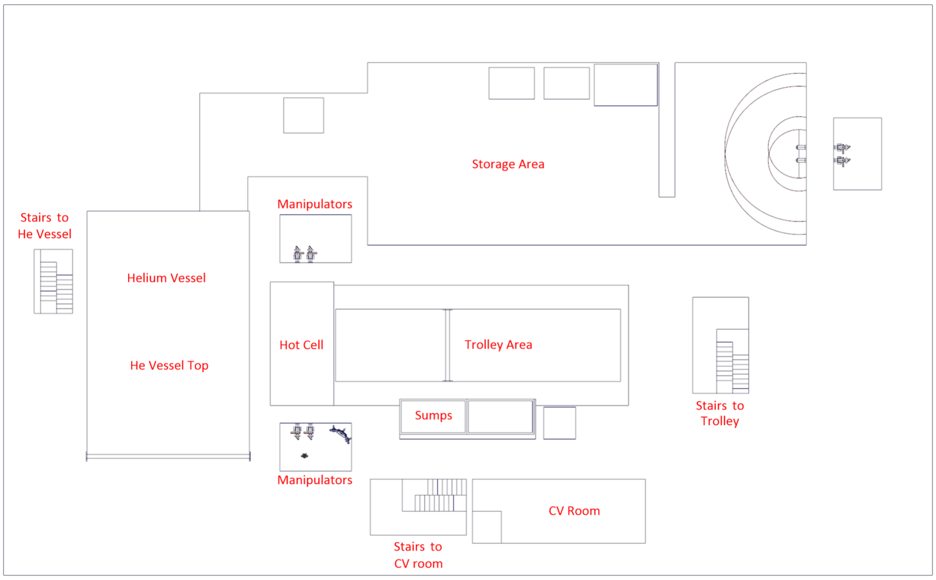

Fig. 6.151: Layout of rooms in the BDF target complex (top view from surface hall)

- manipulator rooms: to manipulate target components during maintenance;
- CV room: to host activated CV equipment underground;
- sump shaft: to allow collection of water leaks at the lowest point;
- He vessel top: to provide a separation layer between the He vessel and the surface hall;
- hot cell: to host the target during maintenance;
- trolley area: to host the target CV systems;
- service room: to host non-activated CV equipment and other services (this area is located in the auxiliary building).

The storage area serves as storage space during maintenance operations; from a ventilation standpoint, it is not separated from the surface hall, despite being underground. The service room is located in the auxiliary building and is shared with the services needed for the extraction tunnel (cooling and ventilation, power converters, etc.).

6.5.1.2 Description of systems

The BDF target complex is designed around a trolley which supports the target and allows its insertion and extraction from the helium vessel for maintenance. The helium vessel contains the following elements (Fig. 6.125):

- target;
- shielding;
- collimator;
- beam window;
- magnetic coil.

All of the services that are directly related to the target are located on the trolley, outside the helium vessel, which is also equipped with a door that seals the helium vessel when the target is inside the helium vessel.

The target can be transported to the storage area and back without having to remove the helium vessel lid and shielding; here, the hydraulic and electrical connections can be maintained via manipulators. The proximity shielding is made of cast iron and allows the target to enter from the side; its cooling connections come from the top of the helium vessel. The entire facility is conceived to allow recovery from failures via remote handling capabilities.

6.5.2 Cooling and ventilation requirements

6.5.2.1 Cooling requirements

The cooling requirements for the BDF water-cooling systems are listed in Table 6.20. The non-activated water-cooling systems (such as the primary system) are located in a service area in the auxiliary building (separated from the target complex), whereas the equipment that will likely be activated is located underground in the CV room, inside the target complex. All secondary cooling circuits are demineralized, to minimize activation of the water.

The target cooling circuit is pressurized to increase the boiling point of the water and avoid an undesired increase in the surface temperature of the blocks that could damage the target. The power deposition is done over a 1 s pulse, every 7.2 s; the power level is roughly 2.5 MW during the first second, and 0 MW during the remaining 6.2 s. The overall thermal load on the target circuit, averaged over 7.2 s, is equal to 350 kW, with the peak power being 7.2 times larger than the average power (see Section 5.2.2). The proximity shielding cooling system provides cooling to the shielding blocks immediately surrounding the target; the thermal load for all blocks is roughly 20 kW (averaged over the 7.2 s cycle). The magnetic-coil cooling system provides cooling for the magnetic coil located inside the helium vessel, immediately downstream of the target. The thermal load generated by the current is 150 kW.

Table 6.20: Cooling-system requirements for the BDF target complex

Parameter	Units	Target	Proximity shielding	Magnetic coil
Location	–	Trolley area	CV room	CV room
T_{supply}	°C	28.0	28.0	28.0
Flow rate	m^3/h	45	6	15
Thermal load	kW	350	20	150
P_{supply}	bar	22	–	–
ΔP	bar	3.5	–	–
Type	–	Demineralized	Demineralized	Demineralized

6.5.2.2 Helium system requirements

The BDF requires two helium systems for the following purposes:

- target helium circulation (Section 6.5.2.2.1): to detect potential leaks from the primary containment of the target;
- helium passivation system (Section 6.5.2.2.2): to purify, circulate, and cool the helium in the helium vessel, to prevent activation and degradation of materials.

The requirements for the two systems are presented in the following sections.

6.5.2.2.1 Requirements for target helium circulation

The target helium circulation system has the primary purpose of circulating pure helium around the primary containment of the target, to allow potential leaks from it to be detected and to prevent undesired target failure or contamination. The requirements for the target helium circulation system are presented in Table 6.21. The helium for the target circulation system is not continuously purified.

Table 6.21: Design requirements for the helium circulation system for the target containment. The system is positioned on the trolley and allows leak detection from the target assembly.

Parameter	Units	Value
Location	–	Trolley area
T_{supply}	°C	28.0
Flow rate	g/s	1.5
Thermal load	kW	0.2
P_{return}	bar	1.0
P_{max}	bar	0.1
Activation	–	Yes

6.5.2.2.2 *Requirements for helium passivation system*

The helium passivation system has the purpose of purifying the helium that circulates through the helium vessel and to cool it. A preliminary design has been developed by ILK (Germany) in collaboration with CERN [16]; ILK has also performed a detailed design of the system [21, 22].

The cooling requirements for the helium passivation system are presented in Table 6.22. The system is capable of circulating 780 m^3/h of helium and cooling a thermal load of 3 kW. Preliminary CFD simulations (Section 6.4.3) have been run on the helium vessel to demonstrate that a 0.2 bar maximum pressure head is sufficient to compensate for the pressure drop in the system and that impurities do not stagnate inside the helium vessel.

Table 6.22: Cooling requirements for the helium passivation system

Parameter	Units	Value
Location	–	CV room
T_{supply}	°C	28.0
Flow rate	m^3/h	780
Thermal load	kW	3
P_{return}	bar	1.0
ΔP	bar	0.2
Activation	–	Yes

The purification requirements for the helium passivation system are presented in Table 6.23. The system is designed to provide a minimum helium purity of 99.9 vol% (averaged over the vessel volume).

Table 6.23: Purification requirements for the helium passivation system

Parameter	Units	Value
Location	–	CV room
Flow rate	m^3/h	75
Design helium purity	%	99.9
$P_{purifier}$	bar	15.0
Activation	–	Yes

6.5.2.3 *Ventilation requirements*

The BDF target complex requires a ventilation system that provides dynamic confinement, to avoid dispersion of contaminants. The design of the ventilation system was done according to the guidelines provided in Ref. [23]; Section 6.5.2.3.1 illustrates the application of that standard to the case of the BDF target complex. The Radiation Protection group at CERN has classified the ventilation areas in the target complex according to these guidelines, and a series of requirements on the ventilation system has been produced (Section 6.5.2.3.2). These requirements, together with the thermal requirements (Sections 6.5.2.3.3 and 6.5.2.3.4), constitute the basis on which the ventilation system was designed. All ventilation units are located in a CV service area located in the auxiliary building, next to the target complex.

6.5.2.3.1 *Design guidelines for nuclear-facility ventilation*

The ISO standard [23] mentioned above provides criteria for the design and operation of ventilation systems for nuclear installations other than nuclear reactors. The guidelines described in the standard are applied according to the following procedure.

1. Each ventilation area is classified on a scale of one to four, on the basis of permanent (surface and airborne) and accidental contamination.
2. An underpressure value is defined for each area, to provide dynamic confinement.
3. An estimated air change rate is determined.
4. Recommendations (such as filtration level) for the design of the specific ventilation system are given, based on the respective classification.

This procedure was applied to the BDF target complex, and the resulting requirements are listed in Section 6.5.2.3.2.

6.5.2.3.2 *Radiation protection requirements*

The application of the ISO standard to the BDF is based essentially on potential accidental conditions that have been postulated by the RP group; these accidental conditions are more stringent than the normal operating conditions in terms of classification, since the expected permanent contamination levels for the BDF are low.

Table 6.24 shows the RP requirements for each ventilated room, in terms of class, underpressure, and minimum air change rate. The pressure cascade produces a dynamic confinement that prevents contaminants being transported from highly critical to non-critical areas in the target complex. The air change rate was also determined so that it was sufficient to replace activated air in passage areas (such as stairs) and the most critical rooms.

Table 6.24: Radiation protection requirements for BDF target complex and nuclear classification of the different areas of the complex.

Room	RP class	Underpressure (Pa)	Air changes (ac/h)
Surface hall	C1	−20	1
Stairs (He vessel)	C1	−40	2
Stairs (CV room)	C1	−40	2
Stairs (trolley)	C1	−40	2
Manipulator rooms	C1	−60	4
CV room	C2	−80	2
Sump shaft	C2	−80	2
He vessel top	C2	−100	5
Hot cell	C2	−100	5
Trolley area	C2	−100	5

As shown in Table 6.24, different underpressure values can be associated with the same class; for this reason, the ventilation rooms were reclassified according to the subclassification shown in Table 6.25, in which each subclass is associated with a specific combination of class and underpressure.

Table 6.25: Radiation protection classes for subclassification

RP subclass	RP class	Underpressure (Pa)	Zone
C1A	C1	−20	Surface hall
C1B	C1	−40	Staircases
C1C	C1	−60	Manipulator rooms
C2A	C2	−80	CV room, sumps
C2B	C2	−100	He vessel top, hot cell, trolley area

The resulting RP requirements following the subclassification are shown in Table 6.26. Figure 6.152 shows the layout of the pressure cascade for dynamic confinement. The minimum supply flow in Table 6.26 accounts only for the radioprotection requirements on the air change rates listed in Table 6.24; the actual design values presented in Section 6.5.3.3 also account for requirements other than RP (e.g. thermal load). The supply air may be recirculated air for subclass C1A; the supply air should be fresh air for all other subclasses.

Table 6.26: Summary of radiation protection requirements according to subclassification

RP subclass	Total volume (m^3)	Underpressure (Pa)	Minimum RP flow (m^3/h)
C1A	28 786	−20	28 786
C1B	618	−40	1 236
C1C	292	−60	1 166
C2A	902	−80	1 803
C2B	746	−100	3 731

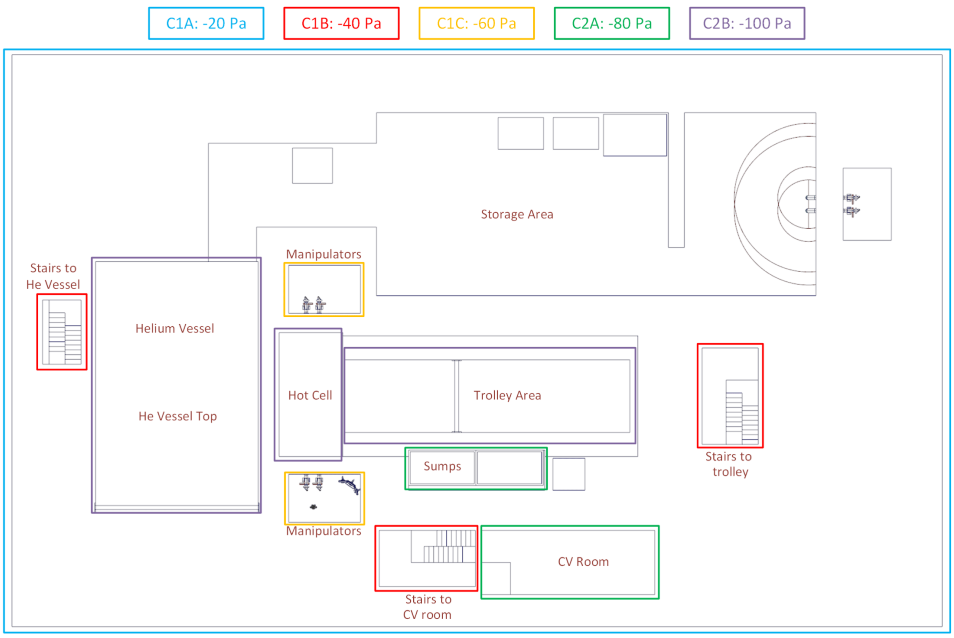

Fig. 6.152: Layout of pressure cascade for dynamic confinement

6.5.2.3.3 *Temperature and humidity requirements*

Table 6.27 presents the requirements for the temperature and humidity range in each room.

Table 6.27: Temperature and humidity requirements for BDF target complex

Room	Temperature range (°C)	RH range (%)
Surface hall	18–26	Not controlled
Stairs	18–26	40–70
Manipulator rooms	18–26	40–70
CV room	18–26	40–70
Sump shaft	18–26	40–70
He vessel top	18–24	40–70
Hot cell	18–24	40–70
Trolley area	18–24	40–70

6.5.2.3.4 Internal heat dissipation

The sources of internal heat dissipation due to equipment and occupational activities inside the conditioned spaces are listed in Table 6.28. At the level of the current design, most of the spaces in the target complex do not present any significant thermal load other than people and lighting; further investigation will have to be done once more accurate information becomes available (electrical loads, power converter requirements, etc.).

Table 6.28: Internal heat load and occupancy for each room in the target complex. Relevant loads are expected only for technical rooms.

Room	Thermal load (kW)	Max. occupancy
Surface hall	–	10
Stairs	–	2
Manipulator rooms	–	3
CV room	10	2
Sump shaft	2	2
He vessel top	–	2
Hot cell	–	2
Trolley area	5	2

6.5.2.4 Other requirements

6.5.2.4.1 Compressed air

A compressed air supply is required inside the BDF target complex. Other than for general use in the surface hall, compressed air is required mainly in the trolley area and CV room, for purging the water circuits and for pneumatic actuators. Table 6.29 shows the compressed air requirements; as the compressed air will be supplied from a technical gallery, the standard dew point and filtration available on the Prévessin site are acceptable.

Table 6.29: Compressed air requirements

Parameter	Value	Units
Flow rate	200	Nm^3/h
Supply pressure	7	bara
Dew point	Not specified	°C
Filtration	Not specified	–

6.5.2.4.2 Rising system

The BDF target complex needs to be provided with sumps to collect activated water arising from the underground services and from leakage through the building walls. The sump area is equipped with pumps to raise the water to surface storage tanks, located on the top floor of the CV room and in the auxiliary building. The sump room is provided with a steel liner to prevent contamination of the concrete.

Table 6.30 lists the volumes of water to be discharged to the sump system every time the circuits are drained and refilled. Because of the high level of activation of the water, the target circuit is the driving factor in sizing the sump system.

Table 6.30: Estimated water volume of cooling circuits

Circuit	Volume (m^3)
Target	1.0
Proximity shielding	0.3
Magnetic coil	0.6

The system is provided with two sump tanks, each sized at 10 m^3, allowing 20 times the volume of the target circuit to be stored, and possibly accommodating water infiltration. Each sump tank is provided with two redundant sump pumps. The target circuit will be drained based on instructions from the RP group. The drain water will be left in the sump for two weeks to allow the decay of short-lived products. After this decay time, the water will be pumped to a dedicated tank at ground level.

6.5.2.4.3 Evaporation system

The auxiliary building is equipped with a room specifically designed for hosting the evaporation system. The evaporation system consists of three evaporation units of type Encon Drum Dryer (or similar), allowing a maximum evaporation rate of 90 m^3/yr. The room includes two redundant 5 m^3 tanks that hold the water before evaporation. The transfer of water from the tank to the evaporator is automatic.

6.5.2.4.4 Smoke extraction system

A smoke extraction system is needed for the target complex. The design of the smoke extraction system needs to be compatible with the confinement of radioactive products provided by the ventilation system. During a fire event, the pressure cascade should be kept in place as much as possible to avoid unforeseen release of potentially contaminated smoke. A 36 $m^3/h/m^2$ extraction flow rate is provided by the surface hall smoke extraction system. Regarding the underground areas, the smoke will be extracted using the standard ventilation system, after cool-down of the smoke. The rooms in the underground area are considered as separate fire compartments; each fire compartment is provided with fire walls and doors according to EN 13501, and the fire dampers required for smoke confinement.

6.5.3 Design of cooling and ventilation systems

6.5.3.1 Cooling systems

6.5.3.1.1 General description

The BDF cooling system is based on a raw-water primary cooling system supplying water at 25°C via cooling towers. Local cooling is provided via demineralized-water secondary circuits; chilled water provides cooling for the air-handling units (AHUs) and the helium purification system. Figure 6.153 shows a schematic view of the cooling systems for the target complex, which are structured as follows.

- primary raw water (Section 6.5.3.1.3):
  - target helium circulation system (Section 6.5.3.1.7), located in the trolley area;

  - secondary demineralized-water cooling systems:
    * target (Section 6.5.3.1.4), located in the helium vessel;
    * proximity shielding (Section 6.5.3.1.5), located in the helium vessel;
    * magnetic coil (Section 6.5.3.1.6), located in the helium vessel;
- chilled water (Section 6.5.3.1.8):
  - helium passivation system, located in the CV room;
  - AHUs, located in the auxiliary building.

Table 6.31 presents a preliminary evaluation of the cooling requirements for the target complex compared with the cooling requirements for the BDF complex, including the extraction tunnel and the SHiP experimental area. A preliminary estimate of the total cooling power needed by the target complex is roughly 600 kW on the demineralized-water circuits and 135 kW on the chilled-water system, whereas the total cooling power for the BDF complex is roughly 5500 kW for the demineralized water and 750 kW for the chilled water.

Table 6.31: Cooling requirements of the BDF target complex compared with the overall needs of the BDF complex.

Cooling type	Target complex only (kW)	BDF complex (kW)
Demineralized water	600	5500
Chilled water	135	750

6.5.3.1.2 Cooling-system piping and instrumentation diagram

The following documentation was prepared during the design process:

- a preliminary synopsis of the cooling system [24];
- a preliminary Piping and Instrumentation Diagram (P&ID) for the cooling system [25];
- a preliminary document on the CV 3D integration [26].

6.5.3.1.3 Primary cooling system

The BDF cooling system is based on a primary circuit that supplies raw water at 25°C. Two options were considered for the supply of the primary water:

- installation of local independent cooling towers;
- connection to the CT2 cooling tower system in the Prévessin area.

In both cases the primary system will have to be sized to cope with the cooling load of the entire experimental facility (5500 kW), which includes needs of the the target complex (600 kW maximum). Table 6.32 presents a high-level comparison between the two options, showing the advantages and disadvantages of each over the other.

Considering the historical operational data, the experience of the operators, the recent upgrades of the CT2 towers, and the future increase in load demand expected, the following assumptions can be made.

- The piping and pumping capacity will not be sufficient to supply raw water for the installations in the new experimental area.
- The CT2 towers will likely not have enough capacity to accommodate the addition of 5.5 MW cooling load.

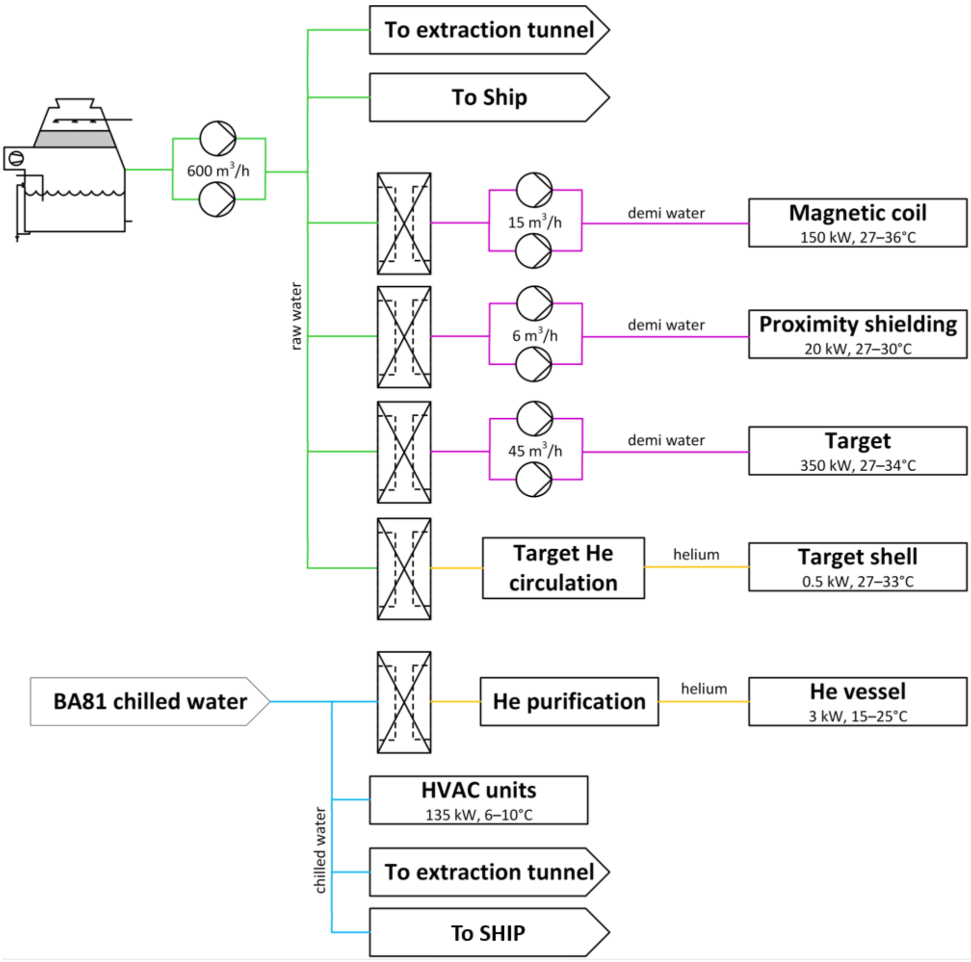

Fig. 6.153: Overview of cooling-system structure for the BDF target complex. The primary (green) and chilled (blue) water circuits are shared with the extraction and experimental areas in the BDF complex.

Since option 1 is the more constraining one, it was selected for the preliminary design phase; option 2 will be maintained as a back-up option, in case the resulting total cooling load on the CT2 towers is lower than expected.

The primary cooling circuit supplies 600 m^3/h at 25°C to handle a total cooling load of 5.5 MW for the entire BDF; the expected temperature increase is 8°C. The estimated diameter of the main piping is DN400; the pressure drop in the circuit is estimated to be around 3 bar, and the required pumping power is roughly 88 kW. The pumping power is provided by two redundant pumps regulated via variable frequency drive (VFD), each one sized for 600 m^3/h; the cooling is provided by three cooling towers ($n + 1$ redundancy), 2.75 MW each. The pumps, the sand filter, the filling circuit, and the other main components of the primary circuit are located in the auxiliary building service area, which is shared with the extraction tunnel services. Figure 6.154 shows the layout of the primary pumping station in the auxiliary building.

The BDF target complex uses a fraction of the 600 m^3/h flow rate, corresponding to 72 m^3/h and 550 kW, for cooling the demineralized-water circuits and the target helium circulation system. The reference size for the primary piping going to the target complex circuits is DN125; within the BDF target complex, primary water reaches the CV room and is distributed locally and in the trolley area.

Table 6.32: Comparison of design options for primary cooling system

Option 1 Local cooling towers	Option 2 CT2 cooling towers
Operation independent from other cooling systems in the Prévessin area	Operation dependent on availability of CT2 towers
Operation and maintenance more complex (water treatment, etc.)	No added complexity from operation and maintenance standpoint
Potential activation confined to new experimental area	Potential activation spreading over CT2 cooling system
Requires installation of cooling towers and pumping station on the new site	Requires upgrade of CT2 pumps and a new pipeline (technical gallery)

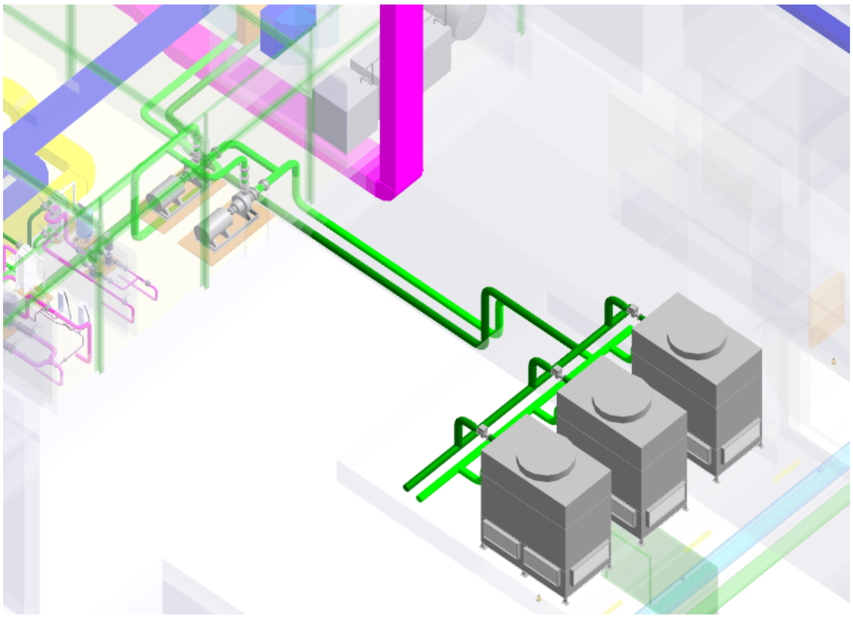

Fig. 6.154: Primary-system pumping station and cooling towers

6.5.3.1.4 *Target cooling system*

The target cooling system provides demineralized-water cooling for the target and is located on the trolley in the underground area (Fig. 6.155). The system supplies 45 m^3/h at 28°C for a thermal load of about 350 kW on average; the estimated return temperature is 35°C. The system is pressurized at 19 bar to avoid local boiling of water on the surface of the target blocks when the beam impacts the target. This pressurization is provided by an automatic expansion tank connected to the circuit before the pumps. Two redundant pumps provide an additional 3.5 bar head to compensate the pressure losses in the circuit, resulting in a supply pressure at the outlet of the pump of 22.5 bar. The size of the piping for the target circuit is DN100, and the estimated pumping power is 10 kW.

All operations on the circuit, such as filling, pressurization, and draining, are automated and do not require physical human intervention to open valves. Draining of the circuit is performed indicatively once a year and is planned based on activation assessments performed by the RP group. The drain water is discharged to the sump; details of the draining operations and the volumes of drain water are provided in Section 6.5.3.4. Draining is followed by a complete demineralized-water refill of the circuit. The actuation of valves for performing this operation is done via pneumatic actuators, which need to function under irradiation; this aspect will be analysed in more depth during the detailed design phase.

The equipment on the skid is provided with a retention basin to collect potential leaks from the system and drain them directly to the sump.

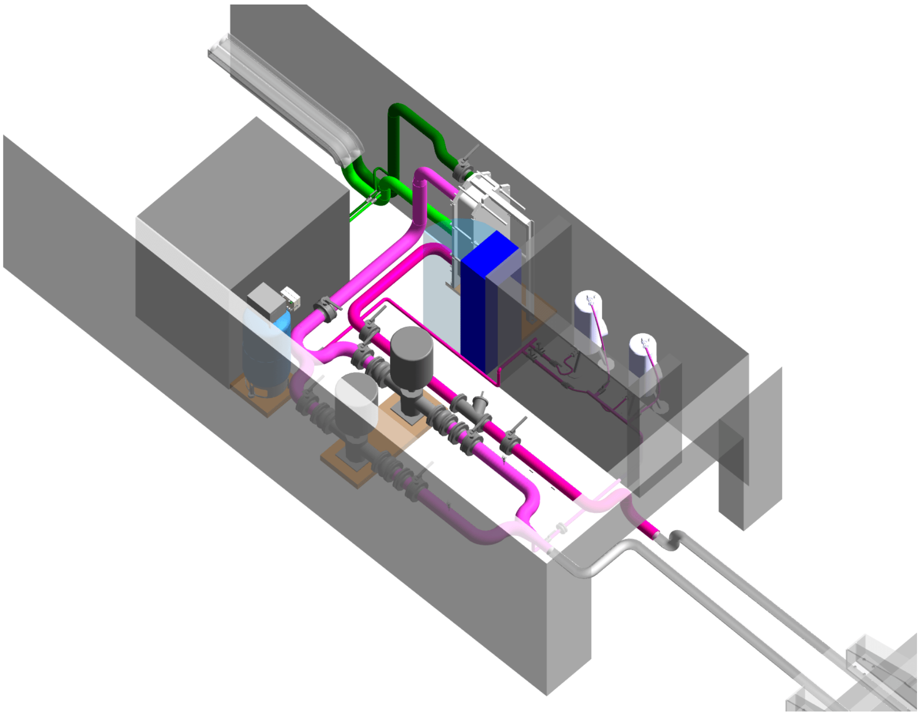

Fig. 6.155: Integration of target cooling system and helium circulation system on trolley. The model also shows the heat exchanger for heat rejection to the primary system.

The system exchanges thermal power with the primary circuit via a plate heat exchanger located on the trolley. To prevent cross-contamination, the heat exchanger plates are double-walled, with EPDM double gaskets. The primary water is delivered to the primary side of the heat exchanger on the trolley via flexible piping. The system operates in a radioactive area: the selection of the equipment, in particular the electronics and the plastic/elastomeric materials for the hydraulic components, needs to take account of this. From preliminary evaluations, EPDM is acceptable for the gaskets, piping, and other components; the correct behaviour of components under irradiation will be confirmed in the detailed design phase, once expected doses estimated via simulations become available. The water in the target cooling system is demineralized by a demineralization circuit in bypass mode, provided with two redundant cartridges; the maximum conductivity of the water supplied will be 0.5 µS/cm. During operation, the cartridges will become activated, because of absorption of radioactive ions from the cooling water; to allow safe maintenance on the trolley during system shutdown, the cartridges are surrounded by iron shielding (Fig. 6.156) 20 cm thick, which reduces the radiation levels generated by the mixed-bed resin.

6.5.3.1.5 Proximity shielding cooling system

The proximity shielding is a set of five blocks located around the BDF target. The beam delivers a thermal load of roughly 20 kW on average to these shielding blocks. This thermal load is cooled by cooling pipes internal to the shielding blocks; the preliminary layout of the cooling pipes is shown in Fig. 6.157.

The cooling is provided by a cooling station located in the CV room (Fig. 6.158). This station supplies 5.75 m^3/h of demineralized water at 28°C at a supply pressure of 5 bar; the expected pressure drop in the proximity shielding is expected to be less than 1 bar. The return temperature is 30°C, and the reference size for the circuit piping is DN32. The pumping is provided by two redundant pumps; the power of each pump is 0.5 kW. The water is demineralized by two redundant cartridges installed in

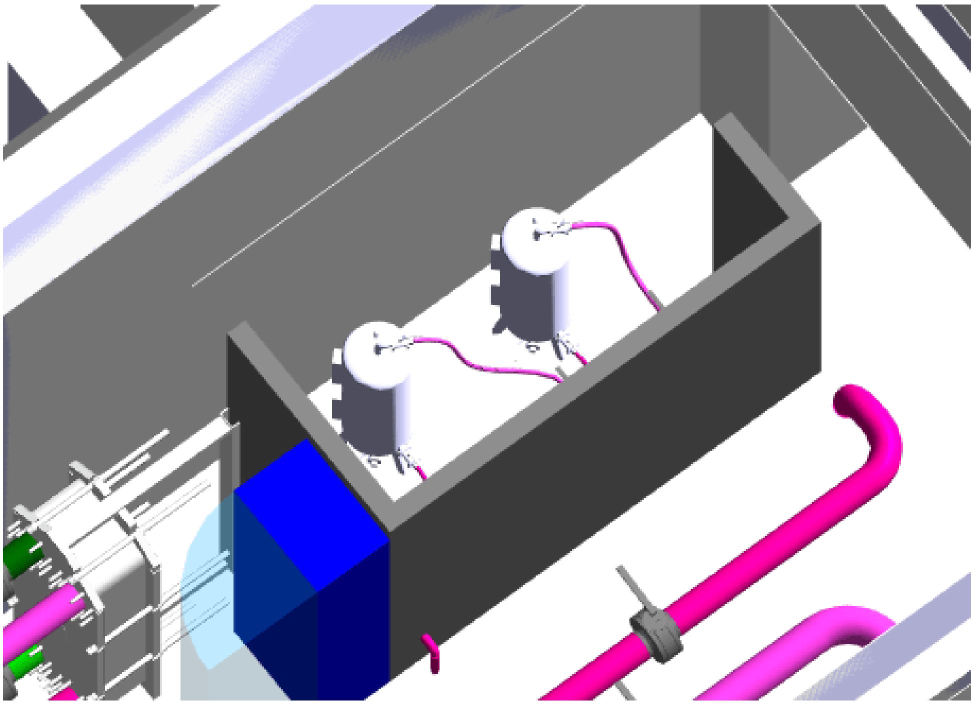

Fig. 6.156: Shielding for primary ion-exchanger cartridges

the CV room; the maximum conductivity of the water supplied will be 0.5 µS/cm. During operation, the cartridges will become activated, similarly to the target demineralization circuit; however, the activation level will be lower than for the target circuit. A 40 cm concrete shield is placed around the cartridge to reduce the dose rate in the CV room during access for maintenance.

The cooling system is connected to the proximity shielding blocks from the top of the helium vessel (Fig. 6.159); the portion of the piping contained inside the helium vessel is removable, to allow positioning and removal of the bunker blocks.

6.5.3.1.6 Magnetic-coil cooling system

A preliminary design of the magnetic coil has been performed (Fig. 6.160), featuring a conductive plate that removes the heat generated by the current flowing through the coil windings. The magnetic coil is located inside the helium vessel, immediately downstream of the target. The cooling for the magnetic coil is provided by a cooling station located in the CV room (Fig. 6.161), supplying demineralized water at 28°C and 15 m^3/h. The cooling system is rated to absorb 150 kW with a return temperature of 37°C. The pumping is provided by two redundant pumps, 15 kW each, supplying water at a maximum pressure of 20 bar; the reference size for the piping is DN65. The demineralization of the water is achieved via two redundant cartridges located in the CV room and shielded by a 40 cm concrete wall, to allow maintenance of the rest of the equipment after their activation; the maximum conductivity of the water supplied will be 0.5 µS/cm.

6.5.3.1.7 Cooling for target helium circulation system

The primary cooling system supplies cooling to the target helium circulation system. The power that needs to be removed from the helium circulation system is expected to be less than 0.5 kW. Details of the circulation system and its cooling are provided in Section 6.5.3.2.1.

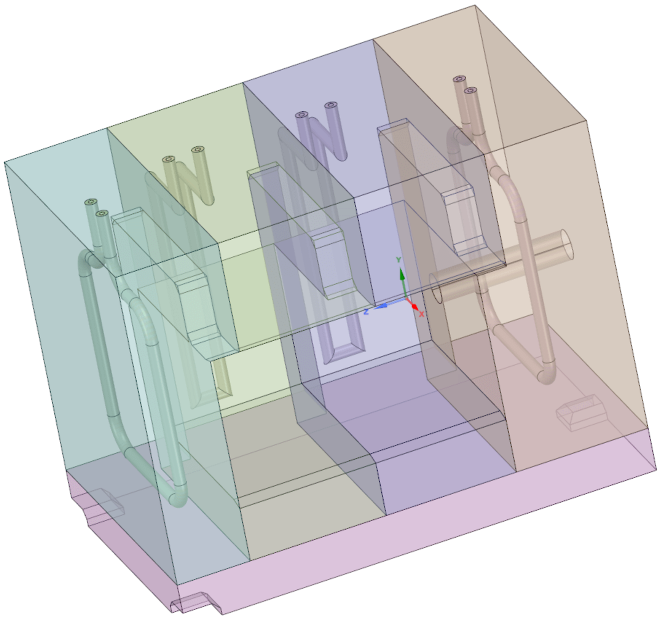

Fig. 6.157: Layout of cooling pipes inside proximity shielding blocks

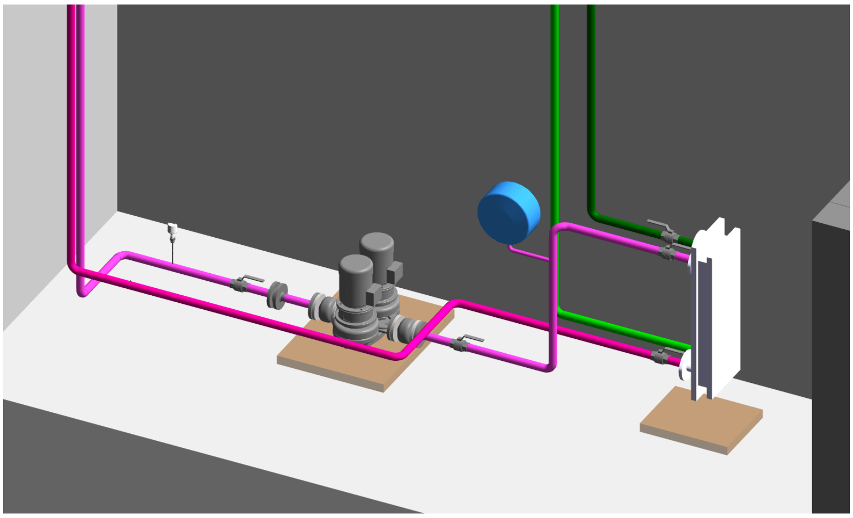

Fig. 6.158: Cooling station for proximity shielding in the CV room

6.5.3.1.8 Chilled water

Chilled water is needed in the BDF target complex building for the cooling of the helium purification system and of the ventilation units in the auxiliary building. The overall requirements in terms of chilled water for the BDF experimental area amount to roughly 750 kW maximum (Table 6.31); this chilled water will be provided by the chilled-water production plant in building BA81, which currently has enough margin to accept this load. If this margin is reduced in the future, a new chilled-water plant will need to be provided in the BDF auxiliary building, supplying chilled water for the entire experimental area.

Of the total amount of chilled-water cooling (750 kW), about 135 kW (corresponding to 29 m^3/h of chilled water at 6–10°C) is needed for the cooling coils of the three AHUs for the BDF target complex

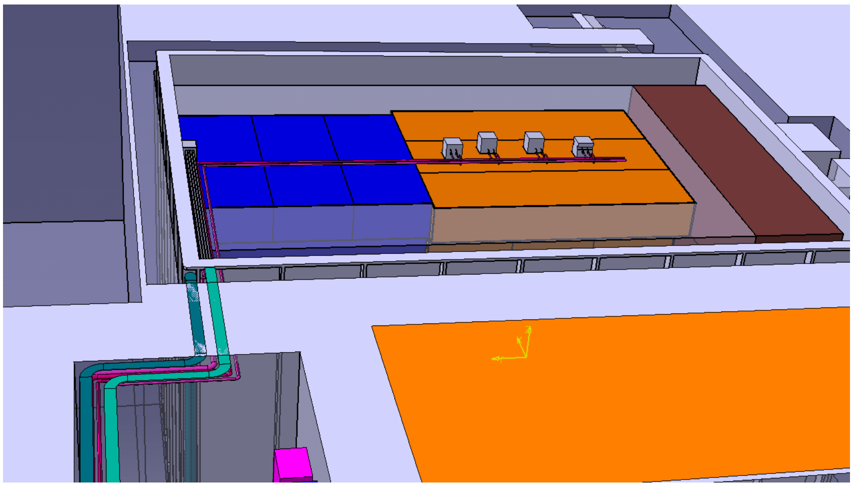

Fig. 6.159: Cooling connections for proximity shielding on top of bunker shielding

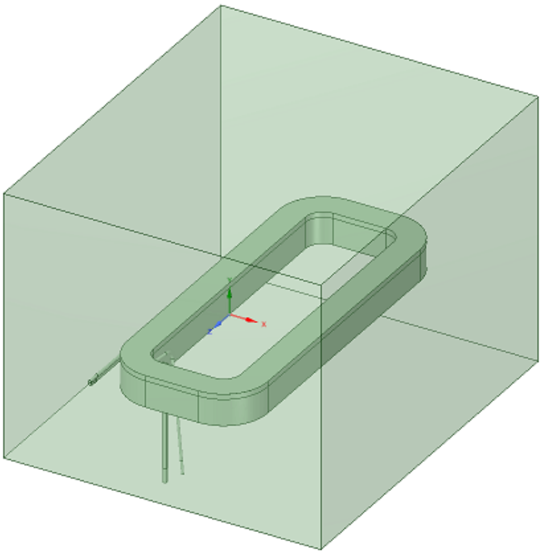

Fig. 6.160: 3D model of muon shield magnet downstream of target

(located in the auxiliary building) and the helium purification system (located in the CV room).

6.5.3.2 Helium systems

The BDF target complex uses two helium systems for cooling, passivation, and monitoring purposes:

- the target helium circulation system (Section 6.5.3.2.1): this system, located on the trolley, is used to flow helium around the target (through the external shell of the target) to detect any leak or release of activated gas from the target containment;
- the helium passivation system (Section 6.5.3.2.2): this system, located in the CV room, is used to cool and purify the helium flowing through the helium vessel.

6.5.3.2.1 Target helium circulation

The helium circulation system for the target blows helium around the target containment in order to make it possible to detect any potential leak from its containment. Figure 6.162 shows the layout of the main components of the circulation system skid, positioned on the trolley; a preliminary P&ID for the system

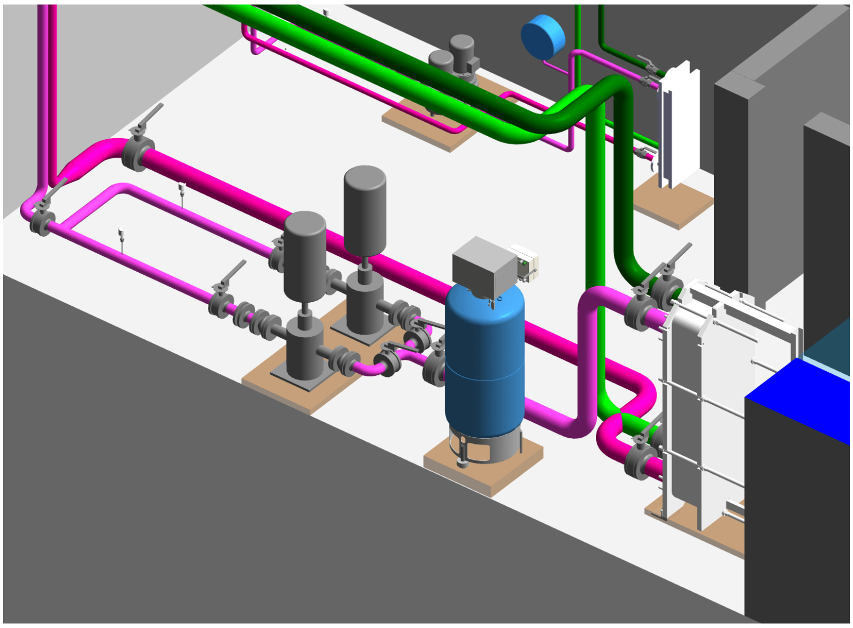

Fig. 6.161: Cooling station for magnetic coil in CV room

is provided in Ref. [27]. Table 6.33 shows the main design parameters for the system.

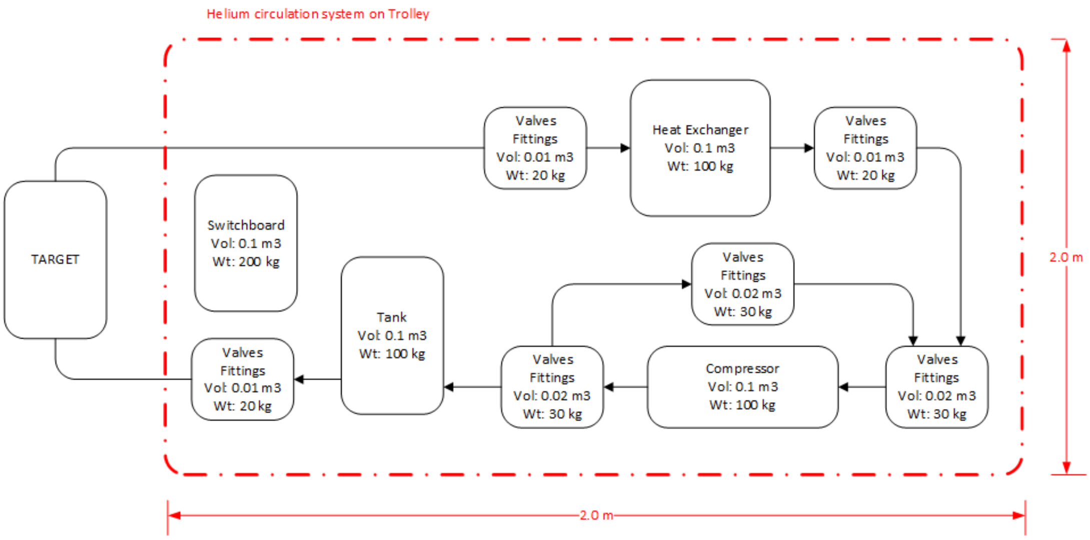

Fig. 6.162: Layout of helium circulation system for target

The main components of the system are a compressor, a helium storage and pressurization tank (positioned immediately after the compressor), and a heat exchanger on the return line. This heat exchanger transfers the heat to the primary circuit.

The target helium circulation system supplies 4.1 g/s of helium at nearly atmospheric pressure; the compressor is sized to overcome a pressure drop of 6000 Pa. The maximum power that can be removed by the system is about 500 W, assuming a maximum temperature for the target containment of 50°C; note that no simulations have been run yet on the helium circulation through the shell, and so this assumption will have to be analysed more deeply at the detailed design stage. In any case, the purpose of the system is primarily helium circulation, and not cooling, so a higher or lower equilibrium temperature for the helium in the target shell is acceptable. The size of the skid is expected to be about 2 m (length) $\times$ 2 m

Table 6.33: Design parameters for the helium circulation system. The system is designed for a maximum flow rate of 4.1 g/s and a thermal power of 500 W.

Parameter	Units	Value
Location	–	Trolley
Flow rate	g/s	4.1
Changes per hour	h^{-1}	1000
T_{in}	°C	28
$T_{\text{out max}}$	°C	50
ΔT_{max}	°C	22
Thermal load	kW	0.5
Piping size	–	DN25
Pressure supply	bar	1.1
Pressure drop	Pa	6000

(width) × 1.5 m (height), resulting in a volume of 6 m^3 and a maximum weight of 1300 kg.

The helium circulation system is cooled via primary raw water at 25°C. The water is supplied by the same primary piping as that connected to the primary side of the heat exchanger of the target secondary circuit (Fig. 6.155); a regulation valve allows one to set the desired flow in this bypass line. Table 6.34 shows the main parameters of the water-cooling circuit.

Table 6.34: Water-cooling specifications for the helium circulation system

Parameter	Units	Value
Location	–	Trolley
T_{in}	°C	25
T_{out}	°C	25.4
ΔT_{max}	°C	0.4
Flow rate	m^3/h	1.1
Piping size	–	DN15
Thermal load	kW	0.5
Type	–	Raw water
Activation	–	No

6.5.3.2.2 Helium passivation system

The helium passivation system supplies purified helium to the helium vessel that contains the BDF target and its shielding; its primary purpose is to remove impurities from the gas mixture so that it is not activated and remains inert from a chemical standpoint. A complete description of the system is provided in Section 6.4.4. Its cooling layout is shown in the preliminary cooling synopsis [24]; Section 6.4.4 provides a preliminary P&ID for the system, and a preliminary integration model is available in Ref. [26].

6.5.3.3 Ventilation systems

6.5.3.3.1 General description

The design approach for the ventilation system was based on the radiation protection and thermal requirements presented in Section 6.5.2.3, and the sizing of the ventilation flow rates was performed in such a way that adequate dynamic confinement and heat removal can be provided. The number of ventilation units was defined based on the number of radiation protection classes involved in the building design (C1/C2) and the position of the rooms to be ventilated (surface or underground). The following three units are needed for ventilation of the target complex:

– surface hall ventilation (C1, on surface): ventilation of surface hall;
– access area ventilation (C1, underground): ventilation of staircases and manipulator rooms;
– hot-area ventilation (C2, underground): ventilation of CV room, trolley, and helium vessel areas.

Figure 6.164 provides a schematic illustration of the ventilation units and their characteristics, and Fig. 6.163 shows a preliminary integration of the ducts within the target complex. All AHUs for the BDF target complex are located in the auxiliary building, as shown in Fig. 6.165.

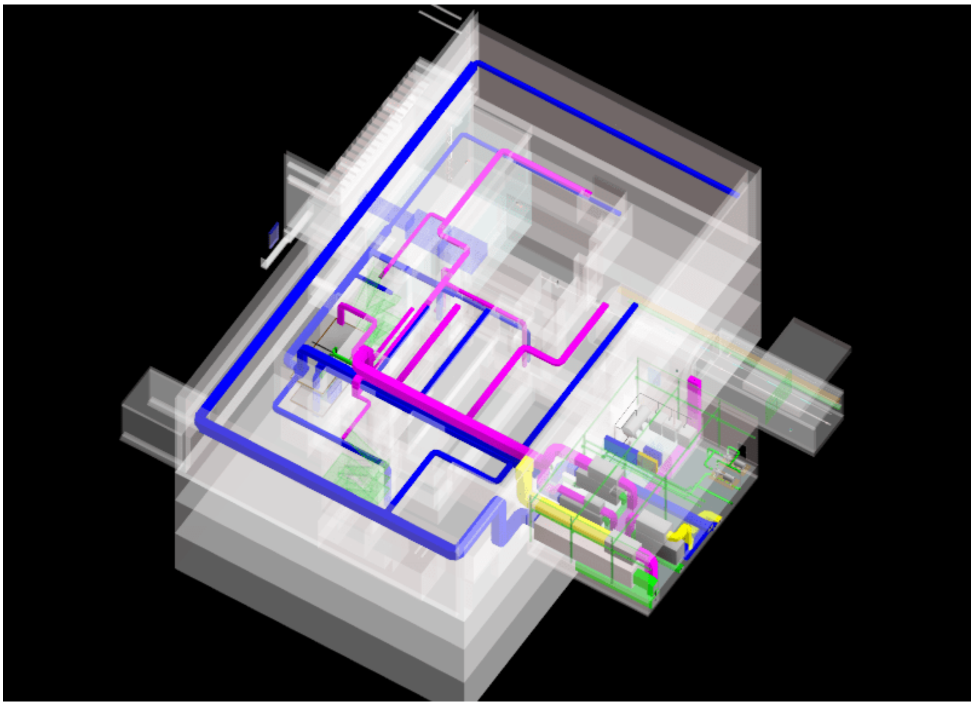

Fig. 6.163: Overview of the ventilation ducts in the target complex building. Blue ductwork represents supply lines, purple ductwork represents extraction lines, and yellow ductwork represents recirculation lines.

A pressure cascade was defined according to the radiation protection requirements listed in Section 6.5.2.3. To maintain the underpressure in each room, it is necessary to have an extraction flow rate that compensates air leaks into the room from higher-pressure levels and from the outside environment. For sizing purposes, it was assumed that the permeability (at 50 Pa) through the walls (both internal and external) of the target complex was equal to 5 $m^3/h/m^2$; the actual value of the permeability will be determined by several factors, mainly the civil engineering design, and will be estimated with more precision in a detailed design phase. In order to be conservative, outgoing leakage (on interfaces where the outside pressure is lower than the inside pressure) has been neglected. The incoming leakage flow rate was calculated for each room in the target complex from the permeability, the pressure distribution determined by the pressure cascade, and the surface area of the walls; the resulting incoming leakage flow rates are listed in Table 6.35. The leakage flow is the minimum air flow rate that needs to be extracted from each volume to maintain the underpressure.

The underpressure set-point for the surface hall is not large (-20 Pa), but, since the surface area of the walls is large, the leakage flow rate is consistent with the supply flow. The hot area also has a consistent leakage flow rate, caused instead by the stronger depressurization value (-80 or -100 Pa).

Table 6.36 summarizes the minimum flow rates for each ventilation system deriving from RP requirements and dynamic confinement considerations.

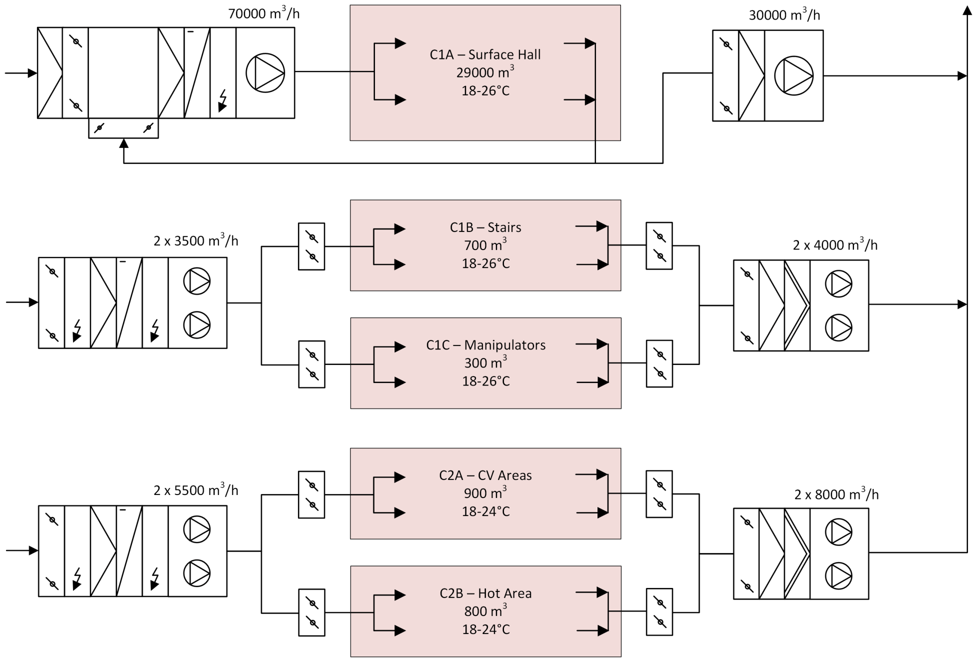

Fig. 6.164: Schematic illustration of ventilation system for the target complex

Table 6.35: Minimum RP flow and leakage flow for each RP subclass

RP subclass	AHU	Underpressure (Pa)	Min. RP flow (m^3/h)	Leakage flow (m^3/h)	Leakage/min. RP flow (%)
C1A	Surface hall	−20	28 786	13 884	48
C1B	Access area	−40	1 236	163	13
C1C	Access area	−60	1 166	206	18
C2A	Hot area	−80	1 803	644	36
C2B	Hot area	−100	3 731	1 770	47

Table 6.36: Minimum supply and extraction flows based on RP requirements

AHU	Min. supply flow (m^3/h)	Min. extraction flow (m^3/h)
Surface hall	28 786	13 884
Access area	2 403	369
Hot area	5 534	2 413

The RP preliminary requirements were used as a starting point for the thermal calculations needed to size the ventilation system. The outdoor design conditions for the Geneva region, defined by the standards and used for the sizing of the air-handling units, are presented in Table 6.37. These values are to be understood as mean-value maxima (95% percentile) for calculation and sizing purposes only. Values outside the range can be observed for short periods of time.

The ventilation units were sized based on the worst cooling and heating conditions in winter and summer; the heat loads for the two conditions were calculated from the temperature requirements (Table 6.27), the internal heat dissipation (Table 6.28), and the outdoor conditions (Table 6.37). Table 6.38 shows the total heat loads in winter and summer for each ventilation area.

The sizing of the ventilation units based on these heat loads is described in Section 6.5.3.3.3 (surface hall), Section 6.5.3.3.4 (access area), and Section 6.5.3.3.5 (hot area).

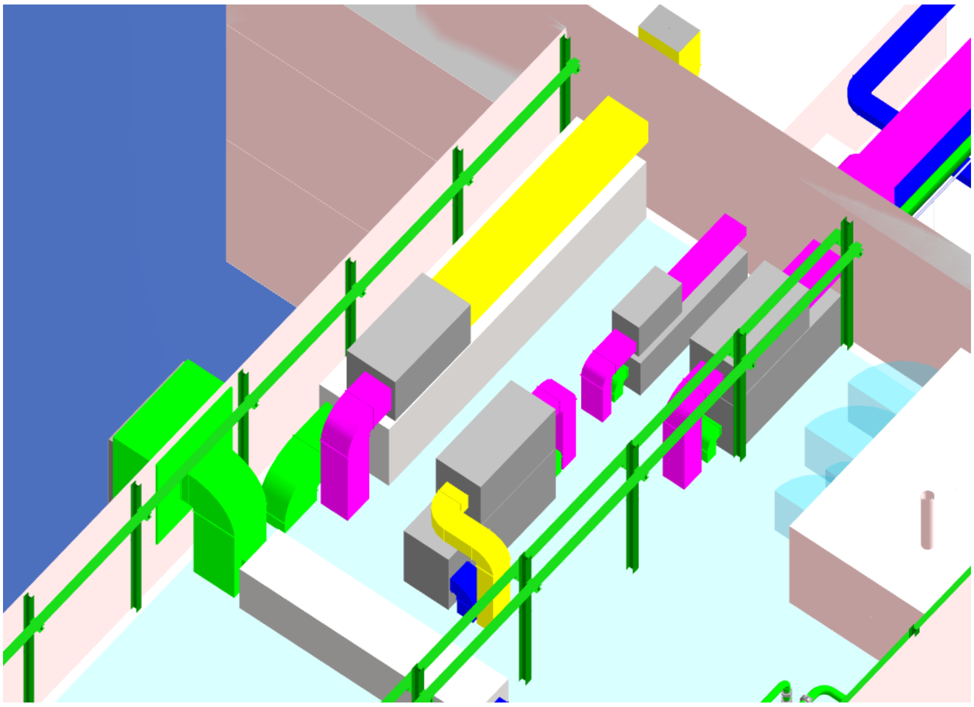

Fig. 6.165: Layout of ventilation units in a dedicated area of the auxiliary building, including all ventilation units for the target complex, the auxiliary building, and the extraction tunnel.

Table 6.37: Reference outdoor conditions for design of ventilation systems in winter and summer in the Geneva area. Actual conditions may be out of this range for a limited time during the year.

Season	Winter	Summer
Dry bulb temperature	−11°C	32°C
Relative humidity	90%	40%
Soil temperature	13°C	17°C

Table 6.38: Overall (internal + external) heat loads for ventilation areas

Ventilation area	Min. heat load (winter) (kW)	Max. heat load (summer) (kW)
Surface hall	−158	62
Access area	−104	−84
Hot area	−10	7

6.5.3.3.2 Piping and instrumentation diagram and synopsis for ventilation

Figure 6.164 shows a schematic illustration of the ventilation system for the target complex. The ventilation of the target complex is provided by three ventilation units. These units share a common fresh air inlet and discharge exhaust air to a shared stack, located in the proximity of the auxiliary building.

The surface ventilation unit takes advantage of recirculation to minimize energy loss. The underground units instead use 100% fresh air, which helps to remove activated components from the ventilation volumes. The two ventilation units for the underground areas each have two pressure levels; automatic dampers will be used to regulate the underpressure in different rooms on each ventilation line.

The following documentation on the BDF ventilation has been developed:

– a preliminary ventilation synopsis [28];

– a preliminary P&ID for each ventilation unit [29];
– a preliminary 3D integration [26].

6.5.3.3.3 Surface hall ventilation

The preliminary P&ID for the surface hall ventilation unit is provided in Ref. [29]. Supply and extraction units are located in the BDF auxiliary building and supply/extract air to/from the surface hall via ductwork. Air is supplied to the surface hall via distribution ducts, whereas the extraction is localized at a single extraction grille in the proximity of the wall that separates the hall from the auxiliary building. Since the volume and the heat loads are large, recirculation is used to minimize energy loss; a minimum amount of fresh air is supplied to maintain optimal conditions. In the worst winter conditions, 70 000 m^3/h of air at 29°C are supplied to maintain at least 18°C in the hall; this compensates for both the heat loss (-158 kW) and the infiltration due to depressurization (14 000 m^3/h at -11°C). The extraction unit extracts at least 14 000 m^3/h to maintain -20 Pa inside the hall. The supply unit needs a 256 kW heating coil to treat the recirculated air. In the worst summer conditions, 40 000 m^3/h of air at 17°C maintain the average temperature in the surface hall below 26°C (accounting for 14 000 m^3/h infiltration at 32°C). The cooling coil needs to be sized for 98 kW.

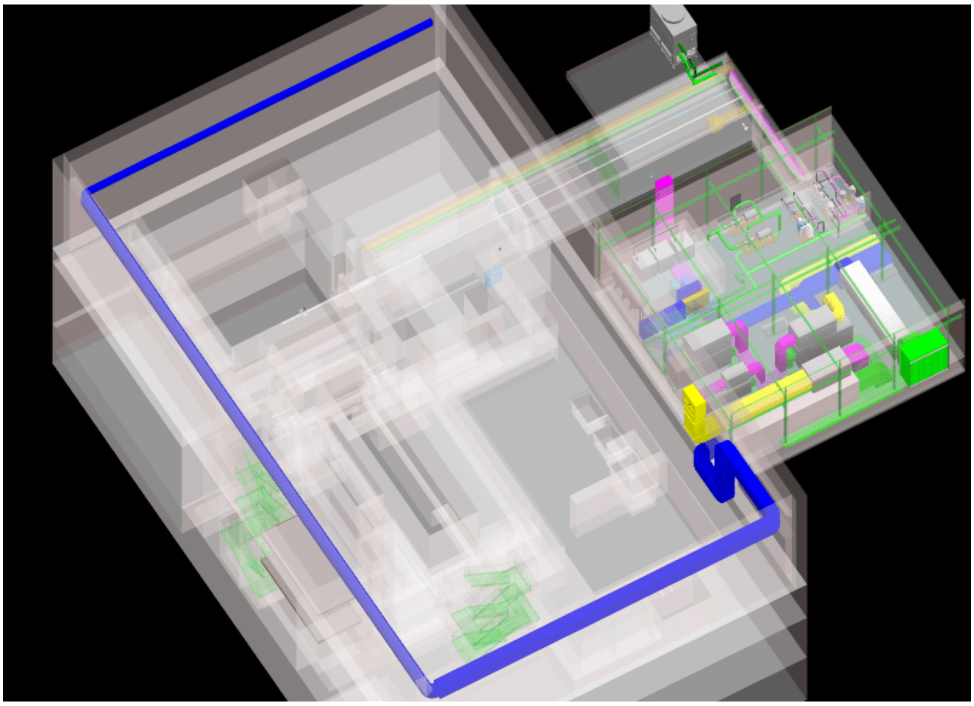

Fig. 6.166: Preliminary integration of surface hall ventilation. The supply duct is shown in blue; air is extracted at a grille in the proximity of the separation wall with the auxiliary building.

The layout of the ducts is shown in Fig. 6.166, and the main parameters of the supply and extraction units are shown in Table 6.39. The extraction flow rate is sized as two times the expected infiltration flow rate to allow some margin for pressure regulation; this margin on the extraction flow can also be used to accelerate the air change rate in the hall and reduce the waiting time before personnel are able to access the area because of air activation.

6.5.3.3.4 Access area ventilation

The access area includes three staircases and two areas for manipulators. The preliminary P&ID for the access area ventilation unit is provided in Ref. [29]. The layout of the ducts is shown in Fig. 6.167, and the main parameters of the supply and extraction units are shown in Table 6.40.

Table 6.39: Parameters of surface hall ventilation unit

Parameter	Units	Value
Supply AHU flow	m^3/h	70 000
Extraction AHU flow	m^3/h	30 000
Supply fan power	kW	27
Extraction fan power	kW	12
Reference duct diameter	m	1.76
Preheat (30% flow) power	kW	100
Heating coil	kW	250
Cooling coil	kW	−100

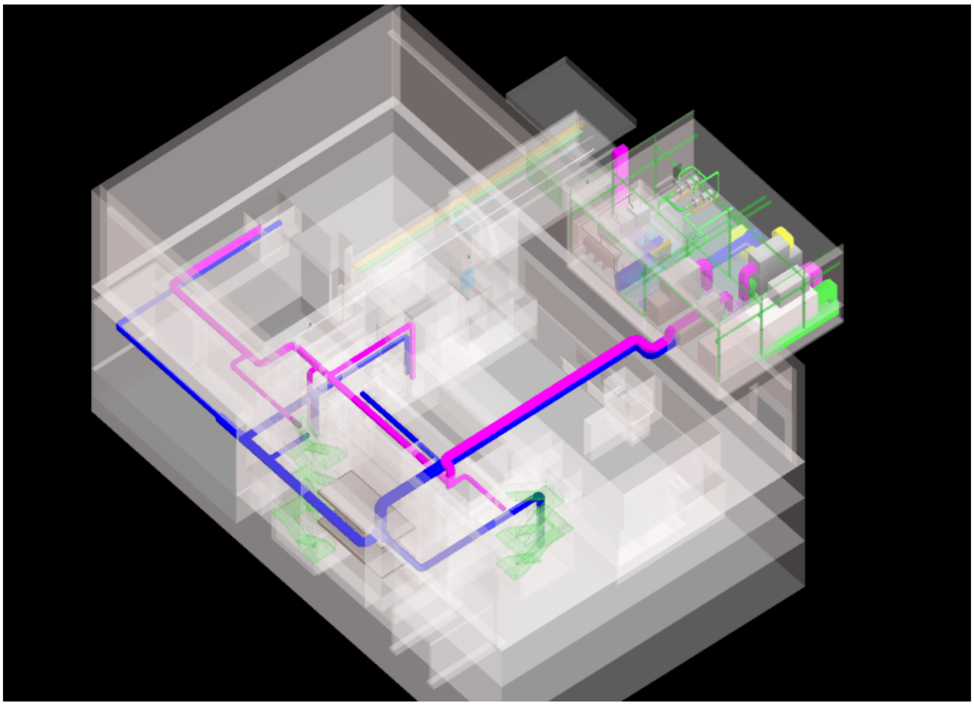

Fig. 6.167: Preliminary integration of access area ventilation. Supply lines to staircases and manipulator areas are shown in blue, and extraction lines are shown in purple.

The supply and extraction units for this ventilation area are located in the auxiliary building. The supply and extraction flows are 3500 and 4000 m^3/h, respectively; the infiltration leakage due to depressurization amounts to about 500 m^3/h under nominal conditions. The ventilation system does not feature recirculation, so that activated air can be immediately extracted and exhausted to the atmosphere. In the worst winter conditions, air is supplied at 27°C and extracted at 19°C. In the worst summer conditions, since these rooms are located underground and do not have a major heat load, about 10 kW of cooling capacity is needed to maintain the temperature in the rooms below 24°C. Table 6.40 lists the heating and cooling power for the ventilation unit.

6.5.3.3.5 Hot-area ventilation

The hot-area ventilation unit supplies ventilation to the CV areas, the trolley, the helium vessel, and part of the storage area. The preliminary P&ID for the hot-area ventilation unit is provided in Ref. [29]. The layout of the ducts is shown in Fig. 6.168, and the main parameters of the supply and extraction units are shown in Table 6.41.

Table 6.40: Parameters of access area ventilation unit

Parameter	Units	Value
Supply AHU flow	m^3/h	3500
Extraction AHU flow	m^3/h	4000
Supply fan power	kW	1.5
Extraction fan power	kW	2.0
Reference duct diameter	m	0.4
Preheat (100% flow) power	kW	20
Heating coil	kW	30
Cooling coil	kW	-10

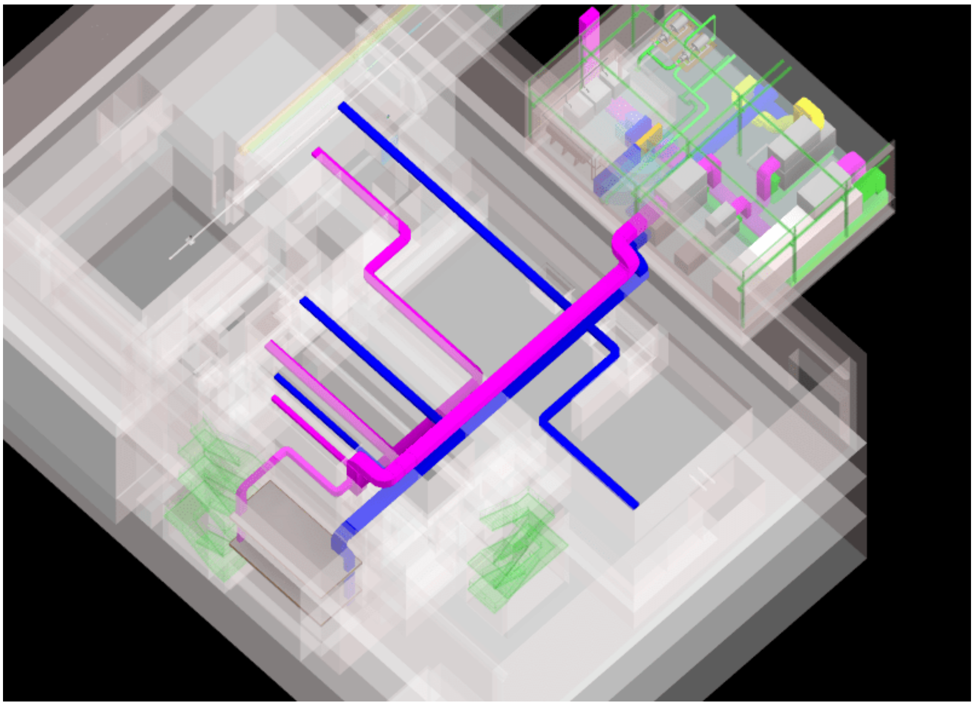

Fig. 6.168: Preliminary integration of hot-area ventilation. Blue ducts are supply lines, and purple ducts are extraction lines.

The structure of the hot-area ventilation is similar to that of the access area ventilation. Since the depressurization is higher, the leakage rate is expected to be about 2500 m^3/h; the supply and extraction flow rates are 5500 and 8000 m^3/h, respectively. The air is not recirculated through the unit, so that activated air is directly discharged to the atmosphere. In the worst winter conditions, air is supplied at 26°C and extracted at 20°C; in the worst summer conditions, air is supplied at 20°C and extracted at 24°C.

6.5.3.3.6 Smoke extraction system

The design of the smoke extraction system for the BDF target complex needs to take into account the fact that the smoke can potentially contain activated gases that should not be released to the environment without proper treatment. Moreover, the operation of the smoke extraction system should not compromise the pressure cascade determined by the ventilation system, so that flow of activated smoke from contaminated areas to non-contaminated areas is prevented. In a fire scenario, the pressure levels can be changed, but the ranking of the areas within the pressure cascade needs to be maintained.

Table 6.41: Design parameters for hot-area ventilation unit

Parameter	Units	Value
Supply AHU flow	m^3/h	5500
Extraction AHU flow	m^3/h	8000
Supply fan power	kW	2
Extraction fan power	kW	3
Reference duct diameter	m	0.5
Preheat (100% flow) power	kW	30
Heating coil	kW	40
Cooling coil	kW	−25

In this context, two different approaches are used for the underground areas and for the surface hall.

The approach for the underground areas is based on shutting off the air supply and letting the fire consume the oxygen in the room as much as possible, potentially until the fire is checked. In the case of fire in one of the underground areas, the supply fire damper closes and the corresponding extraction damper and fan are regulated to maintain the underpressure in the room. If the fire is extinguished, after cool-down and an RP activation check, the smoke can be extracted by the ventilation unit. Instead, if the temperature at the top of the room exceeds 300°C or the exhaust air filtration capability is lost, the extraction fire damper needs to be closed; in this situation, no air is extracted from the room and confinement is lost. To implement this method, all supply and extraction ducts for the underground areas are provided with fire dampers and flow regulation dampers.

For the surface hall, the method implemented for the underground areas cannot be considered, owing to the large amount of air and oxygen in the room. Moreover, since the area is classified and its air requires filtration before being released, natural circulation via skydomes is not applicable. Forced ventilation is needed via smoke extractors; the surface area of the hall is approximately 19 000 m^2, requiring a nominal flow rate for the smoke extractors of 70 000 m^3/h.

6.5.3.4 Rising system

6.5.3.4.1 Overview and layout

The purpose of the rising system is to pump the drain and waste water from the sump area to the surface, to allow its disposal after its activation has decreased below safety limits. Two sumps are foreseen to be included in the target complex, one for the trolley and helium vessel area, and another for the CV room and the rest of the building. Figures 6.169, 6.170, and 6.171 show a preliminary integration for the sump system.

6.5.3.4.2 Description of rising system

The preliminary cooling synopsis [24] and the preliminary P&ID [25] include the layout and components of the rising system. This system is designed to collect any water leaking from the three secondary circuits and any potential infiltration.

The drainage of leaks inside the helium vessel is done by gravity via a pneumatic valve activated by a water leak detector. The detector and valve system is located in a dedicated separation tank next to the sump tanks. The pneumatic valve opens whenever a leak is detected and discharges the water to the sump; during normal operation, the valve is closed and maintains a separation between the helium and the air in the sump.

The sump tanks are provided with a flood detector and a level detector, and two redundant sump

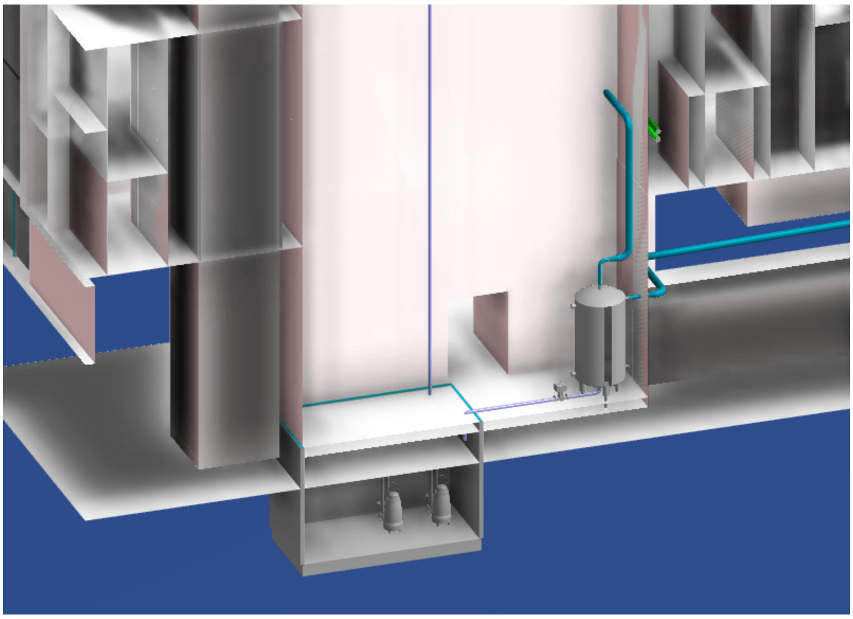

Fig. 6.169: Preliminary integration of rising system in sump area

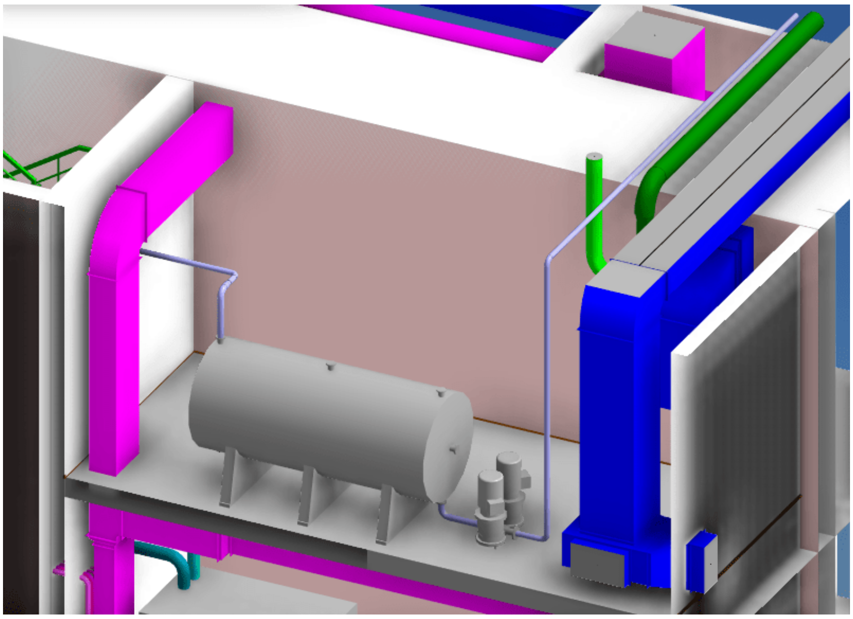

Fig. 6.170: Preliminary integration of intermediate storage tank in CV room

pumps that pump the water to the surface. The sump pumps will provide a flow rate of 15 m^3/h and a minimum pressure head of 3 bar; this flow rate allows moving 2.5 m^3 of water from the sump tanks to the storage tanks in the evaporator room in roughly 10 min.

To allow maintenance of the pump motors without having to physically enter the sump tanks, where the expected dose is high, the sump pumps are provided with an auto-coupling mechanism.

After a decay time determined by RP considerations, the water is pumped to the surface, where it is stored in two redundant storage tanks, of size 5 m^3 each; subsequently, the water is treated according to RP indications.

Two evaporation units are foreseen in the evaporator room, of type ENCON Drum Dryer; these units are provided with a mixer, a mist eliminator, and a power and control cubicle, and can produce a

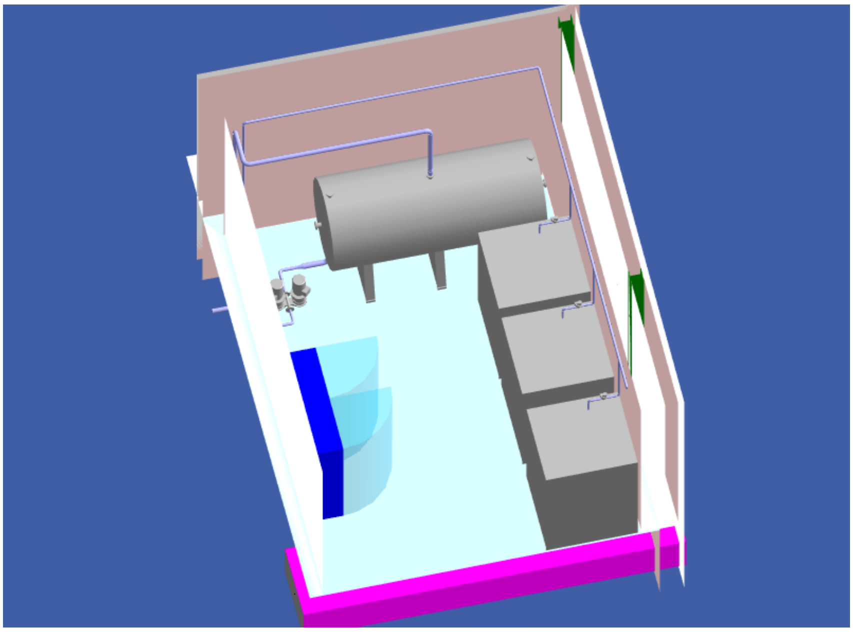

Fig. 6.171: Preliminary integration of evaporator room, including three evaporation units

volumetric air flow of 200 m^3/h. To minimize recondensation of water at the evaporator exhaust, the installation of a ventilation unit will be investigated, specifically dedicated to the evaporator air flow.

Since the evaporator room contains activated components and water, it is provided with shielding to reduce the dose to the outside environment.

6.5.3.5 Electrical and control system

6.5.3.5.1 General description

The electrical and control system for the CV system involves the installation of power and control cubicles in the target complex and auxiliary building. A preliminary sizing has been performed for the target complex components. The installation of sensors and control components in the target complex rooms needs to take account of the expected dose in order to prevent component failure due to radiation. The dose is expected to be low everywhere in the target complex, except in the helium vessel; the most critical area for sensors and control components, in terms of radiation dose, is the trolley area, followed by the CV room. For this reason (and for maintenance/access reasons), control components should be placed in the service area in the auxiliary building, and in the target complex CV room only if strictly needed.

6.5.3.5.2 Integration of electrical cubicles

Figure 6.172 illustrates a preliminary integration of the target complex CV cubicles. The installation is based on an ABB switchboard (5.8 m (width) × 2.37 m (height) × 0.6 m (depth)) located in the service room. The following cubicles are also foreseen in the pre-design:

- cooling systems: all pumps are provided with a variable-frequency drive and a related cubicle (0.3 m (width) × 0.9 m (height) × 0.4 m (depth)); a control cubicle is also foreseen (3.2 m (width) × 2.0 m (height) × 0.4 m (depth));
- ventilation systems: all supply and extraction units are provided with a variable-frequency drive cubicle (0.3 m (width) × 0.7 m (height) × 0.3 m (depth)); all preheating and post-heating coils are provided with a thyristor cubicle (0.6 m (width) × 0.6 m (height) × 0.4 m (depth)); all supply–

extraction unit pairs are provided with a control cubicle (1.6 m (width) × 2.0 m (height) × 3.4 m (depth)).

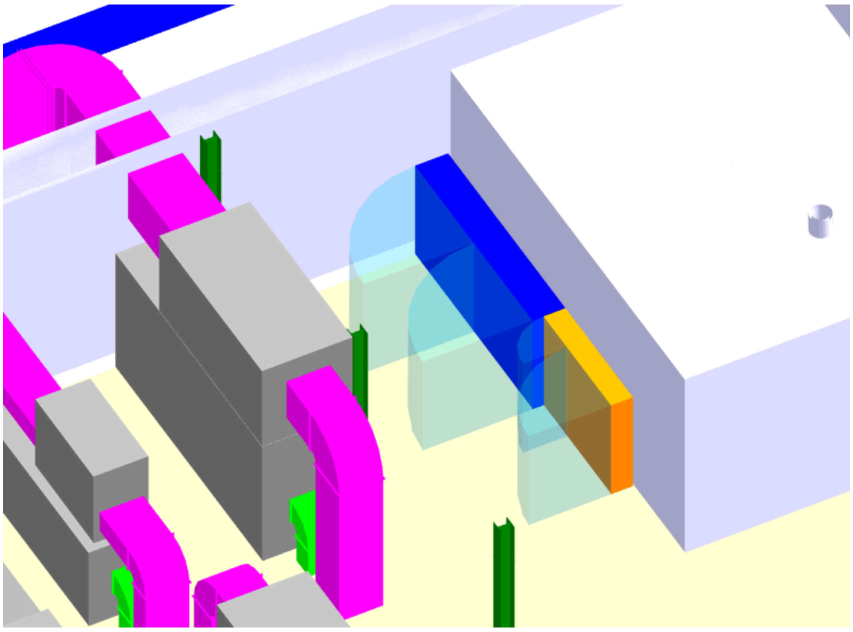

Fig. 6.172: Preliminary integration of electrical cubicles for the target complex services

6.6 Safety considerations for the BDF target complex: identification of main hazards in the target complex and risk assessment

The objective of the hazard identification study was to identify the principal possible failure scenarios related to process control within the target and the target complex, and to suggest possible mitigation measures to the management of the BDF project. The decisions taken on the suggested mitigation measures were considered as an input by the team in charge of safety system engineering, for both the underground and the surface parts of the complex. The hazard identification study was focused on areas accessible to personnel. Details of the study are presented in Tables 6.42–6.52.

Table 6.42: Hazard identification study for the target and target complex, 1

Location	Equipment and operations	Hazardous situation	Causes	Consequences	Existing barriers	Recommendations
Surface building/ building crane SB_BC_Hz1	For the crane concept, for repair/replacement of the target using the building crane, the sequence of component removal from the helium vessel is as follows: (1) He vessel lid; (2) mobile shielding; (3) proximity shielding; (4) target.	Building crane (40 t) gets stuck once floor shielding has been removed.	Failure of electrical supply/motor. Mechanical obstruction.	Radiation (a few microsieverts per hour) in the area due to activated materials present underground [2].	Fence the area. Definition of operational safety procedures. Shielded transfer cask (iron) used for transfer of target from helium vessel to cool-down area.	Full redundancy to be provided: double electrical circuit. Access control system: fence and restrict access to building. Interlock access to the area with the target exchange procedure. Local evacuation system. Remote supervision and access management to the area by CERN Control Centre (CCC).
Surface building/ building crane SB_BC_Hz2	For the crane concept, for repair/replacement of target using the building crane, the sequence of component removal from the helium vessel is as follows: (1) He vessel lid; (2) mobile shielding; (3) proximity shielding; (4) target.	Building crane (40 t) gets stuck during the operation of target transfer from He vessel sited underground to target storage area sited on surface building.	Failure of electrical supply/motor. Mechanical obstruction.	Radiation (a few microsieverts per hour) in the area due to activated materials present underground [2].	Fence the area. Organizational measure: RP procedure. Target iron shielding cask provided, and walls around.	Full redundancy to be provided: double electrical circuit. Interlock access to the area with the target exchange procedure. Local evacuation system. Remote supervision and access management to the area by CCC. Forbid access to building roof.

Table 6.43: Hazard identification study for the target and target complex, 2

Location	Equipment and operations	Hazardous situation	Causes	Consequences	Existing barriers	Recommendations
Surface building/ floor shielding SB_FS_Hz1	Proton beam extracted from SPS and sent to the target. The shielding floor is closed.	Radiation from target pit.	Floor shielding blocks not correctly positioned. Faulty/inadequate shielding.	Elevated radiation levels. Some 5 cm gaps already foreseen in RP simulations, with acceptable radiation levels still maintained. Much higher levels would be seen if a piece of shielding were missing [2].	Definition of shielding verification procedure. DSO tests before and after any intervention on the floor shielding.	RP monitoring system activates local alarms if threshold exceeded. Interlock RP monitors with beam operations. Visual check to confirm all parts of the shielding are present should be part of the patrol before the beam can be turned on.
Surface building/ electrical room SB_ER_Hz1	A technical room is dedicated to the installation of all cabinets needed for power distribution. High-tension and high-current devices are located in this area. Maintenance procedures may imply removal of several protection components.	Exposure to high current/voltage of untrained people present in the area during co-activities. The magnetic coil is expected to be the only high-voltage circuit in the area.	Electrical cabinets with door open (maintenance operation: removal of IP3X protection).	Electrical contact (skin burns). Serious injuries. Death.	IP3X protection. French regulation/ standard. CERN Code C1.	Training and certification of people who have to intervene in such electrical cabinets. Only trained and certified people have authorization to open an electrical-cabinet door. Otherwise, keep the door closed. Interlock access to electrical room for power to magnetic coil during hazardous maintenance operations.

Table 6.44: Hazard identification study for the target and target complex, 3

Location	Equipment and operations	Hazardous situation	Causes	Consequences	Existing barriers	Recommendations
Surface building/ roof SB_Ro_Hz1	Maintenance operation on target. Opening of floor shielding.	Someone present on roof during target exchange.	Work planed on roof when floor shielding is removed or during target exchange. Intrusion.	Exposure to radiation from remote handling of activated materials.	Owing to the distance (15 m), even if the target is exchanged, the shielding is sufficient to have a supervised area.	Padlock ladders, controlled by IMPACT in conjunction with RP.
Hot cell area/trolley HC_Tro_Hz1	For trolley concept, the initial operation is to remove the trolley from the He vessel by withdrawing it along rails into the hot cell and trolley service area. The target and services are located on the trolley on rails.	Trolley immovable. Trolley fails to stop.	Issue with rails. Broken wheel. Motor failure.	Damage to trolley should it fail to stop. Trolley stuck without remote handling access.	Easy access for visual inspection (containment between services which are personnel-accessible areas and hot cell area). Motor/drive chain designed to overcome friction of seized-wheel condition. Target is removed and then wheel is replaced.	Compliant buffers at each end to cushion movement. Speed kept to a minimum. Dual brakes can be considered/located in personnel-accessible area. Define clear recovery procedure. Trolley drive mechanism should be capable of manual override, so that it can be driven into hot cell in the event of a malfunction.

Table 6.45: Hazard identification study for the target and target complex, 4

Location	Equipment and operations	Hazardous situation	Causes	Consequences	Existing barriers	Recommendations
Hot cell area/ Master–Slave Manipulator (MSM) arms HC_MSM_Hz1	The two MSM slave arms can be disconnected from the hot cell side in the case of failure or required maintenance. The arms can be exported from the hot cell using the target export route (used to import and export equipment into and out of the hot cell), and a new one can be imported in a similar way and installed using the hot cell crane.	The two MSM arms fail at the same time (highly unlikely). MSMs become blocked. To repair them, the MSMs have to be removed through the shielding wall into the operator area.	Failure of electrical supply/motor. Mechanical obstruction.	Radiation in operator area from MSM arm. Contamination of the operator zone.	The MSM system has been designed to allow extraction of the MSM without having people enter the hot cell. The MSMs have detachable slave arms which allow them to be lifted off through tubes that pass the mechanical drives from the master arms through the shielding wall. This lifting will be done via the hot cell crane.	Implement special access modes during this procedure. RP procedure with decontamination before allowing access (ensuring distance between activated components and personnel).
Hot cell area/ hot cell crane HC_Cr_Hz1	The hot cell includes a 3 t crane, which is capable of lifting the target from the trolley and assisting the MSMs in lifting and moving heavier items around the hot cell. The crane will be recoverable from failure but maintained during manned access to the hot cell.	Hot cell crane is blocked during repair/replacement of target or before starting repair/replacement of target.	Failure of electrical supply/motor. Mechanical obstruction.	During remote handling operation, increase in radiation level due to remote handling operation becoming stuck while radioactive object is lifted (highly unlikely).		Full redundancy to be implemented: double electrical circuit.

Table 6.46: Hazard identification study for the target and target complex, 5

Location	Equipment and operations	Hazardous situation	Causes	Consequences	Existing barriers	Recommendations
Hot cell area/helium connections HC_HeC_Hz1	Helium connections removed by MSM slave arms.	Helium leak.	Human error/bad manipulation during disconnection operation. Obsolescence of connections.	Helium release (asphyxiation).		Oxygen Deficiency Hazard (ODH) alarm to be provided (ODH risk assessment). Self-rescue mask needed for people who have to intervene. Check He connections (integrity management programme).
Hot cell area/water connections HC_WC_Hz1	Water connections are unclamped from Grayloc connectors using the extension screw and remote handling unbolting tool (bolt runner tool).	Leak of activated water.	Bad manipulation to unclamp.	Activated water in sump.	Grayloc connector (fully metallic seals, operating in elastic domain, allowing seal to be re-used). Double-walled sumps. Facility to pump fluids from sumps via a filter to a containment area in the target hall, and then to an evaporator in the service area.	During target exchange, the operator should stay inside the operator area to unclamp water connections.

Table 6.47: Hazard identification study for the target and target complex, 6

Location	Equipment and operations	Hazardous situation	Causes	Consequences	Existing barriers	Recommendations
Hot cell area/hot cell roof HC_HCroof_Hz1	Above the crane is the hot cell roof, lined to provide a containment barrier. The roof will be placed on installation and will not be removed until decommissioning, unless there are unforeseen circumstances such as replacement of the hot cell crane. Once the hot cell has been repaired/replaced, the hot cell roof is put in the same position as before repair/replacement of the hot cell crane. Then the beam is turned on.	Radiation from the hot cell roof.	Hot cell roof not placed correctly, not put exactly in the same position as before the repair/replacement of the hot cell crane.	Radiation in the area.	Procedural verification/DSO tests before turning beam on.	RP monitoring to detect if radioactive threshold is exceeded. Interlock hot cell roof with beam operations. Need to fence and restrict/forbid access + DIMR.[1]

[1]The DIMR procedure is linked to the access request (IMPACT) and concerns work in activated areas: the interventions are classified into one of three levels of concern, with the aim of limiting received doses. For the higher-level interventions, a detailed work and dose plan is made and approved before working. This procedure will be required for interventions during technical stops and during shutdowns following operation; it will also cover times during shutdowns when shielding blocks are removed, exposing activated materials.

Table 6.48: Hazard identification study for the target and target complex, 7

Location	Equipment and operations	Hazardous situation	Causes	Consequences	Existing barriers	Recommendations
Hot cell area/electric winch HC_EW_Hz1	Electric winch.	Winch not operational.	Failure of electrical system. Pulley failure.	Cask not open. Target remains lifted and radiation level increases (owing to time of lifting longer than foreseen).		Full redundancy of electric winch. Maintenance of pulleys. Fire extinguisher to be provided in operator area. Sprinklers in storage area of lower target building.
Trolley service area/cartridge TS_Car_Hz1	Cartridge with resin (currently foreseen to be Purolite NRW3240 as employed in n_TOF target). Both the National Fire Protection Association (NFPA) fire hazard rating and the Hazardous Materials Identification System (HMIS) flammability rating are 1 on a scale of 0 to 4 for this material.	Cartridge using flammable resin in contact with ignition source.	External ignition source (electrical cables beneath the trolley in the false floor).	Fire (highly unlikely)	Concrete shielding around cartridge. The resin is immersed in water, inside a stainless steel tank.	Suggested extinguishing media: CO_2, dry chemicals, water fog
Underground area/access HC_Ac_Hz1	Short access periods after beam operations.	Activation of material, water, and air due to high level of radiation during beam.	Long phases of beam operations.	Minimum 4 h to access the underground part only if it is possible to flush all air.	CCC supervision. RP access authorization procedure.	Interlock access to underground area with RP monitors.

Table 6.49: Hazard identification study for the target and target complex, 8

Location	Equipment and operations	Hazardous situation	Causes	Consequences	Existing barriers	Recommendations
Target export tunnel/'little' trolley TET_Tro_Hz1	'Little' trolley: the target export tunnel is accessed directly from the hot cell and located beneath a containment door. At the far end of the export tunnel, there is a second containment door providing access for the building crane to remove the target cask (in the trolley concept) from the export tunnel and move it to the cool-down area. A 'little' trolley and a static drive system allow the target cask to be exported via the target export tunnel.	'Little' trolley is blocked during target export operations.	Electrical failure. Static drive system fails. Issue with rails.	Impossible to export target cask into cool-down area.		Provide a redundant system. Integrity management programme for rails. Cask should be such that the dose rate outside is reasonably low.

Table 6.50: Hazard identification study for the target and target complex, 9

Location	Equipment and operations	Hazardous situation	Causes	Consequences	Existing barriers	Recommendations
Sump pumps SB_Pu_Hz1	Activated water has to be pumped out into a dedicated tank and evaporator on surface.	Stagnation of activated water in sumps + radiation.	Deficiency of pump. Failure of power supply. Pump not well designed. Evaporator not well dimensioned.	Radiation in surface building hall due to activated water in the case of a leak or the evaporator not being operational. Current estimation of 1000 l of cooling water in target circuit, 300 l in proximity shielding circuit, and 600 l in magnetic-coil circuit.	The pumps will be located outside the sump, so that they can be accessed in the case of a malfunction.	Alarm level 3. Redundancy of the system. Monitoring with interlocks to the pumps. Fence evaporator area on surface and some shielding.
CV room/compressor CV_Com_Hz1	Compressors.	Fluid leakage.	Worn, misaligned, or damaged sealing system.	Leakage of compressor fluid in CV room could pollute water in drainage system. Leakage from compressors in the exchangers to cooling water could potentially pollute the whole cooling circuit.		Consider implementation of an intermediate closed circuit between the compressor fluid and the water to the cooling towers. Consider implementation of a dual-skin system to prevent leakage even in the event of damage. Compressors should be oil-free.

Table 6.51: Hazard identification study for the target and target complex, 10

Location	Equipment and operations	Hazardous situation	Causes	Consequences	Existing barriers	Recommendations
CV room/compressor CV_Com_Hz2	Compressors.	Noise.	Compressors in operation.	Pain in ears/loss of hearing.	Compressor noise levels will be below regulation limits by design.	Earplugs/system to protect ears; these, along with appropriate signage, should be readily available for use.
CV room/motors CV_Mot_Hz1	Motors.	Hot surface, which can reach more than 80°C.	Ineffective or missing thermal insulation.	Possible burns from skin contact.	The pump motor has thermal protection, but does not have thermal insulation to prevent contact with surface.	Cage off the hazard to prevent accidental contact. Appropriate signage indicating ‘hot surface’ hazard must be in place. Training and certification of people who need to intervene.
CV room/cooling pipes CV_Pip_Hz1	Cooling pipes for the target, proximity shielding, and magnetic-coil circuits.	Leakage of cooling water.	Loss of integrity of cooling pipes.	Flooding. Activated water outside cooling-circuit piping.	Ventilation system already provided, should there be any vapour from leaked water.	Alarm/detector in case of a water-cooling leak. Automatic shut-off of beam on leak detection. Retention tank for activated water. Integrity management programme: 100% radiographic welding tests, thickness measures of pipe, pressure tests.

Table 6.52: Hazard identification study for the target and target complex, 11

Location	Equipment and operations	Hazardous situation	Causes	Consequences	Existing barriers	Recommendations
CV room/cryogenic CV_Cryo_Hz1	Cryogenic equipment for purification system.	Cold surfaces.	Ineffective or missing thermal insulation.	Possible cold burns from skin contact.		Training and certification of people who need to intervene. Appropriate signage indicating hazard must be in place. Self-rescue masks to be provided.
CV room/filters CV_Fil_Hz1	Filters: two filters at exhaust, one medium and one HEPA (according to EN 799:2012). Ventilation rate 5000 m^3/h.	Release of contaminated air into atmosphere.	Filters not well dimensioned.	Air contaminated.		Maintenance plan for filters has to be defined. Environmental monitoring must be put in place.
CV room/electrical cabinets CV_EC_Hz1	Electrical cabinets will be located in CV room.	Exposure to high current and voltage.	Electrical cabinets with door open (maintenance operation: removal of IP3X protection).	Electrical shocks and burns.	Design of cabinets to French standards and CERN code C1. IP3X protection.	Access to CV room restricted to CV operators and authorized workers.
CV room/cartridge CV_Resi_Hz1	Cartridge with resin (currently foreseen to be Purolite NRW3240). Both the NFPA fire hazard rating and the HMIS flammability rating are 1 on a scale of 0 to 4 for this material.	Cartridge using flammable resin in contact with ignition source.	External ignition source (electrical cables).	Fire (highly unlikely).		Suggested extinguishing media: CO_2, dry chemicals, water fog.

6.7 Summary of radiation protection considerations for target complex

This section summarizes the radiological assessment for the design of the BDF target complex. The high-intensity beam power deposited in the target poses challenges for radiation protection in several locations. To reduce the effects and mitigate the impact, the radiological aspects were carefully addressed at the design stage. The studies included expected prompt and residual dose rates in the various areas of the BDF target complex. The risk due to activated air and helium and the consequences of their release into the environment were also evaluated. Finally, studies on radioactive waste zoning were conducted.

The studies were based on extensive simulations with the FLUKA Monte Carlo particle transport code [30, 31] and Actiwiz 3 [32]. Figure 6.173 shows the layout of the facility as implemented in FLUKA. All studies assumed 4×10^{13} protons on target per spill (with a duration of 7.2 s) and an integrated total of 2×10^{20} protons on target over 5 yr of operation, each with 83 days of operation followed by 272 days of shutdown.

The target complex was designed under the condition that the target hall can be accessed during beam operation and be classified as a Supervised Radiation Area (<3 μSv/h) [33]. In contrast, no access during beam operation will be permitted to the underground target bunker or the experimental hall.

In addition to protection of personnel regarding prompt dose rates, considerable shielding is indispensable for reducing the residual dose rates and the environmental impact from activated air and soil, as well as for reducing radiation levels in electronics equipment. The shielding was consequently designed with the objective of keeping the various radiological hazards originating from the operation of the BDF/SHiP facility as low as reasonably possible, while taking into account the constraints from the different stages of the experiment, that is, construction, operation, maintenance, and dismantling. The configuration envisaged is such that it will avoid activation of the fixed concrete civil engineering structures, simplifying not only the dismantling of the installation but also possible changes of scope. The shielding blocks have been specially designed and optimized for remote handling, since they, as well as the target, will become highly activated. The air volumes of the facility have been minimized to reduce the production of airborne radioactivity. In the most critical area, that is, the central region around the target and the hadron absorber, the air is further replaced with a helium environment. This is motivated by the fact that pure helium gives rise only to the formation of tritium, which has a significantly lower radiological impact than the radionuclides arising from air. A pressure cascade between the various compartments of the BDF is therefore foreseen, at least during beam operation, in order to compensate for defects in the static confinement.

The prompt dose rates in the BDF target complex are depicted in Fig. 6.174. As expected, the highest dose rates can be found in the region of the target, reaching a few times 10^{12} μSv/h. They are reduced by a few orders of magnitude in the surrounding iron shielding. Above the helium vessel enclosing the shielding, the prompt dose rates amount to up to 3 mSv/h. The prompt dose rates are reduced further by the concrete shielding above, such that they drop to below 1 μSv/h in the target hall.

Figure 6.175 shows the expected residual dose rates in the BDF target complex after 1 month of cooling time. The highest dose rates can be found in the region of the target and are in the order of a few times 10^8 μSv/h after 1 month of cooling.

The air and helium activation in the target complex was evaluated assuming the maximum beam power for five operational years. When considering the accident of a helium vessel breakdown with complete mixing of activated air and helium, this would result in 2.7 CA[1] and a committed effective dose per hour of stay of 8 μSv on the top of the He vessel. This was used to define the classification of the BDF ventilation system, for which the ISO standard 17873:200 for nuclear installations was taken as a guideline for the BDF. Another important aspect, which has to be taken into account from an environmental point of view, is the activation of the water in the cooling circuits.

[1]A person working 40 h per week, 50 weeks per year with the standard breathing rate in activated air with CA = 1 receives 20 mSv.

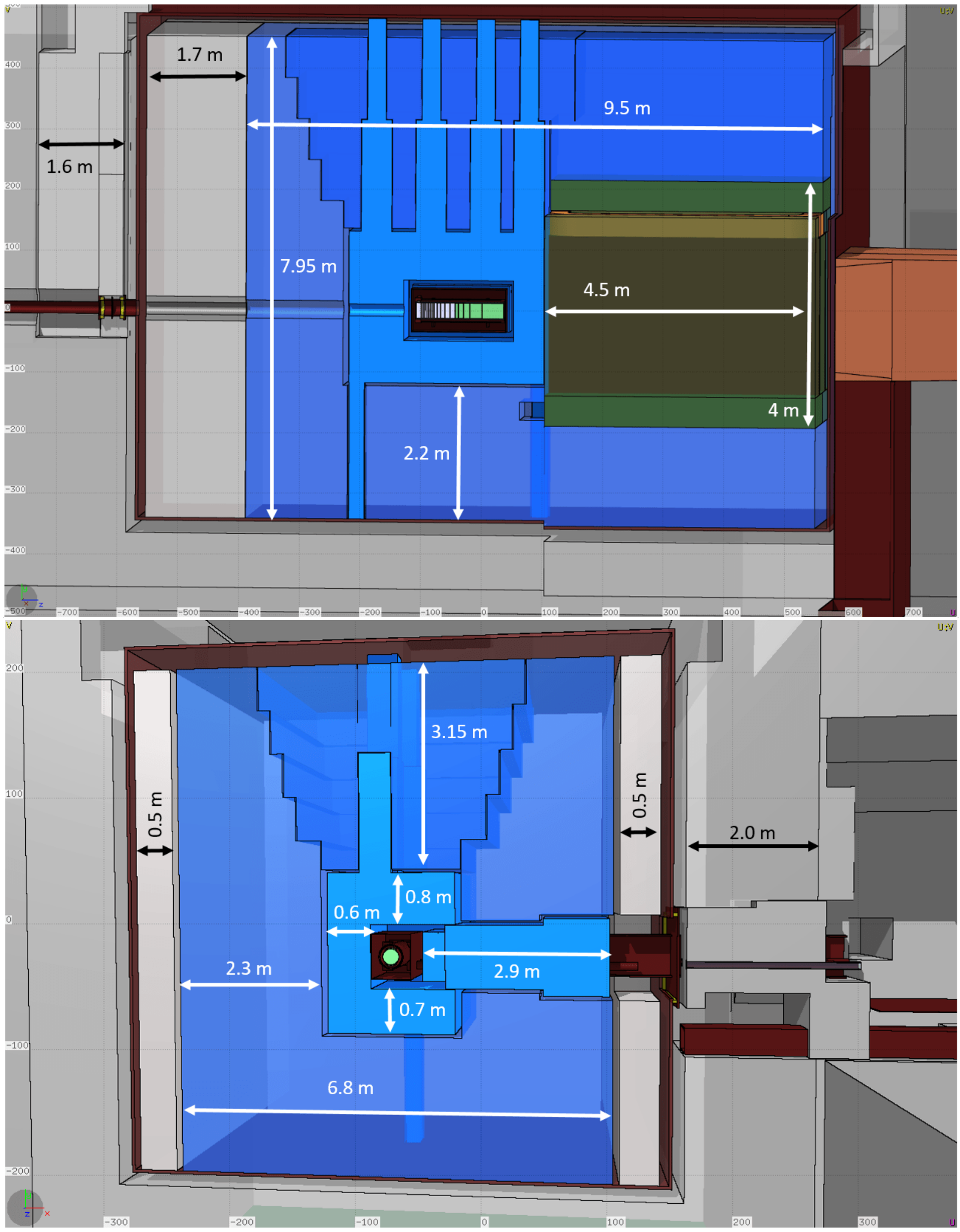

Fig. 6.173: Lateral (a) and perpendicular (b) views of the FLUKA-modelled BDF target complex for the radiation protection calculations.

The environmental impact of air and water releases was studied in detail. It was concluded that the maximum effective dose for airborne release was about 3.3 nSv/yr. The maximum effective dose for airborne release to agriculture was only about 0.2 nSv/yr. Such doses are sufficiently low that their contribution to other sources of exposure on the site (the transfer tunnels TT20, TT26, EHN1, NA62, etc.) would be low enough to fulfil the dose objective of less than 10 μSv/yr for the whole site. The annual release of tritiated water would result in an effective dose of less than 50 nSv/yr. This value is far below the dose constraint of 10 μSv/yr fixed by the Organization for new facilities.

A waste study was performed to predict the amount and characteristics of the radioactive waste that will be produced during operation of the BDF (see Fig. 6.176). The objectives of such a study were to improve the management of radioactive waste and, eventually, to reduce the overall production of radioactive waste. To distinguish areas of radioactive waste from areas of conventional waste, the

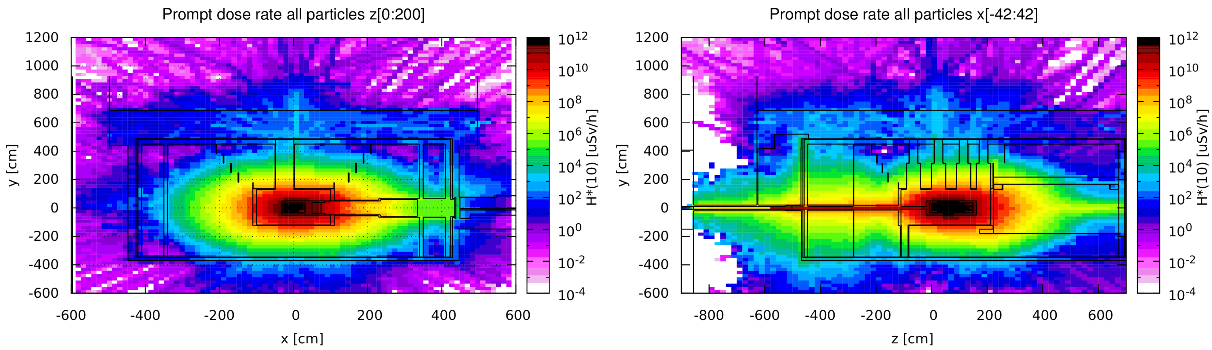

Fig. 6.174: Prompt dose rates in microsieverts per hour in the BDF target complex for all particles. The left plot shows a perpendicular view at target level, and the right plot shows a side view section through the beam line.

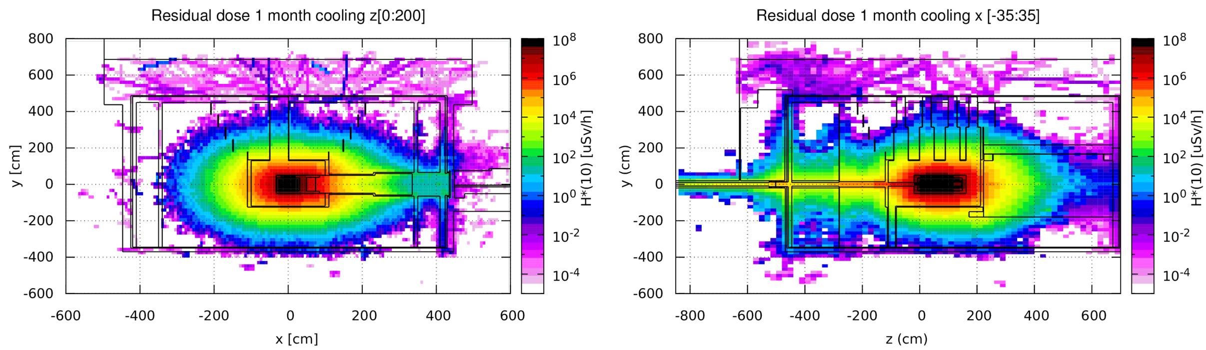

Fig. 6.175: Perpendicular (a) and side view (b) sections through the beam line of residual dose rates in microsieverts per hour in the BDF target complex after 1 month cooling.

liberation limits specified in Swiss legislation [34] were used. Materials with a fraction of the LL larger than one are radioactive according to the Swiss legislation. The zoning plots showed that the most activated parts of the BDF were the target and the cast iron and steel shielding elements. The production of radioactive waste was minimized by making activated parts of the shielding removable so that they could easily be separated from the non-radioactive parts.

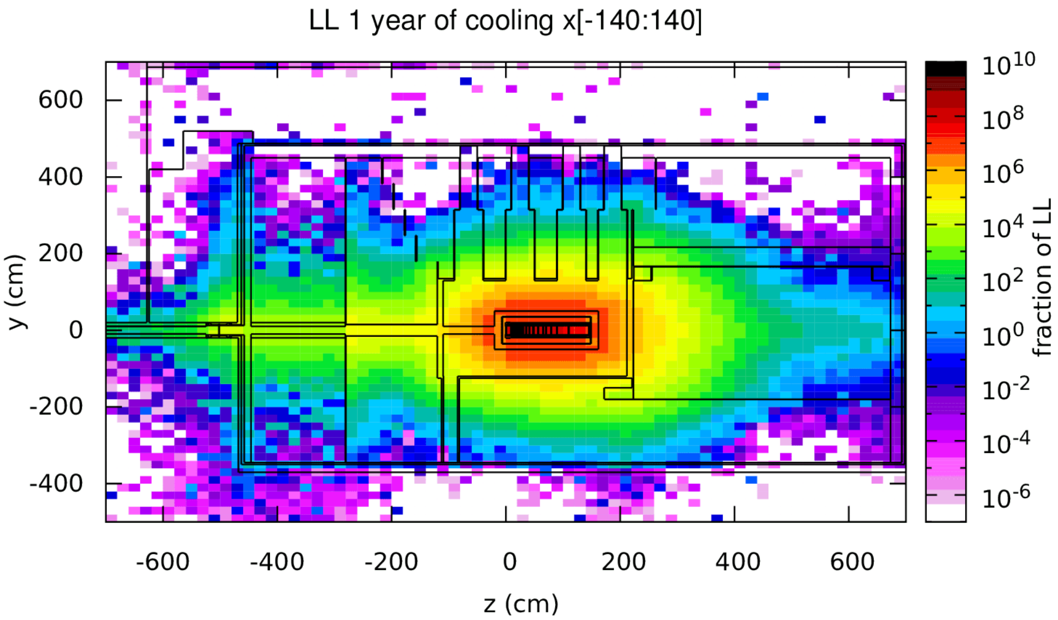

Fig. 6.176: Side view section through the beam line of residual activity, represented as a fraction of the Swiss LL.

References

[1] K. Kershaw, J.-L. Grenard, M. Calviani. *BDF Target Complex Design: Final Results: May 2018*. Tech. rep. EDMS 1977049 v.1, BDF-PM-EN-0002 v.1. CERN, 2018.

[2] K. Kershaw et al. "Design development for the Beam Dump Facility target complex at CERN". In: *J. Instrum.* 13 (2018), P10011. DOI: 10.1088/1748-0221/13/10/P10011. URL: https://cds.cern.ch/record/2631508.

[3] P. Rios Rodriguez. *TIDVG#4 in LSS1 for Operation in 2017 & 2018*. EDMS Document 1720876 v.1. Geneva: CERN, 2017. URL: https://edms.cern.ch/document/1720876/1.0.

[4] S. Garner. *Ultrasonic Testing/SPS Internal DUMP/TIDVG5 Cast-Iron Prototype*. EDMS Document 2028303 v.2. Geneva: CERN, 2018. URL: https://edms.cern.ch/document/2028303/2.0.

[5] SHiP Collaboration. "The active muon shield in the SHiP experiment". In: *J. Instrum.* 12.05, P05011 (2017). DOI: 10.1088/1748-0221/12/05/P05011. arXiv: 1703.03612 [physics.ins-det].

[6] European Union. "Directive 2014/68/EU of the European Parliament and of the Council of 15 May 2014 on the harmonisation of the laws of the Member States relating to the making available on the market of pressure equipment". In: *Off. J. Eur. Union* 189 (June 2014), p. 164.

[7] European Committee for Standardization. *EN 1990 Eurocode: Basis of Structural Design*. 2009.

[8] European Committee for Standardization. *EN 1090-1 Execution of Steel Structures and Aluminium Structures Part 1: Requirements for Conformity Assessment of Structural Components*. 2012.

[9] European Committee for Standardization. *EN 1993-1-1 Eurocode 3: Design of Steel Structures—Part 1-1: General Rules and Rules for Buildings*. 2005.

[10] European Committee for Standardization. *EN 1993-1-5 Eurocode 3: Design of Steel Structures—Part 1-5: Plated Structural Elements*. 2006.

[11] European Committee for Standardization. *EN 1993-1-6 Eurocode 3: Design of Steel Structures—Part 1-6: Strength and Stability of Shell Structures*. 2007.

[12] European Committee for Standardization. *EN 1993-1-8 Eurocode 3: Design of Steel Structures—Part 1-8: Design of Joints*. 2005.

[13] European Committee for Standardization. *EN 10025-2 Hot Rolled Products of Structural Steels—Part 2: Technical Delivery Conditions for Non-alloy Structural Steels*. 2004.

[14] European Committee for Standardization. *EN 13445-3 Unfired Pressure Vessels—Part 3: Design*. 2014.

[15] European Committee for Standardization. *EN 1991-1-1 Eurocode 1: Actions on Structures—Part 1-1: General Actions—Densities, Self-weight, Imposed Loads for Buildings*. 2002.

[16] P. Dalakov. *Pre-design of a Cryogenic System for Helium Purification*. Tech. rep. EDMS 1905338 v.1.0. ILK Dresden, 2018.

[17] P. Avigni, M. Battistin. *Invitation to Tender Documents for the Helium Passivation System for BDF*. IT-4367/EN/BDF, EDMS 1906299 v.0.5. 2018.

[18] P. Avigni et al. “Design of a helium passivation system for the target vessel of the Beam Dump Facility at CERN”. In: *Journal of Instrumentation* 14.12 (Dec. 2019), T12001–T12001. DOI: 10.1088/1748-0221/14/12/t12001. URL: https://doi.org/10.1088%2F1748-0221%2F14%2F12%2Ft12001.

[19] ANSYS. *SpaceClaim*. 2018. URL: http://www.spaceclaim.com/en/default.aspx.

[20] P. Avigni. *BDF Target Complex CV Work Package*. Tech. rep. EDMS 2050757. CERN, 2018.

[21] P. Avigni. *CERN-ILK Collaboration Proposal for Detailed Design of the BDF Helium Vessel Passivation System*. Tech. rep. EDMS 1997873 v.2.0. CERN, 2018.

[22] P. Dalakov. *Detailed Design of the BDF Helium Vessel Passivation System*. Tech. rep. EDMS 1997873 v.2.0. ILK, 2019.

[23] International Organization for Standardization. *Nuclear Facilities—Criteria for the Design and Operation of Ventilation Systems for Nuclear Installations Other Than Nuclear Rreactors*. Standard. 2004.

[24] P. Avigni. *Preliminary Cooling Synoptic for BDF Target Complex*. EDMS 2029615. 2018.

[25] P. Avigni. *Preliminary Cooling PID for BDF Target Complex*. EDMS 2029613. 2018.

[26] M. Archambault, P. Avigni. *Integration Model for the CV Systems of the BDF Target Complex*. Cooling: St0992505; Ventilation: St0865017. 2018.

[27] P. Avigni. *Preliminary PID for Helium Circulation System*. EDMS 2029616. 2018.

[28] P. Avigni. *Preliminary Ventilation Synoptic for BDF Target Complex*. EDMS 2029614. 2018.

[29] P. Avigni. *Preliminary Ventilation PID for BDF Target Complex*. EDMS 2030636. 2018.

[30] T. T. Bohlen, F. Cerutti, M. P. W. Chin, A. Fassò, A. Ferrari, P. G. Ortega, A. Mairani, P. R. Sala, G. Smirnov and V. Vlachoudis. “The FLUKA code: developments and challenges for high energy and medical applications”. In: *Nucl. Data Sheets* 120 (2014), pp. 211–214. ISSN: 0090-3752. DOI: https://doi.org/10.1016/j.nds.2014.07.049. URL: http://www.sciencedirect.com/science/article/pii/S0090375214005018.

[31] A. Ferrari et al. *FLUKA: A Multi-particle Transport Code (Program Version 2005)*. CERN Yellow Reports: Monographs. Geneva: CERN, 2005. URL: https://cds.cern.ch/record/898301.

[32] H. Vincke and C. Theis. “ActiWiz 3 – an overview of the latest developments and their application”. In: *J. Phys. Conf. Ser.* 1046 (June 2018), p. 012007. DOI: 10.1088/1742-6596/1046/1/012007. URL: https://doi.org/10.1088/1742-6596/1046/1/012007.

[33] D. Forkel-Wirth et al. “Radiation protection at CERN”. In: *CAS–CERN Accelerator School: Course on High Power Hadron Machines, 24 May–2 Jun 2011* (Bilbao, Spain). Mar. 2013. eprint: arXiv:1303.6519. URL: http://cds.cern.ch/record/1533023.

[34] Office federal de la santé publique (OFSP). *Ordonnance du 26 avril 2017 sur la radioprotection (ORaP)*. 2017. URL: https://www.admin.ch/opc/fr/classified-compilation/20163016/index.html.

Chapter 7

Experimental hall

7.1 Introduction

The underground experimental hall (ECN4) is located immediately downstream of the target complex, centred on the beam axis, as shown in Fig. 1.2. The design of the experimental area is mainly dictated by the requirements of the proposed SHiP experiment [1, 2, 3] as the first user of the Beam Dump Facility, but also taken into account are possible future extensions and re-use. All phases of the experiment, including assembly, construction, installation, the operational phase, and the dismantling phase, have been taken into consideration. Experience from existing CERN facilities (LHCb, NA62) and other studies of future facilities (CENF, HL-LHC) have provided important input and guidelines.

7.2 General requirements

The Beam Dump Facility is designed to host a multipurpose, large-scale experimental programme using a single beam line and a single main target station. The SHiP experimental set-up (Fig. 7.1) consists of three main components, namely a magnetic deflector composed of six free-standing magnets each $\sim$5 m long, followed by two complementary detector systems. The first detector system is the Scattering and Neutrino Detector (SND), capable of detecting light dark matter through recoil signatures of electrons or nuclei, and of performing measurements on neutrino interactions, in particular those of tau neutrinos. The second detector system is designed to measure decays of Hidden Sector particles, and consists of a large decay volume followed by a spectrometer and particle identification detectors with an aperture of 5 m $\times$ 10 m. The decay volume is kept under a vacuum of 1 mbar by means of a vacuum chamber, 50 m long, with transverse dimensions upstream of 2.2 m$\times$5 m and downstream of 6 m$\times$12 m.

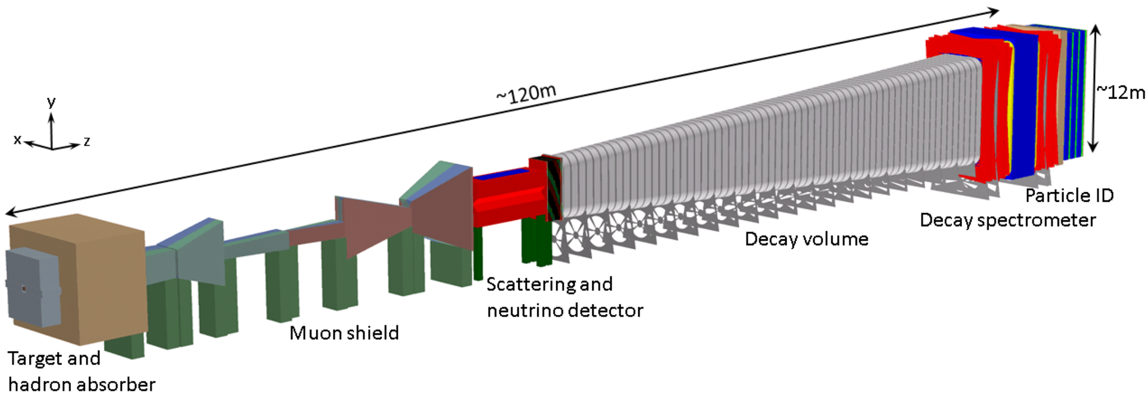

Fig. 7.1: SHiP experimental set-up as implemented in the physics simulation

The total length of the SHiP experimental set-up is 113 m, defining the minimum length of the underground experimental hall. To reduce background from particle scattering in the cavern walls, the width of the cavern will be a minimum of 20 m along the entire length, with the detector located in the centre. No structures or other components will be located between the cavern walls and the detector set-up.

The preliminary dimensions and loads of the detector components are summarized in Table 7.1. The assembly and installation of the muon shield, the two spectrometer magnets, and the vacuum vessel are major undertakings, and these largely determine the layout of the surface hall, its access doors, and the crane configuration, and drive the installation schedule. The current strategy foresees parallel construction of the muon shield magnets and the main spectrometer magnet together with its associated vacuum chamber. A large part of the assembly of both systems will take place in the underground experimental hall. Two overhead bridge cranes are preferred in the underground hall for these and subsequent activities, one with a single-hoist 40 t capacity and the other with a double-hoist 40 t capacity that can be combined into a joint 80 t capacity. They may be located on common rails. This phase is followed by the construction of the decay volume, starting from the larger end and the structural elements of the downstream particle identification detectors. The decay volume will arrive from the factory as pre-manufactured panels. The plan foresees pre-assembly of 7.5 m long sections in the surface hall, with the rectangular vessel sections welded 'lying down', as shown in Work Zone 2 (WZ2) in Fig. 7.2. Each ring is then rotated to its final orientation while being lowered onto the supports in the underground area. This limits the number of welding operations underground, and allows other installation activities to continue in the underground hall. Before shipping of the sections underground, cleaning with high-pressure water will be required to remove dust and oil from the production and welding of the black steel. A similar type of cleaning will also be required after the final welding underground. Suspended protective curtains and recovery of waste water will be required during the cleaning process. The preliminary installation scheme considers installing the decay volume underground on a set of chariots on rails to allow longitudinal displacement of the decay volume during the final assembly and leak tests. As shown in Fig. 7.2, a gap between the decay volume (shown in light green) and the spectrometer section will allow work and leak tests to continue on both systems.

The upstream spectrometer magnet and the upstream muon filters will be installed after the completion of the muon shield, the decay volume, and the spectrometer section.

With the exception of the spectrometer straw tracker stations, which are housed in the vacuum chamber of the spectrometer section, all other detector elements will be assembled directly in situ in the final location. To allow access, the large detectors downstream of the spectrometer straw tracker will be either installed on trolleys on lateral floor rails, or suspended from frames on girders, in a similar manner to the LHCb experiment.

A clean room will be installed in the surface hall, once the large components are installed, to assemble the straw tracker stations before lowering them directly into position in the spectrometer vacuum chamber. The insertion of the 5 m straws will take place in the surface hall, and will require several rotations of the entire frames. Figure 7.3 shows the installation of a straw tracker station inside the spectrometer vacuum vessel.

A preliminary zone arrangement has been designed according to the SHiP assembly procedure. Figure 7.2 shows the proposed layout of the surface hall, with three work zones where the SHiP components will be kept for intermediate storage and pre-assembly, together with two reception areas and two storage areas. The work zones are associated with three strategically located openings leading down to the underground hall. Equipment and components will enter through the two doors of the surface building, shown in dark blue in Fig. 7.2, by truck or semi-trailer and then be moved along the hall by a movable platform, overhead cranes, or a forklift. The SHiP assembly activities are distributed over the three different work zones, allowing parallel operations in order to reduce the duration of the construction and installation. Two overhead bridge cranes on separate rails, with capacities of 40 and 10 t, are required to support these activities.

The muon shield and the Scattering and Neutrino Detector magnet will use Zone 1. The decay volume will alternate between Zones 2 and 3, while the main spectrometer magnet will use Zone 3. Zone 3 will also be used in the second phase for intermediate storage and pre-assembly of the downstream detector systems, and finally for a clean room for the straw tracker stations.

Opening 3 is strategically located directly on top of the main spectrometer section (see Fig. 7.3), allowing construction of the magnet yoke and insertion of the coils. The spectrometer vacuum chamber, consisting of two identical twin boxes, will be constructed in Zone 3 and inserted into the aperture of

Table 7.1: Preliminary space reservation and loads for the SHiP detector components. The 'start' position of each component is relative to the centre of the proton target.

System	Start (m)	Length (m)	Width (m)	Height (m)	Weight (t)
Target	−0.72	–	–	–	–
Absorber magnet	0.82	5.32	7.90	6.80	–
Upstream wall	6.10	0.20	20.00	0.00	–
Muon shield magnet 1	6.30	4.20	3.08	2.02	300.00
Muon shield magnet 2	10.60	4.10	2.46	4.60	330.00
Muon shield magnet 3	14.80	5.60	1.46	1.24	115.00
Muon shield magnet 4	20.60	5.00	1.44	1.14	100.00
Muon shield magnet 5	25.60	6.10	1.54	4.62	200.00
Muon shield magnet 6	31.80	5.00	3.60	6.36	550.00
Emulsion spectrometer magnet	37.90	7.00	2.20	3.40	330.00
Upstream muon system	45.00	1.60	2.20	4.90	85.00
Decay volume front cap	46.60	0.20	2.20	5.00	0.40
Decay volume	46.80	50.00	2.2–5.4	5.0–10.7	650.00
Straw tracker tandem box 1	96.80	3.40	8.50	13.00	120.00
Main spectrometer magnet	100.20	4.00	7.50	13.00	1100.00
Straw tracker tandem box 2	104.20	3.10	8.50	13.00	120.00
Endcap	107.30	0.20	5.80	10.70	3.00
Timing detector	107.55	0.10	7.00	12.00	10.00
Split ECAL	107.70	0.40	5.30	10.60	400.00
Muon pre-filter	108.20	1.10	6.30	12.60	700.00
Muon detector 0	109.40	0.20	6.00	12.00	10.00
Muon filter 0	109.70	0.60	6.00	12.00	400.00
Muon detector 1	110.40	0.20	6.00	12.00	10.00
Muon filter 1	110.70	0.60	6.00	12.00	400.00
Muon detector 2	111.40	0.20	6.00	12.00	10.00
Muon filter 2	111.70	0.60	6.00	12.00	400.00
Muon detector 3	112.40	0.20	6.00	12.00	10.00
Muon filter 3	112.70	0.10	6.00	12.00	60.00

the magnet from both sides. The opening will then allow direct insertion of the straw tracker stations, as well as future access, with the help of the overhead bridge crane in the surface hall.

Table 7.2 summarizes the use of the work zones for the different detector components. The entire installation phase is expected to take 2–2.5 yr.

During the operation of the facility, the three openings will be covered by concrete slabs, and detector tooling and 'detector access' equipment (scaffolding, cherry pickers, etc.) will be stored in the surface hall.

As the surface hall is not accessible during beam operation, control racks, safety and power distribution equipment, computing infrastructure, offices, and a control room will be housed in an adjacent service building (BAE91). Table 7.2 lists the service infrastructure requirements for the SHiP detector, and Table 7.3 summarizes the space requirements in the service building. As listed in the second column, control, computing, and network racks with cooling, ventilation, and power distribution equipment will share the ground floor and the first floor, while laboratories, offices, a cafeteria, a control room, and a conference room will be housed on the second and third floors. In addition, a workshop to support the SHiP construction is planned. For the gas supply and storage, a dedicated gas building (BG91) is required. The liquid scintillator option for the Surrounding Background Tagger of SHiP will also require a platform outside for the storage tanks.

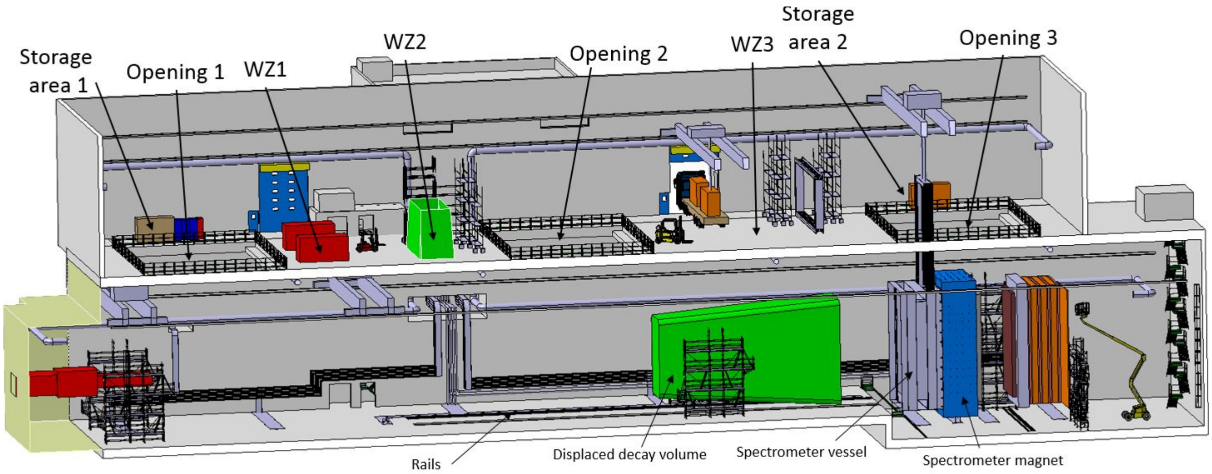

Fig. 7.2: Preliminary organization of the assembly Work Zones (WZ) in the surface hall for the SHiP subsystems.

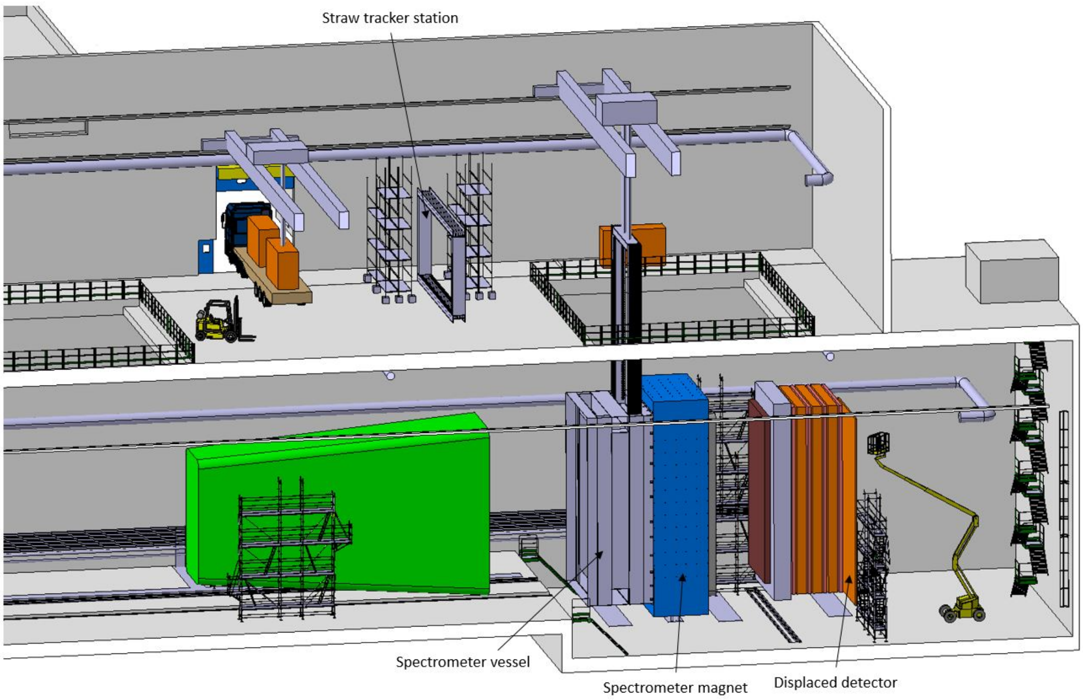

Fig. 7.3: Installation of the SHiP straw tracker

Table 7.2: Preliminary service infrastructure requirements for SHiP, and summary of the use of the work zones for storage and assembly.

	Preliminary infrastructure requirements and services					Installation	
Subsystem	Floor footprint (L × W) (cm)	Supply current (A)	Power cons. detector (kW)	Cooling	Power dissipation into air (kW)	Storage/ pre-assembly	Main assembly
Muon shield magnet 1	416 × 400	50	1	Air	1	WZ1/ECN4	ECN4
Muon shield magnet 2	414 × 400	50	1.5	Air	1.5	WZ1/ECN4	ECN4
Muon shield magnet 3	562 × 300	50	0.9	Air	0.9	WZ1/ECN4	ECN4
Muon shield magnet 4	496 × 300	50	1.4	Air	1.4	WZ1/ECN4	ECN4
Muon shield magnet 5	610 × 300	50	3.5	Air	6.5	WZ1/ECN4	ECN4
Muon shield magnet 6	484 × 460	50	5	Air	5	WZ1/ECN4	ECN4
SND detector magnet	700 × 220	14 600	1900	water (60–80 m^3/h)	100	WZ1/ECN4	ECN4
Emulsion target	Included	0	0	Air	0	WZ1	ECN4
Target tracker	Included		8	Air	8	WZ2	ECN4
Upstream muon ID	160 × 220		10	Air	10	WZ2	ECN4
Decay volume/vacuum	5000 × 600		19	water (65 m^3/h)	2	Outside	WZ2/WZ3
Surround bkg tagger	Included		10	Air	10	WZ2	ECN4
Main spectr. magnet	550 × 763	3000	1083	n/a	100	WZ3	ECN4
Straw tracker	300 × 650		10	Air	10	WZ3	WZ3
Timing detector	100 × 700		10	Air	10	WZ3	ECN4
Split calorimeter	250 × 700		10	Air	10	WZ3	ECN4
Muon system	550 × 800		10	Air	10	WZ3	ECN4
			3093.3	293.3			

Table 7.3: Space reservation for SHiP's services and operational needs. SB, service building; SH, surface hall.

Description	Location	Space (m^2)	Height (cm)	Load (kg/m^2)
Services: voltage transformers	Outside, adjacent to SB	24		
Gas building	Separate building	150	300	
Liquid scintillator tanks (270 m^3)	Outside, adjacent to SB	80		
Services: underground ventilation	Upstream inside SH	100		
Services: safety	SB, ground floor, adjacent to SH	25	250	400
Services: cooling	SB, ground floor, adjacent to SH	100	250	
Services: power distribution	SB, ground floor, adjacent to SH	50	250	
Services: liquid scintillator	SB, ground floor, adjacent to SH	50	250	
Electronics room	SB, ground floor, adjacent to SH	80	250	400
Computing infrastructure	SB, ground floor	80	250	400
Control room	SB, first floor	150	250	300
Lab rooms (4 m × 5 m)	SB, first floor	150	250	300
Common lab	SB, first floor	100	250	300
Workshop	SB, ground floor	150	400	
Clean room	Temporary in SH	100	400	
System management room	SB, ground floor	50	250	300
Office space	SB, second floor	60	250	
Conference room	SB, second floor	150	250	
Kitchen, coffee area	SB, second floor	50	250	
Elevator/staircase	SB	100	250	

7.3 Radiation protection

The high-intensity beam power deposited in the target poses challenges for radiation protection in several locations. To reduce the effect and mitigate the impact, the radiological aspects of the experimental area were carefully addressed at the design stage. The studies included expected prompt and residual dose rates in the various areas of the SHiP experimental area and public areas. The facility was designed under the condition that there is no access to the experimental hall, nor the surface hall on top, during beam operation. The studies were based on past measurements and extensive simulations with the FLUKA Monte Carlo particle transport code [4, 5] and Actiwiz 3 [6]. Figure 7.4 shows a partial layout of the facility (target assembly and muon shield) as implemented in FLUKA. All studies assumed 4×10^{13} protons on target per spill (with a duration of 1 s every 7.2 s) and an integrated total of 2×10^{20} protons on target over 5 yr of operation, each year with ∼280 days of nominal operation followed by ∼80 days of shutdown.

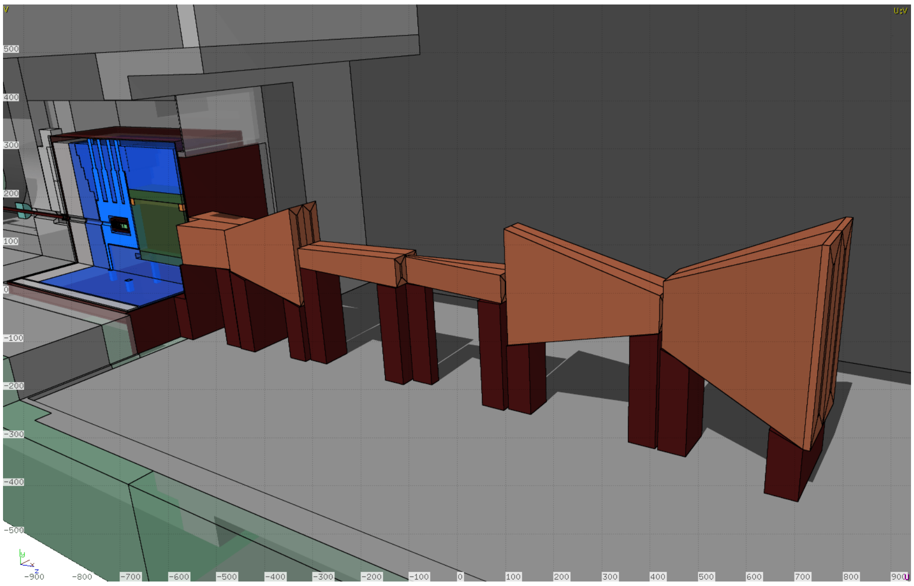

Fig. 7.4: Partial layout of the facility (target assembly and muon shield) as implemented in FLUKA.

Figure 7.5 shows the prompt dose rates from all particles from the muon shield in the experimental hall and in the surface hall in the horizontal (left) and vertical (right) planes through the beam line.

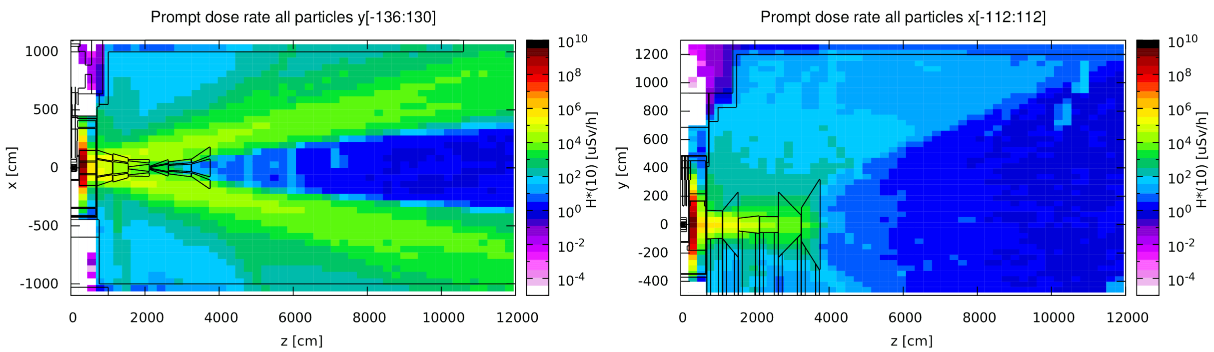

(a) **(b)**

Fig. 7.5: Prompt dose rates in microsieverts per hour in the SHiP experimental hall for all particles: (a) top view, (b) side view section at the level of the beam line.

During operation the dose rates, which are mainly due to muons, reach a few millisieverts per hour along the walls of the experimental hall behind the muon shield and drop to below 1 mSv/h in the surrounding soil, such that the levels of soil activation are considered acceptable.

The side view of the experimental hall shows that muons are also bent towards the ceiling of the experimental hall. The dose reaches a few microsieverts per hour in the surface hall on top of the underground hall, but the surface hall is not designed to be accessible during beam operation. Further simulations demonstrate that the existing beam lines TT81, TT82, and TT83 are not affected by the prompt dose rates originating from the BDF during SHiP operation, nor does the SHiP operation influence the present area classification of the EHN1 experimental hall, which corresponds to a Supervised Radiation Area (<3 µSv/h). Note that these results on long-range effects are conservative because of the assumption of a moraine density 20% lower than that measured in ground samples. Thus, the operation of the SHiP experiment has no impact on the neighbouring experimental areas.

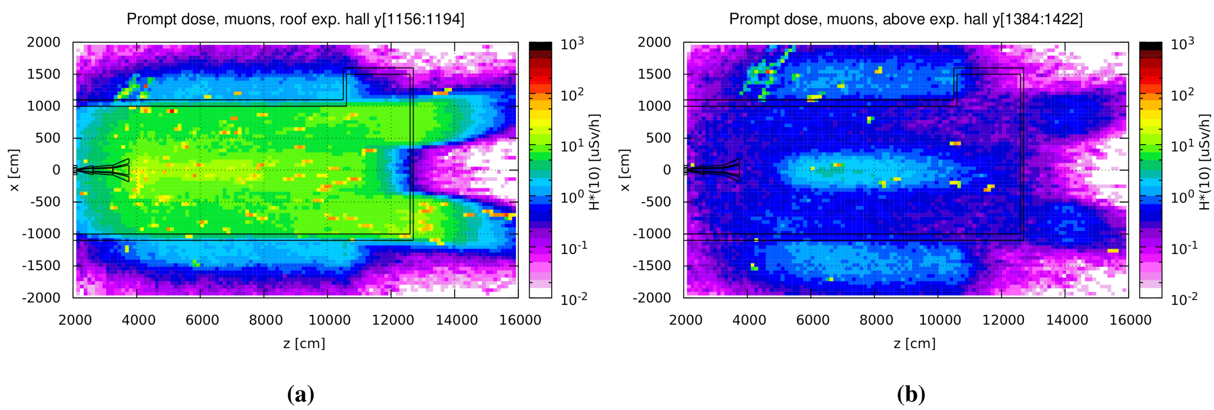

Fig. 7.6: Prompt dose rates in microsieverts per hour inside the experimental hall at level of roof (a) and at ground level in the surface hall (b).

Figure 7.6 shows the prompt dose rates from muons at roof level in the underground experimental hall and at ground level in the above-lying surface hall to show the effectiveness of the 1 m concrete ceiling. This shows that a few microsieverts per hour are expected on top of the ceiling of the underground experimental hall behind the detector surface hall. It is planned to fence this area and cover it with 6 m of the soil remaining from the excavations, such that the dose rate level is brought down to below 0.5 µSv/h, allowing for a Non-Designated Area [7]. A standard stray-radiation monitor for photons, muons, and neutrons is envisaged at the CERN fence closest to the most exposed area.

Assuming 5 yr of operation, the residual dose rates in the SHiP experimental hall are expected to be at most a few microsieverts per hour in contact with the first part of the active muon shield after 4 h of cool-down (see Fig. 7.7), thus allowing for access to this area. The experimental hall up to the end of the active muon shield will be classified as Simple Controlled, while the rest will be classified as a Supervised Radiation Area.

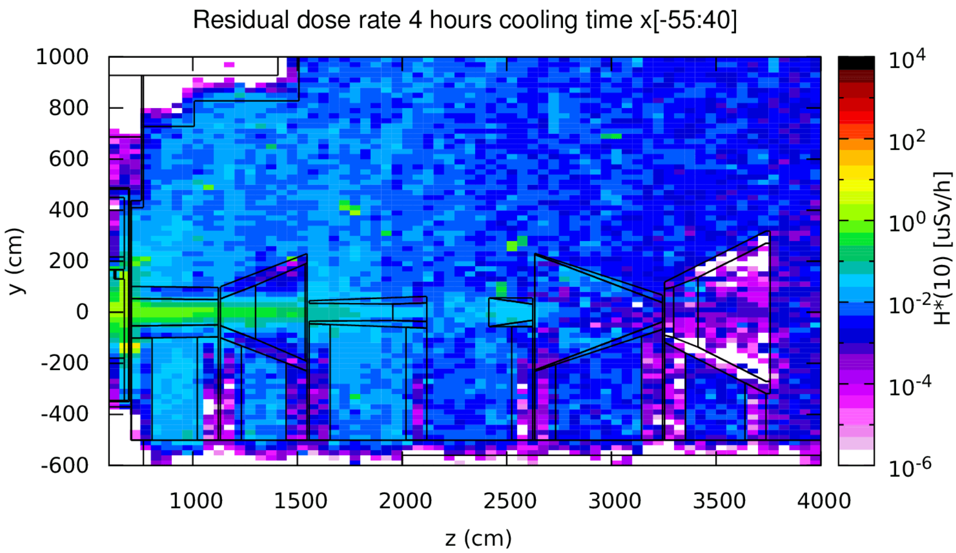

Fig. 7.7: Residual ambient dose equivalent rate in microsieverts per hour for the active muon shield after 5 yr of operation and 4 h of cool-down time.

References

[1] SHiP Collaboration et al. *A Facility to Search for Hidden Particles (SHiP) at the CERN SPS*. Apr. 2015. arXiv: 1504.04956 [physics.ins-det].

[2] C. Ahdida et al. "The experimental facility for the Search for Hidden Particles at the CERN SPS". In: *J. Instrum.* 14.03 (2019), P03025. DOI: 10.1088/1748-0221/14/03/P03025. arXiv: 1810.06880 [physics.ins-det].

[3] C. Ahdida et al. *SHiP Experiment: Progress Report*. Tech. rep. CERN-SPSC-2019-010, SPSC-SR-248. Geneva: CERN, Jan. 2019. URL: http://cds.cern.ch/record/2654870.

[4] T. T. Bohlen et al. "The FLUKA code: developments and challenges for high energy and medical applications". In: *Nucl. Data Sheets* 120 (2014), pp. 211–214. ISSN: 0090-3752. DOI: https://doi.org/10.1016/j.nds.2014.07.049. URL: http://www.sciencedirect.com/science/article/pii/S0090375214005018.

[5] A. Ferrari et al. *FLUKA: A Multi-particle Transport Code (Program Version 2005)*. CERN Yellow Reports: Monographs. Geneva: CERN, 2005. URL: https://cds.cern.ch/record/898301.

[6] H. Vincke and C. Theis. "ActiWiz 3 – an overview of the latest developments and their application". In: *J. Phys. Conf. Ser.* 1046 (June 2018), p. 012007. DOI: 10.1088/1742-6596/1046/1/012007. URL: https://doi.org/10.1088/1742-6596/1046/1/012007.

[7] D. Forkel-Wirth et al. "Radiation protection at CERN". In: *CAS–CERN Accelerator School: Course on High Power Hadron Machines, 24 May–2 Jun 2011* (Bilbao, Spain). Mar. 2013. eprint: arXiv:1303.6519. URL: http://cds.cern.ch/record/1533023.

Chapter 8

Integration

8.1 Introduction

Detailed integration studies have been performed to evaluate the feasibility of siting the Beam Dump Facility within CERN's Prévessin site. All of the infrastructure requirements were defined and integrated within the civil engineering layout, and the locations and numbers of structures and services were optimized in terms of radiation protection, general safety, accessibility, and practicality. Figure 8.1 shows the layout of the integration of the overall facility.

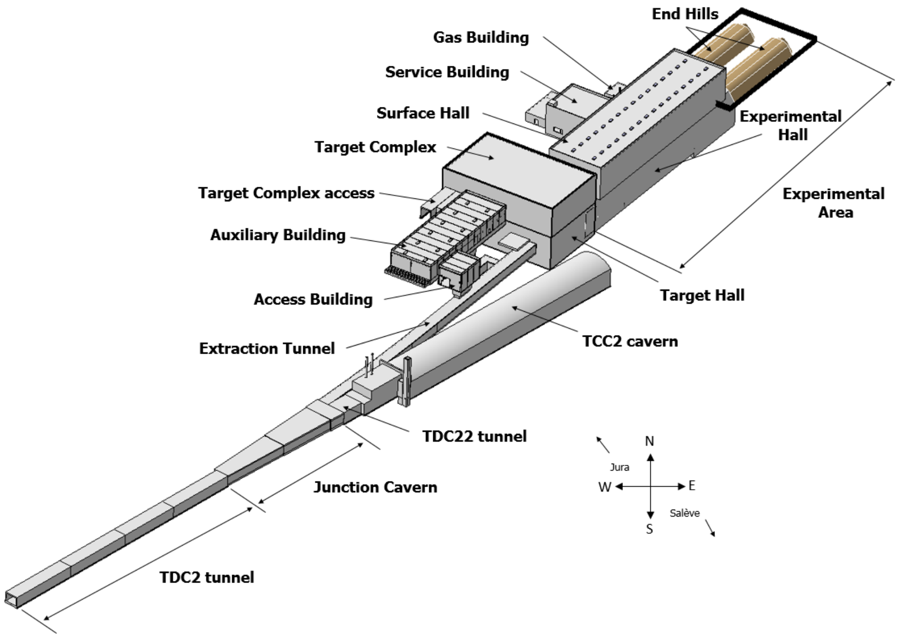

Fig. 8.1: Overview of BDF integration

The integration of the facility is divided into the following four areas:

– *Transfer tunnel:* this houses the BDF beam line equipment and services. It consists of the existing TDC2 tunnel, the junction cavern, and the extraction tunnel.
– *Access building and auxiliary building:* the access building allows the installation of large beam line equipment directly into the transfer tunnel. The auxiliary building houses the cooling, ventilation, and electrical infrastructure for the transfer tunnel, the target complex, and the experimental area. In addition, it includes personnel access to the transfer tunnel.
– *Target complex access:* personnel access and pressurized vehicle access for the target complex.
– *Experimental area:* this is defined and sized to house and allow the assembly of the SHiP experiment inside its experimental hall while providing the services and infrastructure required for the operation of the detector.

A preliminary proposal for the layout of the technical galleries has been produced assuming that the electrical connection of the BDF to the Prévessin network is made through CERN's existing service building, BA80 (see Fig. 11.2). The connection from the existing technical gallery to the BDF first reaches the auxiliary building, where the primary cooling pump and main electrical distribution equipment are located. From here, the water and electrical power are distributed throughout the facility. Further study will be undertaken to determine the optimized layout.

The following sections describe in detail the integration studies performed for each of the four areas listed above. In the appendices to this chapter, Table 8.16 contains the SmarTeam numbers of the integration models (ENOVIA SmarTeam is a product data management tool that enables organizations to manage and collaborate on component information) and Table 8.17 lists the structural specification documents that were developed for the facilities listed above.

8.2 Transfer tunnel

The transfer tunnel for the BDF beam line is located upstream (south-west) of the target complex, as shown in Fig. 8.1. It is composed of the existing TDC2 tunnel, the junction cavern, and the extraction tunnel. The transfer tunnel starts at the existing TDC2 tunnel, from which the BDF bending magnets bend the beam away from the existing North Area beam lines into a new junction cavern. The beam line then branches off the junction cavern into the extraction tunnel and runs alongside the existing TCC2 cavern up to the target complex.

The purpose of the structure is to house the beam line equipment and services that deliver the beam to the target. The equipment includes magnets, beam instrumentation, and vacuum, safety, and alignment equipment. The services include the general electrical distribution, cooling, and ventilation.

8.2.1 TDC2 tunnel

8.2.1.1 Summary

The TDC2 tunnel (shown in Fig. 8.1) is an existing underground tunnel that houses North Area beam lines (TT22, TT23, TT24, and TT25) and their services. The access to the beam lines is from the TCC2 cavern via building BA80, in which the transport access path is located on the Salève (south-east) side.

The new BDF beam line (TT90) starts downstream of the new splitter magnet in the TDC2 tunnel (shown in Fig. 8.2(a)) and runs alongside the existing North Area beam lines for approximately 110 m, as shown in Fig. 8.2(b). As there are only five BDF magnets and one beam monitor on the BDF beam line in the TDC2 tunnel, and as the BDF beam line does not significantly diverge from the existing North Area beam lines until it reaches the junction cavern, the existing tunnel's geometry is sufficient to house this part of the BDF beam line.

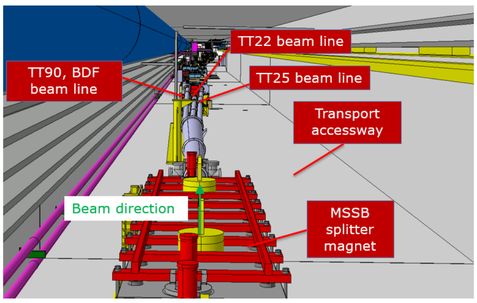

(a)

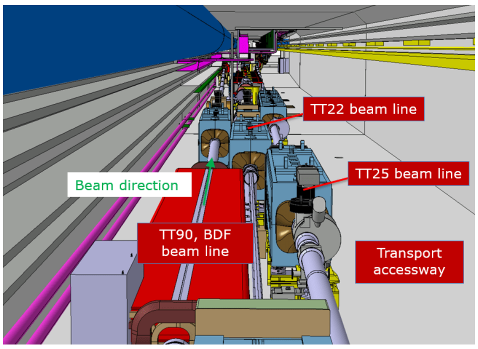

(b)

Fig. 8.2: (a) Start of BDF beam line (TT90) at the first MSSB splitter magnet. (b) BDF beam line (TT90) integrated with the existing North Area beam lines.

8.2.1.2 TDC2 dismantling

As described in Chapter 11, a section of the TDC2 tunnel will be demolished for the construction of the new junction cavern, and all the beam line elements and associated auxiliary infrastructure will be dismantled, starting and finishing 10 m away from the demolition region (see Fig. 8.3). The total extent of the TDC2 demolition will be approximately 75 m, while equipment (including cabling, trays, ventilation ducts, lightning, fire detection, and extinguishing systems, etc.) will be removed from a 95 m long section. Some of this equipment, including magnets, vacuum equipment, and beam instrumentation, will be stored and may be re-used (see Table 8.1 and Fig. 8.4), while other equipment and associated infrastructure will be replaced with new equipment after the construction.

The approach assumes the construction of two shielding walls on both sides of the future junction cavern to reduce the dose from the splitters and the target attenuator experimental areas (XTAX) and to protect the regions from dust and debris, and the use of a portable booster ventilation system before removing the ventilation ducts (this provisional unit is expected to run continuously to guarantee fresh air in TDC2). The beam line equipment in TT22, TT23, TT24, and TT25 within this region will have to be removed with minimum disassembly wherever possible, while destructive work will be acceptable for the associated infrastructure (cutting of ducts and cabling).

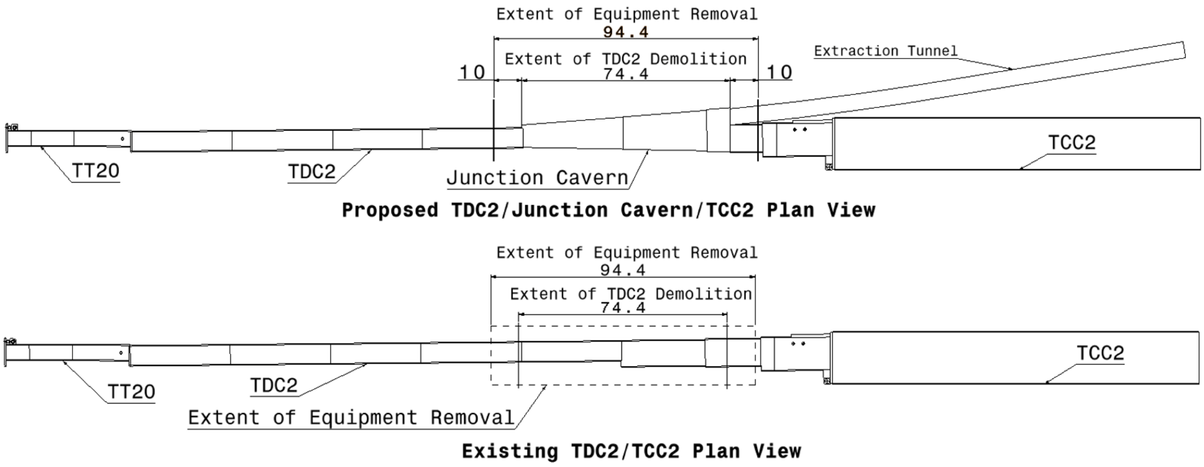

Fig. 8.3: Extent of tunnel demolition and equipment removal in the new junction cavern area [1]

To evaluate the necessary cool-down time, a detailed Work and Dose Planning (WDP) for the given work will be produced. At this stage, only a rough estimate of the WDP can be done, as it largely depends on the detailed methodology of the work (remote handling, shielding, work optimization, etc.).

The estimation of the dose was undertaken by reviewing similar past activities (e.g. removal of magnets) and the associated data available for magnets and beam line elements with different levels of activation. The main assumption in the estimation of the dose during removal of beam line elements was that personnel would spend time continuously in an environment dominated by the background radiation scenario (which assumes that the magnets have been removed).

When looking at the expected dose rates in TDC2 for various cool-down times, the most significant decrease occurs, as expected, in the very first weeks of cool-down (e.g. by a factor of 13 over 4 weeks, typically given by an end-of-year lead ion run). Further cool-down, for example between 9 weeks and 5 months after the proton run, provides a further gain by only a factor of 0.3. At the downstream end of the area under consideration, the dose rates at a distance of 40 cm from the equipment are relatively low (30 μSv/h, 9 weeks after a proton (p^+) run), and thus the cool-down time becomes less critical. For the most activated of the elements to be removed (e.g. beam monitor BSPH.240212), the dose rates are of the order of 590 μSv/h 9 weeks after a p^+ run. These are still much lower than the dose rates at the splitters (11 mSv/h at 40 cm, 9 weeks after a p^+ run), which fortunately do not have to be removed at the

Table 8.1: Main elements to be removed before demolition of TDC2 at the new junction cavern

Beamline	Position (m)	Family	Type	Element
TT23	230084	VGHA	VAC	VGHA.230084
TT23	230111	BSGV	DIAG	BSGV.230111
TT23	230112	MDAV	MAG	MDAV.230112.E
TT23	230116	MDAV	MAG	MDAV.230116.E
TT23	230122	BTV	DIAG	BTV.230122
TT23	230200	QTAD	MAG	QTAD.230200.E
TT23	230300	QTAF	MAG	QTAF.230300.E
TT23	230361	MDAH	MAG	MDAH.230361.E
TT23	230400	QTAF	MAG	QTAF.230400.E
TT23	230500	QTAF	MAG	QTAF.230500.E
TT23	230505	BSG	DIAG	BSG.230505
TT24	240101	VVSA	VAC	VVSA.240101
TT24	240102	VVFT	VAC	VVFT.240102
TT24	240102	BSGV	DIAG	BSGV.240102
TT24	240104	MDLV	MAG	MDLV.240104.E
TT24	240107	MDLV	MAG	MDLV.240107.E
TT24	240119	BTV	DIAG	BTV.240119
TT24	240200	QTLD	MAG	QTLD.240200.E
TT24	240206	MDLV	MAG	MDLV.240206.E
TT24	240209	MDLV	MAG	MDLV.240209.E
TT24	240212	BSPH	DIAG	BSPH.240212
TT24	240214	VVSA	MAG	VVSA.240214
TT24	240300	QTLF	MAG	QTLF.240300.E
TT24	240400	QTLF	MAG	QTLF.240400.E
TT24	240406	MBB	MAG	MBB.240406.E
TT24	240417	MBB	MAG	MBB.240417.E
TT24	240428	MBB	MAG	MBB.240428.E
TT24	240439	MBB	MAG	MBB.240439.E
TT24	240450	MBB	MAG	MBB.240450.E
TT24	240500	QNLF	MAG	QNLF.240500.E
TT24	240600	QNLF	MAG	QNLF.240600.E
TT25	250504	MDLV	MAG	MDLV.250504.E
TT25	250508	BSGV	DIAG	BSGV.250508
TT25	250509	MBB	MAG	MBB.250509.E
TT25	250520	MBB	MAG	MBB.250520.E
TT25	250531	MBB	MAG	MBB.250531.E
TT25	250542	MBB	MAG	MBB.250542.E
TT25	250553	MBB	MAG	MBB.250553.E
TT25	250564	MBB	MAG	MBB.250564.E

same time.

Note that because of the position of some magnets (surrounded by elements from other beam lines), the classical approach of removing the most activated objects (namely the upstream magnets near the splitters) needs further detailed analysis.

The first estimation (based on previous interventions with similar experience and assuming dose rates per item of equipment based on RP measurements and estimates of equipment positions along the

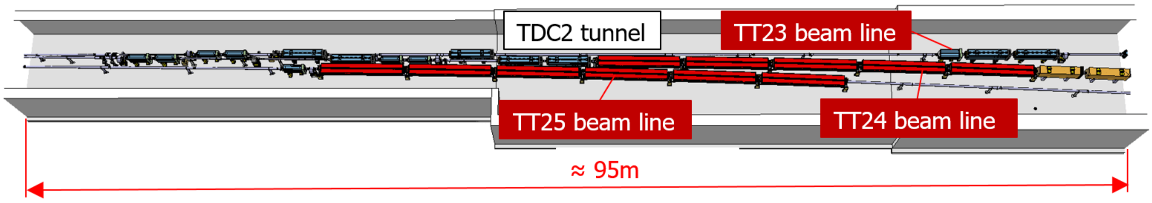

Fig. 8.4: Details of the demolition region, with lines TT23, TT24, and TT25

line) resulted in a total collective dose of the order of 10–20 mSv if the equipment removal starts after 13 weeks (3 months) of cool-down (including a 4 week ion run). This means that the work will clearly be at ALARA level 3 (see Fig. 8.5) from a collective-dose point of view, but this does not seem infeasible. Reducing the cool-down time to 9 weeks (including a 4 week ion run) would increase the collective dose by around 9% (1–2 mSv).

At this stage of the project, and in view of ALARA, the CERN Occupational Health and Safety and Environmental Protection Unit (HSE) RP representatives therefore recommend using the maximum cooling time that is acceptable for the project and one that is at least 9 weeks after the end of the proton run (i.e. 5 weeks in addition to the 4 weeks of an ion run). A further recommendation is to use 13 weeks (3 months) of cooling in the planning process if possible, such that even without an ion run the plan could be met. Furthermore, the dismantling should start at the downstream end of TDC2, giving more cooling time for the hotter elements further upstream. Further details of de-installation are discussed in Sections 8.2.5 and 8.3.4.

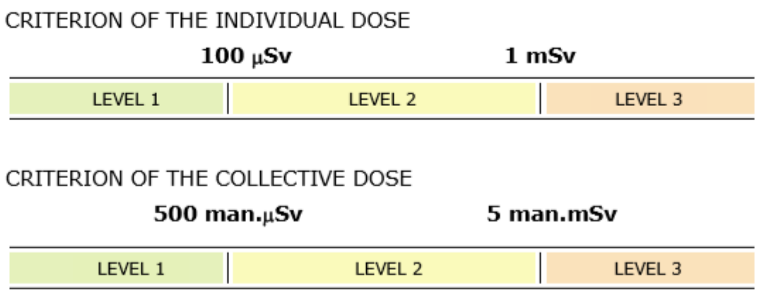

Fig. 8.5: Criteria for ALARA classification at CERN concerning individual and collective doses

8.2.2 Junction cavern (TDC21)

8.2.2.1 Summary

The junction cavern (TDC21) (shown in Fig. 8.1) is an underground cavern that will house four beam lines (TT91, TT23, TT24, and TT25) and their corresponding services. The beam lines enter the junction cavern upstream (south-west) at the TDC2 tunnel, the existing North Area beam lines continue into the TDC22 tunnel, and the BDF beam line (TT90) deviates away towards the Jura side (north-west) into the extraction tunnel. The beam line services include cooling and ventilation, cabling/cable trays, and lighting, among other services, as shown in Fig. 8.6. For the alignment of the beam line equipment in the cavern, there are survey brackets secured to the Jura (north-west) side wall, survey pillars secured to the floor, and survey floor points installed in the cavern floor. During technical stops and long shutdowns of the beam line, personnel and transport vehicles may access the junction cavern for maintenance purposes. The access to the existing North Area beam lines is from the TCC2 cavern via building BA80, in which the transport accessway is located on the Salève (south-east) side. The access to the BDF beam line is from the extraction tunnel, in which the transport accessway is located on the Jura (north-west) side.

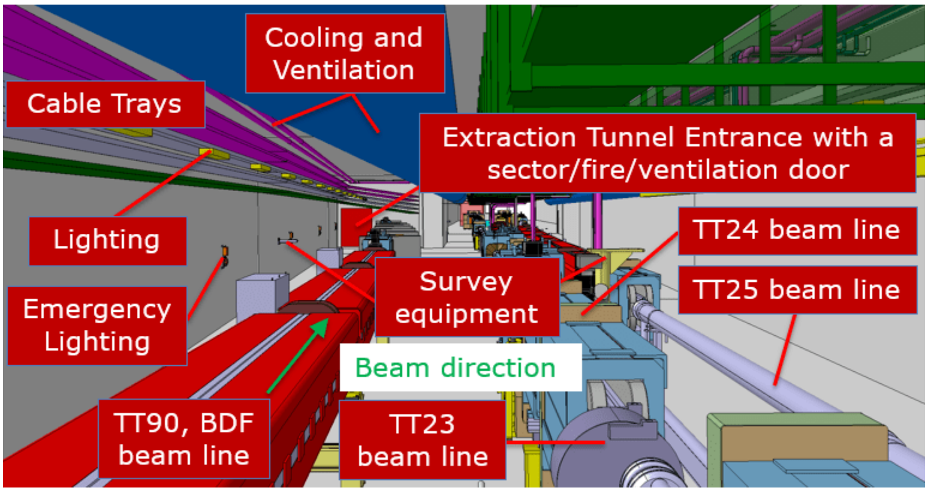

Fig. 8.6: Junction cavern integration layout

8.2.2.2 *Geometry*

Figure 8.7 shows a plan view and sections of the junction cavern. The cavern has a length of 74.1 m, the width of the upstream (south-west) end of the TDC2 tunnel is 7.2 m, and the width of the downstream (north-east) end is 14.2 m. The upstream end is based on an internal opening of size 6.4 m that ties into the existing TDC2 tunnel, and an allowance of 1.5 m between the BDF beam line and the Jura (north-west) side wall of the junction cavern. This allowance is required for a transport vehicle to manoeuvre the MBB bending magnets into position, as shown in Fig. 8.8. There is also a clearance of approximately 1.2 m between the vacuum chamber on the existing beam line TT23 and the new BDF beam line. This allows a smaller handling vehicle to reach the MDLV correction dipoles on the existing beam lines TT23 and TT24, for which a minimum of 1.0 m is required. The downstream end is based on two openings, one 5 m wide that ties into the extraction tunnel and another opening 8 m wide that ties into the existing TDC22 tunnel. The cavern has a height of 4 m, which is the same as that of the existing TDC2 tunnel.

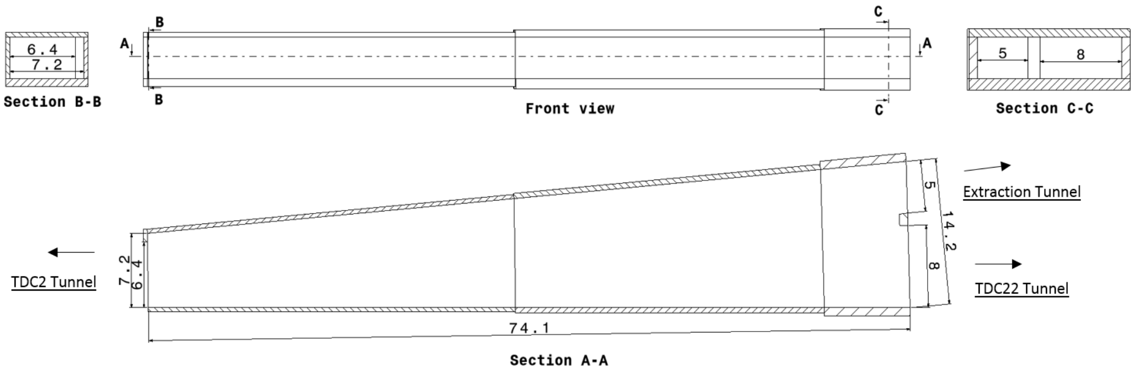

Fig. 8.7: Plan and section views of junction cavern

8.2.3 Extraction tunnel (TT90)

8.2.3.1 *Summary*

The extraction tunnel (TT90) (shown in Fig. 8.1) is a new underground tunnel that houses the BDF beam line and its corresponding services. It allows the beam line to deviate away from the existing North Area beam lines to the target complex. The beam line services include cooling and ventilation, cable trays, and lighting, among other things. For the alignment of the beam line equipment in the tunnel, there are

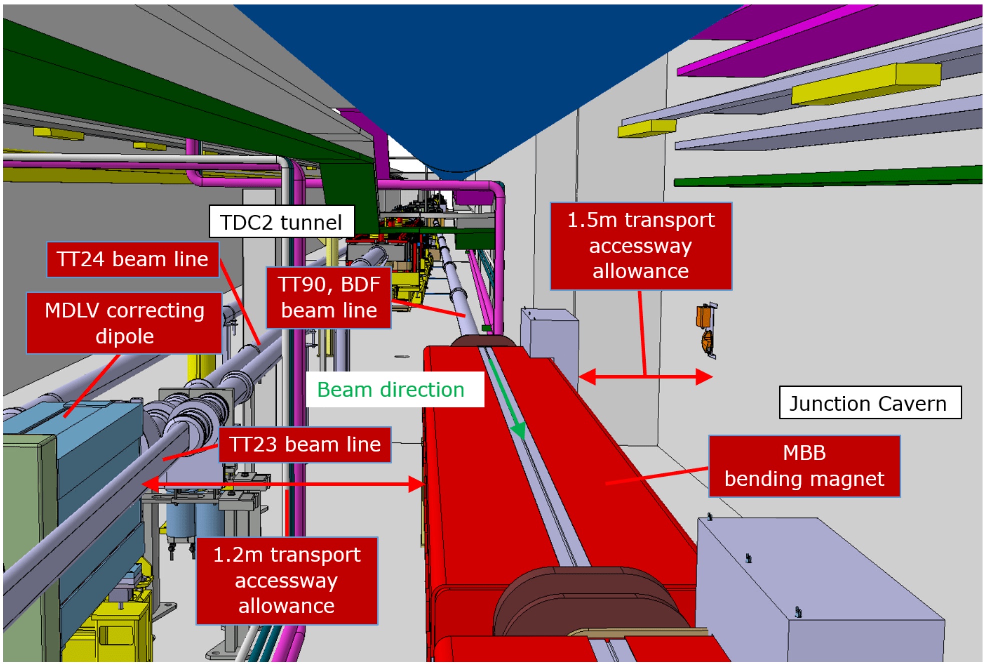

Fig. 8.8: Transport vehicle allowance in junction cavern

survey brackets secured to the Jura side wall and survey floor points installed in the tunnel floor.

During technical stops and long shutdowns of the beam line, personnel and transport vehicles may access the extraction tunnel for maintenance purposes, using the transport accessway located on the Jura side of the tunnel. Personnel access into the extraction tunnel is via the chicane (TA90) connected to the side wall of the extraction tunnel, while transport vehicles and heavy equipment enter the tunnel via the equipment shaft (PA90), as shown in Fig. 8.9 (see Ref. [2] for further details). The equipment shaft is located on the Jura side of the tunnel roof, such that vehicles and equipment lowered into the tunnel do not clash with the services on the Salève side.

The downstream end of the extraction tunnel is connected to the target complex. For emergency purposes, and for ventilation and fire compartmentalization, a sector/fire/ventilation door is located in the target complex alcove; see Fig. 8.10 for further details.

8.2.3.2 Geometry

The structure has a length of approximately 165 m, with an internal height of 4 m and a width of 5 m. The height of the tunnel is the same as that of the junction cavern, and the width of the tunnel is based on the dimensions required for equipment and personnel/transport access, as shown in Fig. 8.11:

- 200 mm allowance for safety lighting and services;
- 1900 mm allowance for transport vehicles;
- 200 mm allowance for the sector door between the junction cavern and the extraction tunnel;
- 1450 mm width for the MBN bending magnet;
- 600 mm allowance for personnel access and maintenance of the cable trays;
- 600 mm allowance for cable trays;
- 50 mm allowance for cabling and the cable tray support structure.

The transport accessway in the extraction tunnel is larger than the 1.5 m allowance in the junction cavern because the MBN bending magnets require a larger transport vehicle to manoeuvre the magnets than that for the MBB bending magnets.

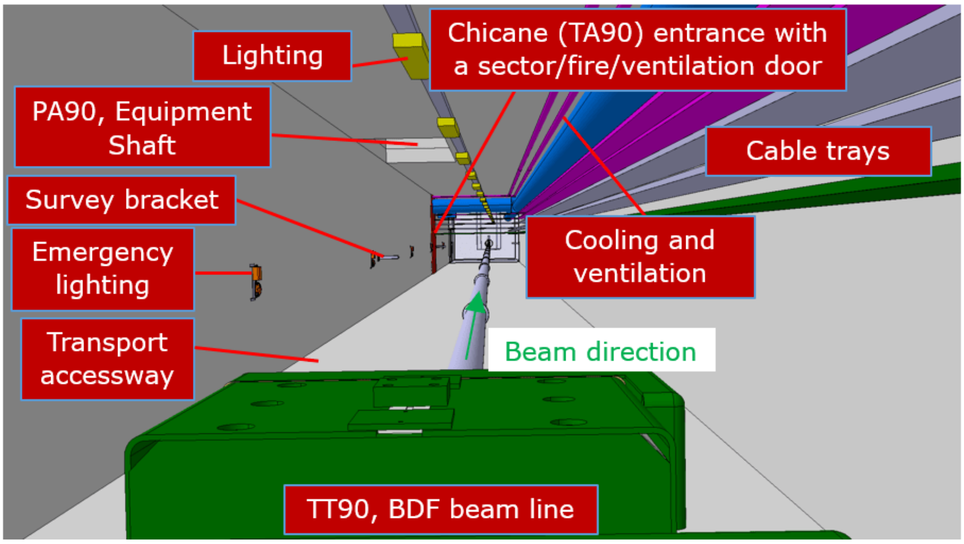

Fig. 8.9: Extraction tunnel integration layout

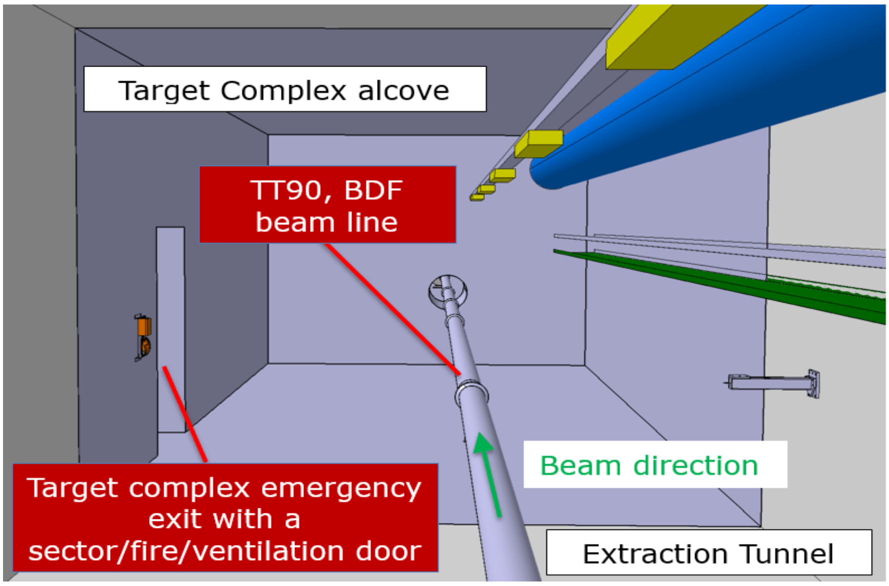

Fig. 8.10: Interface of extraction tunnel with target complex

The chicane is connected to the Jura side of the extraction tunnel, approximately 24 m upstream of the target complex. Approximately 25 m upstream of the chicane entrance is the equipment shaft, connected to the top of the extraction tunnel, as shown in Fig. 8.12.

8.2.4 Beam line equipment

The new BDF beam line (TT90) is approximately 380 m long, and is housed in the following structures:

- 120 m in the existing TDC2 tunnel;
- 75 m in the junction cavern, TDC21;
- 165 m in the extraction tunnel, TT90;
- 20 m in the target complex.

The BDF beam line starts at the first MSSB splitter magnet in the existing TDC2 tunnel (shown in Fig. 8.2(a)) and runs alongside the existing North Area beam lines TT22 and TT25, as shown in

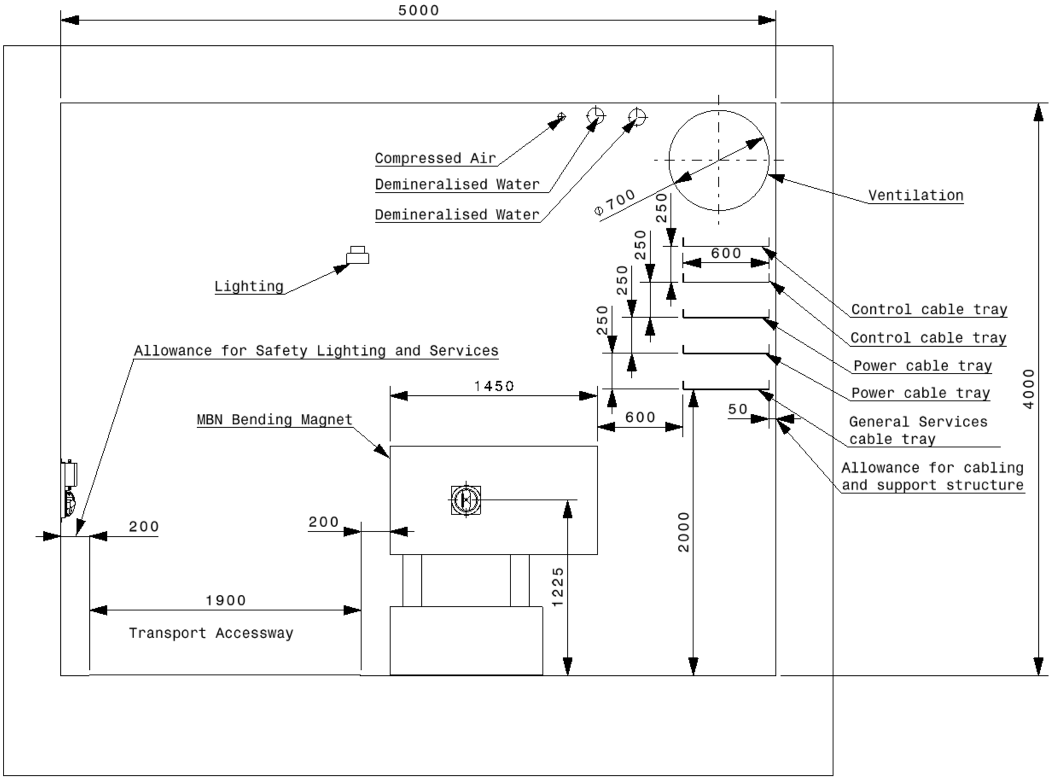

Fig. 8.11: Cross-section of extraction tunnel

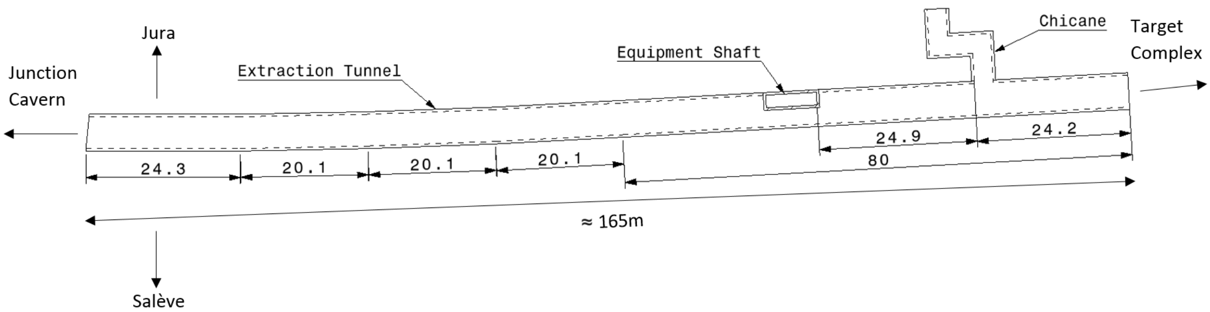

Fig. 8.12: Plan view of extraction tunnel

Fig. 8.2(b) (see Section 4.3.4 for further information on the MSSB splitter magnet). The maintenance of the beam line equipment for both the BDF and the existing North Area beam lines was considered to set the layout of the beam line. To avoid any clashes between the new BDF beam line and beam line TT22, there were a few modifications made to beam line TT22. To determine the precise location of the existing beam line equipment, 3D survey scans were undertaken in the TDC2 tunnel during a technical stop in March 2018. For information on the cooling and ventilation equipment and the transport and handling requirements of the beam line, see Sections 8.3.3 and 8.3.4.

8.2.4.1 Magnets

For the layout of the magnets in the BDF beam line, see Ref. [3]. The types of magnets used in the BDF beam line and their geometry are shown in Table 8.2.

Table 8.2: Characteristics of BDF beam line magnets

Magnet	Quantity	Length (m)	Width (m)	Height (m)	Weight (t)
MBB	5	6.7	0.844	0.685	18
MBN	18	5.51	1.448	0.676	23
MDX	10	0.655	0.73	0.68	1.1
QTG	1	2.2	0.473	0.473	2.65
QTL	5	3.3	0.6	1.057	9.9

8.2.4.1.1 Changes to existing beam line TT22

The existing dipole MDAH.220118 on beam line TT22 clashes with the vacuum chamber on the BDF beam line. The proposed solution is to move dipole MDAH.220118 downstream by approximately 9.4 m next to quadrupole QTAF.220300, as shown in Fig. 8.13.

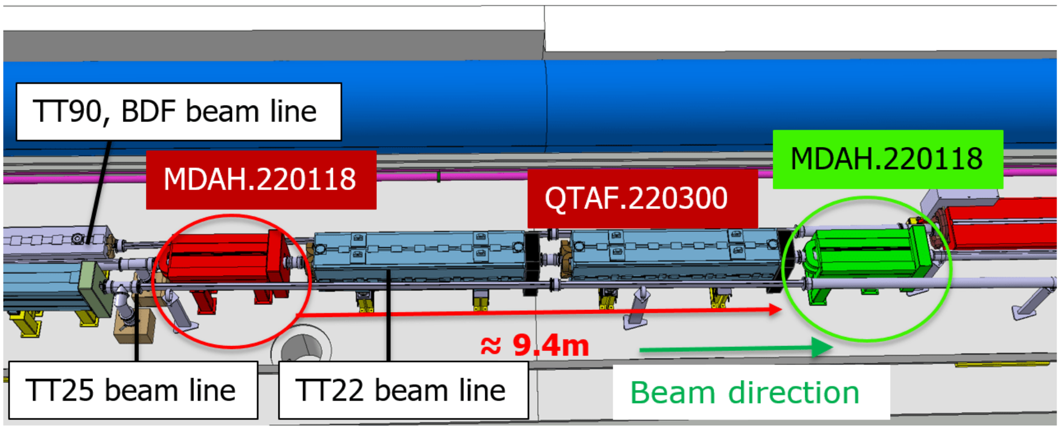

Fig. 8.13: Dipole MDAH.220118 moved 9.4 m downstream

The bending magnet MBB.240500 on the BDF beam line clashes with the vacuum chamber on the TT22 beam line. The magnet is rotated by 0.368° about the centre of the downstream end of the magnet core with respect to the beam line trajectory. The orientation creates a 40 mm offset between the centre line of the magnet and the beam trajectory; it also creates a 15 mm clearance between the magnet and the vacuum chamber, as shown in Fig. 8.14.

8.2.4.2 Beam instrumentation

For the layout of the beam instrumentation in the BDF beam line, see Ref. [3]. The control system for the beam instrumentation is composed of two racks that are to be housed in the auxiliary building.

8.2.4.2.1 Changes to existing beam line TT22

The exterior casing of the existing BSGV.220075[1] monitor (⌀ 436 mm) on beam line TT22 clashes with the vacuum chamber on the BDF beam line. A preliminary design was undertaken by the beam instrumentation group of a new beam monitor with a small exterior casing (⌀ 225 mm), which will fit between the new BDF beam line and the existing TT22 beam line as shown in Fig. 8.15.

8.2.4.3 Vacuum

For the vacuum layout of the BDF beam line, see Ref. [4].

[1] "BSGV" denotes a type of secondary emission monitor.

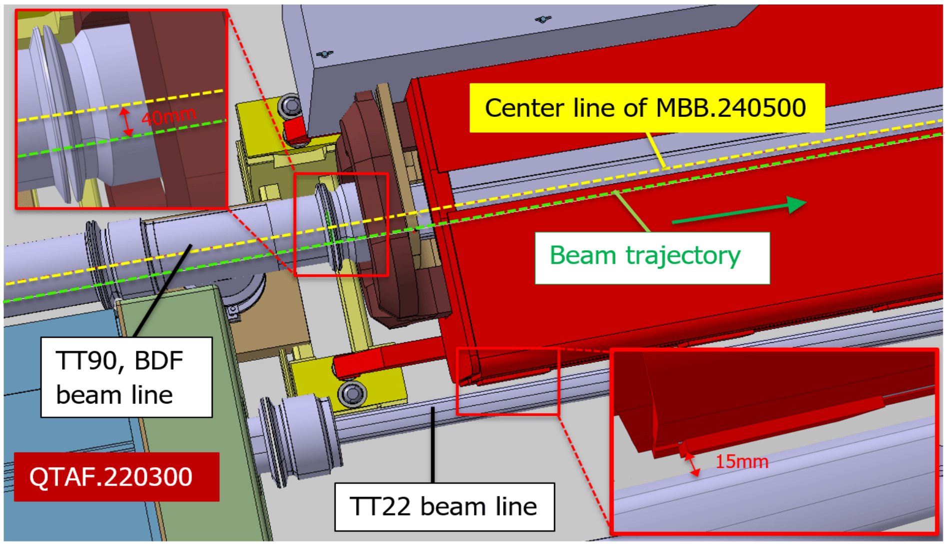

Fig. 8.14: Orientation of MBB bending magnet with respect to the beam line trajectory

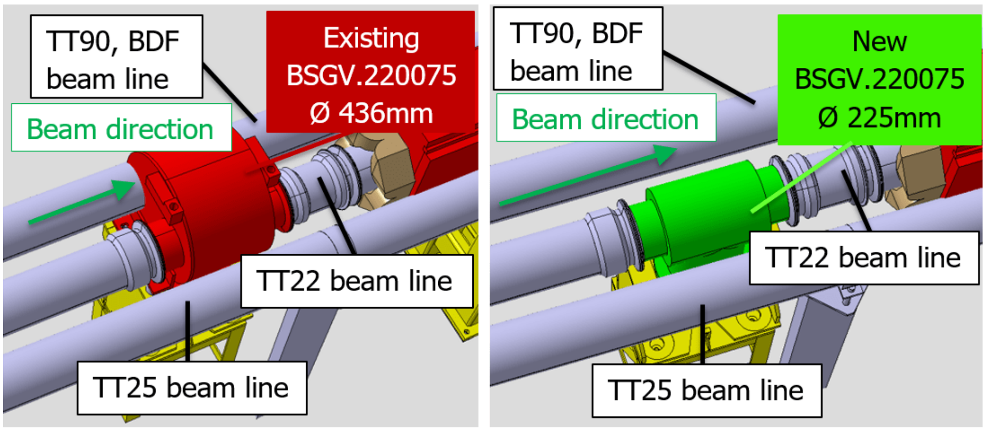

Fig. 8.15: Clash of secondary emission monitor BSGV.220075 with BDF beam line

8.2.4.3.1 New BDF beam line vacuum equipment

Approximately 200 m of new vacuum chamber is required for the BDF beam line (each type of magnet has a specific vacuum chamber, which is not included in the 200 m length). The new vacuum chamber consists of two types, of varying lengths, which are consistent with the existing vacuum chambers in the TDC2 tunnel: a standard circular vacuum chamber with an outer diameter of 159 mm and a rectangular vacuum chamber with an external envelope of 156×64 mm. Each length of vacuum chamber is supported by at least two supports, one of which is fixed and the other free in the longitudinal direction. The number of bellows was chosen such that there is a bellows between any two magnets. The numbers and types of vacuum components for the BDF beam line were qualitatively chosen, as shown in Table 8.3.

The vacuum equipment includes the following items.

- A recombination chamber, for which a new design is required to be undertaken. This vacuum chamber creates a three-way split for the BDF, TT22, and TT25 beam lines (shown in Fig. 8.2(a)). For the purposes of integration, a preliminary model was used in the beam line model.
- Two types of vacuum pump (VPIA and VPIB).
- Roughing valves (type VVRA) equally spaced along the beam line, the first one located at the recombination chamber.
- Two sector valves (type VVS), one after the recombination chamber and one after the MDX mag-

Table 8.3: New vacuum equipment for the BDF beam line

Component	Quantity
Recombination chamber	1
Vacuum pump, VPIA	7
Vacuum pump, VPIB	5
Roughing valve, VVRA	6
Sector valve, VVS	2
Vacuum gauge, VG	2
Venting valve, VVV	2
Vacuum window	1

nets of the dilution system, therefore creating two sectors.
- One vacuum gauge assembly (type VG) per sector (a combination of Pirani and Penning types). For interlock requirements, a vacuum gauge is required to be located before the sector valve.
- One venting valve (type VVV) per sector.
- A vacuum window at the end of the beam line. For the preliminary integration study, a titanium window was used (see Ref. [5] for further details).

A compressed air line is required for the sector valves and roughing valves. The sector valves require a constant compressed air connection; they only require the supply during opening and closing, however. The roughing valves only require a compressed air connection during interventions. Note that the vacuum specifications are the same as for the existing compressed air line in the TDC2 tunnel. The pressure required is between 6 and 7 bar; a pressure of 10 bar is required, however, to account for losses along the compressed air line, which will be regulated down to the required pressure.

A 220 V connection is required for maintenance of the vacuum along the beam line. The vacuum pressure in the BDF beam line will be that of the vacuum system of the existing TDC2 tunnel. There are to be three 45U racks housed in the auxiliary building for the vacuum control system, which will have three 16 A power outlets with 10 sockets (a general network) and three 10 A power outlets with five sockets (an uninterruptible power supply).

8.2.4.3.2 Changes to existing beam line TT22

The vacuum chamber downstream of dipole MDLV.220109 on the TT22 beam line clashes with quadrupole QTG.01 on the BDF beam line. The existing circular vacuum chamber (⌀ 159 mm) with a port for a VPIB vacuum pump was changed to a rectangular vacuum chamber (156×64 mm) with a short circular vacuum chamber (⌀ 159 mm) with a port for a VPIB vacuum pump, as shown in Fig. 8.16.

The vacuum chamber downstream of quadrupole QTAF.220300 on the TT22 beam line clashes with bending magnet MBB.240500 on the BDF beam line. The existing circular vacuum chamber (⌀ 159 mm) with a port for a VPIB vacuum pump was changed to a rectangular vacuum chamber (156×64 mm) with a short circular vacuum chamber (⌀ 159 mm) with a port for a VPIB vacuum pump as shown in Fig. 8.17.

8.2.5 Electrical network system

For details of the main electrical engineering infrastructure required for the beam line, see Section 8.3.5.

To construct the junction cavern, part of the existing TDC2 tunnel will be demolished. During the LS3 long shutdown, all of the equipment in the junction cavern will be removed prior to the demolition (see Ref. [1] for further information on the extent of the equipment removal). The existing cabling in the TDC2 tunnel will be checked during the LS2 long shutdown such that the demolition and the construction

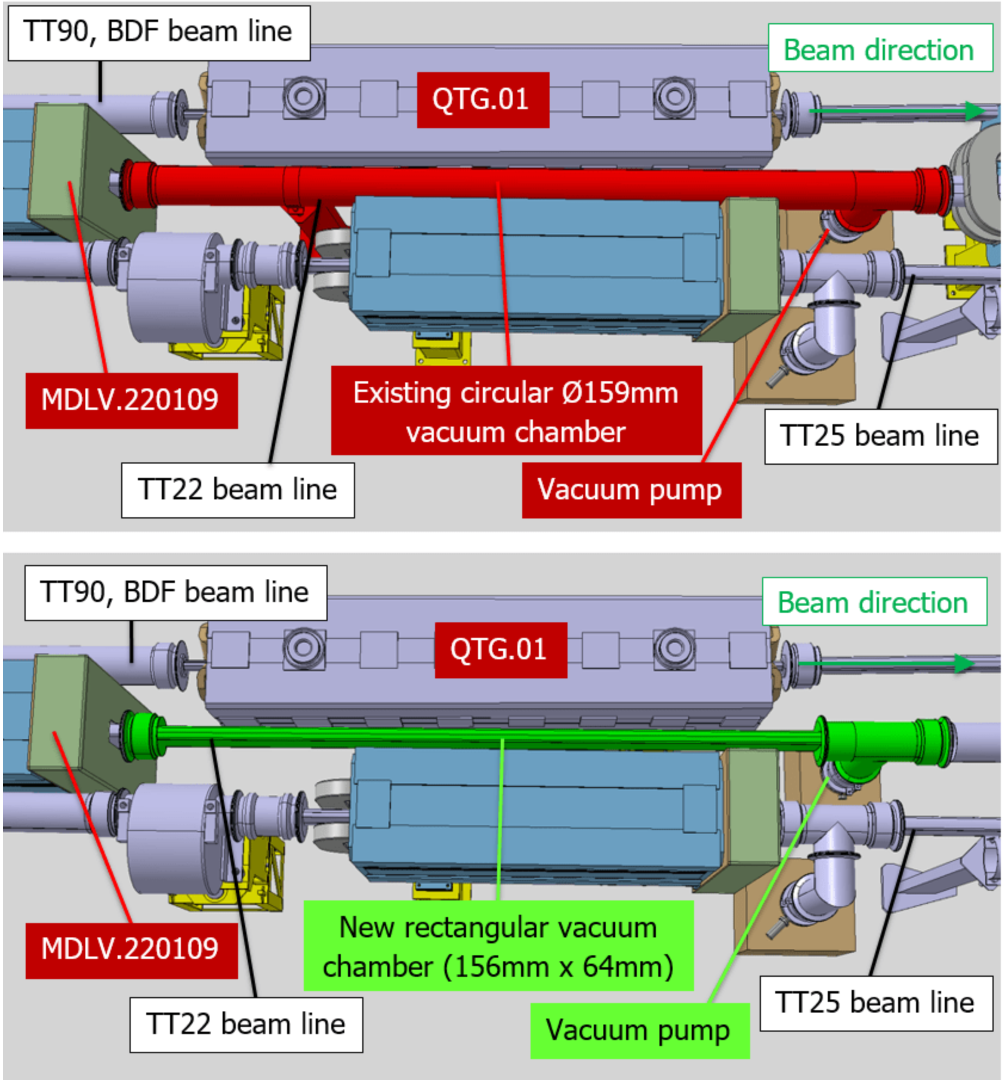

Fig. 8.16: Clash of quadrupole QTG.01 with a vacuum chamber on TT22 beam line

of the junction cavern can be undertaken during LS3. This exercise requires full identification of all electrical services (including cables and fibres installed for the equipment groups) running within the tunnel from the upstream TT20 tunnel that connects with the TDC2 tunnel to the downstream TCC2 cavern, as potentially all of these services will be cut for the duration of the work. For example, if critical services (level 3 alarms or network, fixed, or mobile telephone connectivity) are compromised, a significant period of time will be required to put a temporary solution in place prior to the start of the demolition.

It is foreseen that all the existing cabling in the junction cavern area will be re-used after the equipment de-installation, as the infrastructure is relatively new.

During the construction of the junction cavern and the demolition of the TDC2 tunnel section, lighting is required in the upstream area between the junction cavern and the TDC2 sector door. Therefore, a temporary electrical feed will be required from the upstream TT20 tunnel, for which cabling can be brought from a sump located close to the TDC2 sector door.

The existing TCC2 cavern, downstream of the junction cavern, may be used as a marshalling area during the construction of the cavern. CERN's electrical engineering group's recommendation is that the LED lighting in the TCC2 cavern should be upgraded to increase the power by 30–50%.

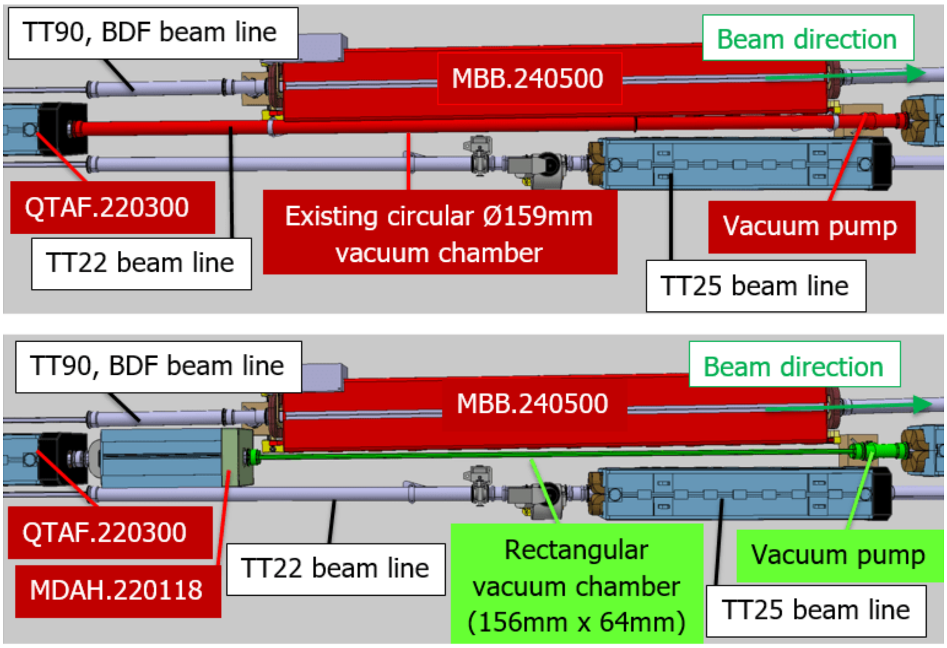

Fig. 8.17: Clash of BDF magnet MBB.240500 with a vacuum chamber on the TT22 beam line

Another recommendation is that HALFEN rails [6] or equivalent should be installed in the junction cavern and the extraction tunnel, as this would prevent drilling into the tunnel and allow some flexibility during installation and maintenance of the electrical infrastructure.

It is expected that the BDF beam line in the existing TDC2 tunnel will not require new cable trays, as the cabling requirements can be integrated into the existing cable trays currently in place.

In the junction cavern, new cable trays are to be installed on the Jura side wall. It is expected that the number of cable trays will be similar to that in the TDC2 tunnel, with two for control, two for power, and one for general services. The cable trays and cabling will be installed before the beam line. As the junction cavern is a new structure, wider than the existing structure, conventional and emergency lighting are to be installed on the Jura side, as shown in Fig. 8.6. The cable trays will continue from the junction cavern into the extraction tunnel; they will be located on the Salève side wall of the extraction tunnel, however. Conventional and emergency lighting are to be installed on the Jura side, as shown in Fig. 8.9. A typical cross-section of the extraction tunnel, showing the various service and geometry requirements, is shown in Fig. 8.11.

8.2.6 Survey

During the process of removal of equipment from the junction cavern, one of the existing survey pillars in the junction cavern area will be removed, and will be replaced with a new survey pillar after construction. During construction, survey floor points will be installed at 25 m intervals, either in the middle of the transport side or on the personnel side. Cast iron covers will be used to enable transport vehicles to drive over the survey points on the floor. The floor points will be installed by the civil engineering group, and the survey group will provide the steel cups and screws; see Ref. [7] for further details.

The reference survey points (fiducials), which will be supplied by the equipment group, will be installed permanently on the equipment before the equipment is installed in the transfer tunnel. The equipment owner may request the survey group's help to align the survey fiducials (fiducialization).

To align the equipment, the reference survey points will include at least one reference point at the beam entry, one reference point at the beam exit, and one reference surface or cylinder for measurement of the roll angle around the beam axis. Each item of equipment must also include an alignment system that can move the equipment vertically, radially, and longitudinally. This alignment system and survey reference must be validated by the survey section.

After construction of the junction cavern and equipment installation, the survey group will align all of the equipment (new and existing). As there is currently some structural movement in the TT20 and TDC2 tunnels, the survey has provided for four different structural movements, in the TDC2 tunnel, the TCC2 cavern, the extraction tunnel, and the SHiP experimental hall. Therefore, the beam equipment has to be monitored every 4–6 months to check for movement.

The new survey reference network consists of new survey pillars and brackets. Each item of equipment must be measurable from at least one pillar position. The positions of the brackets are located within the 200 mm allowance for emergency lighting and services (see Fig. 8.11). The pillars are located between the existing magnets and vacuum chambers. A clear line of sight is required between the brackets and pillars, with the maximum distance between any pillar and any bracket being between 25 and 30 m. Therefore, the new survey system is composed of:

- one survey pillar in the TDC2 tunnel;
- two survey pillars in the junction cavern;
- one survey pillar in the TCC2 cavern;
- one survey bracket in the junction cavern;
- one survey bracket in TDC22 tunnel;
- seven survey brackets in the extraction tunnel.

The positions of the pillars and brackets are shown in Fig. 8.18. Some additional small references may be added later to add redundancy to the survey network. The beam line survey network will be connected to the SHiP alignment network via a clear line of sight through the target complex (see Section 8.5.11 for further details).

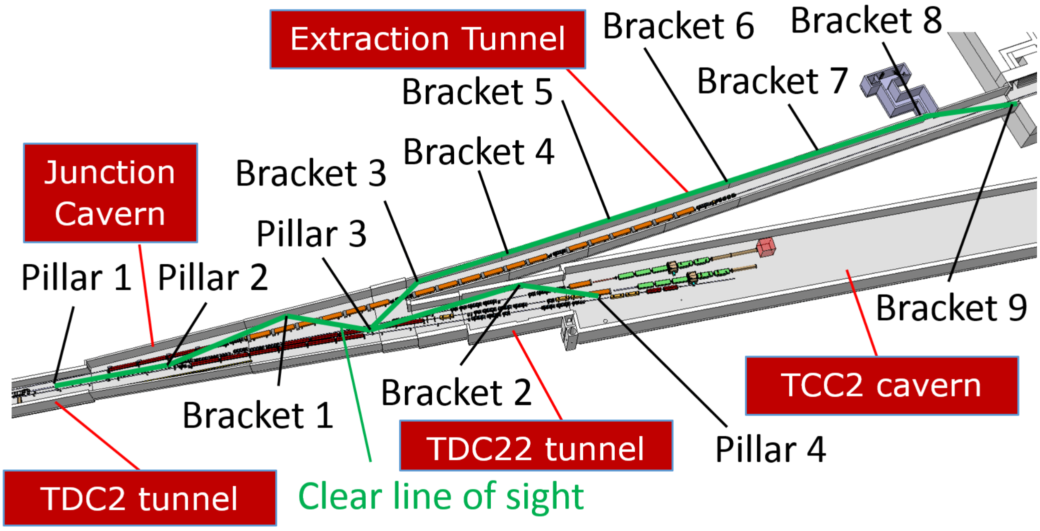

Fig. 8.18: Locations of survey pillars and wall brackets in the transfer tunnel

8.2.7 Radiation protection

The BDF beam line requires important radiation protection constraints to be incorporated into the overall facility layout. This includes specific thicknesses of soil above the tunnel for shielding purposes [8] and suitable fencing requirements at ground level to prevent personnel access (see Section 8.3.2). See Chapter 9 for details of the RP specifications for the facility.

8.2.8 Safety

8.2.8.1 Fire and alarms

The safety requirements for the transfer tunnel were a key aspect in the overall layout of the facility. These include fire protection, detection, alarms, and evacuation. See Chapter 10 for further details.

8.2.8.2 Access control

Access to the BDF will be controlled from the CERN Control Centre, located in building 874 on the CERN Prévessin site. As the target complex, access building, and auxiliary building (including the personnel access to the transfer tunnel) are located next to one another, they will share the same badge control station. The access control system for the transfer tunnel is shown in Figs. 8.19 and 8.20. It includes the following.

1. An emergency exit with a sector/fire/ventilation door between the extraction tunnel and the target complex.
2. A sector/fire/ventilation door between the chicane and the extraction tunnel.
3. A patrolled sector/fire/ventilation door between the junction cavern and the extraction tunnel.
4. Six patrol boxes located throughout the transfer tunnel in accordance with access control recommendations.

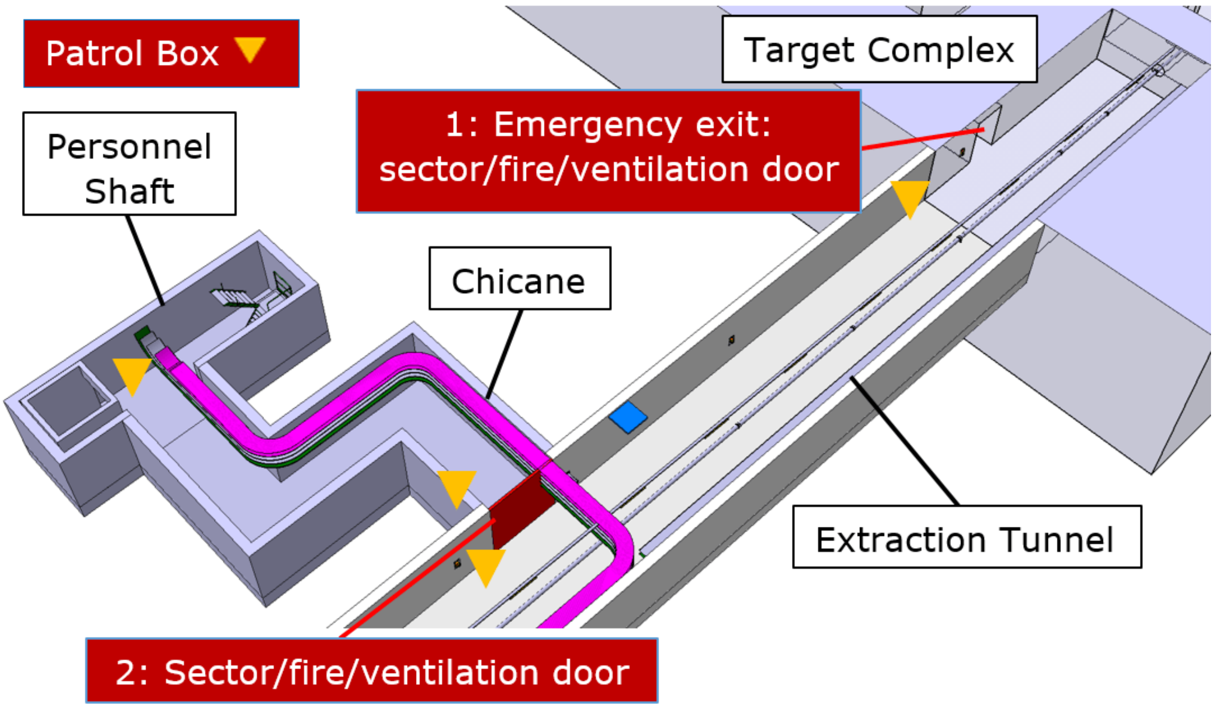

Fig. 8.19: Access control at the downstream end of the extraction tunnel

8.3 Access building and auxiliary building

The service building for the transfer tunnel and the target complex and the equipment access building for the transfer tunnel are located upstream (south-west) of the target complex, on the Jura (north-west) side of the extraction tunnel, as shown in Fig. 8.1.

The structures consist of two surface buildings (access building and auxiliary building), which have a Finished Floor Level (FFL) of 451.1 m above sea level. The auxiliary building's downstream

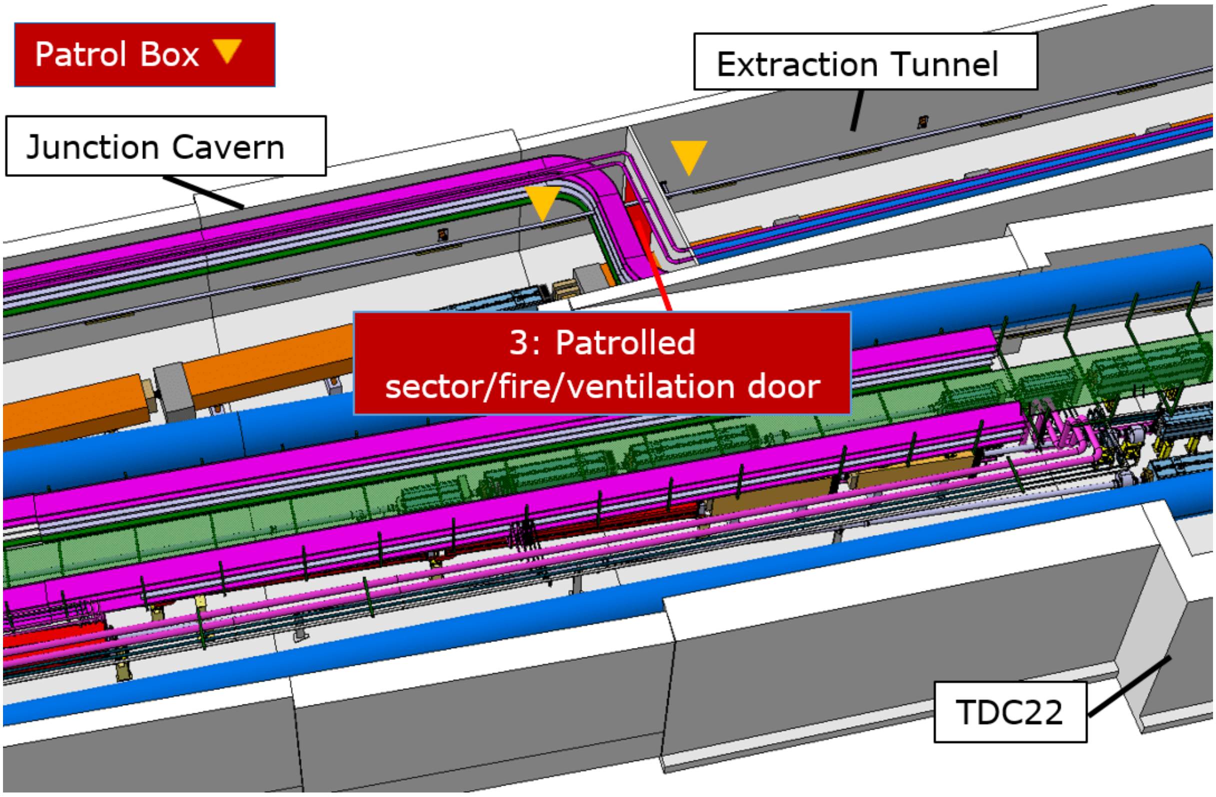

Fig. 8.20: Access control at the upstream end of the extraction tunnel

(north-east) wall is directly next to the target complex, and its Jura (north-west) side wall is next to the target complex's lorry and personnel access. The access building is approximately 46.5 m from the target complex and 4 m from the auxiliary building. Located next to the auxiliary building is a cooling tower base, as shown in Fig. 8.21. Underneath the auxiliary building is a personnel shaft and a chicane, and inside the access building is an equipment shaft, both of which are connected to the extraction tunnel as shown in Fig. 8.22.

The purpose of these structures includes the following:

- access for beam line equipment to the transfer tunnel;
- personnel access to the transfer tunnel;
- service storage and distribution for the transfer tunnel, the target complex, and the experimental area.

The equipment includes magnets, beam instrumentation, vacuum equipment, and general electrical and safety equipment. The services include electrical services, cooling, and ventilation.

8.3.1 Access building (BDN90) and equipment shaft (PA90)

8.3.1.1 Summary

The access building (BDN90) is a single-storey industrial building located directly over the extraction tunnel. Located inside the building is an equipment shaft (PA90) that extends from the floor level of the access building to the top of the extraction tunnel. For the integration studies, a simple single-storey steel frame building with exterior cladding and a concrete floor and equipment shaft was modelled. Figure 8.23 shows the proposed integration layout of the access building and the equipment shaft.

The equipment shaft is located directly over the extraction tunnel, as this allows equipment to be lowered directly onto the extraction tunnel floor. The alternative method would have been a layout

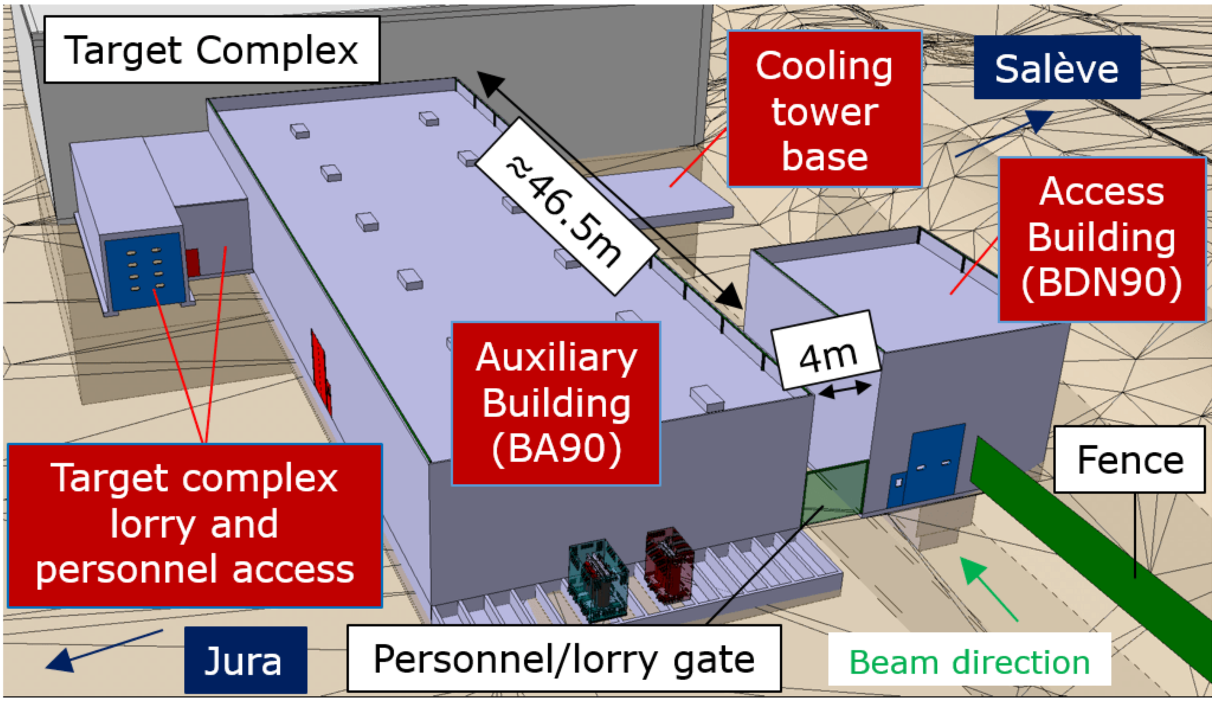

Fig. 8.21: Access and auxiliary buildings

similar to that of the personnel shaft and would have required the tunnel to be locally widened to allow the transport vehicle sufficient space to turn, for which the design was foreseen to be less effective in terms of cost and feasibility.

During the equipment installation, transport vehicles, including a 40 t semi-trailer, a 19 t truck, and a forklift, will move the equipment into the access building, from which a 30 t overhead crane will lift and lower the equipment into the equipment shaft. A handling vehicle inside the extraction tunnel will collect the equipment for positioning along the beam line.

The equipment shaft will be filled with nine concrete shielding blocks during beam operation because of RP considerations, and surrounding the equipment shaft is a guard rail for personnel safety. During installation and de-installation of equipment in the tunnel, the shielding blocks will be removed from the shaft and stored outside the building. The specific storage location for the shielding blocks outside the building has not been defined; however, it is foreseen that the surface outside the building will be of sufficient capacity to temporarily store the shielding blocks during the installation and de-installation procedure.

Inside the building, there is a personnel platform at the height of the crane rail on the Jura (north-west) side to allow personnel to access the crane. To access the platform, there is a ladder attached to the side wall. For ventilation requirements, there will be an air-handling unit supported by the wall/columns inside the building.

8.3.1.2 Geometry

Figure 8.24 shows a plan view and sections of the access building and the equipment shaft. For a detailed layout, see Ref. [9].

The building has an internal geometry 14.2 m long, 11 m wide, and 8.5 m high. The geometry of the structure is based on the distances required for the 30 t overhead crane, transport vehicles, and personnel inside the building.

The width of the structure (11 m) is based on the equipment shaft opening (2.6 m), a personnel

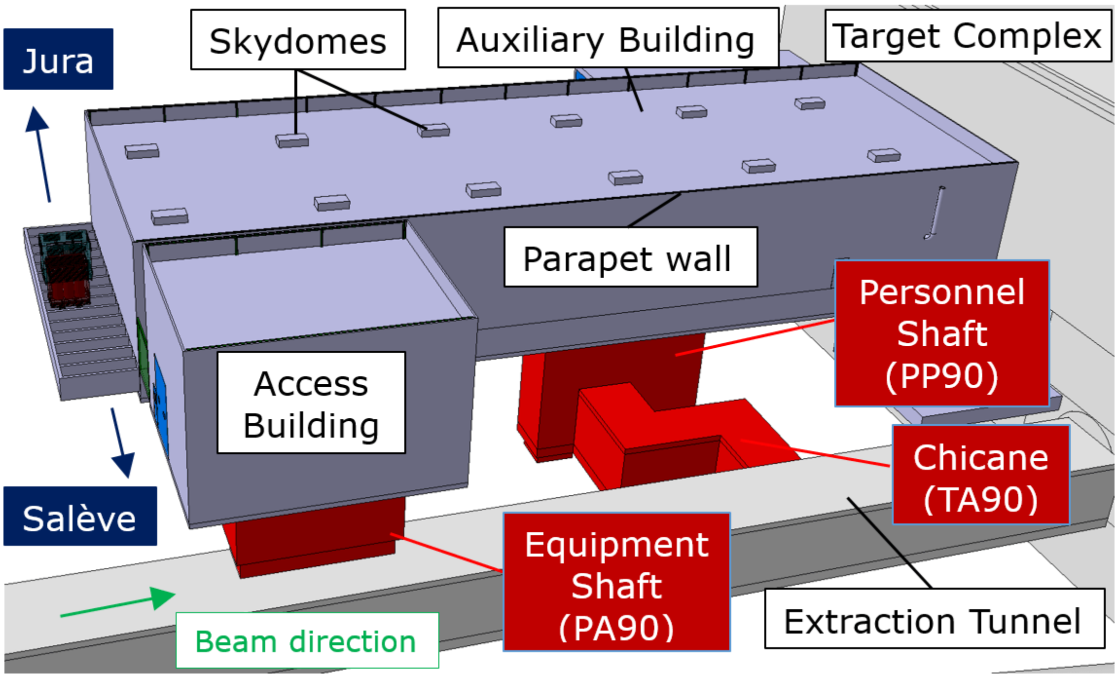

Fig. 8.22: Equipment shaft, personnel shaft, and chicane

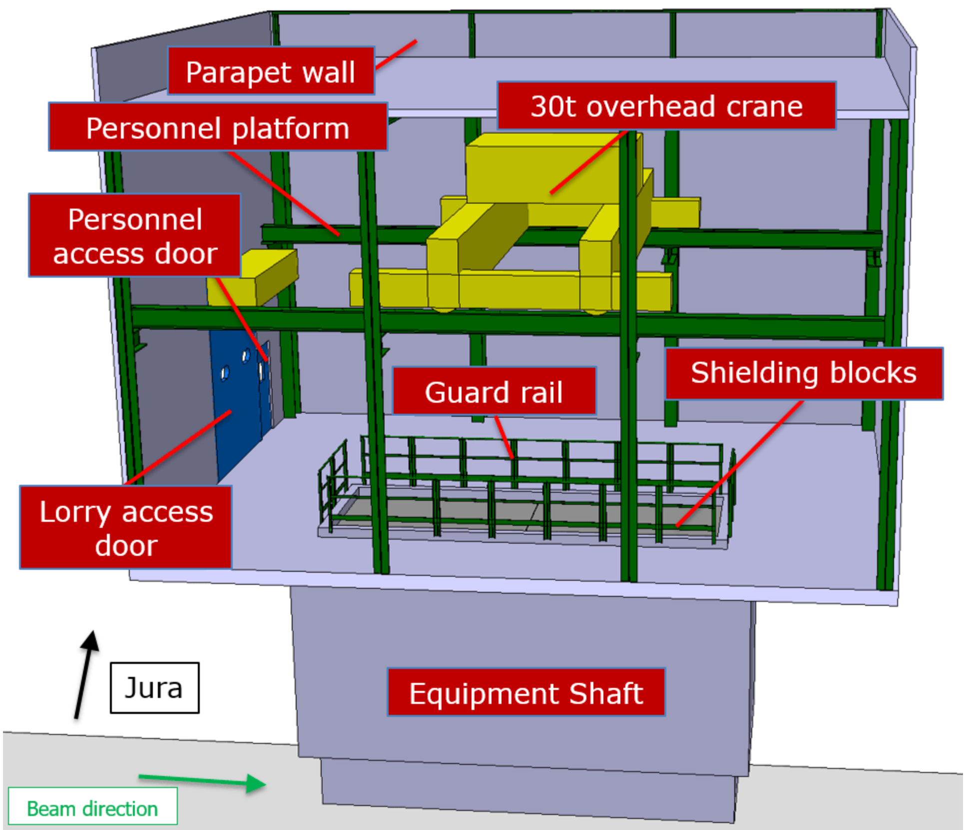

Fig. 8.23: Access building integration layout

accessway (1.5 m), a semi-trailer (2.5 m), and the clearance of the overhead crane on both sides (2 × 2.2 m). The length of the structure (14.2 m) is based on the equipment shaft (8 m) and the clearance of the overhead crane on both sides (2 × 3.1 m).

The shaft is 8 m long and 2 m wide at the bottom, for transporting heavy equipment into and out of the extraction tunnel (the largest magnets are approximately 7 m long and approximately 1.5 m wide). The top of the shaft is 2.6 m wide, as there is a 300 mm wide support on either side of the shaft for the shielding blocks. There is a 200 mm upstand all around the equipment shaft to prevent water entering the extraction tunnel. A preliminary one-way-spanning shielding-block support arrangement has been outlined, as shown in Fig. 8.24.

The height of the structure (8.5 m) is based on the height of the lorry access door (4.7 m), the clearance between the top of the door and the underside of the crane (0.5 m), the height of the crane (2.5 m), the clearance between the top of the crane and the underside of the services (0.5 m), and an allowance for lighting and services (0.3 m).

To access the overhead crane for maintenance, there is a personnel platform, for which the crane is offset from the wall/column by 1 m. On the other side, the crane is offset by 0.5 m to provide the minimum crane clearance. On the roof, there is a 1.1 m parapet wall for personnel access safety.

For details of the minimum thickness of concrete shielding required for the structures, see Ref. [2]. See Chapter 9 for details of the RP specifications for the structures.

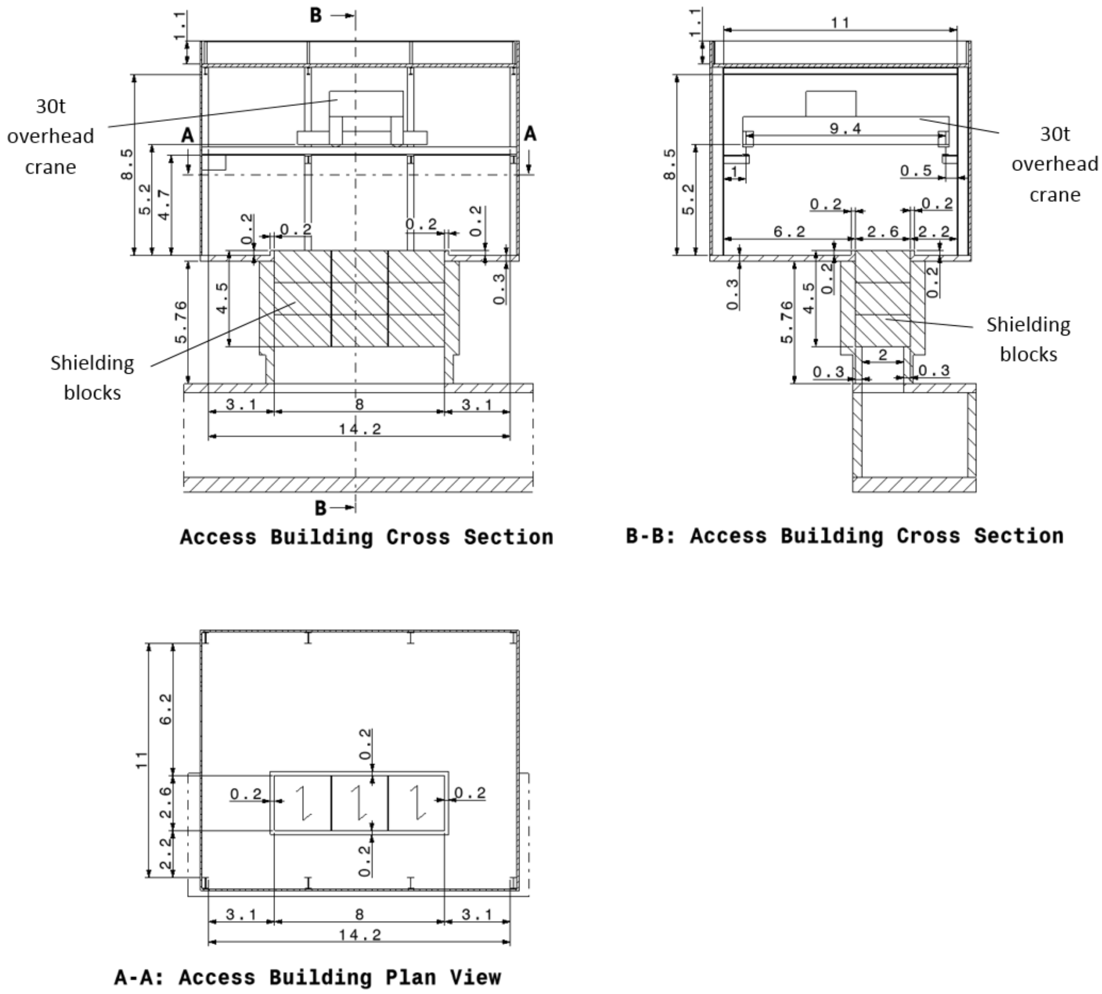

Fig. 8.24: Plan and section views of access building

8.3.2 Auxiliary building (BA90), personnel shaft (PP90), and chicane (TA90)

8.3.2.1 Summary

The auxiliary building (BA90) houses the power supply, the control racks, and the cooling and ventilation equipment for the extraction tunnel and the target complex (the service requirements of the target complex are presented in Ref. [10]). The proposed integration layout is shown in Fig. 8.25; it follows that of a typical service building at CERN.

The cable trays, cooling piping, and ventilation ducts are distributed to the extraction tunnel via the personnel shaft, from which services pass underneath the personnel-accessible false floor and into the personnel shaft via a hole as shown in Fig. 8.26. Services for the target complex housed in the auxiliary building also pass through a hole in the walls between the two structures. Both holes must be sufficiently waterproofed and airtight.

The access control for the extraction tunnel is housed inside the auxiliary building, and is composed of a material access door (MAD), a personnel access door (PAD), and an emergency door. Through the access control there is a personnel lift and stairs, which bring personnel and light equipment down to the chicane. The lift and stairs are fire protected and are not connected to the general electrical circuit for safety. A buffer zone for storing material brought up from the tunnel during maintenance work is located next to the access control.

Transport vehicles, including a 19 t truck and a standard forklift, drive the equipment into the building on the transport accessway. The transport accessway is suspended to allow services to pass beneath the accessway. At end of the transport accessway, next to the access control, there are toilets.

Two 7.5 t overhead cranes move equipment into position throughout the building. There is a ladder attached to the side wall to allow personnel to access and maintain the overhead crane.

On the roof of the auxiliary building there are natural smoke extraction units (skydomes) distributed throughout the roof, as shown in Fig. 8.22. Outside the building, on the upstream side, is a transformer base to support the transformers. The cabling for the transformers will run from the base to underneath the false floor, to be distributed to the various electrical equipment. Also outside, on the Salève side of the building, is a cooling tower base. Because of RP considerations, to access the cooling tower there is a personnel/lorry gate between the access and auxiliary buildings and a fence running alongside the extraction tunnel, as shown in Fig. 8.21.

The personnel shaft (PP90) and chicane (TA90) are located underneath the auxiliary building. The shaft houses a personnel lift, a CAT ladder, a metallic personnel staircase, and the services (ventilation, cooling, and cable trays) from the auxiliary building. The CAT ladder is composed of two sections (maximum height 6 m) with an intermediate platform and a platform at the top. The shaft brings personnel from the FFL of the access building to the FFL of the extraction tunnel. The services are brought into the personnel shaft from underneath the false floor in the auxiliary building to the ceiling level of the chicane (see Figs. 8.26 and 8.27). Personnel and services enter the extraction tunnel via the chicane. At the end of the chicane, at the entrance to the extraction tunnel, there is a sector/fire/ventilation door.

8.3.2.2 Geometry

The auxiliary building is a single-storey steel frame industrial building, 21 m wide between the outer edges of the external columns, which is composed of three columns with a transverse centre-to-centre spacing of approximately 10.4 m. The building is approximately 60 m long, with a longitudinal centre-to-centre column spacing of 5 m. The ceiling-to-floor height is approximately 6.7 m, and there is a 2 m deep false floor to allow personnel to gain access below the false floor. On the roof, there is a 1.1 m parapet wall for personnel access safety (see Fig. 8.28). For a detailed layout of the auxiliary building, see Ref. [11].

The height of the structure (6.7 m) is based on the height of the lorry access door (4 m), the clear-

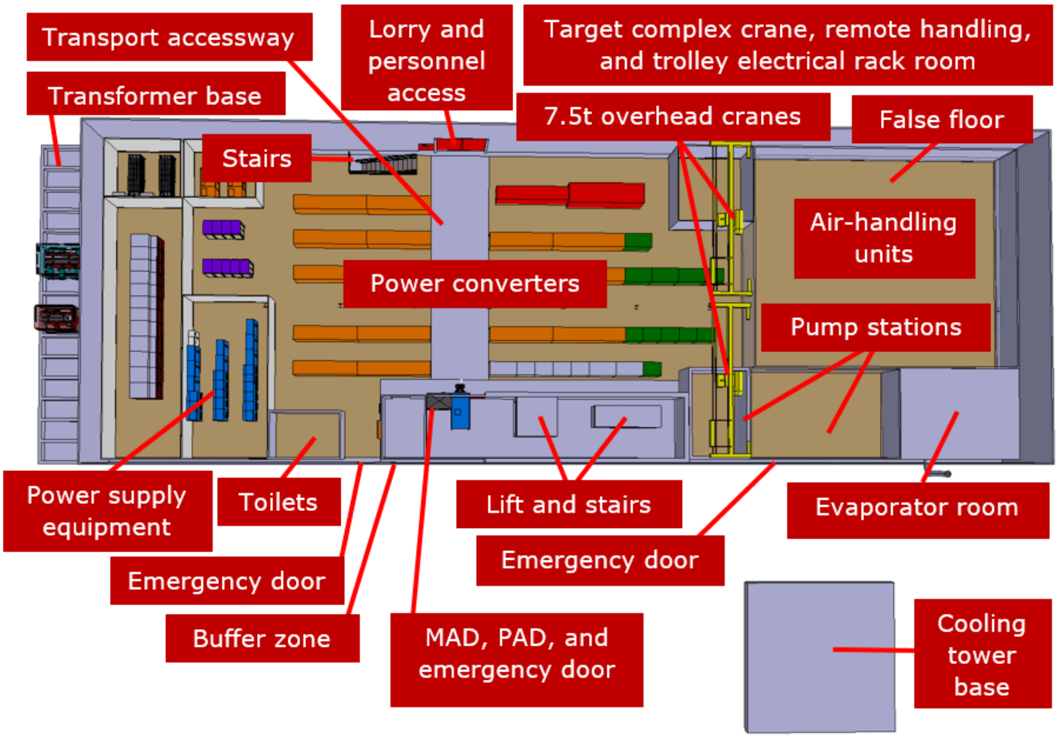

Fig. 8.25: Auxiliary building integration layout

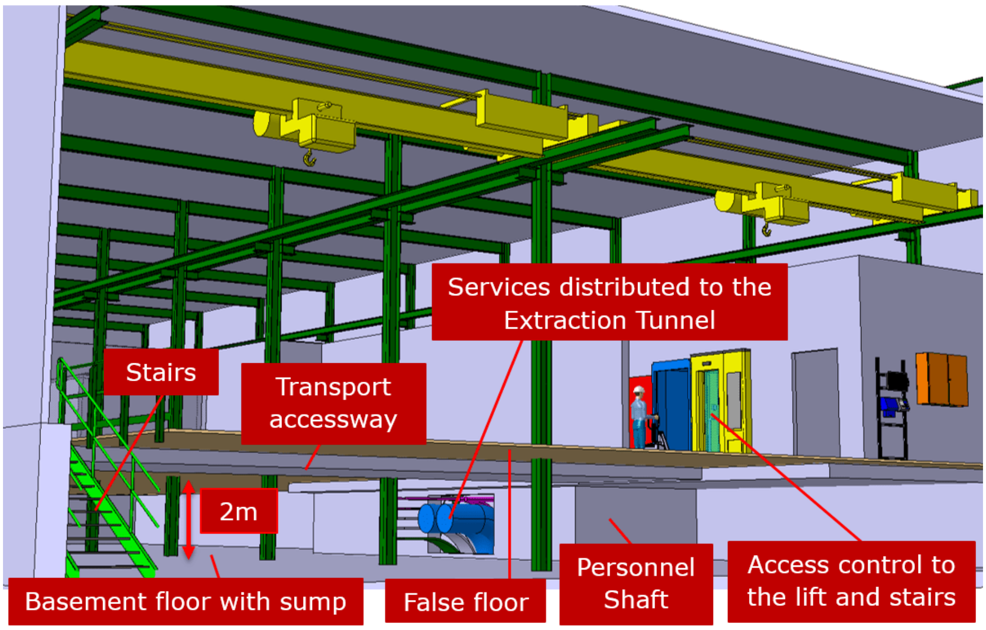

Fig. 8.26: Auxiliary building false floor, transport accessway, and personnel shaft

ance between the top of the door and the underside of the crane (0.5 m), the height of the crane (1.4 m), the clearance between the top of the crane and the underside of the services (0.5 m), and an allowance for lighting and services (0.3 m).

The 2 m deep false floor allows services to be distributed throughout the building and into the extraction tunnel and the target complex.

There is an evaporator room with 0.4 m thick concrete walls and a 0.4 m thick ceiling, with an

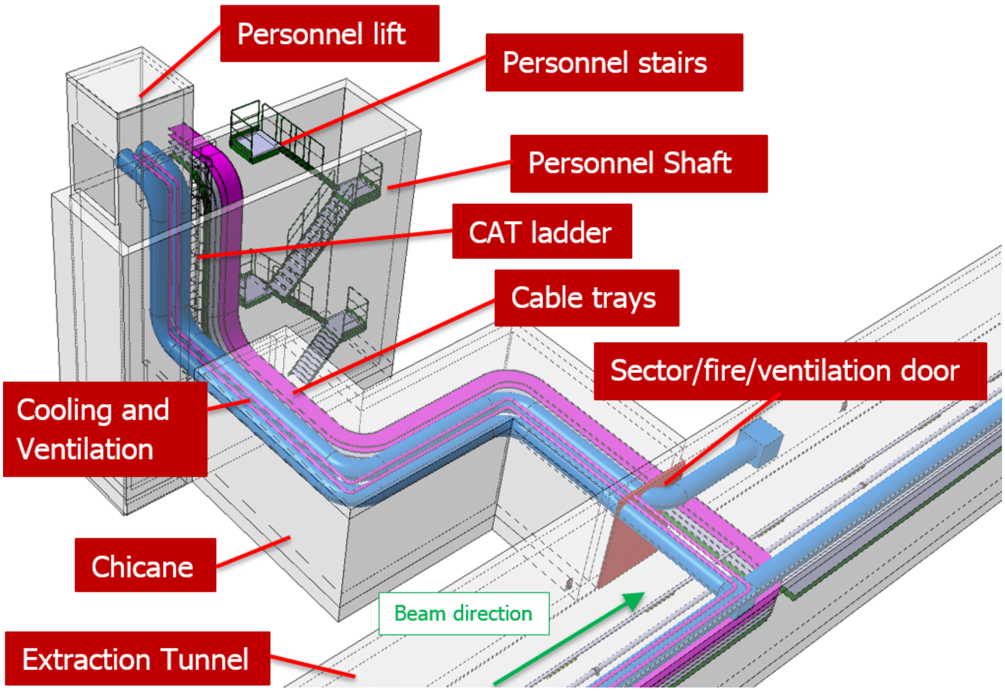

Fig. 8.27: Integration layout of personnel shaft and chicane

internal height of 3.5 m. It is foreseen that equipment housed inside the room may need to be removed for maintenance purposes. Therefore, one proposed structural arrangement is to use removable concrete panels or shielding blocks for the roof and walls, to avoid demolition of the concrete structure during the removal of the equipment.

There is also a secondary pumping station room with 0.2 m thick concrete walls. Surrounding the access control is a 0.3 m thick concrete wall, decreasing to a 0.1 m thick concrete wall at the location of the MAD, PAD, and emergency door. Surrounding the buffer zone is a 0.1 m thick concrete wall. There is also a 1 m wide concrete accessway surrounding the access control, connected to the transport accessway.

As shown in Fig. 8.25, there is a 4.58 m wide transformer base outside the building that the transformers will be supported on. Also outside the building is a 10 m $\times$ 10 m cooling tower base. The base is located 8 m from both the target complex and the auxiliary building, in accordance with cooling and ventilation requirements.

Note that the geometry of the chicane is based on RP requirements, such that there is no direct line of sight between the extraction tunnel and the personnel shaft and that its length is such that the personnel shaft is located at a required distance away from the extraction tunnel. The geometry was checked to ensure that CERN's tunnel fire vehicle (PEFRA [12]) could safely manoeuvre through the chicane to and from the transfer tunnel.

The proposed dimensions of the personnel shaft and chicane are shown in Fig. 8.29. For a detailed layout of the personnel shaft and chicane, see Ref. [13]. The basic geometry of the personnel lift is based on that of a typical lift used at CERN [14].

For further details of the minimum required thickness of concrete shielding for the structures, see Ref. [2].

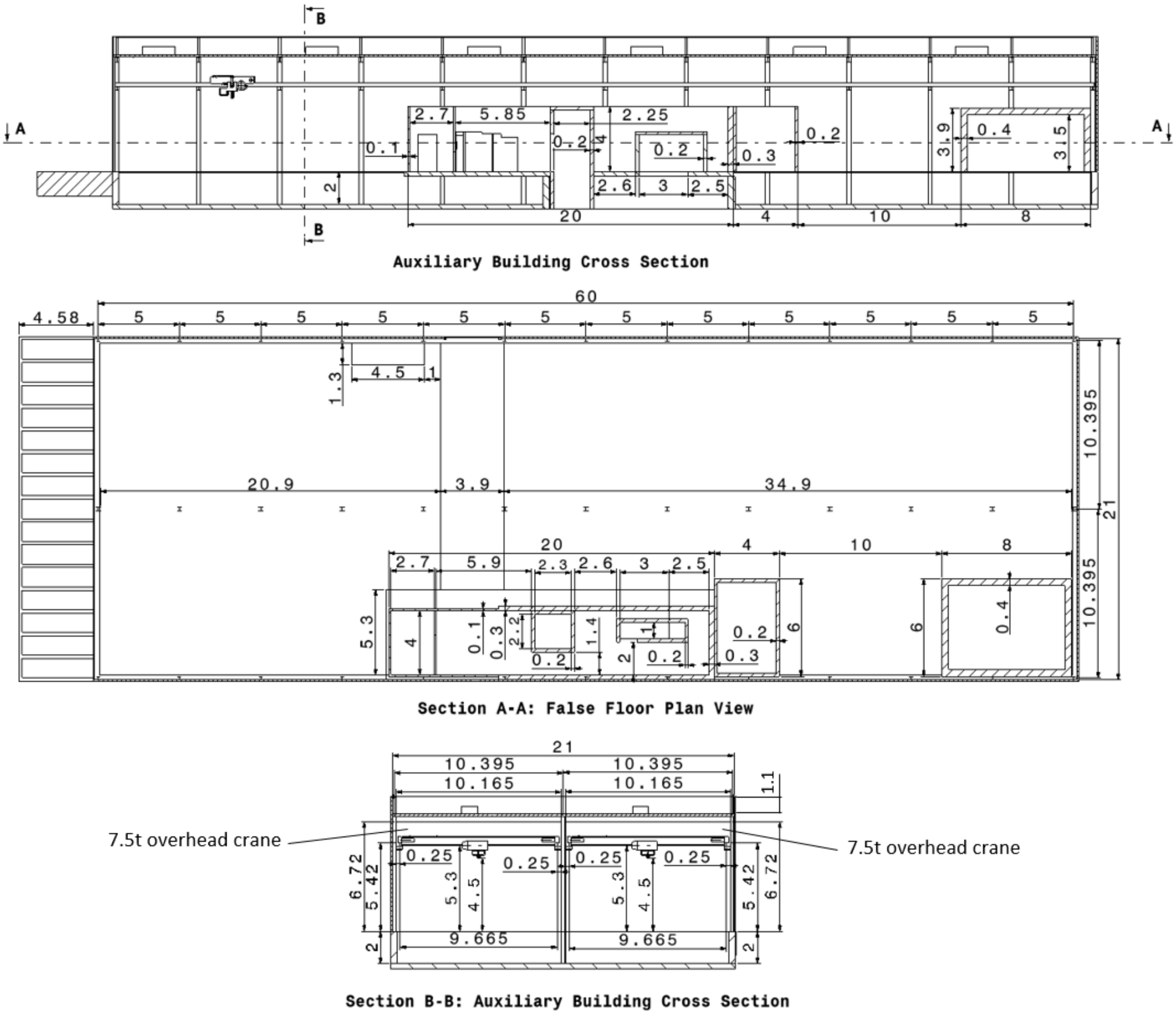

Fig. 8.28: Structural geometry of auxiliary building

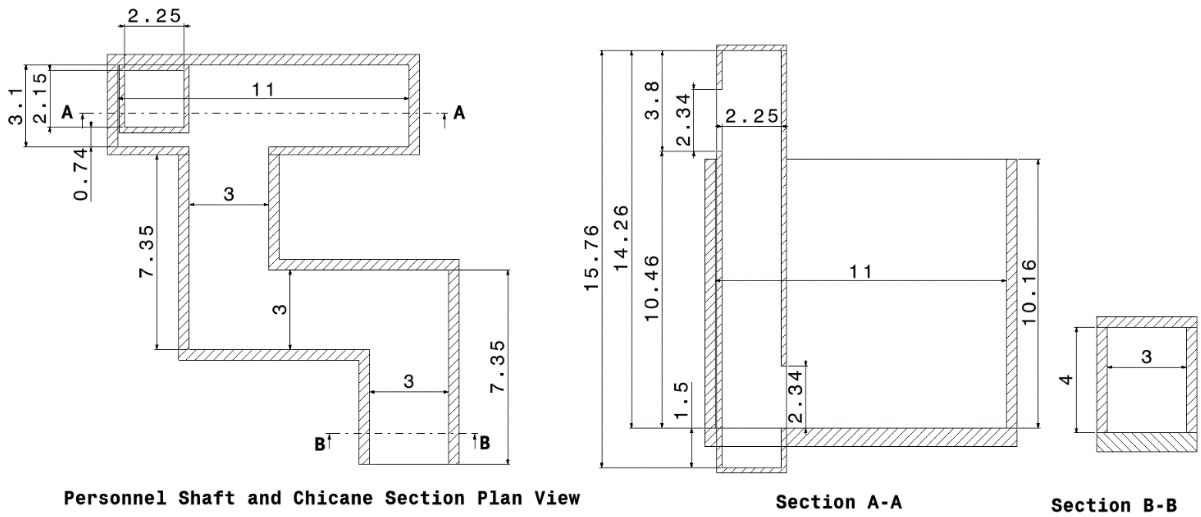

Fig. 8.29: Structural geometry of personnel shaft and chicane

8.3.3 Transport and handling

The possible transport and handling vehicles foreseen to be used in the access building include a 40 t semi-trailer, a forklift, and a 19 t truck. The transport and handling vehicles foreseen to be used inside the transfer tunnel are typical CERN magnet-handling vehicles, as used in the existing TDC2 tunnel.

During technical stops and long shutdowns of the beam line, transport vehicles and beam line equipment may be required in the transfer tunnel. Personnel with light equipment will pass through the access control in the auxiliary building (see Fig. 8.25) and down to the floor level of the transfer tunnel via the lift in the personnel shaft (see Fig. 8.27).

For the larger equipment, the beam-interlocked lorry door of the access building is opened and a semi-trailer or truck is driven in. The 30 t overhead crane lifts the shielding blocks onto the semi-trailer/truck. The semi-trailer or truck moves the shielding blocks outside the building for storage and is driven into the access building loaded with the handling vehicle. The overhead crane lifts the transport vehicle off the semi-trailer or truck and into the equipment shaft to the extraction tunnel floor. The semi-trailer or truck is driven into the access building loaded with beam line equipment (see Table 8.2 for the BDF beam line magnet geometry). The overhead crane lifts the beam line equipment off the semi-trailer or truck and into the equipment shaft to the extraction tunnel floor (see Fig. 8.30).

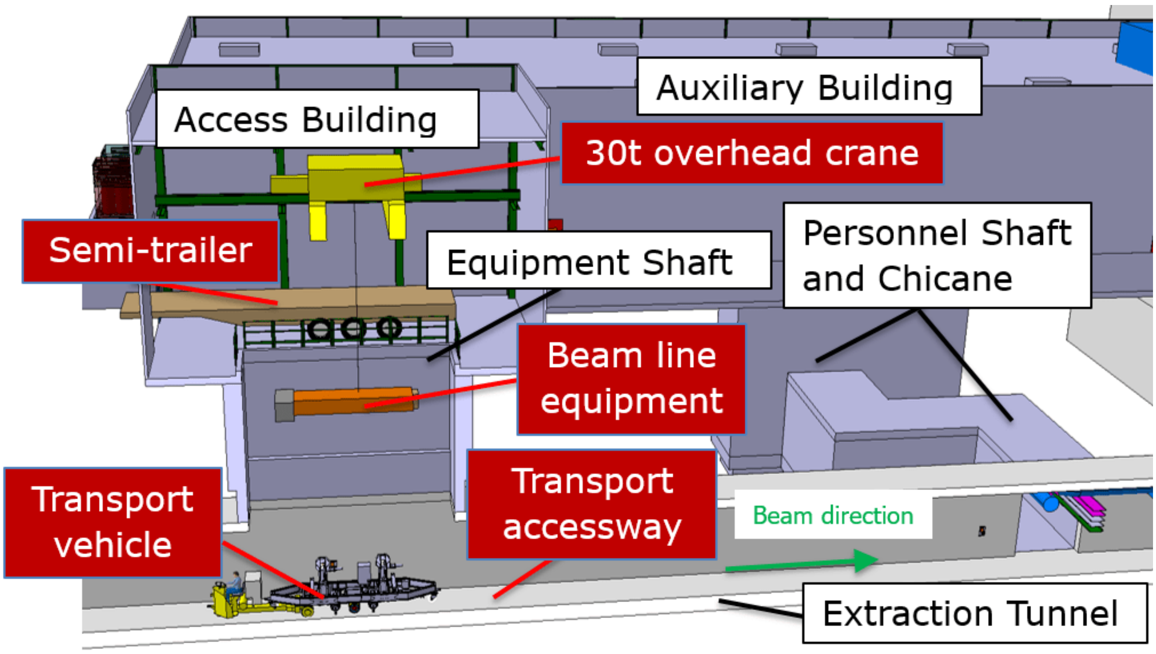

Fig. 8.30: Equipment being transported into the transfer tunnel

The transport vehicle moves along the extraction tunnel and into the junction cavern on the transport accessway. After the equipment has been positioned inside the transfer tunnel, the overhead crane lifts the transport vehicle from the extraction tunnel floor, through the equipment shaft, and onto the semi-trailer. The semi-trailer or truck drives the shielding blocks inside the access building, and the overhead crane lifts the shielding blocks inside the equipment shaft.

The possible transport and handling vehicles foreseen to access the auxiliary building include a standard forklift and a 19 t truck. During installation of equipment in the auxiliary building, a truck or forklift drives onto the transport accessway with the equipment (for typical equipment geometry, see Tables 8.5 and 8.6). The 7.5 t overhead cranes lift and move the equipment throughout the building.

8.3.4 Cooling and ventilation

The CV installations for the target complex and the extraction tunnel are located in the auxiliary building. A description of the CV systems for the extraction tunnel and the surface buildings is provided in Ref. [15].

The extraction tunnel and the surface buildings require the following CV systems:

- demineralized-water cooling for magnets;
- demineralized-water cooling for power converters;
- compressed air for the vacuum equipment in the tunnel and for general use in the auxiliary building;
- ventilation for the auxiliary building, the access building, and the extraction tunnel.

Compressed air for the junction cavern and the extraction tunnel will be supplied from the existing compressed air infrastructure in TDC2. The existing TDC2 ventilation infrastructure will be used for the TDC2 tunnel and the new junction cavern. The existing TDC2 cooling infrastructure will used for the equipment in the TDC2 tunnel, whereas cooling for the new magnets installed in the junction cavern will be provided by the extraction tunnel's demineralized-water cooling. The piping and ductwork layout in TDC2 will remain unchanged, except for minor adaptations in the junction cavern section and the addition of piping (demineralized water and compressed air) for the new BDF beam line magnets on the Jura side of TDC2 and the junction cavern.

The construction of the junction cavern during LS3 will require the demolition of a 75 m long section of the TDC2 tunnel (see Chapter 11 for further details). The CV equipment located in this part of the tunnel is to be dismantled before the work starts. The CV equipment located in the area includes the following:

- supply ventilation duct;
- demineralized-water cooling for magnets;
- raw-water piping (currently not in use);
- compressed air for vacuum equipment.

The systems listed all reach the upstream end of the TDC2 tunnel (leading to the TT20 tunnel). Before the demolition, the parts of the CV systems (mainly piping and ductwork) that are located in the portion of TDC2 that will be demolished will be dismantled. Components that can be re-used will be stored according to RP instructions; parts that cannot be re-used will be replaced with new equipment. After the construction of the junction cavern is finished, piping and ductwork will be reinstalled according to the new layout of the junction cavern; since the layout of the junction cavern simply expands the width of the tunnel on one side, the piping and ductwork can be reinstalled at the same locations as they were in before the demolition; minor adaptations to the layout of the piping will need to be performed in a detailed design phase.

8.3.4.1 Cooling systems

The BDF cooling system is based on a raw-water primary cooling system supplying water at 25 °C via cooling towers. Local cooling is provided via demineralized-water secondary circuits; chilled water provides cooling for the AHUs. The primary system is located in the BDF auxiliary building and provides primary cooling for the entire BDF, including the extraction tunnel, the target complex, and the experimental area. Figure 8.31 shows a synoptic view [16] of the cooling systems for the facility.

The magnet cooling system provides demineralized-water cooling for the magnets in the extraction tunnel; its pumping station is located in the auxiliary building. The system supplies 75 m^3/h at 28 °C and 20 bar for a thermal load of 1200 kW on average; the estimated return temperature is 42 °C, and pressure

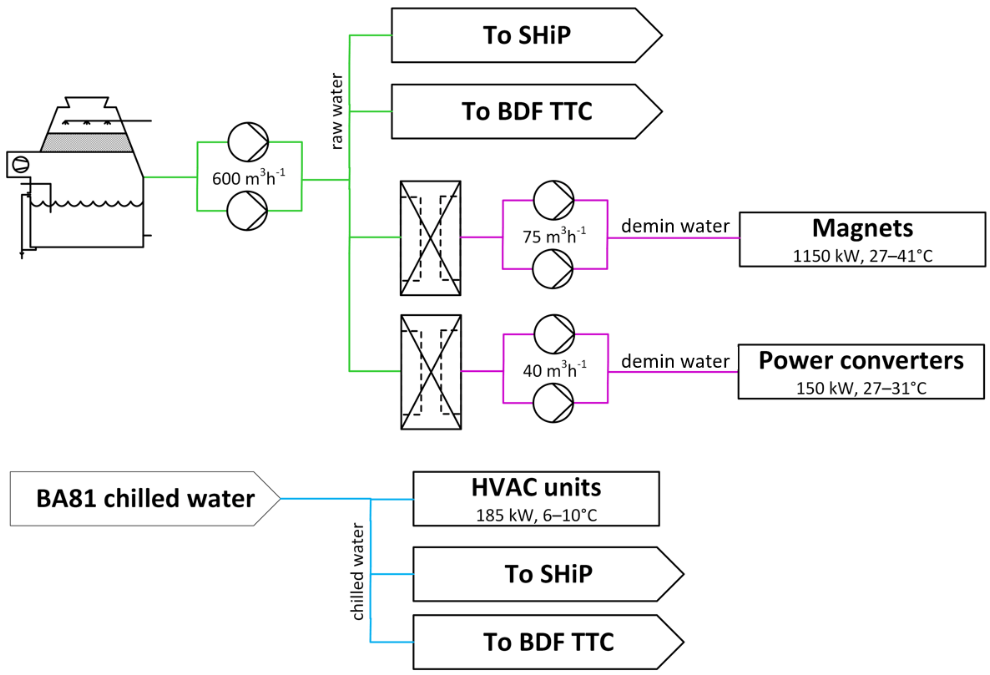

Fig. 8.31: Overview of the cooling systems for the facility

reducers are used to locally reduce the pressure to the needs of the specific magnet. Since the water is likely to become activated, the pumping station located on the surface in the auxiliary building is separated from the rest of the CV equipment.

The power converter cooling system provides demineralized-water cooling for the converters in the auxiliary building. Its pumping station is located in the CV area of the auxiliary building; since the level of activation of this water is expected to be low, the circuit does not need to be separated from the rest of the equipment. The system supplies 40 m^3/h at 28 °C for a maximum thermal load of 150 kW.

Chilled water is needed in the facility for the ventilation units in the auxiliary building and will be provided by the chilled-water production plant in one of CERN's existing service buildings (BA81).

8.3.4.2 Ventilation systems

Ventilation units are required for the following structures:

- extraction tunnel;
- access building;
- auxiliary building.

Figure 8.32 provides a synoptic view [17] of the ventilation units and their characteristics; Fig. 8.33 shows a preliminary integration of the ducts within the facility.

Supply and extraction units for the tunnel ventilation are located in the auxiliary building. Ducts reach the extraction tunnel via the false floor in the auxiliary building and through the chicane. Inside the extraction tunnel, two supply ducts reach the ends of the tunnel, and one extraction grille in the proximity of the chicane extracts the entire flow. Recirculation is normally used during operation; full extraction is activated during shutdowns. The design flow rate for the ventilation units is 12 000 m^3/h.

The ventilation of the access building is done using recirculation; the ventilation unit is located inside the access building and is designed for a flow rate of 6000 m^3/h.

The ventilation supply unit for the auxiliary building is based on recirculation; air is supplied to

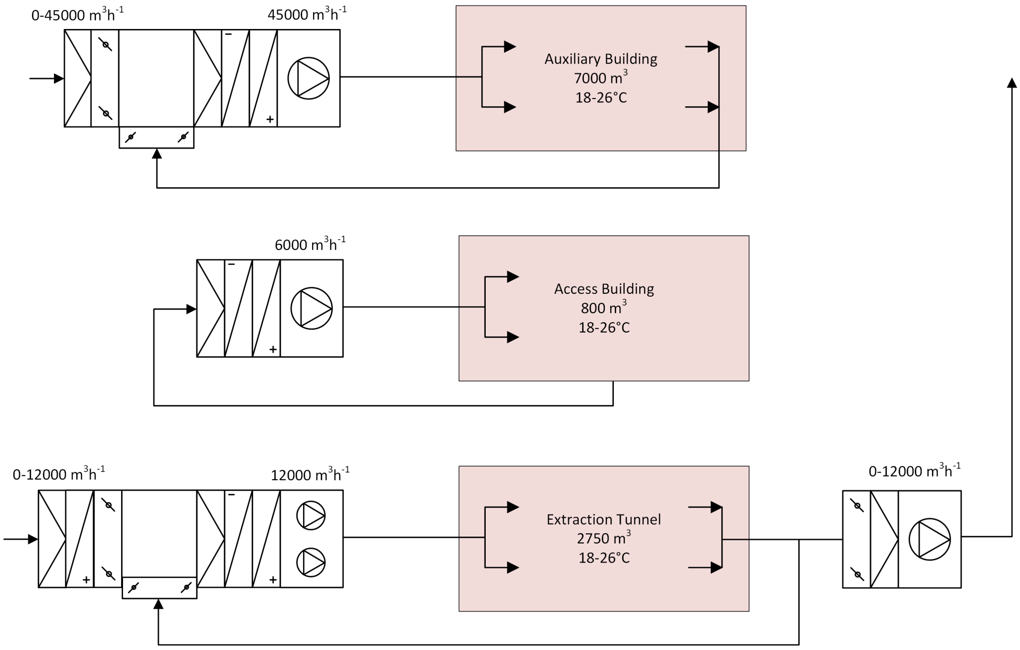

Fig. 8.32: Synoptic view of ventilation system for the extraction tunnel and for access and auxiliary buildings.

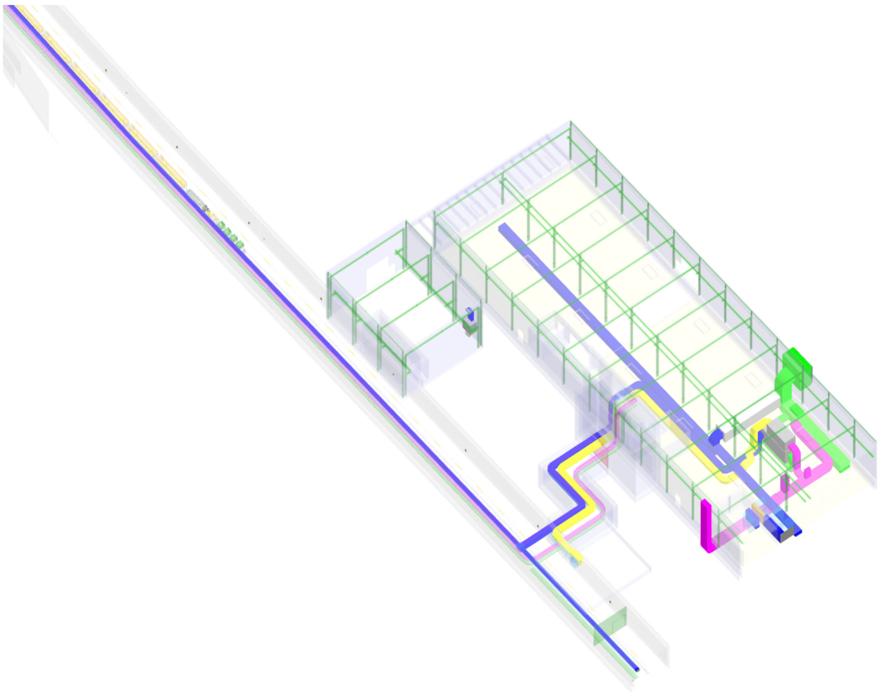

Fig. 8.33: Ventilation duct layout for the extraction tunnel and for access and auxiliary buildings

the room via the false floor and collected directly in the unit. The ventilation approach takes advantage of free cooling whenever possible, to minimize energy loss. The design flow rate is 45 000 m^3/h.

With regard to the smoke extraction system, smoke extraction for the tunnel is provided via portable extractor units and flexible ducts. The smoke extraction method for the auxiliary building is based on natural ventilation and skydomes located on the ceiling or on grilles located on the side walls for improved leak-tightness.

8.3.5 Electrical network system

The BDF electrical feed is foreseen to be supplied from building BA80, for which a minimum of a 1 m wide trench is required from BA80 to the auxiliary building. There may possibly be a technical gallery with cooling and ventilation infrastructure (compressed air, demineralized water, raw water, and chilled water) included; see Fig. 11.2 for the proposed layout of the technical gallery.

Preliminary space reservations in the auxiliary building for the BDF electrical engineering infrastructure have been outlined, as shown in Fig. 8.34.

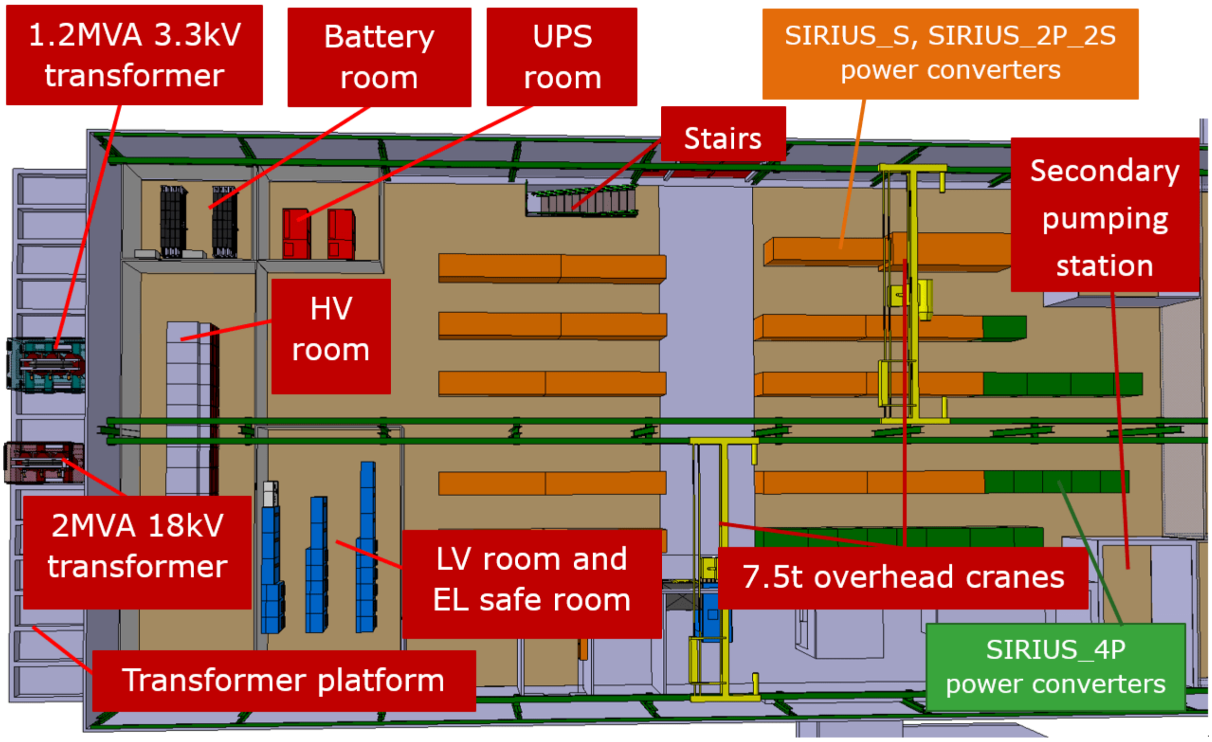

Fig. 8.34: Layout of integration of electrical infrastructure for auxiliary building

The infrastructure includes the following items.

- An Uninterruptible Power Supply (UPS) room for the cooling of the 800 kVA heat load, which can be in a shared space (the cooling for this area must be supplied by a UPS). Two 400 kVA systems provide the requirements for the transfer tunnel, access building, auxiliary building, and target complex with a margin for future expansion.
- A dedicated battery room with smoke extraction in case of fire. It must have an autonomy of 10 min at 800 kVA, and must be cooled to an ideal temperature of 18 °C to maximize battery life.
- An electrical engineering EL safe room, a small rack room with space for six racks to contain electrical-protection and network supervision hardware. This safe room is in a shared space with the low-voltage room. The low-voltage room is sized for the transfer tunnel, access building, auxiliary building, and target complex: 2 MVA normal, 1.2 MVA electrostatic discharge (ESD) protection, and 800 kVA UPS, with no non-electrical engineering racks allowed in front of the switchboards.
- An HV stable switch room (stable and pulsed), 3 m high with a full-height double door, will be accessible to electrical engineers only. The doors will face onto the external perimeter of the building. There will be one switchboard for stable and one switchboard for pulsed power. There

will be a 1.2 m space between the two switchboards and a space reservation in the corner of the switch room for a spare HV circuit breaker (1 m × 1 m) for each switchboard.
– Two transformers, a 2 MVA 18 kV transformer for distribution and a 1.2 MVA 3.3 kV transformer for diesel back-up.

A false floor, 2 m deep, which is personnel accessible via stairs, is included for service distribution throughout the auxiliary building and into the transfer tunnel.

In the access and auxiliary buildings, an 800 mm space reservation is allowed for between the top of the crane and the underside of the ceiling, of which the first 300 mm below the ceiling is reserved for lighting. The lighting will be installed and maintained from the overhead crane.

CERN's electrical engineering group's recommendation is that the cable trays have a minimum of 1.2 m bending radius horizontally and vertically. The control trays will need to be accessed at least once per year for the first 5 yr, and therefore there is a CAT ladder and a metallic staircase in the personnel shaft to inspect and maintain the cable trays as shown in Fig. 8.27.

8.3.6 Electrical power converters

Power converters are required for the magnets on the BDF beam line. They are housed in the auxiliary building, as shown in Fig. 8.34.

A preliminary design of the power converters was provided by CERN's power converter group. Table 8.4 lists the magnet features taken into account in the design. Note that a four-quadrant (4Q) operation mode implies bipolar current and voltage capabilities.

Table 8.4: Design parameters of beam line power converters

Circuit name	No. of magnets in series	R_{mag} (mΩ)	L_{mag} (mH)	I_{max} requested (A)	Quantity	Operation mode
MSSB2117	3	66	140	1100	1	4Q
MBB	5	4.42	9.9	5750	1	4Q
MBN	3	51.5	170	1180	6	4Q
QTG.01	1	57	31	385	1	4Q
QTG.02	1	276	390	345	1	4Q
QTG.03	1	276	390	304	1	4Q
QTG.04	1	276	390	192	1	4Q
QTG.05	1	276	390	354	1	4Q
QTG.06	1	276	390	444	1	4Q
MDX1 corrector	1	320	221	120	6	4Q
MDX1 bend	1	320	221	240	1	4Q
MDX1 dilution	1	320	221	170	4	4Q

The initial request was for one string of 18 magnets with a voltage of 2.7 kV. The solution implemented consists of six strings of three magnets, to guarantee the same current in each magnet. For standardization, the SIRIUS family of power converters were used. The magnet current reference (per unit) for the transfer line is shown in Fig. 8.35. The performance of the current sources requested is 'accuracy class 4', which specifies a long-term (1 yr) stability of 100 ppm, a stability of 20 ppm over 12 h, and a short-term (20 min) stability of 5 ppm

Tables 8.5 and 8.6 show the geometrical specifications of the power converters and the energy storage racks.

The power converters are arranged in two groups (SIRIUS S, SIRIUS 2P 2S) and (SIRIUS 4P), shown in green and orange in Fig. 8.34. The power converters are positioned in the middle of the building, next to both the electrical engineering infrastructure and the transfer tunnel to optimize the length of cabling. The secondary pumping station is located next to the power converters to optimize the length of cooling piping required.

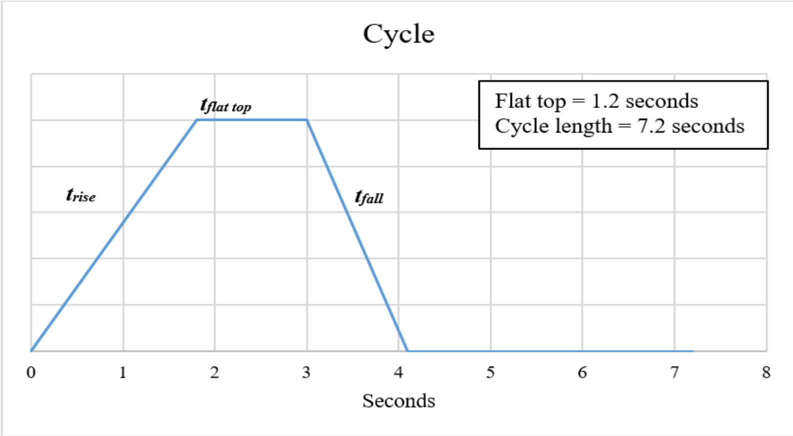

Fig. 8.35: Magnet current reference

The distance between the front and the rear of any two converters/storage racks and the distance between a converter/storage rack and a wall was kept to a minimum of 1.4 m in accordance with the SIRIUS installation guide [18]. This distance was increased to 2 m for the MBB power converter. The power converters and racks were arranged such that the two overhead cranes could manoeuvre them in and out of position for installation and de-installation. The distance between the edge of the wall and the centre of the crane hook was also considered in the layout of the converters.

The existing MSSB2117 splitter magnets will be replaced with new laminated splitter magnets. The existing power converters for these magnets are housed in building BA80. The new magnets, however, require the SIRIUS 4P+ power converter, which is larger than the existing converters; the new power converter is too large to be integrated into building BA80. In addition, the reserve SIRIUS 4P+ is to be housed in the auxiliary building; therefore, the MSSB2117 power converter will also be housed in the auxiliary building.

Table 8.5: Geometry of power converters

Circuit name	Converter type	Qty.	Converter dimensions (per unit) Length (m)	Width (m)	Height (m)	Area (m^2)	Weight/unit (kg)
MSSB2117	SIRIUS 4P+	1	4.2	0.9	2.1	3.8	2600
MBB	NEW 4P+	1	5	1.3	2.4	6.5	5500
MBN	SIRIUS 4P+	6	4.2	0.9	2.1	22.7	2600
QTG.01	SIRIUS S	1	1.2	0.9	2.1	1.1	700
QTG.02	SIRIUS 2P	1	1.8	0.9	2.1	1.6	1100
QTG.03	SIRIUS S	1	1.2	0.9	2.1	1.1	700
QTG.04	SIRIUS S	1	1.2	0.9	2.1	1.1	700
QTG.05	SIRIUS S	1	1.2	0.9	2.1	1.1	700
QTG.06	SIRIUS 2P	1	1.8	0.9	2.1	1.6	1100
MDX1 corrector	SIRIUS S	6	1.2	0.9	2.1	6.5	700
MDX1 bend	SIRIUS S	1	1.2	0.9	2.1	1.1	700
MDX1 dilution	SIRIUS 2S	4	1.8	0.9	2.1	6.5	1100
Reserve	SIRIUS 4P+	1	4.2	0.9	2.1	3.8	2600
Reserve	SIRIUS 2P	1	1.8	0.9	2.1	1.6	1100

The total estimated power dissipated in the air of the auxiliary building from the power converters

Table 8.6: Geometry of energy storage racks

Circuit name	Qty.	Dimensions per unit				
		Length (m)	Width (m)	Height (m)	Area (m^2)	Weight/unit (kg)
MSSB2117 splitter	1	4.8	0.9	2.1	4.3	2400
MBB	1	4.8	0.9	2.1	4.3	2400
MBN	6	4.8	0.9	2.1	25.9	2400
Reserve	1	4.8	0.9	2.1	4.3	2400

is 80 kW, and the total cooling power requested is 150 kW. The cooling is provided by demineralized water with the following features:

- maximum water temperature in circuit 27 °C with $\Delta\theta$ of approximately 10 K;
- total flow rate 660 l/min;
- ΔP 3 bar with a nominal pressure less than 6 bar.

The a.c. and d.c. cabling will be covered by CERN's electrical engineering group. Water-cooled cabling is required for the link between the MSSB2117 splitter, the MBB magnets, and their power converters. Table 8.7 shows the a.c. and d.c. distribution considered in the study. The third column indicates the cable cross-section as recommended by CERN's power converter group in order to keep the voltage drop to a reasonable level. In addition, thermal aspects have to be evaluated by CERN's electrical engineering group. The cable length is twice the distance between the converter and the magnet. The total power to be installed is 1548 kVA.

Table 8.7: A.c and d.c. distribution for power converters

Circuit name	Qty.	Total cable length (m)	I_{rms} (A)	D.c. cable section Cu/Al (mm^2)	Converter type	Electrical feeder (V)	I_{rms} for converters	Total installed r.m.s. power (kVA)
MSSB2117	1	1000	800	480	SIRIUS 4P+	400	125	87
MBB	1	435	3250	1000	NEW 4P+	400	630	436
MBN	6	230	800	480	SIRIUS 4P+	400	125	520
QTG.01	1	278	200	120	SIRIUS S	400	32	22
QTG.02	1	250	400	240	SIRIUS 2P	400	63	44
QTG.03	1	168	200	120	SIRIUS S	400	32	22
QTG.04	1	129	200	120	SIRIUS S	400	32	22
QTG.05	1	90	200	240	SIRIUS S	400	32	22
QTG.06	1	52	400	240	SIRIUS 2P	400	63	44
MDX1 corrector	6	500	200	120	SIRIUS S	400	32	133
MDX1 bend	1	500	200	120	SIRIUS S	400	32	22
MDX1 dilution	4	50	200	120	SIRIUS 2S	400	62	175

8.3.7 Radiation protection

Radiation protection was one of the key aspects in the overall layout of the access and auxiliary buildings. This includes specific concrete and soil thicknesses and specific distances and positions of the buildings away from the beam line. For further details of the minimum required thicknesses of shielding for the structures, see Ref. [2]. See Chapter 9 for details of the RP specifications for the facility.

8.3.8 Safety

8.3.8.1 Fire and alarms

The safety requirements for the access and auxiliary buildings were a key aspect in the overall layout of the buildings. These include natural smoke extraction and safe emergency access throughout the buildings in accordance with safety regulations. See Chapter 10 for further details.

8.3.8.2 Access control

The access control system for the access and auxiliary buildings is shown in Fig. 8.36. It includes the following.

1. Lorry and personnel entrance, badge controlled to allow access to the auxiliary building.
2. Buffer zone with a grilled dosimeter-controlled door.
3. Secondary pumping station in a locked, supervised room.
4. Evaporator for sump in a locked, controlled room.
5. MAD/PAD and emergency door, beam interlocked to allow access to the transfer tunnel.
6. Lorry/personnel gate, badge controlled to allow access to the cooling tower.
7. Lorry/personnel entrance, beam interlocked with badge control for access to the access building.
8. Four patrol boxes located throughout both buildings in accordance with access control recommendations.

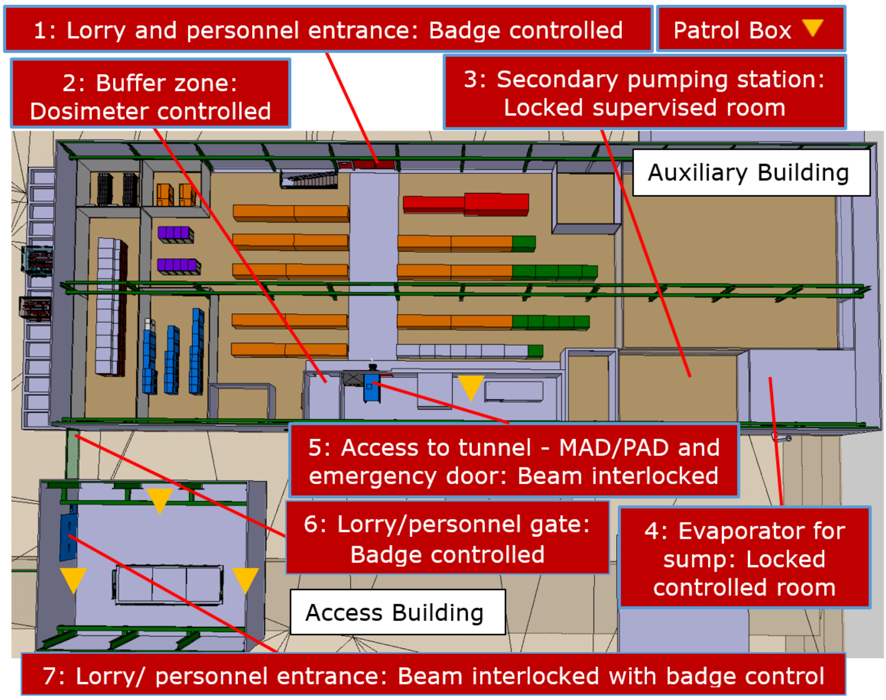

Fig. 8.36: Access control for the access and auxiliary buildings

8.4 Target complex access

The access for the target complex is located on the upstream side of the target complex on the Jura side of the auxiliary building, as shown in Fig. 8.21.

8.4.1 Personnel access

The target complex personnel access is composed of male and female changing rooms, a dirty area, and a decontamination area, as shown in Fig. 8.37. The layout is in accordance with RP requirements and follows a similar arrangement to that of the changing rooms at two of CERN's other target-related facilities, MEDICIS and Building 867. The facility has a plan area of approximately $80\,\mathrm{m}^2$ and the height of the structure is the same as that of the lorry entrance, as this allows a practical structural design and constructability as well as allowing sufficient space for ventilation at ceiling level. For access to the target complex, there is a door locked by an RP veto.

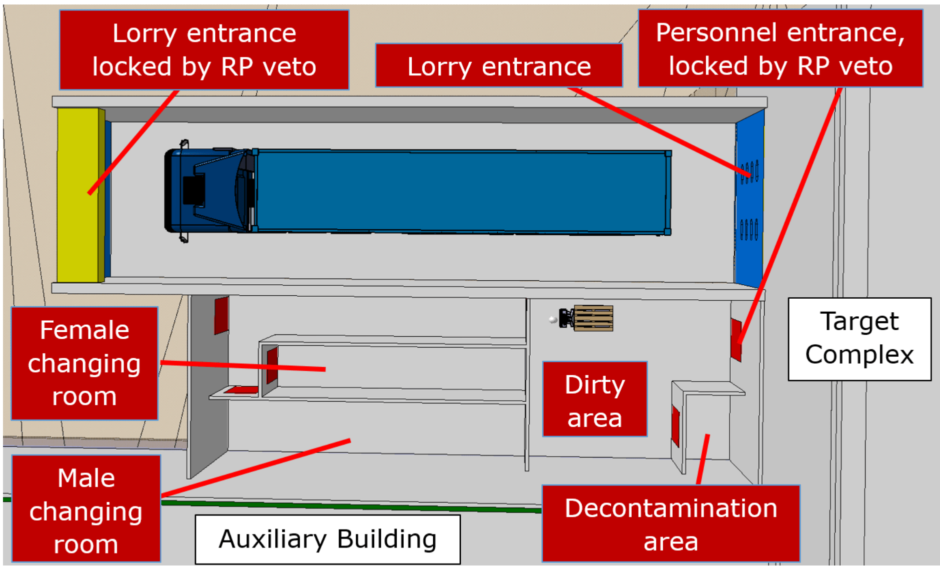

Fig. 8.37: Target complex personnel and vehicle access

8.4.2 Lorry access

The target complex lorry access (shown in Fig. 8.37) is an air-locked compartment to keep the pressure cascade in the target complex, with a large lorry access door locked by an RP veto. The air inside the lorry access has a negative pressure of $-20\,\mathrm{Pa}$, consistent with that of the target complex. This ensures that no contaminated air is released to the external environment during the transport and handling process. The geometry of the facility is in accordance with CERN's Transport and Handling group's requirements. Its geometry is such that the full length of an articulated lorry can fit inside the structure and there is sufficient room for the lorry doors to open on either side, allowing personnel to enter and exit the vehicle. The structure is 20 m long, 5 m wide, and 5 m high. To access the target complex with a vehicle, the external lorry access door is opened and the vehicle is driven in. The pressure inside is decreased to the same negative pressure as in the target complex and the internal lorry door is opened to allow the lorry to access the facility.

8.4.3 Access to the underground area

Inside the target complex, there are two staircases to access the controlled underground area. In front of one staircase there is an end-of-zone door, and in front of the other there is an interlocked PAD. A fence connects the PAD and end-of-zone door, ensuring personnel must pass through the interlocked access control to access the underground area. There are three patrol boxes foreseen in the target complex.

8.5 Experimental area

Particular effort was made in the service integration studies to guarantee a cost-efficient conceptual design. The experimental area is located immediately downstream of the target complex, as shown in Fig. 8.1. Its overall footprint has a maximum length of 180 m, a maximum width of approximately 60 m, a depth of 20 m below ground level, and a height of 16.3 m above ground level. The structure consists of an underground experimental hall and three surface buildings (service and gas buildings and surface hall), which have finished floor levels of approximately 2.1 m (between 1.6 m and 2.6 m) above the existing ground level (≈ 452.4 m above sea level). The current approach is to fill the surrounding area with structural fill to reach the required FFL. The underground experimental hall is situated underneath the surface hall, as shown in Fig. 8.38. The experimental service building and the gas building are located adjacent to the surface hall on the Jura side, and, at the back of the surface hall and in contact with its downstream wall, there are two 6 m high fenced land hills, as required for RP considerations. The layout was defined to house and assemble the SHiP experiment while guaranteeing the operation of the facility from the point of view of RP and safety. The names of the buildings are shown in Fig. 8.38. The purposes of these structures include the following:

- service supply and distribution to the SHiP experiment [19] located in the experimental hall (the requirements are described in Chapter 7);
- assembly and installation of SHiP components and equipment inside the experimental hall;
- personnel access to the experimental hall;
- housing the operational complex, which includes a workshop, laboratories, a control room, offices, and a conference room.

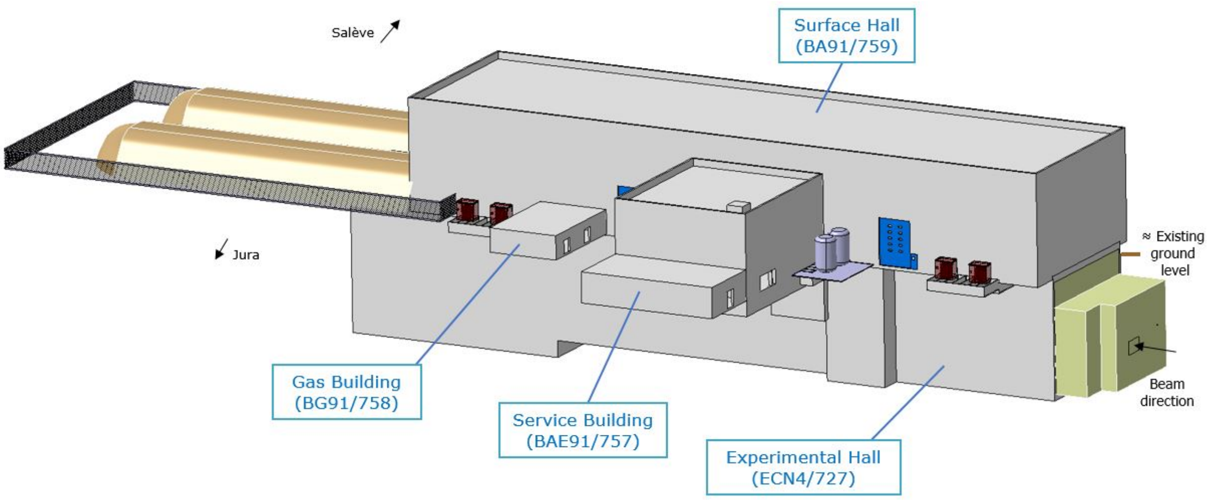

Fig. 8.38: Layout of experimental area

The services include electrical power supply, cooling, ventilation, gas supply, a smoke extraction system, detector support systems, gas distribution, electronics, and readout, network, and computing systems. In addition, the layout provides the required handling equipment, an alignment connection with the beam line, and access control for the facility. The location of the buildings was optimized in accordance with the muon flux during beam operation (see Chapter 9), and thus the service building and gas building are the only two buildings accessible during beam operation, owing to radiation protection constraints. To protect personnel from the muon flux, the service building is located approximately 33 m away from the target interface and is offset approximately 25 m with respect to the 'beam axis'.

Preliminary integration studies have been performed to evaluate the feasibility of housing the SHiP detector inside the experimental area. The following sections describes the geometries of the buildings and halls located inside the experimental area. In addition, they contain an overview of the preliminary design solutions adopted for the key infrastructure, such as ventilation, water cooling, electrical supply, transport, survey, radio-protection, safety, and the access system.

8.5.1 Experimental hall (ECN4)

The underground experimental hall was defined so as to house the SHiP detector, taking into account the assembly of the experiment and the supply of its services. The layout of the experimental hall is detailed in Fig. 8.39, and its geometry is defined in Ref. [20].

The SHiP experiment will be located in the 120 m hall and centred on its 20 m width. The internal height of the structure (19 m) is driven by the space reservation for the spectrometer magnet centred on the beam axis (13 m), the clearance between the top of the magnet and the underside of the crane (0.5 m), the space reservation for the 80 t crane (3.2 m), the clearance between the top of the crane and the underside of the services (0.3 m), and an allowance for lighting and services (0.5 m). To optimize the height structure in accordance with the SHiP detector geometry, the cavern floor has two levels. The floor along the first 88 m is located 5.5 m below the beam axis, and a 2.5 m step brings the floor level down to 8 m below the beam axis to accommodate the large spectrometer section.

There are three openings for equipment access between the surface hall and the underground experimental hall (free space 12.5 m$\times$18 m), through which the large components of the experiment can be lowered. The openings will be left fully open during the assembly phase.

For shielding purposes, each opening will be covered by 18 concrete beams during beam operation. Because of the availability of a crane for assembly and disassembly, each beam has an approximate weight of 37 t and an approximate volume of 14.5 m^3 (14.5 m $\times$ 1 m $\times$ 1 m). The concrete beams will need only temporary storage in the surface hall in the case of an intervention or an exchange of a large SHiP component. The proposed configuration for the support system for the concrete beams is detailed in Fig. 8.40. To avoid 'diagonal' slip of the concrete along the opening, a dowel joint will be considered in their design. The alcove (highlighted in Fig. 8.39) is the volume of the underground hall which is 'inserted' into the target complex structure, and it is the interface between the target hall and the experimental hall (see Fig. 8.41). The target bunker and the experimental hall are separated by a concrete wall with a window made of a thin (approximately 30 mm thick) steel plate centred on the beam axis, allowing the first muon shield magnet to be as close as possible to the magnetized volume in the target shielding (i.e. the hadron stopper). The lateral dimensions of the window, which are driven by the lateral size of the first muon shield magnet, are not yet precisely defined. The window should provide complete airtightness from the target complex.

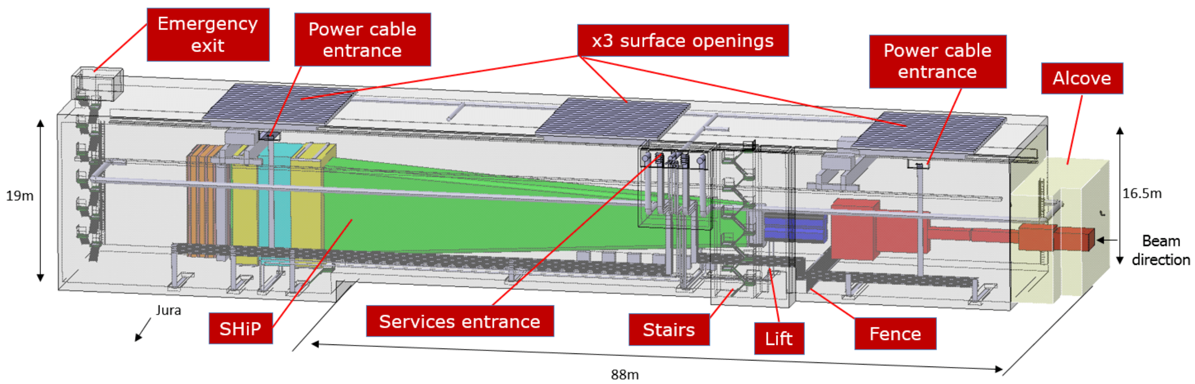

Fig. 8.39: Layout of underground experimental hall

There are two main accesses to the underground hall: at approximately 33 m from the target complex interface, via an elevator and stairs, and at the end of the hall, and also access via a second

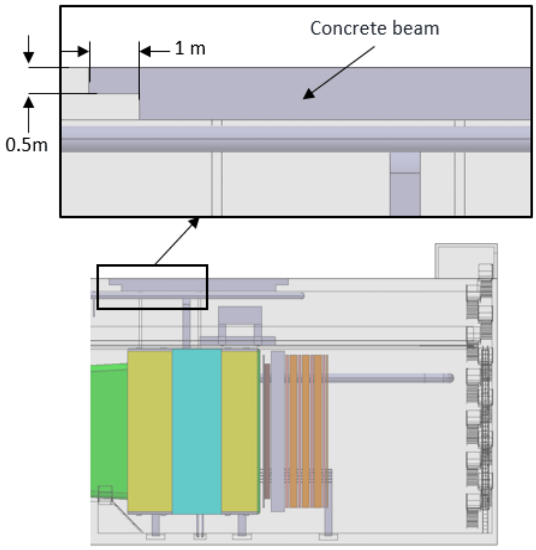

Fig. 8.40: Preliminary support system for the concrete shielding beams

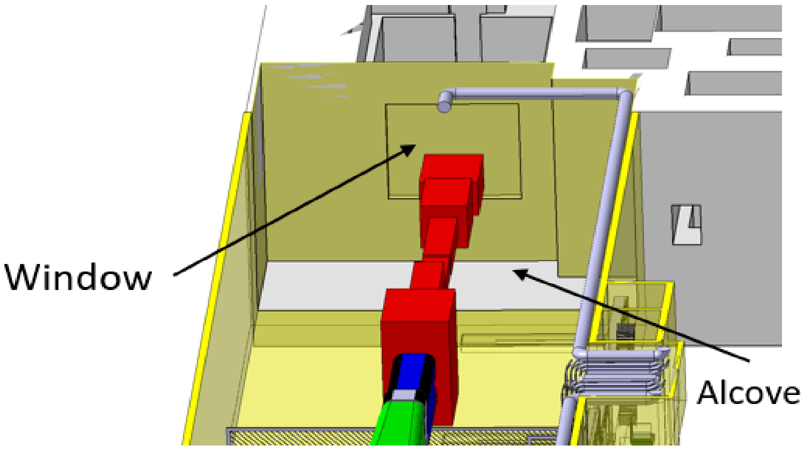

Fig. 8.41: Interface between experimental hall and target complex

set of stairs for emergency purposes (labelled “Emergency exit” in Fig. 8.39), which ends in a small dedicated access shed located at ground level and behind the surface hall.

There is an opening (labelled “Services entrance” in Fig. 8.39) between the service building’s basement and the experimental hall through which the infrastructure and the detector services are routed, i.e. the ventilation ducts, smoke extraction system, cooling, cable trays, etc. In addition, there are two more openings upstream and downstream of the personnel access for routing of the power cables for the magnets. The services are routed along the walls and ceiling (see Fig. 8.42). Channels, approximately 0.5 m deep and 1 m wide, covered by steel plates and fitted with trays for pipes and cabling, in the cavern floor allow routing of services from the wall to the SHiP detector.

For construction and handling purposes, a 40 t overhead crane and an overhead crane with a dual 40 t hoist (80 t capacity) will be provided in the underground hall. There is a personnel platform for maintenance purposes on the right wall (taking the beam direction as a reference), which is accessible by two ladders (see Figs. 8.43 and 8.51b). The smoke extraction system, sprinklers, lighting, etc. will be located above the cranes. Ventilation, cable trays, and cooling pipes will be routed along the walls

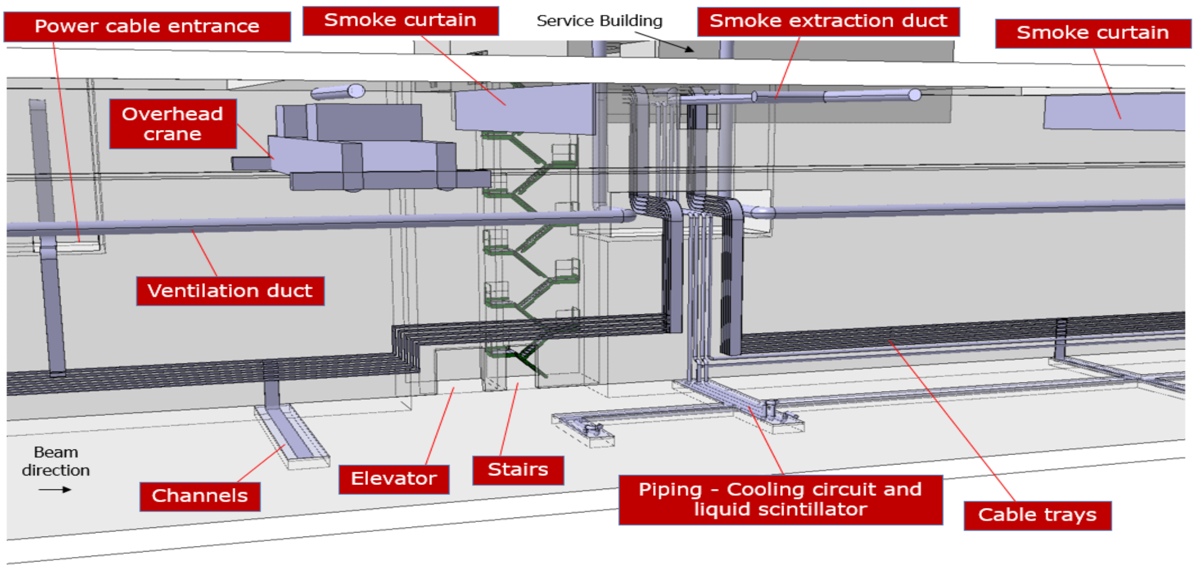

Fig. 8.42: Integration of services in the underground experimental hall. The SHiP detector has been hidden for better illustration.

below the cranes as shown in Fig. 8.42. The smoke extraction curtains can be raised manually to allow movement of the cranes along the hall.

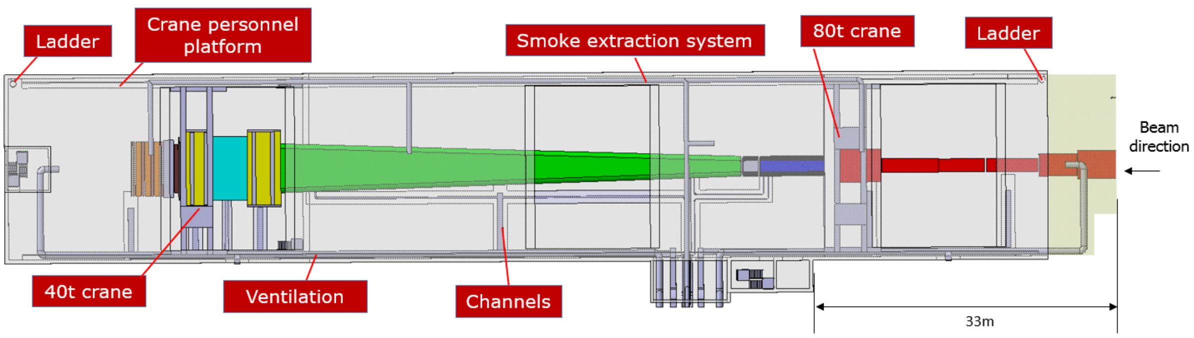

Fig. 8.43: Top view of underground experimental hall

8.5.2 Surface hall (BA91)

The surface hall will be dedicated mainly to the assembly of the SHiP experiment. The building has an internal length of 100 m, an internal width of 26.5 m, and a FFL of approximately 452.4 m above sea level. Its maximum external height is 16.3 m, which does not exceed the height of the EHN1 extension (the highest building on the CERN Prévessin site). The internal height of the structure (14.7 m) is driven by the following requirements:

- the height of the lorry access door (7 m);
- the clearance between the top of the door and the underside of the 10 t crane for installation of services (1.2 m);
- the height of the 10 t crane (2 m);
- the clearance between the top of the 10 t crane and the underside of the 40 t crane (0.5 m);
- the height of the 40 t crane (3 m);
- the clearance between the top of the 40 t crane and the underside of the services (0.5 m);

– an allowance for lighting and services (0.5 m).

The roof has a 1.1 m parapet wall for personnel access safety. The layout of the surface hall is shown in Fig. 8.44, where the surfaces highlighted in green correspond to the ceiling of the underground experimental hall. A plan view and sections can be found in Ref. [21].

The surface hall building is 6.5 m wider than the underground experimental hall owing to RP requirements and for handling purposes (see Fig. 8.38). It has two exterior doors (7 m high and 5 m wide), shown as entrances A and B, and one access to the service building. The large SHiP components will be lowered into the underground experimental hall through the three openings, which will be fully opened during the SHiP assembly period. For this reason, they will be fenced for personnel safety. Concrete beams will cover them when the SHiP installation is completed.

During operation, a MAD/PAD controls the access of personnel and light materials to the surface hall via the service building. The underground hall is accessed by an elevator and stairs located approximately 25 m from the upstream wall of the surface hall.

For handling purposes, the surface hall is equipped with two cranes, namely a 40 t crane and, below it, a 10 t crane, that run along the full length of the 100 m long building. In order for the two cranes to be used independently, each crane is on its own dedicated rails. A personnel platform on the right wall (taking the beam direction as a reference) provides access for maintenance purposes. The platform is reachable by two ladders (see Fig. 8.44).

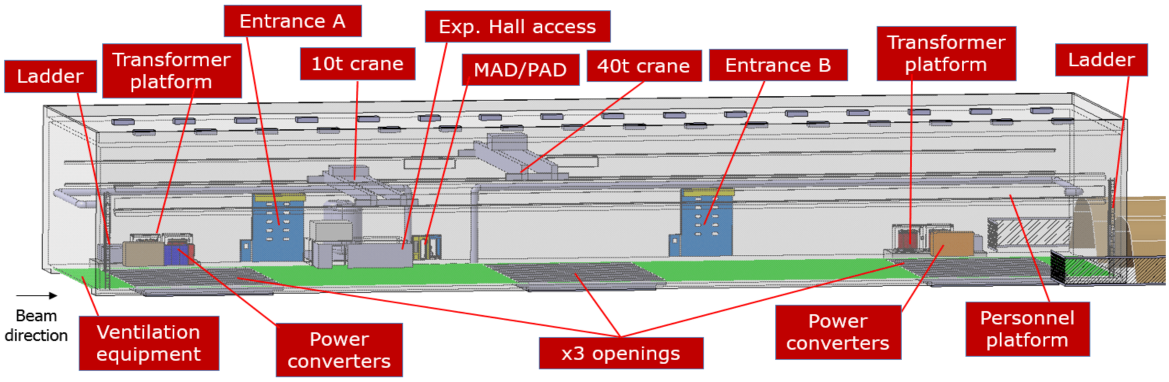

Fig. 8.44: Surface hall layout. The surface highlighted in green corresponds to the ceiling of the underground experimental hall.

Two transformer platforms are located outside the surface hall on the Jura side to connect the experimental area with the CERN electrical network. The base will be designed such that water does not pass from the transformer base into the surface hall. Cabling will pass underground and through a false floor inside the surface hall to where the power converters are located.

The ventilation equipment for the surface hall and the experimental hall is installed in the upstream end of the building between the first access opening and the front wall. Its allocated space reservation is labelled “Ventilation equipment” in Fig. 8.44.

As shown in Fig. 8.45, there are two 6 m high land hills downstream, in contact with the surface hall, for shielding. The hills leave space for a free escape route from the experimental hall’s downstream emergency exit. The hills are fenced to prevent personnel accessing the area during beam operation.

8.5.3 Service building (BAE91)

The service building is located next to the surface hall. Its purpose is to house all of the power supplies, control and electronics racks, and network, computing, cooling, and ventilation equipment and the area

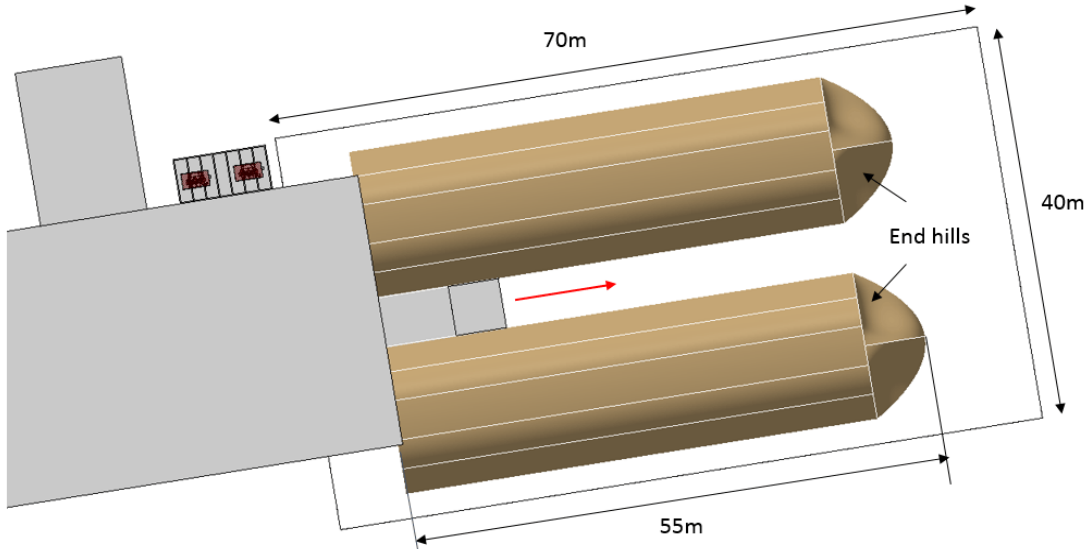

Fig. 8.45: Dimensions of fenced area and land hills. The unobstructed emergency escape route is indicated by the red arrow.

required for operation of the detector. Within its 20 m length and 34 m width, its three floors also include space for offices, laboratories, a control room (for the SHiP detector and remote handling of the target [10]), a conference room, and a workshop as an adjacent independent building. Electrical and electronics racks, ventilation equipment, pumps, etc. will be located on the ground floor. The roof has a 1.1 m parapet wall for personnel safety when accessing the roof (for elevator maintenance). The layout of the surface building is shown in Fig. 8.46.

The three floors of the service building are accessed by stairs and an elevator with a capacity of 13 people. The installation and de-installation of electrical racks, AHUs, pumps, etc. on the ground floor are foreseen to be performed with a pallet truck. As the system management room and the computing infrastructure are located on the first floor, the racks (loaded on a pallet truck) will be taken there via the elevator. There is a personnel and light material access through a MAD/PAD to the surface hall on the ground floor. A 5 t overhead crane is to be installed in the workshop.

Storage tanks (300 m^3 volume in a 50 m^2 space reservation) for the liquid scintillator required by one of the detectors of SHiP are located on one side of the building. The transformer platform is located on the opposite side. The bases will be designed such that water does not pass from them into the service building.

The service building is constructed with a basement dedicated to the distribution of all services throughout the building. The cables and services will pass through the basement wall, which is the interface between the service building and the surface hall, to the underground experimental hall (see Fig. 8.47). The detailed cable layout has yet to be defined.

Figure 8.48 and Ref. [22] show a plan view, the layout, and sections of the service building. Its internal layout, which was determined based on the SHiP requirements (see Tables 7.2 and 7.3), is shown in Fig. 8.49.

8.5.4 Gas building (BG91)

The purpose of this building is to store and supply all of the gases foreseen to be used in the experimental area. For instance, the straw tracker of the SHiP detector will need a gas mixture of CO_2 and Ar. A gas line from the Prévessin gas distribution network is not foreseen, as the required quantity estimated is only a few cubic metres at present. The installation will be designed to be compatible with the storage

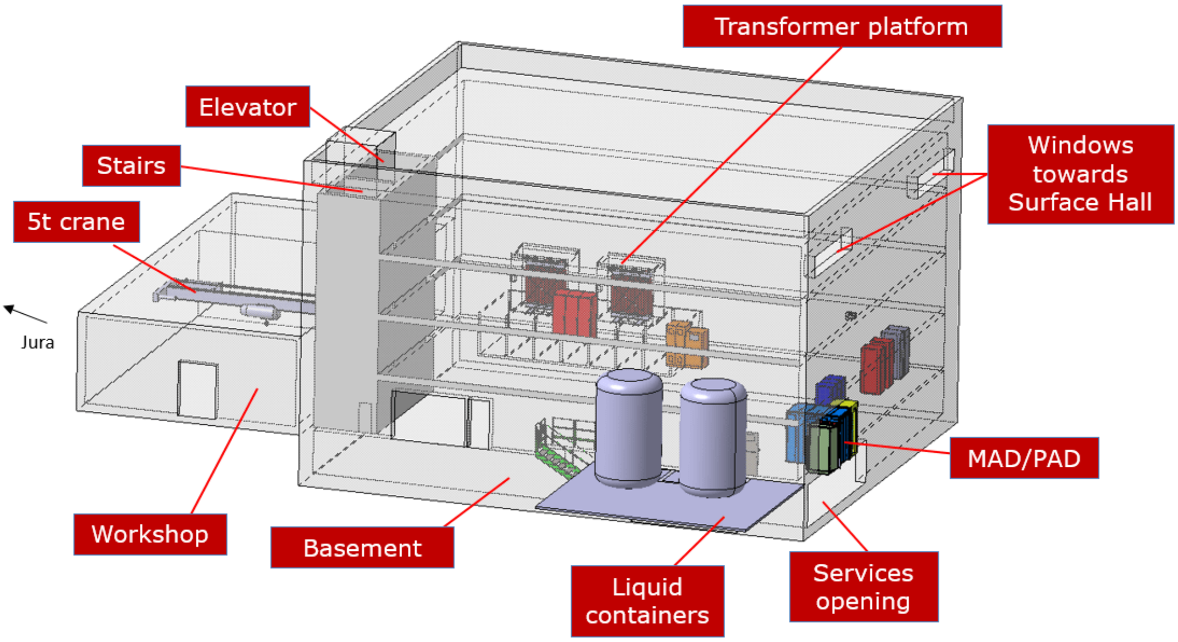

Fig. 8.46: Service building layout (floor layouts have been hidden for clarity)

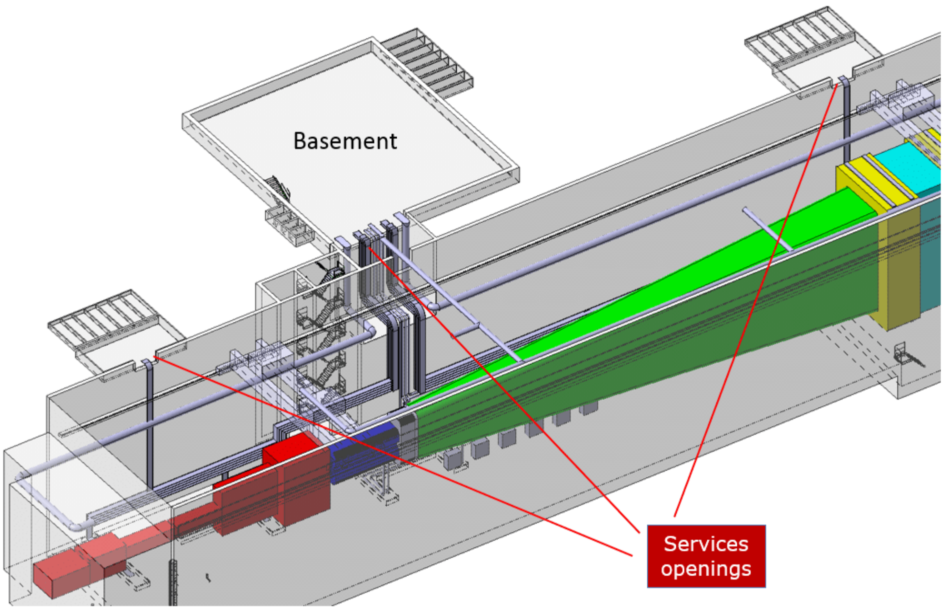

Fig. 8.47: Overview of distribution of services in experimental area

of standard gas bottles.

Its internal layout is not yet specified; however, a reception and a storage area are required. Its estimated ground surface area is 15 m×10 m and a 3 m high ceiling is assumed. The building should comply with the Eurocode guidelines and the relevant National Annexes for a gas installation.

8.5.5 Surface hall and experimental hall cross-sections

Figure 8.50 indicates the location of the cross-sections of the experimental area shown in Fig. 8.51.

Figure 8.51(a) shows a cross-section of the surface hall and the upper floor of the experimental

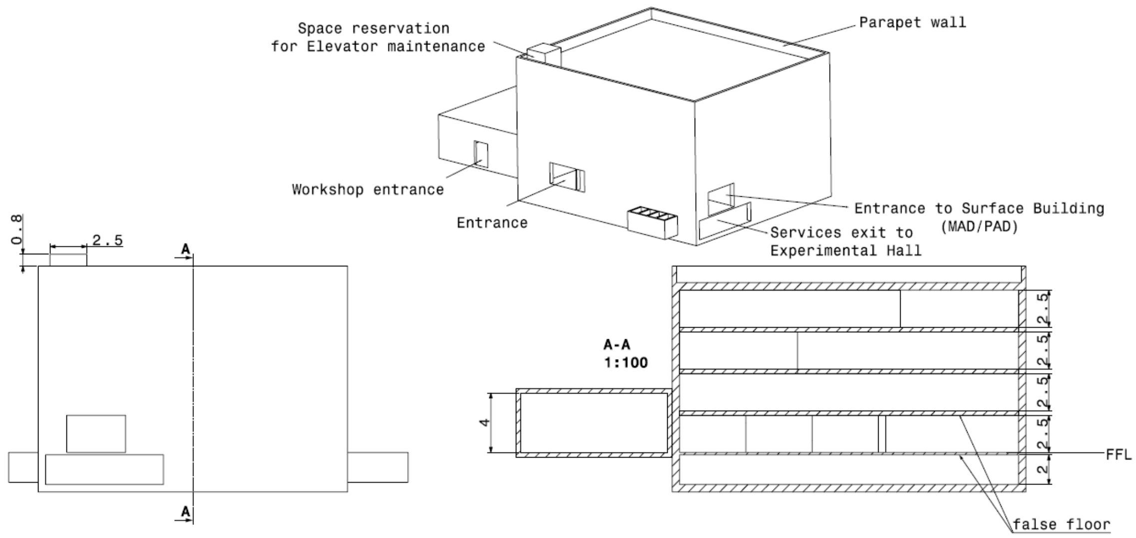

Fig. 8.48: Plan view and sections of service building

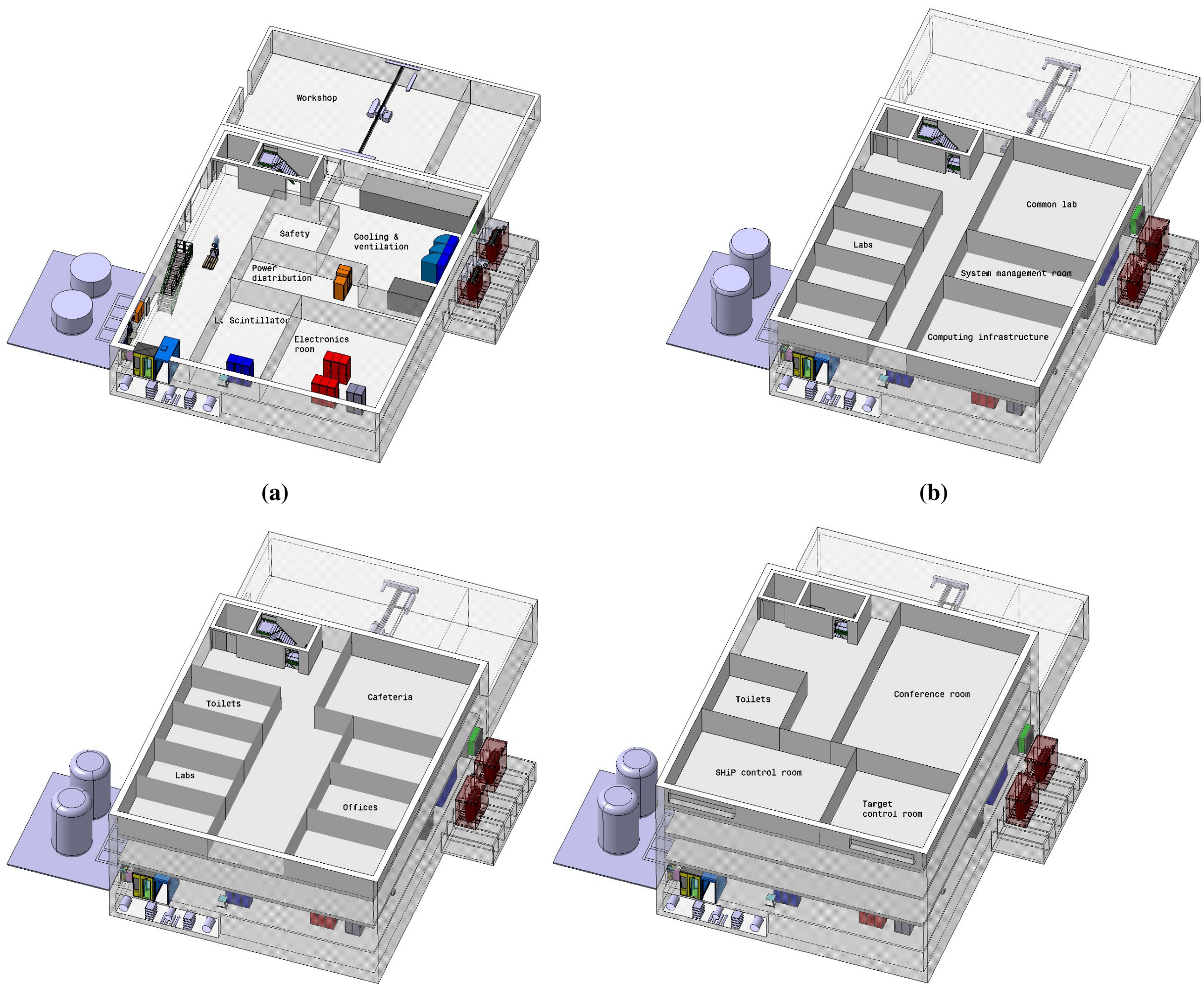

(a)

(b)

(c)

(d)

Fig. 8.49: Internal layout of service building. (a) Ground floor; (b) first floor; (c) second floor; (d) third floor.

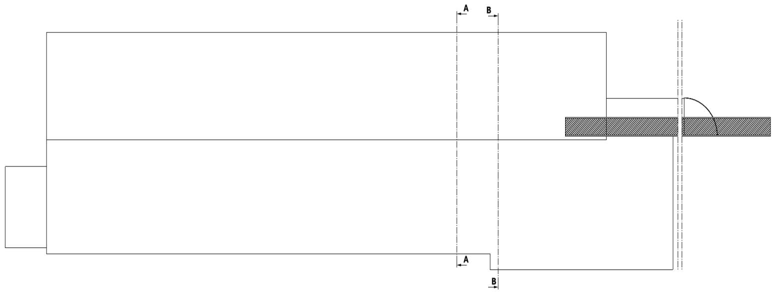

Fig. 8.50: Sections of underground experimental hall shown in Fig. 8.51

hall. Cable trays and piping run along the walls, below and above the 80 t crane, while the SHiP detector is centred in the cavern. In relation to the surface hall, the proposed height breakdown allows the two overhead cranes to run along the length of the entire hall independently.

Figure 8.51(b) shows in detail the integration performed in the most restrictive section of the cavern, the lower floor of the experimental hall. In this location, the 13 m spectrometer magnet has to be centred with respect to the beam axis and, in addition, the crane must pass above it for installation purposes. In the upper floor of the experimental hall, services run along the walls, below and above the crane.

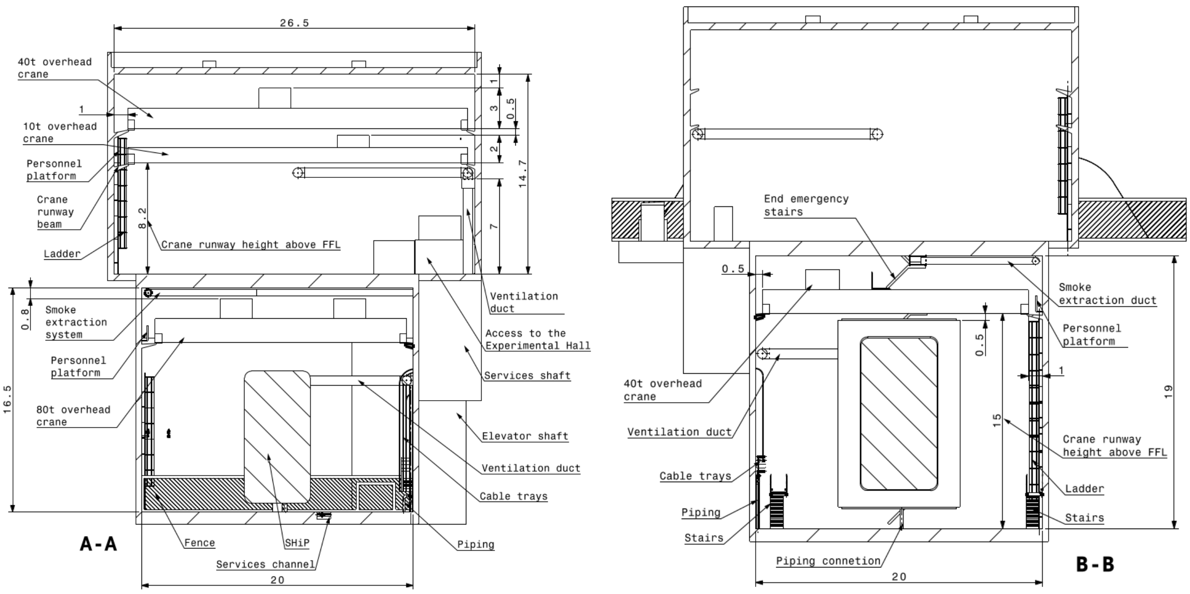

(a) (b)

Fig. 8.51: Cross-sections of experimental area: (a) height breakdown of surface hall; (b) height breakdown of experimental hall.

8.5.6 Civil engineering

The civil engineering studies carried out were based on the activities foreseen and the equipment/SHiP components to be housed inside the buildings.

The study of the estimated service loads foreseen in the service building, gas building, surface hall, and experimental hall based on the infrastructure proposed is detailed in Ref. [23]. In particular, the service loads of the SHiP experiment are described in Ref. [24]. The heavier SHiP components that need to be displaced for maintenance or for equipment replacement (i.e. the subcomponents of the particle ID detector) will be installed on trolleys on floor rails or suspended from frames or girders. Air pads [25] could be used for their movement along the rails.

The key features of the proposed layout are:

– the underground experimental hall, located behind the target complex, to house the SHiP detector;
– the surface hall above the experimental hall, for the assembly of the SHiP experiment;
– the service building on the Jura side of the surface hall, to provide electrical and CV supply (among other things) to the SHiP experiment;
– the gas building for gas supply to the BDF.

As the facility is planned to be located on the CERN site at Prévessin, it is assumed that the existing facilities on this campus such as restaurants, the main access, and the road network are sufficient. For the parts which surround the BDF, however, the following items will have to be included:

– roads and car parks;
– drainage networks;
– lighting;
– fire hoses;
– landscaping and planting.

See Chapter 11 for further details of the civil engineering studies.

8.5.7 Transport and handling

The quantity and variety of equipment to be installed in the experimental area are defined by the SHiP experiment. As set out in Chapter 7, the detector will be assembled in the surface hall with a maximum crane lifting load of 40 t, and the pre-assembled SHiP components will be lowered into the underground experimental hall. In addition, supports, cooling and ventilation ducts, electrical cables, and cable trays will be lowered into and installed in the underground area. Detailed transport and handling solutions will need to be defined for all of the industrial equipment and the pre-assembled and detector components for SHiP, developing special tooling wherever necessary. For the cooling and ventilation equipment, electrical cables, and cable trays, standard industrial handling equipment is foreseen.

The transport and installation operations include:

– unloading materials and equipment;
– transfer within the surface buildings and from the surface hall to the experimental hall for the purposes of assembly, testing, and storage;
– transport in the experimental hall and final installation.

The SHiP parts and materials will arrive at the surface hall in a 40 t semi-trailer or a normal 19 t truck. Then, the overhead cranes or a forklift (30 t/axle) will unload the truck and move the equipment through the surface hall. A 40 t overhead crane and a 10 t crane will lift and lower the parts and materials from the surface hall to the experimental hall. Note that the maximum distance from the FFL to the hook of the 10 t crane is about 8 m and, in the case of the 40 t crane, approximately 11 m.

A 40 t overhead crane and an overhead crane with a dual 40 t hoist (80 t capacity), which can access the full length of the hall, will be provided in the experimental hall. In addition, a few small temporary cranes will support the construction and installation of the detector.

Table 8.8 lists the specifications of the cranes for the experimental area. Cross-sections of the height of the surface hall and experimental hall are shown in Fig. 8.51.

Two lifts are required in the experimental area. The first is located in the service building to allow personnel and light materials to access the three floors. As the system management and computer

Table 8.8: Crane specifications for experimental area

Location	Lifting capacity (t)	Distance from FFL to hook (m)	Span (m)	Travel (m)	Length (m)	Width (m)	Height (m)	Quantity
Surface hall	40	11.2/28.7/31.2	25	97	6	20	3	1
Surface hall	10	8.3/25.8/28.3	25	97	5	20	2	1
Experimental hall	40	13.2/15.7	18.5	109	6	20	3	1
Experimental hall	2×40	13.2/15.7	18.5	109	6	20	3.2	1
Workshop	5	2.5	9	20	3	10	1.5	1

rooms are housed on the first floor [22], the lift should have the capacity to raise electronics racks and laboratory equipment. The second lift provides personnel and material access (e.g. pallets, chariots, and light equipment) from the surface hall to the experimental hall. Technical details of the lifts are described in Ref. [26]. Table 8.9 shows the main specifications of the lifts in the experimental area.

Table 8.9: Specifications of lifts for experimental area

Location	Number of levels	Depth (m)	Capacity
Access to experimental cavern	2	17.5	3 t
Service building	4	9	1 t

8.5.8 Electrical network system

The SHiP detector is expected to consume approximately 3.1 MW (see Table 7.2), with a total of six magnets for the muon shield, one emulsion spectrometer magnet, and a spectrometer magnet with a weight of more than 1000 t. The electrical power system is divided into two subsystems:

– conventional power (magnet power supplies, electronics racks, cooling and ventilation systems, and infrastructure components);
– emergency power provided by back-up generators (emergency lighting, sump pumps, and ventilation systems for subsurface enclosures).

Any critical system that cannot accept any power interruption will need to be provided with an uninterruptible power supply system. The emergency supply system is based on batteries, located in the auxiliary building (see Fig. 8.25); therefore, its supply will be routed through the technical galleries to reach the experimental area. A proposal for the layout of the technical galleries has been produced assuming that the electrical connection of the BDF to the Prévessin network is made through the CERN service building BA80 (see Fig. 11.2).

A description of the electrical power supply has been estimated from the CENF study [27]. The proposal considers only the electrical power infrastructure, and thus the cabling and the fibre-optical infrastructure are yet to be studied. The numbers of cable trays shown in Figs. 8.47 and 8.51 are only for illustration.

The general infrastructure required for electrically safe operation and personnel safety is the following:

– installation of the electrical systesm's SCADA monitoring equipment to supervise the installation and the status of the electrical services from the CERN Control Centre;
– electrical containment, normal lighting, emergency lighting, and power distribution in all of the buildings and technical galleries.

The transformer locations and the space reserved for the electrical distribution equipment inside the service building are shown in Fig. 8.52. A total of three slabs are provided for the transformers, two of which are positioned in such a way that the distance between them and the power converters is optimized. The number of transformers has yet to be defined. The transformers located next to the service building (highlighted in green in Fig. 8.52) will supply the general services of the experimental area, which include:

- overhead cranes;
- cooling and ventilation supplies;
- general lighting and small power;
- racks and electronics;
- offices;
- workshop.

The power for the magnets of the experiment will be supplied through the transformers shown in red in Fig. 8.52 from dedicated Type 1 and Type 2 distribution boards located in the surface hall. Table 8.10 lists the estimated power loads in the experimental area.

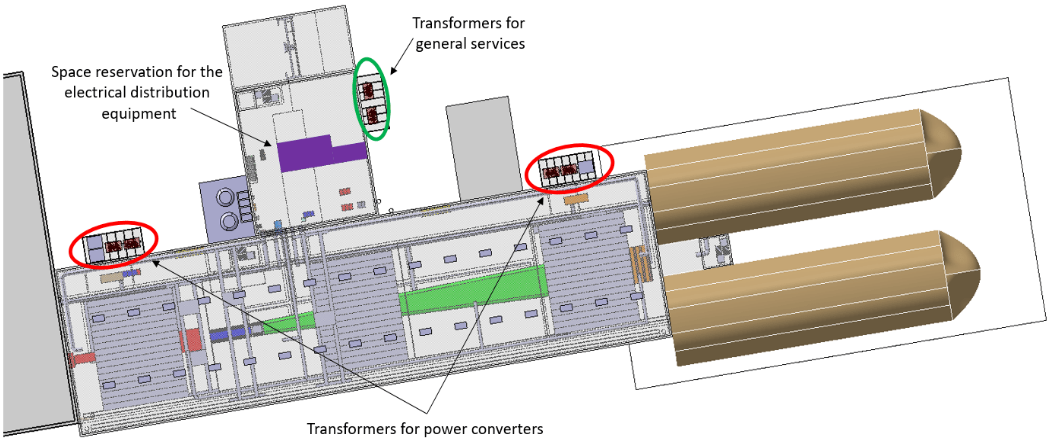

Fig. 8.52: Location of transformers in experimental area

Table 8.10: Experimental Area electrical power loads

Pulsed loads	
Not applicable	
TOTAL	0 W
Stable loads	
Power converters (experiments magnets)	3.1 MW
Ventilation and cooling	320 kW
General services	280 kW
Racks and electronics	200 kW
TOTAL	3.9 MW
Secure networks loads	Located in the Auxiliary Building

8.5.9 Electrical power converters

Power converters are required for the magnets of the muon shield, the emulsion spectrometer magnet, and the decay spectrometer magnet. The criterion applied was to locate the power converters in such a way that the cable length between the magnets and them was minimized. Therefore, as the decay

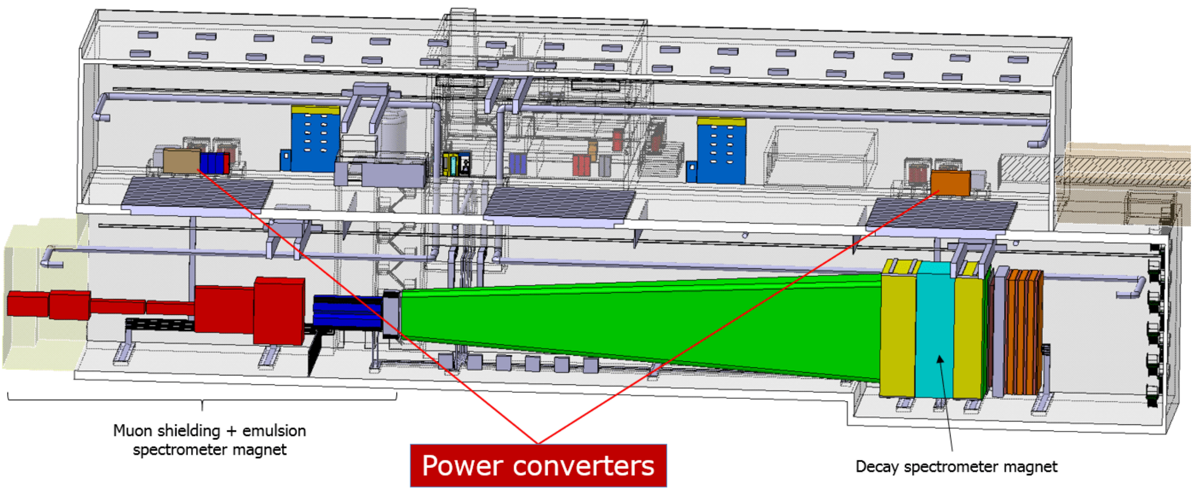

Fig. 8.53: Layout of power converters

spectrometer magnet is about 60 m away from the emulsion spectrometer magnet, two locations for the power converters were chosen (see Fig. 8.53).

A preliminary design for the power converters was produced based on the current and power inputs given in Chapter 7, excluding the resistance of the d.c. cables. Table 8.11 lists the characteristics of the magnets taken into account in the design. The performance of the current sources requested is 'accuracy class 4', which specifies a long-term (1 yr) stability of 100 ppm, a stability of 20 ppm over 12 h, and a short-term (20 min) stability of 5 ppm. The modules will be controlled by an FGC3 platform, taking into consideration that in the d.c. operation mode, there is no control of the current during ramp-up and ramp-down.

Table 8.11: Design parameters for power converters

Circuit name	No. of magnets in series	R_{mag} at 20°C	I_{max} requested (A)	No. of converters	Operation mode
Emulsion spectrometer magnet	1	8.9	14 600[a]	1	d.c. bipolar
Decay spectrometer magnet	1	111	3000	1	d.c.
Muon shield magnet 1	1	400	50	1	d.c. unipolar
Muon shield magnet 2	1	600	50	1	d.c. unipolar
Muon shield magnet 3	1	360	50	1	d.c. unipolar
Muon shield magnet 4	1	560	50	1	d.c. unipolar
Muon shield magnet 5	1	1400	50	1	d.c. unipolar
Muon shield magnet 6	1	2000	50	1	d.c. unipolar

[a] Aluminium pancake design.

The design criterion was to use standard CERN power converters or a combination of them to reduce the cost and optimize the design timing (the proposed design is shown in Table 8.12). The design for the muon shield magnets is based on three racks, each of them populated with two converters and a spare. The total numbers of power converters is eight, and its running cost, assuming 4000 h of operation per year, is about 690 kCHF per year.

Table 8.12: Preliminary design of SHiP power converters

Circuit name	Converter type	No. of converters	Operation mode
Emulsion spectrometer magnet	New ALICE_4P, $2 \times$ (150 V/8 kA)	1	d.c. bipolar (4-quadrant operation)
Decay spectrometer magnet	New design, 4P_B	1	d.c. unipolar (1-quadrant operation)
Muon shield magnet 1	Combo	1	d.c. unipolar (1-quadrant operation)
Muon shield magnet 2	Combo	1	d.c. unipolar (1-quadrant operation)
Muon shield magnet 3	Combo	1	d.c. unipolar (1-quadrant operation)
Muon shield magnet 4	Combo	1	d.c. unipolar (1-quadrant operation)
Muon shield magnet 5	Combo	1	d.c. unipolar (1-quadrant operation)
Muon shield magnet 6	Combo	1	d.c. unipolar (1-quadrant operation)

Regarding the cooling requirements and the ventilation contribution, the total estimated power dissipated in the surface hall environment is 56 kW and the total cooling power requested is 126 kW. The use of demineralized water in the cooling circuit is foreseen, in addition to the following features:

– the maximum water temperature in the circuit will be 27 °C with a $\Delta\theta$ of approximately 10 K;
– the total flow rate will be 480 l/min;
– ΔP will be 3 bar with a nominal pressure less than 6 bar.

The integration specifications of the power converters are listed in Table 8.13. The requirements include the following.

– Each of the power converters should be accessible from the front and the rear.
– The ALICE4P modules for the emulsion spectrometer magnet require an outdoor platform for 18 kV transformers and an additional 15 m^2 space reservation for two electrical boxes.
– The new 4PB modules for the decay spectrometer magnet require an outdoor platform for 18 kV transformers and an additional 8 m^2 space reservation for one electrical box.
– An additional control rack for Ethernet connections (dimensions 0.6 m$\times$0.9 m$\times$2 m) is required.

Figure 8.54 shows the integration of the power converters inside the surface hall, which complies with the requirements specified. As the surface hall is not accessible during beam operation owing to radiation protection requirements, maintenance when the beam is running is not allowed.

Because of the high current required, water-cooled cables may be considered for the link between the emulsion spectrometer and decay spectrometer magnets and their respective power converters. Table 8.14 shows the a.c. and d.c distribution considered in the study. The second column indicates the cable cross-section, as recommended by the CERN power converters group in order to keep the voltage

Table 8.13: Integration and cooling specifications of power converters

Circuit name	Converter type	Dimensions (length/width/height) (m)	Weight/unit (t)	Power dissipated in air (kW)	Water cooling (kW)
Emulsion spectrometer magnet	New ALICE_4P, 2 × (150 V/8 kA)	7.6/1.3/2.4	6	36	84
Decay spectrometer magnet	New design, 4P_B	4.0/1.3/2.4	4	18	42
Muon shield magnet 1	Combo	0.8/0.9/2.1	0.5	0.84	0
Muon shield magnet 2	Combo	0.84			0
Muon shield magnet 3	Combo	0.8/0.9/2.1	0.5	0.84	0
Muon shield magnet 4	Combo	0.84			0
Muon shield magnet 5	Combo	0.8/0.9/2.1	0.5	0.84	0
Muon shield magnet 6	Combo	0.84			0

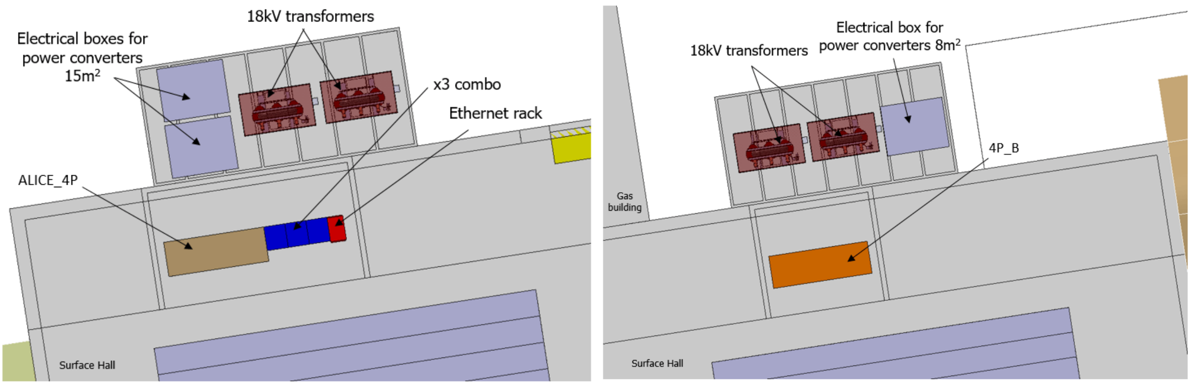

(a) **(b)**

Fig. 8.54: Integration of power converters. (a) Power converter for emulsion spectrometer magnet and muon shield. (b) Power converter for decay spectrometer magnet.

drop to a reasonable level. In addition, thermal aspects have to be evaluated. The total cable length was estimated from the integration model and is twice the distance between the converters and the magnets. The total power to be installed is about 3823 kVA.

8.5.10 Cooling and ventilation

The CV installations for the SHiP experimental area comprise the following systems:

– raw-water system;
– demineralized-water system for the cooling of magnets and power converters;
– chilled-water system for the cooling of ventilation units;
– ventilation units and ductwork;
– smoke extraction system.

Specific details of the design of the cooling and ventilation systems are provided in Ref. [28]. Inside the experimental area, two areas are reserved for the installation of CV equipment.

– 100 m^2 on the ground floor of the service building [22], which will house the secondary pumping system, the AHUs for the service building, and the smoke extraction system. This area is accessible at any time.
– 100 m^2 area next to the separation wall between the target complex and the surface hall (see Fig. 8.44) for the AHUs for the surface hall and experimental hall. These units will be accessible

Table 8.14: A.c. and d.c. distribution for power converters

Circuit name	Total cable length (m)	I_{rms} (A)	D.c. cable section Cu/Al (mm^2)	Converter type	Electrical feeder (V)	I_{rms} for I_{rms} converters	Total installed r.m.s. power (kVA)
Emulsion spectrometer magnet	80	16 000	2000	ALICE_4P	18 000	0	2526
Decay spectrometer magnet	100	3000	1440	New 4P_B	18 000	0	1263
Muon shield magnet 1	110	50	25	Combo	400	16	11
Muon shield magnet 2	100	50	25	Combo	400	0	0
Muon shield magnet 3	90	50	25	Combo	400	16	11
Muon shield magnet 4	80	50	25	Combo	400	0	0
Muon shield magnet 5	80	50	25	Combo	400	16	11
Muon shield magnet 6	90	50	25	Combo	400	0	0

only during technical shutdowns of the machine, and, in the case of a major failure, an intervention of 1 day is allowed.

8.5.10.1 Cooling

Since little activation of cooling water is expected in the underground hall, pumping stations and the main cooling equipment can be placed in the service building. Preliminary user requirements for the cooling of the SHiP components are presented in Ref. [28].

The SHiP cooling system is based on a raw-water primary cooling system supplying water at 25 °C via cooling towers. Local cooling is provided via demineralized-water secondary circuits (e.g. for the power converter cooling circuit); chilled water provides cooling for the AHUs. Figure 8.55 illustrates the cooling system structure.

Cooling for SHiP represents about half of the cooling requirements of the entire BDF primary circuit. The primary flow rate to the experimental area amounts to 270 m^3/h at 25 °C, with a total cooling load of 3.1 MW; the expected temperature increase is 10 °C and the estimated diameter of the main piping is DN250. The pressure drop of the circuit is assumed to be 3 bar, and the required pumping power is roughly 40 kW.

A secondary cooling system provides demineralized-water cooling to the magnets and detectors in the experimental hall. Located at ground level and inside the surface building, it supplies 215 m^3/h at 28 °C for a thermal load of about 3100 kW on average; the estimated return temperature is 40.5 °C. The system is equipped with an expansion tank and two redundant pumps which supply demineralized water at 20 bar; pressure reducers are used to lower the pressure for equipment that needs a lower supply pressure. The size of the piping circuit is DN250, and the estimated pumping power is 180 kW.

Chilled water is needed in the experimental area for the ventilation units in the service building and the surface hall. The overall requirements in terms of chilled water amount to roughly 750 kW maximum; this cooling capacity is provided by the BA81 chilled-water production plant. Of this amount, about 450 kW (corresponding to 80 m^3/h of chilled water at 6 °C to 10 °C) is needed for the cooling coils of the three AHUs.

Chilled water, demineralized-water filling, and compressed air are supplied from a new technical gallery. Moreover, since the primary water production is located next to the auxiliary building, a trench from the auxiliary building to the service building is required. The pipes are routed through the trench up to the ground floor of the service building. A proposal for the layout of the trenches is detailed in Fig. 11.2.

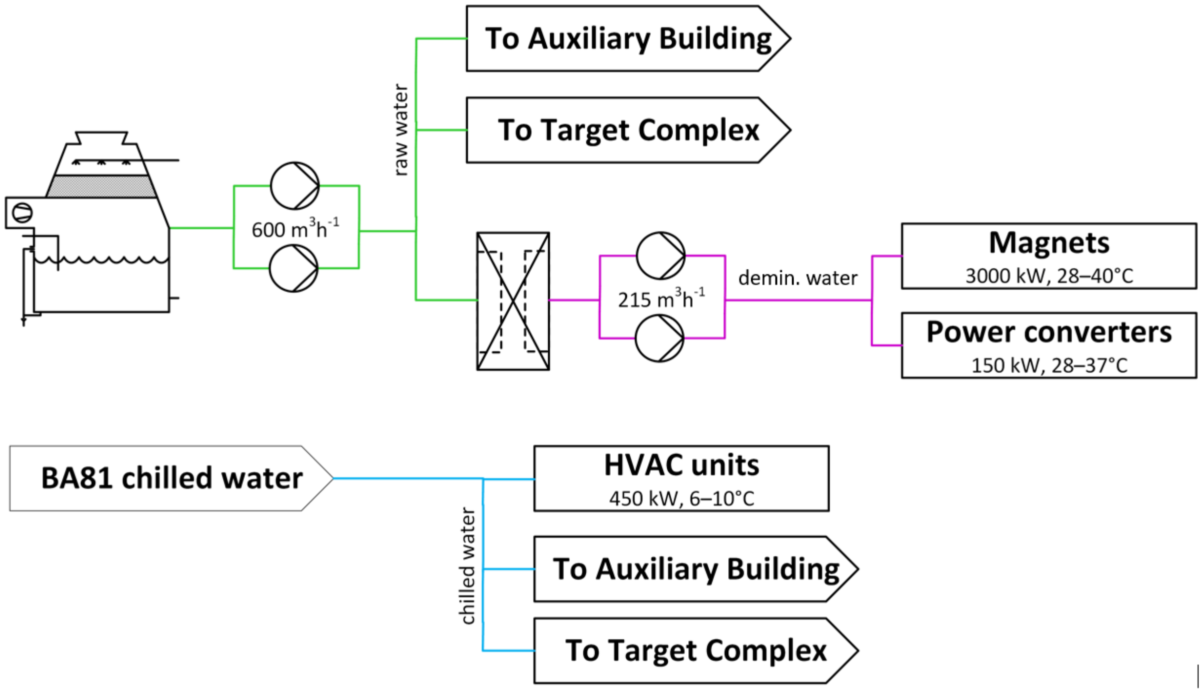

Fig. 8.55: Schematic illustration of cooling system for experimental area

8.5.10.2 Ventilation

Preliminary user requirements for the ventilation of SHiP equipment are presented in Ref. [28]. As mentioned in the cooling section above (8.5.10.1), owing to the low expected activation of the area, dynamic confinement is not required. The ventilation system is designed to supply fresh air and provide adequate temperature and humidity conditions in the buildings. Figure 8.56 shows a preliminary integration of the ventilation ducts inside the buildings.

The following ventilation units are needed in the context of the experimental area's ventilation system:

– ventilation for the experimental hall (plus smoke extraction);
– ventilation for the surface hall;
– ventilation for the service building.

Regarding the system in the experimental hall, the ventilation unit is located in the surface hall, next to the upstream wall that separates the surface hall from the target complex; at this location, activation of equipment is minimized. Air is supplied to the experimental hall via distribution ducts and extracted from grilles, whose optimal position will be determined via CFD analysis. Owing to the volume of the hall and the heat loads, recirculation is used to minimize the energy requirements; a minimum amount of fresh air is supplied to maintain optimal conditions. The nominal flow rate of the unit is 85 000 m^3/h for a reference duct diameter of 1.94 m. The emulsion spectrometer magnet will require a dedicated local temperature and humidity control owing to its special requirements.

The surface hall is a large building located on top of the experimental hall. The supply unit for this ventilation area is located inside the surface hall, so that ductwork is minimized. The maximum supply flow is 55 000 m^3/h for a reference duct diameter of 1.56 m; the ventilation system takes advantage of recirculation.

In relation to the service building, ventilation needs to be supplied to the service equipment area on the first floor, and to the offices, control rooms, and laboratories on the higher floors. The preliminary

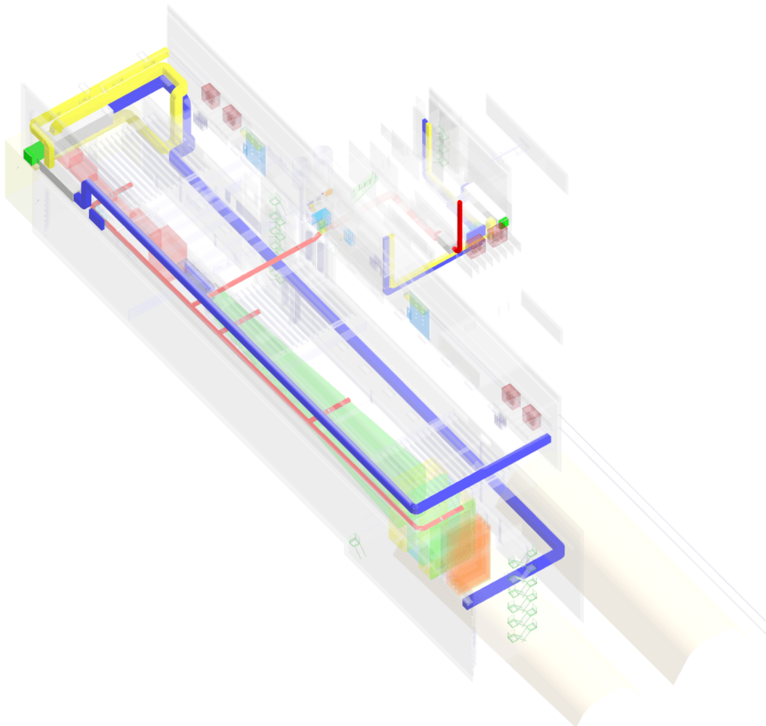

Fig. 8.56: Preliminary integration of ventilation ducts in experimental area

design foresees a single ventilation unit for the entire building. A more detailed design will be performed when the layout of the internal rooms is established and the heat load distribution computed. The nominal flow rate considered for the unit is 45 000 m^3/h, for a reference duct diameter of 1.4 m.

With respect to the smoke extraction system (the design parameters are detailed in Section 8.5.13.1), the experimental hall is divided into four smoke extraction sectors (see Fig. 8.60); the same extraction unit is used for all sectors, and only one sector at a time can be activated. The maximum extraction flow per sector is 24 000 m^3/h. In the case of fire in the surface hall, the smoke will be ventilated via natural ventilation and skydomes located on the ceiling (see Fig. 8.58).

8.5.11 Survey

For the SHiP experiment, large-scale metrology survey work will be performed at several different steps: design, construction, assembly, and alignment of the detector elements. This means the following.

- Participating in the project at an early stage, e.g. collecting the geometrical parameters and alignment needs or discussing the integration of the survey needs during the design of the infrastructure, tools, or detector elements.
- Providing the necessary geometrical data for adjustment and control of the assembly infrastructure.
- Providing position and orientation information related to the assembly and testing of the SHiP detector, i.e. geometrical information for the following purposes:
  - alignment of the detector assembly tooling;
  - the geometrical follow-up and adjustment of the detector elements during assembly;
  - positioning of the detector elements for tests.
- Establishing, measuring, computing, and maintaining geodetic networks or coordinate systems

and defining the parameters linking different networks or systems when needed.
- Providing surveyed position and orientation information to locate the detector in the CERN Coordinate System (CCS) and to link it to the upstream beam line.
- Providing, when necessary, metrology measurements for the fiducialization of the detector elements and of module assemblies.
- Providing control of the position and the alignment of stand-alone elements and module assemblies in the experimental area.
- Participating in any upgrades at an early stage to ensure high-quality geometrical information during the lifetime of the detector.

This covers both the theoretical and the practical aspects of the large-scale metrology work for the SHiP project, knowing that the theoretical positions of the beam line elements will be provided by the accelerator optics team.

In the field, measurements will be performed using suitable survey instrumentation and methods such as total stations, optical levelling, photogrammetry, 3D laser scanners, and laser trackers.

8.5.11.1 Specifications

The positioning and stability tolerances and requirements of each subsystem of the SHiP experiment need to be identified in order for one to make an estimate of the necessary means of adjustment. A more detailed analysis of the survey tasks will need the following input from the various persons responsible for the detector in the experimental collaboration:

- the expected positioning tolerances after installation of all subsystems;
- the further displacements that may be observed during the assembly process of the experiment;
- the future displacements induced by the operation of the detector because of vacuum forces or because of deformations over time at the civil engineering level (i.e. floor stability).

The positioning tolerances should be expressed in a physicist's reference frame, where Z is parallel to the beam and X lies in a horizontal plane.

8.5.11.2 Support and alignment reference system

A geodetic network has to be established that includes the upstream beam line up to the SHiP experimental hall. Additional geodetic points will be installed in the SHiP experimental hall. These points will be materialized by either wall brackets, permanent tripods, or ground inserts equipped with CERN Standard Survey (CSS) reference sockets. The complete network will be determined in the CSS and measured by total stations, laser trackers, and direct levelling. The geodetic network of the area will need to be updated periodically.

All of the elements to be aligned will be equipped with survey reference points or a tilt reference surface, or both. Typical detector elements will be equipped with a minimum of three (preferably more) fiducials that are distributed in space to allow one to determine the position and rotation in space of the element.

The supports of the elements should dissociate movements in the horizontal and vertical planes and also shifts and rotations. Each element needs a corresponding adjustment system with a sufficient adjustment range.

The survey team should help with the definition and placement of these fiducials/supports and should be included in the approval of the final designs.

8.5.11.3 Link of machine geometry to experimental area

The very first geometrical link between the machine geometry and the experimental hall is expected to pass through the target complex while a line of sight is still available. In parallel, a dedicated 0.4 m diameter pipe that traverses the target complex should be used for the geometrical link. At least four survey reference points on dedicated brackets (at minimum, two on the machine side and two in the experimental hall) should be considered as the main geometrical references for the transfer of the machine geometry to the experimental hall after completion of the target complex. The length of the line of sight passing through the machine (∼23 m), the target complex (∼27 m), and the experimental hall (∼10 m) is nearly 60 m in total (see Fig. 8.57).

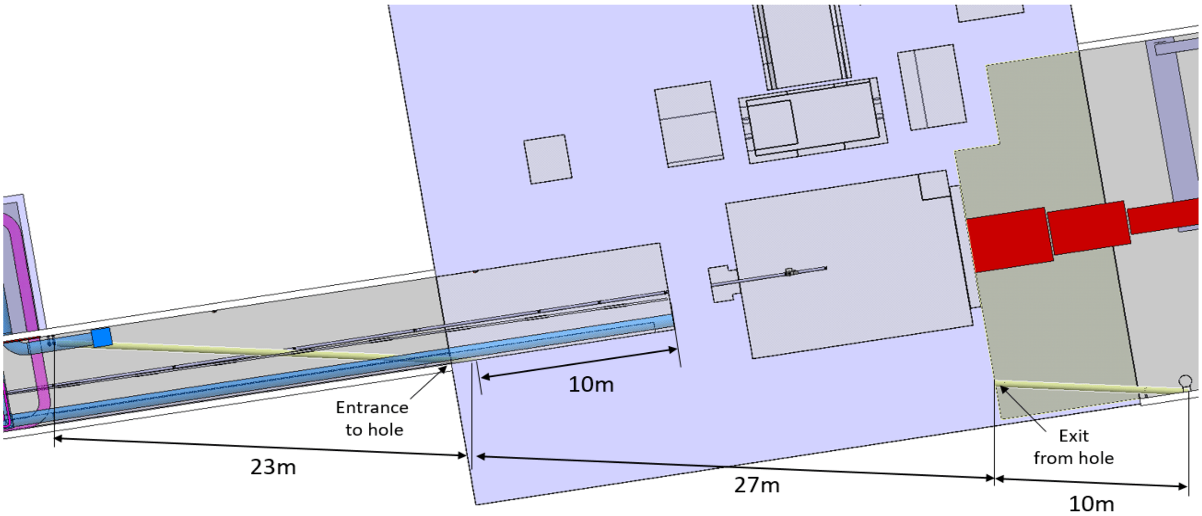

Fig. 8.57: Preliminary integration of the connection of the beam line and SHiP alignment networks

8.5.11.4 Geometrical quality control measurement

The survey team should provide on demand some of the geometrical and dimensional control measurements for the prototype and production elements.

8.5.11.5 Fiducialization measurements

The determination of the reference target positions for the survey with respect to the reference system of the element or module on which they are placed is called a fiducialization. If the fiducialization of an element cannot be guaranteed by construction or achieved by the metrology laboratory owing to the size or specific details of the object, it could be carried out by the survey team after a dedicated discussion with the technical co-ordination and the survey team.

The parameters of the fiducializations are stored in survey reports and, depending on the object, can be extracted from metrology reports, geometrical quality control measurements, or reports of a specific fiducialization operation. The external fiducials are expected to remain visible and accessible during the various measurement operations.

8.5.11.6 Theoretical data

The spatial position and orientation data for the beam line elements, including the SHiP detector, need to be extracted from the results of beam optics calculations such as BEATCH/ beam line definition files. Additional parameters necessary for large-scale metrology can be derived from the layout drawings of the detector. The files and the layout plans have to be provided to the survey team prior to any survey or alignment work. If possible, all measurements and results from the metrology, survey, and alignment activities should be documented in measurement reports and stored in EDMS.

8.5.11.7 Marking out

With respect to the geodetic network, reference marks representing the projected beam line and the elements to be aligned may be painted on the floor and walls by the survey team. These marks will help in the installation of the services and beam line elements. Everyone working in their vicinity should ensure that these marks remain visible. The required marks and annotations have to be defined in collaboration with the technical co-ordination of the experiment.

8.5.11.8 Positioning

Before the installation of the detector elements, their supports will be installed by others and be pre-adjusted to their nominal position by the survey team. Such survey interventions can happen also before the installation of supports if shims are required to counteract local floor deformations. Once the detector elements are installed, their initial positioning will be carried out with respect to the geodetic network of the area. Precise survey methods and instrumentation will have to be used, such as laser trackers, total stations, and direct levelling.

8.5.11.9 As-built measurements

To save time during the infrastructure installation, and to provide 3D documentation of the experimental area, a number of as-built measurements of the civil engineering structures could be done, followed by as-built measurements of the installed infrastructure and, finally, of the experiment.

It is recommended to make 3D scans in the experimental hall at the end of the civil engineering work, and after the installation work. These measurements should be pre-processed by the survey team to give point clouds and their 3D coordinates in the CCS or a defined experimental coordinate system to the SHiP integration team.

8.5.12 Radiation protection

The high-intensity beam power deposited in the target poses challenges for radiation protection in several locations. To reduce the effect and mitigate the impact, the radiological aspects have been carefully addressed at the design stage. The studies included expected prompt and residual dose rates in the various areas of the SHiP experimental area and public areas. The studies were based on past measurements and extensive simulations with the FLUKA Monte Carlo particle transport code and ActiWiz 3. The results of the study are shown in Chapter 9.

The RP requirements integrated into the experimental area layout are the following:

- 1 m concrete thickness for the ceiling of the underground experimental hall;
- 0.4 m concrete thickness for the walls, floor, and elevator/stairs shaft of the experimental hall;
- 6 m high and 40 m long land hills behind the surface building (see Fig. 8.45);
- a surface fence behind the building to avoid personnel accessing the area during operation (see Fig. 8.45);
- the underground experimental hall and surface hall are not accessible during beam operation.

8.5.13 Safety

The proposed layout of the experimental area complies with CERN safety rules and has been analysed from the point of view of safety. The main safety requirements taken into account are the following.

– The lift and stairs are protected against fire, and their lighting is not connected to the general electrical circuit (they will be connected to the UPS network); therefore, they can be used at any time.
– Fire equipment and Fire Brigade vehicles (e.g. PEFRA [12]) can descend to the underground experimental hall through the lift, especially for rescue operations.
– Two escape routes from the experimental hall are provided (see Fig. 8.39). One is located 33 m away from the target hall/alcove interface, and the other at the end of the underground hall.
– A 1.1 m high parapet is provided around the roof of the surface hall and service building (see Fig. 8.58).
– Ladders to access the roofs and the crane platforms are provided inside the surface hall and the underground experimental hall. The maximum step height and exact location will be determined in further studies.
– As concrete beams will close the openings inside the surface hall at the end of the SHiP installation phase, barriers must be installed around the three openings.
– A safe zone against fire is required in the underground area. One option could be a room prepared against fire at the entrance to the lift, allocated out of the 20 m wide hall to reduce the detector background. The safe area must be overpressurized and linked to a vertical egress path. The location and configuration will be studied in more detail.
– Regarding the fire/sector door locations and sizing, the underground experimental hall is considered as one fire compartment in itself, completely independent of the target complex.
– A fire detection system is installed to ensure early detection. Early detection is such that it allows evacuation (the last occupant out) before untenable conditions are reached.
– A system capable of transmitting an alarm, along with a message containing safety instructions, to occupants anywhere in the North Area, is installed. This alarm should be triggered upon detection of a fire, operation of evacuation push buttons, action by the CERN Fire Brigade out of the CERN Fire Brigade Safety Control Room (SCR) or the CCC, or BIW (Beam Imminent Warning) situations. Evacuation push buttons should cover all premises.
– Fire detection and evacuation push buttons are integrated with safety actions such as compartmentalization, stopping ventilation, and other machine functions according to a predefined fire protection logic.
– The fire resistance of ducts and fire compartments is respected, with appropriate fire dampers as they pass across fire resistance partitions.

See Chapter 10 for further information on safety considerations.

8.5.13.1 Fire system and alarms

For the service building, standard fire safety requirements in building codes are very likely to be applicable wherever fire-induced radiological risk is not an issue. Concerning the surface hall, natural ventilation through skydomes (see Fig. 8.58) is an easy technical solution for implementation/integration.

The smoke extraction system of the experimental hall falls outside the applicable building codes. Therefore, it should be fine-tuned by means of CFD simulations in a performance-based design effort. The HSE Fire Safety Engineering Team has provided preliminary estimates based on regulations and previous similar experience. Further studies will have to be performed by CFD simulations. The present rough estimates cannot be taken as definitive functional requirements; at this stage of the project, however, they will help in sizing the elements for integration purposes.

The features of the proposed smoke extraction system for the experimental hall are as follows.

– The 2400 m^2 (120 m$\times$20 m) experimental hall is split into four smoke extraction areas of area approximately 600 m^2.
– Smoke extraction flow rates will be in the order of 1 m^3/s for every 100 m^2 surface.

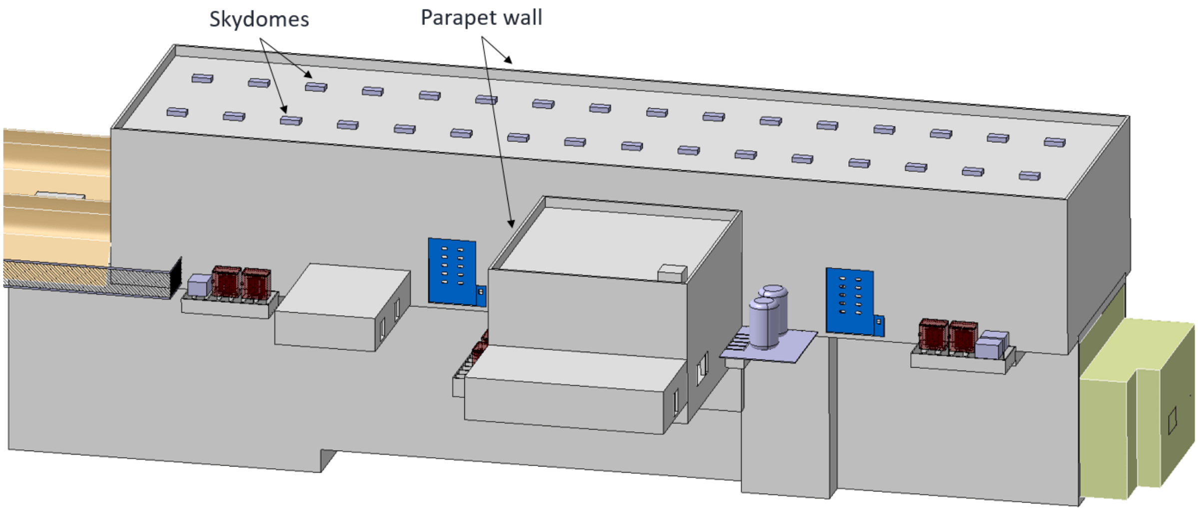

Fig. 8.58: Fire evacuation system of surface hall

- The smoke extraction system shares the main duct and extraction equipment for the four areas.
- Only one smoke extraction area is triggered at a time (the one where the origin of the fire is located).
- The target velocity in the ducts is 10 m/s.
- A 0.5 m diameter shaft is provided.
- There are four extraction sectors.
- There are four smoke extraction points.
- There are three 'smoke curtains' (2 m$\times$20 m). These are screens directly connected to the ceiling with the aim of containing the smoke in the case of fire (see Fig. 8.59). They should remain extended but can be raised promptly, and manually.

Fig. 8.59: Smoke curtain [29]

Therefore, the smoke extraction flow rate should be in the order of 6.6 m^3/s (24 000 m^3/h), and a DN1000 extraction duct (0.785 m^2 cross-section) allows a velocity of 8.4 m/s, below the 10 m/s target. The smoke extraction equipment is foreseen to be allocated inside the service building, where it can be accessible during beam operation. It will be integrated with the cooling and ventilation equipment (see Section 8.5.10). Figure 8.60 shows the smoke extraction ducts and the smoke curtains highlighted in red and black, respectively. The ducts run above the overhead cranes and on the right wall of the underground hall (taking the beam direction as a reference).

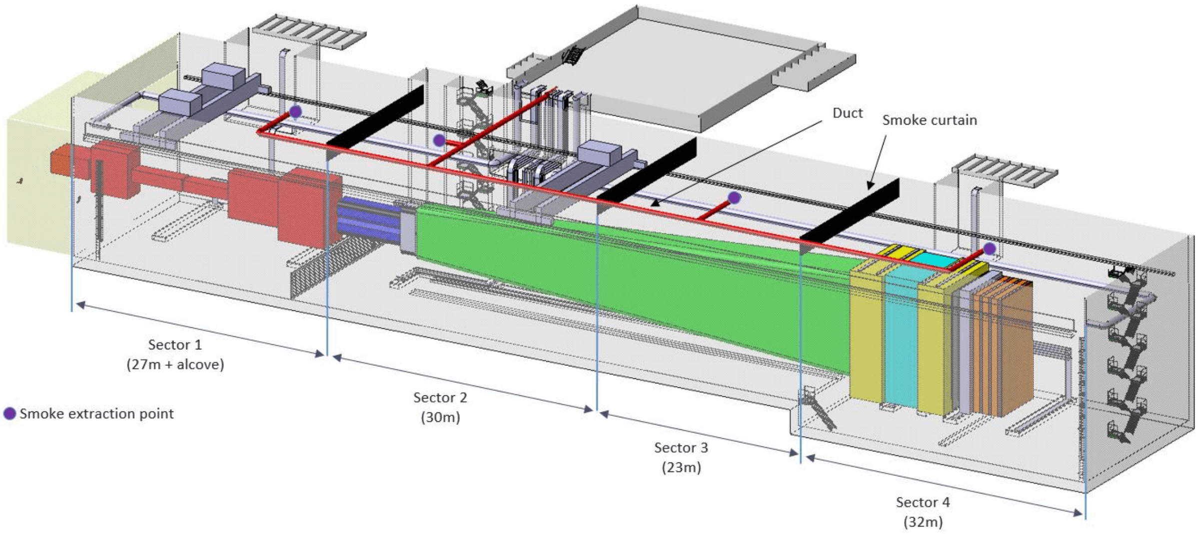

Fig. 8.60: Smoke extraction system of experimental hall

8.5.14 Access control

The BDF access control will be controlled from the CERN Control Centre, located in building 874 on the CERN Prévessin site. Therefore, a connection between the two is required.

The access control system of the experimental area includes the following.

- Badge access to enter the service building, workshop, and control room.
- No access to the surface hall and underground experimental hall during beam operation, owing to RP constraints.
- Material access door/personnel access door to gain access from the service building to the surface hall. A maintenance fence inside the surface hall could be added to allow maintenance of the MAD/PAD during beam operation.
- Exterior doors (personnel and material) of surface hall beam interlocked. The emergency exit from the experimental hall is also beam interlocked.
- Two patrolled installations, one in the surface hall and another in the experimental hall.
- Sector door to access the experimental hall from the surface hall (dosimeter required).

Figure 8.61 represents the scheme of the access control system at ground level. During construction and installation, large pieces, pre-assembled SHiP components, and personnel will enter the surface hall through the doors located on the Jura side (shown in Fig. 8.61 as "Beam-interlocked door/emergency door"). During beam operation and technical stops, these doors will be interlocked and personnel access to the surface hall must be through the MAD/PAD to avoid losing the patrol of the surface hall. To access the underground experimental hall, personnel, tooling, and materials will have to pass through the sector door. If a large detector part has to be replaced, it will enter through the large doors of the surface hall and be lowered underground through the openings. As a consequence, the patrol of the surface hall and experimental hall will be lost. A presence detection system on the concrete beams may be required to ensure that the openings are completely closed.

Figure 8.62 shows the approximate location of the patrol boxes in the underground experimental hall. There are two at the extremes of the hall and one more next to the elevator.

Finally, an estimated list of the hardware included in the access control system is shown in Table 8.15. Beam interlock logic modifications, cabling, and programmable logic controllers (PLCs) are not included.

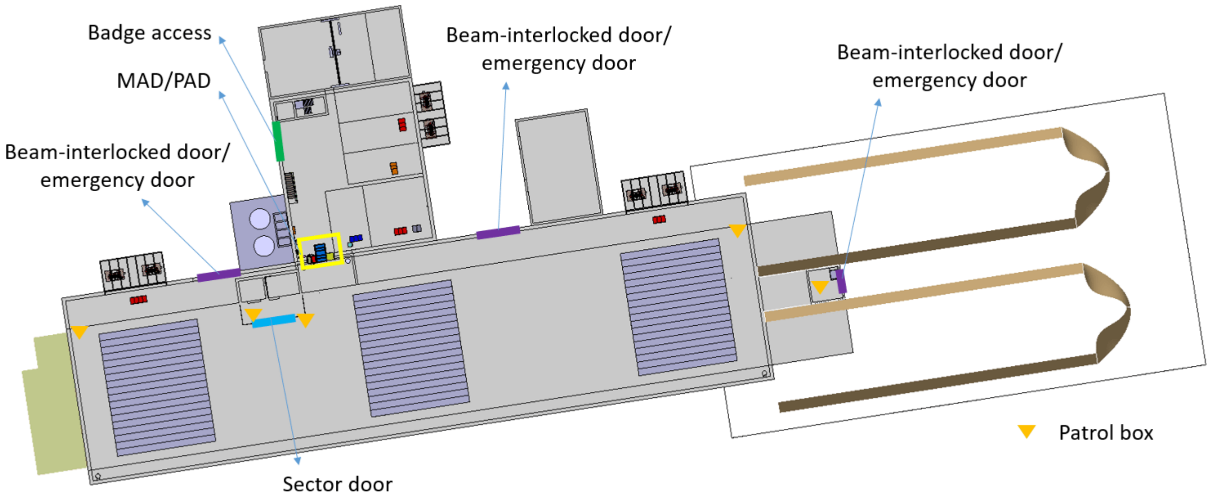

Fig. 8.61: Access control scheme of experimental area

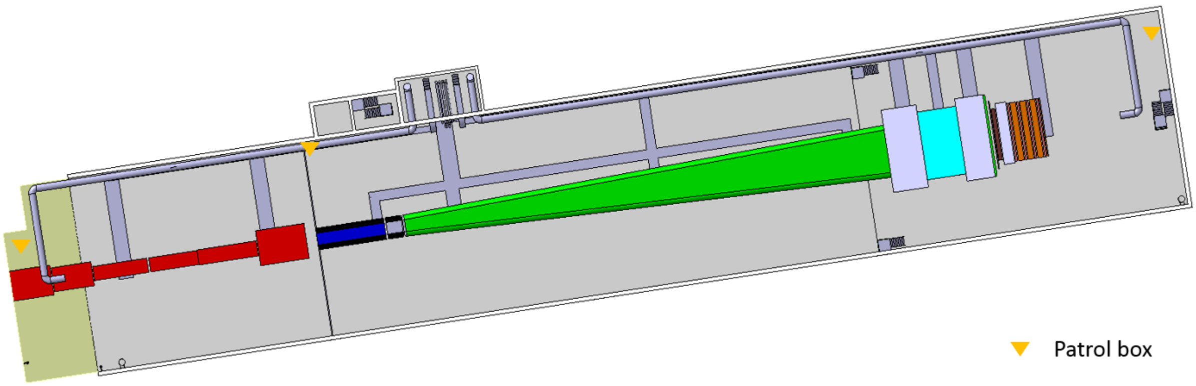

Fig. 8.62: Location of access control equipment inside experimental hall

Table 8.15: Access system hardware

Item	Quantity
MAD/PAD	1
Beam-interlocked doors	3
Badge control station	1
Badge control readers	≈5
Patrol boxes	8

References

[1] L. Dougherty. *BDF—TDC2 Equipment Removal*. Tech. rep. EDMS 2084770. 2019. URL: https://edms.cern.ch/document/2084770.

[2] L. Dougherty, P. Santos Diaz. *Structural Specifications for the Access Building, Auxiliary Building, Personnel Shaft and Chicane*. Tech. rep. EDMS 2000961. 2018. URL: https://edms.cern.ch/document/2000961.

[3] L. Dougherty. *BDF Beam Line Integration Study*. Tech. rep. EDMS 2046922. 2018. URL: https://edms.cern.ch/document/2046922.

[4] L. Dougherty. *BDF Beam Line Vacuum Layout Integration Study*. Tech. rep. EDMS 2052532. 2018. URL: https://edms.cern.ch/document/2052532.

[5] R. Ricol. *Fenetre titane TED*. Tech. rep. CRNHZMW 1271. 2013. URL: https://edms.cern.ch/document/1264344.

[6] HALFEN. *HALFEN Rails*. 2019. URL: https://www.halfen.com (visited on 02/18/2019).

[7] P. Dewitte. *Procédure montage GGPSO*. Tech. rep. EDMS 1744694. 2017. URL: https://edms.cern.ch/document/1744694.

[8] L. Dougherty. *Structural Specifications for the Transfer Tunnel*. Tech. rep. EDMS 2037312. 2018. URL: https://edms.cern.ch/document/2037312.

[9] L. Dougherty. *BDF Access Building and Equipment Shaft Layout Drawing*. Tech. rep. EDMS 2028013. 2018. URL: https://edms.cern.ch/document/2028013.

[10] K. Kershaw. *Service Building for BDF Target Complex*. Tech. rep. EDMS 2009818 v.01. 2018. URL: https://edms.cern.ch/document/2009818.

[11] L. Dougherty. *BDF Auxiliary Building Layout Drawing*. Tech. rep. EDMS 2028014. 2018. URL: https://edms.cern.ch/document/2028014.

[12] L. A. Dougherty. *Tractor Chariot (PEFRA)*. Tech. rep. EDMS 2028971. 2018. URL: https://edms.cern.ch/document/2028971.

[13] L. Dougherty. *Personnel Shaft and Chicane Layout*. Tech. rep. EDMS 2028016. 2018. URL: https://edms.cern.ch/document/2028016.

[14] L. A. Dougherty. *Schindler Lift Specification*. Tech. rep. EDMS 2028012. 2018. URL: https://edms.cern.ch/document/2028012.

[15] P. Avigni. *BDF Extraction Tunnel CV Work Package*. Tech. rep. EDMS 2050765. 2018. URL: https://edms.cern.ch/document/2050765.

[16] P. Avigni. *BDF Cooling Synoptic*. Tech. rep. EDMS 2029613. 2018. URL: https://edms.cern.ch/document/2029613.

[17] P. Avigni. *BDF Ventilation Synoptic*. Tech. rep. EDMS 2029614. 2018. URL: https://edms.cern.ch/document/2029614.

[18] S. Reignier. *Sirius TN 5 Installation Specification*. Tech. rep. EDMS 1870848. 2018. URL: https://edms.cern.ch/document/1870848.

[19] SHiP Collaboration. "The experimental facility for the Search for Hidden Particles at the CERN SPS". In: *J. Instrum.* 14.3 (Mar. 2019), P03025. DOI: 10.1088/1748-0221/14/03/P03025. arXiv: 1810.06880 [physics.ins-det].

[20] P. Santos Diaz. *BDF Experimental Hall Concept*. EDMS 2027681 v.2. January 2019. URL: https://edms.cern.ch/document/2027681.

[21] P. Santos Diaz. *BDF Surface Hall Concept*. EDMS 2027705 v.2. January 2019. URL: https://edms.cern.ch/document/2027705.

[22] P. Santos Diaz. *BDF Service Building Concept*. EDMS 2027708 v.3. January 2019. URL: https://edms.cern.ch/document/2027708.

[23] P. Santos Diaz. *BDF—Structural Specifications for the Experimental Area*. Tech. rep. EDMS 2011390 v.1. 2018. URL: https://edms.cern.ch/document/2011390.

[24] P. Santos Diaz. *SHiP Load Layout*. EDMS 2027693 v.2. January 2019. URL: https://edms.cern.ch/document/2027693.

[25] *CERN Bulletin*. "CMS: riding on a cushion of air". In: *CERN Bulletin* 23/98 (1998).

[26] P. Santos Diaz. *Experimental Area Lift Specifications*. EDMS 2032342. 2018. URL: https://edms.cern.ch/document/2032342.

[27] J. Devine. *CENF Target Facility Electrical Engineering Specification*. EDMS 1440310. 2014. URL: https://edms.cern.ch/document/1440310.

[28] P. Avigni. *SHiP CV Work Package*. Tech. rep. EDMS 2050772. 2019. URL: https://edms.cern.ch/document/2050772.

[29] MultiMedia LLC. *Supercoil*. 2019. URL: https://www.stoebich.com/en/product/supercoil/10087 (visited on 01/24/2019).

Integration: appendices

8.A SmarTeam numbers

The SmarTeam references of the 3D models of the top-level assemblies for the Beam Dump Facility are listed in Table 8.16.

Table 8.16: SmarTeam references of the integration 3D models

Description	SmarTeam number
BDF transfer line integration study	ST0890663
BDF access and auxiliary buildings and target complex access	ST1054816
BDF experimental area layout	ST0964387
BDF–SHiP assembly mock-up	ST1095050
SHiP conceptual layout	ST0947198

8.B Structural specification documents

The structural specification documents for the transfer tunnel, the surface buildings, and the experimental area stored in the CERN EDMS are listed in Table 8.17.

Table 8.17: Structural specification documents

Title	EDMS number
Transfer Tunnel	2037312
Access Building, Auxiliary Building, Personnel Shaft and Chicane	2000961
Experimental Area	2027772

Chapter 9

Radiation protection

9.1 Introduction

The main radiation protection challenges for the BDF arise from the high beam power and the proximity to the surface, to other experimental facilities, and to the CERN fence, but also from the need to retain flexibility for future installations. To respect the applicable CERN radiation protection legislation regarding doses to personnel as well as the environmental impact, a full radiological assessment was carried out for the design of the BDF. The facility was optimized based on general radiation protection guidelines and specific studies on prompt and residual dose rates, air and helium activation, ground and water activation, and radioactive waste production, as they heavily influence the design. To assess the above-mentioned radiation protection aspects, extensive simulations were performed with the FLUKA Monte Carlo particle transport code [1, 2].

Next to the radiological assessment of the facility itself, the evaluation of its primary beam extraction from the SPS is also a crucial factor. Since the dedicated BDF beam line branches off at the top of the existing TT20, in the TDC2 cavern, studies of ground activation around TT20 and TDC2 were conducted. These are particularly relevant for the civil engineering works (see Chapter 11). Also, the necessary cool-down times for the existing tunnels before any works can start were evaluated. In addition, beam losses in the dedicated BDF transfer line were studied with the help of FLUKA.

Furthermore, tritium out-diffusion experiments for all materials relevant to the BDF were performed. The contribution of tritium out-diffusion is particularly relevant to the activation of the cooling water of the BDF target. This chapter focuses on the primary beam extraction for the BDF, the BDF itself, the SHiP experimental area, and the tritium out-diffusion measurement.

9.2 BDF beam line

The extraction of the beam for SHiP from the SPS will be by slow resonant extraction from the SPS LSS2 using existing extraction equipment and transfer of the beam along TT20 up to a switch in the TDC2 tunnel that leads into a dedicated BDF transfer line (Section 11.3.2). The TDC2 tunnel is an existing underground tunnel that houses the North Area beam lines (TT22, TT23, TT24, and TT25) and their services. The new BDF beam line (TT90) starts downstream of the new splitter magnet in the TDC2 tunnel and runs alongside the existing North Area beam lines for approximately 110 m, as shown in Fig. 9.1.

With the SHiP extraction in addition to the North Area requirement, the total number of protons extracted per year will increase by a factor of approximately 4. Thus, to keep the activation of the SPS extraction region to a level comparable to that of today, a reduction of the beam losses during extraction by a similar factor is envisaged, to be achieved by several techniques as described in Chapter 3.

9.2.1 Junction cavern

The junction cavern (TDC21) is an underground cavern that houses four beam lines (TT90, TT23, TT24, and TT25) and their corresponding services (see Fig. 9.1). To enable the construction of the junction cavern, part of the existing TDC2 tunnel must first be demolished. To assess the radioactivity levels that will be encountered during the civil engineering works, concrete and soil samples have been taken and analysed.

Concrete samples were taken at three different locations from the slab of the existing TDC2 tunnel

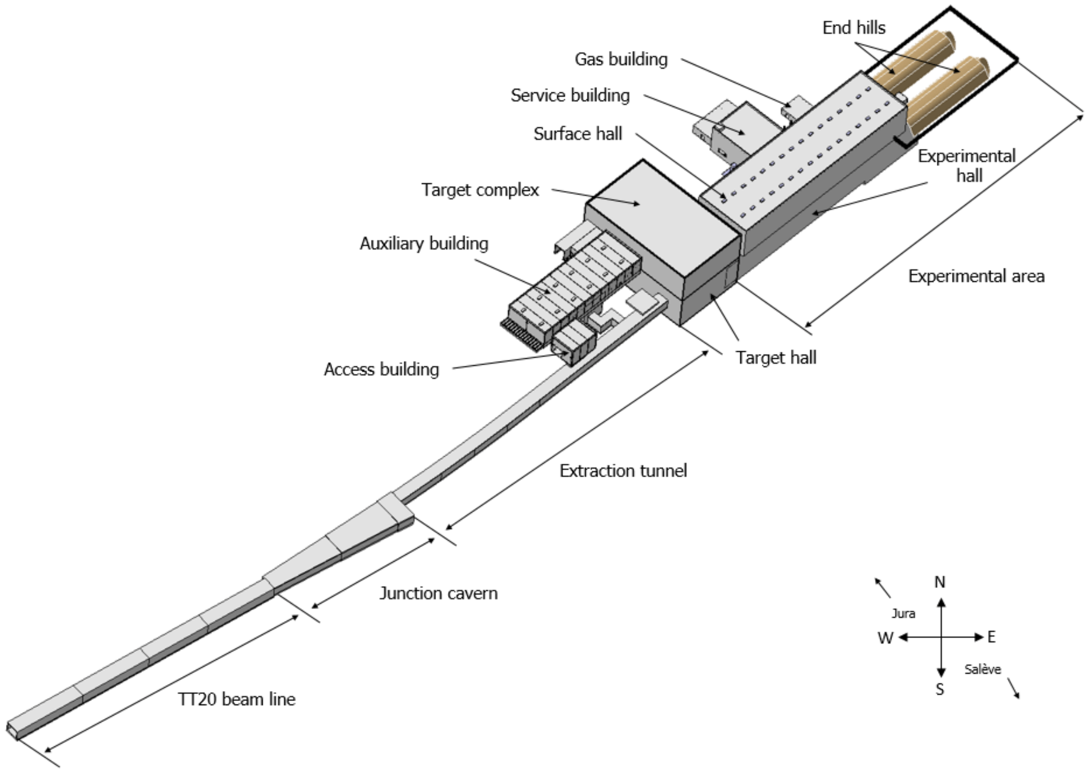

Fig. 9.1: Overview of BDF integration

(see Fig. 9.2) during the 2016–2017 Year End Technical Stop (beginning in April) after a cool-down period of 4.5 months (the stop of the proton run was in mid November, and the stop of the ion run in mid December). The results of gamma spectrometry of the concrete samples showed radioactivity above the Swiss liberation limit [3] for all of them, with values of 145–404 times the LL. This means that the concrete will be considered as radioactive in every location, and at every depth, in the TDC2 tunnel.

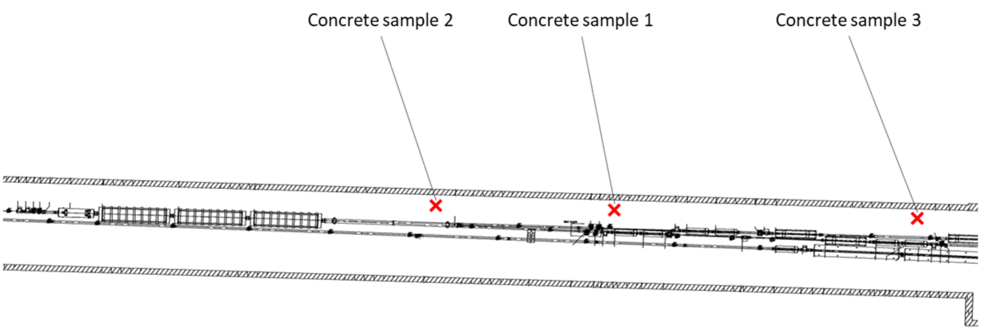

Fig. 9.2: Locations of concrete sampling

Fig. 9.3: Locations of soil sampling

Surface soil sampling was carried out during the 2017–2018 Year End Technical Stop (on 21 March 2018) after a cool-down of approximately 5 months (the stop of the proton run was at the end of October, and the stop of the ion run at the beginning of December). The locations, shown in Fig. 9.3, were chosen to be where the activation of the equipment in the tunnel was highest. The drilling stopped at 1.5 m from the roof of the tunnel, which corresponds to approximately 5.5 m depth. Na-22 was found in the results of the gamma spectrometry, with values of up to 5% of the LL. Based on the results, the soil up to 5.5 m depth from the surface can be considered non-radioactive. The soil even closer to the cavern, however, could show a different gradient of activation, and therefore special measures should be taken if activation levels prove to be significant. Thus, the soil excavations, demolition, and construction works for the new junction cavern require radiation workers.

For any civil engineering works in the area under consideration, it has to be taken into account further that a minimum soil thickness of 8 m must be kept around the walls of the TDC2 and TCC2 tunnels during beam operation in the North Area [4]. For the start of the soil excavations and demolition works, from an ALARA point of view, the cooling time should be as long as possible. However, it is clear that, from the point of view of the project, the opposite is the case. Therefore, a compromise has to be found which is acceptable for the project.

When we look at the expected dose rates in TDC2 for various cooling times, the most significant decrease occurs during the very first weeks of cool-down (by a factor of approximately 13 during a 4 week Pb run). But between, for example, 9 weeks and 5 months after the proton run, the further gain amounts to about 30%. At the downstream end of the TDC2 area, in which equipment will have to be removed, the dose rates at 40 cm from the equipment are relatively low (30 µSv/h, 9 weeks after the proton run), and therefore the cooling time becomes less critical. For the hottest elements to be removed (e.g. BSPH.240212), the dose rates are of the order of 590 µSv/h 9 weeks after the proton run. These are still much lower than the dose rates at the splitters (11 mSv/h at 40 cm, 9 weeks after the proton run), which fortunately do not have to be removed for the civil engineering works.

To evaluate the necessary cool-down time, a WDP for any given works should also usually be looked at. At this stage, only a preliminary estimate of the WDP can be done, as it largely depends on the detailed methodology for the works (remote handling, shielding, work optimization, etc.). However, an estimate can suggest an order of magnitude for the cool-down time. A collective dose of about 10–20 mSv for equipment removal after 13 weeks (3 months) of cooling (including 4 weeks of Pb run) was estimated. Reducing the cooling time to 9 weeks (including 4 weeks of Pb run) would increase the collective dose by approximately 9% (1–2 mSv).

At this stage of the project, and in view of ALARA, it is recommended to use the maximum cooling time that is acceptable for the project, and on that is at least 9 weeks after the end of the proton run (i.e. 5 weeks in addition to the 4 weeks of the Pb run). From a radiation protection point of view, it is recommended to use 13 weeks (3 months) of cooling in the plan if possible, such that even without an ion run the plan could be met. Note that for both construction scenarios there is a contingency of more than 15 weeks, part of which could possibly be used for additional cool-down. Furthermore, the dismantling should start at the downstream end of TDC2, giving more cooling time for the hot elements further upstream.

9.2.2 Extraction tunnel

The extraction tunnel is an underground tunnel that houses the BDF beam line and its services. A personnel shaft from the auxiliary building serves as an entrance to the extraction tunnel (see Fig. 9.4). A chicane was designed in order to reduce the direct shining into the auxiliary building arising from beam losses in the extraction tunnel (see Fig. 9.5).

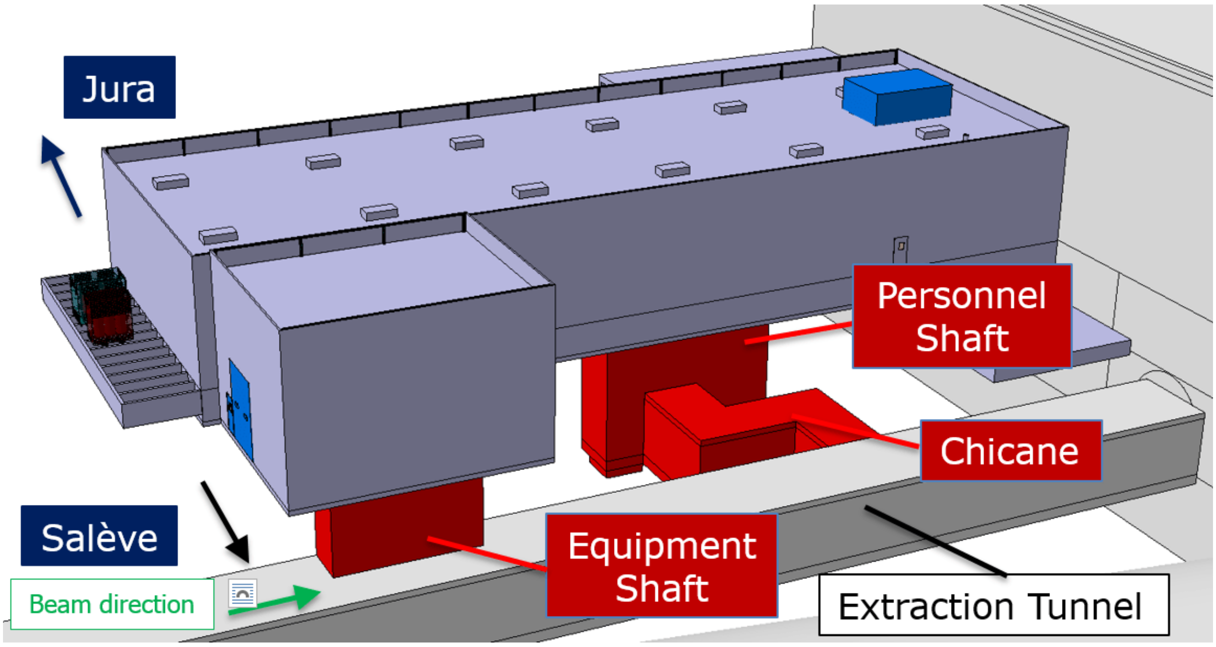

Fig. 9.4: Equipment shaft, personnel shaft, and chicane

In principle, no major beam losses are expected in the BDF beam line. To assess the radiological aspects, a conservative beam loss of 5% of the BDF spill (4×10^{13} protons on target in 7.2 s) on a cylindrical copper target (loss on a magnet) was assumed. However, any such kind of continuous loss would not be acceptable for the operation of the facility. In the case of such losses, further measures (e.g. optimization of beam transfer, shielding around hot spots) should be put in place to minimize the activation of the beam line and soil and to minimize radioactive waste production. The prompt dose rate is depicted in Fig. 9.6. The chicane reduces the prompt dose rate by five orders of magnitude. The dose rate is further reduced in the personnel shaft, and the shielding provided by the above-ground building structures (see Section 8.3) is such that the radiation reaches acceptable levels in the accessible areas of the auxiliary building. Furthermore, the access building and the personnel access in the auxiliary building are not accessible when the beam is on.

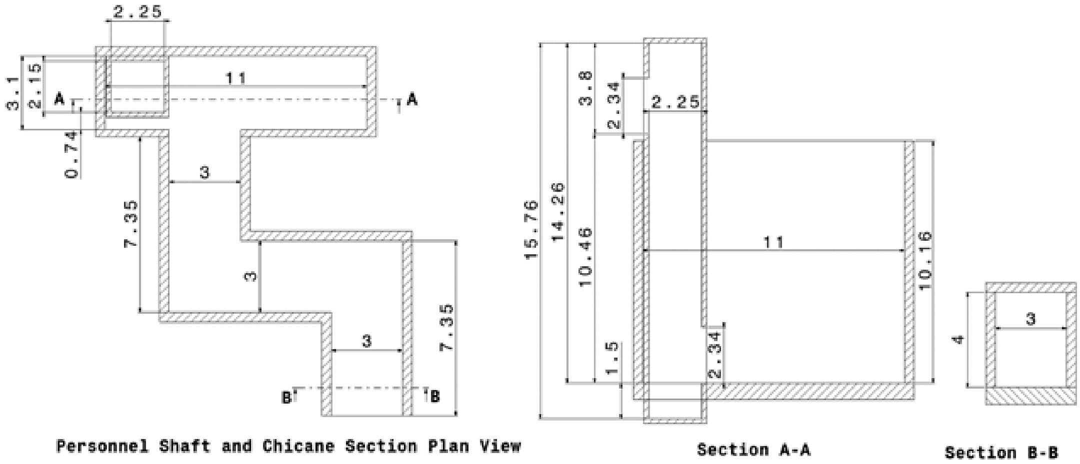

Fig. 9.5: Plan view of chicane section

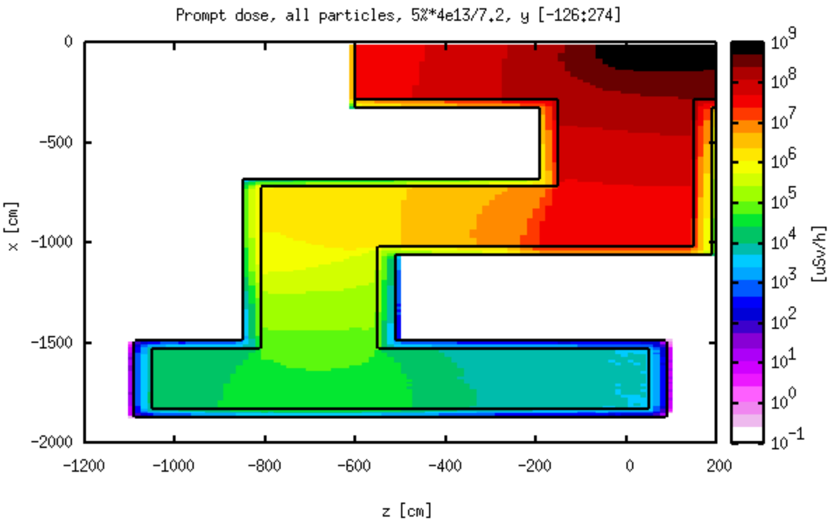

Fig. 9.6: Prompt dose rate in microsieverts per hour in the access chicane for the SHiP transfer line.

9.3 The BDF FLUKA model

The Monte Carlo particle code FLUKA was used to evaluate the radiation protection requirements for the entire BDF/SHiP facility. The FLUKA model of the facility was developed in collaboration with the EN-STI group at CERN. Figure 9.7 depicts the most critical areas of the facility from a radiation protection point of view: the target complex and the active muon shield.

The coordinate system used in the model is a right-handed Cartesian coordinate system with its origin at the target. The orientation of the coordinate system is defined by the width (x) and height (y) of the target complex and the beam direction (z). Because of the proximity of SHiP to ground level ($\approx$ 10 m), other experimental facilities ($\approx$ 20 m), and public areas ($\approx$ 70 m), massive shielding is required to keep the prompt radiation in the various accessible areas of the facility and the surroundings

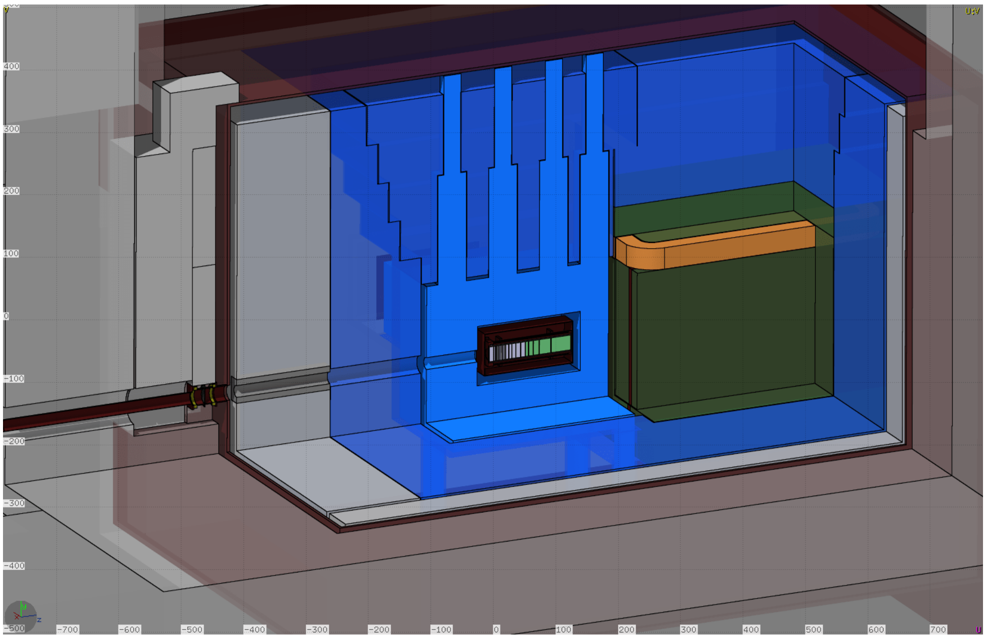

(a)

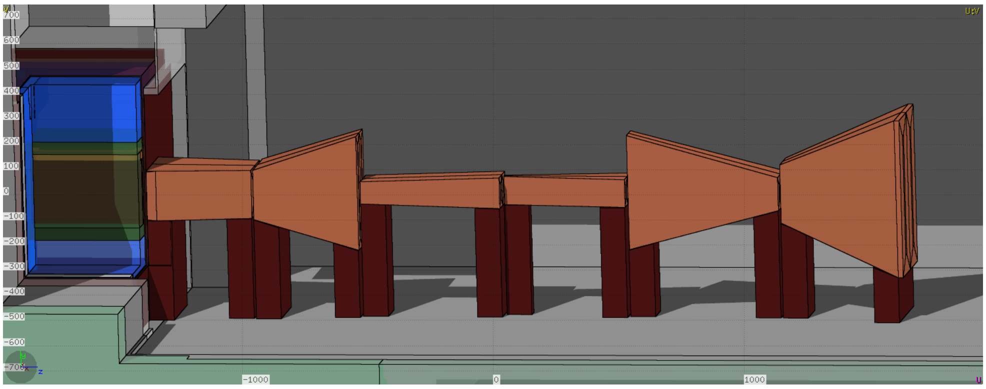

(b)

Fig. 9.7: View of target complex (a) and of active muon shield (b)

reasonably low. In addition to personnel protection regarding prompt dose rates, considerable shielding is indispensable for reducing the residual dose rates from and the environmental impact of activated air and soil, as well as for reducing radiation levels in electronic equipment (see also Ref. [5]). The shielding was consequently designed with the objective of keeping the various radiological hazards originating from the operation of the facility as low as reasonably possible, while taking into account the constraints of the various stages of the experiment, that is, construction, operation, maintenance, and dismantling. The configuration envisaged is such that activation of the fixed concrete civil engineering structures is avoided, simplifying not only the dismantling but also possible changes in the scope of the installation.

The shielding in the target area was therefore modelled with massive iron and concrete blocks with the thicknesses specified in Fig. 9.8. The iron blocks were specially designed for remote handling, as they will become highly activated. Several gaps were included between the blocks to account for imperfect alignment, ducts for cooling, electronics, etc. The innermost shielding blocks will include stainless steel water-cooling pipes for heat removal. The water-cooling circuits for these elements, as well as those for the target, will be closed and separated from other circuits. The downstream shielding, which has a thickness of 4.8 m, is magnetized and also acts as a hadron stopper with the objective of

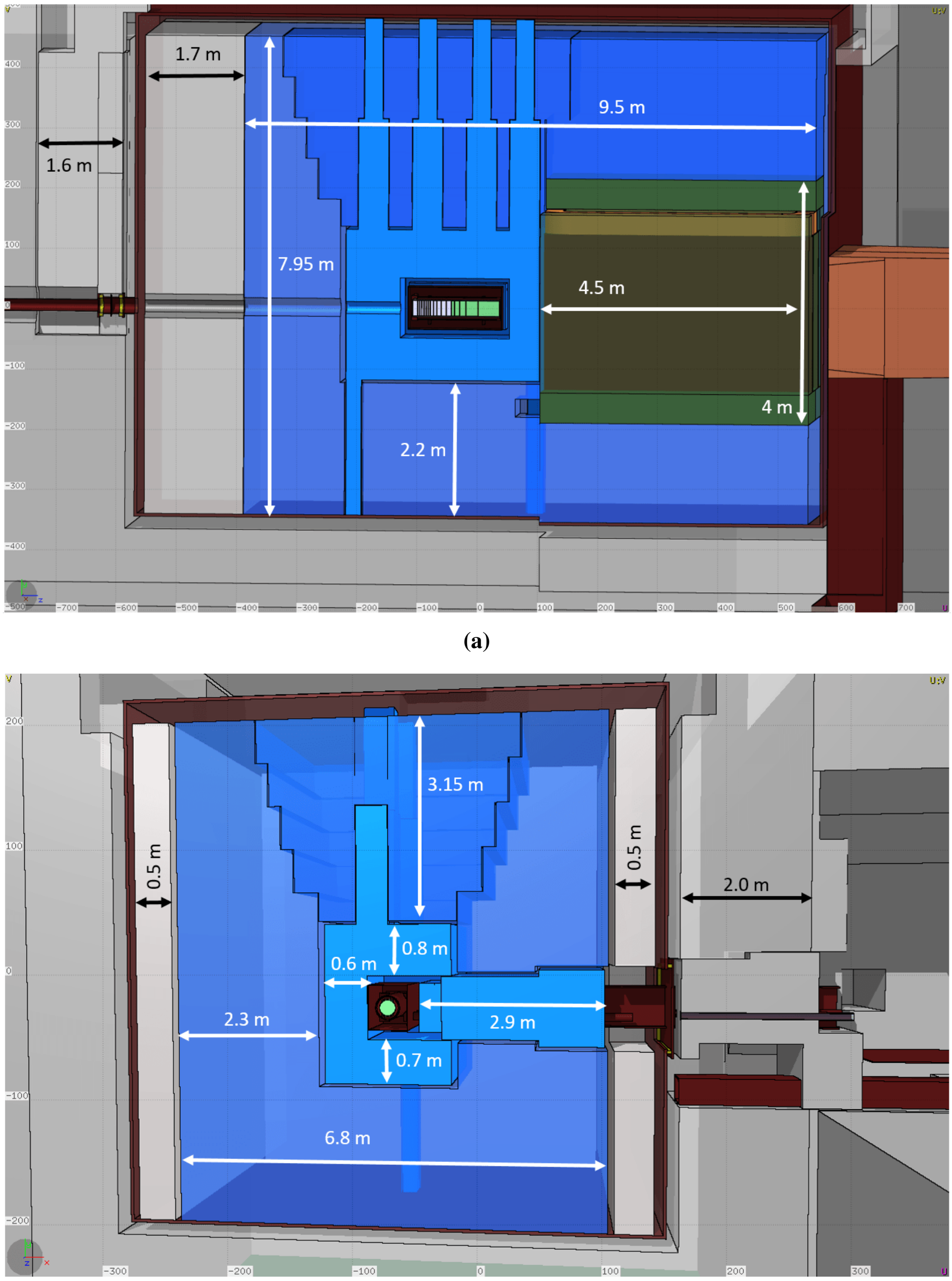

(a)

(b)

Fig. 9.8: Lateral (a) and perpendicular (b) views of the target complex

absorbing the secondary hadrons and the residual non-interacting protons emerging from the target, to significantly reduce the exposure of the active muon shield to radiation and to start bending the muons to increase the fiducial volume of the SHiP experiment. The iron shielding is embedded in a helium vessel to reduce corrosion. The remaining gaps between the iron shielding and the helium vessel structure are filled with removable concrete shielding blocks. The helium vessel is further surrounded by the fixed concrete civil engineering structures. On the sides and on the bottom of the vessel, the main requirement on the thickness of the concrete shielding comes from civil engineering. A minimum concrete shielding thickness of 2.4 m towards the target hall was further estimated based on the required prompt-dose-rate reduction. The iron shielding around the beam window has to minimize the air volume and be dismountable to minimize prompt dose rates and air activation in the backward region. Upstream of the window, the shielding has an aperture for the primary beam 20 cm in radius. This passage towards the primary beam line will be filled with removable iron bricks to reduce 'back splash' of particles into the primary beam area, which will lead to activation of the upstream beam line components and the surrounding air. To further reduce the 'back splash', two absorbers (preferably made out of polyethylene of lengths 1 m and 1.5 m) will be placed in the extraction tunnel. For further information about the conceptual design of the target area station, see Chapter 6.

The material properties employed for the shielding components were chosen such that they resulted in rather conservative estimates of the prompt and residual dose rates. The compositions assumed for the shielding materials are given in Table 9.1. Note that the self-shielded low-energy neutron cross-sections were utilized for cast iron and US1010 iron to correct for self-shielding effects. Pessimistic cobalt concentrations of 0.035% and 0.04% were assumed for cast iron and US1010 iron, respectively. Densities of 7.85, 7.87, and 2.34 g/cm^3 were utilized for the cast iron, US1010 iron, and concrete components, respectively. The soil surrounding the whole facility was modelled with a density of 1.9 g/cm^3, which is lower than the result of the measurement performed nearby for CENF, 2.3 g/cm^3. In this way, location-dependent density differences and a local decrease due to civil engineering works were conservatively taken into account. The chemical composition of the soil, as specified in Table 9.1, was determined from core samples taken for CENF. A water content of 7.5%, as measured from the samples, was furthermore assumed. The soil around the SHiP facility was modelled according to the current ground level in that area, with the smallest distance to the SHiP beam line being 10.3 m.

Table 9.1: Chemical composition of cast iron and US1010 iron as used in the FLUKA studies.

Material	Element	Weight percentage (%)
Cast iron	Iron (self-shielded)	94.267
	Carbon	3.399
	Silicon	1.799
	Manganese	0.5
	Cobalt	0.035
US1010	Iron (self-shielded)	99.14
	Carbon	0.105
	Sulfur	0.05
	Manganese	0.45
	Phosphorus	0.04
	Cobalt	0.04

9.4 BDF target area

9.4.1 Prompt and residual dose rates

The BDF target complex was designed under the condition that the target hall can be accessed during beam operation and be classified as a Supervised Radiation Area (<3 µSv/h). In contrast, no access during beam operation will be permitted to the target bunker. The prompt dose rates in the BDF target complex are depicted in Fig. 9.9. As expected, the highest dose rates can be found in the region of the target, reaching a few times 10^{12} µSv/h. They are reduced by a few orders of magnitude in the surrounding iron shielding. Above the helium vessel enclosing the shielding, the prompt dose rates are up to 3 mSv/h. The prompt dose rates are further reduced by the concrete shielding above the vessel, such that they drop to below 1 µSv/h in the target hall.

Figures 9.10 and 9.11 show the expected residual dose rates in the SHiP target complex for dif-

Table 9.2: Chemical composition of concrete and soil [6] as used in the FLUKA studies

Material	Element	Weight percentage (%)
Concrete	Hydrogen	0.6
	Carbon	5.62
	Silicon	18.867
	Magnesium	0.663
	Sulfur	0.012
	Oxygen	49.287
	Potassium	0.656
	Sodium	0.453
	Calcium	20.091
	Aluminium	2.063
	Iron	1.118
	Phosphorus	0.048
	Titanium	0.347
	Manganese	0.0387
	Zinc	0.0241
	Zirconium	7.4×10^{-3}
	Barium	0.0179
	Lead	0.0464
	Strontium	0.399
	Europium	4.2×10^{-5}
Moraine	Oxygen	3.90×10^{-1}
	Calcium	2.41×10^{-1}
	Silicon	1.83×10^{-1}
	Carbon	5.03×10^{-2}
	Iron	4.88×10^{-2}
	Aluminium	4.35×10^{-2}
	Potassium	2.16×10^{-2}
	Magnesium	8.07×10^{-3}
	Titanium	4.46×10^{-3}
	Sodium	3.34×10^{-3}
	Manganese	1.47×10^{-3}
	Barium	9.41×10^{-4}
	Strontium	8.68×10^{-4}
	Phosphorus	6.20×10^{-4}
	Chromium	5.28×10^{-4}
	Zinc	2.92×10^{-4}
	Zirconium	2.57×10^{-4}
	Sulfur	2.32×10^{-4}
	Nickel	1.72×10^{-4}
	Vanadium	1.40×10^{-4}
	Cerium	1.32×10^{-4}
	Chlorine	1.25×10^{-4}
	Lanthanum	1.10×10^{-4}
	Tungsten	1.05×10^{-4}
	Copper	6.37×10^{-5}
	Neodymium	5.48×10^{-5}
	Cobalt	4.27×10^{-5}
	Yttrium	4.07×10^{-5}
	Lead	3.78×10^{-5}
	Gold	3.48×10^{-5}
	Gallium	2.54×10^{-5}
	Lithium	5.73×10^{-6}
	Europium	6.87×10^{-8}

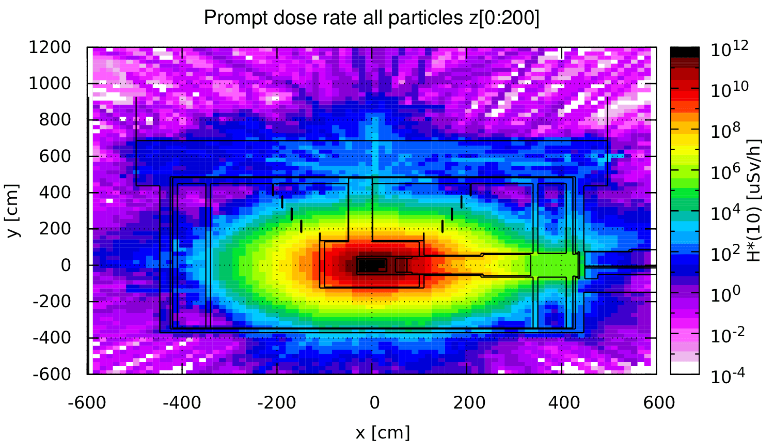

(a)

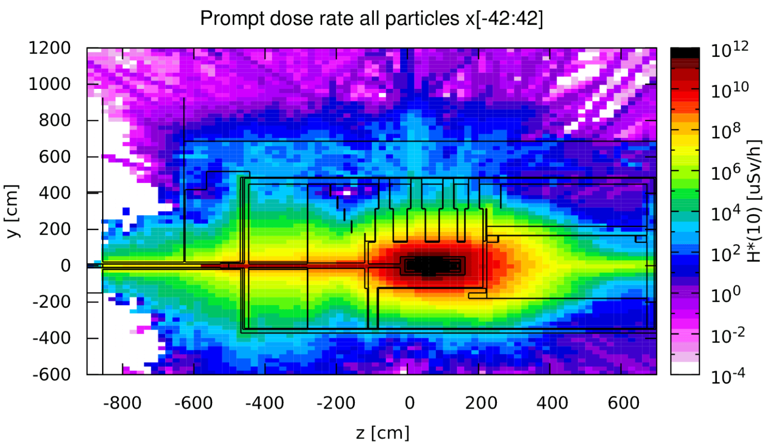

(b)

Fig. 9.9: Prompt dose rates in microsieverts per hour in the BDF target complex for all particles. (a) Perpendicular view at target level; (b) side view section through beam line.

ferent cooling times. The highest dose rates can be found in the region of the target, and they are in the order of a few times 10^8 µSv/h after 1 month of cooling.

For this reason, the facility design was such that all interventions planned in the target area will be executed remotely. The closest personnel-accessible area is above and next to the helium vessel enclosing the shielding. Here, maximum residual dose rates of a few microsieverts per hour after 1 week of cooling are reached, assuming that the helium vessel is closed and all shielding elements are in place. The residual dose rates in the target hall can be considered negligible.

9.4.2 Helium and air activation

The air and helium activation in the target complex was evaluated assuming the maximum beam power for five operational years. To evaluate the production of radionuclides in the air, a total of 39 isotopes were considered, including the radiologically most relevant short-lived isotopes ^{11}C, ^{13}N, ^{14}O, ^{15}O, and ^{41}Ar, as well as ^{3}H, ^{7}Be, ^{14}C, ^{32}P, ^{33}P, and ^{35}S among those with long half-lives. The highest air activation resulted in the air surrounding the helium vessel having 1.7×10^7 Bq after 60 s of cooling.

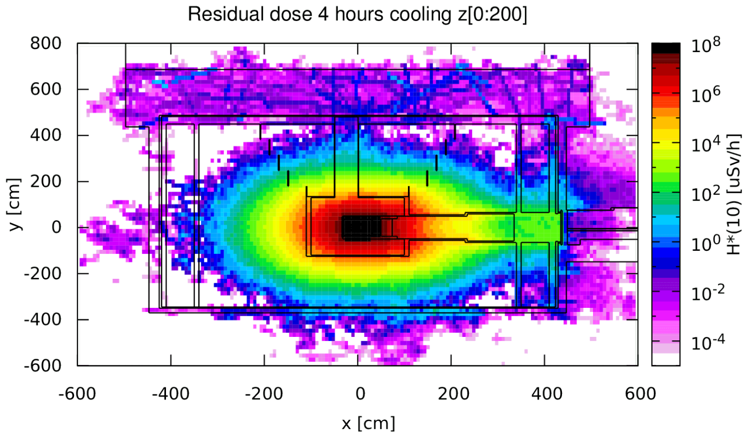

(a)

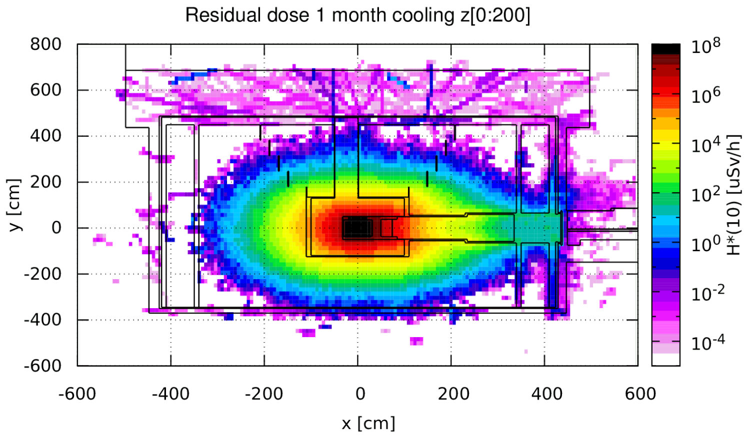

(b)

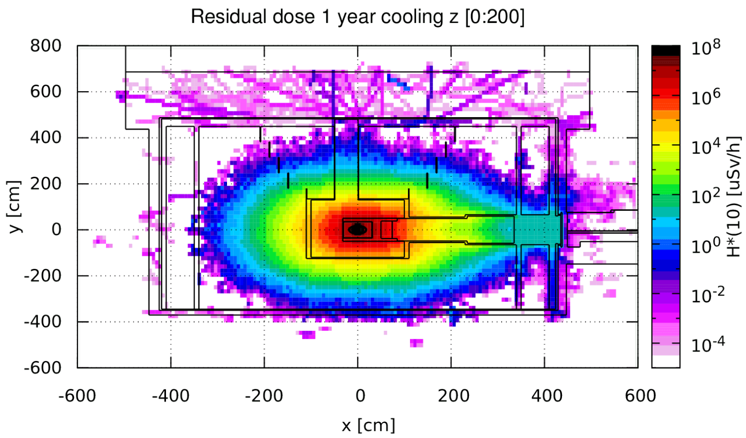

(c)

Fig. 9.10: Perpendicular view at target level of residual dose rates in microsieverts per hour in the BDF target complex after 4 h (a), 1 month (b), and 1 yr (c) of cooling.

When this value is compared with the CA[1] values of Swiss legislation [3], it results in 0.7 CA.

[1]A person working 40 h per week, 50 weeks per year with the standard breathing rate in activated air with CA = 1 receives 20 mSv.

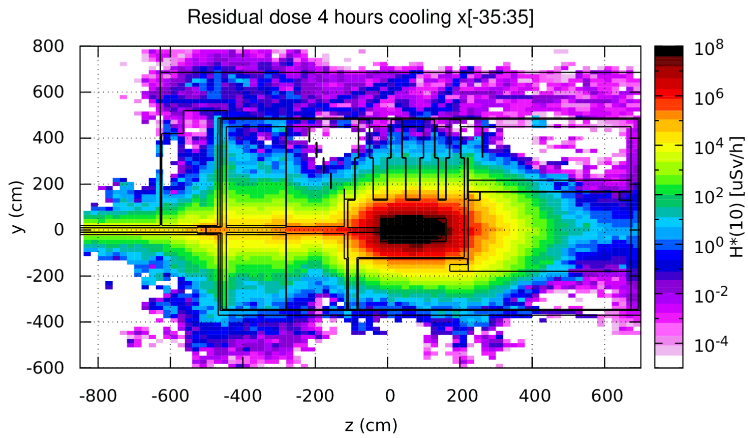

(a)

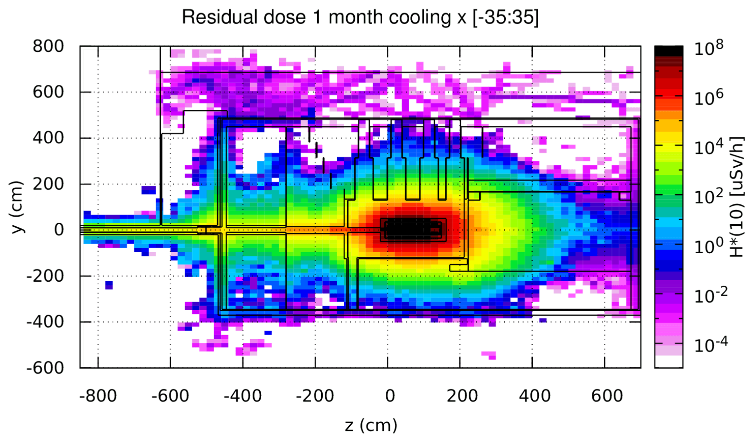

(b)

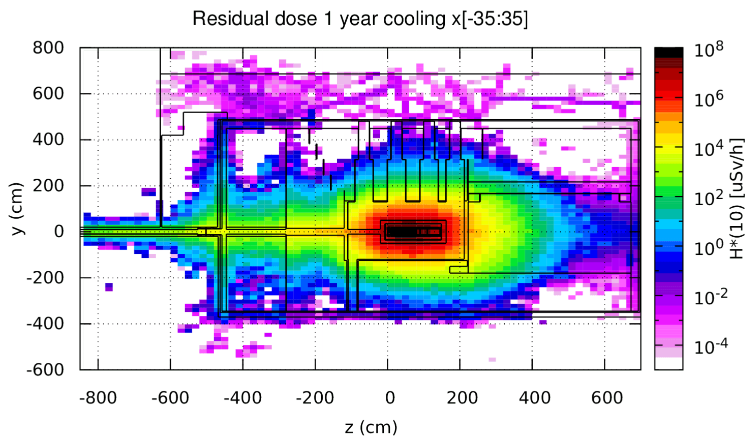

(c)

Fig. 9.11: Side view section through the beam line of residual dose rates in microsieverts per hour in the BDF target complex after 4 h (a), 1 month (b), and 1 yr (c) of cooling.

For all helium-filled regions, a realistic purity of 99.9% helium and 0.1% air contamination was considered. In the most critical helium region, that is, the innermost region of the helium vessel surrounding the target, a total activity of 2.8×10^9 Bq for helium and 6.1×10^7 Bq for air after 60 s of cooling was found. This results in 0.4 CA for helium and 7.5×10^5 CA for air. This demonstrates the effectiveness of helium, which gives rise only to the formation of tritium, which has a significantly lower radiological impact than the radionuclides arising from air.

Note that these results do not yet take into account the out-diffusion of tritium from the iron and concrete shielding into the air and helium environments, owing to the limited availability of diffusion constants for tritium at the moment. However, tritium out-diffusion experiments for all of the materials relevant to the BDF are currently being performed (see Section 9.7).

When the accident of a breakdown of the helium vessel with complete mixing of activated air and helium, this would result in 2.7 CA and a committed effective dose per hour of stay of 8 μSv. This was used to define the classification of the BDF ventilation system, for which the ISO standard 17873:2004 for nuclear installations was taken as a guideline. The ventilation system guarantees a pressure cascade from low- to high-contamination areas (see Section 6.5) sufficient to compensate for the defects of the static confinement. The air around the helium vessel will be injected at a flow rate of 5500 m^3/h and extracted at a flow rate of 8000 m^3/h, leading to an average irradiation time of approximately 7 min. The activation in the air surrounding the helium vessel with 7 min irradiation and no cooling time results in a total activity of 2.61×10^6 Bq, leading to 0.11 CA.

The ventilation circuits should be equipped with high-efficiency particle and aerosol (HEPA) filters to remove activated dust particles and aerosol-bound radionuclides from the air. Also, the air exhaust should be provided with such filters, and the airborne radioactivity released into the environment should be monitored.

9.4.3 Water activation

Another important aspect, one which has to be taken into account from an environmental point of view, is the activation of the water in the cooling circuits. The expected radioactivity in the water was evaluated assuming the expected beam power over five operational years and assuming that all of the water was concentrated statically in the target. The results give a conservative estimate because the speed of the water in the circuits will be 5 m/s and the cooling circuits of the proximity shielding and the magnetic coil are far away from the target area. The production of radionuclides in the water and the resulting activities were used to define the shielding around the demineralization cartridges, where most of the radionuclides will be trapped. For the cartridge in the target water-cooling circuit, 50 cm cylindrical concrete shielding is foreseen, and for the roof of the trolley service area, 165 cm of concrete. For the cartridge in the shielding/coil water-cooling circuit, which is located in the CV room, 40 cm cylindrical shielding is envisaged, like that for the roof of the room itself. The water, after passing through the cartridges, will mostly contain tritium. The tritium concentration arising from direct activation was estimated to be 0.5 GBq/l. Because of the high tritium production in the target (approximately 18 TBq during 5 yr of operation), a significant contribution to the tritium concentration in the water may come from out-diffusion of gaseous tritium from the blocks of the target and subsequent trapping in the cooling water. Tritium out-diffusion experiments at CERN are being performed to overcome the lack of experimental data (see Section 9.7). Assuming 1% of out-diffusion every 2 months and 100% trapping, the tritium concentration from out-diffusion will be around 60 MBq/l every 2 months. The exchange of cooling water (1 m^3) in 1 yr would result in 280 GBq of tritium activity.

9.4.4 Radioactive waste zoning

A waste study was performed to predict the amount and the characteristics of the radioactive waste that will be produced during operation of the BDF. The objectives of this study were to improve the management of radioactive waste and, eventually, to reduce the overall production of radioactive waste.

To distinguish areas of radioactive waste from areas of conventional waste, the liberation limits from Swiss legislation [3] were used. To exempt a material containing a mixture of radionuclides of artificial origin from any further regulatory control, the following sum rule must be respected:

$$\sum_{i=1}^{n} \frac{a_i}{\mathrm{LL}_i} < 1\,, \tag{9.1}$$

where a_i is the specific activity (in Bq/kg) or the total activity (in Bq) of the ith radionuclide of artificial origin in the material, LL_i is the Swiss liberation limit for radionuclide i in the material, and n is the number of radionuclides present. If the sum rule is not obeyed, the material is radioactive according to Swiss legislation. Twelve different cooling times, ranging from 15 min to 30 yr, were assessed. Figure 9.12 shows the waste zoning of the BDF target area after 1 yr of cooling time. Note that the values in air- and helium-filled regions are so far not representative, as the air and helium will be diluted by leakage or extraction into the environment, or both. The zoning plots show that the most activated parts of the BDF are the target and the iron shielding elements. It can be seen that the target and part of the iron shielding remain radioactive. In the design of the shielding, the minimization of radioactive waste was taken into account by having a modular iron bunker such that activated parts might easily be separated from ones that are below the liberation limits.

9.4.5 Soil activation

The production of radioactivity in the soil and water surrounding the SHiP facility is a significant environmental concern. Particularly soluble radionuclides likely to pass through the karstic system are critical for the protection of groundwater resources. To minimize related radiological risks, the specific activities of the leachable radionuclides H-3 and Na-22 should lie below the following design goals [6]:

- H-3 < 10 Bq/kg;
- Na-22 < 2 Bq/kg.

The leachable radionuclide Na-24 was neglected because it is too short-lived to survive the journey from its place of creation to its place of consumption. When the relation between prompt radiation and soil activation was studied for the CENF facility, it was estimated that the limits given above were not exceeded for prompt dose rates of 1 mSv/h or below. As can be seen in the previous subsection, the design of the facility is such that it avoids activation of the fixed concrete civil engineering structures and, as a consequence, of the soil; in fact, the the soil is below 1 LL and the prompt dose rate at the soil level is kept below 1 mSv/h.

9.5 Environmental impact

The environmental impact from releases of radioactive air and helium was studied in detail. The annual releases from the target pit around the He vessel and from the He vessel are listed in Table 9.3.

In total, 44 GBq and 16 MBq of short-lived gases (^{11}C, ^{13}N, ^{14}O, ^{15}O, and ^{41}Ar) will be released annually from the target pit and the helium vessel, respectively. Note that the BDF target complex will be equipped with standard ventilation-monitoring stations to measure short-lived radioactive gases online, taking samples of aerosol-bound radioactivity and enabling tritium sampling (the two latter categories are analysed in a laboratory).

Several different residential groups and an agricultural group were taken as representative for airborne exposure. The locations of the reference groups relative to the source are shown in Fig. 9.13. The dose coefficients (in Sv/Bq), which have to be multiplied by the annual long-term releases (in Bq/yr) for each radionuclide to obtain the annual effective dose (in Sv/yr), are listed in Table 9.4 for each reference population group and each radionuclide. The release from the helium vessel was assumed to

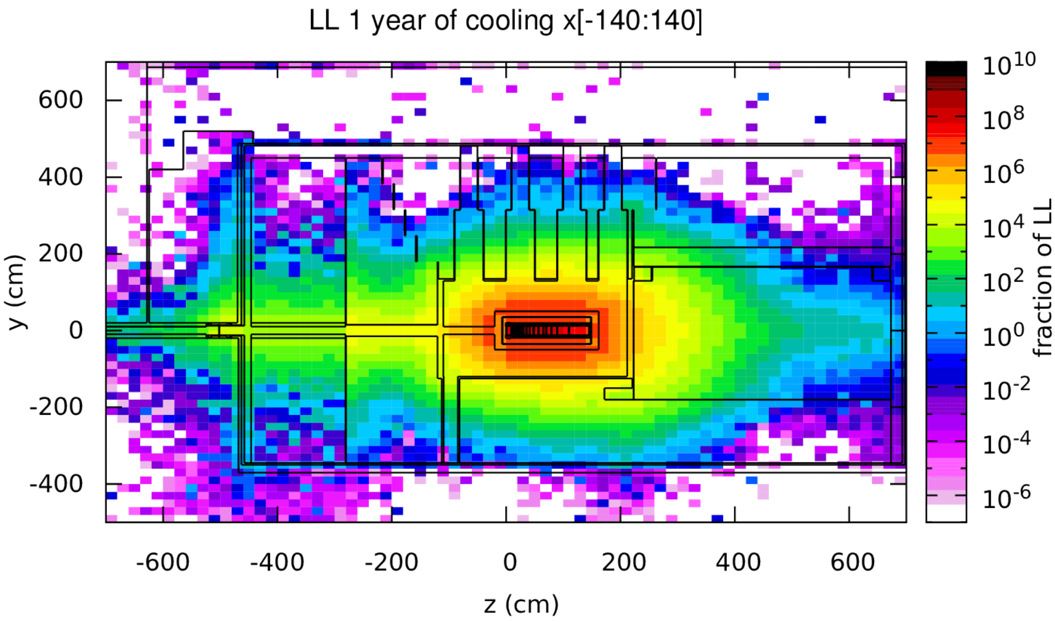

Fig. 9.12: Side view section through the beam line of residual activity, represented as a fraction of the Swiss LL.

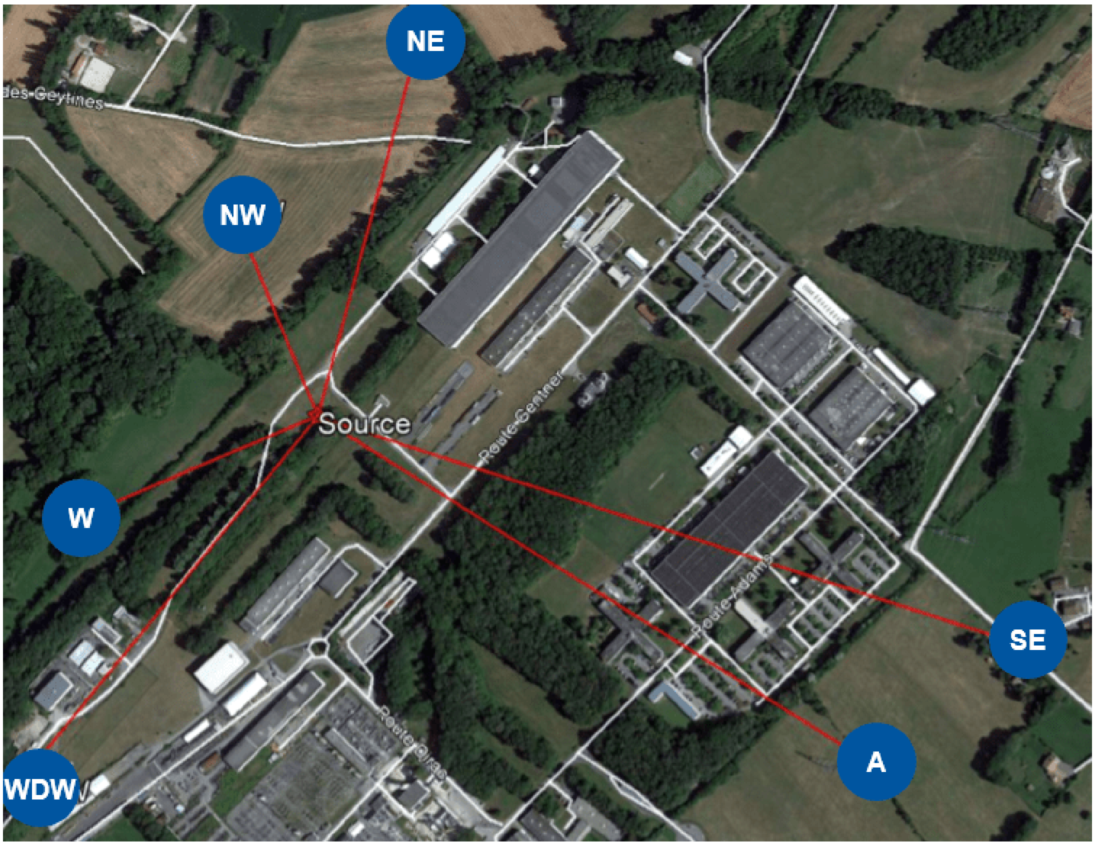

Fig. 9.13: Locations of the reference groups around the CERN site

happen once at the end of a yearly run, and thus the dose coefficients in Table 9.4 have been multiplied by a factor of 20 to take into account short-term effects. The greatest effective doses to the residential

Table 9.3: Annual releases from the target pit around the He vessel

Radioisotope	Activity flushed from target pit (Bq/yr)	Activity flushed from helium vessel (Bq/yr)
H-3	5.5×10^{4}	1.44×10^{9}
Be-7	9.0×10^{5}	1.46×10^{6}
Be-10	1.5×10^{-1}	3.57×10^{-1}
C-11	3.9×10^{9}	2.77×10^{6}
C-14	9.4×10^{3}	2.66×10^{4}
N-13	1.8×10^{10}	7.81×10^{6}
O-14	7.5×10^{8}	1.29×10^{5}
O-15	2.0×10^{10}	3.60×10^{6}
O-19	2.0×10^{6}	1.02×10^{3}
F-18	2.0×10^{5}	1.39×10^{3}
Ne-23	3.2×10^{6}	1.06×10^{3}
Ne-24	7.9×10^{5}	4.60×10^{2}
Na-22	2.4×10^{1}	9.44×10^{1}
Na-24	3.3×10^{4}	1.51×10^{3}
Na-25	5.9×10^{6}	1.73×10^{3}
Mg-27	5.0×10^{6}	2.70×10^{3}
Mg-28	1.2×10^{4}	8.41×10^{2}
Al-26	6.6×10^{-5}	2.10×10^{-4}
Al-28	4.0×10^{7}	7.89×10^{3}
Al-29	1.4×10^{7}	5.01×10^{3}
Si-31	1.7×10^{6}	8.91×10^{3}
Si-32	5.3×10^{-1}	1.57
P-30	1.6×10^{7}	2.86×10^{3}
P-32	3.7×10^{4}	2.17×10^{4}
P-33	2.2×10^{4}	2.13×10^{4}
P-35	2.6×10^{7}	4.15×10^{3}
S-35	1.3×10^{4}	2.22×10^{4}
S-37	5.7×10^{7}	1.35×10^{4}
S-38	6.2×10^{5}	4.01×10^{3}
Cl-34	1.2×10^{6}	1.19×10^{3}
Cl-36	1.7×10^{-2}	3.83×10^{-2}
Cl-38	3.6×10^{7}	3.94×10^{4}
Cl-39	6.8×10^{7}	1.12×10^{5}
Cl-40	1.4×10^{8}	1.82×10^{4}
Ar-37	6.2×10^{4}	6.67×10^{4}
Ar-39	1.4×10^{2}	3.08×10^{2}
Ar-41	5.4×10^{8}	1.70×10^{6}
K-38	3.1×10^{4}	8.54
K-40	4.3×10^{-9}	1.19×10^{-8}

reference groups were reached for the NW group for all sources. To simplify the presentation, only the effective doses for this group and for the agricultural group will be presented. These are listed for each radionuclide and each group in Table 9.5.

One can conclude that the maximum effective dose for the NW group is about 9.8 nSv/yr. The maximum effective dose to the agricultural group is only about 5.3 nSv/yr. Such doses are sufficiently low that they will not contribute significantly to the total dose received by any member of the public due to operation of all facilities on the Prévessin site (TT20, TT26, EHN1, NA62, etc.), the new facilities included. CERN aims to keep this dose below a dose objective of 10 µSv/yr. Considerably exceeding the latter would require optimization of the facilities. With the BDF in operation, this will not be the case. In our experience, those radionuclides which stick to aerosols are very efficiently removed by HEPA filters. Hence, radionuclides such as ^{7}Be, ^{22,24}Na, ^{32,33}P, and ^{35}S could be released with activities a few orders of magnitude lower than those calculated.

The environmental impact of releases of water was studied in detail (see Section 9.4.3). The tritium

Table 9.4: Dose coefficients (Sv/Bq) for the different groups. A, agricultural group.

Radioisotope	WDW	NE	NW	W	SE	A
H-3	2.54×10^{-20}	9.66×10^{-20}	1.64×10^{-19}	1.55×10^{-19}	3.31×10^{-20}	8.40×10^{-20}
Be-7	1.04×10^{-17}	3.21×10^{-17}	5.46×10^{-17}	5.18×10^{-17}	1.10×10^{-17}	2.23×10^{-19}
B-10	5.84×10^{-17}	2.35×10^{-16}	3.99×10^{-16}	3.78×10^{-16}	8.05×10^{-17}	3.16×10^{-17}
C-11	2.14×10^{-20}	8.74×10^{-20}	1.53×10^{-19}	1.46×10^{-19}	2.59×10^{-20}	0.00
C-14	2.83×10^{-18}	1.39×10^{-17}	2.35×10^{-17}	2.23×10^{-17}	4.75×10^{-18}	5.83×10^{-17}
N-13	1.18×10^{-20}	5.33×10^{-20}	9.59×10^{-20}	9.12×10^{-20}	1.28×10^{-20}	0.00
O-14	2.56×10^{-21}	1.33×10^{-20}	3.65×10^{-20}	2.90×10^{-20}	3.54×10^{-22}	0.00
O-15	1.55×10^{-21}	1.10×10^{-20}	2.18×10^{-20}	1.90×10^{-20}	5.20×10^{-22}	0.00
O-19	5.50×10^{-23}	6.37×10^{-22}	3.59×10^{-21}	1.77×10^{-21}	5.79×10^{-24}	0.00
F-18	3.67×10^{-19}	1.26×10^{-18}	2.17×10^{-18}	2.07×10^{-18}	4.08×10^{-19}	6.13×10^{-24}
Ne-23	2.48×10^{-23}	2.89×10^{-22}	8.58×10^{-22}	7.10×10^{-22}	1.39×10^{-24}	0.00
Ne-24	1.78×10^{-21}	1.08×10^{-20}	2.07×10^{-20}	1.94×10^{-20}	1.10×10^{-21}	0.00
Na-22	4.38×10^{-15}	1.35×10^{-14}	2.30×10^{-14}	2.18×10^{-14}	4.64×10^{-15}	3.14×10^{-14}
Na-24	9.49×10^{-18}	3.03×10^{-17}	5.16×10^{-17}	4.89×10^{-17}	1.03×10^{-17}	2.26×10^{-17}
Na-25	1.94×10^{-22}	1.51×10^{-21}	4.25×10^{-21}	3.61×10^{-21}	2.60×10^{-23}	0.00
Mg-27	2.98×10^{-19}	1.31×10^{-18}	2.06×10^{-18}	2.20×10^{-18}	2.63×10^{-19}	0.00
Mg-28	7.53×10^{-18}	3.10×10^{-17}	5.27×10^{-17}	5.00×10^{-17}	1.05×10^{-17}	1.30×10^{-16}
Al-26	5.32×10^{-14}	1.61×10^{-13}	2.73×10^{-13}	2.59×10^{-13}	5.51×10^{-14}	1.68×10^{-16}
Al-28	6.13×10^{-20}	7.41×10^{-19}	8.11×10^{-19}	9.42×10^{-19}	3.24×10^{-20}	0.00
Al-29	1.72×10^{-20}	8.88×10^{-20}	1.44×10^{-19}	1.47×10^{-19}	1.59×10^{-20}	0.00
Si-31	1.01×10^{-19}	5.28×10^{-19}	9.08×10^{-19}	8.66×10^{-19}	1.71×10^{-19}	2.30×10^{-23}
Si-32	1.56×10^{-16}	4.99×10^{-16}	8.46×10^{-16}	8.02×10^{-16}	1.71×10^{-16}	1.47×10^{-17}
P-30	6.03×10^{-21}	3.85×10^{-20}	5.65×10^{-20}	5.51×10^{-20}	2.14×10^{-21}	0.00
P-32	5.02×10^{-18}	8.10×10^{-17}	1.38×10^{-16}	1.30×10^{-16}	2.77×10^{-17}	4.96×10^{-15}
P-33	2.12×10^{-18}	1.31×10^{-17}	2.22×10^{-17}	2.10×10^{-17}	4.47×10^{-18}	6.32×10^{-16}
P-35	3.26×10^{-20}	3.05×10^{-19}	3.27×10^{-19}	3.55×10^{-19}	1.78×10^{-21}	0.00
S-35	1.99×10^{-18}	1.16×10^{-17}	1.97×10^{-17}	1.87×10^{-17}	3.97×10^{-18}	3.65×10^{-16}
S-37	2.19×10^{-20}	1.10×10^{-19}	1.80×10^{-19}	1.84×10^{-19}	1.75×10^{-20}	0.00
S-38	1.10×10^{-18}	4.22×10^{-18}	7.23×10^{-18}	6.89×10^{-18}	1.39×10^{-18}	1.55×10^{-20}
Cl-34	2.06×10^{-19}	8.13×10^{-19}	1.41×10^{-18}	1.38×10^{-18}	2.38×10^{-19}	9.63×10^{-33}
Cl-36	2.48×10^{-17}	1.08×10^{-14}	1.84×10^{-14}	1.74×10^{-14}	3.70×10^{-15}	5.00×10^{-13}
Cl-38	1.74×10^{-19}	6.99×10^{-19}	1.22×10^{-18}	1.18×10^{-18}	2.08×10^{-19}	1.04×10^{-30}
Cl-39	2.49×10^{-19}	9.22×10^{-19}	1.60×10^{-18}	1.53×10^{-18}	2.86×10^{-19}	7.85×10^{-27}
Cl-40	3.47×10^{-21}	2.31×10^{-20}	5.12×10^{-20}	4.27×10^{-20}	9.10×10^{-22}	0.00
Ar-37	6.77×10^{-26}	2.04×10^{-25}	3.47×10^{-25}	3.29×10^{-25}	7.00×10^{-26}	0.00
Ar-39	2.57×10^{-22}	7.75×10^{-22}	1.32×10^{-21}	1.25×10^{-21}	2.66×10^{-22}	0.00
Ar-41	4.47×10^{-20}	1.51×10^{-19}	2.40×10^{-19}	2.27×10^{-19}	5.68×10^{-20}	0.00
K-38	1.10×10^{-19}	4.92×10^{-19}	7.64×10^{-19}	8.13×10^{-19}	9.09×10^{-20}	0.00
K-40	3.18×10^{-15}	2.44×10^{-14}	4.14×10^{-14}	3.92×10^{-14}	8.34×10^{-15}	2.06×10^{-13}

activity concentration of 0.3 GBq/l at the end of each operational year is too high for rapid discharge of water from a sump into the receiving river Le Lion, because the emission limit for water accessible to the public could be exceeded. A new evaporator was therefore included in the design of the BDF to evaporate the water slowly into the atmosphere, benefiting from long-term variations in the wind direction. The dosimetric impact of a similar facility was studied in the past [6]. Several hypothetical population groups were examined, and a maximum effective dose per becquerel of released activity of 1.64×10^{-19} Sv/Bq was obtained [6]. The annual release of 280 GBq of tritium would result in an effective dose of less than 50 nSv/yr. This value is far below the dose constraint of 10 μSv/yr fixed by the Organization for new facilities.

Table 9.5: Effective doses (Sv/yr) for the NW and agricultural reference groups

Radioisotope	NW	A
H-3	4.73379×10^{-9}	2.42462×10^{-9}
Be-7	1.64454×10^{-9}	6.71669×10^{-12}
Be-10	2.9091×10^{-15}	2.30395×10^{-16}
C-11	6.10442×10^{-10}	0
C-14	1.27261×10^{-11}	3.15714×10^{-11}
N-13	1.79319×10^{-9}	0
O-14	2.73733×10^{-11}	0
O-15	4.48658×10^{-10}	0
O-19	7.182×10^{-15}	0
F-18	4.96779×10^{-13}	1.40334×10^{-18}
Ne-23	2.76003×10^{-15}	0
Ne-24	1.65388×10^{-14}	0
Na-22	4.39769×10^{-11}	6.0038×10^{-11}
Na-24	3.25718×10^{-12}	1.42659×10^{-12}
Na-25	2.53092×10^{-14}	0
Mg-27	1.03207×10^{-11}	0
Mg-28	1.4961×10^{-12}	3.69057×10^{-12}
Al-26	1.16683×10^{-15}	7.18052×10^{-19}
Al-28	3.22696×10^{-11}	0
Al-29	2.02626×10^{-12}	0
Si-31	1.74293×10^{-12}	4.41491×10^{-17}
Si-32	2.70759×10^{-14}	4.70469×10^{-16}
P-30	9.3639×10^{-13}	0
P-32	6.49838×10^{-11}	2.33565×10^{-9}
P-33	9.95586×10^{-12}	2.83428×10^{-10}
P-35	8.69143×10^{-12}	0
S-35	9.02045×10^{-12}	1.6713×10^{-10}
S-37	1.02981×10^{-11}	0
S-38	5.07684×10^{-12}	1.0884×10^{-14}
Cl-34	1.78834×10^{-12}	1.2214×10^{-26}
Cl-36	1.44043×10^{-14}	3.91422×10^{-13}
Cl-38	4.53519×10^{-11}	3.86606×10^{-23}
Cl-39	1.12714×10^{-10}	5.53001×10^{-19}
Cl-40	7.20983×10^{-12}	0
Ar-37	4.84585×10^{-19}	0
Ar-39	8.3041×10^{-18}	0
Ar-41	1.37001×10^{-10}	0
K-38	2.39231×10^{-14}	0
K-40	1.00467×10^{-20}	4.9991×10^{-20}
Total	9.78×10^{-9}	5.31×10^{-9}

9.6 Experimental area

9.6.1 Prompt radiation and shielding requirements

Similarly to the target complex, no access will be permitted to the underground experimental hall during beam operation. Furthermore, no access during operation is required to the above-ground access building for the experimental hall (in the surface hall building). The prompt dose rates were investigated to illustrate the effectiveness of the active muon shield and to provide information for a further risk analysis. Figures 9.14 and 9.15 present different views of the distributions of the prompt dose rate in the underground experimental hall from all particles and for muons and neutrons. They demonstrate that the muons are swept away from the beam line by the active muon shield and retain their direction owing to the small amount of large-angle scattering behind the muon shield, while the neutrons show a relatively direction-independent shape. The dose rates reach a few millisieverts per hour on the side of the experimental hall behind the muon shield and drop below 1 mSv/h in the surrounding soil. The level of soil activation is considered acceptable, particularly so because the dose rates are dominated by muons. The side view of the experimental hall illustrates that the muons are also bent towards the top of the experimental hall. Thanks to the 1 m concrete shielding between the experimental hall and the surface hall, only a few microsieverts per hour are reached in the surface hall. The latter could in principle be classified as a Supervised Radiation Area; since there is no need, however, for personnel in this area during beam operation, no permanent radiation monitoring is foreseen for this area.

9.6.2 Muon flux in surrounding areas

The prompt radiation at ground level above the underground experimental hall was analysed to define the dose rates next to the surface hall building, which covers only the first 100 m of the underground experimental hall. Figure 9.16 presents the above-ground prompt dose rates in the area of the experimental hall. It shows that the highest dose rates are reached behind the surface hall building, amounting to a few microsieverts per hour up to approximately 30 m behind and 5 m beside the experimental hall. This area will be fenced off and covered with 6 m of soil from the excavations, such that the dose rates will be further reduced to a level allowing for a non-designated area (<0.5 μSv/h).

Figure 9.17 shows the expected prompt dose rates in the ground and the experimental facilities surrounding the SHiP facility. It demonstrates that the existing beam lines TT81, TT82, and TT83 are not affected by the prompt dose rates originating from the SHiP facility. Note that any excavation of soil downstream of the underground experimental hall is forbidden.

The SHiP operation also does not influence the present area classification of the EHN1 experimental hall, which corresponds to a permanently occupied Supervised Radiation Area (<3 μSv/h). It should be borne in mind that the results given are conservative estimates because a moraine density 20% lower than the measured value was assumed. The operation of the SHiP facility as designed should not therefore have any impact on the surrounding experimental areas. According to CERN's radiation protection code F [5], if the total annual effective dose from all CERN facilities to any member of the public remains below 10 μSv/yr, the exposure does not require any justification and the facilities are considered as optimized. In SHiP, the effective dose to members of the public is expected to be dominated by stray radiation from muons (see Fig. 9.18), which means prompt radiation that still penetrates outside the shielded zones to the environment and beyond the fenced areas of CERN. The prompt radiation outside the fenced CERN site, and thus the publicly accessible area, was envisaged to stay below 5 μSv/yr. The latter condition is fulfilled for SHiP, as can be seen from Fig. 9.18. A standard stray-radiation monitor for photons, muons, and neutrons should be installed at the fence closest to the most exposed area.

9.6.3 Residual dose rate

Assuming 5 yr of operation, the residual dose rates in the SHiP target bunker are expected to be on the order of a few microsieverts per hour in contact with the first part of the active muon shield after 4 h hours of cooling (see Fig. 9.19), thus allowing access to this area. The experimental hall up to the active muon shield will be classified as Simple Controlled, while the rest will be classified as a Supervised Radiation Area.

9.7 Tritium out-diffusion

As discussed in Section 9.4.3, most of the tritium (≈95%) produced at the BDF will be contained in the target (≈18 TBq). Because of high volatility of tritium, releases of tritium from the target are expected (out-diffusion) into the target cooling water during operation and into the air during shutdowns and after target decommissioning. Tritium can also outgas from the iron and concrete shielding into the helium and air environment. Even if tritium releases have a negligible dosimetric impact, they may have a negative public relations impact. Based on the available literature, mostly from fusion facilities and nuclear power plants, tritium diffusion coefficients for the BDF materials in the operational temperature range are available, but have considerable uncertainty. The fraction of tritium released to the water circuit and by out-diffusion into the air during storage will need an experimental evaluation to assess how to meet all safety requirements for the new facility without consistent oversizing. For this reason, during the beam test of the BDF target prototype, several samples of the materials that compose the target (TZM, W, and Ta) and that will be used in the facility (concrete, iron, stainless steel, and aluminium) were placed on the side of the target prototype (see Fig. 9.20) to be irradiated under conditions similar to those of the future BDF target. The dose rates for those samples are shown in Table 9.6.

Table 9.6: Dose rates for samples used for the tritium out-diffusion measurements. The cooling time was 2 months except for concrete and aluminium, for which it was 1 week.

Material	Dose rate at 40 cm (μSv/h)
Concrete	2.5
Aluminium	6.5
Cast iron	35
SS316	18
TZM	25
W	18
Ta	200

To measure the tritium out-diffusion, the samples have been placed in a container connected to a bubbler (MARC 7000; see Fig. 9.21), which circulates air through the container. The air flow passes through flasks filled with water to capture the tritium released. The flasks are analysed by liquid scintillation to quantify the release. Another measurement method that has been employed is immersion in water to measure out-diffusion in a different environment. These measurements will benchmark an out-diffusion plug-in for FLUKA and, for the first time, furnish tritium out-diffusion rates which can be used at CERN.

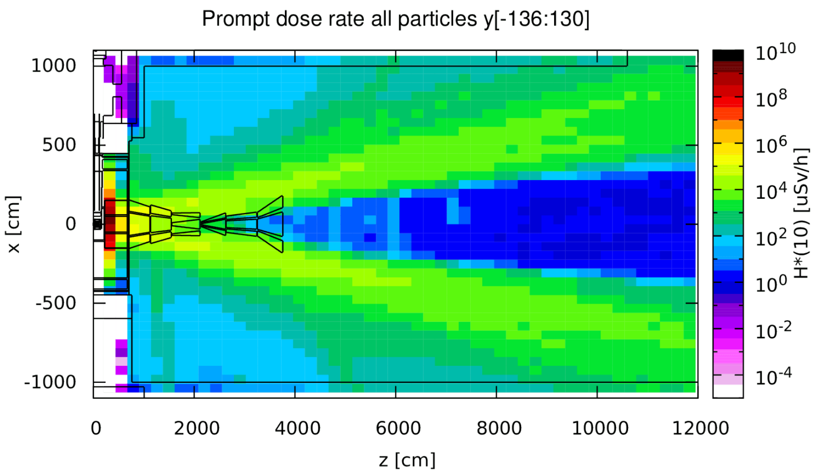

(a)

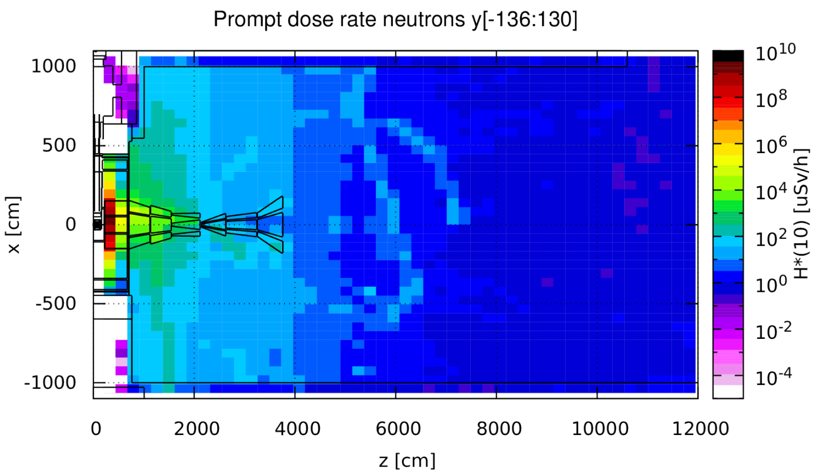

(b)

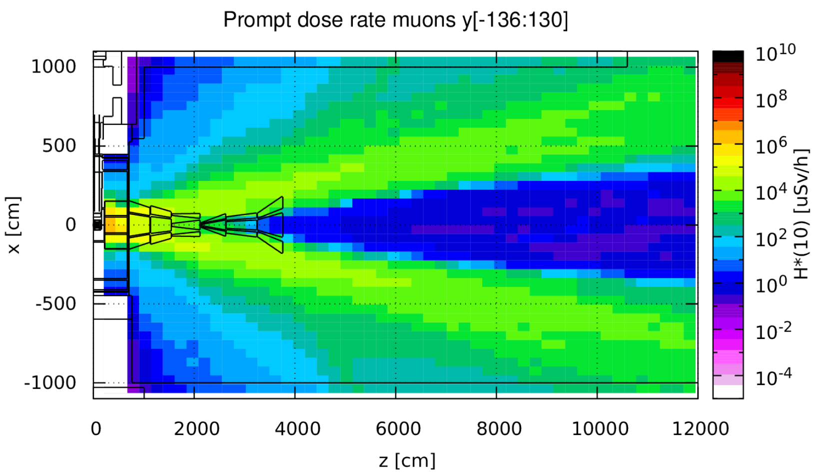

(c)

Fig. 9.14: Top view of prompt dose rates in microsieverts per hour in the experimental cavern for all particles (a), neutrons only (b), and muons only (c).

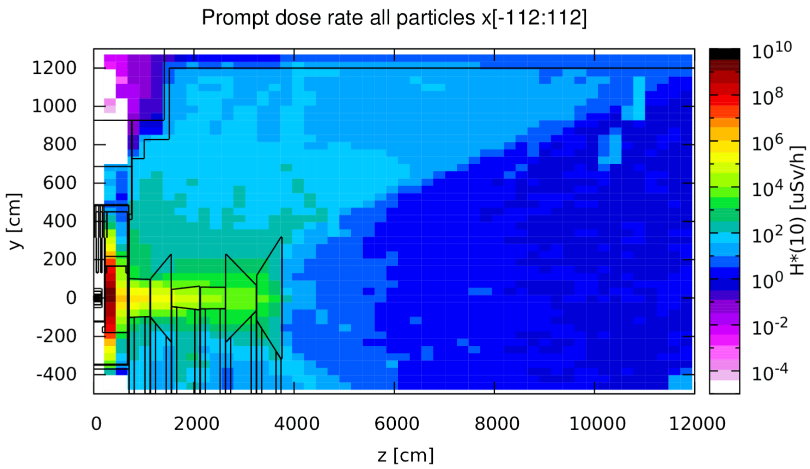

(a)

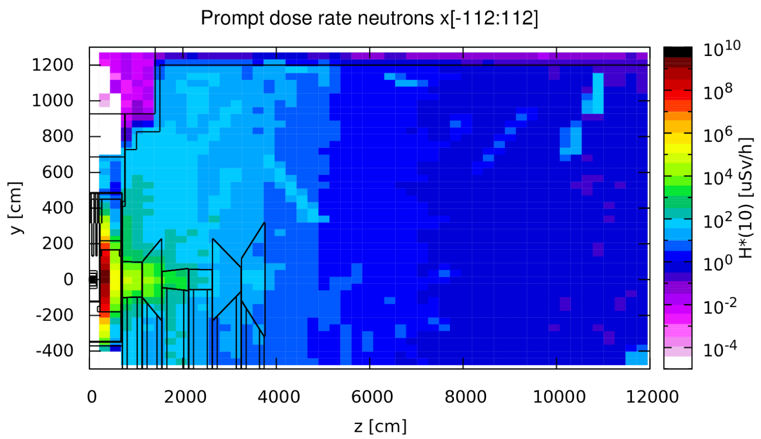

(b)

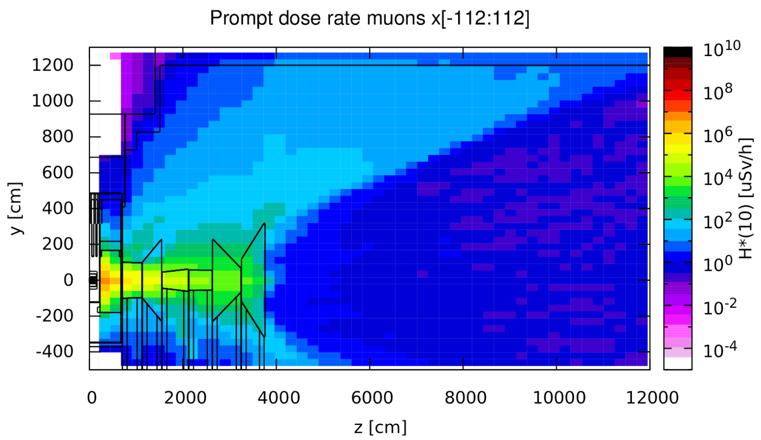

(c)

Fig. 9.15: Lateral view of prompt dose rates in microsieverts per hour in the experimental cavern for all particles (a), neutrons only (b), and muons only (c).

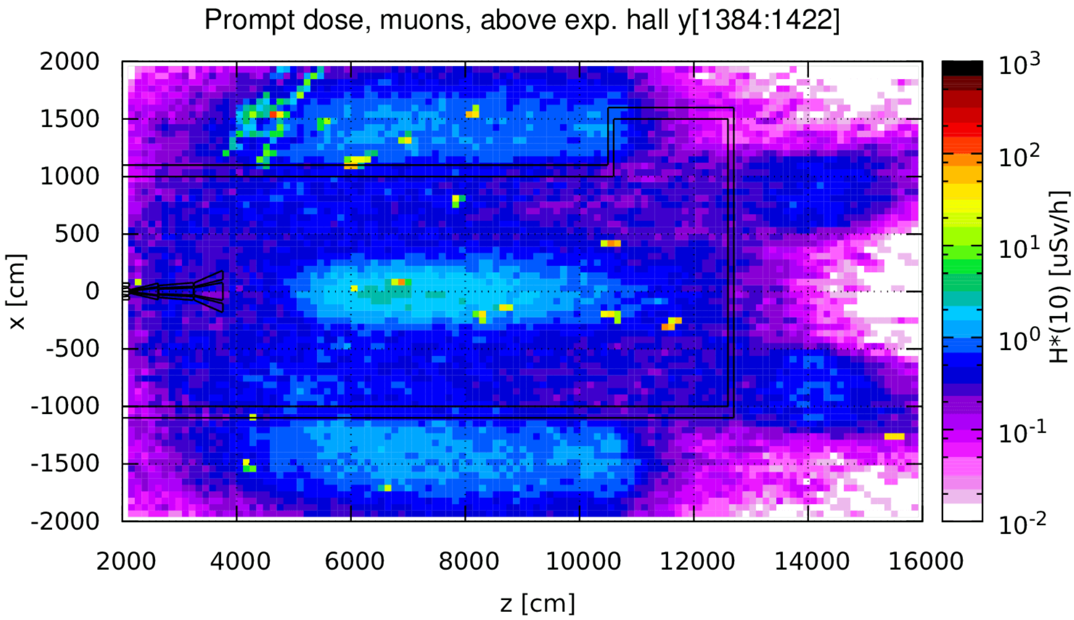

Fig. 9.16: Muon flux in microsieverts per hour at ground level in surface hall

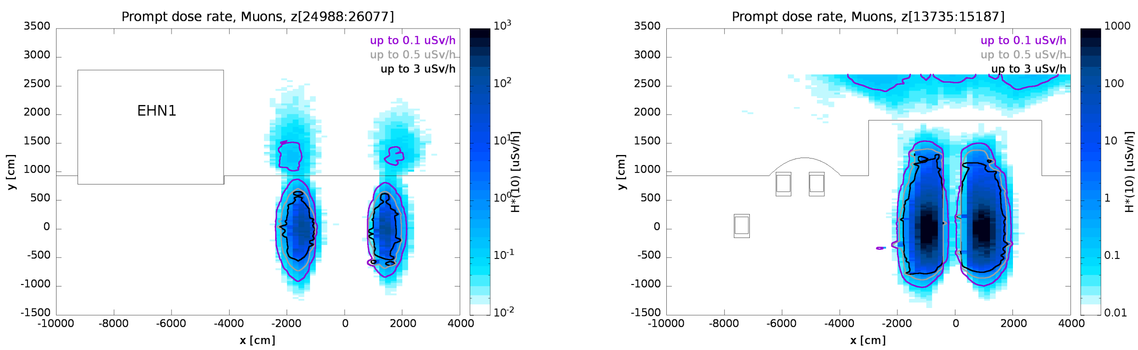

(a) **(b)**

Fig. 9.17: Muon flux in microsieverts per hour in the proximity of EHN1 (a) and tunnels TT81, TT82, and TT83 (b).

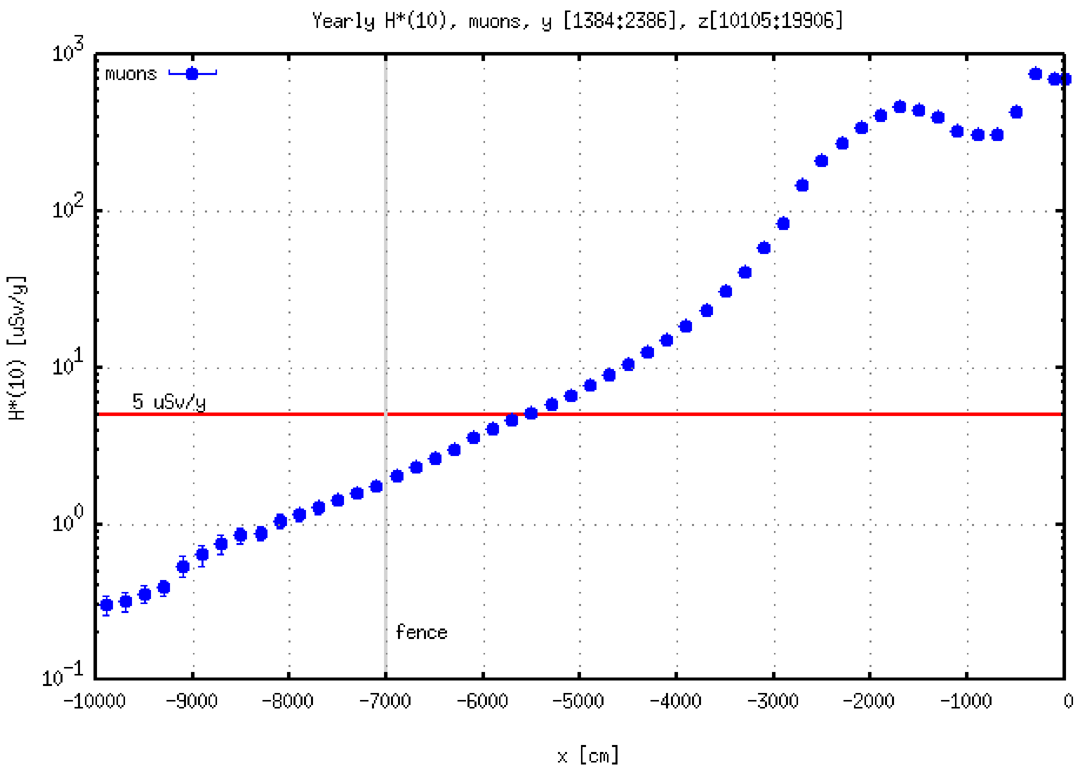

Fig. 9.18: Muon prompt dose rates in µSv/yr at the CERN fence. The histogram was averaged over the most critical area 1384 < y < 2386 and 10105 < z < 19906. The contribution from neutrons was furthermore estimated to be below 1 µSv/yr.

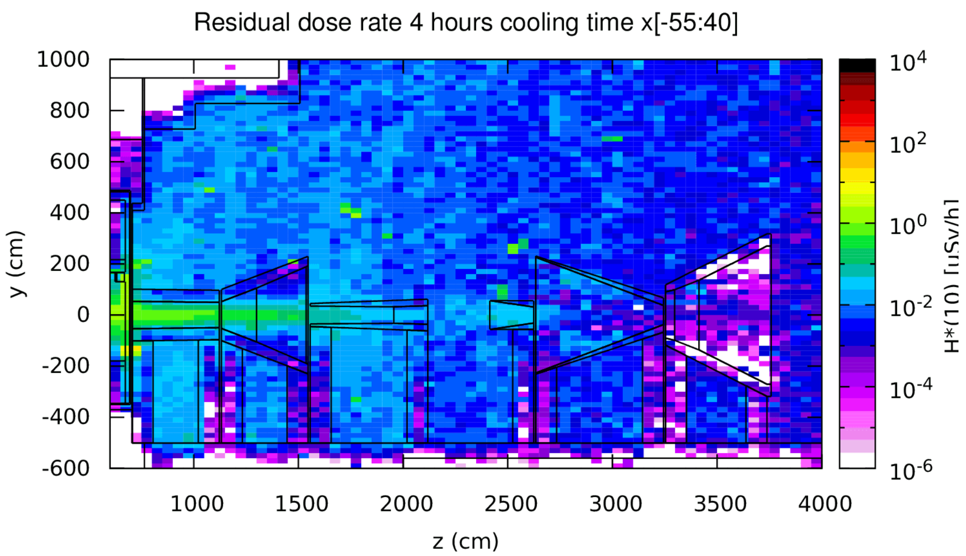

Fig. 9.19: Residual ambient dose equivalent rate in microsieverts per hour for the active muon shield after 5 yr of operation and 4 h of cooling time.

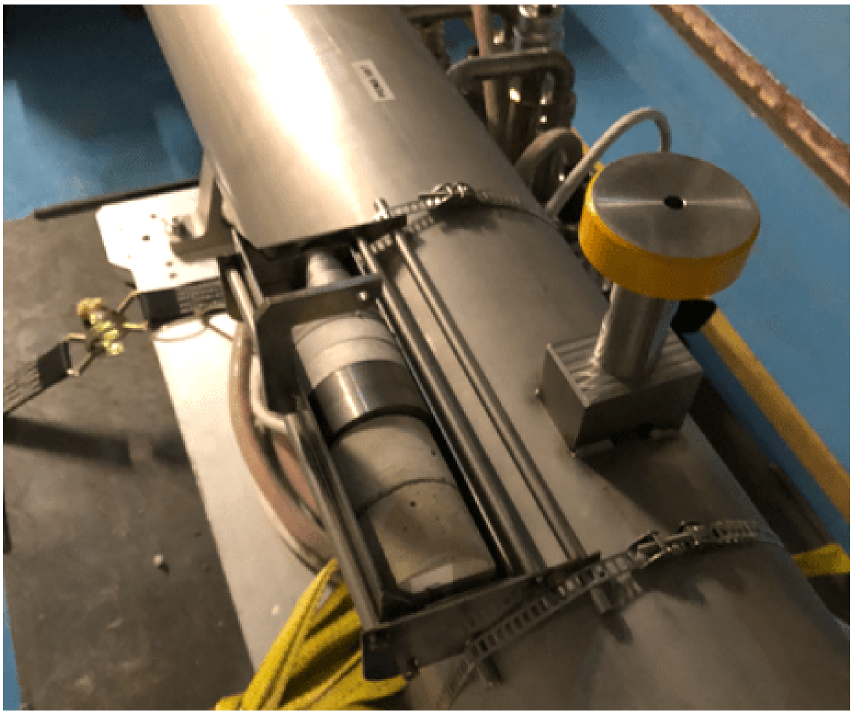

Fig. 9.20: Location of samples around the BDF target prototype

Fig. 9.21: Bubbler (left); box hosting sample, where air is recirculated (centre); lead shielding for samples (right).

References

[1] A. Ferrari et al. *FLUKA: A Multi-particle Transport Code (Program Version 2005)*. CERN Yellow Reports: Monographs. Geneva: CERN, 2005. URL: https://cds.cern.ch/record/898301.

[2] G. Battistoni et al. "Overview of the FLUKA code". In: *Ann. Nucl. Energy* 82 (2015). Joint International Conference on Supercomputing in Nuclear Applications and Monte Carlo 2013, SNA + MC 2013. Pluri- and Trans-disciplinarity, Towards New Modeling and Numerical Simulation Paradigms, pp. 10–18. ISSN: 0306-4549. DOI: https://doi.org/10.1016/j.anucene.2014.11.007. URL: http://www.sciencedirect.com/science/article/pii/S0306454914005878.

[3] Office federal de la santé publique (OFSP). *Ordonnance du 26 avril 2017 sur la radioprotection (ORaP)*. 2017. URL: https://www.admin.ch/opc/fr/classified-compilation/20163016/index.html.

[4] M. Anelli et al. *A Facility to Search for Hidden Particles (SHiP) at the CERN SPS*. Tech. rep. CERN-SPSC-2015-016, SPSC-P-350. CERN, 2015. arXiv: 1504.04956 [physics.ins-det].

[5] D. Forkel-Wirth et al. "Radiation protection at CERN". In: *CAS–CERN Accelerator School: Course on High Power Hadron Machines, 24 May–2 Jun 2011* (Bilbao, Spain). Mar. 2013. eprint: arXiv:1303.6519. URL: http://cds.cern.ch/record/1533023.

[6] P. Vojtyla, C. Strabel and H. Vincke. *CENF Radiological Environmental Considerations*. Tech. rep. EDMS 1427092, CERN (2015).

Chapter 10

Safety engineering

10.1 Introduction

In all of the technical considerations for a facility such as the BDF, it is essential to consider safety and environmental protection as an integral part of the comprehensive design, taking conscious decisions early on to eliminate or significantly reduce potential hazards, in a cost-effective, pragmatic manner.

10.2 Legal context of CERN

By virtue of its intergovernmental status, CERN is entitled to adopt its own internal organizational rules, which prevail over national laws, to facilitate the execution of its mission. In the absence of specific CERN regulations, the laws and regulations of the Host States generally prevail.

In response to its unique geographical situation (straddling the Swiss–French border without discontinuity) and its highly specific technical needs, the Organization stipulates its own safety policy, in the frame of which it establishes and updates rules aimed at ensuring uniform safety conditions across its sites. CERN's safety rules apply to the Organization's activities, as well as to persons participating in CERN's activities or present on its site.

When establishing its own safety rules, CERN takes into account the laws and regulations of the Host States, EU regulations and directives, and international regulations, standards, and directives; as a general principle, CERN aligns with these as much as reasonably possible. Where such compliance is not possible or desirable owing to technical or organizational constraints, such as for equipment and facilities not covered by normal standards, specific clearance from CERN's HSE Unit based on a risk assessment and compensatory measures is required.

10.3 Occupational Health and Safety

CERN's Safety Policy, in order of priority, sets out to protect all persons affected by its activities, to limit the impact of the Organization's activities on the environment, and to protect its equipment and ensure continuity of operations. The agreed safety objectives for the BDF project are shown in Table 10.1.

10.4 Hazard identification study for BDF TTC

A specific hazard identification study for the BDF target and target complex was presented in Section 6.6. The objective of the hazard identification study was to identify as early as possible the principal failure scenarios leading to critical accident situations, as well as the consequences, and to define essential mitigation measures or redesigns.

10.5 Fire safety

The goal of fire safety at CERN is to protect occupants, rescuers, the external population, the environment, the facility itself, and continuity of operation. To this end, all buildings, experimental facilities, equipment, and experiments installed at CERN should comply with CERN Safety Code E. In view of the special nature of the use of certain areas, in particular underground area, with increased fire risk, the HSE Unit is to be considered the authority for approving and stipulating special provisions.

As the project moves to the Technical Design Report stage, when layouts and interconnecting ventilation systems will be finalized, detailed fire risk assessments will have to be done for all areas of

Table 10.1: Agreed safety objectives for the BDF project

	A: Life safety	B: Environmental protection	C: Property protection	D: Continuity of operation
1	Safe evacuation of uninjured occupants	Limited release of pollutants to air	Continuity of essential services	Limit downtime
2	Safe evacuation or stabilization of injured occupants	Limited release of pollutants to water	Incident should not cause further incidents	
3	Safe intervention of rescue teams		Limit property loss	

the BDF complex, i.e. the extraction tunnel, target complex, and experimental hall. At this stage, a general fire safety strategy has been produced, based on the location and current level of design, along with the latest fire safety strategies employed at CERN. The complex will be considered as an extension of the fire concept developed for the whole of the North Area [1].

The most efficient protection strategy is one that uses multilevel ‘safety barriers’, with a bottom-up structure, to limit fires at the earliest stages with the lowest consequences, thus considerably limiting the probability and impact of the largest events.

To ensure that large adverse events are possible only in very unlikely cases of failure of many barriers, measures at every possible level of functional design need to be implemented:

– in the conception of every piece of equipment (e.g. materials used in electrical components, circuit breakers, etc.);
– in the grouping of equipment in racks or boxes (e.g. generous cooling of racks, use of fire-retardant cables, and fire detection with power cut-off within each rack);
– in the creation and organization of internal rooms (e.g. fire detection, power cut-off, and fire suppression inside rooms with equipment);
– in the definition of fire compartments;
– in the definition of firefighting measures.

The key concepts of the fire safety strategy can be split into compartmentalization, fire detection, smoke extraction, and fire suppression, as set out below.

10.5.1 Compartmentalization

Compartmentalization impedes the propagation of fire and potentially activated smoke through a facility, allowing occupants to escape to a comparatively safe area much more quickly than otherwise, as well as facilitating the effective fighting of the fire, and the evacuation of victims by the Fire Brigade. In the North Area fire concept, the following requirements have been set:

– all ventilation doors must be EI90 fire doors;
– communicating galleries must be isolated with EI90 fire doors;
– neighbouring surface facilities must be isolated with EI120 fire doors;

– compartments longer than 450 m must be avoided;
– normally open fire doors must be equipped with a remote action release mechanism, monitoring position, and self-action thermal fuse.

10.5.1.1 *Extraction tunnel*

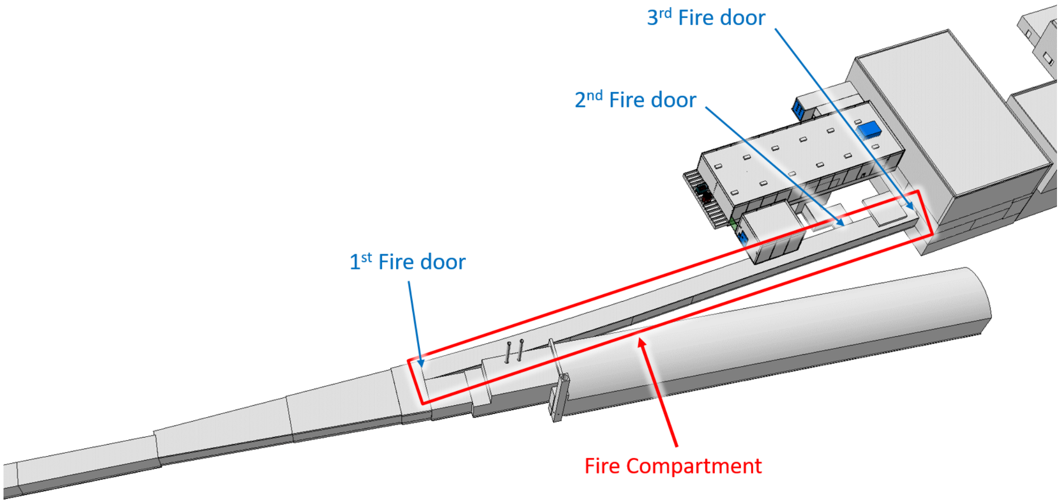

Fig. 10.1: Compartmentalization in the BDF extraction tunnel

The new extraction tunnel will be considered as one single fire compartment, requiring three fire doors (as shown in Fig. 10.1). The fire doors will follow the standard requirements for the North Area fire concept: 0.9 m minimum width, with fire doors EI90 or greater. They will be set to a normally closed configuration, owing to the ventilation specification and needs of the extraction tunnel. The door separating the extraction tunnel from the SPS will be EI120.

10.5.1.2 *Extraction tunnel*

The following areas will be divided into separate fire compartments (shown in Fig. 10.2):

– auxiliary building;
– access building;
– target building;
– lower target building;
– surface hall;
– experimental hall.

Note that both the experimental hall and the lower target building will be separate compartments from the corresponding surface hall and target building, accounting for the differing uses of the spaces. The lower target building will also be divided into several separate fire compartments, corresponding to the pressure cascades implemented for radiation containment.

10.5.2 Fire detection

An early fire detection system, integrated into the safety action system, is a crucial component of the North Area fire strategy. Early detection is such that allows evacuation (last occupant out) before un-tenable conditions are reached; the CERN HSE Unit Fire Safety team should be consulted about the design. The system must be capable of transmitting an alarm, along with a message containing safety

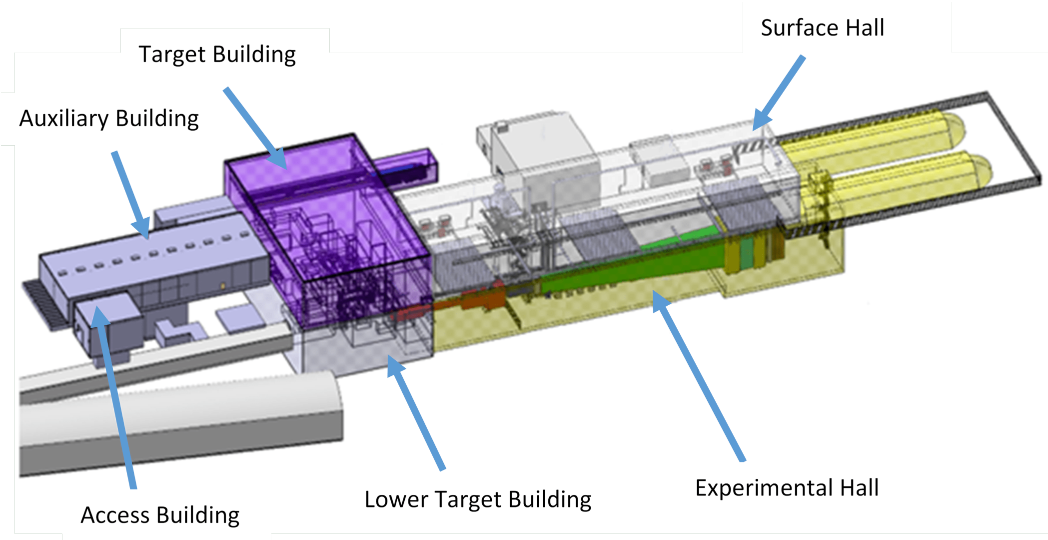

Fig. 10.2: Compartmentalization areas of the BDF complex

instructions, to occupants anywhere in the North Area. This alarm should be triggered upon fire detection, action on evacuation push buttons, CERN Fire Brigade action out of the CERN Fire Brigade SCR or the CCC, or Beam Imminent Warning situations. Evacuation push buttons should cover all premises. The fire detection and evacuation push buttons must also be integrated with safety actions such as compartmentalization, stopping of ventilation, and other machine functions according to a predefined fire protection logic. Fire detection encompasses the following actions:

- close all fire doors in the fire compartment of origin and the adjacent fire compartments;
- trigger an evacuation alarm in the fire compartment of origin and the adjacent fire compartments;
- stop free-cooling ventilation;
- broadcast an information message through the public address system;
- trigger a level 3 alarm in the CSAM system, which alerts the CERN Fire Brigade control room and results in crews being dispatched immediately.

10.5.3 Smoke extraction

One of the key findings from the North Area fire risk assessment was the need for careful risk assessment of the effects of smoke in the event of a fire in the underground and surface areas, taking into account both the safe evacuation of occupants and the effective intervention of the Fire Brigade to locate victims and prevent the further spread of fire. A build-up of smoke can also result in lasting damage to the sensitive and valuable equipment present, an effect that can be limited through extraction.

In accordance with CERN Safety Guideline SG-FS-0-0-2, premises with a surface area exceeding 2000 m^2 or with a length exceeding 60 m should be divided into smoke zones with a maximum surface area of 1600 m^2 and a maximum length of 60 m. The smoke curtains between smoke zones should be made out of a non-combustible material (B-s3, d0) with a fire resistance of at least $\frac{1}{4}$ h. The height of roof screens should be 25% of the average height of the building when this height is less than 8 m, or 2 m when the height of the building is more than 8 m. Depending on the specific requirements of the building design, these can be retractable, with automatic release on fire detection.

An additional consideration for fires in accelerator tunnels is the danger of potentially activated smoke, and the need to handle this in a controlled manner to limit the release of polluting agents to the environment. A fire assessment methodology that entails the radiological hazard induced by a fire event is currently under development by the FIRIA project, led by the HSE Unit. Many of the concepts featured in the FIRIA methodology have been incorporated into the safety support provided by the HSE Unit to the BDF project. However, once the FIRIA Methodology is fully available in July 2021, it is recommended to consider carrying out a FIRIA exercise as part of the Technical Design Report phase. A description of the FIRIA project is available in Ref. [2].

10.5.3.1 Extraction tunnel

The extraction tunnel will follow the strategy set out for the North Area, namely containment via both the automatic closing of any ‘normally open’ fire doors and the stopping of ventilation on fire detection. Potentially activated smoke will therefore remain in the fire compartment for assessment by the Radiation Protection (HSE-RP) group, who can then make a decision on the release delay, extraction flow rate, and options for smoke filtering or scrubbing to minimize the dose to the public, using a portable system of ducts and smoke extraction devices to remove the smoke as needed.

10.5.3.2 Auxiliary building

The auxiliary building is generally unclassified, with just two smaller radiation-classified zones, and controlled access to the extraction tunnel. The surface footprint is less than 2000 m^2, and no side is longer than 60 m. Natural smoke extraction is therefore appropriate, through the use of skydomes.

10.5.3.3 Lower target building

The lower target building will contain radioactive areas, with cascaded pressures to prevent the escape of activated material to areas with lower radiation classifications. In the absence of prescriptive codes for the design of smoke extraction strategies for such areas, the detailed design should be *performance based*, and done in conjunction with the HSE Unit Fire Safety team. Mechanical extraction is an intrinsic part of the design for this system, and the fire safety strategy will govern the logic behind the automatic actions on detection of a fire in a particular area. Where the air temperature in the compartment of origin of the fire is below 300°C (and so will not damage the extraction ducts), the strategy will be to immediately turn off the air supply to the compartment, while maintaining the air extraction. The strategy is to starve the fire of oxygen, choking it before significant quantities of smoke can be produced. In this way, the negative impacts of the fire can be minimized. Where the air temperature has already exceeded 300°C, both the air supply and air extraction will be turned off, and the containment actions will be extended to the surrounding fire compartments. For the Technical Design Report stage, further studies will be required in this area, in line with the FIRIA methodology.

10.5.3.4 Target building

The target building will be a separate fire compartment from the lower target building, but will not be sealed against smoke. A mechanical smoke extraction strategy will therefore be employed, in tandem with a central smoke curtain, which will divide the hall into two areas of less than 1600 m^2, ensuring compliance with the CERN safety guidelines.

10.5.3.5 Experimental hall

The experimental hall will use mechanical smoke extraction, with four smoke curtains dividing the hall into five sectors of less than 1600 m^2. As the experimental hall will be a Radiologically Classified Area, the strategy will be to contain any potentially activated smoke for assessment by the HSE-RP group, who can then make a decision on the release delay, extraction flow rate, and options for smoke filtering or scrubbing to minimize the dose to the public. The initial design details of this system are discussed in Chapter 9, and should be fine-tuned using computational fluid dynamics simulations and a performance-based design methodology as the project moves to the Technical Design Report stage.

10.5.3.6 Surface hall

The surface hall will be a separate fire compartment from the experimental hall below, and will have a lower radiological classification. A natural smoke extraction strategy is therefore currently foreseen, using skydomes, in tandem with smoke curtains. The arrangement of smoke curtains will be the same as that employed for the experimental hall, dividing the hall into five sectors of less than 1600 m^2.

10.5.4 Fire suppression

The CERN Fire Brigade need adequate means of fighting a fire on arrival, including a surface hydrant network, which will be provided as the project moves to the Technical Design Report stage, in tandem with the HSE Unit fire safety specialists.

10.5.4.1 Extraction tunnel, lower target building, experimental hall

Dry risers will be installed throughout the underground areas, allowing the CERN Fire Brigade to choose to supply water to them for firefighting as required. The additional fire loads and radiation risks present in the lower target building require the addition of a suppression system, to be specified in detail as the project moves into the Technical Design Report phase. A number of fire suppression solutions for such challenging environments are being considered at CERN, such as the delivery of fire suppression by remotely operated drones, which may be applied in this area.

10.5.5 Access safety

For the underground access, it must be ensured that the following are true.

- The lift and stairs are protected against fire, and not connected to the general electrical circuit (i.e. they can be used at any time).
- A safe area, with an overpressure relative to the surroundings, is available at the base of the lift (or another vertical egress path). The size of this area should be commensurate with the number of occupants, in addition to the time taken for evacuation, and should be determined as the project moves to the Technical Design Report stage.

For the extraction tunnel, it is important in addition that fire equipment and Fire Brigade vehicles (e.g. PEFRA, shown in Fig. 10.3) can move freely in and out of the lift and pass through the chicane immediately before the lift and stairs without any problem, especially during a rescue operation.

Fig. 10.3: The CERN Fire Brigade vehicle PEFRA

10.6 Safety of civil engineering structures

The installation of the BDF complex will involve a significant amount of civil engineering works, including tunnel modifications, numerous new buildings, and a challenging target complex. At CERN, all structures must be designed and manufactured according to the Eurocodes, accounting especially for local seismic action. Because of the estimated levels of radiation foreseen across the facility, along with environmental considerations, the control of water ingress and egress is of particular interest. It is important to note that this is not an exhaustive list of requirements, and that further analyses will be required as the project moves into the Technical Design Report stage.

10.6.1 Drainage

The objective of the design of underground drainage systems in areas subject to HSE-RP control or chemical contamination is to ensure that any water at risk of activation or contamination is collected and controlled before it can pass into the external drainage networks.

A preliminary study of the groundwater at the Prévessin site was performed during the Comprehensive Design Study phase to tackle the risk of radionuclide transfer into groundwater [3]. The aim of this study was to provide information on the present hydrological situation by means of collecting historical data and by performing new water level measurements in the area concerned, since the most recent previous data were taken in 2014.

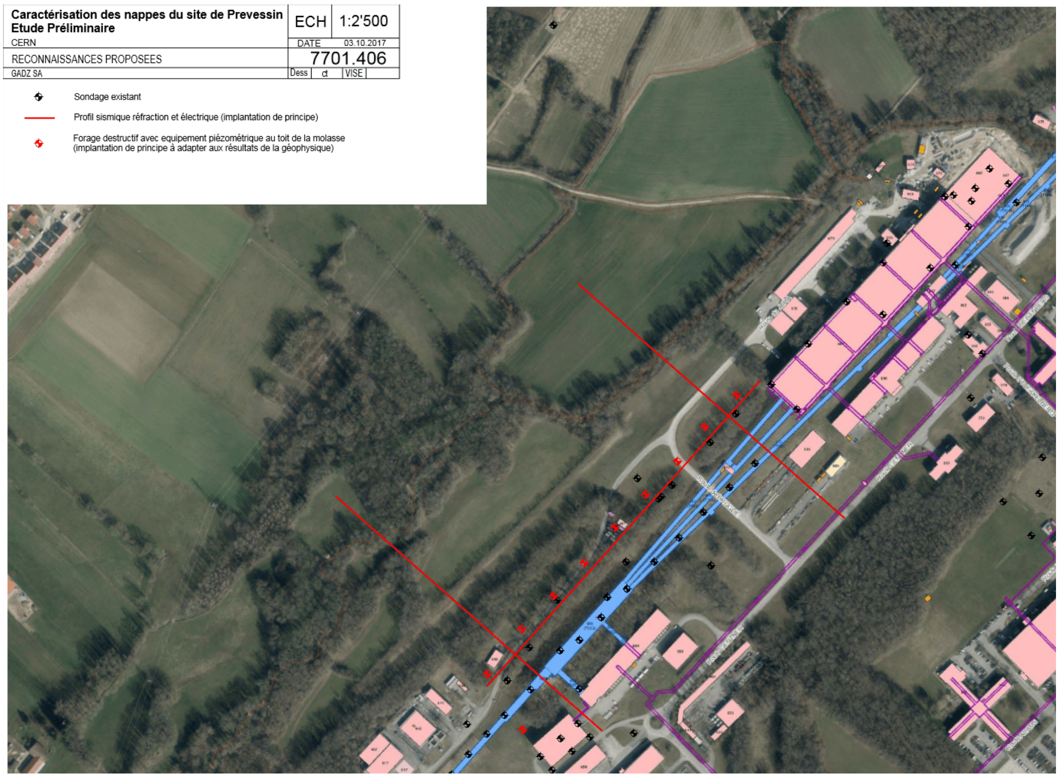

Fig. 10.4: Key area of interest identified in the hydrological and geotechnical studies of the North Area on the Prévessin site.

The outcome of the study was that further investigations by CERN should focus on an area 400 m to the south west of EHN1, as shown in Fig. 10.4. While the shallow water lenses identified are not thought to represent a risk from an environmental point of view, a 30 m deep aquifer may require further consideration. Water from the surface could potentially reach the deep aquifer if the water infiltrated the ground locally or if the existing drainage was not perfect (i.e. tight). Most probably, this deep aquifer flows in a north-westerly direction towards the Sillon de Saint-Genis and joins the Allondon river. The study has therefore highlighted an existing area of consideration for CERN, separate from the BDF project. It can be assumed that the lower aquifer exists and that the current TT20 tunnel links the level of the BDF to the aquifer. The integrity of the drainage in the TT20 may potentially be compromised by construction quality issues and ground movement. The tunnel could therefore in principle transmit water from the upper level to the lower aquifer either via the central drain or via the peripheral drainage of the tunnel itself. The BDF project should therefore ensure that no water from the facility drains into the TT20 tunnel, employing the strategies outlined below.

The water entering the drainage network can be considered to originate from:

- groundwater: subsurface water occupying the saturation zone, from which wells, springs, or streams are fed;
- machine-originated water: water from leaks in the chilled-water supply or of machine cooling water, or water escaping from other pipework such as dry risers;
- infiltration water (groundwater plus rain infiltration): this usually enters the underground area through failed or failing waterproofing membranes and cracks in the lining at construction joints or shrinkage cracks; in some areas with a high water table and hydrostatic head, water may enter though the floor or surcharging of the main drains;
- fire suppression water: water originating from the fire-extinguishing system in the lower target building.

It is assumed that the groundwater is unlikely to be activated, whereas water originating from the underground building or the tunnel has a higher risk of activation, and water contained in closed-circuit cooling is highly likely to be activated. The design approach for each source of water will be as follows.

Groundwater should not be allowed to enter the underground area directly. A free-flowing drainage layer should be provided to allow water to drain away from the underground area to a central drain pipe, which carries the water to a sump and a pumping station for evacuation to the surface and appropriate handling. The central drain should be sealed from the underground area to prevent water ingress into it. Watertight covers every 50 m must be provided to allow access for inspection and cleaning of the network. Any collector drains (usually slotted land drains) must also have rodding eyes accessible from the inside of the underground area. Any change in section size or direction must also have an access chamber to allow inspection and cleaning. The waterproofing and drainage systems should always be detailed to minimize the risk of water leaving the drainage network and finding its way back into the surrounding water table. Siphons and areas of standing water should be avoided and alternative details found.

Machine-originated water is mainly from closed-circuit cooling systems, and has the potential to be highly activated (including the danger of contamination with tritiated water). This water must be collected at its source and a drip tray created to collect any water leaking from the installation. A drain tap must be provided to channel the water into storage containers. The potentially contaminated water must then be stored locally in containers for verification by the HSE-RP group before being transported to the surface for disposal.

Both infiltration water and fire suppression water can be considered as being at risk of activation, as they may collect near radiation sources and stand for periods of time, leading to activation. For this reason, a second drain dedicated to water from the interior of the underground area must be provided, from which this water should be pumped to the surface for testing. The capacity of this network should be sized to cope with these loads, based on an analysis of the flows involved, as the project moves to the Technical Design Report stage. Water from the network must not reach the TT20 tunnels, in which leak paths are known to exist. There should, additionally, be no connection between this network and the drain taking the groundwater. Constriction joints should be detailed to provide either a self-sealing gasket or a resealable injection tube to keep the joint watertight. In areas of known high water table pressures, both measures may be needed. The joints should also be designed to allow easy channelling of any water ingress by the installation of a simple gutter to guide the water to the floor and away from the machine. This same approach is equally valid for shrinkage crack inducers.

Water from tunnel vaults must be collected in a channel at the interface between the tunnel vault and the floor. This channel should then be connected to the central drain (internal water) via pipes buried in the concrete invert. The design of the channels and interceptor drains must be done so as to minimize the risk of water on the transport path of the tunnel.

10.6.2 General structural safety aspects of buildings

10.6.2.1 Fire resistance

New structures and infrastructure should be designed and executed to guarantee mechanical resistance for 120 min of exposure to the design fire. Passive protection systems, e.g. intumescent paints and plasters, should be provided only for those elements that are unable to comply with such a requirement. The structural assessment will need to be carried out in accordance with EN 1991-1-2, EN 1992-1-2, and EN 1993-1-2.

10.6.2.2 False floors

A false or raised floor is a floor that provides a void or space for the technical installations and maintenance thereof in a building or part of the infrastructure. Such floors have been the cause of a number of incidents and near misses at CERN in recent years, and so incorporating safe design at an early stage will help to avoid potential hazards.

The objective of the design of false floors is therefore to provide a suitable environment for the services foreseen, allowing access for the installation, maintenance, and eventual removal of the installed equipment. The services may include, but are not limited to:

- electrical cabling;
- signal cabling;
- heating and ventilation;
- water supply and distribution;
- gas supply and distribution;
- fire detection;
- a fire main.

A number of considerations must be taken into account when deciding on the type of floor to install and the space required to meet the above criteria. Each phase of the floor's life must also be designed for and must allow safe installation, utilization, and finally decommissioning of the floor. Key design criteria include the following.

- Minimize the area of floor that is freely removable (this reduces the risk of damage to and deterioration of the floor from multiple interventions).
- Where possible, provide full-height access to the cable trays and pipework.
- Identify cable-pulling routes for the current layout and, where possible, future modifications, and try to identify locations of smaller access points for pulling the cables.
- Identify points of access to and egress from the floor for maintenance purposes that have the minimum impact on the normal walkways through the building.
- Detail the pulling points and access points such that there is a rigid barrier integrated into the access trapdoor (access should be via a trapdoor which in the open position is supported by barriers that protect the opening).
- Provide a suitable ladder or steps to access the area under the floor.

– Consult all groups who may need to pull cables to ensure that the layout chosen is suitable and, if necessary, pre-equip the cable trays with pulleys and pulling wires.
– Consult with transport staff to identify the methods of transport of foreseen equipment into the building and to verify the floor loadings.
– Develop a plan of the building showing all access and egress points for daily use and for access under the floor for works, all fire escape routes, and all transport routes. This can be used to quickly validate the loadings and mark the floor areas with the permissible loads.
– Once the basic layout of the floor and structures has been produced, the removable parts can be either designed in house or bought in as a system. In either case, it is highly recommended to have a system that fixes the position of the tiles with a solid frame to prevent creep of the tiles when repeatedly lifted and replaced. It is also worth considering a numbering system or pattern to help ensure that tiles are replaced in the correct orientation and position.

10.6.3 Target complex

The target of the BDF target complex is embedded in shielding blocks, and a study of the impact of such heavy shielding blocks on the floor level with respect to the beam alignment has been taken into account. The structural safety of the BDF helium vessel was considered in accordance with the following parameters:

– material: structural steel;
– self-supporting structure: 12 m $\times$ 9 m $\times$ 9 m;
– operational helium pressure: 0.05–0.1 barg (test pressure 0.5 barg);
– maximum load on vessel floor: 60 tons/m^2;
– compatibility with the flat concrete floor of the building (civil engineering tolerances);
– one drain point on the bottom to evacuate water leaks, and also for flushing out air with helium.

The requirements are the following:

– partial safety factor as per EN 1990;
– seismic action with a peak ground acceleration of 1.1 m/s^2 (soil type A) and with EN 1998-1 for the definition of the response spectrum;
– structural assessment in accordance with EN 1993-1-1, EN 1993-1-5, and EN 1993-1-6;
– anchors to the surrounding concrete elements to be assessed according to EN 1992-4;
– executional aspects to be treated in accordance with EN 1090.

10.7 Chemical safety

The chemicals currently foreseen for the BDF project represent standard risks seen in many other facilities at CERN. As these are subject to change as the project moves to the Technical Design Report stage, and as the exact quantities and storage conditions are not yet known, the installations will require proper risk assessment according to CERN Safety Form C-0-0-1 when these details become fixed. As for all such facilities at CERN, activities involving chemical agents should comply with the following CERN safety rules:

– Safety Regulation on Chemical Agents (SR-C);
– General Safety Instruction (GSI-C-1) on Prevention and Protection Measures;
– General Safety Instruction (GSI-C-3) on Monitoring of Exposure to Hazardous Chemical Agents in Workplace Atmospheres (where required).

Activities involving asphyxiant chemical agents should comply with the following CERN safety rules:

Table 10.2: Summary table of properties of possible solvents for liquid scintillator candidates [4]

Solvent	Density (g/cm^3)	Relative light yield	Flash point (°C)	Emission max. (nm)	Attenuation length (m)	HMIS		
						Flammability	Reactivity	Health
LAB	0.863	0.98	140	283	20	1	0	1
PXE	0.985	0.87	145	290	12	1	0	1
PC	0.889	1	48		10	2	0	2

– Safety Regulation on Chemical Agents (SR-C);
– General Safety Instruction (GSI-C-1) on Prevention and Protection Measures.

Should any additional chemicals be proposed for use in the facility, the chemical specialists in the HSE Unit must be consulted.

10.7.1 Liquid scintillator used in the BDF experimental area

Certain chemicals are already being considered within the scope of the integration of the BDF. The liquid scintillator chemicals foreseen to be used in the initial detectors of the proposed SHiP experiment consist of two organic compounds: a solvent, and a solute in the form of a powdered fluor. Such mixtures have been evaluated by the SHiP Collaboration [4], taking into account each chemical's flammability and flashpoint, as well as other health, safety, and environmental risks. Table 10.2 summarizes the properties of these solvents and fluors.

The currently selected mixture is one of Linear Alkyl Benzene (LAB) with 2,5-diphenyloxazole (PPO). The solvent, LAB, has a relatively high flash point of 140°C, with PPO added in small quantities (1.5–3 g/l). The chemicals are foreseen to be stored in two liquid containers of total volume 270 m^3, located immediately outside the service building. This quantity falls below the thresholds classified by the applicable regulations in force at the time of authoring this document. However, should the quantities being stored change significantly, this situation must be revaluated and, in addition, respect the legislation in force at the time of installation.

From a safety perspective, both LAB and PPO are classified as hazardous chemicals, and must be handled with suitable precautions and protection measures. LAB represents an aspiration hazard, and must therefore be stored and disposed of appropriately. PPO presents acute toxicity (oral), eye irritation, and chronic aquatic toxicity hazards. A chemical risk assessment must be carried out at the Technical Design Report stage, based on a safety data sheet prepared for the mixture in accordance with the REACH directive (see CERN Safety Guideline C-0-0-4). All appropriate preventive measures should be taken against environmental pollution; the regulatory requirements and the best available techniques should be applied, including putting in place a suitable retention basin to retain spilt chemicals, creating a loading/unloading area, and installation of all necessary means to detect a chemical leak.

In addition to the risk assessment, the following safety forms should be completed, when required, for the use of hazardous chemical agents:

– Safety Form C-1-0-2—Chemical Inventory (Example);
– Safety Form C-1-0-3—Tests of Safety Showers/Eye Washes;
– Safety Form C-1-0-4—Respirator Use (Example);
– Safety Form C-3-0-1—Exposure Form for Hazardous Chemicals and CMR.

10.7.2 Helium

The target bunker will be housed within a helium vessel to prevent air activation, with a nominal volume of approximately 82 m^3 of helium in the system, split between the vessel, the helium passivation system, and the helium circulation system on the trolley. This will be supplied from 60 cylinders located immediately outside the target complex. The current level of design detail is insufficient to assess the oxygen deficiency hazard level represented by the helium in this area. This will depend on what (if any) rate of leakage from the system is found, and if such leakages will reach confined spaces within the facility. On moving into the Technical Design Report stage, a chemical risk assessment should be carried out to determine the level of risk present, and the mitigation strategies required. Because of its low density, helium will collect predominantly at the ceilings of buildings; in the case of the target complex, this could include rising to the roof of the surface target building. It will therefore be necessary to include this area in the risk assessment, in particular because of the potential hazard it could represent to personnel operating cranes at this height in the building.

10.7.3 Liquid nitrogen

Liquid nitrogen is foreseen for the helium passivation system; it is currently expected to be provided by a cryogenic dewar located in the CV room, containing approximately 120 l of liquid nitrogen. At 10 l/h, the design flow rate in the system is relatively low, and will all be extracted and vented to the atmosphere. As with the helium in the system, a chemical risk assessment should be conducted for the area, to determine whether the nitrogen presents an ODH risk.

10.7.4 Gas building

The design of the supplies and facilities includes a gas building, intended to store and supply all of the gases foreseen to be used in the experimental area. As the design of the experimental area is still developing, a full inventory of the gases that will be contained in this building is not available. It is currently expected, however, to house CO_2 and Ar for the straw tracker of the SHiP detector. As for the helium and nitrogen for the target complex, once the details of the gas inventory in this area have been finalized, a chemical risk assessment will be required to determine the risks present. Should flammable gases be added to the inventory, an explosion risk assessment should be carried out, and the hazardous areas should be classified as required. The following safety forms should be completed for the use of flammable gases:

- Safety Form C-2-0-1—Explosion Risk Assessment;
- Safety Form C-2-0-2—Classification of Hazardous Areas (when required);
- Safety Form C-2-0-3—Declaration/Cancellation of the Use of Flammable Gas in an Experiment Area (when required).

The following guideline documents should be consulted when completing the safety forms:

- Safety Guideline C-2-0-1—Explosion Protection Measures;
- Safety Guideline C-2-0-2—Identification and Prevention of Explosion Hazards;
- Safety Guideline C-2-0-3—Practical Guide for Classification of Hazardous Areas;
- Safety Guideline C-1-0-1—Storage of Hazardous Chemical Agents.

All purchases of flammable gases should be authorized by the Flammable Gas Safety Officer of the relevant Department, and the use of the relevant areas should be subject to authorization by the HSE Unit.

10.7.5 Lead

Lead is not currently part of the shielding design for the target area. As the design is still at a preliminary stage, and that for the experimental hall is still under development, however, it is important to note that lead can present significant hazards. Care must be taken that the necessary procedures are followed for purchasing, shipping, storing, and handling the blocks to limit the dangers of lead poisoning and of exposure to activated materials. In particular, blocks should arrive at CERN pre-painted or adequately protected by equivalent means, to ensure that risks from dust are contained. Should lead be required, a chemical risk assessment should be carried out, and the following safety form should be completed:

– Safety Guideline C-0-0-3—Lead.

10.8 Electrical safety

The design of the electrical infrastructure for the BDF is currently at a general level, but will incorporate subsystems that either produce or use high voltage or current, both of which represent electrical hazards to personnel. Dedicated electrical rooms will be used to contain all the electrical cabinets required for power distribution. The hazards are expected to be standard for such installations, and should be mitigated through sound design practice and execution. The CERN Electrical Safety rules, alongside NF C 18-510, should be followed throughout the design process; where exceptions are required, these should be subject to an appropriate level of risk assessment to evaluate the residual risk and to determine the mitigation strategies required. NF C 18-510-compliant covers, interlocks preventing access to high-voltage equipment, and restriction of access to the electrical rooms to those with the appropriate level of CERN electrical *habilitation* training should be used to protect personnel from any electrical hazards present.

10.8.1 Electromagnets

Of particular interest from an electrical safety perspective will be the magnetic coil and steel yoke, located downstream of the target. These are likely to be the highest-voltage component in the system. For all electromagnets, appropriate grounding measures should be implemented for the magnet yokes, and all live parts protected to a minimum of IPXXB for low-voltage and IPXXC for high-voltage circuits or locked out for any intervention in their vicinity. Interventions may be carried out only by personnel with the necessary training, after following the work organization procedures and authorization (VICs, IMPACT, etc.) of the facility co-ordinator.

10.9 Mechanical safety and design of the target complex

The cooling requirements of the target due to the high energy levels deposited by the beam, along with the high radiological activation levels of the materials surrounding the target, have led to the need for a number of different pressurized fluid circuits within the target complex.

All pressure equipment should comply with the following CERN safety rules:

– CERN Safety Regulation SR-M—Mechanical Equipment;
– CERN General Safety Instruction GSI-M-2—Standard Pressure Equipment.

Moreover, there are specific sets of rules applicable only to certain types of standard pressure equipment. These rules are defined in the following Specific Safety Instructions, of which the following may be applicable to the BDF project:

– CERN Specific Safety Instruction on Pressure Vessels (SSI-M-2-1);
– CERN Specific Safety Instruction on Safety Accessories for Standard Pressure Equipment (SSI-M-2-3);
– CERN Specific Safety Instruction on Metallic Pressurized Piping (SSI-M-2-4);
– CERN Specific Safety Instruction on Vacuum Chambers and Beam Pipes (SSI-M-2-5);
– CERN Specific Safety Instruction on Transportable Pressure Equipment (SSI-M-2-6).

According to CERN safety rules, pressure equipment should meet the essential requirements set by the following applicable European directives:

– Directive 2014/68/EU on pressure equipment (Pressure Equipment Directive);
– Directive 2010/35/EU on transportable pressure equipment (Transportable Pressure Equipment Directive).

Pressure equipment designed and manufactured according to harmonized European standards benefits from a presumption of conformity with the essential requirements laid down in the above-mentioned European directives. According to the CERN safety rules, the use of harmonized European standards is compulsory for pressure equipment designed or manufactured at CERN. The use of other design codes or national standards should be reviewed and approved by the HSE Unit.

10.9.1 Cooling-water circuit

The highest pressure in the pressurized systems foreseen within the facility is in the pressurized cooling-water circuit, which pumps demineralized water around the target and proximity shielding. The system is currently foreseen to operate at approximately 25 barg, and, owing to the high radiation levels in the target area, will be inaccessible to personnel during operation. Limiting spillages of highly activated (and tritiated) water will, however, be a key part of the risk assessment of the area. It is therefore essential that the system should be able to withstand the internal pressure loads without critical failure in all conceivable modes of operation. Standard mitigation strategies must be put in place, in line with the requirements of the CERN rules and the Pressure Equipment Directive, but a number of complicating factors make the target relatively unique as a pressure vessel. A key failure mode for the system will be the event of a cooling-water pump malfunctioning, causing a 'natural convection scenario'. The design must show (through a combination of simulation and testing) that the high energy deposition at the end of the target will not cause localized boiling (and high pressures) sufficient to cause critical failure of the pressure envelope. Complicating factors in this include the significant pressure drop across the target, and the high localized stresses in the material due to heating. In light of the criticality of the facility, a higher-level quality assurance programme should also be implemented for this system during fabrication and installation, requiring 100% volumetric inspection of all welds.

In addition to the dangers of overheating during operation, consideration must be given to the effects of afterheat after the beam is turned off. As a mitigation measure, a jockey pump should be considered, to provide additional redundancy and to keep pressure and some flow in the target should the main pump fail or be turned off outside of beam time.

A key mitigation measure (and an essential feature for the target complex) will be the ability of the system to deal with water leaks and to prevent contamination of other water sources. To this end, there must be capacity within the system to detect leaks, to retain the entire inventory of cooling water in the event of a leak, and to be able to effectively drain the whole circuit if required (with no significant areas inaccessible to drainage of the activated water).

10.9.2 Helium purification circuit

To ensure that the helium delivered to the helium vessel remains at 99.9% purity, the helium purification circuit will operate at 15 barg in the condenser–freezer and adsorber components of the system, with a maximum allowable pressure of 30 barg. As with the target cooling-water circuit, the criticality of this system requires a higher degree of quality assurance during fabrication and installation, in addition to fulfilling the design and quality assurance requirements of the Pressure Equipment Directive and the CERN safety rules, including 100% volumetric inspection of all welds in the system.

10.9.3 Cryogenics

The helium purification system will also require cooling in the condenser–freezer and adsorber components. To this end, the adsorber will be submerged in a liquid nitrogen dewar, while the condenser–freezer will pre-cool the impure helium via heat exchange with cold nitrogen vapour supplied from the dewar at 1.5 barg. This equipment should comply with the following CERN safety rules:

- CERN Safety Regulation SR-M—Mechanical Equipment;
- CERN General Safety Instruction GSI-M-4—Cryogenic Equipment.

In accordance with the rules above, cryogenic pressure equipment should comply with the following European directive:

- Directive 2014/68/EU on pressure equipment (Pressure Equipment Directive).

For the pressurized cryogenic piping, it is required that:

- the equipment complies with Directive 2014/68/EU on pressure equipment;
- the equipment is delivered with an EC declaration of conformity.

Cryogenic pressure vessels should be equipped with pressure relief devices to ensure the safe release of the working fluid in the case of overpressure. Piping sections that may become isolated with cryogenic liquid or cold gas in them should also be equipped with pressure relief devices to ensure safe release of the working fluid in the case of overpressure. The pressure relief devices should:

- be installed, commissioned, and periodically tested according to the General Safety Instruction on Cryogenic Equipment (GSI-M-4);
- be sized in accordance with:
  - EN 13648-3: Cryogenic Vessels—Safety Devices for Protection against Excessive Pressure—Part 3: Determination of Required Discharge: Capacity and Sizing; and the applicable part of
  - ISO 4126: Safety Devices for Protection against Excessive Pressure;
- be CE marked and delivered with an EC declaration of conformity with Directive 2014/68/EU. Pressure relief devices must be classified in category IV and their conformity assessed accordingly. By way of exception and in agreement with the HSE Unit, however, pressure relief devices manufactured for specific equipment may be classified in the same category as the equipment they protect. They should additionally be Pi-marked whenever installed on transportable cryogenic storage vessels.
- The exhausts of all cryogenic safety valves should vent to a safe location.

10.9.4 Heating, ventilation, and air conditioning (HVAC)

10.9.4.1 Pressurized Areas

Pressurized areas and controlled ventilation are key parts of both the radiation protection and the fire safety strategies for this facility, helping to prevent the spread of airborne particles or smoke beyond their areas of origin. Typically, at CERN pressurized areas meet the fire safety requirements set by the French Instruction technique 246 (overpressure of 20–80 Pa in stairwells of buildings with public access) and the safety requirements for airborne radioactive particles set by the Ventilation Working Group Report EDMS N. 1226988, for particle-accelerator-type environments, where the overpressure between the accelerators and the ‘safe area’ is from 20 to 30 Pa.

For areas with higher radiation levels, a case-specific risk assessment should be done by the BDF project and the HSE-RP group together to define the correct values of the pressure cascade. The target complex, owing to the significant containment needs driven by the high radiation levels in this area, may require values well above the ones mentioned above. In any case, the force required to manually open emergency exit doors must not exceed 100 N.

10.9.5 HVAC equipment

Equipment purchased on the market (e.g. air-handling units, chillers, boilers, fan coils) should comply with the applicable European directives and should bear the CE marking.

Ductwork (supply or exhaust air) and piping systems incorporated in a permanent manner into a building should comply with the following European regulations:

– European Regulation 305/2011—Construction Products Regulation;
– EN 1505—Ventilation for Buildings. Sheet Metal Air Ducts and Fittings with Rectangular Cross-Section;
– EN 1506—Ventilation for Buildings. Sheet Metal Air Ducts and Fittings with Circular Cross-Section;
– EN 12097—Ventilation for Buildings. Requirements for Ductwork Components to Facilitate Maintenance of Ductwork Systems;
– EN 13480—Metallic Industrial Piping.

These standards provide a presumption of conformity with the safety requirements regarding the design laid down in the applicable European regulations. Electrical components related to HVAC installations should respect the general safety requirements as indicated in Section 10.8.

10.9.6 Trolley mechanics

A key mechanical consideration for the target trolley itself will be the danger of a malfunction causing the trolley to become stuck at some point along its path of travel. A recovery procedure will therefore be needed for each of the potential failure modes, identified through a Failure Mode and Effects Analysis (FMEA) risk assessment. The most likely of these is a failure of drive motor; this could be overcome by ensuring that the trolley drive system can be overridden, either manually using a crank handle or with a supplementary back-up motor. Additionally, care should be taken that the drive motor has sufficient capacity to ensure that the trolley can still be driven in the event of a seized wheel or similar obstruction.

10.9.7 End-of-life considerations for mechanical components

An important consideration for a facility such as the BDF target complex is the design for the end of its operational life. Thought should be given to facilitating disassembly and disposal of the highly activated materials at the decommissioning of the facility. This may include separating out, as far as possible, different materials within the helium vessel, and making disassembly of dissimilar materials as easy as possible. Keeping witness samples of all the materials used inside the vessel (and exposed to the highest levels of radiation) will allow easy examination of the effects of the actual radiation dose on the mechanical properties of the exact materials used. This could be invaluable for disassembly, for example by revealing the radiation hardening that has occurred in the metallic components should cutting operations be required. Maintaining modularity and designing in significant temperature measurement capacity in components in the helium vessel will also be important for extending the life of the facility, should this be required towards the end of the predicted initial operational time.

10.10 Lifting and handling equipment

The BDF is expected to use a significant quantity of lifting equipment, including hoists, cranes, and personnel lifts. Most notably, all three of the proposed concepts for the target complex require a 40 t crane in the ground-level target hall to perform maintenance activities and to lift equipment (including highly activated material) in and out of the helium vessel. All lifting and handing equipment installed at CERN should comply with the following CERN safety rules:

– Safety Regulation on Mechanical Equipment (SR-M);
– General Safety Instruction on Lifting Equipment and Accessories (GSI-M-1).

10.10.1 Target complex

Because of the radiation levels foreseen in the target complex, remote handling equipment has been designed to deal with the need for regular maintenance of the technical equipment in the area. All of the concepts for the complex, but most particularly the crane concept, will require remote handling operations to be carried out using the cranes in the target area. Because of the activation of the material, it is essential that there is sufficient redundancy in this system to deal with crane malfunctions. Mitigation will include redundancy in lifting capacity, as well as planned strategies for handling malfunctions using detailed FMEA. All cranes, bridge cranes, gantry cranes, and power-driven hoists must conform to the following:

– CERN Specific Safety Instruction (SSI-M-1-2)—Design, Installation, and Use;
– CERN Specific Safety Instruction (SSI-M-1-4)—Manually Powered Lifting Equipment.

All remote handling equipment and tooling must additionally conform to the following:

– CERN Specific Safety Instruction (SSI-M-1-3)-—Non-fixed Load-lifting Accessories.

Overhead travelling cranes should also respect the following general standards:

– EC Machinery Directive (European Directive 2006/42/EC);
– FEM 1.001, 3rd edition, revised 1998.10.01;

as well as the following CERN safety documents:

– Safety Regulation on Mechanical Equipment (SR-M);
– General Safety Instruction on Lifting Equipment and Accessories (GSI-M-1);
– Electrical Safety Code C1;
– Safety Instruction IS23 Rev. 2. Criteria and Standard Test Methods for the Selection of Electrical Cables, Wires and Insulated Parts with Respect to Fire Safety and Radiation Resistance;
– Safety Instruction IS24. Regulations Applicable to Electrical Installations;
– Safety Instruction IS41. The Use of Plastic and Other Non-metallic Materials at CERN with Respect to Fire Safety and Radiation Resistance;
– Safety code A3 Rev. Safety Colours and Safety Signs.

The following specific safety aspects for cranes should also be respected:

– drainage apertures in all places where water or oil may collect;
– catwalk to access the rails;
– catwalks on the main beam and on the crab for safe maintenance on the crane; headroom above the catwalks of at least 1.8 m; mobile ladder to reach the crane catwalk; safe access to the crab catwalk from the crane catwalk;
– maintenance access platform;
– noise level index (defined by ISO Standard No. R.1996) maximum 65 dB;
– protection against overturning;

– overhanging system for equipment mounted beyond the steelwork of the crane;
– end stops for travelling, traversing, and hoisting; end stop for upper overtravel of hoisting;
– earthing of structural steelwork and crab;
– load limiter;
– floodlights to illuminate the area under the crane;
– overspeed detection.

10.10.1.1 Hot cell winch

As with all hoists in the facility, the winch should respect the following general standards:

– EC Machinery Directive (European Directive 2006/42/EC);
– FEM 1.001, 3rd edition, revised 1998.10.01;

as well as the following CERN safety documents:

– Safety Regulation on Mechanical Equipment (SR-M);
– General Safety Instruction on Lifting Equipment and Accessories (GSI-M-1);
– Electrical Safety Code C1;
– Safety Instruction IS23 Rev. 2. Criteria and Standard Test Methods for the Selection of Electrical Cables, Wires and Insulated Parts with Respect to Fire Safety and Radiation Resistance;
– Safety Instruction IS24. Regulations Applicable to Electrical Installations;
– Safety Instruction IS41. The Use of Plastic and Other Non-metallic Materials at CERN with Respect to Fire Safety and Radiation Resistance;
– Safety Code A3 Rev. Safety Colours and Safety Signs.

The following specific safety aspects for winches and hoists should also be respected:

– noise level index (defined by ISO Standard No. R.1996) maximum 65 dB;
– protection against overturning;
– overhanging system for equipment mounted beyond the steelwork of the hoist;
– end stops for travelling, traversing, and hoisting; end stop for upper overtravel of hoisting;
– earthing of structural steelwork and crab;
– load limiter;
– overspeed detection.

10.10.2 Personnel lifts

Personnel lifts in the facility should respect the following general standards:

– European Standard EN 81.1;
– EN 94:1992 and EN 811:1997;
– EC Directive 95-16 (EC conformity certification);

as well as the following safety documents:

– European Directive 95/16C;
– EN 81-72 Firefighter Lifts;
– EN 81-73 Behaviour of Lifts in Case of Fire;
– Electrical Safety Code C1;
– Safety Code E Rev. Fire Protection;
– Safety Instruction IS23 Rev. 2. Criteria and Standard Test Methods for the Selection of Electrical Cables, Wires and Insulated Parts with Respect to Fire Safety and Radiation Resistance;

- Safety Instruction IS24. Regulations Applicable to Electrical Installations;
- Safety Instruction IS37 Rev. 2. Alarms and Alarm Systems;
- Safety Instruction IS41. The Use of Plastic and Other Non-metallic Materials at CERN with Respect to Fire Safety and Radiation Resistance;
- Safety Code A3 Rev. Safety Colours and Safety Signs.

The following specific safety aspects for personnel lifts should also be respected:

- automatic lighting, with economizer, provided by a recessed ceiling fitting with emergency lighting;
- hands-free telephone integrated in car control panel;
- overload/full load indicator via electronic sensors with notification in cab (full load = 100%, overload = 110%); load sensor precision 5% rated load;
- car door with variable-speed drive and preliminary unlocking in levelling zone;
- electrical manoeuvring system;
- emergency escape hatch onto the car roof.

10.11 Non-ionizing radiation

The high magnetic fields from the proposed electromagnets in the current BDF design represent a hazard similar to that found in many of the facilities at CERN, and should be handled with standard mitigation strategies. The facility should follow Directive 2013/35/EU on the occupational exposure of workers, alongside CERN Safety Instruction IS 36 and its Amendment. Any activity inside a static magnetic field should be subject to risk assessment and ALARA. Personnel should be informed about the hazards and appropriately trained. Areas with magnetic flux densities exceeding 0.5 mT should be delimited (pacemaker warning signs should be used), while areas with magnetic flux densities exceeding 10 mT should be rendered inaccessible to the public.

10.11.1 Extraction tunnel

Electromagnets are foreseen in the BDF extraction beam line, with modified splitter magnets, quadrupoles, dilution kickers, and dipole magnets present in the optics design, all of which are to be largely identical to those already in use in the North Area. All magnets foreseen for the facility are warm magnets.

10.11.2 Target area

The major novelty will be the active muon shield, to be installed immediately downstream of the target and the hadron stopper. A warm 1.4 T magnetic coil will be installed within the larger shielding surrounding the target. The restrictions around this magnet are expected to be enforced as a natural result of the radiation levels around the magnet when it is in operation. The expected risk is therefore only foreseen for commissioning, testing, and maintenance of the magnet, which should be mitigated by ensuring that these operations are carried out only by appropriately qualified personnel, in line with the rules and processes outlined at the start of this section.

10.12 Noise

The BDF facilities are located in the North Area on the Prévessin site, close to the fence line of CERN's property. To ensure occupational health and safety of people exposed to noise, the BDF project should be compliant with the following rules and regulations:

- CERN Safety Code A8—Protection against Noise;

– Directive 2003/10/EC of the European Parliament and of the Council of 6 February 2003 on the minimum health and safety requirements regarding the exposure of workers to the risks arising from physical agents (noise);
– the French Code du travail.

Emissions of environmental noise related to neighbourhoods should respect the thresholds indicated in the following French regulation:

– Arrêté du 23 janvier 1997 relatif à la limitation des bruits émis dans l'environnement par les installations classées pour la protection de l'environnement.

10.13 Asbestos

As the extraction tunnel was constructed before 1997, an asbestos survey was carried out by the HSE Unit. The findings of the investigation are summarized in EDMS 2054048. If the presence of asbestos is ascertained, necessary protective measures will have to be put in place following the applicable CERN safety rule:

– Safety Instruction IS 43—Asbestos: Dangers and Precautions.

10.14 Protection of the environment

With regard to protection of the environment, the CERN Safety Policy states that the Organization is committed to ensuring the best possible protection of the environment. This can be achieved by ensuring that the regulations given are followed for the different activities and experiments.

As the project moves to the Technical Design Report stage, a review with the environmental protection specialists in the HSE Unit should be held to determine whether the relevant technical provisions of the following regulations should apply to the BDF project:

– Arrêté du 29/05/00 relatif aux prescriptions générales applicables aux installations classées pour la protection de l'environnement soumises à déclaration sous la rubrique n° 2925;
– Arrêté du 14/12/13 relatif aux prescriptions générales applicables aux installations relevant du régime de l'enregistrement au titre de la rubrique n° 2921 de la nomenclature des installations classées pour la protection de l'environnement.

The technical environmental mitigation measures should be determined more precisely once information about technical details is available, such as the type and the quantity of chemicals or the solution chosen for cooling.

10.14.1 Air

Atmospheric emissions should be limited at source and should comply with the relevant technical provisions of the following regulations:

– Arrêté du 02 février 1998 relatif aux prélèvements et à la consommation d'eau ainsi qu'aux émissions de toute nature des installations classées pour la protection de l'environnement soumises à autorisation, Articles 26, 27, 28, 29, and 30.

The design of exhaust air discharge points should comply with the requirements of Section 5.1.3 of CERN Safety Guideline C-1-0-3—Practical Guide for Users of Local Exhaust Ventilation (LEV) Systems.

Whenever greenhouse gases are used, relevant technical provisions contained in the following regulations apply:

– Regulation (EU) No. 517/2014 of the European Parliament and of the Council of 16 April 2014 on fluorinated greenhouse gases and repealing Regulation (EC) No. 842/2006;
– Code de l'environnement Livre V : Titre II (Art. R521-54 to R521-68) and Titre IV (Art. R543-75 to R543-123).

All appropriate preventive measures should be taken against the release of greenhouse gases into the atmosphere. Working procedures should be established and implemented for activities involving the use of those gases, including storage, handling, transport, recovery, and disposal. Additionally, such activities should be performed by trained personnel. The emissions of fluorinated gases should be registered during the entire life cycle of the equipment or experiment.

In accordance with the siting of the facility on French territory, the design, operation, and maintenance of cooling tower water circuits should comply with the relevant technical provisions of the following regulations and standards in order to limit the risk of *Legionella* bacteria and their dispersion in the atmosphere:

– NF E38-424 Aéroréfrigérants humides : terminologie et exigences de conception vis-à-vis du risque légionellose;
– Arrêté du 14 décembre 2013 relatif aux prescriptions générales applicables aux installations relevant du régime de l'enregistrement au titre de la rubrique n° 2921 de la nomenclature des installations classées pour la protection de l'environnement;
– Guide des bonnes pratiques *Legionella* et tours aéroréfrigérantes.

10.14.2 Water

The BDF project should ensure rational use of water. The discharge of effluent water into the CERN clean water and sewage networks should comply with the relevant technical provisions contained in the following regulations:

– Loi n° 2006-1772 du 30 décembre 2006 sur l'eau et les milieux aquatiques;
– Arrêté du 02 février 1998 relatif aux prélèvements et à la consommation d'eau ainsi qu'aux émissions de toute nature des installations classées pour la protection de l'environnement soumises à autorisation.

The direct or indirect introduction of potentially polluting substances into water, including their infiltration into the ground, is prohibited. Applicable values of emission limits for effluent water discharged in the Host States' territory are defined in the following regulations:

– Arrêté du 02 février 1998 relatif aux prélèvements et à la consommation d'eau ainsi qu'aux émissions de toute nature des installations classées pour la protection de l'environnement soumises à autorisation, Art. 31 and Art. 32.

Complementarily, if independent cooling towers are installed, the cooling circuit should be equipped with a recycling process, and the effluent resulting from the recycling process should be discharged into the sanitary network.

Retention measures for fire-extinguishing water are required for any CERN project in which large quantities of hazardous or potentially polluting substances are used or stored. As the project moves to the Technical Design Report stage, through discussions with the environmental protection specialists from the HSE Unit, it will be determined whether the following guidance documents should be applied (in accordance with the French Code de l'Environnement):

– Référentiel APSAD D9 : Dimensionnement des besoins en eau pour la défense contre d'incendie;
– Référentiel APSAD D9A : Dimensionnement des rétentions des eaux d'extinction.

These documents are available from the Centre National de Prévention et de Protection (http://www.cnpp.com/).

10.14.3 Energy

The use of energy should be as efficient as possible. For the entire facility, adequate measures should be taken to comply with the relevant technical provisions contained in the following regulation:

- Loi n° 2010-788 du 12 juillet 2010 portant engagement national pour l'environnement (Grenelle II).

In addition, the construction of new buildings sited in France should comply with the relevant technical provisions relating to thermal efficiency contained in the following regulations:

- Décret n° 2012-1530 du 28 décembre 2012 relatif aux caractéristiques thermiques et à la performance énergétique des constructions de bâtiments;
- Arrêté du 26 octobre 2010 relatif aux caractéristiques thermiques et aux exigences de performance énergétique des bâtiments nouveaux et des parties nouvelles de bâtiments;
- Réglementation Thermique 2012 (RT 2012);
- NF EN 15232 Performance énergétique des bâtiments—Impact de l'automatisation, de la régulation et de la gestion technique.

10.14.4 Soil

The natural physical and chemical properties of the soil must be preserved. All relevant technical provisions related to the usage or storage of hazardous substances in the environment should be fulfilled to avoid any chemical damage to soil. Furthermore, the excavated material should be handled adequately, and further site contamination should be prevented. All excavated material must be disposed of appropriately in accordance with the associated waste regulations.

10.14.5 Waste

The selection of construction materials, design, and fabrication methods should be such that the generation of waste is both minimized and limited at source. Waste should be handled from its collection to its recovery or disposal according to:

- Code de l'environnement, Livre V : Titre IV—Déchets;
- Loi n° 2009-967 du 3 août 2009 de programmation relative à la mise en œuvre du Grenelle de l'environnement (1), Art. 46.

Traceability of the waste should be guaranteed at all times.

10.14.6 Preservation of the natural environment

The BDF project should ensure the preservation of the natural environment (e.g. the landscaping, fauna, and floral reserve) according to the relevant technical provisions contained in the following regulation:

- Code de l'environnement, Art. L411-1.

Plant species (e.g. orchids) listed in this regulation should be protected, restored, or adequately replaced. Whenever natural areas at CERN are affected by a project, the Civil Engineering and Buildings (SMB-SE-CEB) section of the Site Management and Buildings (SMB) Department should be contacted for authorization and definition of appropriate measures.

References

[1] A. Arnalich. *North Area—Fire Risk Assessment*. Tech. rep. CERN, 2018. URL: https://edms.cern.ch/document/1895523.

[2] A. Arnalich. *FIRIA Project Kickoff*. Tech. rep. CERN, 2018. URL: https://edms.cern.ch/document/1982653.

[3] GADZ. *Sondates et Etude Geotechnique concernant le projet Neutrino Base Line CENF. Final Report*. 2014. URL: https://edms.cern.ch/document/1311633.

[4] M. Anelli et al. *A Facility to Search for Hidden Particles (SHiP) at the CERN SPS*. Tech. rep. CERN-SPSC-2015-016, SPSC-P-350. CERN, 2015. arXiv: 1504.04956 [physics.ins-det].

Chapter 11

Civil engineering

11.1 Overview

Civil Engineering (CE) costs for projects such as the BDF typically represent a significant proportion of the overall implementation budget. For this reason, particular emphasis has been placed on CE studies to ensure a cost-efficient conceptual design and construction methodology. This chapter provides an overview of the designs adopted for CE along with the key considerations. The design developed has been used to provide an estimated cost and schedule for CE elements.

The CE studies were based on the assumption that the BDF will be sited at the CERN Prévessin laboratory in France. A junction with the existing tunnel TDC2 will be required to enable a new machine extraction tunnel in the North Area, leading to a new target complex and experimental facility. All CE works for the project are fully located within existing CERN land. The area foreseen for the development of the new BDF is highlighted in Fig. 11.1.

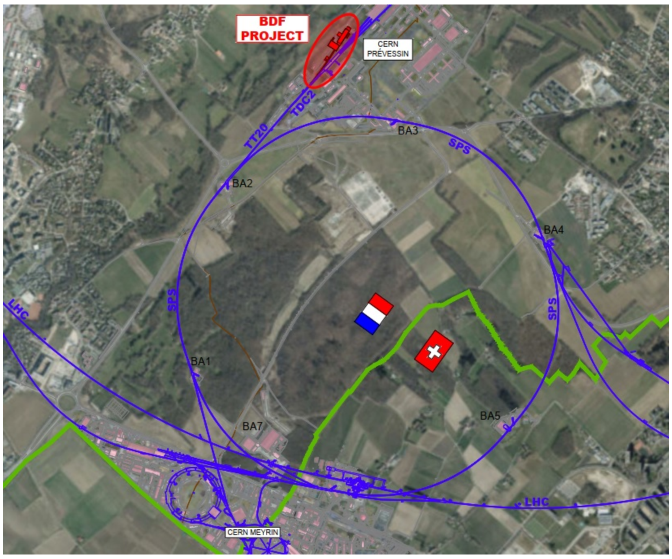

Fig. 11.1: Location of the BDF project on the French CERN site at Prévessin

A plan overlay of the proposed BDF facilities on the existing site is shown in Fig. 11.2. The key features of this layout are:

- demolition of a section of the existing TDC2 tunnel to form a 75 m long junction cavern;
- a 165 m long extraction tunnel, 5 m wide × 4 m high (internal dimensions);
- a 15 m long × 12 m wide access building, including a heavy-equipment access shaft;
- a 60 m long × 20 m wide auxiliary building, servicing the extraction tunnel and target complex;
- a 36 m long × 58 m wide target complex along with an associated vehicle airlock and personnel access;
- a 120 m long × 20 m wide experimental hall;
- a 100 m long × 27.5 m wide surface building above the experimental hall;
- a 21 m long × 35 m wide service building and workshop and a 10 m long × 15 m wide gas building.

The civil engineering studies presented in this chapter were performed by the SMB-SE Future

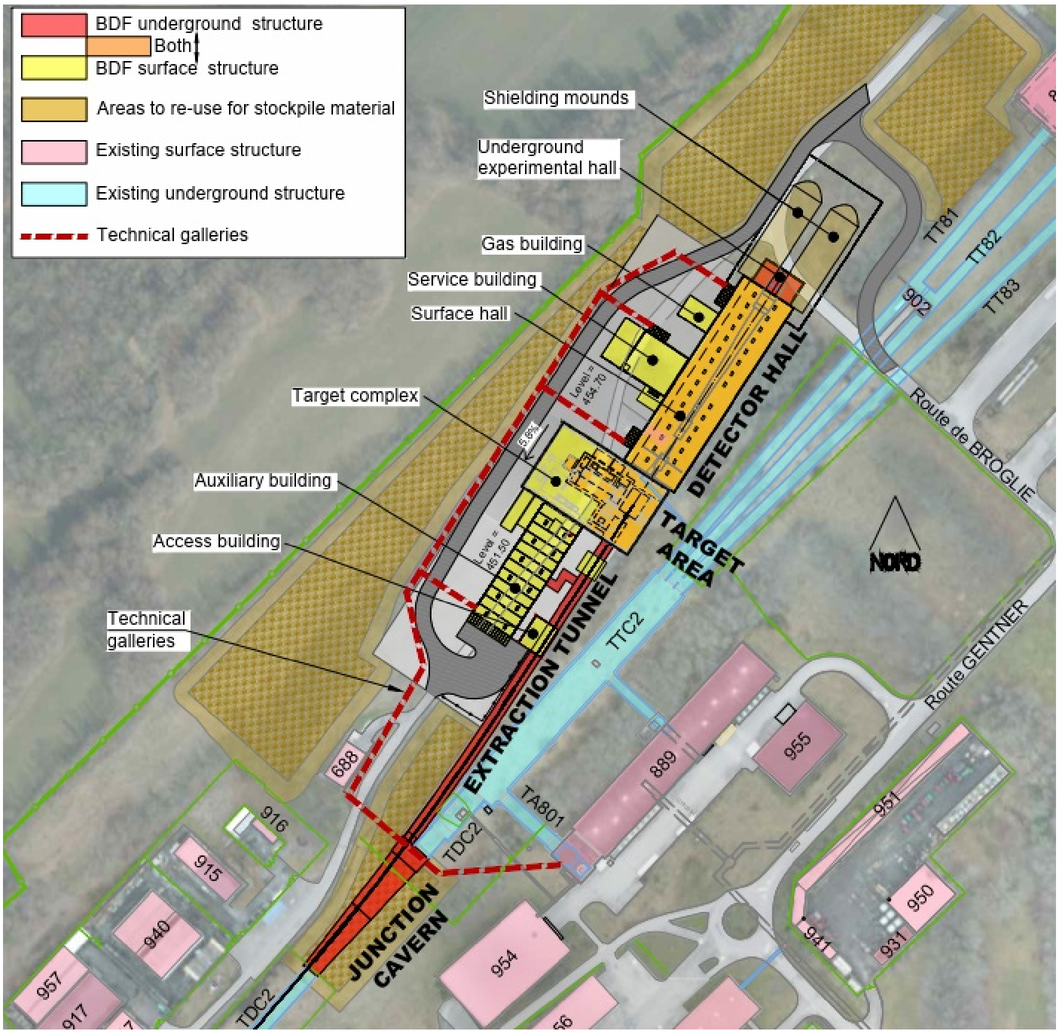

Fig. 11.2: Existing CERN infrastructure and proposed BDF facilities, indicating above- and below-ground installations.

Accelerator Studies (FAS) section with various inputs from technical experts across the BDF project team. The engineering consultants Arup have also worked on the study, along with specialist radiation subconsultants Studsvik. A more detailed report on the CE study produced in collaboration with Arup is also available [1].

11.2 Location and existing infrastructure

11.2.1 Location

The proposed site for the BDF project is entirely located within existing CERN land on the Prévessin campus. The existing site is composed of green areas and existing roads. There is also a small SMB depot/storage area, designated 'Zone 9103'. This comprises building 687, the demountable buildings 6357 and 6575, and a steel container 6361.

This location is well suited to housing the BDF project from a CE perspective, primarily because of the relatively stable and well-understood ground conditions. Quite detailed geological records exist for this area, and these were utilized in this study to minimize the costs and risk of the project. The underground works will be constructed in the stable moraine glacial deposits at depths of up to 20 m below ground level.

11.2.2 Geology and hydrology

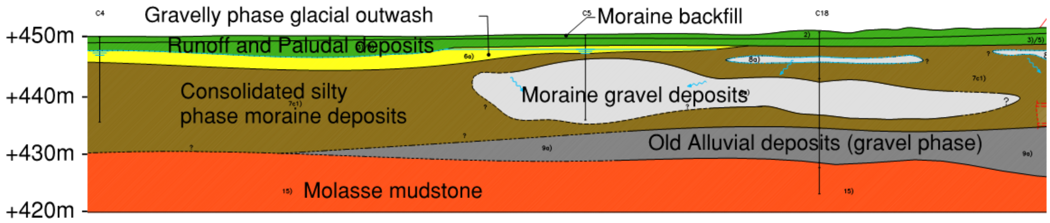

Fig. 11.3: Typical geological long section of the area (based on a study by GADZ in 2014 [2])

The proposed location of the BDF is situated in the Geneva Basin, a subbasin of the large North Alpine Foreland (or Molasse) Basin. This is a large basin which extends along the entire Alpine front from south-eastern France to Bavaria, and is infilled by clastic 'Molasse' deposits of Oligocene and Miocene age. The basin is underlain by crystalline basement rocks and formations of Triassic, Jurassic, and Cretaceous age. The Molasse, comprising an alternating sequence of marls and sandstones (and formations of intermediate compositions), is overlain by Quaternary glacial moraines related to the Wurmian and Rissian glaciations. Figure 11.3 shows a typical geological cross-section of the moraines in the vicinity of the BDF.

A ground investigation has previously been carried out in this area. The findings were summarized by the geotechnical consultant GADZ [2]. Although the ground investigation was carried out for an earlier stage of the CERN Neutrino Platform (CENF) project, the results are both applicable to the BDF and sufficiently detailed to be used for a feasibility review of the foundations and other CE infrastructure.

According to the GADZ report, several groundwater tables were in the area, independent of one another. Careful consideration will be required during detailed design and construction both to optimize the design and to prevent any contamination of groundwater. Future project-specific ground investigations will provide an opportunity for more detailed examination.

11.2.3 Existing infrastructure

Fig. 11.4: Photograph from May 1972 taken at the start of tunnelling for TT20, looking towards the SPS

The proposed works connect with the existing TDC2 tunnel, which was excavated in 1972 using the 'cut and cover' technique as shown in Fig. 11.4.

The proposed BDF facilities will be close to the existing TCC2 cavern as well as to the transfer tunnels TT81, 82, and 83. The existing tunnels are likely to be sensitive to vibration and excavation carried out as part of the construction works. The CE study proposals aim to avoid any impact on existing infrastructure; however, tunnel monitoring will be required before, during, and after construction works. It will be particularly important to monitor and manage construction-induced vibration during 'beam on' to avoid disruption to operations.

The age and use of the existing infrastructure also has an impact on the planning of the works owing to radiological activation of the tunnels and surrounding earth. Existing concrete in TDC2 has been tested and was found to be up to 400 times the liberation limit, meaning that it must be classified and treated as radioactive. Simulations have also indicated that it was likely the soil surrounding TDC2 would be highly irradiated. As part of this study, soil samples were taken and testing was carried out to a depth of 1.5 m above the tunnel roof slab. No levels above the LL were found. A conservative assumption that all soil within 1.5 m of the tunnel walls is activated has been proposed by CERN's Radiation Protection team until further testing can confirm this or show otherwise. The full findings and conclusions are detailed in an RP report [3].

RP studies [4] have shown that work cannot be carried out within 8 m of the existing beam line. Again, this is an important factor in the planning and scheduling of CE works. This was taken into account in this study.

11.3 Description of Civil Engineering design

This section details the proposals for each part of the planned infrastructure, including requirements and considerations in relation to CE.

11.3.1 TDC2 junction cavern

The junction cavern consists of a new tunnel measuring 75 m long, 5.3 m high, and varying between 8 and 16 m in width (external dimensions). The proposed design for the tunnel involves a cast-in-situ reinforced concrete (RC) base slab and pre-cast RC 'n' sections on top. Pre-cast sections were chosen to increase the speed of construction and reduce the time operatives will need to be next to activated soil. The sections will be between 1 and 2 m in length. The cast-in-situ base will reduce differential settlement.

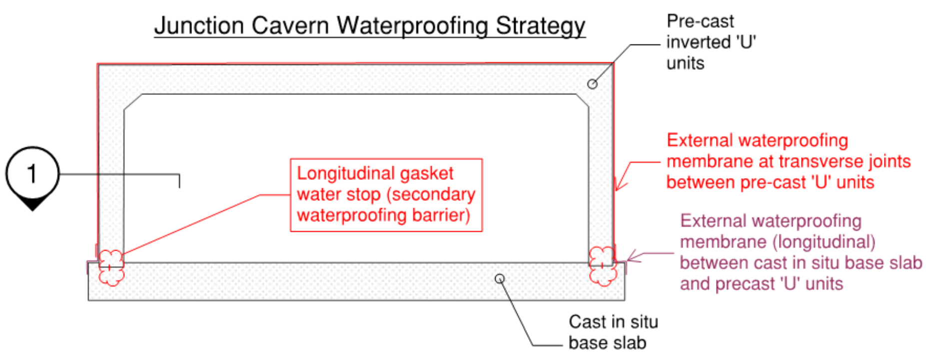

Fig. 11.5: Typical cross-section through junction cavern, showing the proposed form of construction

Waterproofing will be provided via a multilayer passive system, as shown in Fig. 11.5, with an external membrane and gaskets between sections. The junction cavern will provide a connection with the existing TDC2 tunnel, allowing sufficient space for extraction beam line equipment, services, and future maintenance access. The dimensions of the cavern have been sized accordingly.

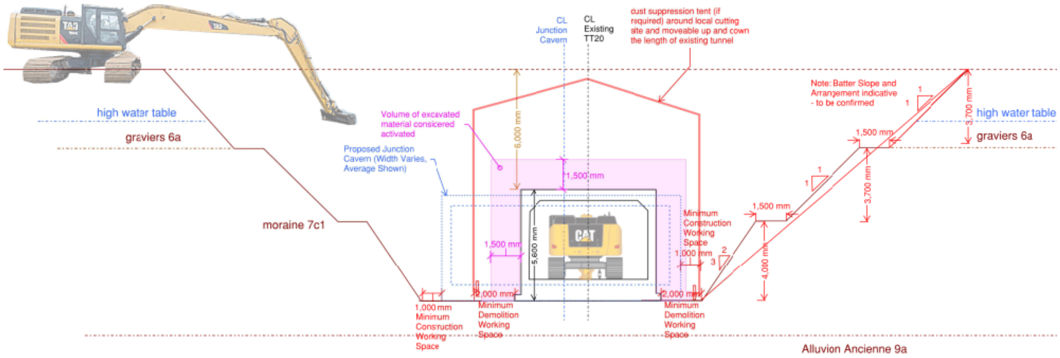

Fig. 11.6: Illustration of cross-section during works for traditional demolition of the existing TDC2 tunnel.

To enable construction of the junction cavern, first the relevant part of the existing TDC2 tunnel must be demolished. A detailed analysis of the options was undertaken to determine the best demolition approach, cognizant of both civil engineering and radiation protection constraints [5].

The outcome of the process was a decision to demolish TDC2 in full over the required length via traditional methods using crushing and hammering in an open-cut excavation, as shown in Fig. 11.6. This has significant advantages in that it reduces the duration of construction works in comparison with more specialist methods such as dry diamond rope saw cutting (DDRWC) into sections. The shorter duration will lead to a reduction in cost and in the radiation dose received by the construction workforce. DDRWC will, however, be used at the points where TDC2 will be retained to ensure that a neat joint can be achieved.

Note that Arup's study concluded that a tent would not be needed for this operation. Standard methods of dust suppression and control of inhalation will be sufficient to prevent any internal dose issues for construction operatives. The spread of dust to areas outside CERN must be evaluated in more detail to ensure that any dose received by the public is within acceptable levels. This will need to be evaluated further at later stages of the project to ensure that the measures in place will prevent any release of contaminated material. A tent is shown in Fig. 11.6 for illustrative purposes only.

Before demolition, approximately 100 m length of machine and services will have to be removed from TDC2 to allow demolition. To prevent the spread of dust and debris from construction into the retained sections of TDC2, sealed walls will be built at each end.

The demolished concrete and activated earth will be re-used as backfill above the new junction cavern and extraction tunnel to avoid disposal off-site and to avoid producing additional activated soil in the future around the BDF. The soil will be backfilled such that the most activated soil will be placed closest to the new junction cavern or extraction tunnel structure.

Construction sequencing will also be optimized to avoid double-handing, i.e. storage of material prior to deposition will be minimized.

11.3.2 Extraction tunnel

Following a detailed integration study, the internal dimensions required for the extraction tunnel were set. The resulting dimensions of the 165 m long extraction tunnel will be 5.8 m wide × 5.1 m high (Fig. 11.7).

The form of construction will be similar to that used for the junction cavern, i.e. pre-cast RC 'n' units 1–2 m long on a cast-in-situ RC base slab. For the majority of its length, however, diaphragm walls will also be required for two reasons: to allow construction close to TCC2 and to significantly reduce

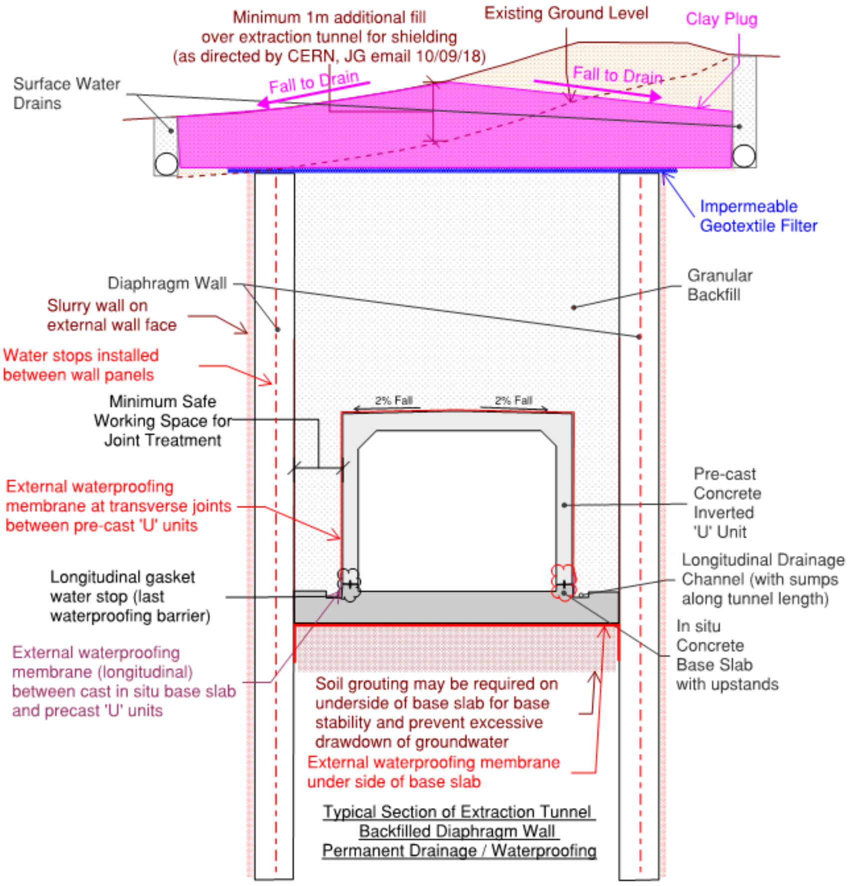

Fig. 11.7: Typical cross-section through the extraction tunnel, showing diaphragm walls and multilayer passive waterproofing systems.

the extent of excavation required in comparison with an open-cut solution (Fig. 11.8). Some propping within TCC2 may still be required for stability during the works, depending on the extent of asymmetric loading applied.

The approach followed in the junction cavern will be replicated here for waterproofing, but with an additional clay 'plug' and geomembrane used above the diaphragm walls and with formalized drainage provided to collect surface water.

As noted earlier in the chapter, the works to construct the junction cavern and the first approximately 80 m of the extraction tunnel (within an 8 m offset from the beam line) will need to be executed outside operational beam runs. Despite selecting options to reduce the duration of these works as far as practical, this will still mean aligning the programme with a long shutdown.

11.3.3 Access and auxiliary buildings

Above ground, the auxiliary and access buildings will be basic steel portal frame structures with cladding to provide watertightness and insulation.

The 60 m long × 20 m wide auxiliary building has a false floor to allow maintenance access to the large quantity of services contained within. It will be supported on RC shallow strip foundations, since it does not bear directly on the extraction tunnel.

At the auxiliary building, the extraction tunnel diaphragm walls will extend to form a 'box' to enable construction within (Fig. 11.9). This will maintain a watertight perimeter. The walls will con-

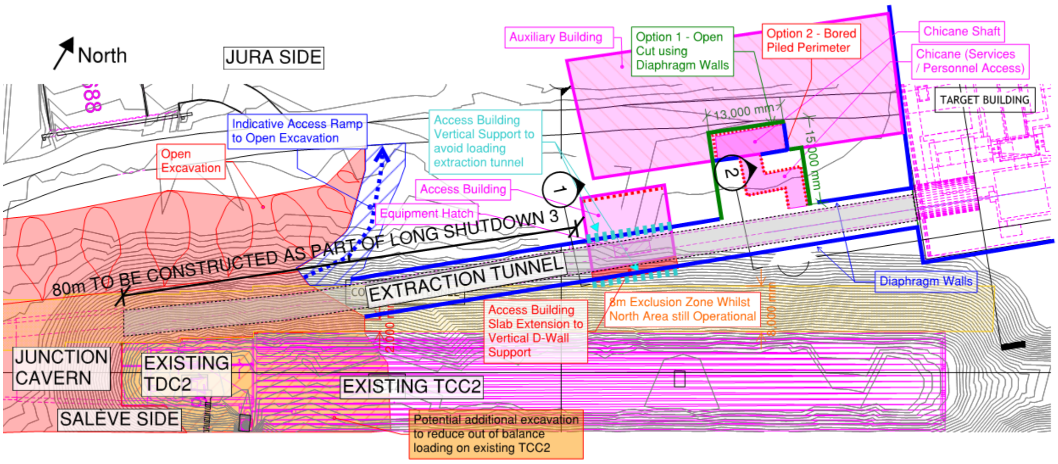

Fig. 11.8: Plan view of extraction tunnel, showing extents of open cut (shaded red) and diaphragm walls (blue).

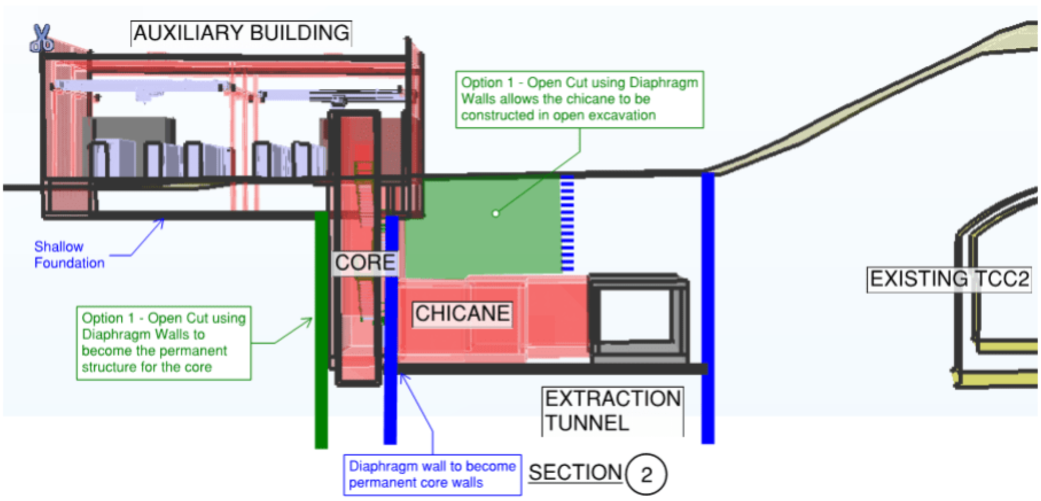

Fig. 11.9: Sectional schematic view showing the access core and chicane within diaphragm wall 'box'

tinue to provide a permanent shell to an underground core providing personnel and service access to the extraction tunnel.

The 15 m long × 12 m wide access building is located above the extraction tunnel (Fig. 11.10). It will require a deep foundation to avoid uneven loading on the extraction tunnel. A transfer structure will be required to support the shaft and concrete shielding, potentially utilizing the diaphragm walls via a shear connection if required.

11.3.4 Target complex

The target complex building will be a 58 m × 36 m building with 15 m above ground and 17 m below. The structure will be characterized at the surface by a steel frame main hall equipped with a 40 t crane. The wall to the north-west will, however, be partly formed from a retaining wall to accommodate a ramp. The basement structure will be formed from diaphragm walls with RC internal structures.

Several target-handling options remained in discussion at the time the CE study was undertaken. The 'trolley concept' option, as shown in Fig. 11.11, was agreed on as a baseline for CE work. The principles of the CE study could be equally applied to other options nonetheless.

Because of potential radioactive contamination, special measures need to be taken in the target complex to minimize the amount of groundwater that is able to seep into the underground facility or,

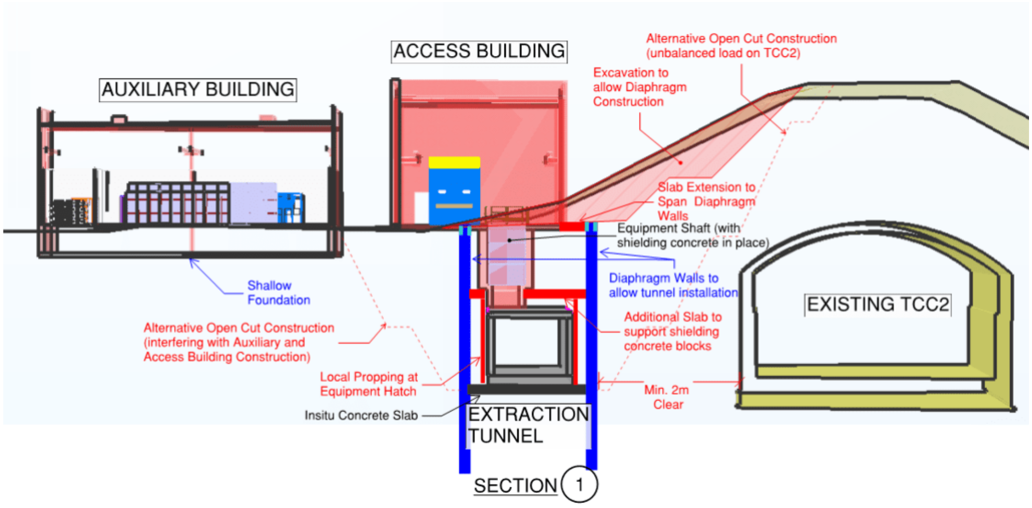

Fig. 11.10: Sectional schematic view showing the proposed arrangement around the access building heavy equipment shaft and its relationship with TCC2.

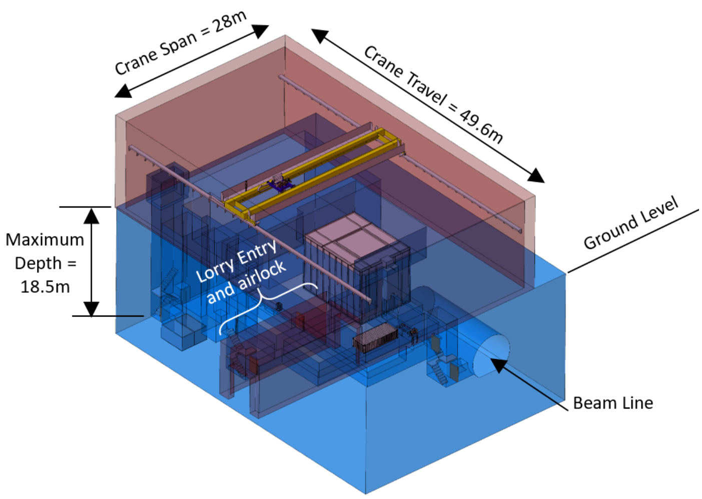

Fig. 11.11: Isometric view of 'trolley concept' target building, showing above-ground surface hall in red and underground areas in blue.

alternatively, permeate from within to the surrounding soil and groundwater. This has dictated the use of diaphragm walls, which provide the best solution in terms of permeability to groundwater. Further details of the necessary measures are noted in the full civil engineering feasibility review [1].

The diaphragm walls will be lined to provide an acceptable interior for the basement of the complex.

Tolerances and settlement were looked at as part of the study, since they are key to the operation and installation of the target and helium vessel (as they are very sensitive to movement).

The roughness and evenness of the slabs in the area supporting the helium vessel are critical to evenly distributing the very significant point loading generated by the cast iron shielding. An evenness of 3 mm per 3 m straight edge could be achieved by use of a combination of the following measures:

– enhanced preparation of subgrade (if ground-bearing) or specialist formwork and falsework;
– pouring concrete in thin strips (this would add to the duration of the works);
– specialist concrete mixes to reduce shrinkage;

– trial slabs;
– self-levelling toppings (which may be placed at the final fit-out stage to allow construction traffic).

Steel-lamina-reinforced elastomeric strips or pads, similar to those used in bridge bearings, are also suggested for reducing the sensitivity to any discontinuities. Elsewhere, tolerances are achievable within industry norms for a very flat/even specification.

An overarching strategy has been adopted to minimize settlement between the extraction tunnel, the target complex, and the experimental area. The following measures are proposed.

– The target complex is massive and will act as an anchor point for other structures, which will be stabilized by it.
– Shared diaphragm walls between the target complex and both the experimental area and the extraction tunnel will help to limit differential movement between areas.
– Specific connection details will be provided at joints between areas.
– This arrangement will allow continuity of the base slab between the target and experimental areas.

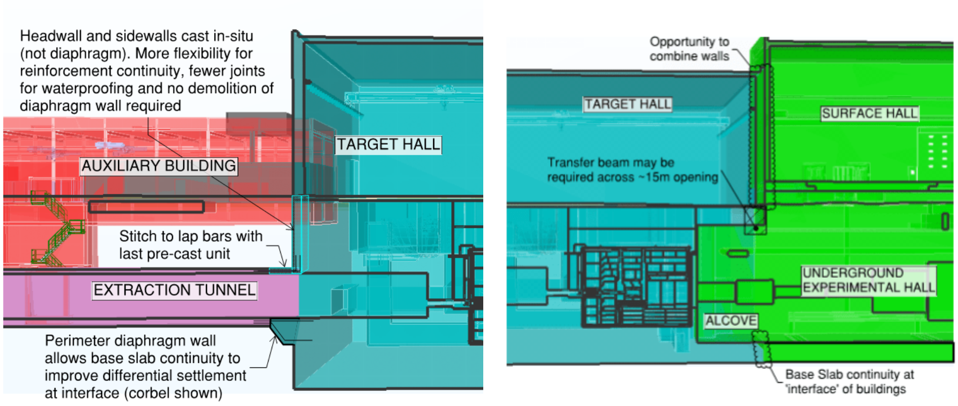

Fig. 11.12: Sectional schematic views showing the specific connection details to be used at the interfaces between the target complex and the extraction tunnel (left) and between the target complex and the experimental area (right).

Since the target is the most sensitive element for settlement, differential settlement will be controlled relative to it. The above measures should be sufficient to limit differential settlement to levels which can be dealt with through adjustment of supports along the beam line and the detector equipment. Elsewhere, however, ground movements are hard to predict, and detailed numerical analysis will be required as part of the design development.

The target complex is also characterized by several underground areas of different size, depth, and internal dimensions (i.e. the target bunker, the muon shield tunnel, cooling and ventilation rooms, and a storage area), as well as a trolley and crane for remote handling and operation. The technical aspects of these areas have been fully described in Chapter 6.

11.3.5 Experimental area

The experimental area's main structures are the underground experimental hall and the surface hall (Fig. 11.13). The experimental hall measures 120 m long × 20 m wide, with two sections of lengths 88 and 32 m at floor levels of 16.5 and 19 m depth, respectively, below ground level. The building will be composed of a diaphragm wall perimeter with a large RC base slab. At the top of this 'box', another RC floor slab spans between the walls, with three openings of 14.5 m × 18 m to allow vertical access for assembled components from above. The openings will be filled with eighteen 1 m deep removable pre-cast, pre-stressed, pre-tensioned RC beams. The underground area will be equipped with two cranes of 40 and 80 t capacity running at the same height. Access will also be provided for services and personnel via an underground core with stairs and lift, offset from the main hall. An alcove projects into the target hall at the joint between the structures, as shown in Fig. 11.12. The foundation of the hall will be thickened beneath the main detector components where necessary to accommodate the large punching shear and allow distribution of loads.

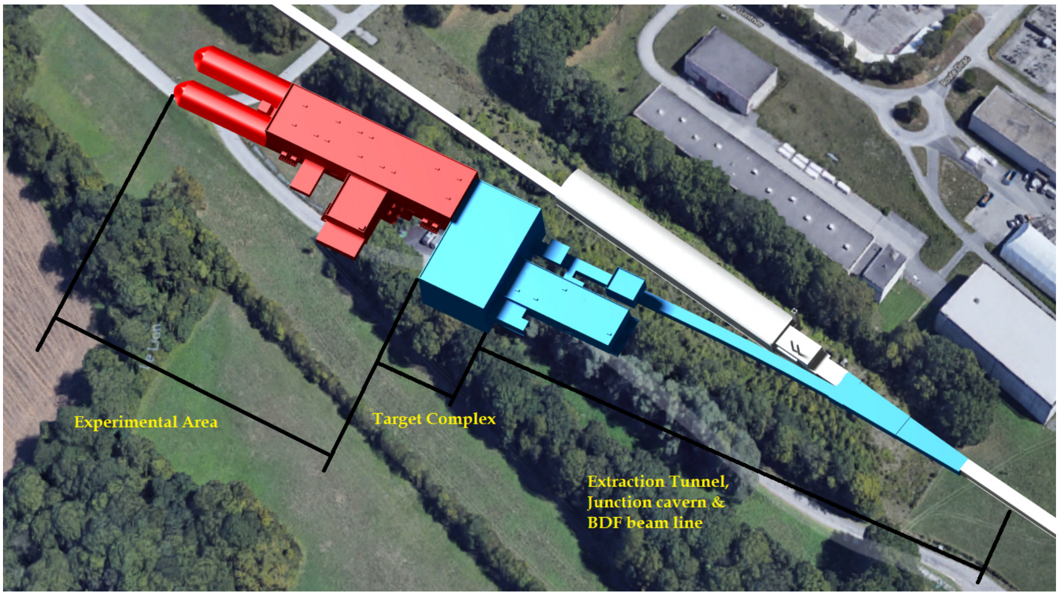

Fig. 11.13: 3D Aerial view of experimental area in relation to other infrastructure

The surface hall will be a more conventional clad steel frame structure, 100 m long and 26.5 m wide with a maximum height of 16.5 m. The structure will be just slightly wider than the hall below. This building will be served by independent 40 t and 10 t cranes supported by separate rails.

It is envisaged that the experimental hall could be extended a further 100 m on the same alignment if required in the future for further developments, assuming similar extents of shielding and fenced supervised area beyond.

11.3.6 Service and gas buildings

A three-storey service building with a basement structure will be provided within the experimental area, although it will also provide facilities for the target complex. This building measures 20 m $\times$ 34 m in plan, extending 12 m above ground and 2.4 m below. The building extends on the Jura side at ground level to house a workshop with a 5 t capacity crane. The building foundation will also form the basement structure, with a perimeter of RC cantilever retaining walls sharing a common footing constituting a floor slab. The reminder of the structure will be a simple steel frame building, with a lift and stairs in an RC core providing stability. This building is at a preliminary design stage.

A basic steel frame gas building measuring 15 m $\times$ 10 m, 3 m tall on a simple RC raft foundation is to be located close by.

11.3.7 Ancillary infrastructure and general considerations

11.3.7.0.1 Loading

Detailed specifications were produced for the loading in each area by the teams responsible in collaboration with the FAS team [6, 7, 8, 9]. These were used in the development of CE proposals.

11.3.7.0.2 Site levels and hardstanding

The existing site levels vary significantly, and the design has looked to tie into these while ensuring that the finished floor levels of buildings are suitable for avoiding surface water flooding issues [10]. Approximate finished levels for areas of hardstanding have been proposed, along with a ramp of suitable gradient between the differing site levels outside the experimental area and the remainder of the site as noted in Fig. 11.2. A requirement of a maximum gradient of 6% has been respected in line with the requirements of CERN's transportation service.

Vehicle swept path analysis was carried out to ensure that the operation of the access roads and access to facilities will be suitable for all necessary vehicles.

Assumptions were made about the areas of parking to be provided for each facility, which will need to be refined at a later stage when the building occupancy is fully defined. Estimated parking needs can be accommodated within the area of hardstanding provided. Specific parking areas are not shown on drawings.

11.3.7.0.3 Access roads and technical galleries

An access road will be provided, linking to existing roads at the Route de Broglie and an unnamed road to the south-west, allowing access to each part of the BDF.

Technical galleries have been assumed alongside access roads to allow connection of the proposed facilities to the existing service networks. Culvert-type galleries 2 m wide and 1 m deep with RC removable concrete lids at regular intervals are envisaged for access. An indicative layout is shown in Fig. 11.2, but this will need to be refined when service supplies are studied in more detail.

11.3.7.0.4 Earthworks

The volume of earthworks arising out of the project is significant, predominantly because of the substantial underground structures required. Excavated material will be re-used as far as possible for backfill above structures and to create the required levels across the site. A large amount of fill material will be required to bring the access road to the north and the hardstanding levels at various points across the site up to the required levels. Imported structural fill will be used to provide a solid foundation for the roads and hardstanding, while lower levels, verges, and the surrounding area will be infilled with excavated material. Careful selection and control of materials during placement and recompaction will be needed close to roads.

There will still be a large volume of excess 'cut' material beyond this, and it is assumed that this can be stockpiled permanently on-site to minimize costs. Areas have been identified as suitable for stockpiling. Weaker materials will be permanently stockpiled in mounds.

11.3.7.0.5 Drainage

Drainage needs have been looked at along with the impact on existing site drainage. Outline design assumptions have been made to enable costing, although a full design cannot be completed until the capacity of the existing drainage systems is better understood.

11.3.7.0.6 Seismic design

According to the Décret no 2010-1255 du 22 Octobre 2010 portant délimitation des zones de sismicité du territoire français, CERN is classified as in seismic zone 3, 'sismicité modérée'. The requirements on the project for dealing with seismic response should be achievable through careful design to Eurocode 8. The seismic response is highly dependent on ground conditions, and so more detailed work will be needed on this, following ground investigation at the next stage of development.

11.3.7.0.7 Existing infrastructure

The 'Zone 9103' buildings and an area of hardstanding will need to be relocated or reprovided as part of the project.

11.4 Recommendations for work at the next stage of project development, and opportunities

The CE study carried out has necessarily worked to an appropriate level of detail for this stage of project development. At the next stage, more detailed studies will be required to inform the detailed design. The following further studies and investigation work have been identified:

- A detailed ground investigation will be required to confirm or disprove existing assumptions and, in particular, obtain more detailed boreholes extending to bedrock in this area. The opportunity should be taken to gain detailed information on groundwater movement and perched water tables.
- Activation of soil around the existing TDC2 should be confirmed, as this will help to enable planning and tendering of works.
- Further study will be required to confirm service supplies from existing networks and then optimize the location of the technical galleries needed.
- Consideration will be required to avoid or minimize any impact on adjacent beam line operations and experiments during construction work. Vibration could be an issue, and mitigation measures may be required for work carried out during 'beam on'. Tunnel monitoring is also likely to be required during works.
- Flood risk assessment and basic hydrological modelling will be required to ensure that the risks and requirements are fully understood, to be able to confirm design levels for parking areas, thresholds, and waterproofing details.
- A ground-penetrating radar survey should be carried out to confirm the location of services.
- A survey and study of existing drainage systems should be done to assess their condition and capacity in order to design connections and replacement drainage systems where necessary.
- An optimization exercise for reduction or substitution of concrete fills in the target complex should be carried out.

It is recommended that, if the project receives approval, this additional work should be carried out as soon as possible.

References

[1] Arup. *CERN SPS Beam Dump Facility (BDF) Civil Engineering Feasibility Study: Arup Task 2 Feasibility Design Evaluation*. 2018. URL: https://edms.cern.ch/document/2058818.

[2] GADZ. *Sondates et Etude Geotechnique concernant le projet Neutrino Base Line CENF. Final Report*. 2014. URL: https://edms.cern.ch/document/1311633.

[3] F. Aberle. *First Radiological Assessment: Impact Study of the Civil Engineering Works for the BDF Excavation of TDC2*. Unpublished. 2018.

[4] M. Calviani et al. *Conceptual Design of the SHiP Experiment Target and Target Complex*. 2016. URL: https://edms.cern.ch/document/1465053.

[5] Arup. *CERN SPS Beam Dump Facility (BDF) Feasibility Study: Task 1 Radionuclide Study of Junction Cavern Area*. 2018. URL: https://edms.cern.ch/document/2030381.

[6] L. Dougherty. *BDF—Structural Specifications for the Access Building, Auxiliary Building, Personnel Shaft and Chicane*. 2018. URL: https://edms.cern.ch/document/2000961.

[7] L. Dougherty. *BDF—Structural Specifications for the Transfer Tunnel*. 2018. URL: https://edms.cern.ch/document/2037312.

[8] K. Kershaw. *Input to Civil Engineering for BDF Target Complex Main Building*. 2018. URL: https://edms.cern.ch/document/2019052.

[9] P. Santos Diaz. *BDF—Structural Specifications for the Experimental Area*. 2018. URL: https://edms.cern.ch/document/2011390.

[10] Arcadis. *Civil Engineering Feasibility Study Report, Main Structural Calculation Notes and Preliminary Layouts Concerning the Target Complex Developed in the Frame of the CENF Project*. 2015. URL: https://edms.cern.ch/document/1508827.

Appendices

Appendix A

Road map

A.1 Status

In 2016, the BDF team were charged by CERN management to complete key technical feasibility studies of the proposed facility in time for the European Strategy for Particle Physics (ESPP) update process. This was in conjunction with a recommendation by the CERN SPS and PS Experiments Committee (SPSC) to the SHiP experiment to prepare a Comprehensive Design Study as an input to the ESPP update. Material and personnel resources were made available to perform in-depth studies and prototyping. The key areas addressed were extraction and beam transfer, the target and target complex, radiation protection, safety engineering, integration, and civil engineering.

Since inception, there has been sustained effort with good progress on all fronts as described in detail in this report. In brief, the study has addressed all pertinent technological challenges, and in-depth studies and prototyping have been performed or are already well under way for all critical components and systems. Through a mixture of novel hardware development, beam physics, and technology, the study and prototype validation have shown that the SPS can deliver a beam with the required characteristics, with acceptable losses, to a robust target housed in a functional and secure target complex. The radiological implications appear manageable, the technologies and their deployment, although challenging, appear to be within CERN's established competencies, and the project, given the resources, is ready to move towards the detailed design and execution phase.

A.2 Feasibility study phase

The feasibility study phase will come to an end with the delivery of this Comprehensive Design Study, which is timed to coincide with the ESPP update process.

With the go-ahead from CERN management, under the continuing auspices of Physics Beyond Colliders, it is foreseen to continue these studies in 2019 and 2020. Specific areas include:

- post-irradiation examination of the target prototype tested in 2018;
- design of helium vessel and preparation for prototyping;
- construction and testing of a prototype laminated switch/splitter magnet;
- an intermediate iteration of system integration;
- development and possible prototyping of the hadron absorber magnetization system;
- continued studies of techniques for loss reduction during slow extraction from the SPS and deployment of these techniques with operational beams (planned for the SPS run starting in 2021);
- the site investigation required for a definitive civil engineering study.

A.3 Studies during the Technical Design Report phase

By 2020, the BDF team will be in a position to seek approval to go ahead with the preparation of a Technical Design Report. While working towards the delivery of the Technical Design Report, it is envisioned that it will commence:

- detailed engineering studies and specification of deliverables for both the standard and the novel systems;
- detailed integration plans;

– civil engineering pre-construction activities, i.e. environmental impact study, build permit submission/approval, tender process, and detailed civil engineering design;
– definitive radiation protection studies.

Appropriate progress with these activities, some of which would follow after approval, could lead to the delivery of the Technical Design Report in 2022. The aim would be to seek project approval in 2023, allowing subsequent project execution to take advantage of the North Area stop during LS3.

A summary of the possible evolution of the BDF project is shown in Table A.1.

Table A.1: Outline of a possible time line for the BDF

2020	Approval to go ahead with Technical Design Report
2020	Continued design studies and prototyping
2021–2022	Engineering design studies towards Technical Design Report
	Detailed integration studies
	Specification towards production
	Begin CE pre-construction activities: environmental impact study and detailed CE design and pre-tender process
2022	Technical Design Report delivery
2023	Seek approval
2023+	Tender, component production, CE contracts

Some further investigation work, as detailed in Chapter 11, will need to be carried out before detailed civil engineering design can begin with specialist external consultancies. Once these designs are complete, tendering for the civil engineering construction contracts can start. In parallel, an environmental impact study must be prepared and approved by the local authorities, prior to timely submission of a building permit application for the project, to allow construction works to commence.

A.3.1 Civil engineering schedule and resource considerations

The civil engineering work is split into four main packages, as indicated in Fig. A.1. The WP1, WP2, and WP3 activities can be performed during normal beam operation in the North Area, where the only constraint is a requirement to maintain 8 m of earth shielding on TCC2 given by radiation protection considerations. This is discussed in more detail in Chapter 11.

WP4 includes all of the activities that must be carried out during a beam stop, which is likely to be during the Long Shutdown 3 of the injectors. This will include the demolition and reconstruction of the junction cavern along with the construction of the extraction tunnel up to the point where the distance between proposed extraction tunnel and TCC2 increases to 8 m.

The current beam operation schedule includes approximately 12 months of shutdown without beam during LS3. This is unlikely to be sufficient to carry out the required civil engineering works. Other activities such as cool-down of the machine and tunnel, infrastructure dismantling/re-installation, and testing/commissioning must also be considered in the works schedule to calculate the required period of North Area shutdown. An extension of the North Area shutdown to, say, 24 months would also be beneficial for addressing important requirements for the consolidation of the overall SPS NA complex. Any extension of the long shutdown of the injectors would be in parallel with an ongoing LHC stop.

The working assumption for the moment is that the reconstruction of the junction cavern and construction of the first part of the new transfer line will take around 1.25 yr. The required cool-down period after the stop of North Area operation could be partially covered by an ion run at the end of the preceding operating period. As this work package is not on the critical path, a generous cool-down period

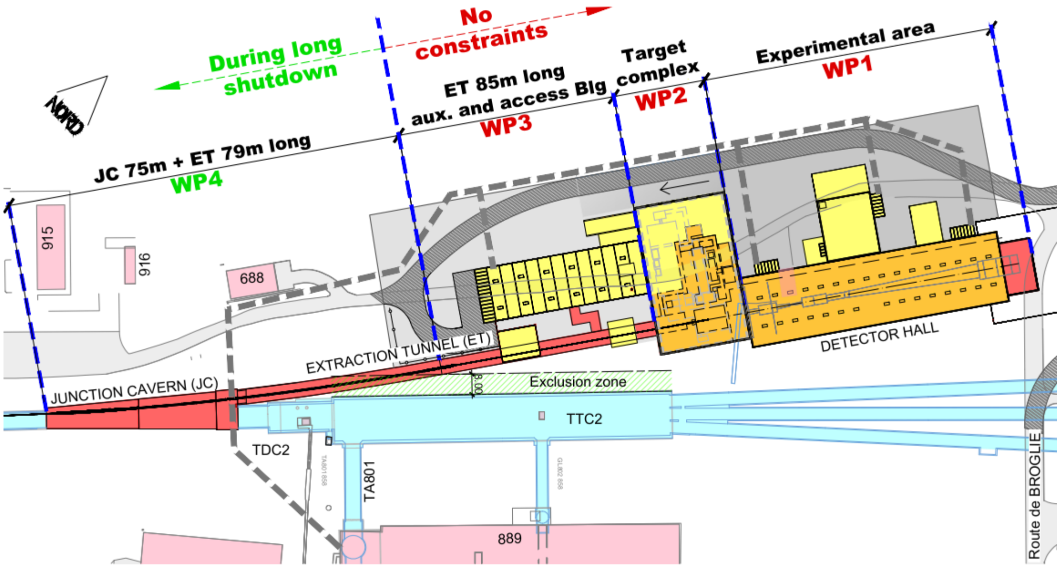

Fig. A.1: Indicative division and sequence of work packages for delivery of BDF project

can be allowed, increasing the duration of the work package to 1.75 yr, including 1.5 months for removal of services and equipment.

In principle, work packages can be partially executed in parallel, although this needs to be studied in more detail and set out carefully in contract documents to avoid cost increases arising from contractors working in close proximity to one another. Various activities, including construction of access roads, technical galleries, and other non-area-specific tasks, have been included as miscellaneous works and have not been assigned specifically to any work package. It is likely that these activities will need to be done as advanced enabling works or as part of the first work package (WP4).

The key drivers of the construction phase are outlined below. The figures shown do not include contingency. Radiological considerations have been taken into account.

- *Civil engineering underground works* are estimated to take 3 yr:
  - 1.75 yr for the reconstruction of the junction cavern and the construction of the first part of the new transfer line, including cool-down etc. (WP4);
  - 1.25 yr for the final part of the new transfer line and access shafts (WP3);
  - 1.5 yr for the target complex (WP2);
  - 1.75 yr for the experimental hall (WP1);
  - 0.75 yr for the foundations of the service buildings.
- *Civil engineering surface works*, following on from the associated underground works, are estimated to take 2.5 yr:
  - 0.75 yr for the access building and auxiliary building;
  - 1.0 yr for the service building and target hall;
  - 1.0 yr for the experimental hall;
  - 1.0 yr for the experimental-area service buildings.

  These work packages can be executed in parallel with underground work where appropriate.

A.3.2 Component production and installation

Component production and preparation can continue during the execution of the civil engineering phase. This will include production and preparation of standard beam line elements (magnet refurbishment, and production of splitters, power converters, beam instrumentation, vacuum components, etc.) and delivery of the target assembly, helium vessel, target handling, shielding, and other components for the target complex.

Installation can be staged as the structures become available. Approximate time estimates for this phase are given below:

- junction cavern hardware and services: 6 months for re-installation, including testing and commissioning;
- installation of hardware and services for the extraction beam line: 6 months;
- installation of hardware and services for the target complex: 2.5 yr;
- installation of hardware, services, access and safety systems, and metallic structures, electrical and cabling activities, and installation of IT network, for the access and auxiliary buildings: 15 months;
- experimental hall: the entire installation phase, including the detector, around 2.5 yr.

A.3.3 Schedule

The medium-term schedule (circa 2019) of the injector complex and the LHC foresees a long shutdown (LS3) for the injectors in 2025. LS3 stretches from 2024 to midway through 2026 for the LHC.

An indicative schedule for the preparation and execution of the BDF project is shown in Table A.2. The uncertainties are significant at the present study phase of the project. The time estimates on the civil engineering front are based on knowledge acquired from construction for previous similar projects at CERN, and the analysis performed in conjunction with an external company as described in Chapter 11. The production and preparation of beam line components is something that CERN is well versed in. The truly novel exercise will be the installation, testing, and commissioning of the target complex, and this will be an exploratory process for CERN.

The following points should be noted.

- Component production and preparation can continue in parallel with civil engineering.
- Non-junction-cavern work packages can take place in parallel with beam operation. They would be staged and start as soon as feasible.
- Surface work can begin when associated underground structures are complete or in some cases before, to provide protection from the weather.
- The overall goal is to commence data taking as soon as reasonably possible in Run 4.

Table A.2: Outline of an indicative time line for execution of the BDF project

Indicative dates	Years	Activity
2023–2024	2.0	*CE pre-construction*
		Environmental impact study
		Building permit submission/approval
		Tender and CE detailed design
2023–2025	3.0	*Component production*
		Beam line systems and components
		Tender for production of technical services
		Target assembly
		Handling systems etc. for target complex
2025–2027	3.0	*Underground CE*
	1.25	Junction cavern/beam line part 1
	1.25	Beam line part 2/access building
	1.5	Target complex
	1.75	Experimental hall
2026–2028	2.5	*Surface CE*
	0.75	Access and auxiliary buildings
	1.0	Service building/target hall
	1.0	Experimental hall
2026–2028	2.5	*Installation*
	0.5	Junction cavern/beam line part 1
	0.5	Beam line part 2
	1.25	Access and auxiliary buildings
	2.5	Service building/target hall
	2.0	Experimental hall

Appendix B

Cost estimates

B.1 Introduction

The cost estimates presented here essentially map on to the work package breakdown of the study:

– extraction, targeting SPS losses, activation, and mitigation measures;
– design of TT20, switch, and new transfer line;
– target and target complex;
– radiation protection;
– safety engineering;
– integration (junction cavern, beam line, target complex, detector hall);
– civil engineering.

Overall, a class 4 (intermediate, i.e. concept or feasibility study) cost estimate has been performed. An outline justification for this categorization follows.

B.2 Material

B.2.1 Junction cavern and dump line

In terms of relative expense, the slow extraction system of the SPS and the transfer line TT20 are in place, and, although these are critical, future developments will not represent a major capital investment. Once constructed, the new beam line will be a relatively standard CERN design, and the associated cost estimates for services and integration can be taken as solid. The hardware for the switch and the new transfer line are well defined and certainly well within CERN's expertise and, again, the figures quoted below can be taken with a reasonable degree of confidence.

The hardware costs for the junction cavern and the new transfer line to the target complex are shown in Table B.1. The costs for global systems (cooling and ventilation, electricity distribution, survey, access system, radiation monitoring, and handling engineering) are covered in Section B.2.3 below.

B.2.2 Target and target complex

The target itself is a challenging development. Good anticipatory understanding of the costs has been gained in the production of the prototype, and it will certainly be a relatively expensive component.

The target complex design team have worked with an external company that specializes in the design of high-radiation complexes and the handling in them. In collaboration with this company, two handling concepts, based on a trolley and overhead access, were developed and costed (see Chapter 6).

In the summary shown in Table B.1, the trolley concept is taken as the baseline. Another proposal incorporating features of both concepts is under study, with anticipated costs potentially lower than for the pure trolley concept.

B.2.3 Global systems

The cost estimates for the standard global systems have benefited from our working with the respective CERN groups (cooling and ventilation, access, radiation protection, safety, survey). These groups are generally well versed in the production and deployment of the solutions foreseen, and the estimates may be considered sound. Owing to lack of resources, the costs of electrical distribution are based on a previous estimate and must be regarded as approximate. The cost estimates for global systems and services are summarized in Table B.1.

B.2.4 Civil engineering

The estimates for the largest work package in terms of cost, civil engineering, have benefited from collaboration with specialized external companies with a history of working with CERN. These companies have scrutinized and endorsed the CE cost estimate presented below. Here, the uncertainties have been reduced with respect to the 2015 exercise [1] and the quoted total can be regarded with some degree of confidence. However, until the required ground investigations have been performed, the estimate remains class 4.

B.2.4.1 Basis of estimate

The cost estimate for the BDF project was based on the layouts presented in Chapter 11. The estimate produced includes all aspects of construction, detailed engineering design work, and construction management except where stated otherwise. Many of the rates used to formulate this estimate are based on real construction costs from experience with the Large Hadron Collider (1998–2005), on cost studies of a future circular collider by a consultant (ILF) [2], and on recent tendering for similar projects at CERN such as CENF and the HL-LHC. In addition to this process, Arup independently reviewed the cost estimate as part of their scope of work, and the results were fed back into the costing process to ensure a robust estimate.

The civil engineering activities have been split into four primary work packages, as shown in Appendix A. The provisional costs for the main tasks identified and included in each package are shown in Table B.1.

Table B.1: Summary cost estimates for the CE work packages

Work package	Cost (MCHF)
Work Package 1	31.7
Work Package 2	16.5
Work Package 3	10.9
Work Package 4	7.3
Work Package 5	1.3
Site investigation	0.6
Facility total	68.3

The accuracy of the estimate is considered class 4, study or feasibility, and the final cost could be 15–30% lower or 20–50% higher (in line with AACE International's best practice recommendations [3], as have been used for previous CERN projects). Until the project requirements are further developed, it is suggested that a suitable band to adopt would be −20% to +40% for CE costs.

B.2.4.2 Costing assumptions and exclusions

The cost estimate is based on the following assumptions.

- Spoil can be retained on CERN land with no tipping and disposal costs. If this were to change, the cost increase would be significant.
- The proposed drainage can be connected into existing drainage without significant capacity enhancement of the existing system.

- Build-up of hardstanding areas and access roads can be carried out using site-won material with only 1.5 m depth of road construction.
- The radiation protection measures required for the works and the assumptions agreed are as stated in Ref. [4, 5].
- The construction works programme will be as stated in the schedule noted in Appendix A. This programme is outline and will need to be reviewed to optimize activities to allow multiple work packages to progress in parallel.
- Ground and groundwater conditions do not vary significantly from those previously found in the area.
- No improvements are required to the wider Prévessin site for office space, restaurants, main access, road network, etc.
- Building 687 will be demolished and a replacement constructed elsewhere, while the demountable buildings 6357 and 6575 and a container, 6361, will be relocated. An area of hardstanding will be provided to replace the existing area.
- Assumptions have been made about the required depth of diaphragm walling; however, the cost is very sensitive to changes in depth owing to the large proportion of total costs of the scheme relating to diaphragm wall construction (approximately 27%).
- Allowances have been made for temporary propping of TCC2 and excavations during diaphragm wall construction; however, this will depend on ground conditions, meaning that they are subject to change.
- An allowance has been made for four tensile fabric structures to temporarily house activated soil before re-use, with two thirds of the material re-used directly without intermediate storage.

All temporary facilities needed for the civil engineering works have been included in the cost estimate, but nothing for any temporary areas or buildings needed for machine or detector assembly/installation.

For clarity, the overall cost estimate does not include:

- SMB-SE resources;
- special foundation support for facilities (e.g. a detector);
- pre-cast concrete shielding blocks;
- tenting over the excavation and demolition of TDC2.

B.2.5 Material costs: overall summary

A breakdown of the material cost estimate is shown in Table B.2. A breakdown of the items in each of the main work packages is shown here.

A high-level summary of the estimated material costs for construction is shown in Table B.3.

B.2.6 Personnel

The breakdown shown below addresses the requirements for staff and fellows foreseen; both of these classes are identified as CERN personnel (member of personnel (MPE)). The installation of hardware, cabling, etc. will generally be performed by field support units. This is covered in the material budget summarized above.

The personnel estimate is based largely on the experience of the groups concerned. For well-established activities such as those associated with power converters and magnets, the estimates can be viewed with reasonable confidence; for more novel endeavours such as the target complex, the estimates should be regarded as preliminary at this stage.

Table B.2: Summary of material costs for BDF construction

Work package	Estimate (MCHF)
Civil engineering	68.2
Work Package 1	31.7
Work Package 2	16.5
Work Package 3	10.9
Work Package 4	7.3
Work Package 5	1.3
Site investigation	0.6
Extraction and beam line	9.6
Magnet refurbishment	0.7
Switch/splitters	2.1
Dilution system (MDX magnet)	0.52
Power converters	3.0
Beam instrumentation	0.8
Vacuum system	0.6
Interlocks	0.2
D.C. cabling	1.62
Target and target complex	45.5
Target assembly and annexe equipment	5.6
Instrumentation package	0.9
Bunker iron shielding and US1010	14.0
Concrete shielding	0.85
Magnetizing coil for US1010 shield	1.0
Target and coil handling system	19.1
Target and coil shielding casks	0.2
Helium vessel	2.3
Integration	0.6
Beam window(s)	0.6
Collimator(s)	0.5
Infrastructure and services	31.5
Cooling	7.4
Ventilation	6.3
Electrical distribution	5.6
Survey and alignment	1.1
Access system	1.4
Fire safety system	3.5
Radiation monitoring	0.4
Transport (inc. cranes and lifts)	5.1
Control infrastructure	0.7
Integration and installation	3.6
Installation	2.6
Installation, design support	0.6
Preparation, dismantling	0.4
Total	158.4

Table B.3: Overview summary of material cost estimates for the main BDF work packages

Work package/system	Estimate (MCHF)
Beam line and junction cavern hardware	9.6
Target and target complex infrastructure	45.5
Civil engineering	68.2
Cooling and ventilation	13.7
Electrical distribution	5.6
Survey and alignment	1.1
Access, safety, RP, controls	6.0
Transport (including cranes and lifts)	5.1
(De-)installation	3.6
Total	158.4

Table B.4: Summary of personnel requirements for BDF construction

Work package	Staff (FTE yr)	Fellows (FTE yr)
Civil engineering	23.5	7
Site investigation		
Junction cavern		
Extraction tunnel		
Target complex		
Experimental area		
Infrastructure and services	18.9	10
Cooling	3	–
Ventilation	3	–
Electrical infrastructure	1.3	1
Access and safety systems	5	–
Radiation protection	4.3	7
Survey	1	2
Transport: cranes, lifts, tooling	1.3	–
Extraction and beam line	28.0	11.5
Power converters	12	3
Magnets	4.5	–
Vacuum	2	–
Beam instrumentation	4	4
Interlocks	1	0.5
Optics design and commissioning	2	2
Software, layout, integration	2.5	2
Target and target complex	77.0	5.4
Target assembly and annexe equipment	15	0.9
Instrumentation package	5	0.45
Bunker iron shielding and US1010	3	0.6
Concrete shielding	3	–
Magnetizing coil for US1010 shielding	3	0.3
Target and coil handling system	25	1.8
Target and coil shielding casks	0.5	–
Helium vessel	11	0.6
Integration	6	–
Beam window(s)	2	0.3
Survey and alignment	3	0.3
Collimator(s)	0.5	0.15
Integration and installation	10.2	6
Integration and co-ordination	3	–
Installation, design support	4.2	6
Removal/installation in TDC2	3	–
Total	158	40

References

[1] SHiP Collaboration et al. *A Facility to Search for Hidden Particles (SHiP) at the CERN SPS*. Apr. 2015. arXiv: 1504.04956 [physics.ins-det].

[2] ILF. *FCC Cost and Schedule Study*. 2017. URL: https://edms.cern.ch/document/2050504/1.

[3] P. Christensen et al. *Cost Estimate Classification System—as Applied in Engineering, Procurement, and Construction for the Process Industries*. AACE, Inc., 2005.

[4] Arup. *CERN SPS Beam Dump Facility (BDF) Feasibility Study: Task 1 Radionuclide Study of Junction Cavern Area*. 2018. URL: https://edms.cern.ch/document/2030381.

[5] Arup. *CERN SPS Beam Dump Facility (BDF) Civil Engineering Feasibility Study: Arup Task 2 Feasibility Design Evaluation*. 2018. URL: https://edms.cern.ch/document/2058818.

Appendix C

Potential siting of a lepton flavour violation experiment

C.1 Introduction and experimental requirements

The BDF beam line offers a potential opportunity to host and operate in parallel an experiment (named 'TauFV' [1]) to search for lepton flavour violation and rare decays by taking advantage of the possibility of producing a very large sample of tau leptons and D mesons. Using a thin in-line target to intercept about 2% of the intensity delivered to the SHiP target, the experiment would have access to close to 8×10^{13} tau lepton and 5×10^{15} D^0 meson decays. The detector under study consists of a spectrometer 7.5 m long and 3 m wide including a vertex detector, a tracker, potentially a fast timing detector, an electromagnetic calorimeter, and a muon system. The experimental dipole produces a field of 2.5 T·m over a length of 2 m. It is desirable to be able to swap the polarity to manage systematic errors in the physics measurements.

The reconstruction of secondary vertices and suppression of background can be significantly enhanced by using a target made up of several very narrow blades, orthogonal to the beam and spaced by a few centimetres, in conjunction with a highly elliptic transverse beam profile with a beam sigma of greater than 4 mm in the plane parallel to a target blade, and preferably less than 1 mm orthogonal to a blade. This allows the secondary vertices to be discerned in two dimensions, and the interactions to be diluted along the blade to reduce pile-up. As discussed in detail below, from the point of view of beam optics, several locations can provide the required beam conditions and the beam drift space required to accommodate the detector along the BDF transfer tunnel between the TDC2 switchyard cavern and the BDF target station without affecting the location of the BDF experimental area and without significant changes to the configuration of the beam line. The choice is instead driven by considerations related to the civil engineering in the vicinity of existing installations, radiological protection, and access and transport requirements above ground and underground. Lateral space is required on both sides for shielding to limit the radiation exposure of the surrounding underground area to levels typical of the rest of the beam line.

Further simulation studies must be done to understand the impact on the SHiP experiment in terms of background. The flux arising from intercepting 2% of the beam is small, but the residual muon flux penetrating the target bunker enters the SHiP muon shield at a location and with an angular distribution for which it was not designed. This could potentially lead to capture of a fraction of the muons, increasing significantly the flux in the SHiP acceptance. This will be studied as the TauFV experimental configuration reaches more maturity.

C.2 Implementation on BDF beam line

C.2.1 Lattice modifications

The most suitable location to implement the TauFV experiment is about 100 m upstream of the BDF target. Figure C.1 summarizes the changes required to accommodate the TauFV requirements and the associated shielding. The detector is represented by the plain red rectangle.

The last four main dipoles must be moved downstream by around 40 m. This allows separating the beam axes of the TauFV experiment and the SHiP experiment by an angle of 21.9 mrad. An additional quadrupole, referred to as the 'New QTL', needs to be added after the TauFV detector to control the evolution of the beam size.

Beam sizes are represented by solid lines in Fig. C.1, and the apertures of the elements in the

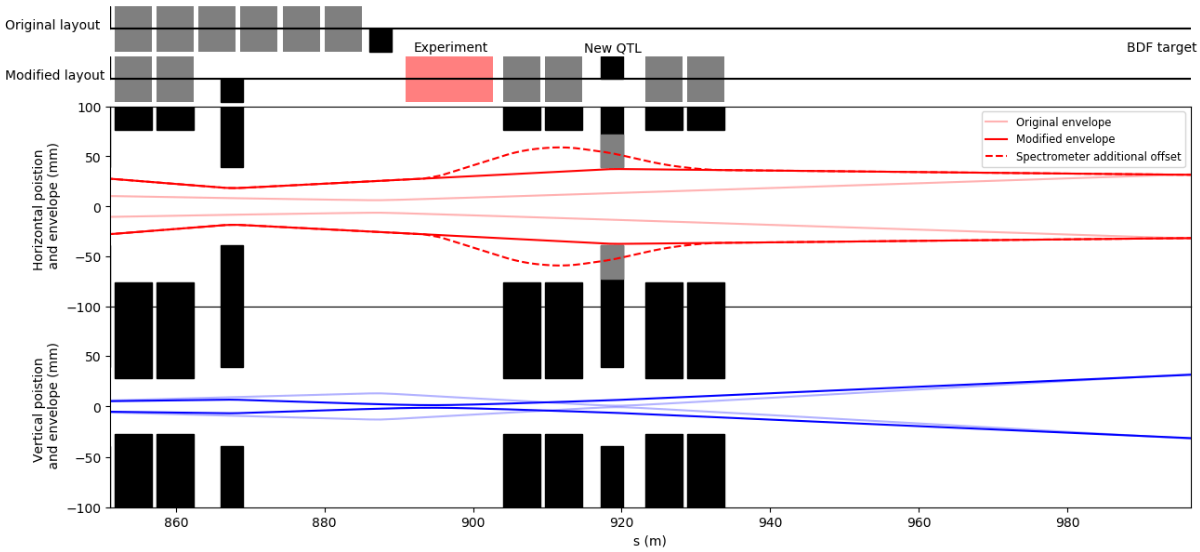

Fig. C.1: Synoptic view of the later part of the new BDF beam line, and apertures and beam sizes, without and with the TauFV experiment. In the synoptic view, dipoles are represented as grey bars, while quadrupoles are represented as black squares above the centre line for focusing magnets and below it for defocusing magnets.

modified layout are shown as black rectangles. The beam size is plotted as $\pm 4\sigma$, using $N = 4$ in Eq. (4.1) with the beam parameters discussed in Section 4.2.1. Comparing this with the original beam size in the nominal layout, shown by light red lines, the figure also demonstrates that the beam dimensions on the BDF target are preserved. The new beam line design allows producing a beam spot with $\sigma_x =$ 6.8 mm and σ_y = 0.34 mm in the horizontal and vertical planes, respectively, at the TauFV target.

The beam size and the magnet currents along the first part of the transfer line are very similar to the nominal case. Very small adjustments are required to satisfy the combined requirements of the TauFV target and the BDF target. The complete trajectory correction scheme has not been simulated for the new configuration, but with only small differences in the strengths of the quadrupoles, the correction scheme can remain the same. Studies of specific locations, such as around and immediately downstream of the splitter (see Fig. 4.5), confirm that the modified optics is compatible with the nominal design.

C.2.2 Spectrometer compensation

The experiment will use a 2.5 T·m spectrometer that will cause a deflection of the primary beam of up to 1.87 mrad. It is planned to be able to switch the polarity of the spectrometer magnet. To correct for the angle produced by the magnet of the experiment, the four downstream main dipoles will be employed in pairs. The first pair of dipoles generates a kick in a direction opposite to that of the spectrometer, while the second pair provides a kick in the same direction as the spectrometer. At most, the first pair will be powered to around 1400 A to provide up to 9.45 T·m per magnet. This is slightly beyond the maximum nominal strength of the magnets but remains achievable, since these magnets will only be pulsed to follow the BDF cycle. The second pair will be powered to up to 1240 A, or 8.32 T·m, which is below the maximum nominal strength for this type of magnet. This scheme allows compensation of the effect of the spectrometer without an additional magnet.

Horizontal apertures on both sides need to be considered, owing to the closed bump in the trajectory created by the spectrometer and its compensation. Figure C.1 shows in dashed red lines the additional apertures required to operate this scheme. The smallest aperture, shown in grey, at the level of the new QTL refers to a circular aperture. This considerably underestimates the available space, as the beam is much larger horizontally than vertically at this location. Because of the non-circular section of the vacuum chamber in this quadrupole, a more realistic representation of the available aperture is shown in black.

C.2.3 BDF dilution system

Lastly, the dilution system discussed in Section 4.3.3.1 will need to be strengthened. Its new location will be 40 m closer to the BDF target, which will thus require a system which is around 70% stronger. This has not been studied in detail, but the same design as chosen for the nominal layout can easily be scaled up by adding more units.

C.3 Target system

The TauFV target system consists of five tungsten blades of dimensions $40 \times 2 \times 0.4\,\mathrm{mm}^3$. The energy deposition on the target blades was estimated with FLUKA simulations [2]. The average energy density in each blade after one pulse is expected to be of the order of $450\,\mathrm{J/cm}^3$. Figure C.2 displays the energy density along the longitudinal axis for the different target blades, assuming 2×10^{20} protons on target.

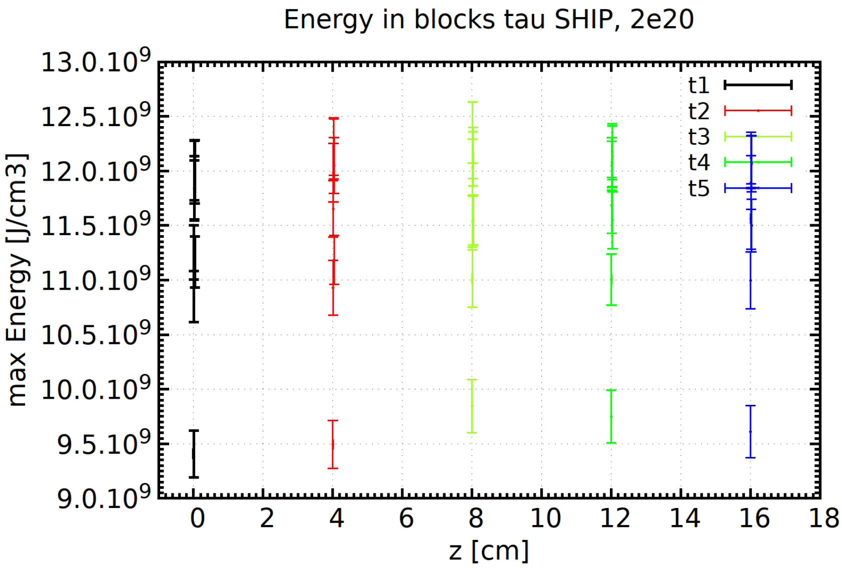

Fig. C.2: Energy distribution along the Z axis for five tungsten blades assuming 2×10^{20} protons on target.

Because of the high beam power deposited on such thin blades, and the fact that the surrounding vertex detector must operated with cooling, the target must be actively cooled.[1] The initial studies assumed an inert gas such as helium as the cooling medium for the target. Preliminary CFD simulations have been carried out to calculate the heat transfer coefficient that could be achieved with forced circulation of helium around the blades.

The preliminary study assumed that the thin tungsten blades are contained in a closed-loop tank in which the helium-cooling circulation system is enclosed. The horizontal cross-section of the helium volume is tentatively assumed to be $160 \times 40\,\mathrm{mm}^2$, designed in such a way that the whole volume of the target blades is contained. The blades are clamped on the top and bottom edges; the supports for the blades have also been included in the 3D CFD model. Figure C.3 presents the fluid-flow model of the whole helium circuit and a simplified quarter model of one of the blades used for simulation of the helium cooling.

[1]Otherwise, a radiatively cooled assembly under vacuum could have been proposed, as refractory metals could be operated at very high temperature.

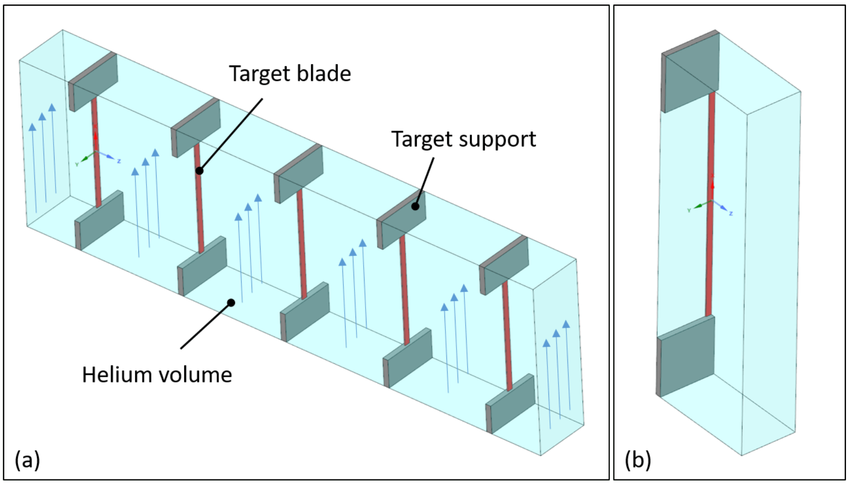

Fig. C.3: (a) Full 3D model of the design of the helium cooling system; (b) quarter model used for CFD calculations of the helium cooling circuit.

An initial flow rate of 684 m^3/h (equivalent to 34.2 m^3/h for the quarter case illustrated in Fig. C.3(b)) was assumed, which is expected to be realistic for the cooling system of such a device. This helium flow rate leads to an average helium velocity in contact with the blades of around 50 m/s, illustrated in Fig. C.4(a). The average heat transfer coefficient obtained at the surface of the tungsten blades is estimated at around 350 W/(m^2·K), as shown in Fig. C.4(b).

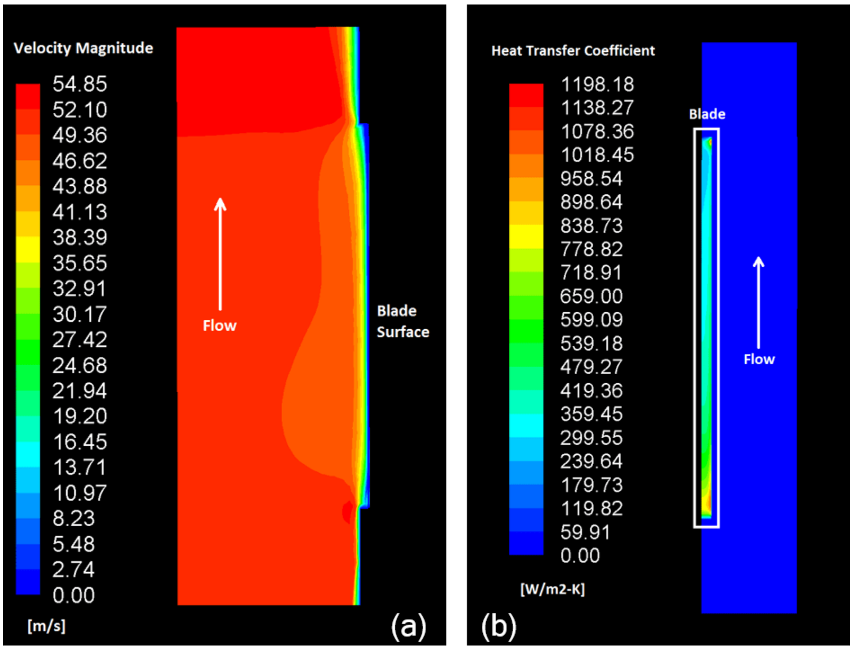

Fig. C.4: (a) Contours of velocity magnitude in a plane containing the blade centre lines. (b) Heat transfer coefficient on the surface of a blade.

The HTC value obtained was used as a boundary condition for FEM calculations aimed at validating the current target design from a thermomechanical point of view. The thermal simulations performed showed that the estimated convection through the helium leads to an acceptable temperature in the target blades, around 220 °C after a beam impact (see Fig. C.5). Given that tungsten is a refractory metal with a high melting point suitable for high-temperature applications, the temperature reached is within the limits for safe operation of the target. The compatibility of the resulting temperature and the helium flow with the global assembly will depend on the vertex detector system and its associated cooling system, which will operate close to the target assembly.

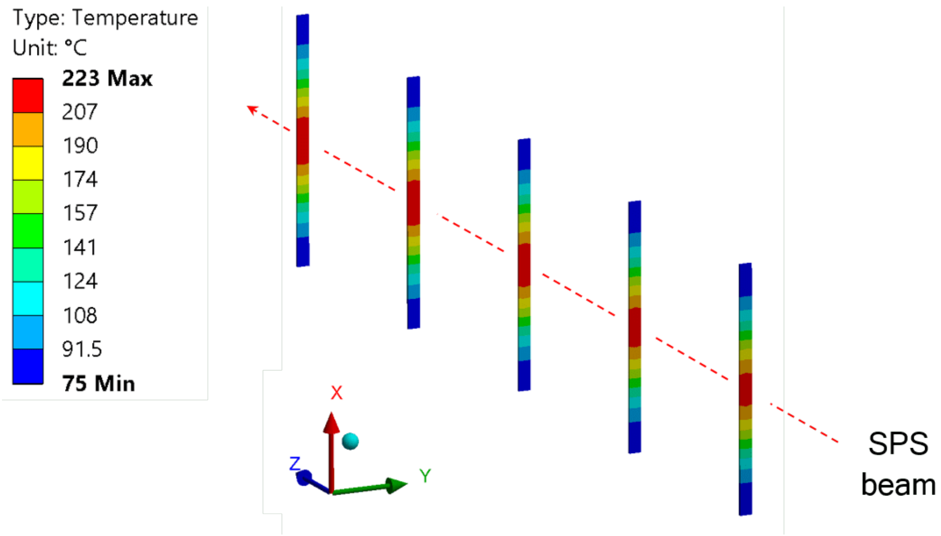

Fig. C.5: Temperature distribution in the target blades at the pulse peak. Maximum temperature ≈ 220 °C.

The thermal stresses induced by the temperature increase in the target materials were also calculated. As mentioned above, the blades are assumed to be clamped at the edges. Given the low ductility of tungsten at temperatures below 300 °C, the maximum-principal-stress criterion is the most suitable one for evaluating the safety margin of the target blades against failure. However, the stresses induced by the beam are purely compressive, and the calculated maximum principal stress is negligible. The maximum von Mises equivalent stress is equal to the maximum compressive stress, and is around 220 MPa, significantly below the tensile strength of the material at the operational temperatures (550 MPa at 300 °C [3]). The distribution of the von Mises equivalent stress in one of the target blades obtained from the structural calculations is presented in Fig. C.6.

Fig. C.6: Distribution of von Mises equivalent stress in a target blade at the pulse peak. Maximum stress ≈ 220 MPa.

In conclusion, this very preliminary analysis shows that the temperatures and stresses expected in the tungsten blades are well within the material limits, thus validating the preliminary target design for the current experimental set-up. The main challenges in the manufacturing of the target are associated with the production and machining of such thin tungsten blades, pure tungsten being a very brittle material at room temperature. Alternatively, a tungsten alloy with a NiFe or NiCu content could be considered, allowing a similar density but higher strength and ductility. Otherwise, slightly lighter materials with much more ductility, such as tantalum or tantalum alloys, could potentially be employed.

C.4 Radiation protection

C.4.1 Introduction

The main radiation protection challenges for TauFV arise from the high beam power, the proximity to the surface and the CERN fence, and the goal of minimizing the impact on the rest of the BDF complex. To respect the applicable CERN radiation protection legislation regarding doses to personnel as well as the environmental impact [4], a preliminary radiological assessment was carried out for the proposed set-up of the TauFV experiment. Specific studies of prompt and residual dose rates, as well as considerations of air and ground activation, will be described. To assess the above-mentioned radiation protection aspects, extensive simulations were performed with the FLUKA Monte Carlo particle transport code [2, 5].

C.4.2 FLUKA model

In the FLUKA model, for simplicity, the target was modelled as a 40 mm $\times$ 2 mm $\times$ 2 mm single tungsten blade. The experimental set-up modelled is shown in Fig. C.7. A helium vessel is provided to host the target and the vertex locator detector (VELO) to avoid corrosion. A spectrometer magnet[2] with downstream tracking stations is used for momentum measurement. The spectrometer is followed by a calorimeter, simulated as a gadolinium aluminium gallium garnet block with a density of 6.67 g/cm^3 20 cm thick, and a muon detector with iron filters, simulated as a 1.6 m thick iron block. The first 5.3 m downstream of the experiment are reserved for shielding. The shielding is followed by a 2.5 m long magnet to correcting the trajectory of the beam with a field inverse to that of the spectrometer magnet. Six dipole skeletons (without a magnetic field) of 50 cm $\times$ 50 cm $\times$ 500 cm are implemented downstream of the correcting magnet. The beam pipe, made of stainless steel, is cylindrical upstream of the detector, with a radius of $\sim$5 cm. In the experimental apparatus and inside the downstream magnets, the beam pipe is elliptical, with an aperture of 20 cm $\times$ 1 cm and 36 cm $\times$ 12 cm, respectively.

The shielding surrounding the helium vessel is composed of iron and concrete as follows:

– iron shielding on the top of (195 cm), on the bottom of (50 cm), on the side of (120 cm), and upstream of (80 cm) the helium vessel;
– concrete shielding upstream of the helium vessel and around the beam pipe, of dimensions 150 $\times$ 150 $\times$ 220 cm;
– iron (280 cm long) and concrete (90 cm long) shielding upstream of the top and bottom shielding of the helium vessel.

The iron shielding is 140 cm thick on the top of and 65 cm thick on the sides of the spectrometer magnet, the calorimeter, and the muon spectrometer. Downstream of the experiment, shielding 5.3 m long is provided. It consists of several layers:

– an elliptical inner layer of 5 cm tungsten encasing the beam pipe;
– an iron cylinder with a radius of 60 cm encasing the tungsten;
– a concrete parallelepiped of dimensions 390 cm $\times$ 390 cm $\times$ 530 cm surrounding the iron cylinder.

The magnets downstream of the shielding are surrounded by 80 cm $\times$ 240 cm $\times$ 160 cm (x, y, z) standard blocks of concrete for 10 m. To further improve the shielding and reduce the prompt dose to the downstream magnets, and to the tunnel and the soil:

[2]Only the yoke was included in the FLUKA simulations; the coil has not yet been included.

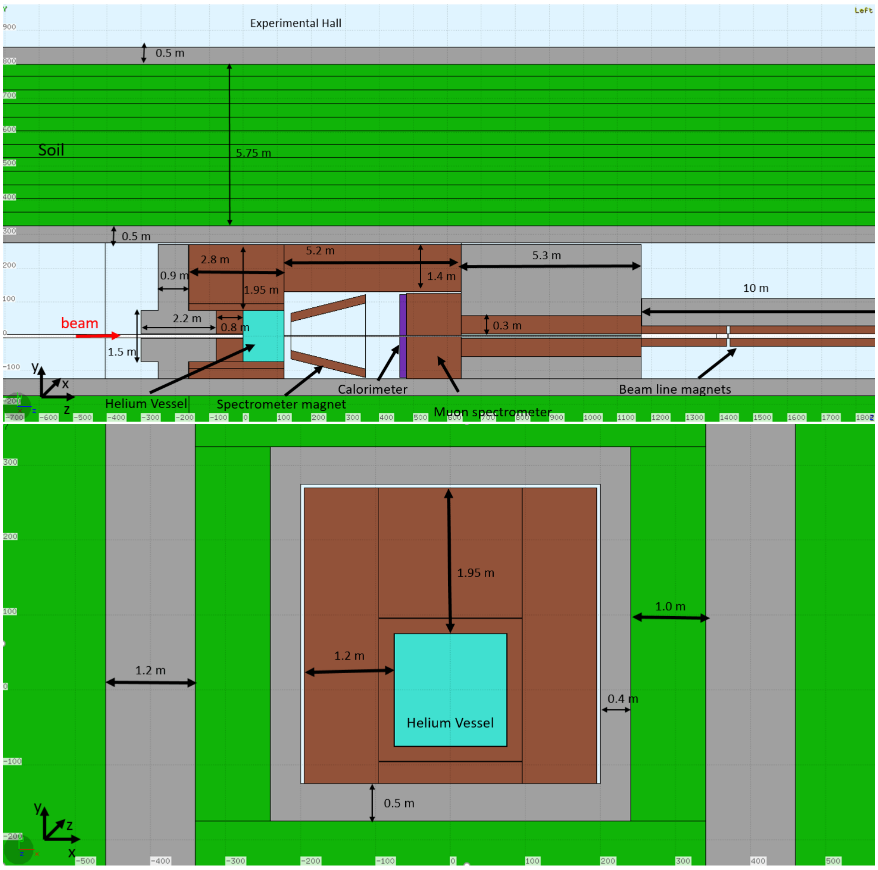

Fig. C.7: FLUKA model for TauFV. Vertical (top) and horizontal (bottom) views.

- the concrete shielding can be partially exchanged with iron;
- more collimators can be added further downstream;
- the shape of the beam pipe can be optimized inside the shielding.

The material compositions and densities used in the FLUKA simulation are as given in Section 9.3.

C.4.3 Radiation protection assessment

FLUKA simulations were performed assuming 4×10^{13} protons per spill with one spill every 7.2 s. The resulting prompt ambient dose equivalent rates for the experiment and the shielding are shown in Fig. C.8, while Fig. C.9 shows the prompt ambient dose equivalent rates for the tunnel, soil, and experimental hall.

As expected, the highest dose rates can be found in the region of the target, calorimeter, and muon spectrometer, reaching a few times 10^{11} µSv/h. The levels are reduced by several orders of magnitude in the surrounding shielding. The prompt dose rates are further reduced by the soil above, such that they drop to a few µSv/h in the above-ground experimental hall.

Figure C.10 shows the expected residual dose rates after one day of cool-down time. The highest dose rates can be found in the region of the detector, reaching the order of a few times 10^{6} µSv/h. For this reason, the facility should be designed such that interventions will be performed with remote handling systems.

In the next phase of the study, it is planned to perform optimization of the shielding to further reduce the prompt and residual dose rates. The impact of the remnant beam on the activation of the BDF downstream should be evaluated. The environmental impact from releases of radioactive air and from

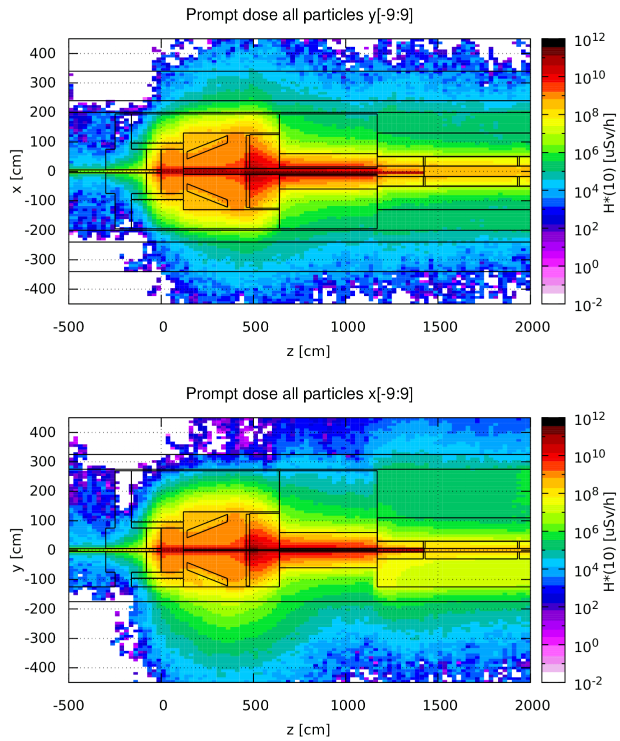

Fig. C.8: Prompt ambient dose equivalent rates for experiment and shielding: horizontal (top) and vertical (bottom) sectional views.

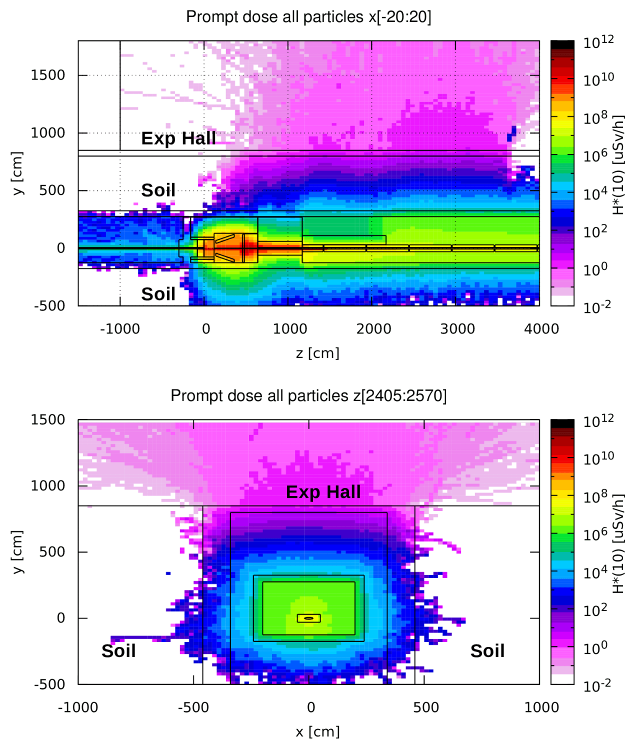

Fig. C.9: Prompt ambient dose equivalent rates for tunnel, soil, and experimental hall: vertical (top) and perpendicular (bottom) sectional views.

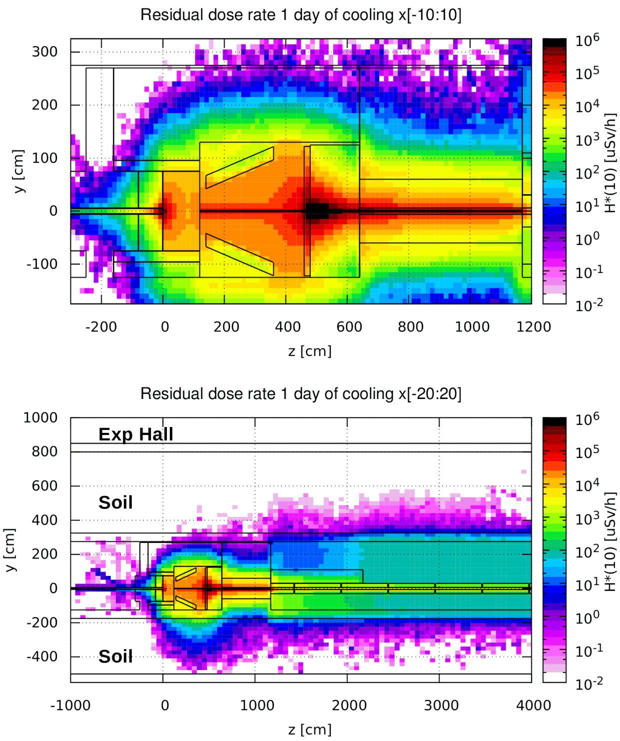

Fig. C.10: Residual ambient dose equivalent rates after one day of cool-down for the experiment (left) and the surroundings (right).

soil activation should also be carefully addressed in future studies. Finally, the production of radioactive waste should be evaluated.

C.5 Civil engineering

C.5.1 Introduction

The civil engineering required to implement TauFV has been studied at a conceptual level to ensure that the project is feasible. The CE involved in TauFV is no more complex than that involved in the wider BDF project. This section briefly details the CE requirements specific to TauFV and, as such, must be read in conjunction with the CE chapter (Chapter 11) for the wider BDF project for context and detail relating to these proposals.

C.5.2 Civil engineering requirements

TauFV is to be located on the existing beam line within the BDF extraction tunnel as detailed in Section C.2. The positioning has been driven primarily by beam dynamics constraints. The location is also favourable from a CE perspective, allowing synergy between the proposed BDF infrastructure and that for TauFV.

The TauFV experimental arrangement would take up the full width of the planned extraction tunnel. Therefore additional space is required to allow access to the rest of the BDF transfer line for the following purposes:

- passage of personnel;
- transport of materials and equipment past the experiment;
- space reservation for cable trays and services;

- prevention of any dead ends which would not allow acceptable evacuation routes from certain lengths of tunnel.

Several options to facilitate access past the TauFV detector bunker were considered. The options reviewed included a bypass tunnel and alternative access arrangements, but the preferred option was to widen the tunnel. Tunnel enlargement would provide sufficient space to bypass the experiment with enough shielding between the experiment and the access route to make the arrangement acceptable for RP. This was clearly the most cost-effective option, as well as providing flexibility for change in the future.

To allow installation, operation, and maintenance of the TauFV experiment, a shaft above this area will be needed over the full width and length of the experiment with direct vertical access.

A full summary of the requirements generated by TauFV is therefore as follows.

- Tunnel widening to 8.35 m at a point 94 m upstream of the BDF target over a distance of approximately 41 m.
- A shaft above the proposed location of the TauFV experiment measuring 5 m wide by 10 m long. The shaft must be capable of being filled with concrete shielding blocks when the beam is in operation.
- An access, assembly, and storage building above the experiment to house:
  - a suitably sized crane serving both the heavy-equipment shaft and the TauFV shaft;
  - sufficient shared circulation space for transport and handling of detector components, magnets, beam line equipment, and shielding;
  - flexible space to be used for temporary storage of activated equipment or assembly/maintenance related to the detector;
  - vehicle access to the building to enable all of the above.
- Concrete shielding blocks to fill the shaft and also to provide a partition between the experiment and the passageway.

C.5.3 Civil engineering infrastructure

The proposed layout of the CE infrastructure to meet the needs of the TauFV experiment is shown in Fig. C.11.

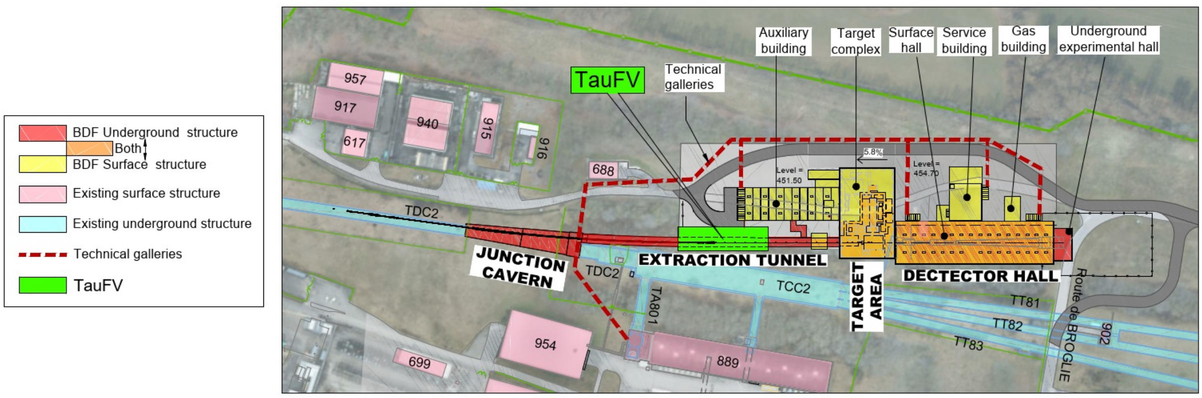

Fig. C.11: Location plan showing the position of TauFV and the CE modifications required for implementation.

C.5.3.1 Tunnel enlargement

The proposed form of construction for the tunnel enlargement will be exactly the same as that used elsewhere on the BDF. The layout of the below-ground infrastructure is shown in Fig. C.12.

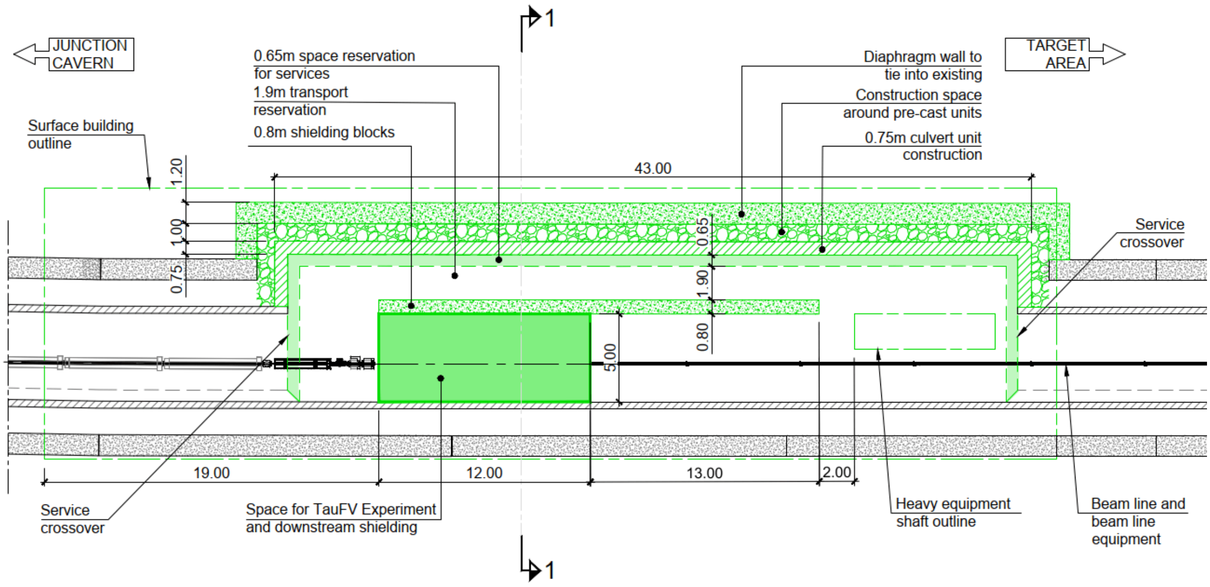

Fig. C.12: Plan view of the proposed subsurface CE infrastructure, shown in green, with wider BDF proposals shown in grey.

Widening is only practical on the north-west side of the BDF extraction tunnel, owing to the proximity of the existing TCC2 tunnel and the constraints with which working close to it are associated.

Owing to the CE requirements of the wider project, it is essential that a watertight perimeter is maintained around the BDF installation. Therefore, the proposed diaphragm walls for the enlargement will tie into those already proposed for the BDF. This will maintain continuity of the perimeter as well as provide benefit from the efficiencies associated with a consistent form of construction.

The widened tunnel itself will again be constructed from pre-cast 'n' units on a cast-in-situ concrete base. The pre-cast units will be widened and have a deeper roof slab, but in all other respects will be similar. A cast-in-situ joint will need to be formed between the two sections of differing widths. The same approach to waterproofing will be adopted, with a multilayer passive system maintained through this area.

The proposed cross-section of the BDF extraction tunnel (Fig. C.13) includes a 650 mm wide space reservation for cable trays and services. This extends to 700 mm for a ventilation duct close to the tunnel roof. The enlargement for TauFV will require a 650 mm wide strip to be maintained, with the ventilation duct running outside the required access area. This will allow continuity of the services past the TauFV experiment as well as provide acceptable levels of radiation shielding for cabling and other radiation-sensitive infrastructure. A crossover from one side of the tunnel to the other will be required for the services at each end of the TauFV experiment. This should not be problematic, as a crossover is already planned for the BDF. The option to keep services on the Jura side of the tunnel throughout could be explored at future stages if TauFV is implemented.

The transport-handling team have been consulted to ensure that sufficient space is allowed at either end of the enlarged area for movement and turning of the longest and largest components. A minimum width of 1.9 m will be maintained, as well as a maximum angle of 30°.

C.5.3.2 TauFV access shaft

The experimental team has calculated the required cross-section of the shaft as 5 m by 10 m, which has been used to inform this study. The form of construction will again be similar to that used for the heavy-equipment shaft. There may be scope to optimize this when the design moves past the conceptual stage

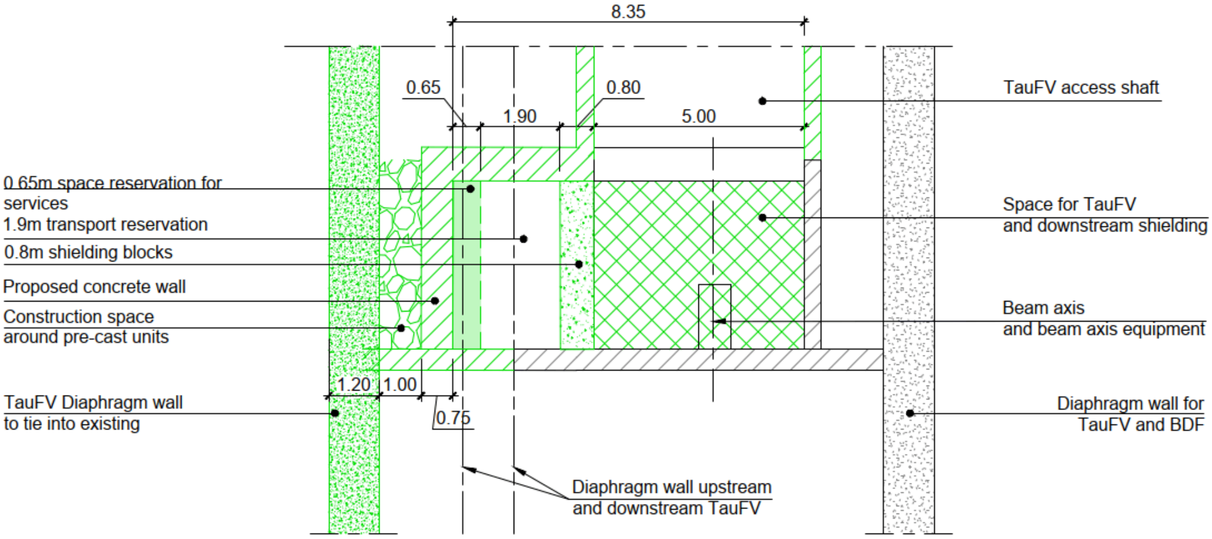

Fig. C.13: Schematic typical section through TauFV access shaft, showing proposed TauFV infrastructure in green, with wider BDF proposals shown in grey.

and when requirements are fully understood. In the meantime, it is sufficient to say that the shaft is entirely feasible using the same techniques. Where necessary, there is also the option to use diaphragm walls to support the roof slab and the concrete shielding blocks, with connections as shown in Fig. C.14. An interlocking arrangement will be adopted for stacking the shielding.

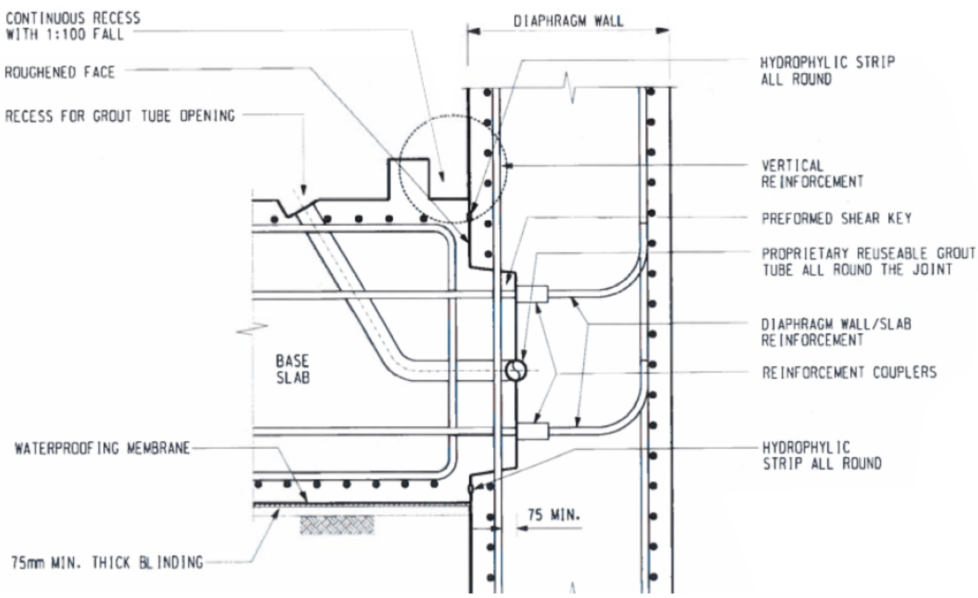

Fig. C.14: Typical detail of coupler connection between diaphragm wall and slab

C.5.3.3 Concrete shielding blocks

RP requirements dictate a requirement for 0.8 m thick shielding blocks to be positioned alongside the TauFV experiment and the downstream magnets over a total distance of 25 m. The shielding blocks will be pre-cast concrete blocks stacked to form walls. The block walls can be dismantled to allow any future change in the experimental arrangement.

C.5.3.4 Access building

An access building above the TauFV shaft is required to house a crane and space for handling, storage, and work on components. The additional area required to accommodate the needs of the experiment was agreed between the transport-handling and experimental area teams as 625 m^2.

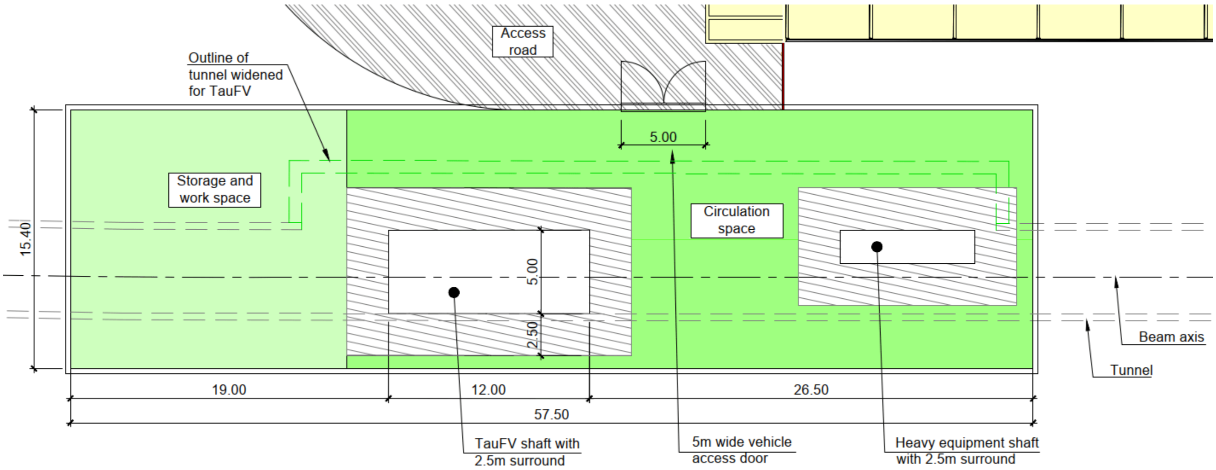

Fig. C.15: Schematic layout of TauFV building floor plan

Since the building is already close to the proposed BDF access building, it is more efficient to provide this space by extending the building south-west to cover both shafts. In this way, one set of crane rails and one crane will serve both shafts. Circulation space will also be shared between the two, and only one access door needs to be provided, again helping to reduce the overall floor space required. Initial discussions suggest that a 40 t crane will be suitable to serve both purposes.

The expanded access building will be of the same type of construction as that for the BDF. An opportunity was identified in this instance to have the building share the diaphragm walls as a foundation. The building outline was designed to follow the same alignment as the diaphragm walls to enable this.

An indicative layout of the building floor plan is included in Fig. C.15. This layout has been agreed with the experimental and transport-handling teams. Further optimization will be carried out as the design is developed.

C.5.4 Further civil engineering considerations

In general, the same considerations apply to the TauFV experiment CE infrastructure as to the wider BDF proposals. One point to note is that the scheduling of the construction of these elements would need careful consideration. The TauFV infrastructure is predominantly outside the 8 m exclusion zone around TCC2; however, a substantial proportion of the access building and some of the subsurface infrastructure are not. Planning how these elements could be scheduled most effectively will be key to delivery of the BDF programme in full. TauFV construction work could be included in either Work Package 3 or Work Package 4, or alternatively split between the two. Procurement of these works could be optimized at the next stage of project development.

References

[1] I. Bezshyiko et al. “TauFV: a fixed-target experiment to search for flavour violation in tau decays”. Submitted to European Particle Physics Strategy Update 2018–2020.

[2] T. T. Bohlen et al. “The FLUKA code: developments and challenges for high energy and medical applications”. In: *Nucl. Data Sheets* 120 (2014), pp. 211–214. ISSN: 0090-3752. DOI: https://doi.org/10.1016/j.nds.2014.07.049. URL: http://www.sciencedirect.com/science/article/pii/S0090375214005018.

[3] F. F. Schmidt, H. R. Ogden. *The Engineering Properties of Tungsten and Tungsten Alloys*. Defense Metals Information Center, Sept. 1963.

[4] D. Forkel-Wirth et al. “Radiation protection at CERN”. In: *CAS–CERN Accelerator School: Course on High Power Hadron Machines, 24 May–2 Jun 2011* (Bilbao, Spain). Mar. 2013. eprint: arXiv:1303.6519. URL: http://cds.cern.ch/record/1533023.

[5] A. Ferrari et al. *FLUKA: A Multi-particle Transport Code (Program Version 2005)*. CERN Yellow Reports: Monographs. Geneva: CERN, 2005. URL: https://cds.cern.ch/record/898301.

Appendix D

Applications of the BDF to nuclear astrophysics and material irradiation

D.1 Introduction

The unique capabilities of the particle field created by the high-energy, high-intensity proton beam from the SPS impacting on the production target could be exploited for other purposes also. In fact, because of the large beam power on the target, and without perturbing the main physics goal of the installation, the facility could be parasitically exploited for other scientific and technical goals, which are described further in Sections D.2 and D.3.

The capabilities would indeed be unique in terms of total doses, particle spectra, and fluences: similar values could be reached at 'standard' spallation neutron sources but are not easily exploitable owing to the specific physics and engineering criteria that apply at those facilities, including closely coupled cryogenic moderators and reflectors, which deplete significantly the high-energy components of the particle spectra.

D.2 Nuclear astrophysics applications

D.2.1 Introduction and physics case

Almost all elements heavier than iron are produced in the Universe by neutron-induced reactions, in particular neutron capture processes. In the stellar environment, in particular in the Asymptotic Giant Branch (AGB) phase, characterized by relatively low temperatures and neutron densities, nuclei close to the beta-stability line (i.e. stable or with a long half-life) are produced in the so-called s-process (with 's' standing for 'slow'), where neutron capture times are typically much longer than competing beta decays. In contrast, extremely high temperatures and neutron densities are reached in explosive scenarios, such as supernovae or binary Neutron Star (NS) merger events, leading to the production of neutron-rich nuclei in rapid capture processes (r-processes). Modelling of both s- and r-process nucleosynthesis requires neutron capture cross-section data for isotopes along the valley of beta-stability. In fact, accurate (n,γ) cross-sections are needed in order to reliably determine s-process abundances, which on the one hand provide important information on stellar evolution and on the other hand allow the r-process counterpart to be obtained from the differences from the observed abundances ($N_{\mathrm{r}} = N_{\mathrm{obs}} - N_{\mathrm{s}}$).

Recently, studies of stellar nucleosynthesis have received a boost thanks to the enormous progress made in astronomical observations, as well as important developments in modelling stellar evolution. A huge step forward in this respect has resulted from the recent multimessenger observation of an NS–NS merger in August 2017. The simultaneous detection of gravitational waves, a gamma-ray burst, and electromagnetic radiation in the optical and near-optical range has unequivocally demonstrated that NS–NS mergers are an important, if not the most important, site for r-process nucleosynthesis. All this now calls for new data on neutron-induced reactions, in particular on short-lived radioactive isotopes. More details of the need for neutron data of interest for nuclear astrophysics can be found in Ref. [1].

An important feature of s-process nucleosynthesis is the branching of the reaction path when isotopes with half-lives comparable to the neutron capture time are produced (called, for this reason, branching-point isotopes). The analysis of such branchings provides crucial information on the physical conditions (temperature, neutron density, etc.) of the stellar site in which s-process nucleosynthesis takes place. A complete list of the most important branching-point isotopes can be found in Ref. [2]. Neutron cross-section data on these isotopes are scarce, if they exist at all, and are often discrepant. Two major problems hinder reliable measurements of these reactions: on the one hand, samples of sufficient mass of such radioactive isotopes are extremely difficult to procure and, on the other hand, even when samples are available, the background related to the natural radioactivity of the sample often dominates over capture count rates. Both problems can be minimized only by the use of intense neutron beams.

Taking advantage of the high luminosity of the neutron beam, some branching-point isotopes, with a relatively long half-life of tens or hundreds of years, have been measured at n_TOF, and at new high-flux activation facilities, such as SARAF in Israel. In all of these cases, sample masses of several milligrams (in some cases hundreds of milligrams) were used. An important step forward in these measurements would require neutron fluxes orders of magnitude higher than currently available. If this were possible, a reasonable reaction count rate could still be obtained with submilligram or even submicrogram sample masses, making feasible measurements that at present are considered unrealistic. The use of extremely low sample masses has several advantages, in particular the availability of the material and the low associated background (and safety limitations). In fact, a sufficient amount of short-lived isotopes can be obtained, for example, by irradiation of a stable or long-lived progenitor, or extracted from irradiated structural components in nuclear reactors or at spallation neutron sources. Most importantly, suitable samples of short-lived isotopes could be obtained by implantation with a radioactive ion beam at currently available radioactive ion beam facilities. A successful attempt in this respect has recently been made at n_TOF, where a 90 ng sample of the short-lived isotope ^{7}Be was produced by implantation at the CERN ISOLDE facility and irradiated with a neutron beam in the second experimental area (EAR2) at n_TOF [3]. The second advantage is that an extremely small-mass sample of a short-lived isotope would be characterized by a manageable total activity and related background. The only limitation in this case might be posed by the background related to neutron beam itself and its interaction with the experimental set-up, as well as by the gamma-ray and charged-particle contamination in the beam. For these reasons, the measurements must rely on high-sensitivity techniques, such as activation analysis, either offline or online (i.e. in between irradiation pulses), or accelerator mass spectroscopy.

D.2.2 Neutron flux at the Beam Dump Facility complex for nuclear astrophysics

In this context, the availability of an extremely intense neutron flux at the BDF would offer a unique opportunity to study neutron-induced reactions on short-lived isotopes, of interest for nuclear astrophysics as well as for various applications. Preliminary Monte Carlo simulations indicate that a flux of around 10^{13}–10^{14} neutrons/cm^2/pulse could be available in the proximity of the BDF target (see Fig. D.1), with a spectrum covering the range from thermal energy to 100 MeV, with a peak around 1 MeV.

Since the long duration of the proton pulse (1 s) does not allow one to use the time-of-flight technique for neutron energy determination, only integral cross-section measurements can be performed. To this end, the neutron spectrum has to be suitably tailored to the needs of the study. In particular, for studies related to nuclear astrophysics, it is desirable to rely on a Maxwellian-like neutron spectrum, with kT between 10 and 100 keV. Such a spectrum can be obtained with an additional (small) moderation of the BDF neutron beam, so as to lower the average neutron energy, and with the use of suitable filters (or absorbers) to suppress the thermal and epithermal region. Studies in this direction are already ongoing in the n_TOF Collaboration, aimed at setting up an irradiation station near the spallation target. In fact, a BDF neutron facility might greatly benefit from the experience that will be gained in the next few years at the n_TOF near-target irradiation facility. The huge flux envisaged for a neutron beam at the BDF would surpass any other activation facility now being constructed or planned for the near future. In fact, even assuming a reduction due to the moderation and filtering process of two orders of magnitude, a flux of 10^{12} neutrons/cm^2/pulse would be available for the measurements, three orders of magnitude higher than expected, for example, at the near-target irradiation station at n_TOF mentioned above and two orders of magnitude higher than at the most intense Maxwellian neutron source currently available, at SARAF, which is characterized by an average neutron flux of 1.2×10^{10} n/cm^2/s.

The great potentiality of the BDF neutron beam can be illustrated with a few examples of measurements that could be performed at the facility. The short-lived ^{147}Nd ($t_{1/2} = 11$ days) is an important

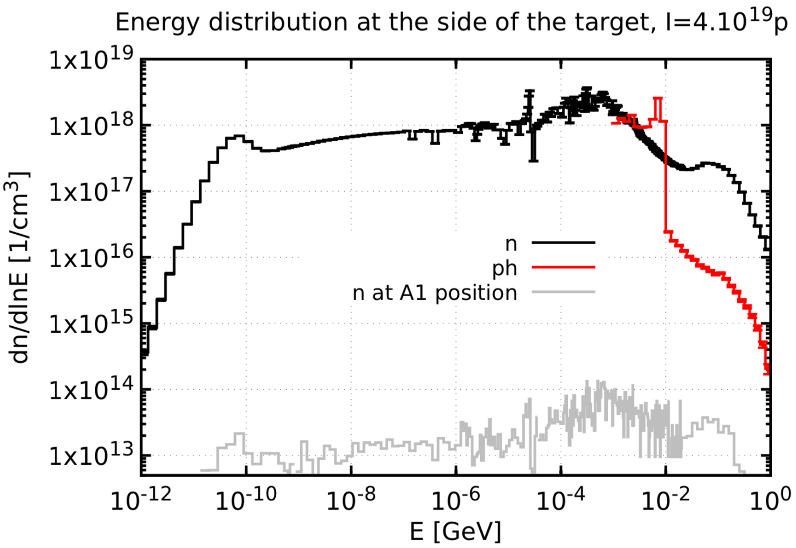

Fig. D.1: Neutron spectrum on the side of the target, at roughly 70 cm from the axis of the assembly. The black line shows the neutron spectrum, while the red line shows the photon background (cut at 10 MeV). The grey lines represent the neutron fluence at 3.4 m at 90° with respect to the target centre, assuming an opening through the target bunker shielding, representing a potential irradiation port.

s-process branching isotope that constrains the neutron density of low-mass AGB stars [2]. Its very short half-life, however, makes it extremely difficult at present to measure its neutron capture cross-section, a key factor in the determination and modelling of the nucleosynthesis path around this branching point. In fact, only a small amount of this isotope (a few tens of nanograms) can be produced by irradiation of the stable isotope ^{146}Nd, for example in the core of a nuclear reactor. Such a small amount of material makes it mandatory, for measuring the ^{147}Nd(n,γ) cross-section, to use an extremely intense neutron beam, at present not available anywhere. At the BDF, the predicted flux of 10^{12} neutrons/cm^2/pulse would result (assuming a realistic Maxwellian averaged cross-section of 100 mb) in 10^4 neutron capture reactions per day, leading to the production of the stable isotope ^{148}Nd. The number of reactions could later be determined offline with sufficient accuracy by measuring the number of ^{148}Nd atoms produced with accelerator mass spectroscopy.

Other important branching isotopes of short half-life that could be measured at the BDF are ^{179}Ta and ^{134}Cs, with a $t_{1/2}$ of roughly 2 yr, and ^{170}Tm, with a $t_{1/2}$ of 0.35 yr. In this case as well, high-purity samples with a mass of a few nanograms (or a few tens of nanograms) might reasonably be produced by implantation of a radioactive beam and later be irradiated with the BDF neutron beam. This would be the case for the particularly important branching isotope ^{134}Cs, which is sensitive to the s-process temperature in low-mass AGB stars. At present, a measurement of the neutron capture cross-section of this isotope is not considered feasible, at least in the near future. The availability of a BDF neutron beam, in combination with the ISOLDE beam, might finally make this measurement possible. The yield of this isotope at ISOLDE exceeds 10^9 ions/µC, so that a sample of 10^{14} atoms (corresponding to $\sim$10 ng) could be produced by implantation in a few days at ISOLDE. The result of the capture reaction is ^{135}Cs, a radioactive nucleus with very long half-life (2.3×10^6 yr), which again could be measured by means of accelerator mass spectroscopy. Similar considerations apply also to ^{170}Tm, which could be produced at a nuclear reactor (or with the same BDF beam) starting from the stable isotope ^{169}Tm, with the only difference being that the measurement in this case would rely on the activation technique, given the short half-life of the reaction product ^{171}Tm. As for ^{179}Ta, if a production mechanism could be found (for example by means of the ^{180}Ta(n,2n) reaction), a similar measurement may also become feasible at the

BDF.

In summary, the availability of an extremely high-flux neutron beam at the BDF would open the way to very challenging measurements of interest for nuclear astrophysics, for both s- and r-process nucleosynthesis, that are not feasible at neutron facilities currently operating or planned for the near future.

D.3 Electronics and material irradiation

D.3.1 Introduction

The BDF infrastructure and operation provide a unique opportunity for hosting irradiation test facilities for materials and electronics. The unparalleled mixed-field radiation levels expected near the target, reaching integral annual levels of roughly 400 MGy and 10^{18} 1 MeV neutron equivalent per square centimetre (see Fig. D.2), would allow accelerated testing in a highly representative environment for future accelerator applications, including for instance ones linked to the HE-LHC, FCC-hh, and potentially FCC-ee.

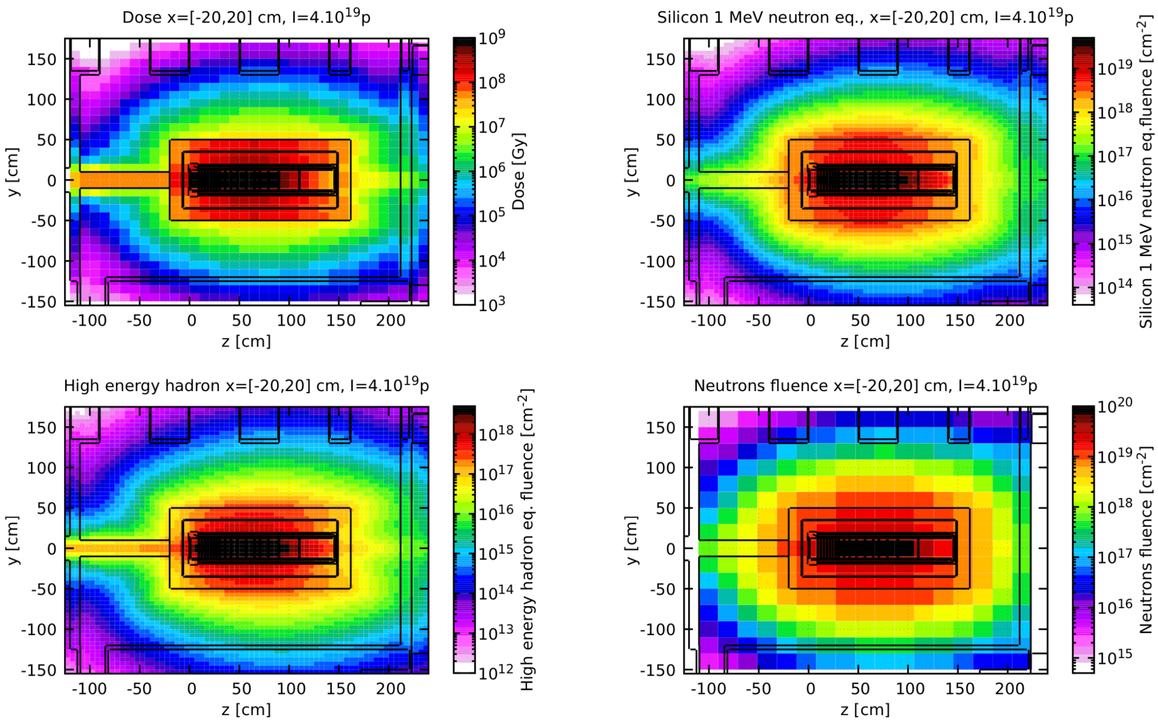

Fig. D.2: Longitudinal section of target bunker showing relevant prompt radiation quantities averaged around the target centre line. The values are normalized per yearly protons on target.

D.3.2 Irradiation capabilities

D.3.2.1 Near-target station

Irradiation of materials would be performed in passive mode, with a remote handling and transport system that places the samples in the irradiation areas and is able to retrieve them into hot cell zones for post-irradiation analysis. The levels attained would be sufficient to study both the Total Ionizing Dose (TID) (mainly affecting insulating, polymeric materials) and the dpa (mainly affecting the mechanical and thermophysical properties of metals).

Electronics would be tested in a similar way to perform passive, unbiased displacement damage studies, or active (i.e. biased) studies of TID effects. In both cases, lifetime levels compatible with those expected in the most exposed detector areas in the FCC-hh would be attained, providing an excellent opportunity to evaluate the radiation tolerance of electronics, certainly beyond the limit of what present silicon-based technologies can withstand.

An in-beam irradiation station, directly facing the diluted primary beam, could also be envisaged in order to further increase the TID and dpa levels that could be reached.

D.3.2.2 Irradiation outside the proximity shielding

In addition to the near-target irradiation stations, providing a broad range of dose rates and fluxes for ultrahigh-dose and ultrahigh-fluence sample irradiation, a more accessible area with a lower radiation level could be constructed for testing electronic components, boards, and systems. Such an area would require neutron fluxes (>10 MeV) in the 10^4–10^8 n/cm^2/s range, and would allow qualification of electronic equipment to be operated in an accelerator environment. Ideally, surface areas of several square metres should be available, enabling the radiation qualification of bulky systems, such as power converters.

With the increased interest in and need for using commercial off-the-shelf electronic components and systems-on-chip, large-scale irradiation is in principle the only viable solution to ensure adequate radiation tolerance. Such conclusions apply not only to accelerator applications but also to ground-level (e.g. automotive applications and high-reliability servers), avionic, and so-called new space applications. An area for this purpose could be obtained in the BDF target complex, with a dedicated irradiation bunker on the side of the target, without perturbing the main physics aim of the facility. Fluxes of the same order of magnitude as those mentioned above could be reached, as evident in Fig. D.3.

Radiation protection aspects will have to be analysed further in the future to find the best-suited configuration.

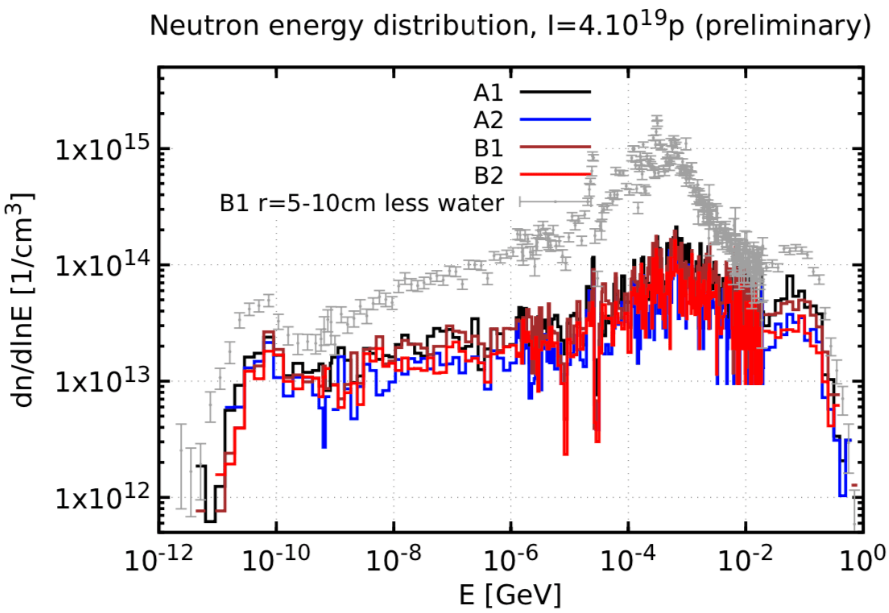

Fig. D.3: Neutron spectrum on the side of the target, at different distances from the centre. Positions A1 and B1 are at 3.4 m from the centre, while A2 and B2 are at 4.1 m. The values could be further optimized with an improved configuration of the neutron collimation system: for example, the grey line shows the values at 3.4 m with a larger collimator opening.

D.3.3 Synergies with other CERN facilities

The unique capabilities of a potential material irradiation facility could be well coupled with other facilities on the CERN site, for example HiRadMat, allowing the possibility of executing beam shock experiments on previously irradiated material. This would create a world-class installation in the field of high-power targets, beam windows, collimators, and absorbers, which would be of interest for all high-power and high-intensity accelerator endeavours worldwide. Complementarity could be further explored with the CHARM and Co-60 irradiation facilities.

References

[1] N. Colonna, F. Gunsing, and F. Käppeler. "Neutron physics with accelerators". In: *Prog. Part. Nucl. Phys.* 101 (2018), pp. 177–203. ISSN: 0146-6410. DOI: "10.1016/j.ppnp.2018.02.002". URL: http://www.sciencedirect.com/science/article/pii/S014664101830019X.

[2] F. Käppeler et al. "The s process: nuclear physics, stellar models, and observations". In: *Rev. Mod. Phys.* 83 (1 2011), pp. 157–193. DOI: 10.1103/RevModPhys.83.157. URL: https://link.aps.org/doi/10.1103/RevModPhys.83.157.

[3] L. Damone et al. "$^7\mathrm{Be}(n,p)^7\mathrm{Li}$ reaction and the cosmological lithium problem: measurement of the cross section in a wide energy range at nTOF at CERN". In: *Phys. Rev. Lett.* 121 (4 July 2018), p. 042701. DOI: 10.1103/PhysRevLett.121.042701. URL: https://link.aps.org/doi/10.1103/PhysRevLett.121.042701.